CODEN: JASMAN

The Journal of the Acoustical Society of America

ISSN: 0001-4966

Vol. 120, No. 2 August 2006

(Continued)

CONTENTS—*Continued from preceding page*

(Continued)

CONTENTS—*Continued from preceding page*

(Continued)

CONTENTS—*Continued from preceding page*

Results from an autonomous underwater vehicle towed hydrophone array experiment in Nantucket Sound

Jason D. Holmes and William M. Carey
Department of Aerospace and Mechanical Engineering, Boston University, Boston, Massachusetts 02215
jholmes@bu.edu, wcarey@bu.edu

James F. Lynch
Department of Applied Ocean Physics and Engineering, Woods Hole Oceanographic Institution, Woods Hole, Massachusetts 02543
jlynch@whoi.edu

Abstract: Shallow water experiments have been conducted in Nantucket Sound with an autonomous underwater vehicle towed hydrophone array system in an area proximate to that of a previous experiment [Frisk and Lynch, J. Acoust. Soc. Am. **86**, 1928–1939 (1989)]. Transmission loss was measured, for frequencies between 220 and 1228 Hz in an ocean waveguide, under conditions of an isovelocity water column with an approximate depth of 13 m over a sandy-silty bottom. Results obtained at 415 Hz show classic isovelocity waveguide phenomena that include interference effects, mode stripping due to modal attenuation, and transmission loss proportional 15 to 10 $\log_{10}(R)$.

PACS numbers: 43.30.Xm, 43.30.Yj, 43.30.Ma, 43.30.Bp [D. Keith Wilson]
Date Received: March 17, 2006 **Date Accepted:** July 17, 2006

1. Introduction

In the mid-1980s Lynch *et al.* published a series of papers,[1–3] demonstrating the power of synthetic aperture Hankel transform technique for effectively characterizing the geoacoustic profiles in the ocean bottom. The experimental technique required a moored receiver, a source deployed from a drifting ship, and the measurement of range to form a spatial synthetic aperture. The measurement of the complex pressure to a 5 km range took up to 8 h, over which the tides and currents were changing the character and depth of the water column. Carey *et al.*[4] extended this technique, by the use of a vertical array and a moving source emitting four frequencies, and showed that coherent processing of frequencies up to 275 Hz covering ranges of 4 km over a 2 h period were possible. Motivated by the quality of results obtained using the synthetic aperture technique and inspired by current autonomous underwater vehicle (AUV) technology, an effort was initiated to determine if a synthetic aperture measurement could be cost-effectively and efficiently performed using a single ship and an AUV with a towed array. A physical aperture was required to improve the signal-to-noise ratio (SNR) of the measurements but, at low frequencies, the dimensions would be large and thus require a synthetic aperture approach. Additionally, measured radiated vehicle noise from the REMUS AUV (Ref. 5) contained broad-band and narrow-band components, comparable in level to the expected experimental signal level, which would degrade the SNR for a sensor not spatially separated from the vehicle. These constraints of frequency and noise are satisfied by the prototype REMUS-towed-array system (RTAS), a six-channel towed-hydrophone array.

Between December of 2004 and 2005, six experiments were conducted to determine the ability of RTAS to perform the desired long-range transmission experiments culminating with the Nantucket Sound experiments. This paper discusses the results from these experiments and presents preliminary conclusions on the characteristics of sound propagation and attenuation in a waveguide that was practically the ideal Pekeris waveguide.

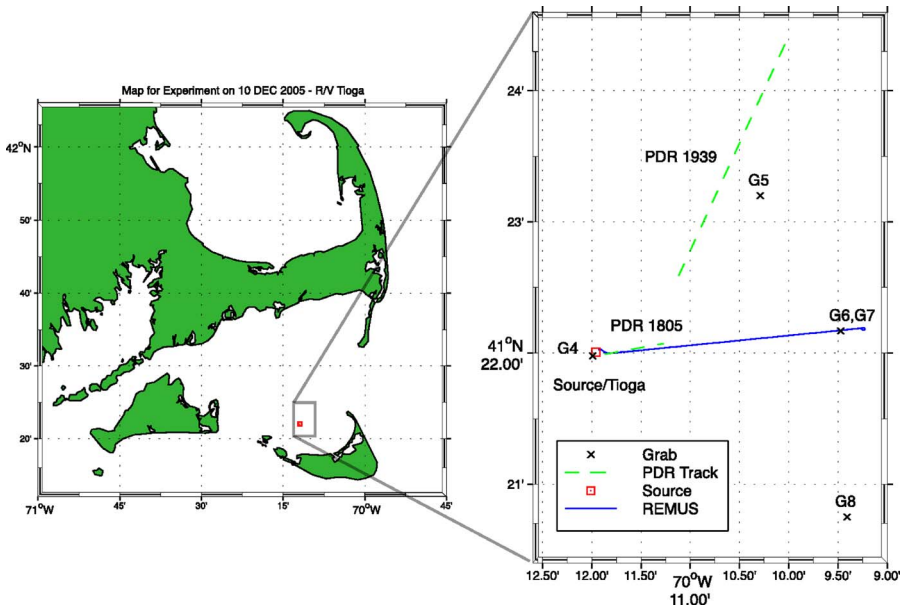

Fig. 1. (Color online) Map showing the location of the 10 DEC 2005 experiment. Grab sample locations are labeled with a G followed by sample bottle number. The two precision depth recorder tracks closest to the experimental mission path are shown and labeled by a PDR and the file number.

2. The Nantucket Sound Experiment

2.1 The REMUS towed-array system

The AUV used for the Nantucket sound experiments was a standard REMUS 100 (Ref. 5) modified to have an aluminum shroud on the tail to protect the array-tow cable from the propeller and control surfaces. The vehicle obtained an initial and final global positioning system (GPS) reading for each mission, and navigated by deadreckoning while submerged because the GPS receiver is hull mounted and does not work under water. Vehicle orientation, velocity, latitude, and longitude, as well as estimates of the water sound speed and bathymetry and other environmental parameters, were recorded on an onboard computer approximately every second.

The array system attached to REMUS consisted of a recording canister, a tow cable, the acoustic array, and a drogue. The acoustic section was constructed from a 9.2 m long 2.8 cm outer diameter Kevlar reinforced impedance matched tube. Six hydrophone groups, each with a 20 dB preamplifier and wired in parallel, were spaced at 0.75 m ($\lambda/2$ for 1 kHz). Each channel had a calibrated sensitivity of -174 ± 1 dB re 1 V/μPa over 100 Hz to 10 kHz. The tow cable was a 10 m long, neutrally buoyant, cable, and the drogue was a 10 m long section of 1 cm diameter high drag rope. Data recording was performed inside a 10 cm diameter 61 cm long sealed canister, strapped to the underside of the vehicle. A conditioning board interfaced the six hydrophone channels with three off-the-shelf minidisk recorders, each with 90 min of uncompressed 16-bit 44,100 sample per second recording capability for two channels. Synchronization of the recorders was performed by a custom pulse generator on the conditioning board.

2.2 Site survey

Before conducting the two Nantucket Sound experiments, a site survey was performed to determine the characteristics of the waveguide. Grab samples of the sediment and a precision depth recorder operating at 33 and 200 kHz were used to characterize the bottom in the area around the experimental track of the AUV. Figure 1 shows the location of the experimental site,

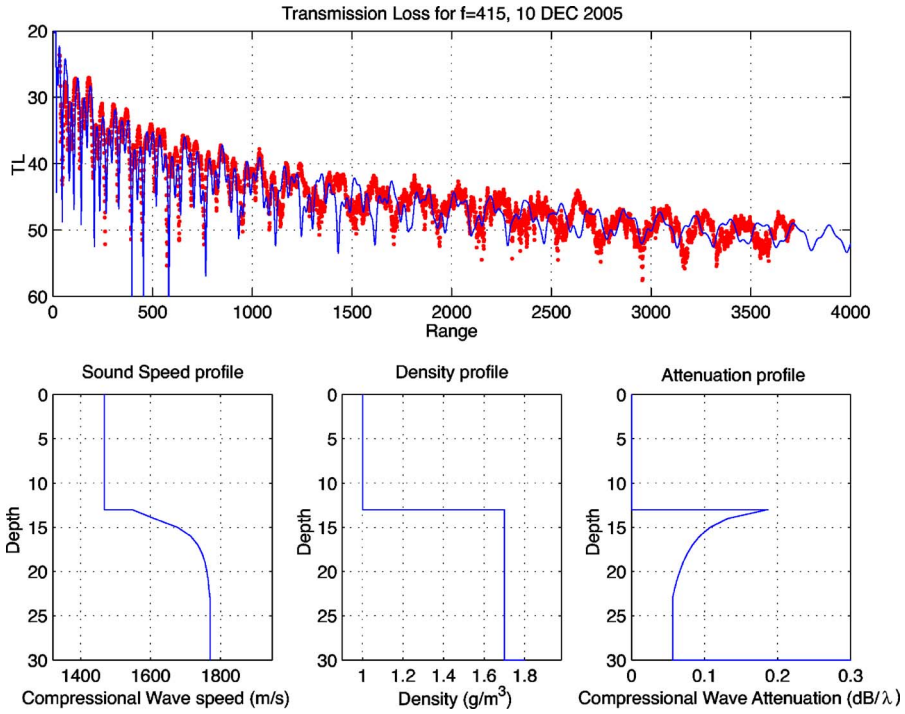

Fig. 2. (Color online) TL vs range for 415 Hz on the outbound leg of the experiment conducted on 10 DEC 2005. Dots indicate measured TL and the solid line indicates the predicted transmission loss using a range independent normal mode code and the geoacoustic profiles shown.

as well as the grab sample locations and depth recorder tracks that were closest to the experimental track. The site was chosen because of its sandy-silty bottom, constant bathymetry (which is protected on the north and west by Tuckernuck Shoal and on the south and east by Nantucket) and its proximity to the Frisk-Lynch-Rajan site.

Analysis of the grab samples showed that the sediment in the upper layers of the bottom was 97% sand and 3% silt with a mean grain size of 115 μm ($\phi \approx 3.1$). The porosity was measured to be 49% and the density 1.7 g/cm^3. These values are consistent with archival grab sample data,[6] as well as with United States Geological Survey data for the Nantucket Sound.[7]

Using the site survey data, as well as previous inversions in the area,[2] sound speed, attenuation, and density profiles as a function of depth were determined. These profiles are shown in Fig. 2, and can be considered as ideal profiles corresponding to the average bottom properties in the area. Attenuation used in the model was consistent with a modified Biot model,[8] and was extrapolated from Hamiltons[9] value at 1 kHz using a quadratic dependence as predicted by the theory. The sound speed in the water was measured using a sound speed, temperature, and depth probe on the ship as well as one on board the vehicle, to be 1467 ± 0.25 m/s and constant over depth due to mixing from a storm the previous day. The sound speed profile in the sediment increases from 1550 m/s to 1800 m/s with a gradient consistent with the Hamilton.[9] The attenuation versus depth follows the functional form:

$$\alpha(z) = K z_{\mathrm{ref}}^{-b}, \tag{1}$$

where K is a constant, z_{ref} is the depth below the surface plus 1 to accommodate modeling between 0 and 1 m below the surface, and b is one-sixth to be consistent with historical measurements.[9] Density is considered to be a constant over depth down to the acoustic basement, as the small gradient predicted by theory would not be influential at the frequencies employed in this study.

2.3 Experimental geometry

The experimental geometry for the Nantucket Sound experiments consisted of mooring the support ship in a two-point mooring, and deploying the AUV with the array attached from the stern of the ship. A U.S. Navy calibrated source was deployed with a winch cable from the stern A-frame. An anchor attached to the source and cable tension minimized source motion and kept a constant 6 m source depth.

The vehicle mission geometry for the second experiment is shown as a solid curve in Fig. 1; it consisted of a 4 km straight course radially out from the source at 6.0 m depth, a turnaround controlled to keep the array shape stable, and a 4 km course back. The first experiment geometry was similar, and consisted of a 2 km outbound track. In both experiments, the vehicle was navigated by deadreckoning using acoustic Doppler current profiler ground tracking, and the range to the source was determined using latitude and longitude from the ship's GPS receiver and AUV sensors.

The continuous-wave (cw) frequencies of sound transmissions were as follows: The first experiment (September) outbound, 635, 823, 1031, and 1228 Hz; the second experiment (December) outbound, 220.5, 415, and 635 Hz; and inbound, 635, 823, 1031, and 1228 Hz.

3. Results

If one considers a water column of thickness h with a constant density and a sound speed given by $c(z)$, bounded on the top and bottom by horizontally stratified media, then the acoustic field satisfies the inhomogeneous Helmholtz equation:

$$\left[\frac{1}{r}\frac{\partial}{\partial r}\left(r\frac{\partial}{\partial r}\right)+\frac{\partial^2}{\partial z^2}+k^2(z)\right]p(r;z,z_0)=-2\left(\frac{\delta(r)}{r}\right)\delta(z-z_0), \tag{2}$$

where the wave number is $k(z)=\omega/c(z)$, z is the receiver depth, and z_0 is the source depth. Solutions to this equation can be expressed via the zero-order Hankel transform pair defined by

$$p(r)=\int_0^\infty g(k_r)J_0(k_r r)k_r dk_r, \quad g(k_r)=\int_0^\infty p(r)J_0(k_r r)r dr, \tag{3}$$

where J_0 is the zeroth-order Bessel function, r is the horizontal range, and k_r is the horizontal wave number. The depth dependent Green's function, $g(k_r)$, satisfies

$$\left(\frac{\partial^2}{\partial z^2}+k^2(z)-k_r^2\right)g(k_r;z,z_0)=-2\,\delta(z-z_0), \tag{4}$$

as well as the boundary conditions at the surface and the bottom. Due to this fact, the horizontal wave number spectrum contains information about the geoacoustic properties in the bottom.

Methods for evaluating the Hankel transform include evaluation of the asymptotic form by fast Fourier transform,[1,4]. Filon quadrature,[10] and trapezoidal rule quadrature integration,[10] which we use in this analysis. The Hankel transform is thus evaluated as

$$g(k_r)=\sum_{i=1}^{N} W_i P_i r_i J_o(k_r r_i), \tag{5}$$

where P_i is the complex pressure of the ith data sample, r_i is the range associated with that sample, and W_i is a Newton-Cotes quadrature weighting factor. For a trapezoidal rule with equal range spacing, $W_i=\Delta R/2$ for $i=1$ or N, and $W_i=\Delta R$ for all other i. With modern computing power, the zeroth-order Bessel function is easy to evaluate by a series expansion, and the time constraints associated with quadrature evaluation were not important because the data were postprocessed.

Propagating modes, evanescent modes, and leaky modes are all needed to describe the entire pressure field in the water but, for long-range propagation when shear is not important (as is the case for sandy silty sediments) the pressure is simply

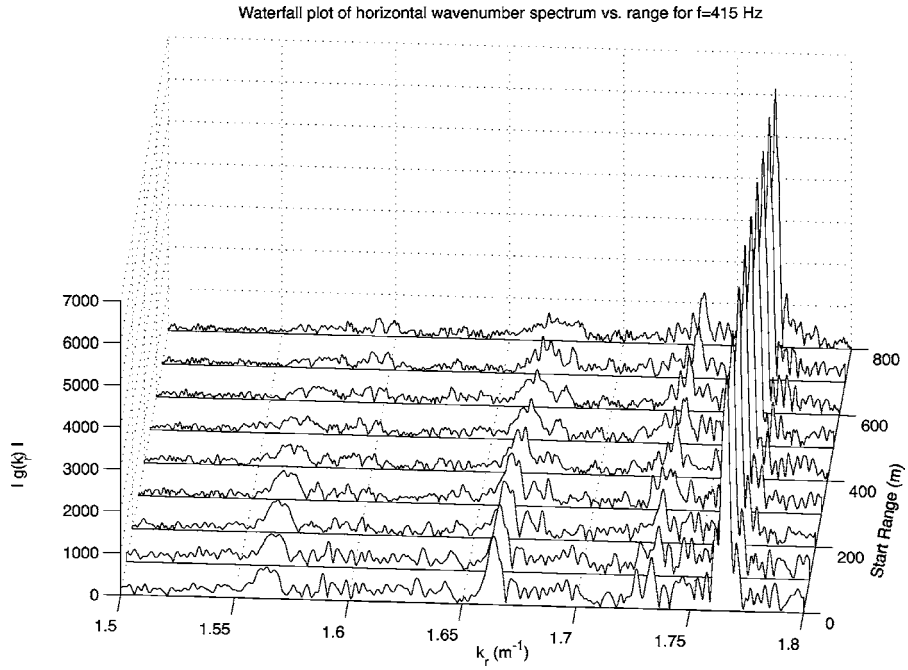

FIG. 3. Waterfall plot of the horizontal wave number spectrum of 415 Hz measured over 2 km long finite apertures stating at increasing ranges. Four modes are present and the higher-order (lower-k) modes display mode stripping.

$$p(r) \approx \sum_{n=1}^{M} a_n \phi_n(z) \phi_n(z_0) H_0^{(1)}[(k_n + i\beta_n)r], \tag{6}$$

where ϕ_n, k_n, and β_n are the modal eigenfunction, the modal eigenvalue (or modal wave number), and modal attenuation coefficient of the nth propagating mode, respectively. A perturbation solution for the modal coefficients, that was originally developed by Kornhauser and Raney,[11] Ingenito,[12] and Pierce,[8] gives the modal attenuation coefficient as

$$\beta_n(\omega) = v_{\mathrm{ph},n} \frac{\int [\alpha(\omega)/\rho c] \phi_n^2 dz}{\int (\phi_n^2/\rho) dz}. \tag{7}$$

The frequency dependence of the attenuation was explicitly included to stress its importance. In general, the modal attenuation coefficients will be larger for the higher-order modes due to the shape of ϕ_n and the steeper mode angles. These steeper mode angles result in mode stripping, which in turn results in the deep nulls with a short interference length at close range and a longer interference length at a longer range. This result is clearly evident in the measured transmission loss (TL) for 415 Hz, as shown in Fig. 2. Calculated TL results, using the range independent Kraken normal mode program[13] [using Eq. (6)] with the idealized ocean bottom model, are also shown and are in good agreement with the measured results. While TL calculations at the other experimental frequencies agree well with theory, the 415 Hz case is chosen here as particularly illustrative because it contains enough propagating modes to demonstrate the relevant phenomena, yet few enough such that the results are not cluttered. The disagreement with respect to the nulls at longer ranges, between the measured and modeled results, is most likely due to range dependencies that are not modeled.

Propagating modal eigenvalues are shown in the measured horizontal wave number spectrum given by an evaluation of Eq. (5) by sharp peaks centered at each k_n. Because the complex pressure versus range is necessarily measured over a finite aperture, the modal ampli-

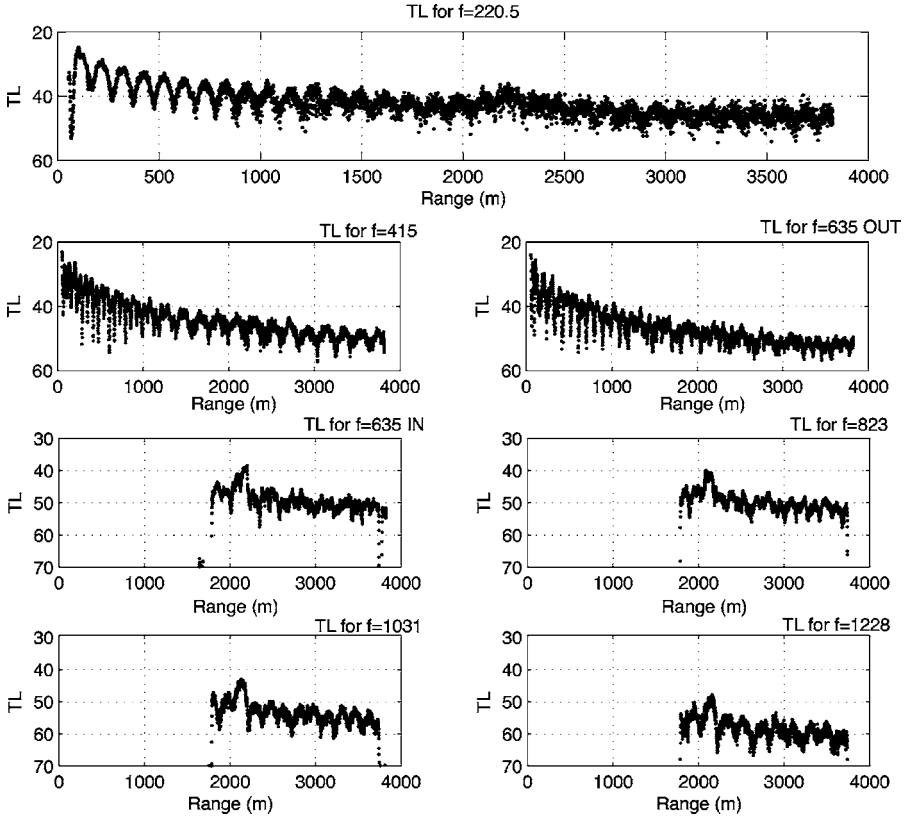

Fig. 4. TL vs range for all frequencies used in the experiment. Only long-range TL measurements are available for the high frequencies used on the inbound leg due to recorder disk space limitations.

tude can be recovered. Thus, if successive finite apertures are used, the modal attenuation coefficients for each mode can be estimated by the decay of the modal amplitudes with range. This effect is shown in Fig. 3 with a waterfall plot of the horizontal wave number spectra evaluated over a 2 km aperture, starting at successively further starting ranges from the beginning of the data set and extending to 800 m. The high modal attenuation is also clearly evident by the broad width of the higher-order modal peaks.

TL results for all frequencies from the experiments are shown in Fig. 4. Source levels were kept to a minimum for environmental impact reasons, and SNRs at 4 km were generally over 6 dB. The SNR for 220.5 Hz was, however, reduced to 0 dB past 1.2 km. Further, the shipping noise is evident in the 220.5 Hz data near 2.2 km, which is consistent with noise coming from the local shipping lane to Nantucket Harbor. Despite these poor SNR issues on each individual channel, the modal interference pattern, at long ranges for 220.5 Hz, is still easily recovered by overlap processing. This is accomplished by making complex pressure measurements for every 0.75 m advance of the array when the physical aperture of the array is 3.75 m. By using this overlap processing technique, six measurements of the complex pressure are made at each range, and thus the coherent gain of the signals allows for an increased SNR. By fitting the envelope of the TL versus $\log_{10}(R)$ with straight lines at short and long ranges, the range dependence of TL is shown to be between 15 $\log_{10}(R)$, and 10 $\log_{10}(R)$; consistent with Urick.[14]

These results are for the case of a 13 m water depth with source-to-receiver ranges of 4 km. Extension to deeper water and longer ranges with the RTAS is straightforward given the previous results in deeper water[3,4] and properties of the vehicle.[5]

4. Conclusions

This paper has presented preliminary results from a series of synthetic aperture AUV-towed-hydrophone array experiments, under conditions equivalent to a Pekeris waveguide. The sound transmission results were found to agree well with calculations, as well as the Pekeris solutions, when based on a geoacoustic profile calculated by the Hamilton formulations with attenuation given by a modified Biot theory. The experimental transmission results were found to clearly show the physical phenomena expected for sound transmission in an isovelocity waveguide; that is, a modal interference pattern and mode stripping. The ability of RTAS to characterize the ocean waveguide, through the synthetic aperture Hankel transform technique with the accuracy, efficiency, and cost effectiveness discussed in this paper, is a significant advance in sound transmission measurements and sound field characterizations, and demonstrates a new ocean-acoustics tool.

Acknowledgments

The authors gratefully acknowledge the hard work and dedication of the members of the Ocean Systems Laboratory (OSL), the Ocean Acoustics Laboratory (OAL), the rigging shop, and the Captain and Crew of the R/V Tioga at the Woods Hole Oceanographic Institution. Support for this work was provided by the Office of Naval Research through Program Manager Dr. Ellen Livingston (Code 321), as well as Dr. Tom Curtin (Code 322). Steve Savitsky (Code 72) and Joseph Kaminski (Code 1511) of the Naval Undersea Warfare Center provided the sound sources and test facilities prior to the experiment. Boston University supplied the funding for the array and recording equipment. Finally, the authors are grateful for ONR's support of the first author's National Defense Science and Engineering Graduate (NDSEG) fellowship.

References

[1]G. V. Frisk and J. F. Lynch, "Shallow water waveguide characterization using the Hankel transform," J. Acoust. Soc. Am. **76**(1), 205–216 (1984).
[2]G. V. Frisk, J. F. Lynch, and S. D. Rajan, "Determination of compressional wave speed profiles using modal inverse techniques in a range-dependent environment in Nantucket Sound," J. Acoust. Soc. Am. **86**(5), 1928–1939 (1989).
[3]J. F. Lynch, S. D. Rajan, and G. V. Frisk, "A comparison of broadband and narrow-band modal inversions for bottom geoacoustic properties at a site near Corpus Christi, Texas," J. Acoust. Soc. Am. **89**(2), 648–665 (1991).
[4]W. Carey, J. Doutt, R. Evans, and L. Dillman, "Shallow-water sound transmission measurements on the New Jersey continental shelf," IEEE J. Ocean. Eng. **20**(4), 321–336 (1995).
[5]Hydroid, LLC, REMUS 100 Autonomous Underwater Vehicle, brochure, Falmouth, MA (2006).
[6]J. C. Hathaway, "Data file: Continental margin program Atlantic Coast of the United States, Vol. 2—Samples collection and analytical data," Ref. No. 71-15, Woods Hole Oceanographic Institution, Falmouth, MA.
[7]C. J. O'Hara and R. N. Oldale, "Geology, shallow structure, and bedform morphology, Nantucket Sound, Massachussets. 1:125,000," MF 1911, United States Geological Survey.
[8]A. D. Pierce, W. M. Carey, and M. Zampoli, "Low-frequency attenuation of sound in marine sediments," in *Proc. Oceans 2005* (IEEE/OES, Brest, France, 2005).
[9]E. L. Hamilton, "Geoacoustic modeling of the sea floor," J. Acoust. Soc. Am. **68**(5), 1313–1340 (1980).
[10]F. Jensen, W. Kuperman, M. Porter, and H. Schmidt, *Computational Ocean Acoustics* (American Institute of Physics, New York, 1994).
[11]E. T. Kornhauser and W. P. Raney, "Attenuation in shallow-water propagation due to an absorbing bottom," J. Acoust. Soc. Am. **27**(4), 689–692 (1955).
[12]F. Ingenito, "Measurements of mode attenuation coefficients in shallow water," J. Acoust. Soc. Am. **53**(3), 858–863 (1973).
[13]M. B. Porter, "The KRAKEN normal mode program," SACLANT Undersea Research Center.
[14]R. J. Urick, *Principles of Underwater Sound for Engineers* (McGraw–Hill, New York, 1967).

ACOUSTICAL NEWS—USA

Elaine Moran
Acoustical Society of America, Suite 1NO1, 2 Huntington Quadrangle, Melville, NY 11747-4502

***Editor's Note**: Readers of the journal are encouraged to submit news items on awards, appointments, and other activities about themselves or their colleagues. Deadline dates for news items and notices are 2 months prior to publication.*

John Horne awarded the 2006 Medwin Prize in Acoustical Oceanography

ASA member John K. Horne was selected the recipient of the 2006 Medwin Prize in Acoustical Oceanography.

John Horne is Research Assistant Professor at the University of Washington School of Aquatic and Fishery Science. He received a B.Sc. (Hons.) and M.Sc. degrees from Dalhousie University and a Ph.D. from the Memorial University of Newfoundland.

The prize was awarded to Dr. Horne at the meeting of the Acoustical Society of America held in Providence, RI, 5–9 June 2006. During the meeting he presented the Acoustical Oceanography Prize Lecture titled "Acoustic species identification: When biology collides with physics."

The Medwin Prize in Acoustical Oceanography was established in 2000 through a grant made to the Acoustical Society Foundation by Herman and Eileen Medwin to recognize a person for the effective use of sound in the discovery and understanding of physical and biological parameters and processes in the sea. Previous recipients have been Timothy J. Leighton (2001), Bruce D. Cornuelle (2002), Jeffrey A. Nystuen (2003), Stan E. Dosso (2004), and Svein Vagle (2005).

Applications and/or nominations for the award are due in September each year. For further information about the award, please contact the Acoustical Society of America, Suite 1NO1, 2 Huntington Quadrangle, Melville, NY 11747-4502, Tel: 516-576-2360; Fax: 516-576-2377; E-mail: asa@aip.org; Web: http://asa.aip.org. Application information can also be found on the ASA Home Page at ⟨http:// asa.aip.org/fellowships.html⟩.

USA Meetings Calendar

Listed below is a summary of meetings related to acoustics to be held in the U.S. in the near future. The month/year notation refers to the issue in which a complete meeting announcement appeared.

2006

17–21 Sept.	INTERSPEECH 2006 (ICSLP 2006), Pittsburgh, PA [www.interspeech2006.org ⟨http://www.interspeech2006.org/⟩]
28 Nov.–2 Dec.	152nd Meeting of the Acoustical Society of America joint with theAcoustical Society of Japan, Honolulu, HI [Acoustical Society of America, Suite 1NO1, 2 Huntington Quadrangle, Melville, NY 11747-4502; Tel.: 516-576-2360; Fax: 516-576-2377; E-mail: asa@aip.org; WWW: http://asa.aip.org].

2007

4–8 June	153rd Meeting of the Acoustical Society of America, Salt Lake City, UT [Acoustical Society of America, Suite 1NO1, 2 Huntington Quadrangle, Melville, NY 11747-4502; Tel.: 516-576-2360; Fax: 516-576-2377; E-mail: asa@aip.org; WWW: http://asa.aip.org].
27 Nov.–2 Dec.	154th Meeting of the Acoustical Society of America, New Orleans, LA (note Tuesday through Saturday) [Acoustical Society of America, Suite 1NO1, 2 Huntington Quadrangle, Melville, NY 11747-4502; Tel.: 516-576-2360; Fax: 516-576-2377; E-mail: asa@aip.org; WWW: http://asa.aip.org].

2008

28 July–1 Aug.	9th International Congress on Noise as a Public Health Problem (Quintennial meeting of ICBEN, the International Commission on Biological Effects of Noise), Foxwoods Resort, Mashantucket, CT [Jerry V. Tobias, ICBEN 9, Post Office Box 1609, Groton, CT 06340-1609, Tel.: 860-572-0680; Web: www.icben.org; E-mail icben2008@att.net].

Cumulative Indexes to the Journal of the Acoustical Society of America

Ordering information: Orders must be paid by check or money order in U.S. funds drawn on a U.S. bank or by Mastercard, Visa, or American Express credit cards. Send orders to Circulation and Fulfillment Division, American Institute of Physics, Suite 1NO1, 2 Huntington Quadrangle, Melville, NY 11747-4502; Tel.: 516-576-2270. Non-U.S. orders add $11 per index.

Some indexes are out of print as noted below.

Volumes 1–10, 1929–1938: JASA and Contemporary Literature, 1937–1939. Classified by subject and indexed by author. Pp. 131. Price: ASA members $5; Nonmembers $10.

Volumes 11–20, 1939–1948: JASA, Contemporary Literature, and Patents. Classified by subject and indexed by author and inventor. Pp. 395. Out of Print.

Volumes 21–30, 1949–1958: JASA, Contemporary Literature, and Patents. Classified by subject and indexed by author and inventor. Pp. 952. Price: ASA members $20; Nonmembers $75.

Volumes 31–35, 1959–1963: JASA, Contemporary Literature, and Patents. Classified by subject and indexed by author and inventor. Pp. 1140. Price: ASA members $20; Nonmembers $90.

Volumes 36–44, 1964–1968: JASA and Patents. Classified by subject and indexed by author and inventor. Pp. 485. Out of Print.

Volumes 36–44, 1964–1968: Contemporary Literature. Classified by subject and indexed by author. Pp. 1060. Out of Print.

Volumes 45–54, 1969–1973: JASA and Patents. Classified by subject and indexed by author and inventor. Pp. 540. Price: $20 (paperbound); ASA members $25 (clothbound); Nonmembers $60 (clothbound).

Volumes 55–64, 1974–1978: JASA and Patents. Classified by subject and indexed by author and inventor. Pp. 816. Price: $20 (paperbound); ASA members $25 (clothbound); Nonmembers $60 (clothbound).

 0001-4966/2006/120(2)/559/2/$22.50

Volumes 65–74, 1979–1983: JASA and Patents. Classified by subject and indexed by author and inventor. Pp. 624. Price: ASA members $25 (paperbound); Nonmembers $75 (clothbound).

Volumes 75–84, 1984–1988: JASA and Patents. Classified by subject and indexed by author and inventor. Pp. 625. Price: ASA members $30 (paperbound); Nonmembers $80 (clothbound).

Volumes 85–94, 1989–1993: JASA and Patents. Classified by subject and indexed by author and inventor. Pp. 736. Price: ASA members $30 (paperbound); Nonmembers $80 (clothbound).

Volumes 95–104, 1994–1998: JASA and Patents. Classified by subject and indexed by author and inventor. Pp. 632. Price: ASA members $40 (paperbound); Nonmembers $90 (clothbound).

Volumes 105–114, 1999–2003: JASA and Patents. Classified by subject and indexed by author and inventor. Pp. 616. Price: ASA members $50; Nonmembers $90 (paperbound).

ACOUSTICAL NEWS—INTERNATIONAL

Walter G. Mayer
Physics Department, Georgetown University, Washington, DC 20057

Acoustical News

International Meetings Calender

Below are announcements of meetings and conferences to be held abroad. Entries preceded by an asterisk are new or updated listings.

August 2006

22–26 **Ninth International Conference on Music Perception and Cognition**, Bologna, Italy (Web: www.icmpc2006.org).

September 2006

6–8 **Second International Symposium "Material-Acoustics-Place 2006,"** Zvolen, Slovakia (Web: www.acoustics.sk/map/).

11–12 *__International Conference on Synthetic Aperture Sonar and Synthetic Aperture Radar__, Lerici, Italy (Web: www.ioa.org.uk/viewupcoming.asp).

13–15 **Autumn Meeting of the Acoustical Society of Japan**, Kanazawa, Japan (Acoustical Society of Japan, Nakaura 5th-Bldg., 2-18-20 Sotokanda, Chiyoda-ku, Tokyo 101-0021, Japan; Fax: +81 3 5256 1022; Web: www.asj.gr.jp/index-en-html).

18–19 **Greek National Conference on Acoustics**, Heraklion, Crete, Greece (Web: www.iacm.forth.gr/~acoustics2006).

18–20 **Sixth International Symposium on Active Noise and Vibration Control (ACTIVE2006)**, Adelaide, Australia (Web: www.active2006.com.).

18–20 **International Conference on Noise and Vibration Engineering (ISMA2006)**, Leuven, Belgium (Fax: 32 16 32 29 87; Web: www.isma-isaac.be).

18–20 **12th International Conference on Low Frequency Noise and Vibration and its Control**, Bristol, UK (Web: www.lowfrequency2006.org).

October 2006

3–6 *__IEEE International Ultrasonics Symposium__, Vancouver, BC, Canada (Web:www.ieee-ultrasonics2006.org).

4–6 **33rd International Acoustical Conference "Acoustics High Tatras 06"-EAA Symposium**, Štrbské Pleso, Slovakia (e-mail: 33iac@skas.sk; Web: www.skas.sk/acoustics/2006).

11–13 **Annual Conference of the Canadian Acoustical Association**, Halifax, Nova Scotia, Canada (Web: www.caa-aca.ca/halifax-2006.html).

16–17 **Institute of Acoustics Autumn Conference**, Oxford, UK (web: www.ioa.org.uk/viewupcoming.asp).

18–20 **37th Spanish Congress on Acoustics-EAA Symposium of Hydroacoustics-Iberian Meeting on Acoustics**, Gandia-Valencia, Spain (Web:www.ia.csic.es/sea/index.html).

25–28 **Fifth Iberoamerican Congress on Acoustics**, Santiago, Chile (Web: www.fia2006.cl).

November 2006

2–3 **Swiss Acoustical Society Fall Meeting**, Luzern, Switzerland (Web: www.sga-ssa.ch).

3–4 *__Reproduced Sound 22__, Oxford, UK (web: ioa.org.uk/viewupcoming.asp).

20–22 **First Joint Australian and New Zealand Acoustical Societies Conference**, Christchurch, New Zealand (Web: www.acoustics.org.nz).

April 2007

10–12 **Fourth International Conference on Bio-Acoustics**, Loughboro, UK (Web:www.ioa.org.uk/viewupcoming).

16–18 *__29th International Symposium on Acoustical Imaging__, Shonan Village Center, Kanagawa Pref., Japan (Web: publicweb.shonan-it.ac.jp/ai29/AI29.html).

June 2007

3–7 *__11th International Conference on Hand-Arm Vibration__, Bologna, Italy (Web: associazioneitalianadiacustica.it/HAV2007/index.htm)

18–21 *__Oceans07 Conference__, Aberdeen, Scotland, UK (Web: www.oceans07ieeeaberdeen.org).

July 2007

2–6 *__Eight International Conference on Theoretical and Computational Acoustics__, Heraklion, Crete, Greece (Web: www.iacm.forth.gr/~ictca07).

4–7 *__International Clarinet Association Clarinetfest__, Vancouver, British Columbia, Canada (e-mail: john.cipolla@wku.edu; phone: 1 270 745 7093).

9–12 **14th International Congress on Sound and Vibration (ICSV14)**, Cairns, Australia (e-mail: n.kessissoglou@unsw.edu.au).

22–27 *__12th Internation Conference on Phonon Scattering in Condensed Matter__, Paris, France (e-mail: bper@ccr.jussieu.fr).

August 2007

6–10 **16th International Congress of Phonetic Sciences (ICPhS2007)**, Saarbrücken, Germany (Web:www.icphs2007.de).

26–29 **Inter-noise 2007**, İstanbul, Turkey (Web: www.internoise2007.org.tr).

27–31 **Interspeech 2007**, Antwerp, Belgium (Web: www.interspeech2007.org).

September 2007

2–7 **19th International Congress on Acoustics (ICA2007)**, Madrid, Spain (SEA, Serrano 144, 28006 Madrid, Spain; Web: www.ica2007madrid.org).

9–12 **ICA Satellite Symposium on Musical Acoustics (ISMA2007)**, Barcelona, Spain (SEA, Serano 144, 28006 Madrid, Spain; Web: www.ica2007madrid.org).

9–12 **ICA Satellite Symposium on Room Acoustics (ISRA2007)**, Sevilla, Spain (Web: www.ica2007madrid.org).

17–19 *__Third International Symposium on Fan Noise__, Lyon, France (Web: www.fannoise.org).

July 2008

7–10 **18th International Symposium on Nonlinear Acoustics (ISNA18)**, Stockholm, Sweden (temporary e-mail:⟨Bengt Enflo⟩ benflo@mech.kth.se).

28–1 **Ninth International Congress on Noise as a Public Health Problem**, Mashantucket, Pequot Tribal Nation (ICBEN 9, P.O. Box 1609, Groton CT 06340-1609, USA: Web: www.icben.org).

September 2008

22–26 **INTERSPEECH 2008-10th ICSLP**, Brisbane, Australia (Web: www.interspeech2008.org).

November 2008

1–5 *__IEEE International Ultrasonics Symposium__, Beijing, China (Web: www.ieee-uffc.org/ulmain.asp?page=symposia).

 0001-4966/2006/120(2)/563/2/$22.50

August 2010

23–27 **20th International Congress on Acoustics (ICA2010)**, Sydney, Australia (Web: www.ica2010sydney.org/).

Swiss Acoustical Society Moves

The Swiss Acoustical Society has moved to new quarters and their new address is Swiss Acoustical Society, P.O. Box 164, 6203 Sempach-Station, Switzerland. Their fax number is +41 469 40 50 and their e-mail address is info@sga-ssa.ch. Their Web site has not changed and remains http://www.sga-ssa.ch.

Great Britain's Institute of Acoustics appoints new Chief Executive

The Institute of Acoustics has appointed Kevin Macan-Lind as its new Chief Executive who will succeed Roy Bratby who has retired after nine years of service to the IOA. The new Chief Executive started his professional life in the Australian and New Zealand Banking Group and Barclays. He also has years of experience in publishing and event management and as director of an established health product mail order company. Dr. Tony Jones, President of IOA, said, "We are delighted to have Kevin on board…. I have high expectations that Kevin's entrepreneurial experience, knowledge, and enthusiasm will ideally suit him to the task of building upon the substantial progress already achieved by the Institute."

BOOK REVIEWS

P. L. Marston
Physics Department, Washington State University, Pullman, Washington 99164

These reviews of books and other forms of information express the opinions of the individual reviewers and are not necessarily endorsed by the Editorial Board of this Journal.

Editorial Policy: *If there is a negative review, the author of the book will be given a chance to respond to the review in this section of the Journal and the reviewer will be allowed to respond to the author's comments. [See "Book Reviews Editor's Note," J. Acoust. Soc. Am.* **81***, 1651 (May 1987).]*

Shakespeare's Songbook

Ross W. Duffin

W. W. Norton & Company, New York, 2004.

496 pp. Price: $39.95 (hardcover), ISBN: 0393058891.

Late at night in Lady Olivia's great house in Illyrium, three friends—Sir Toby, the lady's uncle, Feste her fool, and Sir Andrew Aguecheek, her hapless suitor—sing drunken songs that resound loudly through the empty halls. Malvolio, Lady Olivia's stern steward and "something of a Puritan," rises from bed to chide the drunkards, but they respond by mocking him with more songs:

> Sir Toby: Shall I bid him go?
> Feste: What an if you do?
> Sir Toby: Shall I bid him go, and spare not?
> Feste: O no, no, no, no, you dare not (*Twelfth Night 2.3*).

The scene, like the play as a whole, dramatizes a confrontation of two Elizabethan subcultures, the bawdy festive world of taverns and the strict moralistic world of Puritanism.

For the original audiences of Shakespeare's play, the confrontation would have been more obvious than it is to us, since Shakespeare borrowed the lines that Toby and Feste exchange from a popular song of the period, first published in Robert Jones' *First Booke of Songs* (1600). The song is, as Stephen Orgel says in the foreword to Ross Duffin's *Shakespeare's Songbook*, one of the "songs that drunken revelers really did sing in Elizabethan England" (p. 13). Shakespeare used Jones' song the way a director might insert a snatch of Bob Dylan into a movie soundtrack, put lines from a rap song in the mouths of characters, or name one of his characters "Bobbie McGee." Duffin's book enables us to hear the joking musical allusions that would have been second nature to Shakespeare and his audiences.

Music and dance always accompanied Shakespeare's plays, like their Greek predecessors, but this aspect of Elizabethan drama has been difficult to reconstruct. Scholars have pieced together the musical aspects of his drama from scattered sources, but *Shakespeare's Songbook* is a unique achievement, the first time anyone has "brought all of the Shakespearean tunes and texts together" (p. 25). Duffin, the Fynette H. Kulas Professor of Music at Case Western Reserve University in Cleveland, has compiled all the songs in Shakespeare's plays, whether they were written by Shakespeare or borrowed from elsewhere. Wherever available, he provides the full text of each song, even when Shakespeare includes only a stanza or two, or even only a few lines. Because he includes contemporary tunes for all of the songs, Duffin's book is as useful to performers, producers, and directors as it is to scholars. He admits that he is more confident of some tunes than of others, but all the tunes were theoretically available to Shakespeare. The songs are arranged alphabetically by title, but an index of first lines and another index arranged by play make the book very easy to use. The book comes with a CD containing 81 songs, about half of the songs discussed in the book.

Shakespeare's Songbook is a treasure for Shakespearean scholars, demonstrating that Shakespeare quotes from and alludes to popular songs far more than has commonly been recognized. This raises many questions, but let me limit myself to two. First, there is the question of Shakespeare's sources. Shakespeare's allusions to ancient myths have often been taken as evidence of his familiarity with Ovid's *Metamorphoses* and other ancient literature, all available in English translations in Shakespeare's time. As Duffin points out, however, Shakespeare's audience would more likely have gained their knowledge of myth and history from popular song than from Ovid himself, and perhaps the same was true of the Bard himself. This might even hold some implications for the always-renewed debate over the playwright's identity. If the plays draw from popular songs about Apollo and Daphne rather than from Ovid, perhaps the author really was an actor with an elementary education rather than a university-educated aristocrat.

Second, Duffin understandably does not attempt to explain the significance of all the quotations and allusions to songs, but that leaves a vast interpretive task to others. When Shakespeare quotes the title of a ballad, does he intend it to evoke the entirety of the ballad, so that the ballad becomes an internal commentary on the play itself? Does he intend it as a joke, a sop to hip groundlings? When he quotes the same song in two different plays (there are five allusions to "King Cophetua and the Beggar Maid" in four different plays), are we supposed to recognize the repetition and muse on larger parallels between the plays? Like the best books of criticism, Duffin's lays out a program of new research even as it brings another research program to an impressive culmination.

Shakespeare's Songbook is a wonderfully planned and executed piece of scholarly detection and an indispensable resource for anyone interested in Elizabethan popular music, or, more broadly, early modern popular culture.

PETER J. LEITHART
Senior Fellow, Theology and Literature
New St. Andrews College, Moscow, Idaho

 0001-4966/2006/120(2)/565/1/$22.50

REVIEWS OF ACOUSTICAL PATENTS

Lloyd Rice
11222 Flatiron Drive, Lafayette, Colorado 80026

The purpose of these acoustical patent reviews is to provide enough information for a Journal reader to decide whether to seek more information from the patent itself. Any opinions expressed here are those of reviewers as individuals and are not legal opinions. Printed copies of United States Patents may be ordered at $3.00 each from the Commissioner of Patents and Trademarks, Washington, DC 20231. Patents are available via the Internet at http://www.uspto.gov.

Reviewers for this issue:

GEORGE L. AUGSPURGER, *Perception, Incorporated, Box 39536, Los Angeles, California 90039*
ANGELO CAMPANELLA, *3201 Ridgewood Drive, Hilliard, Ohio 43026-2453*
DIMITRI DONSKOY, *Stevens Institute of Technology, Castle Point on the Hudson, Hoboken, New Jersey 07030*
JOHN M. EARGLE, *JME Consulting Corporation, 7034 Macapa Drive, Los Angeles, California 90068*
JOHN ERDREICH, *Ostergaard Acoustical Associates, 200 Executive Drive, West Orange, New Jersey 07052*
SEAN A. FULOP, *California State University, Fresno, 5245 N. Backer Avenue M/S PB92, Fresno, California 93740-8001*
JEROME A. HELFFRICH, *Southwest Research Institute, San Antonio, Texas 78228*
DAVID PREVES, *Starkey Laboratories, 6600 Washington Ave. S., Eden Prarie, Minnesota 55344*
DANIEL R. RAICHEL, *2727 Moore Lane, Fort Collins, Colorado 80526*
CARL J. ROSENBERG, *Acentech Incorporated, 33 Moulton Street, Cambridge, Massachusetts 02138*
NEIL A. SHAW, *Menlo Scientific Acoustics, Inc., Post Office Box 1610, Topanga, California 90290*
WILLIAM THOMPSON, JR., *Pennsylvania State University, University Park, Pennsylvania 16802*
ERIC E. UNGAR, *Acentech, Incorporated, 33 Moulton Street, Cambridge, Massachusetts 02138*
ROBERT C. WAAG, *University of Rochester, Department of Electrical and Computer Engineering, Rochester, New York 14627*

7,007,546

43.20.Ye MEASUREMENT, COMPENSATION AND CONTROL OF EQUIVALENT SHEAR RATE IN ACOUSTIC WAVE SENSORS

Jeffrey C. Andle, assignor to Biode Incorporated
7 March 2006 (Class 73/54.41); filed 22 December 2003

The viscosity of material **10** determines the attenuation of shear waves **35** in piezoelectric crystal **25**, in traveling from wave source **30** to wave

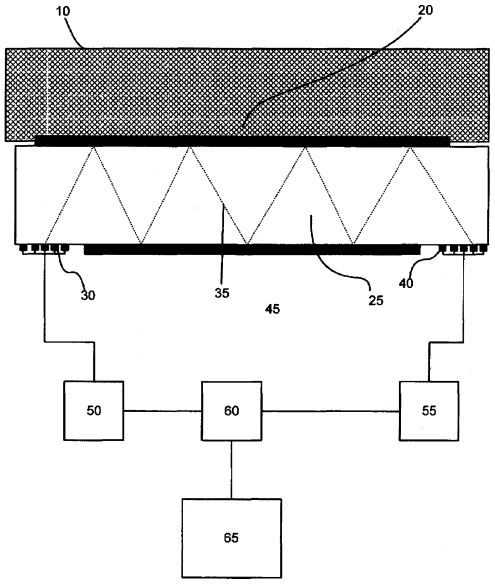

receiver **40**. Viscosity is computed by module **65** from the signal from comparator **60**.—AJC

7,009,326

43.28.Tc ULTRASONIC VIBRATION APPARATUS USE AS A SENSOR HAVING A PIEZOELECTRIC ELEMENT MOUNTED IN A CYLINDRICAL CASING AND GROOVES FILLED WITH FLEXIBLE FILLER

Kenji Matsuo and Junshi Ota, assignors to Murata Manufacturing Company, Limited
7 March 2006 (Class 310/324); filed in Japan 28 October 1999

This patent describes an ultrasonic object sensor with improved beam width comprising a circular plate **2′** at the end of a cylinder **2**, driven by a piezoelectric transducer **1** on the center of that plate. Inner and outer plate

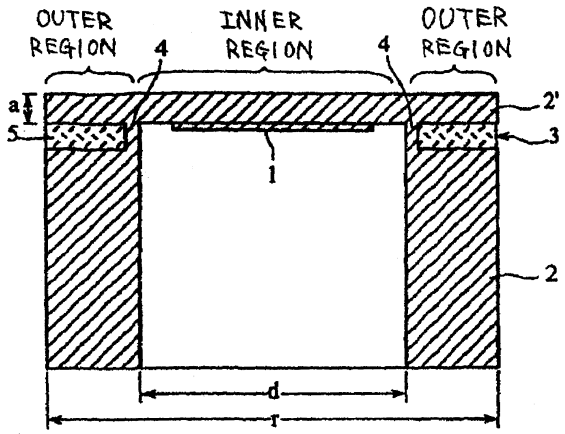

regions vibrate while the support web **4** is between regions. The beam width is improved (broadened in this case) when damping material is placed in a groove under the outer region.—AJC

 0001-4966/2006/120(2)/567/18/$22.50

7,002,877

43.30.Gv METHOD AND APPARATUS FOR ACTIVE SONAR PERFORMANCE PREDICTION

Juan I. Arvelo and Bruce Newhall, assignors to The Johns Hopkins University
21 February 2006 (Class 367/131); filed 3 November 2004

A computer-based system is discussed for predicting active, low-frequency, sonar array performance in shallow coastal waters. The sonar operator can select an arbitrary geographical location, specify details of the sonar system's transmitter and receivers, and define a target to be searched for. The operator can also specify appropriate bathymetric data, bottom composition, and sound-speed profile, which choices lead to the calculation of the major component of surface reverberation. In a refinement of the procedure, surface reverberation may also be calculated using a semiempirical scattering strength derived from wind-speed data, plus a component of volume reverberation calculated from a biological population database.—WT

7,006,081

43.35.Pt ACOUSTIC TOUCH SENSOR WITH LAMINATED SUBSTRATE

Joel Kent *et al.*, assignors to Elo TouchSystems, Incorporated
28 February 2006 (Class 345/177); filed 5 October 2001

This patent describes a transverse surface (Lamb) wave touch screen comprising a slow wave-speed thin polymer **23** on a high wave-speed glass plate **7**. Wave energy concentrates in polymer **23** for good touch sensitivity.

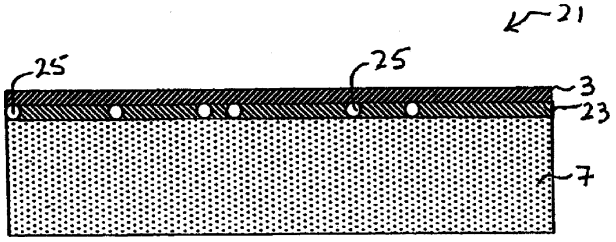

Cast polymer thickness, e.g., 30 μm as set by spacers **25**, is selected for constant group velocity over 4–40 MHz to preserve pulse shape. The touch surface is protected by micro-sheet **3**.—AJC

7,000,474

43.35.Yb ACOUSTIC DEVICE USING HIGHER ORDER HARMONIC PIEZOELECTRIC ELEMENT

Joel C. Kent, assignor to ELO Touchsystems, Incorporated
21 February 2006 (Class 73/579); filed 28 February 2003

This patent describes the use of high-order harmonic transducers in the operation of touch-screen devices. The motivation for using high-order harmonics is that the transducers can be thicker and less susceptible to breakage during assembly and handling. The inventor calls for coupling to Love waves in the substrate, although use with SH and Rayleigh waves is discussed. The patent is well written and detailed, even having some performance data and a brief tutorial on shear waves in thin plates. However, there is nothing here that would not be instantly familiar to anyone involved in ultrasonic testing, and the only aspect that this reviewer found novel was the claim that thicker transducers are better.—JAH

7,004,031

43.35.Zc ULTRASONIC SENSOR

Kiyonari Oda *et al.*, assignors to Denso Corporation
28 February 2006 (Class 73/602); filed in Japan 16 May 2003

This patent discloses a control scheme for temperature compensation of ultrasonic transducers used in automobile backup warning sensors. The concern is that the shifting resonant and antiresonant frequencies will cause the transducer to ring too long for good obstacle range resolution. The inventors chose to control this through the switching of capacitors in parallel with the transducer and subsequent measurement of the ringdown time below a pre-established threshold. The approach seems both naive and primitive to this reviewer, as it does not account for changes in signal amplitude with capacitive loading, and the use of switched capacitors does nothing to change the damping properties of the system.—JAH

7,004,025

43.38.Ar COMPOSITE SENSOR DEVICE AND METHOD OF PRODUCING THE SAME

Masaya Tamura, assignor to Murata Manufacturing Company, Limited
28 February 2006 (Class 73/511); filed in Japan 23 June 2000

This patent discloses a composite accelerometer/gyroscope sensor. The inventor has chosen to segregate the two devices into separate chambers as shown. The inventor had concerns about the driving frequency of the 1-kHz gyro in the upper half of the sensor package coupling to the accelerometer in the lower half, so he took the measure of sealing them into two separate cavities and introducing an inert gas at atmospheric pressure into the lower

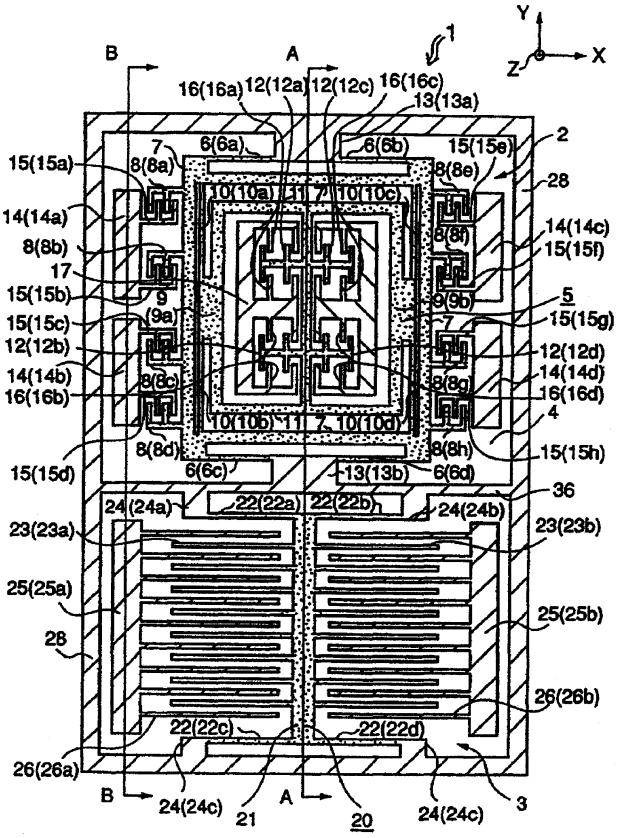

one and evacuating the upper one. The argument is made that the use of a high-pressure gas fill is for introducing damping of vibrations coupled from the gyroscope, but neglects to mention that this increases the broadband noise level of the accelerometer. None of this is novel and the patent is focused almost entirely on the fabrication details.—JAH

6,997,178

43.38.Ar OXYGEN INHALER MASK WITH SOUND PICKUP DEVICE

Gérard Reynaud, assignor to Thomson-CSF Sextant
14 February 2006 (Class 128/201.19); filed in France 25 November 1998

The patent deals with microphones integrated into oxygen masks used by pilots and in other similar applications. The aim is to achieve better response by moving the microphone element closer to the user's mouth and to minimize noises produced by the associated intake and exhalation valves.—JME

7,007,901

43.38.Ar MICROPHONE SUPPORT

Kazuhisa Kondo, assignor to Kabushiki Kaisha Audio-Technica
7 March 2006 (Class 248/75); filed in Japan 20 November 2002

Described here is a swivel microphone mount that prevents a microphone, so mounted, from being "swiveled" beyond fixed limits, ostensibly to prevent fraying of wires and running the risk of feedback.—JME

7,002,441

43.38.Bs MICRO-ELECTRO-MECHANICAL SWITCH, AND METHODS OF MAKING AND USING IT

Brandon W. Pillans and David I. Forehand, assignors to Raytheon Company
21 February 2006 (Class 335/78); filed 9 August 2004

This patent discloses the design of a long-lifetime RF-MEMS switch for use in applications where longevity is important. The inventors address a common failure mode of these electrostatically actuated switches, in which charge gets trapped on the surface of the switch over repeated actuation cycles, ultimately causing the switch to stay closed. Referring to the figure, a small boss is created on the lower conductor **21**. Through the application of a dc switching voltage to conducting membrane **31**, the two are caused to come into contact at the boss; typically this voltage is 50–70 V. In the

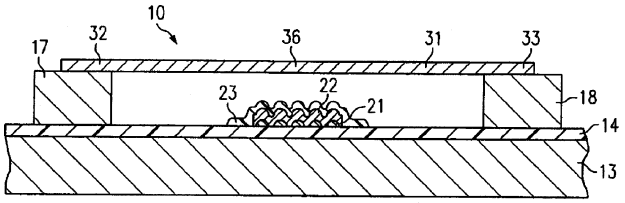

collapsed state the switch is closed with the insulating nodules **22** separating the electrodes just enough to attain a capacitance ratio C(on)/C(off) of 100:1. This is sufficient isolation for many rf applications. The inventors assert that, as a result of the lower contact area, charge buildup is reduced and the switch lifetime is extended. The solution they provide would be rather obvious to those with knowledge in the art and would also be of dubious effectiveness. There is little discussion of the physical basis for their longevity claim and there are no results given to substantiate it either.—JAH

6,975,741

43.38.Dv ELECTROACOUSTIC TRANSDUCER BEING ACOUSTICAL TIGHT IN THE AREA OF ITS AIR GAP FOR ITS MOVING COIL

Heinz Renner, assignor to Koninklijke Philips Electronics N.V.
13 December 2005 (Class 381/411); filed in the European Patent Office 13 February 2001

An electrodynamic transducer is described that has a very small air gap around the moving coil. By use of ball bearings **38** and **39** (!), glides **36**, two-magnet motor assembly **6**, and distinctive coil carrier **28**, among other

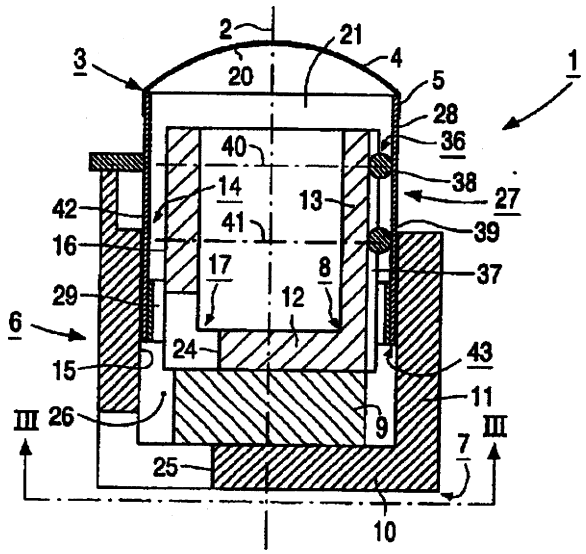

improvements over prior art, the patent says, in essence, that the smaller the air gap, the lower the frequency at which the gap is "acoustically impermeable" and thus, "perfect signal reproduction can be obtained down to a low frequency" that is equal to the limit of impermeability. The patent states that this has been accomplished down to 10 Hz. The size of the transducer and efficiency, among other parameters that may be of interest to a loudspeaker engineer, are not discussed. Several readings of the patent did not yield or reveal the purpose of the device to this reviewer.—NAS

6,998,940

43.38.Fx COMPONENT OPERATING WITH BULK ACOUSTIC WAVES AND A METHOD FOR PRODUCING THE COMPONENT

Thomas Metzger, assignor to EPCOS Incorporated
14 February 2006 (Class 333/187); filed in Germany 15 January 2003

This patent discloses a method for fabricating a film bulk acoustic resonator using more or less standard silicon processing. The main advantages of this method are in the reduction of electrical cross-coupling between resonators and in simplifications of the processing. This is not particularly novel from a conceptual standpoint, the primary differences between this and current design being in the planarization steps that the author inserts in the process. There is no performance or design data to indicate how well this technique works.—JAH

7,002,436

43.38.Fx VACUUM-CAVITY MEMS RESONATOR

Qing Ma *et al.*, assignors to Intel Corporation
21 February 2006 (Class 333/186); filed 19 August 2004

This patent discloses the construction of a flexural bar type of resona-

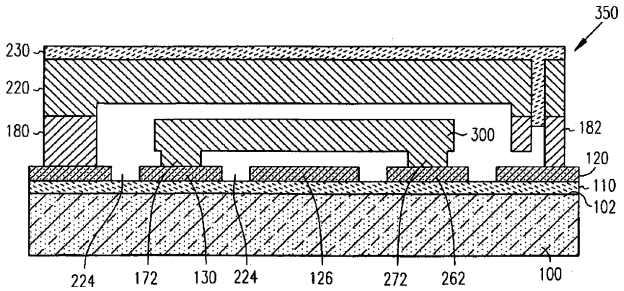

tor for GHz frequencies. The patent is more concerned with the packaging and evacuation of the device than with the resonator design, an example of

which is shown in the figure. A single process is described for fabricating any of three different varieties of resonators. The process is based on the use of silicon nitride as a sealant and cover of the devices, which are made of silicon using wet etching processes. The presentation is sparing in details and doesn't address thermal expansion or materials selection issues, so it seems unlikely to be of interest to anyone. The patent is brief and easy to read.—JAH

6,981,570

43.38.Ja LOUDSPEAKER SYSTEM WITH COMMON LOW AND HIGH FREQUENCY HORN MOUNTING

Richard H. Dalbec, Rensselaer, New York
3 January 2006 (Class 181/182); filed 8 May 2003

The invention describes a means of mounting a high-frequency horn **304**, high-frequency driver **303**, and two low-frequency drivers **502** and **506** to a common panel **301** in an enclosure **501**. The opening in which the horn

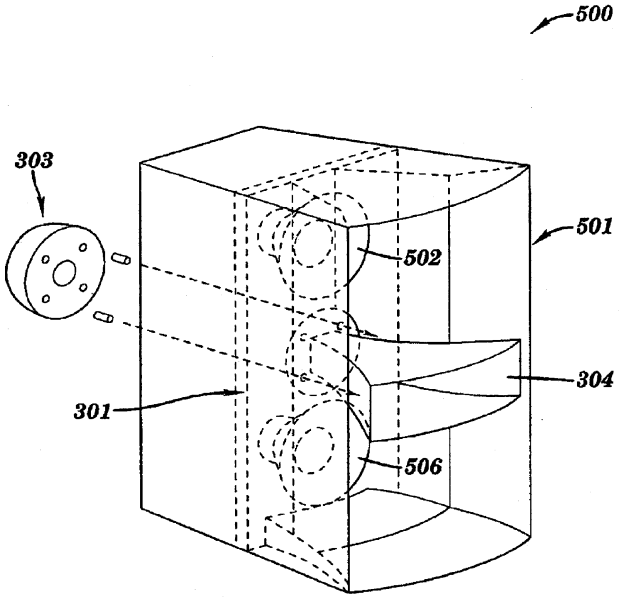

sits appears to be, in later figures, some type of horn-loaded geometry. This is said (a favorite word in the application) to reduce the destructive interference of the drivers.—NAS

6,978,861

43.38.Ja CONNECTION OF SOUND BOWL OF LOUDSPEAKER

A. Wen Yu, Taipei, Taiwan, Province of China
27 December 2005 (Class 181/172); filed 26 June 2002

Various means are described for attaching the cone to the surround of what appears to be an electrodynamic loudspeaker. The prior art described is vague and the drawing misleading. The preferred embodiment of the invention seems to be in wide use and employs mature techniques. "Thereby the tolerance of the loudspeaker is enhanced. Thus, the loudspeaker is tolerable to vibration and produces sound with precise tunes, and stabilizes the quality

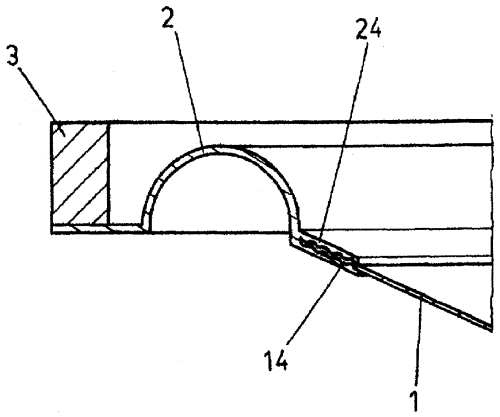

of sound." All this with no mention of reflections at the interface or any of the bulk parameters of the materials.—NAS

6,983,819

43.38.Ja ENTERTAINMENT SOUND PANELS

Christian Busque *et al.*, assignors to AWI Licensing Company
10 January 2006 (Class 181/150); filed 8 November 2002

There are many flat panel transducers on the market now. This patent describes improvements in the design, for both ceiling-grid and non-ceiling-grid applications, of the mounting for exciter **620**, connection to the panel via pad **222**, and the perimeter support assembly **230**, **220** for panel **200**. The

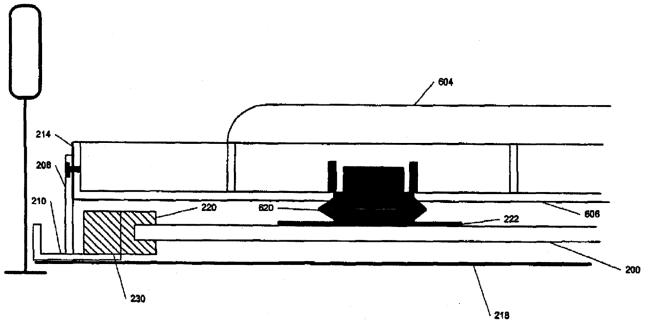

patent is well written and easy to follow and will provide the reader with a short introduction to this class of loudspeaker. The inventors are employed by a large ceiling manufacturer, a loudspeaker design firm, and an offshore manufacturer.—NAS

7,003,130

43.38.Ja RESONANCE FREQUENCY CORRECTION METHOD AND VIBRATION SPEAKER

Seuk Hwan Chung, assignor to Samsung Electro-Mechanics Company, Limited
21 February 2006 (Class 381/396); filed 29 January 2003

When fabricating combination vibrator-loudspeakers, it may be difficult to hold the vibrator resonant frequency within acceptable tolerances. This patent describes an automated production system that can add and cure

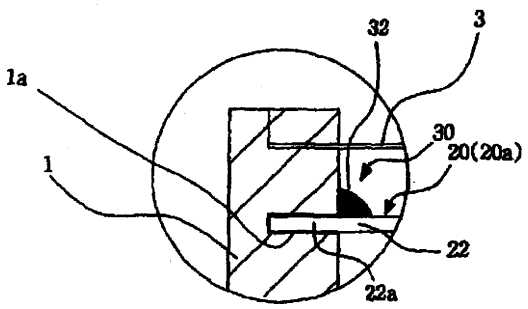

an elastomer to increase stiffness or trim a portion of the suspension to decrease stiffness.—GLA

7,010,140

43.38.Ja ELECTROACOUSTIC TRANSDUCER

Masahito Furuya, assignor to Citizen Electronics Company, Limited
7 March 2006 (Class 381/396); filed in Japan 25 July 2002

According to this patent, a conventional miniature loudspeaker vents rear radiation through slits around the perimeter of the casing. If the diaphragm is clamped in place, it is likely that there will be small air leaks from the front chamber immediately adjacent to the slits. Thus, a portion of the

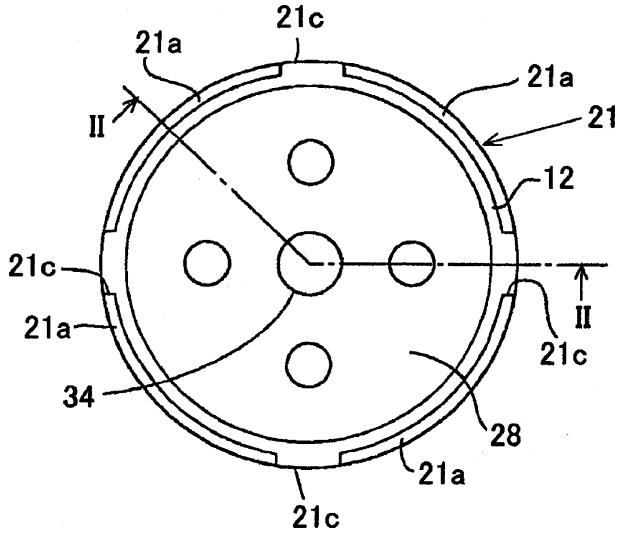

front radiation is canceled by rear radiation rather than emanating from the front port as intended. An improved design is described that includes the fairly obvious solution of adding adhesive to the edge of the diaphragm.—GLA

7,006,643

43.38.Lc DIFFERENTIAL AUDIO AMPLIFICATION SYSTEM

Jeffrey S. Anderson, assignor to Logitech Europe S.A.
28 February 2006 (Class 381/120); filed 8 June 2001

Differential audio power amplifiers are commonly used in automotive sound systems to achieve maximum output from a limited-voltage dc supply. It is well known that this configuration also rejects common-mode

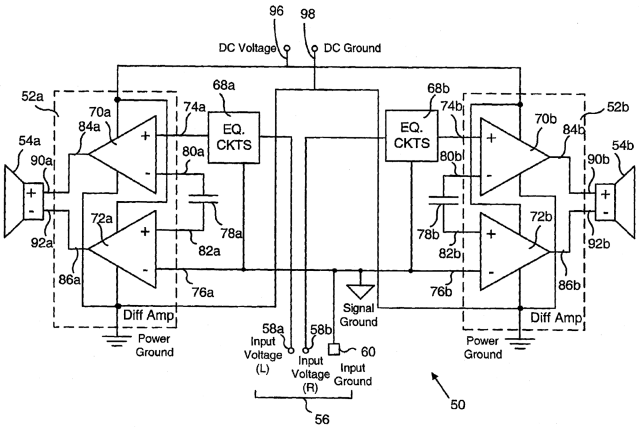

power supply noise. Most multimedia computer systems include a noisy, low-voltage power supply. Can you guess what has been patented here?—GLA

6,978,031

43.38.Ne LOUDSPEAKER SOUND MODULATION APPARATUS

Joseph K. Garretson and Lewis C. Iby, assignors to Scosche Industries, Incorporated
20 December 2005 (Class 381/162); filed 24 May 2004

A grill **13** that can be perforated in many different ways is connected to a motor **20**. These are mounted within the cone void of a loudspeaker. The motor turns the grill. In addition to the modulation of the sound that a perforated grill can produce, if the interior of the cone void is illuminated,

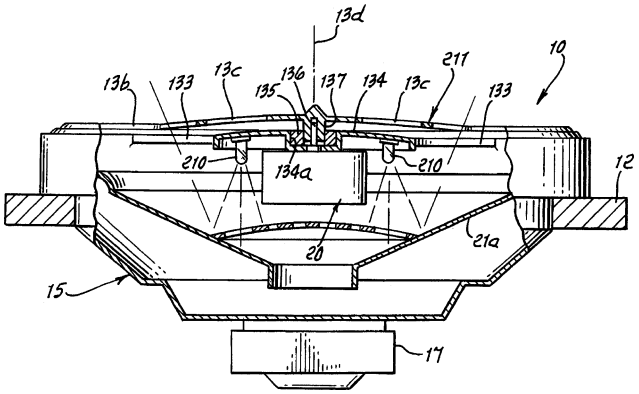

say by LEDs **210**, visual effects may be provided. "There is a need for speaker accessories characterized as producing motion to complement sound, such as music, produced by such speakers."—NAS

7,009,325

43.38.Rh SURFACE ACOUSTIC WAVE DEVICE

Hajime Kando and Michio Kadota, assignors to Murata Manufacturing Company, Limited
7 March 2006 (Class 310/313 A); filed in Japan 7 January 2003

Miniature communication devices operating at GHz frequencies require faster phase-velocity substrates for SAW devices. Leaky (modified Rayleigh) waves that have a larger longitudinal component also have a greater velocity. The coupling efficiency for shear waves is greater. High-density materials such as gold and silver have less propagation loss. The author considers the optimum to be a SAW device on a hexagonal or a

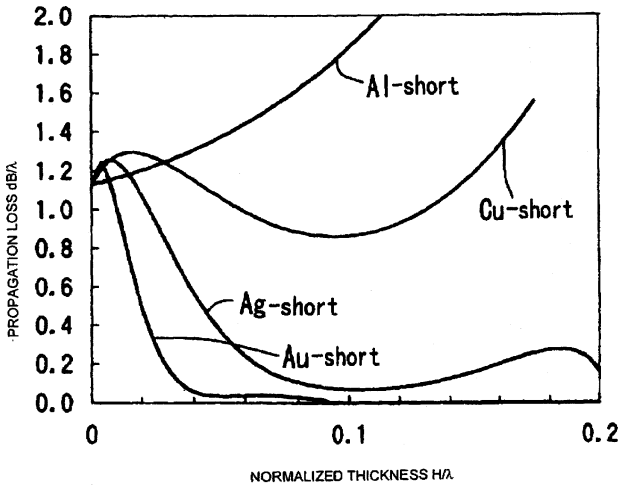

trigonal piezoelectric crystal substrate, such as lithium tantalate, with a specific range of IDT gold conductor thickness versus wavelength ratio, and a specific range of crystal orientation Euler angles.—AJC

7,009,468

43.38.Rh SURFACE ACOUSTIC WAVE DEVICE AND ELECTRONIC DEVICE USING THE SAME

Michio Kadota *et al.*, assignors to Murata Manufacturing Company, Limited
7 March 2006 (Class 333/195); filed in Japan 27 April 2001

Selection of the Euler angle of the crystal increases the SAW coupling factor and hence the efficiency. Miniature communication SAW devices can be made smaller by operating in the horizontal shear (SH) mode. Gold electrodes provide high coupling efficiency. The authors claim a SAW de-

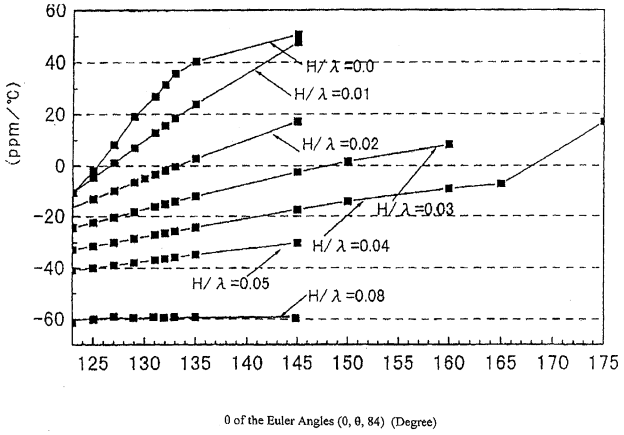

vice on a quartz substrate with a minimal temperature coefficient when gold electrodes have thickness to wavelength ratios between 0.01 and 0.08, when the crystal Euler orientation angle is between 120° and 150°.—AJC

7,002,616

43.38.Si CELLULAR TELEPHONE

Yuichi Taneya *et al.*, assignors to Sanyo Electric Company, Limited
21 February 2006 (Class 348/14.02); filed in Japan 31 January 2002

The cellular telephone in question is a multipurpose device that doubles as a digital movie camera capable of recording a simultaneous sound track. It seems wasteful to incorporate two microphones, one for

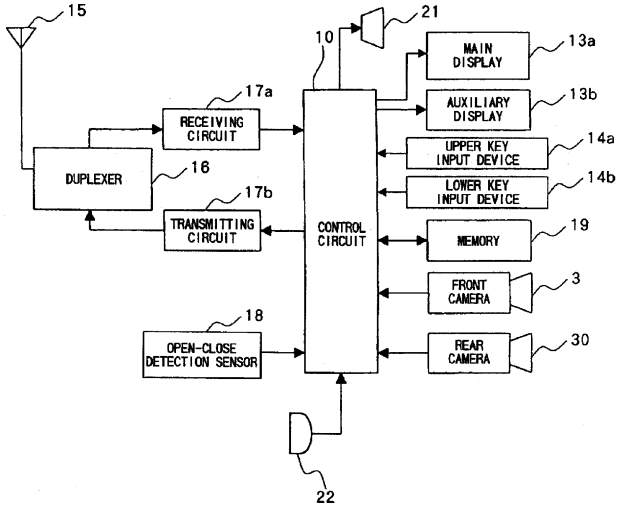

phone calls and one for recordings. With a little additional (fairly sophisticated) circuitry, the sensitivity of a single microphone can be automatically controlled as needed.—GLA

7,006,641

43.38.Si DRIVING CIRCUIT, ELECTRO-MECHANICAL-ACOUSTIC TRANSDUCER, AND PORTABLE TERMINAL APPARATUS

Shuji Saiki and Sawako Usuki, assignors to Matsushita Electric Industrial Company, Limited
28 February 2006 (Class 381/98); filed in Japan 14 April 1999

This is a fairly long patent, culminating in 54 equally long claims. It deals with combination vibrator-loudspeakers used in cellular telephones. Since the vibrator resonant frequency is difficult to control and may vary

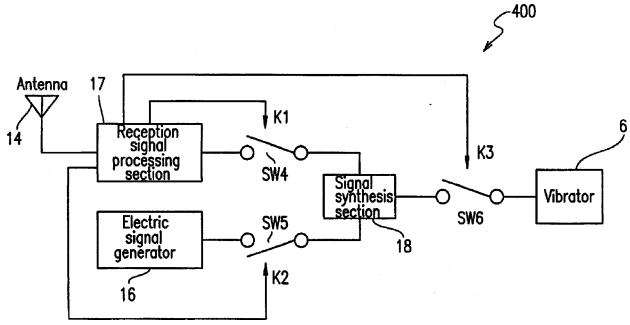

with vibration amplitude, conventional phones drive the vibrator with a swept signal rather than a single frequency. A more efficient scheme is described that synthesizes a drive signal from at least two individual frequencies.—GLA

7,003,329

43.38.Si DEVICE, SYSTEM AND METHOD FOR AUGMENTING CELLULAR TELEPHONE AUDIO SIGNALS

Mark Kirkpatrick, assignor to BellSouth Intellectual Property Corporation
21 February 2006 (Class 455/567); filed 21 March 2002

This patent assumes that cellular telephone users crave access to a much greater variety of custom ring signals than is available from current commercial phones. The proposed solution is a snap-on auxiliary device

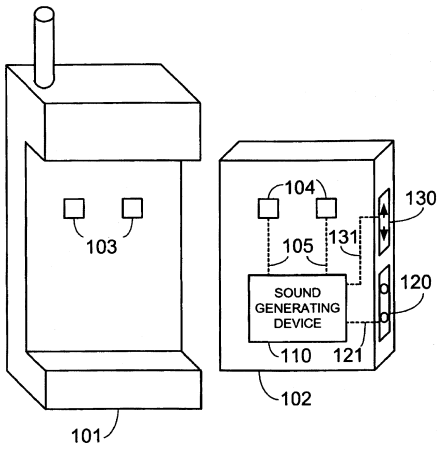

containing multiple digital sound files that can be edited as desired. Thus, the user can "scroll through a selection of audio files on the audio signal device, hearing the selections, and choosing one to be the designated alert signal for incoming telephone calls."—GLA

7,010,139

43.38.Si BONE CONDUCTING HEADSET APPARATUS

Kees Smeehuyzen, Delray Beach, Florida
7 March 2006 (Class 381/380); filed 2 December 2003

This patent describes "a bone conducting headset apparatus specifically designed for military and/or high decibel industrial environments." Rather than being incorporated into a military helmet, the device is light-

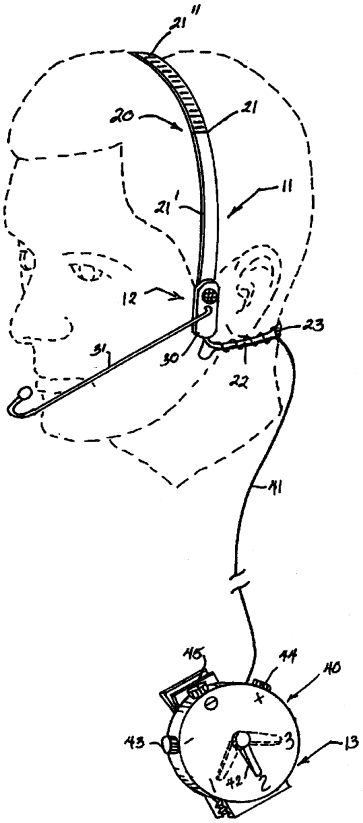

weight and self-contained. It includes a head strap and a neck strap to securely position microphone-speakers **12** plus an optional boom microphone **31**. A clip-on control box provides selection of several modes of operation, including "push-to-talk" operation.—GLA

7,003,119

43.38.Vk MATRIX SURROUND DECODER/ VIRTUALIZER

John Eric Arthur, assignor to Qsound Labs, Incorporated
21 February 2006 (Class 381/17); filed 31 March 1999

The patent describes methods of processing matrix-encoded stereo programs for playback over surround-sound loudspeaker arrays, taking into account certain differences among commercial surround encoding-decoding

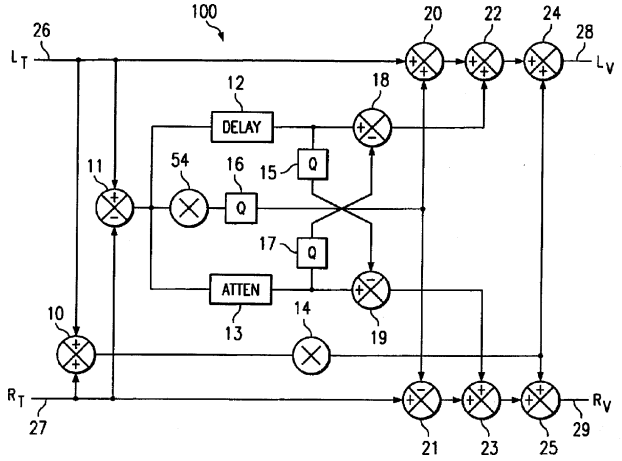

standards. Those elements in the figure labeled "Q" represent certain proprietary filters already described in earlier patents.—JME

7,003,467

43.38.Vk METHOD OF DECODING TWO-CHANNEL MATRIX ENCODED AUDIO TO RECONSTRUCT MULTICHANNEL AUDIO

William P. Smith *et al.*, assignors to Digital Theater Systems, Incorporated
21 February 2006 (Class 704/500); filed 6 October 2000

The patent text begins with a good summary of various multichannel formats for theater sound and notes that the majority of DVDs available to the home theater owner are supplied in a two-channel matrix encoded format. A method is then disclosed for decoding such two-channel audio in a way that more closely approximates discrete 5.1 recordings. "This is accom-

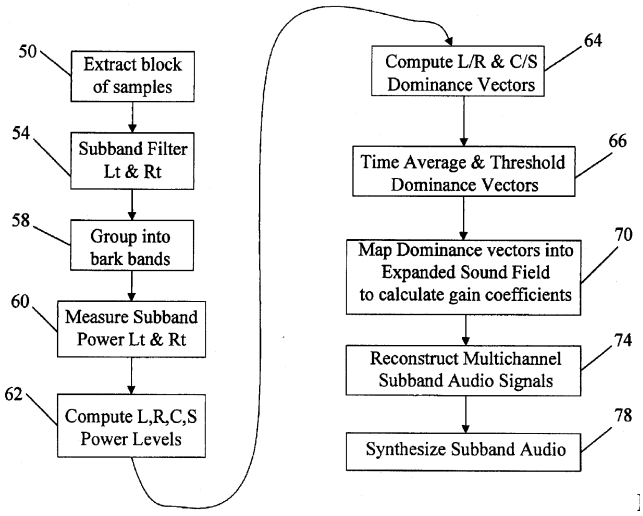

plished by subband filtering the two-channel audio, steering the subband audio within an expanded sound field that includes a discrete point with optimized gain coefficients for each of the speaker locations and then syn-

thesizing the multichannel subbands to reconstruct the multichannel audio."—GLA

7,010,128

43.38.Vk METHOD OF PROCESSING AND REPRODUCING AN AUDIO STEREO SIGNAL AND AN AUDIO STEREO SIGNAL REPRODUCTION SYSTEM

Christer Heed and Fredrik Gunnarsson, assignors to Embracing Sound Experience AB
7 March 2006 (Class 381/1); filed 25 November 1999

Closely spaced stereophonic loudspeakers, provided with a judicious amount of antiphase crosstalk, can give rise to an "out of bounds" localization of the stereo program for a listener precisely on-axis. The patent describes a simple way of doing this. First, the stereo L and R signals are added and subtracted to produce a sum signal **M** and a difference signal **S**. A simple signal attenuator α is placed in the **M** channel to reduce the level of the sum signal as the M-S pair is rematrixed to produce stereo **L**′ and **R**′

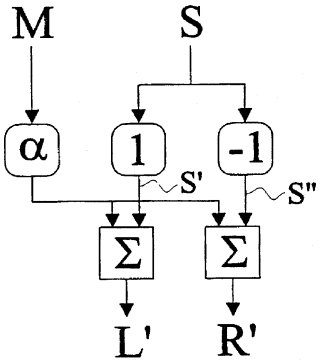

signals. With values of α in the range of a few dB, an on-axis listener in the near field of the loudspeakers will then hear a widened stereo image, produced by individual phasor relationships at each ear. All of this is included in a single package consisting of two loudspeaker systems. A small added baffle is mounted between the mid- and high-frequency transducers to heighten the effect at high frequencies. The techniques for doing this have been around for more than a half-century (Heegaard, J. Audio Eng. Soc., Vol. 40, No. 10).—JME

6,975,738

43.38.Vk TELEVISION SYSTEM WITH DIGITAL SOUND

Fuzhong Yang and Fayong Cai, both of Shenzhen, China
13 December 2005 (Class 381/306); filed in China 18 February 2000

Disclosed is a means of turning off the scanning and high-voltage circuits of a cathode ray tube (CRT) television set using a microprocessor

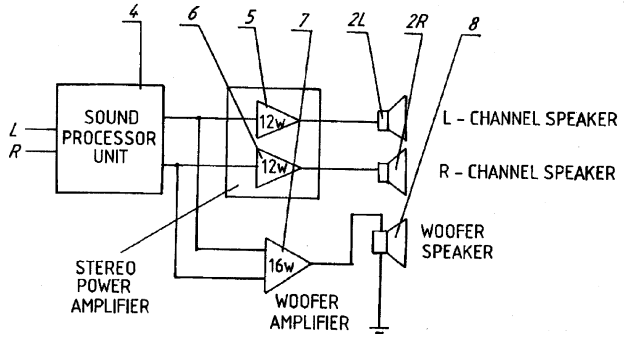

control board in response to a sound command signal. This is done so that only the sound system in the television consisting of sound processor unit **4**, amplifiers **5**, **6**, and **7**, and speakers **2L**, **2R**, and **8** are active. This is described in the concise patent description in less than two pages of text, including the single claim.—NAS

6,999,590

43.38.Vk STEREO SOUND CIRCUIT DEVICE FOR PROVIDING THREE-DIMENSIONAL SURROUNDING EFFECT

Chien Cheng Chen, assignor to Sunplus Technology Company, Limited
14 February 2006 (Class 381/1); filed 19 July 2001

A great many circuits have been developed to create pseudo-stereo from monophonic program material or to create an expanded sound field from two-channel stereo program sources. The simple circuit shown here

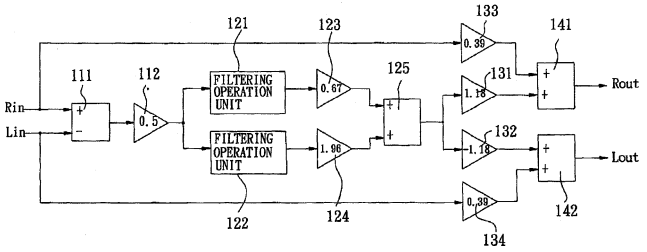

falls into the latter category. The two "filtering operation" units are bandpass filters centered at 318 Hz and 7.23 kHz. These two frequencies (three significant figures, no less) are specified explicitly in the patent claims.—GLA

6,997,887

43.40.Qi EVALUATION OF REFLECTED TIME-ENERGY PROFILE FOR DETERMINATION OF DAMPING CAPACITY

James C. Earthman, Irvine and Cherilyn G. Sheets, Newport Beach, both of California
14 February 2006 (Class 600/590); filed 25 September 2003

When a structure is subjected to an impact force, a stress wave is transmitted through the structure and causes deformation. As the structure deforms, it acts, in part, as a shock absorber, dissipating a portion of the mechanical energy associated with the impact. The ability of the structure to

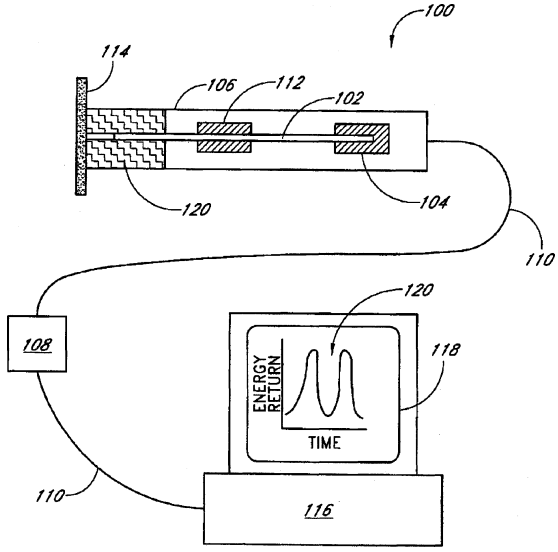

dissipate mechanical energy is referred to as the "damping capacity," which depends on the type and structural integrity of the materials forming the structure. This patent entails a method for measurement of the acoustic

damping capacity of a material or a structure, in particular, a layered honeycomb. The method consists of tapping the structure with a tapping rod, thereby imparting energy to the honeycomb structure. The energy reflected from the material is then measured over a specific time interval. A time-energy profile is created on the basis of the energy reflected from the honeycomb structure during that time internal. The evaluation of the time-energy profile determines the acoustic damping capacity of the honeycomb structure.—DRR

7,005,946

43.40.Sk MEMS PIEZOELECTRIC LONGITUDINAL MODE RESONATOR

Amy E. Duwel *et al.*, assignors to The Charles Stark Draper Laboratory, Incorporated
28 February 2006 (Class 333/187); filed 31 July 2003

The authors describe a fabrication method for a mechanical resonant bar for use in the 0.5–2-GHz regime. Their goal is to circumvent the shortcomings of traditional crystal and SAW devices in terms of Q factor in this frequency range. Their solution is to fabricate the resonant structure as a bar supported primarily at its center. This is very nice, but the concept of

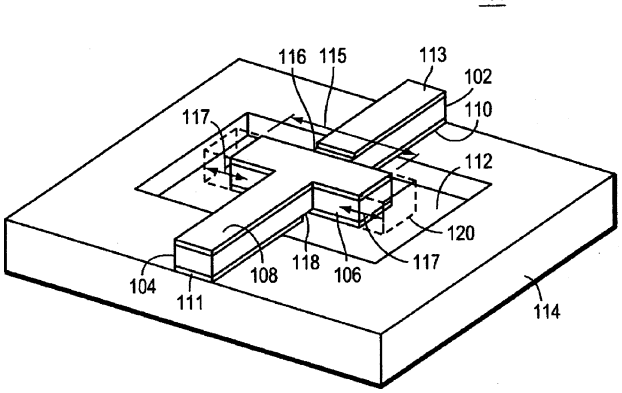

supporting a resonant bar at its nodes in order to minimize energy leakage has been known since the time of the ancient Greeks. While it is somewhat uncommon to operate these devices in the 3-1 mode as shown, this is not unheard of. Perhaps there is something novel about the electrode configuration, but it escapes this reviewer.—JAH

7,004,201

43.40.Tm VIBRATION ABSORBING HOSE

Tetsuya Arima *et al.*, assignors to Tokai Rubber Industries, Limited
28 February 2006 (Class 138/121); filed in Japan 23 June 2003

A pressure-resistant bellowslike hose, intended to reduce vibration transmission, is constructed of a multiplicity of rubber layers and reinforcing layers, with the latter made of braided yarns. Rings inserted in the ''valleys'' of the corrugations keep the hose from enlarging in the radial direction and longitudinal reinforcing yarns restrain elongation in the longitudinal direction.—EEU

7,007,896

43.40.Tm SHOCK AND VIBRATION ISOLATION SYSTEM

Kenneth N. Telford and Chris M. Paavola, assignors to The Boeing Company
7 March 2006 (Class 244/158 R); filed 13 November 2003

This system for connecting a spacecraft to a launch vehicle consists of a spring element that includes excursion limit stops and dampers. The spring element is configured essentially like two parallel plates that are connected to each other at only one pair of opposite edges and that have a gap between them. Bolts interconnecting the two plates with appropriately chosen clearances provide the desired limit stops. Damping is provided by arrangements in which a magnetic piston moves within a housing that contains magnetorheological fluid.—EEU

7,002,282

43.40.Tm SURFACE ACOUSTIC WAVE DEVICE AND METHOD OF FABRICATING THE SAME

Naoyuki Mishima, assignor to Fujitsu Media Devices Limited
21 February 2006 (Class 310/313 R); filed in Japan 28 January 2003

SAW chips in TV, VTR, DVD, and cell phone devices are often located on the device lid where flexure can perturb circuit performance. Lid flexure is not a problem for a 2 mm × 2mm 1-GHz SAW chip. Stressing flexure of lid **41** can be communicated to chip **1** via enclosure **10** through

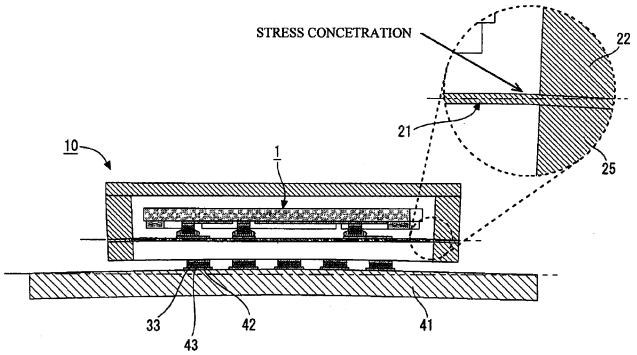

solder lands **42**, **43**, **33**. Enclosure **10** and card **21** are intentionally arranged to confine strain to be mainly at card **21** near enclosure sides **22** and **25**. The 18 claims include several mounting pad configurations.—AJC

7,003,380

43.40.Vn SYSTEM FOR COMPUTATIONALLY EFFICIENT ADAPTATION OF ACTIVE CONTROL OF SOUND OR VIBRATION

Douglas G. MacMartin *et al.*, assignors to Sikorsky Aircraft Corporation
21 February 2006 (Class 700/280); filed 27 February 2002

A sound and vibration control scheme is presented where a variety of sensors **128a**, **128b**, **128c**, and **128d** are placed on an airframe, and their

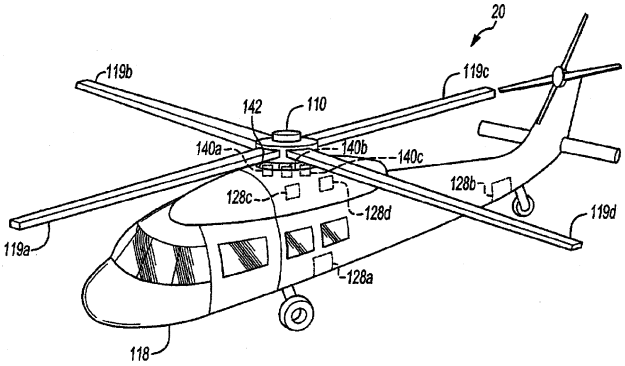

signals are processed by a T-matrix scheme using Cholesky decomposition to feed drive signals to actuators (not shown).—AJC

7,010,420

43.40.Vn VIBRATION CONTROLLER FOR ACTIVE VIBRATION INSULATORS AND METHOD FOR CONTROLLING VIBRATIONS FOR THE SAME

Hiroyuki Ichikawa *et al.*, assignors to Tokai Rubber Industries, Limited
7 March 2006 (Class 701/111); filed in Japan 13 April 2004

This patent describes an active-vibration insulator comprising a sensor **12** and a controller **20** that drives an actuator **26** to counteract the vibration motion of engine mount **16**. To reduce the computation load for the controller, module **20** includes a preconstructed data storage map **22** of a few common engine torque values versus frequency. Instantaneous local values are interpolated from these.—AJC

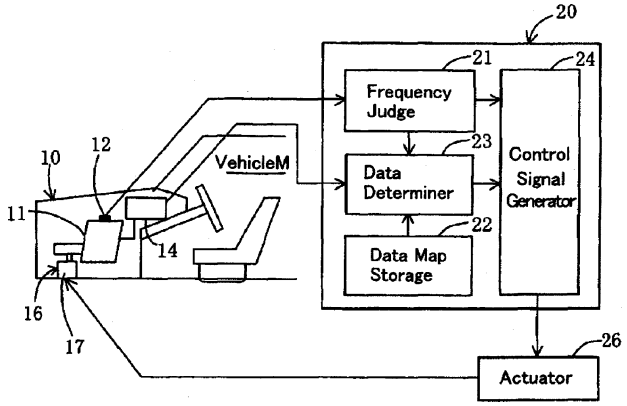

7,007,774

43.40.Yq ACTIVE HORIZONTAL VIBRATION REDUCING DEVICE FOR ELEVATOR

Kenji Utsunomiya *et al.*, assignors to Mitsubishi Denki Kabushiki Kaisha
7 March 2006 (Class 187/292); filed in Japan 29 July 2002

Active devices for limiting an elevator's horizontal vibrations, such as may be caused by insufficiently straight guide rails or sway of the building due to wind, typically employ vibration detection arrangements and application of forces to the guide rollers, actuated via electronic controllers and power amplifiers. In order to protect the active control apparatus from excessive current or voltage, as may occur when a passenger jumps about in the elevator cab, there are provided means for shutting down the control system during intervals in which the current exceeds a preselected value.—EEU

7,000,729

43.55.Ev FIVE-LAYER SOUND ABSORBING PAD: IMPROVED ACOUSTICAL ABSORBER

William W. Jacobsen, assignor to Acoustek Nonwovens
21 February 2006 (Class 181/290); filed 8 July 2003

This sound absorbing pad has five layers: an outer scrim, a protective film, a core of batt insulation, another film, and an outer scrim. The pad is flexible and compressible so it can be bunched up and then installed in a tight area and it will then expand to fill the void where it was placed. It can be used in this manner in an automobile for insulation in pillars, wheelhouses, roof rails, and such. And it could be used in a wall or ceiling or floor.—CJR

7,003,128

43.58.Vb HEARING DEVICE SET FOR TESTING A HEARING DEVICE

Maurice Boonen, assignor to Phonak AG
21 February 2006 (Class 381/322); filed 7 April 2003

We have here a hearing-device testset for evaluating hearing devices of the sort having an input acoustical/electrical converter, a computing unit, and an output electrical/acoustical converter. The device being tested may be an in-the-ear or outside-the-ear hearing aid, or it may be a consumer hearing device such as a headset, earpiece, earphone, active anti-noise device, etc. The testset consists of a box designed to properly hold at least one device being tested and an acoustic coupler applicable to the acoustical input and/or output of the tested device.—DRR

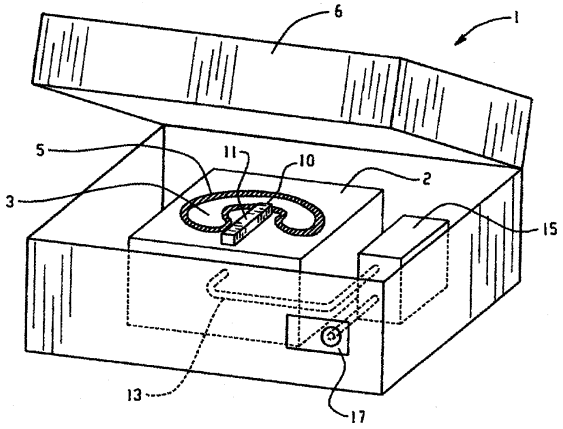

6,997,052

43.58.Wc VIBRATION LEVEL SENSOR

Siegbert Woehrle, assignor to VEGA Grieshaber KG
14 February 2006 (Class 73/290 V); filed in Germany 17 September 2002

A tuning fork resonator is employed to measure a level of liquid in a tank. Piezo sensors and tunable electrical circuitry measure variation in the resonant frequency of the fork immersed into the liquid. A change in the resonant frequency correlates with the level of liquid, as known in prior art. It is said that additional measurements of vibration amplitude can be used to detect a malfunction of the mechanical resonator due to various reasons including mechanical blockage, deposits, or damage to the resonator. The control logic and mechanical design are described in sufficient detail.—DMD

7,006,930

43.60.Cg METHOD OF ANALYZING TIRE PITCH SEQUENCE BASED ON LUG STIFFNESS VARIATIONS

Jon Irvin Stuckey, assignor to Bridgestone/Firestone North American Tire, LLC
28 February 2006 (Class 702/39); filed 21 August 2002

The author claims a superior tire noise analysis comprising a Fourier analysis of the arc lengths between tread lug road contacts combined with

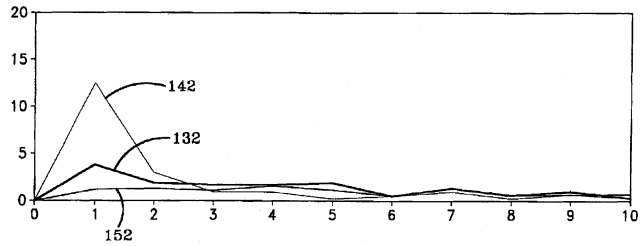

the stiffness (cross section) of each lug. (A ''lug'' is one individual block of tread rubber.) The resulting Fourier spectrum depicts the amplitude of harmonics of pattern repetition. Of three patterns, this analysis shows **142** to be worst with concentrated forces at the rate of pattern repetition, while pattern **152** is best with a broad range of low-amplitude forces.—AJC

7,002,281

43.60.Qv MULTI-REFLECTIVE ACOUSTIC WAVE DEVICE

Jeffrey C. Andle, assignor to BIODE Incorporated
21 February 2006 (Class 310/313 B); filed 16 July 2003

One side of a thin piezoelectric substrate **400** is either bare or coated with an enzyme or antibody material **470**. The other side has a SAW interdigital transducer (IDT) comprising stripes of a deposited conductor spaced 50%. Conductors in zone **410** are connected to a 160-MHz oscillator. Zone **430** is connected to an amplifier that may also replace the oscillator to form a feedback loop. The center zone **420** acts as a narrow-band filter. The input

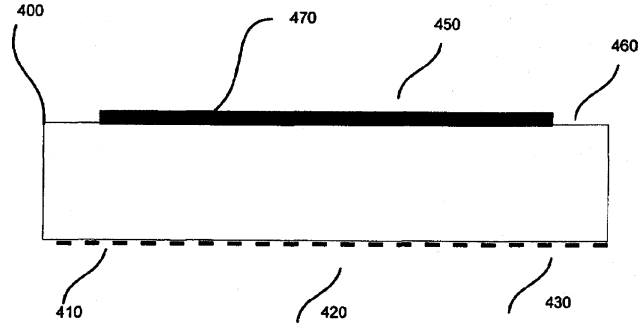

and output zones each contain about 200 conductor pairs, while the center filter has about 100 pairs. An additional set of ten electrode pairs is added at each outer end as ''guard'' electrodes. The arrangement is termed ''multi-reflective'' by the author. Presence of material **450** by the sensing surface **470** will vary the transmitted signal, or the operating frequency in the case of the feedback oscillator. The claims include adaptations for comparator circuitry, power absorption circuits, temperature compensation, etc.—AJC

7,003,123

43.60.Qv VOLUME REGULATING AND MONITORING SYSTEM

Dimitri Kanevsky *et al.*, assignors to International Business Machines Corporation
21 February 2006 (Class 381/72); filed 27 June 2001

This system will be a boon to those unable to detect when their headphones are playing at a deafening volume. ''A warning indicator indicates to the user that the volume is set too high.'' For the very lazy, the system can automatically reduce the volume in the event that it is too loud.—SAF

7,005,947

43.60.Qv SURFACE ACOUSTIC WAVE ELEMENT, FREQUENCY FILTER, OSCILLATOR, ELECTRONIC CIRCUIT, AND ELECTRONIC INSTRUMENT

Setsuya Iwashita *et al.*, assignors to Seiko Epson Corporation
28 February 2006 (Class 333/193); filed in Japan 26 March 2003

This author describes a specific cell phone device whose SAW chip consists of deposited single-crystal piezoelectric material of the lithium niobate family, using conventional cell telephone circuitry.—AJC

7,003,126

43.66.Ts DYNAMIC RANGE ANALOG TO DIGITAL CONVERTER SUITABLE FOR HEARING AID APPLICATIONS

Mead C. Killion and Dan Mapes-Riordan, assignors to Etymotic Research, Incorporated
21 February 2006 (Class 381/312); filed 15 November 2002

During high-level inputs, the dynamic range of an analog-to-digital (A-to-D) converter is extended by switching in a lower-gain preamplifier in front of the A-to-D converter. In another embodiment, a digital signal pro-

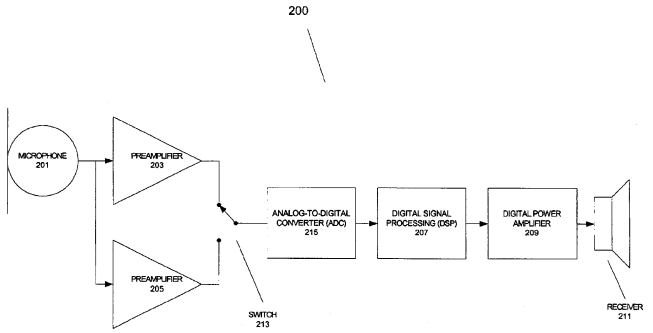

cessor selects outputs from a low-amplitude or a high-amplitude A-to-D converter, or both, depending on the input signal level.—DAP

7,006,646

43.66.Ts DEVICE FOR ADAPTING AT LEAST ONE ACOUSTIC HEARING AID

Herbert Baechler, assignor to Phonak AG
28 February 2006 (Class 381/314); filed 27 June 2000

An I2C- or I2S-type hi-directional communications interface is connected to a computerized fitting calculator, a hearing aid, and a patient response unit. The hearing aid wearer provides voice or keypad ratings about hearing aid-processed auditory stimuli. The communication interfaces meet electrical safety requirements for medical devices.—DAP

7,006,647

43.66.Ts HEARING AID WITH A MICROPHONE SYSTEM AND AN ANALOG/DIGITAL CONVERTER MODULE

Christoph Wuersch, assignor to Phonak AG
28 February 2006 (Class 381/324); filed 11 February 2000

A detachable EMI-shielded analog-to-digital converter module may be combined with different EMI-shielded housings containing various microphone assemblies.—DAP

7,003,127

43.66.Ts HEARING AID WITH LARGE DIAPHRAGM MICROPHONE ELEMENT INCLUDING A PRINTED CIRCUIT BOARD

Walter P. Sjursen *et al.*, assignors to Sarnoff Corporation
21 February 2006 (Class 381/322); filed 6 January 2000

A disposable hearing aid has an amplifier on a printed-circuit board with a ground plane that seals off the back volume of the microphone inside a metal housing. The combined assembly acts as an EMI shield for the microphone and amplifier. The large diaphragm of the microphone is divided by a support into several smaller active areas to produce low noise with a relatively high signal output.—DAP

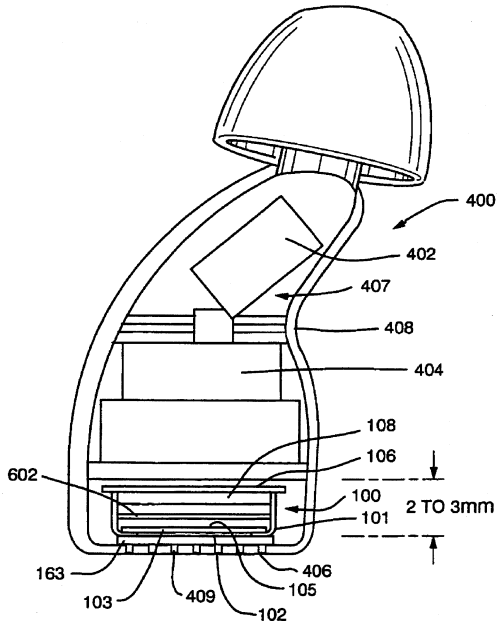

7,010,133

43.66.Ts METHOD FOR AUTOMATIC AMPLIFICATION ADJUSTMENT IN A HEARING AID DEVICE, AS WELL AS A HEARING AID DEVICE

Josef Chalupper and Patrick Mergell, assignors to Siemens Audiologische Technik GmbH
7 March 2006 (Class 381/312); filed in Germany 26 February 2003

The levels of speech and background noise are determined in multiple frequency bands. The resulting overall level of speech and noise, in combination with audiometric data, a speech comprehension model, and a loudness model, somehow determines time-segmented automatic updates for setting the gain in each frequency band.—DAP

7,010,132

43.66.Ts AUTOMATIC MAGNETIC DETECTION IN HEARING AIDS

Henry Luo *et al.*, assignors to Unitron Hearing Limited
7 March 2006 (Class 381/312); filed 3 June 2003

Either an acoustic or a magnetic input to a hearing aid is selected automatically by a magnetic signal detector based on whether audio information is present in the magnetic input signal. This invention is said to overcome shortcomings of systems that use magnetic switching sensors that are triggered by a dc magnetic field. Applicable systems include audio loops

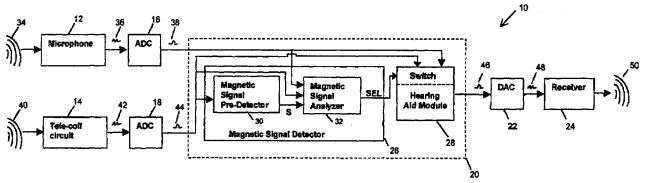

that do not have a dc magnetic field and phones with dc magnetic fields too weak to trigger the sensor.—DAP

7,003,876

43.66.Ts METHOD OF CONSTRUCTING AN IN THE EAR AUXILIARY MICROPHONE FOR BEHIND THE EAR HEARING PROSTHETIC

Scott A. Crawford and C. Geoffrey E. Fernald, assignors to Advanced Bionics Corporation
28 February 2006 (Class 29/859); filed 9 December 2003

An in-the-ear microphone is connected via a short tubing to the ear hook on the post auricular housing of a cochlear implant. Advantages over a post auricular microphone position are said to include better acoustical coupling to a telephone handset, less ambient noise pickup during telephone use, and acoustical advantages of the sound pickup in the concha rather than over the ear.—DAP

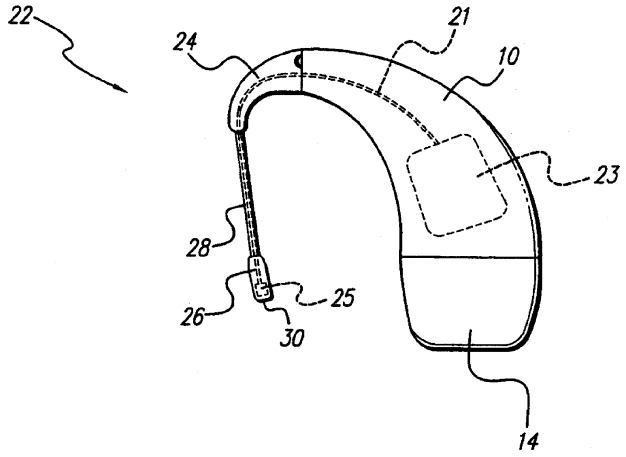

7,010,135

43.66.Ts METHOD TO DETERMINE A FEEDBACK THRESHOLD IN A HEARING DEVICE

Andreas Von Buol, assignor to Phonak AG
7 March 2006 (Class 381/318); filed 2 October 2002

The feedback threshold in a hearing aid fitting is useful to determine the maximum amount of amplification a hearing aid can provide on a wearer before becoming oscillatory. Maximum gain may be preset during fitting so the wearer will never be allowed to exceed this threshold. Methodology is recommended to determine the mechanical/acoustic feedback threshold of a hearing aid in multiple frequency bands while it is being worn.—DAP

7,010,134

43.66.Ts HEARING AID, A METHOD OF CONTROLLING A HEARING AID, AND A NOISE REDUCTION SYSTEM FOR A HEARING AID

Lars Baekgard Jensen, assignor to Widex A/S
7 March 2006 (Class 381/313); filed in Denmark 18 April 2001

To suppress multiple noise sources that are separated both spatially and in frequency, a directional hearing aid with band-limited delay processors consists of at least two omnidirectional microphones that produce adap

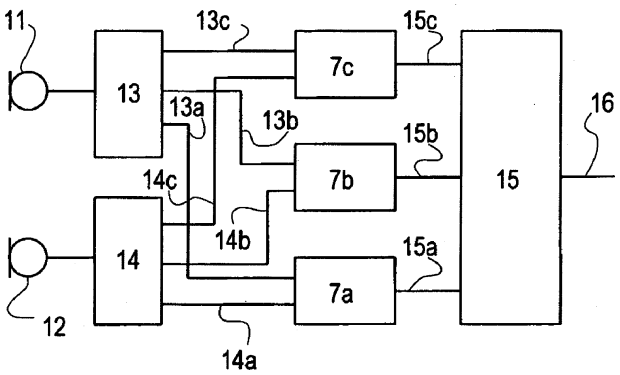

tively variable polar patterns. Automatic adjustment of the polar pattern in multiple frequency bands is implemented via sum and difference nodes in conjunction with varying the attenuation and time delay of the microphone outputs.—DAP

7,010,136

43.66.Ts RESONANT RESPONSE MATCHING CIRCUIT FOR HEARING AID

Randall W. Roberts *et al.*, assignors to Micro Ear Technology, Incorporated
7 March 2006 (Class 381/320); filed 17 February 1999

The frequency response of a hearing aid is tuned by a variable low-pass filter with overshoot, placed in series with the amplifier, to match the

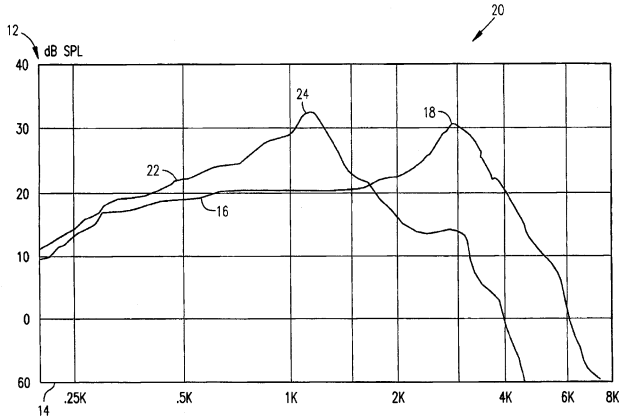

frequency response of the unaided ear canal of the hearing aid wearer.—DAP

7,010,137

43.66.Ts HEARING AID

Marvin A. Leedom *et al.*, assignors to Sarnoff Corporation
7 March 2006 (Class 381/328); filed 13 March 2000

The housing of a nonremovable custom battery used in a disposable hearing aid is designed to conform to the shape of a typical human ear canal between the aperture and first bend.—DAP

7,006,650

43.66.Vt DEVICE FOR ATTENUATING SOUND ON THE HUMAN EAR

Lars Wild, Bad Salzdetfurth, Germany
28 February 2006 (Class 381/380); filed in Germany 5 February 1999

Miniature radio receivers are incorporated into foam earplugs. This permits a base unit to send alarm signals to the wearer while preventing sleep interference from outside noise sources.—JE

6,999,924

43.72.Ar SYSTEM AND METHOD FOR CHARACTERIZING VOICED EXCITATIONS OF SPEECH AND ACOUSTIC SIGNALS, REMOVING ACOUSTIC NOISE FROM SPEECH, AND SYNTHESIZING SPEECH

Greg C. Burnett *et al.*, assignors to The Regents of the University of California
14 February 2006 (Class 704/233); filed 11 July 2002

Speech recognition and related applications would generally improve if the computer could somehow be absolutely certain whether or not someone's vocal cords were vibrating at a particular moment. This patent proposes to enhance speech recognition performance by adding a voicing detector which consists of a kind of electromagnetic analog to medical ultrasound. By placing a 2-GHz EM transmitter and receiver near a speaker's throat, it is possible to detect the motion of tracheal and esophageal tissue in sympathy with the vocal cords to sufficient accuracy to permit the reliable determination of a voicing condition during speech. The details of the EM radar technique are provided in previous patents.—SAF

7,003,455

43.72.Dv METHOD OF NOISE REDUCTION USING CORRECTION AND SCALING VECTORS WITH PARTITIONING OF THE ACOUSTIC SPACE IN THE DOMAIN OF NOISY SPEECH

Li Deng *et al.*, assignors to Microsoft Corporation
21 February 2006 (Class 704/233); filed 16 October 2000

This patent discloses a different method of noise reduction in which a speech signal is compared with a "noisy" version using feature vectors of each. This yields a collection of noise correction and scaling vectors and

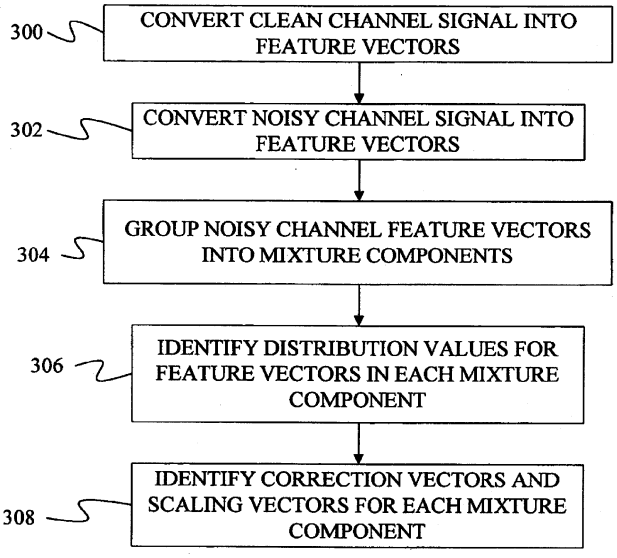

these can be applied when a noisy signal is later received to provide a noise-reduced feature vector. It is not immediately obvious how this scheme would work for arbitrary noise.—SAF

6,999,926

43.72.Fx UNSUPERVISED INCREMENTAL ADAPTATION USING MAXIMUM LIKELIHOOD SPECTRAL TRANSFORMATION

Dongsuk Yuk and David M. Lubensky, assignors to International Business Machines Corporation
14 February 2006 (Class 704/244); filed 23 July 2001

Maximum likelihood methods select modeling parameters with the goal of maximizing the probability of the actual observations given the model. This patent offers a method of speaker adaptation in this spirit, in which a speech signal's cepstral feature vectors are transformed by the transformation yielding the maximum likelihood for the actual speech under the recognition models.—SAF

6,999,929

43.72.Fx RECOGNIZING SPEECH BY SELECTIVELY CANCELING MODEL FUNCTION MIXTURE COMPONENTS

Ralf Kompe and Silke Goronzy, assignors to Sony International (Europe) GmbH
14 February 2006 (Class 704/255); filed in the European Patent Office 6 September 2000

An approach to speaker adaptation in a speech recognition system is proposed, which involves modifying the acoustic models by removing mixture components which make a negligible contribution to the description of the incoming signal. The objective is to reduce acoustic model size in a speaker adaptive fashion, resulting in improved system efficiency even for large speaker-independent recognizers.—SAF

7,003,458

43.72.Fx AUTOMATED VOICE PATTERN FILTER

Kai-Ten Feng *et al.*, assignors to General Motors Corporation
21 February 2006 (Class 704/236); filed 15 January 2002

It is proposed to add to a typical distributed client-server speech recognition setup a ''voice pattern filter,'' which would attempt to make a speaker's voice (client side) better conform to the speech recognition models (server side) by adjusting the spectral characteristics during the transmission. Some details are provided, but the patent is extremely terse.—SAF

7,003,465

43.72.Fx METHOD FOR SPEECH RECOGNITION, APPARATUS FOR THE SAME, AND VOICE CONTROLLER

Keiko Morii and Yoshio Ohno, assignors to Matsushita Electric Industrial Company, Limited
21 February 2006 (Class 704/275); filed in Japan 12 October 2000

A speaker-adaptive scheme is devised for a speech recognition system in which a first input utterance is used to select a best ''training pattern'' from among a training set of such models which are classified by speaker. This is similar to selecting a speaker model, only on a pattern-by-pattern basis, it seems. The best selected pattern is then compared to the input to determine a ''distortion coefficient'' that measures the degree of difference in the spectra between training and input speech. Said spectral difference is then applied in further recognition attempts for the speaker at hand.—SAF

6,963,838

43.72.Ja ADAPTIVE HOSTED TEXT TO SPEECH PROCESSING

Jacob Christfort, assignor to Oracle International Corporation
8 November 2005 (Class 704/260); filed 3 November 2000

This speech generator system uses a combination of audio waveform playback and speech synthesis, synthesizing items which are not available in an audio form. The notable feature is that statistical records are kept of synthesized words and when, as determined by the statistics, a word's frequency of use would justify having a recording made, the system prompts for such a recording. The approach would seem to lead to a conglomeration of speaking styles in the stored items.—DLR

7,003,082

43.72.Kb SYSTEM FOR TEXT ASSISTED TELEPHONY

Robert M. Engelke and Kevin Colwell, assignors to Ultratec, Incorporated
21 February 2006 (Class 379/52); filed 5 August 2003

This appears to be another variation of a system for providing telephone services to people with hearing difficulties by providing captioning. Two telephone lines are involved. The arrangement is this: a personal interpreter-captioned telephone device dials a relay on a second telephone

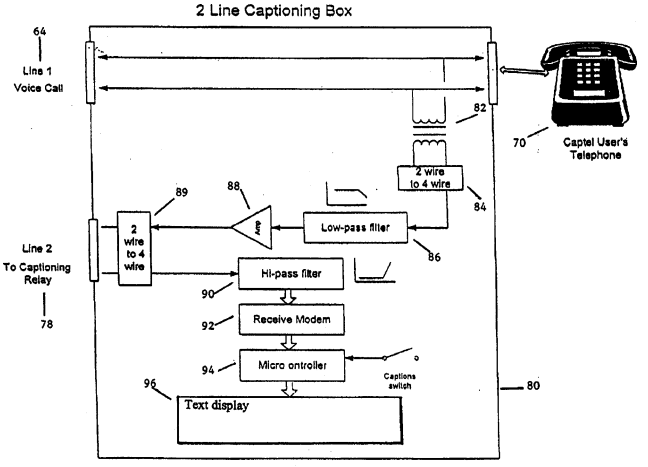

line while the assisted user is conversing with a hearing user over a first telephone line. The second telephone line connects to a relay that provides voice-to-text translation service and returns, a text stream to the captioned telephone device.—DRR

7,006,604

43.72.Kb RELAY FOR PERSONAL INTERPRETER

Robert M. Engelke, assignor to Ultratec, Incorporated
28 February 2006 (Class 379/52); filed 14 July 2003

This is a relay to facilitate communication between hearing users and users who need or desire assistance in understanding verbal communications over a telephone system. In order to circumvent the delay inherent in typing, the call assistant at the relay does not type most words but, instead, revoices the words spoken by the hearing user into a voice recognition program trained to the voice of the call assistant. The text stream generated by the computer and the voice of the hearing user are both sent to the assisted user so that the latter is supplied with a visual text stream to supplement the

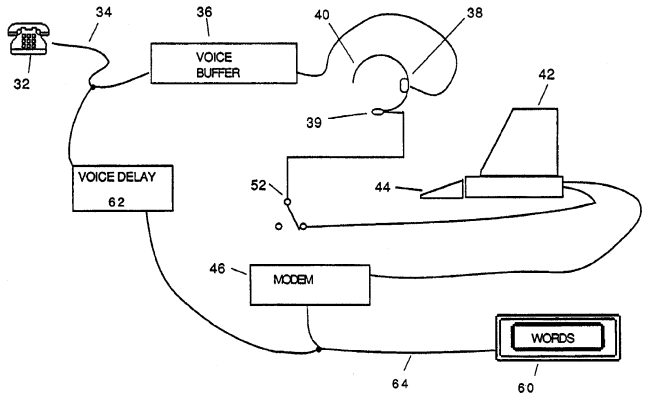

voice communications. A time delay in transmitting the voice of the hearing user through the relay helps the assisted user to better comprehend the communications session.—DRR

7,010,481

43.72.Lc METHOD AND APPARATUS FOR PERFORMING SPEECH SEGMENTATION

Takuya Takizawa, assignor to NEC Corporation
7 March 2006 (Class 704/220); filed in Japan 28 March 2001

This patent presents an approach to dividing a speech signal into phone-sized segments. It appears that the speech is intended to be also entered as a text string, because the general method here involves comparing a synthesized speech signal corresponding to the spoken text with the actual speech signal. A dynamic programming matching operation is then carried out in an effort to segment the input speech in accordance with the actual segments in the synthesized speech.—SAF

6,963,832

43.72.Ne MEANING TOKEN DICTIONARY FOR AUTOMATIC SPEECH RECOGNITION

Michael Vanhilst, assignor to Hewlett-Packard Development Company, L.P.
8 November 2005 (Class 704/9); filed 9 October 2001

The lexicon of this speech recognition system would be semantically organized. Lexical entries, with keys referred to as ''meaning tokens,'' also include sets of related words. When any of these words appears in the speech input, the key meaning token is listed in a semantic structure being built for that input. Clearly, multiple lexical entries may contain words

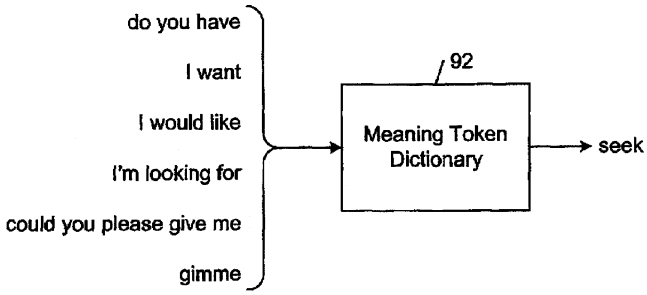

which match each word in the input, a situation not well covered in the patent. Perhaps the intended domain is too small for that. A rule-based language analyzer would then ''extract meaning from the sequence of meaning tokens.'' The acoustic/phonetic recognition system is not discussed except to note its presence.—DLR

6,963,834

43.72.Ne METHOD OF SPEECH RECOGNITION USING EMPIRICALLY DETERMINED WORD CANDIDATES

Matthew W. Hartley *et al.*, assignors to International Business Machines Corporation
8 November 2005 (Class 704/235); filed 29 May 2001

This speech recognizer produces a confidence score along with each of several word candidates found by the sketchily specified acoustic recognizer. The confidence scores are then used by an *n*-best procedure to pick the recognized word. It seems clear that the patent has nothing new to say and should not have been granted.—DLR

6,963,836

43.72.Ne SPEECHDRIVEN SETTING OF A LANGUAGE OF INTERACTION

Henricus Antonius Wilhelmus Van Gestel, assignor to Koninklijke Philips Electronics, N.V.
8 November 2005 (Class 704/251); filed in the European Patent Office 20 December 2000

This voice-operated device controller recognizes the spoken device command, but also identifies the language used by the speaker. Obviously, for this to work, the range of possible input commands must be sharply limited. This is accomplished by defining the recognition vocabulary as consisting of commands for a specific machine, such as a CD player. Possible commands are then such things as ''stop,'' ''play,'' ''louder,'' ''softer,'' and a few other similar actions. The general context is a video-system set-top box. As described, the device can handle six common European languages.—DLR

6,999,925

43.72.Ne METHOD AND APPARATUS FOR PHONETIC CONTEXT ADAPTATION FOR IMPROVED SPEECH RECOGNITION

Volker Fischer *et al.*, assignors to International Business Machines Corporation
14 February 2006 (Class 704/243); filed in the European Patent Office 14 November 2000

This patent proposes a method for adapting a speech recognition system to a specific domain of application. A generic speech recognizer is used as a starting point, from which a second, more domain-specific, recognizer is produced by simply re-estimating the parameters of the generic decision network and phonetic context values when provided with new domain-specific training data.—SAF

7,003,460

43.72.Ne METHOD AND APPARATUS FOR AN ADAPTIVE SPEECH RECOGNITION SYSTEM UTILIZING HMM MODELS

Udo Bub and Harald Höge, assignors to Siemens Aktiengesellschaft
21 February 2006 (Class 704/256); filed in Germany 11 May 1998

An effort is described by which a typical hidden Markov modeling approach to speech recognition could be made adaptive to new speaking styles or even out-of-vocabulary utterances by means of ''splitting'' the probability density function used for acoustic modeling. It is envisioned that splitting the density can ''create new regions in a feature space erected by the feature vectors, these new regions comprising significant information ...

and thus assuring an improved recognition.'' Although the idea is presented in some detail, the patent language obscures its essence.—SAF

7,006,969

43.72.Ne SYSTEM AND METHOD OF PATTERN RECOGNITION IN VERY HIGH-DIMENSIONAL SPACE

Bishnu Saroop Atal, assignor to AT&T Corporation
28 February 2006 (Class 704/238); filed 1 November 2001

Although not strictly acoustic in nature, this patent deserves some attention for its revival of the ''hypersphere'' method of pattern recognition in a speech recognition context. Feature vectors associated with phonemes in speech recognition systems are indeed very high-dimensional, and this patent invokes a number of public-domain results, some of which are quite old, in an effort to improve upon the classification performance of typical Gaussian mixture approaches. The main innovation involves geometric transformation of both training and input sounds into a hypersphere shape, in order to locate clusters so that they have maximal separation and minimal overlap. The general approach of hyperspherical pattern recognition can be found in the papers cited.—SAF

6,999,928

43.72.Pf METHOD AND APPARATUS FOR SPEAKER IDENTIFICATION USING CEPSTRAL COVARIANCE MATRICES AND DISTANCE METRICS

Zhong-Hua Wang *et al.*, assignors to International Business Machines Corporation
14 February 2006 (Class 704/250); filed 21 August 2001

A common method for speaker identification is further developed, which computes a number of distance metrics between cepstral covariance matrices. This includes an effort to compensate for the speaker's telephone handset. Although the metrics are the chief innovation, they all seem to be *ad hoc*, and no basis for their success is provided here besides references to the literature.—SAF

7,006,638

43.80.Qf ELECTRONIC STETHOSCOPE

Knud Erik Baekgaard and Torben Naurbo Dalgaard, assignors to Bang & Olufsen Technology A/S
28 February 2006 (Class 381/67); filed in Denmark 30 August 1994

This electronic stethoscope consists of a vibration transducer, an amplifier, provisions for accommodating a headphone, and at least one digital filter with a transfer function corresponding to at least one acoustic stethoscope type. While the signals will correspond to those learned, the stethoscope bears the advantages of greater amplification, elimination of noise sources, and compensation for an individual physician's hearing loss. With stereoscopic embodiments, sound-frequency distributions can be transformed into spatial or temporal sound distributions perceivable by the user, thereby facilitating, for example, the detection of heart murmurs and measurement of blood pressure.—DRR

7,010,342

43.80.Qf METHOD AND APPARATUS FOR DETECTING AND TRANSMITTING ELECTRICAL AND RELATED AUDIO SIGNALS FROM A SINGLE, COMMON ANATOMICAL SITE

Peter M. Galen *et al.*, assignors to Inovise Medical, Incorporated
7 March 2006 (Class 600/513); filed 14 March 2003

For the purpose of body-activity monitoring, this apparatus utilizes a remote, reusable or disposable, combined electrical/audio sensor to simultaneously pick up an electrical signal and site-related audio signal for coupling to external monitoring apparatus. A preferred embodiment for the purpose of heart monitoring entails a small, largely self-contained sensor unit, in which an audio transducer (e.g., a small microphone) is combined with a common detection axis with an acoustic and shrouding structure. This structure has an opening, like a circular mouth, which is defined, at least in part, by an annular electrical conductor that functions as an electrically conductive element for picking up an ECG electrical signal.—DRR

6,999,592

43.80.Qf TIME AND FREQUENCY WINDOWED POCKET CARDIAC STETHOSCOPE

William E. Chelen, Pittsburgh, Pennsylvania
14 February 2006 (Class 381/67); filed 8 August 2002

This electronic stethoscope allows the electronic selection of portions of the cardiac cycle to be amplified and tuned, so as to be more easily heard and identified. An automatic compensation for cardiac size is provided through an automatic gain control to precisely establish the beginning of each cardiac cycle. The main objects of the device are (a) to provide for the selection of a time window for selective variable amplification, (b) to provide frequency windowing/bandpass tuning of the phonocardiogram signal, and (c) to provide automatic processing of all necessary functions, save

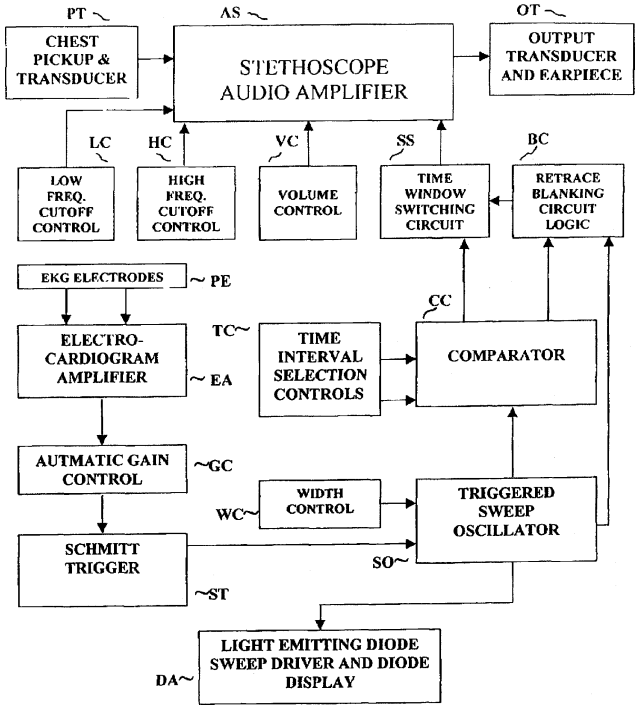

those of the operator-selected time and frequency parameters. The device, which is miniaturized to permit it to be carried in, say, a shirt pocket and used in a clinic or at bedside, is based on the electrocardiographic QRS complex/electronic Schmitt trigger of a sweep generator and comparator. The synchronization signal, in connection with manual user inputs, allows

for the control of digital/analog switching of on/off time intervals of a variable frequency-response electronic stethoscope.—DRR

7,003,121

43.80.Qf METHOD AND AN APPARATUS FOR PROCESSING AN AUSCULTATION SIGNAL

Lars Arknæs-Pedersen, assignor to Bang & Olufsen Technology A/S
21 February 2006 (Class 381/67); filed in Denmark 8 April 1998

The object of the method and apparatus is to provide a technique that slows down sound signals, particularly sound signals representing auscultation signals such as heart sounds, while still obtaining the original pitch with a minimum of echo in the resulting slow-downed signal. The method involves processing an input sound signal so that it is divided in time into multiple signal segments, each with a specific time duration. The signal

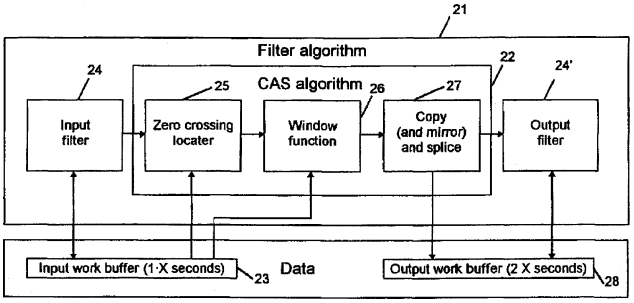

segments are processed into an output signal of successive signal segments, processing these in such a manner that at least one but preferably all signal segments are repeated at least once in the output signal. Each signal segment is established such that the time duration of substantially all the equal segments is less than 50 ms.—DRR

7,001,335

43.80.Sh ULTRASONIC WAVE GENERATING/ TRANSMITTING APPARATUS

Kazunari Adachi and Tsuneyoshi Sugimoto, assignors to Aisin Kiko Company, Limited
21 February 2006 (Class 600/437); filed in Japan 21 December 2000

This ultrasonic generating and transmitting apparatus is designed for use in destruction of calculi, such as biliary calculus and renal calculus, destruction of cancerous cells, and ultrasonic cleaning. The device is essentially a generating/transmission system equipped with an ultrasonic vibrator

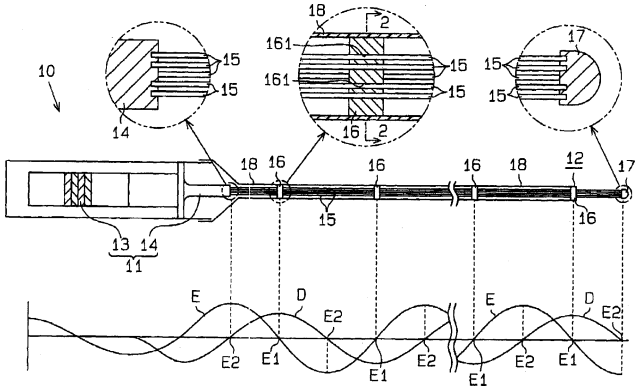

section and a transmission section for transmitting ultrasonic vibration from the vibrating section. Multiple linear members are provided for transmitting vibration and binding plates that bind the linear members in such a manner that they are apart from one another.—DRR

7,004,940

43.80.Sh DEVICES FOR PERFORMING THERMAL ABLATION HAVING MOVABLE ULTRASOUND TRANSDUCERS

Thomas P. Ryan and Gennady Kleyman, assignors to Ethicon, Incorporated
28 February 2006 (Class 606/41); filed 10 October 2002

Thermal ablation therapy is provided by a hand-held device having one or more transducer assemblies that can be activated to emit ultrasound energy capable of ablating tissue. These transducer assemblies are movable

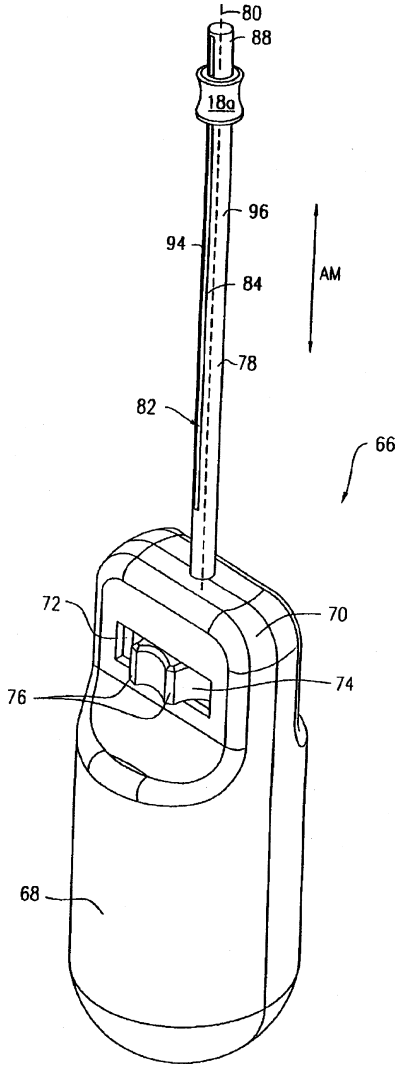

relative to the handle and can be adjusted to appropriate positions relative to the tissues to be ablated.—DRR

7,001,355

43.80.Sh SKIN CARE DEVICE

Mahito Nunomura *et al.*, assignors to The Procter & Gamble Company
21 February 2006 (Class 604/22); filed in Japan 21 January 2002

This is a device for introducing a skin care agent through the skin into the human body by ultrasonic penetration. The penetrating composition consists of a specific amount of the skin agent, a viscosifying agent that provides the composition with a viscosity in the range from approximately 1000

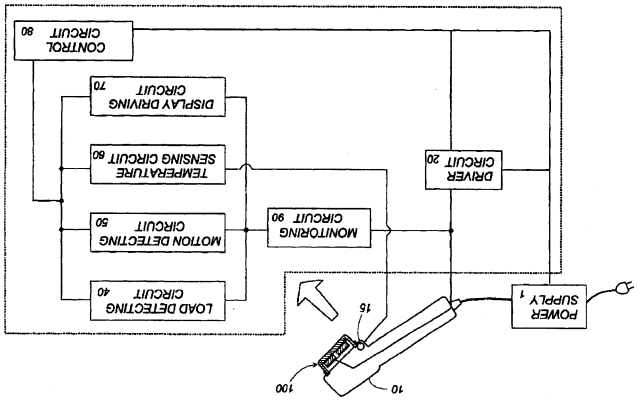

mPas to 106 MPas, 0.1% to 30% of a water soluble humectant, and an aqueous carrier. The ultrasound apparatus consists of (a) an application element for applying ultrasound to the skin at a frequency of around 3 to 10 MHz and an intensity ranging from 0.1 to 2 W/cm^2 and (b) a control element to adjust conditions of the application element.—DRR

6,997,875

43.80.Vj ACOUSTIC BORDER DETECTION USING POWER MODULATION

George A. Brock-Fisher and David M. Prater, assignors to Koninklijke Philips Electronics N.V.
14 February 2006 (Class 600/443); filed 8 April 2002

Two ultrasonic beams, each at a different power level, are transmitted after a contrast agent is present in the region of interest. Echoes from the beams are processed to detect a phase change that occurs at the boundary of tissue and blood-containing contrast agent. The time of the phase change is used to identify the position of the boundary.—RCW

6,997,876

43.80.Vj ULTRASOUND CLUTTER FILTERING WITH ITERATIVE HIGH PASS FILTER SELECTION

Larry Y. L. Mo *et al.*, assignors to Zonare Medical Systems, Incorporated
14 February 2006 (Class 600/455); filed 16 April 2004

Ultrasound colorflow imaging data are separated from low-frequency Doppler clutter signals by using a high-pass filter with a low-frequency cutoff that is adjusted iteratively on a point-by-point or region-by-region basis dynamically in real time.—RCW

7,004,904

43.80.Vj IMAGE ENHANCEMENT AND SEGMENTATION OF STRUCTURES IN 3D ULTRASOUND IMAGES FOR VOLUME MEASUREMENTS

Vikram Chalana *et al.*, assignors to Diagnostic Ultrasound Corporation
28 February 2006 (Class 600/443); filed 31 July 2003

A volume of an organ or fluid-filled structure is located and measured by applying a segmentation algorithm to a sequence of two-dimensional images for the estimation of areas in cross sections that span the volume of interest.—RCW

7,004,905

43.80.Vj FINITE AMPLITUDE DISTORTION-BASED INHOMOGENEOUS PULSE ECHO ULTRASONIC IMAGING

Ted Christopher, assignor to Research Corporation Technologies, Incorporated
28 February 2006 (Class 600/443); filed 23 March 2004

Echos are processed from an ultrasound beam at a power level that produces first-order and higher-order signal components as it propagates through tissues and an image is formed from one of the higher-order signal components.—RCW

7,004,906

43.80.Vj CONTRAST AGENT IMAGING WITH AGENT SPECIFIC ULTRASOUND DETECTION

Ismayil M. Guracar *et al.*, assignors to Siemens Medical Solutions USA, Incorporated
28 February 2006 (Class 600/447); filed 26 July 2004

Ultrasonic contrast agent velocity is determined from the third order of the fundamental signal and displayed along with the amount of energy using a map indexed by both energy and velocity.—RCW

LETTERS TO THE EDITOR

Prediction of absolute thresholds and equal-loudness contours using a modified loudness model (L)

Brian R. Glasberg[a] and Brian C. J. Moore[b]
Department of Experimental Psychology, University of Cambridge, Downing Street, Cambridge CB2 3EB, England

(Received 16 February 2006; revised 19 May 2006; accepted 22 May 2006)

The loudness model described by Moore *et al.* [J. Audio Eng. Soc. **45**, 224–240 (1997)] forms the basis for a recent ANSI standard for the calculation of the loudness of steady sounds. However, the model does not give accurate predictions of the absolute thresholds published in a recent ISO standard. Here it is described how the assumed middle-ear transfer function in the model can be modified to give more accurate absolute threshold predictions. The modified model also gives reasonably accurate predictions of the equal-loudness contours published in a recent ISO standard. © *2006 Acoustical Society of America.* [DOI: 10.1121/1.2214151]

PACS number(s): 43.66.Cb, 43.66.Ba [AJO] Pages: 585–588

I. INTRODUCTION

The recently published ANSI standard for calculation of the loudness of steady sounds (ANSI, 2005) is based on the loudness model of Moore *et al.* (1997). The model gives reasonably accurate predictions of a wide range of data on loudness perception (Moore *et al.*, 1997; Chouard, 1997; Subedi *et al.*, 2004). However, the equal-loudness contours predicted by the model (shown as the dotted lines in Fig. 1) differ substantially from those in the ISO standard that was applicable at the time (ISO 226, 1987), which were based on the data of Robinson and Dadson (1956).

A revised ISO standard for equal-loudness contours has recently been published (ISO 226, 2003), based on the data from several different laboratories (Suzuki and Takeshima, 2004); these contours are shown as the solid lines in Fig. 1. The 1997 model predicts these new contours reasonably well (Suzuki and Takeshima, 2004). However, some discrepancies remain. In particular, the shapes of the contours predicted by the model for frequencies between 1 and 6 kHz differ from those in the standard. One reason for the discrepancy is that the 1997 model was designed to give accurate predictions of the absolute threshold for pure tones presented in free field with frontal incidence (binaural listening), as published in ISO 389-7 (1996). These absolute thresholds differ in value and in form as a function of frequency from those used in the standard for the equal-loudness contours (ISO 226, 2003).

Recently, a revised standard for the absolute threshold for pure tones presented in free field with frontal incidence has been published (ISO 389-7, 2005). This revised standard is consistent with the latest standard for equal-loudness contours (ISO 226, 2003). In the present paper, we describe how the 1997 model has been modified so as to predict accurately the absolute thresholds in ISO 389-7 (2005). With this revision, the loudness model also gives somewhat more accurate predictions of the equal-loudness contours in ISO 226 (2003).

II. OUTLINE OF THE MODEL

To help the reader understand the modifications to the model, we first give a brief outline of the stages of the model (Moore *et al.*, 1997).

A. Transmission through the outer ear

For a sound presented in free field from a frontal direction, the transformation from free-field sound pressure (measured in the absence of the listener at the position corresponding to the center of the listener's head) to eardrum sound pressure was assumed to be as specified in Shaw (1974). At 1 kHz, this function has a value of +2.6 dB; the sound level at the eardrum is 2.6 dB higher than the free-field level. Similar values for the free field to eardrum transformation are given in recent standards (ISO 11904-1, 2002; ISO 11904-2, 2004). In the computer program implementing the loudness model, the function is represented as a table of values (with smooth interpolation). Therefore, it is easy to incorporate the transformations corresponding to other directions of sound incidence.

[a]Electronic mail: bgl2@cus.cam.ac.uk
[b]Author to whom correspondence should be addressed. Electronic mail: bcjm@cam.ac.uk

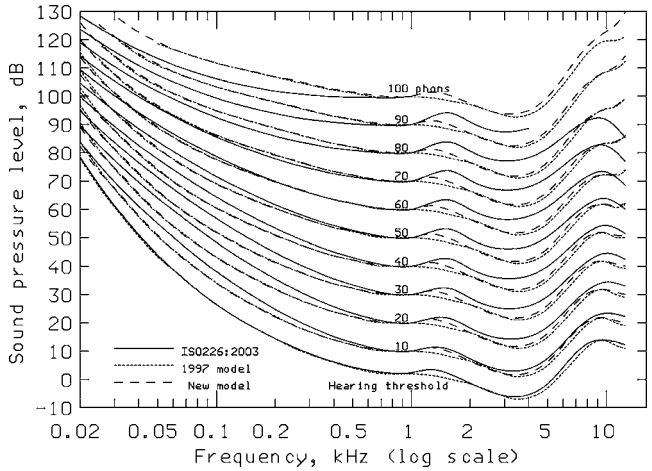

FIG. 1. The bottom curves show the absolute thresholds (free field, frontal incidence, binaural listening) predicted by the original (1997) model (dotted line), the modified model (dashed line), and as published in ISO 389-7 (2005, solid line). The other curves show equal-loudness contours as predicted by the original model, the modified model, and as published in ISO 226 (2003) (dotted, dashed, and solid lines, respectively).

B. Transmission through the middle ear

Above 0.5 kHz, the function describing transmission through the middle ear (the ratio of sound pressure in the cochlea to sound pressure at the eardrum) is assumed to be similar in form to the absolute threshold curve (minimum audible pressure at the eardrum) but inverted in shape. This is based on the assumption that the cochlea is equally sensitive to all frequencies in the range 0.5 to about 15 kHz. The transmission function above 0.5 kHz was based on the absolute thresholds specified in ISO 389-7 (1996). Below 0.5 kHz, middle-ear transmission is assumed to "roll off," in a manner broadly consistent with the data of Puria *et al.* (1997) and Aibara *et al.* (2001). The whole transmission function is scaled so that its value at 1 kHz is −2.6 dB. Thus, for a 1-kHz tone presented in free field with frontal incidence, the gain produced by the outer ear is canceled by the loss produced by the middle ear, and the effective level of the tone reaching the cochlea is equal to its free-field level. This is done for computational convenience.

C. Calculation of the excitation pattern

The excitation pattern is calculated from the effective spectrum reaching the cochlea, i.e., the spectrum after filtering to allow for the effects of transmission through the outer and middle ear. The excitation pattern evoked by a given sound is defined as the output from the auditory filters, plotted as a function of filter center frequency, in response to that sound. The method of calculating excitation patterns is essentially as described by Glasberg and Moore (1990), except that the constant 0.38 in their Eq. (5) is changed to 0.35.

It is assumed that auditory filter center frequencies are limited to the range 0.05–15 kHz. Signals with extremely low and high frequencies are detected because they produce outputs from filters tuned below or above those frequencies (Buus *et al.*, 1986; Ruggero and Temchin, 2002; Ashihara *et al.*, 2006; Yasin and Plack, 2005). The frequency scale of the excitation pattern is transformed to the ERB_N-number scale (Glasberg and Moore, 1990; Moore, 2003), where ERB_N stands for the mean value of the equivalent rectangular bandwidth of the auditory filter as determined using young, normally hearing listeners at moderate sound levels.

D. Variation in the excitation required for absolute threshold as a function of frequency

The absolute threshold at low frequencies rises somewhat more steeply with decreasing frequency than the assumed transmission characteristic of the middle ear. To account for this, it is assumed that the excitation level at absolute threshold increases with decreasing frequency below 0.5 kHz. The rise may be due to reduced gain from the cochlear active mechanism (Yates, 1995; Sellick *et al.*, 2006) and to the shunting effect of the helicotrema (Cheatham and Dallos, 2001). Above 0.5 kHz, the excitation at absolute threshold is assumed to be constant. The excitation level at absolute threshold was chosen for each frequency below 0.5 kHz so as to predict the binaural absolute thresholds in ISO 389-7 (1996). However, predicted absolute thresholds at low frequencies depend both on the assumed transmission characteristic of the middle ear and on the excitation required to reach threshold at each frequency.

E. Transformation from excitation to specific loudness and summation across frequency and ears

The excitation at each center frequency is transformed to specific loudness, N', which is the loudness per ERB_N. The transform involves a compressive nonlinearity, and the amount of compression is assumed to decrease for center frequencies below 0.5 kHz. Full details are given in Moore *et al.* (1997). The overall loudness of a sound for monaural presentation is obtained by summing the specific loudness across the whole ERB_N-number scale. For binaural presentation, the overall loudness is obtained by summation of the loudness at the two ears, which is broadly consistent with empirical data (Fletcher and Munson, 1933; Hellman and Zwislocki, 1963; Chouard, 1997). For diotic presentation, the overall loudness is double that for each ear separately.

F. Conversion from sones to phons

The output of the model is a loudness estimate in sones, where 1 sone is defined as the loudness of a 1-kHz tone with a level of 40 dB SPL presented binaurally in free field with frontal incidence. A table relating loudness in sones to loudness level in phons is generated by using as input to the model a 1-kHz tone with various levels. That table (with interpolation) is used to give a predicted loudness level for any input sound.

III. MODIFICATION OF THE MODEL

It is assumed in the model that a sound at absolute threshold has a small fixed loudness of 0.003 sones, which is equivalent to a loudness level of 2.2 phons. Based on this assumption, the absolute threshold for a pure tone of a given frequency can be predicted by using a tone of that frequency as input to the model, and adjusting the input level until the

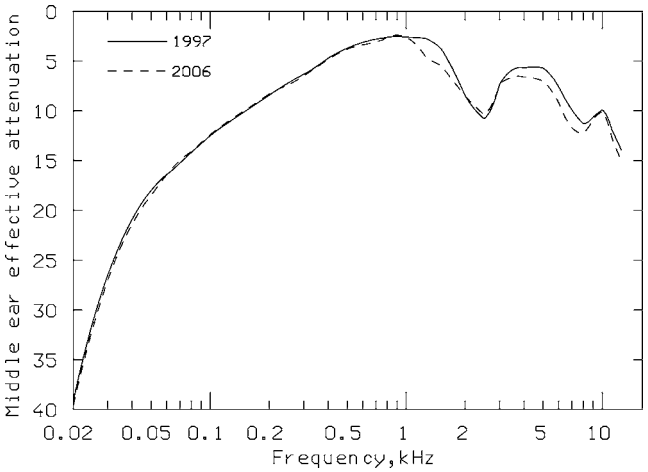

FIG. 2. Comparison of the middle-ear transfer function assumed in the original model (solid curve) and in the modified version of the model (dashed curve).

predicted loudness level is between 2.0 and 2.5 phons. It has been suggested that the loudness at absolute threshold varies somewhat with frequency (Hellman and Zwislocki, 1968), but this suggestion was based on extrapolation, since loudness judgments were not obtained for levels below 4 dB SL. Furthermore, the loudness at threshold estimated by Hellman and Zwislocki (1968) varied only by a factor of about 2 over the frequency range from 100 to 1000 Hz. Since loudness varies very rapidly with level at low SLs, small changes in the assumed loudness at threshold have only a small effect on the predicted absolute threshold.

The model was modified to predict the absolute thresholds specified in ISO 389-7 (2005) by altering the assumed middle-ear transfer function, but keeping the value at 1 kHz equal to −2.6 dB. The "old" and "new" middle-ear transfer functions are shown in Fig. 2. The final predicted thresholds were within 0.2 dB of the values specified in ISO 389-7 (2005) for all frequencies from 0.05 to 12.5 kHz (bottom curve of Fig. 1; the dashed-line representing the predictions is not visible since it lies on top of the solid line).

The model was then used to predict equal-loudness contours, for loudness levels from 10 to 100 phons. The predictions are shown as dashed lines in Fig. 1. The equal-loudness contours predicted by the modified model are closer to the measured contours (solid lines) than are the contours predicted by the old model, in the frequency range from 1 to 8 kHz. Some clear discrepancies remain at low frequencies, especially around 0.1 kHz, where the predicted contours lie a little below the measured contours for loudness levels up to 50 phons, and a little above the measured contours for loudness levels of 80 phons and above. The predicted and measured contours match well for loudness levels of 60 and 70 phons. There are also some discrepancies between 2 and 5 kHz, where the predicted contours lie a little below the measured contours. The model predicts that the rate of growth of loudness with increasing sound level is similar for frequencies from 1 to 5 kHz, loudness roughly doubling for each 10-dB increase in sound level above 40 dB. This is consistent with empirical data (Hellman, 1976). However, the equal-loudness contours in ISO 226 (2003) can only be accounted for if it is assumed that the growth of loudness with increasing sound level is slower around 3–4 kHz than at 1 kHz. In any case, the discrepancies between the measured and predicted equal-loudness contours are small relative to the likely errors of measurement, as indicated by the differences in the contours measured in different laboratories (Suzuki and Takeshima, 2004).

IV. CONCLUSIONS

We have described how a loudness model (Moore *et al.*, 1997) that forms the basis for a new ANSI standard for the calculation of the loudness of steady sounds (ANSI, 2005) can be modified to predict the absolute thresholds in ISO 389-7 (2005) and to give reasonably accurate predictions of the equal-loudness contours in ISO 226 (2003). The modifications involve changes to the assumed middle-ear transfer function in the model. The executable code for the modified model can be obtained from: ⟨http://hearing.psychol.cam.ac.uk/Demos/demos.html⟩.

ACKNOWLEDGMENTS

This work was supported by the MRC (UK). We thank Yoiti Suzuki and an anonymous reviewer for helpful comments on an earlier version of this paper.

Aibara, R., Welsh, J. T., Puria, S., and Goode, R. L. (**2001**). "Human middle-ear sound transfer function and cochlear input impedance," Hear. Res. **152**, 100–109.

ANSI (**2005**). ANSI S3.4-2005. Procedure for the Computation of Loudness of Steady Sounds (American National Standards Institute, New York).

Ashihara, K., Kurakata, K., Mizunami, T., and Matsushita, K. (**2006**). "Hearing threshold for pure tones above 20 kHz," Acoust. Sci. & Tech. **27**, 12–19.

Buus, S., Florentine, M., and Mason, C. R. (**1986**). "Tuning curves at high frequencies and their relation to the absolute threshold curve," in *Auditory Frequency Selectivity*, edited by B. C. J. Moore and R. D. Patterson (Plenum, New York).

Cheatham, M. A., and Dallos, P. (**2001**). "Inner hair cell response patterns: Implications for low-frequency hearing," J. Acoust. Soc. Am. **110**, 2034–2044.

Chouard, N. (1997). "Loudness and unpleasantness perception in dichotic conditions," Ph.D. thesis, Universite du Maine.

Fletcher, H., and Munson, W. A. (**1933**). "Loudness, its definition, measurement, and calculation," J. Acoust. Soc. Am. **5**, 82–108.

Glasberg, B. R., and Moore, B. C. J. (**1990**). "Derivation of auditory filter shapes from notched-noise data," Hear. Res. **47**, 103–138.

Hellman, R. P. (**1976**). "Growth of loudness at 1000 and 3000 Hz," J. Acoust. Soc. Am. **60**, 672–679.

Hellman, R. P., and Zwislocki, J. J. (**1963**). "Monaural loudness summation at 1000 cps and interaural summation," J. Acoust. Soc. Am. **35**, 856–865.

Hellman, R. P., and Zwislocki, J. J. (**1968**). "Loudness determination at low sound frequencies," J. Acoust. Soc. Am. **43**, 60–64.

ISO 226 (**1987**). Acoustics - Normal equal-loudness contours (International Organization for Standardization, Geneva).

ISO 389-7 (**1996**). Acoustics - Reference zero for the calibration of audiometric equipment. Part 7: Reference threshold of hearing under free-field and diffuse-field listening conditions (International Organization for Standardization, Geneva).

ISO 11904-1 (**2002**). Acoustics - Determination of sound immission from sound sources placed close to the ear - Part 1: Technique using microphone in real ear (MIRE-technique) (International Organization for Standardization, Geneva).

ISO 226 (**2003**). Acoustics - Normal equal-loudness contours (International Organization for Standardization, Geneva).

ISO 11904-2 (**2004**). Acoustics - Determination of sound immission from sound sources placed closed the ear - Part 2: Technique using a manikin (International Organization for Standardization, Geneva).

ISO 389-7 (**2005**). Acoustics - Reference zero for the calibration of audiometric equipment. Part 7: Reference threshold of hearing under free-field and diffuse-field listening conditions (International Organization for Standardization, Geneva).

Moore, B. C. J. (**2003**). *An Introduction to the Psychology of Hearing*, 5th ed. (Academic, San Diego).

Moore, B. C. J., Glasberg, B. R., and Baer, T. (**1997**). "A model for the prediction of thresholds, loudness and partial loudness," J. Audio Eng. Soc. **45**, 224–240.

Puria, S., Rosowski, J. J., and Peake, W. T. (**1997**). "Sound-pressure measurements in the cochlear vestibule of human-cadaver ears," J. Acoust. Soc. Am. **101**, 2754–2770.

Robinson, D. W., and Dadson, R. S. (**1956**). "A re-determination of the equal-loudness relations for pure tones," Br. J. Appl. Phys. **7**, 166–181.

Ruggero, M. A., and Temchin, A. N. (**2002**). "The roles of the external, middle, and inner ears in determining the bandwidth of hearing," Proc. Natl. Acad. Sci. U.S.A. **99**, 13206–13210.

Sellick, P. M., Robertson, D., and Patuzzi, R. (**2006**). "The effect of BAPTA and 4AP in scala media on transduction and cochlear gain," Hear. Res. **211**, 7–15.

Shaw, E. A. G. (**1974**). "Transformation of sound pressure level from the free field to the eardrum in the horizontal plane," J. Acoust. Soc. Am. **56**, 1848–1861.

Subedi, J. K., Yamaguchi, H., and Matsumoto, Y. (**2004**). "Masked perception thresholds of low frequency tones under background noises and their-estimation by loudness model," J. Low Freq. Noise Vib. Active Cont. **23**, 145–157.

Suzuki, Y., and Takeshima, H. (**2004**). "Equal-loudness-level contours for pure tones," J. Acoust. Soc. Am. **116**, 918–933.

Yasin, I., and Plack, C. J. (**2005**). "Psychophysical tuning curves at very high frequencies," J. Acoust. Soc. Am. **118**, 2498–2506.

Yates, G. K. (**1995**). "Cochlear structure and function," in *Hearing*, edited by B. C. J. Moore (Academic, San Diego).

Comment on paper entitled, "An inversion of Freedman's 'image pulse' model in air" [J. Acoust. Soc. Am. 119(2), 965–975 (2006)] (L)

Robert Hickling
Sonometrics Inc., 8306 Huntington Road, Huntington Woods, Michigan 48070

Guillermo C. Gaunaurd
Army Research Laboratory, Code AMSRD-ARL- SE-RU, 2800 Powder Mill Road, Adelphi, Maryland 20783-1197

(Received 31 March 2006; revised 11 May 2006; accepted 12 May 2006)

Echolocation (i.e., perceiving objects using acoustic echoes) is well-known in underwater detection and to a lesser extent in robot guidance and machine perception. The paper by Tsakiris and McKerrow is concerned with machine perception in air using Freedman's asymptotic model, which was originally developed to predict the backscattering multiple-echo effect observed in sonar detection. This effect was subsequently shown to be due to the elastic response of underwater targets. Freedman's model can be used in air because the acoustic target is assumed to be rigid. Also, the model's prediction of multiple echoes can be used to obtain information about the shape of the target. This is the so-called inversion of the Freedman model by Tsakiris and McKerrow. In their paper, various simple bodies are tested in air using ultrasound and it is shown that the model provides relatively poor information about body shape. Several explanations are given. However, one explanation is not considered, namely that the model itself is not satisfactory. First, there is poor agreement with exact backscattering theory. Second, deriving information about target shape from the multiple echoes predicted by the model is a highly questionable procedure. Both these aspects are examined here. © *2006 Acoustical Society of America.* [DOI: 10.1121/1.2211487]

PACS number(s): 43.60.Lq, 43.20.Fn, 43.30.Gv, 43.60.Jn [EJS] Pages: 589–590

I. INTRODUCTION

In the paper by Tsakaris and McKerrow, the only reference provided for Freedman's model is his 1961 Ph.D. thesis, which is not readily accessible. We therefore obtained an understanding of the model from Freedman's subsequent papers.[1,2] One of us (R.H.) shared an office with Dr. Freedman at the British Underwater Detection Establishment during the years 1955–57, where we both were concerned with the multiple-echo effect in sonar detection. The effect continues to high frequencies for a spherical target in water, even though this is not predicted by Stenzel's exact solution[3] for a rigid immovable sphere. It would appear then that the effect is due to vibrations resulting from the elastic interaction of sound with a solid in water. However, Dr. Freedman found that asymptotic theory predicted multiple echoes from a rigid sphere (as indicated in Fig. 1 of the paper by Tsakiris and McKerrow). This then was his explanation of the multiple-echo effect. In the paper the inverse of the multiple-echo effect is used by Tsakaris and McKerrow in an attempt to derive information about the shape of acoustic targets. It can be shown mathematically[4] that the sonar cross section for a rigid sphere using Freedman's model is the same as that using the classical Kirchhoff method. Moreover, the key equation of the model was used previously.[5] Hence, the model is not entirely original. In our Fig. 1, we show a comparison[6] between the exact theory of backscattering from a rigid immovable sphere[1] and the Kirchhoff asymptotic method. It is seen that, although the trend is similar, there are major differences. Clearly this relates to the lack of agreement between theory and experiment reported in the paper by Tsakiris and McKerrow.

II. THE ELASTIC RESPONSE OF ACOUSTIC TARGETS

It is necessary to discuss the multiple-echo effect observed with sonar targets because it is the origin of the procedure used by Tsakiris and McKerrow to derive information about targets in air. An understanding of this effect developed over a number of years. First, there was the exact analytical solution of Faran[7] for scattering by solid spheres and cylinders that included shear and compressional waves in the solid. This was followed by a similar solution[8] by Goodman and Stern for spherical shells. The availability of computers then permitted the computation of echo pulses in water using digital Fourier transforms. Exact agreement was found between theory and experiment for spherical aluminum shells in water at the Lake Travis facility of the Advanced Research Laboratory at the University of Texas.[9] This work, and earlier related papers,[10] clearly showed that the multiple-echo effect observed in sonar detection is due to vibrations associated with the elastic response of the target and not to the predictions of Freedman's asymptotic theory.

III. EXACT SOLUTIONS FOR RIGID BODIES WITH SIMPLE SHAPES

Tsakiris and McKerrow perform tests in air on rigid targets with simple shapes. The wave equation can be solved

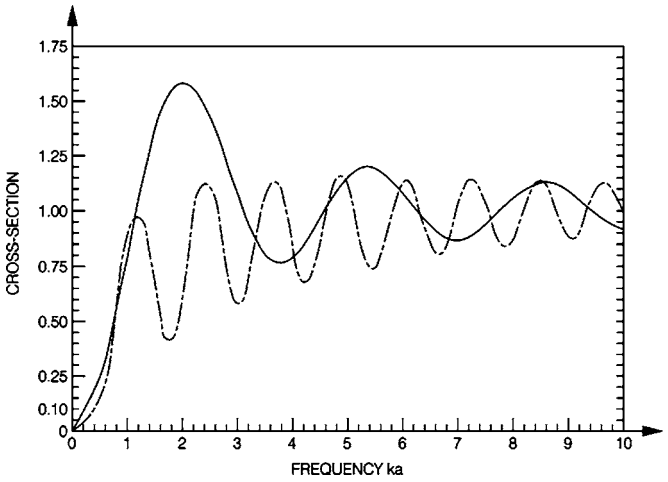

FIG. 1. Comparison of exact theory (dashed line) with the Kirchhoff approximation (solid line) for the acoustic backscattering cross section for a rigid immovable sphere of radius a. This figure is a modified version of Fig. 3 in Ref. 5. (The cross section is the square of the backscattered pressure amplitude in Fig. 2.)

exactly for such shapes by the method of separation of variables.[11] Also, exact solutions can be obtained using numerical methods such as finite-element and finite-difference techniques. From these it is possible to compute echo pulses and determine their nature and origin. For large bodies and/or high frequencies the echoes are specular and are returned directly to the source from the closest part of the target surface. This is exemplified in our Fig. 1 for the exact solution for a rigid immovable sphere where the region for specular echoes occurs when ka is large and the cross section tends to 1. For lower values of ka the cross section oscillates. Tsakiris and McKerrow state their measurements may be too close to the target for good agreement with Freedman's model. Figure 2 shows the effect of distance on backscattering from a rigid immovable sphere.[12] (In this figure the pressure amplitude is equal to the square root of the acoustic cross section in Fig. 1.) It is seen that backscattering in the far field, where $R=10$ or more, is distinctly different from backscattering between $R=2$ and 5, where their measurements appear to have been made. This then would be another reason for the discrepancy between theory and experiment.

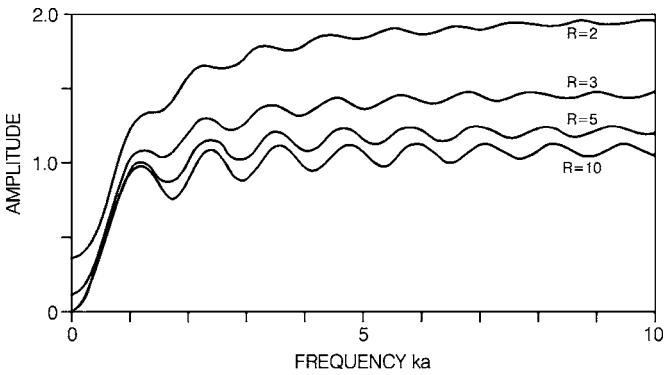

FIG. 2. Backscattered pressure amplitude for a rigid immovable sphere of radius a as a function of frequency ka, for different source distances Ra from sphere. (The pressure amplitude is the square root of the cross section in Fig. 1.)

As previously stated, the purpose of the paper by Tsakiris and McKerrow is to use the multiple-echo feature of Freedman's model to obtain information about the shapes of acoustic targets in air using ultrasound. It seems unlikely, however, that they can obtain anything more than specular echoes. This is evident from an early paper on scattering from acoustic targets of different shapes (a sphere, a cylinder, and a prolate spheroid) using exact solutions[13] in which it is shown that only specular echoes occur at high frequencies.

IV. CONCLUDING REMARKS

It is not easy for humans, whose dominant sense is vision, to relate to echolocation. Vision operates passively, objects being perceived only when illuminated by natural or artificial light. Echolocation, on the other hand, is an active process, objects being perceived when the sound emitted by a source operates in conjunction with a receiver of echoes. In addition, there is a major difference between reflected light and reflected sound. Except for polished surfaces, light is usually scattered in all directions from points on an object, so that every point can be seen by the eye. On the other hand, sound is usually backscattered by mirror-like or specular highlights that are the only parts of a surface perceived at any instant in time. Tsakiris and McKerrow use a single ultrasonic transducer for emitting and receiving. This transducer has to wait until it receives an echo before it emits another signal. In contrast, bats and porpoises, which have highly developed echolocation abilities, have separate emitters and receivers. Echolocation has an advantage over computer vision using cameras, because it has better depth perception.

The use of echolocation in machine perception needs to be encouraged and placed on a rigorous basis. We hope our comments are helpful.

[1]A. Freedman, "A mechanism of acoustic echo formation," Acustica **12**, 10–21 (1962).
[2]A. Freedman, "An experimental examination of acoustic echo structure," Acustica **14**, 89–104 (1964).
[3]H. Stenzel, *Leitfaden zur Berechnung von Schallvorgagen* (Springer, Berlin, 1939).
[4]H. Gaunaurd, Unpublished derivation (2006).
[5]*Propagation of Short Radio Waves*, edited by D. E. Kerr, Vol. 13, MIT Radiation Lab. Series (McGraw-Hill, New York, 1952).
[6]G. Gaunaurd, "Monostatic and bistatic cross sections of a large (capped) sphere partially insonified at a circular spot," J. Acoust. Soc. Am. **61**(5), 1121–1132 (1977).
[7]J. J. Faran, "Sound scattering by solid cylinders and spheres," J. Acoust. Soc. Am. **23**(4), 405–418 (1951).
[8]R. R. Goodman and R. Stern, "Reflection and transmission of sound by elastic spherical shells," J. Acoust. Soc. Am. **34**, 338–344 (1962).
[9]K. J. Diercks and R. Hickling, "Echoes from hollow aluminum spheres in water," J. Acoust. Soc. Am. **41**(2), 330-393 (1967).
[10]R. Hickling, "Analysis of echoes from a solid elastic sphere in water," J. Acoust. Soc. Am. **34**(10), 1582–1592 (1962).
[11]P. M. Morse and H. Feshbach, *Methods of Theoretical Physics* (McGraw-Hill, New York, 1953), Vol. I, pp. 655–666.
[12]R. Hickling, "Acoustic Radiation and Reflection from Spheres," Part I of Ph.D. thesis, California Institute of Technology (1962), p. 30.
[13]R. Hickling, "Frequency dependence of echoes from bodies of different shapes," J. Acoust. Soc. Am. **30**(2), 137–139 (1958).

Comment on "Auditory-nerve first-spike latency and auditory absolute threshold: A computer model" [J. Acoust. Soc. Am. 119, 406–417 (2006)] (L)

B. Suresh Krishna[a)]
Mahoney Center for Brain and Behavior, Center for Neurobiology and Behavior, Columbia University College of Physicians and Surgeons, and the New York State Psychiatric Institute, New York, New York 10032

(Received 22 February 2006; revised 11 May 2006; accepted 18 May 2006)

A recent paper by Meddis [J. Acoust. Soc. Am. **119**, 406–417 (2006)] shows that an existing model of the auditory nerve [Meddis and O'Mard, J. Acoust. Soc. Am. **117**, 3787–3798 (2005)] is consistent with experimentally-measured first-spike latencies in the auditory nerve [Heil and Neubauer, J. Neurosci. **21**, 7404–7415 (2001)]. The paper states that this consistency emerges because in the model, the calcium concentration inside the inner hair cell builds up over long periods of time (up to at least 200 ms) during tone presentation. It further states that integration over long time-scales happens despite the very short time constants (<1 ms) used for the calcium dynamics. This letter demonstrates that these statements are incorrect. It is shown by simulation that calcium concentration inside the hair cell stage of the Meddis model rapidly reaches a steady state within a few milliseconds of a stimulus onset, exactly as expected from the short time-constant in the simple first-order differential equation used to model the calcium concentration. The success of the Meddis model in fitting experimental data actually confirms earlier results [Krishna, J. Comput. Neurosci. **13**, 71–91 (2002a)] that show that the experimental data are a natural result of stochasticity in the synaptic events leading up to spike-generation in the auditory nerve; integration over long time scales is not necessary to model the experimental data. © *2006 Acoustical Society of America.*
[DOI: 10.1121/1.2213569]

PACS number(s): 43.64.Bt [BLM] Pages: 591–593

Meddis (2006) has recently shown that an existing biophysically detailed model of the auditory nerve (Meddis and O'Mard, 2005) produces first-spike latencies that are qualitatively consistent with experimentally measured first-spike latencies in the auditory nerve (Heil and Neubauer, 2001). The paper asserts (p. 412) that this consistency emerges because "model latencies can be attributed to the accumulation of presynaptic calcium during tone presentation." The buildup of calcium is ascribed to a mismatch between calcium influx and efflux and is supposed to "operate at least up to tone durations of 200 ms" (p. 412). The paper states that such long time-scale integration over periods up to 200 ms can happen despite the very short time constants (<1 ms) used for the calcium dynamics in the model.

These statements are incorrect, because there is no long-term calcium integration inside the hair cell stage of the Meddis (2006) model. To show this, the calcium concentration inside the inner hair cell stage of the Meddis model in response to a 10 dB sound-pressure level, 200 ms long pure tone was obtained using simulation. In published examples from both the experimental data (Heil and Irvine, 1997) and the Meddis model (Meddis 2006), stimuli at this sound-pressure level and duration fail to elicit a spike after stimulus onset in low spontaneous-rate (SR) fibers on each of 20 presentations; mean first-spike latency was roughly between 10 and 20 ms in high SR fibers.

The inner hair cell potential variation in response to this stimulus is identical for all the parameter variations considered in Meddis (2006); this inner hair cell potential variation serves as the input that drives calcium influx into the hair cell. The inner hair cell potential was obtained using the publicly available Development System for Auditory Modeling (DSAM) of Meddis and O'Mard. All parameter settings were identical to those in Meddis (2006) except that the simulation time step was set to 1 μs for improved accuracy, instead of the 10 μs in Meddis (2006); the output inner hair cell potential from DSAM was essentially unchanged by this change in time step. The remaining stages between the inner hair cell potential and calcium concentration were simulated in MATLAB using a 1 μs time-step: this includes Eqs. (A7)–(A10) in Meddis (2006).

Figure 1(a) plots the inner hair cell potential obtained using DSAM in response to a 200 ms long pure tone (at 10 dB sound pressure level and 4 kHz frequency) shaped by a cosine-squared ramp with 1.7 ms rise/fall time at onset and offset, respectively. According to Meddis (2006, p. 410), such a stimulus fails to elicit a spike in low SR fibers possibly because "the time taken to accumulate enough presynaptic calcium to initiate a spike is greater than the duration of the signal," clearly implying that calcium is building up over the entire duration of the tone, but at too slow a rate to elicit a spike. Figures 1(c) and 1(e) plot the calcium concentration inside the inner hair cell with parameters set for low SR fibers exactly as in Meddis (2006). Calcium concentration rises rapidly to reach 99% of its peak deviation from baseline within about 4.97 ms after stimulus onset. Since the inner

[a)]Electronic mail: ssk2031@columbia.edu

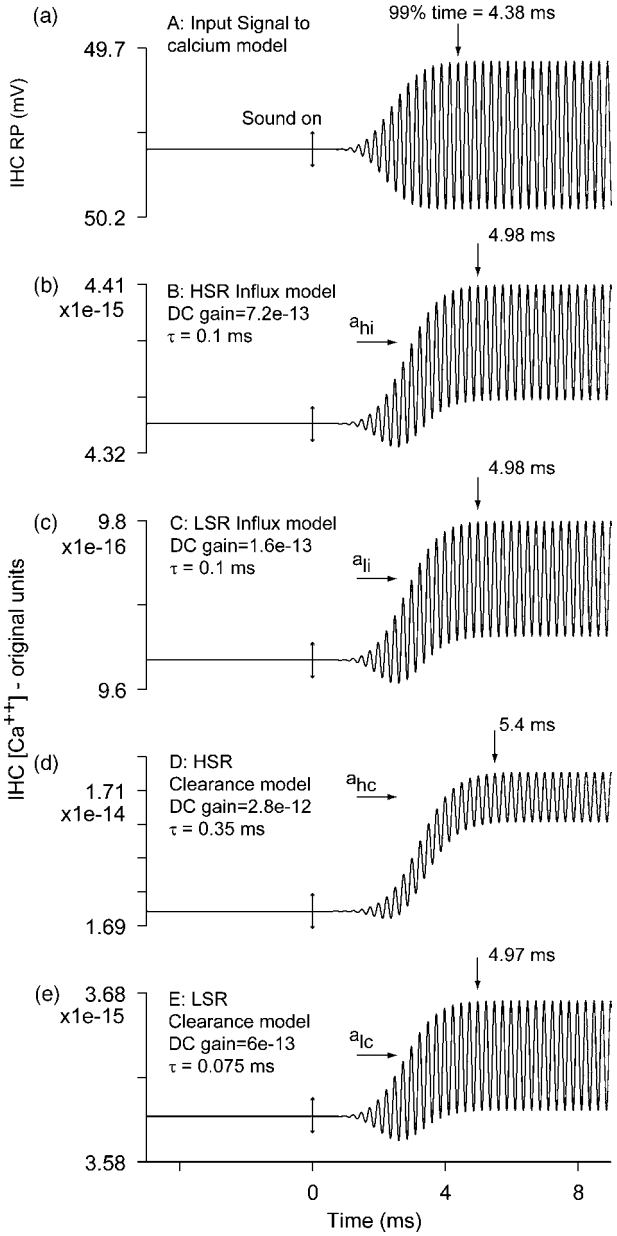

FIG. 1. Calcium concentration in the Meddis inner hair cell reaches steady state within a few milliseconds of sound onset: there is no long-term buildup of calcium. (a) Plot of inner hair cell receptor potential (mV) as a function of time (ms) in response to a 4 kHz tone (10 dB sound pressure level, 1.7 ms cosine-squared rise-fall times). Small double-headed arrow at time=0 ms indicates sound onset. Also indicated is the time required for the potential to reach 99% of its peak excursion; in this case, it is 4.38 ms. (b)–(e) Plots of calcium ion concentration [units identical to Meddis (2006)] in the inner hair cell as a function of time (ms) with parameters set to those of the high SR influx model (b), the low SR influx model (c), the high SR clearance model (d), and the low SR clearance model (e), respectively. The rightward arrows labeled a_{hi}, a_{li}, a_{hc}, and a_{lc} show the steady-state dc component of calcium concentration, obtained as the mean calcium concentration from 100 to 150 ms after sound onset, for each model. The dc gain (obtained as $\tau_{Ca} * G_{Ca}^{max}$) and time constant of calcium clearance (τ_{Ca}: shown as τ) of the models are indicated in each graph. Sound onset and time for ordinate value to reach 99% of its peak excursion are shown as in (a).

hair cell potential reaches 99% of its peak deviation from baseline about 4.38 ms after stimulus onset, it is clear that the added lag due to the dynamics of calcium influx and clearance is extremely small. Importantly, the calcium concentration does not steadily increase over the duration of the tone, as implied by Meddis (2006) on the basis that calcium dynamics show long-term integration. The results for high SR fibers are similar. Since the time constants in the influx model are identical for low, medium, and high SR fibers in Meddis (2006), the time for calcium concentration in the high SR case to reach 99% of peak deviation [Fig. 1(b)] is identical to that for low SR fibers [Fig. 1(c)]. In the clearance model, the time constant (τ_{Ca}) of clearance for high SR fibers is slightly longer, and therefore the time to reach 99% of peak deviation is also slightly longer by about 0.4 ms [Figs. 1(d) and 1(e)]. Importantly, in contrast to the similarity in rise times, there is a large difference in both transient and average steady-state concentrations between high and low SR fibers; this is true for both influx and clearance models. This difference in concentrations is expected from the analytical expression for the transfer gain of a first-order low-pass filter. For frequency components that are small compared to $(1/\tau_{Ca})$, the gain relating calcium concentration to the input (third power of proportion of open channels multiplied by driving potential, after absorbing the G_{max}^{Ca} term into the gain) in the Meddis model [Eq. (A7)] is approximately equal to $(G_{max}^{Ca} * \tau_{Ca})$; the expression is exactly correct at a frequency of 0 (dc). For the influx model, only G_{max}^{Ca} is changed (by a factor of 4.5) to model the differences in calcium dynamics between high and low SR fibers; therefore the only change in model output is a simple scaling that is independent of frequency. The model calcium concentration for high SR fibers is simply 4.5 times the model calcium concentration for low SR fibers. For the clearance model, since τ_{Ca} is varied between high and low SR fibers, the gain is frequency dependent; however, at dc, the gain ratio is 4.67 and therefore the average steady-state calcium concentration for high SR fibers is 4.67 times the average steady-state concentration for low SR fibers. But neither fiber type shows any sign of long-term integration in the calcium concentration profile.

The Meddis (2006) model fits experimental latency data not because of long-term calcium integration, but because of its stochastic spike-generation process. Ignoring refractory effects from spikes prior to stimulus onset, the Meddis model generates a spike whenever any of q available quanta is released, with each of the q quanta having a fixed small stimulus-dependent probability p of generating a spike in a single simulation epoch. If the mean rate of quantal release is higher, then the mean first-spike latency will be lower. For small values of p (p can be made as small as necessary by decreasing the simulation time step dt), and for purposes of calculating first-spike latency, the spike train from the Meddis model's spiking algorithm can be approximated by a Poisson process with a time varying firing rate roughly equal to qp/dt. If this spike train fires at a mean rate of 10 spikes/s, a reasonable value for firing rates of low-SR fibers to near-threshold stimuli, the expected mean first-spike latency is 100 ms. Thus, this approximate calculation shows that the mean first-spike latencies are essentially consistent with the firing rates obtained from auditory nerve fibers. Further, this reasoning also shows why changes in SR in the Meddis model lead to differences in first-spike latency. The main effect of the parameter changes that are used to model differences in SR in the Meddis (2006) model is an approxi-

mately 4.5-fold difference in gain. This difference in gain is the primary contributor to the observed latency effects; the changes in rise time (i.e., "integration time") between fibers of different SR are minor (zero for the influx model, and less than 0.5 ms for the clearance model: see Fig. 1). When the gain is higher, so is the driven spike rate and the mean first-spike latency is therefore smaller.

The above-presented argument is a summary of the one in Krishna (2002a), where it was shown that the experimental data can be captured at a quantitative level by a minimal model that relies upon stochastic spiking at a rate proportional to an *almost* instantaneous function of sound pressure; no long-term integration of stimulus magnitude is required to capture the data. This minimal model was a simplified version of current standard models of the auditory periphery, including the Meddis (2006) model. Krishna (2002a, p. 86) implied that all such standard models could be expected to capture the data successfully; indeed, this is exactly what Meddis (2006) confirms. The above-noted argument also enables a long-due clarification of the physiological basis for the Poisson model used in Krishna (2002a). Krishna (2002a) did not explicitly localize the physiological basis for his spike-generation process. Specifically, despite what the regrettably confusing phrasing in one section might appear to possibly imply, the paper did not intend to suggest that the stochasticity in spike generation arises postsynaptically (see criticism in Heil, 2004). The most likely physiological basis for the Poisson model is the approximately Poisson nature of the vesicle release process; if each random vesicle release leads to a reliably timed spike as has been suggested in the physiological literature (Siegel, 1992), then the spike train will also possess Poisson properties (as explicitly stated in Krishna 2002b, p. 216). Available extracellular data strongly support the use of a Poisson process (modified by a refractory period) to model auditory nerve spike-train data (Johnson, 1978). It is important to emphasize that just like the model in Krishna (2002a), the Meddis model also contains what Meddis (2006, p. 407) calls an "explicit integration module;" this integration module resides not in the calcium dynamics, but in the stochastic vesicle release process. This is because models that characterize the analog to discrete-event conversion stage of auditory transduction (including the processes of vesicle release and post-synaptic spiking) as a point process can equivalently be interpreted as incorporating a stage where the conditional intensity function of the point process is integrated until the integral crosses an exponentially distributed random threshold. This fact was stated for the Poisson case in Krishna (2002a); the general version of this theorem can be found in Brown *et al.* (2002).

Krishna (2002a) did not imply that calcium dynamics have no role to play in determining first-spike latency, as stated in Meddis (2006). The specific objection in Krishna (2002a) was to the idea that the latency data were best modeled using a calcium integrator that, to paraphrase Heil and Neubauer (2001, p. 7414), can be "conceptualized using the metaphor of a barrel that has an inflow component that is directly proportional to stimulus peak-pressure and an inflow/outflow component that is constant; the first spike is triggered when the amount of fluid in the barrel reaches a critical value." It is not at all obvious how such a "barrel" model would be consistent with the known ability of auditory-nerve fibers to follow stimulus variations up to several kilohertz. It is important to note that Heil and Neubauer have since explicitly disclaimed this "barrel" metaphor and state that "we do not assume the existence of a response which is directly proportional to the continuously increasing integral of $P(t)$ or of $P(t)$ raised to some power and which could be measured during a given trial;" here $P(t)$ refers to the peak pressure of the stimulus (Neubauer and Heil, 2004, p. 438). Instead, they now favor a stochastic interpretation (Heil and Neubauer, 2003; Neubauer and Heil, 2004) that is somewhat different from the one discussed earlier. This explanation, in apparent agreement with Krishna (2002a), also relies partially upon the fact that long first-spike latencies will emerge from low driven spike rates. However, from their cursory description, it is unclear how their empirical law governing spike timings (and hence the spike rate) can be derived from their stochastic formulation of calcium dynamics. Further, while the details are unclear, this stochastic formulation still appears to retain a similar problematic dependence upon a long-term running average of stimulus pressure. It remains to be demonstrated that their new proposal is consistent with other aspects of the data like the variability of first-spike latency and the ability of auditory-nerve fiber responses to follow high stimulus frequencies. In any event, the "widely-held objection" (Meddis 2006, p. 407) to the idea that short-term submillisecond dynamics in the auditory periphery can be used to create long-term temporal integration over periods up to 100 ms or more is well-founded and remains entirely valid.

The author thanks Laurel Carney for reading and commenting on the first draft.

Brown, E. N., Barbieri, R., Ventura, V., Kass, R. E., and Frank, L. M. (**2002**). "The time-rescaling theorem and its application to neural spike train data analysis," Neural Comput. **14**, 325–346.

Heil, P. (**2004**). "First-spike latency of auditory neurons revisited," Curr. Opin. Neurobiol. **14**, 461–467.

Heil, P., and Irvine, D. R. (**1997**). "First-spike timing of auditory-nerve fibers and comparison with auditory cortex," J. Neurophysiol. **78**, 2438–2454.

Heil, P., and Neubauer, H. (**2001**). "Temporal integration of sound pressure determines thresholds of auditory-nerve fibers," J. Neurosci. **21**, 7404–7415.

Heil, P., and Neubauer, H. (**2003**). "A unifying basis of auditory thresholds based on temporal summation," Proc. Natl. Acad. Sci. U.S.A. **100**, 6151–6156.

Johnson, D. H. (**1978**). "The relationship of post-stimulus time and interval histograms to the timing characteristics of spike trains," Biophys. J. **22**, 413–430.

Krishna, B. S. (**2002a**). "A unified mechanism for spontaneous-rate and first-spike timing in the auditory nerve," J. Comput. Neurosci. **13**, 71–91.

Krishna, B. S. (**2002b**). "Temporal response properties of single neurons in the inferior colliculus of the anesthetized gerbil," PhD dissertation, Center for Neural Science, New York University.

Meddis, R. (**2006**). "Auditory-nerve first-spike latency and auditory absolute threshold: A computer model," J. Acoust. Soc. Am. **119**, 406–417.

Meddis, R., and O'Mard, L. P. (**2005**). "A computer model of the auditory-nerve response to forward-masking stimuli," J. Acoust. Soc. Am. **117**, 3787–3798.

Neubauer, H., and Heil, P. (**2004**). "Towards a unifying basis of auditory thresholds: The effects of hearing loss on temporal integration reconsidered," J. Assoc. Res. Otolaryngol. **5**, 436–458.

Siegel, J. H. (**1992**). "Spontaneous synaptic potentials from afferent terminals in the guinea pig cochlea," Hear. Res. **59**, 85–92.

Repetition Pitch glide from the step pyramid at Chichen Itza (L)

Frans A. Bilsen[a)]
van Boisotstraat 1, 2631BE Nootdorp, The Netherlands

(Received 1 May 2006; revised 18 May 2006; accepted 18 May 2006)

Standing at the foot of the Mayan step pyramid at Chichen Itza in Mexico, one can produce a pitchy "chirp" echo by handclapping. As exposed by Declercq *et al.* [J. Acoust. Soc. Am. **116**, 3328–3335 (2004)], an acoustic model based on optical Bragg diffraction at a periodic structure cannot explain satisfactorily the chirp-echo sonogram. Alternatively, considering the echo as a sequence of reflections, and given the dimensions of the pyramid and source-receiver position, the chirp is predicted correctly as a Repetition Pitch glide of which the pitch height is continuously decreasing within 177 ms from 796 to 471 Hz-equivalent. © *2006 Acoustical Society of America.*
[DOI: 10.1121/1.2213570]

PACS number(s): 43.20.El, 43.66.Hg [RW] Pages: 594–596

I. INTRODUCTION

At Chichen Itza in Mexico there is a Mayan ruin with a pyramid named El Castillo that produces an echo, in response to a handclap, which sounds like the chirp of a Quetzal bird. It was correctly suggested by Lubman[1] and others that the periodic structure of, in particular, the central staircase is responsible for the chirp-like sound of the echo. In search for an explanation, Declercq *et al.*[2] performed sonogram analysis of the echo as recorded by Lubman,[1] and applied the monofrequent single homogeneous plane wave (Rayleigh) diffraction theory to the periodic structure of the steps of the pyramid and the handclap pulse under consideration.

In Fig. 1, the gray-scaled background constitutes the sonogram of the chirp echo as reproduced from Fig. 8 of Declercq *et al.*;[2] they applied a time-limited Fourier transform with a Gaussian window of 2 ms width to the chirp echo as recorded by Lubman.[1] Time is plotted horizontally on a linear scale from 0 to 200 ms, and frequency vertically on a linear scale from 0 to 5000 Hz. In the text below their Fig. 8, they state that "it can already be concluded that these patterns cannot simply be the result of pure Bragg diffraction and that an extra effect must be involved."[3]

It occurred to the present author, within the framework of the Repetition Pitch theory, that the lighter areas in this sonogram suggest the presence of spectral energy at the second, third, and fourth harmonic of a gliding (absent) fundamental frequency. The other lighter regions immediately above 0 Hz are ascribed by Declerq *et al.*[2] to low-frequency noise coming from the interaction of wind with the microphone. Therefore, an alternative explanation based on the perception of Repetition Pitch is proposed in this letter.

II. AN ALTERNATIVE MODEL BASED ON REPETITION PITCH

When a sound and its (delayed) repetition(s) are added together, a compound signal is obtained having a rippled spectrum. In particular, the power spectrum of a white signal with one added repetition is a cosinusoidal function of frequency with spectral maxima at multiples of a "fundamental" corresponding to the reciprocal value of the delay time. With such a signal, one generally perceives a pitch, Repetition Pitch (RP), corresponding to the fundamental.[4,5] This is true for different kinds of RP signals ranging from pulse pairs to continuous white noise added to itself delayed.[6–8] In the present case, the original sound is a handclap, to be idealized as a (dirac) pulse. Paired reflections (repetitions) from successive steps will be considered as pulse pairs of which a (gliding) fundamental together with its harmonics is calculated.

Adopting the data of pyramid dimensions, handclap and sound recording positions by Lubman from Declercq *et al.*,[2] the drawing in Fig. 2 is obtained. The steps of the staircase are numbered $n=-7$ to 84, with $n=0$ being the step at ear (microphone) height. Dimensions are given in meters.

The sound path length $S(n)$ from source-receiver position to step n of the staircase is calculated with Pythagoras' theorem as follows:

$$S(n) = [(11.8 + n \times 0.263)^2 + (n \times 0.263)^2]^{1/2} \quad \text{with } n = -7, \ldots, 0, \ldots, 84. \tag{1}$$

Then, with a sound velocity at the site of 343 m/s, the traveling time back and forth, $T(n)$ (in seconds), follows as

$$T(n) = 2 \times S(n)/343 \quad \text{with } n = -7, \ldots, 0, \ldots, 84. \tag{2}$$

The time interval or delay time $\tau(n)$ between successive reflections at the receiver position then is given by

$$\tau(n) = T(n+1) - T(n) \quad \text{with } n = -7, \ldots, 0, \ldots, 84. \tag{3}$$

Finally, the instantaneous value of the "fundamental" follows as the reciprocal value of $\tau(n)$ and the "harmonics" f_m of the fundamental are given by

$$f_m(n) = m/\tau(n) \quad \text{with } m = 1,2,3,4, \ldots . \tag{4}$$

The course (glide) of the first four harmonics is given in Fig. 1 by the dotted lines numbered 1 through 4, with each dot representing the instantaneous value of a RP harmonic following Eq. (4). The calculated fundamental glides from 796 to 471 Hz within a time span of 177 ms, the latter value

[a)]Electronic mail: fabilsen@xs4all.nl

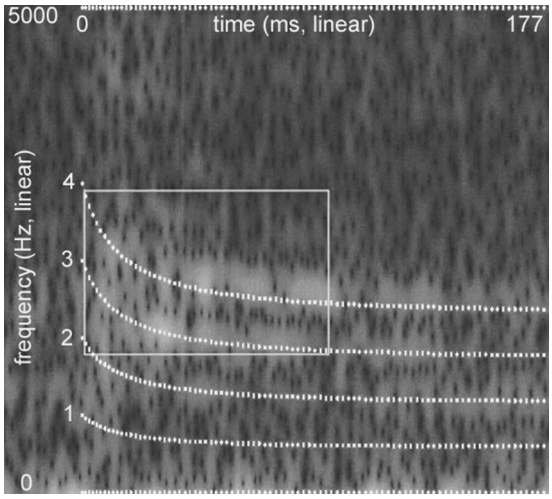

FIG. 1. Sonogram produced by Declercq *et al.* (Ref. 2, their Fig. 8) of the isolated chirp echo as recorded by Lubman (Ref. 1). Time-limited Fourier transformation with a Gaussian window of 2 ms was applied. Vertical axis: frequency linear from 0 to 5000 Hz; horizontal axis: time linear from 0 to 200 ms; white indicates high intensity. The white rectangle has no specific meaning for the present considerations. Dotted lines marked 1 through 4 constitute the present model predictions (see the text).

being the sum of all individual delays. For easy comparison with the sonogram of the recorded chirp echo, the dotted lines are superimposed on the sonogram (total span 200 ms) so that the 177-ms span of the model (91 dots) coincides as well as possible with the extent of the lighter areas of the sonogram in the horizontal direction (three dots fall outside the figure). Horizontal dotted lines at 0 Hz and 5 kHz coincide with the frequency scale of the sonogram. It can be concluded that the dotted lines fit nicely to the lighter regions in the sonogram.

III. CONCLUDING REMARKS

In order to correctly appreciate the fit between the sonogram and the theoretical curves, one has to take into account that the 2-ms Gaussian time window of the sonogram's running Fourier transform (see Declercq *et al.*[2]) covered mainly two reflections, given a delay time interval of 1.95 ms (=177/91) on average. This implies that, in accordance with

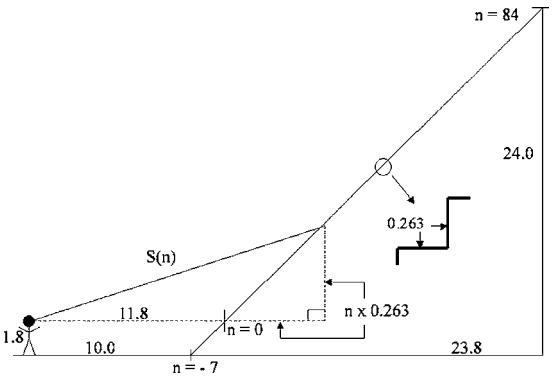

FIG. 2. Schematics of El Castillo pyramid in Chichen Itza following the data by Lubman as adopted by Declercq *et al.* (Ref. 2). Dimensions are given in meters. Source-receiver position is at a height of 1.8 m at a distance of 10 m from the foot of the pyramid. Step width is 0.263 m. Steps are numbered $n=-7$ to 84.

our calculations based on pulse pairs, the vertical width of the lighter areas is expected to reflect cosinusoidal power spectra.[9]

As far as perception is concerned, it should be noticed that no spectral energy is present in the signal at the "fundamental." Thus, a Repetition Pitch is predicted due to the presence of the second and, more important, the third and fourth "harmonics" (the so-called dominant harmonics[5,6]). It glides from 796 to 471 Hz-equivalent. That is to say: in theory, because we have not considered the short-term characteristics of the cochlear frequency analysis as well as the integration characteristics of the human pitch processor. This would be beyond the limited scope of the present letter. By informal listening, instead, to a synthesized RP glide following the above-noted model, great similarity with the chirp recorded by Lubman[1] (downloaded from his website) was observed. This confirms also the perceptual relevance of the present considerations.

Additionally, it is worthwhile mentioning an original observation by Christian Huygens[10] in 1693 at the castle of Chantilly de la Cour in France. Standing at the foot of the majestic stone staircase in the garden he noticed that the noisy sound from a fountain produced a certain pitch. This was confirmed at later occasions by handclapping. Acoustic registrations show a regular reflection pattern due to the equality in width of the steps of the staircase, resulting in a stationary Repetition Pitch of 370 Hz-equivalent. Thus, both continuous (fountain) noise and handclap are understood to be appropriate source signals in Chantilly. In this context, it is tempting to predict that a setting with continuous noise would most probably not work at Chichen Itza, because of the simultaneous mixing of all the different time delays in the chirp echo.

ACKNOWLEDGMENT

The present study was triggered by a presentation by Dr. N. F. Declercq on 23 November 2005 for the Dutch Acoustical Society.

[1]D. Lubman, http://www.ocasa.org/MayanPyramid.htm (site visited on 24-11-2005).

[2]N. F. Declercq, J. Degrieck, R. Briers, and O. Leroy, "A theoretical study of special acoustic effects caused by the staircase of the EL Castillo pyramid at the Maya ruins of Chichen Itza in Mexico," J. Acoust. Soc. Am. **116**, 3328–3335 (2004).

[3]Exact, though cumbersome simulations, based on amplitude calculations by means of an extension of the Rayleigh theory of diffraction, produce better results, in agreement with experiments. The theoretical model reveals the amplitude distribution in a sonogram representation of the echo in front of the pyramid. From this amplitude distribution it is also possible to extract the "delay lines" of the echo [N. F. Declercq (private communication)].

[4]F. A. Bilsen, "Repetition Pitch: Monaural interaction of a sound with the repetition of the same, but phase shifted, sound," Acustica **17**, 295–300 (1966).

[5]F. A. Bilsen, "Pitch of noise signals: Evidence for a central spectrum," J. Acoust. Soc. Am. **61**, 150–161 (1977).

[6]F. A. Bilsen and R. J. Ritsma, "Some parameters influencing the perceptibility of pitch," J. Acoust. Soc. Am. **47**, 469–475 (1970).
[7]W. M. Hartmann, *Signals, Sound, and Sensation* (AIP Press, New York, 1997), pp. 361–376.
[8]T. D. Rossing, *The Science of Sound* (Addison-Wesley, New York, 1990), pp. 121–122.
[9]A prediction of the complete sonogram instead of only spectral maxima (dotted lines) seems feasible partly by incorporating (running) cosinusoidal power spectra of pulse pairs multiplied with the spectrum of the handclap. However, also including reflection properties of the steps (amplitude and phase) is beyond the scope of the present approach.
[10]C. Huygens, " En envoiant le probleme d'Alhazen en France," Correspondence No. 2840 (November 1693) printed in Oeuvres Complètes, Vol. **10**, edited by Societý Hollandaise des Sciences (Nijhoff, Den Haag, 1950), pp.570–571.

Image-source method and truncation of a series expansion of the integral solution—Case of an angular sector in two dimensions

Vincent Martin[a)]
Laboratoire de Mécanique Physique, CNRS, 2, place de la Gare de Ceinture, F-78210 St-Cyr l'Ecole, France

Thomas Guignard[b)]
Laboratoire d'Electromagnétisme et d'Acoustique, EPFL, STI-ITOP-LEMA, Station 11, CH-1015 Lausanne, Switzerland

(Received 14 September 2005; revised 16 May 2006; accepted 19 May 2006)

The acoustic ray method rests upon specular reflection, an intuition that gives access only to an approximation of the solution by not taking into account the parts of the field called diffusion and diffraction. In trying to understand rationally the roots of the approximation, it has appeared that the image source could be generalized and also that errors may be partially due to missing generalized sources, already in elementary geometries such as obtuse angles. Indeed, it is shown that the exact integral solution of a two dimensional acoustic problem, expressed as a series of terms, could be seen as the contribution of the different image sources, via a partial use of the Huygens' principle. With the correspondence between the terms and the image sources shown, the missing sources would appear and the method would thereby be refined. © *2006 Acoustical Society of America.*
[DOI: 10.1121/1.2214133]

PACS number(s): 43.20.Dk [NX] Pages: 597–610

I. INTRODUCTION

In acoustic cavities such as concert halls or passengers' spaces in vehicles, the numerical description of classical sound fields—those satisfying the Helmholtz equation in space-frequency domain with local boundary conditions—stems from various methods, the choice of which depends first of all on the ratio of the wavelength to a linear dimension of the considered cavity. The reasons for this choice are either of conceptual or practical nature and each method has its own advantages and drawbacks. For example, the boundary finite element method, developed from the exact integral representation of the Helmholtz operator solution, is impractical for high frequencies, as the necessary fine discretization of the boundaries would then lead to large and full matrices, taking a long time to build and inverse. In the adequate frequency range, the method cannot be extended to nonlinear problems (at least not directly). It needs knowledge of the acoustic field everywhere on the boundaries before giving access to the field at the points of interest inside the domain.

The finite element method (finite elements of volume), resting on the variational form stemming from the weak form of the equation under study, is also confined to sufficiently long wavelengths for the same practical reasons of discretization, this time of the domain, even if the matrices are more quickly built and inversed as they can be made with a large number of null terms. As an indication, it is not easy to describe sound fields in the audible medium frequency range (1 kHz–5 kHz) in passengers' space in aircrafts, helicopters, cars, etc. The method is appropriate for nonlinear problems. It necessarily describes the field everywhere within the domain and on the boundaries (substructuration could lead directly to the boundary values but at the expense of supplementary calculation time).

As for the ray method, it is restricted to the description of fields arising from specular reflections and does not take diffraction into account. Diffusion effects can be inserted but require great precaution. However, it gives access to the medium frequency range mentioned above. Specular reflection—originating from geometrical optics concepts—applied to sound waves in air is quoted as early as the 1940s (Ref. 1) if not before, with experimental validation. The principle of specular reflection on perfectly rigid walls is compatible with the modal theory in waveguides and in rectangular cavities.[2] It is also with specular reflection that it has been possible to obtain an understanding of some-causality problems in the field of active acoustic control,[3] as long as the geometrical configuration is very simple. In architectural acoustics, it is commonly accepted that the ray method is able to describe sound fields above 100 Hz in large auditoriums.[4] Here, the calculation of the field at some particular point within the domain does not require that of the entire domain (contrarily to the finite element method) nor on all the boundaries (contrarily to the boundary element method). However, one must remember that the method is not rigorous and that the reaction taken only at the impact point of reflection is an approximation of the more global reaction properly described by the integral representation; this is probably the reason why calculation on all the boundaries is not needed.

[a)]Electronic mail: vmartin@ccr.jussieu.fr
[b)]Electronic mail: thomas.guignard@epfl.ch

The ray method, so widely known for room acoustics in the years around 1960–1990,[5] has been revisited over the last 10 years or so for its use in vehicle passengers' space, with the sound field descriptions in the audible medium frequency range in view.[6,7] Concerning the algorithmic procedure, improvements carried out by previous authors in two different directions are helpful:[4,8,9] one is called *ray-tracing*, the other *virtual image sources*, and their history shows that they were developed quite simultaneously.

In a *ray-tracing*, algorithm, rays "leave" a point source emitting an impulse (in theory an infinity of rays) and, for each of them, the first point of impact on a wall is sought and from there on the next impact point on another wall, etc. Nothing prevents this method from being used within nonconvex cavities. A priori, the procedure goes on indefinitely for each ray. Given a receiver point R, rays originating from the source that, after a certain number of reflections, go through R, make up the sound history—called impulse response or histogram or echogram—at point R. In practice, the number of rays leaving the source is finite and the rays propagate in a divergent way with the consequence that the weaker the probability for the rays to go through the receiver R, the smaller the number of permitted reflections. This is the reason why the histogram is made for a neighborhood of R rather than the point alone. In these conditions the procedure can be quite short but at the price of uncertainty. Nevertheless, this ray-tracing version has the great advantage of being able to insert diffusive walls (because of their geometry and not of their behavior).

The *virtual image sources* algorithm identifies the images of the real source by a mirror effect on each wall, then the images of the images are nought, etc., a priori indefinitely. However all these images are only potentially useful for calculating the acoustic field (except for rectangular enclosures) and only a small number of them actually "light" the domain, while still less are "seen" by the-given receiver point. Validity (for "lighting" the domain) and visibility, (of the receiver point) tests reduce hugely the number of images and a proximity test restricts their number by limiting the acceptable distance between the images and the receiver point. Nonconvex domains need an obstruction test[9] or call for another approach.[7,10] The algorithm is precise in giving the rays leaving the source and propagating to the receiver, but distinguishing the useful sources from the potential ones is a heavy task and moreover it is difficult here to take diffusion into account. However, this procedure is chosen in this paper for its precision. It must be mentioned that the virtual sources procedure can also be understood as that of virtual receivers. Indeed, by determining the receiver images it is possible to retropropagate rays issued from R until the real source is reached.[9] At this stage, it must be noted that the definition of image sources makes the problem independent of the type of signal emitted by the primary source and of the usage of the signal at the reception point. For example, in Refs. 4, 8, and 9, rays are energy carriers and are used to assess sound intensity (under consideration of the form of the sound field). Here, phased (therefore in terms of complex amplitudes) sound fields in the frequency domain are considered, so as to observe systems of standing waves forming resonances and antiresonances.

In that sense, comparison between acoustic fields calculated by the finite element method and the ray method (with the image source algorithm) has shown-differences which constitute a handicap for going further in small enclosures with the latter method.[7] What should then be done in order to reduce the differences? It is known qualitatively that the ray method does not take into account diffraction and/or diffusion and that the solution obtained cannot in general be exact. But even by dealing only with the part of the acoustic field made up of specular reflections, what do we know quantitatively about the ability of the image sources to reveal the field? In trying to answer this question, it would first be necessary to sustain the intuitive notion of image sources by a rational formulation and, in doing so, to have a tool to master their contribution to the sound field. Looking in that direction in the framework of a very elementary geometrical configuration, it has been found that sources said to be invalid by the current source-choosing algorithm could improve the description of the acoustic field. This being said, it has not yet been possible to know if this improvement resulted from a better-description of diffraction, or of the reflected field, or of both. Thus, the work presented here has the form of a theoretical investigation in a simple configuration, an investigation not yet found in the acoustic literature.

The beginning of this paper is a recall of one of the algorithms of the ray method that defines the image sources, and also emphasizes two figures of an angular sector in the plane which motivate the study. After a first premiss that sets out a particular presentation of the acoustic field in presence of a reflective wall in a two-dimensional (2D) half-space, the exact solution of the angular sector arises from the integral representation. The solution thus obtained on the walls is liable to be developed in series, and arguments associated with the Huygens' principle lead us to think that each term of the series could reveal the contribution of an image source. The same formalism is then extended to the case of walls with damping material. Then, the transformation of the pressure on the walls into the pressure inside the sector shows the possible contribution of image sources inside the domain. Numerical experiments in the third section of this paper support broadly the hypothesis of a correspondence between terms of the series and image source contributions, opening a door towards an improvement of the current algorithms for identifying the useful virtual sources.

At this point it is necessary to cite in more detail the work of Mechel,[10] presenting a comprehensive overview of the image sources method. The reassembling of sources in a 2D angular sector and the development of the exact solution into a modal series (different from the series development presented in this paper) are of particular interest here. The reassembling of sources leads to the definition and the insertion of a "corner source," along with a particular directivity, and to an algorithm to compute the validity of images. The modal series suggests the idea of inserting the exact solution into the image sources method, thereby resulting in a mixed analytical-image source method. Although the approach presented here has not been inspired by Mechel's work and

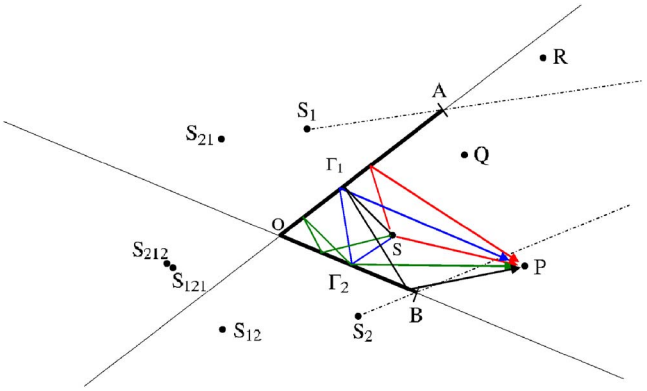

FIG. 1. (Color online) Set of image-sources liable to give rise to reflected rays for points in the angular sector; set of rays (i.e., of sources) contributing to the calculation of the acoustic field at point P.

follows a different path, a certain, relation between the objectives of both approaches must be assessed. In fact, these two approaches could converge by extrapolation of the fact that the elementary solution classically associated with each image source could be replaced by a more complete solution (including diffraction) associated with a -certain set of images.

The present text develops, extends, and explores in greater depth the subject of a relatively short communication given recently at a congress.[11]

II. FORMALISM ON THE BOUNDARIES AND IN THE DOMAIN

A. Preamble, configurations and premisses

Any comparison between acoustic fields obtained by the image source method and by the boundary integral method needs, as a preliminary, to speak of the algorithm which usually chooses the image sources. The image from a wall numbered n originates by a mirror effect on that wall from a source, that could itself be the image from wall numbered k. It is convenient to write it as

$$S_{\underbrace{\ldots kn}_{l\text{indices}}}$$

to signify that it will give rise to l reflections from the actual source, the last one on wall n, the previous one on wall k, etc. For example, the source denoted S_5 is the image of the real source through wall 5, and source S_{53} is the image of source S_5 through wall 3. Its presence will show two reflections. This can happen only if the last reflection is able to reach a point inside the domain. To clarify, Fig. 1 presents a 2D domain made up of an angular sector defined by two semi-infinite straight lines, in fact two segments (of finite length). Six image sources are liable to reveal reflections. However to reach point P, only four image sources are useful; only source S_{212} would give a reflected ray reaching point Q; for R, three image sources intervene. In Fig. 1, it appears that an image source with last index n plays a role, for point P forinstance, if the ray from that source goes through wall n to reach P. In these conditions, source S_{212} is of no use for point Q as the ray from S_{212} does not go through wall Γ_2 to reach Q.

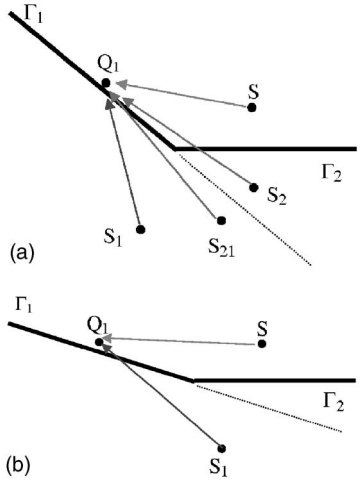

FIG. 2. The implementation of the algorithm for determining the useful image sources for point Q_1 results in three images in (a) and only one in (b).

Having thus in mind the algorithm for determining the sources, the motivation of the present work arises from both diagrams in Fig. 2. The sector is now defined by the semi-infinite straight lines Γ_1 and Γ_2. The configuration on Fig. 2(a) leads to four sources (three images and the real source). However, the validity of the field obtained at point Q_1, is not guaranteed. On the contrary, on Fig. 2(b), the only image source available definitively instills a doubt regarding the field obtained, as it is not expected that wall Γ_2 plays no role at all (source S_1, reveals the presence of wall Γ_1 only). Nevertheless, it is possible to enlighten the degree of precision of the field obtained by rays by comparing it to the exact solution given by the integral representation. To begin with, the particularly simple situation of a single reflecting plane is observed to gain access to the definition of the first order image source, the wall pressure (in a discretized form) and an iterative access to it. Notations will be defined in the course of development. In Fig. 3, a point source S_0 radiates an acoustic pressure. In particular at point Q on the perfectly reflecting wall Γ, the elementary solution of the Helmholtz operator is shown to be

$$p(Q) = G_\infty(Q,S_0) + G_\infty(Q,S_0), \tag{1}$$

where $G_\infty(Q,S_0)$ is the elementary solution of the Helmhotz operator in an open domain (the source flow amplitude is chosen so that the right-hand side of the Helmholtz wave equation is unity); here, in 2D, it has the form $+(i/4)H_0^-(k|Q-S_0|)$ with H_0^- the Hankel function of the second kind of zeroth order. In fact, for any point R in the

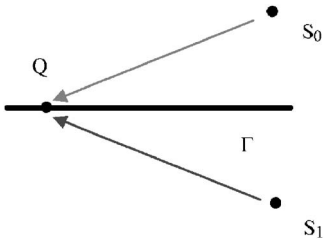

FIG. 3. Reflection of an acoustic wave on a totally reflecting plane in the half-infinite space.

domain, the integral representation (also called Green's third formula) leads to

$$p(R) = G_\infty(R,S_0) + \int_\Gamma \partial_{n_M} G_\infty(R,M) p(M) dM, \tag{2}$$

where $G_\infty(R,S_0)$ is the result of the operation $\int_\Omega G_\infty(R,S)\,\delta(S-S_0)dS$ taking into account the excitation on the right-hand side of the wave equation.

When point R in the domain tends toward point Q on Γ, the principal part of the double layer potential leads to

$$p(Q) = G_\infty(Q,S_0) + \tfrac{1}{2}p(Q) \tag{3}$$

which can also be written

$$p(Q) = 2G_\infty(Q,S_0) \quad \forall\, Q \in \Gamma \tag{4}$$

and $p(\Gamma)=2G_0(\Gamma)$ will now be a shorthand representation for $p(Q)=2G_\infty(Q,S_0)$ when the observation points Q are on the boundary Γ. The subscript 0 is linked to the source S_0 (the index ∞ of G has been removed when indication of the source occurs). The image source S_1 can be made apparent by noting

$$p(\Gamma) = \underbrace{G_0(\Gamma)}_{\text{cominng from } S_0} + \underbrace{\frac{1}{2}p(\Gamma)}_{\text{coming from } S_1}. \tag{5}$$

In fact, the term $\frac{1}{2}p(\Gamma)$ in (5) is equal to $G_\infty(Q,S_0)$ by identification in (3) and (4). It indeed represents the free-field pressure on the geometrical locus Γ due to S_0 but also the pressure on the same locus due to S_1, since S_1, is the mirror image of S_0 relative to Γ.

Now, out of the continuous form

$$p(Q) = G_\infty(Q,S_0) + \int_\Gamma p(M)\partial_{n_M} G_\infty(Q,M) dM \tag{6}$$

a discrete form can be deduced. By decomposing the wall Γ (which is a straight line in this bi-dimensional space) into elementary facets Γ_j such as $\Gamma \equiv \cup\Gamma_j$ with $j=1,\infty$, Eq. (6) can be approximated by

$$p(Q) = G_\infty(Q,S_0) + \sum_{j=1}^{\infty} p(M_j) \times \int_{\Gamma_j} \partial_{n_M} G_\infty(Q,M) dM, \quad \text{where } M_j \in \Gamma_j \tag{7}$$

provided the pressure can be considered constant on each facet. For a particular point Q_i, the pressure can be written

$$p_i = G_\infty(Q_i,S_0) + \sum_{j=1}^{\infty} a_{ij} p_j \tag{8}$$

or, for a set of points on the wall, by the matrix equation

$$\mathbf{p}(\Gamma) = \mathbf{g}_0(\Gamma) + \mathbf{A}\cdot\mathbf{p}(\Gamma), \tag{9}$$

where the vertical (columns) dimension of matrix $\mathbf{A}$ is infinite. Following the usual convention, bold lowercase letters represent vectors and bold uppercase ones represent matrices; accordingly $G_\infty(Q_i,S_0)$ becomes $\mathbf{g}_0(\Gamma)$. For the resolution of the problem, $\mathbf{A}$ will be made square and (3) provides that

$$\mathbf{A} = \tfrac{1}{2}\mathbf{I} \tag{10}$$

in that case.

At this stage, a side remark will be useful for the later developments. In (9), the wall pressure $\mathbf{p}(\Gamma)$ is the final solution sought, which will be written $\mathbf{p}_E$ (E for "end"). The term $\mathbf{g}_0(\Gamma)$ comes from the free-field pressure on the geometrical locus on the wall and will be thus written $\mathbf{p}_F$ (F for "free"). In these conditions, (9) becomes

$$\mathbf{p}_E = [\mathbf{I}-\mathbf{A}]^{-1}\cdot\mathbf{p}_F \tag{11}$$

which describes the effect of the wall on the free-field emitted by the source S_0. This formulation can also be differently interpreted if one considers Eq. (11) with the matrix term formally developed as a series,

$$\mathbf{p}_E = \underbrace{\mathbf{p}_F}_{\text{contribution from } S_0} + \underbrace{[\mathbf{A}+\mathbf{A}^2+\mathbf{A}^3+\ldots]\cdot\mathbf{p}_E}_{\text{contribution from } S_1 \text{ taling the wall into account}}. \tag{12}$$

In fact, with no absorption where (10) is valid, the second term of the right-hand side of (12) leads to

$$\left(\tfrac{1}{2}+\tfrac{1}{4}+\tfrac{1}{8}+\cdots\right)\mathbf{p}_F = \mathbf{p}_F \tag{13}$$

which is the contribution of the image source S_1. The existence of this source takes the wall into account and its contribution with $\mathbf{p}_F = 1/2\mathbf{p}_E$ reveals that the wall reflects perfectly.

Furthermore, if $\mathbf{A}$ is seen as revealing the radiation of a pressure source upon itself, the modified pressure value becomes the new pressure source, which is again modified by $\mathbf{A}$, etc., and the pressure at the source converges towards the pressure value $1/2\mathbf{p}_E=\mathbf{p}_F$ in vector notation. This interpretation would then be a special case of what will be discussed later on. It should also be noted that the development of $[\mathbf{I}-\mathbf{A}]^{-1}$ is legitimate as long as the series converges. It is evidently the case here, but in a more general case, the convergence of the series should be assessed.

B. A possible origin of the image sources and of their relative importance

Were the ray method exact, the pressure on point Q_1 on wall Γ_1 in Fig. 2(a) would be, with the notations mentioned before

$$p_{\text{ray}}(Q_1) = G_0(Q_1) + G_1(Q_1) + G_2(Q_1) + G_{21}(Q_1). \tag{14}$$

As previously stated, (14) is more precisely written in 2D as

$$p_{\text{ray}}(Q_1) = +\frac{i}{4}(H_0^-(k|Q_1-S_0|) + H_0^-(k|Q_1-S_1|) + H_0^-(k|Q_1-S_2|) + H_0^-(k|Q_1-S_{21}|)). \tag{15}$$

What would be the outcome of a computation from integral representation, which is known to be exact? To start with, the development is done with nonabsorbing walls.

Green's third formula leads to

$$p(Q_1) = G_\infty(S_0,Q_1) + \underbrace{\int_{\Gamma_1} p(M)\partial_{n_M} G_\infty(Q_1,M)dM}_{=1/2p(Q_1)} + \int_{\Gamma_2} p(M)\partial_{n_M} G_\infty(Q_1,M)dM \tag{16}$$

or, in matrix form, with still further obvious shorthand representation

$$\mathbf{p}(\Gamma_1) = \mathbf{p}_1 = \mathbf{g}_0(\Gamma_1) + \mathbf{A}_{11}\cdot\mathbf{p}_1 + \mathbf{A}_{12}\cdot\mathbf{p}_2 \tag{17}$$

with

$$\mathbf{A}_{11} = \tfrac{1}{2}\mathbf{I} \tag{18}$$

in the case of a perfectly reflecting wall Γ_1. In a similar way,

$$\mathbf{p}_2 = \mathbf{g}_0(\Gamma_2) + \mathbf{A}_{21}\cdot\mathbf{p}_1 + \mathbf{A}_{22}\cdot\mathbf{p}_2 \tag{19}$$

with

$$\mathbf{A}_{22} = \tfrac{1}{2}\mathbf{I} \tag{20}$$

with a perfectly reflecting wall Γ_2. It is to be noted that (18) and (20) reveal infinite and perfectly reflecting walls. The matrices $\mathbf{A}_{12}$ and $\mathbf{A}_{21}$ therefore contain information about the finiteness of the walls (they are of semi-infinite dimensions) and border effects.

Equations (17) and (19) lead to

$$\mathbf{p}_1 = \underbrace{[\mathbf{I}-\mathbf{A}_{11}]^{-1}\cdot\mathbf{g}_0(\Gamma_1)}_{\substack{=2\mathbf{I} \text{ when } \beta=0 \\ \text{contributions of } S_0 \text{ and } S_1 \text{ on } \Gamma_1 \\ \text{respectively noted } \mathbf{g}_0(\Gamma_1) \text{ and } \mathbf{g}_1(\Gamma_1)}} + \underbrace{[\mathbf{I}-\mathbf{A}_{11}]^{-1}\cdot\mathbf{A}_{12}}_{=2\mathbf{A}_{12} \text{ noted } 2\ \mathbf{C}}\cdot\mathbf{p}_2,$$

$$\mathbf{p}_2 = \underbrace{[\mathbf{I}-\mathbf{A}_{22}]^{-1}\cdot\mathbf{g}_0(\Gamma_2)}_{\substack{\text{contributions of } S_0 \text{ and } S_2 \text{ on } \Gamma_2 \\ \text{respectively noted } \mathbf{g}_0(\Gamma_2) \text{ and } \mathbf{g}_2(\Gamma_2)}} + \underbrace{[\mathbf{I}-\mathbf{A}_{22}]^{-1}\cdot\mathbf{A}_{21}}_{=2\mathbf{A}_{21} \text{ noted } 2\ \mathbf{B}}\cdot\mathbf{p}_1, \tag{21}$$

where Eq. (10) with reflecting walls (admittance $\beta=0$) has been used and where matrices $\mathbf{B}$ and $\mathbf{C}$ are a notation used for brevity's sake. Solving this system provides

$$\mathbf{p}_1 = [\mathbf{I}-2\mathbf{C}\cdot2\mathbf{B}]^{-1}\cdot(\mathbf{g}_0(\Gamma_1)+\mathbf{g}_1(\Gamma_1)) + [\mathbf{I}-2\mathbf{C}\cdot2\mathbf{B}]^{-1}\cdot2\mathbf{C}\cdot(\mathbf{g}_0(\Gamma_2)+\mathbf{g}_2(\Gamma_2)),$$

$$\mathbf{p}_2 = [\mathbf{I}-2\mathbf{B}\cdot2\mathbf{C}]^{-1}\cdot(\mathbf{g}_0(\Gamma_2)+\mathbf{g}_2(\Gamma_2)) + [\mathbf{I}-2\mathbf{B}\cdot2\mathbf{C}]^{-1}\cdot2\mathbf{B}\cdot(\mathbf{g}_0(\Gamma_1)+\mathbf{g}_1(\Gamma_1)). \tag{22}$$

Formally, developing in series would result in the expressions

$$\mathbf{p}_1 = \mathbf{g}_0(\Gamma_1)+\mathbf{g}_1(\Gamma_1) + 2\mathbf{C}\cdot(\mathbf{g}_0(\Gamma_2)+\mathbf{g}_2(\Gamma_2)) + 2\mathbf{C}\cdot2\mathbf{B}\cdot(\mathbf{g}_0(\Gamma_1)+\mathbf{g}_1(\Gamma_1)) + 2\mathbf{C}\cdot2\mathbf{B}\cdot2\mathbf{C}\cdot(\mathbf{g}_0(\Gamma_2)+\mathbf{g}_2(\Gamma_2)) + \cdots,$$

$$\mathbf{p}_2 = \mathbf{g}_0(\Gamma_2)+\mathbf{g}_2(\Gamma_2) + 2\mathbf{B}\cdot(\mathbf{g}_0(\Gamma_1)+\mathbf{g}_1(\Gamma_1)) + 2\mathbf{B}\cdot2\mathbf{C}\cdot(\mathbf{g}_0(\Gamma_2)+\mathbf{g}_2(\Gamma_2)) + 2\mathbf{B}\cdot2\mathbf{C}\cdot2\mathbf{B}\cdot(\mathbf{g}_0(\Gamma_1)+\mathbf{g}_1(\Gamma_1)) + \cdots. \tag{23}$$

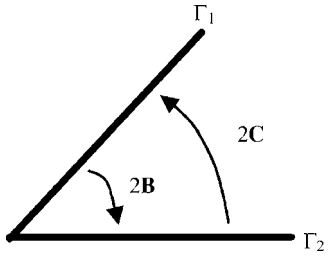

FIG. 4. Matrices **2B** and **2C** transfer, respectively, pressure from wall Γ_1, toward wall Γ_2 and inversely.

Now, Huygens' principle posits that the field emitted from a source to a reception point can be regarded as the contribution of fictitious sources located on the wave front between the source and the reception point.[12] This assertion, qualitative at this stage, argues in favor of establishing a correlation between the terms of the series and the image sources. Indeed, keeping an eye on $\mathbf{p}_1$, in (23), it should be noted that $2\mathbf{C}\cdot\mathbf{g}_0(\Gamma_2)$ is the pressure radiated by S_0 toward Γ_2 transferred to Γ_1 through the multiplication by $2\mathbf{C}$ (cf. Fig. 4). It is also the pressure originating from S_2 on Γ_2 transferred to Γ_1, i.e., pressure from S_2 radiated to Γ_1 denoted $\mathbf{g}_2(\Gamma_1)$. This last deduction lacks rigor for the time being. In fact, it would be necessary to know the pressure radiated by S_2 on the whole (infinite) wall Γ_2 for the pressure transferred to points of Γ_1 to be comparable with that radiated by S_2. To this first reasoning, another is added. Term $2\mathbf{C}\cdot\mathbf{g}_2(\Gamma_2)$ represents the pressure due to S_2 on Γ_2 transferred to Γ_1, i.e., pressure from S_2 on Γ_1. It is also the pressure from S_{21} to Γ_1 or $\mathbf{g}_{21}(\Gamma_1)$, with the same lack of rigour as written above (the notation $\mathbf{g}_{21}$ for source S_{21} is clear, see Sec. II A for the definition of S_{21}). With both reasonings, it appears from (23) (terms of the same order are in square brackets),

$$\mathbf{p}_1 = [\mathbf{g}_0(\Gamma_1)+\mathbf{g}_1(\Gamma_1)] + [\mathbf{g}_2(\Gamma_1)+\mathbf{g}_{21}(\Gamma_1)] + [\mathbf{g}_{12}(\Gamma_1) + \mathbf{g}_{121}(\Gamma_1)] + [\mathbf{g}_{212}(\Gamma_1)+\mathbf{g}_{2121}(\Gamma_1)] + \cdots,$$

$$\mathbf{p}_2 = \underbrace{[\mathbf{g}_0(\Gamma_2)+\mathbf{g}_2(\Gamma_2)]}_{\text{0th order terms}} + \underbrace{[\mathbf{g}_1(\Gamma_2)+\mathbf{g}_{12}(\Gamma_2)]}_{\text{1st order terms}} + \underbrace{[\mathbf{g}_{21}(\Gamma_2)+\mathbf{g}_{212}(\Gamma_2)]}_{\text{2nd order terms}} + \underbrace{[\mathbf{g}_{121}(\Gamma_2)+\mathbf{g}_{1212}(\Gamma_2)]}_{\text{3rd order terms}} + \cdots. \tag{24}$$

To put the above formalism in relation with the diagrams of motivation in Fig. 2, we should conclude that the sources S_{12}, S_{121}, etc., are missing on the configuration on Fig. 2(a) and sources S_2, S_{21}, etc., for the configuration on Fig. 2(b). Moreover, taking into account the natural order of terms in the series for $\mathbf{p}_1$, the first source that should be added to the configuration on Fig. 2(a) would be S_{12}, which is not suitable since it is inside the domain. On Fig. 2(b), source S_2 should be considered next. The algorithm for determining the sources would take it into account, were wall 2 lengthened towards the left. Let us also note that the order of sources for $\mathbf{p}_1$ is not the same as for $\mathbf{p}_2$.

Studying the same problem with an admittance β_1 on Γ_1 and β_2 on Γ_2 enables us on the one hand, to refine the transfer terms towards walls Γ_1 and Γ_2 and, on the other hand, to take the admittance of the reflections associated with the im-

age sources into account. The development resembles the one presented at the start of this section, but with a further degree of generalization along with some refinements in the possible understanding of the image sources origin.

In this case also, some preliminary remarks are necessary and one returns to Fig. 3, where the wall Γ now has an admittance β_Γ (the inverse of the reduced impedance Z_Γ). Equation (6) is now to be written as

$$p(R) = G_\infty(R,S_0) + \int_\Gamma \underbrace{(\partial_{n_M} G_\infty(R,M) + ik\beta_\Gamma G_\infty(R,M))}_{(*)} \times p(M)dM. \tag{25}$$

So the wall itself takes on the role of a source with pressure $p(M)$, transmitted to point R while considering the wall admittance β_Γ and the radiation via $\partial_{n_M} G_\infty$ and G_∞ applied to the distance $|R-M|$. From a physical viewpoint, the so-called source pressure $p(M)$ must act on the internal source impedance Z_Γ combined with the load impedance coming from the medium in which the acoustical pressure is propagating. The resulting pressure must then be propagated to point R. All these roles are described by part $(^*)$ of Eq. (25). In terms of discrete operators, making point R tend toward point Q on wall Γ leads to

$$p(Q) - \int_\Gamma (\partial_{n_M} G_\infty(Q,M) + ik\beta_\Gamma G_\infty(Q,M))p(M)dM = G_\infty(Q,S_0) \tag{26}$$

or, by using the same notations as in (11)

$$\mathbf{p}_E(\Gamma) = [\mathbf{I} - \mathbf{A}_{\Gamma\Gamma}]^{-1} \cdot \mathbf{p}_F(\Gamma), \tag{27}$$

where the matrix $\mathbf{A}_{\Gamma\Gamma}$ [a generalization of the form $\mathbf{A}$ in (11), representing the influence of the wall facets on observation points on the wall] stems from a discretized form of the expression

$$\int_\Gamma (\partial_{n_M} G_\infty(Q,M) + ik\beta_\Gamma G_\infty(Q,M))p(M)dM \tag{28}$$

In the whole domain, with $\mathbf{p}_E(\Omega)$ noting the vector containing pressure values on points inside the domain and with $\mathbf{A}_{\Omega\Gamma}$ noting the matrix originating from the discretization of

$$\int_\Gamma (\partial_{n_M} G_\infty(R,M) + ik\beta_\Gamma G_\infty(R,M))p(M)dM \tag{29}$$

the components of which represent the influence on the facets on the reception point in the domain, Eq. (25) becomes

$$\mathbf{p}_E(\Omega) = \mathbf{A}_{\Omega\Gamma} \cdot [\mathbf{I} - \mathbf{A}_{\Gamma\Gamma}]^{-1} \cdot \mathbf{p}_F(\Gamma) + \mathbf{g}_0(\Omega). \tag{30}$$

This can be interpreted as follows: $\mathbf{p}_F(\Gamma)$ is the pressure coming from source S_0 radiated on the geometrical locus defined by the wall Γ, S_0 loaded by both its internal impedance Z_{S_0} and the radiating impedance Z_{rad_Ω}. This pressure is therefore more precisely written

$$\mathbf{p}_F(\Gamma) = \mathbf{g}_0(Z_{S_0} \cup Z_{\mathrm{rad}_\Omega}, \Gamma^{\mathrm{geom}}). \tag{31}$$

The operator $[\mathbf{I}-\mathbf{A}_{\Gamma\Gamma}]^{-1}$ applied to this quantity does consider the wall impedance (in fact the combination of the wall and propagation medium impedances) and one writes

$$\mathbf{p}_E(\Gamma) = [\mathbf{I} - \mathbf{A}_{\Gamma\Gamma}]^{-1} \cdot \mathbf{p}_F(\Gamma) = \underbrace{\mathbf{g}_0(Z_{S_0} \cup Z_{\mathrm{rad}_\Omega}, \Gamma(Z_\Gamma))}_{\mathbf{g}_1(Z_{S_0} \cup Z_{\mathrm{rad}_\Omega}, \Gamma(Z_\Gamma))}, \tag{32}$$

where it has been emphasized that Γ is now no longer only a geometrical locus but also an actual wall with some kind of internal impedance if this wall is to be seen as a source. Furthermore, as for Eq. (5), it appears that the pressure emitted by S_0 on the wall is also the pressure emitted by image S_1.

Finally, the right-hand side of Eq. (30), except the direct contribution, is interpreted as the pressure coming from the image source on a geometrical locus of the domain and will be written

$$\mathbf{A}_{\Omega\Gamma} \cdot [\mathbf{I} - \mathbf{A}_{\Gamma\Gamma}]^{-1} \cdot \mathbf{p}_F(\Gamma) = \mathbf{g}_1(Z_{S_0} \cup Z_{\mathrm{rad}_\Omega}, Z_\Gamma \cup Z_{\mathrm{rad}_\Gamma}, \Omega^{\mathrm{geom}}). \tag{33}$$

This rich notation reveals that the image source S_1 emits a pressure towards a point inside the domain Ω, taking into account the fact that it is the image of source S_0 (together with its internal impedance Z_{S_0} and load Z_{rad_Ω}) relatively to wall Γ (with internal impedance Z_Γ and load Z_{rad_Γ}).

The notion of a wall seen as a source with its own pressure and having an internal impedance that must be combined with the load impedance in order to radiate into the domain—or toward the geometrical locus of another wall—is the key to interpreting the terms of the series development of the solution obtained by the integral equations method.

Going back to the situations in Fig. 2, the continuous form of the coupled problem on both walls is now the extended form of (16),

$$\begin{aligned} p(Q_1) &= G_\infty(Q_1,S_0) + \int_{\Gamma_1} p(M)(\partial_{n_M} G_\infty(Q_1,M) \\ &\quad + ik\beta_1 G_\infty(Q_1,M))dM + \int_{\Gamma_2} p(M) \\ &\quad \times (\partial_{n_M} G_\infty(Q_1,M) + ik\beta_2 G_\infty(Q_1,M))dM, \\ p(Q_2) &= G_\infty(Q_2,S_0) + \int_{\Gamma_1} p(M)(\partial_{n_M} G_\infty(Q_2,M) \\ &\quad + ik\beta_1 G_\infty(Q_2,M))dM + \int_{\Gamma_2} p(M) \\ &\quad \times (\partial_{n_M} G_\infty(Q_2,M) + ik\beta_2 G_\infty(Q_2,M))dM, \end{aligned} \tag{34}$$

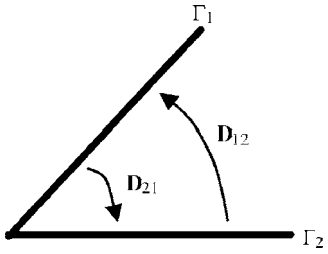

FIG. 5. Operators $\mathbf{D}_{21}$ and $\mathbf{D}_{12}$ transfer, respectively, pressure from wall Γ_1, toward wall Γ_2 and inversely (the order of the indices comes from the matrix representation and is to be read from right to left).

or in discrete form [this time, unlike (21), without simplification]

$$\begin{aligned}\mathbf{p}_1 &= [\mathbf{I}-\mathbf{A}_{11}]^{-1}\cdot\mathbf{g}_0(\Gamma_1)+[\mathbf{I}-\mathbf{A}_{11}]^{-1}\cdot\mathbf{A}_{12}\cdot\mathbf{p}_2,\\ \mathbf{p}_2 &= [\mathbf{I}-\mathbf{A}_{22}]^{-1}\cdot\mathbf{g}_0(\Gamma_2)+[\mathbf{I}-\mathbf{A}_{22}]^{-1}\cdot\mathbf{A}_{21}\cdot\mathbf{p}_1,\end{aligned} \tag{35}$$

out of which one obtains, for example, the extended form of (22),

$$\begin{aligned}\mathbf{p}_1 = [\mathbf{I}-[\mathbf{I}-\mathbf{A}_{11}]^{-1}\cdot\mathbf{A}_{12}\cdot[\mathbf{I}-\mathbf{A}_{22}]^{-1}\cdot\mathbf{A}_{21}]^{-1}\\ \cdot[[\mathbf{I}-\mathbf{A}_{11}]^{-1}\cdot\mathbf{g}_0(\Gamma_1)+[\mathbf{I}-\mathbf{A}_{11}]^{-1}\cdot\mathbf{A}_{12}\\ \cdot[\mathbf{I}-\mathbf{A}_{22}]^{-1}\cdot\mathbf{g}_0(\Gamma_2)].\end{aligned} \tag{36}$$

Using the notations $\mathbf{D}_{21}=[\mathbf{I}-\mathbf{A}_{22}]^{-1}\cdot\mathbf{A}_{21}$ and $\mathbf{D}_{12}=[\mathbf{I}-\mathbf{A}_{11}]^{-1}\cdot\mathbf{A}_{12}$ the terms responsible for the pressure transfer from Γ_1 to Γ_2 and inversely appear; they generalize matrices $2\mathbf{B}$ and $2\mathbf{C}$ in (21). The order of the indices comes from the matrix equations and must be read from right to left to reveal the direction of transfer from one wall to the other. The analysis of $\mathbf{D}_{21}$, for example, shows that $\mathbf{A}_{21}$, which originates from

$$\int_{\Gamma_1}(\partial_{n_M}G_\infty(Q_2,M)+ik\beta_1G_\infty(Q_2,M))p(M)dM \tag{37}$$

applied to $p(\Gamma_1)$ makes wall Γ_1 [with pressure $p(\Gamma_1)$ and internal impedance Z_1] radiate towards the locus defined by wall Γ_2. Moreover, according to Eq. (27) the operator $[\mathbf{I}-\mathbf{A}_{22}]^{-1}$ modifies the pressure radiated at Γ_2 so as to consider the absorption described by β_2. Figure 5 illustrates the action of the operators $\mathbf{D}_{21}$ and $\mathbf{D}_{12}$. At this stage, the pressure at Eq. (36) is now

$$\begin{aligned}\mathbf{p}_1 = [\mathbf{I}-\mathbf{D}_{12}\cdot\mathbf{D}_{21}]^{-1}\cdot[[\mathbf{I}-\mathbf{A}_{11}]^{-1}\cdot\mathbf{g}_0(\Gamma_1)\\ +\mathbf{D}_{12}\cdot[\mathbf{I}-\mathbf{A}_{22}]^{-1}\cdot\mathbf{g}_0(\Gamma_2)]\end{aligned} \tag{38}$$

and, using Eq. (12) as well as the remarks in Eq. (21), it can be written

$$\begin{aligned}\mathbf{p}_1 = [\mathbf{I}-\mathbf{D}_{12}\cdot\mathbf{D}_{21}]^{-1}\cdot[(\mathbf{g}_0(\Gamma_1)+\mathbf{g}_1(\Gamma_1,\beta_1))\\ +\mathbf{D}_{12}\cdot(\mathbf{g}_0(\Gamma_2)+\mathbf{g}_2(\Gamma_2,\beta_2))],\end{aligned} \tag{39}$$

where the expression $\mathbf{g}_1(\Gamma_1,\beta_1)$ stipulates that S_1 radiates on Γ_1, taking the wall admittance β_1 into account, and similarly for $\mathbf{g}_2(\Gamma_2,\beta_2)$. By developing the inverse term in (35) we obtain

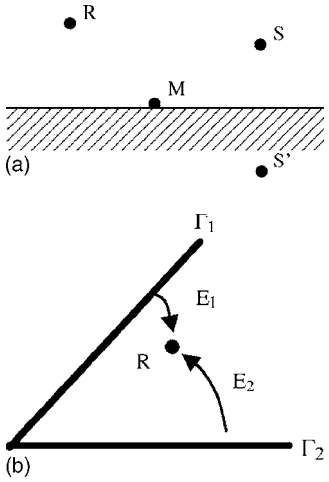

FIG. 6. (a) Elementary configuration with a reflection on the wall; (b) transfer of pressures from the wall toward the inside of the domain.

$$\begin{aligned}\mathbf{p}_1 = (\mathbf{g}_0(\Gamma_1)+\mathbf{g}_1(\Gamma_1,\beta_1))+\mathbf{D}_{12}\cdot(\mathbf{g}_0(\Gamma_2)+\mathbf{g}_2(\Gamma_2,\beta_2))\\ +\mathbf{D}_{12}\cdot\mathbf{D}_{21}\cdot(\mathbf{g}_0(\Gamma_1)+\mathbf{g}_1(\Gamma_1,\beta_1))\\ +\mathbf{D}_{12}\cdot\mathbf{D}_{21}\cdot\mathbf{D}_{12}\cdot(\mathbf{g}_0(\Gamma_2)+\mathbf{g}_2(\Gamma_2,\beta_2))+\cdots\end{aligned} \tag{40}$$

which is a generalization of (23).

The terms in Eq. (40) should be analyzed as follows. The symbol $\mathbf{g}_0(\Gamma_1)$ is the pressure radiated at geometrical locus Γ_1 coming from source S_0 (with its own pressure and impedance). The radiation uses a combination of source and radiation impedances and one notes more precisely as in (31)

$$\mathbf{g}_0(\Gamma_1)=\mathbf{g}_0(Z_{S_0}\cup Z_{\mathrm{rad}_\Omega},\Gamma_1^{\mathrm{geom}}) \tag{41}$$

and accordingly

$$\mathbf{g}_0(\Gamma_2)=\mathbf{g}_0(Z_{S_0}\cup Z_{\mathrm{rad}_\Omega},\Gamma_2^{\mathrm{geom}}). \tag{42}$$

Similarly to the case with reflecting walls, it is supposed that the term $\mathbf{D}_{12}\cdot\mathbf{g}_0(\Gamma_2)$ is at the origin of term $\mathbf{g}_2(\Gamma_1)$, but now for absorbing walls a more precise interpretation is sought. With the notations introduced before, this term is

$$\mathbf{D}_{12}\cdot\mathbf{g}_0(\Gamma_2)=[\mathbf{I}-\mathbf{A}_{11}]^{-1}\cdot\mathbf{A}_{12}\cdot\mathbf{g}_0(\Gamma_2). \tag{43}$$

The operator $\mathbf{A}_{12}$ applied to $\mathbf{g}_0(\Gamma_2)$ [the precise form of which is written as (42)] arises from the continuous term

$$\begin{aligned}\int_{\Gamma_2}\underbrace{(\partial_{n_M}G_\infty(Q_1,M)+ik\beta_2G_\infty(Q_1,M))}_{(*)}\\ \times G_0(Z_{S_0}\cup Z_{\mathrm{rad}_\Omega},\Gamma_2^{\mathrm{geom}}(M))dM\end{aligned} \tag{44}$$

(G_0 is the Green function corresponding to vector $\mathbf{g}_0$) where some conjectures had to be accepted in order to go further in the interpretation. In Eq. (44), the term $G_0(Z_{S_0}\cup Z_{\mathrm{rad}_\Omega},\Gamma_2^{\mathrm{geom}}(M))$ could have the role of the pressure coming from Γ_2 seen as a source radiating toward geometrical locus

Γ_1^{geom}. To this end, it should have a source impedance and a radiation impedance. This source would then be revealed by the existence of the image source S_2. The term $(^*)$ in Eq. (44) could have this role of combining both source and radiation impedances. In these conditions,

$$\mathbf{A}_{12}\cdot\mathbf{g}_0(Z_{S_0}\cup Z_{\text{rad}_\Omega},\Gamma_2^{\text{geom}}) \equiv \mathbf{g}_2(Z_{S_0}\cup Z_{\text{rad}_\Omega},Z_2\cup Z_{\text{rad}_{\Gamma_2}},\Gamma_1^{\text{geom}}) \tag{45}$$

and, following the interpretation of (37),

$$\mathbf{D}_{12}\cdot\mathbf{g}_0(\Gamma_2)=[\mathbf{I}-\mathbf{A}_{11}]^{-1}\cdot\mathbf{A}_{12}\cdot\mathbf{g}_0(Z_{S_0}\cup Z_{\text{rad}_\Omega},\Gamma_2^{\text{geom}}) \equiv \mathbf{g}_2((Z_{S_0}\cup Z_{\text{rad}_\Omega}),(Z_2\cup Z_{\text{rad}_{\Gamma_2}}),\Gamma_1(Z_1)) \tag{46}$$

thus confirming the first supposition. Encouraged by this understanding of the term $\mathbf{D}_{12}\cdot\mathbf{g}_0(\Gamma_2)$, a similar interpretation of term $\mathbf{D}_{21}\cdot\mathbf{D}_{12}\cdot\mathbf{g}_0(\Gamma_2)$ is sought. It is expected that expression (46) allows for

$$\mathbf{D}_{21}\cdot\mathbf{D}_{12}\cdot\mathbf{g}_0(\Gamma_2) \equiv \mathbf{g}_{21}(Z_{S_0}\cup Z_{\text{rad}_\Omega},Z_2\cup Z_{\text{rad}_{\Gamma_2}},Z_1\cup Z_{\text{rad}_{\Gamma_1}},\Gamma_2(Z_2)). \tag{47}$$

Indeed, $\mathbf{A}_{21}$ multiplied by Eq. (46) can be understood as the pressure coming from Γ_1 radiating towards Γ_2 with the needed impedances. Particularly, the "internal" impedance of Γ_1 and the pressure on Γ_1 are united in the existence of source S_{21}, so the right-hand term of Eq. (46) can now be understood as the source pressure

$$\mathbf{g}_{21}(Z_{S_0}\cup Z_{\text{rad}_\Omega},Z_2\cup Z_{\text{rad}_{\Gamma_2}},\Gamma_1(Z_1)). \tag{48}$$

Upon multiplication by $\mathbf{A}_{12}$, (48) becomes

$$\mathbf{g}_{21}(Z_{S_0}\cup Z_{\text{rad}_\Omega},Z_2\cup Z_{\text{rad}_{\Gamma_2}},Z_1\cup Z_{\text{rad}_{\Gamma_1}},\Gamma_2^{\text{geom}}) \tag{49}$$

and finally via $[\mathbf{I}-\mathbf{A}_{22}]^{-1}$,

$$\mathbf{g}_{21}(Z_{S_0}\cup Z_{\text{rad}_\Omega},Z_2\cup Z_{\text{rad}_{\Gamma_2}},Z_1\cup Z_{\text{rad}_{\Gamma_1}},\Gamma_2(Z_2)). \tag{50}$$

Each impedance grouping is linked to a particular propagation path, so there are as many reflections as groupings. The interpretation of all other terms follows the same procedure. But even if these conclusions give meaning to the image sources and to the number of reflections that are associated with them, they still remain to be formally demonstrated. For it is at first sight surprising that an incident pressure wave on a wall would lead to a source pressure as soon as the wall impedance is considered *and* that this very impedance would be considered *a second time* when this source radiates [again, part $(^*)$ of Eq. (44) shows a combination of this wall impedance and the radiation impedance].

C. Integral representation inside the domain and series development

The investigation proposed in this paper of the rational origins of the notion of image sources associated with the acoustical ray method rests entirely on the series development of the exact solution of the wall pressure. This development could not have been directly applied to the exact solution within the domain. Whereas, now that the wall pressure can be developed as a series, an extension toward an expression of the pressure inside the domain is possible. Only the case of perfectly reflecting walls is considered here. Again, some preliminary remarks are needed.

In the elementary configuration of Fig. 6(a), pressure at point R is expressed by

$$p(R)=G_\infty(R,S)+\underbrace{\int_\Gamma p(M)\partial_{n_M}G_\infty(M,R)dM}_{\text{contribution from S', or } G_\infty(R,S')} \tag{51}$$

with [according to (4)]

$$p(M)=G_\infty(M,S)+G_\infty(M,S')=2G_\infty(M,S') \tag{52}$$

thus leading to the following matrix equation (with our notation conventions)

$$\mathbf{p}=\mathbf{g}(\Omega)+\mathbf{E}_\infty\cdot\mathbf{p}(\Gamma)=\mathbf{g}(\Omega)+\mathbf{E}_\infty\cdot 2\mathbf{g}'(\Gamma). \tag{53}$$

For the two-walled configuration under study here [Fig. 6(b)], we write similarly

$$\mathbf{p}=\mathbf{g}_0(\Omega)+\mathbf{E}_1\cdot\mathbf{p}_1+\mathbf{E}_2\cdot\mathbf{p}_2. \tag{54}$$

During the analysis of the series development to obtain the source contribution, it appears that the terms are counted by pairs. Indeed, the formulation is also

$$\begin{aligned}\mathbf{p}=\mathbf{g}_0(\Omega)&+\mathbf{E}_1\cdot(\underbrace{\mathbf{g}_0(\Gamma_1)+\mathbf{g}_1(\Gamma_1)}_{2\cdot\mathbf{g}_1(\Gamma_1)}+\underbrace{\mathbf{g}_{12}(\Gamma_1)+\mathbf{g}_{121}(\Gamma_1)}_{2\cdot\mathbf{g}_{121}(\Gamma_1)}+\underbrace{\mathbf{g}_{1212}(\Gamma_1)+\mathbf{g}_{12121}(\Gamma_1)}_{2\cdot\mathbf{g}_{12121}(\Gamma_1)}+\cdots)\\&+\mathbf{E}_1\cdot(\underbrace{\mathbf{g}_2(\Gamma_1)+\mathbf{g}_{21}(\Gamma_1)}_{2\cdot\mathbf{g}_{21}(\Gamma_1)}+\underbrace{\mathbf{g}_{212}(\Gamma_1)+\mathbf{g}_{2121}(\Gamma_1)}_{2\cdot\mathbf{g}_{2121}(\Gamma_1)}+\underbrace{\mathbf{g}_{21212}(\Gamma_1)+\cdots}_{2\cdot\mathbf{g}_{21212}(\Gamma_1)}+\cdots)\\&+\mathbf{E}_2\cdot(\underbrace{\mathbf{g}_0(\Gamma_2)+\mathbf{g}_2(\Gamma_2)}_{2\cdot\mathbf{g}_2(\Gamma_2)}+\underbrace{\mathbf{g}_{21}(\Gamma_2)+\mathbf{g}_{212}(\Gamma_2)}_{2\cdot\mathbf{g}_{212}(\Gamma_2)}+\underbrace{\mathbf{g}_{21212}(\Gamma_2)+\mathbf{g}_{212121}(\Gamma_2)}_{2\cdot\mathbf{g}_{212121}(\Gamma_2)}+\cdots)\\&+\mathbf{E}_2\cdot(\underbrace{\mathbf{g}_1(\Gamma_2)+\mathbf{g}_{12}(\Gamma_2)}_{2\cdot\mathbf{g}_{12}(\Gamma_2)}+\underbrace{\mathbf{g}_{121}(\Gamma_2)+\mathbf{g}_{1212}(\Gamma_2)}_{2\cdot\mathbf{g}_{1212}(\Gamma_2)}+\underbrace{\mathbf{g}_{12121}(\Gamma_2)+\mathbf{g}_{121212}(\Gamma_2)}_{2\cdot\mathbf{g}_{121212}(\Gamma_2)}+\cdots).\end{aligned} \tag{55}$$

Transferring the pressures from the walls towards the domain through $\mathbf{E}_1$, and $\mathbf{E}_2$ leads to

$$\mathbf{p} = \mathbf{g}_0(\Omega) + \mathbf{g}_1(\Omega) + \mathbf{g}_2(\Omega) + \mathbf{g}_{12}(\Omega) + \mathbf{g}_{21}(\Omega) + \mathbf{g}_{121}(\Omega) + \mathbf{g}_{212}(\Omega) + \mathbf{g}_{1212}(\Omega) + \cdots , \quad (56)$$

where assembling terms by pairs always takes into account terms of the same order in the series revealing the pressures on the walls. It must be noted that this particular order of terms is of no significance, and it would have been quite possible to write, for example,

$$\mathbf{p} = \mathbf{g}_0(\Omega) + \mathbf{g}_2(\Omega) + \mathbf{g}_1(\Omega) + \mathbf{g}_{12}(\Omega) + \mathbf{g}_{21}(\Omega) + \mathbf{g}_{212}(\Omega) + \mathbf{g}_{121}(\Omega) + \cdots . \quad (57)$$

However, in the present case, the relative order of the terms series stemming from S_1 and S_2 remains. This question about the order of terms radiating toward the domain will appear in the conclusion.

III. NUMERICAL EXPERIMENTS

The reasoning correlating the terms of the series development and the image sources may lack rigor and an analysis of this reasoning will sooner or later prove necessary, but as a first step, numerical experiments can yield results faster and provide a factual confirmation of the interpretation presented here.

All the experiments presented here were done in the situation depicted in Fig. 7 composed of two perfectly reflecting walls Γ_1 and Γ_2, at an angle θ. The present study is concerned with the justification of a possible term-by-term relation between the series development of the integral solution and the series of image sources. Therefore, work has been concentrated on the case of perfectly reflecting walls (except for situation B presented in Fig. 10, see below), deliberately setting aside the case of absorbing walls. Only after this term-by-term correspondence has been assessed will it be possible to compare a series term with wall impedance and an image source contribution with specular absorption. In this second step, the difference between a local specular reaction and the nonlocal reaction present in the integral equations (diffusion) could then be verified. Both walls, theoretically of infinite length, are in fact 5 m long for numerical reasons; the source is located at the coordinates (x_S, y_S). The values of θ, x_S, and y_S used in the different situations referred to in this section are summed up in Table I. The walls are discretized into 250 facets of a length of 0.02 m each (the wavelength is ca. 0.7 m). The pressure is computed on both walls at 500 Hz. In the following tests, the solution obtained by the image sources method is compared with the corresponding series development. The reference solution in all cases is computed with the integral method. This solution isassumed to be exact, but with an approximation brought by the discretization and the finite length of the walls.

TABLE I. Considered situations.

Label	θ	(x_s, y_s) in m	Z_r.	Corresponds to Figure
A	$\pi/2$	(3.0,3.0)	∞	13
B	$\pi/2$	(0.5,0.5)	9	10
C	$5\pi/8$	(0.5,2.0)	∞	11(a), 14(a)
D	$5\pi/8$	(−0.5,2.0)	∞	11(b), 14(b)
E	$7\pi/2$	(0.1,0.3)	∞	14(c)
F	$\pi/6$	$(3.0, 3.0\cdot\tan(\theta/2))$	∞	12(a), 12(b)

Seeking a way to observe if there is a correspondence between the terms of the series development and the image sources for the computation of the wall pressure, the first test comes from an intuitive consideration. For an acute angle θ, a great number of reflections can occur between the walls, so a great number of image sources is expected; it is noticeable that the image choice algorithm shows that all image sources are visible for the wall pressure. For $\theta > \pi/2$ (obtuse), a small number of sources should intervene. It could be that the number of image sources is a monotonous function of the angle, so the convergence speed of the series should increase from acute to obtuse angles. To verify this assertion, a distance between the exact solution (actually the expression "exact" is incorrect since the solution is only numerically approached) and the solution obtained with a number N_t of terms of the series development or obtained with a number N_s of image sources is defined as

$$d(N_t) = \int_{\Gamma_1} |p_{\text{series}}(N_t, x) - p_{\text{exact}}(x)|^2 \, dx \quad \text{and}$$

$$d(N_s) = \int_{\Gamma_1} |p_{\text{sources}}(N_s, x) - p_{\text{exact}}(x)|^2 \, dx. \quad (58)$$

Figure 8 shows that the convergence curves of both the ray method and series development solutions are closely related and verify the fact that the convergence is faster for wider angles. For acute angles, the extra terms of the series development (those without an image source equivalent) appear to be of weak or even negligible contribution compared to the first terms. From a more physical point of view, the development series and its interpretation *via* Huygens' principle lead to the same conclusion, since the specular part of the sound field (located in the first terms of the series) is of

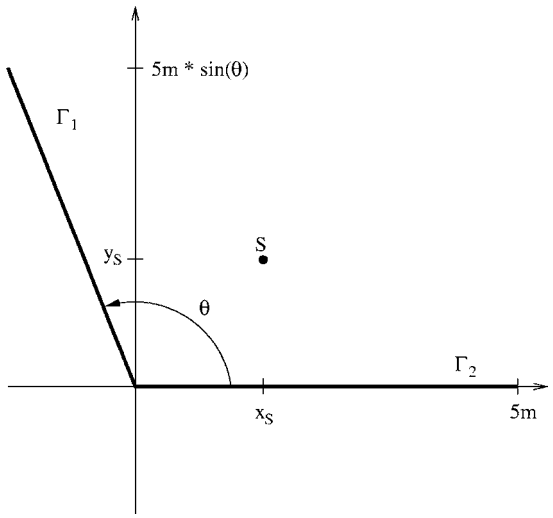

FIG. 7. Geometrical configuration for the numerical tests.

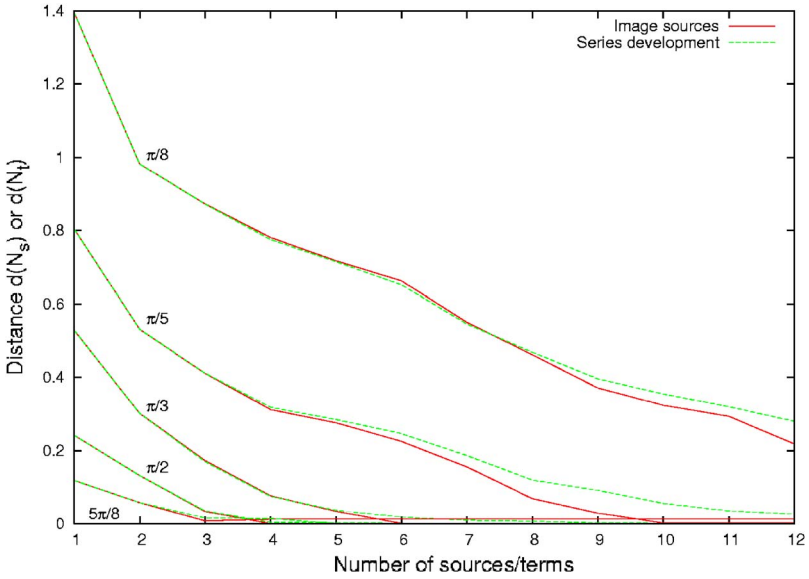

FIG. 8. (Color online) Convergence speed as function of aperture angle θ.

greater importance than the diffracted part (in the higher order terms). Therefore the correspondence between the terms of the series development and the image sources can be further explored. Let us remark that in the case of an open sector, no resonances with infinite amplitudes at some frequencies are expected, which has indeed been observed.

A special situation is the so-called quarter-infinite space (in 2D), where $\theta=\pi/2$ (situation A). It has been previously observed that the image source method is in very good agreement with the reference solution in the case of perfectly rigid walls and also of those with a local impedance.[13] This also means that the visible sources (of which there are 4: the real source plus 3 images) contain the majority if not all of the needed information. Figure 8 shows that the reference solution is reached in four terms both by the series development and by the corresponding image sources. However, a closer observation (induced by the strong convergence, as we shall see) shows a very slight difference between the two convergence curves: the terms of the series development converge a little more slowly than the sum of the image sources contributions. This could be due to the numerical approximation of the exact (reference) solution, and will be further examined. This situation where the first four terms are sufficient to obtain a good solution should be revealed in Eq. (23) if the product of the matrices $\mathbf{C}\cdot\mathbf{B}$ were null for $\theta=\pi/2$ without $\mathbf{B}$ or $\mathbf{C}$ being zero. In practice, this would be highlighted by a norm of the product. Figure 9 shows the maximum singular value of the product $\mathbf{C}\cdot\mathbf{B}$ along with the convergence [according to (58)] of the fifth term of the series development on Γ_1, i.e., $2\mathbf{C}\cdot 2\mathbf{B}\cdot\mathbf{g}_0(\Gamma_1)$. Both values are seen to decrease from acute angles toward $\pi/2$. The convergence stabilizes at zero from there on, signifying that the fifth term is superfluous for obtuse angles. On the other hand, the fact that the maximum singular value of $\mathbf{C}\cdot\mathbf{B}$ is not null at $\theta=\pi/2$ could hint that this norm is perhaps not appropriate to treat the expected vanishing of $\mathbf{C}\cdot\mathbf{B}$ at $\theta=\pi/2$.

Despite the fact that the numerical experiments presented in this paper focus on the case $\beta=0$, to gain confidence in the well-founded base of the work, a comparison is

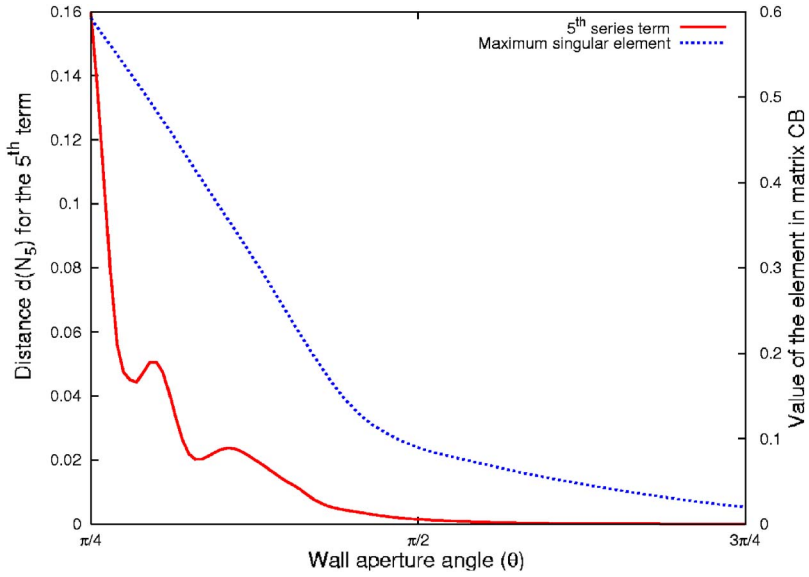

FIG. 9. (Color online) The contribution of $\mathbf{C}\cdot\mathbf{B}$ decreases when going from acute to obtuse angles.

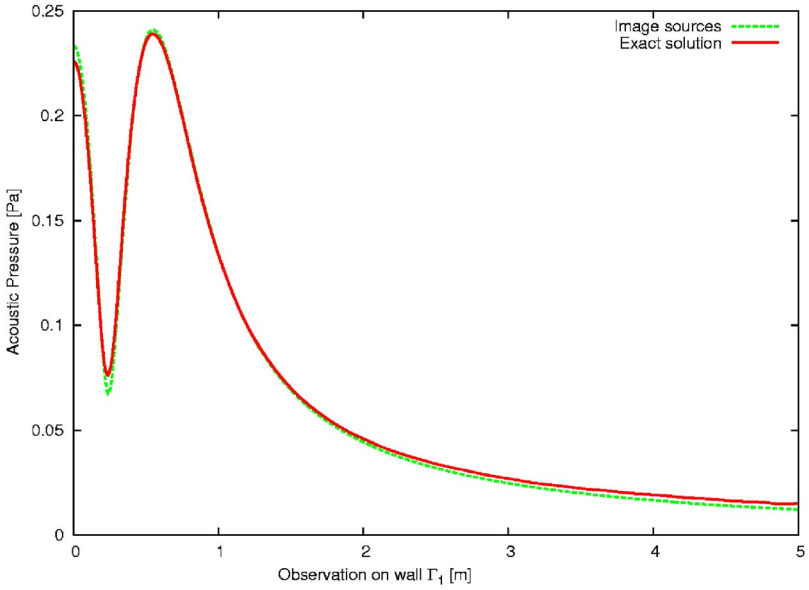

FIG. 10. (Color online) Pressure levels on wall Γ_1, in situation B, with absorbing walls (Z_r=9).

proposed in Fig. 10 between the pressure field on the boundaries of a quart-infinite space (situation B) with an arbitrary impedance (reduced impedance Z_r=9, which characterizes an absorption of about 36% at normal impedance) calculated with the integral method and the pressure calculated with the four images. The very good agreement between both fields lead us to believe that the first four terms of the series still correspond to the four sources, probably resulting therefore in product $\mathbf{D}_{12}\cdot\mathbf{D}_{21}$ in Eq. (39) null without both of the matrices being zero, but this still remains to be demonstrated.

The weak convergence in Fig. 8 for an acute angle θ shows that the interpretation of the series development proves coherent at first sight and hints at a formal justification of the image sources method, but offers no improvement of this method, since the extra terms (not corresponding to visible sources) are of negligible contribution. On the contrary, for obtuse angles one can show the effects of adding the "supplementary" sources, coming from the terms of the series development without a "real" corresponding image source ["invisible" source as mentioned in Fig. 2(b)]. To show the impact of this extra source, two situations, showing characteristic features of the method, are displayed here. The situations considered are as defined in Table I. Figure 11(a) (situation C) shows an increase in precision when an extra source (in this case S_2) is added. For another situation, however, Fig. 11(b) (situation D) seems to show that adding a source can indeed weaken the solution. This puts the distance as defined above into question and leads to the observation of the strong convergence, i.e., the comparison between the

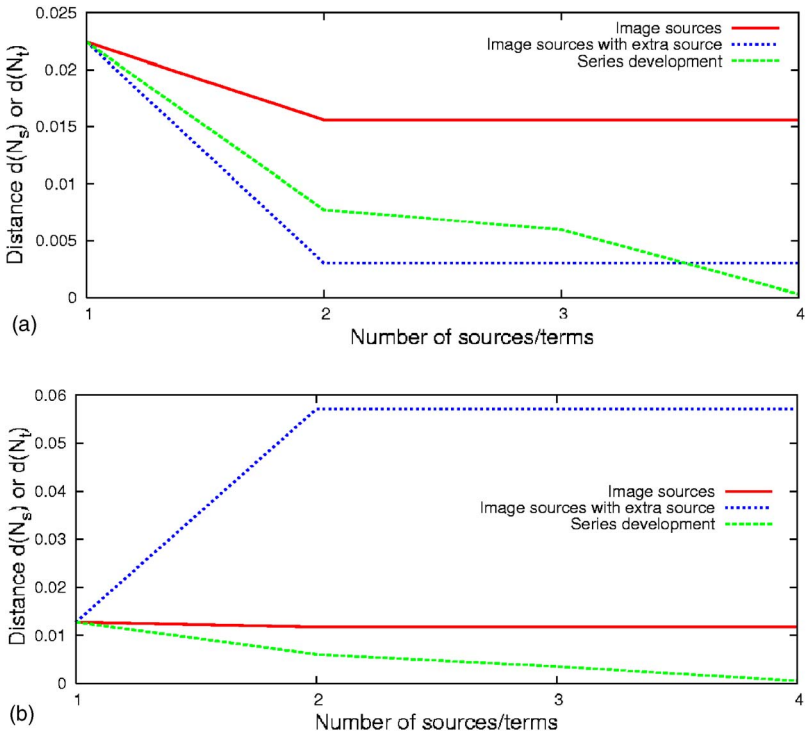

FIG. 11. (Color online) Weak convergence on wall Γ_1: (a) Situation C, (b) Situation D.

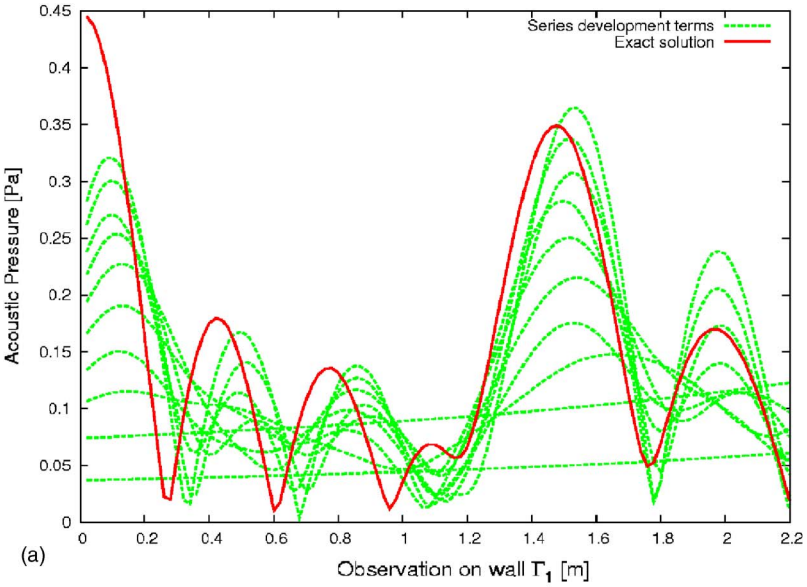

FIG. 12. (Color online) Strong convergence in situation F: (a) convergence of the series development terms toward the exact solution (for clarity, only the first 10 terms are shown); (b) contribution of the first six terms of the series development and corresponding image sources.

actual pressure levels obtained by each method. The horizontal lines in Fig. 11 occur when no additional sources are considered.

Instead of observing a mean value between the reference solution and the computed one, the actual pressure level on each point of the wall is observed. Figure 12(a) shows the strong convergence in the case of acute θ (situation F). The terms of the series development can be seen to converge toward the exact solution. In Fig. 12(b), a more detailed view shows the first six terms and their corresponding image sources. An almost perfect coherence between the terms and the sources can be observed. This is expected for the first two terms, since they are conceptually identical, but the coherence of the higher terms is significant for the validity of the interpretation.

As said earlier for $\theta=\pi/2$, the series development converges more slowly than the sum of the image sources contributions. Figure 13 shows the strong convergence for situation A, which has $\theta=\pi/2$ and confirms this remark, for only four image sources are necessary to converge toward the reference solution, whereas six series development terms are needed (although four terms already lead to a very acceptable result).

Observing the pressure level on the walls (strong convergence) for cases with an obtuse angle θ [situation C in Fig. 14(a), D in Fig. 14(b), and E in Fig. 14(c)] reveals the enhancement brought about by adding an extra invisible source (in this case S_2). The oscillatory behavior of the wall pressure is not taken into account if only the visible sources are used. This valuable information is added when an extra source is used [but was not accessible when only observing the weak convergence, as in Fig. 11(b)].

IV. CONCLUSION

The acoustic ray method rests upon specular reflection—combined with the notion of associated image sources in one version of the method—that has been intuitively accepted following geometrical optics. Sound fields in cavities have thus been computed and the results compared

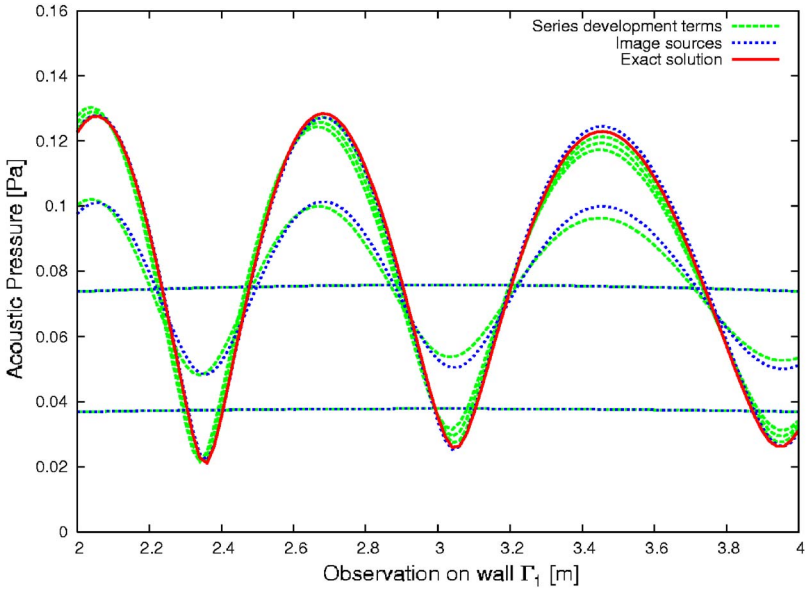

FIG. 13. (Color online) Strong convergence in situation A.

with finite element method results, shedding light on differences between the two methods, which we seek to reduce. Acoustic rays, not taking diffraction into account, will always show different results. Nevertheless, and having a possible improvement of the ray method in mind, the primary goal of this research was to identify the analytical origin of image sources and so tackle the problem in a rational way.

For this purpose, the analysis of the exact solution of the harmonic wall pressure in an elementary domain (angular sector in two dimensions, bounded by two "walls," totally

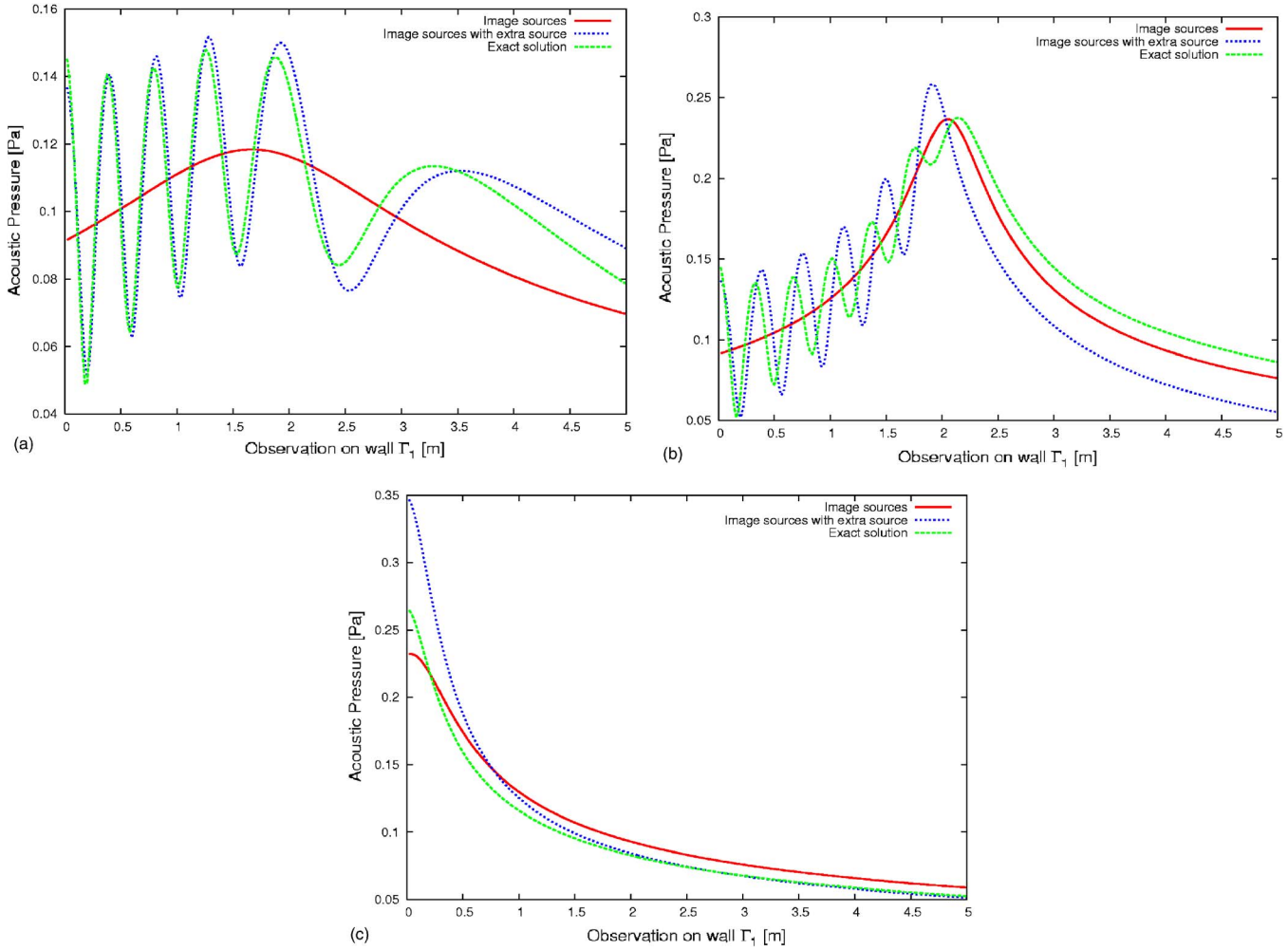

FIG. 14. (Color online) Effect of an "invisible" source (a) situation C, (b) situation D, (c) situation E.

reflective to start with, and then absorbent) has brought interesting results. Of particular interest was the generalization of the notion of image-sources, of which some that are normally not considered in the classical image source method could lead to better results, were they used. In fact, the exact solution (obtained by an integral representation of the problem) can be developed into a series after being discretized and written in matrix form. Thanks to Huygens' principle, the first terms of this series could represent the contributions of the image sources that are given by the method currently used. The other terms in the series would then be represented by generalized image sources. Such sources are actually missing in the classical ray method and could be used to refine the sound field computation results. To assert that a particular solution comes closer to a reference solution, a distance must be defined, in this case an euclydian norm in L^2.

The numerical experiments—where no absorption has been-considered at this stage of the investigation, except for a short illustration—have greatly confirmed the correspondence between the contributions of the first terms of the series development and the corresponding image sources. Moreover, it has been shown that in certain cases, a "missing" image source brings significant extra information (either directly visible with the chosen distance, or visually observable on the graph but not revealed by the chosen distance).

At this level, mentioning the "first" missing source again implies having defined a distance to establish a relation that enables a classification of the image sources' importance. In the configuration proposed in this paper, the euclydian norm used calls "first missing source" the first term of the series that does not correspond to an image source visible at the reception point. As long as this point is located on a wall and at a certain distance from the corners, an idea for the algorithm to make this first missing source appear is envisaged. But the problem requires further investigation for cases where the reception point is near the wall limits.

In the same vein, it has been shown that the acoustic pressure in the domain can also be developed in series, but not immediately. Contrary to the wall pressure case, the order of the terms is in this case still unknown and further research is necessary to identify it. This problem is directly linked to the classification of the influences of walls on the solution at a particular point in the domain. As soon as a rational way to identify these influences is found, physical information on the role of the different walls will be available. This role is for the moment only derived intuitively from simple cases.

Finally, this paper has shown that a solution obtained by current ray methods is an approximation taking into account the first terms of an exact solution obtained via integral representation. But a weak point still remains: ideally the contribution of each source should have been shown to be concentrated in a single series development term, and not spread in multiple terms instead. Nevertheless, this point has been observed in numerical results, although it has not been demonstrated mathematically.

ACKNOWLEDGMENTS

This research is supported by the Swiss CTI-7294.1 EUS-IW project within the framework of the European program EUREKA 2790 and is partly funded by *RIETER Automotive Management Corp.*, Winterthur, Switzerland.

[1] V. O. Knudsen and C. M. Harris, *Acoustical Designing in Architecture* (Wiley, New York, 1947).
[2] J. Allen and D. A. Berkley, "Image method for efficiently simulating small-rooms acoustics," J. Acoust. Soc. Am. **65**, 943–950 (1979).
[3] L. Allard, V. Martin, and M. Rossi, "Réponse impulsionnelle d'un contrôleur actif par anticipation dans un semi-espace; analyse physique et problème de causalité associé" (Impulse response of an active controller by anticipation in half-space; physical analysis and associated causality problem), *Proceedings of the 5th French Congress on acoustics*, Lausanne, Switzerland, 2000, pp. 630–631.
[4] A. Kroksad, S. Strom, and S. Sordal, "Calculating the acoustical room response by the use of a ray-tracing technique," J. Sound Vib. **8**, 118–125 (1968).
[5] H. Kuttruff, *Room Acoustics*, 4th ed. (Spon Press, London, 2000).
[6] P. Jean, "Coupling integral and geometrical representations for vibro-acoustical problems," J. Sound Vib. **224**, 475–487 (1999).
[7] T. Courtois and V. Martin, "Spectral quality of acoustic predictions obtained by the ray method in coupled two-dimensional damped cavities," J. Sound Vib. **270**, 259–278 (2004).
[8] J. Borish, "Extension of the image model to arbitrary polyhedra," J. Acoust. Soc. Am. **75**, 1827–1836 (1984).
[9] M. Vorländer, "Simulation of the transient and steady-state sound propagation in rooms using a new combined ray-tracing/image-source algorithm," J. Acoust. Soc. Am. **86**, 172–178 (1989).
[10] F. M. Mechel, "Improved mirror source method in room acoustics," J. Sound Vib. **256**, 873–940 (2002).
[11] V. Martin and T. Guignard, "Justification of the image sources in ray method," *Proceedings of the 12th International Congress on sound and vibration*, Lisbon, Portugal, Paper 178, 2005.
[12] B. B. Baker and E. T. Copson, *The Mathematical Theory of Huygens' Principle*, 3rd ed., (Chelsea, New York, 1987).
[13] T. Guignard, V. Martin, and T. Courtois, "Interpolated identified reflection coefficients for acoustic ray method," *Proceedings of the 11th International Congress on sound and vibration*, St. Petersburg, Russia, 2004, pp. 3707–3714.

An orthogonality relation-based technique for post-processing finite element predictions of waves scattering in solid waveguides

L. Moreau,[a] M. Castaings, and B. Hosten
Laboratoire de Mécanique Physique, University Bordeaux 1, UMR CNRS 5469, 351 cours de la Libération, 33405 Talence Cedex, France

M. V. Predoi
Department of Mechanics, University Politehnica Bucharest, Calea Plevnei 94, Bl. 10D2, Ap.12, Sect. 1, 010236-Bucharest, Romania

(Received 21 December 2005; revised 24 May 2006; accepted 27 May 2006)

In this paper we propose an efficient way to post-process output data predicted by Finite Element (FE) or Boundary Element (BE) codes, when the scattering of Lamb modes by defects in plate-like structures is considered. The use of a general orthogonality relation is compared to classical post-processing made with spatial FFT. To get the amplitudes of incident or scattered modes, this orthogonality relation requires the numerical prediction of the through-thickness displacements, and stress-fields distributions, on each side of the scatterer. The distance between the location where these fields are predicted and the scatterer can be very small, thus allowing huge reductions in the size of the mesh. Through two examples, this orthogonality relation is used to calculate the reflection and transmission coefficients of a pure Lamb mode incident on a notch-like defect, in either an elastic or a viscoelastic plate. Thanks to efficient absorbing regions, the FE meshed domains are reduced to the vicinity of the defects, thus allowing several advantages of the method to be demonstrated in comparison to some weaknesses of the classical post-processing based on spatial FFT. © *2006 Acoustical Society of America.* [DOI: 10.1121/1.2216563]

PACS number(s): 43.20.El, 43.20.Fn, 43.20.Gp [DSB] Pages: 611–620

I. INTRODUCTION

Ultrasonic waves are commonly used for detecting defects in materials, which is becoming a major preoccupation in industrial context. Lamb modes are particularly well suited for testing large structures since they can propagate along long distances, while interrogating the whole through-thickness of the guide.[1,2] Nondestructive tests are based on the fact that an incident Lamb mode would share its energy into several diffracted wave packets, the proportion in amplitude of which will depend on the geometry, the location, and the dimension of the defect. Even if the incident wave is a pure Lamb mode, the diffracted wave packets can be very complicated, since at least two Lamb modes exist at any given frequency.[3] This is an advantage since the more modes, the more information about the defect, but the more complicated the interpretation of the diffracted Lamb waves. Numerical simulations are therefore necessary for predicting the scattering of Lamb waves by defects of various geometries. Numerous works have been published on the subject, often based on the completeness principle of Lamb modes stipulating that any acoustic field in a solid waveguide can be described in the modal basis of Lamb modes.[4] In the 1980s, a modified version of the Wiener-Hopf technique has been proposed for simulating the reflection of an incident Lamb mode from a finite horizontal crack situated on the plane of symmetry of an elastic layer.[5,6] In the same period, a variational method has been used for predicting the reflection of Lamb modes from a crack normal to the surfaces of an isotropic plate.[7] Later, the semianalytical reciprocal work method or modal decomposition method, which are based on the consideration of nonpropagating modes for satisfying boundary conditions in the vicinity of defects, have been successfully used for modeling the reflection by a free edge of a plate,[8,9] or the reflection from and transmission past either a weld between two steel plates of the same thickness,[10] an opening crack in an aluminium plate,[11] or a circular cylinder embedded in an elastic plate.[12] These semianalytical methods allow fast computations to be performed. Furthermore, they require a truncation in the infinite series of nonpropagating modes. Therefore, the quality of the results depends on the way this truncation is made. Moreover, these techniques are not easy to use for defects running along the guide since changes in phase for various positions along the defect must be properly taken into account for all propagating or nonpropagating modes. Finally, numerical or hybrid solutions based on the FE method are good candidates for simulating problems of Lamb modes scattering,[13] since they consist in solving the equation of mechanical dynamic equilibrium without having to consider propagating or nonpropagating wave modes, these being implicitly included in the solutions. Solutions are supplied in terms of displacements, strains, or stresses, and adequate post-processing is usually necessary for interpreting them in terms of wave propagation or scattering phenomena. Moreover, in order to reduce the number of elements necessary for meshing waveguides,

[a]Corresponding author. Electronic mail: l.moreau@lmp.u-bordeaux1.fr

simulations are generally restricted to two-dimensional problems. In these conditions, plane-strain problems are solved for simulating the diffraction of modes by strip-like defects,[14] or plane-stress problems for simulating modes producing uniform stresses through the guide-thickness and their scattering by defects of uniform size through the thickness.[15] The two-dimensional (2-D) approach considerably limits the information that is sought concerning the effect of 3-D shaped defects on the scattering of an incident finite-beam Lamb mode.

In this paper we present the use of an orthogonality relation-based technique for post-processing FE predictions of fields scattered by defects in 2-D waveguides. In the literature, several orthogonality relations for wave propagation in solids exist,[3] the most common being used with various objectives concerning elastic guides,[16–18] for example to model scattering of waves by welded junctions in elastic plates.[10] Recently, Gunawan and Hirose[19] proposed the mode-exciting method to solve Lamb wave-scattering problems in infinite elastic plates. In this method, a set of Lamb modes is excited by appropriate boundary conditions given on virtual edges of a finite plate. After solving numerically the elastodynamic problem defined in the finite domain (using a finite element or boundary element), the numerical solution is decomposed into Lamb modes constituting a system of equations, which has to be solved to determine the scattering coefficients of Lamb modes for the original problem in the infinite plate. However, the process requires the definition and the use of as many sets of exciters as there are propagating modes in the plate, and the amplitudes of the incident propagating modes must be linearly independent for all sets of exciters given on the virtual edges.

In the present paper, the post-processing technique uses a simpler process based on a general orthogonality relation, valid for both elastic and viscoelastic media, contrary to that used by Duquenne and Moulin,[20] which is valid for elastic media only and which is used to post-process FE solutions simulating the generation of modes by PZT transducers coupled to plates having negligible damping. The general relation is applied between two sets of fields, one set being predicted by the finite-element method and the other one corresponding to a selected mode (propagating or nonpropagating), the amplitude of which is sought. The fields supplied by the FE method correspond to the total field including an incident mode and all propagating and nonpropagating modes scattered by a local inhomogeneity in the plate. In comparison to the mode-exciting method,[19] the FEM requires to be run only once and not for a numerous series of sets of exciters. Furthermore, the FE data are produced in the Fourier domain, so that the model can properly take into account the viscoelasticity of the material constituting the guide,[21] the length of which is significantly shortened due to the use of efficient absorbing regions.[22,23] The scattering of an incident Lamb mode by a notch either in an elastic aluminium plate or in a viscoelastic Perspex plate are two examples investigated. The advantages brought by this technique are emphasized in each of these two applications. Also, the interest it represents for post-processing future 3-D simulations is discussed.

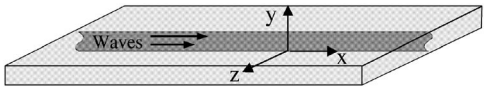

FIG. 1. Schematic of a 3-D plate-like guide with plane of propagation ***Oxy***.

II. THE ORTHOGONALITY RELATION-BASED POST-PROCESSING TECHNIQUE

As shown by Kirrmann,[4] the basis of Lamb modes is complete. Thus, any acoustic field in a solid waveguide can always be decomposed in this basis. The post-processing technique proposed in this paper is based on this principle.

A. Background and notations

We consider the propagation of several Lamb modes along the x direction of the Cartesian coordinate axis and producing nonzero strains in the ***Oxy*** plane only of a solid, plate-like guide (Fig. 1). Plane strain conditions are therefore considered. In these conditions, each mode n produces displacements and stresses that can be expressed, in two dimensions, by the following vector and tensor, respectively:

$$\boldsymbol{u^n} = \begin{pmatrix} U_x^n \\ U_y^n \end{pmatrix} e^{i(\omega t - k_n x)}, \tag{1}$$

$$\boldsymbol{\sigma^n} = \begin{pmatrix} T_{xx}^n & T_{xy}^n \\ T_{xy}^n & T_{yy}^n \end{pmatrix} e^{i(\omega t - k_n x)}, \tag{2}$$

where t is the time, $\omega = 2\pi f$ is the angular frequency, and i is the complex number such as $i^2 = -1$. $k_n = k_n' - ik_n''$ is the complex wavenumber of mode n. Sign − in Eqs. (2) and (3) indicates a forward traveling wave, while a sign + would refer to a backward traveling wave. With these conventions, k_n' and k_n'' are chosen to be positive numbers so that any backward or forward traveling wave has a decaying amplitude in its direction of propagation. The complex amplitude of the mode is arbitrary and is included in the displacement and stress field distributions.

The general expression for the time-averaged acoustic power flow $\langle P_x \rangle_n$ carried by a mode n through the guide thickness is[3]

$$\langle P_x \rangle_n = \mathrm{Re}\left(\int_0^h \frac{-(\boldsymbol{\sigma^n} \boldsymbol{\nu^n}^*) \cdot \mathbf{x}}{2} dy \right) = \mathrm{Re}\left[-\frac{1}{2} \int_0^h \boldsymbol{\sigma^n} \left(\frac{\partial \boldsymbol{u^n}}{\partial t} \right)^* \cdot \mathbf{x}\, dy \right], \tag{3}$$

where h is the thickness of the waveguide, and $\boldsymbol{\nu^n}$ is the particle velocity for the Lamb mode n. Re$[\cdots]$ is the real part of quantity $[\cdots]$ and the asterisk means complex conjugation. Substituting Eqs. (1) and (2) into (3), one obtains

$$\langle P_x\rangle_n = \mathrm{Re}\left[-\frac{1}{2}\int_0^h (-i\omega T_{xx}^n e^{-k_n'' x} U_x^{n^*} e^{-k_n'' x} - i\omega T_{xy}^n e^{-k_n'' x} U_y^{n^*} e^{-k_n'' x}) dy\right] = \underbrace{e^{-2k_n'' x}}_{\substack{\text{attenuation of energy}\\ \text{flow with distance}\\ \text{of propagation}}} \mathrm{Re}\left[\frac{i\omega}{2}\int_0^h (T_{xx}^n U_x^{n^*} + T_{xy}^n U_y^{n^*}) dy\right]. \tag{4}$$

For elastic waveguides, Eq. (4) reduces to zero if the mode n has a purely imaginary or a complex wavenumber, since such modes are well known to not carry energy in elastic guides.[3] If the wavenumber is real, then $\langle P_x\rangle_n$ is the time-averaged power flow carried by the mode all along the elastic guide ($e^{-2k_n'' x}=1$). For absorbing waveguides, it can be shown that all modes have complex wavenumbers, and that they all have a propagating behavior while being attenuated.[24] In these conditions, $\langle P_x\rangle_n$ represents the time-averaged power flow carried by each mode n and decreasing along the guide according to the $e^{-2k_n'' x}$ law.

It can be of interest to consider power-normalized mode fields (or modes with unit amplitude) rather than fields corresponding to arbitrary power (or arbitrary amplitudes) of modes. In this purpose, the displacement and stress fields given by Eqs. (1) and (2) are rewritten in the form

$$\tilde{\boldsymbol{u}}^{\boldsymbol{n}} = \begin{pmatrix} \tilde{U}_x^n \\ \tilde{U}_y^n \end{pmatrix} e^{i(\omega t - k_n x)}, \tag{5}$$

$$\tilde{\boldsymbol{\sigma}}^{\boldsymbol{n}} = \begin{pmatrix} \tilde{T}_{xx}^n & \tilde{T}_{xy}^n \\ \tilde{T}_{xy}^n & \tilde{T}_{yy}^n \end{pmatrix} e^{i(\omega t - k_n x)}, \tag{6}$$

where $\tilde{U}_k^n = 1/\sqrt{|P_{x_0}|}\,U_k^n$ and $\tilde{T}_{kl}^n = (1/\sqrt{|P_{x_0}|})T_{kl}^n$ with $k,l=x,y$ are the power-normalized displacement and stress fields of the mode n, respectively, and P_{x_0} is the value of $\langle P_x\rangle_n$ given by Eq. (4) with $x=0$, i.e., for $e^{-2k_n'' x}=1$. Then the time-averaged power flow is expressed as

$$\langle P_x\rangle_n = \frac{1}{|P_{x_0}|} e^{-2k_n'' x} \underbrace{\mathrm{Re}\left[\frac{i\omega}{2}\int_0^h (T_{xx}^n U_x^{n^*} + T_{xy}^n U_y^{n^*}) dy\right]}_{P_{x_0}}$$

$$= \pm e^{-2k_n'' x} \tag{7}$$

thus allowing to check that it is unity at $x=0$ and that it decreases according to $e^{-2k_n'' x}$ as x increases. Signs ± indicate the direction of the flow: sign + corresponds to a flow in the x direction, and sign − to a flow in the opposite direction.

With regard to Eqs. (5) and (6), if the mode n is now supposed to have a complex amplitude $\alpha_n = \beta_n e^{-2k_n'' x}$, rather than a unit amplitude, then the expression of its time-averaged power flow would be

$$\langle P_x\rangle_n = \pm |\beta_n|^2 e^{-2k_n'' x} = \pm |\alpha_n|^2, \tag{8}$$

where β_n is the intrinsic amplitude of the mode, which does not depend on the attenuation due to propagation, and α_n is the amplitude that mode n has at a given position.

B. Basis of the post-processing technique

The post-processing technique proposed in this paper is based on the use of a general orthogonality relation, which involves a scalar product between the displacement and stress distributions of two modes m and n, considered at a given position along the guide. This relation is valid for both elastic or viscoelastic media, and has been established and used by Shkerdin for modeling the conversion of Lamb modes by a delamination in a plate:[25]

$$\int_0^h (T_{xy}^n U_y^m + T_{xy}^m U_y^n - T_{xx}^n U_x^m - T_{xx}^m U_x^n) dy = A(n)\,\delta_{mn}, \tag{9}$$

where δ_{mn} is the Kronecker symbol, thus meaning that any different modes m and n are orthogonal to each other. For $m=n$, $A(n)$ is the result of the integral, which can be used to calculate the complex amplitude α_n of the mode n, as shown later.

Let us now consider a complex acoustic field, called the "total field," composed of several modes propagating in a waveguide. The total displacement and stress distributions can be expressed as

$$\boldsymbol{u}_{\mathrm{tot}} = \sum_{j=1}^{J} \alpha_j \tilde{\boldsymbol{u}}_{\boldsymbol{j}} \quad \text{and} \quad \boldsymbol{\sigma}_{\mathrm{tot}} = \sum_{j=1}^{J} \alpha_j \tilde{\boldsymbol{\sigma}}_{\boldsymbol{j}}, \tag{10}$$

where α_j is the complex amplitude of each mode j in the total field. J is the total number of modes, which can either be a finite number or tend toward infinity. To calculate the complex amplitude of any guided mode n in this total field, the previous orthogonality relation is applied between the power-normalized fields of this mode and the total field. Practically, in Eq. (9), the terms U_k^m and T_{xk}^m are replaced by Eq. (10), and the terms U_k^n and T_{xk}^n are replaced by $\tilde{U}_k^n$ and $\tilde{T}_{xk}^n$, with $k=x,y$, thus leading to

$$\int_0^h \left[\tilde{T}_{xy}^n \left(\sum_{j=0}^{J} \alpha_j \tilde{U}_y^j\right) + \left(\sum_{j=0}^{J} \alpha_j \tilde{T}_{xy}^j\right)\tilde{U}_y^n - \tilde{T}_{xx}^n \left(\sum_{j=0}^{J} \alpha_j \tilde{U}_x^j\right) - \left(\sum_{j=0}^{J} \alpha_j \tilde{T}_{xx}^j\right)\tilde{U}_x^n\right] dy = A(n)\,\delta_{jn}. \tag{11}$$

Thanks to the orthogonality property of modes, if $n \notin [1 \ldots J]$, then the result of the integral is equal to zero. On the other hand, if $n \in [1 \ldots J]$ then the expression implies that

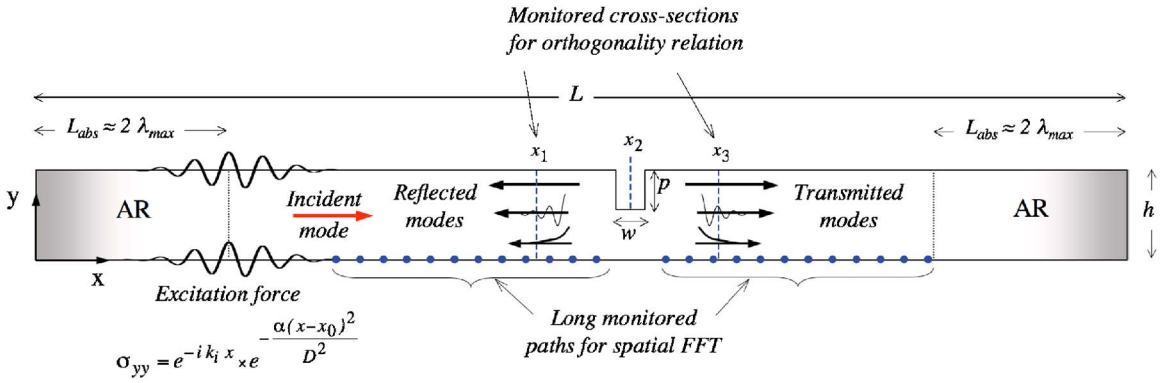

FIG. 2. (Color online) Schematic of the model for guided plate waves scattered by a notch.

$$A(n) = \int_0^h [\tilde{T}^n_{xy}(\alpha_n \tilde{U}^n_y) + (\alpha_n \tilde{T}^n_{xy})\tilde{U}^n_y - \tilde{T}^n_{xx}(\alpha_n \tilde{U}^n_x) - (\alpha_n \tilde{T}^n_{xx})\tilde{U}^n_x]dy \tag{12}$$

and

$$A(n) = \int_0^h 2\alpha_n(\tilde{T}^n_{xy}\tilde{U}^n_y - \tilde{T}^n_{xx}\tilde{U}^n_x)dy. \tag{13}$$

As long as the result of the previous orthogonality relation between a power-normalized mode and a total acoustic field is known, i.e., when $A(n)$ in Eq. (11) is given a numerical value, then the complex amplitude α_n of any mode n existing (or not) in the total acoustic field, can be calculated by inverting the Eq. (13), so leading to

$$\alpha_n = \frac{A(n)}{2\int_0^h (\tilde{T}^n_{xy}\tilde{U}^n_y - \tilde{T}^n_{xx}\tilde{U}^n_x)dy}. \tag{14}$$

C. Use of the post-processing technique for scattering problems

The orthogonality relation-based method described previously is used in this paper for quantifying the complex amplitudes of Lamb wave modes existing in solid waveguides when scattering occurs. Figure 2 presents the geometry of the problems considered here. A pure Lamb mode is incident on an opening notch in a plate, located at position x_2 along the guide. Mode conversion phenomenon will cause the scattering of Lamb modes, reflected from and transmitted past the notch. The total acoustic field in the guide can therefore be very complicated since it results from the superposition of the incident and all the diffracted modes: propagating modes, plus an infinity of evanescent or attenuated modes having non-negligible amplitudes in the vicinity of the notch.[3] In our study, this total field is predicted using a Finite Element code, as described in Ref. 26. Its complex through-thickness displacement and stress fields, U^{tot}_k and T^{tot}_{xk} with $k=x,y$, are monitored on each side of the notch, at positions labeled x_1 and x_3, while the power-normalized fields, $\tilde{U}^n_k$ and $\tilde{T}^n_{xk}$ with $k=x,y$, of any mode n, are calculated using a semianalytical method based on the surface impedance matrix method.[27] In the Finite Element code, the equations of dynamic equilibrium are solved in the Fourier domain, for a series of N frequencies corresponding to the nonzero amplitude components of the spectrum of a temporal excitation applied to the plate for launching the incident mode.[20] The excitation signal is usually chosen to be a Gaussian-windowed toneburst, the center frequency f_0 and the number of cycles of which will take different values in the examples of Sec. III.

When the complex amplitude α_i of the incident mode, the complex amplitude α^r_n of any reflected mode n, or the complex amplitude α^t_n of any transmitted mode n are calculated, using Eq. (14), then the ratios between the amplitude of any scattered mode and that of the incident mode can be derived:

$$\{r_n\}_{x_1} = \left\{\frac{\alpha^r_n}{\alpha_i}\right\}_{x_1} \quad \text{and} \quad \{t_n\}_{x_3} = \left\{\frac{\alpha^t_n}{\alpha_i}\right\}_{x_3}. \tag{15}$$

These complex ratios established for positions x_1 and x_3, respectively, can then be calculated at any position x along the guide by applying exponential correcting factors, as

$$\{r_n\}_x = \frac{\alpha^r_n e^{ik_n(x-x_1)}}{\alpha_i e^{-ik_i(x-x_1)}} = \{r_n\}_{x_1} \times \frac{e^{ik_n(x-x_1)}}{e^{-ik_i(x-x_1)}}$$

and

$$\{t_n\}_x = \frac{\alpha^t_n e^{-ik_n(x-x_3)}}{\alpha_i e^{-ik_i(x-x_3)}} = \{t_n\}_{x_3} \times \frac{e^{-ik_n(x-x_3)}}{e^{-ik_i(x-x_3)}} \tag{16}$$

It is also possible to calculate the proportion between any scattered mode n and the incident mode in terms of energy, by quantifying the ratio between the time-averaged power flow of the scattered mode n and that of the incident mode. As shown by Eq. (8), such quantities are the square of the modulus of the ratios between amplitudes, given in Eq. (16). Note that Eq. (16) allows calculating ratios of amplitudes for any type of modes, i.e., propagating, attenuated, or evanescent modes, in elastic or viscoelastic plates. However, since evanescent modes in elastic plates do not carry energy, ratios between time-averaged power flows will concern propagating modes only. But, for viscoelastic plates, since all modes propagate while being attenuated,[24] ratios between time-averaged power flows is a sensible quantity for any type of modes.

In comparison to the standard post-processing technique based on spatial FFT, which also supplies the amplitudes of the incident, reflected, or transmitted modes, the orthogonality relation-based method allows huge reductions in the size of the model to be made. Indeed, as illustrated in Fig. 2, the spatial FFT requires monitoring the displacements over distances, on each side of the defect, that must be large enough for the lobes in the wavenumber diagram to be accurately defined,[28] whereas the orthogonality relation technique requires monitoring through-thickness displacements and stresses at a given position along the guide, only. This advantage will be even more important for 3-D models, since meshing a surface through the guide thickness, around the defect, will be sufficient to apply the orthogonality relation, thus eliminating numerous elements of a large volume around the defect that would be necessary for applying the spatial FFT-based post-processing. Note that the elimination of large domains around the defect is also rendered possible by the use of efficient absorbing regions that suppress undesired reflections from the edges of the domain.

Furthermore, in viscoelastic media, this method directly supplies the amplitudes of modes at a selected position along the guide, while the spatial FFT supplies an average amplitude of each mode at a position along the monitored path, this position being dependent on the attenuation of the mode. Since all modes do not have the same attenuation, and since these attenuations vary with frequency, the amplitudes obtained for the different modes monitored along a given path correspond to different positions along this path. Therefore, it becomes very difficult to calculate the ratios between the amplitudes of scattered modes and that of the incident mode,[26] since this would require us to recalculate these amplitudes for a same position, taking into account the frequency-dependent attenuation of each mode.

III. APPLICATIONS

The propagation of Lamb waves along a plate made of either an isotropic elastic material (Sec. III B) or an isotropic viscoelastic material (Sec. III C) is considered. In the models, ***x*** and ***y*** indicate the direction of the propagation and the out-of-plane direction, respectively (Fig. 2). The reflection and transmission coefficients of a pure incident mode scattered by a notch-like defect are calculated, and the efficiency of the orthogonality relation-based technique is discussed.

A. Finite Element simulations

The FE simulations are made using the commercially available software COMSOL.[29] As mentioned in Sec. II A, plane strain conditions ($\varepsilon_{xz}=\varepsilon_{yz}=\varepsilon_{zz}=0$) are applied, so that the two-dimensional partial differential equations solved in the frequency domain are

$$C_{11}\frac{\partial^2 u_x}{\partial x^2}+C_{66}\frac{\partial^2 u_x}{\partial y^2}+(C_{12}+C_{66})\frac{\partial^2 u_y}{\partial x\ \partial y}=-\rho\omega^2 u_x,$$
$$C_{22}\frac{\partial^2 u_y}{\partial y^2}+C_{66}\frac{\partial^2 u_y}{\partial x^2}+(C_{21}+C_{66})\frac{\partial^2 u_x}{\partial x\ \partial y}=-\rho\omega^2 u_y, \tag{17}$$

where u_x and u_y are the displacement components, in the Fourier domain. As explained in Refs. 21 and 22, these equations are written in a specific COMSOL formalism, and solved for each frequency of the spectrum of a temporal excitation. Although the examples in Secs. III B and III C concern isotropic materials, the model is written for the case of a plane of propagation ***Oxy*** coinciding with a plane of symmetry of an anisotropic material. Moreover, the moduli C_{ij} in Eq. (17) can be defined to be complex quantities if the material is viscoelastic: $C_{ij}=C'_{ij}+iC''_{ij}$, the real part representing the material stiffness and the imaginary part its viscoelasticity.[21] This allows efficient absorbing regions (AR in Fig. 2) to be added at the edges of the plates, so that the model can represent the behavior of a structure that is infinitely long, while still using a small number of mesh elements. Instead of simply increasing the imaginary parts of the C_{ij}, as done before for defining these absorbing regions,[22,23] a frequency-dependent coefficient $A(f)$ is implemented for improving their efficiency in absorption. According to the geometry used in this study and shown in Fig. 2, the imaginary parts of the C_{ij} are then defined as follows:

$$\mathrm{Im}(C_{ij})=\begin{cases} C''_{ij}, & \text{if } x\in[L_{\mathrm{abs}},L-L_{\mathrm{abs}}] \quad (C''_{ij}=0 \text{ if material is elastic})\\ C''_{ij}+A(f)\left(\dfrac{|x^{l,r}_{\mathrm{abs}}-x|}{L_{\mathrm{abs}}}\right)^3 C'_{ij}, & \text{if} \quad x\notin[L_{\mathrm{abs}},L-L_{\mathrm{abs}}], \end{cases} \tag{18}$$

where L is the length of the plate, L_{abs} the length of the absorbing regions, $x^{l}_{x_{\mathrm{abs}}}$ and $x^{r}_{x_{\mathrm{abs}}}$ are the starting positions of the left and right absorbing regions, respectively. $A(f)$ is chosen to have large values at low frequencies, where modes are less sensitive to the material viscoelasticity, and low values at high frequencies or at frequencies close to frequency cutoff, where modes are more sensitive to changes in the acoustic impedances between the main domain of the plate and the absorbing regions. In this way, the length L_{abs} can be chosen to be equal to about twice the maximum wavelength of the waves existing in the whole frequency range of investigation, in comparison to previous studies where it had to be about three times this maximum wavelength.[23] In these conditions, the absorbing regions cause a reflection smaller than −60 dB of the energy of the incident wave, which is an acceptable crite-

TABLE I. Properties of the materials.

Material	Thickness (mm)	Density (g/cm3)	C_{11} (GPa)	C_{66} (GPa)
Aluminium	8	2.66	106	27
Perspex	3.9	1.2	$8.5+0.4i$	$2.1+0.1i$

rion for such scattering problems. This reduction of L_{abs} will be even more beneficial in further 3-D models for which the absorbing regions will have to be volumes instead of surfaces.

In the two following applications, the incident mode is generated by an excitation locally applied at the surface of the plate as a normal force, with a Gaussian-windowed spatial distribution corresponding precisely to the stress produced by the desired incident mode, using the following function:

$$\sigma_{yy} = e^{-ik_i x} \cdot e^{-\alpha(x-x_0)^2/D^2}, \tag{19}$$

where α (chosen equal to 20) and x_0 define the width and the center of the Gaussian envelope, respectively. D is the length of the excitation zone, which is chosen to be twice the maximum wavelength of the incident mode in the frequency domain, and k_i is the frequency-dependent wavenumber of the incident mode.

B. Diffraction by a notch in an aluminium plate

This first example concerns the scattering of an incident A_0 mode by a square notch of depth $p=2$ mm and width $w=2$ mm (Fig. 2), in an 8 mm thick aluminium plate, the properties of which are given in Table I. The incident mode is generated at 47 discrete frequencies comprised between 140 and 500 kHz, so that the total acoustic field in the plate can be composed of the incident mode plus up to six propagative scattered modes, according to the dispersion curves shown in Fig. 3. Also an infinity of nonpropagative modes can be scattered by the notch.

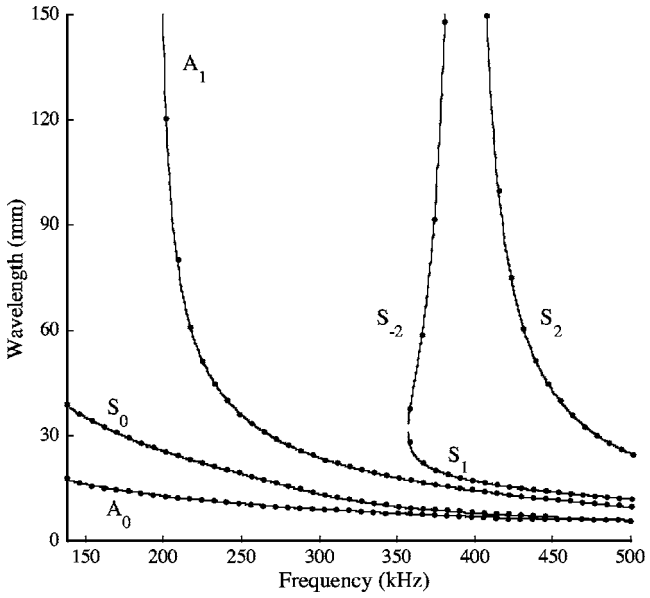

FIG. 3. Wavelength dispersion curves for Lamb modes in the 8 mm thick aluminium plate.

Two models of the scattering are realized for post-processing the FE data, the first one using the spatial FFT, and the other using the orthogonality relation. The length of each absorbing region is $L_{abs}=300$ mm (twice the maximum wavelength, which is that of the S_2 mode at 407 kHz), and the total length of the plate is equal to 2560 mm in the first case and to 760 mm in the second case. This reduction in length is due to the strong difference in the monitoring zones required to apply the two post-processing techniques. Indeed, the orthogonality relation was performed at the notch sides, i.e., at $x_1=x_2-w/2$ and $x_3=x_2+w/2$, while the spatial FFT required 900 mm ($6\lambda_{max}$) long zones on each side of the defect, for the lobes of the six propagative modes to be well resolved in the wavenumber diagram. Since 1 mm square Lagrange quadratic elements were used in the mesh, the reduction in the number of degrees of freedom (DoF) is therefore a factor 3.3 for this 2-D model.

As explained in Sec. II C, the orthogonality relation-based technique has been used for calculating the energy reflection and transmission coefficients, R_n^e and T_n^e, respectively, which correspond to the square of the modulus of the ratios given in Eq. (15):

$$R_n^e = |\{r_n\}_{x1}|^2 \quad \text{and} \quad T_n^e = |\{t_n\}_{x3}|^2. \tag{20}$$

Figure 4 compares the results of these energy coefficients to those calculated by using the spatial FFT post-processing, as described in Ref. 23. The good correlation allows validating the method based on the use of the general orthogonality relation. Moreover, the energy balance, i.e. (*incident power flow—total diffracted power flow*)/ *incident power flow*, calculated from the results obtained with each of these techniques shows that the orthogonality relation leads to less than 1% of error while the spatial FFT has up to 3% of error.

C. Diffraction by a notch in a viscoelastic plate

In this section, the scattering of a pure incident S_0 mode on a notch with depth $p=2$ mm and width $w=0.1$ mm, located at $x_2=260$ mm in a 3.9 mm thick Perspex plate is considered (Fig. 2). The properties of this material are given in Table I. The mesh is made of 0.1 mm by 0.325 mm Lagrange quadratic elements, so that the boundaries of the notch are discretized by 13 elements.

Equations (17) are solved for a series of 25 frequencies comprised between 88 and 205 KHz, using a distribution of complex amplitudes for the input corresponding to that of a four-cycle, Gaussian-windowed toneburst with a center frequency $f_0=146$ kHz. The wavelength and attenuation dispersion curves for this Perspex plate (Fig. 5) show that, between 88 and 205 kHz, the modes A_1, A_2, S_1, S_3, and S_4 are much more strongly attenuated than the modes A_0 and S_0, and that the maximum wavelength is that of A_1 at 136 kHz, which is equal to 700 mm. Consequently, the length of the absorbing regions should be about 1400 mm ($2\lambda_{max}$), but a series of tests showed that the very high attenuation of A_1 at frequencies for which its wavelength takes very large values, allows 145 mm long absorbing regions to efficiently remove its re-

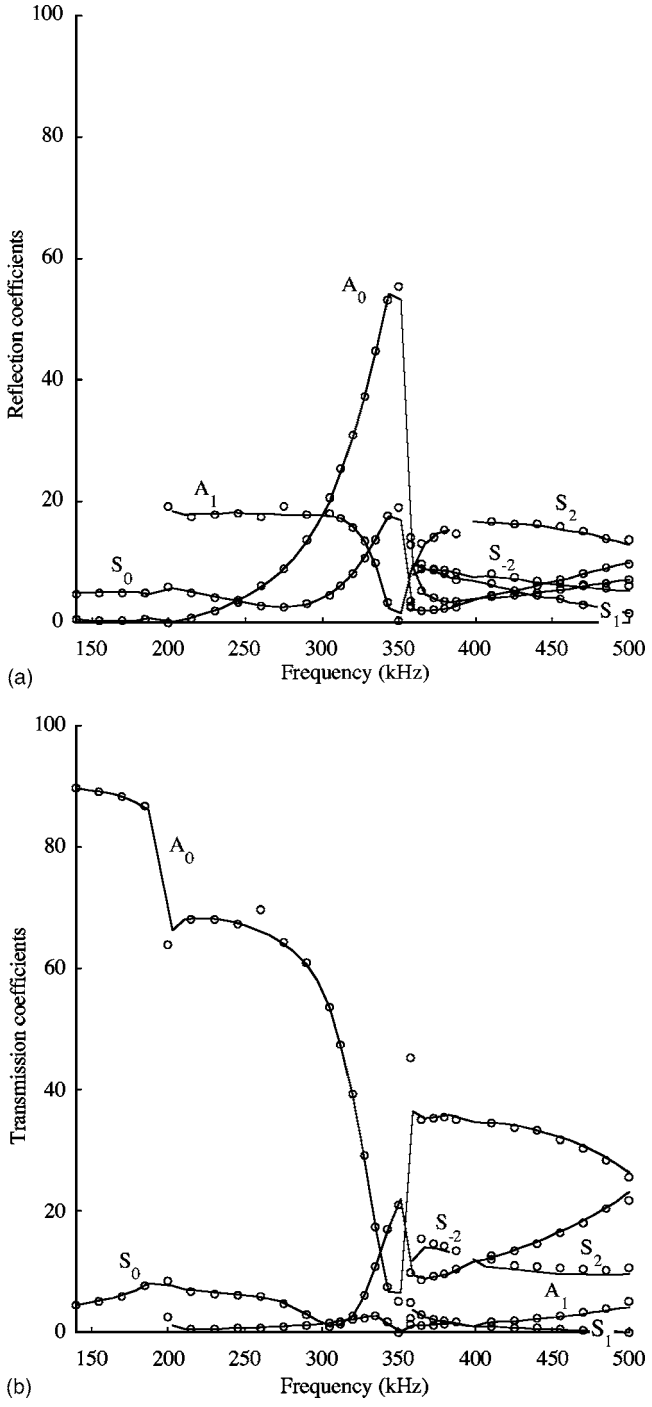

FIG. 4. (a) Reflection and (b) transmission coefficients, in terms of energy, for an incident A_0 mode on a 2 mm square notch in an aluminium plate. FE solution + post-processing using either the orthogonality relation (—) or the spatial FFT (◦).

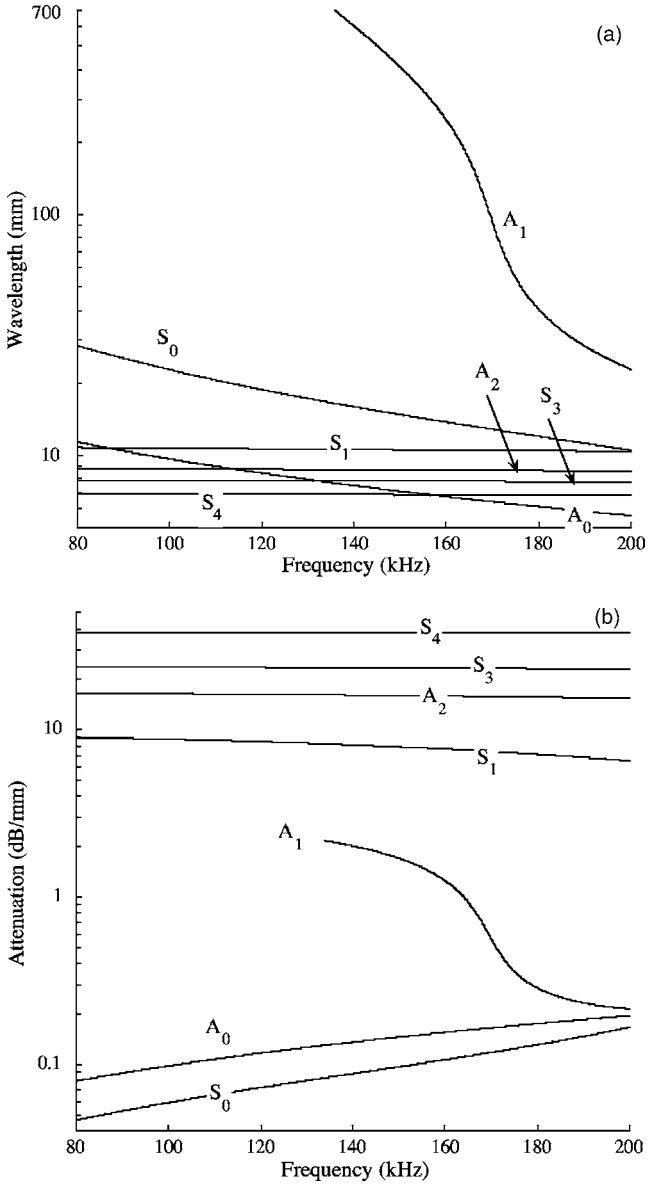

FIG. 5. Dispersion curves of Lamb modes in the 3.9 mm thick Perspex plate; (a) wavelengths and (b) attenuations.

flection from the plate ends. The total length of the plate is therefore set equal to 350 mm, including the two absorbing regions, the length of the excitation zone, i.e., $2\lambda_{S_0}^{\max} \approx 60$ mm, where $\lambda_{S_0}^{\max}$ is the maximum wavelength of the incident mode in the frequency domain of interest, plus a very small domain for the notch.

The reflection and transmission coefficients, in terms of amplitudes, are calculated for the modes A_0, S_0, A_1, A_2, S_1, S_3, and S_4, using Eq. (15), with $x_1 = x_2 - (w/2) = 259.95$ mm and $x_3 = x_2 + (w/2) = 260.05$ mm. Figure 6 presents the modulus of these coefficients, and shows that even the amplitudes of the strongly attenuated modes A_1, A_2, S_1, S_3, and S_4 can be calculated with the orthogonality relation-based method, as long as the positions of the monitored cross sections are chosen close enough to the notch. More high-order modes with even stronger attenuation exist in the same frequency range, but these are not shown in Fig. 5. Their amplitudes could also be quantified since the monitored cross sections run right along the notch sides, but it has been chosen to limit the calculations of the amplitudes of the first seven modes to demonstrate the potential of the method. It is interesting to note that not only the propagative modes have significant amplitudes at the notch location, but also the strongly attenuated modes that have amplitudes up to ten percent that of the incident mode, in the transmitted field. This implies that they have a non-negligible contribution in the total field close to the defect.

In order to validate the reflection and transmission coef-

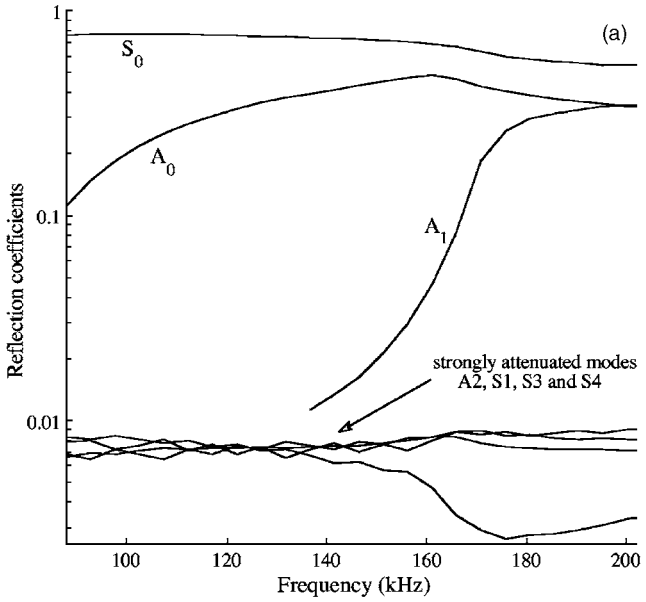

FIG. 6. (a) Reflection and (b) transmission coefficients, in terms of amplitude, calculated by post-processing the FE predictions with the orthogonality relation-based technique, for the S_0 mode incident on the notch in the 3.9 mm thick Perspex plate.

ficients given in Fig. 6, a reconstruction of temporal waveforms reflected from and transmitted past the notch has been made, corresponding to the total U_x displacement on the plate surface and at a distance $d=15$ mm away from the notch (about one wavelength of the incident mode S_0 at the center frequency 146 kHz). As shown in Fig. 7, at such a distance, all the strongly attenuated modes have negligible amplitudes. Two independent procedures are used for reconstructing these temporal signals. The first one is made of the following steps.

(1) Quantifying the complex amplitude of each mode at the notch location ($x=x_1$ or $x=x_3$), as explained before, i.e., using the orthogonality relation technique.
(2) Applying the change in phase (due to the propagation path of length d) to each of these amplitudes, in the same way as that defined in Eq. (16).

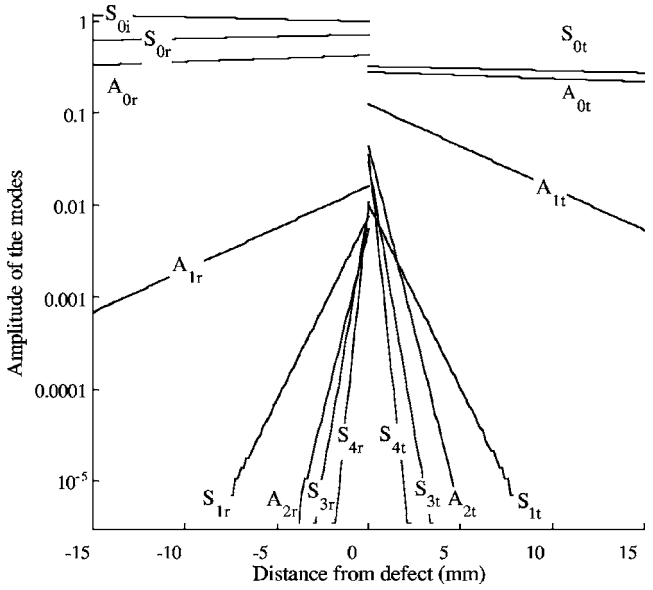

FIG. 7. Decreasing of the scattered-modes amplitudes versus the distance from the defect, at the central frequency (146 kHz).

(3) Using the power-normalized mode-shapes for calculating the complex U_x displacement produced by each mode at the plate surface and at $x=x_1-d$ or $x=x_3+d$.
(4) Summing all these U_x displacements to get the total U_x displacement produced by all modes that are not completely attenuated after the propagation along the distance d.
(5) Applying an inverse FFT after the four previous steps have been done for each frequency of the excitation.

The resulting waveforms are compared to those obtained by applying an inverse FFT to the complex displacements U_x directly monitored at the positions $x=x_1-d$ and $x=x_3+d$. Note that a specific model with a longer plate has been especially run in this purpose since the two aimed positions were in the absorbing regions of the initial model. Figure 8 shows the very good agreement between the two types of reconstruction, thus proving that the orthogonality relation-based processing technique supplies correct complex amplitudes of the modes, thus validating the reflection and transmission coefficients given in Fig. 6.

IV. CONCLUSIONS

A technique based on a general orthogonality relation has been proposed for post-processing FE output data, and, more specifically, for quantifying the complex amplitudes of guided wave modes diffracted in scattering problems. In comparison to the classical spatial FFT post-processing technique, which requires long paths to be monitored on each side of a scatterer, the orthogonality relation-based method allows to significantly reduce the number of mesh elements since it requires monitoring the through-thickness scattered field, at two single positions on each side of the scatterer, only. Two examples have been investigated for illustrating the advantages offered by this technique: the diffraction of the incident A_0 mode by a notch in an elastic aluminium plate, and the diffraction of the incident S_0 mode by a notch

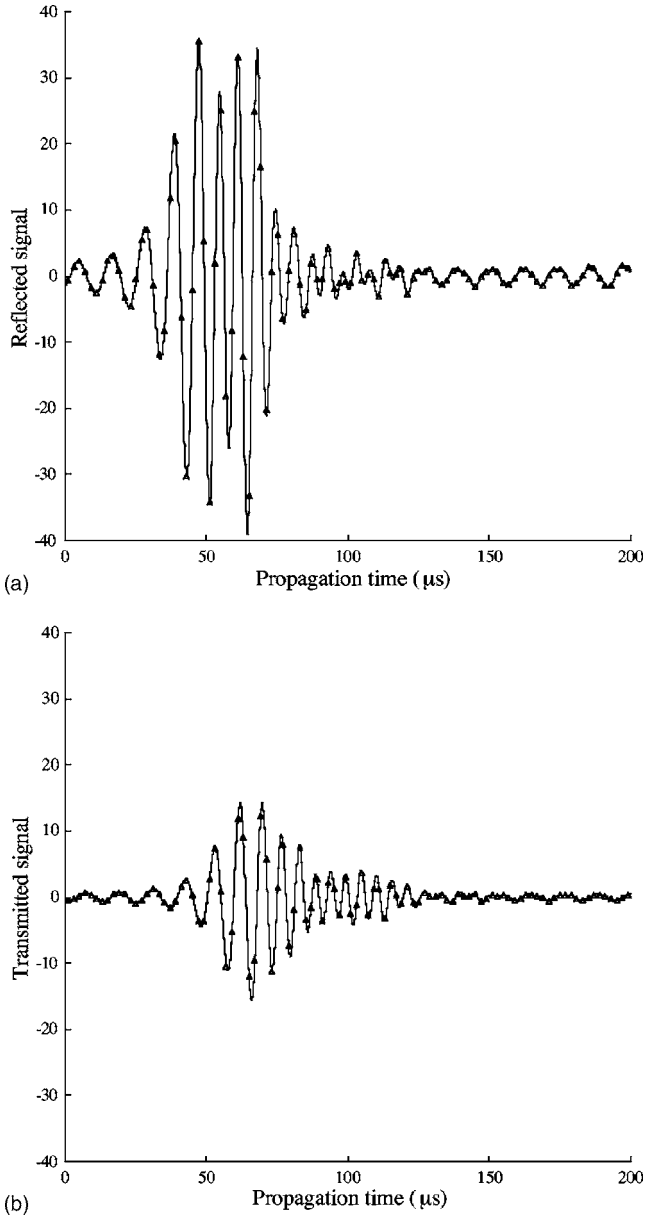

FIG. 8. Reconstructed temporal waveforms for in-plane displacement at the surface of the Perspex plate and at a distance $d=15$ mm away from the notch (a) to the left and (b) to the right; (△): inverse FFT from U_x directly monitored at the two positions, and (—): inverse FFT from U_x obtained from complex amplitudes calculated with the orthogonality relation + change in phase and mode shapes.

in the viscoelastic Perspex plate. Ratios between amplitudes or averaged power flow of scattered and incident modes have been predicted for these two cases. The method was shown to give results in very good agreement with data obtained by spatial FFT processing, in the case of the aluminium plate, where up to six propagating modes were diffracted. Furthermore, this method makes it easy to define ratios of amplitudes (or of power flows) between modes in viscoelastic media, while this is very difficult to achieve if the spatial FFT-based processing technique is used. Temporal waveforms of displacements at locations remote from the notch have been successfully reconstructed in the case of the Perspex plate, and used to validate the complex amplitudes of the scattered modes estimated with the orthogonality relation. The use of the general orthogonality relation for post-processing FE output data seems to be a very promising way to consider the simulation of scattering problems in three dimensions, since the reduction in the number of degrees of freedom it allows will be much more significant than in 2-D problems. Indeed, a reduction of N elements in a 2-D model would lead to a reduction of N^2 elements in three dimensions, if the width and the length of the 3-D geometry are considered to be equal to the length of the 2-D geometry.

ACKNOWLEDGMENTS

The authors are grateful to professors G. Shkerdin and C. Glorieux for supplying complementary explanations on the general orthogonality relation they propose in their publication.[25]

[1]P. Cawley, "The rapid non-destructive inspection of large composite structures," Composites **25**, 351–357 (1994).
[2]K. Diamanti, J. M. Hodgkinson, and C. Soutis, "Detection of low-velocity impact damage in composite plates using lamb waves," Structural Health Monitoring **3**, 33–41 (2004).
[3]B. A. Auld, *Acoustic Fields and Waves in Solids*, (R. Krieger, Malabar, FL, 1990).
[4]P. Kirrmann, "On the completeness of Lamb Waves," J. Elast. **37**, 39–69 (1995).
[5]S. Rokhlin, "Diffraction of Lamb waves by a finite crack in an elastic layer," J. Acoust. Soc. Am. **67**, 1157–1165 (1980).
[6]S. Rokhlin, "Resonance phenomena of Lamb waves scattering by a finite crack in a solid layer," J. Acoust. Soc. Am. **69**, 922–928 (1981).
[7]M. Tan and B. A. Auld, "Normal mode variational method for two and three dimensional acoustic scattering in an isotropic plate," Ultrason. Symp. Proc. **1**, 857–861 (1980).
[8]E. Le Clezio, M. V. Predoi, M. Castaings, B. Hosten and M. Rousseau, "Numerical predictions and experiments on the free-plate edge mode," Ultrasonics **41**, 25–40 (2003).
[9]B. Morvan, N. Wilkie-Chancellier, H. Duflo, A. Tinel, and J. Duclos, "Lamb wave reflection at the free edge of a plate," J. Acoust. Soc. Am. **113**, 1417–1425 (2003).
[10]M. V. Predoi and M. Rousseau, "Lamb waves propagation in elastic plane layers with a joint strip," Ultrasonics **43**, 551–559 (2005).
[11]M. Castaings, E. LeClezio and B. Hosten, "Modal decomposition method for modeling the interaction of Lamb waves with cracks," J. Acoust. Soc. Am. **112**, 2567–2582 (2002).
[12]X. M. Wang and C. F. Ying, "Scattering of Lamb waves by a circular cylinder," J. Acoust. Soc. Am. **110**, l752–1763 (2001).
[13]J. Mackerle, "Finite-element modelling of non-destructive material evaluation, an addendum: a bibliography (1997–2003)," Modell. Simul. Mater. Sci. Eng. **12**, 799–834 (2004).
[14]M. J. S. Lowe, P. Cawley, J.-Y. Kao, and O. Diligent, "Prediction and measurement of the reflection of the fundamental anti-symmetric lamb wave from cracks and notches," AIP Conf. Proc. **19A**, 193–200 (2000).
[15]O. Diligent, T. Grahn, A. Bostrom, P. Cawley, and M. J. S. Lowe, "The low-frequency reflection and scattering of the S0 lamb mode from a circular through-thickness hole in a plate: FE, analytical and experiments," J. Acoust. Soc. Am. **112**, 2589–2601 (2002).
[16]W. B. Fraser, "Orthogonality relation for the Rayleigh-Lamb modes of vibration of a plate," J. Acoust. Soc. Am. **59**, 215–216 (1976).
[17]J. E. Murphy, G. Li, and S. A. Chin-Bing, "Orthogonality relation for Rayleigh-Lamb modes of vibration of an arbitrary layered elastic plate with and without fluid loading," J. Acoust. Soc. Am. **96**, 2313–2317 (1994).
[18]B. S. Ramachandra Rao and J. K. Sridhara, "On some bi-orthogonality relations for semi-infinite strip problems," J. Math. Phys. **8**, 219 (1974).
[19]A. Gunawan and S. Hirose, "Mode-exciting method for Lamb wave-scattering analysis," J. Acoust. Soc. Am. **115**, 996–1005 (2004).
[20]L. Duquenne, E. Moulin, J. Assaad, and S. Grondel "Transient modelling of Lamb waves generated in viscoelastic materials by surface bonded piezoelectric transducers," J. Acoust. Soc. Am. **116**, l33–141 (2004).
[21]M. Castaings, C. Bacon, B. Hosten, and M. V. Predoi, "Finite element predictions for the dynamic response of thermo-viscoelastic material struc-

tures," J. Acoust. Soc. Am. **115**, 1125–1133 (2004).
[22]B. Hosten and M. Castaings, "Finite methods for modelling the guided waves propagation in structures with weak interfaces," J. Acoust. Soc. Am. **117**, 1108–1113 (2004).
[23]M. Drozdz, L. Moreau, M. Castaings, M. J. S. Lowe, and P. Cawley, "Efficient numerical modelling of absorbing regions for boundaries of guided waves problems," *Review of Progress in Quant. Non Destruct. Eval*, edited by D. O. Thompson and D. E. Chimenti, AIP Conf. Proc., New York, 2006, Vol. **25**.
[24]F. Simonetti and M. J. S. Lowe, "On the meaning of Lamb mode non-propagating branches," J. Acoust. Soc. Am. **118**, 186–192 (2005).
[25]G. Shkerdin and C. Glorieux, "Lamb mode conversion in a plate with a delamination," J. Acoust. Soc. Am. **116**, 2089–2100 (2004).
[26]B. Hosten and M. Castaings, "FE modeling of Lamb mode diffraction by defects in anisotropic viscoelastic plates," NDT & E Int. **39**, 195–204 (2006).
[27]B. Hosten and M. Castaings, "Surface impedance matrices to model the propagation in multilayered media," Ultrasonics **41**, 501–507 (2003).
[28]D. Alleyne and P. Cawley, "A two dimensional Fourier transform method for the measurement of propagating multimode signals," J. Acoust. Soc. Am. **89**, 1159–1168 (1991).
[29]COMSOL, *User's Guide*. Version 3.2 by COMSOL AB 2004 ⟨http://www.consol.com/⟩. Website last viewed on September 2005, the 6th.

Effect of ground variability on acoustic-to-seismic transfer function and false alarms in landmine detection

Vladimir N. Fokin,[a),e)] Margarita S. Fokina,[b),e)] James M. Sabatier,[c)] and Zhiqu Lu[d)]
National Center for Physical Acoustics, The University of Mississippi, 1 Coliseum Drive, University, Mississippi, 38677

(Received 26 May 2005; revised 21 May 2006; accepted 24 May 2006)

The spatial variability of ground properties leads to fluctuations in the acoustic-to-seismic transfer function (A/S TF), the ratio of the normal particle velocity on the ground to sound pressure. In some cases, these fluctuations may lead to false landmine detection alarms. This work shows that small variations in the ground properties may cause strong variations in the A/S TF. Experimental measurements of the A/S TF performed at a US Army eastern temperate site are presented and a correlation between high magnitudes of the A/S TF (false alarms) and moisture content on the surface is shown. A simple model of the ground explaining this correlation is suggested. This model was used to describe spatial distribution of high magnitudes in the TF and natural spatial variability of the TF. Results of calculations were compared with experimental data. Two frequency modulation scales in the A/S TF are observed at positions on the ground where land mines are not located. It was hypothesized that these are due to influence of wheeled vehicular traffic on the acoustic parameters in the ground layers. A comparison between numerical modeling of the A/S TF and the experimental data was performed. Direct measurements of acoustic parameters confirmed conclusions obtained from analysis of the A/S TF. [DOI: 10.1121/1.2214159]

PACS number(s): 43.20.El, 43.28.En, 43.40.At, 43.35.Mr [ADP] Pages: 621–630

I. INTRODUCTION

Investigations of the effects of the natural variability of ground on the interaction of sound with the ground are important for landmine detection research and agricultural soils studies. In this paper, the effects of natural variability of acoustical properties of the ground, i.e., compressional and shear wave speeds, density, thickness of the layers, on landmine detection are considered. Acoustic landmine detection utilizes the difference in the values of the acoustic-to-seismic transfer function (A/S TF) measured over the mine and away from the mine. For some types of mines, the A/S TF over the mine lies within the range of the natural variability of the ground admittance. This may lead to an increase in the false alarm rate. Understanding the nature of acoustic false alarms and their connection with the environmental phenomenology will directly contribute to both increased probability of detection of a mine and a decreased false alarm rate. These tasks require thorough investigations of ground variability.

Analysis of outdoor sound interaction with the ground has received considerable attention in a number of papers[1,2] in which a poro-elastic model of the ground was explored. These studies have concentrated on sound propagation over the ground. Several authors have observed that an airborne acoustic wave incident on a ground surface could couple energy into the ground.[3,4] These observations were based on measurements of ground vibration normal velocity using a buried geophone. In the work of Arnott and Sabatier,[5] it was shown that the A/S TF measured with geophone is in good agreement with the A/S TF measured by laser Doppler vibrometer (LDV). This pioneering technique was successfully used for acoustic landmine detection.[6,7] Many works deal with the scattering problem (which involves determining the scattering field as well as the internal field) arising when a known incident field impinges on a porous material with known physical properties.[8]

A poro-elastic model that considers propagation of two types of compressional waves in the media, known as "fast" and "slow" waves, and a shear wave, is the most adequate theory for the description of the ground. This poro-elastic model is complicated by the requirement for 14 input parameters for each poro-elastic layer. Some of the parameters are easily determined physical parameters; but others, such as air permeability, air porosity, and pore tortuosity, are difficult to measure *in situ*.[2] Because of this, it is difficult to properly apply and test this model in uncontrolled outdoor conditions.

It is possible to consider the A/S coupling within the framework of a visco-elastic model of the ground due to fact that ground motion in the poro-elastic model is associated with the "fast" compression wave. The main energy of this wave is in the frame displacement. Frame displacement may be detected by a LDV. On the other hand the "slow" wave is due to the oscillation of air in the pores and has little effect on the frame displacement. There are investigations that show that the A/S TFs predicted in the framework of the visco-elastic and the poro-elastic models are very close to each other,[9,10] when attenuation in the visco-elastic model is only slightly different from the attenuation in the poro-elastic model. In comparison with the poro-elastic model, the visco-elastic model needs six parameters for each layer. Therefore,

[a)]Electronic mail: vlfok@yahoo.com
[b)]Electronic mail: rtfok@yahoo.com
[c)]Electronic mail: sabatier@olemiss.edu
[d)]Electronic mail: zhiqulu@olemiss.edu
[e)]Present address: NSF Nanoscale and Engineering Center (NSEC), 243 Hesse Hall, University of California, Berkeley, California 94720–1740.

it is reasonable to use the simpler, layered visco-elastic model in the initial effort to understand the effect of natural ground variability on the A/S TF over a broad range of frequencies and plane wave incident angles.

The mathematical model for the reflection of plane waves from the multilayered elastic media has been developed in a number of papers[11–14] and has been successfully used for predicting sound propagation and reflection. Specific computational schemes were discussed in Refs. 15–18 and the effects of gradients of parameters in the layers were considered by a number of authors.[19–21] However, the sensitivity of the TF to different parameters of a layered ground and the effects of the natural variability of ground are not analyzed yet and need to be addressed.

II. PHYSICAL MODEL AND MATHEMATICAL BACKGROUND

The physical model used in the study of the acoustic-to-seismic transfer function (A/S TF) consists of $\boldsymbol{n}$ elastic layers covering an elastic half-space. Layers are parallel to x-y plane, z axis look upward, layers lay within negative z and $z=0$ correspond to upper boundary of first layer. This briefing has primarily been documented elsewhere,[22] but this section introduces its derivation in matrix form, which may add another view of the model and help readers grasp the mathematical background by consulting with both ways. The ground parameters are assumed to be constant within an elastic layer. The air and elastic half-spaces are assumed to be homogeneous and semi-infinite. Attenuation effects are taken into account in the layers and in the half-spaces assuming that the compression and shear wave velocities are complex values. We assume that the displacement fields $\boldsymbol{U}$ can be written in the terms of the scalar and the vector potentials φ and $\boldsymbol{\psi}$,

$$\boldsymbol{U} = \mathbf{grad}\,\varphi + \mathbf{curl}\,\boldsymbol{\psi}. \tag{1}$$

When taking only waves of vertical polarization into account, then the displacement fields are not dependent upon the y-coordinate $\boldsymbol{U}=\boldsymbol{U}(\boldsymbol{U}_x,\boldsymbol{U}_y=\mathbf{0},\boldsymbol{U}_z)$. $\boldsymbol{U}$ is expressible as the sum of an irrotational component, which represents a compression wave, and a solenoidal component, which represents a shear wave. The vector potential $\boldsymbol{\psi}$ represents the component of motion with nonzero vorticity. The reference axis of the system can be chosen such that $\boldsymbol{\psi}$ has only one component along the y axis, that is to say $\boldsymbol{\psi}=(\mathbf{0},\boldsymbol{\psi}_y,\mathbf{0})$. Stress and strain relations for a locally isotropic solid in a linear approach to determine the amplitude of strain are given by the generalized Hooke's law written in the tensor form. Using Eq. (1) and the generalized Hooke's law, the normal and tangential components of the displacement and the stress tensor in isotropic media can be written in terms of the potentials φ and $\boldsymbol{\psi}_y$. The components of the displacement and stress tensor involved in the boundary conditions are continuous across the liquid/elastic ($z=\mathbf{0}$) and the elastic/elastic ($z=\boldsymbol{d}_j$) interfaces:

$$z=0,\begin{cases}\boldsymbol{U}_z|_0=\boldsymbol{U}_z|_1,\\ 0|_0=\boldsymbol{\sigma}_{xz}|_1,\\ -\boldsymbol{p}|_0=\boldsymbol{\sigma}_{zz}|_1,\end{cases}\qquad z=\boldsymbol{d}_j,\begin{cases}\boldsymbol{U}_x|_j=\boldsymbol{U}_x|_{j+1},\\ \boldsymbol{U}_z|_j=\boldsymbol{U}_z|_{j+1},\\ \boldsymbol{\sigma}_{xz}|_j=\boldsymbol{\sigma}_{xz}|_{j+1},\\ \boldsymbol{\sigma}_{zz}|_j=\boldsymbol{\sigma}_{zz}|_{j+1}.\end{cases} \tag{2}$$

The potentials φ and $\boldsymbol{\psi}_y$ are governed by the Helmholtz equations:

$$\begin{aligned}&\Delta\varphi+\boldsymbol{\alpha}^2\varphi=0,\\ &\Delta\boldsymbol{\psi}_y+\boldsymbol{\beta}^2\boldsymbol{\psi}_y=0,\end{aligned} \tag{3}$$

where $\boldsymbol{\alpha}^2$ and $\boldsymbol{\beta}^2$ are the squares of the vertical components of the wave numbers for the compression and shear wave velocities. We will write the set of waves in layers and half-space through potentials taking into account the radiation conditions at infinity, and substituting them in the boundary conditions (2). Therefore, $\mathbf{4}(\boldsymbol{n}-\mathbf{1})$ equations are obtained with $\mathbf{4}(n-\mathbf{1})$ unknowns. A direct method of solution of the problem would be to construct $\mathbf{4}(\boldsymbol{n}-\mathbf{1})$ algebraic equations with the help of boundary conditions for the amplitudes of $\mathbf{4}(\boldsymbol{n}-\mathbf{1})$ waves, including the reflected wave, and then solving the set of equations using matrix inversion. Using the matrix propagator method based on the use of recurrence formulas which relate the amplitudes of waves in adjacent layers, it is possible to obtain six boundary equations for the combined description of the upper air half-space and multilayered elastic media. For solving the system of linear algebraic equations with respect to the reflection coefficient, the refraction indices expressed in terms of the elements of the matrix propagator $\boldsymbol{D}$, one may use Cramer's rule. However, the matrix method has an essential limitation due to the accumulation of the errors in numerical calculations of the matrix propagator for a great number of layers or at high frequencies. In this connection associated matrices are used, which allows one to extend the domain of validity of the matrix method and to eliminate the basic restrictions of the Thomson-Haskell[12,13] approach. In this case, the determinations of the set of boundary equations can be expressed in terms of the elements of the matrices of the second and sixth orders.

The direct transition from matrixes of the fourth order to the matrixes of the six order was based on the theorem of the properties of the associated matrices, when the characteristic matrix of the fourth order $\boldsymbol{D}$ is set in correspondence with the matrix of the sixth order $\tilde{\boldsymbol{D}}$, with the elements being second-order minors of the matrix of the fourth order $\boldsymbol{D}$. From the theorem on the properties of associated matrices, it follows that the minor matrices $\tilde{\boldsymbol{D}}$, $\tilde{\boldsymbol{A}}_j^{-1}$, $\tilde{\boldsymbol{A}}_j$, $\tilde{\boldsymbol{L}}_j$ corresponding to the matrices $\boldsymbol{D}$, $\boldsymbol{A}_j^{-1}$, $\boldsymbol{A}_j$, $\boldsymbol{L}_j$ satisfy the relationship $\tilde{\boldsymbol{D}}=\tilde{\boldsymbol{A}}_1^{-1}\cdot\tilde{\boldsymbol{A}}_2\cdot\tilde{\boldsymbol{L}}_2\cdot\tilde{\boldsymbol{A}}_2^{-1}\cdot\ldots\cdot\tilde{\boldsymbol{A}}_j\cdot\tilde{\boldsymbol{L}}_j\cdot\tilde{\boldsymbol{A}}_j^{-1}\cdot\ldots\cdot\tilde{\boldsymbol{A}}_n\cdot\tilde{\boldsymbol{L}}_n\cdot\tilde{\boldsymbol{A}}_n^{-1}\cdot\tilde{\boldsymbol{A}}_\infty$ and represent the sixth-order matrix. $\tilde{L}_j$ is the diagonal matrix of the sixth order. Every matrix D of the fourth order corresponds to matrix of the sixth order, if we will rename all combinations from four indexes 1, 2, 3, 4 by couples, arranging them in the next order: (1 3) (2 4) (1 4) (3 2) (1 2) (4 3), then

$$\boldsymbol{D} = \begin{vmatrix} d_{11} & d_{12} & d_{13} & d_{14} \\ d_{21} & d_{22} & d_{23} & d_{24} \\ d_{31} & d_{32} & d_{33} & d_{34} \\ d_{41} & d_{42} & d_{43} & d_{44} \end{vmatrix},$$

$$\tilde{\boldsymbol{D}} = \begin{vmatrix} D_{13}^{13} & D_{24}^{13} & D_{14}^{13} & D_{23}^{13} & D_{12}^{13} & D_{34}^{13} \\ D_{13}^{24} & D_{24}^{24} & D_{14}^{24} & D_{23}^{24} & D_{12}^{24} & D_{34}^{24} \\ D_{13}^{14} & D_{24}^{14} & D_{14}^{14} & D_{23}^{14} & D_{12}^{14} & D_{34}^{14} \\ D_{13}^{32} & D_{24}^{32} & D_{14}^{32} & D_{23}^{32} & D_{12}^{32} & D_{34}^{32} \\ D_{13}^{12} & D_{24}^{12} & D_{14}^{12} & D_{23}^{12} & D_{12}^{12} & D_{34}^{12} \\ D_{13}^{43} & D_{24}^{43} & D_{14}^{43} & D_{23}^{43} & D_{12}^{43} & D_{34}^{43} \end{vmatrix}, \tag{4}$$

with the elements being the second-order minors of the matrix $\boldsymbol{D}$. The diagonal matrix of the sixth order for interlayer contacts $\tilde{\boldsymbol{L}}$ was obtained using the same procedure. For transition from fluid to elastic media the transfer matrix $\boldsymbol{K}_{\ell S}$ should be introduced,

$$\boldsymbol{K}_{\ell S} = \begin{vmatrix} 0 & 0 & 0 & -1 & 0 & 0 \\ 0 & 1 & 0 & 0 & 0 & 0 \end{vmatrix}. \tag{5}$$

Then, the reflection coefficient and the refraction indices for two types waves are determined by

$$\boldsymbol{R} = \frac{\{\boldsymbol{Q} \cdot \boldsymbol{K}_{\ell S} \cdot \tilde{\boldsymbol{D}}\}_{22}}{\{\boldsymbol{Q} \cdot \boldsymbol{K}_{\ell S} \cdot \tilde{\boldsymbol{D}}\}_{32}}, \tag{6}$$

$$\boldsymbol{W}_{\ell} = \frac{\tilde{\boldsymbol{D}}_{34}}{\{\boldsymbol{Q}\boldsymbol{K}_{\ell S} \cdot \tilde{\boldsymbol{D}}\}_{32}}, \tag{7}$$

$$\boldsymbol{W}_{t} = -\frac{\tilde{\boldsymbol{D}}_{33}}{\{\boldsymbol{Q} \cdot \boldsymbol{K}_{\ell S} \cdot \tilde{\boldsymbol{D}}\}_{32}}. \tag{8}$$

Using the sixth-order matrices has some advantages, because large and small matrix elements emerging in ccomputations at high frequencies and for thick layers are canceled in the computation of the elements of sixth-order matrix. If the pressure P and the reflection coefficient R are known, the impedance Z_{in}, the A/S TF (the admittance function), may be determined and expressed as

$$Z_{\text{in}} = \frac{\rho c_0}{\cos \vartheta_0} \cdot \frac{1+R}{1-R}, \quad \text{TF}(f,\theta) = \frac{1}{Z_{\text{in}}(f,\theta)}, \tag{9}$$

where θ_0, ρ, c_0 are angle of incidence, density, and sound speed. A matrix technique was implemented as a functioning computer code[14] to obtain $\mathbf{TF}(f,\theta)$.

III. EFFECT OF GROUND PARAMETERS' NATURAL VARIABILITY ON THE A/S TF

The number of ground parameters affecting the A/S TF dramatically increases with increasing numbers of layers in the ground. A model with one viscoelastic layer covering an elastic half space will have 11 independent parameters. A model with 3 viscoelastic layers will have 23 independent parameters. Analytical expressions for layered, elastic media are very cumbersome and, in explicit form, limited to the case of single elastic layer covering an elastic half space.[23] Though recurrent expressions for the sound reflection coefficient from multilayered media are available,[11,23,24] it is highly unlikely that explicit analytical expressions may be analyzed for the A/S TF in the multilayered media. To understand the interconnection between the A/S TF and the parameters of a layered model of the ground, numerical investigations were performed. In this section, results of the numerical investigations of the A/S TF for a model of the ground containing 1–3 viscoelastic layers covering the viscoelastic half space are presented.

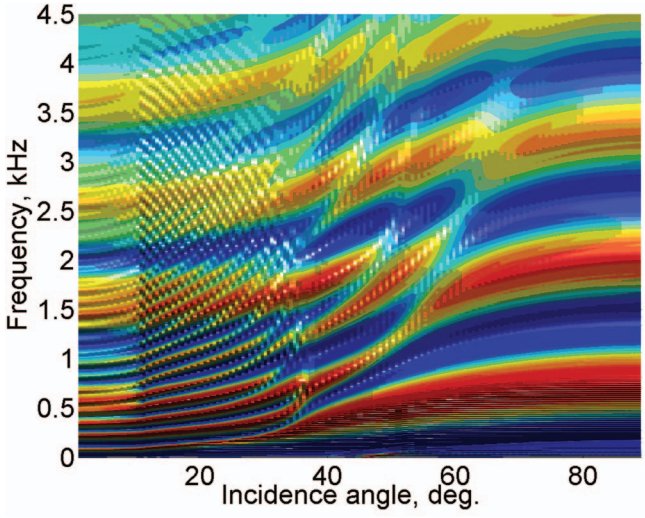

FIG. 1. Calculated acoustic-to-seismic transfer function (admittance function) on angle-frequency plane for twelve viscoelastic layers covering the elastic half-space.

The A/S TF depends on frequency f, angle of incidence of the acoustic wave θ, density ρ, complex compressional and shear sound speeds $(C_{\ell}+i\eta_{\ell},\ C_t+i\eta_t)$ of the media $\text{TF}(f,\theta,C_{\ell 1}+i\eta_{\ell 1},C_{t1}+i\eta_{t1},\rho_1,\ldots)$. Most often frequency or incident angle on the A/S TF are analyzed.[22]

The A/S TF on the frequency-angle plane is characterized by periodic modulation along the frequency axis and quasiperiodical modulation along the angle axis. The results of computations of the $\text{TF}(f,\theta)$ for 12 elastic homogeneous layers, covering an elastic half-space, are given in Fig. 1 in the form of a surface on the "frequency-incidence angle" plane. The properties of the ground for numerical modeling are shown in Table I. In Table I, upper and lower compression and shear velocities in an inhomogeneous elastic layer are tabulated. To model gradients of the parameter within inhomogeneous layer this inhomogeneous layer was subdivided into 12 "sublayers," in which the density, the compression, and shear velocities were constant. In the $\text{TF}(f,\theta)$ critical angles caused by compressional and shear speeds in the layered system may be found. To analyze effect of ground parameters' variability on AS TF we will consider models of the ground which have 1–3 homogeneous viscoelastic layers.

Though behaviors of the $\text{TF}(f,\theta)$ are complicated (Fig. 1) in the vicinity of every point on the frequency-angle plane, the A/S TF may be described in the terms of positions and amplitudes of nearby maxima and minima. This resonance approach was developed[25,26] and was successfully

TABLE I. Physical properties of the ground.

Media	c_ℓ (m/s)	η_ℓ (m/s)	c_t (m/s)	η_t (m/s)	ρ(kg/m^3)	D(m)
Air	340	0.017	⋯	⋯	1.225	∞
Inhomogeneous elastic layer	207–1590	9.93	80.2–116.25	1.4035	1700	1.98
Homogeneous elastic half-space	1800	7.32	500	2.03	2400	∞

used to describe the reflection coefficient in the vicinity of resonances. To describe the effect of ground parameter variability on the reflection coefficient or the A/S TF, it seems reasonable to analyze the frequency position of resonances and their amplitude in order to characterize the TF. Such consideration helps determine groups of ground parameters responsible for the natural variability of the A/S TF.

In landmine detection, the most interesting spatial scales of ground variability are at ranges from a few centimeters to a few tens of centimeters. These scales are most interesting because they are the same as the landmine dimensions and therefore cause false alarms. Natural ground variability in these scales may lead to high false alarm rates and hinder landmine detection. Inhomogeneity within these scales is likely due to the upper layer of the ground because it may be strongly affected by external mechanical stresses produced by different objects on the surface. These mechanical stresses may be connected both with human activity and wildlife activity in less habitant areas. Variability parameters in deeper layers have much less influence on AS TF and due to natural reasons inhomogeneity with spatial scales from few centimeters to a few tens of centimeters are less probable in deeper layers. It is also hypothesized that amplitudes of fluctuations of the parameters will be much greater in the top layers of the ground than those in the elastic substrate. The period of modulation of the A/S TF and positions of extremes are determined by parameters of the layers. Since the natural variability of the A/S TF seems mostly due to variability in the frequency positions of resonances and since the sensitivity of the A/S TF to variations of parameters in deeper layers is smaller than the sensitivity to variations of the parameters in the upper layer, the dependence of the A/S TF on the parameters of the elastic substrate will not be analyzed here.

A. Effect of parameter variability in the top layer of the ground

Numerous measurements of the A/S TF for detection of landmines in outdoor conditions show that the magnitude of the TF has strong spatial variability.[7] This variability is thought to be due to the natural variability of acoustical properties of the ground (compressional and shear wave speeds, density, thickness of the layers). Experimental data show that the variability of the TF at low frequencies is minimal and increases dramatically with increasing frequency. As a result, the A/S TF measured over the same region of the ground has practically no spatial variability at frequencies less than 100 Hz, but has a strong spatial variability at frequencies above 300 Hz. Since the majority of antipersonnel mines have maximum responses for frequencies higher than 300 Hz, this effect essentially increases the false alarm rate for antipersonnel mines. An understanding of the factors that cause this variability in the magnitude of the A/S TF from one spatial point to another will help to reduce the false alarm rate. To understand the effect of the natural variability of the ground on the A/S TF, numerical investigations were performed for a model consisting of one elastic layer covering an elastic half-space and three elastic layers covering the elastic half-space.

The dependence of the A/S TF on shear speed in the layer and thickness of the layer was analyzed elsewhere.[22] It was shown that variability of these parameters will lead to significant changes in the magnitude of the TF and increasing of false alarm rates.

To further analyze the effects of variations of the ground parameters on the A/S TF, it is reasonable to consider the TF on the frequency-ground parameter plane. All other parameters of the media and incident angle are fixed. Sets of parameters used for computations are shown in Table II. For computations, a model consisting of one elastic layer covering the elastic half space was used. The dependencies of the A/S TF on compressional speed in the layer were computed for angle of incidence equal to 1°. Amplitude of the A/S TF is presented in color with red corresponding to maximum and blue for minimum.

The compressional speed in the layer should have significant influence on the TF. The calculated A/S TF on the f-C_ℓ plane is shown in Fig. 2. Initial parameters of the layer used for computations are shown in Table II. The section of the A/S TF along the frequency axis with a fixed value of C_ℓ gives the frequency dependence of the A/S TF. A section along the C_ℓ axis will show the dependence of the A/S TF on the C_ℓ in the layer at a fixed frequency. Based on the as-

TABLE II. The set of parameters for one layer model of the ground.

Media	c_ℓ (m/s)	η_ℓ (m/s)	c_t (m/s)	η_t (m/s)	ρ (kg/m^3)	d(m)
Air	340	0.017	0	0	1.225	∞
Layer	80	3.5	70.1	1.0	1400	1.32
Half-space	1800	3.5	500	2.2	2400	∞

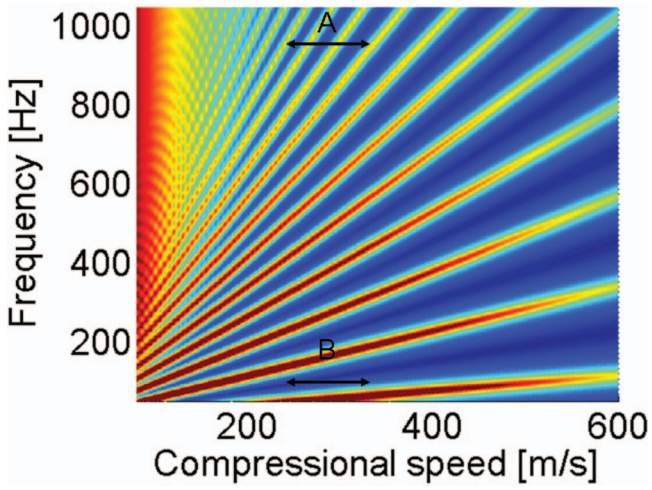

FIG. 2. Calculated acoustic-to-seismic transfer function: on frequency-compressional wave speed in the layer plane. All other parameters of viscoelastic model of the ground are fixed (Table II).

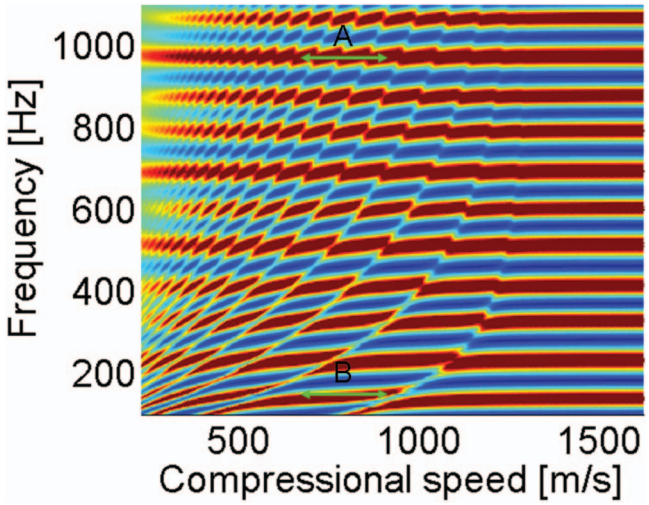

FIG. 3. Calculated acoustic-to-seismic transfer function: on the plane frequency-compressional wave speed in the third layer. All other parameters of viscoelastic model of the ground are fixed.

sumption that the compressional speed in the layer varies from one spatial point to another, this section may be used for estimation of spatial variability of the A/S TF due to variability of the C_ℓ. Analysis of this dependence at different frequencies shows that spatial variations of C_ℓ will cause much less change in the values of the TF at lower frequencies than at higher frequencies. For example, variation of the compressional speed in the layer at 50 Hz (arrow B) will cause no significant changes in the TF. The same variation of compressional speed in the layer at 1000 Hz (arrow A) will cause changes in the TF from minima to maxima three times. Thus small fluctuations of compressional speed will lead to strong spatial variability of the TF at higher frequencies but will cause no spatial variability at lower frequencies. This sensitivity analysis contributes to understanding of experimental data described elsewhere.[7]

With the assumption that all other parameters of the model are fixed, the shift of the position of first maxima of the transfer function may be used as an indicator of changes in the compressional wave speed in the layer or thickness of the layer.

B. Effect of variability in the third layer of the ground

Though the model of a single elastic layer covering the elastic half-space gives a qualitative description of the effects due to variability of top layer of the ground, models with a greater number of layers will better describe the reality. For more realistic modeling, a ground model consisting of three viscoelastic layers lying on the elastic substrate was investigated. The sound speed and density increase with the depth. To take into account effects due to critical angles in the layered system, calculations were made for an angle of incidence equal to 60°. The physical constants used for calculations are shown in Table III. Figure 3 shows the dependence of the A/S TF on the compressional speed in the third layer. In Fig. 3 one can see two sets of modulations. The first modulation has maxima and minima parallel to the compressional speed axis. These maxima and minima are due to wave reflections in the top two layers of the ground. The parameters of the top two layers are kept constant and frequency modulation of the TF due to interference of the waves inside these two layers is practically independent of parameters in the third layer. At low frequencies ($f < 200$ Hz) and for low values of compressional speed in the third layer ($C_\ell < 500$ m/s) this dependence may be essential.

The second modulation has a parabolic form and is due to the varying compressional speed in the third layer. If the wave speed in the third layer is higher than the sound speed in air a critical angle should exist at the boundary of the air half space. For angles greater than this critical angle, energy will not penetrate into the third layer. With increasing compressional wave speed in the layer, the critical angle corresponding to this wave speed will decrease. When the speed of the compressional wave in the third layer becomes greater than 1300 m/s, the layer becomes completely reflective. This occurs when the angle of incidence of the plane wave in the air equals the critical angle for the third layer. Energy can no longer penetrate the layer and additional increase in the

TABLE III. The set of parameters for three layer model of the ground.

Media	c_ℓ (m/s)	η_ℓ (m/s)	c_t (m/s)	η_t (m/s)	ρ (kg/m^3)	d(m)
Air	340	0.017	0	0	1.225	∞
Layer 1	150	0.5	80	1.0	1400	0.5
Layer 2	180	0.5	100.0	1.0	1530	1.38
Layer 3	230	3.5	150	1.0	1560	1.52
Half-space	1800	3.5	500	2.2	2400	∞

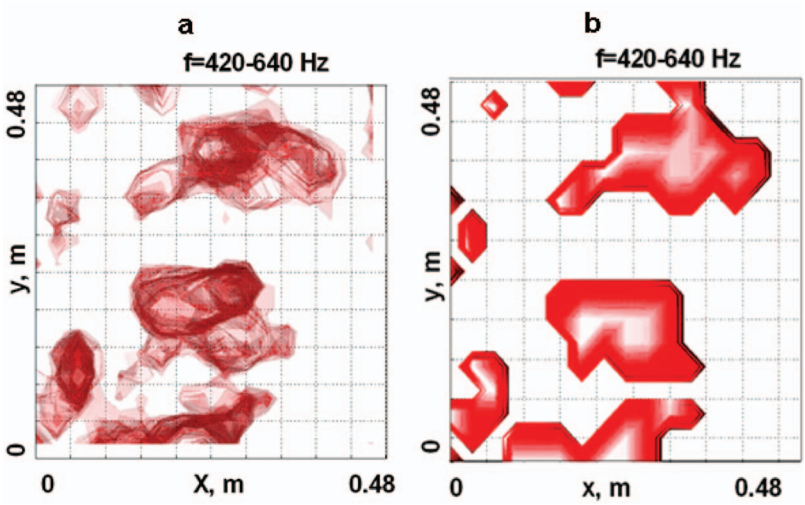

FIG. 4. Spatial distribution of higher intensity points in the measured transfer function (a) and spatial distribution of higher intensity points in the calculated transfer function (b).

compressional speed in the layer will have no effect on the A/S TF. Analogous to the consideration of Fig. 2, it easy to see that variability of the parameters of the third layer within certain limits marked by arrows (Fig. 3) will cause more fluctuations at high frequencies (about 1000 Hz, arrow A) than at low frequencies (about 150 Hz, arrow B).

The effects of the third layer in the ground on the A/S TF is smaller than the effect of the first layer, but it may be essential for an explanation of some experimentally observed effects.

IV. EXPERIMENTAL INVESTIGATION OF NATURAL VARIABILITY OF THE GROUND AND FALSE ALARMS

In this section, analysis of experimental data of natural variability of the ground is presented. The experimental investigations were performed at an US Army eastern temperate site, in 2001 and 2003. The test site consisted of several square meters of a constructed gravel road and measuring procedure is described elsewhere.[7] Analysis of experimental data reveals mine like high TF region unchanged over several frequency subbands located on a blank site. The high velocity response on the blank site exists in the frequency band from 480 to 580 Hz.

At the time of the measurements, the surface of the ground within the measurement site visually consisted of wet and dry regions of irregular shapes. Analysis of LDV data revealed that locations of the wet regions on the ground surface and the high velocity regions in the LDV images are highly correlated. A simple model was suggested to explain this phenomenon.[22]

The spatial locations of the strongest response of the experimentally measured TF may be revealed in the space-frequency volume by drawing contours of different levels for the normalized TF. The normalized TF for a fixed frequency was obtained by dividing the velocity response at each point by the maximum value of the velocity at this frequency. This processing was done for all frequencies. The maximal value of the normalized TF will be equal to unity. The image of the normalized TF was plotted in the frequency-space volume. Figure 4(a) shows contours of the experimentally measured normalized transfer function with a level equal to 0.6 on the projection of the x,y plane in the frequency band between 420 and 640 Hz.

The model of a layered, viscoelastic ground was used to numerically model the spatial distribution of the high values of the A/S TF. During this effort, it was hypothesized that the model of the ground for the wet regions consisted of two different elastic layers covering an elastic substrate. The upper layer was less dense and had a lower sound speed than the second layer. The model of the ground outside the wet regions consisted of one elastic layer in which the parameters are equal to the parameters of the second layer in the wet region model. The thickness of this layer was equal to the total thickness of two layers. The spatial distribution of the different models was estimated from the spatial distribution of high values in the measured A/S TF.

The results of computations of the A/S TF are presented in Fig. 4(b) in a form analogous to Fig. 4(a). Regions of the normalized transfer function with a level equal to 0.6 were isolated by red contours in the space-frequency volume. Figure 4(b) is the top view on these contours. In general Figs. 4(a) and 4(b) are very similar although the experimental picture has a more complicated structure. The spatial distribution of the colored regions is the same. It is difficult to model the fine structure of the TF on the experimentally obtained TF [Fig. 4(a)]. The rough model used for calculations utilized only two different models for all spatial points. Nevertheless it permits prediction of main features of the experimentally measured TF.

V. INFLUENCE OF WHEELED VEHICULAR TRAFFIC ON THE ACOUSTIC-TO-SEISMIC TRANSFER FUNCTION

In the previous sections, experimentally measured dependencies of the amplitude of the A/S TF at some frequencies in the X-Y plane were considered. In this section, frequency dependence of the A/S TF along one spatial coordinate (x or y) will be analyzed. We will specify the x coordinate as along the road and the y coordinate as across the road. Measurements were performed on "gravel" and "dirt roads" at the test site. Soil properties corresponding to

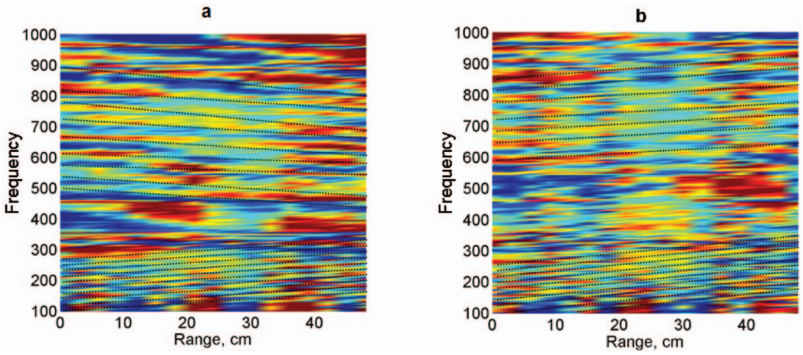

FIG. 5. Experimentally measured TF[1] (a) along the dirt road, (b) across the dirt road.

these sites are described elsewhere.[7] During measurement, the sound field interacting with the ground excites vibrations in the LDV too. These vibrations are added to the measured vibrations of the ground and may mask the frequency and spatial dependencies of the A/S TF. To remove modulations due to LDV vibration one can utilize the fact that LDV vibrations have the same Fourier spectrum at all spatial points and can be eliminated by subtraction from the measured TF averaged by the range TF,

$$\mathbf{TF}'(\boldsymbol{f},\boldsymbol{r}_i) = \mathbf{TF}(\boldsymbol{f},\boldsymbol{r}_i) - \frac{1}{\boldsymbol{n}}\sum_{i=1}^{n}\mathbf{TF}(\boldsymbol{f},\boldsymbol{r}_i).$$

This processing makes spatial variations of the TF more visible. In Figs. 5(a) and 5(b), $\mathbf{TF}'(\boldsymbol{f},\boldsymbol{r}_i)$ measured along the x and y axes on the dirt road are shown. Two different structures may be found in Figs. 5(a) and 5(b). Each maximum or minimum in Figs. 5(a) and 5(b) fluctuates in amplitude when the range increases. For better visualization, dotted black lines were placed over these trends in Figs. 5(a) and 5(b). These lines do not exactly follow actual maxima or minima in the $\mathbf{TF}'(\boldsymbol{f},\boldsymbol{r}_i)$ but are useful to highlight these structures. The first structure can be seen at low frequencies and has a small period of frequency modulation. The second structure is located at high frequencies and has larger period of frequency modulation. There is an essential difference between sections across and along the road. In Figs. 5(a) and 5(b) the lines due to the first structure have positive inclination or a positive derivative along the range. The lines due to second structure have a negative derivative along the road [Fig. 5(a)] and positive derivative across the road [Fig. 5(b)]. Analysis of measurements in other spatial points confirms that these two structures are stably present in sites located on a dirt road.

To model this spatial variability of the A/S TF, models of the layered ground are considered. Variability of layer depth and wave speed in the layer have similar effects on the TF. It was hypothesized that the depth of the layer is constant and that there is a horizontal gradient of the compressional wave speed in the layer. The compressional wave speed increases or decreases when range increases. The results of modeling the spatial variability of the ground for three layered models of the ground are shown in Figs. 6(a)–6(c). Figure 6(a) shows variability of the A/S TF for one elastic layer covering the elastic half space. Parameters of the half space are constant. Compressional speed in the layer decreases with range. In Fig. 6(a) one can see regular modulation in the TF. The period in this modulation decreases with range so lines of frequency modulation have negative inclination. The model consisting of one elastic layer covering an elastic half space may qualitatively explain the existence of one period of modulation in the experimental A/S TF. For two layers lying on elastic half space, the results of modeling the A/S TF are shown in Fig. 6(b). In the top layer, sound speed decreases with distance and, in the second layer, sound speed increases with the distance. As a result of different horizontal gradients in the layers, the two different modulations may be seen in Fig. 6(b). The additional modulation with a smaller frequency period and positive inclination may be observed in the low frequency band. Two modulations in Fig. 6(b) have

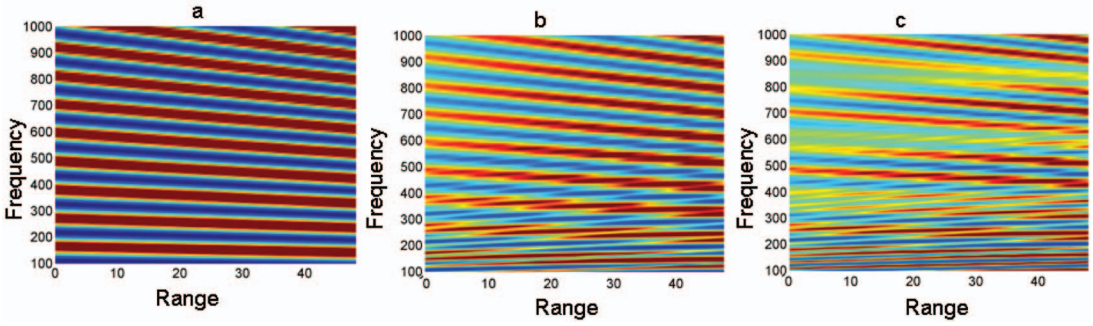

FIG. 6. Calculated transfer function for ground with horizontal gradient of compressional wave speed in the layers: (a) one viscoelastic layer covering half-space, (b) two viscoelastic layers covering half-space, (c) three viscoelastic layers covering half-space.

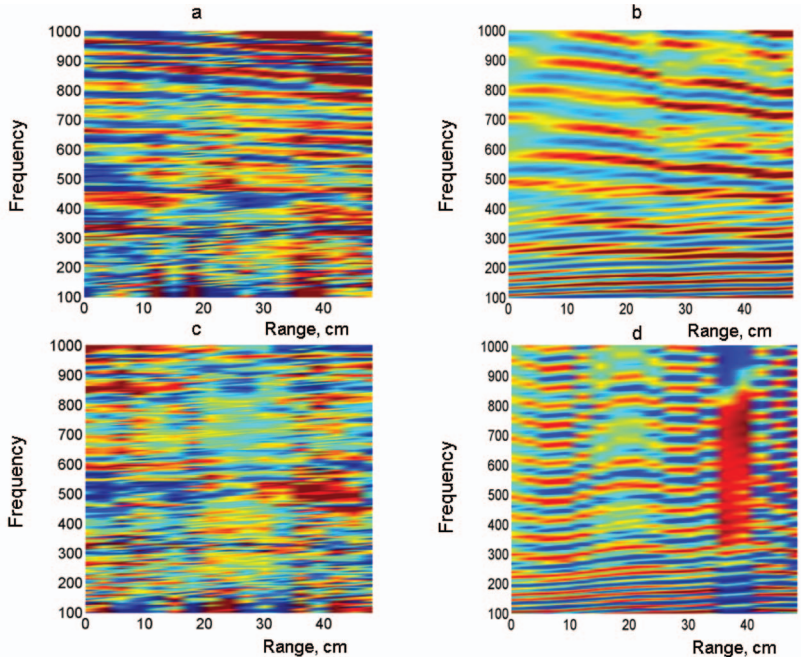

FIG. 7. Comparison between measured $\mathbf{TF}'(\boldsymbol{f},\boldsymbol{r}_i)$ (a), (c) and calculated $\mathbf{TF}(\boldsymbol{f},\boldsymbol{r}_i)$ (b), (d).

the opposite inclination and different frequency periods. The frequency modulations in Fig. 6(b) are regular and have high contrast between minima and maxima.

Though two layers are enough for qualitative description of experimentally observed phenomena in real conditions, it is unlikely that two adjacent layers will have horizontal gradients of compressional speeds in opposite directions. To make the physical model more realistic, a third layer is placed between these two layers. The parameters of the third layer are kept constant. The results of the A/S TF computations are shown in Fig. 6(c). After adding the third layer, transfer function on Fig. 6(c) became more similar to the experimental graphs. The contrasts between minima and maxima are decreased and the modulation with a small frequency period becomes more visible. The additional modulation due to the third layer makes the amplitude of the first two modulations frequency dependent.

To add additional realism to the three-layer model, fluctuations in the compressional speed and the thickness of the layers was added in addition to regular dependencies of compressional wave speed on distance. Two different realizations are shown in Figs. 7(b) and 7(d) along with two different experimental, horizontal sections of the site located on the dirt road. [Figs. 7(a) and 7(c)]. It is impossible to exactly model the experimentally measured TF due to lack of information about the parameters of the layered ground. In qualitative modeling only common features may be compared. One can notice the discontinuous lines of maxima and minima in the range dependence of the extremes of the modeled TF [Fig. 7(b)] which are clearly seen in the experimentally measured A/S TF [Fig. 7(a)]. Another important feature is the high values of the TF at distances at 35–40 cm in frequency range 350–800 Hz in the numerically modeled TF [Fig. 7(d)]. These high values in the experimentally measured TF [Fig. 7(c)] located between 30 and 50 cm in the 400–600 Hz frequency band potentially may be a false alarm. The calculated TF [Fig. 7(d)] roughly reproduces this feature. This supports the idea that fluctuations of the compressional speed along with fluctuations of layer depths may lead to false alarms. The low values of the experimental TF in Fig. 7(c) in frequency band 550–950 Hz at range between 20 and 30 cm seem to be in common with the low intensity regions located in Fig. 7(d) at distances 12–25 cm in frequency bands 300–500 and 600–800 Hz. It is thought that the regular variability of the ground parameters combine with the fluctuations of the parameters to produce the majority of experimentally observed effects. The regular changes in the properties of the layers will lead to the inclination of the lines of the local minima and maxima in the TF. Fluctuation of the parameters will lead to irregularities in this structure. A comparison of the experimental and the modeled A/S TF illustrates that layered, elastic model of the ground with horizontal gradients and fluctuations of compressional wave speed and thickness of the layer may be used for study of the A/S TF and for physical explanation of the experimental phenomena.

It was also thought that the different spatial dependencies of the TF, along and across the road, were due to the additional stress produced by the wheels of vehicles driving through the same places on the road, repeatedly. To confirm the existence of the different velocities in the wheeled and undisturbed parts of the road, measurements of the compressional velocity were made on the dirt lane by measuring delays of signal propagated along the ground. To emphasize the possible effects of additional stress on the compressional wave speed in the wheeled soil, measurements were performed along the track and in undisturbed regions. One way roads used for measurements have two ruts located near sides of the road. The results of measuring the time delay versus range for the wheeled and undisturbed sections were used for calculation of the compressional wave speed. It was found that the effect of wheeled vehicle traffic strongly de-

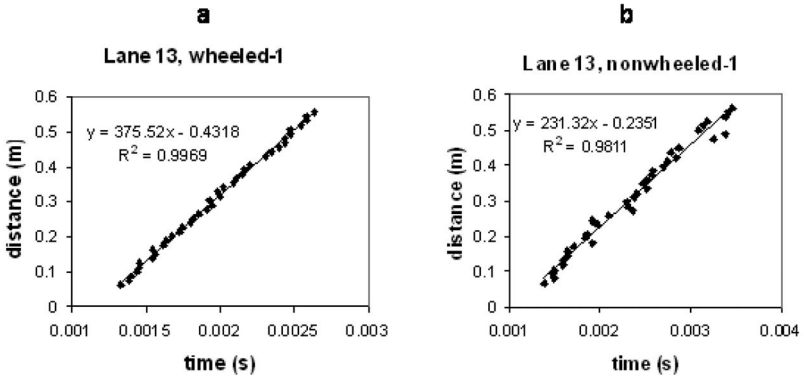

FIG. 8. Experimentally measured dependencies of propagation time for front of the impulse from distance for two sides of the road (a) of track and (b) on track.

pends on the type of the road. On the gravel road no significant difference in the compressional wave speeds for undisturbed and wheeled sections were found.

For the dirt road, tests were conducted on the undisturbed road and wheeled track at both sides of the same road. Average compressional wave speeds equal to 231.3 and 267.6 m/s were obtained for nonwheeled soil. The compressional wave speeds for wheeled track were equal to 375.5 and 337.9 m/s. The results of the measurements and equations of straight lines with best fitting the experimental data for wheeled track and nonwheeled track shown in Fig. 8. Due to time delays in the experimental equipment, the straight lines in Fig. 8 did not originate from the point (0,0). It is clear that in this case the compressional wave speed in wheeled track is significantly higher than compressional wave speed in the undisturbed road. For the dirt road, compaction exhibits stronger influence on soil properties and results in a higher compressional wave speed value for the wheeled track than that for the undisturbed road. Similar results regarding the effect of stress on the compressional wave speed in soil were obtained in laboratory experiments.

Measurements of wave speed in wheeled and undisturbed soil confirm the assumption that horizontal gradients of compressional speed may produce inclined lines in dependencies of the TF on the distance. It was shown that the A/S TF has high sensitivity to sound speeds in the layered ground and may be used for detection of horizontal gradients of sound speed in the ground.

VI. CONCLUSION

In this paper, the layered, visco-elastic model of the ground was used to describe airborne sound interaction with the ground. The influence of the natural variability of ground parameters on the A/S TF was numerically investigated. Analysis of dependencies of the TF on physical parameters for a model consisting of one elastic layer overlaying an elastic substrate was used to explain that the natural variations of ground parameters will cause stronger fluctuations in the magnitude of the TF at higher frequencies than at lower frequencies over the same region of the ground.

The model and data analysis confirm a strong influence of the layered ground parameters on the A/S TF. Variability of the ground properties causes variability in the magnitude of the A/S TF and false alarms in acoustic landmine detection. Due to these variations, different regions of the ground will provide different values of the TF. Comparison of computed distribution of regions with high values of the TF with experimental data shows good agreement and confirms validity of the suggested physical model for false alarms.

Comparison between results of numerical modeling and experimental data confirm that elastic model of the ground with horizontal gradients and fluctuations of compressional wave speed and thickness of the layer may be used for physical explanation of the experimental phenomena. The assumption that horizontal gradients of compressional speed in the top layer are due to alterations in the soil properties due to wheeled vehicular traffic was confirmed by direct measurements of the compressional speed. It was shown that, for a dirt road, additional stress from vehicular traffic causes an increase in the compressional wave speed in the wheeled part of road.

The layered, visco-elastic model of the ground is a very simple model. However, it explains the experimentally observed phenomena. The results of this paper may aid in understanding the nature of the variability of the A/S TF and in establishing an improved acoustic prediction capability in natural ground environments.

ACKNOWLEDGMENTS

This work was funded by the Office of Naval Research under Grant No. N00014-02-1-0878. The authors are grateful to Ning Xiang for his dedication and expertise in collecting the data for this paper.

[1]T. F. W. Embleton, J. E. Piercy, and N. Olson, "Outdoor sound propagation over ground of finite impedance," J. Acoust. Soc. Am. **61**, 659–674 (1977).
[2]K. Attenborough, J. M. Sabatier, H. E. Bass, and L. N. Bolen, "The acoustic transfer function at the surface of a layered poroelastic soil," J. Acoust. Soc. Am. **79**, 1353–1358 (1986).
[3]H. E. Bass, L. N. Bolen, D. Cress, J. Lundien, and M. Flohr, "Coupling of airborne sound into the earth: Frequency dependence," J. Acoust. Soc. Am. **67**, 1502–1506 (1980).
[4]J. M. Sabatier, H. E. Bass, and G. R. Elliott, "On the location of frequencies of maximum acoustic-to-seismic coupling," J. Acoust. Soc. Am. **80**, 1200–1202 (1986).
[5]P. W. Arnott and J. M. Sabatier, "Laser doppler vibrometer measurements of acoustictoseismic coupling," Appl. Acoust. **30**, 279–291 (1990).
[6]J. Sabatier and N. Xiang, "Laser-Doppler based acoustic-to-seismic detection of buried mines," Proc. SPIE **3710**, 215–222 (1999).
[7]N. Xiang and J. Sabatier, "An experimental study on antipersonnel landmine detection using acoustic-to-seismic coupling," J. Acoust. Soc. Am. **113**, 1333–1341 (2003).

[8]Z. E. A. Fellah *et al.*, "Determination of transport parameters in air-saturated porous materials via reflected ultrasonic waves," J. Acoust. Soc. Am. **114**, 2561–2569 (2003).
[9]M. S. Fokina, V. N. Fokin, and J. M. Sabatier, "Propagator matrix for plane wave reflection–poroelastic and elastic layered models," *Proceedings of the Seventh European Conference on Underwater Acoustics*, edited by D. G. Simons, Delft, The Netherlands, 2004, pp. 71–78.
[10]N. D. Harrop, "The exploitation of acoustic-to-seismic coupling for the determination of soil properties," Ph.D. thesis, The Open University, UK, 1999, pp. 1–395.
[11]L. M. Brekhovskikh and O. A. Godin, *Acoustics of Layered Media* (Springer, Berlin, 1999).
[12]W. T. Thomson, "Transmission of elastic waves through a stratified solid material," J. Appl. Phys. **21**, 89–93 (1950).
[13]N. A. Haskell, "The dispersion of surface waves on multilayered media," Bull. Seismol. Soc. Am. **43**, 17–34 (1953).
[14]M. S. Fokina and V. N. Fokin, "Numerical modeling of plane waves reflection coefficients from elastic layered bottom," Acoust. Phys. **46**, 479–487 (2000).
[15]I. W. Dunkin, "Computation of modal solutions in layered elastic media at high frequencies," Bull. Seismol. Soc. Am. **55**, 335–358 (1965).
[16]E. N. Thrower, "The computation of the dispersion of elastic waves in layered media," J. Sound Vib. **2**, 210–226 (1965).
[17]H. Schmidt and F. B. Jensen, "Efficient numerical solution technique for wave propagation in horizontally stratified environments," Comput. Math. Appl. **11**, 699–714 (1985).
[18]S. Ivansson, "Low-frequency slow-wave dispersion computations by compound-matrix propagation," J. Acoust. Soc. Am. **106**, 61–72 (1999).
[19]B. Ursin, "Review of elastic and electromagnetic wave propagation in horizontally layered media," Geophysics **48**, 1063–1081 (1983).
[20]A. J. Robins, "Plane-wave reflection from a solid layer with nonuniform density, sound speed, and shear speed," J. Acoust. Soc. Am. **103**, 1337–1345 (1998).
[21]M. S. Fokina and V. N. Fokin, "Influence of gradients in inhomogeneous elastic media on resonances of the plane wave reflection coefficient," Acta. Acust. Acust. **88**, 703–706 (2002).
[22]V. N. Fokin, M. S. Fokina, J. M. Sabatier, N. Xiang, and W. B. Howard, "Effect of variability of soil physical properties on clutter and false alarms in land mine detection," Radio Sci. **39**, RS4S04 (2004).
[23]L. M. Brekhovskikh and O. A. Godin, *Acoustics of a Layered Media* (Nauka, Moscow, 1989).
[24]A. D. Pierce, *Acoustics: An Introduction to its Physical Principles and Applications* (Acoustical Society of America, Woodbury, 1994).
[25]R. Fiorito, W. Madigosky, and H. Uberall, "Acoustic resonance and the determination of the material parameters of a viscous fluid layer," J. Acoust. Soc. Am. **69**, 897–903 (1981).
[26]M. S. Fokina and V. N. Fokin, "Resonances of acoustic waves interacting with an elastic seabed," J. Comput. Acoust. **9**, 1079–1093 (2001).

Improved theory of acoustic elementary edge waves

Pyotr Ya. Ufimtsev
EM Consulting, 1959 Barry Avenue, Los Angeles, California, 90025

(Received 9 February 2006; revised 10 May 2006; accepted 10 May 2006)

The high-frequency asymptotic theory of acoustic edge waves [P. Ya. Ufimtsev, J. Acoust. Soc. Am. **86**, 463–74 (1989)] is well suited for investigation of backscattering from perfectly reflecting (*soft or hard*) three-dimensional objects with edges. However, it needs to be improved for calculation of forward scattering, especially in the directions grazing to the edge faces, where it predicts infinite values. The present paper removes this singularity by the appropriate choice of the so-called *uniform* component of the surface field. It is defined here as the field induced on the half-plane tangential to the *illuminated face* of the scattering edge (and to the edge itself). An improved theory of elementary edge waves is proposed, which is valid for all directions of scattering, including the forward grazing directions. © *2006 Acoustical Society of America.* [DOI: 10.1121/1.2211447]

PACS number(s): 43.20.El, 43.20.Fn [AJMD] Pages: 631–635

I. INTRODUCTION

Edges are constituent elements of many radiating and scattering structures, where incident waves undergo diffraction and transform into other types of waves that can exist within and around these structures. The design of such constructions with appropriate properties stimulates continuing research on the edge diffraction. Two basic types of approaches are usually used for the solution of related diffraction problems: direct numerical methods are applied in the low-frequency region, and asymptotic techniques are utilized in the high-frequency region.

Among high-frequency techniques are the geometrical optics (GO) (ray acoustics), the physical optics[1] known in acoustics as the Kirchhoff approximation (KA), the geometrical theory of diffraction (GTD),[2] the physical theory of diffraction (PTD),[3] their various modifications, and the matched asymptotic expansions (MAE).[4,5] Notice that Fourier transforms of impulse responses also provide valuable information on high-frequency diffraction. Besides, the study of wave diffraction in the time domain allows one to estimate local scattering contributions by different elements of a scattering object, and in this way it clarifies the scattering physics.

The following papers show some examples of applications of these techniques. Partridge and Smith[6] applied the GO and KA approaches to investigate the scattering from a rigid tapered parabolic cylinder. In comparison with the solution of the boundary integral equations, Fawcett[7] examined the KA and MAE approximations in the scattering problems related to smooth objects and flat-ended cylinders. Menounou *et al.*[8] analyzed the Kirchhoff approximation for the edge waves scattered by an aperture with a ragged edge. Brill and Gaunaurd[9] and Moser *et al.*[10] applied the KA and GTD techniques to evaluate the scattering from finite cylinders with ribs. Tran Van Nhieu[4,5] studied the scattering from cylinders and a circular disk, utilizing the GTD, PTD, and MAE approaches. Wolf[11] developed an asymptotic approach similar to PTD for the investigation of diffraction at plane screens. Ufimtsev[3] derived the PTD asymptotics for diffracted rays, caustic fields, slope, and multiple diffraction, as well as for the field scattered from bodies of revolution. Based on the exact Biot-Tolstoy solution,[12] Medwin, Childs, and Jebsen[13] introduced the concept of "secondary edge sources" and applied it to the study of double diffraction. This concept was extended by Svensson and Fred,[14] who derived the analytical directivity functions for these sources and investigated the scattering from a circular disk and a rectangular plate.

In the present paper we focus on the further development of PTD. This theory was originally developed for electromagnetic waves.[15] A recent monograph. "Theory of Edge Diffraction in Electromagnetics,"[16] contains a revised and extended version of the original PTD. Its modern form (based on the concept of elementary edge waves) has been published in articles (see Refs. 3 and 17). References [9–11] and [67–116] cited in the review article, "Comments on diffraction principles and limitations for RCS reduction techniques,"[18] demonstrate various applications and modifications of PTD related to electromagnetic diffraction problems.

Now, it is well established that PTD is helpful for asymptotic analysis of antennas and scattering problems. However, it has an essential limitation in evaluation of the forward scattering: It predicts infinite values for the field in the directions grazing to the edge faces. An example of the grazing configuration is shown in Fig. 1. The main purpose of the present paper is to develop a new version of the theory of elementary edge waves, which would be free from the grazing singularity.

To identify a key point in the current theory[3] where it should be improved, let us review its basic elements. It is a source-based theory. It calculates the scattered field by the integration of the surface field. The central idea is the separation of the surface field into the so-called uniform and nonuniform components, with the subsequent separate calculation of the field generated by each component. The uniform component is determined according to the geometrical optics as $j_s^{(0)} = \partial u / \partial N$ on the acoustically soft objects, and as $j_h^{(0)} = u$ on the acoustically hard objects. Here, $\hat{N}$ is the outward normal to the scattering surface, and the quantity u is the

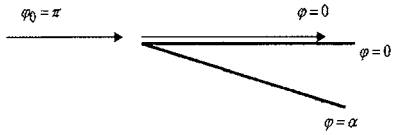

FIG. 1. Grazing incidence on the wedge under the angle $\varphi_0=\pi$ and grazing scattering in direction $\varphi=0$. In this case, the current theory (Ref. 3) predicts infinite values for the scattered field. No singularity exists in the reverse situation, when $\varphi_0=0$ and $\varphi=\pi$.

geometrical optics field that consists of the incident and reflected waves ($u=u^{\text{inc}}+u^{\text{ref}}$). The nonuniform component is defined as the difference between the total field on the tangential wedge ($j^w_{s,h}$) and the uniform component ($j^{(1)}_{s,h}=j^{(w)}_{s,h}-j^{(0)}_{s,h}$). This component concentrates near the edge, while the uniform component dominates away from the edge.

Analysis of the grazing singularity shows that these definitions are not adequate for the actual surface field under the grazing incidence ($\varphi_0=\pi$ or $\varphi_0=\alpha-\pi$). In particular, the nonuniform component $j^{(1)}_h$ does not vanish away from the edge, but instead transforms into a plane wave there. Also, the uniform component $j^{(0)}_h$ includes the absent reflected wave. Thus, the separation of the surface field into components $j^{(0)}$ and $j^{(1)}$ is a key element that needs to be improved.

The appropriate candidate for a new definition of $j^{(0)}_{s,h}$ is the field $j^{hp}_{s,h}$, induced by the incident wave on the illuminated side of the half-plane tangential to the illuminated face of the scattering edge (and to the edge itself). This component $j^{hp}_{s,h}$ is described by the Fresnel integral[19,20] [see Eqs. (32) and (33) below]. Then, the new nonuniform component should be defined as $j^{(1)}_{s,h}=j^w_{s,h}-j^{hp}_{s,h}$. The next section calculates the elementary edge waves generated by the new component $j^{(1)}_{s,h}$, as well as the field generated by the component $j^{hp}_{s,h}$.

One should mention that the PTD grazing singularity can be removed without changing its original definitions of the uniform and nonuniform components. For instance, Michaeli[21] and Johanson[22] suggested the modified versions of PTD with truncated elementary strips (shown below in Fig. 2). In the version of Ref. 21, the scattered field is found as the difference of two terms related to the leading and trailing ends of the strip. These terms become singular under the grazing incidence, but their singularities cancel each other. The version in Ref. 22 is more suitable for applications, because it does not contain singular terms. In distinction to these versions, the present paper reveals the nature of the grazing singularity and removes it with an appropriate redefinition of uniform and nonuniform components of the surface sources. In addition, it allows for the extraction of the edge contribution (in the explicit form) from the total diffracted field.

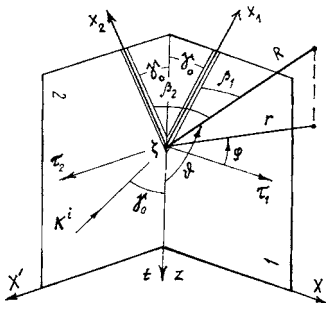

FIG. 2. Element of the tangential wedge with faces 1 ($\varphi=0$) and 2 ($\varphi=\alpha$). It is assumed that $\pi<\alpha\leqslant 2\pi$. Elementary scattering strips 1 and 2 are oriented along the axes x_1 and x_2. Vector $\hat{k}^i$ shows the direction of the incident wave. Symbols R, ϑ, φ and r, φ, z are, respectively, the local spherical and cylindrical coordinates of the observation point.

II. ASYMPTOTIC EXPRESSIONS OF ELEMENTARY WAVES

Elementary edge waves (EEWs) are the waves $du_{s,h}$ scattered in the vicinity of an infinitely small element of a scattering edge. With analytic expressions for EEWs, one can calculate the field scattered by objects with curved edges (under the condition that their radii of curvature are large compared to the wavelength) just by integrating EEWs over the edge, $u_{s,h}=\int du_{s,h}$. According to the high-frequency localization principle,[23] the EEWs scattered at a curved edge are asymptotically equivalent to those scattered at a straight edge of the tangential wedge. The exact solution of the wedge diffraction problem is well known[20,24–26] and it can be used to construct high-frequency asymptotics of EEWs.

We follow Refs. 3, 17, and 27, and calculate the EEWs scattered at the wedge by integrating the surface field induced on two elementary strips oriented along the surface-diffracted rays (Fig. 2) (which belong to the Rubinowicz diffraction cone,[28] known also as the Keller cone). The integral expressions for EEWs are the following:

$$du^{(1)}_s=-d\zeta\,\frac{\sin\gamma_0}{4\pi}\left[\int_0^\infty j^{(1)}_s\frac{e^{ikr_1}}{r_1}d\xi_1+\int_0^\infty j^{(1)}_s\frac{e^{ikr_2}}{r_2}d\xi_2\right], \tag{1}$$

$$du^{(1)}_h=d\zeta\,\frac{\sin\gamma_0}{4\pi}\left[\int_0^\infty j^{(1)}_h\frac{\partial}{\partial N}\frac{e^{ikr_1}}{r_1}d\xi_1+\int_0^\infty j^{(1)}_h\frac{\partial}{\partial N}\frac{e^{ikr_2}}{r_2}d\xi_2\right]. \tag{2}$$

Here, $du^{(1)}_s$ and $du^{(1)}_h$ are the velocity potentials of acoustic EEWs scattered at edges with acoustically soft and hard faces, respectively, and $\hat{N}$ is the outward normal to the edge faces. The quantity $d\zeta$ is a differential element of the edge; $r_{1,2}=\sqrt{(x_{1,2}-\xi_{1,2})^2+y^2_{1,2}+z^2_{1,2}}$ is the distance between the integration and observation points; $x_{1,2}$, $y_{1,2}$, $z_{1,2}$ are local Cartesian coordinates associated with faces 1 and 2 (and with strips 1 and 2), respectively. The quantity $j^{(1)}_{s,h}$ is defined as $j^{(1)}_{s,h}=j^w_{s,h}-j^{hp}_{s,h}$, where $j^w_{s,h}$ and $j^{hp}_{s,h}$ are known functions related to the tangential wedge and half-plane, respectively.[19,20,24]

Because these integrals are calculated exactly in the same way as in Refs. 3, 17, and 27, we explain here only key details. The functions $j^{(1)}_{s,h}$ are expressed in the form of the Sommerfeld integrals[20,24] in the complex plane. For the Green function of free space, we use Eq. (6.616-3) from Ref. 29,

$$\frac{e^{ikr_{1,2}}}{r_{1,2}} = \frac{i}{2}\int_{-\infty}^{\infty} e^{ip(x_{1,2}-\xi_{1,2})} H_0^{(1)}(qh_{1,2})dp, \tag{3}$$

where $q=\sqrt{k^2-p^2}$ with $\mathrm{Im}(q)\geqslant 0$ and $h_{1,2}=\sqrt{y_{1,2}^2+z_{1,2}^2}\geqslant 0$. With these observations, the fields (1,2) can be written in the form of triple integrals. We change the order of integration and calculate in closed form the integrals over variables ξ_1 and ξ_2 associated with axes x_1 and x_2, respectively. The Sommerfeld-type integrals in the complex plane (related to functions $j_{s,h}^{(1)}$) are evaluated in closed form by application of the Cauchy residue theorem. The final integrals over the variable p [associated with the Green function (3)] are calculated asymptotically under the condition $kR\gg 1$.

The results of the calculations are

$$du_{s,h}^{(1)} = u^{\mathrm{inc}}(\zeta)\frac{d\zeta}{2\pi}F_{s,h}^{(1)}(\vartheta,\varphi)\frac{e^{ikR}}{R}, \tag{4}$$

where $u^{\mathrm{inc}}(\zeta)$ stands for the incident field at the point ζ on the scattering edge. The directivity patterns of EEWs are described as

$$F_s^{(1)} = -[U(\sigma_1,\varphi_0)+U(\sigma_2,\alpha-\varphi_0)]\sin^2\gamma_0, \tag{5}$$

$$F_h^{(1)} = -[V(\sigma_1,\varphi_0)\sin\varphi + V(\sigma_2,\alpha-\varphi_0)\sin(\alpha-\varphi)]\sin\gamma_0\sin\vartheta, \tag{6}$$

with

$$U(\sigma,\psi) = U_t^w(\sigma,\psi) - \varepsilon(\psi)U_t^{\mathrm{hp}}(\sigma,\psi), \tag{7}$$

$$V(\sigma,\psi) = V_t^w(\sigma,\psi) - \varepsilon(\psi)V_t^{\mathrm{hp}}(\sigma,\psi), \tag{8}$$

$$U_t^w(\sigma,\psi) = \frac{\pi}{2\alpha\sin^2\gamma_0}\times\left[\cot\frac{\pi(\sigma+\psi)}{2\alpha}-\cot\frac{\pi(\sigma-\psi)}{2\alpha}\right], \tag{9}$$

$$U_t^{\mathrm{hp}}(\sigma,\psi) = \frac{1}{4\sin^2\gamma_0}\left[\cot\frac{\sigma+\psi}{4}-\cot\frac{\sigma-\psi}{4}\right], \tag{10}$$

$$V_t^w(\sigma,\psi) = \frac{\pi}{2\alpha\sin^2\gamma_0\sin\sigma}\times\left[\cot\frac{\pi(\sigma+\psi)}{2\alpha}+\cot\frac{\pi(\sigma-\psi)}{2\alpha}\right]. \tag{11}$$

$$V_t^{\mathrm{hp}}(\sigma,\psi) = \frac{1}{4\sin^2\gamma_0\sin\sigma}\left[\cot\frac{\sigma+\psi}{4}+\cot\frac{\sigma-\psi}{4}\right]. \tag{12}$$

Functions U_t^w, V_t^w and U_t^{hp}, V_t^{hp} are associated with the solution of the wedge and half-plane diffraction problems, respectively. It is clear that functions U_t^{hp}, V_t^{hp} follow from functions U_t, V_t by setting $\alpha=2\pi$. Parameters $\sigma_{1,2}$ are defined by the equation

$$\cos\sigma_{1,2} = (\cos^2\gamma_0-\cos\beta_{1,2})/\sin^2\gamma_0, \tag{13}$$

where

$$\cos\beta_1 = \sin\gamma_0\sin\vartheta\cos\varphi-\cos\gamma_0\cos\vartheta, \tag{14}$$

$$\cos\beta_2 = \sin\gamma_0\sin\vartheta\cos(\alpha-\varphi)-\cos\gamma_0\cos\vartheta. \tag{15}$$

More details on $\sigma_{1,2}$ are shown in Refs. 3 and 17. Function $\varepsilon(x)$ is determined by

$$\varepsilon(x) = \begin{cases} 1 & \text{if } 0\leqslant x\leqslant\pi \\ 0 & \text{if } x>\pi. \end{cases} \tag{16}$$

Asymptotics of functions $F_{s,h}^{(1)}(\vartheta,\varphi)$ are simplified for the directions $\vartheta=\pi-\gamma_0$ related to the Rubinowicz-Keller diffraction cone,

$$F_s^{(1)}(\pi-\gamma_0,\varphi) = f(\varphi,\varphi_0,\alpha)-f^{\mathrm{hp}}(\varphi,\varphi_0), \tag{17}$$

$$F_h^{(1)}(\pi-\gamma_0,\varphi) = g(\varphi,\varphi_0,\alpha)-g^{\mathrm{hp}}(\varphi,\varphi_0), \tag{18}$$

where

$$f(\varphi,\varphi_0,\alpha) = \frac{\sin\frac{\pi}{n}}{n}\left[\left(\cos\frac{\pi}{n}-\cos\frac{\varphi-\varphi_0}{n}\right)^{-1}-\left(\cos\frac{\pi}{n}-\cos\frac{\varphi+\varphi_0}{n}\right)^{-1}\right], \tag{19}$$

$$g(\varphi,\varphi_0,\alpha) = \frac{\sin\frac{\pi}{n}}{n}\left[\left(\cos\frac{\pi}{n}-\cos\frac{\varphi-\varphi_0}{n}\right)^{-1}+\left(\cos\frac{\pi}{n}-\cos\frac{\varphi+\varphi_0}{n}\right)^{-1}\right], \tag{20}$$

with $n=\alpha/\pi$, and

$$f^{\mathrm{hp}}(\varphi,\varphi_0) = (A+B)/4,$$

$$A = \varepsilon(\varphi_0)\left[\cot\frac{\pi-\varphi-\varphi_0}{4}-\cot\frac{\pi-\varphi+\varphi_0}{4}\right], \tag{21}$$

$$B = \varepsilon(\alpha-\varphi_0)\left[\cot\frac{\pi+\varphi+\varphi_0-2\alpha}{4} - \cot\frac{\pi+\varphi-\varphi_0}{4}\right], \tag{22}$$

$$g^{\mathrm{hp}}(\varphi,\varphi_0) = -(C+D)/4, \tag{23}$$

$$C = \varepsilon(\varphi_0)\left[\cot\frac{\pi-\varphi+\varphi_0}{4}+\cot\frac{\pi-\varphi+\varphi_0}{4}\right], \tag{24}$$

$$D = \varepsilon(\alpha-\varphi_0)\left[\cot\frac{\pi+\varphi+\varphi_0-2\alpha}{4} + \cot\frac{\pi+\varphi-\varphi_0}{4}\right]. \tag{25}$$

Functions f^{hp}, g^{hp} are associated with the field scattered by the tangential half-plane. Namely, they relate to that part

of the field which is radiated by the scattering sources $j_{s,h}^{hp}$ induced on the one (illuminated) side of the half-plane. In distinction to them, functions f,g describe the field generated by the sources distributed on both sides of the half-plane. Because of that, functions f,g do not transform into f^{hp}, g^{hp} by setting $n=2$.

All functions f, g and f^{hp}, g^{hp} are singular in the directions of the incident and reflected rays ($\varphi=\pi+\varphi_0, \pi-\varphi_0, 2\alpha-\pi-\varphi_0$), but their combinations [(17) and (18)] are always finite. For instance, in the direction of the specular reflection ($\varphi=\pi-\varphi_0$) from face $\varphi=0$ (Figs. 1 and 2),

$$F_h^{(1)}(\pi-\gamma_0,\pi-\varphi_0)=-\frac{1}{2n}\cot\frac{\varphi_0}{n}+\frac{1}{4}\cot\frac{\varphi_0}{2}-\frac{1}{2n}\cot\frac{\pi-\varphi_0}{n}+\varepsilon(\alpha-\varphi_0)\frac{1}{4}\times\cot\frac{\pi-\varphi_0}{2}+\frac{1}{2n}\cot\frac{\alpha-\pi}{n}-\varepsilon(\alpha-\varphi_0)\frac{1}{4}\cot\frac{\alpha-\pi}{2}, \tag{26}$$

$$F_s^{(1)}(\pi-\gamma_0,\pi-\varphi_0)=-\frac{1}{2n}\cot\frac{\varphi_0}{n}+\frac{1}{4}\cot\frac{\varphi_0}{2}-\frac{1}{2n}\cot\frac{\pi-\varphi_0}{n}+\varepsilon(\alpha-\varphi_0)\frac{1}{4}\times\cot\frac{\pi-\varphi_0}{2}-\frac{1}{2n}\cot\frac{\alpha-\pi}{n}+\varepsilon(\alpha-\varphi_0)\frac{1}{4}\cot\frac{\alpha-\pi}{2}. \tag{27}$$

The following asymptotics are valid for the field in the direction of the specular reflection ($\varphi=2\alpha-\pi-\varphi_0$) from the face $\varphi=\alpha$:

$$F_h^{(1)}(\pi-\gamma_0,2\alpha-\pi-\varphi_0)=\frac{-1}{2n}\cot\frac{\varphi_0-\alpha+\pi}{n}+\varepsilon(\varphi_0)\frac{1}{4}\cot\frac{\varphi_0-\alpha+\pi}{2}+\frac{1}{2n}\cot\frac{\alpha-\pi}{n}-\varepsilon(\varphi_0)\frac{1}{4}\cot\frac{\alpha-\pi}{2}-\frac{1}{2n}\cot\frac{\alpha-\varphi_0}{n}+\frac{1}{4}\cot\frac{\alpha-\varphi_0}{2}, \tag{28}$$

$$F_s^{(1)}(\pi-\gamma_0,2\alpha-\pi-\varphi_0)=\frac{-1}{2n}\cot\frac{\varphi_0-\alpha+\pi}{n}+\varepsilon(\varphi_0)\frac{1}{4}\cot\frac{\varphi_0-\alpha+\pi}{2}-\frac{1}{2n}\cot\frac{\alpha-\pi}{n}+\varepsilon(\varphi_0)\frac{1}{4}\cot\frac{\alpha-\pi}{2}-\frac{1}{2n}\cot\frac{\alpha-\varphi_0}{n}+\frac{1}{4}\cot\frac{\alpha-\varphi_0}{2}. \tag{29}$$

These equations clearly show that functions $F_{h,s}^{(1)}$ are free from the grazing singularity. Indeed, for the grazing directions of the incident wave ($\varphi_0=\pi$, $\varphi_0=\alpha-\pi$) these functions have the finite values

$$F_h^{(1)}(\pi-\gamma_0,0)=F_h^{(1)}(\pi-\gamma_0,\alpha)=-\frac{1}{n}\cot\frac{\pi}{n}+\frac{1}{4}\tan\frac{\alpha}{2}, \tag{30}$$

$$F_s^{(1)}(\pi-\gamma_0,0)=F_s^{(1)}(\pi-\gamma_0,\alpha)=-\frac{1}{4}\tan\frac{\alpha}{2}. \tag{31}$$

It is also seen that functions $F_{h,s}^{(1)}$ are equal to zero, when $\alpha=2\pi$ and the wedge transforms into the half-plane.

The above asymptotics describes the field generated by the nonuniform component $j_{s,h}^{(1)}$ of the surface scattering sources. The total scattered field also includes the contribution generated by the uniform component $j_{s,h}^{(0)}$. On strip 1 (Fig. 2) these components are determined as

$$j_h^{(0)}\equiv j_h^{hp}=2u_0e^{-ik\zeta\cos\gamma_0}e^{ik\xi_1\cos^2\gamma_0}\times[-I(\xi_1,\varphi_0)+e^{-ik\xi_1\sin^2\gamma_0\cos\varphi_0}], \tag{32}$$

$$j_s^{(0)}\equiv j_s^{hp}=2u_0e^{-ik\zeta\cos\gamma_0}e^{ik\xi_1\cos^2\gamma_0}\times\left[ik\sin\gamma_0\sin\varphi_0 I(\xi_1,\varphi_0)+\sqrt{\frac{k}{2}}\sin\frac{\varphi_0}{2}\frac{e^{-i\pi/4}}{\sqrt{\pi}}\frac{e^{ik\xi_1\sin^2\gamma_0}}{\sqrt{\xi_1}}-ik\times\sin\gamma_0\sin\varphi_0 e^{-ik\xi_1\sin^2\gamma_0\cos\varphi_0}\right], \tag{33}$$

where

$$I(\xi_1,\varphi_0)=e^{-ik\xi_1\sin^2\gamma_0\cos\varphi_0}\frac{e^{-\pi/4}}{\sqrt{\pi}}\times\int_{\sqrt{2k\xi_1}\sin\gamma_0\cos\frac{\varphi_0}{2}}^{\infty}e^{it^2}dt. \tag{34}$$

The last terms in Eqs. (32) and (33) (together with the factor 2 in front of the brackets) relate to the sum of the incident and reflected plane waves. When $\varphi_0\to\pi$, these equations transform into

$$j_h^{(0)}=u_0e^{-ik\zeta\cos\gamma_0}e^{ik\xi_1}, \tag{35}$$

$$j_s^{(0)}=u_0e^{-ik\zeta\cos\gamma_0}\sqrt{\frac{2k}{\pi\xi_1}}e^{i(k\xi_1-\pi/4)}. \tag{36}$$

Here, $j_h^{(0)}$ is actually the grazing incident wave and $j_s^{(0)}$ represents the edge wave. The quantities $j_{h,s}^{(0)}$ on strip 2 (on the half-plane $\varphi=\alpha$) can be found from (32) and (33) with the replacement of φ_0 by $\alpha-\varphi_0$ and ξ_1 by ξ_2.

Consider the field created by the scattering sources $j_{h,s}^{(0)}$ distributed over the finite elementary strips ($0\leqslant\xi_{1,2}\leqslant l$). In the far zone ($R\gg kl^2$), it is determined by the integrals

$$du_{h1}^{(0)}=\frac{d\zeta}{4\pi}ik\sin\gamma_0\sin\vartheta\sin\varphi\frac{e^{ikR}}{R}\times\int_0^l j_{h1}^{(0)}(\xi_1,\varphi_0)e^{-ik\xi_1\cos\beta_1}d\xi_1, \tag{37}$$

$$du_{s1}^{(0)} = -\frac{d\xi}{4\pi}\sin\gamma_0\frac{e^{ikR}}{R}\int_0^l j_{s,1}^{(0)}(\xi_1,\varphi_0)e^{-ik\xi_1\cos\beta_1}d\xi_1. \quad (38)$$

Replacing ξ_1, β_1, φ, φ_0 here with ξ_2, β_2, $\alpha-\varphi$, $\alpha-\varphi_0$, one obtains the equations associated with the field from strip 2 ($0\leqslant\xi_2\leqslant l$). These integrals are easily calculated in closed form. We show only those results which relate to the grazing incidence ($\varphi_0=\pi$),

$$du_{h1}^{(0)} = u_0 e^{-ik\zeta\cos\gamma_0}\frac{d\zeta}{4\pi}\frac{e^{ikR}}{R} \times \frac{\sin\gamma_0\sin\vartheta\sin\varphi}{1-\cos\beta_1}[e^{ikl(1-\cos\beta_1)}-1], \quad (39)$$

$$du_{s1}^{(0)} = u_0 e^{-ik\zeta\cos\gamma_0}\frac{d\zeta}{2\pi}\frac{e^{ikR}}{R}\sin\gamma_0 \times \sqrt{\frac{2}{1-\cos\beta_1}}\frac{e^{i3\pi/4}}{\sqrt{\pi}}\int_0^{\sqrt{kl(1-\cos\beta_1)}} e^{it^2}dt. \quad (40)$$

For the grazing direction ($\beta_1=0$, $\varphi=0$), it follows from these equations that $du_{h1}^{(0)}=0$ and

$$du_{s1}^{(0)} = u_0 e^{-ik\zeta\cos\gamma_0}\frac{d\zeta}{2\pi}\frac{e^{ikR}}{R}\sin\gamma_0\sqrt{\frac{2kl}{\pi}}e^{i3\pi/4}. \quad (41)$$

As expected, the field $du_{h,s}^{(0)}$ is free from the grazing singularity.

III. CONCLUSION

High-frequency asymptotics of elementary edge waves derived in this paper are free from the grazing singularity and well suited for investigation of bistatic scattering from soft and hard objects with plane facets, especially in the case when both faces of the edge are illuminated by the incident wave ($\alpha-\pi\leqslant\varphi_0\leqslant\pi$). For other incidence directions φ_0, one can apply the existing theory.[3,27]

A distinctive feature of the present theory is as follows: It introduces a new nonuniform scattering source $j_{h,s}^{(1)}$ that generates an elementary edge wave regular in all scattering directions. In other words, it allows the extraction of the fringe component from the total field in a pure/explicit form.

ACKNOWLEDGMENTS

The author appreciates the careful reading of the manuscript by the reviewers and their useful comments. He also thanks Ms. Sophie Spurrier for her assistance.

[1]H. M. Macdonald, "The effect produced by an obstacle on a train of electric waves," Philos. Trans. R. Soc. London, Ser. A **212**, 299–337 (1912).
[2]J. B. Keller, "Geometrical theory of diffraction," J. Opt. Soc. Am. **52**(2), 116–130 (1962).
[3]P. Ya. Ufimtsev, "Theory of acoustical edge waves," J. Acoust. Soc. Am. **86**(2), 463–474 (1989).
[4]M. Tran Van Nhieu, "Diffraction by plane screens," J. Acoust. Soc. Am. **97**(2), 796–806 (1995).
[5]M. Tran Van Nhieu, "Diffraction by the edge of a three-dimensional object," J. Acoust. Soc. Am. **99**(1), 79–87 (1996).
[6]C. Partridge and E. R. Smith, "Acoustic scattering from a rigid tapered finite parabolic cylinder," J. Acoust. Soc. Am. **98**(4), 2328–2335 (1995).
[7]J. A. Fawcett, "Modeling of high-frequency scattering from objects using a hybrid Kirchhoff/diffraction approach," J. Acoust. Soc. Am. **109**(4), 1312–1319 (2001).
[8]P. Menounou, M. R. Bailey, and D. T. Blackstock, "Edge wave on axis behind an aperture or disk having a ragged edge," J. Acoust. Soc. Am. **107**(1), 103–111 (2000).
[9]D. Brill and G. C. Gaunaurd, "Approximate description of the sound fields scattered by insonified, submerged, ribbed, flat-ended cylindrical structures," J. Acoust. Soc. Am. **93**(1), 71–79 (1993).
[10]P. J. Moser, H. Uberall, and J. R. Yuan, "Sound scattering from a finite cylinder with ribs," J. Acoust. Soc. Am. **94**(6), 3342–3351 (1993).
[11]P. Wolf, "A new approach to edge diffraction," SIAM J. Appl. Math. **15**(6), 1434–1469 (1967).
[12]M. A. Biot and I. Tolstoy, "Formulation of wave propagation in infinite media by normal coordinates with an application to diffraction problem," J. Acoust. Soc. Am. **29**(3), 381–391 (1957).
[13]H. Medwin, E. Childs, and G. M. Jebsen, "Impulse studies of double diffraction: A discrete Huygens interpretation," J. Acoust. Soc. Am. **72**(3), 1005–1013 (1982).
[14]U. P. Svensson and R. I. Fred, "An analytic secondary source model of edge diffraction," J. Acoust. Soc. Am. **106**(5), 2331–2344 (1999).
[15]P. Ya. Ufimtsev, *Method of Edge Waves in the Physical Theory of Diffraction* (in Russian) (Sovetskoe Radio, Moscow: 1962) [Translated into English by the U.S. Air Force, Foreign Technology Division (National Air Intelligence Center), Wright-Patterson AFB, OH, 1971. Technical Report AD 733203, Defense Technical Information Center of USA, Cameron Station, Alexandria, VA, 22304–6145.]
[16]P. Ya. Ufimtsev, *Theory of Edge Diffraction in Electromagnetics* (Tech. Science, Encino, CA, 2003).
[17]P. Ya. Ufimtsev, "Elementary edge waves and the physical theory of diffraction," Electromagnetics **11**(2), 125–160 (1991).
[18]P. Ya. Ufimtsev, "Comments on diffraction principles and limitations for RCS reduction techniques," Proc. IEEE **84**(12), 1828–1851 (1996).
[19]A. Sommerfeld, "Mathematische Theorie der Diffraction" (Mathematical theory of diffraction), Math. Ann. **47**, 317–374 (1896).
[20]*Electromagnetic and Acoustic Scattering by Simple Shapes*, edited by J. J. Bowman, T. B. A. Senior, and P. L. E. Uslenghi (Hemisphere, New York, 1987).
[21]A. Michaeli, "Equivalent currents for second order diffraction by the edges of perfectly conducting polygonal surfaces," IEEE Trans. Antennas Propag. **AP-35**(2), 183–190 (1987).
[22]P. M. Johansen, "Uniform physical theory of diffraction equivalent edge currents for truncated wedge strips," IEEE Trans. Antennas Propag. **AP-44**(7), 989–995 (1996).
[23]V. A. Fock, *Electromagnetic Diffraction and Propagation Problems* (Pergamon, London, 1965).
[24]A. Sommerfeld, "Theorie der Beugung" (Theory of diffraction), in *Die Differential-und Integralgleichungen der Mechanik und Physik*, Vol. 2, Physical Part, edited by F. Frank and R. V. Mizes (Vieweg, Braunschweig, Germany, 1935), Chap. 20. (American publications: New York 1943, 1961).
[25]H. M. Macdonald, *Electric Waves* (The University Press, Cambridge, England, 1902), pp. 186–198.
[26]H. M. Macdonald, "A class of diffraction problems," Proc. London Math. Soc. 14, 410–427 (1915).
[27]D. I. Butorin and P. Ya. Ufimtsev, "Explicit expressions for an acoustic edge wave scattered by an infinitesimal edge element" (in Russian), Akust. Zh. **32**(4), 450–456 (1986); [English transl.:Sov. Phys. Acoust. **32**, 283–287 (1986)].
[28]A. Rubinowicz, "Zur Kirchhoffschen Beugungstheorie" (The Kirchhoff theory of diffraction). Ann. Phys. **4**(73), 339–364 (1924).
[29]I. S. Gradshteyn and I. M. Ryzhik, *Tables of Integrals, Series, and Products* (Academic New York, 1994).

A phenomenological model for sonic crystals based on artificial neural networks

E. Fuster-Garcia, V. Romero-García, and Juan V. Sánchez Pérez[a)]
Grupo de Acústica Arquitectónica y del Medio Ambiente and Departamento de Física Aplicada, ETSICCP, UPV, Cno. de Vera s/n, 46020 Valencia, Spain

L. M. García-Raffi and Enrique A. Sánchez Pérez
Instituto de Matemática Pura y Aplicada and Departamento de Matemática Aplicada, ETSICCP, UPV, Cno. de Vera s/n, 46020 Valencia, Spain

(Received 13 January 2006; revised 30 May 2006; accepted 1 June 2006)

A phenomenological model that simulates the acoustic attenuation behavior of sonic crystals is developed in this paper. The input of the model is a set of parameters that characterizes each experimental setup, and the output is a simulation of the associated attenuation spectrum. The model consists of a combination of a multiresolution analysis based on wavelet functions and a set of artificial neural networks. An optimized coupling of these tools allows us to drastically reduce the experimental data needed, and to obtain a fast computational model that can be used for technological purposes. © *2006 Acoustical Society of America.* [DOI: 10.1121/1.2217127]

PACS number(s): 43.20.Fn, 43.60.Np [KA] Pages: 636–641

I. INTRODUCTION

Sonic crystals (SCs) are structures formed by a periodic array of acoustic scatterers embedded in a homogeneous material, with strong modulation of the elastic constants between the scatterers and the surrounding materials. The periodicity in these materials results in the appearance of sonic band gaps, a range of frequencies for which sound propagation is forbidden inside the crystal. These stop bands have induced several application proposals, such as acoustic filters and shield devices.[1–6]

In recent years, a great experimental and theoretical effort has been made in order to improve the knowledge of the acoustical properties of these systems. Theoretical simulation programs have been developed to predict the behavior of such structures. Some of them calculate the acoustic band structure of infinite crystal using the plane-wave expansion method.[7,8] Other approaches, based on a variational method[9] and a Korringa-Khon-Rostoker method,[10] have been developed. Also, finite systems have been studied using the transfer-matrix method[4,11] and multiple scattering theory[12–14] (MST). Experimental measurements, under controlled and outdoor conditions, have been performed[2] in the audible range.

It has been observed that the acoustic attenuation spectra produced by SCs depend not only on the lattice constant but also on the filling factor, type of array, sound incidence angle, and measure distance. Small variations on them can produce big changes in the shape and position of the attenuation peaks in the spectrum.[9]

Moreover, although it has been proved that the simulation programs provide satisfactory results, there is still a gap between theoretical and experimental spectra. Theoretical models give us qualitative information about the shape and variation of the attenuation peaks, but this information is not as complete as is required for the technological development of the SCs. In this sense, it would be interesting to perform models based on experimental data that have been obtained in situations that are close to the use of SCs, such as acoustic filters or shield devices. Our paper presents this type of model. It is based on the interplay between two well-known mathematical techniques: Multiresolution analysis (MRA),[15–17] and artificial neural networks (ANNs).[18–20] Our procedure consists of a four-step scheme. First, we have to measure attenuation spectra corresponding to different values of the parameters defining both the crystal and the experimental conditions of the measurement (SC setups). Second, in order to present the experimental information to the ANN in a compressed and arranged format, we analyze attenuation spectra with MRA based on wavelet transform. In the third step, we train a set of neural networks with the experimental data. The objective is that ANNs correlate pairs formed by a vector of n parameters, that define the SC setup and the corresponding experimental attenuation spectrum. This correlation will allow us to simulate attenuation spectra. The fourth step consists of a test of the model; comparing simulated with experimental spectra specifically preserved as samples for this purpose.

Note that the conditions under which the model works consider only SC setups defined by a vector of parameters whose values lie inside the range of values used in the construction of the model.

We present results of our model for a well-known two-dimensional SCs configuration, formed by hollow aluminium cylinders rods arranged in triangular cells embedded in air,[9] in order to allow the comparison between the results obtained with our model and the theoretical calculation using MST.

[a)]Electronic mail: jusanc@fis.upv.es

II. MATHEMATICAL APPROACH

The core of our model is composed of a set of ANNs that compute the correlation between vectors of parameters corresponding to different SC setups and the associated experimental spectra. To achieve this objective, we perform a supervised training of networks with pairs formed by a vector and an associated spectrum. These spectra are defined by a great number of channels (512, in our case) to obtain a good resolution. If raw spectra were used, a complex ANN structure would be needed, and a great number of experimental samples would be necessary to train it. A natural way to overcome this problem is to try to characterize the attenuation peaks in spectra by a few number of parameters. We can try to use classical spectroscopic techniques for a systematic analysis of peaks, such as, fitting peaks with respect to a well-known base of functions to obtain a characterization of them (centroid, width, tail, etc.). But, as we have mentioned in Sec. I, the nature of the physical processes involved produces a great variety of attenuation peak shapes. Consequently, these classical techniques are not appropriate for this purpose. Therefore, we have decided to use another mathematical tool for analyzing attenuation spectra; the MRA based on the wavelet transform.[15] Moreover, the MRA allows us to present experimental spectra to the network in a very compressed and arranged format, which drastically reduces the number of degrees of freedom of our model and the error associated to the simulated spectra. The MRA uses the properties of wavelets basis to decompose the signal into a sequence of different resolution levels. Roughly speaking, this analysis allows us to distinguish between the spectrum's tendencies and fluctuations.[16] This property of MRA facilitates both data compression—via the deletion of the coefficients of the nonrelevant levels easily—and also filtering data—which establishes suitable thresholds for the value of the coefficients. For these reasons, MRA turns out to be extremely effective for the systematization of the analysis of the peaks in acoustic attenuation spectra.

An ANN is composed of many simple nonlinear computational elements; operating in parallel and densely interconnected. Several interconnected neurons organized in layers can form an ANN. In this work, we have used a feedforward network topology, where the data processing can extend over multiple layers of neurons but no feedback connections are present (connections extending from outputs of neurons to inputs of neurons in the same layer or previous layers).

In order to set up the ANN for a specific use, a training process and a learning process are needed. The training process consists of feeding the ANN with teaching patterns, and letting it change its weights and bias according to some learning rule. The algorithm used in this work for training is the *Levenberg-Marquardt optimization algorithm*.[20] The learning rules are methods of deriving the next changes that might be made in a network. In our case, we use the learning function *Gradient descent with momentum weight and bias*.[19]

III. DEVELOPMENT OF THE MODEL

As we have just mentioned, our model is constructed following a four-step procedure indicated in Fig. 1.

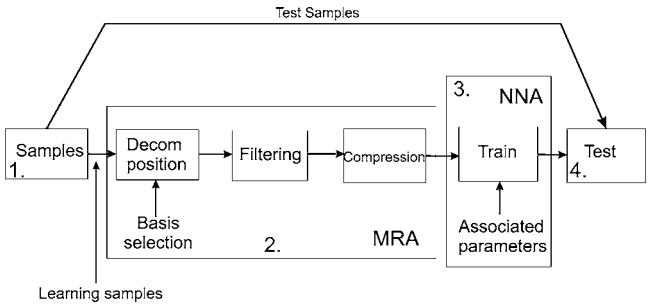

FIG. 1. Diagram of procedure for building the model.

A. Experimental data set

The first step consists of obtaining a significant set of experimental data corresponding to a region of the parameters space where we want to use the model.

The experiments have been performed in an anechoic chamber of $8\times6\times3$ m^3. We use a sound source with a speaker placed at the focus of a parabolic reflector to obtain a plane wave. However, since the dimension of the chamber is not much larger than the SC size, sound waves are not full plane waves when the wavefronts reach the SC. The SCs are built up by hanging cylindrical rods on a frame with triangular symmetry. The frame can rotate around the vertical axis, so one can explore any direction of the wave vector perpendicular to the cylinder axis. Here, we use 1 m length hollow aluminium rods. The points of measurements are always placed on the axis defined by the center of the SC and the source. In these points, the continuous white noise emitted by the source is recorded by a microphone with and without SC (insertion loss). The attenuation spectrum is obtained from the difference between the two signals. A dual-channel signal analyzer (type *B&K* 2148) has been used throughout all experiments. The analyzer makes the fast Fourier transform (FFT) of the data and produces the corresponding spectrum with a resolution of 8 Hz. A range from 800 to 4888 Hz is analyzed, and a total of 512 channels have been taken to generate a spectrum.

We have assigned a vector of five parameters (input vector) to every SC setup. These parameters are: Incidence angle, cylinders radii, lattice spacing, distance from the point of measurement to the center of the structure, and number of rows of the SC.

The incidence angle (θ), calculated between the direction of the wave vector ($\mathbf{k}$) (see Fig. 2) and the symmetry axis of the crystal, ranges from 0° to 30° (5° step). The values of the radii of used scatterers (r) are: 0.8, 1, 1.25, 1.5,

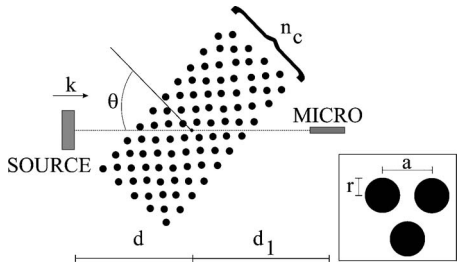

FIG. 2. Definition of parameters used for characterizing every SC setup.

1.75, and 2 cm. The lattice constant (a) can take two values: 6.35 and 12.7 cm. The distance between the center of the structure and the point of measurement (d_1) has been chosen from 1 m to 4 m (0.5 m step). The number of rows (N_r) varies from 3 to 9. Finally, the number of columns (N_c) of every SC is fixed to 10, and the distance between the source and the center of the structure (d) is also fixed to 1.35 m.

By means of a random procedure, we have defined a set of 151 combinations of these parameters that produce 151 input vectors. Next, the corresponding experimental spectrum is measured for every vector. We have selected a sample of 145 of these pair vector-spectrum for ANNs learning process, and the remaining 6 pairs have been preserved to check the accuracy of the model (test).

B. MRA of the experimental spectra

Once we have obtained the experimental data, and before presenting them to ANNs, an adequate treatment is needed in order to simplify the information contained in them. As we have explained above, the mathematical tool chosen for doing that has been the MRA that allows us to: Divide the information contained in each spectrum into different resolution levels, filter each of these levels independently in order to delete noise, and compress all the information contained using a number of coefficients as smaller as possible to characterize the spectrum.

Attending to the shape of the peaks in the attenuation spectra, we have selected Daubechies 2 as the most convenient wavelet basis to perform the MRA analysis, since it allows one to represent attenuation peaks in a very accurate way with a very small set of coefficients. This can be seen in Fig. 3.

Now, we can perform the MRA of each spectrum up to the *9th wavelet level*.

Once we have divided the information contained in each spectrum in different resolution levels, we can perform a filtering process which sets an independent threshold value for each level.

The final step is the reduction of the number of coefficients (compression of the information). To do that, we delete the two most detailed wavelet resolution levels. This does not affect the shape of the spectrum, although they represent a large number of coefficients (75% of the total). To illustrate this, Fig. 4 shows the reconstruction of a spectrum computing the inverse wavelet transform with only the remaining coefficients (25% of the total). As the reader can see, there is a remarkable coincidence between the reconstructed spectrum and the original one. In this sense, we obtain a high rate of compression of the spectra. For the MRA and the inverse wavelet transform, we have used the *Wavelet* MATLAB toolbox.[22]

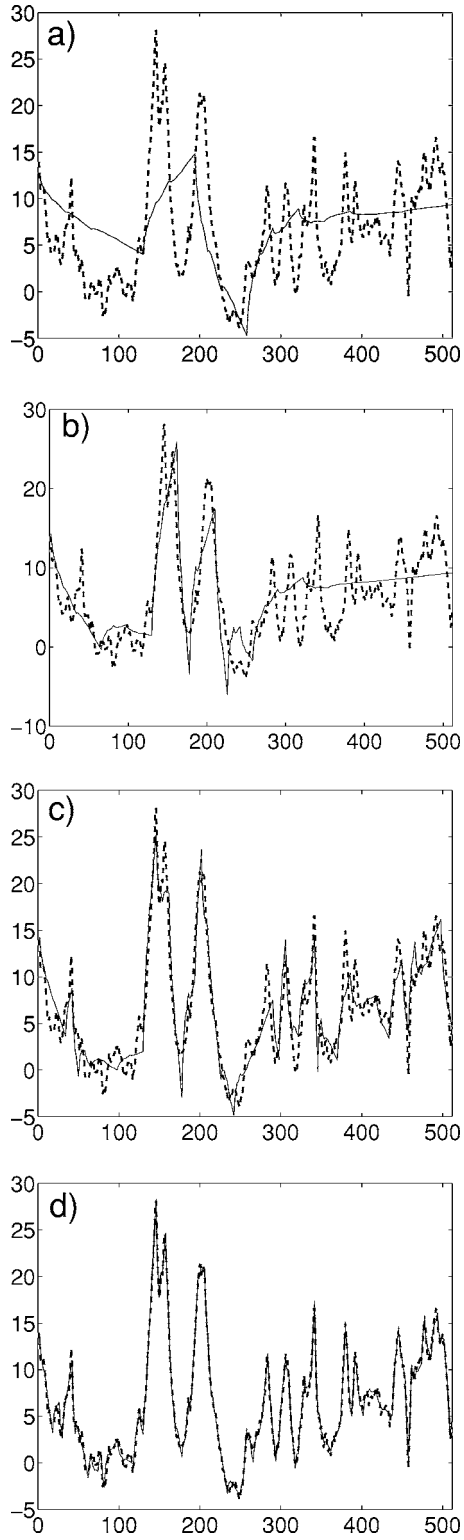

FIG. 3. Reconstruction of a typical experimental spectrum of 512 channels using (a) 5, (b) 10, (c) 30, and (d) 100 wavelet coefficients, respectively. The y axis represents the pressure attenuation in dB. The dashed line represents the reconstructed spectrum; and the continuous line, the original one.

C. Design and training of the ANN

In our model, we have considered eight neural networks, one for each resolution level of the MRA analysis of experimental spectra, that work independently. The input in each of them is the parameter vector that determines the SC setup (input vector), and the output is a real-valued vector that gives us the wavelet coefficients of the simulated spectrum for the corresponding resolution level. Consequently, the main mathematical assumption is that every resolution level can be computed independently.

Due to the small size of the set of experimental spectra chosen, a simple neural network architecture is proposed: A

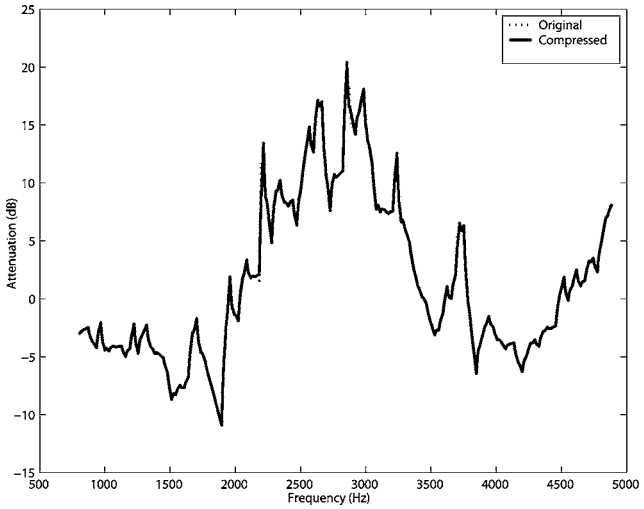

FIG. 4. Experimental spectrum versus its compressed version. It can be seen that the compressed versions cannot be distinguished from the original.

two-layer feedforward backpropagation network type. The first layer contains five neurons (the number of parameters that define the SC setup) with an *tansin*[21] activation function, and the second layer contains as many neurons as coefficients that have to be predicted with a *linear* activation function. This number varies depending on the MRA resolution level simulated by the neural network.

For the learning procedure, we feed the 8 networks with the experimental set of 146 inputs/outputs, and an optimization procedure of connection weights and bias is performed. At the very end, we have a final and optimal set of weights and bias for all networks. Then, the model is ready for simulating spectra: Giving to each neural network the same vector of parameters as input, they will return the wavelet coefficients corresponding to the MRA level assigned to each one. Computing the inverse wavelet transform of all of these coefficients together (all levels), we obtain the simulated spectrum associated with the SC setup encoded with this vector of parameters. For the effective computation of the model, we have used the *Neural Network* MATLAB toolbox.[21]

D. Test and results of the model

Once the ANNs have been trained, a test of the model must be performed. For this purpose, we have preserved six experimental spectra that have not been used for the training. In Fig. 5, we compare experimental and simulated spectra associated with three test SC setups.

The parameters corresponding to the simulated spectra are: Fig. 5(a): Incidence angle 5° cylinders radii 0.02 m, lattice spacing 0.0635 m, distance from the point of measurement to the center of the structure 4 m, and a number of rows 7; Fig. 5(b): Incidence angle 20°, cylinders radii 0.02 m, lattice spacing 0.0635 m, distance from the point of measurement to the center of the structure 2 m, and number of rows 6; and Fig. 5(c): Incidence angle 5° cylinders radii 0.0175 m, lattice spacing 0.0635 m, distance from the point of measurement to the center of the structure 4 m, and number of rows 9.

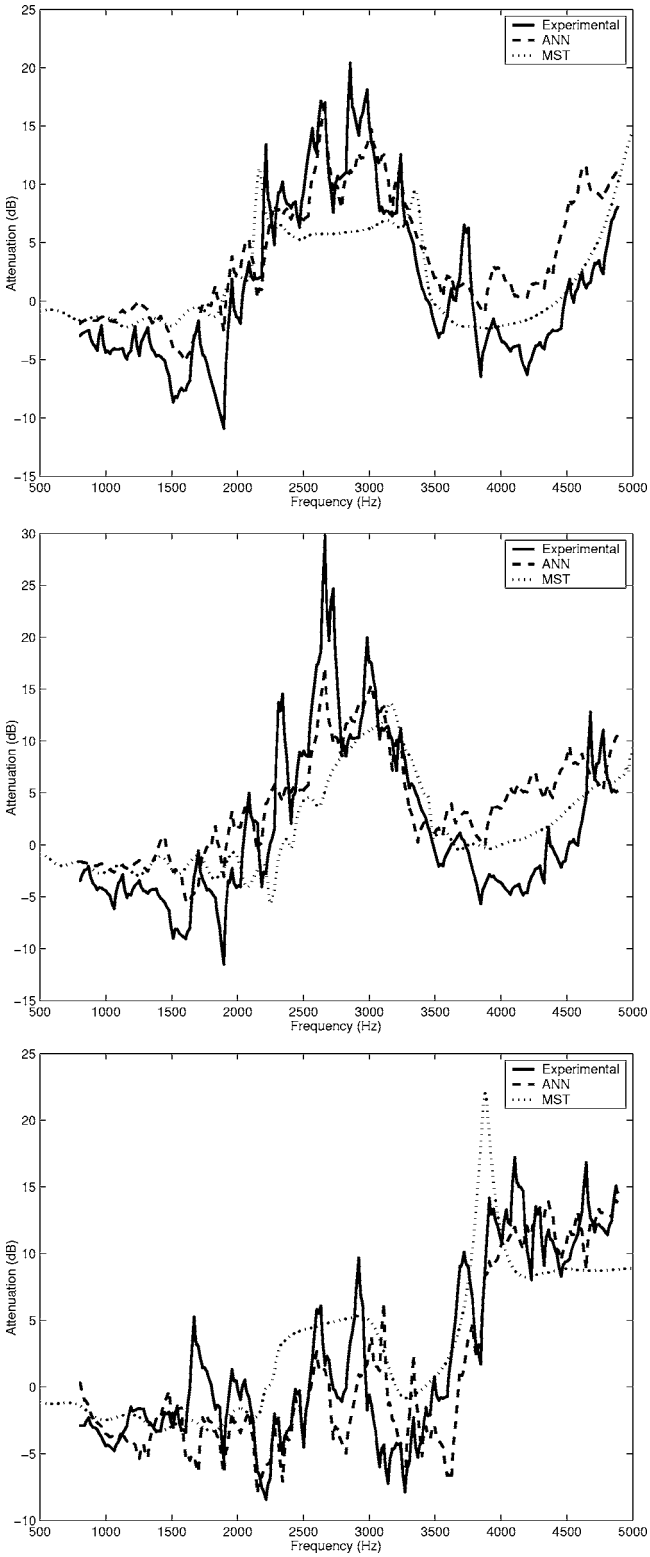

FIG. 5. Results of the test of the model for three of the test samples: Experimental spectra (continuous line), simulated spectra using our model (dashed line), and simulated spectra using MST (dotted line).

A very good agreement between simulation and experiment can be observed. Practically all simulated peaks in the whole spectrum have a correct centroid, width, and tail, i.e., the shape of the simulated spectrum is very similar to the experimental one. The simulated attenuation level is also in

TABLE I. Quadratic error values associated with the test spectra. In the second column, we show the errors associated with the MST predictions. The third column shows the errors associated with our model.

Test spectrum	ϵ_{MST}	ϵ_{ANNs}
1	2.54	1.96
2	4.42	4.24
3	6.28	4.71
4	7.22	4.45
5	8.48	5.08
6	7.7	3.4

good agreement with experimental data. There are no spurious peaks, that is, peaks that appear in the simulated spectra but are absent in the experimental ones.

1. Comparison with MST

The reason for choosing the SCs setup mentioned above is that it allows us to compare our model with the MST. In Fig. 5 (dotted line), we can see that—although MST provides a general representation of the tendencies of the experimental spectra—it does not perform a good prediction of the shape of the spectrum.

In order to quantify the accuracy of each model, we define a quadratic error by

$$\epsilon^2 = \frac{\sum_{i=1}^{512} [p_{\mathrm{theo}}(f_i) - p_{exp}(f_i)]^2}{512}, \tag{1}$$

where we divide by the total number of channels (512). The results for the tests spectra are shown in Table I. The average errors are 6.11 dB for MST, and 3.97 dB for our model (35% smaller). As can be seen, our model reproduces the shape of the experimental spectrum and has an associated error smaller than the MST in all cases.

2. Dependence of the model on the training samples

To complete the test of the model, we analyze its dependence on the number of training samples. To do so, we have trained the ANNs with populations of 40, 80, and 146 spectra. In each case, we have obtained different weights for the ANNs connections, which produce different predicted spectra. In Fig. 6, we show the comparison between these predictions and the associated experimental spectra for one of the test spectra.

Looking at these results, and assuming that we want to work with simulated spectra with a correct shape and an error associated at least smaller than the one associated with MST, we are encouraged to use more than 100 training samples to build our model. But taking into account that we want to use a number of training samples, as small as possible in order to reduce the effort in the experimental measurements, we have arrived at a compromise of 146 training samples.

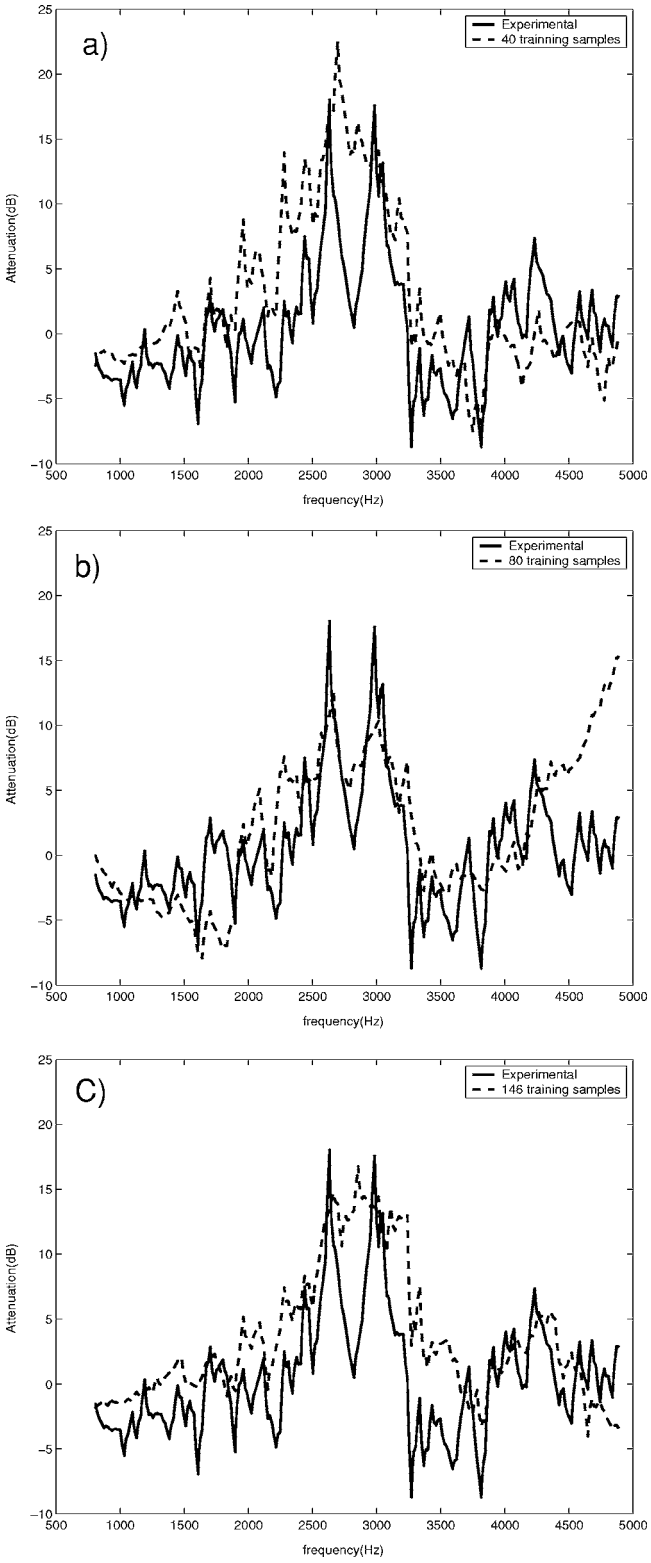

FIG. 6. Test spectrum obtained using a different number of training samples: (a) 40 training samples, (b) 80 training samples, and (c) 146 training samples.

IV. CONCLUSIONS

In this paper, we have obtained a general procedure to simulate attenuation spectra generated by SCs exclusively based on experimental data, i.e., we have developed a phenomenological model of the behavior of SCs.

It is a general procedure that produces specific models, which effectively include the experimental conditions of measurements. This is an interesting property for technologi-

cal purposes. In this sense, the closer the experimental data to the technological situation where we want to use the SC, the more reliable the simulation.

In this case, we have used a simple experimental situation, where the MST applies, in order to compare it with our model. However, we want to remark that our model has the advantage of easy use in experimental situations, where other models cannot be used. For example, it can be used in the case of SCs with scatterers of complex geometry, or composed by materials of unknown acoustic impedance, or for any frequency range (ultrasound).

The training and learning of ANNs take a short time (a few minutes) and every simulation takes only a few seconds in a standard Pentium IV personal computer platform. Our procedure is extremely fast in comparison with other procedures based, for example, in multiple scattering. Once trained, it is very useful when combined with optimization technics (genetics algorithms).

The use of MRA based on wavelets, and the selection of an adequate basis, allows us to optimize the representation of the spectra via a small set of wavelet coefficients. We have been able to reduce 75% of the initial coefficients that characterize each spectrum without losing the main details.

Moreover, the combination of wavelet codification and a neural network structure allows us to construct a parallel computation model. The splitting of the signal into different resolution levels, that can be computed independently, makes it possible to divide a complex ANN that computes all spectra at the same time into eight simpler ANNs—all computing only one resolution level.

As a result of these two features mentioned above, a drastic reduction in experimental data needed for the training processes is possible. The fewer connections the ANNs have, the fewer experimental data are needed to adjust weights and bias.

We want to emphasize that this procedure can be used for other experimental goals that have an experimental spectrum associated as an output, such as the design of sound and ultrasound lenses, barriers, photonic crystals, and any filter device in general.

ACKNOWLEDGMENTS

This research has been partially supported by the Generalitat Valenciana (Spain), under Grant No. GV04B-371, by Comisión Interministerial de Ciencia y Tecnología of Spain, under Grant No. BFM2003-02302, and by Comisión Interministerial de Ciencia y Tecnología of Spain, Contract No. MAT 2003-04993-03.

The authors would like to thank the R+D+i Linguistic Assistance Office at the Universitat Politècnica de València, Aloma Domènech i Gamez, and Teba Olcina Rambla for their help in revising this paper.

[1] R. Martínez-Sala, J. Sancho, J. V. Sánchez-Pérez, J. Llinares, and F. Meseguer, "Sound attenuation by sculpture," Nature (London) **378**, 241 (1995).
[2] J. V. Sánchez-Pérez, C. Rubio, R. Martínez-Sala, R. Sánchez-Grandía, and V. Gómez, "Acoustic barriers based on periodic arrays of scatterers," Appl. Phys. Lett. **81**, 5240–5242 (2002).
[3] A. Uris, C. Rubio, H. Estellés, J. V. Sánchez-Pérez, R. Martínez-Sala, and J. Llinares, "Design of lightweight multilayer partitions based on sonic crystals," Appl. Phys. Lett. **79**, 4453–4454 (2001).
[4] M. S. Kushwaha, "Stop-bands for periodic metallic rods: Sculptures that can filter the noise," Appl. Phys. Lett. **70**, 3218–3220 (1997).
[5] M. Shen and W. Cao, "Acoustic band-gap engineering using finite-size layered structures of multiple periodicity," Appl. Phys. Lett. **75**, 3713–3715 (2001).
[6] Y. Lai, X. Zhang, and Z. Zhang, "Engineering acoustic band gaps," Appl. Phys. Lett. **79**, 3224–3226 (2001).
[7] M. S. Kushwaha, P. Halevi, L. Dobrzynski, and B. Djafari-Rouhani, "Acoustic band structure of periodic elastic composites," Phys. Rev. Lett. **71**, 2022–2025 (1993).
[8] E. N. Economou and M. M. Sigalas, "Classical wave propagation in periodic structures: Cermet versus network topology," Phys. Rev. B **48**, 13434–13438 (1993).
[9] J. V. Sánchez-Perez, D. Caballero, R. Martínez-Sala, C. Rubio, J. Sánchez Dehesa, F. Meseguer, J. LLinares, and F. Gálvez, "Sound attenuation by a two-dimensional array of rigid cylinders," Phys. Rev. Lett. **80**, 5325–5328 (1998).
[10] M. Kafesaki and E. N. Economou, "Multiple scattering theory for 3D periodic acoustic composites," Phys. Rev. B **60**, 11993–11999 (1999).
[11] M. M. Sigalas and N. Economou, "Attenuation of multiple-scattered sound," Europhys. Lett. **36**, 241–246 (1996).
[12] Y. Y. Chen and Z. Ye, "Theoretical analysis of acoustic stop bands in two-dimensional periodic scattering arrays," Phys. Rev. E **64**, 0366161–0366165 (2001).
[13] L. Sanchis, F. Cervera, J. Sánchez-Dehesa, J. V. Sánchez-Pérez, C. Rubio, and R. Martínez-Sala, "Reflectance properties of two-dimensional sonic band-gaps crystals," J. Acoust. Soc. Am. **109**, 2598–2605 (2001).
[14] O. Umnova, K. Attenborough, and C. Linton, "Effects of porous covering on sound attenuation by periodic arrays of cylinders," J. Acoust. Soc. Am. **119**, 278–284 (2006).
[15] I. Daubechies, *Ten Lectures on Wavelets* (SIAM, Philadelphia, 1999).
[16] L. Debnat, *Wavelets and signal processing* (Birkhauser, Boston, 2003).
[17] R. A. Devore and B. J. Lucier, *Wavelets*. Acta Numerica, edited by A. Iserles (Cambridge University Press, Cambridge, UK, 1992), Vol. **1**, p. 1.
[18] B. Krse and B. Van der Smagt, *Introduction to Neural Networks* (University of Amsterdam, The Netherlands, 1996).
[19] M. T. Hagan, H. B. Demuth, and M. H. Beale, *Neural Network Design* (PWS, Boston, MA, 1996).
[20] K. Levenberg, "A method for the solution of certain problems in least squares," Q. Appl. Math. **2**, 164–168 (1944).
[21] H. Demuth and M. Beale, *Neural Network Toolbox Users Guide* (The MathWorks, Inc., 1998).
[22] M. Misiti, Y. Misiti, G. Oppenheim, and J. M. Poggi, *Wavelet Toolbox Users Guide* (The MatheWorks, Inc., 2005).

Pore scale numerical modeling of elastic wave dispersion and attenuation in periodic systems of alternating solid and viscous fluid layers

Radim Ciz[a)]
CSIRO Petroleum, ARRC, 26 Dick Perry Avenue, Kensington, Perth, WA 6151, Australia

Erik H. Saenger[b)]
Fachrichtung Geophysik, Freie Universitaet Berlin, Malteserstr. 74-100, 12249 Berlin, Germany

Boris Gurevich[c)]
Department of Exploration Geophysics, Curtin University of Technology, GPO Box U1987, Perth, Western Australia 6845 and CSIRO Petroleum, ARRC, 26 Dick Perry Avenue, Kensington, Perth, WA 6151, Australia

(Received 7 September 2005; revised 3 May 2006; accepted 30 May 2006)

Numerical pore-scale simulation of elastic wave propagation is an emerging tool in the analysis of static and dynamic elastic properties of porous materials. Rotated staggered-grid (RSG) finite difference method has proved to be particularly effective in modeling porous media saturated with ideal fluids. Recently this method has been extended to viscoelastic (Maxwell) media, which allows simulation of wave propagation in porous solids saturated with Newtonian fluids. To evaluate the capability of the viscoelastic RSG algorithm in modeling wave dispersion and attenuation we perform numerical simulations for an idealized porous medium, namely a periodic system of alternating solid and viscous fluid layers. Simulations are performed for a single frequency of 50 kHz (for shear waves) and 500 kHz (for compressional waves) and a large range of fluid viscosities. The simulation results show excellent agreement with the theoretical predictions. Specifically the simulations agree with the prediction of Biot's theory of poroelasticity at lower viscosities and with the viscoelastic dissipation at higher viscosities. The finite-difference discretization is required to be sufficiently fine for the appropriate sampling of the viscous boundary layer to achieve accurate simulations at the low values of viscosity. This is an additional accuracy condition for finite-difference simulations in viscoelastic media. © *2006 Acoustical Society of America.* [DOI: 10.1121/1.2216687]

PACS number(s): 43.20.Jr [JBS] Pages: 642–648

I. INTRODUCTION

Despite five decades of research into acoustics of porous media, many questions concerning the nature of acoustic attenuation and dispersion in such media remain unresolved. Some of these questions can be addressed by numerical simulations performed on the microscale, that is, on the scale of individual pores and grains. This approach, which can be called digital (or computational) rock physics, is increasingly used to model the effect of pores, fractures, and fluid on the effective acoustic properties (Roberts and Garboczi, 2000; Arns *et al.*, 2002; Grechka, 2003; Saenger *et al.*, 2004) as well as geometrical, hydraulic, and electrical properties of rocks (Schwartz *et al.*, 1994; Spanne *et al.*, 1994; Auzerais *et al.*, 1996; Arns *et al.*, 2001; Keehm *et al.*, 2004). Until recently, most of the computational methods for effective *acoustic* properties focused on ideally elastic materials saturated with ideal fluids; however, understanding of acoustic dissipation requires taking into account the viscosity of the pore fluids.

Recently Saenger *et al.* (2005) developed viscoelastic rotated staggered grid (VRSG) algorithm that can perform pore-scale simulation of wave propagation in porous materials saturated with Newtonian fluids. The algorithm of Saenger *et al.* (2005) is essentially an extension to viscous pore fluids of the rotated staggered grid (RSG) finite difference (FD) method developed by Saenger *et al.* (2000). The fluid viscosity is included by modeling the pore fluid as a special case of the generalized Maxwell body (GMB), which in a wide range of viscosities and frequencies is equivalent to a Newtonian fluid.

In order to use the VRSG algorithm for the study of wave propagation in porous media, it is necessary to investigate whether this algorithms can accurately simulate known effects in wave propagation in such media. It is known that attenuation and dispersion of elastic waves in poroelastic media mainly occurs due to the flow of the pore fluid induced by the propagating waves. Such wave-induced fluid flow can occur due to pressure gradients between peaks and troughs in the wave [Biot's global flow (Biot, 1956a, 1956b)], between more compliant and stiff pores [local or squirt flow (Mavko and Jizba, 1991; Dvorkin *et al.*, 1995)] and between regions of lower and higher compliance [meso-

[a)]Electronic mail: radim.ciz@csiro.au
[b)]Electronic mail: saenger@geophysik.fu-berlin.de
[c)]Electronic mail: boris.gurevich@geophy.curtin.edu.au

scopic flow (Pride and Berryman, 2003)]. The global flow attenuation and dispersion can occur in homogeneous single-porosity-media described by the classical Biot's equations of poroelasticity (Biot, 1956a, 1956b), and has a peak at the so-called Biot's characteristic frequency

$$\omega_B = \frac{\eta}{\rho_f \kappa}, \tag{1}$$

where η and ρ_f are the viscosity and density of the pore fluid and κ is the permeability of the medium. The local flow attenuation is less well understood. While there is no universally accepted model of this phenomenon, it is generally believed that its characteristic frequency is given by

$$\omega_R = \frac{B}{\eta}\left(\frac{b}{a}\right)^n, \tag{2}$$

where B is characteristic rock stiffness, a is characteristic size of the (stiff) pores, $b \ll a$ is characteristic thickness of compliant pores (cracks), and n is a dimensionless constant usually taken to be equal to 3 (Mavko and Nur, 1975). The characteristic frequency of the mesoscopic attenuation is given by equation (1) with $n=2$ (Pride *et al.*, 2003). The principle difference between Eqs. (1) and (2) is in the role of fluid viscosity: Increase of fluid viscosity causes an increase of Biot's characteristic frequency but a decrease of the characteristic frequency for local and mesoscopic flow. One can also note that for single porosity medium (that is, a medium where the size of all pores is of the same order of magnitude) $b/a = O(1)$ so that

$$\omega_R = \frac{B}{\eta}. \tag{3}$$

Therefore, for the single-porosity medium frequency ω_R is the same as that for attenuation due to the classical viscoelastic effect, also known as viscous shear relaxation, that is, stiffening of the material due to fluid viscosity at high frequencies. In other words, in single porosity medium local flow attenuation reduces to classical viscoelastic attenuation.

In order to be applicable for a detailed simulations of porous media, the VRSG algorithm needs to be able to simulate phenomena with characteristic frequencies given by Eqs. (1) and (2) or (3). To do this, one needs to simulate the dynamic behavior of a porous medium with the VRSG algorithm and compare the results with known expressions for attenuation and dispersion in such media. While explicit expressions are known for global-flow (Biot's) attenuation (Biot, 1956a, 1956b), they are not known for local flow mechanism, which is the least understood.

This problem can be at least partially resolved by considering an idealized porous medium, such as a periodic system of alternating solid and viscous fluid layers. Such a system, although very idealized, is known to possess many features of saturated porous media. In particular, shear and compressional waves propagating in the plane of the layers of such system and polarized in the same plane have exhibit both Biot's and viscoelastic attenuation with characteristic frequencies given by Eqs. (1) and (3), respectively. At the same time, such a layered system represents the only case of a porous medium for which exact expressions for attenuation and dispersion are known. For these reasons the periodic system of alternating solid and viscous fluid layers is ideally suited for testing of the VRSG algorithm.

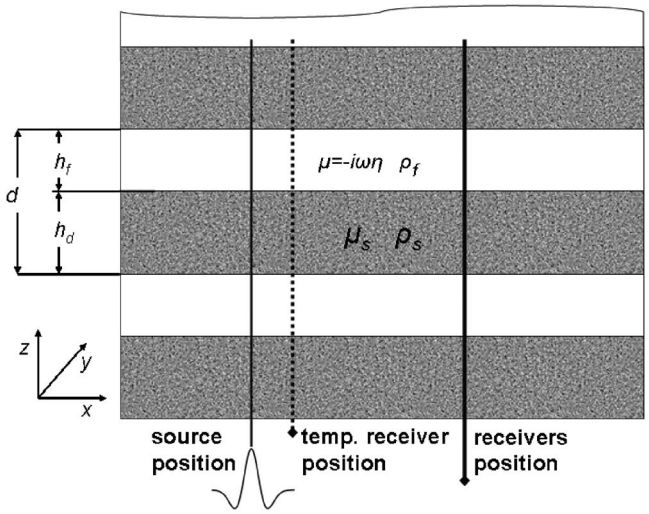

FIG. 1. Medium of alternating solid and viscous fluid layers.

The objective of this paper is: (1) to perform numerical simulations of compressional as well as shear wave propagation, (2) to compute attenuation as well as dispersion of these waves, and (3) to compare the numerical and theoretical results for both global and local-flow mechanisms.

First, we review the exact dispersion equations for such layered systems (Sec. II) and give the basic description of the VRSG algorithm (Sec. III). Numerical setup and simulation results are presented in Sec. IV followed by conclusions (Sec. V).

II. THEORETICAL BACKGROUND

Consider a system of periodically alternating solid and fluid layers of period d (Fig. 1). The elastic solid has density ρ_s, bulk modulus K_s, and shear modulus μ_s. The viscous fluid has density ρ_f, bulk modulus (inverse compressibility) K_f, and dynamic viscosity η. The solid and fluid layer thicknesses are h_s and h_f, respectively, so that $h_s + h_f = d$.

We analyze the propagation of shear and compressional waves in the x direction parallel to the layering, with the displacement in the direction y (for the shear or SH wave) and to x (for the compressional wave), both parallel to the bedding. For a given frequency ω the solutions can be sought in the form of plane waves

$$u_y = u_{y0} \exp i\omega(x/b - t), \tag{4}$$

for the SH wave and

$$u_x = u_{x0} \exp i\omega(x/c - t), \tag{5}$$

for the P wave.

A. Shear waves

Propagation of the SH wave in a periodic system of solid and viscous fluid layers is governed by an exact dispersion equation (Rytov, 1956; Brekhovskikh, 1981; Gurevich, 2002):

$$p\left[\tan^2\frac{\beta_s h_s}{2}+\tan^2\frac{\beta_f h_f}{2}\right]+(1+p^2)\tan\frac{\beta_s h_s}{2}\tan\frac{\beta_f h_f}{2}=0. \tag{6}$$

Here $\beta_s^2=\omega^2(1/b_s^2-1/b^2)$, $\beta_f^2=\omega^2(1/b_f^2-1/b^2)$, where $b_s=(\mu_s/\rho_s)^{1/2}$, and $b_f=(\mu_f/\rho_f)^{1/2}$ are shear velocities in the materials s and f, respectively, $p=\mu_f\beta_f/\mu_s\beta_s$ and $\mu_f=-i\omega\eta$.

Our aim is to solve the dispersion equation (6) on a macroscale, that is for long waves, to obtain the phase velocities b and c as a function of ω for long waves such that $|\omega d/b|\ll 1$. In this limiting case equation (6) reduces to (Gurevich and Ciz, in press):

$$\frac{1}{b^2}=\frac{1}{\mu}\left[\rho-\frac{\rho_f^2\phi^2}{q(\omega)}\right]\left[1+i\omega/\omega_V\frac{\phi}{1-\phi}\right], \tag{7}$$

where $\phi=h_f/d$ is the volume fraction of the fluid layers (porosity), $\mu=\mu_s(1-\phi)$ is the static shear modulus of the system, $\rho=(1-\phi)\rho_s+\phi\rho_f$ is the average density, and

$$q(\omega)=\phi\rho_f[1-(i\omega/\omega_b)^{-1/2}\tan(i\omega/\omega_b)]^{1/2-1}, \tag{8}$$

is generalized virtual mass coefficient of the layered system. ω_B has the role of characteristic frequency and is given by an equation similar to Eq. (1):

$$\omega_B=\eta\phi/3\kappa\rho_f=4\eta/\rho_f h_f^2 \tag{9}$$

with permeability of porous slabs given by (Bedford, 1986):

$$\kappa=\frac{\phi h_f^2}{12}. \tag{10}$$

In turn, ω_V is viscoelastic characteristic frequency, Eq. (3). According to Eq. (7), the behavior of SH-wave velocity dispersion and attenuation in the layered system depends on the ratio ω_B/ω_V. When $\omega_B\ll\omega_V$, Eq. (7) reduces to

$$\frac{1}{b^2}=\frac{1}{\mu}\left[\rho-\frac{\rho_f^2\phi^2}{q(\omega)}\right]. \tag{11}$$

The dispersion equation (11) is identical to the dispersion equation for S waves in a porous medium described by Biot's theory of poroelasticity with permeability (10) and virtual mass coefficient (8), thus confirming the system of solid and fluid layers as a particular (limiting) case of a poroelastic medium. In the opposite case $\omega_B\ll\omega_V$, we have

$$\frac{1}{b^2}=\frac{1}{\mu}\left[1+i\omega/\omega_V\frac{\phi}{1-\phi}\right]. \tag{12}$$

This equation describes the standard viscoelastic dispersion (Gurevich, 1999, 2002).

The theoretical solutions presented earlier give the complex shear-wave velocity (or slowness) as a function of frequency. The real part of the complex velocity yields the phase velocity of the wave, while the ratio of imaginary to real part of the squared slowness yields the dimensionless attenuation (inverse quality factor)

$$Q_{Sh}^{-1}=\frac{\mathrm{Im}\,b^{-2}}{\mathrm{Re}\,b^{-2}}. \tag{13}$$

B. Compressional waves

Propagation of the P wave in a periodic system of solid layers denoted by s and f is governed by an exact dispersion equation (Rytov, 1956; Brekhovskikh, 1981; Gurevich, 2002):

$$\begin{aligned}&4(\mu_s-\mu_f)^2K_1K_2+\omega^2\rho_s[c^2\rho_s-4(\mu_s-\mu_f)]K_2\tan\frac{\beta_s h_s}{2}\\&+\omega^2\rho_f[c^2\rho_f+4(\mu_s-\mu_f)]K_1\tan\frac{\beta_f h_f}{2}\\&-\omega^2\rho_f\rho_s c^2\left[L_1\tan\frac{\beta_f h_f}{2}+L_2\tan\frac{\beta_s h_s}{2}\right]=0.\end{aligned} \tag{14}$$

where $\alpha_s^2=\omega^2(1/c_s-1/c)$, $\alpha_f^2=\omega^2(1/c_f-1/c)$ and $c_s=[(K_s+4\mu_s/3)/\rho_s]^{1/2}$, $c_f=[(K_f+4\mu_f/3)/\rho_f]^{1/2}$ are compressional velocity in the material s and f, respectively, $\mathrm{Im}\,\mu_f=\mathrm{Im}\,\lambda_f=-\omega\eta$, $K_f=(\lambda_f+2\mu_f)/3$, and

$$\begin{aligned}K_1&=\frac{\omega^2}{c^2}\tan\frac{\beta_s h_s}{2}+\alpha_s\beta_s\tan\frac{\alpha_s h_s}{2},\\K_2&=\frac{\omega^2}{c^2}\tan\frac{\beta_f h_f}{2}+\alpha_f\beta_f\tan\frac{\alpha_f h_f}{2},\\L_1&=\frac{\omega^2}{c^2}\tan\frac{\beta_s h_s}{2}-\alpha_f\beta_s\tan\frac{\alpha_f h_f}{2},\\L_2&=\frac{\omega^2}{c^2}\tan\frac{\beta_f h_f}{2}-\alpha_s\beta_f\tan\frac{\alpha_s h_s}{2}.\end{aligned} \tag{15}$$

Similarly to the shear wave case, Eq. (6) needs to be analyzed on the macroscale, that is in the limit $|\omega d/c|\ll 1$. However, such a theoretical analysis appears to be too involved, and the analytical solution is only known in the low-frequency limit (Gurevich, 2002). However, it has been shown numerically (Bedford, 1986), that for sufficiently small values of $|\omega d/c|$ attenuation and dispersion predicted by Eq. (14) are the same as given by Biot's dispersion equation for fast compressional waves in a porous medium with steady state permeability (10) and virtual mass coefficient given by (8). Note that both Eq. (14) and Biot's theory predict another type of compressional wave, so-called Biot's slow wave. However, analysis of this highly dispersive wave is beyond the scope of this paper.

The theoretical expressions summarized in this section will be used for comparison with numerical simulations.

III. ALGORITHM

To model wave propagation in a solid-fluid mixture, we apply displacement-stress rotated staggered finite-difference

grid (Saenger *et al.*, 2000) to solve the elastodynamic wave equation. With a viscoelastic extension (described in detail in Saenger *et al.*, 2005) we are able to model wave propagation in different kinds of porous media.

The theoretical model of viscoelasticity is based on an approach described by Emmerich and Korn (1987). Incorporation of viscosity based on the GMB means that Hooke's law is modified

$$\sigma_{ij} = c_{ijkl}\varepsilon_{kl} - \sum_{m=1}^{n} \xi_m^{ij}. \tag{16}$$

In this equation, $\sigma_{ij}, c_{ijkl}, \varepsilon_{kl}$ denote the stresses, the elastic tensor, and the strains, respectively. The number of relaxation mechanisms is equal to m. The anelastic functions ξ_m^{ij} are determined by

$$\dot{\xi}_m^{ij} + \omega_m \xi_m^{ij} = \omega_m \tilde{Y}_m^{ijkl} \varepsilon_{kl}, \tag{17}$$

with $\tilde{Y}_m^{ijkl}$ as the tensors of anelastic coefficients and ω_m as angular relaxation frequencies. The GMB frequency-dependent viscoelastic modulus $C_{ijkl}(\omega)$ can be derived by inserting the Fourier transform of Eq. (17) into Eq. (16):

$$C_{ijkl}(\omega) = c_{ijkl} - \sum_{m=1}^{n} \tilde{Y}_m^{ijkl} \frac{\omega_m}{i\omega + \omega_m}. \tag{18}$$

A second order discretization of Eq. (6) is implemented in the rotated staggered grid algorithm. As a result the anelastic functions ξ_m^{ij} and coefficients $\tilde{Y}_m^{ijkl}$ are located in the center of an elementary FD cell at the same position as the stress tensor [see Fig. 1(d) of Saenger *et al.*, 2000]. The exact position of a boundary between two different materials is exactly the bound of the appendant elementary cells.

A compressible viscous fluid (i.e., Newtonian fluid) can be characterized by the following frequency-dependent elastic moduli:

$$C_{44}(\omega) = \mu(\omega) = i\omega\eta_\mu, \tag{19}$$

$$C_{12}(\omega) = \lambda(\omega) = \lambda(0) + i\omega\eta_\lambda, \tag{20}$$

with $\lambda(\omega)$ and $\mu(\omega)$ as angular-frequency dependent Lamé parameters. For all examples in this paper we assume that the dynamic fluid viscosity η is equal to η_μ and η_λ. However, the key question is how to approximate the viscous behavior given by Eqs. (19) and (20) with a GMB. The following strategy is based on a Taylor expansion of Eq. (18) for $\omega = 0$:

- We use one relaxation mechanism ($n=1$).
- $\tilde{Y}_1^{44} = c_{44}$. Only in this case it is possible that $C_{44}(0)=0$.
- In the low frequency range of the GMB for one relaxation mechanism one can determine the wanted fluid-viscosity by using the following relations:

$$\eta_\mu = \frac{1}{i} \left. \frac{\partial C_{44}(\omega, \tilde{Y}_1^{44} = c_{44})}{\partial\omega} \right|_{\omega=0} = \frac{c_{44}}{\omega_1}, \tag{21}$$

$$\eta_\lambda = \frac{1}{i} \left. \frac{\partial C_{12}(\omega)}{\partial\omega} \right|_{\omega=0} = \frac{\tilde{Y}_1^{12}}{\omega_1}. \tag{22}$$

- For $\eta_\mu = \eta_\lambda$ one can show that $\tilde{Y}_1^{12} = c_{44}$. Further, with Eqs. (18), (20), and the known relation $c_{11} = c_{12} + 2c_{44}$ one can derive (for $\omega = 0$):

$$c_{11} = \lambda(0) + 3c_{44}. \tag{23}$$

- For FD approaches it is necessary to take into account the stability criterion. For the rotated staggered grid with FD operators of second order in time and space the following relation is valid (Saenger *et al.* 2000):

$$\sqrt{\frac{c_{11}}{\rho_{fluid}}} = \nu_p \leqslant \gamma, \quad \gamma = \frac{\Delta h}{\Delta t}. \tag{24}$$

- We choose c_{44} the following restriction [given by the "stability criterion"-relation (24) and Eq. (23)]:

$$c_{44} \leqslant \frac{\gamma^2 \rho_{\text{fluid}} - \lambda(0)}{3}. \tag{25}$$

- Together with the choice of the angular relaxation frequency ω_1 one can determine the wanted dynamic viscosity η [compare with Eq. (21)].
- We choose a source signal in the low frequency range of the applied GMB ($\omega_{\text{source}} \ll \omega_1$).

IV. NUMERICAL SIMULATIONS AND RESULTS

A. Numerical setup

To obtain effective velocities and attenuation coefficients in layered media we choose the following numerical setup. The full synthetic model contains two horizontal thin layers of viscous fluid and elastic solid of equal size (30×3000 grid points with an interval of $\Delta x = 0.0001$ m for the SH wave and $\Delta x = 0.00001$ m for the P wave). The solid has the P-wave velocity $\nu_p = 5100$ m/s, S-wave velocity $\nu_s = 2944$ m/s, density $\rho_s = 2540$ kg/m^3, and viscosity $\eta = 0$ kg/m s. For the viscous fluid we always set $c_{11} = 3.922 \times 10^{11}$, $c_{44} = 1.3 \times 10^{11}$, and $\rho_f = 1000$ kg/m^3. The fluid viscosity η is varied with the choice of ω_1 [see Eq. (21)]. To generate a plane SH wave (Rickerl, $f_{\text{dom}} = 50$ kHz, $\Delta t = 5e-9$ s) or a P-wave (Rickerl, $f_{\text{dom}} = 500$ kHz, $\Delta t = 5e-10$ s), we apply a line source in horizontal or vertical direction and perform the finite-difference simulations with periodic boundary conditions in the same direction. The effective velocity is estimated by measuring the time of the zero crossing of the plane wave over a distance of 1000 grid points. All computations are carried out with the second order spatial FD operators and with the second order time update.

To obtain attenuation coefficients from simulation data we analyze the amplitude decaying with distance over one wavelength. Based on the constant "Q" model (Knopoff, 1964; Pilant, 1979; Mavko *et al.*, 1998) the attenuation $1/Q$ reads

$$\frac{1}{Q} = -\frac{1}{\pi} \left. \frac{\Delta A}{A} \right|_{L_W}, \tag{26}$$

where ΔA is the change in amplitude A over one wavelength "L_W." This methodology is used to derive the attenuation from the numerically simulated wave forms at the distance of one wavelength.

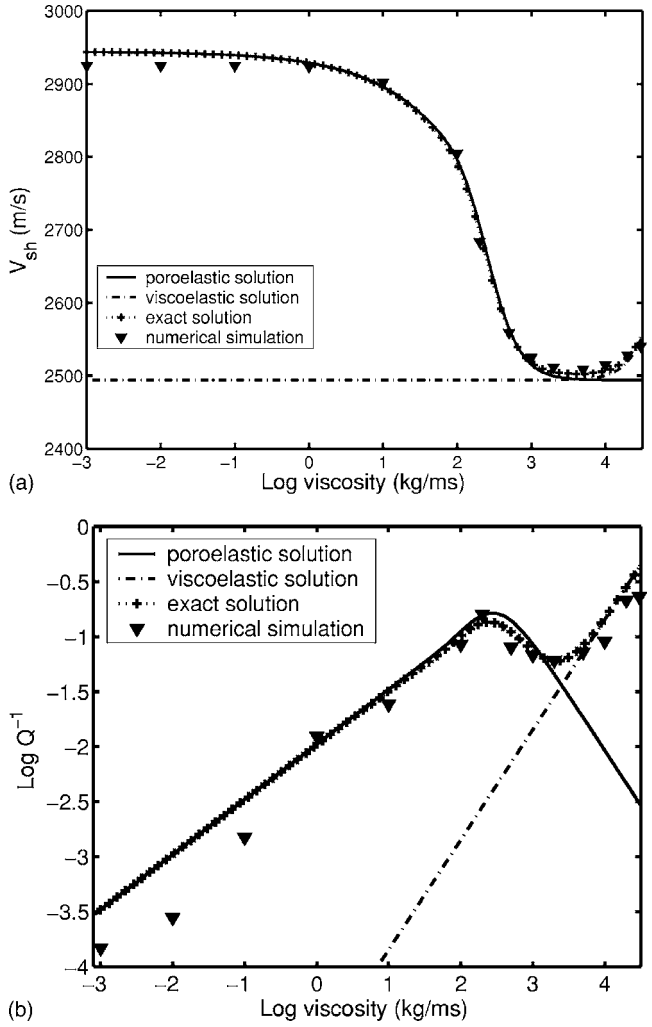

FIG. 2. Shear wave velocity (a) and attenuation (b) vs viscosity. The triangles represent values of shear wave velocity obtained from numerical simulations for models with different viscosity values. The cross-dotted line corresponds to exact solution (6), the solid line represents the poroelastic solution (7), and the dash-dotted line denotes the viscoelastic solution (12).

B. Numerical results

The results of shear wave simulations are summarized in Figs. 2(a) and 2(b) which show the shear wave velocity and attenuation plotted versus the fluid viscosity. The solid triangles are simulations results, and the solid line is, the theoretical solution obtained by numerically solving the exact dispersion equation (6). Also shown are theoretical solution in poroelastic (11) and viscoelastic (12) limits. We observe a very good agreement between the full theoretical solutions and the numerical simulations for almost the full range of viscosities. Up until viscosity of about 3000 kg/ms the numerical solution also agrees with poroelastic (Biot's) solution (11), after which it tends to follow the viscoelastic solution (12). This latter effect is shown only for a relatively narrow range of frequencies, as the viscoelastic solution is only valid as long as the parameter $\omega/\omega_V=\omega\eta/\mu_s$ is small, that is, for viscosities $\eta \ll \mu_s/\omega$. At higher viscosities when the viscoelastic term begins to dominate, the waves become strongly dispersive and our method of velocity estimation no longer applies. We did not focus on these high viscosities as they are unphysical (in the sense that Newtonian fluid model is no longer valid, see Landau and Lifshitz, 1987). The viscoelastic behavior is much more clearly visible on attenuation than on the dispersion plot, since the first-order viscoelastic term in (12) is purely imaginary and therefore does not contribute to the phase velocity.

Some discrepancies are observed for very low and very high viscosities. These discrepancies cannot be explained by numerical dispersion because we use over 500 grid points per dominant wavelength. The discrepancy at low viscosity is likely to be caused by insufficient sampling of the viscous boundary layer near the solid/fluid interface. For instance, at viscosity $\eta=10$ kg/ms and frequency 50 kHz, the thickness of the boundary layer (viscous skin depth) is already about $(2\eta/\omega\rho_f)^{1/2}=2.5\times10^{-4}$ m, or about less than three grid points of the FD grid. Thus the value $\eta=10$ kg/m s is the minimum value of viscosity for which the boundary layer is adequately sampled. From a practical point of view this gives a general physical accuracy condition for simulations of wave propagation in viscoelastic media

$$\sqrt{\frac{2\eta}{\omega\rho_f}} \geqslant \xi\Delta x; \quad \xi \approx 3. \tag{27}$$

In our setup this condition is not fulfilled at viscosities lower than $\eta=10$ kg/m s, which causes the errors in attenuation observed in Fig. 2(b). Note also corresponding errors in phase velocity [Fig. 2(a)]; however, the velocity errors are smaller. Again, as mentioned earlier, this accuracy condition should not be mixed with the classical dispersion accuracy condition derived for wave propagation in an elastic solid or ideal fluid. The dispersion condition is discussed in detail for the RSG in Saenger *et al.* (2000) and Saenger and Bohlen (2004) and gives rules for a proper ratio of grid points per wavelength. For pore-scale simulations this is typically not a crucial condition because the main focus is on effective elastic properties in the long wavelength limit. One needs several grid points to discretize the pores properly (~30 grid points) and the wavelength must be at least 10 times larger than the pores. The resulting ratio of 300 or more grid points per wavelength is therefore not crucial with respect to the numerical dispersion.

To further investigate the relationship between the thickness of the viscous solid/fluid boundary and the number of grid points, the computation of shear velocities was performed for different number of grid points and different size of spatial steps. The results are summarized in Fig. 3. These results demonstrate that insufficient spatial sampling causes the observed velocity errors at low viscosities, in situations when the viscous skin depth is small.

The results for *P*-wave dispersion and attenuation are shown in Figs. 4(a) and 4(b). The numerically simulated values of *P*-wave velocities [Fig. 4(a)] and inverse quality factor [Fig. 4(b)] are consistent with the exact solution. This agreement is observed in a wide range of viscosities. A small discrepancy appears at viscosities as low as $\eta<0.1$ kg/m s. At these very low viscosities the very thin solid/fluid boundary layer is still not properly discretized.

It is useful to note that Biot's theory of poroelasticity neglects the bulk viscosity of the pore fluid. Our numerical

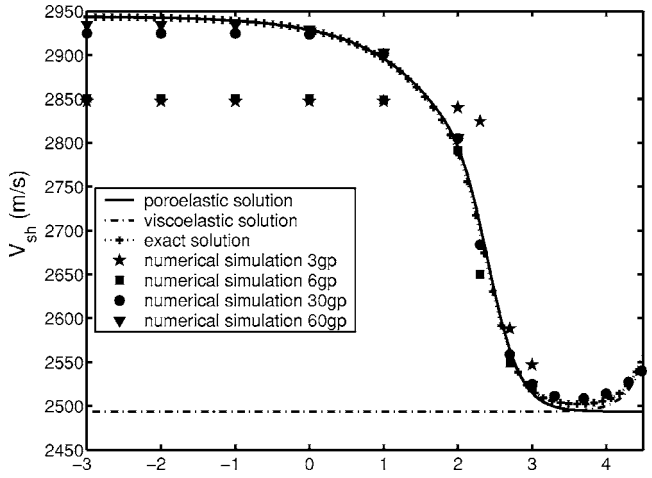

FIG. 3. SH-wave velocity vs viscosity. The solid line corresponds to the poroelastic solution [Eq. (7)]. The discrete points represent values of SH-wave velocity obtained from numerical simulations for models with varying number of grid points.

simulations include the effects of both bulk and shear viscosities. The theoretical solution for shear waves includes only the effect of shear viscosity. The good agreement between the numerical simulation and the theoretical attenuation and dispersion proves the legitimacy of Biot's assumption as expected. For compressional waves Figs. 4(a) and 4(b) show solutions both with ($\mathrm{Im}\,\lambda_f = \mathrm{Im}\,\mu_f = -\omega\eta$) and without ($\mathrm{Im}\,\lambda_f = 0$) bulk viscosity. We see that influence of bulk viscosity on the dispersion and attenuation of compressional waves is negligible in the poroelastic regime, and becomes significant only in the viscoelastic regime, again confirming Biot's assumption.

V. CONCLUSIONS

The main result of this paper is an excellent agreement between the numerical simulations and theoretical predictions of shear and compressional wave velocities and attenuation factors. This agreement is observed in a wide range of fluid visocities. In the lower viscosity range the solution shows excellent agreement with the poroelastic solution as predicted by Biot's theory of poroelasticity. At higher viscocities the behavior of viscosities and, in particular, attenuation factors is consistent with classical viscoelastic dissipation. This confirms that the viscoelastic rotated staggered grid FD method of Saenger *et al.* (2005) is capable of modeling both poroelastic (associated with global flow) and viscoelastic effects with high accuracy. The finite-difference discretization required to achieve this accuracy must be sufficiently fine to ensure adequate sampling of viscous boundary layer near the pore wall. At least two grid points with spatial distance less than the viscous skip depth are required for the accurate computation. This can be regarded as general (physical) accuracy condition for wave simulation on a microscale in presence of viscosity.

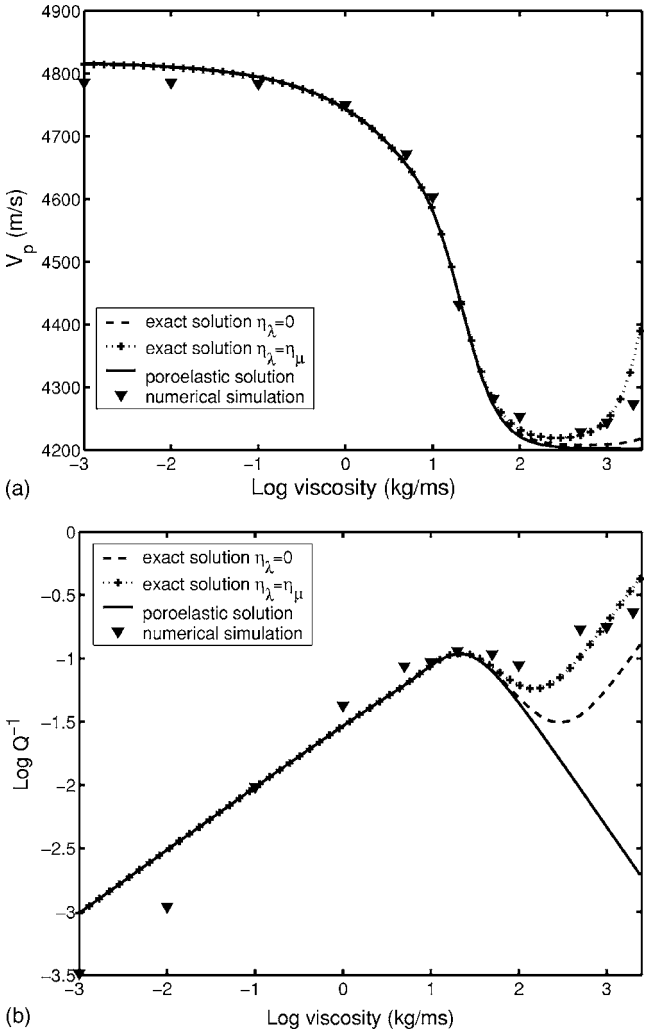

FIG. 4. Compressional wave velocity (a) and attenuation (b) vs viscosity. The dashed line corresponds to the exact Rytov's dispersion equation (14) for the case when the bulk viscosity of the fluid layer is neglected. The cross-dotted line represents the exact Rytov's dispersion equation when the solution accounts for the bulk viscosity of the fluid layer. The solid line corresponds to the Biot's dispersion equation for compressional waves. The triangles represent values of compressional wave velocity obtained from numerical simulations for models with varying viscosities for spatial step $\Delta x = 1e-5$.

ACKNOWLEDGMENTS

The work was supported by the Centre of Excellence for Exploration and Production Geophysics, CSIRO Division of Petroleum Resources, Curtin Reservoir Geophysics Consortium, and CSIRO Postdoctoral Fellowship Program.

Arns, C. H., Knackstedt, M. A., Pinczewski, W. V., and Garboczi, E. G. (**2001**). "Accurate estimation of transport properties from microtomographic images," Geophys. Res. Lett. **28**, 3361–3364.

Arns, C. H., Knackstedt, M. A., Pincewski, W. V., and Garboczi, E. J. (**2002**). "Computation of linear elastic properties from microtomographic images: Methodology and agreement between theory and experiment," Geophysics **67**, 1396–1405.

Auzerais, F. M., Dunsmuir, J., Ferreol, B. B., Martys, N., Olson, J., Ramakrishnan, T. S., Rothman, D. H., and Schwartz, L. M. (**1996**). "Transport in sandstone: A study based on three dimensional microtomography," Geophys. Res. Lett. **23**, 705–708.

Bedford, A. (**1986**). "Application of Biot's equations to a medium of alternating fluid and solid layers," J. Wave-Mater. Interact. **1**, 34–53.

Biot, M. A. (**1956a**). "Theory of propagation of elastic waves in a fluid-saturated porous solid. I. Low-frequency range," J. Acoust. Soc. Am. **28**, 168–178.

Biot, M. A. (**1956b**). "Theory of propagation of elastic waves in a fluid-saturated porous solid. II. Higher frequency range," J. Acoust. Soc. Am.

28, 179–191.
Brekhovskikh, L. M. (**1981**). *Waves in Layered Media* (Academic, New York).
Dvorkin, J., Mavko, G., and Nur, A. (**1995**). "Squirt flow in fully saturated rocks," Geophysics **60**, 97–107.
Emmerich, H., and Korn, M. (**1987**). "Incorporation of attenuation into time-domain computations of seismic wavefields," Geophysics **52**, 1252–1264.
Grechka, V. (**2003**). "Effective media: A forward modeling view," Geophysics **68**, 2055–2062.
Gurevich, B. (**1999**). "Low-frequency shear wave propagation in periodic systems of alternating solid and viscous fluid layers," J. Acoust. Soc. Am. **106**, 57–60.
Gurevich, B. (**2002**). "Effect of fluid viscosity on elastic wave attenuation in porous rocks," Geophysics **67**, 264–270.
Gurevich, B., and Ciz, R. (in press). "Shear wave dispersion and attenuation in periodic systems of alternating solid and viscous fluid layers," Int. J. Solids Struct..
Keehm, Y., Mukerji, T., and Nur, A. (**2004**). "Permeability prediction from thin sections: 3D reconstruction and lattice-boltzmann flow simulation," Geophys. Res. Lett. **31**, L04, 606.
Knopoff, L. (**1964**). "Q," Rev. Geophys. **2**, 625–660.
Landau, L., and Lifshitz, E. (**1987**). *Fluid Mechanics* (Pergamon, New York).
Mavko, G., and Jizba, D. (**1991**). "Estimating grain-scale fluid effects on velocity dispersion in rocks," Geophysics **56**, 1940–1949.
Mavko, G., Mukerji, T., and Dvorkin, J. (**1998**). *The Rock Physics Handbook* (Cambridge University Press, Cambridge).
Pilant, W. L. (**1979**). *Elastic Waves in the Earth* (Elsevier, New York).
Pride, S. R., Harris, J., Johnson, D. L., Mateeva, A., Nihei, K., Nowack, R. L., Rector, J., III, Spetzler, H., Wu, R., Yamomoto, T., Berryman, J., and Fehler, M. (**2003**). "Permeability dependence of seismic amplitudes," The Leading Edge **22**, 518–525.
Pride, S. R., and Berryman, J. G. (**2003**). "Linear dynamics of double-porosity double-permeability materials, I. Governing equations and acoustic attenuation," Phys. Rev. E **68**, 036603-1–036603-10.
Roberts, A. P., and Garboczi, E. J. (**2000**). "Elastic properties of model porous ceramics," J. Am. Ceram. Soc. **83**, 3041–3048.
Rytov, S. M. (**1956**). "Acoustical properties of a thinly laminated medium," Sov. Phys. Acoust. **2**, 68–80.
Saenger, E. H., Gold, N., and Shapiro, S. A. (**2000**). "Modeling the propagation of elastic waves using a modified finite-difference grid," Wave Motion **31**, 77–92.
Saenger, E. H., and Bohlen, T. (**2004**). "Finite-difference modeling of viscoelastic and anisotropic wave propagation using the rotated staggered grid," Geophysics **69**, 583–591.
Saenger, E. H., Shapiro, S. A., and Keehm, Y. (**2005**). "Seismic effects of viscous Biot-coupling: Finite difference simulations on micro-scale," Geophys. Res. Lett. **32**, L14310.
Saenger, E. H., Krüger, O. S., and Shapiro, S. A. (**2004**). "Numerical considerations of fluid effects on wave propagation: Influence of the tortuosity," Geophys. Res. Lett. **31**, L21613.
Schwartz, L. M., Auzerais, F. M., Dunsmuir, J., Martys, N., Bentz, D. P., and Torquato, S. (**1994**). "Transport and diffusion in three-dimensional composite media," Physica A **207**, 28–36.
Spanne, P., Thovert, J., Jacquin, J., Lindquist, W. B., Jones, K., and Coker, D. (**1994**). "Synchotron computed microtomography of porous media: Topology and transports," Phys. Rev. Lett. **73**, 2001–2004.
Mavko and Nur (1975).

Revisiting the edge resonance for Lamb waves in a semi-infinite plate

Vincent Pagneux[a)]
Laboratoire d'Acoustique de l'Université du Maine, UMR CNRS 6613 Faculté des Sciences, 72095 Le Mans

(Received 30 January 2006; revised 11 May 2006; accepted 23 May 2006)

The resonance for the elastic plate with a free edge is studied from the point of view of complex resonance. The variations of the real part and of the imaginary part of the complex resonance frequency as a function of the Poisson ratio ν are determined numerically. The results confirm the real resonance frequency theoretically predicted in I. Roitberg *et al.*, Q. J. Mech. Appl. Math. **51**, 1–13 (1998) for a zero Poisson ratio $\nu_1=0$, and a real resonance frequency that corresponds to a Lamé mode is discovered for a Poisson ratio $\nu_2=0.2248$. It is shown that both real resonance frequencies may exist, at these two particular values of ν, because of the decoupling between the propagating Lamb mode and the set of evanescent Lamb modes. © *2006 Acoustical Society of America.* [DOI: 10.1121/1.2214153]

PACS number(s): 43.20.Px, 43.20.Gp, 43.20.Mv [RMW] Pages: 649–656

I. INTRODUCTION

The study of Lamb wave propagation in elastic waveguides is an active domain of research, notably because of the important applications it may have in nondestructive testing.[1] It remains also an interesting domain of research on its own because of its intrinsic and complicated vectorial character due to the coupling between longitudinal and transversal modes. It is remarkable that, for such a venerable subject, there remain fundamental open questions; e.g., the mathematical proof of the completeness of the Lamb modes has not yet been achieved entirely.[2]

Another fundamental problem for Lamb waves that is not fully understood is the edge resonance for a semi-infinite plate with a free edge.[3–9] This resonance occurs for symmetric vibration at frequencies such that only the lowest order symmetric Lamb mode S_0 can propagate, and it is characterized, near a particular frequency, by the abrupt change of the reflection coefficient of the mode S_0 and by the excitation of a localized motion of the plate at the edge. Actually, in Refs. 3–9, it appears as a quasiresonance with a large but finite amplitude response when the incident wave is the S_0 mode, and for Poisson ratio near 0.3. That resonant phenomenon was discovered in an experiment by Glazis in 1956.[3] Thereafter, several authors confirmed the existence of this resonance[4–7] owing to numerical calculations based on modal or finite-element methods. Recently, new experimental and numerical studies[8,9] have shown the same kind of resonances, and the results in Ref. 9 suggest that the resonance persists by coupling symmetric and antisymmetric Lamb modes when the free edge is beveled. Other geometries corresponding to rods[10] or cylindrical shells[11] have also been shown to display the same kind of resonant behavior. Mathematically, the edge resonance for semi-infinite plate has been studied by Roitberg *et al.*[12] who were able to apply the tools of functional analysis to obtain a proof of the existence of a trapped mode for a real frequency in the particular case of zero Poisson ratio ($\nu=0$). One fundamental idea in their paper was to use the absence of coupling between the only propagating Lamb mode S_0 and the remaining infinity of evanescent Lamb modes at $\nu=0$.

In this paper, the aim is to bridge the gap between the particular result of Ref. 12 corresponding to a real resonance frequency at $\nu=0$ and the other results[3–9] corresponding to a quasiresonance and obtained for much higher Poisson ratio $\nu\sim0.3$. We use the concept of complex resonance that has been widely used in acoustics in the resonance scattering theory,[13,14] and that corresponds to a resonance frequency for which a nonzero imaginary part is allowed. For the semi-infinite plate, a complex resonance is associated with a pole in the complex plane of the reflection coefficient[15] of the incident mode S_0, and it corresponds also to an eigenmode with a complex frequency of the elasticity equations without incident wave. Since the problem, when cast in dimensionless form, has only two parameters, the dimensionless frequency and the Poisson ratio, we seek complex resonance frequencies as a function of ν in the physically acceptable range of Poisson ratio $\nu=0$ to $\nu=0.5$.

The paper is organized as follows. The scattering problem is formulated in Sec. II. Section III presents the behavior of the real and imaginary parts of the complex resonance frequency as a function of the Poisson ratio, and the resonant mode is displayed. In Sec. IV, we discuss the results, and the concluding remarks are presented in section V. The numerical method used to obtain the results is briefly described in the Appendix.

II. FORMULATION OF THE PROBLEM

The problem under study corresponds to the bidimensional geometry shown in Fig. 1, with the vertical edge at $x=0$ and the horizontal surfaces at $y=\pm h$. Symmetric in-plane displacements are considered and the frequency is such

a)Electronic mail: vincent.pagneux@univ-lemans.fr

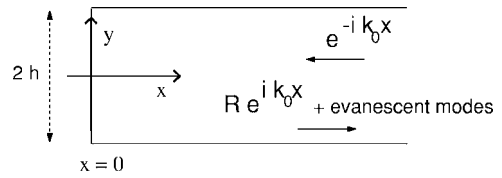

FIG. 1. Geometry of the semi-infinite plate.

that only the first Lamb mode S_0 is propagating. The harmonic time dependence $e^{-i\omega\tau}$ will be omitted in the following. The elasticity equations are

$$-\rho\omega^2\mathbf{w} = \nabla\cdot\sigma, \tag{1}$$

where ρ is the density, $\mathbf{w}=(u,v)^T$ is the displacement, and

$$\sigma = \begin{pmatrix} s & t \\ t & r \end{pmatrix} \tag{2}$$

the stress tensor, with

$$\begin{aligned} &s = \lambda\partial_y v + (\lambda+2\mu)\partial_x u, \\ &t = \mu(\partial_y u + \partial_x v), \quad r = (\lambda+2\mu)\partial_y v + \lambda\partial_x u, \end{aligned} \tag{3}$$

where (λ,μ) are the Lamé's constants. The boundary conditions correspond to traction-free surface of the plate, $\sigma\cdot\mathbf{n}=0$, where $\mathbf{n}$ is the normal to the surface boundary, and are given by $t=r=0$ for $y=\pm h$ and $t=s=0$ for $x=0$.

These equations can be made dimensionless by renormalizing the components of the displacement $\mathbf{w}$ by h, the components of the stress tensor σ by μ, and the coordinates x and y by h. The resulting dimensionless equations are

$$-\Omega^2 u = \partial_x s + \partial_y t, \quad -\Omega^2 v = \partial_x t + \partial_y r, \tag{4}$$

$$\begin{aligned} &s = \gamma\partial_x u + (\gamma-2)\partial_y v, \\ &t = \partial_x v + \partial_y u, \quad r = (\gamma-2)\partial_x u + \gamma\partial_y v, \end{aligned} \tag{5}$$

with dimensionless frequency $\Omega=\omega h/c_T$ and $\gamma=c_L^2/c_T^2=(\lambda+2\mu)/\mu\geq 2$, where $c_T=\sqrt{\mu/\rho}$ and $c_L=\sqrt{(\lambda+2\mu)/\rho}$ are, respectively, the transversal and longitudinal wave speeds. The boundary conditions are

$$r=t=0 \quad \text{at } y=\pm 1, \quad t=s=0 \quad \text{at } x=0. \tag{6}$$

It is important to note that the set of equations (4)–(6) has only two parameters, which are the frequency Ω and the Poisson ratio $\nu=(\gamma-2)/[2(\gamma-1)]$ with $0<\nu<0.5$. In Eq. (5), γ is expressed as a function of ν by $\gamma=2(1-\nu)/(1-2\nu)$.

Since we are interested in the scattering of the propagating mode S_0 by the free edge, the solution can be written[16] in the form of an incident left-going Lamb mode S_0 and a reflected right-going Lamb mode S_0 plus right-going evanescent Lamb modes S_n $(n\geq 1)$,

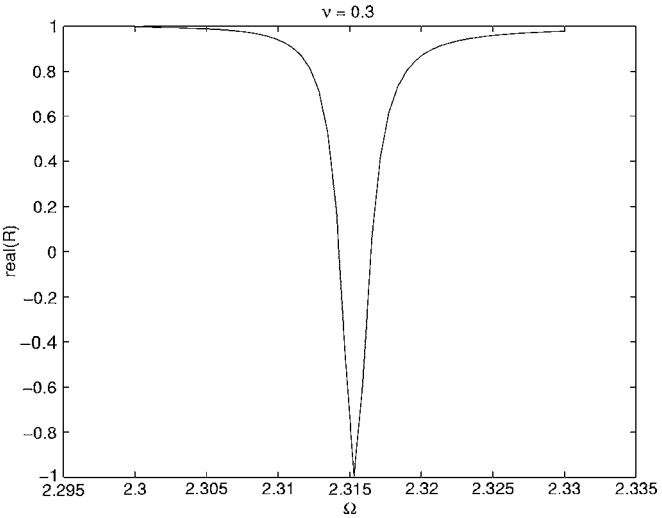

FIG. 2. Real part of the reflection coefficient as a function of frequency. $\nu=0.3$.

$$\begin{pmatrix} u \\ v \\ s \\ t \end{pmatrix} = e^{-ik_0 x}\begin{pmatrix} u_0^- \\ v_0^- \\ s_0^- \\ t_0^- \end{pmatrix} + Re^{ik_0 x}\begin{pmatrix} u_0^+ \\ v_0^+ \\ s_0^+ \\ t_0^+ \end{pmatrix} + \sum_{n=1}^{+\infty} a_n e^{ik_n x}\begin{pmatrix} u_n^+ \\ v_n^+ \\ s_n^+ \\ t_n^+ \end{pmatrix}. \tag{7}$$

The left-going Lamb S_0 mode corresponds to eigenvectors $[u_0^-(y),v_0^-(y),s_0^-(y),t_0^-(y)]^T$ with wave number $-k_0$, and the right-going Lamb modes correspond to eigenvector $[u_n^+(y),v_n^+(y),s_n^+(y),t_n^+(y)]^T$ with wave number k_n $(n\geq 0)$. To completely define R we need to specify that we use the symmetry[17,16] between right-going and left-going Lamb modes such that $(u_n^-,t_n^-)^T=(u_n^+,t_n^+)^T$ and $(s_n^-,v_n^-)^T=-(s_n^+,v_n^+)^T$.

To calculate the solution of the problem, we use a hybrid method with a collocation discretization along the coordinate y and a modal approach along the coordinate x. This method allows us to find the reflection coefficient R and the coefficients a_n. For the sake of clarity, it is described in the Appendix.

For real Ω, the conservation of energy implies[17] that $|R(\Omega,\nu)|=1$. Figure 2 shows an example for $\nu=0.3$ of the behavior of the real part of R as a function of frequency. It is the classical type of result that has been shown in earlier paper on the edge resonance (see Refs. 4–8 for instance); it displays an abrupt change of R in a narrow range of frequencies typical of the edge resonance.[5] This is the typical behavior for a quasiresonance.

For complex Ω, R is not constrained to be on the unit circle, and complex resonances correspond to frequency where R is infinite. These poles of R in the complex Ω plane have negative imaginary part $\mathrm{Im}(\Omega)<0$ (see Ref. 15 for a clear discussion) and they correspond to a solution (7) which is an eigensolution of the elasticity equations with only right-going waves. This eigenmode has a temporal dependence $e^{-i\omega\tau}$ and is thus decaying with time at a rate which is given by the imaginary part of the complex resonance frequency. In physical units, the decaying rate (the inverse of the "ringing time") is given by $\alpha=(c_T/h)\mathrm{Im}(\Omega_R)$, where Ω_R is the com-

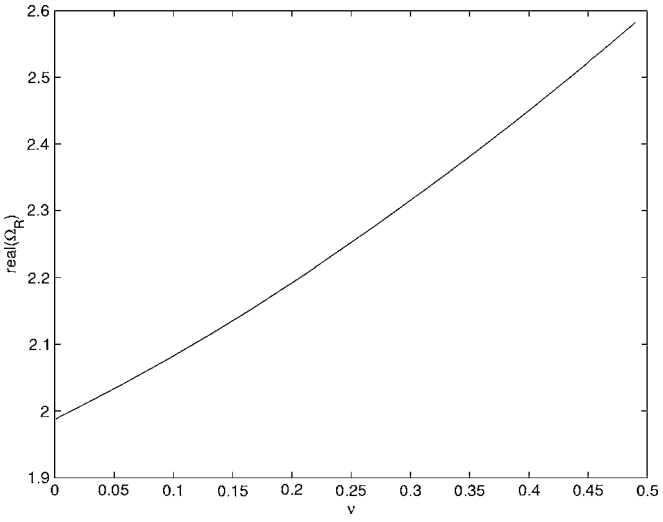

FIG. 3. Real part of the complex resonance frequency as a function of the Poisson ratio ν.

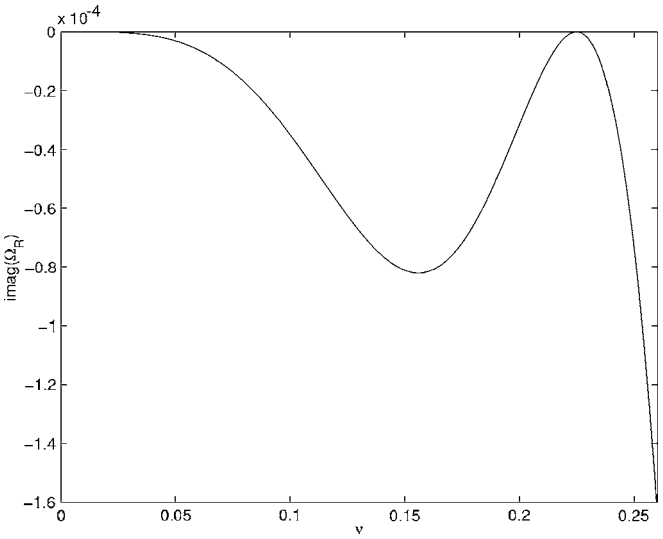

FIG. 5. Detail of the preceding Fig. 4.

plex resonance frequency. Moreover, to poles Ω_R of R with $\mathrm{Im}(\Omega_R)<0$ correspond the complex conjugates $\bar{\Omega}_R$, with $\mathrm{Im}(\bar{\Omega}_R)>0$, which are zeros of R such that $R(\bar{\Omega}_R)=0$.[15] Numerically we seek these zeros of R by a Newton-Raphson method.

III. RESULTS

In this section we present the results of the problem posed in Sec. II owing to the numerical method described in the Appendix. Numerically, one and only one complex resonance frequency Ω_R has been found for each value of the Poisson ratio ν. Figures 3–5 display the principal results of that paper. They show the behavior of the complex resonance frequency as a function of the Poisson ratio. The real part of the complex resonance frequency (Fig. 3) varies almost linearly with ν. For practical purpose, a very good approximation of this real part is given by the empirical formula

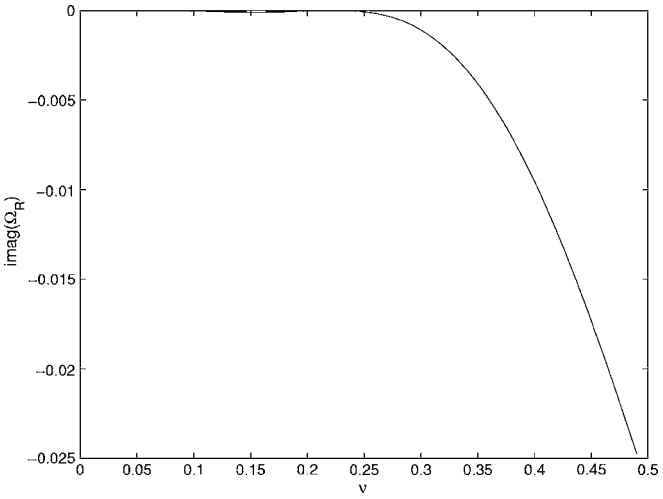

FIG. 4. Imaginary part of the complex resonance frequency as a function of the Poisson ratio ν.

$$\mathrm{Re}(\Omega_R)=0.652\nu^2+0.898\nu+1.9866, \tag{8}$$

whose error is less than 10^{-3}. The values of the real resonance frequencies existing in the literature[4–9] are recovered and are very well approximated by the formula (8). This correspondence between the real part of the complex resonance frequency computed in this work and the real frequency obtained in Refs. 4–9 by looking at real frequency where the reflection coefficient changes abruptly is guaranteed by the very small values of the imaginary part of the complex resonance frequency. This fact is confirmed in Fig. 4, where the imaginary part of Ω_R is plotted as a function of the Poisson ratio. It can be seen that $\mathrm{Im}(\Omega_R)$ remains close to zero for $\nu<0.25$ and decreases substantially for higher ν. To gain insights into the behavior of $\mathrm{Im}(\Omega_R)$ in the range $0<\nu<0.25$, Fig. 5 shows a magnified view of Fig. 4. It appears that $\mathrm{Im}(\Omega_R)$ is zero for two values of the Poisson ratio: $\nu_1=0$ and $\nu_2=0.2248$. The first value, $\nu_1=0$, corresponds to the real frequency resonance discovered in Ref. 12. The second value, $\nu_2=0.2248$, corresponds to numerical accuracy to a resonance frequency $\Omega_R=\pi/\sqrt{2}$, i.e., to an S_0 Lamé mode as will be seen in the following section. Note that if the value $\Omega_R=\pi/\sqrt{2}$ is used in Eq. (8), it yields a second-degree equation with unknown ν, the solution of which is $\nu=\nu_2=0.2248$. Note also that near the two real resonance frequencies the local behavior of $\mathrm{Im}(\Omega_R)$ is $\mathrm{Im}(\Omega_R)\sim C_1\nu^4$ when $\nu\to\nu_1=0$ and $\mathrm{Im}(\Omega_R)\sim C_2(\nu-\nu_2)^2$ when $\nu\to\nu_2$, where C_1 and C_2 are constants. It would be interesting to theoretically find these asymptotic expressions with the techniques presented in Ref. 15. In the same manner as for the real part of Ω_R, the imaginary part is well approximated by the empirical formula

$$\mathrm{Im}(\Omega_R)=-\frac{c\nu^4(\nu-\nu_2)^2}{1+\left(\frac{\nu-\nu_3}{a}\right)^2+\left(\frac{\nu-\nu_3}{b}\right)^4}, \tag{9}$$

where $\nu_3=0.2062$, $a=0.1696$, $b=0.2606$, and $c=1/0.0313$. This empirical formula has been guessed owing to the

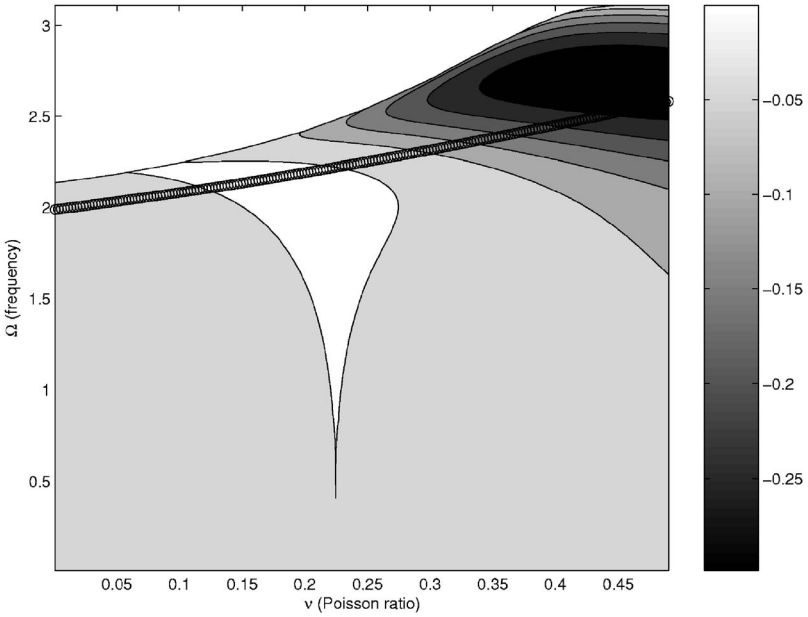

FIG. 6. Background phase ϕ as a function of the frequency Ω and of the Poisson ratio ν. Circles (○) correspond to the real part of the complex resonance frequency Ω_R as a function of ν.

known local behavior of $\mathrm{Im}(\Omega_R)$ near ν_1 and ν_2 and gives an error less than 1% on the full range of Poisson ratio. Actually, if the curves associated with Eqs. (8) and (9) were plotted on the corresponding figures, it could not be distinguished from the curves already displayed. A quite remarkable point is the symmetry with respect to ν_3 in the expression (9), and it remains an open question to know if it occurs only by chance or if it is due to some hidden mathematical symmetry in the problem.

Another quantity of interest is the background phase ϕ that can be defined for real frequency Ω by the relation[14]

$$R = \frac{\Omega - \bar{\Omega}_R}{\Omega - \Omega_R} e^{i\phi}. \tag{10}$$

This relation is valid for real frequency Ω, i.e., when $|R|=1$, and it reflects the fact that the complex Ω_R and its conjugate $\bar{\Omega}_R$ are, respectively, a pole and a zero of R. The background phase ϕ represents the slow variation of the reflection coefficient superposed on the rapid variation due to the presence of the pole Ω_R. Figure 6 shows the behavior of ϕ on the whole range of Poisson ratio ν and for real frequency Ω sustaining one propagating Lamb mode (note that in the limit $\nu \to 0.5$ the first cut-on frequency for higher order modes is known[18] to be $\Omega_c = \pi$). It can be seen that the values of the background phase ϕ are very low in the major part of the (ν, Ω) plane, with a maximum amplitude of 0.3 for the higher Poisson ratio (around 0.45). Consequently, because of the low value of ϕ, the variations of R are almost entirely due to the presence of the complex resonance frequency Ω_R.

Figures 7–10 represent the patterns of the elastic fields $u(x,y)$, $v(x,y)$, $s(x,y)$, and $t(x,y)$ at the second real resonance frequency $\Omega_R = \pi/\sqrt{2}$ with $\nu = \nu_2 = 0.2248$. These patterns are almost the same as for the other real resonance frequency $\Omega_R = 1.9866$ with $\nu = \nu_1 = 0$. Because of the symmetry of the motion, only the upper part, $y > 0$, of the geometry, $x \geq 0$ and $|y| \leq 1$, of the semi-infinite plate is shown. In Figs. 7 and 8, it can be seen that the motion is localized near the edge and the largest amplitudes are at the corners. Incidentally, the representation in Figs. 9 and 10 of the two components, s and t, of the stress tensor permits us to verify that they satisfy the boundary condition, $s = t = 0$ at $x = 0$ and $t = 0$ at $y = 1$. It is interesting to note that the lines of equal values of t form small closed contours in the vicinity of the corner; it has to be associated with the type of local behavior of the stress at corner (stress singularity) which is similar to the corner eddies for creeping flows in fluid mechanics.[19] An illustration of the shape of the resonant mode for the entire plate is given in Fig. 11 and can help one have a clearer view of the phenomenon. In this figure, the amplitude of the mode has been chosen arbitrarily so that the shape of the motion can be seen easily.

IV. INTERPRETATION OF THE RESULTS FOR THE TWO REAL RESONANCES

In the preceding section it has been shown that there exists a complex resonance frequency for $0 \leq \nu < 0.5$ and,

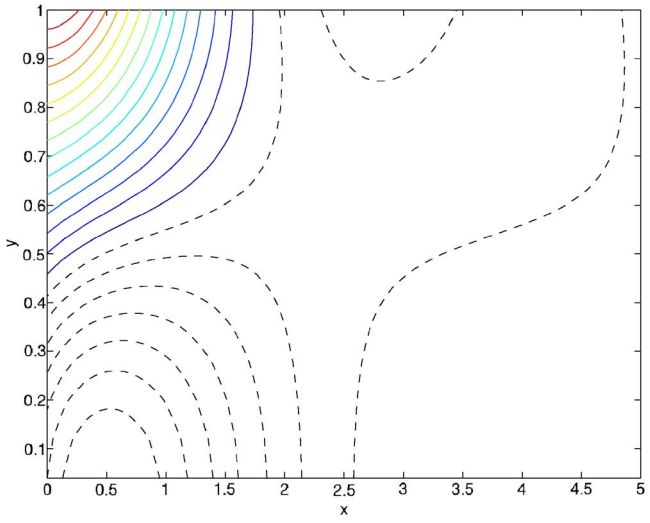

FIG. 7. (Color online) Contour lines for the displacement u at the resonance $\nu = \nu_2 = 0.2248$. Plain lines for positive values and dashed lines for negative values.

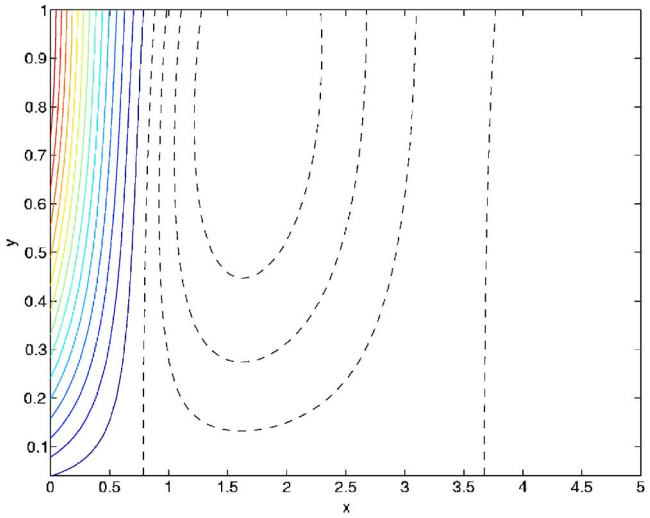

FIG. 8. (Color online) Contour lines for the displacement v at the resonance $\nu=\nu_2=0.2248$. Plain lines for positive values and dashed lines for negative values.

that for two particular values of the Poisson ratio, $\nu_1=0$ and $\nu_2=0.2248$, the imaginary part of the complex resonance frequency is zero. In the following, the existence of the two real resonance frequencies for ν_1 and ν_2 is explained by showing that in both cases there is a decoupling between the propagating Lamb mode S_0 and the higher order evanescent Lamb modes.

The solution in term of Lamb modes [Eq. (7)] can be rewritten as

$$\begin{pmatrix} \mathbf{X}(x,y) \\ \mathbf{Y}(x,y) \end{pmatrix} = \begin{pmatrix} \mathbf{X}_0(y) \\ -\mathbf{Y}_0(y) \end{pmatrix} e^{-ik_0 x} + \sum_{n\geqslant 0} a_n \begin{pmatrix} \mathbf{X}_n(y) \\ \mathbf{Y}_n(y) \end{pmatrix} e^{ik_n x}, \quad (11)$$

with $a_0=R$ and where $\mathbf{X}=(u,t)^T$, $\mathbf{Y}=(-s,v)^T$ and $\mathbf{X}_n=(u_n^+,t_n^+)^T$, $\mathbf{Y}_n=(-s_n^+,v_n^+)^T$. The symmetry between right-going and left-going modes has been used so that $(u_n^-,t_n^-)^T=(u_n^+,t_n^+)^T=\mathbf{X}_n$ and $(-s_n^-,v_n^-)^T=-(-s_n^+,v_n^+)^T=-\mathbf{Y}_n$. The interest of this formulation is that it can be easily projected owing to the biorthogonality relation[17,16,20]

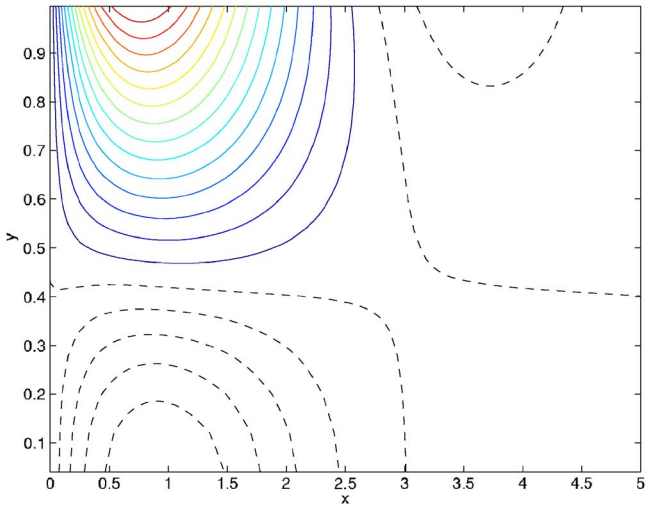

FIG. 9. (Color online) Contour lines for the stress tensor component s at the resonance $\nu=\nu_2=0.2248$. Plain lines for positive values and dashed lines for negative values.

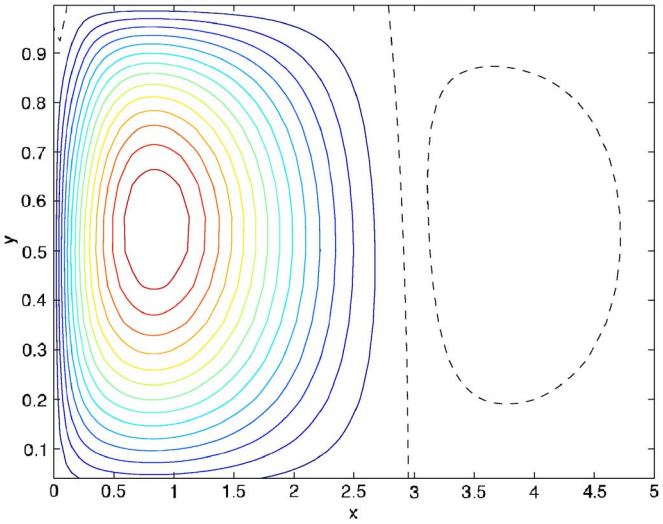

FIG. 10. (Color online) Contour lines for the stress tensor component t at the resonance $\nu=\nu_2=0.2248$. Plain lines for positive values and dashed lines for negative values.

$$\int_{-h}^{h} \mathbf{X}_n \cdot \mathbf{Y}_m dy = J_n \delta_{nm}. \quad (12)$$

To find the unknown components, a_n $(n\geqslant 0)$, the two lines of Eq. (11) are projected[16], using Eq. (12), at $x=0$ where $t=0$ and $s=0$. The following system of equations is then obtained:

$$J_m(\delta_{0m}+a_m) = -\sum_{n\geqslant 0} (a_n+\delta_{0n}) \int_{-h}^{h} u_n^+ s_m^+ dy, \quad (13)$$

$$J_m(-\delta_{0m}+a_m) = \sum_{n\geqslant 0} (a_n-\delta_{0n}) \int_{-h}^{h} v_n^+ t_m^+ dy. \quad (14)$$

Generally, this system of equations is not easy to solve because when truncated to a finite size, say N, it seems to be redundant with $2N$ equations and N unknowns a_n. Actually, this intricacy comes from the boundary conditions at $x=0$ which impose one component of $\mathbf{X}$ $(t=0)$ and one compo-

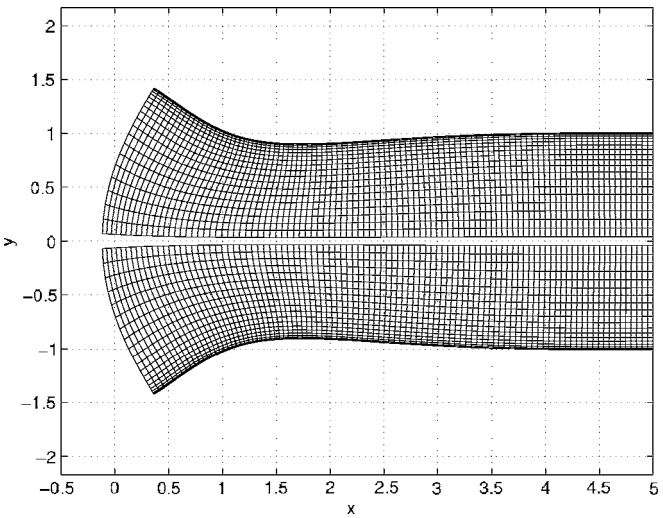

FIG. 11. Shape of the semi-infinite plate at the resonance $\nu=\nu_2=0.2248$.

nent of $\mathbf{Y}$ ($s=0$). If the boundary conditions were entirely on $\mathbf{X}$ or on $\mathbf{Y}$ (often called mixed boundary conditions; see for instance Ref. 21), the resulting system would not be redundant and the situation would be easier. The difficulty to solve the system (13) and (14) is one reason why, in this particular free-edge problem, we choose another numerical method (see the Appendix) to solve the scattering problem. Nevertheless, the system is greatly simplified for $\nu=0$ and for Lamé mode where $\Omega=\pi/\sqrt{2}$ and $\nu\neq 0$. In fact, these two cases correspond to the two real resonance frequencies found in Sec. III.

For the first case where $\nu=0$, studied in Ref. 12, Eqs. (4) and (5) are greatly simplified since $\gamma=2$. It appears that the mode S_0 is such that $u_0^+=1$, $t_0^+=0$, $s_0^+=2ik_0$, $v_0^+=0$, and $k_0=\Omega/\sqrt{2}$. For the second case, where $\Omega=\pi/\sqrt{2}$ and $\nu\neq 0$, the mode S_0 is a Lamé mode[22] such that $u_0^+=d\psi_0/dy$, $t_0^+=0$, $s_0^+=2ik_0u_0$, $v_0^+=-ik_0\psi_0$, and $k_0=\Omega/\sqrt{2}=\pi/2$, where $\psi_0(y)$ is the transverse potential. The Lamé mode is a purely transversal wave that corresponds to transversal plane waves reflecting on the horizontal boundaries with angle $\pi/4$ and for which there is no mode conversion with longitudinal waves. In fact, the first case is also a Lamé mode with $k_0=\Omega/\sqrt{2}$, but it is a degenerate Lamé mode for the special case of zero Poisson ratio ν; it is purely longitudinal with a constant longitudinal potential $\phi_0(y)=C$.

For both cases, by using the biorthogonality relation (12) and the fact that $t_0^+=0$, it can be verified that we have the following useful relations:

$$\int_{-h}^{h} u_0^+ s_n^+ dy = \int_{-h}^{h} u_n^+ s_0^+ dy = -J_0\delta_{0n}, \tag{15}$$

$$\int_{-h}^{h} v_0^+ t_n^+ dy = \int_{-h}^{h} v_n^+ t_0^+ dy = 0. \tag{16}$$

Then, Eq. (13) gives no information for $m=0$ and becomes, for $m\geqslant 1$,

$$J_m a_m = -\sum_{n\geqslant 1} a_n \int_{-h}^{h} u_n^+ s_m^+ dy, \tag{17}$$

which involves only the evanescent modes and is thus decoupled from the propagating mode S_0. Equation (14) for $m\geqslant 1$ becomes

$$J_m a_m = \sum_{n\geqslant 1} a_n \int_{-h}^{h} v_n^+ t_m^+ dy. \tag{18}$$

For $m=0$, i.e., the projection on mode S_0, Eq. (14) becomes

$$J_0(a_0-1)=0, \tag{19}$$

which yields immediately $R=a_0=1$.

Consequently, it appears that, for both cases, the scattering problem of the mode S_0 can be solved analytically to give $R=1$ [from Eq. (19)]. Besides, the components of the evanescent modes have to verify the homogeneous Eqs. (17) and (18). This means that for $\nu=0$ and for $\Omega=\pi/\sqrt{2}$, the mode S_0 is very simply reflected by the free edge since it is not coupled to the evanescent modes. In addition, the elastic field spanned by all the evanescent modes cannot propagate toward infinity, but there may be a nontrivial solution to Eqs. (17) and (18); it is the typical situation for the existence of trapped modes which have discrete eigenvalue embedded in the continuum of scattering eigenvalues,[23–26] below the first cutoff frequency of the evanescent modes. Here, for the first case, $\nu=0$, Ω plays the role of the eigenvalue while, for the second case, $\Omega=\pi/\sqrt{2}$, ν is the eigenvalue. Usually, for a scalar case such as acoustic waveguides, the decoupling between evanescent and propagative waves is simply due to spatial symmetries between even and odd (i.e., symmetric and antisymmetric) solutions. Here, the decoupling between the propagative mode and the evanescent modes is subtler and is due to an internal[12] (hidden) symmetry of the elasticity equations. For the Lamé mode the decoupling can be also physically understood by noting that, if there is no mode conversion at the horizontal boundaries, there is no more mode conversion at the vertical boundary, which is also impinged with an angle of $\pi/4$.

V. CONCLUDING REMARKS

We have shown the existence of a complex resonance frequency Ω_R when the Poisson ratio ν varies between 0 and 0.5. The real part of Ω_R gives the frequency of the usual edge (quasi-)resonance that had been discussed in the literature; it increases monotonically from about 2 at $\nu=0$ up to about 2.6 at $\nu=2.5$. The imaginary part of Ω_R gives the decaying rate of the resonance and has a more complicated behavior; it is zero for two values of the Poisson ratio, $\nu_1=0$ and $\nu_2=0.2248$, and decreases up to -2.510^{-3} at $\nu=0.5$. The two values of ν where the complex resonance frequency has a zero imaginary part correspond to trapped modes for which there is a decoupling between the propagating waves and the evanescent waves. The first decoupling at $\nu=\nu_1=0$ is due to the special structure of the elasticity equations at this particular Poisson ratio value, and the second decoupling is due to the decoupling between the propagating Lamé mode and the higher order evanescent modes. Besides, it is amusing to note that, on the one hand, these two trapped modes can exist due to the decoupling between the Lamb mode S_0 and the higher order Lamb modes and, on the other hand, the edge resonance is often presented[8] as a consequence of the coupling between the mode S_0 and the higher order modes (which is not false). In the future, it would be interesting to study the complex resonance frequency for more complicated edge geometries such as the beveled edge, for instance.

APPENDIX: NUMERICAL METHOD

The elasticity equations (4) and (5) can be written [see also Ref. 17]

$$\partial_x \begin{pmatrix} \mathbf{X} \\ \mathbf{Y} \end{pmatrix} = \begin{pmatrix} 0 & F \\ G & 0 \end{pmatrix} \begin{pmatrix} \mathbf{X} \\ \mathbf{Y} \end{pmatrix}, \tag{A1}$$

where $\boldsymbol{X}=(u,t)^T$, $\boldsymbol{Y}=(-s,v)^T$, and where F and G are the operator-matrices,

$$F=\begin{pmatrix} -\frac{1}{\gamma} & -\frac{\gamma-2}{\gamma}\partial_y \\ \frac{\gamma-2}{\gamma}\partial_y & -\Omega^2-4\frac{\gamma-1}{\gamma}\partial_{y^2} \end{pmatrix}, \tag{A2}$$

$$G=\begin{pmatrix} \Omega^2 & \partial_y \\ -\partial_y & 1 \end{pmatrix}. \tag{A3}$$

Concerning the boundary conditions (6), since the problem is considered as an evolution equation [Eq. (A1)] on $\boldsymbol{X}$ and $\boldsymbol{Y}$, we always use the expressions of r written as a linear function of $\boldsymbol{Y}$,

$$r:\mathbf{Y}\to r(\mathbf{Y})=(\gamma-2)/\gamma s+4(\gamma-1)/\gamma\partial_y v, \tag{A4}$$

which implies that the boundary conditions are entirely expressed in terms of $\boldsymbol{X}$ and $\boldsymbol{Y}$.

We use the Differentiation Matrix Suite proposed by Weideman and Reddy[27] to construct the numerical method that solves the scattering problem of Sec. II. This is a spectral collocation method based on Chebyshev polynomials which yields the discretization of the differential operators ∂_y and ∂_y^2. An unknown function q is written as $q=\Sigma_{n=1}^{N}\tilde{q}_n\chi_n(y)$, where the χ_n are expressed in terms of Chebyshev polynomials. Practically, in the discretization along y, the function q will be replaced by the vector $\tilde{\mathbf{q}}$, the first derivative dq/dy will be replaced by $D_1\tilde{\mathbf{q}}$, and d^2q/dy^2 will be replaced by $D_2\tilde{\mathbf{q}}$. Besides, with this collocation method $\tilde{q}_n=q(y_n)$ where $y_n=\cos[(n-1)\pi/(N-1)]$[27].

In our problem the displacement and the stress tensor components are written as

$$(u,v,s,t,r)^T=\sum_{n=1}^{N}(\tilde{u}_n,\tilde{v}_n,\tilde{s}_n,\tilde{t}_n,\tilde{r}_n)^T\chi_n(y).$$

Some care has to be taken to impose the boundary conditions at $y=\pm1$. One pair of conditions, $t(y\pm1)=0$, yields immediately $\tilde{t}_1=\tilde{t}_N=0$. The other boundary condition, $r(y\pm1)=0$, yields $\tilde{r}_1=\tilde{r}_N=0$ and needs to be translated in terms of quantities appearing in Eq. (A1). From Eq. (A4) we have $\tilde{\mathbf{r}}=(\gamma-2)\tilde{\mathbf{s}}+4(\gamma-1)D_1\tilde{\mathbf{v}}$ which yields $\tilde{r}_1=(\gamma-2)\tilde{s}_1+4(\gamma-1)\mathbf{l}_1^T\tilde{\mathbf{v}}$ and $\tilde{r}_N=(\gamma-2)\tilde{s}_N+4(\gamma-1)\mathbf{l}_N^T\tilde{\mathbf{v}}$, where $\mathbf{l}_1$, respectively $\mathbf{l}_N$, is the vector of the first row, respectively, last row, of the matrix D_1. Eventually the boundary conditions $r(y\pm1)=0$ are written as $\tilde{s}_1=-4(\gamma-1)/(\gamma-2)\mathbf{l}_1^T\tilde{\mathbf{v}}$ and $\tilde{s}_N=-4(\gamma-1)/(\gamma-2)\mathbf{l}_N^T\tilde{\mathbf{v}}$. Since the boundary conditions impose the values of $\tilde{t}_1$, $\tilde{t}_N$, $\tilde{s}_1$, and $\tilde{s}_N$, in the following the vectors of unknowns $\tilde{\mathbf{t}}$ and $\tilde{\mathbf{s}}$ are to be understood with components $(\tilde{t}_2,\ldots,\tilde{t}_{N-1})$ and $(\tilde{s}_2,\ldots,\tilde{s}_{N-1})$. With this discretization, the elasticity Eqs. (A1) become

$$\frac{d}{dx}\begin{pmatrix}\tilde{\mathbf{u}}\\ \tilde{\mathbf{t}}\end{pmatrix}=\begin{pmatrix} -\frac{1}{\gamma}I & M_1 \\ \frac{\gamma-2}{\gamma}D_1 & M_2 \end{pmatrix}\begin{pmatrix}-\tilde{\mathbf{s}}\\ \tilde{\mathbf{v}}\end{pmatrix}, \tag{A5}$$

$$\frac{d}{dx}\begin{pmatrix}-\tilde{\mathbf{s}}\\ \tilde{\mathbf{v}}\end{pmatrix}=\begin{pmatrix} \Omega^2 I & D_1 \\ -D_1 & I \end{pmatrix}\begin{pmatrix}\tilde{\mathbf{u}}\\ \tilde{\mathbf{t}}\end{pmatrix}, \tag{A6}$$

with

$$M_1=-\frac{\gamma-2}{\gamma}D_1-4\frac{\gamma-1}{\gamma-2}\begin{pmatrix}\mathbf{l}_1^T\\ 0\cdots0\\ \vdots\\ 0\cdots0\\ \mathbf{l}_N^T\end{pmatrix} \tag{A7}$$

and

$$M_2=-\Omega^2 I-4\frac{\gamma-1}{\gamma-2}D_2+4\frac{\gamma-1}{\gamma}(\mathbf{c}_1\mathbf{l}_1^T+\mathbf{c}_N\mathbf{l}_N^T), \tag{A8}$$

where $\mathbf{c}_1$, respectively $\mathbf{c}_N$, is the vector of the first column, respectively, last column, of the matrix D_1 and I is the identity matrix. Each system of ordinary differential equations (ODE) in Eqs. (A5) and (A6) is of size $2(N-1)$. For the sake of clarity and to keep the notation from becoming messy, all the matrices are to be understood as having the dimension corresponding to the vectors that they link together; for instance, the identity matrix in the first entry of Eq. (A5) is of dimension $N\times(N-2)$ because it links $d\tilde{\mathbf{u}}/dx$ and $\tilde{\mathbf{s}}$. It remains to impose the assumption of symmetric motion on the system of ODE. First, we impose that N is an even number so that $N=2N_e$. Thereafter, the symmetric motion implies that u and s are even functions of y and that v and t are odd functions of y, which is translated to $u_{2N_e-n+1}=u_n$, $s_{2N_e-n+1}=s_n$, $v_{2N_e-n+1}=-v_n$, and $t_{2N_e-n+1}=-t_n$ for $1\leqslant n\leqslant N_e$.

At this point, the problem is discretized with respect to the coordinate y and it remains to solve the system of ordinary differential Eqs. (A5) and (A6). To do that, the matrix of this system of ODE is diagonalized, yielding $4(N_e-1)$ eigenvalues and eigenvectors. Actually, it is equivalent to obtain numerically the Lamb modes with the Chebyshev polynomials; there are $2(N_e-1)$ eigenvectors corresponding to left-going Lamb modes and $2(N_e-1)$ eigenvectors corresponding to right-going Lamb modes. The solution to the ODE needs the $4(N_e-1)$ coefficients corresponding to the $4(N_e-1)$ eigenvectors. The $2(N_e-1)$ coefficients of the numerical left-going Lamb modes are given by the radiation condition: the incident S_0 mode is given and the $2N_e-3$ left-going evanescent numerical modes are set to zero. The $2(N_e-1)$ coefficients of the numerical right-going Lamb modes are given by the boundary condition at $x=0$ that imposes $\tilde{\mathbf{s}}(x=0)=0$ (N_e conditions) and $\tilde{\mathbf{t}}(x=0)=0$ (N_e-1 conditions). Finally, the resulting system of $2(N_e-1)$ equations is solved and permits one to obtain the reflection coefficient R as well as the elastic fields u, v, s, and t. The complex resonance frequency is found by seeking complex Ω where R is zero by a Newton-Raphson method.

In practice, the computations have been done with $N_e=20$. The advantage of this spectral collocation method is that it is very accurate: for real frequency Ω the conservation of energy is well respected since typically $|R|-1\sim10^{-10}$ and the accuracy on the resonance frequencies Ω_R is 10^{-8}.

Note added in proofs: During the reviewing of this paper, the author has been informed of a related study (V. Zernov, A. A. Pichugin and J. Kaplunov, Proc. R. Soc. A 2006, vol. 462, p. 1255–1270) confirming the real resonances.

[1]D. Ensminger, *Ultrasonics, Fundamentals, Technology, Applications* (Marcel Dekker, New York, 1988).
[2]H. Besserer and P. G. Malishewsky, "Mode series expansions at vertical boundaries in elastic waveguides," Wave Motion **51**, 1–13 (2004).
[3]E. A. G. Shaw, "On the resonant vibrations of thick barium titanate disks," J. Acoust. Soc. Am. **28**, 38–50 (1956).
[4]P. J. Torvik, "Reflection of wave trains in semi-infinite plates," J. Acoust. Soc. Am. **41**, 346–353 (1967).
[5]B. A. Auld and E. M. Tsao, "A variational analysis of edge resonance in a semi-infinite plate," IEEE Trans. Sonics Ultrason. **24**, 317–326 (1977).
[6]M. Koshiba, S. Karakida, and M. Suzuki, "Finite-element analysis of edge resonance in a semi-infinite plate," Electron. Lett. **19**, 256–257 (1983).
[7]R. D. Gregory and I. Gladwell, "The reflection of a symmetric Rayleigh-Lamb wave at the fixed or free edge of a plate," J. Elast. **13**, 185–206 (1983).
[8]E. Le Clezio, M. V. Predoi, M. Castaings, B. Hosten, and M. Rousseau, "Numerical predictions and experiments on the free-plate edge mode," Ultrasonics **41**, 25–40 (2003).
[9]N. Wilkie-Chancelier, H. Duflo, A. Tinel, and J. Duclos, "Numerical description of the edge mode at the beveled extremity of a plate," J. Acoust. Soc. Am. **117**, 194–199 (2005).
[10]M. de Billy, "End resonance in infinite immersed rods of different cross sections," J. Acoust. Soc. Am. **100**, 92–97 (1996).
[11]J. Kaplunov, L. Y. Kossovich, and M. V. Wilde, "Free localized vibrations of a semi-infinite cylindrical shell," J. Acoust. Soc. Am. **107**, 1383–1393 (2000).
[12]I. Roitberg, D. Vassiliev, and T. Weidl, "Edge resonance in an elastic semi-strip," Q. J. Mech. Appl. Math. **51**, 1–13 (1998).
[13]L. Flax, L. R. Dragonette, and H. Überall, "Theory of elastic resonance excitation by sound scattering," J. Acoust. Soc. Am. **63**, 723–731 (1978).
[14]L. Flax, G. Gaunaurd, and H. Überall, "Theory of resonance scattering," in *Physical Acoustics*, edited by W. P. Mason and R. N. Thurston (Academic, New York 1981), Vol. **XV**, pp. 191–294.
[15]A. Aslanyan, L. Parnovski, and D. Vassiliev, "Complex resonances in acoustic waveguides," Q. J. Mech. Appl. Math. **53**, 429–447 (2000).
[16]V. Pagneux and A. Maurel, "Lamb wave propagation in inhomogeneous elastic waveguides," Proc. R. Soc. London, Ser. A **458**, 1913–1930 (2002).
[17]V. Pagneux and A. Maurel, "Scattering matrix properties with evanescent modes for waveguides in fluids and solids," J. Acoust. Soc. Am. **116**, 1913–1920 (2004).
[18]A. Freedman, "The variation, with the Poisson ratio, of Lamb modes in a free plate. I. General spectra," J. Sound Vib. **137**, 209–230 (1990).
[19]V. V. Meleshko, "Selected topics in a history of the two-dimensional biharmonic problem," Appl. Mech. Rev. **56**, 33–85 (2003).
[20]W. B. Fraser, "Orthogonality relation for the Rayleigh-Lamb modes of vibration of a plate," J. Acoust. Soc. Am. **59**, 215–216 (1976).
[21]J. D. Achenbach, *Wave Propagation in Elastic Solids* (North Holland, Amsterdam, 1987).
[22]D. Royer and E. Dieulesaint, *Elastic Waves in Solids I: Free and Guided Propagation*, Advanced Texts in Physics (Springer, New York 2000).
[23]F. Ursell, "Trapping modes in the theory of surface waves," Proc. Cambridge Philos. Soc. **47**, 347–358 (1951).
[24]D. S. Jones, "The eigenvalues of $\Delta u+\lambda u=0$ when the boundary conditions are given on semi-infinite domains," Proc. Cambridge Philos. Soc. **49**, 668–684 (1953).
[25]D. V. Evans, M. Levitin, and D. Vassiliev, "Existence theorems for trapped modes," J. Fluid Mech. **261**, 21–31 (1994).
[26]A. S. Bonnet-Ben Dhia and F. Mahé, "A guided mode in the range of the radiation modes for a rib waveguide," J. Opt. **28**, 41–43 (1997).
[27]J. A. C. Weideman and S. C. Reddy, "A MATLAB differentiation matrix suite," ACM Trans. Math. Softw. **26**, 465–519 (2000).

Measurement of the frequency dependence of the ultrasonic parametric threshold amplitude for a fluid-filled cavity

A. Teklu
Department of Physics & Astronomy, College of Charleston, 66 George Street, Charleston, South Carolina 29424

Michael S. McPherson, M. A. Breazeale, Roger D. Hasse, and Nico F. Declercq[a)]
National Center for Physical Acoustics, The University of Mississippi, 1 Coliseum Drive, University, Mississippi 38677

(Received 19 August 2005; revised 22 May 2006; accepted 25 May 2006)

By driving a transducer at one end of a fluid-filled cavity parallel to a rigid plane reflector at the other end, standing ultrasonic waves can be generated. Variations in the cavity length resulting from transducer motion lead to the generation of resonant frequencies lower than the drive frequency (known as fractional harmonics). This excitation of fractional harmonics in a liquid-filled cavity by ultrasonic waves was described previously as a parametric phenomenon [Laszlo Adler and M. A. Breazeale, J. Acoust. Soc. Am. **48**, 1077–1083 (1970)]. This system was modeled by using a modified Mathieu's equation whose solution resulted in the prediction of critical threshold drive amplitude for the excitation of parametric oscillation. The apparatus used by Adler and Breazeale was recently refined for accurate measurements of the threshold amplitude for parametric excitation at frequencies ranging from 2 to 7 MHz. The measurements showed that in this range the threshold amplitude increases with increasing drive frequency in apparent discrepancy with the results of Adler and Breazeale. Analysis of the theory indicates, however, that both past and current results lie in two different stability zones and each is in agreement with the existing theory.
 [DOI: 10.1121/1.2214457]

PACS number(s): 43.25.Gf [MFH] Pages: 657–660

I. BACKGROUND

Parametric excitation of a resonant system is the self-excitation of a non-characteristic mode of the system. This is caused by a periodic variation of a parameter of the system upon which the natural frequency of the mode depends.[1] For this excitation to occur, the resonant frequency of the system must be nearly equal to one-half the frequency at which the parameter varies. In addition, the parameter must vary with an amplitude that is greater than a critical threshold value. This threshold amplitude for the generation of fractional harmonics is determined by the amount of dissipation in the system as well as the relationship between the exciting frequency and the excited frequency. Stabilization of the amplitude depends on the amount of dissipation and nonlinearity of the system.

Numerous examples of parametric phenomena are observed in different branches of physics. Perhaps the most familiar example is the operation of a playground swing. The child on the swing must periodically vary the vertical position of the center of mass so that the effective length of the pendulum changes. Synchronization of this change with the oscillation causes the oscillation amplitude to increase gradually from a small initial amplitude. The important point is that the resonant frequency of the swing, determined by the swing's effective length, is modulated by the periodic raising and lowering of the center of mass.[1] The amplitude is limited by the nonlinearity of the system.[1]

Other examples include the following: a driven tuning fork with one prong changing the length of a stretched string;[2] transverse vibration of a rod under the action of a longitudinal periodic force at twice the resonant frequency;[3] parametrically excited fractional phonons in solids;[4] electromechanical oscillator;[5] and liquid-filled ultrasonic resonant system operated as an acoustical parametric generator.[6–8]

II. THEORY

Adler and Breazeale made the first detailed investigation of a fluid-filled cavity caused to parametrically resonate by ultrasound.[9] Further investigations were made by Yen.[10] Such a cavity has standing-wave solutions satisfying the acoustic boundary conditions only for a series of specific frequencies known as the resonant frequencies. The values of these frequencies depend on the physical dimensions and geometrical shape of the cavity.

The apparatus used in the experiments of Adler and Breazeale utilized a water-filled, one-dimensional cavity terminated by two parallel planes at each end of the cavity. One end is a rigid plane reflector and the other end is a transducer driven by an external rf voltage of frequency 2ω. As the transducer at the end of the cavity oscillates back and forth, the length of the cavity changes, and this variation of the cavity length also causes the resonance frequency to vary. In addition, nonlinear effects of the medium in which the waves

[a)]Permanent address: George W. Woodruff School of Mechanical Engineering, Georgia Institute of Technology, 801 Ferst Drive, Atlanta, GA 30332-0405 and Georgia Tech Lorraine, 2 rue Marconi, 57070 Metz, France. Electronic mail: nico.declercq@me.gatech.edu

propagate cause the generation of frequency doublets. These frequencies (ω_1 and ω_2) occur at approximately half the drive frequency (2ω) in such a manner that $\omega_1+\omega_2 \approx 2\omega$.[11,12]

Parametric excitation is possible only if the energy input to the system due to periodic variation of its resonant frequencies reaches a critical threshold value that is large enough to overcome the energy dissipated by the system. Therefore, the amplitude of the varying parameter must satisfy a threshold condition. In fact, it has been observed that frequencies other than the resonant frequencies can be generated by the nonlinearity of the medium when any of the acoustical parameters of the system are varied periodically.[11] Since some of these frequencies have values below the drive frequency, they are usually referred to as subharmonics or fractional harmonics.

Another important criterion for the observation of parametric oscillation is the aspect ratio, defined as the ratio of transverse to longitudinal dimensions of the cavity. The aspect ratio is related to the Fresnel number, defined as[12]

$$F = \frac{r^2}{\lambda L}, \tag{1}$$

where r is characteristic of the transverse size of the cavity (for example, the square root of the area of a plane radiator or reflector), λ is the wavelength of the ultrasonic wave, and L is the longitudinal length of the cavity in the direction of propagation of the wave. As a result of a transition from an initially stable to an unstable state, parametric resonance can be observed when the aspect ratio or the Fresnel number is large ($F \geq 1$). For the cavity used here $F=95$, satisfying the physical conditions for the observation of parametric excitation.

For the fluid-filled cavity resonator, the vibration of the transducer causes the length of the cavity, and hence the resonant frequency, to be periodic functions of time. The time-dependent cavity length can be expressed as[11]

$$l(t) = l_0(1 + h\cos 2\omega t) \tag{2}$$

with

$$h = \frac{A}{l_0}, \tag{3}$$

where A is the vibration amplitude of the drive transducer, l_0 is the unperturbed length of the cavity, and 2ω is the frequency of the driver. Similarly, the time-dependent resonant frequency may be expressed as

$$\omega_n(t) = \omega_{n_0}(1 + h\cos 2\omega t), \tag{4}$$

where ω_{n_0} is the unperturbed characteristic frequency of the nth mode given by

$$\omega_{n_0} = \frac{n\pi c}{l_0} \tag{5}$$

and c is the speed of sound in the medium.

The wave equation governing the particle displacement $y(x,t)$ in an ultrasonic wave in a dissipative medium is given by[11]

$$\frac{\partial^2 y(x,t)}{\partial t^2} = c^2\frac{\partial^2 y(x,t)}{\partial x^2} + \frac{\alpha c^3}{\omega^2}\frac{\partial^3 y(x,t)}{\partial x^2\,\partial t}, \tag{6}$$

where α is the acoustical absorption coefficient of the medium. Assuming a solution of the form

$$y(x,t) = g(t)\sin\frac{n\pi x}{l(t)} \tag{7}$$

and using Eq. (2), one can rewrite the dissipative wave equation and get

$$\frac{d^2 g'}{dz^2} + (\bar{a} - 2q\cos 2z)g' = 0, \tag{8}$$

where

$$g'(z) = g(z)\exp\left(\frac{-a\alpha c}{\omega}z\right), \tag{9}$$

$$\bar{a} = \left(a - \frac{a^2\alpha^2 c^2}{\omega^2}\right), \tag{10}$$

$$z = \omega t, \quad q = ah, \quad \text{and} \quad a = \frac{\omega_n^2}{\omega^2}. \tag{11}$$

Equation (8) is a differential equation whose solution is given by a damped Mathieu's function satisfying the boundary conditions that the particle displacement y must vanish at $x=0$ and $x=l_0$. Depending on the value of a, the excited frequencies can be integral or fractional multiples of the natural resonance frequency. Furthermore, the solutions can be stable, unstable, or neutral.[13]

Since the fractional harmonics are generated from nonlinear interactions in the medium, it is necessary to consider the effects that such nonlinearities might have on the threshold drive amplitude. Our analysis, and that in Ref. 1, shows that the nonlinearity does not impact the threshold amplitude h. Thus, Eq. (8) is sufficient for the analysis of the threshold drive amplitude behavior.

In Eq. (11), the term ω_n represents the set of possible harmonics generated by the system. When these harmonics correspond to parametric resonance regions (where $a=1$, $a=4$, $a=9$, etc.[13]), one can observe parametric resonance. The solution to Eq. (8) leads to a condition on the drive amplitude h, for the onset of parametric amplification. This condition defines a region of instability as follows:

$$h\omega \geq \sqrt{(\omega_n - \omega_o)^2 + (a\alpha c)^2}, \tag{12}$$

where the equality represents the threshold condition for the onset of parametric amplification. There are several possible zones where parametric amplification occurs. In the case $\omega_n = \omega \approx \omega_o$, we have the condition $a=1$, so that the first term under the radical vanishes. In this case, with the harmonics near a physical resonance of the system, the threshold behavior is limited only by the dissipation in the system. Hence, for $a=1$, we have a threshold given by

$$h\omega > \alpha c, \tag{13}$$

which was the case observed in the initial experiments of Adler and Breazeale.[8] However, for the other regions of

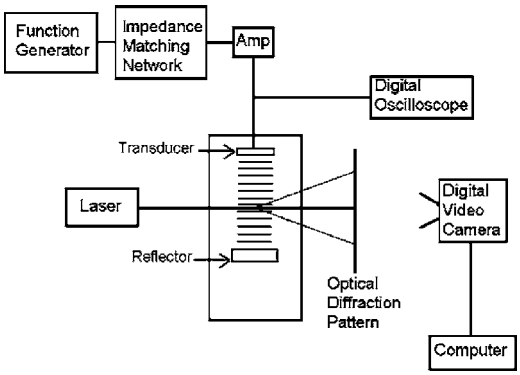

FIG. 1. Block diagram of the acoustic parametric generator.

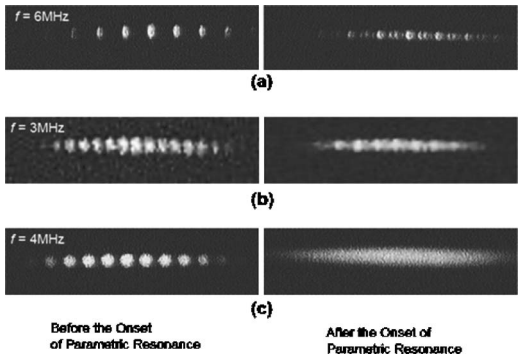

FIG. 2. Photos of diffraction patterns before and after the onset of parametric resonance: (a) The after photo shows a few intermediate orders; (b) The after photo shows a larger number of intermediate orders; and (c) The after photo shows essentially a continuum when the number of subharmonics becomes great enough.

parametric oscillation (with corresponding threshold amplitude minima at $a=4$, 9, 16, 25, etc.), one must include both terms under the radical. In the case to be described, $a=4$. This means that the threshold becomes

$$h\omega \geq \sqrt{(\omega_n - \omega_o)^2 + (4\alpha c)^2}. \tag{14}$$

In this case, the threshold condition is determined by both the attenuation and the resonant frequency.

Here, we report observation of the generation of fractional harmonics due to parametric oscillation in a liquid-filled, ultrasonic system similar to that originally used by Adler and Breazeale.[8] The data show a more complicated threshold amplitude behavior than the $1/\omega$ frequency dependence observed by Adler and Breazeale[8] (which is the behavior predicted by Eq. (13) for the $a=1$ region). The data in the present experiment require a fit with both terms of Eq. (12), and they correspond to the stability region defined by $a=4$. We have improved the oscillator stability and present new measurements of the frequency dependence of the drive threshold amplitude for the generation of parametric oscillation.

III. EXPERIMENT

A block diagram of the system used to study the frequency dependence of the threshold amplitude for generation of parametric resonances is shown in Fig. 1. It consists of a liquid-filled one-dimensional cavity bounded by a drive transducer (which acts as an oscillating boundary) at one end and by a rigid plane reflector at the other end. The reflector is a plane plate aligned parallel to the radiating transducer. The transducer is a 1-in. diameter, x-cut, quartz transducer driven by a rf signal generator. The impedance of the generator was matched to the quartz drive transducer by an impedance matching network. The frequencies ranged from 2 to 7 MHz.

The transducer-reflector assembly is designed to allow minute adjustments to achieve very accurate parallel alignment of the transducer and reflector. This assembly is immersed in a water-filled tank at room temperature. The periodically varying parameter in this case is the distance between the rigid reflector and the drive transducer, which changes as the transducer oscillates back and forth with a given drive frequency.

The periodic variations in the density of the liquid produced by a standing wave can act as an optical diffraction grating. Laser light passing through the standing wave from a direction perpendicular to the cavity length diffracts and creates a diffraction pattern as shown on the left side in Fig. 2.

The presence of fractional harmonics produces extra diffraction orders between the ordinary diffraction orders resulting from standing waves in the cavity as shown on the right side of Fig. 2. Thus, the appearance of intermediate diffraction orders provides an indication of the onset of parametric excitation. The drive voltage was reduced until the extra diffraction orders disappeared in order to determine the minimum threshold voltage required for parametric excitation.

To observe parametric excitation, two experimental factors are critical: the parallelism between the transducer and reflector and the amplitude of the drive threshold. It is possible to overcome slight misalignment of the parallelism of the plate relative to the reflector by increasing the amplitude. Therefore, once parametric oscillation is observed, the parallelism is carefully adjusted so that the onset of parametric oscillation occurs at the lowest possible drive voltage.

IV. RESULTS AND DISCUSSIONS

Figure 2 shows diffraction patterns for three different frequencies both before and after the onset of parametric excitation. In Fig. 2(a), parametric resonance causes additional orders to appear. In Fig. 2(b), the number of intermediate orders has increased. In Fig. 2(c), the number of intermediate orders is so great that it is impossible to resolve individual orders in the spectrum, and they appear as a continuum.

Measurements of the threshold value of the transducer drive voltage for the onset of parametric oscillation were performed at different frequencies. Figure 3 shows a plot of the frequency dependence of the threshold drive voltage for the original data of Adler and Breazeale. As seen in the figure, the threshold value of the drive voltage decreases with increasing frequency. The theoretical curve indicated is a fit of Eq. (13) to the data. In the case of the original experiment of Adler and Breazeale, the physical parameters of the system preferentially excited the $a=1$ mode.

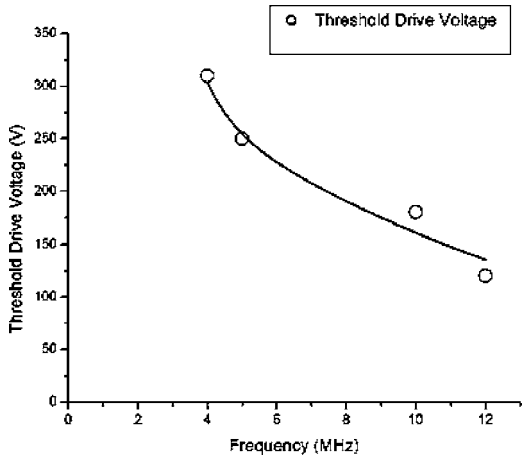

FIG. 3. Data of Adler and Breazeale (Ref. 8) with theoretical curve indicating stability criteria given in Eq. (13) (with $a=1$).

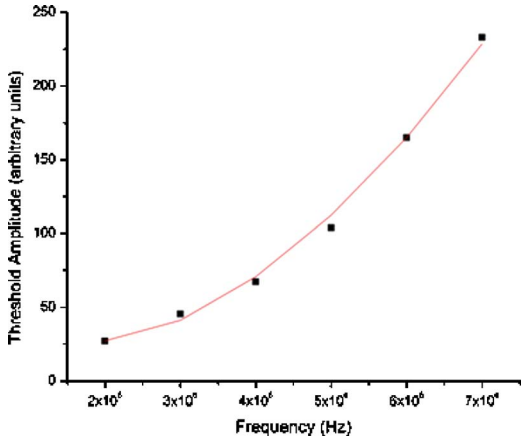

FIG. 4. Current results with theoretical curve indicating stability criteria given in Eq. (14) (with $a=4$).

The data of the original experiment were fit with the theoretical expression given in Eq. (13). Dividing both sides of Eq. (13) by ω and using the equality to determine the minimum allowed value of the input parameter h, one has

$$h = \frac{1}{\omega}\alpha c. \tag{15}$$

Therefore, with $a=1$, the critical threshold amplitude has a $(1/\omega)$ dependence on drive frequency. This theoretical fit is shown in Fig. 3, and it is in good agreement with the data.

The results of the current experiment, which had different cavity dimensions, do not show a $(1/\omega)$ frequency dependence. However, by considering both terms in Eq. (14), one can understand why this is true. The region defined by $a=4$ also is a parametric region. Using $a=4$, one has a threshold dependence given in Eq. (14). This is the curve shown in Fig. 4 as a theoretical curve. This curve agrees well with the experimental data for a value of $a=4.08\pm0.72$, as shown, and indicates that the different frequency dependence of the threshold amplitude observed in this experiment results from the fact that the physical parameters of this experimental configuration (the same frequency range but considerably smaller cavity size than in the original experiment) are preferentially causing parametric excitation in the $a=4$ stability region.

V. CONCLUSIONS

The results of a new investigation of parametric resonance in a fluid-filled, one-dimensional cavity are presented. The threshold drive amplitude for the onset of parametric oscillations has been measured as a function of frequency. These data show an upward trend in apparent contradiction with previously published results.[1,8] This apparent discrepancy is resolved by analysis of the theory. We demonstrate that the different experimental arrangements (with different characteristic frequencies) result in different regions of instability. This accounts for the different data trends.

ACKNOWLEDGMENTS

We would like to thank Dr. L. Mills (College of Charleston) for his helpful discussions. The Ph.D. dissertation of Wayne Prather helped understand the implications of the relevant theory. This work was supported by the NATO Collaborative Linkage Grant No. PST.NR.CLG.980315. Nico F. Declercq is a Postdoctoral Fellow of the Fund for Scientific Research Flanders (FWO - Vlaanderen).

[1] L. Adler and M. A. Breazeale, "Parametric phenomena in physics," Am. J. Phys. **39**, 1522–1527 (1971).
[2] F. Melde, "Poggendorff's Ueber die Erregung Stehender Wellen eines fadenförmigen Körpers (About excitation of standing waves of a string)," Ann. Phys. Chem. **109**, 193–215 (1860).
[3] N. N. Bogoliubov and Y. A. Mitropolsky, *Asymptotic Methods in the Theory of Nonlinear Oscillations* (Hindustan, India Delhi-6, 1961).
[4] M. Luukkala, W. G. Proctor, H. Mahon, and H. Brun, "Excitation of fractional harmonics in solids," Phys. Rev. Lett. **19**, 430–432 (1967).
[5] Lord Rayleigh, *The Theory of Sound* (Dover, New York, 1945).
[6] A. Korpel and R. Adler, "Parametric phenomena observed on ultrasonic waves in water," Appl. Phys. Lett. **7**, 106–108 (1965).
[7] M. A. Breazeale and R. McCluney, "Subharmonic generation in a resonant cavity," J. Acoust. Soc. Am. **40**, 1262(A) (1966).
[8] L. Adler and M. A. Breazeale, "Generation of fractional harmonics in a resonant ultrasonic wave system," J. Acoust. Soc. Am. **48**, 1077–1083 (1970).
[9] L. Adler and M. A. Breazeale, "Excitation of subharmonics in a resonant ultrasonic wave system," Naturwiss. **55**, 385–386 (1968).
[10] N. Yen, "Experimental investigation of subharmonic generation in an acoustic interferometer," J. Acoust. Soc. Am. **57**, 1357–1362 (1975).
[11] L. Adler, Ph. D. dissertation (The University of Tennessee, 1969).
[12] V. J. Sanchez-Morcillo, "Spontaneous pattern formation in an acoustical resonator," J. Acoust. Soc. Am. **115**(1), 111–119 (2004).
[13] N. W. McLachlan, *Theory and Application of Mathieu Functions* (Oxford University Press, Oxford, 1947).

Spatio-temporal dynamics of an encapsulated gas bubble in an ultrasound field

Alexander A. Doinikov[a)]
Institute of Nuclear Problems, Belarus State University, 11 Bobruiskaya Street, Minsk 220050, Belarus

Paul A. Dayton[b)]
Department of Biomedical Engineering, University of California, 451 East Health Sciences Drive, Davis, California 95616

(Received 14 February 2006; revised 25 May 2006; accepted 26 May 2006)

Coupled equations describing the radial and translational dynamics of an encapsulated gas bubble in an ultrasound field are derived by using the Lagrangian formalism. The equations generalize Church's theory [J. Acoust. Soc. Am. **97**, 1510 (1995)] by allowing for the translation motion of the bubble and radiation losses due to the compressibility of the surrounding liquid. The expression given by Church for the inner bubble radius corresponding to the unstrained state of the bubble shell is also refined, assuming that the shell can be of arbitrary thickness and impermeable to gas. Comparative linear analysis of the radial equation is carried out relative to Church's theory. It is shown that there are substantial departures from predictions of Church's theory. The proposed model is applied to evaluate radiation forces exerted on encapsulated bubbles and their translational displacements. It is shown that in the range of relatively high frequencies encapsulated bubbles are able to translate more efficiently than free bubbles of the equivalent size.
 [DOI: 10.1121/1.2215228]

PACS number(s): 43.25.Yw, 43.35.Ei, 43.80.Qf, 43.80.Ev [CCC] Pages: 661–669

I. INTRODUCTION

Interest in theoretical models describing the dynamics of encapsulated gas bubbles in an ultrasound field is motivated by increasingly growing use of contrast agents in ultrasound biomedical applications. Of special interest are models in the form of a Rayleigh-Plesset-type equation as they are more amenable to theoretical analysis, more convenient for numerical simulations, and can with comparative ease be applied to model the dynamics of more than one bubble. The first of such models was proposed by de Jong *et al.*[1,2] They modified the Rayleigh-Plesset equation by phenomenologically introducing an additional restoring force due to the stiffness of the bubble shell and an additional damping due to internal friction inside the shell. The modified equation was used to model the radial oscillation of Albunex contrast agent. Subsequently, Frinking and de Jong[3] proposed another version of this equation that was intended to model the radial dynamics of thick-shelled contrast agents such as Quantison and Myomap. It should be emphasized that both of the above-mentioned models are based on qualitative arguments rather than rigorous theoretical derivations.

A more sophisticated and theoretically justified model was developed by Church.[4] He considered a spherical encapsulated gas bubble enclosed in an incompressible solid elastic shell and surrounded by an incompressible viscous Newtonian liquid. The viscous damping inside the shell was also taken into account. Using a consistent theoretical approach, Church derived a Rayleigh-Plesset-type equation describing the radial motion of the bubble. The only *ad hoc* assumption that he used concerns determination of the inner radius of the bubble shell corresponding to the unstrained state of the shell.

More recently, using a modified Herring equation[5] along with some elements of Church's theory, the behavior of a contrast agent bubble was modeled by Morgan *et al.*[6] and Dayton *et al.*[7] In the latter work, the radial equation was also supplemented with a translational equation to estimate the magnitude of radiation force on contrast agents and compare the theoretical results with experiments.

All the above-mentioned papers show that, as a matter of fact, any modification of the Rayleigh-Plesset equation, based on reasonable assumptions, can be fitted to provide good agreement with specific experiments. However, models that involve *ad hoc* parameters cannot guarantee reliable predictions for cases different from that to which they were fitted, even if distinctions are physically insignificant. This fact is well illustrated by Frinking and de Jong's[3] article, where an effective bulk modulus, K_{eff}, is introduced to describe the elasticity of the encapsulating shell of contrast agents such as Quantison, Myomap, and Albunex. All of these agents consist of air bubbles encapsulated by a shell of human albumin. They differ only in diameter and the shell thickness. For Quantison, which has a mean diameter of 3.2 μm and the shell thickness of which is 200–300 nm and proportional to the bubble diameter, Frinking and de Jong obtained $K_{\text{eff}}=17.4$ MPa. For Myomap, which has a mean diameter of 10 μm and the shell of which is approximately three times thicker than the Quantison shell, $K_{\text{eff}}=78.4$ MPa. Measurements for Albunex filtered with 12-, 8-, 5-, and 3-μm pore size mechanical filters yielded the follow-

a)Electronic mail: doinikov@bsu.by
b)Electronic mail: padayton@ucdavis.edu

ing values of K_{eff}, respectively: 1.3, 2.0, 6.2, and 9.8 MPa. These results are believed to be explained by the fact that the thickness of the Albunex shell, which is about 15–20 nm, is independent of the bubble diameter, the latter being about 3.8 μm. It is evident that such a model is very inconvenient, especially if we are going to simulate the dynamics of a contrast agent cluster consisting of bubbles of different size. When a model is based on real physical parameters, distinctions in the behavior of the above-mentioned contrast agents should arise in a natural way, just varying sizes instead of fitting K_{eff} to every new set of the bubble geometrical adjectives.

Models accounting for the translational motion of contrast agents deserve special notice. They have not received proper consideration so far. If a model incorporates translation, this makes it more complicated. However, such a model provides an additional means for adjusting the parameters responsible for the radial dynamics of a contrast agent bubble, among other things. With an adequate expression for the drag force, the translational displacement of a contrast agent bubble is determined mainly by the intensity of its radial oscillation, i.e., the translational displacement can serve as a direct measured performance of the radial oscillation. In many cases, the translational displacement can be measured more precisely than the radius-time curves, especially since the translational displacement is in fact a time-average quantity. Hence, fitting theoretical and experimental displacements can be used to improve values of the model parameters which were initially estimated by other methods, such as radius-time curves, scattering spectra, etc. It should also be remembered that in many applications, such as targeted drug delivery, the translational dynamics of contrast agents is of great independent interest.

The purpose of this paper is to derive rigorously coupled equations governing the spatio-temporal dynamics of an encapsulated gas bubble in an ultrasound field. The present derivation improves Church's theory by allowing for the translation motion of the bubble and radiation losses due to the compressibility of the surrounding liquid. The expression given by Church for the inner bubble radius corresponding to the unstrained state of the encapsulating shell is also refined, assuming that the shell can be of arbitrary thickness and impermeable to gas.

II. THEORY

Let us consider an encapsulated gas bubble surrounded by a liquid and undergoing radial and translational motions in response to an imposed acoustic field. It is assumed that the surrounding liquid is a slightly compressible Newtonian liquid and the bubble shell behaves as a viscoelastic solid. It is also assumed that the bubble translates along a straight line that is specified by the wave vector of the acoustic field. To describe the motion of the bubble, spherical coordinates (r, θ, ε) are introduced, the origin of which is at the moving center of the bubble. The geometry of the system is shown in Fig. 1. The aim of this section is to derive coupled equations of radial and translational bubble motions by using the Lagrangian formalism. Using the Lagrangian procedure is not new in fluid arid bubble dynamics.[8–15] However, with respect to encapsulated bubbles, this approach has not been used much so far.[16]

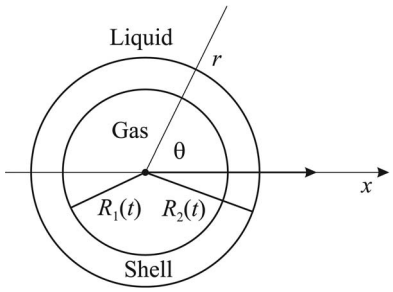

FIG. 1. Schematic sketch of an encapsulated bubble.

A. Lagrangian equations

The Lagrangian equations are given by[17]

$$\frac{d}{dt}\frac{\partial L}{\partial \dot{q}_i} - \frac{\partial L}{\partial q_i} = -\frac{\partial F}{\partial \dot{q}_i}, \tag{1}$$

where L is the Lagrangian function, q_i and $\dot{q}_i$ are called generalized coordinates and velocities, respectively, and F is the dissipative function that is entered to account for dissipative effects such as viscosity. The Lagrangian function is defined as $L=T-U$, where T and U are the kinetic and potential energies of the system, respectively. Expressions for T, U, and F are sequentially calculated in the following subsections.

B. Kinetic energy

The kinetic energy can be represented as

$$T = \tfrac{1}{2} m_b \dot{x}^2 + T_L + T_S, \tag{2}$$

where m_b is the mass of the bubble, $x(t)$ is the position of the center of the bubble in an inertial frame, the overdot denotes the time derivative, T_L is the kinetic energy of the liquid, and T_S is the kinetic energy of the shell.

It is shown in Ref. 18 that the kinetic energy of a slightly compressible liquid that encloses a spherical bubble with the time-varying radius $R_2(t)$, assuming also that the bubble can translate, is given by

$$T_L = 2\pi\rho_L \left(R_2^3 \dot{R}_2^2 + \frac{1}{6} R_2^3 \dot{x}^2 + \frac{2}{c} R_2^2 \dot{R}_2 \dot{f}(t) + \frac{1}{c}\int_0^t [f'(\tau)]^2 \, d\tau \right) + O(c^{-2}), \tag{3}$$

where ρ_L is the equilibrium density of the liquid, c is the sound speed in the liquid, and $f(t) = -\dot{R}_2(t) R_2^2(t)$. Note that if we substitute the explicit expression for $f(t)$ into Eq. (3), we will get a second-order time derivative of the radius in the third term in brackets, which is inadmissible in the Lagrangian formalism. To avoid this problem, $\dot{f}(t)$ in T_L will be treated just as a function of time and the explicit expression for $f(t)$ will be used only in final equations. We will see below that this approach gives a correct result.

Assuming that the volume of the bubble shell, V_S, remains constant in the process of bubble motion and that the effect of translation on the deformation of the shell is negligible, the velocity inside the shell can be written as

$$v_S = \frac{R_1^2 \dot{R}_1}{r^2}, \tag{4}$$

where $R_1(t)$ is the inner radius of the bubble shell. The kinetic energy of the shell is then calculated as

$$T_S = \frac{1}{2}\int_{V_S} \rho_S v_S^2 \, dV = 2\pi\rho_S R_1^3 \dot{R}_1^2 \left(1 - \frac{R_1}{R_2}\right), \tag{5}$$

where ρ_S is the density of the shell. Applying to the shell the same approach that was used in Ref. 18 for calculating Eq. (3), it can be shown that compressibility corrections to Eq. (5) can not be lower order than c_l^{-2}, where c_l denotes the longitudinal speed of sound in the shell. Note also that the assumption of incompressible shell gives the following equations, which will be used below,

$$R_2^3 - R_1^3 = R_{20}^3 - R_{10}^3, \quad R_1^2 \dot{R}_1 = R_2^2 \dot{R}_2, \quad \frac{dR_2}{dR_1} = \frac{R_1^2}{R_2^2}, \tag{6}$$

where R_{10} and R_{20} are, respectively, the inner and the outer radii of the bubble shell at rest.

C. Potential energy

The total potential energy of the system can be written as the following sum:

$$U = U_g + U_{\mathrm{st}} + U_{\mathrm{ex}} + U_L + U_S. \tag{7}$$

U_g is the internal energy of the gas core. Assuming that the behavior of the gas is adiabatic, one has[19]

$$U_g = \frac{P_{g0} V_{g0}}{\gamma - 1}\left(\frac{R_{10}}{R_1}\right)^{3(\gamma-1)}, \tag{8}$$

where P_{g0} is the equilibrium pressure of the gas within the bubble, $V_{g0} = (4\pi/3)R_{10}^3$ is the equilibrium gas volume, and γ is the ratio of specific heats.

The term U_{st} describes contributions due to surface tension at the gas-shell and the shell-liquid interfaces,

$$U_{\mathrm{st}} = 4\pi R_1^2 \sigma_1 + 4\pi R_2^2 \sigma_2. \tag{9}$$

Here σ_1 and σ_2 denote the surface tension coefficients for the corresponding interfaces.

U_{ex} is the contribution due to work done by the external pressure on the outer bubble surface. This contribution can be represented as

$$U_{\mathrm{ex}} = \frac{4\pi}{3} R_2^3 [P_0 + P_{\mathrm{ac}}(x,t)], \tag{10}$$

where P_0 is the hydrostatic pressure in the liquid and $P_{ac}(x,t)$ is the acoustic pressure at the location of the bubble.

U_L is the potential energy of the surrounding liquid due to its compressibility. It is shown in Ref. 18 that U_L is given by

$$U_L = \frac{2\pi\rho_L}{c}\int_0^t [f'(\tau)]^2 \, d\tau + O(c^{-2}). \tag{11}$$

Finally, U_S is the elastic energy of the shell defined by

$$U_S = \int_{V_S} \mathcal{E} \, dV, \tag{12}$$

where $\mathcal{E}$ is the elastic energy density which is given by[20]

$$\mathcal{E} = \mu_S\left(u_{ij} - \tfrac{1}{3}\delta_{ij}u_{kk}\right)^2 + \tfrac{1}{2}K_S u_{kk}^2. \tag{13}$$

Here μ_S and K_S are respectively the shear modulus and the bulk modulus of the shell, δ_{ij} is the Kronecker delta, u_{ij} is the linear strain tensor, and summation over double indices is implied. The linear strain tensor is defined as

$$u_{ij} = \frac{1}{2}\left(\frac{\partial u_i}{\partial x_j} + \frac{\partial u_j}{\partial x_i}\right), \tag{14}$$

with u_i denoting the ith component of the displacement vector. Since the shell is assumed to be incompressible, which results in $u_{kk}=0$, and in view of spherical symmetry, Eq. (13) takes the form

$$\mathcal{E} = \mu_S (u_{ij})^2 = \mu_S\left[\left(\frac{\partial u}{\partial r}\right)^2 + \frac{2u^2}{r^2}\right], \tag{15}$$

where u is the radial displacement. Using again the fact that the shell is incompressible, u can be written as

$$u = \frac{R_1^2}{r^2}(R_1 - R_{1e}), \tag{16}$$

where R_{1e} is the unstrained equilibrium position of the gas-shell interface. Note that R_{1e} does not coincide with R_{10}. The expression for R_{1e} is calculated below.

Substitution of Eqs. (15) and (16) into Eq. (12) yields

$$U_S = 8\pi\mu_S (R_{20}^3 - R_{10}^3)\frac{R_1 (R_1 - R_{1e})^2}{R_2^3}. \tag{17}$$

As with T_S, it can be shown that compressibility corrections to Eq. (17) are on the order c_1^{-2} and therefore they are neglected here.

D. Dissipative function

The total dissipative function of the system can be represented as

$$F = F_L + F_S = \int_{V_L} f_L \, dV + \int_{V_S} f_S \, dV, \tag{18}$$

where V_L is the volume occupied by the liquid, F_L and F_S are the dissipative functions of the liquid and the shell, and f_L and f_S are the densities of the dissipative functions.

For the surrounding liquid, f_L, can be written as[20,21]

$$f_L = \eta_L\left(v_{ij} - \tfrac{1}{3}\delta_{ij}v_{kk}\right)^2 + \tfrac{1}{2}\zeta_L v_{kk}^2, \tag{19}$$

where η_L and ζ_L are, respectively, the shear and the bulk viscosity coefficients of the liquid, and v_{ij} is the rate-of-strain tensor of the liquid, defined as

$$v_{ij} = \frac{1}{2}\left(\frac{\partial v_i}{\partial x_j} + \frac{\partial v_j}{\partial x_i}\right), \tag{20}$$

with $\boldsymbol{v}$ denoting the liquid velocity. Neglecting the compressibility of the liquid, one has $v_{kk} = \boldsymbol{\nabla}\cdot\boldsymbol{v} = 0$ so Eq. (19) reduces to

$$f_L = \eta_L (v_{ij})^2. \tag{21}$$

To satisfy the boundary condition of adhesion of the liquid particles to the bubble surface, which is expressed as

$$\boldsymbol{v} = \dot{R}_2 \boldsymbol{e}_r + \dot{\boldsymbol{x}} = (\dot{R}_2 + \dot{x}\cos\theta)\boldsymbol{e}_r - \dot{x}\sin\theta\,\boldsymbol{e}_\theta \quad \text{at } r = R_2, \tag{22}$$

the liquid velocity can be represented as $\boldsymbol{v} = \boldsymbol{\nabla}\varphi + \boldsymbol{\nabla}\times\boldsymbol{\psi}$, where the scalar potential φ must obey the Laplace equation, $\Delta\varphi = 0$. Expressions for φ and $\boldsymbol{\psi}$ satisfying these two conditions are given by

$$\varphi = -\frac{R_2^2\dot{R}_2}{r} + \frac{R_2^3\dot{x}\cos\theta}{4r^2}, \tag{23}$$

$$\boldsymbol{\psi} = \tfrac{3}{4}R_2\dot{x}\sin\theta\,\boldsymbol{e}_\varepsilon. \tag{24}$$

The liquid velocity are then calculated as

$$\boldsymbol{v} = \left[\frac{R_2^2\dot{R}_2}{r^2} + \frac{\dot{x}}{2}\left(\frac{3R_2}{r} - \frac{R_2^3}{r^3}\right)\cos\theta\right]\boldsymbol{e}_r - \frac{\dot{x}}{4}\left(\frac{3R_2}{r} + \frac{R_2^3}{r^3}\right)\sin\theta\,\boldsymbol{e}_\theta. \tag{25}$$

Considering the form of Eq. (25), $(v_{ij})^2$ can be written as[20]

$$(v_{ij})^2 = v_{rr}^2 + v_{\theta\theta}^2 + v_{\varepsilon\varepsilon}^2 + 2v_{r\theta}^2 = \left(\frac{\partial v_r}{\partial r}\right)^2 + \frac{1}{r^2}\left(v_r + \frac{\partial v_\theta}{\partial\theta}\right)^2 + \frac{1}{r^2}\left(v_r + v_\theta\frac{\cos\theta}{\sin\theta}\right)^2 + \frac{1}{2}\left(\frac{1}{r}\frac{\partial v_r}{\partial\theta} + \frac{\partial v_\theta}{\partial r} - \frac{v_\theta}{r}\right)^2. \tag{26}$$

On substitution of Eq. (25) into Eq. (26), one has

$$(v_{ij})^2 = \frac{6R_2^4\dot{R}_2^2}{r^6} + \frac{9R_2^6\dot{x}^2}{8r^8} + \frac{9R_2^2\dot{R}_2\dot{x}}{r^4}\left(\frac{R_2}{r} - \frac{R_2^3}{r^3}\right)\cos\theta + \frac{\dot{x}^2}{8}\left(\frac{27R_2^2}{r^4} - \frac{54R_2^4}{r^6} + \frac{18R_2^6}{r^8}\right)\cos^2\theta. \tag{27}$$

Finally, integrating this equation over V_L, one finds

$$F_L = 8\pi\eta_L R_2\dot{R}_2^2 + 3\pi\eta_L R_2\dot{x}^2. \tag{28}$$

Calculation of the dissipative function for the shell is much easier. For f_S, one has[20]

$$f_S = \eta_S (v_{ij})^2 = \eta_S\left[\left(\frac{\partial v_S}{\partial r}\right)^2 + \frac{2v_S^2}{r^2}\right], \tag{29}$$

where η_S is the shear viscosity of the shell and v_S is given by Eq. (4). Integrating Eq. (29), one obtains

$$F_S = 8\pi\eta_S(R_{20}^3 - R_{10}^3)\frac{R_1\dot{R}_1^2}{R_2^3}. \tag{30}$$

E. Equations of motion

Calculating the functions L and F by using the equations obtained above, substituting the resulting expressions into Eq. (1), taking R_1 and x as generalized coordinates, and using Eq. (6) to express R_2 in terms of R_1, one obtains the following equations of bubble motion:

$$\begin{aligned} R_1\ddot{R}_1\left[1 + \left(\frac{\rho_L - \rho_S}{\rho_S}\right)\frac{R_1}{R_2}\right] + \dot{R}_1^2\left[\frac{3}{2} + \left(\frac{\rho_L - \rho_S}{\rho_S}\right)\times\left(\frac{4R_2^3 - R_1^3}{2R_2^3}\right)\frac{R_1}{R_2}\right] - \frac{1}{c}\frac{\rho_L}{\rho_S}(R_2^2\dddot{R}_2 + 6R_2\dot{R}_2\ddot{R}_2 + 2\dot{R}_2^3) \\ = \frac{\rho_L\dot{x}^2}{\rho_S 4} + \frac{P_{g0}}{\rho_S}\left(\frac{R_{10}}{R_1}\right)^{3\gamma} - \frac{2\sigma_1}{\rho_S R_1} - \frac{2\sigma_2}{\rho_S R_2} - \frac{P_0 + P_{ac}(x,t)}{\rho_S} \\ - \frac{4\dot{R}_1}{\rho_S R_1 R_2^3}[\eta_L R_1^3 + \eta_S(R_{20}^3 - R_{10}^3)] - \frac{4\mu_S(R_{20}^3 - R_{10}^3)}{\rho_S R_2^3} \\ \times\left(1 - \frac{R_{1e}}{R_1}\right)\left[1 + \frac{1}{2}\left(1 - \frac{R_{1e}}{R_1}\right)\left(1 - \frac{3R_1^3}{R_2^3}\right)\right], \end{aligned} \tag{31}$$

$$m_b\ddot{x} + \frac{2\pi}{3}\rho_L\frac{d}{dt}(R_2^3\dot{x}) = -\frac{4\pi}{3}R_2^3\frac{\partial}{\partial x}P_{ac}(x,t) - 6\pi\eta_L R_2\dot{x}. \tag{32}$$

Equation (31) governs the radial pulsation of the bubble and Eq. (32) its translation. The first term on the right-hand side of the translational equation is the acoustic radiation force and the second term is the viscous drag force in the form of the Stokes law, which is only natural as we used the no-slip boundary condition on the bubble surface. However, it is common practice to replace the Stokes drag force with a more accurate equation resulting from experimental measurements.

If the c^{-1} term on the left-hand side, the translational term $\rho_L\dot{x}^2/(4\rho_S)$ on the right-hand side, and the $(1 - R_{1e}/R_1)$ correction within the square brackets in the elastic term on the right-hand side are omitted, Eq. (31) becomes identical to that obtained by Church.[4] Note that Church's theory implicitly supposes that the deformation of the shell is small and therefore the elastic term in Church's radial equation is taken only to the first order in $(1 - R_{1e}/R_1)$. The $(1 - R_{1e}/R_1)$ correction in the elastic term partly extends the range of Eq. (31) towards finite deformations.

When the sound is off and the bubble is at rest, from Eq. (31) it follows that

$$P_{g0} = P_0 + \frac{2\sigma_1}{R_{10}} + \frac{2\sigma_2}{R_{20}} + 4\mu_S\left(1 - \frac{R_{10}^3}{R_{20}^3}\right)\left(1 - \frac{R_{1e}}{R_{10}}\right)\times\left[1 + \frac{1}{2}\left(1 - \frac{R_{1e}}{R_{10}}\right)\left(1 - \frac{3R_{10}^3}{R_{20}^3}\right)\right]. \tag{33}$$

Church used this equation, neglecting the $(1 - R_{1e}/R_1)$ correction in the elastic term, to get an expression for R_{1e}. As-

suming that the encapsulating layer is thin and fully permeable to gas, he set $P_{g0}=P_0$ and obtained

$$R_{1e}^{Ch}=R_{10}\left[1+\frac{1}{4\mu_S}\left(\frac{2\sigma_1}{R_{10}}+\frac{2\sigma_2}{R_{20}}\right)\frac{R_{20}^3}{R_{20}^3-R_{10}^3}\right]. \tag{34}$$

However, for thick-shelled contrast agents, such as Quantison and Myomap,[3] it is unlikely that such an approximation will be appropriate. In the following subsection, a more correct calculation of R_{1e} is given.

Next, $\dot{x}$ in Eqs. (31) and (32) is in fact the velocity of the bubble with respect to the velocity of the surrounding liquid. That is, if there is a stream in the bulk liquid, due to the propagation of the acoustic wave, acoustic streaming, and so forth, $\dot{x}$ should be replaced with $\dot{x}-v_{ex}$, where v_{ex} denotes the liquid velocity unrelated to the presence of the bubble.

It is easy to see that the compressibility correction, the c^{-1} term in Eq. (31), is similar to that obtained by Prosperetti for a free bubble.[22] The striking feature of this term is the appearance of the third-order derivative $\dddot{R}_2$. This is just a consequence of using Taylor series expansions to express time-retarded quantities, e.g., $\ddot{R}_2(t-R_2/c)\approx\ddot{R}_2(t)-(R_2/c)\dddot{R}_2(t)$. The third derivative can be eliminated as follows. It is easily shown by using Eq. (6) that

$$R_2^2\dddot{R}_2+6R_2\dot{R}_2\ddot{R}_2+2\dot{R}_2^3=R_1^2\dddot{R}_1+6R_1\dot{R}_1\ddot{R}_1+2\dot{R}_1^3, \tag{35}$$

i.e., R_2 in the compressibility correction can be replaced with R_1. Further, since the compressibility correction is already of order c^{-1}, the right-hand side of Eq. (35) can be evaluated from Eq. (31) omitting the c^{-1} term. This results in

$$\begin{aligned}R_1^2\dddot{R}_1+6R_1\dot{R}_1\ddot{R}_1+2\dot{R}_1^3=&\left[1+\left(\frac{\rho_L-\rho_S}{\rho_S}\right)\frac{R_1}{R_2}\right]^{-1}\\&\times\left\{R_1\frac{dG}{dt}+2R_1\dot{R}_1\ddot{R}_1\left[1+\left(\frac{\rho_L-\rho_S}{\rho_S}\right)\frac{R_1^4}{R_2^4}\right]\right.\\&\left.+2\dot{R}_1^3\left[1+\left(\frac{\rho_L-\rho_S}{\rho_S}\right)\frac{R_1^4(2R_2^3-R_1^3)}{R_2^7}\right]\right\},\end{aligned} \tag{36}$$

where G denotes the right-hand side of Eq. (31). On substitution of this equation into Eq. (31), the third derivative vanishes.

F. Expression for R_{1e}

The radius R_{1e} (as well as R_{2e} for the outer interface) corresponds to the unstrained state of the shell material when any internal stresses within the shell are absent. Knowledge of R_{1e} is necessary because by definition the displacement vector is reckoned from the unstrained position. Clearly R_{10} does not meet the unstrained state since even if the sound is off, stresses within the shell are not zero as there exists surface tension at the interfaces and in general $P_0\neq P_{g0}$.

To calculate R_{1e}, we need to know the strain distribution inside the shell when the sound is off. Solution to this problem can be found, for example, in Ref. 20. Applying it to the present case, one has

$$u=ar+b/r^2, \tag{37}$$

where

$$a=\frac{R_{10}^3(P_{g0}-2\sigma_1/R_{10})-R_{20}^3(P_0+2\sigma_2/R_{20})}{3K_S(R_{20}^3-R_{10}^3)}, \tag{38}$$

$$b=\frac{(P_{g0}-P_0-2\sigma_1/R_{10}-2\sigma_2/R_{20})R_{10}^3R_{20}^3}{4\mu_S(R_{20}^3-R_{10}^3)}. \tag{39}$$

These equations give the strain distribution inside a resting spherical layer with inner and outer radii of R_{10} and R_{20}. At $r=R_{10}$, the deformation is equal to $u_1=R_{10}-R_{1e}$. Setting $u=u_1$ and $r=R_{10}$ in Eq. (37) and using Eq. (33), one obtains

$$R_{1e}=R_{10}\left[1-\frac{1}{4\mu_S}\left(P_0+\frac{2\sigma_2}{R_{20}}\right)\frac{R_{20}^3}{R_{10}^3}\right]. \tag{40}$$

Similarly, for R_{2e}, one has

$$R_{2e}=R_{20}\left[1-\frac{1}{4\mu_S}\left(P_0+\frac{2\sigma_2}{R_{20}}\right)\right]. \tag{41}$$

Equations (40) and (41) show that $R_{1e}<R_{10}$ and $R_{2e}<R_{20}$, i.e., the internal gas pressure expands the shell outwards with respect to its unstrained position. Note that $R_{1e}^{Ch}>R_{10}$, i.e., Church's approximation predicts an opposite effect, namely that the shell shrinks due to surface tension with respect to its unstrained position. This discrepancy can be important because it affects the sign of the elastic term in Eq. (31). Note also that for the case of a free bubble, when $R_{20}^3-R_{10}^3=0$ the elastic term in Eq. (31) tends to zero as it must, whereas in Church's theory this term tends to a finite quantity as is seen from Eq. (34).

Completing this main section, some remarks concerning the limits of validity of the proposed model should be made. Although no explicit restrictions are imposed on the amplitude of radial oscillation, the model, like the others mentioned in the Introduction, in fact is valid for moderate acoustic pressures at best. First, it ignores nonlinear elastic effects in the shell. Second, if compression is strong enough, the shell buckles. Even if the buckling is reversible, it is evident that the dynamics of the shell will change. If the buckling is irreversible, then the response of the bubble to repeating acoustic pulses can change. Third, the shell can break up during expansion and the bubble will lose gas. Finally, the bubble can also lose gas due to the shell permeability, the radial and translational motions of the bubble can be affected by a constrained environment of a blood vessel, etc. All these effects are still beyond the capabilities of existing models.

III. LINEAR ANALYSIS

Let us assume that the amplitude of the radial oscillation is small. Then we can write

$$R_1=R_{10}+\xi(t),\quad R_2=R_{20}+\frac{R_{10}^2}{R_{20}^2}\xi(t), \tag{42}$$

where it is assumed that $|\xi|\ll R_{10}$. Substituting Eqs.(42) into Eq. (31) and linearizing it with respect to ξ, one obtains the equation of a linear harmonic oscillator:

$$\ddot{\xi} + \delta\dot{\xi} + \omega_0^2\xi = -\frac{P_{ac}(t)}{\alpha\rho_S R_{10}}. \tag{43}$$

It is assumed in Eq. (43) that $P_{ac}(t)$ is of the form $P_{ac}(t) = P_a \exp(i\omega t)$, where P_a is the acoustic pressure amplitude and ω is the angular driving frequency. The coefficient α, the damping constant δ, and the undamped linear resonance frequency ω_0 are given by

$$\alpha = 1 + \left(\frac{\rho_L - \rho_S}{\rho_S}\right)\frac{R_{10}}{R_{20}}, \tag{44}$$

$$\delta = \delta_\eta + \delta_r, \tag{45}$$

$$\delta_\eta = \frac{4}{\alpha\rho_S R_{10}^2 R_{20}^3}[\eta_L R_{10}^3 + \eta_S(R_{20}^3 - R_{10}^3)], \tag{46}$$

$$\delta_r = \frac{\rho_L R_{10}\omega^2}{\alpha c \rho_S}, \tag{47}$$

$$\omega_0 = \frac{1}{R_{10}\sqrt{\alpha\rho_S}}\left\{3\gamma P_{g0} - \frac{2\sigma_1}{R_{10}} - \frac{2\sigma_2 R_{10}^3}{R_{20}^4} + \frac{4\mu_S(R_{20}^3 - R_{10}^3)}{R_{20}^3}\left[1 - D\left(1 + \frac{3R_{10}^3}{R_{20}^3}\right)\right]\right\}^{1/2}, \tag{48}$$

$$D = \frac{1}{4\mu_S}\left(P_0 + \frac{2\sigma_2}{R_{20}}\right)\frac{R_{20}^3}{R_{10}^3}. \tag{49}$$

It is instructive to compare these quantities to those obtained by Church.[4] Differences are observed for δ_r, and ω_0:

$$\delta_r^{Ch} = \omega^2 R_{20}/c, \tag{50}$$

$$\omega_0^{Ch} = \frac{1}{R_{10}\sqrt{\alpha\rho_S}}\left\{3\gamma P_0 - \frac{2\sigma_1}{R_{10}} - \frac{2\sigma_2 R_{10}^3}{R_{20}^4} + \frac{4\mu_S(R_{20}^3 - R_{10}^3)}{R_{20}^3}\left[1 + Z\left(1 + \frac{3R_{10}^3}{R_{20}^3}\right)\right]\right\}^{1/2}, \tag{51}$$

$$Z = \frac{1}{4\mu_S}\left(\frac{2\sigma_1}{R_{10}} + \frac{2\sigma_2}{R_{20}}\right)\frac{R_{20}^3}{R_{20}^3 - R_{10}^3}. \tag{52}$$

It should be noted that Eq. (50) was not formally derived by Church as part of Eq. (31); it was introduced by *ad hoc* assumption, modifying the relevant expression for a free bubble. The difference between Eqs. (48) and (51) is accounted for by Church's assumption that $P_{g0} = P_0$ and his resulting expression for R_{1e}, Eq. (34). Figures 2 and 3 show the ratios δ_r/δ_r^{Ch} and ω_0/ω_0^{Ch} as functions of R_{20}. The solid lines in the figures correspond to the shell thickness $R_S = R_{20} - R_{10} = 20$ nm (Albunex bubble), and the dashed lines to $R_S = 200$ nm (Quantison bubble). The values of the physical parameters required for these calculations were taken from Church's work:[4] $P_0 = 101.3$ kPa, $\rho_L = 1000$ kg/m^3, $\eta_L = 0.001$ Pa s, $c = 1500$ m/s, $\rho_S = 1100$ kg/m^3, $\eta_S = 1.77$ Pa s, $\mu_S = 88.8$ MPa, $\sigma_1 = 0.04$ N/m, and $\sigma_2 = 0.005$ N/m. Figures 2 and 3 show that the discrepancy with Church's theory increases as the bubble radius decreases and the shell thickness increases, but is not very significant for bubbles with $R_{20} > 1$ μm. However, it is known that the real resonance frequency of a system with dissipation differs from ω_0 and depends on δ. The behavior of δ_r, and ω_0 suggests that the damped (real) resonance frequency of an encapsulated bubble differs more significantly from that given by Church's theory. To clarify this point, let us consider a solution to Eq. (43). This is

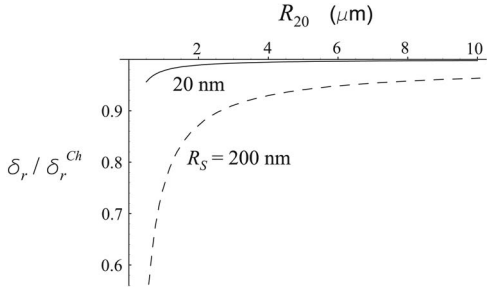

FIG. 2. The ratio of the radiation damping constants δ_r/δ_r^{Ch} as a function of equilibrium bubble radius for two values of the shell thickness R_S.

$$\xi(t) = A\exp(i\omega t + i\phi), \tag{53}$$

where

$$\phi = \arctan[\omega\delta/(\omega^2 - \omega_0^2)], \tag{54}$$

$$A = P_a Q(\omega)/(\alpha\rho_S R_{10}\omega_0^2), \tag{55}$$

$$Q(\omega) = \omega_0^2/[(\omega^2 - \omega_0^2)^2 + \omega^2\delta^2]^{1/2}. \tag{56}$$

The resonance response corresponds to a maximum of $Q(\omega)$. If δ is independent of ω, the damped resonance frequency is equal to $\omega_r = \sqrt{\omega_0^2 - \delta^2/2}$. However, in the present case δ_r is frequency dependent and therefore ω_r is defined by a more complicated expression

$$\omega_r = \frac{1}{\beta\sqrt{3}}(\sqrt{\beta^2\delta_\eta^2 + 4\beta\delta_\eta + 6\beta^2\omega_0^2 + 1} - 2\beta\delta_\eta - 1)^{1/2}, \tag{57}$$

where $\beta = \delta_r/\omega^2 = \rho_L R_{10}/(\alpha c\rho_S)$. The value of the damped resonance frequency given by Church's theory, ω_r^{Ch}, is obtained from Eq. (57) by replacing ω_0 with ω_0^{Ch} and β with $\beta^{Ch} = R_{20}/c$. Figure 4 shows the ratio ω_r/ω_r^{Ch} as a function of R_{20} for the same values of the parameters as in Fig. 3. Figure 5 presents the absolute values of the

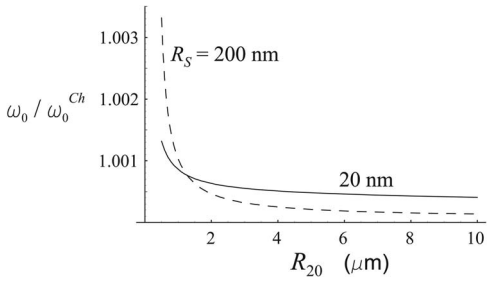

FIG. 3. The ratio of the undamped resonance frequencies ω_0/ω_0^{Ch} as a function of equilibrium bubble radius for two values of the shell thickness R_S.

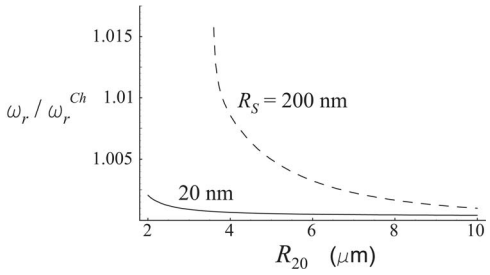

FIG. 4. The ratio of the damped resonance frequencies ω_r/ω_r^{Ch} as a function of equilibrium bubble radius for two values of the shell thickness R_S.

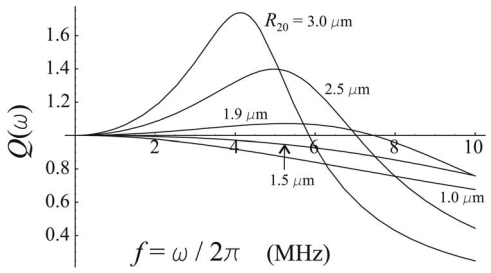

FIG. 6. Behavior of the resonance function $Q(\omega)$ at $R_S=20$ nm for various values of the equilibrium bubble radius R_{20}.

damped resonance frequency $f_r=\omega_r/2\pi$; the dashed line corresponds to a free bubble of the equivalent size. It is seen from Fig. 4 that the ratio ω_r/ω_r^{Ch} is really noticeably larger than the ratio ω_0/ω_0^{Ch} in Fig. 3. Figure 5 points to one more feature of damped oscillations, which is not considered in Church's analysis, namely that strong damping can lead to the absence of resonance. This occurs when the expression in brackets in Eq. (57) becomes negative, which in turn results from the fact that δ_η very strongly increases as the bubble radius decreases. It is for this reason that the solid lines in Fig. 5 go down and stop at small values of R_{20}, and the corresponding lines in Fig. 4 are terminated at approximately 3.5 and 2 μm. Figure 6 illustrates the process of vanishing resonance response, showing the function $Q(\omega)$ at $R_S=20$ nm for various values of R_{20}. It is seen that when R_{20} is smaller than a threshold value, the resonance peak is absent and the amplitude of the radial oscillation monotonically decreases as the driving frequency increases. Figure 5 also shows that the thicker the bubble shell, the larger the threshold bubble radius.

IV. COMPARISON WITH ZERO-THICKNESS ENCAPSULATION MODELS

Most of the existing models having the form of a Rayleigh-Plesset-type equation can be referred to as zero-thickness encapsulation models, since these, explicitly or implicitly, assume the bubble shell to be very thin and describe only the dynamics of the outer bubble radius. If we neglect the translational term in Eq. (31) and assume that $\rho_S \approx \rho_L$, the deformation of the shell is small, and $R_S \ll R_{10}, R_{20}$, Eq. (31) reduces to an equation of the above-named type:

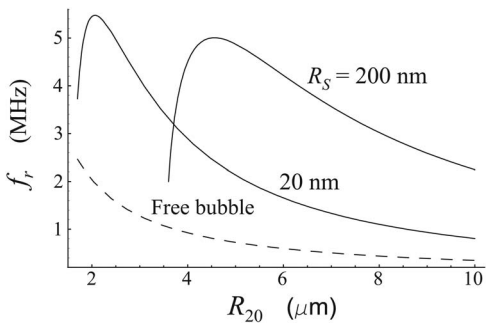

FIG. 5. Damped resonance frequency $f_r=\omega_r/2\pi$ versus equilibrium bubble radius for two values of the shell thickness R_S. The dashed line corresponds to a free bubble of the equivalent size.

$$\rho_L\left(R\ddot{R}+\frac{3}{2}\dot{R}^2\right)=P_{g0}\left(\frac{R_0}{R}\right)^{3\gamma}-\frac{2\sigma}{R}-P_0-P_{\mathrm{ac}}-4\eta_L\frac{\dot{R}}{R}-12\eta_S R_S\frac{\dot{R}}{R^2}-12\mu_S R_S\frac{R_0}{R}\left(\frac{1}{R_0}-\frac{1}{R}\right), \tag{58}$$

where R denotes the outer bubble radius and $\sigma=\sigma_1+\sigma_2$. It is easy to see that Eq. (58) is practically identical to the equation proposed by de Jong *et al.* for Albunex microspheres[1,2] provided that

$$S_p=6R_S\mu_S \quad \text{and} \quad S_f=48\pi R_S\eta_S, \tag{59}$$

where S_p and S_f are, respectively, the shell elasticity parameter and the shell friction parameter that appear in de Jong *et al.*'s model. Using Eqs. (59) and the results of de Jong *et al.*, we can estimate values of μ_S and η_S for albumin-shelled bubbles. Assuming $R_S=15$ nm, one has $\mu_S=88.8$ MPa and $\eta_S=1.77$ Pa s, in agreement with Church's estimates.[4] By using Ref. 23, the parameters S_p and S_f can also be evaluated for lipid-shelled bubbles. For example, setting $R_S=1$ nm as is proposed by Morgan *et al.*[6] for lipid coatings, one finds $\mu_S=333.3$ MPa and $\eta_S=2.4$ Pa s. Note that the value of η_S is of the same order of magnitude as that obtained by Morgan *et al.*[6] by fitting experimental radius-time curves. As regards the elastic term used in the model of Morgan *et al.*, Marmottant *et al.*[23] have recently shown that it is incorrect. Therefore comparison of the value of μ_S is impossible.

Marmottant *et al.*[23] also showed that for lipid-shelled bubbles, the elastic behavior of the bubble shell can occur only for very small oscillations of the bubble radius about its equilibrium value. For larger oscillations, the shell buckles when the bubble is compressed and breaks up when the bubble expands. Therefore a continuous elastic model like Eq. (58) is not a good approximation for lipid-shelled contrast agents. However, for bubbles with a sufficiently thick encapsulation, such as polymer- or albumin-shelled contrast agents, Eqs. (31) and (32) can be quite adequate.

V. RADIATION FORCE AND TRANSLATIONAL MOTION

In this section, we apply Eqs. (31) and (32) to calculate the radiation force experienced by an encapsulated bubble and the translational displacement of the bubble due to this force. Let us first consider radiation force in a weak field,

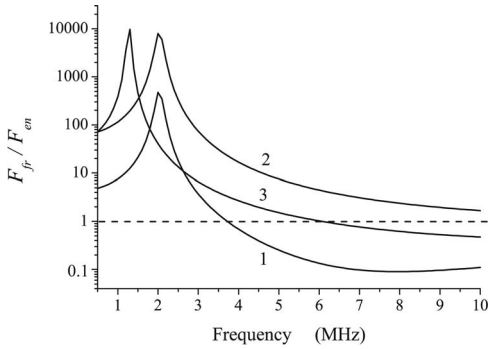

FIG. 7. Comparison of radiation force experienced by an encapsulated bubble in a weak field with that on a free bubble of the equivalent size at various driving frequencies. (1) $R_{20}=2$ μm, $R_S=15$ nm; (2) $R_{20}=2$ μm, $R_S=200$ nm; and (3) $R_{20}=3$ μm, $R_S=200$ nm.

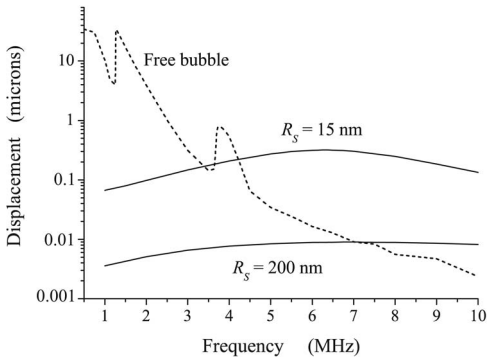

FIG. 8. Translational displacement versus driving frequency for a free and an encapsulated bubble. The driving field is a single 20-cycle acoustic pulse with a pressure amplitude of 150 kPa. The displacement is fixed after the termination of the pulse. The outer radius of the bubbles is 2 μm.

assuming that the radial oscillation of the bubble is described by Eq. (43). The radiation force exerted on the bubble can be calculated as

$$\boldsymbol{F}_{\mathrm{en}} = -\frac{4\pi}{3}\langle R_2^3(t)\boldsymbol{\nabla} P_{ac}(\boldsymbol{r},t)\rangle, \tag{60}$$

where $\langle\rangle$ means the time average and $\boldsymbol{r}$ is the position vector of the bubble centroid. Substituting $R_2(t)$ from Eq. (42), one obtains

$$\boldsymbol{F}_{\mathrm{en}} = -4\pi R_{10}^2\langle \xi(t)\boldsymbol{\nabla} P_{ac}(\boldsymbol{r},t)\rangle. \tag{61}$$

In the case of a plane traveling wave, $P_{ac}(\boldsymbol{r},t)=P_a\exp(i\omega t - i\boldsymbol{k}\cdot\boldsymbol{r})$, where $k=\omega/c$ is the wave vector. Substituting this expression into Eq. (43), one finds $\xi(t)$ to be

$$\xi(t) = \frac{P_{ac}(\boldsymbol{r},t)}{\alpha\rho_S R_{10}(\omega^2-\omega_0^2-i\omega\delta)}. \tag{62}$$

Substitution of Eq. (62) into Eq. (61) finally yields

$$F_{\mathrm{en}} = \frac{2\pi P_a^2 R_{10}\omega\delta k}{\alpha\rho_S[(\omega^2-\omega_0^2)^2+\omega^2\delta^2]}. \tag{63}$$

The radiation force on a free bubble of the equivalent radius is given by[24]

$$F_{\mathrm{fr}} = \frac{2\pi P_a^2 R_{20}\omega\delta_f k}{\rho_L[(\omega^2-\omega_{0f}^2)^2+\omega^2\delta_f^2]}, \tag{64}$$

where

$$\delta_f = \frac{\omega^2 R_{20}}{c} + \frac{4\eta_L}{\rho_L R_{20}^2}, \tag{65}$$

$$\omega_{0f} = \frac{1}{R_{20}\sqrt{\rho_L}}\left(3\gamma P_0 + \frac{2(3\gamma-1)\sigma}{R_{20}}\right)^{1/2}. \tag{66}$$

Figure 7 displays the ratio $F_{\mathrm{fr}}/F_{\mathrm{en}}$ as a function of driving frequency for three bubbles with different values of equilibrium radius and shell thickness. The presence of encapsulation decreases the amplitude of the radial oscillation of contrast agent bubbles. For this reason, it is commonly supposed that the radiation force on an encapsulated bubble should be considerably smaller than that on a free bubble of the equivalent size. Figure 7 reveals, however, that this is not true throughout the whole frequency range. At relatively low frequencies, near the resonance of the free bubble, the radiation force on the free bubble is really much larger than that on the encapsulated bubbles. However, for higher frequencies, in the range of resonances of the encapsulated bubbles, the radiation force on the encapsulated bubble exceeds that on the free bubble. Curve 3 shows that this effect can occur even for a thick-shelled bubble with $R_S=200$ nm if its outer radius is large enough.

Figure 8 shows the translational displacement of a free bubble (dashed line) and two equivalent encapsulated bubbles with $R_S=15$ nm and 200 nm under stronger driving. The bubbles are subjected to a single 20-cycle acoustic pulse with a pressure amplitude of 150 kPa. The displacement is fixed after the termination of the pulse. The outer radius of all the bubbles is 2 μm. The simulation was carried out by numerically calculating Eqs. (31) and (32). It is again seen that at high frequencies the displacement of the encapsulated bubbles is considerably larger, this time even for the 2-μm-radius bubble with $R_S=200$ nm. Thus, it is found that in the range of relatively high frequencies encapsulated bubbles are able to translate more efficiently than free bubbles of equivalent size.

VI. CONCLUSIONS

In this work coupled equations describing the radial and translational dynamics of an encapsulated gas bubble are derived. It is assumed that the encapsulating layer is an incompressible elastic solid with viscous damping and the surrounding medium is a slightly compressible viscous Newtonian liquid. The proposed model improves Church's theory[4] by allowing for the translation motion of the bubble and radiation losses due to the compressibility of the surrounding liquid. It is also shown that the expression obtained by Church for the inner bubble radius corresponding to the unstrained state of the encapsulating shell gives an incorrect result when the shell thickness tends to zero. The expression for the unstrained radius is recalculated by using equations from the theory of elasticity.

Comparative analysis of the linearized radial equation is carried out relative to Church's theory. In the course of the analysis, the expression for the acoustic damping constant of

an encapsulated bubble is refined, and it is shown that Church's theory underestimates the damped resonance frequencies of encapsulated bubbles. It is also shown that the viscous damping in the bubble shell can lead to the absence of resonance response. This effect is observed when the bubble radius is smaller than a threshold value; the thicker the bubble shell, the larger the threshold bubble radius. Below the threshold radius, the amplitude of the radial oscillation monotonically decreases as the driving frequency increases.

The acoustic radiation force experienced by an encapsulated bubble in a weak field is calculated analytically and compared with the radiation force on a free bubble of the equivalent size. It is shown that for high frequencies, the radiation force on the encapsulated bubble exceeds that on the free bubble. For the case of stronger driving, comparison of the radiation forces is carried out by numerically calculating the translational displacement of the bubbles, using the nonlinear coupled equations of the radial and translational motions. It is shown again that at high frequencies the displacement of encapsulated bubbles is considerably greater than that of free bubbles of equivalent size.

ACKNOWLEDGMENT

A.A.D. wishes to acknowledge the financial support of the International Science and Technology Center (ISTC) under Contract No. B-1213.

[1]N. de Jong, R. Cornet, and C. T. Lancee, "Higher harmonics of vibrating gas-filled microspheres. Part one: simulations," Ultrasonics **32**, 447–453 (1994).
[2]N. de Jong and L. Hoff, "Ultrasound scattering of Albunex microspheres," Ultrasonics **31**, 175–181 (1993).
[3]P. J. A. Frinking and N. de Jong, "Acoustic modeling of shell-encapsulated gas bubbles," Ultrasound Med. Biol. **24**, 523–533 (1998).
[4]C. C. Church, "The effect of an elastic solid surface layer on the radial pulsations of gas bubbles," J. Acoust. Soc. Am. **97**, 1510–1521 (1995).
[5]K. Vokurka, "Comparison of Rayleigh's, Herring's, and Gilmore's models of gas bubbles," Acustica **59**, 214–219 (1986).
[6]K. E. Morgan, J. S. Allen, P. A. Dayton, J. E. Chomas, A. L. Klibanov, and K. W. Ferrara, "Experimental and theoretical evaluation of microbubble behavior: Effect of transmitted phase and bubble size," IEEE Trans. Ultrason. Ferroelectr. Freq. Control **47**, 1494–1509 (2000).
[7]P. A. Dayton, J. S. Allen, and K. W. Ferrara, "The magnitude of radiation force on ultrasound contrast agents," J. Acoust. Soc. Am. **112**, 2183–2192 (2002).
[8]H. Lamb, *Hydrodynamics* (Cambridge U. P., Cambridge, 1957).
[9]O. V. Voinov and A. G. Petrov, "Motion of a sphere of changing volume in an ideal fluid near a flat surface," Izv. Akad. Nauk SSSR, Mekh. Zhidk. Gaza **5**, 94–103 (1971).
[10]M. Ceschia and R. Nabergoj, "On the motion of a nearly spherical bubble in a viscous liquid," Phys. Fluids **21**, 140–142 (1978).
[11]B. B. Chakraborty and G. S. Tuteja, "Motion of an expanding, spherical gas bubble in a viscous liquid under gravity," Phys. Fluids A **5**, 1879–1882 (1993).
[12]S. Luther, R. Mettin, and W. Lauterborn, "Modeling acoustic cavitation by a Lagrangian approach," in *Proceedings of the 15th International Symposium on Nonlinear Acoustics*, edited by W. Lauterborn and T. Kurz (AIP, Melville, NY, 2000), pp. 351–354.
[13]A. A. Doinikov, "Translational motion of two interacting bubbles in a strong acoustic field," Phys. Rev. E **64**(2), 026301 (2001).
[14]A. A. Doinikov, "Translational motion of a spherical bubble in an acoustic standing wave of high intensity," Phys. Fluids **14**, 1420–1425 (2002).
[15]A. A. Doinikov, "Mathematical model for collective bubble dynamics in strong ultrasound fields," J. Acoust. Soc. Am. **116**, 821–827 (2004).
[16]E. A. Zabolotskaya, Yu. A. Ilinskii, G. D. Meegan, and M. F. Hamilton, "Modifications of the equation for gas bubble dynamics in a soft elastic medium," J. Acoust. Soc. Am. **118**, 2173–2181 (2005).
[17]L. D. Landau and E. M. Lifshitz, *Mechanics* (Pergamon, Oxford, 1976).
[18]A. A. Doinikov, "Equations of coupled radial and translational motions of a bubble in a weakly compressible liquid," Phys. Fluids **17**(12), 128101 (2005).
[19]S. Y. Emelianov, M. F. Hamilton, Y. A. Ilinskii, and E. A. Zabolotskaya, "Nonlinear dynamics of a gas bubble in an incompressible elastic medium," J. Acoust. Soc. Am. **115**, 581–588 (2004).
[20]L. D. Landau and E. M. Lifshitz, *Theory of Elasticity* (Pergamon, Oxford, 1986).
[21]L. D. Landau and E. M. Lifshitz, *Fluid Mechanics* (Pergamon, Oxford, 1987).
[22]A. Prosperetti, "The equation of bubble dynamics in a compressible liquid," Phys. Fluids **30**, 3626–3628 (1987).
[23]P. Marmottant, S. van der Meer, M. Emmer, M. Versluis, N. de Jong, S. Hilgenfeldt, and D. Lohse, "A model for large amplitude oscillations of coated bubbles accounting for buckling and rupture," J. Acoust. Soc. Am. **118**, 3499–3505 (2005).
[24]A. A. Doinikov, "Bjerknes forces and translational bubble dynamics," in *Bubble and Particle Dynamics in Acoustic Fields: Modern Trends and Applications*, edited by A. A. Doinikov (Research Signpost, Trivandrum, Kerala, 2005), pp. 95–143.

Translation of bubbles subject to weak acoustic forcing and error in decoupling from volume oscillations

Dagmar Krefting[a)]
Institute for Medical Informatics, Charité - Universitätsmedizin Berlin, Hindenburgdamm 30, 12200 Berlin, Germany

Jean O. Toilliez and Andrew J. Szeri
Department of Mechanical Engineering, University of California, Berkeley, California 94720-1740

Robert Mettin and Werner Lauterborn
Drittes Physikalisches Institut, Georg-August-Universität Göttingen, Friedrich-Hund-Platz 1, 37077 Göttingen, Germany

(Received 28 December 2005; revised 10 May 2006; accepted 19 May 2006)

A microbubble in a sound wave oscillates in volume and translates unsteadily. The two motions are coupled. In large-scale simulations of the structure of bubble clouds driven by acoustic fields, it has been of significant convenience to decouple volume oscillations and translation, as an approximation. The errors of this decoupling approximation were considered in an earlier presentation [A. J. Reddy and A. J. Szeri, J. Acoust. Soc. Am. **112**, 1346–1352 (2002)], in the parameter range of interest in medical ultrasound. In this work, the approximation is reexamined for a much broader range of driving frequencies and bubble sizes. Solving the equation of motion for linearly oscillating bubbles, it is found that even for weak acoustic forcing, the translation speed obtained with the decoupling approximation can be in error as much as 30% relative to the translation speed in the full equations. The error depends on the bubble size, the driving frequency, and the liquid properties. The results are presented in a form convenient for applications. The principal utility of the analysis is for bubbles in microgravity, or in normal gravity driven by a soundfield with a horizontal wave-number vector. © *2006 Acoustical Society of America.*
[DOI: 10.1121/1.2214132]

PACS number(s): 43.25.Yw, 43.25.Ts [MFH] Pages: 670–675

I. INTRODUCTION

Pressure gradients force bubbles into translational motion relative to the surrounding liquid. The best known example is the rising of bubbles due to gravity induced hydrostatic pressure. Though pressure gradients in harmonic standing wave fields are periodic and the mean pressure gradient is zero, radial oscillations of the bubble may lead to a nonvanishing net force that results in mean translational motion of the bubble. A single bubble can be trapped near a pressure antinode, if the net force—the primary Bjerknes force—balances buoyancy over a driving cycle. In multibubble systems, complex spatio-temporal structures form. Acoustically driven bubbles are important in ultrasonic cleaning, sonochemistry and in certain medical applications. Knowledge of the underlying principles is necessary to predict and control the behavior of the bubble field and to improve and develop technical applications.

The radial pulsation of a bubble including strong nonlinear behavior at high acoustic pressures and violent collapses is described by the Rayleigh-Plesset equation and its extensions.[1] The translational dynamics of a single bubble in a stationary sound field were first investigated by Crum and Eller.[2] The equation of mean translational motion of a linear oscillating bubble is derived by the forces acting over one cycle of acoustic driving. This idea of averaging and decoupling the equation of motion to calculate the long term behavior of bubble movement in acceptable computational time was later adapted by Parlitz *et al.*[3]

Reddy and Szeri recently considered the averaged and decoupled and the full time resolved equation of motion for a single microbubble at different external forcing and frequencies.[4] To illustrate their point, they give the error for two sets of parameters at moderate pressure amplitude. In the case of a strong collapse in subresonant driving, they obtain an error of approximately 35%. Superresonant driving results in a mild collapse with an error of about 120% in the average velocity. The main reason for the differing solution is the inaccurate decoupling of the time average of the drag force term. The drag force term contains the product of radius and translational velocity. Crum and Eller decoupled the averaged drag force term by using the product of the averaged radius and averaged speed. In the regime investigated of weak external forcing, Reddy and Szeri find good agreement between the averaged speed obtained by the full equation and the averaged equation of motion. Therefore they postulate that the decoupled average suffices as an estimate for the drag force term. However, the focus by Reddy and Szeri was on conditions relevant to medical ultrasound—i.e., bubble radii of few microns and frequencies on the order of a few megahertz. In the present work we examine a much broader

a)Electronic mail: dagmar.krefting@charite.de

 0001-4966/2006/120(2)/670/6/$22.50

range of radii and driving frequencies and find that even in the case of weak forcing, the decoupling approximation can lead to considerable errors on the order of 30%. This is a significant result to bear in mind, particularly if one wants to use a decoupling approximation to enable large-scale simulation of the translation dynamics of many bubbles in a cloud.[3]

Hence the objective of this work is to investigate the error induced by decoupling radial oscillations and translation. The behavior of a single bubble subject to acoustic forcing—even if nonlinear—can be solved quite rapidly on a desktop computer. However, the strategy implemented here may be more appropriate in computationally intensive cases, such as the study of multibubble systems, as mentioned above.

II. EQUATION OF TRANSLATIONAL MOTION

A. The full equation

The translational motion of a spherical bubble in an uncompressible liquid was derived in different ways,[2,5–7] but results in mainly the same equation. The general differential form of the one-dimensional equation of motion

$$\frac{dP}{dt} = \sum_i F_i$$

can be used as a starting point. The momentum P of a void bubble is given by the added momentum of the surrounding liquid, in the case of a spherical object the added mass is one-half of a liquid drop of the size of the bubble[8]

$$P = -\frac{\rho 2\pi R^3}{3} U, \tag{1}$$

where ρ describes the density of the liquid, $R(t)$ the bubble radius, and $U(t)$ the liquid velocity in the far field relative to the bubble. As external forces F_i we consider the acoustical driving F_p and the viscous drag force F_d. Buoyancy is not included, assuming an acoustical forcing perpendicular to gravity or under microgravity conditions. The situation of motion in line with gravity will be discussed later. The first external force, F_p, is—as known from hydrodynamics—the pressure acting on the surface of the bubble. Using the Gauss theorem this can be written in terms of the pressure gradient ∇p and bubble volume V,

$$F_p = -V \nabla p = -\frac{4\pi R^3}{3} \nabla p, \tag{2}$$

assuming that the pressure gradient is constant over the area of integration; or that the bubble is small compared to the wavelength of the acoustic wave. In the case of a sound field, this force is referred to as the primary Bjerknes force, although the name was originally used for the net force over one period of driving. The primary Bjerknes force can be identified with the inertia force in the approach of Magnaudet and Legendre[6] by using the Euler equation for the liquid in the far field.[4]

When considering a viscous fluid, we must add the viscous drag force. The drag force depends on the Reynolds number

$$\mathrm{Re} = \frac{\rho R|u|}{\eta}.$$

Here, η is the dynamic viscosity of the liquid. Generally, the characteristic velocity u is the translational speed $u = U(t)$. Magnaudet and Legendre[6] introduced the radial velocity $\dot{R}$ of the bubble wall as a second characteristic velocity. This leads to the definition of two different Reynolds numbers for the bubble motion

$$\mathrm{Re}_U = \frac{\rho R|U|}{\eta}, \quad \mathrm{Re}_{\dot{R}} = \frac{\rho R|\dot{R}|}{\eta}.$$

They distinguished two limiting cases for which they could derive the viscous drag force. For $\mathrm{Re}_U \gg 1$ *or* $\mathrm{Re}_{\dot{R}} \gg 1$ the viscous drag force is similar to the case of a nonoscillating spherical void at high Reynolds numbers[8]

$$F_d = 12\pi\eta R U. \tag{3}$$

At $\mathrm{Re}_U \ll 1$ and $\mathrm{Re}_{\dot{R}} \ll 1$ the expression splits in two parts, a term analogous to expression (3) but three times smaller, and a memory-integral term analogous to the Basset-Boussinesq force.[4,9] In this paper the first case is chosen, for reasons explained in Appendix B. Combining these terms and letting the hydrodynamic force go to zero—the mass of the bubble is negligible—lead to the equation of motion

$$\frac{\rho 2\pi}{3} \frac{d}{dt} R^3 U = \frac{4\pi R^3}{3} \nabla p - 12\pi\eta R U. \tag{4}$$

For mathematical purposes it is conveniently recast as

$$\dot{U} = -\left[\frac{18\eta}{\rho} \frac{1}{R^2} + \frac{3\dot{R}}{R} \right] U + \frac{2\nabla p}{\rho}. \tag{5}$$

In this paper we propose to first solve the equation for the velocity explicitly, and later, compare it to the mean velocity found from the averaged and decoupled equation of motion.

B. The averaged and decoupled equation of motion

Let us introduce the operator $\langle \cdots \rangle_T$, such that

$$f_T = \langle f(t) \rangle_T := 1/T \int_0^T f(t) dt.$$

Now, in the case of a standing wave ultrasonic field, the pressure gradient can be separated in the following form:

$$\nabla p(x,t) = \nabla p_a(x) \sin \omega t.$$

Therefore, averaging the equation of motion (4) over one period of acoustic driving $T = 2\pi/\omega$ yields

$$\frac{\rho 2\pi}{3}\langle R^3\dot{U}\rangle_T = \frac{4\pi\nabla p_a}{3}\langle R^3 \sin\omega t\rangle_T - 12\pi\eta\langle RU\rangle_T. \quad (6)$$

The added momentum and drag force terms feature the averages of coupled functions, namely radius and velocity. The objective of this work is to study the error made by decoupling these terms, that is, by rewriting the equation of motion in its averaged and decoupled form,

$$\frac{\rho 2\pi R_T^3}{3}\dot{U}_T = \frac{4\pi\nabla p_a}{3}\langle R^3 \sin\omega t\rangle_T - 12\pi\eta R_T U_T. \quad (7)$$

The decoupling process is of significant benefit: once the average radial motion is known, it becomes straightforward to integrate the average velocity. This decoupling operation can be considered a good approximation if two conditions are respected:

(i) The bubble undergoes weak oscillations $\tilde{R}(t)$ with respect to R_T,

$$R(t) = R_T + \tilde{R}(t), \quad \mathcal{O}(\tilde{R}(t)) = \epsilon R_T.$$

(ii) The oscillatory component of the translational motion $\tilde{U}(t)$ remains small compared to the mean velocity U_T,

$$U(t) = U_T + \tilde{U}(t), \quad \mathcal{O}(\tilde{U}(t)) = \epsilon U_T.$$

Conditions (i) and (ii) allow one to write the time dependent part of the averaged drag force in the form

$$\langle RU\rangle_T = R_T U_T + \langle\tilde{U}\rangle_T R_T + \langle\tilde{R}\rangle_T U_T + \tilde{R}\tilde{U}. \quad (8)$$

The second and third term of right-hand side of (8) are eliminated, since by definition $\langle\tilde{R}\rangle_T = \langle\tilde{U}\rangle_T = 0$. The last term of the equation is of order $\mathcal{O}(\epsilon^2)$ and may therefore be neglected and

$$\langle RU\rangle_T \approx \langle R\rangle_T\langle U\rangle_T, \quad (9)$$

hence justifying the form of (7).

C. Discussion

In the case of sufficiently large acoustic pressure, condition (i) is not applicable: violent bubble collapses contradict any linear radial approximation. In the case of weak forcing, as considered in this paper, it is met within the limits of linear radial oscillation. Condition (ii) consists in having a large average translation velocity, supplemented by a smaller oscillatory component. Let us examine the situation where gravity is included in the problem (5) (Ref. 10) and lines up with the acoustic pressure gradient. A consequence of it is an averaged translational component of order ϵ^0, which is solely due to the buoyancy force—e.g., a rising bubble in a supersaturated solution of carbon dioxide. Condition (ii) is satisfied in this case. A straightforward analysis yields the minimal pressure gradient necessary to achieve bubble levitation. In the latter case, only a pure oscillatory motion, induced by acoustic forcing, is achieved[10] and condition (ii) is violated. Because of zero speed over a period of driving, the present analysis is not necessary. In the present work, we focus on bubble motion in between these two limiting cases, where condition (ii) is likely to be violated.

III. THE EQUATION OF MOTION WITH LINEARIZED RADIAL OSCILLATION

We assume weak harmonic radial oscillations in the form

$$R(t) = R_0[1 - \epsilon\sin\omega t]. \quad (10)$$

The result may be obtained by linearizing one of the numerous equations modeling the radial bubble dynamics.[1,3,11] Unidirectional coupling of the radial and translational dynamics was chosen in a way that the radial oscillation is not influenced by the translational motion of the bubble. Doinikov pointed out that the correct equation of radial motion includes an additional term of $U^2/4$ to the external force.[7] As he showed numerically, this term has mainly an effect at higher pressure amplitudes. Therefore we neglect this term following Watanabe and Kukita[5] as well as Reddy and Szeri.[4] The phase of oscillation was chosen to be valid for subresonant forced bubbles (see Appendix A). The equation of motion (5) can then be written in the following form:

$$\dot{U} = -\left[\frac{18\eta}{\rho R_0^2}[1 + 2\epsilon\sin\omega t] - 3\epsilon\omega\cos\omega t\right]U + \frac{2\nabla p_a}{\rho}\sin\omega t \quad (11)$$

$$= -\left[k_1 + \epsilon\sqrt{(2k_1)^2 + (3\omega)^2}\times\sin\left(\omega t - \tan^{-1}\frac{3}{2k_1\omega}\right)\right]U + k_2\sin\omega t, \quad (12)$$

with

$$k_1 = \frac{18\eta}{\rho R_0^2} \quad \text{and} \quad k_2 = \frac{2\nabla p_a}{\rho}. \quad (13)$$

A. The mean velocity obtained by the full equation

Equation (12) is an ordinary differential equation which can be solved using variation of constants. The full solution is given in (C11) in Appendix C. In this work we are mainly interested in the mean velocity. Furthermore, the equation of motion was developed for the relative liquid velocity, which can be expressed by the absolute liquid velocity U_a (relative to an inertial frame) and the bubble motion $\dot{x}$ in the inertial frame,

$$U = U_a - \dot{x}. \quad (14)$$

The absolute velocity of the liquid is given by the acoustic sound field and is strictly periodic, so its mean value vanishes, hence

$$\langle U\rangle_T = -\langle\dot{x}\rangle_T. \quad (15)$$

In the quasistationary case the averaged speed is

$$\langle \dot{x} \rangle_T = \frac{3\epsilon k_2}{2k_1} \sqrt{1 + \left(\frac{2k_1}{3\omega}\right)^2} \cdot \frac{\omega/k_1}{1 + \omega^2/k_1^2} \times \left[\frac{\omega}{k_1} \sin \tan^{-1} \frac{3\omega}{2k_1} + \cos \tan^{-1} \frac{3\omega}{2k_1} \right]. \quad (16)$$

For further use, the parameter c is defined by

$$c = \frac{\omega}{k_1}.$$

We note that this parameter corresponds to the dimensionless viscosity: $18\nu^* = 1/c$—or a Reynolds number—mentioned by Popinet and Zaleski.[10] They derived a linearized equation identical to (11), but included the buoyancy force and used a different approach to obtain the oscillatory component of the motion around the equilibrium point. The mean speed can then be recast as a function of this parameter, multiplied by a factor $3\epsilon k_2/2k_1$, containing the information about the pressure distribution,

$$\langle \dot{x} \rangle_T = \frac{3\epsilon k_2}{2k_1} \sqrt{1 + \left(\frac{2}{3c}\right)^2} \cdot \frac{c}{1 + c^2} \times \left[\cos \tan^{-1} \frac{3c}{2} + c \cdot \sin \tan^{-1} \frac{3c}{2} \right] = \frac{3\epsilon k_2}{2k_1} f(c). \quad (17)$$

B. The averaged velocity obtained by time averaging and decoupling the equation of motion

Using the assumption (10), one can average the equation of motion as stated in (6) over one period of time and apply the decoupling approximation to obtain (7). From

$$R^3 \sin \omega t \approx R_0^3 (1 - 3\epsilon \sin \omega t) \sin \omega t + \mathcal{O}(\epsilon^2),$$

one may approximate

$$\langle R^3 \sin \omega t \rangle_T \approx -R_0^3 \langle \sin^2 \omega t \rangle_T = -\frac{3\epsilon R_0^3}{2}.$$

This, in conjunction with (13), allows for rewriting (7) as

$$\frac{\rho 2\pi R_0^3}{3} \dot{\bar{U}} = -\pi \rho k_2 \epsilon R_0^3 - 12\pi \eta R_0 \bar{U}.$$

Assuming all transients have expired, hence letting $\dot{\bar{U}} = 0$, and according to (14), it follows that

$$\bar{U} = -\frac{3\epsilon k_2}{2k_1} \Leftrightarrow \bar{\dot{x}} = \frac{3\epsilon k_2}{2k_1}. \quad (18)$$

IV. RESULTS

We compare the averaged velocity $\bar{\dot{x}}$ from the decoupling approximation with the mean velocity $\langle \dot{x} \rangle_T$ from the full equation. The solution differs in the parameter dependent part

$$\langle \dot{x} \rangle_T = \bar{\dot{x}} f(c). \quad (19)$$

In Fig. 1 we show the function $f(c)$. As $c \to \infty$, $\langle \dot{x} \rangle_T \to \bar{\dot{x}}$.

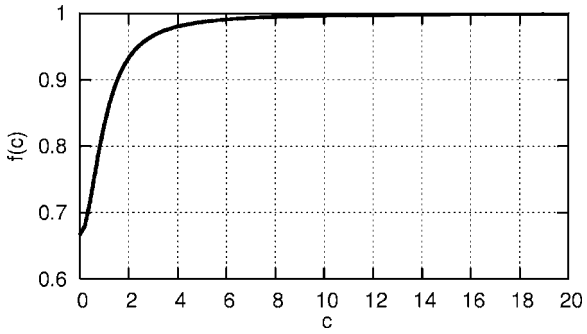

FIG. 1. Plot of the correction function, $f(c)$.

The actual bubble motion may be slower than predicted by the averaged and decoupled equation of motion at small c. The mean velocity is the limit case for large c. Upon writing out the definition of the parameter c,

$$c = \frac{\omega}{k_1} = \frac{\omega \rho R_0^2}{18\eta}, \quad (20)$$

it is easy to determine the influence of the experimental parameters and liquid characteristics. The condition of high c is satisfied for liquids with high density and low viscosity. For water with a density of $\rho = 10^3$ kg/m^3 and a dynamic viscosity of $\eta = 10^{-3}$ kg/ms, the parameter c is given by

$$c_{\text{water}} = \frac{10^6}{18} \omega R_0^2. \quad (21)$$

An error on the averaged (decoupled) velocity of less than 1% is given by

$$c > c_{0.01} \approx 6; \quad (22)$$

the averaged (decoupled) velocity is the same as the mean velocity with an accuracy better than 99.9% for

$$c > c_{0.001} \approx 20. \quad (23)$$

The corresponding radii R_0 are given approximately by

$$R_{0,0.01} > \sqrt{\frac{10^{-4}}{\omega}}, \quad (24)$$

$$R_{0,0.001} > \sqrt{\frac{4 \times 10^{-4}}{\omega}}. \quad (25)$$

This can also be written in terms of the resonance radius R_r for a given sound frequency f_0, using it as the Minnaert frequency[1]

$$f_0 = \frac{\omega}{2\pi} = \frac{3}{R_r} \frac{m}{s}, \quad (26)$$

$$R_{0,0.01} > \sqrt{6 \times 10^{-6} R_r}, \quad (27)$$

$$R_{0,0.001} > \sqrt{2 \times 10^{-5} R_r}. \quad (28)$$

In Fig. 2 we show the minimum equilibrium radius R_0 satisfying these conditions and the linear resonance radius R_r in the low ultrasound regime. The graph shows that there is a significant range of bubble sizes where the averaged equa-

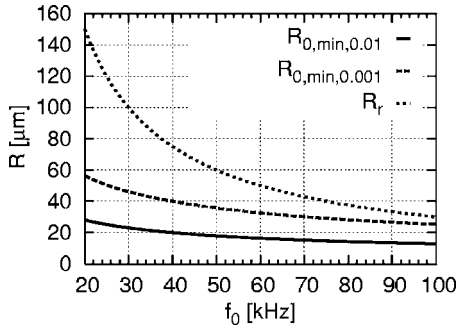

FIG. 2. Minimum equilibrium radius to achieve an error between the averaged (decoupled) velocity and the mean velocity of less than 1% ($R_{0,\min,0.01}$, solid line), respectively, 0.1% ($R_{0,\min,0.001}$, dashed line), and the corresponding linear resonance radius (R_r, dotted line) in the low ultrasound regime.

tion of motion gives the same result as the full time resolved case. For smaller bubbles the translational velocity is less. The error is up to 30%, but can be corrected by multiplying the correction function $f(c)$ *a posteriori*. The present work shows that even if the bubble undergoes only weak radial oscillations, the average of radius and velocity is *not* necessarily equal to the product of the averages. In particular, small bubbles having a low added inertial mass follow the quickly oscillating pressure gradient, which results in a significant time-varying part of the translational velocity. We want to emphasize that the correction function obtained above does not depend upon the acoustic pressure. The Rayleigh-Plesset equation determines the radial amplitude and gives the limits of the linearization. In the present work, we expand the findings of Reddy and Szeri to the case of mild forcing and weak linear oscillations in the subresonant case, and determined the limits of the validity of the decoupling approximation in the drag force term.

ACKNOWLEDGMENTS

One of the authors (D. K.) was supported by the Graduiertenkolleg "Strömungsinstabilitäten und Turbulenz" and the BMBF Projekt "Untersuchung von Kavitationsfeldern." Two of the authors (J. O. T. and A. J. S.) were supported by the NASA Program in Microgravity Fluid Physics. The authors thank Matthias Grott for helpful discussions.

APPENDIX A: SUBRESONANT DRIVING

In subresonant driving, the driving frequency f_0 is less than the bubble's linear resonance frequency f_R, which is given for air bubbles of size R_0 in water approximately by the Minneart frequency f_R,[1]

$$f_0 < f_R, \quad f_R = \frac{3}{R_0}\frac{m}{s}. \tag{A1}$$

Conversely, the bubble's radius is less than the resonance radius R_r,

$$R_0 < R_r, \quad R_r = \frac{3}{f_0}\frac{s}{m} = \frac{6\pi}{\omega}\frac{s}{m}. \tag{A2}$$

APPENDIX B: THE CHOICE OF THE DRAG FORCE TERM

We assume linear radial oscillations as given in (10). The radial velocity is $\dot{R}(t) = -\epsilon\omega R_0 \cos(\omega t)$. The second Reynolds number can be evaluated

$$\mathrm{Re}_{\dot{R}} \approx \frac{\rho R_0^2 \epsilon\omega}{\eta} \approx 10^6 R_0^2 \epsilon\omega, \tag{B1}$$

by using the water properties $\rho = 10^3\ \mathrm{kg/m^3}$ and $\eta = 10^{-3}$ kg/ms. The lower limit for the accuracy of (3) is set to the value of $\mathrm{Re}_{\dot{R}} \geq 12$. This is in accordance to the verification calculations by Magnaudet and Legendre.[6] The upper linearization limit for the radial amplitude is set to $\epsilon \leq 0.1$, giving an error of 1%. The range of bubble sizes relative to the resonance radius, where (5) is accurate, is determined by the following expression:

$$\frac{R_0}{R_r} \geq \sqrt{\frac{2f_0 \times 10^{-5}}{3\pi}}.$$

At $f_0 = 20$ kHz the condition is satisfied by bubbles of size $30\ \mu\mathrm{m} < R_0 \leq 150\ \mu$m, at $f_0 = 100$ kHz the range is $14\ \mu\mathrm{m} \leq R_0 < 30\ \mu$m. Furthermore, Reddy and Szeri propose to use expression (3) even for bubbles with $\mathrm{Re}_U \ll 1$ and $\mathrm{Re}_{\dot{R}} \ll 1$: for microbubbles driven at MHz frequencies, reasonably accurate results are obtained.[4]

APPENDIX C: SOLUTION OF THE DIFFERENTIAL EQUATION

First, the radius dependent terms in (5) are approximated as a Taylor series, where $\epsilon \ll 1$. Hence,

$$\frac{1}{R^2(t)} = \frac{1}{R_0^2(1-\epsilon\sin\omega t)^2} \approx \frac{1}{R_0^2}[1 + 2\epsilon\sin\omega t] + \mathcal{O}(\epsilon^2), \tag{C1}$$

$$\frac{\dot{R}(t)}{R(t)} = \frac{-\epsilon\omega\cos\omega t}{1-\epsilon\sin\omega t} = -\epsilon\omega\cos\omega t(1-\epsilon\sin\omega t)^{-1} \approx -\epsilon\omega\cos\omega t + \mathcal{O}(\epsilon^2). \tag{C2}$$

Using these results, (12) is recast in the form

$$\dot{U} = -[k_1 + \epsilon k_3 \sin(\omega t + k_4)]U + k_2 \sin\omega t, \tag{C3}$$

with

$$k_3 = ((2k_1)^2 + (3\omega)^2)^{1/2} \quad \text{and} \quad k_4 = -\tan^{-1}\frac{3\omega}{2k_1}.$$

We approach a solution of the form

$$U(t) = c(t)\exp(A(t)),$$

where $A(t)$ is obtained by solving the homogeneous differential equation,

$$A(t) = \int_{t_0}^{t} -[k_1 + \epsilon k_3 \sin(\omega s + k_4)]\mathrm{d}s$$

$$= -k_1 t + \frac{\epsilon k_3}{\omega}\cos(\omega t + k_4). \tag{C4}$$

By approximation of the oscillatory component

$$\exp\left(\frac{\epsilon k_3}{\omega}\cos(\omega t + k_4)\right) \approx 1 + \frac{\epsilon k_3}{\omega}\cos(\omega t + k_4),$$

we obtain

$$\exp(A(t)) = \exp(-k_1 t) + \epsilon k_5 \cos(\omega t)\exp(-k_1 t) - \epsilon k_6 \sin(\omega t)\exp(-k_1 t), \tag{C5}$$

with

$$k_5 = k_3 \cos(k_4)/\omega \quad \text{and} \quad k_6 = k_3 \sin(k_4)/\omega.$$

$c(t)$ is given by

$$c(t) = c(t_0) + \int_{t_0}^{t} [k_2 \sin(\omega s)\exp(-A(s))]ds$$

$$= c_0 \tag{C6}$$

$$+ k_2 \int_{t_0}^{t} \sin(\omega s)\exp(k_1 s)ds \tag{C7}$$

$$- \epsilon k_2 k_5 \int_{t_0}^{t} \sin(\omega s)\cos(\omega s)\exp(k_1 s)ds \tag{C8}$$

$$+ \epsilon k_2 k_6 \int_{t_0}^{t} \sin^2(\omega s)\exp(k_1 s)ds. \tag{C9}$$

By applying the initial condition $U(t=0)=0$, we set $c(t_0)=0$. Then, integrating from $t_0=0$ to t yields

$$c(t) = k_7 \sin(\omega t)\exp(k_1 t) + k_8 \cos(\omega t)\exp(k_1 t) - k_8 + \epsilon k_9 \cos(\omega t)\sin(\omega t)\exp(k_1 t) - \epsilon k_{10}\exp(k_1 t) + \epsilon k_{11}\sin^2(\omega t)\exp(k_1 t) - \epsilon k_{10}, \tag{C10}$$

with

$$k_7 = k_2 \cos(\tan^{-1} c)(k_1^2 + \omega^2)^{-1/2},$$

$$k_8 = k_2 - \sin(\tan^{-1} c)(k_1^2 + \omega^2)^{-1/2},$$

$$k_9 = k_2(k_5 + 2ck_6)(k_1(1 + (2c)^2))^{-1},$$

$$k_{10} = k_9 c,$$

$$k_{11} = 2k_{10} - k_2 k_6/k_1.$$

Multiplication of (C5) with (C10) results in

$$U(t) = -\epsilon[k_{10} + k_5 k_8 \cos^2(\omega t) + (k_1 1 + k_6 k_7)\sin^2(\omega t)] + k_7 \sin(\omega t) + k_8 \cos(\omega t) + \epsilon(k_5 k_7 + k_6 k_8 - k_9)\cos(\omega t)\sin(\omega t) + \exp(-k_1 t)[U_0 - k_8 - \epsilon k_{10} + \epsilon k_5(U_0 - k_8)\cos(\omega t) + \epsilon k_6(U_0 - k_8)\sin(\omega t)] + \mathcal{O}(\epsilon^2). \tag{C11}$$

We look for a quasistatic solution: we therefore neglect all transient terms in $\exp(-k_1 t)$. The integral of $\sin \omega t, \cos \omega t$, and $\sin \omega t \cdot \cos \omega t$ over one period are all equal to zero. To obtain the mean speed, we need only take the first four terms of (C11) into account. The result is given in (16).

[1] T. Leighton, *The Acoustic Bubble* (Academic, New York, 1994).
[2] L. Crum and A. Eller, "Motion of bubbles in a stationary sound field," J. Acoust. Soc. Am. **48**, 181–189 (1970).
[3] U. Parlitz, R. Mettin, S. Luther, I. Akhatov, M. Voss, and W. Lauterborn, "Spatio-temporal dynamics of acoustic cavitation bubble clouds," Philos. Trans. R. Soc. London, Ser. A **357**, 313–334 (1999).
[4] A. Reddy and A. Szeri, "Coupled dynamics of translation and collapse of acoustically driven microbubbles," J. Acoust. Soc. Am. **112**, 1346–1352 (2002).
[5] T. Watanabe and Y. Kukita, "Translational and radial motions of a bubble in an acoustic standing wave field," Phys. Fluids A **5**, 2682–2688 (1993).
[6] J. Magnaudet and D. Legendre, "The viscous drag force on a spherical bubble with a time-dependent radius," Phys. Fluids **10**, 550–554 (1998).
[7] A. Doinikov, "Translational motion of a spherical bubble in an acoustic standing wave of high intensity," Phys. Fluids **14**, 1420–1425 (2002).
[8] L. Landau and E. Lifschitz, *Hydrodynamik*, number 6 in Lehrbuch der Theoretischen Physik, 5th ed. (Akademie Verlag, Berlin, 1991).
[9] S. Yang and L. Leal, "A note on memory-integral contributions to the force on an accelerating spherical drop at low reynolds number," Phys. Fluids A **3**, 1822–1824 (1991).
[10] S. Popinet and S. Zaleski, "Coupling of radial and translational motion in small viscous bubbles," in *Proceeding of FEDSM99, 3dr ASME/JSME Joint Fluids Engineering Conference* (American Society of Mechanical Engineering, New York, NY, 1999).
[11] A. Prosperetti, L. Crum, and K. Commander, "Nonlinear bubble dynamics," J. Acoust. Soc. Am. **83**, 502–514 (1988).

Measurement of high intensity focused ultrasound fields by a fiber optic probe hydrophone

Yufeng Zhou, Liang Zhai, Rebecca Simmons, and Pei Zhong[a)]
Department of Mechanical Engineering and Materials Science, Duke University, Durham, North Carolina 27708

(Received 31 January 2006; revised 16 May 2006; accepted 19 May 2006)

The acoustic fields of a high intensity focused ultrasound (HIFU) transducer operating either at its fundamental (1.1 MHz) or third harmonic (3.3 MHz) frequency were measured by a fiber optic probe hydrophone (FOPH). At 1.1 MHz when the electric power applied to the transducer was increased from 1.6 to 125 W, the peak positive/negative pressures at the focus were measured to be $p^+=1.7-23.3$ MPa and $p^-=-1.2--10.0$ MPa. The corresponding spatial-peak pulse-average (I_{SPPA}) and spatial-average pulse-average (I_{SAPA}) intensities were $I_{SPPA}=77-6000$ W/cm^2 and $I_{SAPA}=35-4365$ W/cm^2. Nonlinear propagation with harmonics generation was dominant at high intensities, leading to a reduced −6 dB beam size (L×W) of the compressional wave (11.5×1.8–8.8×1.04 mm) but an increased beam size of the rarefactional wave (12.5×1.6–13.2×2.0 mm). Enhancement ratio of absorbed power density in water increased from 1.0 to 3.0. In comparison, the HIFU transducer working at 3.3 MHz produced higher peak pressures ($p^+=3.0-35.1$ MPa and $p^-=-2.5--13.8$ MPa) with smaller beam size (0.5×4 mm). Overall, FOPH was found to be a convenient and reliable tool for HIFU exposimetry measurement. © *2006 Acoustical Society of America.* [DOI: 10.1121/1.2214131]

PACS number(s): 43.25.Zx, 43.80.Ev, 43.25.Cb [CCC] Pages: 676–685

I. INTRODUCTION

In recent years, high intensity focused ultrasound (HIFU) has been used increasingly as a new and effective treatment modality for cancer therapy.[1–4] By focusing acoustic energy into a small cigar-shaped volume, HIFU ($I_{SPTA}>1000$ W/cm^2) can produce thermal ablation (temperature >65 °C) and tissue necrosis (i.e., a lesion) in a well-defined volume in the target tumor.[5] Treatment of the whole tumor is accomplished by scanning the HIFU beam line-by-line and layer-by-layer under the guidance of B-mode ultrasound or MRI imaging. For safe and effective HIFU treatment in the clinic, it is critical to predict and control the lesion size produced.[6] Towards this goal, a fundamental knowledge of the acoustic field and acoustic energy output of the HIFU system is essential and needs to be accurately determined.

Several techniques have been developed to measure the acoustic output of HIFU transducers. For example, calorimetry[7] and radiation force measurements[8] have been used to determine the total acoustic power produced by a HIFU transducer, from which the total energy flux through the beam cross-sectional area (or intensity) can be estimated. Although convenient to use, these techniques cannot resolve the pressure variation and distribution within the focal volume. Currently, polyvinylidene fluoride (PVDF) membrane or needle hydrophones (with a sensing element of 0.5–1.0 mm) are often used for mapping the acoustic field of a HIFU transducer. However, to avoid cavitation damage to the hydrophone, measurements were typically carried out first at a low output level, and then the pressure amplitudes and distribution at high output levels were extrapolated based on linear propagation model.[9,10] Since wave form distortion due to nonlinear propagation and cavitation produced at high output levels will significantly alter the size and shape of the lesion formed,[6,11–14] the extrapolation method may not provide accurate and satisfactory results. Moreover, once cavitation damage is produced on the surface of the sensing element of the hydrophone, the probe must be repaired and recalibrated before further use. Alternatively, optical methods based on Schlieren imaging[15] and optical diffraction tomography[16] have been used to quantify the pressure field of ultrasound transducers. Yet, the applicability of these optical methods is also limited to conditions under low-pressure amplitudes associated with linear wave propagation. Altogether, current methods used for HIFU exposimetry measurement are either limited by their spatial or temporal resolutions or unreliability in determining the HIFU field at clinically relevant high intensity output levels.

In this work, a self-calibrated fiber optic probe hydrophone (FOPH)[17] was used for HIFU exposimetry measurement. FOPH was originally developed for measurement of shock waves of high pressure amplitude with short risetime in a lithotripter field.[17] Because of its small probe size (0.1 mm sensing element), broad bandwidth (50 MHz), improved robustness in high tensile pressure field, and longevity (a probe tip can be easily prepared after cavitation damage), it may provide a reliable and accurate means for HIFU exposimetry measurement. Using a FOPH, we have measured the pressure wave forms produced in the focal volume of a focused HIFU transducer operating at either its fundamental (1.1 MHz) or third harmonic (3.3 MHz) frequency. It was found that pressure wave form distortion appeared at moderate output levels and grew significantly at high output

[a)]Electronic mail: pzhong@duke.edu

 0001-4966/2006/120(2)/676/10/$22.50

levels of the HIFU transducer. Based on the pressure wave forms measured, the beam size, intensity, and acoustic power of the HIFU transducer were calculated and the primary features of nonlinear propagation and associated energy absorption enhancement were quantified.

II. MATERIALS AND METHODS

A. Fiber optic probe hydrophone (FOPH) and PVDF membrane hydrophone

In this study, a fiber optic probe hydrophone (FOPH-500, RP Acoustics, Leutenbach, Germany) was used for HIFU field measurement. The working principle of FOPH has been described previously.[17] Briefly, the FOPH-500 employs a pigtailed laser diode ($\lambda=810$ nm) that is connected to one leg of a 1×2 fiber coupler. The light reflection at a 100 μm fiber/water interface is measured by a fast photodetector with an integrated amplifier of 30 MHz bandwidth, connected to the other leg of the coupler. Conversion of the reflected light intensity to pressure can be carried out off-line using a calibration program based on the Fresnel formula for the pressure-dependent refractive index at the fiber tip/water interface. With deconvolution process, the bandwidth of the FOPH can be enhanced to 50 MHz without loss in the signal-to-noise ratio (SNR) and the sensitivity of hydrophone is about 2 mV/MPa based on the specification of the manufacturer. The measurements of the FOPH was first compared with a recently calibrated PVDF membrane hydrophone (GEC-Marconi Research Center, Essex, UK) with an active element of 0.5 mm diameter, operated in combination with a matched amplifier, yielding a sensitivity of 41 mV/MPa at 1 MHz.

B. HIFU transducer and pressure measurement protocol

An annular focused HIFU transducer (H-102, Outer Diameter=69.94 mm, Inner Diameter=22.0 mm, F =62.64 mm, Sonic Concepts, Woodinville, WA) was used in this study (Fig. 1). The HIFU transducer, mounted at the bottom of a Lucite tank ($L\times W\times H=40.5\times30.5\times15$ cm) filled with degassed and deinoized water ($O_2<4$ mg/L, $T\approx25$ °C), was driven by sinusoidal bursts produced by a function generator (33120A, Agilent, Palo Alto, CA) together with a 55 dB power amplifier (A150, ENI, Rochester, NY). A 50 Ω attenuator (up to 22.1 dB attenuation, Kay Elemetrics Corp., Lincoln Park, NJ) could be inserted between the function generator and the power amplifier to further reduce the electric power input to the HIFU transducer. The HIFU transducer was running either at its fundamental (1.1 MHz) or third harmonic (3.3 MHz) frequency. To map the acoustic field of the HIFU transducer, the FOPH probe was connected to a three-dimensional positioning system (step motors: VXM-2, lead screws: BiSlide-M02, Velmex, Bloomfield, NY), which has a minimum step size of 5 μm and a maximum scan range of 250 mm. The output of the FOPH was first recorded by a digital oscilloscope (LeCroy 9310A, Chestnut Ridge, NY) operated at 100 MHz sampling rate, and then transferred to a PC for off-line pressure conversion and analysis. To streamline the experiment, a Visual Basic program was written and used to control automatically the output of the function generator, data acquisition and transfer, and scanning of the FOPH probe via GPIB bus and RS-232 port, respectively.

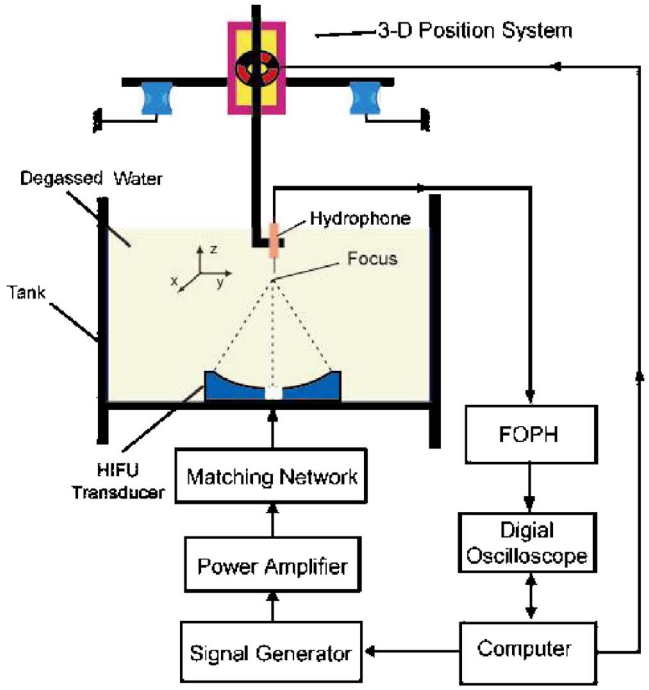

FIG. 1. (Color online) A schematic diagram of the experimental setup for HIFU exposimetry measurement using a computer controlled three-dimensional pressure mapping system.

To minimize temperature increase and cavitation activity near the probe tip, the HIFU transducer was operated in burst mode with a duty cycle of 0.1 %–0.2 % (i.e., 10–20 cycles/burst), and the peak-to-peak output voltage from the function generator, V_{pp}, was set to be less than 0.5 V. Above this output level, cavitation was frequently induced at the probe tip, leading to wave form contamination and probe damage. Averaging over 300 bursts was used to improve the SNR of the measured pressure wave forms. The geometric focus of the HIFU transducer was determined by searching for the location of maximum signal strength at a low output level with a burst delay time of ~41.76 μs, which is the time needed for a linear acoustic wave to propagate from the surface to the focus of the HIFU transducer. At the low output level the geometric focus was assumed to coincide with the acoustical focus of the HIFU transducer. An x-y-z coordinate system was then established with its origin coinciding with the geometric focus of the transducer and the z axis along the transducer axis (Fig. 1). Acoustic field characterization of the HIFU transducer was carried out by line or area scan. For line scan, the pressure distributions transverse to and along the transducer axis within the range of $x=-3-3$ mm and $z=-50-50$ mm were measured at a step size of $\Delta x=0.12$ mm and $\Delta z=0.5$ mm, respectively. For area scan, the pressure distributions in the x-y or x-z plane ($x=-2-2$ mm, $y=-2-2$ mm, $z=-10-10$ mm, $\Delta x=\Delta y=0.1$ mm, $\Delta z=1$ mm) were recorded.

C. Data analysis

Following the measurements, the peak positive/negative (compressional/rarefactional) pressure distributions were plotted, respectively, from which the −6 dB beam size and main lobe size were calculated. Spectrum analysis was performed by using fast Fourier transform (FFT) with minimal spectrum leakage techniques. First, the recorded full amplitude wave form was truncated to an integer number of cycles with zero-crossing points on both ends. Second, the truncated wave form was replicated to about 4000 sampling points. Third, Fourier transformation was performed on the stretched wave form to determine its fundamental frequency and harmonics. The spectrum could be further normalized by the total energy of the wave form. In addition, the spectra of the compressional and rarefactional components of the wave form were analyzed individually to evaluate their different nonlinear propagation characteristics.[18]

Based on the pressure wave-form data, the spatial-peak pulse-average intensity (I_{SPPA}), typically at the focus of the HIFU transducer, can be calculated by

$$I_{SPPA} = \frac{1}{nT}\int_{t_0}^{t_0+nT} \frac{p^2(t)}{\rho_0 c_0} dt, \tag{1}$$

where ρ_0 is the ambient density of water, c_0 is the small-signal sound speed in water, $p(t)$ is the time varying pressure wave form, T is the period of the wave form, n is the integer number of cycles in the selected pressure wave form, t_0 is the retarded time for the first full amplitude period, and t is time.[19] In addition, the spatial-average pulse-average intensity (I_{SAPA}) can be calculated as

$$I_{SAPA} = \int_S I_{SPPA} dS \Big/ \int_S dS, \tag{2}$$

where S is the integration area, which is usually the −6 dB beam area in the focal plane. Here the I_{SPPA} as defined in Eq. (1) is used in a broad sense to indicate pulse-average intensity at the measurement point.

The electrical input power to the HIFU transducer (P_{in}) was determined by $P_{in}=V_{rms}^2 \cos\vartheta/|Z|$, where V_{rms} is the rms voltage applied to the HIFU transducer, $|Z|$ is the magnitude and ϑ is the phase angle of the impedance Z. According to the specifications from the manufacturer, the impedance parameters of the HIFU transducer at 1.1 and 3.3 MHz with the 50 Ω matching unit are $|Z|=62.5$ Ω, 43.9 Ω, and $\vartheta=0.334°$, 0.925°, respectively. The acoustic power of the HIFU transducer (P) was estimated by integrating I_{SPPA} through a large area including the main and side lobes of the HIFU transducer. Subsequently the energy conversion efficiency of the HIFU transducer was determined by P/P_{in}.

D. Power absorption

In the focal region of a HIFU transducer, significant nonlinear propagation will cause the acoustic energy to shift from the fundamental frequency to higher harmonics, each of which has a different focal geometry and absorption property. As shown previously by Clarke and ter Haar[12] the absorbed acoustic power density $A(P)$ can be calculated from spectra data by

$$A(P) = \sum_{n=1}^{6} I_n(P)\alpha(f_n), \tag{3}$$

where $I_n(P)$ is the acoustic intensity of nth harmonic at acoustic power P, $\alpha(f_n)=2.5\times10^{-4} f_n^2 Np/cm/MHz$ is the absorption coefficient at the harmonic frequency f_n in water. Here only six harmonics are included because of their satisfactory SNRs. The initial lesion formation in a HIFU field is believed to occur at the point where the absorbed power density reaches a maximum.[9]

When the output of the HIFU transducer increases, the rate of harmonics generation and acoustic to thermal energy conversion will also change nonlinearly. The enhancement ratio for the absorbed acoustic power per unit volume, $E_A(P)$, can be determined using the following equation:

$$E_A(P) = \frac{A(P)}{P} \Big/ \frac{A(P_{ref})}{P_{ref}}, \tag{4}$$

where P_{ref} is the lowest power of the HIFU transducer (i.e., in this study the output voltage of the function generator was 0.05 V with additional 22.1 dB attenuation at 1.1 MHz) in the range of linear acoustics.[5]

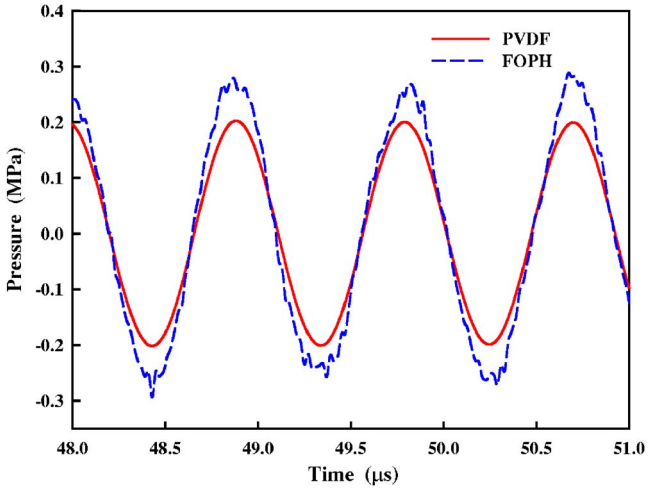

FIG. 2. (Color online) Comparison of the measured pressure wave forms by the FOPH and the PVDF membrane hydrophone in the 1.1 MHz HIFU field produced at a peak-to-peak output voltage of 50 mV with 15 dB insert attenuation.

III. RESULTS

A. Comparison of FOPH and PVDF membrane hydrophone

The acoustic pressures produced by the 1.1 MHz HIFU transducer in the linear range measured by the FOPH and the PVDF membrane hydrophone, respectively, were compared in Fig. 2. At low output level the noise in the FOPH measured wave form was significant even after signal averaging, especially at the wave crest and trough. Overall, however, the wave-form profiles measured by these two different hydrophones were symmetric and similar to each other. It was

noticed that in the linear range the measured peak-to-peak pressure by the FOPH was usually higher than that of the PVDF membrane hydrophone and this difference was proportional to the output voltage of the HIFU transducer.

When converting the electric signal to the corresponding acoustic pressure measured by a PVDF membrane hydrophone, the sensitivity at the fundamental frequency of the measured pulse is often used. At high output levels shift of the acoustic energy from the fundamental frequency to its harmonics due to nonlinear propagation is significant. The sensitivity of the PVDF membrane hydrophone used in this study decreases by about 20% from 1 MHz to 20 MHz. Hence, the use of the full calibration chart in the frequency range (deconvolution of the frequency response of the hydrophone) may lead to more accurate conversion of the pressure wave form. For example, at V_{pp}=0.5 V the deconvoluted wave form produced by the 3.3 MHz HIFU transducer had a 5% higher peak positive pressure than the corresponding value calculated using only the sensitivity at the fundamental frequency [Fig. 3(a)].

Figure 3(b) compares the lateral pressure distributions of the 3.3 MHz HIFU transducer at V_{pp}=0.2 V, measured by using the FOPH (solid line) and the PVDF membrane (long dashed line) hydrophone, respectively. The FOPH measurements revealed much higher peak pressure at the focus (17.9 MPa) and smaller −6 dB beam width (0.37 mm), compared to the corresponding values measured by the PVDF membrane hydrophone (8.9 MPa and 0.48 mm). It is interesting to note that if the FOPH measured pressure distribution was averaged through an area of 0.5 mm in diameter (representing the sensor size of the PVDF membrane hydrophone), the final results would change significantly [short dashed line in Fig. 3(b)]. The pressure distribution looks similar to that of the PVDF membrane hydrophone with the peak pressure decreasing to 12 MPa and the −6 dB beam width increasing to 0.63 mm. According to the International Electrotechnical Commission standards (IEC 61102), the maximum hydrophone size for measuring this 3.3 MHz HIFU field should be less than 0.27 mm in order to avoid the spatial averaging effect imposed by the size of the sensor.[20]

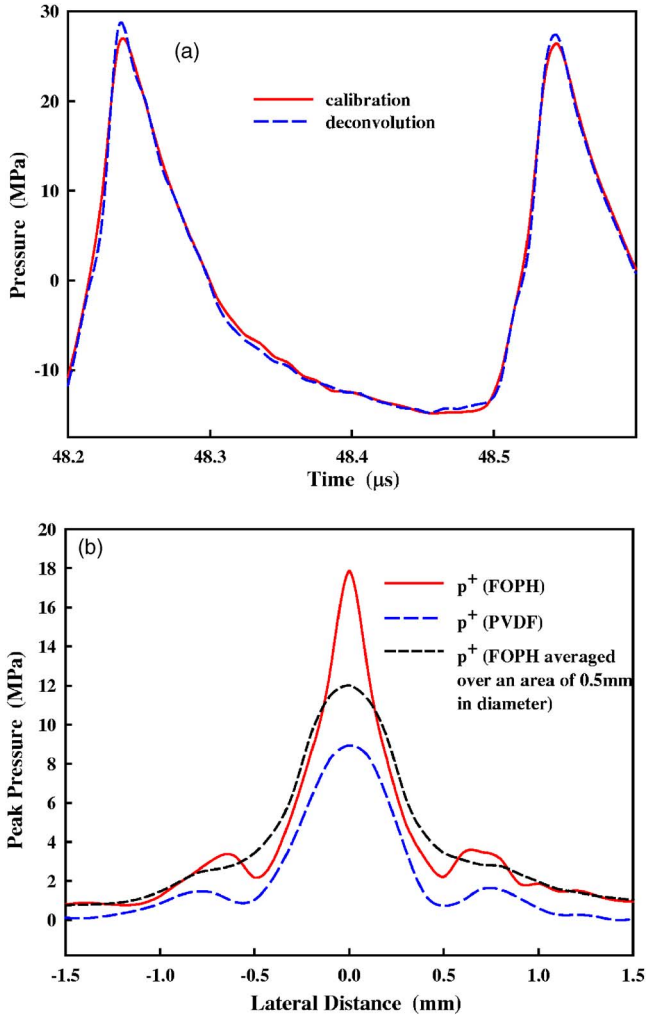

FIG. 3. (Color online) (a) The effect of deconvolution on the conversion of electric signal to pressure wave form measured by the PVDF membrane hydrophone at the focus of a 3.3 MHz HIFU transducer with V_{pp}=0.5 V. (b) Comparison of the pressure distribution measured by the FOPH (solid line) and the PVDF membrane hydrophone (long dashed line) in the focal plane of the 3.3 MHz HIFU transducer with V_{pp}=0.2 V. Furthermore, the pressure distribution measured by the FOPH was averaged through an area of 0.5 mm in diameter (short dashed line). V_{pp}: peak-to-peak output voltage of the function generator.

B. Nonlinear effects in HIFU field

The pressure wave forms produced by the 1.1 MHz HIFU transducer were measured in the range of V_{pp} =0.05–0.5 V (Fig. 4). Combined with the 55 dB power amplifier, the corresponding electrical input power into the transducer was calculated to be 1.6–125 W (Table I). The pressure wave forms measured by the FOPH are consistent and reproducible. Over a 2-month period, the variations in peak positive (p^+) and negative (p^-) pressures from six experiments were found to be within 5% except at the lowest output level (~10%) that may be caused partially by a possible longtime baseline variation of the oscilloscope or the laser intensity of the FOPH (~0.1 MPa at V_{pp}=50 mV), a system error that cannot be reduced by signal averaging. The acoustic intensities and acoustic powers were calculated based on the measured pressure wave forms (Table I). Within this output range I_{SPPA} and I_{SAPA} were found to increase from 77 to 6000 W/cm^2 and from 37 to 4365 W/cm^2, respectively. When the acoustic power was increased from 1.1 to 81.6 W, the corresponding power conversion efficiency was found to vary in the range of 62%–73%, which is close to the value specified by the manufacturer based on radiation force measurements.

At the geometric focus, wave-form distortion from sinusoidal to "sawtooth" shape due to nonlinear propagation[21] was observed as the output of the transducer was increased [Fig. 5(a)]. The nonlinear effects in the HIFU field led to significantly different electric input-dependent relationship of p^+ and p^-. Within the range of V_{pp}=0.05–0.5 V, p^- increased almost linearly from −1.2 to −10.0 MPa while p^+ rose much more rapidly from 1.7 to 23.3 MPa (Fig. 4). The nonlinear propagation was also manifested by harmonics generation in the wave forms [Fig. 5(b)]. At low output level (V_{pp}=0.05 V), the fundamental frequency was found to account for about 85% in the normalized spectrum while the

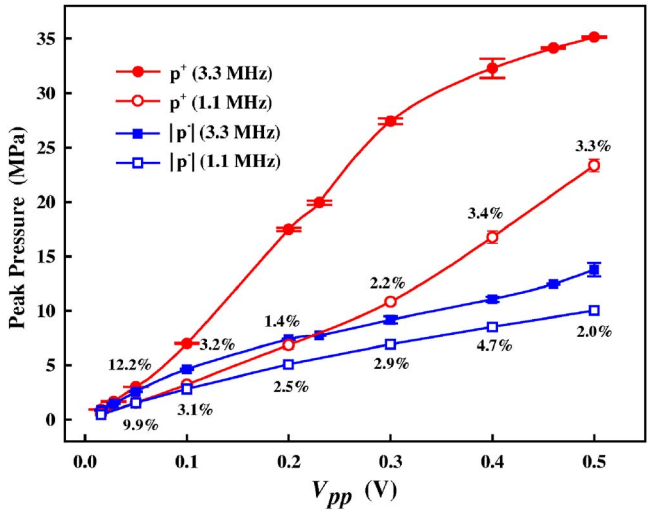

FIG. 4. (Color online) The electric input dependency of peak positive (p^+) and negative (p^-) pressure at the focus of the HIFU transducer working at either 1.1 or 3.3 MHz. V_{pp} is the peak-to-peak output voltage of the function generator. The percentage of standard deviation over mean value is listed in the plot for the 1.1 MHz HIFU transducer. Results were calculated from six experiments performed in a 2-month period.

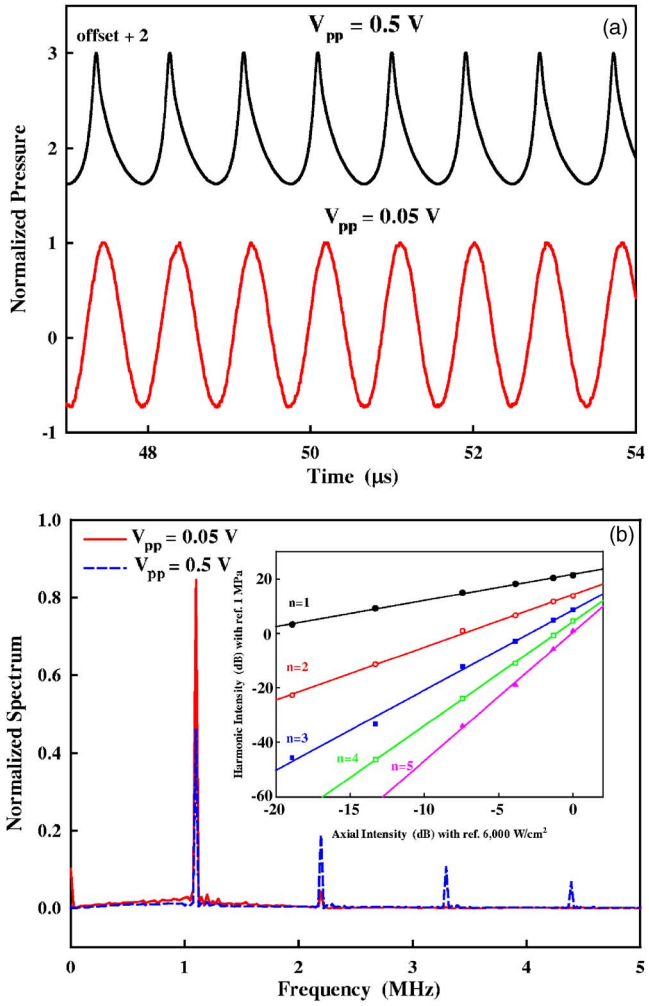

FIG. 5. (Color online) (a) Normalized pressure wave forms measured by the FOPH at the focus of the 1.1 MHz HIFU transducer when the peak-to-peak output voltage (V_{pp}) of the function generator was set at 0.05 and 0.5 V, respectively, and (b) the corresponding normalized spectra and harmonic intensities of the pressure wave forms and the electric input dependency of harmonic generation (inset) with respect to the referenced pressure of 1 MPa.

second harmonic was less than 5% [solid line in Fig. 5(b)]. Hence, most acoustic energy was stored in the fundamental frequency. In contrast, at high output level (0.5 V), the fundamental frequency decreased to 46% while the second harmonic increased to 19%, and higher (third and fourth) harmonics became significant [dashed line in Fig. 5(b)]. Therefore, substantial portion of the wave form energy was shifted from the fundamental frequency into higher harmonics. Furthermore, the intensities of all harmonics were found to increase linearly with the acoustic intensity, I_{SPPA}, [inset in Fig. 5(b)] and the calculated slopes (Table II) were found to be similar to the results of previous studies.[12,18] Furthermore, the nonlinearity has different influence on compressional and rarefactional waves. The fundamental frequency of the compressional wave was found to shift upwards from 1.1 MHz while that of the rarefactional wave shifted downwards. At higher output the rate of harmonics generation for the compressional components increased much faster than that of the rarefactional components (Table II). As a result, these changes lead to the asymmetric distortion of the wave form [Fig. 5(a)].

The pressure distributions along the transverse (x) and axial (z) direction of the 1.1 MHz HIFU transducer are shown in Fig. 6, which were found to be fairly symmetric in the focal plane. Although the peak pressures increased with the output power, the size of the main lobe remained almost unchanged, i.e., $L \times W = 20.5 \times 2.7$ mm. At the highest output level (V_{pp}=0.5 V), the maximum p^+ was measured at a position slightly (~0.5 mm) beyond the geometric focus of the transducer, while the maximum p^- was found to shift ~2.5 mm proximal to the transducer. Similar phenomenon has been observed in a lithotripter field, which is attributed to nonlinear propagation of the shock wave.[22] The correspond-

TABLE I. Acoustic intensity, power output, and electric-to-acoustic energy conversion efficiency of the 1.1 MHz HIFU transducer.

Output V_{pp} (V)	I_{SPPA} (W/cm^2)	I_{SAPA} (W/cm^2)	$I_{\mathrm{SAPA}}/I_{\mathrm{SPPA}}$	P_{in} (W)	P (W)	P/P_{in}
0.05	77.4	36.5	0.47	1.56	1.14	72.7%
0.1	281	146	0.52	6.36	3.95	62.1%
0.2	1082	605	0.56	23.5	15.0	63.0%
0.3	2458	1426	0.58	51.5	33.1	64.3%
0.4	4433	2657	0.60	86.2	59.6	69.2%
0.5	5996	4365	0.73	125	81.6	65.6%

TABLE II. Slopes of harmonic intensity vs axial intensity for different harmonic components.

	1.1 MHz			3.3 MHz		
n	Whole	Compressional	Rarefactional	Whole	Compressional	Rarefactional
1	0.96	1.16	0.81	0.95	1.07	0.88
2	1.93	2.41	1.56	1.91	2.20	1.42
3	2.94	N/A	1.63	2.69	N/A	1.55
4	3.81	3.44	1.85	3.58	2.70	1.83
5	4.71	4.11	2.08	4.47	4.10	2.14

ing −6 dB beam sizes both in the focal plane and along the central axis of the 1.1 MHz HIFU transducer were calculated (Fig. 7). Because of the strong nonlinear propagation and the associated harmonics generation, the −6 dB beam size of p^+ was found to decrease significantly with output power. In contrast, the −6 dB beam size of p^- was found to increase slightly, presumably because of the downwards shift of the fundamental frequency of the rarefactional wave at higher output levels.

The distribution of normalized harmonic spectra and absolute harmonic intensities along the x and z axis at V_{pp} =0.1 V and 0.3 V are shown in Fig. 8. At the focus of the HIFU transducer, a significant portion of the wave energy shifted from the fundamental frequency to higher order harmonics. Therefore, the focal point becomes a local minimum for the normalized fundamental component but a maximum for harmonic components at V_{pp}=0.1 V. In particular, the harmonic generation is more apparent at high output level (0.3 V). In addition, along the x and z axis, the maxima and minima of the fundamental component correspond to the minima and maxima of the second harmonic. It was found that the −6 dB beam size along both the transverse and central axis of the transducer decreases with the harmonic number by $n^{-1/2}$, which is consistent with results from previous studies.[12]

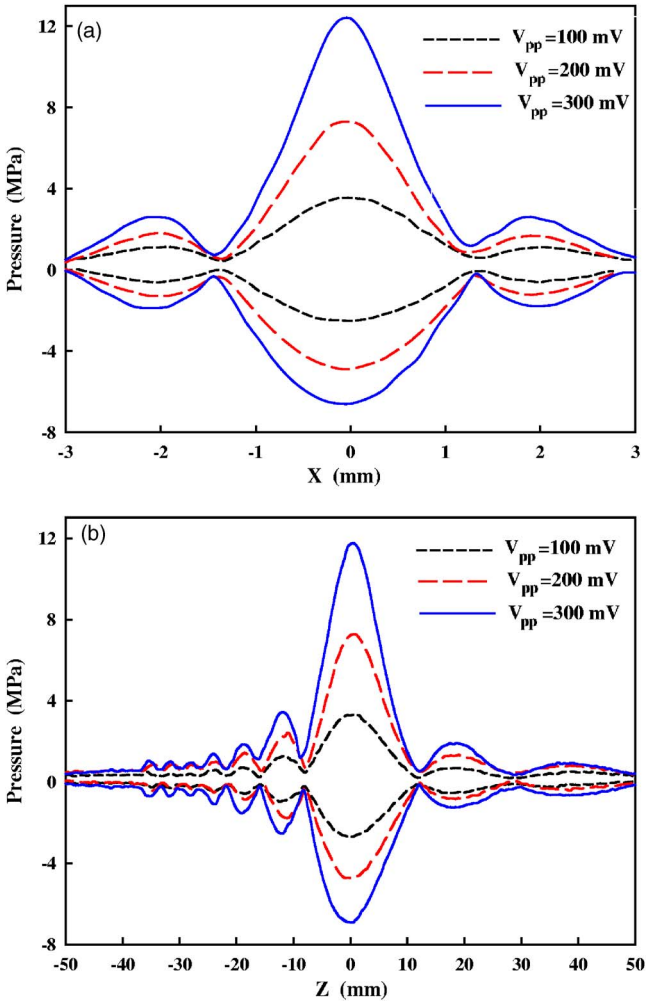

FIG. 6. (Color online) Pressure distribution (a) transverse to and (b) along the 1.1 MHz HIFU transducer axis at the peak-to-peak output voltage of the function generator V_{pp}=0.1, 0.2, and 0.3 V.

C. Comparison of HIFU fields at 1.1 and 3.3 MHz

At the same output voltage, V_{pp}, the peak pressures produced by the HIFU transducer at 3.3 MHz were much higher than the corresponding values at 1.1 MHz (Fig. 4). For example, at V_{pp}=0.5 V the peak positive and negative pressures at 3.3 MHz were 35.1±0.1 MPa and −13.8±0.6 MPa; while the corresponding values at 1.1 MHz were 23.3±0.6 MPa and −10±0.4 MPa, respectively. In consequence, the calculated I_{SPPA} at 3.3 MHz was much higher (Table III). When $V_{pp}>0.3$ V, the rate of increase for p^+ began to saturate, presumably because of the significantly increased attenuation of higher order harmonics during non-

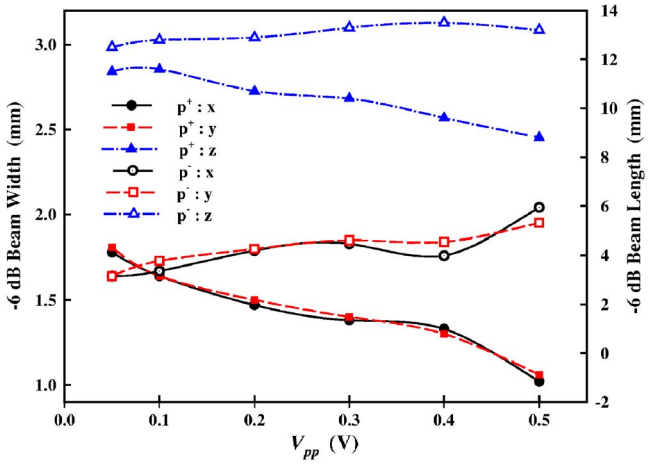

FIG. 7. (Color online) The −6 dB beam size of the peak positive (p^+) and negative (p^-) pressure distribution around the focus of the 1.1 MHz HIFU transducer at different peak-to-peak output voltage of the function generator V_{pp}.

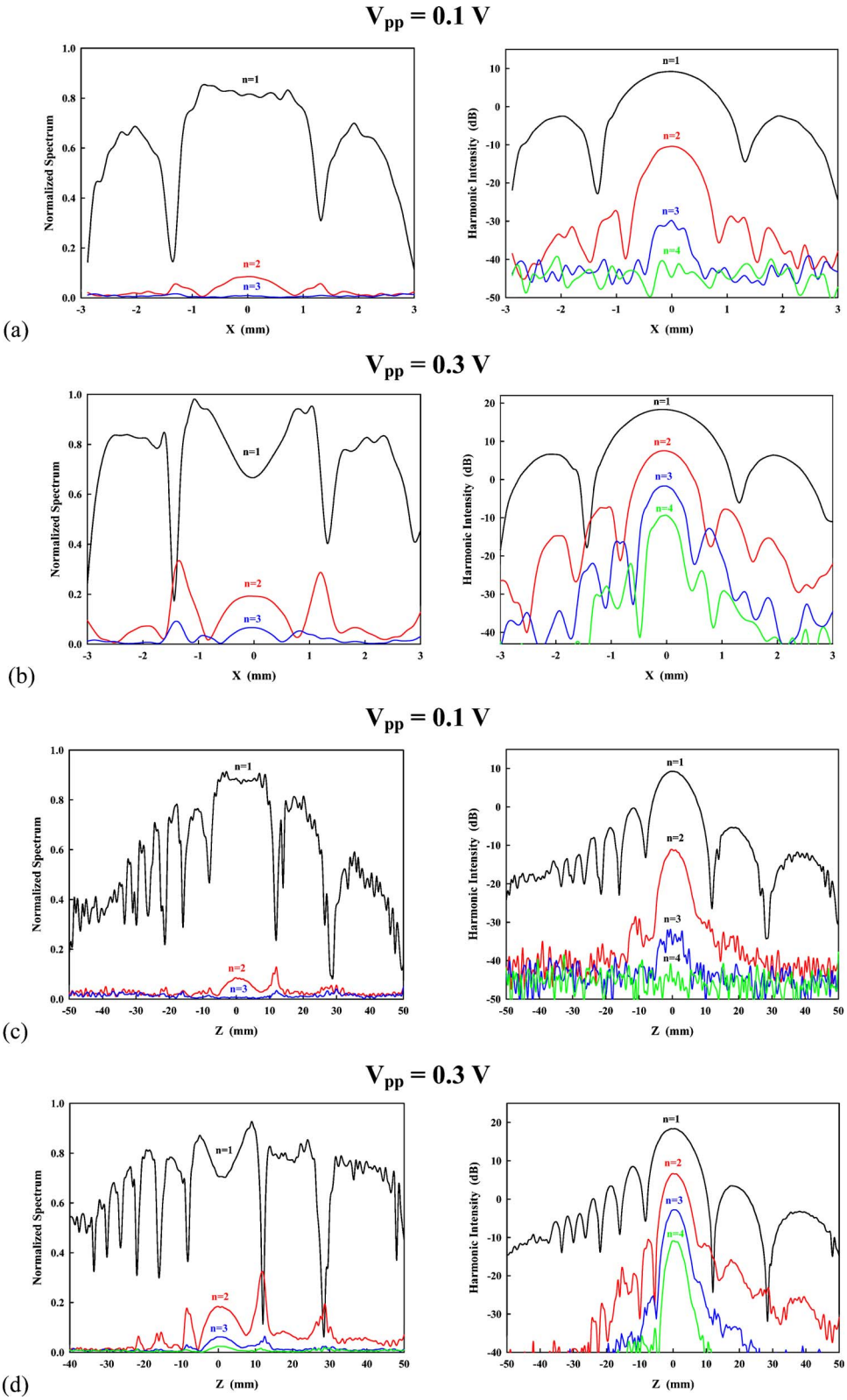

FIG. 8. (Color online) Harmonics distribution of the 1.1 MHz HIFU transducer at different peak-to-peak output voltage of the function generator V_{pp} (0.1 V and 0.3 V). Left column is normalized spectrum and right column is harmonic intensity with respect to the reference pressure of 1 MPa. Plots in (a) and (b) are transverse (x) while plots in (c) and (d) are along (z) the transducer axis.

linear wave propagation. It was found that the electric input power and electric-to-acoustic energy conversion ratio of the HIFU transducer at 3.3 MHz were similar to those at 1.1 MHz (Tables I and III). In addition, the nonlinear effects on wave-form distortion and the beam size change at 3.3 MHz were found to be similar to those at 1.1 MHz. For example, there is no significant difference in the calculated slopes of the acoustic intensities from all harmonics produced at either 3.3 MHz or 1.1 MHz (Table II), which suggests that harmonics generation is independent to the central frequency of the burst.

The pressure distributions of the 3.3 MHz HIFU transducer both transverse to and along the central axis of the HIFU transducer are shown in Fig. 9. In comparison to those produced at 1.1 MHz, the beam size became much smaller ($\sim 0.5 \times 4$ mm) and the side lobe was less significant, sug-

TABLE III. Acoustic intensity, power output, and electric-to-acoustic energy conversion efficiency of the 3.3 MHz HIFU transducer.

Output V_{pp} (V)	I_{SPPA} (W/cm^2)	I_{SAPA} (W/cm^2)	I_{SAPA}/I_{SPPA}	P_{in} (W)	P (W)	P/P_{in}
0.05	240	127	0.53	1.10	0.72	65.4%
0.1	981	551	0.56	4.38	2.92	66.8%
0.2	3728	2338	0.63	17.52	12.71	72.5%
0.3	7088	4801	0.68	40.75	28.05	68.8%
0.4	9730	6849	0.70	73.36	50.54	68.9%
0.5	10 967	8144	0.74	109.56	62.90	57.4%

gesting that the acoustic energy is concentrated more towards the focus. As a result, the peak pressure and acoustic intensity become much larger at the similar electric input power. At higher output voltage, the nodes in the pressure distribution of the compressional wave at 3.3 MHz, both transverse to and along the central axis of the HIFU transducer, gradually disappeared and began to merge with the main lobe. In contrast, the node in the rarefactional pressure distribution always existed. In addition, when $V_{pp}>0.2$ V, two pressure peaks, both compressional wave and rarefactional wave, appeared along the central axis of the HIFU transducer at about $z=2$ mm. The reason for this unique feature is not completely known.

As a result of nonlinear propagation in water, the enhancement ratio of absorbed acoustic power density of the HIFU transducer at the beam focus was found to increase from 1.0 to 3.0 at 1.1 MHz (Fig. 10). In comparison, the corresponding enhancement ratio at 3.3 MHz was lower at a given intensity and the theoretically predicted reduction in enhancement factor at higher power ($I_{SPPA}>10\,000$ W/cm^2) was also observed.[12,18] The initial increase of the enhancement ratio at 1.1 MHz was very slow up to 100 W/cm^2, which was similar to the nonlinear propagation threshold for 1.7 MHz focused ultrasound in water based on the measurements by a PVDF membrane hydrophone.[12] Above 100 W/cm^2, the enhancement ratio grew much more quickly. It should be noted that because ultrasound absorption coefficients in water and biological tissues are frequency dependent, the total acoustic power absorbed at 3.3 MHz is significantly higher than that at 1.1 MHz, which has been confirmed by thermocouple measurement (data not shown).

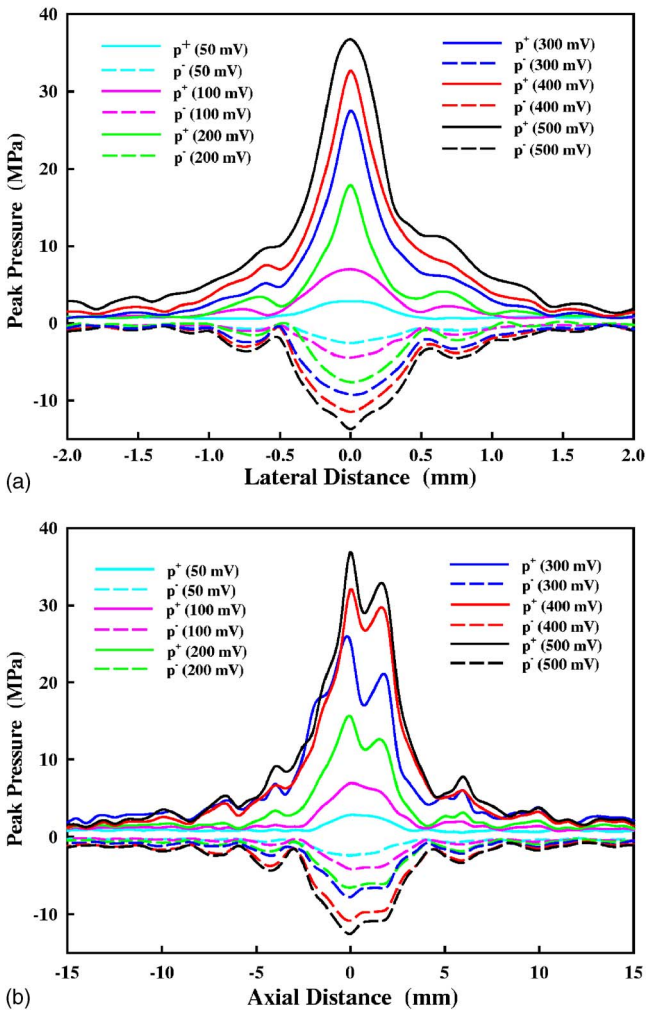

FIG. 9. (Color online) Pressure distribution (a) transverse to and (b) along the 3.3 MHz HIFU transducer axis with the output voltage in the range of 0.1–0.5 V.

IV. DISCUSSION

Accurate exposimetry measurement of HIFU systems is essential for determining the causal relationship between ul-

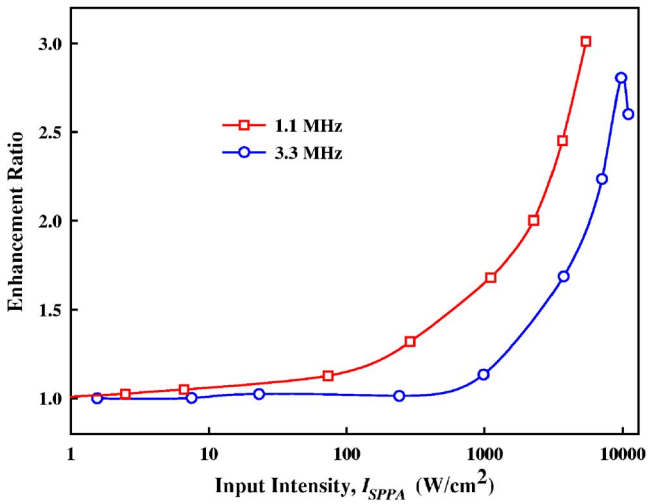

FIG. 10. (Color online) The enhancement ratio for absorbed acoustic power per unit volume at the focus of the HIFU transducer operating at either 1.1 or 3.3 MHz.

trasound exposure and resultant bioeffects, and for ensuring the effectiveness and safety of clinical HIFU treatment. From the regulatory point of view, exposimetry information is also important for quality control and comparison between different HIFU systems. Currently available methods are either limited by their temporal and spatial resolution (calorimetry and radiation force measurement) or their accuracy and reliability under clinically relevant HIFU intensities (optical techniques, PVDF membrane and needle hydrophones). In this study, we evaluated the feasibility of using a self-calibrated FOPH[17] for HIFU exposimetry measurement, which offers the unique advantages of small probe size (0.1 mm), broad bandwidth (50 MHz), robustness under high-pressure amplitude, and longevity. The calibration of the FOPH is done strictly based on the relation between pressure and reflection coefficient at the fiber tip (measured by the photodetector) that is defined exclusively by the material properties of the fiber and surround medium (i.e., water).[17] For calibration of the FOPH only a dc-photodiode voltage needs to be determined before the measurement without any reference standards. Therefore, FOPH is especially convenient for harmonics measurement in a HIFU field compared to PVDF membrane and needle hydrophones, which, in addition to their susceptibility to cavitation damage, must be calibrated at different discrete frequencies.

The small sensor size of the FOPH is also advantageous for resolving high frequency components in HIFU fields. According to the IEC 61102 guideline, in order to reduce the influence of spatial averaging the effective diameter (d_h) of the hydrophone active element must satisfy the following criterion:

$$d_h < \begin{cases} 0.5\lambda z/d_s, & z/d_s > 1, \\ 0.5\lambda, & z/d_s < 1, \end{cases} \tag{5}$$

where λ is the acoustic wavelength at the center frequency, z is the source-to-hydrophone distance, and d_s is the relevant source dimension.[20] Based on this criterion, both the FOPH and PVDF hydrophone can resolve well the 1.1 MHz HIFU field (see Fig. 2). However, the PVDF membrane hydrophone will suffer significantly from signal averaging effect when measuring the 3.3 MHz HIFU field (see Fig. 3). Furthermore, low frequency response of a hydrophone is also important for reliable measurement of lithotripsy and diagnostic pulses.[23] With deconvolution, the bandwidth of FOPH can be extended towards both low and high frequencies. In contrast, the low frequency response of PVDF membrane hydrophone is limited (i.e., its sensitivity at frequency lower than 100 kHz is usually very weak).[24] It should be noted, however, that when the criterion is satisfied and for weak pressure signals within linear propagation range, the PVDF membrane hydrophone can resolve the pressure signals much better because of its significantly higher sensitivity than the FOPH (see Fig. 2).

Using the FOPH we have measured the pressure wave forms produced by a focused HIFU transducer working at either 1.1 or 3.3 MHz in a wide range of output intensities (I_{SPPA}=1–11 000 W/cm^2). Significant wave-form distortion, which is characteristic of nonlinear propagation,[21] was produced at mediate and high output levels (Fig. 5). The characteristics of harmonics generation [see Fig. 5(b) and Table II] and harmonics beam size variation (Fig. 8) at both 1.1 and 3.3 MHz are similar to the results of 1.7 MHz HIFU field reported previously using a PVDF membrane hydrophone.[12] The most immediate consequence of nonlinear propagation is the narrowing of beam size due to harmonics generation with the associated increase of energy concentration toward the focus. This can be seen from the increased ratio of I_{SAPA}/I_{SPPA} within the output range investigated in this work (Tables I and III). Moreover, harmonics generation can lead to significant enhancements in energy absorption due to higher attenuation coefficients at harmonic frequencies.[12,21] Previous studies have suggested that the enhancements may contribute primarily to the initiation of lesion or cavitation on the transducer axis.[6,12]

Theoretical modeling of acoustic and thermal field produced by a HIFU transducer is important for better predicting and controlling lesion formation in clinical therapy. Several numerical simulations have been carried out, using the Khokhlov-Zabolotskaya-Kuznetsov (KZK) equation for modeling nonlinear propagation of high intensity acoustic beams[25,26] and the BioHeat transfer equation (BHTE)[27] to model the temperature elevation in tissue. A reliable characterization of the HIFU field (pressure wave form, pressure and thermal distribution) will be important for validating these numerical simulations.

In summary, FOPH has been shown to be an appropriate and reliable tool for HIFU exposimetry measurement, especially at high output intensity levels. It can be used to measure the pressure wave forms, distribution, and characterize the nonlinear propagation features in a HIFU field. Furthermore, the measurement data can be used to calculate the acoustical power and intensity output of the HIFU transducer, and to provide essential and critical information for device characterization and comparison, as well as for modeling nonlinear wave propagation and cavitation effect in a HIFU field.

ACKNOWLEDGMENTS

This work was supported in part by NIH through Grants Nos. RO1-DK52958, RO1-EB02682, and R21-EB03299. The authors also wish to thank George Keilman of Sonic Concepts for helpful discussion on determination of the electrical input power to the HIFU transducer and Professor Wolfgang Eisenmenger and Dr. Rainer Pecha for their helpful comments on the paper.

[1] G. Vallancien, M. Harouni, B. Guillonneau, B. Veillon, and J. Bougaran, "Ablation of superficial bladder tumors with focused extracorporeal pyrotherapy," Urology **47**, 204–207 (1996).
[2] A. G. Visioli, I. H. Rivens, G. R. ter Haar, A. Horwich, R. A. Huddart, E. Moskovic, A. Padhani, and J. Glees, "Preliminary results of a phase I dose escalation clinical trial using focused ultrasound in the treatment of localised tumours," Eur. J. Ultrasound **9**, 11–18 (1999).
[3] F. Wu, W. Z. Chen, J. Bai, J. Z. Zou, Z. L. Wang, H. Zhu, and Z. B. Wang, "Pathological changes in human malignant carcinoma treated with high-intensity focused ultrasound," Ultrasound Med. Biol. **27**, 1099–1106 (2001).
[4] F. Wu, Z. B. Wang, W. Z. Chen, J. Z. Zou, J. Bai, H. Zhu, K. Q. Li, F. L. Xie, C. B. Jin, H. B. Su, and G. W. Gao, "Extracorporeal focused ultrasound surgergy for treatment of human solid carcinomas: early Chinese clinical experience," Ultrasound Med. Biol. **30**, 245–260 (2004).

[5]G. R. ter Haar, "Ultrasound focal beam surgery," Ultrasound Med. Biol. **21**, 1089–1100 (1995).
[6]N. A. Watkin, G. R. ter Haar, and I. H. Rivens, "The intensity dependence of the site of maximal energy deposition in focused ultrasound surgery," Ultrasound Med. Biol. **22**, 483–491 (1996).
[7]P. N. T. Wells *et al.*, "The dosimetry of small ultrasonic beams," Ultrasonics **1**, 106–110 (1963).
[8]C. R. Hill, "Calibration of ultrasonic beams for bio-medical applications," Phys. Med. Biol. **15**, 241–248 (1970).
[9]C. R. Hill, H. Rivens, M. G. Vaughan, and G. R. ter Haar, "Lesion development in focused ultrasound surgery: a general model," Ultrasound Med. Biol. **20**, 259–269 (1994).
[10]S. Sokka, R. King, and K. Hynynen, "MRI-guided gas bubble enhanced ultrasound heating in in vivo rabbit thigh," Phys. Med. Biol. **48**, 223–241 (2003).
[11]K. Hynynen, "The threshold for thermally significant cavitation in dog's thigh muscle," Ultrasound Med. Biol. **17**, 157–169 (1991).
[12]R. L. Clarke and G. R. ter Haar, "Production of harmonics in vitro by high-intensity focused ultrasound," Ultrasound Med. Biol. **25**, 1417–1424 (1999).
[13]F. Chavrier, J. Y. Chapelon, A. Gelet, and D. Cathignol, "Modeling of high-intensity focused ultrasound-induced lesions in the presence of cavitation bubbles," J. Acoust. Soc. Am. **108**, 432–440 (2000).
[14]M. R. Bailey, L. N. Couret, O. A. Sapozhnikov, V. A. Khokhlova, G. R. ter Haar, S. Vaezy, X. G. Shi, R. Martin, and L. A. Crum, "Use of overpressure to assess the role of bubbles in focused ultrasound lesion shape in vitro," Ultrasound Med. Biol. **27**, 695–708 (2001).
[15]B. Schneider and K. K. Shung, "Quantitative analysis of pulsed ultrasonic beam patterns using a Schlieren system," IEEE Trans. Ultrason. Ferroelectr. Freq. Control **43**, 1181–1186 (1996).
[16]A. Holm, H. W. Persson, and K. Lindstrom, "Measurements of ultrasonic fields with optical diffraction tomography," Ultrasound Med. Biol. **17**, 505–512 (1991).
[17]J. Staudenraus and W. Eisenmenger, "Fiberoptic probe hydrophone for ultrasonic and shock-wave measurements in water," Ultrasonics **31**, 267–273 (1993).
[18]W. Swindell, "A theoretical study of nonlinear effects with focused ultrasound in tissues: an acoustic bragg peak," Ultrasound Med. Biol. **11**, 121–130 (1985).
[19]W. L. Nyborg and J. Wu, "Relevant field parameter with rationale," in *Ultrasonic Exposimetry*, edited by M. C. Ziskin and P. A. Lewin (CRC Press, Boca Raton, FL, 1992), pp.85–112.
[20]G. R. Harris, "A discussion of procedures for ultrasonic intensity and power calculations from miniature hydrophone measurements," Ultrasound Med. Biol. **11**, 803–817 (1985).
[21]T. G. Muir and E. L. Carstensen, "Prediction of nonlinear acoustic effects at biomedical frequencies and intensities," Ultrasound Med. Biol. **6**, 345–357 (1980).
[22]M. A. Averkiou and R. O. Cleveland, "Modeling of an electrohydraulic lithotripter with the KZK equation," J. Acoust. Soc. Am. **106**, 102–112 (1999).
[23]G. R. Harris, "Pressure pulses distortion by hydrophones due to diminished low frequency response," IEEE Trans. Ultrason. Ferroelectr. Freq. Control **42**, 989–992 (1995).
[24]A. S. DeReggi, S. C. Roth, J. M. Kenney, S. Edelman, and G. R. Harris, "Piezoelectric polymer probe for ultrasonic applications," J. Acoust. Soc. Am. **69**, 853–859 (1981).
[25]N. S. Bakhvalov, Y. M. Zhileikin, and E. A. Zabolotskaya, *Nonlinear Theory of Sound Beams* (AIP, New York, 1987).
[26]P. M. Meaney, M. D. Cahill, and G. R. ter Haar, "The intensity dependence of lesion position shift during focused ultrsound surgery," Ultrasound Med. Biol. **26**, 441–450 (2000).
[27]H. H. Pennes, "Analysis of tissue and arterial blood temperature in the resting human forearm," J. Appl. Physiol. **1**, 93–122 (1948).

On the modeling of sound propagation over multi-impedance discontinuities using a semiempirical diffraction formulation

Yiu Wai Lam and Mohammad Reza Monazzam
Acoustics Research Centre, School of Computing, Science and Engineering, University of Salford, Salford M5 4WT, United Kingdom

(Received 11 October 2005; revised 30 May 2006; accepted 31 May 2006)

Several approximate extensions of the semi-empirical De Jong model [De Jong *et al.*, J. Sound and Vib. **86**, 23–46 (1983)] are considered for the prediction of sound propagation over multiple impedance discontinuities. A limitation in the original formulation of the De Jong model is highlighted and a modified form that overcomes this limitation is derived based on reciprocity. This leads to the development of a model for multiple impedance discontinuities that can be used for the investigation of sound-wave propagation above a mixed, striped soft ground that is created by either porous absorbent strips, embedded grooves, or wells with different depths. The accuracy of the model is validated against the boundary element method. It is then used to evaluate the importance of the imaginary part of the admittance of the ground strips on sound attenuation along welled surface. It is shown that the attenuation performance of a surface with multiple impedance discontinuities is high when the imaginary part of the average admittance is large and negative (with an $-i\omega t$ convention), but the magnitudes of the attenuation peaks are also substantially affected by diffraction from the impedance discontinuities. © *2006 Acoustical Society of America.*
[DOI: 10.1121/1.2216905]

PACS number(s): 43.28.En, 43.50.Vt, 43.28.Fp [DKW] Pages: 686–698

I. INTRODUCTION

Sound-wave propagation above a surface with multiple impedance discontinuities has been a subject of continuing interest, particularly due to the possibility of enhancing ground attenuation through diffraction at the discontinuities. A practical application of this problem is in the prediction of traffic noise, for example, which is usually produced above hard ground (e.g., asphalt or concrete), and crosses a discontinuity as it propagates over to a softer ground (e.g., grass or snow). Another example of this problem is in the study of wave propagation over a series of ribs or grooves, which can provide extra attenuation of environmental noise. van Der Heijden and Marten[1] measured the sound attenuation by a set of parallel wells on the ground, and van Tol and Holties[2] investigated low, close to track barriers and absorptive layers on a slab track. A further possibility of using such an impedance surface is in novel reactive barrier designs. Fujiwara *et al.*[3] predicted the performance of a series of wells on the top surface of a T-shaped barrier. Recently, the authors showed that adding a Schroeder-type diffuser surface on top of a T-shaped barrier can provide substantial improvement on the barrier's insertion loss.[4]

It should also be noted that the ability of an impedance discontinuity to generate surface waves can also be used to enhance instead of attenuate sound propagation. Zhu *et al.*[5] have demonstrated such a possibility by means of an impedance strip with finite width. However, the focus of this paper is attenuation rather than amplification of sound propagating along impedance surfaces. In particular, the possibility of using impedance discontinuities to enhance attenuation is considered.

Many different methods of solution for the case of a two-impedance, single-discontinuity bounsdary have been presented in the literature. Enflo and Enflo[6] derived a solution in the form of a triple integral. Simpler asymptotic approximations can be obtained when the source and receiver are far from the impedance discontinuity and are both on the ground, and when the distance from the source to the discontinuity is much less than that from the source to the receiver. Rasmussen[7] also provides an approximate solution for the propagation over an impedance discontinuity. Zhu *et al.*[5] showed that this approximation has good agreement with a boundary element method prediction over a simple impedance jump that generates a surface wave.

Unfortunately, the above methods for a single-impedance discontinuity are not easily amendable to the more complex case of multiple impedance discontinuities that are not necessarily far from each other. Numerical methods of calculations such as parabolic equation[8] and boundary integral equation[9] can provide accurate prediction, but they are generally expensive in terms of computation resources and do not always give an insight into the physical mechanisms of the sound attenuation.

The method presented by De Jong *et al.*[10] and Koers[11] can be considered as a different class of solution that uses semiempirical modifications of analytical expressions for diffraction by a rigid half-plane, which is used to represent an admittance step from a hard surface to air. This method has been shown to produce good predictions under a variety of conditions, although Daigle *et al.*[12] and Hothersall *et al.*[13] found that it has serious limitations in certain geometries involving near-grazing angles and at low frequencies. It was suggested that more accurate results can be obtained at greater source and receiver heights and shorter source to re-

ceiver distances. Hothersall *et al.*[13] also presented an extension of the De Jong model to the case of one impedance strip (two impedance discontinuities) and found good agreement with predictions by the numerical boundary element method. However, as pointed out by Boulanger *et al.*,[14] their extension has an inconsistency with the original De Jong model. Boulanger *et al.*[14] examined the De Jong method at short distances and close to the ground. Very good agreement with measurements was reported for a single discontinuity. However, their extension of the method, which is similar to that given by Bassiouni *et al.*[15] and is corrected for the inconsistency noted in the equation of Hothersall *et al.*,[13] to a surface with periodic multiple impedance strips was found to produce clear discrepancies when compared with measurements.

Nyberg [16] introduced a solution of the Helmholtz equation for a mixed ground using a Fourier transform technique. He showed that this problem under certain conditions may be estimated by using area-averaged admittance. Although it seems to give a good approximation for a periodic mixed impedance ground in a limited range of frequency, it cannot distinguish the situations where one strip or another is at the specular reflection point for a given percentage of hard surfaces.

The purpose of this paper is to examine the attenuation of sound propagation over a ground with multiple impedance discontinuities that are created by a series of rigid wells with different depths. The width of the wells in the direction of the propagation is generally smaller or comparable to the acoustic wavelength such that the discontinuities cannot be considered to be far from each other. The impedances of these wells can have large variations in values due to well resonances. We wish to derive an approximate analytical solution for this problem to provide some insight into the attenuation mechanism that will allow us to obtain guidelines for design optimization. Of the methods identified from the literature, the approximation method by De Jong is chosen as the basis for further development. First, we examine the De Jong model and explain the apparent inconsistence in the extension[13] for one impedance strip and the failure of the existing extension[14,15] for multiple strips. A new extension of the method for multi-impedance ground will then be introduced, and the accuracy of the new model on grounds with single and multiabsorbent strips will be examined. The numerical boundary element method (BEM), which has been shown to be very accurate and reliable in previous studies,[9,14] will be used as a basis for comparisons and validation. Finally, the model will be applied to multiwelled surfaces with various depth sequences to examine the factors that influence the excess attenuation, with the view of understanding how such surfaces can affect the performance of a T-shaped barrier.

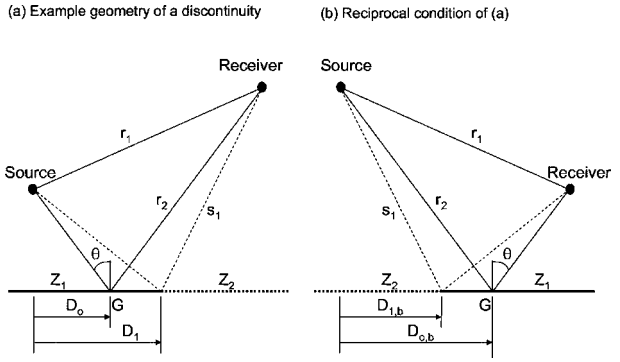

FIG. 1. Definition of the different paths for a single impedance discontinuity. *G* is the specular reflection point. (a) is an example with the specular reflection point on the source side of the discontinuity and (b) is the reciprocal case of (a).

II. DIFFRACTION MODELS FOR WAVE PROPAGATION OVER MIXED IMPEDANCE GROUND

A. Original De Jong model

De Jong *et al.*[10] introduced a solution by comparing the case of an admittance step at a transition between a hard to a soft ground with the case of a semi-infinite screen. It was suggested that the solution for the diffraction by the latter can be used to represent the diffraction by an admittance step from an acoustically hard surface to the atmosphere. Using $e^{-i\omega t}$ to represent the time dependence, the De Jong equation for the relative pressure above a plane containing a single-impedance discontinuity can be written as

$$\frac{p}{p_1} = 1 + \frac{r_1}{r_2} Q_G e^{ik(r_2-r_1)} + (Q_2 - Q_1) e^{-i\pi/4} \frac{1}{\sqrt{\pi}} \frac{r_1}{s_1} \times [F_2(\sqrt{k(s_1-r_1)}) \pm F_2(\sqrt{k(s_1-r_2)}) e^{ik(r_2-r_1)}]. \quad (1)$$

The different path lengths including r_1, r_2, *and* s_1 are shown in Fig. 1. The total pressure at the receiver point is p, and p_1 is the free-field pressure. Q_1 and Q_2 are the spherical wave reflection coefficients calculated for an infinite ground of impedance Z_1 and Z_2, respectively, and are calculated at the specular reflection point G. Table I summarizes the choices of Q_G and the ± sign inside the right-hand-side square bracket in Eq. (1).

TABLE I. Choice of Q_G and +/− sign inside the right-hand side square bracket in the original De Jong model, Eq. (1).

	Z_1 on source side [e.g., Fig. 1(a)]	Z_2 on source side [e.g., Fig. 1(b)]
Specular reflection point G on impedance Z_1	$Q_G=Q_1$ + sign inside the square bracket (Q_2-Q_1) in front of square bracket	$Q_G=Q_1$ − sign inside the square bracket (Q_1-Q_2) in front of square bracket
Specular reflection point G on impedance Z_2	$Q_G=Q_2$ − sign inside the square bracket (Q_2-Q_1) in front of square bracket	$Q_G=Q_2$ + sign inside the square bracket (Q_1-Q_2) in front of square bracket

The third term on the right-hand side of the equation can be seen as the contribution from the diffraction by the impedance discontinuity, and is equal to a correction term (Q_2-Q_1) times the approximate diffracted field from a hard half-plane. The term (Q_2-Q_1) corrects for the surfaces having finite impedance Z_1 and Z_2. It is empirically constructed by physical arguments to give the correct prediction when $Q_1=1$ (acoustically hard) and $Q_2=0$ (air), and when Z_1 approaches Z_2. Because of the empirical nature of this correction, its limitations are not mathematically explicit. Daigle *et al.*[12] conducted a thorough study on the behavior of the De Jong model. They found that the model has difficulties dealing with situations when the grazing angles are small, but they were not able to formulate firm criteria for the use of the model.

Of the diffraction terms inside the square bracket in Eq. (1), $F_2(x)$ is the integral

$$F_2(x) = \int_x^\infty e^{(iw^2)} dw. \tag{2}$$

The first F_2 term inside the square bracket can be considered as the diffraction contribution associated with the direct source, while the second F_2 term is that associated with the image source. The sign change for the second term is therefore understandable as the reflected path r_2 moves from the source side to the receiver side of the discontinuity. Note that the diffraction terms used here are derived with an assumption that $k\, s_1 \gg 1$. Daigle *et al.*[12] found that the differences between the use of this approximation and an exact formulation of the diffracted field in the De Jong model are not significant in the cases that they studied. The observed errors of the model at small grazing angles are not caused by the approximation of the hard half-plane diffracted field, but rather by the empirical correction for the finite impedances.

The spherical reflection coefficient can be calculated by the Weyl–van der Pol approximation,[17]

$$Q = R_P + (1 - R_P) F(z), \tag{3}$$

where R_p is the plane-wave reflection coefficient,

$$R_p = \frac{\cos\theta - \beta}{\cos\theta + \beta}. \tag{4}$$

In this paper the normalized surface admittance β for absorptive fibrous material is calculated by the empirical equations of Delany and Bazely.[18] For narrow wells, the model described by Eq. (8) of Wu *et al.*[19] is used to compute β. Briefly, the model assumes plane-wave propagation in the well but adjusted to incorporate the effects of thermal wave and shear wave in the boundary layers. Full details can be found in Sec. I A of Ref. 19.

The argument z in the function $F(z)$ is called the numerical distance. To help the discussion in later sections, the following equations, which are well documented in the literature,[20–22] are given:

$$z = + \frac{1+i}{2} \sqrt{k r_2} (\beta + \cos\theta). \tag{5}$$

The function $F(z)$, which describes the interaction between the spherical wavefront with the impedance boundary, is approximated by

$$F(z) = 1 + iz\sqrt{\pi}\,\mathrm{cerfe}(z), \tag{6}$$

where cerfe(z) is the scaled complemented error function. In the range of $|\beta|^2 k r_2 \gg 1$, the absolute value of the numerical distance is much bigger than unity. The error function complement can then be approximated by an asymptotic expansion, and the boundary factor $F(z)$ for large $|z|$ may be written as

$$F(z) = 2i\sqrt{\pi} z H[-\mathrm{Im}(z)] e^{-z^2} - \left\{ \frac{1}{2z^2} + \frac{3}{4z^4} + \cdots \right\}, \tag{7}$$

where H is the Heaviside step function—it is unity when its argument is positive, and zero when its argument is negative.

The excess attenuation can now be calculated as

$$\mathrm{EA} = -20 \log\left(\frac{p}{p_1}\right) \mathrm{dB}. \tag{8}$$

B. Modified De Jong model

The original De Jong model is derived for the case of an impedance step from a harder ground to a softer ground $(Z_1 \rangle Z_2$ in Fig. 1). The model has been shown by De Jong *et al.* and others[10,13,14] to have good accuracy under a variety of conditions for a single-impedance jump from hard to soft ground, which satisfy De Jong's assumption of hard to soft transition in his derivation of the model. Unfortunately, this assumption has been overlooked in other studies and caused some confusion when the model is extended to cover multiple impedance discontinuities. The implication of this assumption of hard to soft transition can be clearly seen by considering Eq. (1) under reciprocal conditions. An example is shown in Fig. 1, where Fig. 1(b) is the reciprocal case of Fig. 1(a). Applying the original De Jong model, i.e., Eq. (1), to Fig. 1(a), gives the total pressure p_a as

$$\frac{p_a}{p_1} = 1 + \frac{r_1}{r_2} Q_1 e^{ik(r_2 - r_1)} + (Q_2 - Q_1) e^{-i\pi/4} \frac{1}{\sqrt{\pi}} \frac{r_1}{s_1} \times [F_2(\sqrt{k(s_1 - r_1)}) + F_2(\sqrt{k(s_1 - r_2)}) e^{ik(r_2 - r_1)}]. \tag{9}$$

On the other hand, applying the model to the reciprocal case of Fig. 1(b) gives the total pressure p_b as

$$\frac{p_b}{p_1} = 1 + \frac{r_1}{r_2} Q_1 e^{ik(r_2 - r_1)} + (Q_2 - Q_1) e^{-i\pi/4} \frac{1}{\sqrt{\pi}} \frac{r_1}{s_1} \times [-F_2(\sqrt{k(s_1 - r_1)}) + F_2(\sqrt{k(s_1 - r_2)}) e^{ik(r_2 - r_1)}]. \tag{10}$$

Note that in Eq. (10) we have already adjusted for the reversal of the $(Q_1$-$Q_2)$ term and the change of sign of the second F_2 term inside the square bracket for the reciprocal case. It can be clearly seen that Eq. (10) differs from Eq. (9) by the negative sign in front of the first F_2 term inside the square

bracket. Consequently $p_a \neq p_b$, which violates the reciprocity condition. Due to this difference the original model, i.e., Eq. (1), does not satisfy acoustic reciprocity and is therefore invalid for a soft to hard transition.

In order for the model to satisfy the reciprocity condition, we can impose a further condition on the sign of the first F_2 term. By comparing Eqs. (9) and (10), and knowing that Eq. (1) works for hard to soft transition, we modified the De Jong model into the following equation:

$$\frac{p}{p_1} = 1 + \frac{r_1}{r_2} Q_G e^{ik(r_2-r_1)} + (Q_2 - Q_1) e^{-i\pi/4} \frac{1}{\sqrt{\pi}} \frac{r_1}{s_1} \times [\mu F_2(\sqrt{k(s_1 - r_1)}) + \gamma F_2(\sqrt{k(s_1 - r_2)}) e^{ik(r_2-r_1)}], \quad (11)$$

where, as before, $\gamma = 1$ for $D_o < D_1$ and $=-1$ for $D_o > D_1$. The new parameter μ is introduced to account for the reciprocity requirement such that $\mu = 1$ when the admittance $\beta_2 > \beta_1$, and $=-1$ for $\beta_2 < \beta_1$. Equation (11) will be referred to as the modified De Jong model.

C. Extension to multiple impedance discontinuities

Due to the assumption of hard to soft transition in the original De Jong model, any extension of this model to multiple impedance discontinuities that involves transitions to a harder ground is bound to be in error. Bassiouni *et al.*[15] extended the De Jong method for the sound propagation over a ground surface containing any finite number of impedance discontinuities. Their equation is a straightforward application of the original De Jong model to each of the impedance discontinuities in turn. As such, it will not work if any of the consecutive impedance changes is from a softer to a harder ground. Unfortunately, Bassiouni *et al.*[15] does not contain any data to support its claim of the model's accuracy.

Boulanger *et al.*[14] used the same approach to extend the original De Jong model to calculate sound propagation over a ground with periodic impedance changes. Equation (18) of Boulanger *et al.*[14] is essentially the same as Bassiouni's equation, but simplified to periodic changes between two impedances. This periodic impedance changes clearly violate the assumption of only hard to soft transition in the original De Jong model. Therefore, it is not surprising that the extended model shows clear discrepancies when compared with measured data (see Fig. 12 of Boulanger *et al.*[14]).

In another study, Hothersall *et al.*[13] presented an extension of the De Jong model to one strip of impedance change, i.e., two impedance discontinuities. In their description of the De Jong model, they have in fact correctly stated that the choice of Z_2 and Z_1 in Eq. (1) should be such that Z_1 is the more rigid of the two. In their extension of the De Jong model to two discontinuities, there is a sign change in the Fresnel integral that corresponds to the $F_2(\sqrt{k(s_1 - r_1)})$ term [see Eqs. (10)–(12) in Hothersall *et al.*[13]] that accounts for the diffraction from the second discontinuity (transition from softer to harder impedance). Unfortunately, they did not give any description or justification for the change. Indeed, they suggested that their equations follow Bassiouni's approach[15] and did not point out the differences. Consequently, there is confusion in later literature[14] that claims that their equations were inconsistent with De Jong's model, and it was suggested[14] that $a-1$ should be multiplied to the Fresnel integral in question. It is now clear that that suggestion is incorrect and should not be carried out.

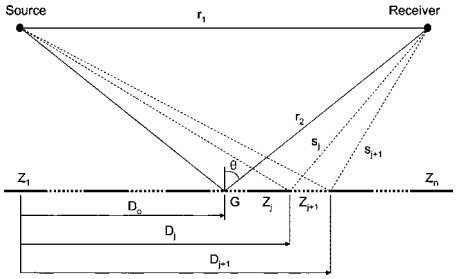

FIG. 2. Definition of the different paths for multiple impedance discontinuities. G is the specular reflection point.

D. The new Multi-impedance Discontinuities Model (nMID)

The above observations clearly show that the original De Jong model [Eq. (1)] cannot be extended to cases with multiple impedance discontinuities without incorporating the modifications suggested here in Eq. (11) to deal with the case of an impedance transition from softer to harder ground. Based on reciprocity requirement, it has been shown earlier that a sign change in the diffraction term associated with the direct path is necessary to account for the soft to hard transition. Based on this modification, we can now extend the modified De Jong model to multiple impedance ground by applying Eq. (11) to each of the discontinuities in turn. For a ground with n impedance sections, and hence $(n-1)$ impedance discontinuities, the total pressure p is approximately given by

$$\frac{p}{p_1} = 1 + \frac{r_1}{r_2} Q_G e^{ik(r_2-r_1)} + \sum_{j=1}^{n-1} (Q_{j+1} - Q_j) \frac{e^{-i\pi/4}}{\sqrt{\pi}} \frac{r_1}{s_j} \times [\mu_j F_2(\sqrt{k(s_j - r_1)}) + \gamma_j F_2(\sqrt{k(s_j - r_2)}) e^{ik(r_2-r_1)}], \quad (12)$$

where $\gamma_j = 1$ for $D_o < D_j$ and $=-1$ for $D_o > D_j$, and $\mu_j = 1$ when the admittance $\beta_{j+1} > \beta_j$ and $=-1$ for $\beta_{j+1} < \beta_j$. The geometry and the definition of the paths and symbols are as shown in Fig. 2.

Obviously this straightforward application of the single-discontinuity diffraction formula, Eq. (11), to multiple discontinuities will inherit the limitation of the base formula, i.e., that the accuracy decreases with larger reflection angles (nearer grazing). Furthermore, such a simple combination does not consider possible interactions between the discontinuities, and is therefore expected to work best when the discontinuities are far apart relative to the acoustic wavelength. Note that when there is only one impedance strip, i.e., $n=3$ with $Z_3 = Z_1$, Eq. (12) reduces to the same Eqs. (10)–(12) of Hothersall *et al.*[13]

Also, for a ground with a periodic arrangement of identical strips of impedance Z_2 embedded in a ground of impedance Z_1, such as the case considered in Boulanger *et al.*,[14] the equation can be rewritten in terms of the diffraction terms from the two edges of each strip as

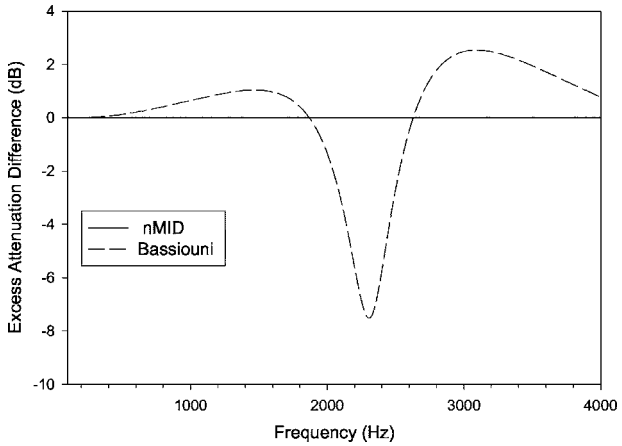

FIG. 3. Error in applying the original De Jong model to reciprocal cases of propagation over a hard ground with a 0.12-m absorbent strip placed at the midpoint between source and receiver. Distance from source to receiver is 1 m.

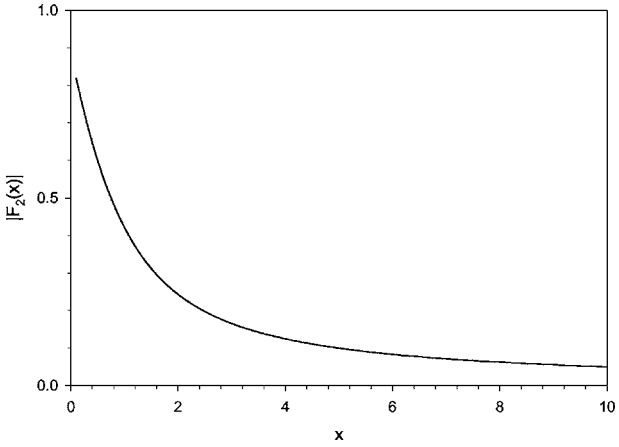

FIG. 4. The absolute value of the Fresnel integral $F_2(x)$.

$$\frac{p}{p_1} = 1 + \frac{r_1}{r_2} Q_G e^{ik(r_2 - r_1)} + (Q_2 - Q_1) \frac{e^{-i\pi/4}}{\sqrt{\pi}} \times \sum_{k=1}^{m} \left[\frac{r_1}{s_{2k-1}} \{ F_2(\sqrt{k(s_{2k-1} - r_1)}) + \gamma_{2k-1} \times F_2(\sqrt{k(s_{2k-1} - r_2)}) e^{ik(r_2 - r_1)} \} + \frac{r_1}{s_{2k}} \times \{ F_2(\sqrt{k(s_{2k} - r_1)}) - \gamma_{2k} F_2(\sqrt{k(s_{2k} - r_2)}) e^{ik(r_2 - r_1)} \} \right], \tag{13}$$

where m is the total number of strips.

E. The significance of the modification

In Sec. II B we have shown mathematically that the original De Jong model does not satisfy reciprocity requirement. The consequence of this in application to a simple case of a single-impedance strip (two impedance discontinuities) is shown in Fig. 3. The impedance strip is placed perpendicular to the source to receiver direction and has a width of 12 cm. This width is much narrower, compared with acoustic wavelength, than those used in a previous study.[13] The reason for choosing such a narrow width is that our eventual purpose is to use the model to investigate the excess attenuation created by embedded wells that have widths that are less than the acoustic wavelength. In Fig. 3 the strip has a porous-type flow resistivity (200 000 N s m^{-4}) that is typical of grassland. The source to receiver distance is 1 m, and the strip is placed on a rigid ground midway between the source and the receiver. Calculations are first made for a source height of 0.1 m and a receiver height of 0.4 m, and then for the corresponding reciprocal situation. The differences in the excess attenuation between the two cases are shown in Fig. 3. The result from the extension by Bassiouni *et al.*, which is based on the original De Jong model, is labeled as "Bassiouni."

Because the two cases are the reciprocal of each other, we expect the difference between the calculated excess attenuation to be exactly zero. This is indeed the case with the nMID model. On the other hand the extension (Bassiouni) based on the unmodified De Jong model produces differences of up to 8 dB, proving that it does not satisfy the reciprocity requirement.

Another way to look at the significance of the modification is to examine the differences between the equations representing the two models. The only difference between the modified model, Eq. (11), and the original De Jong model, Eq. (1), is the reversal of the sign of the $F_2(\sqrt{k(s_1 - r_1)})$ term when the transition is from a softer impedance to a harder impedance, i.e., the introduction of the parameter μ in Eq. (11). Hence, the significance of the modification can be seen by examining the behavior of this F_2 term. Figure 4 shows the absolute value of this term as a function of its argument x, which is given by $\sqrt{k(s_1 - r_1)}$. As can be seen from the figure, the value of F_2 increases as its argument gets smaller. Therefore, it is expected that the effect of the modification, or in other words the error in any extensions to multiple impedance strips that are based on the original formulation, will be greater when $\sqrt{k(s_1 - r_1)}$ is smaller. This occurs at lower frequencies and, from the geometry of Figs. 1 and 2, when the source and receiver heights are low and the propagation is close to grazing. Generally the nMID model provides more significant improvements over the incorrect model at lower frequencies and at smaller grazing angles. Note that this only applies to soft to hard impedance transitions, but in the case of multiple impedance strips such transitions will inevitably occur. To demonstrate this, Fig. 5 compares the result of predictions using the nMID model and Bassiouni's equation on the single-impedance strip configuration of Fig. 10(a) of Hothersall *et al.*[13] The source and receiver heights are both at 4 m. The distance between them is 20 m. The strip width is 5 m. The position of the strip is changed from below the source to below the receiver. The excess attenuation is plotted against the horizontal distance from the source to the center of the strip in Fig. 5 for the frequency of 500 Hz. The flow resistivity of the strip is taken to be 200 000 N s m^{-4} as in Hothersall *et al.*,[13] but the depth of the absorbent is taken to be 0.032 m. The source and receiver geometry is symmetrical. Therefore, we expect the results to be symmetrical about the center point (when the distance from the source to the center of the strip is 10 m). In

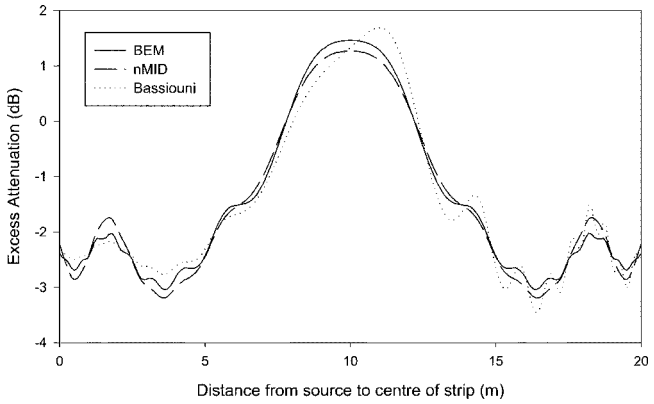

FIG. 5. Comparison between calculations of propagation over an absorbent strip of width 5 m. Source and receiver heights are both 4 m. Distance from source to receiver is 20 m. The source frequency is 500 Hz.

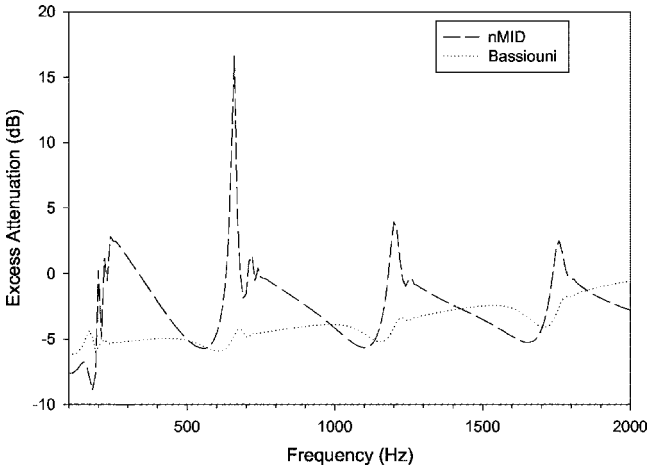

FIG. 6. Predicted attenuation over a rigid ground with a well of width 0.12 m and depth 0.3 m located midway between source and receiver. Distance from source to receiver is 10 m and source and receiver heights are 0.1 and 0.2 m, respectively.

this configuration the nMID is the same as Eqs. (10)–(12) of Hothersall *et al.*[13] Indeed, the nMID model shows good agreement with BEM that is similar to that found in Hothersall *et al.*[13] On the other hand, the incorrect Bassiouni model shows an asymmetric result in Fig. 5 because of the lack of reciprocity in its formulation.

One particular case where extensions based on the original De Jong model will always fail to predict the correct attenuation occurs when the specular reflection point is outside but close to either side of a narrow impedance strip. This can be seen by examining the nMID model for a single impedance strip [i.e., $m=1$ in Eq. (13)], and with the reflection point at the source side of the strip. Under this condition the incorrect extension based on the original De Jong equation (e.g., Bassiouni *et al.*[15] and Boulanger *et al.*[14]) is similar to the nMID model but has a -1 sign in front of the third Fresnel integral inside the square bracket [i.e., the $F_2(\sqrt{k(s_2-r_1)})$ term]. If the strip is narrow such that the difference between s_1 and s_2 is small, then the F_2 terms inside the square bracket in this incorrect extension will largely cancel. This will then leave only the first two terms (representing spherical reflection from an infinite ground) in the equation, even though the discontinuities are close to the specular reflection point. On the other hand, the nMID model will have correctly a significant diffraction contribution from the addition of the two F_2 terms associated with r_1. The difference is large especially when the difference between the two impedances is large such that (Q_2-Q_1) returns a large value. One such example is when the impedance strip is created by a well that has a large swing of extreme impedance values due to resonances in the well at different frequencies. Figure 6 shows the result of such a case. The strip is a narrow well of depth 0.3 m and a width (in the source to receiver direction) of 0.12 m. It is placed on a rigid ground midway between the source and the receiver. The source height is 0.1 m and the receiver height is 0.2 m. The source to receiver distance is 1 m. The reflection point is on the source side of the strip. The figure shows clearly the failure of the incorrect extension (labeled "Bassiouni" in the figure) to predict the diffraction effect from the strip. In comparison, the nMID prediction clearly shows strong attenuation patterns created by the embedded well.

III. PROPAGATION OVER MIXED POROUS IMPEDANCE SURFACES

Although there have been previous studies[13–15] in the literature on the application of De Jong's model to mixed impedance grounds, not all the results are positive due to the incorrect application of the original De Jong model and the confusion over the apparent inconsistence[14] of Hothersall *et al.*'s equations[13] with the De Jong equation. Hothersall *et al.*[13] studied single-impedance strip configurations with strips that were 5 to 10 m wide at frequencies not lower than 500 Hz. Good accuracy was found except at close to grazing propagation. Because of our eventual goal of using the nMID model for wells that are narrower than a wavelength, we wish to conduct further investigations on propagation over narrow impedance strips. In all our tests, the strips are all 0.12 m wide, and the source to receiver distance is always 1 m. The source and receiver heights are in the range from close to the ground to 0.4 m. In other words the effect of mixed impedance boundaries that are close to each other is considered in situations where source and receiver are close to the surface and separated by a short distance. The short separation of the source and receiver provides a reflection angle θ that is largely different from grazing (about 60° to 70° from the normal of the reflecting surface in most cases) for most of the source and receiver heights of interest. With this arrangement the path lengths s_j (see Fig. 2) are of the order of 1 m. The assumption of $ks_j \gg 1$ that is inherent to the diffraction approximation used in the nMID model should therefore be satisfied at frequencies above 300 Hz when $ks_j > 5$.

The accuracy of the nMID model is first examined on a single absorbent strip, and then on a mixed impedance surfaces in which seven different admittance strips in a rigid ground are used. As in Hothersall *et al.*,[13] the boundary element method, which has been shown to have good agreement with measured data in previous works on mixed impedance plans,[9,14] is used to provide data for the validation of

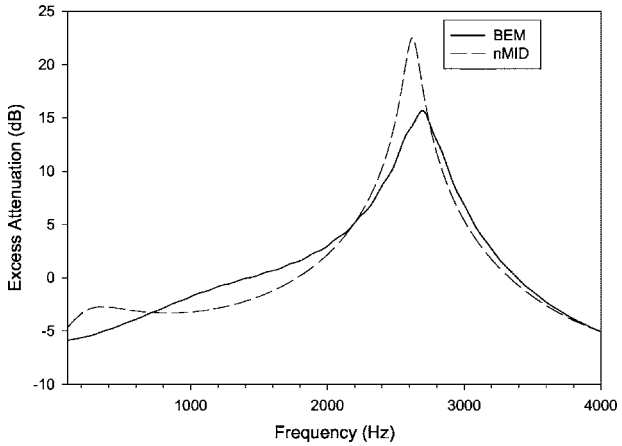

FIG. 7. Propagation over one porous absorbent strip. Source and receiver heights are 0.1 and 0.4 m, respectively, the strip is located at midpoint between source and receiver. The flow resistivity $\sigma=20\,000$ N s m^{-4}.

the nMID model. Full details of the boundary element method (BEM) used in this investigation can be found in Monazzam and Lam.[4]

A. One absorbent strip

Figure 7 shows the prediction of the excess attenuation for wave propagation over a narrow strip of porous material (flow resistivity $\sigma=20\,000$ N s m^{-4}). The source and receiver heights are 0.1 and 0.4 m, respectively. It can be seen that the nMID model has good agreement with the BEM prediction except for the attenuation peak at around 2.5 kHz. The reflection angle θ is 63.4° and should be far enough from grazing for the nMID model to work. On the other hand, the width of the strip, 12 cm, is less than an acoustic wavelength at frequencies below about 2.8 kHz. The discrepancy in the attenuation peak is therefore likely to be caused by the interactions between the two discontinuities due to their small separation (less than a wavelength below 2.8 kHz). In this case the BEM prediction, which takes into account the interactions, has a significantly lower peak magnitude. However, the interactions do not always result in a reduction in peak magnitude, as it can be seen in the example in the next section where the magnitude predicted by the BEM can be smaller than that predicted by the nMID model. Overall though the main features of the attenuation variation with frequency are well predicted. The nMID model appears to provide a reasonably good prediction of the attenuation even when the two impedance discontinuities are closer than a wavelength to each other.

B. Multiabsorbent strips

A mixed surface with seven absorbent strips placed back to back to each other and located perpendicularly to the direction from source to receiver on a rigid ground is used for this investigation. The predictions by the nMID and by the BEM are shown in Fig. 8. The surface in Fig. 8 has an arbitrary arrangement of absorbent strips. The flow resisitivities of the absorbents, which are stated in the figure, are chosen to be typical of soft to grass-covered grounds. The strips are all given a fixed depth of 0.1 m for the simulation.

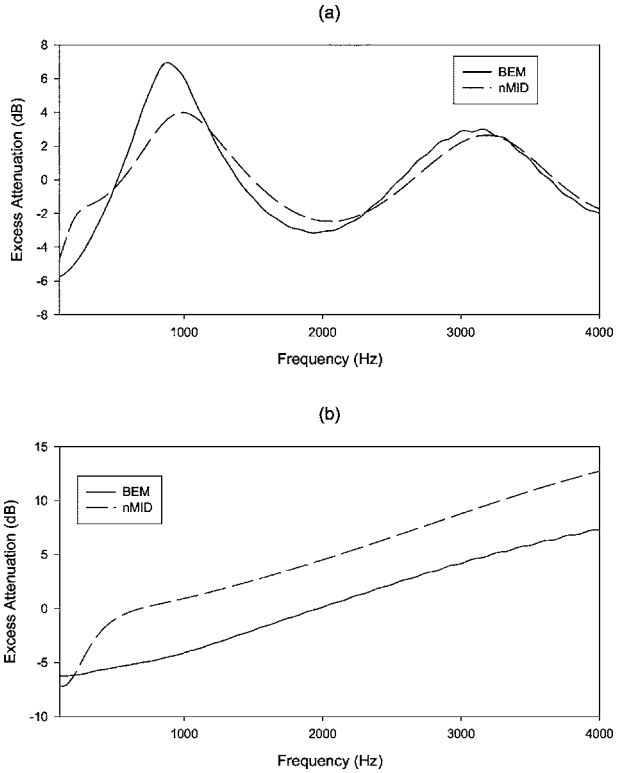

FIG. 8. Wave propagation over a mixed impedance surface containing seven strips placed on a rigid ground midway between the source and receiver. The flow resistivity of the strips from source to receiver are 250 000, 200 000, 20 000, 300 000,120 000,180 000, and 350 000 N s m^{-4}. Source and receiver heights are (a) 0.4 and 0.2 m; (b) 0.01 and 0.01 m, respectively.

Reasonable agreement is seen between the nMID model and the boundary element method in Fig. 8(a) when the source and receiver are high above the surface (0.4 and 0.2 m high, respectively, with a separation of 1 m). The closeness of the discontinuities once again created shifts in the frequency and the magnitude of the attenuation peaks that are similar to that seen in Fig. 7, which has similar source and receiver heights. Again, the overall trend of the attenuation is well predicted. As the source and receiver are moved close to the ground (both are 0.01 m above ground and the reflection angle becomes $\theta=88.9°$) in Fig. 8(b), a consistent error relative to the BEM prediction is seen over most of the frequency range shown in the figure. This consistent error seems to be a result of the limited accuracy of the De Jong model when the propagation is close to grazing. Apart from the constant shift in magnitude, the nMID still matches the trend of the attenuation increase with frequency that is predicted by the BEM. It seems that the nMID model can provide a good indication of the essential features of the attenuation.

IV. PROPAGATION OVER WELLED SURFACES

A. Effect of imaginary part of admittance for welled surface

The use of wells of different depths to create a mixed impedance surface is of particular interest here. This is the base design for the well-known Schroeder-type diffusers. It has been shown by numerical simulation that putting such a

surface on top of a T-shaped barrier can substantially increase the insert loss of the barrier.[4] However, modeling such welled surfaces in the analytical multiple impedance discontinuities model presents more difficulties than modeling porous absorbent strips. With a porous strip, the surface admittance (the inverse of impedance) varies smoothly with frequency. The real part, which corresponds to resistive loss, is generally significant. When the strip is created by a well, the admittance at the entrance to the well can vary widely due to resonances. For example, for a rigid well that is narrow enough such that plane wave propagation can be assumed, the value of the normalized input admittance β changes from negative infinity to positive infinity when passing through a resonance.

The behavior of the spherical wave boundary factor $F(z)$, Eq. (6), has been studied extensively in the past.[23] It is known that the approximation is only valid when the value of β satisfies certain conditions. Additionally, the attenuation effect represented by the boundary factor $F(z)$ is likely to change considerably due to the extreme variation of the β value with frequency for welled surfaces. Hence, it is necessary to examine the effect of β on the spherical reflection coefficient for propagation over a boundary with embedded rigid wells.

The boundary factor $F(z)$ can be approximated by Eq. (7) for large values of the numerical distance $|z|$. However, Eq. (7) is only bounded for certain range of the argument of z. The suggested substitution by Stinson[23] for Eq. (7) is

$$\begin{cases} F(z) = 2i\sqrt{\pi} z H[-\mathrm{Im}(z)] e^{-z^2} - \left\{ \dfrac{1}{2z^2} + \dfrac{3}{4z^4} + \cdots \right\}, & \dfrac{-\pi}{4} < \arg z < \dfrac{3\pi}{4} \\ F(z) = 0 & \text{otherwise} \end{cases} . \tag{14}$$

From Eq. (5) the real and imaginary part of the numerical distance z are given by

$$\mathrm{real}(z) = \frac{\sqrt{kr_2}}{2}(a - b + \cos\theta), \text{ and}$$
$$\mathrm{imag}(z) = \frac{\sqrt{kr_2}}{2}(a + b + \cos\theta), \tag{15}$$

$$\arg(z) = \arctan\left(\frac{a + b + \cos\theta}{a - b + \cos\theta}\right), \tag{16}$$

where a and b are the real and imaginary parts of the admittance β, respectively. The real part of the numerical distance z is negative if the imaginary part of the admittance β is positive and bigger than the sum of the cosine of the reflection angle and the real part of the admittance. At the entrance to a rigid well, the real part of the admittance is positive but very small (≈ 0), but the imaginary part is very large, particularly around resonant frequencies. When the reflection angle θ is large and therefore $\cos\theta$ is small, $\arg(z)$ is determined mainly by b, the imaginary part of β. From Eq. (15), a large and positive imaginary part of the admittance β (i.e., masslike reactance) will result in the real part of numerical distance z being negative and the imaginary part of z being positive. When the imaginary part of β is large and negative (i.e., springlike reactance), the real part of the numerical distance z is positive and the imaginary part of z is negative. In both cases, since the real part of β is positive and small for a rigid well, we have $|a| \ll |b|$ and the value of $\arg(z)$ is always within the valid range ($-\pi/4 < \arg z < 3\pi/4$). Therefore, Eq. (7) is valid for the welled surface. However, $\arg(z)$ will be close to the limit of $3\pi/4$ when the imaginary part of β is large and positive, and close to $-\pi/4$ when the imaginary part of β is large and negative.

A closer look at the equations for the spherical reflection coefficient can also reveal the behavior of the apparent sound attenuation over a welled surface at resonant frequencies where large values of admittance β occur. From Eq. (4) it can be seen that the plane-wave reflection coefficient approaches -1 when β is much larger than $\cos\theta$, where θ is the reflection angle from the surface normal. The numerical distance z is large when β is large. For large values of z, the boundary factor $F(z)$, from Eq. (7), will approach zero. Hence, the spherical reflection coefficient, Eq. (3), will approach -1 when β is large at resonance. For a surface with a uniform admittance and without discontinuities, the sound propagation is given by Eq. (1) without the diffraction terms [the third term on the right-hand side of Eq. (1)], and with Q_G calculated from the admittance of the well. When Q_G approaches -1, the reflected pressure largely cancels the incident pressure to give large ground attenuation. The amplitude factor (r_1/r_2) and the phase factor $e^{ik(r_2-r_1)}$ will modify the exact frequency at which the attenuation peak occurs, but it will be close to the resonant frequencies of the well, especially at lower frequencies. This is what one would expect since physically the sound energy will be trapped by the resonating well. Therefore, we can expect the imaginary part of the admittance β of rigid wells to have a significant correlation with the attenuation of sound propagation over a surface embedded with such rigid wells.

When there is an impedance discontinuity nearby, the reflected pressure is modified by the diffraction terms in Eq. (1), even if the reflection point is still on the surface of the well. To see how the discontinuity modifies the attenuation, we can make further approximations to simplify Eq. (1). Since the integral F_2 decays rapidly with its argument (Fig.

4), one may ignore the first F_2 term that involves the bigger argument $\sqrt{k(s_1-r_1)}$ when the source and receiver are not close to the ground, and write

$$\frac{p}{p_1} \approx 1 + \frac{r_1}{r_2} e^{ik(r_2-r_1)}\Gamma, \tag{17}$$

where

$$\Gamma = \left[Q_2 - (Q_2 - Q_1)\frac{(1-i)}{\sqrt{2\pi}} F_2(x) \right], \text{ with } x = \sqrt{k(s_1 - r_2)}. \tag{18}$$

If the ground reflection point is close to the discontinuity, then x is small and a crude approximation of the F_2 integral based on a simple step approximation of the integration is

$$F_2(x) \approx \left(\sqrt{\frac{\pi}{8} - x} \right) + i\sqrt{\frac{\pi}{8}}, \tag{19}$$

and Γ is then

$$\Gamma = \left[Q_2 - (Q_2 - Q_1)\left\{ \left(\frac{1}{2} - \frac{x}{\sqrt{2\pi}} \right) + i\frac{x}{\sqrt{2\pi}} \right\} \right]. \tag{20}$$

We can see that, because of the imaginary part in Eq. (20), Γ will not be exactly -1. Therefore, the attenuation peak will be greatly reduced due to the presence of the diffraction from the discontinuity. Moreover, at resonance, $Q_2 \approx -1$ and $Q_1 = 1$ if the other side of the discontinuity is a hard ground. Then, Γ is approximately $\sqrt{(2/\pi)}x(1+i)$, which approaches zero rather than -1 when x is small. Hence, large cancellation will not occur at resonance. The attenuation peak will be shifted away significantly from the resonant frequency. To see whether the shift is to a lower or higher frequency, we can examine the behavior of the Qs to find the condition under which Γ may regain a value of -1. When $x \ll 1$ and ignoring the imaginary part, Eq. (20), with $Q_1 = 1$ being a hard surface, becomes

$$\Gamma \approx \frac{Q_2 + 1}{2}. \tag{21}$$

For Γ to approach -1 for maximum attenuation, Q_2 needs to have a largely real and negative value close to -3.

Close to resonance, the admittance is large. For a large admittance $\beta = a + ib$, with a small and negligible, the numerical distance z is approximately

$$z \approx \frac{-(1-i)}{2}\sqrt{kr_2 b}, \text{ and } z^2 = -kr_2(a + \cos\theta)b - i\frac{kr_2 b^2}{2}. \tag{22}$$

Note that we have retained the small $(a+\cos\theta)$ term in the expression for z^2 to show the decay factor in the exponential term in $F(z)$. If b is positive and large (just above a resonance), then the Heaviside factor in Eq. (7) is zero and the boundary factor $F(z)$ is again small,

$$F(z) \approx -\frac{1}{2z^2} \approx \frac{1}{kr_2(2(a+\cos\theta)b + ib^2)} \approx \frac{-i}{kr_2 b^2}. \tag{23}$$

In this case the real value of Q_2 above resonance does not change much from the value of -1 given by R_p. Hence, the attenuation peak frequency is not shifted towards higher frequencies. Indeed, the increasing value of the imaginary part in Eq. (23) as b becomes smaller (moving away from resonance) means that the attenuation at frequencies just above resonance should decrease.

At frequencies just below resonance, b is negative and large. The Heaviside function is 1 and $F(z)$ has an additional term,

$$F(z) \approx 2i\sqrt{\pi} z e^{-z^2} - i\frac{1}{kr_2 b^2}. \tag{24}$$

At resonance b is very large and the real part of z^2 in Eq. (22) gives rise to a large decay factor in e^{-z^2}. $F(z)$ is again very small, providing continuity in $F(z)$ between Eqs. (23) and (24) when b changes from large negative values to large positive values. However, when b becomes smaller [but still >1 and $(a+\cos\theta)$] moving away from resonance to lower frequencies, z^2 will be dominated by the imaginary term and e^{-z^2} becomes a largely oscillating phase factor. In this case the first term in Eq. (24) for $F(z)$ can produce reasonably large, negative real values for Q_2 to come close to -3, and hence for Γ to approach -1 for maximum cancellation and attenuation. Therefore, it is likely that the attenuation peak will shift to lower frequencies in the presence of a discontinuity.

Although the above analysis is based on just one discontinuity, it is expected that the general behavior should be similar when there are multiple discontinuities. However, the specific values of the attenuation will change according to specific configurations. This will be confirmed in the following sections with simulations on a variety of surfaces embedded with wells.

B. Propagation over a rigid surface embedded with one well

As discussed above, it is expected that the excess attenuation over welled surfaces will have notable changes around their resonant frequencies. This is investigated by using the nMID model to calculate the excess attenuation of a ground embedded with narrow wells. One case with a single well embedded in a rigid ground is used as examples in Fig. 9. The well has a width of 0.12 m and the well depth is 0.245 m. The excess attenuation over this surface, with source and receiver heights at, respectively, 0.001 and 0.35 m, is shown in Fig. 9. As before, the horizontal source to receiver distance is 1 m and the well is placed with its width in the source to receiver direction and placed midway between the source and receiver. The very small source height used here is to simulate the propagation of sound over the top surface of a T-shaped barrier where the source incidence may be considered as mostly parallel to the top surface. The small source height means that the ground reflection point is mostly on the hard portion of the ground at the

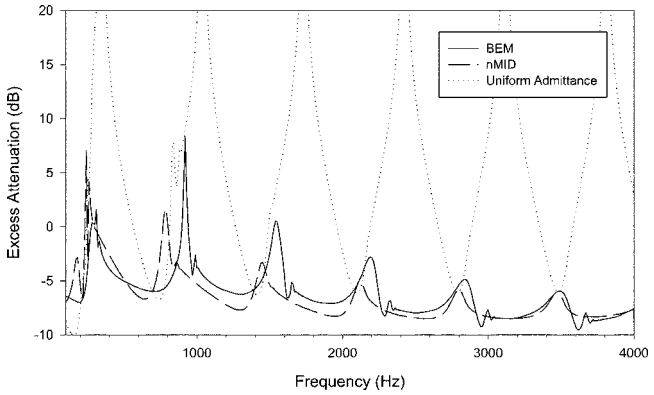

FIG. 9. Excess attenuation of propagation over a 0.12-m-wide well embedded in a rigid ground located midway between source and receiver that are 1 m apart. The well depth is 0.245 m. Source and receiver heights are 0.001 and 0.35 m, respectively.

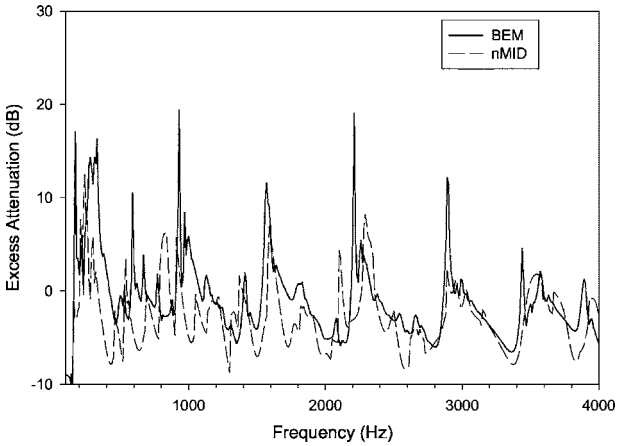

FIG. 10. Excess attenuation of propagation over seven 0.12-m-wide wells embedded in a rigid ground located midway between source and receiver that are 1 m apart. The well depths are 0.25, 0.4, 0.35, 0.3, 0.45, 0.2, and 0.18 m. Source and receiver heights are 0.001 and 0.35 m, respectively.

source side before the start of the well. Figure 9 shows that the nMID model has reasonable agreement with the reference BEM calculation, and predicted the main features, i.e., the peaks in the excess attenuation just before the resonant frequencies of the wells. The discrepancies seen around the peaks are similar to those found in the cases with absorbent strips (Figs. 7 and 8) due to the closeness of the discontinuities and the near-grazing propagation. However, in the welled case the peaks are much sharper due to resonances and small losses, and the discrepancies are more apparent. The discrepancies also appear to be larger at lower frequencies. Since $ks_j > 5$ at frequencies above approximately 300 Hz, the assumption inherent to the hard half-plane diffraction formulation used in the model should be satisfied at frequencies above 300 Hz. The larger discrepancies at low frequencies but above 300 Hz are more likely to be caused by the empirical correction for the finite impedances in the De Jong model and the interactions between the discontinuities that are ignored in the nMID model.

The result in Fig. 9 shows that the excess attenuation is indeed highly correlated with the resonances, at which the imaginary part of the admittance crosses over from a large negative value to a large positive value. The attenuation peaks just before each resonant frequency, where $\mathrm{Im}(\beta)$ is large and negative, then drops quickly to small values (negative attenuation) when $\mathrm{Im}(\beta)$ becomes large and positive. This correlates very well with our predictions from Eq. (7) on the dependence of the boundary factor $F(z)$ on the imaginary part of the admittance. Indeed, this can be seen clearly by comparing the results with that calculated for a hypothetical surface that has a uniform admittance equals to that of the well. Using this hypothetical surface, the attenuation, also shown in Fig. 9, shows strong attenuation peaks at well resonances. The peaks are much stronger than those of the BEM and nMID calculations that also account for the effect of the surrounding hard ground and the diffraction from the discontinuities. This confirms that the imaginary part of the admittance pays a crucial part in the attenuation of sound propagation over a welled surface, but the effect of the impedance discontinuities must be correctly accounted for also. The nMID model thus proves to be useful in providing some insight into the main factors affecting the attenuation.

C. Propagation over multiple embedded wells

In order to see the effect on a multiwelled surface the investigation was extended to a case with seven wells. The wells all have the same width of 0.12 m but the well depths are all different. The well depths from source to receiver are arbitrarily chosen to be 0.25, 0.4, 0.35, 0.3, 0.45, 0.2, and 0.18 m. The source and receiver separation and their heights are identical to the single-well case. The result of this calculation is shown in Fig. 10. With more well depths there are more resonances within the frequency range. There are corresponding increases in the number of attenuation peaks in the graph. Thus, the general relationship between attenuation and well resonances is maintained even in the case of multiple wells. However, the magnitude and extent of these attenuation peaks do vary. Some resonances do not produce noticeable attenuation peaks at all. This is possibly caused by the diffraction effect of multiple impedance discontinuities that modifies the reflected wave. The trend of the attenuation peaks is reasonably predicted by the nMID in comparison with the BEM prediction. The nMID seems capable of accounting for the diffraction from multiple impedance discontinuities. There are however discrepancies in the positions and absolute values of the peaks between the two methods, similar to that observed earlier in Fig. 9, especially at low frequencies. Considering the closeness of the discontinuities (less than a wavelength at frequencies below 2.8 kHz) and the closeness of the source to the ground (source height is 0.001 m), both of which are limitations of the nMID model, the nMID approximation is reasonably accurate in predicting the trend of the attenuation changes and the influences of the well resonances. Indeed, the accuracy of the nMID model improves with frequency as the width of the wells becomes comparable and eventually larger than the wavelength. The agreement between nMID and BEM is noticeably better at frequencies above 2 kHz.

Our next test surface is a rigid surface embedded with wells that corresponds to a quadratic residue diffuser (QRD) design. The reason for choosing this surface is that previous work[4] has shown that the insertion loss of a T-shaped barrier can be significantly improved by placing such a structure on the top of the T-shape. It is therefore of interest to see if this improvement in barrier performance is due to extra attenuation of sound when it propagates over the QRD covered top surface. The nMID model should be able to provide some insight into the factors that create this extra attenuation if it can correctly predict the attenuation. Again, the BEM is used as a reference in this investigation.

A QRD surface is created by a sequence of wells that have depths that are determined from a quadratic residue sequence according to the formula

$$d_i = \frac{c(i^2 \bmod N)}{N(2f_r)}, \tag{25}$$

where d_i is the depth of the ith well, N is the length of the quadratic sequence, and f_r is the design frequency of the diffuser. Note that the design frequency is not the same as the first resonant frequency of the well with the maximum depth, which occurs at $f_o = c/(4^* d_{\max})$, where $d_{\max}$ is the maximum depth. Full details on QRD design can be found in the literature.[24]

The QRD surface used in this simulation has an $N=7$ design. The design frequency is 400 Hz. Due to the numbering sqeuence, there are only three distinct well depths and one zero depth (rigid surface). The well widths are fixed at 0.12 m as before. The results are shown in Fig. 11 for two source heights. The propagation geometry in Fig. 11(a) is the same as that of Fig. 10, while the source height is raised to 0.1 m in Fig. 11(b). Because of the smaller number of distinct well depths there are less distinct resonant frequencies, and Fig. 11 shows correspondingly less attenuation peaks than Fig. 10, which has seven distinct wells. Note that once again the nMID model provides reasonable prediction over the trend of the attenuation despite noticeable errors in the peak magnitudes. As the source height is raised in Fig. 11(b), the accuracy of nMID improves, as is expected from the assumption of the nMID model.

When the source height is very close to the surface (0.001 m), which we used to approximate the incidence condition over the top surface of a T-shaped noise barrier, the results in Figs. 10 and 11 show that the nMID predictions have tolerable agreement with the BEM predictions. There are still noticeable discrepancies in the values of the peak frequencies and magnitudes at low frequencies. However, the general trends of the attenuation, and in particular the influence of the well resonances and the effect of multiple diffractions, between the two predictions are in good agreement. We believe that this shows that the nMID is sufficiently accurate to explain the effect of a QRD surface on the top of a T-shaped barrier, although it may not be accurate enough to be used as a means to predict the absolute magnitude of the barrier performance.

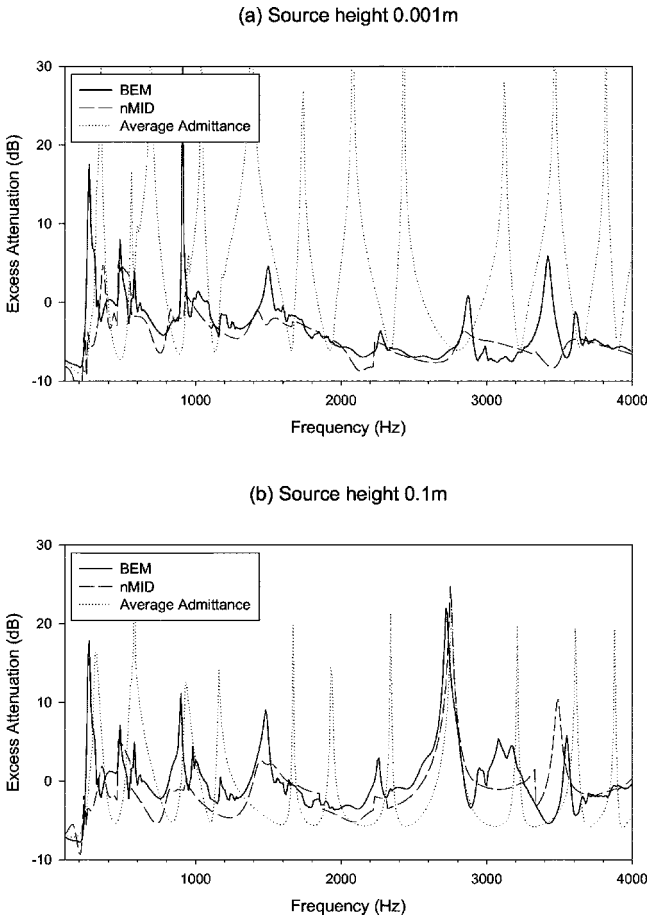

FIG. 11. Excess attenuation of propagation over $N=7$ QRD surfaces embedded in a rigid ground located midway between source and receiver that are 1 m apart. The well widths are fixed at 0.12 m. Source and receiver heights are 0.001 and 0.35 m, respectively.

D. Average admittance effect

Nyberg[16] demonstrated that the Helmholtz equation with the boundary condition for a point source above an infinite plane surface with periodic impedance strips can be solved by using a Fourier transform approach. The wave propagation over a two-valued, infinitely periodic striped impedance can be approximated by employing the area-averaged admittance in the calculation of the reflection coefficient,

$$\beta_{\text{ave}} = \frac{(w_1\beta_1 + w_2\beta_2)}{(w_1 + w_2)}, \tag{26}$$

where w_1 and w_2 are the widths of the two types of strips, and β_1 and β_2 are the corresponding admittance values. The assumption made is that (w_1+w_2) is much smaller than the acoustic wavelength. In our case the width of each well (strip) is smaller than a wavelength. However, since the strips are not periodic, the total width of all the nonperiodic strips added together is larger than or comparable to a wavelength in most of the frequency range. Hence, Nyberg's approximation cannot be applied directly here. In earlier sections we have seen that the admittance of the well plays a deterministic role in the attenuation of sound propagation over a surface with a single well. It is therefore of interest to see if the area-averaged admittance over multiple wells also

correlates with the attenuation phenomenon. At resonance the average admittance is dominated by that of the well in resonance and therefore the attenuation should be correlated with the average admittance. In Fig. 11 the prediction using the averaged admittance without the diffraction terms from the discontinuities, i.e., on a hypothetical surface of uniform admittance equals to the average admittance, is also shown. Without accounting for the diffraction, the prediction shows a strong attenuation peak at every resonant frequency. Although some of these peaks do coincide with the attenuation peaks predicted by the BEM and nMID models (especially at frequencies below 1 kHz when the acoustic wavelength is longer than the overall width of all the wells), fewer peaks appear in the more accurate predictions. This again shows the importance of accounting for the diffraction from the impedance discontinuities, and suggests that the effect of the discontinuities actually reduces the attenuation peaks both in number and in magnitude. However, there is also evidence, most noticeably at frequencies below 1 kHz in Fig. 11, that the diffraction terms also broaden the peaks slightly and also do not allow the attenuation to drop to large negative values immediately after each resonance. It therefore appears that the imaginary part of the area-averaged admittance can be used as a pointer for optimizing the attenuation provided by such surfaces, provided that the effect of the diffraction from the discontinuities is accounted for properly, by either the BEM or nMID to obtain the correct attenuation levels.

V. CONCLUSIONS

The original De Jong model for the calculation of diffraction from an impedance discontinuity has an inherent assumption of transition from a hard to a softer impedance. Unfortunately this assumption has been overlooked in many of the subsequent works[13,14] that attempted to extend the model to cases with multiple impedance discontinuities. This paper has shown that such extensions are invalid because of this assumption of hard to soft transition. In one previous work[13] where the extension to one impedance strip (two impedance discontinuities) did work, there was no clear explanation as to the adjustment in the equations that were used. Consequently, some confusion was found in later work which considered the extension to be inconsistent and should be corrected. In this paper we used the acoustic reciprocity condition to derive a modified form of the De Jong equation that does not have the restriction of hard to soft impedance transition. This modification clarifies the previously unexplained adjustment made in the equations of Hothersall *et al.*[13] This modified equation was then used to obtain a new multiple impedance discontinuities model, the nMID. It was shown that this nMID model agrees well with the accurate boundary element method when applied to single and multiple impedance strips that are made up of typical porous surfaces. As expected, due to the inherent assumption of the De Jong approximation and the disregard of intercoupling effects between discontinuities, the accuracy decreases as the source or receiver height decreases (nearer grazing incidence) and when the width of the strips or the distance between the discontinuities becomes shorter than the acoustic wavelength. Nevertheless, the simulations presented in this paper have shown that the nMID is still capable of predicting the main features of the excess attenuation spectrum under these unfavorable conditions.

One of the main objectives of this work is to investigate the attenuation of sound propagation over multiple impedance strips that are created by rigid wells of different depths. The admittance of rigid wells has a different behavior from that of porous surfaces. The extreme values created by well resonances mean that the admittance value can be close to the limits of the valid range of useful approximations that are used to calculate the spherical reflection coefficient. It has been shown, by examining the behavior of the spherical reflections coefficient at different values of admittance, that the wells can have large effect on the sound propagation when the imaginary part of the admittance is large and negative (with a $e^{-i\omega t}$ convention), which occurs just before a well resonance. This correlation was confirmed by simulations on surfaces with single and multiple wells. It was found that the attenuation peaks at frequencies just below the resonant frequencies, at which the imaginary part of the admittance becomes very large and negative. In case of multiple wells, the area-average admittance gives a rough indication to this behavior and can be considered as a first approximation pointer for quick optimization of the attenuation over such surfaces. However, diffraction from the impedance discontinuities modifies and substantially reduces the magnitudes of the attenuation peaks, and therefore must be properly accounted for. Overall, it was found that the nMID model is capable of accounting for these effects, although discrepancies are more noticeable at the sharp attenuation peaks at lower frequencies.

[1] L. A. M. van Der Heijden and M. J. M. Martens, "Traffic noise reduction by means of surface wave exclusion above parallel grooves in the roadside," Appl. Acoust. **15**, 329–339 (1982).

[2] P. F. van Tol and H. A. Holties, "A reciprocal method to evaluate low, close to track noise barriers," J. Acoust. Soc. Am. **105**(2), 949 (1999).

[3] K. Fujiwara, D. C. Hothersall, and C. H. Kim, "Noise barriers with reactive surfaces," Appl. Acoust. **53**(4), 225–272 (1998).

[4] M. R. Monazzam and Y. W. Lam, "Performance of profile single noise barriers covered with quadratic residue diffusers," Appl. Acoust. **66**, 709–730 (2005).

[5] W. Zhu, M. R. Stinson, and G. A. Daigle, "Scattering from impedance gratings and surface wave formation," J. Acoust. Soc. Am. **111**(5), 1996–2012 (2002).

[6] B. O. Enflo and P. H. Enflo, "Sound wave propagation from a point source over a homogeneous surface and over a surface with an impedance discontinuity," J. Acoust. Soc. Am. **82**, 2123–2135 (1987).

[7] K. B. Rasmussen, "A note on the calculation of sound propagation over impedance jumps and screens," J. Sound Vib. **84**, 598–602 (1982).

[8] K. E. Gilbert and M. J. White, "Application of the parabolic equation to sound propagation in a refracting atmosphere," J. Acoust. Soc. Am. **85**, 630–637 (1989).

[9] S. N. Chandler-Wilde and D. C. Hothersall, "Sound propagation above an inhomogeneous impedance plane," J. Sound Vib. **98**, 475–491 (1985).

[10] B. A. De Jong, A. Moerkerken, and J. D. Van Der Toorn, "Propagation of sound over grassland and over an earth barrier," J. Sound Vib. **86**(1), 23–46 (1983).

[11] P. Koers, "Diffraction by an absorbing barrier or by an impedance transition," Proceedings of Internoise'83, 311–314 (1983).

[12] G. A. Daigle, J. Nicolas, and J.-L. Berry, "Propagation of noise above ground having an impedance discontinuity," J. Acoust. Soc. Am. **77**(1), 127–138 (1985).

[13]D. C. Hothersall and J. N. B. Harriott, "Approximate models for sound propagation above multi-impedance plane boundaries," J. Acoust. Soc. Am. **97**(2), 918–926 (1995).
[14]P. Boulanger, T. Waters-Fuller, K. Attenborough, and K. M. Li, "Models and measurements of sound propagation from a point source over mixed impedance ground," J. Acoust. Soc. Am. **102**(3), 1432–1442 (1997).
[15]M. R. Bassiouni, C. R. Minassian, and B. Chang, "Prediction and experimental verification of far-field sound propagation over varying ground surface," Proceedings of Internoise'83, 287–290 (1983).
[16]C. Nyberg, "The sound field from a point source above a striped impedance boundary," Acta Acust. (Beijing) **3**, 315–322 (1995).
[17]C. F. Chien and W. W. Soroka, "Sound propagation along an impedance plane," J. Sound Vib. **43**(1), 9–20 (1975).
[18]M. E. Delany and E. N. Bazely, "Acoustical properties of fibrous absorbent materials" Appl. Acoust. **3**, 105–116 (1970).
[19]T. Wu, T. J. Cox, and Y. W. Lam, "From a profiled diffuser to an optimized absorber," J. Acoust. Soc. Am. **108**(2), 634–650 (2000).
[20]R. B. Lawhead and I. Rudnick, "Acoustic wave propagation along a constant normal impedance boundary," J. Acoust. Soc. Am. **23**, 546–549 (1951).
[21]L. E. Vogler, "A note on the attenuation function for propagation over a flat layered earth," IEEE Trans. Antennas Propag. **AP-12**, 240–242 (1964).
[22]R. J. King and G. A. Schalk, "Ground wave attenuation function for propagation over a highly inductive earth," Radio Sci. **2** (New Series), 687–693 (1967).
[23]M. R. Stinson, "A note to the use of an approximate formula to predict sound field above an impedance plane due to a point source," J. Acoust. Soc. Am. **98**, 1810–1812 (1995).
[24]M. R. Schroeder, "Binaural dissimilarity and optimum ceilings for concert halls: More lateral sound diffusion," J. Acoust. Soc. Am. **65**, 958–963 (1979).

Frame bulk modulus of porous granular marine sediments

Masao Kimura
School of Marine Science and Technology, Tokai University, 3-20-1 Orido, Shimizu-ku, Shizuoka, Shizuoka 424-8610, Japan

(Received 18 August 2005; revised 2 May 2006; accepted 10 May 2006)

Frame bulk modulus is important for analyzing the acoustic wave propagation in porous water-saturated marine sediments such as sands. Previous measurements of the longitudinal wave velocities in air-saturated glass beads of uniform grain size showed that the longitudinal wave velocity increased with the grain size. This result cannot be explained by using a classical contact theory such as the Hertz-Mindlin model. It was speculated that this phenomenon is due to the effect of air elasticity between the grains. In this study, the longitudinal and shear wave velocities in samples of vacuum-, air-, and water-saturated glass beads as well as beach sands at a lower stress were measured. The results obtained were used to estimate the corresponding values of the frame bulk modulus. In the water-saturated samples, these values are about 10^9 Pa at a frequency of 500 kHz and about ten times greater than those in air-saturated samples at a frequency of 11.8 kHz. The grain size dependence was also observed. These measurements are explained in terms of the effect of fluid elasticity at the grain-to-grain contact in the context of a modified gap stiffness model. © *2006 Acoustical Society of America.* [DOI: 10.1121/1.2211427]

PACS number(s): 43.30.Ma [RR] Pages: 699–710

I. INTRODUCTION

The Biot-Stoll model is used extensively for analyzing acoustic wave propagation in porous water-saturated marine sediments.[1–6] However, velocity dispersion in marine sediment is one of the important subjects that has been unresolved in the community of sediment acoustics.[7,8] Among the 13 physical parameters that are required by the model, the value of the frame bulk modulus is one of the most difficult to estimate.[9] The frame bulk modulus is an important parameter because it is expected to be considerably related to the velocity dispersion. Some researchers have used constant values in the region of 10^8 Pa.[6] However, the measured frequency dependence of the longitudinal wave velocity is not consistent with the calculated characteristics using a frequency-independent frame bulk modulus. The reported velocity dispersion is greater than the calculated dispersion using the frequency-independent frame bulk modulus.[7,10] Further, the measurements in air-saturated almost-uniform glass beads of four different grain sizes, but with almost the same porosity, show that the longitudinal wave velocity increases significantly with the grain size. These results cannot be explained by a contact theory such as the Hertz-Mindlin model.[11] It is assumed that the value of the frame bulk modulus used by some researchers is obtained from the values of the longitudinal and shear wave velocities of air-saturated samples.[12] The frame bulk modulus is defined as the ratio of the externally applied isotropic pressure to the dilatation in the jacketed test.[13] Pore fluid in the medium is free to flow out of the bag through an upper tube such that the pore fluid pressure remains unchanged during slow loading. A significant problem is whether the pore fluid between the grains has any influence on the frame bulk modulus. The possibility of the influence of elasticity of the pore fluid between the grains was suggested by Chotiros[14] and Chotiros and Isakson.[15] Murphy *et al.* proposed the gap stiffness model for describing an acoustic relaxation caused by the local fluid flow in the gap between the grains of rocks.[16] To investigate the influence of the pore fluids such as air and water between the grains on the frame bulk modulus, it is necessary to obtain the frame bulk modulus of vacuum-, air-, and water-saturated samples. Moreover, marine sediments have different grain sizes, grain size distributions, grain shapes, and porosity, so it is desirable to use many kinds of samples.

In this study, the longitudinal and shear wave velocities in samples of vacuum-, air-, and water-saturated glass beads with four different grain sizes as well as 85 kinds of beach sands at a lower stress were measured in order to investigate the influence of pore fluids such as air and water between the grains on the frame bulk modulus. The values of the frame bulk moduli were estimated from the measured velocities and known physical properties. These results are explained in terms of the modified gap stiffness model; this model also predicts the frequency dependence of the frame bulk modulus.

II. THEORY

A. The Biot-Stoll model

Marine sediments are composed of an assemblage of grains—a porous skeletal frame saturated with seawater, as shown in Fig. 1. In the Biot-Stoll model, two energy-loss mechanisms exist during the acoustic wave propagation: (1) viscous loss caused by the relative motion of the pore fluid to the frame and (2) friction loss caused by the friction due to grain-to-grain contact. The wave equations for the longitudinal wave in a porous saturated medium are expressed as follows:[13]

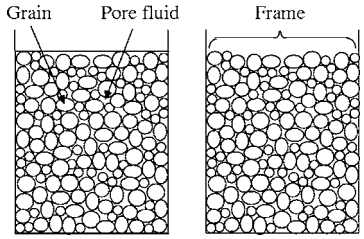

FIG. 1. Grain, pore fluid, and an assemblage of grains comprising the frame in the Biot-Stoll model.

$$\nabla^2(He - C\zeta) = \frac{\partial^2}{\partial t^2}(\rho e - \rho_f \zeta),$$
$$\nabla^2(Ce - M\zeta) = \frac{\partial^2}{\partial t^2}(\rho_f e - m\zeta) - \frac{F\eta}{k}\frac{\partial \zeta}{\partial t}, \tag{1}$$

$$e = \mathrm{div} u, \quad \zeta = \beta\, \mathrm{div}(u - U), \tag{2}$$

where $\boldsymbol{u}$ and $\boldsymbol{U}$ denote the displacements of the frame and pore fluid, respectively. The parameters H, C, and M are determined from the elasticity of the frame, grains, and pore fluid, respectively. Further, parameters ρ and ρ_f are the densities of the sediment and pore fluid, respectively. Furthermore, m is the virtual mass; k, the permeability; η, the viscosity; and F, the viscous correction factor. The solutions for e and ζ of the forms

$$e = A_1 \exp[j(\omega t - k_l x)], \quad \zeta = A_2 \exp[j(\omega t - k_l x)], \tag{3}$$

are assumed in order to obtain a solution at an angular frequency ω. Here, k_l is the wave number for the longitudinal wave; it is expressed as follows:

$$k_l = k_{lr} + jk_{li}. \tag{4}$$

Upon transformation to the frequency domain, the following equation is obtained:

$$\begin{vmatrix} Hk_l^2 - \rho\omega^2 & \rho_f\omega^2 - Ck_l^2 \\ Ck_l^2 - \rho_f\omega^2 & m\omega^2 - Mk_l^2 - j\dfrac{\omega F\eta}{k} \end{vmatrix} = 0. \tag{5}$$

That is,

$$(C^2 - HM)k_l^4 + \left(Hm + \rho M - 2\rho_f C - jH\frac{F\eta}{\omega k}\right)\omega^2 k_l^2 + \left(\rho_f^2 - \rho m + j\rho\frac{F\eta}{\omega k}\right)\omega^4 = 0. \tag{6}$$

The roots of Eq. (6) give the velocities for the first and second kinds of longitudinal waves as functions of frequency as follows:

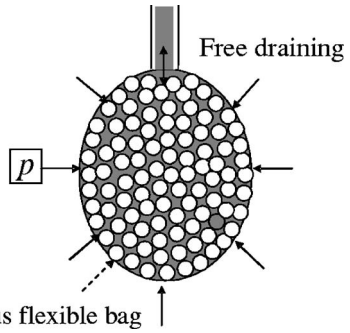

FIG. 2. Jacketed test for deriving the frame bulk modulus. The saturated porous medium is placed in an impervious, flexible bag; it is loaded by means of an external pressure p. The pore fluid in the medium is free to flow out of the bag through an upper tube.

$$c_l = \frac{\omega}{k_{lr}}. \tag{7}$$

The frame bulk modulus is defined as the ratio of the externally applied isotropic pressure p to the dilatation e in the jacketed test,[13] as shown in Fig. 2. In the jacketed test, a saturated porous medium is placed in an impervious, flexible bag, and loaded by means of an external pressure. The pore fluid in the medium is free to flow out of the bag through an upper tube such that the pore fluid pressure remains unchanged during slow loading. An important question is whether the pore fluid has any influence on the frame bulk modulus. It seems that the pore fluid has no effect at lower frequencies. However, there must be an effect at higher frequencies because the pore fluid between the grains is trapped and forced to support the normal stress between the grains. Therefore, it is considered that the frame bulk modulus must have a frequency dependence. Some researchers in the community have used constant values of approximately 10^8 Pa for the frame bulk modulus, as shown in Table I. It is assumed that some of these values are obtained form the values of the longitudinal and shear wave velocities of the air-saturated samples.[12] However, Chotiros and Isakson suggested that this value must have a frequency dependence.[15] The frame bulk modulus is an important parameter because it is expected to be related considerably to the velocity dispersion.

B. Gap stiffness model

The gap stiffness model was developed by Murphy *et al.*[16] This model describes an acoustic relaxation due to the local fluid flow in the gap between the grains. A fraction of the frame is permeated by sheet-like gaps, as shown in Fig. 3(a). The incomplete grain-to-grain contact permits the existence of an interconnected fluid film between the grain sur-

TABLE I. Values of the frame bulk modulus in the Biot-Stoll model (after N. P. Chotiros, J. Acoust. Soc. Am., 1995).

Frame bulk modulus	Hovem and Ingram	Stoll and Kan	Stern *et al.*	Ogushwitz	Turgut and Yamamoto
K_b (Pa)	1.00×10^8	4.36×10^7	4.36×10^8	1.99×10^8	1.08×10^8

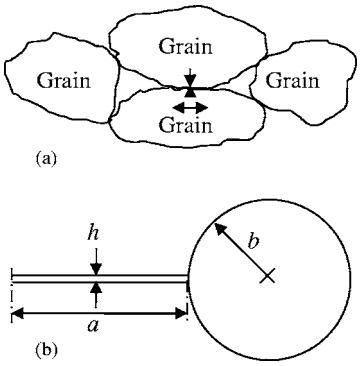

FIG. 3. Configuration in the gap stiffness model. (a) Grain-to-grain contact of sand. (b) Axisymmetric section through the model. The model consists of a narrow gap connected to a finite annular pore. Here, h denotes the gap separation distance; a, the contact radius; and b, the radius of the annular pore.

faces. This model consists of a narrow gap connected to a finite annular pore, as shown in Fig. 3(b). In Fig. 3(b), h is the gap separation distance; a, the contact radius; and b, the radius of the annular pore. An acoustic wave drives the fluid film out of the narrow gap region and into the annular pore. The effective stiffness of the gap k_g, which is the resistance of the gap to the applied dynamic loadings, is expressed as follows:

$$k_g = \frac{\Delta F}{-\Delta h}, \tag{8}$$

where ΔF denotes the acoustic load and Δh is the increment of the gap separation distance. The volume capacity of the annular pore region per unit increase in acoustic pressure is

$$C_v = \frac{2\pi^2(a+b)b^2}{K_f}, \tag{9}$$

where K_f denotes the bulk modulus of the pore fluid. Here, C_v is a function of the pore volume and the bulk modulus of the pore fluid. The gap stiffness k_g is expressed as follows:

$$k_g = \frac{\pi a^2 K_f}{h_0}\left[1 - \frac{2C_v K_f J_1(\kappa a)}{2\pi a^2 h_0 J_1(\kappa a) + \kappa a C_v K_f J_0(\kappa a)}\right] = \frac{\pi a^2 K_f}{h_0}\left(1 - \frac{1}{\dfrac{V_{\text{gap}}}{V_{\text{pore}}} + \dfrac{\kappa a}{2}\dfrac{J_0(\kappa a)}{J_1(\kappa a)}}\right), \tag{10}$$

where h_0 denotes the initial value of the separation distance. Here, J_0 and J_1 are the Bessel functions of the first kind of zeroth and first orders, respectively, and κa is defined as follows:

$$\kappa a = \sqrt{-j\left(\frac{12\eta}{K_f}\right)\left(\frac{a}{h_0}\right)^2\omega}, \tag{11}$$

where η denotes the viscosity of the pore fluid. The volume of the gap V_{gap} and that of the pore V_{pore} are expressed as follows:

$$V_{\text{gap}} = \pi a^2 h_0, \tag{12}$$

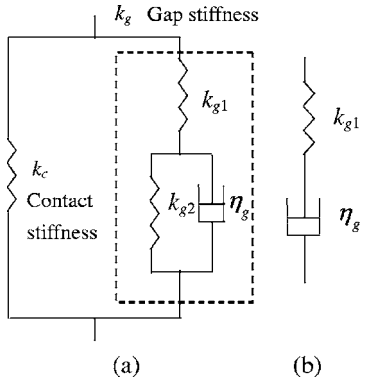

FIG. 4. Spring and dashpot model. (a) Contact stiffness and gap stiffness. (b) Approximated gap stiffness.

$$V_{\text{pore}} = 2\pi^2(a+b)b^2. \tag{13}$$

In Eq. (10),

$$1 \le \left|\frac{\kappa a}{2}\frac{J_0(\kappa a)}{J_1(\kappa a)}\right| < \infty\left(\left|\frac{\kappa a}{2}\frac{J_0(\kappa a)}{J_1(\kappa a)}\right| \to 1(\omega \to 0), \left|\frac{\kappa a}{2}\frac{J_0(\kappa a)}{J_1(\kappa a)}\right| \to \infty\,(\omega \to \infty)\right), \tag{14}$$

and

$$\frac{V_{\text{gap}}}{V_{\text{pore}}} \ll \left|\frac{\kappa a}{2}\frac{J_0(\kappa a)}{J_1(\kappa a)}\right|. \tag{15}$$

Therefore, Eq. (10) is approximated to

$$k_g = \frac{\pi a^2 K_f}{h_0}\left(1 - \frac{1}{\dfrac{\kappa a}{2}\dfrac{J_0(\kappa a)}{J_1(\kappa a)}}\right). \tag{16}$$

A porous grain contact has an effective normal stiffness. The effective normal stiffness k_n is the sum (in parallel) of the elastic stiffness of the solid-to-solid contact (contact stiffness) k_c and the effective stiffness of contact gap (gap stiffness) k_g; this stiffness is expressed as follows:

$$k_n = k_c + k_g. \tag{17}$$

A spring and dashpot model for the contact stiffness and gap stiffness is shown in Fig. 4(a). In this figure, k_{g1} and k_{g2} are expressed as follows:

$$k_{g1} = \frac{\pi a^2 K_f}{h_0}, \tag{18}$$

$$k_{g2} = \frac{\pi a^2 K_f}{h_0}\frac{V_{\text{gap}}}{V_{\text{pore}}}, \tag{19}$$

and η_g is the loss factor of the gap stiffness; this factor is not a constant but a function of frequency. The loss factor η_g is expressed as follows:

$$\eta_g = \frac{\pi a^2 K_f}{h_0}\frac{\dfrac{\kappa a}{2}\dfrac{J_0(\kappa a)}{J_1(\kappa a)} - 1}{j\omega}. \tag{20}$$

Using the approximated Eq. (16), k_{g2} can be neglected, as shown in Fig. 4(b). More specifically, the gap stiffness k_g is

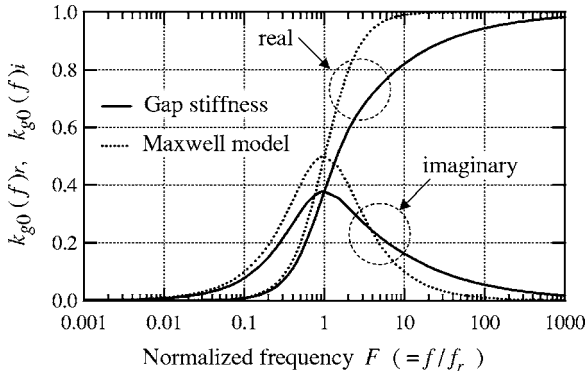

FIG. 5. Frequency dependence of the real and imaginary parts of the gap stiffness and Maxwell models.

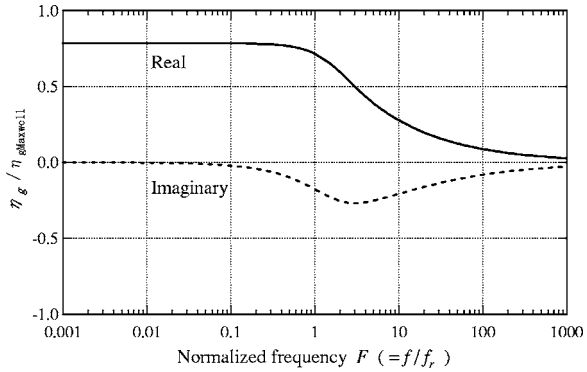

FIG. 6. Frequency dependence of the loss factor of the gap stiffness η_g.

in series with k_{g1} and η_g; it reduces to the form of the Maxwell model. Chotiros and Isakson used the Maxwell model for evaluating the frame bulk modulus.[15] However, our model is different from the Maxwell model because η_g is a function of frequency. At a lower frequency, the gap stiffness k_g approaches the following limit:

$$k_{g0} = \frac{k_{g1}k_{g2}}{k_{g1}+k_{g2}} = \frac{\pi a^2 K_f}{h_0}\frac{V_{\text{gap}}}{V_{\text{gap}}+V_{\text{pore}}} \approx 0\ (\omega \to 0). \quad (21)$$

At a higher frequency, the fluid has no time to flow in and out. The only compliant part of the gap is the bulk modulus of the fluid in the gap. Thus, k_g reduces to

$$k_{g\infty} = k_{g1} = \frac{\pi a^2 K_f}{h_0}(\omega \to \infty). \quad (22)$$

At an intermediate frequency, the real part of the gap stiffness k_{gr} increases from the minimum k_{g0} to the maximum $k_{g\infty}$. The normalized gap stiffness k_{g0} is expressed as follows:

$$k_{g0} = 1 - \frac{1}{\frac{\kappa a}{2}\frac{J_0(\kappa a)}{J_1(\kappa a)}}, \quad (23)$$

$$\kappa a = \sqrt{-j2\pi\frac{f}{f_r}}, \quad (24)$$

where f_r is the relaxation frequency of the gap stiffness that is dependent on the aspect ratio $\alpha(=h_0/a)$, the bulk modulus K_f, and viscosity η of the pore fluid as follows:[17]

$$f_r = \frac{1}{12}\frac{K_f}{\eta}\alpha^2. \quad (25)$$

On the other hand, the stiffness of the Maxwell model is expressed as follows:

$$k_{gM0} = \frac{1}{1 - j\frac{f}{f_{rM}}}, \quad (26)$$

where f_{rM} is the relaxation frequency of the Maxwell model. The normalized frequency characteristics of the real and imaginary parts of the gap stiffness and those of the Maxwell model are shown in Fig. 5. The characteristics of the gap stiffness are different from those of the Maxwell model, particularly at higher frequencies. This is because the loss factor of the gap stiffness η_g is dependent on frequency. The loss factor normalized to that of the Maxwell model is expressed as follows:

$$\frac{\eta_g}{\eta_{g\text{Maxwell}}} = \frac{\frac{\kappa a}{2}\frac{J_0(\kappa a)}{J_1(\kappa a)} - 1}{j\frac{f}{f_r}}, \quad (27)$$

$$\kappa a = \sqrt{-j2\pi\frac{f}{f_r}}. \quad (28)$$

The normalized frequency dependence of η_g is shown in Fig. 6. From this figure, it is seen that η_g is almost independent of frequency at lower frequencies but is dependent on frequency at higher frequencies.

III. MEASUREMENTS OF VELOCITIES

We have shown the measured results of the longitudinal wave velocity in air-saturated glass beads of different grain sizes (0.125, 0.192, 0.451, and 0.781 mm) but with almost the same porosity.[10] The results showed that the longitudinal wave velocity increases significantly with the grain size. Measured results of this type were reported also by Prasad and Meissner;[18] however, these could not be explained. These results cannot be explained by a contact theory such as the Hertz-Mindlin model.[11] The longitudinal and shear wave velocities in vacuum-saturated glass beads were measured by a pulse-transmitting method in order to investigate the effect of air elasticity in the gap between the grains. The sample in the vessel is densely packed by a vibrator. The vessel used for the measurements is shown in Fig. 7. Piezoelectric transducers with a resonance frequency of 50 kHz and a diameter of 3.8 cm were used for transmitting and receiving. A single-cycle sine wave pulse with a frequency of 11.8 kHz was used for the transmitting waveform. The resonant frequencies of the transmitting and receiving transducers were 50 kHz; however, their operating frequencies were 11.8 kHz; the received signal was maximum at this frequency. The received signal could not be detected at a frequency of 50 kHz because of the very high attenuation of the longitudinal wave at higher frequencies in the air- and vacuum-saturated

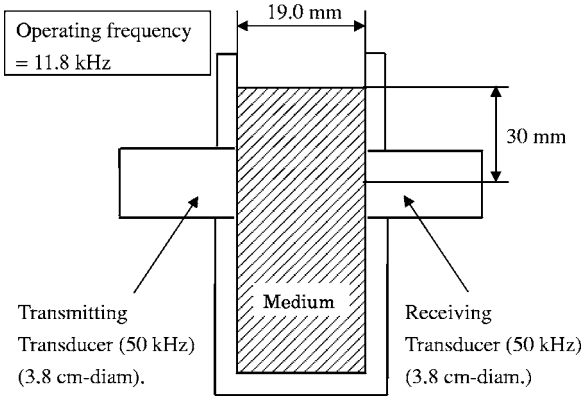

FIG. 7. Vessel used for the measurements for the longitudinal wave velocity in air-saturated samples.

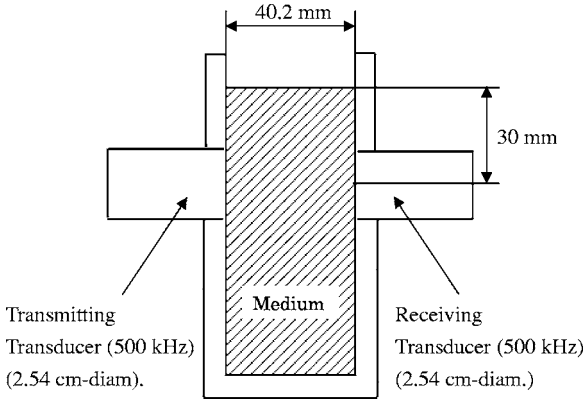

FIG. 9. Vessel used for the measurements for the longitudinal wave velocity in water-saturated samples.

samples. The depth for the measurement was set at 30 mm in order to obtain the same stress condition. The propagation distance is 19.0 mm. The longitudinal wave velocity is obtained using the following equation:

$$c_l = c_a \frac{1}{1 - \frac{\Delta t c_a}{d}}, \tag{29}$$

where c_a(=343 m/s) is the velocity in air at a temperature of 20 °C, d is the propagation distance, and $\Delta t = t_a - t_l$ (t_l, t_a=57.49 μs: propagation time in the sample and air, respectively). The measurements were conducted at temperatures of 26–28 °C. The vacuum-saturated measurements were carried out in a vacuum chamber. The measured results are shown in Fig. 8. The grain size parameter ϕ is defined as the negative of the $\log_2$ of the grain diameter in millimeters. From this figure, it is observed that the longitudinal wave velocity decreases with the removal of air. The difference between the air- and vacuum-saturated values increases with the grain size. The residual grain size dependence in the vacuum-saturated case is relatively small, and it is adequately explained by the Hertz-Mindlin model. These unexpected results demonstrate that the presence of air has a significant effect on the elasticity in the gap between the grains.

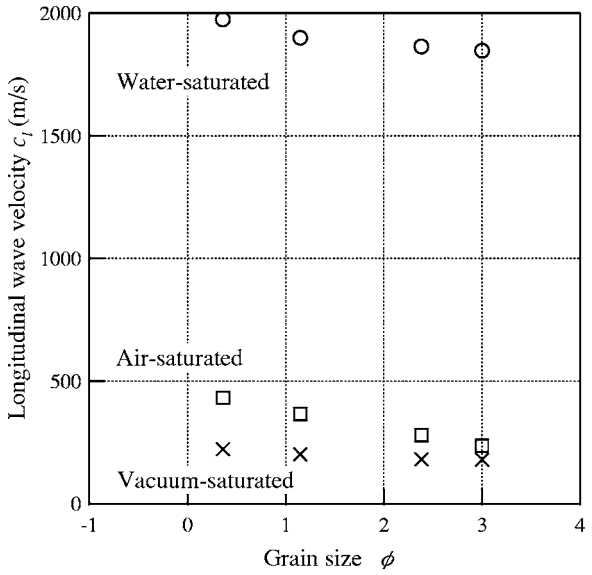

FIG. 8. Longitudinal wave velocity vs grain size for water-, air-, and vacuum-saturated glass beads. Measurements were carried out at a frequency of 500 kHz for the water-saturated samples and at 11.8 kHz for the vacuum- and air-saturated samples.

The longitudinal wave velocities in the water-saturated glass beads of the four grain sizes mentioned above were also measured. For measurements in the water-saturated case, how to remove the air in the samples is important. In the first step, the water-saturated sample was boiled in order to remove the air. Next, the water, which was degassed by vacuum deaeration for an hour, was poured into the vessel, and then the glass beads were poured into the water little by little and carefully. The sample was deaerated in the vacuum chamber for an hour again. As mentioned above, the samples in the vessel were densely packed by the vibrator. The vessel for the measurements is shown in Fig. 9. It is difficult to use the same operating frequency for the water-saturated measurements as that for the air- and vacuum-saturated measurements, because the wavelength in water-saturated sample corresponding to the frequency of 11.8 kHz is long; therefore, the velocity measurements in a small vessel in laboratory are difficult. Then, piezoelectric transducers with a resonance frequency of 500 kHz and a diameter of 2.54 cm were used for transmitting and receiving. A five-cycle sine wave pulse with a frequency of 500 kHz was used for the transmitting waveform. The depth for the measurement was again set at 30 mm. The propagation distance is 40.2 mm. The longitudinal wave velocity is obtained using the following equation:

$$c_l = c_w \frac{1}{1 - \frac{\Delta t c_w}{d}}, \tag{30}$$

where c_w(=1483 m/s) is the velocity in water at a temperature of 20 °C, d is the propagation distance, and $\Delta t = t_w - t_l$ (t_l, t_w=28.75 μs: propagation time in sample and water, respectively). The measurements were conducted at a temperature of 20 °C in a constant-temperature bath. The measured parameters for the glass beads of different grain sizes are shown in Table II. The grain size and its standard

TABLE II. Measured values of parameters for the glass beads of different grain sizes.

Grain size	d	mm	0.125	0.192	0.451	0.781
	ϕ	$(=-\log_2 d)$	3.00	2.38	1.15	0.36
Standard deviation	ϕ_{sd}		0.20	0.23	0.12	0.15
Total density (air-saturated)	ρ	kg/m^3	1507	1541	1553	1565
Total density (water-saturated)	ρ	kg/m^3	1930	1955	1942	1949
Grain density	ρ_r	kg/m^3	2471	2498	2457	2465
Porosity (air-saturated)	β		0.390	0.383	0.368	0.365
Porosity (water-saturated)	β		0.367	0.362	0.353	0.352

deviation were obtained using the sieving method. The porosity is expressed as follows:

$$\beta = \frac{\rho_r - \rho}{\rho_r - \rho_f}. \tag{31}$$

It is obtained from the measured total density, ρ; grain density, ρ_r; and pore fluid density ρ_f. The total density was obtained using the weight and volume of the sample in a vessel that was the same size as the vessel for the velocity measurement. The grain density was obtained from the total density and the difference between the weights of the samples in the vessel before and after drying in the case of the water-saturated sample. The measured results along with the results for the vacuum- and air-saturated samples are shown in Fig. 8. It is observed that the longitudinal wave velocities for the water-saturated glass beads increase with the grain size in a manner similar to those in the case of the air-saturated sample; this suggests that the presence of water also has an effect on the gap elasticity.

The glass beads are spherical, and their standard deviation of the grain size is small. On the other hand, the marine sediments have different grain sizes, grain size distributions, grain shapes, and porosities. Many kinds of beach sands are expected to be used as samples. Therefore, the longitudinal wave velocities in 85 kinds of beach sands were measured under vacuum-, air-, and water-saturated conditions. We have obtained 50 kinds of sand samples from beaches ranging from Aomori to Yamaguchi in Honshu Island in Japan, and 35 kinds of sand samples from beaches ranging from Perth to Sydney in Australia. Before the measurements, each beach sand was washed by boiling three times. The measurements were carried out in the same vessel by the same method that was used in the previous case. The measured parameters for 85 kinds of beach sands are shown in Table III. The circularity C_i in Table III expresses the roundness of the two-dimensional figure of the grain and is defined by the following equation:

$$C_i = \frac{4\pi(\text{area})}{(\text{perimeter})^2}. \tag{32}$$

We measured the circularity for 85 kinds of beach sands using IMAGE PRO PLUS—a software for image processing developed by Media Cybernetics. The number of the grain samples was 200 for each kind of sand. The measured results of the longitudinal wave velocities are shown in Fig. 10. A reduction in the longitudinal wave velocity is observed when the air is removed. These results again suggest that air has an effect on the elasticity of the grain-to-grain contact. The longitudinal wave velocities of air- and water-saturated beach sands increase with the grain size in the same manner as in the case of the glass beads.

The shear wave properties were also investigated in a similar manner. The shear wave velocity c_s was measured in vacuum-, air-, and water-saturated glass beads of the same four different grain sizes and in the same set of 85 kinds of beach sands using a pulse method. The vessel used in the measurements is shown in Fig. 11. As mentioned above, the samples were densely packed by the vibrator, and the measurement depth was 30 mm. Bimorph-type piezoelectric transducers with dimensions of $20\times15\times0.5$ mm^3 were used for transmitting and receiving. A five-cycle sine wave pulse with a frequency of 3.5 kHz was used for the transmitting waveform. The measurement of the shear wave velocity at a frequency of 500 kHz cannot be carried out because the attenuation at this frequency is quite large; therefore, a frequency of 3.5 kHz was used for the shear wave velocity measurement. The propagation distance is 38.5 mm. The shear wave velocity was obtained from the time delay and

TABLE III. Measured parameters for 85 kinds of beach sands.

			Mean	Minimum	Maximum	Standard deviation
Grain size	d	mm	0.319	0.163	0.747	0.134
	ϕ	$(=-\log_2 d)$	1.76	0.42	2.62	0.54
Standard deviation	ϕ_{sd}		0.39	0.22	0.89	0.12
Total density (air-saturated)	ρ	kg/m^3	1626	1446	1789	95.3
Total density (water-saturated)	ρ	kg/m^3	2049	1903	2204	74.8
Grain density	ρ_r	kg/m^3	2716	2622	2881	77.1
Porosity (air-saturated)	β		0.401	0.333	0.463	0.028
Porosity (water-saturated)	β		0.389	0.333	0.454	0.029
Circularity	C_i		0.923	0.903	0.953	0.013

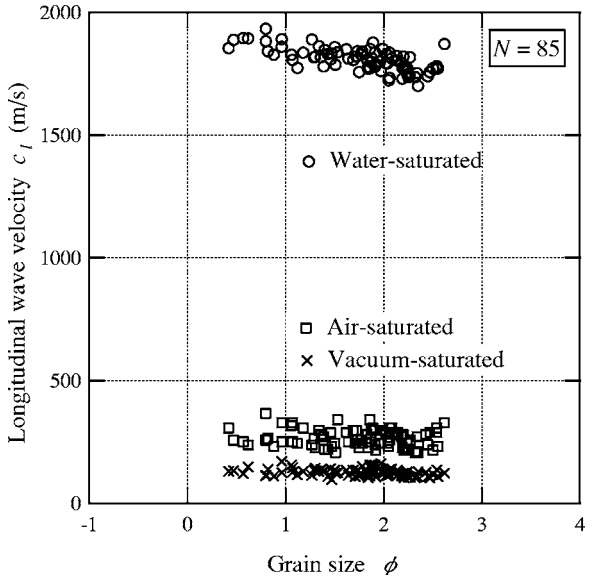

FIG. 10. Longitudinal wave velocity vs grain size for water-, air-, and vacuum-saturated beach sands (85 samples). Measurements were carried out at a frequency of 500 kHz for the water-saturated samples and at 11.8 kHz for the vacuum and air-saturated samples.

transmitter-receiver separation. The relationship of the measured shear wave velocity in air-saturated or water-saturated glass beads of four different grain sizes and 85 kinds of beach sands to the grain size is shown in Fig. 12. From this figure, it is observed that the shear wave velocity in water-saturated sample is greater than that in air-saturated sample. The shear wave velocities in vacuum- and air-saturated samples were found to be almost the same for both the glass beads as well as beach sands. The average shear wave velocity is 68 m/s for vacuum- and air-saturated glass beads; 59 m/s, water-saturated glass beads; 68 m/s, vacuum- and air-saturated beach sands; and 57 m/s, water-saturated beach sands.

The Poisson's ratios of samples of vacuum-, air-, and water-saturated glass beads as well as beach sands were obtained using the measured longitudinal and shear wave velocities. The Poisson's ratio σ is expressed as follows:

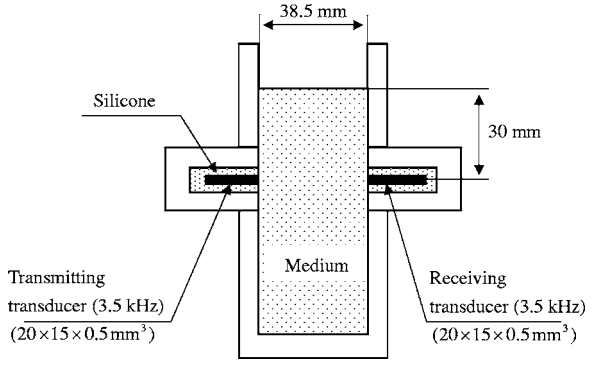

FIG. 11. Vessel used for the measurements for the shear wave velocity in air- and water-saturated samples.

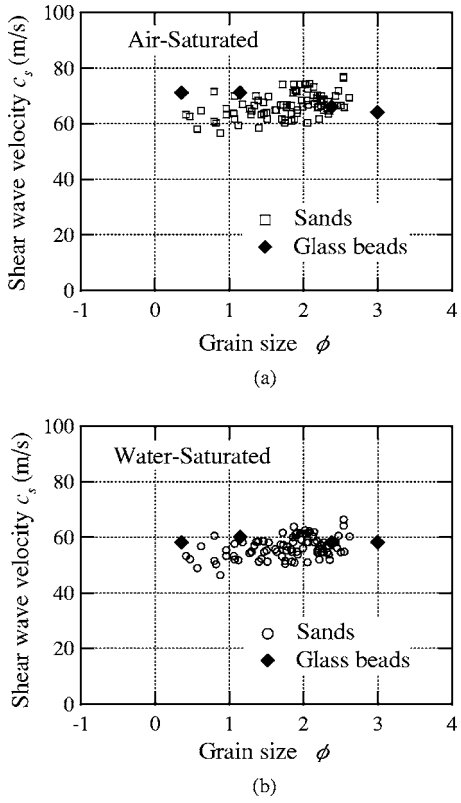

FIG. 12. Relationships of the measured shear wave velocity with the grain size for (a) air-saturated sand, and (b) water-saturated sand.

$$\sigma = \frac{1}{2}\frac{1-2\left(\frac{c_s}{c_l}\right)^2}{1-\left(\frac{c_s}{c_l}\right)^2}. \tag{33}$$

The Poisson's ratio as a function of grain size is shown in Fig. 13. From this figure, it is observed that the values of the Poisson's ratio for glass beads and beach sands are close to 0.5 for the water-saturated samples; they range from approximately 0.44 to 0.49 for the air-saturated samples. For the vacuum-saturated samples, they range from approximately 0.43 to 0.44 for glass beads and from 0.1 to 0.4 for beach sands. In the air-saturated case, there is a small degree of dependence on the grain size. On the other hand, in the vacuum-saturated case, the grain size dependence is large for beach sands.

IV. FRAME BULK MODULUS

The frame bulk modulus is related to the longitudinal and shear wave velocities. In the case of vacuum- and air-saturated samples, the longitudinal wave velocity c_l and the shear wave velocity c_s are expressed by the following equations:

$$c_l = \sqrt{\frac{K_b + \frac{4}{3}\mu}{\rho}}, \quad c_s = \sqrt{\frac{\mu}{\rho}}, \tag{34}$$

where K_b denotes the frame bulk modulus; μ, the frame shear modulus; and ρ, the total density. Thus, the frame bulk

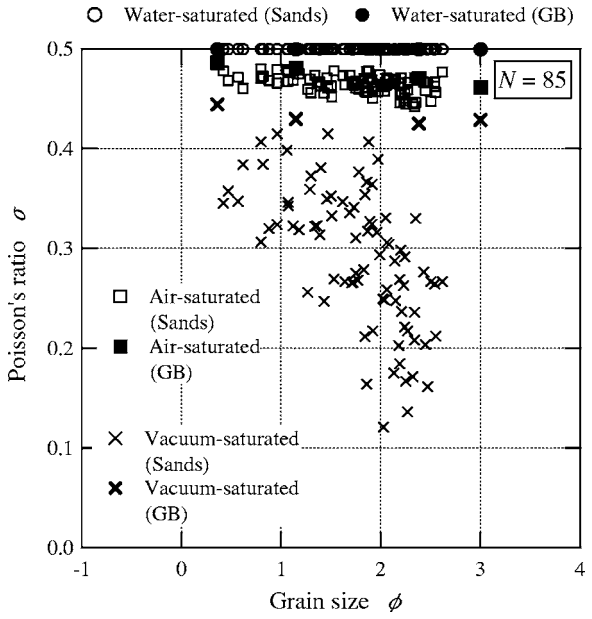

FIG. 13. Poisson's ratio as a function of grain size. The Poisson's ratios of samples of vacuum-, air-, and water-saturated glass beads as well as beach sands were obtained by using the measured longitudinal and shear wave velocities.

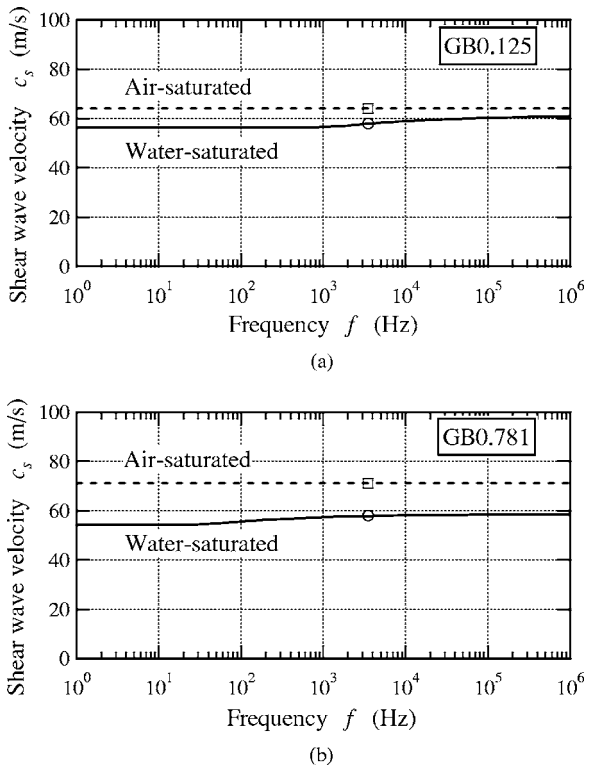

FIG. 14. Shear wave velocity as a function of frequency for glass beads with the grain sizes of (a) 0.125 mm, and (b) 0.781 mm.

modulus K_b is determined by using the following equations:

$$K_b = \rho\left(c_l^2 - \frac{4}{3}c_s^2\right). \tag{35}$$

Therefore, the frame bulk modulus can be obtained by using the measured results of the longitudinal and shear wave velocities and the densities. The operating frequencies for the measurements of the longitudinal and shear waves were different. The frequency of the longitudinal wave velocity was 11.8 kHz; on the other hand, that of the shear wave velocity was 3.5 kHz. However, velocity dispersion in the shear wave is not observed in the air-saturated samples according to the calculated results for glass beads with grain sizes of 0.125 and 0.781 mm using the Biot-Stoll model as shown in Fig. 14. The values of the parameters as shown in Table II were used for the calculation. There is no difference between the shear wave velocities at frequencies 3.5 and 11.8 kHz.

On the other hand, in the case of the water-saturated samples, the frame bulk modulus cannot be obtained by using Eq. (35). This is due to the significant inertial and viscous interactions between the frame and pore fluid in porous granular marine sediments. Using the measured longitudinal wave velocity, Eqs. (6) and (7) in the Biot-Stoll model were inverted to obtain the frame bulk modulus. The values of the parameters used for calculating the frame bulk modulus are shown in Table IV. In the parameters, the frame shear modulus cannot be obtained from the shear wave velocity at the frequency of 3.5 or 500 kHz because velocity dispersion exists in the shear wave in the water-saturated samples as shown in Fig. 14. Therefore, by using the measured shear wave velocity at a frequency of 3.5 kHz, the next shear wave equation of the Biot-Stoll model was inverted to obtain the frame shear modulus that is necessary for deriving the frame bulk modulus.

$$\left(m\mu - j\mu\frac{\eta F}{k\omega}\right)k_s^2 + \left\{(\rho_f^2 - \rho m) + j\rho\frac{\eta F}{k\omega}\right\}\omega^2 = 0, \tag{36}$$

where μ is the frame shear modulus and k_s, the wave number for the shear wave, which is expressed as follows:

$$k_s = k_{sr} + jk_{si}. \tag{37}$$

The roots of Eq. (36) yield the velocities for the shear wave as a function of frequency as follows:

$$c_s = \frac{\omega}{k_{ls}}. \tag{38}$$

The permeability and pore size were obtained by using the following equations:[19]

$$k = \frac{d^2}{36k_0}\frac{\beta^3}{(1-\beta)^2}\ (k_0 = 5), \tag{39}$$

$$a = \frac{d}{3}\frac{\beta}{1-\beta}. \tag{40}$$

The grain size characteristics of the frame bulk moduli of vacuum-, air-, and water-saturated glass beads as well as beach sands are shown in Figs. 15 and 16, respectively. The values of parameters for the calculations of the Hertz-Mindlin frame bulk modulus are shown in Table V. The Hertz-Mindlin frame bulk modulus is expressed as follows:

TABLE IV. Values of parameters used for the calculation of the frame bulk modulus.

Grain	Diameter	ϕ	measured
		d (mm)	measured
	Density	ρ_r (kg/m^3)	measured
	Bulk modulus	K_r (Pa)	3.6×10^{10}
Pore fluid	Density	ρ_f (kg/m^3)	998
	Bulk modulus	K_f (Pa)	2.195×10^9
	Viscosity	η (Pa s)	1.00×10^{-3}
Frame	Porosity	β	measured
	Permeability	k (m^2)	$k=\frac{d^2}{36k_0}\frac{\beta^3}{(1-\beta)^2}$ $(k_0=5)$
	Pore size	a (m)	$a=\frac{d}{3}\frac{\beta}{1-\beta}$
	Structure factor	α_t	1.25
	Shear modulus	μ (Pa)	μ(inverted using the measured c_s)
	Longitudinal logarithmic decrement	δ_l	0.15
	Shear logarithmic decrement	δ_s	0.15

$$K_{b\mathrm{HM}}=\sqrt[3]{\frac{C_n^2(1-\beta)^2\mu_r^2}{18\pi^2(1-\sigma_r)^2}P}, \tag{41}$$

where β denotes the porosity; C_n, the coordination number; μ_r, the shear modulus of the grain; σ_r, the Poisson's ratio of the grain; and P, the hydrostatic confining pressure. From Fig. 15, it is observed that the frame bulk modulus values in the vacuum-saturated glass beads are in good agreement with those of the Hertz-Mindlin model. The values for the air-saturated samples are significantly higher. The values for the water-saturated samples are about 10^9 Pa at a frequency of 500 kHz and about ten times greater than those in the corresponding air-saturated samples at a frequency of 11.8 kHz. In all the samples, there is some degree of dependence on the grain size. In the vacuum-saturated sample, the grain size dependence is small but measurable, suggesting the involvement of additional forces in addition to the mechanical forces predicted by the Hertz-Mindlin model. In the case of the air- and water-saturated samples, the grain size dependence is higher. With regard to the sands, it is shown in Fig. 16 that the values of the frame bulk moduli of water-saturated beach sands are also about 10^9 Pa at a frequency of 500 kHz and about ten times greater than those in the corresponding air-saturated samples at a frequency of 11.8 kHz, and these, in turn, are about five times greater than those in the vacuum-

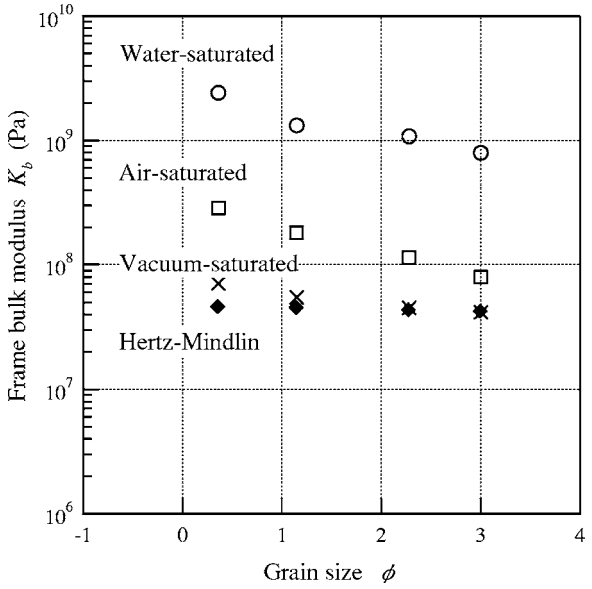

FIG. 15. Frame bulk modulus vs grain size for the water-, air-, and vacuum-saturated glass beads. Values of the frame bulk modulus at a frequency of 500 kHz for the water-saturated samples and at 11.8 kHz for the vacuum- and air-saturated samples.

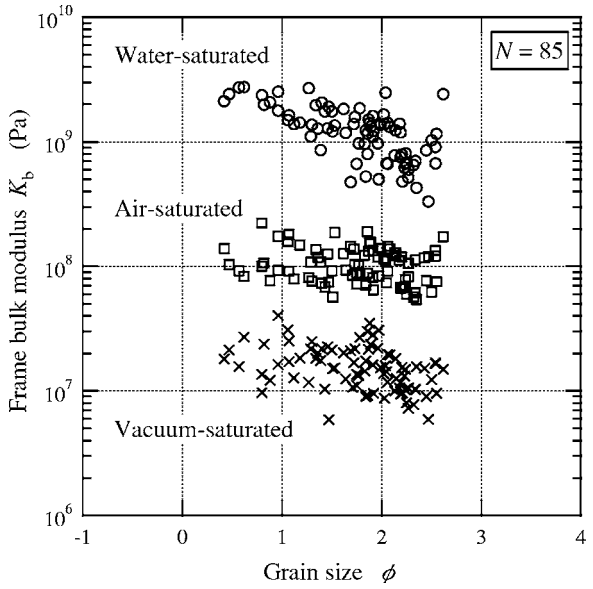

FIG. 16. Frame bulk modulus vs grain size for water-, air-, and vacuum-saturated beach sands (85 samples). Values of the frame bulk modulus at a frequency of 500 kHz for the water-saturated samples and at 11.8 kHz for the vacuum- and air-saturated samples.

TABLE V. Values of parameters for the calculations of the frame bulk modulus in the Hertz-Mindlin model.

Grain size	d	mm	0.125	0.192	0.451	0.781
	ϕ (=$-\log_2 d$)		3.00	2.38	1.15	0.36
Porosity	β		0.390	0.383	0.368	0.365
Grain density	ρ_r	kg/m^3	2471	2498	2457	2465
Coordination number	C_n		8.6	8.7	9.1	9.2
Grain shear modulus	μ_r	Pa	2.92×10^{10}	2.92×10^{10}	2.92×10^{10}	2.92×10^{10}
Hydrostatic confining pressure	P	Pa	$P=(2/3)(1-\beta)\rho_r g d, g=9.8\ \mathrm{m/s^2}, d=0.03\ \mathrm{m}$			

saturated samples. The frame bulk moduli of vacuum-, air-, and water-saturated sands have a significant dependence on the grain size, although there is a random spread of the experimental values caused by the variety in the grain size distribution and grain shape. In the context of the modified gap stiffness model, the grain size dependence suggests that there must also be a corresponding frequency dependence.

The results may be explained in terms of the modified gap stiffness model. Using Eq. (16), the calculated results of the normalized frequency characteristics of the real and imaginary parts of the gap stiffness for air- and water-saturated sands are shown in Figs. 17 and 18, respectively. The frequency characteristics of the gap stiffness are dependent on the aspect ratio α, bulk modulus K_f, and viscosity η of the pore fluid. The values of the parameters used for the calculations of the frequency characteristics of the gap stiffness are shown in Table VI. Comparing the frequency dependence of the gap stiffness of the air-saturated sample with that of the water-saturated sample, the relaxation frequency as shown in Eq. (25) for water-saturated sample is approximately 320 times that of the air-saturated sample ($K_f/\eta|_{\mathrm{water}} \approx 320 K_f/\eta|_{\mathrm{air}}$), assuming that both aspect ratios are the same. An operating frequency of 500 kHz for water-saturated measurements is considered to be a higher frequency at which the approximated Eq. (22) is applicable. Similarly, at the operating frequency of 11.8 kHz for the air-saturated measurements, Eq. (22) is applicable.

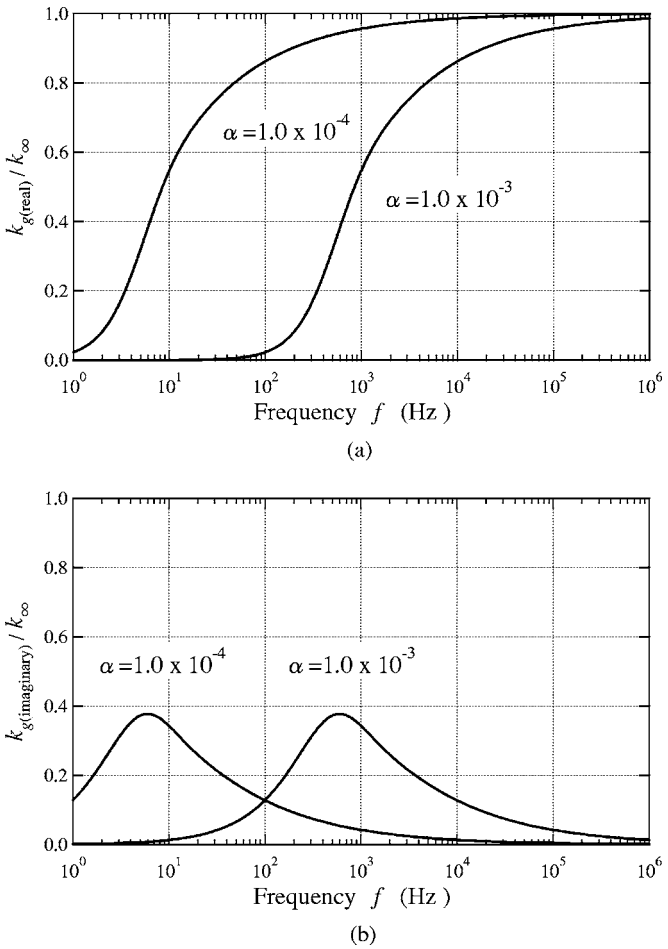

FIG. 17. Frequency characteristics of (a) the real part and (b) the imaginary part of the gap stiffness for air-saturated sand.

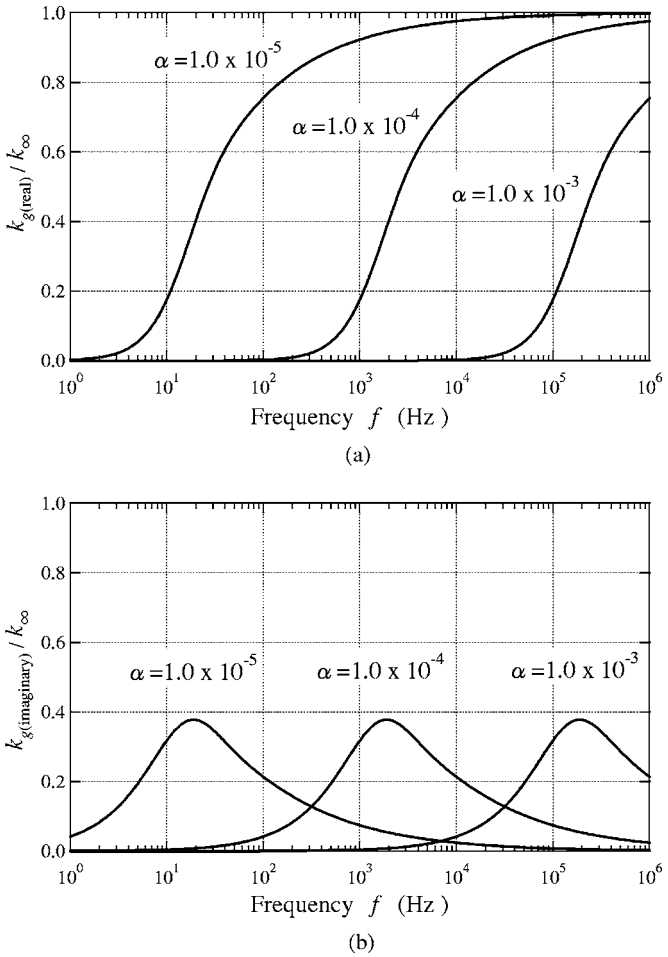

FIG. 18. Frequency characteristics of (a) the real part and (b) the imaginary part of the gap stiffness for water-saturated sand.

TABLE VI. Values of parameters used for the calculation of the frequency characteristics of the gap stiffness.

			Air-saturated	Water-saturated
Fluid bulk modulus	K_f	Pa	1.28×10^5	2.25×10^9
Viscosity	η	Pa s	1.80×10^{-5}	1.00×10^{-3}
Aspect ratio	$\alpha=\frac{h_0}{a}$		1.0×10^{-4}	1.0×10^{-5}
			1.0×10^{-3}	1.0×10^{-4}
				1.0×10^{-3}

The frame bulk modulus K_b is determined by the contact stiffness k_c and gap stiffness k_g by using the following equation:

$$K_b = \frac{C_n(1-\beta)}{12\pi r}(k_c + k_g) = \sqrt[3]{\frac{C_n^2(1-\beta)^2\mu_r^2}{18\pi^2(1-\sigma_r)^2}P} + \frac{C_n(1-\beta)}{12\pi r}k_g = K_{b\mathrm{HM}} + K_{bg}(f), \quad (42)$$

where r denotes the grain radius. Here, $K_{b\mathrm{HM}}$ is the frequency-independent term (Hertz-Mindlin term) and $K_{bg}(f)$ is the frequency-dependent term (gap stiffness term).

With regard to frequency dependence, by using the gap stiffness model, the calculated results of the frame bulk moduli of the air- and water-saturated glass beads of 0.192-mm grain size are shown in Fig. 19. The open circles indicate the derived values of the frame bulk moduli for the air- and water-saturated glass beads of the 0.192-mm grain size obtained from the measurements at the corresponding measurement frequencies. In the calculations, the frequency-independent term (Hertz-Mindlin term) $K_{b\mathrm{HM}}=4.31\times10^7$ Pa for the glass beads of 0.192 mm in Table V was used. The parameter $K_{bg}(f)_{\max}$ was adjusted in a manner such that the values obtained from the model and measurement at the appropriate measurement frequency of 11.8 kHz for the air-saturated sample and 500 kHz for the water-saturated sample would be in agreement. From Fig. 19, it is observed that the frame bulk modulus is predicted to start from a low-frequency asymptote and increase toward a high-frequency asymptote value for both the air- and water-saturated samples. The transition occurs over a frequency range that is approximately centered around the relaxation frequency. Therefore, the frequency characteristics of the frame bulk modulus can be defined using the Hertz-Mindlin term $K_{b\mathrm{HM}}$ and the gap stiffness term $K_{bg}(f)$. The former is completely governed by the physical properties of the grains, while the latter is governed by the grain-fluid interactions. The undetermined parameters of the latter, $K_{bg}(f)_{\max}$, and α may be inverted from velocity measurements at two frequencies, one near the relaxation frequency and another at a much higher frequency. The $K_{bg}(f)_{\max}$ could be determined by measuring the longitudinal wave velocities at much higher frequencies in the air- and water-saturated samples in this study. It is necessary to measure the longitudinal wave velocities in the region of the relaxation frequencies in air- and water-saturated samples to determine each aspect ratio.

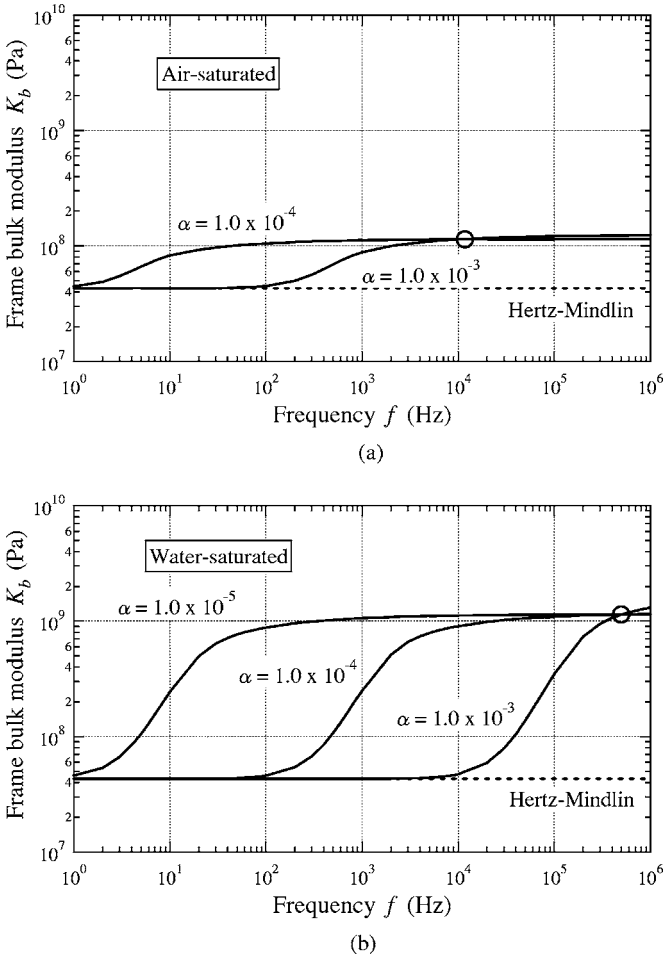

FIG. 19. The real part of the frame bulk modulus vs frequency for (a) air-saturated and (b) water-saturated glass beads (0.192 mm). The open circles indicate the derived values of the frame bulk modulus for glass beads of 0.192 mm-grain size.

V. CONCLUSIONS

The influence of the pore fluid and grain size on the frame bulk modulus of unconsolidated granular marine media at a lower stress was investigated. The density and longitudinal and shear wave velocities in vacuum-, air-, and water-saturated glass beads of four different grain sizes and those of 85 kinds of beach sands were measured. In each case, the values of the frame bulk modulus were inverted from the measured velocity values by using appropriate acoustic wave propagation equations. The results show that the values of the frame bulk moduli of water-saturated glass beads and beach sands are approximately 10^9 Pa at a frequency of 500 kHz and are about ten times greater than those of the corresponding air-saturated samples at 11.8 kHz. An operating frequency of 500 kHz for water-saturated measurements and 11.8 kHz for the air-saturated measurements is considered to be a higher frequency at which the approximated Eq. (22) is applicable. It is shown that these phenomena can be explained by using the modified gap stiffness model; this model also predicts that the frame bulk modulus

must have a dependence on the frequency and grain size. As the frequency increases, the frame bulk modulus is predicted to increase from a low-frequency asymptote toward a high-frequency asymptotic value. This transition occurs over a frequency range that is approximately centered around the relaxation frequency. It is predicted that the frequency characteristics of the frame bulk modulus can be completely defined by two independent terms: the Hertz-Mindlin and gap stiffness terms. The former may be calculated from the physical properties of the grains, and the undetermined parameters of the latter may be inverted from two velocity measurements: one in the region of the relaxation frequency and another at a much higher frequency. We plan to measure the longitudinal wave velocity in the region of the relaxation frequency in air- and water-saturated samples to determine each aspect ratio.

The velocity dispersion in marine sediment is the one of the important subjects that has been unresolved in the community of sediment acoustics. This study showed that the values of the frame bulk modulus of water-saturated glass beads and beach sands at higher frequency are approximately ten times greater than those used in the community of sediment acoustics. Moreover, our results show that the frame bulk modulus has frequency dependence. It is necessary to investigate the dispersion characteristics theoretically and experimentally by using our results about the frame bulk modulus.

ACKNOWLEDGMENTS

The author wishes to express his appreciation to Dr. Nicholas P. Chotiros for his valuable suggestions, extensive assistance for the premeasurements in vacuum-saturated glass beads in the Applied Research Laboratories, the University of Texas at Austin, and revising the manuscript. The author is grateful to Mr. Masahiro Noguchi, a 2003 graduate student of Graduate School of Marine Science and Technology, Tokai University for his assistance with the longitudinal wave velocity measurements in water-saturated sands.

[1]M. A. Biot, "Theory of elastic waves in a fluid-saturated porous solid. I. Low frequency range," J. Acoust. Soc. Am. **28**, 168–178 (1956).
[2]M. A. Biot, "Theory of elastic waves in a fluid-saturated porous solid. II. Higher frequency range," J. Acoust. Soc. Am. **28**, 179–191 (1956).
[3]M. A. Biot, "Mechanics of deformation and acoustic propagation in porous dissipative media," J. Appl. Phys. **33**, 1482–1498 (1962).
[4]M. A. Biot, "Generalized theory of acoustic propagation in porous dissipative media," J. Acoust. Soc. Am. **34**, 1254–1264 (1962).
[5]R. D. Stoll, "Wave attenuation in saturated sediments," J. Acoust. Soc. Am. **47**, 1440–1447 (1970).
[6]N. P. Chotiros, "Biot model of sound propagation in water-saturated sand," J. Acoust. Soc. Am. **97**, 199–214 (1995).
[7]R. D. Stoll, "Velocity dispersion in water-saturated granular sediment," J. Acoust. Soc. Am. **111**, 785–793 (2002).
[8]K. L. Williams, D. R. Jackson, E. I. Thorsos, D. Tang, and S. G. Schock, "Comparison of sound speed and attenuation measured in a sandy sediment to predictions based on the Biot theory of porous media," IEEE J. Ocean. Eng. **27**, 413–428 (2002).
[9]C. J. Hickey and J. M. Sabatier, "Choosing Biot parameters for modeling water-saturated sand," J. Acoust. Soc. Am. **102**, 1480–1484 (1997).
[10]M. Kimura, "Velocity dispersion in granular marine sediment," 144th ASA meeting J. Acoust. Soc. Am. **111**, 2230 (2002).
[11]G. Mavko, T. Mukerji, and J. Dvorkin, *The Rock Physics Handbook: Tools for Seismic Analysis in Porous Media* (Cambridge University Press, Cambridge, 1998).
[12]R. D. Stoll, "Comments on 'Biot model of sound propagation in water-saturated sand,' [J. Acoust. Soc. Am. **97**, 199–214 (1995)]," J. Acoust. Soc. Am. **103**, 2723–2725 (1998).
[13]R. D. Stoll, *Sediment Acoustics* (Springer, Berlin, 1989).
[14]N. P. Chotiros, "Response to: "Comments on 'Biot model of sound propagation in water-saturated sand'" [J. Acoust. Soc. Am. **103**, 2723–2725 (1998)]," J. Acoust. Soc. Am. **103**, 2726–2729 (1998).
[15]N. P. Chotiros and M. Isakson, "A broadband model of sandy ocean sediments: Biot-Stoll with contact quirt flow and shear drag," J. Acoust. Soc. Am. **116**, 2011–2022 (2004).
[16]W. F. Murphy III, K. W. Winkler, and R. L. Kleinberg, "Acoustic relaxation in sedimentary rocks: Dependence on grain contacts and fluid saturation," Geophysics **51**, 757–766 (1986).
[17]G. A. Gist, "Fluid effects on velocity and attenuation in sandstones," J. Acoust. Soc. Am. **96**, 1158–1173 (1994).
[18]M. Prasad and R. Meissner, "Attenuation mechanisms in sands: Laboratory versus theoretical (Biot) data," Geophysics **57**, 710–719 (1992).
[19]J. M. Hovem and G. D. Ingram, "Viscous attenuation of sound in saturated sand," J. Acoust. Soc. Am. **66**, 1807–1812 (1979).

Increases in deep ocean ambient noise in the Northeast Pacific west of San Nicolas Island, California

Mark A. McDonald[a)]
WhaleAcoustics, 11430 Rist Canyon Road, Bellvue, Colorado 80512

John A. Hildebrand and Sean M. Wiggins
Marine Physical Laboratory, Scripps Institution of Oceanography, University of California San Diego, La Jolla, California 92093-0205

(Received 10 October 2005; revised 12 May 2006; accepted 30 May 2006)

Recent measurement at a previously studied location illustrates the magnitude of increases in ocean ambient noise in the Northeast Pacific over the past four decades. Continuous measurements west of San Nicolas Island, California, over 138 days, spanning 2003–2004 are compared to measurements made during the 1960s at the same site. Ambient noise levels at 30–50 Hz were 10–12 dB higher (95% CI=2.6 dB) in 2003–2004 than in 1964–1966, suggesting an average noise increase rate of 2.5–3 dB per decade. Above 50 Hz the noise level differences between recording periods gradually diminished to only 1–3 dB at 100–300 Hz. Above 300 Hz the 1964–1966 ambient noise levels were higher than in 2003–2004, owing to a diel component which was absent in the more recent data. Low frequency (10–50 Hz) ocean ambient noise levels are closely related to shipping vessel traffic. The number of commercial vessels plying the world's oceans approximately doubled between 1965 and 2003 and the gross tonnage quadrupled, with a corresponding increase in horsepower. Increases in commercial shipping are believed to account for the observed low-frequency ambient noise increase. © *2006 Acoustical Society of America.*
[DOI: 10.1121/1.2216565]

PACS number(s): 43.30.Nb, 43.50.Lj, 43.60.Cg [DRD] Pages: 711–718

I. INTRODUCTION

Deep ocean ambient noise has been predicted to be increasing over the past few decades due to anthropogenic sources (National Research Council, 2003). Increases in the number, size, speed, and horsepower of commercial ships led Ross (1976, 1993, and 1974) to predict that ocean ambient noise levels at low frequencies (10–150 Hz) had increased 15 dB between 1950 and 1975. At frequencies above about 150 Hz, ocean ambient noise levels are dominated by wind driven surface waves (National Research Council, 2003). At frequencies below 5 Hz, the dominant noise source is microseisms (Webb, 1998).

In the 1960s, the US Navy conducted ambient noise measurements using cabled hydrophones at a series of deep ocean sites off the west coast of North America (Wenz, 1969). These sites were situated at water depths of about 1000 m and were coupled to the deep sound channel. Measurements of ocean ambient noise in the deep sound channel are a summation of sound sources across the ocean basin plus local noise. Andrew *et al.* (2002) re-examined one of those sites off Point Sur, on the coast of central California, providing an ocean ambient noise level comparison spanning nearly four decades. They found about a 10 dB increase in ambient noise level in the 20–80 Hz range which they attribute primarily to increases in commercial shipping. This study reports on changes in ambient noise from measurements made west of San Nicolas Island, off the coast of southern California, a site previously characterized by Wenz (1968a).

II. MEASUREMENTS, 1960s AND NOW

A. Cabled hydrophone recordings, 1964–1966

A cabled seafloor hydrophone array is located on the continental slope approximately 80 km southwest of San Nicolas Island, California (Fig. 1). This hydrophone array was part of the US Navy's sound surveillance system, and is referred to as San Nicolas South. An ocean ambient noise study was conducted using this array from January 1964 through June 1966 by making magnetic tape recordings from a single hydrophone channel. A detailed analysis of these ambient noise data was reported by Wenz (1968a) in which analog filters were used to analyze 200 s segments of data three times each hour over the entire 30 months of data. Analyses included distributions, means, standard deviations, and variability by time of day, by month, and by year. Wenz (1969) also discusses transient events and compares this site with four other sites labeled Point Sur, Coos Bay, Pacific Beach North, and Pacific Beach South. Wind speed, shipping departure time data, and biological sources were considered in an attempt to explain the significant diel (day/night) and other temporal variations in these data.

Transient signals, including ships passing nearby, greater than 3 dB above ambient noise were examined by Wenz (1968a) for the San Nicolas South data. About 10% of the data contained transients more than 3 dB above the back-

[a)]Electronic mail: mark@whaleacoustics.com

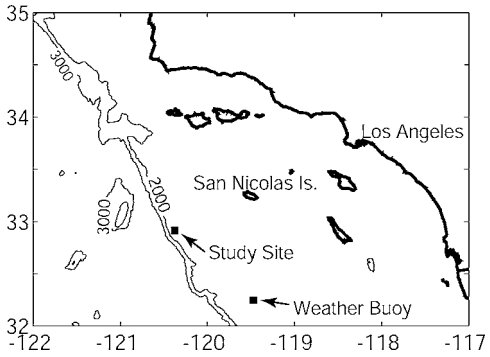

FIG. 1. Location of the ambient noise study site off southern California, west of San Nicolas Island. Bathymetric contours (2000 and 3000 m) delineate the continental shelf. A nearby weather buoy gives detailed information on wind and wave conditions.

ground average and were removed from the analysis, yet the overall average was changed by less than 1 dB by doing so.

B. Autonomous hydrophone recordings, 2003–2004

A seafloor autonomous acoustic recording package (ARP), similar to that described by Wiggins (2003), was used to collect ambient noise data during 2003–2004 at the same site as Wenz's 1964–1966 cabled hydrophone measurements. The recorder was deployed at location 32° 54.932′ N, 120° 22.580′ W, at a depth of 1090 m, with the hydrophone suspended 10 m above the seafloor. The San Nicolas South location used for Wenz's study is reported as 32° 54.913′ N, 120° 22.548′ W at a depth of 1106 m (Curtis *et al.*, 1999). To within the potential inaccuracies in both measurements, the ARP was at the same location as studied by Wenz (1968a). The hydrophone used by Wenz is thought to have been on or very near the seafloor, but not buried within the seafloor sediments.

Continuous recordings were made at a sampling rate of 1000 Hz from November 3, 2003 to March 19, 2004. Initial quality control and inspection of the data was conducted by producing spectrograms as 5 min average spectra in 1 Hz bins. Review of the data in this form revealed no evidence of instrumental problems throughout the recording period. In high current areas ($>$2 kts) mechanical noise is induced by flow and strum on the hydrophone, but at this site, as is typical of most deep water sites, there is no evidence of flow noise. As with all near seafloor acoustic recorders, there are occasional "fish bumps" or brief impulsive sounds of unknown, possibly biological origin (Buskirk, 1981). Other common transient sounds can be readily classified as blue whales, fin whales, humpback whales, ships, and low frequency active sonar. There is no distinct evidence of fish sounds.

Transients due to nearby ships were not removed in the 2003–2004 data analysis as these are uncommon events. Also, based on Wenz's evaluation of transient impact (1968a), we do not believe shipping transient removal would significantly change the average ambient noise levels at this site, especially since this site is in relatively deep water and outside major shipping lanes.

C. Calibration

ARP calibration was conducted using a reference hydrophone at the U. S. Navy's Transducer Evaluation Center facility in San Diego (TRANSDEC), to verify the theoretical calibration which was based on nominal component specifications. Calibration was conducted from 10 to 250 Hz. These calibrations were extrapolated (from 230 to 470 Hz) to account for the sampling limit of the recorder used in this study. Differences between the actual instrument used for measurements at the San Nicolas South site and the one tested at TRANSDEC are expected to be less than 1 dB, due to slight differences in hydrophone sensitivity and circuitry. The ARP hydrophone consisted of six Benthos AQ-1 elements electrically joined and effectively colocated to make one effective hydrophone. Corrections for hydrophone pressure and temperature at the seafloor site were not included. Manufacturer's specifications for these corrections and with independent testing (Lastinger, 1982) suggest these corrections are less than 0.5 dB for the data presented in this study.

The calibration testing showed the theoretical response of the instrument to be within 1 dB of the measured response. The seafloor recorder is not expected to have a meaningful response below 2 Hz. The high frequency rolloff of the recorder used at San Nicolas South begins at 470 Hz, and provides 30 dB/octave of protection from aliasing. The noise floor of the instrument is approximately 53 dB re 1 μPa^2/Hz.

D. Spectral averaging

To be consistent with the analysis of Wenz (1968a), 200 s of data were used for each spectral average. Wenz used only three averages per hour, presumably because of data processing limitations, while this study used continuous data with no overlap between spectral averages, processed with a Hanning window. All of the spectra were calculated in 1 Hz bins, however, when a direct comparison to Wenz's data was desired, 1/3 octave band levels were computed from the 1 Hz bin data. The 1 Hz bin data provide more detailed information to help identify sound sources and presumably would have been used by Wenz, if the computational technology had been readily available at the time.

III. RESULTS

Average pressure spectrum levels for the 4.5 months recorded in 2003–2004, were elevated at low frequencies, when compared to averages for the 30 month period recorded in 1964–1966 (Fig. 2). Ambient pressure spectrum levels at low frequencies (30–50 Hz) were 10–12 dB higher in 2003–2004. Level comparisons in the 10–30 Hz band are complicated by whale calling. Above 50 Hz the differences between recording epochs decrease, and were only 1–3 dB at 80–200 Hz. Above 200 Hz the 1964–1966 average ambient spectrum levels were higher than those in 2003–2004, owing partially to a diel component in the 1964–1966 data (discussed later), which was absent in the recent data.

One approach to estimating uncertainty in the average spectrum levels for 2003–2004 is by combining an estimated 95% confidence interval for the calibration errors of 1 dB

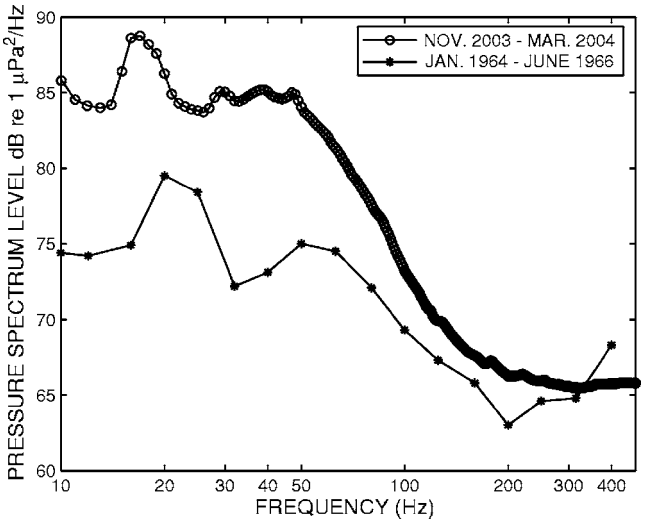

FIG. 2. Mean pressure spectrum levels (1 Hz bins) at the San Nicolas South site for November 2003 to March 2004, compared to January 1964 to June 1966. Band level averages were reported by Wenz (1968a, 1968b) as corrected to units of pressure spectrum level.

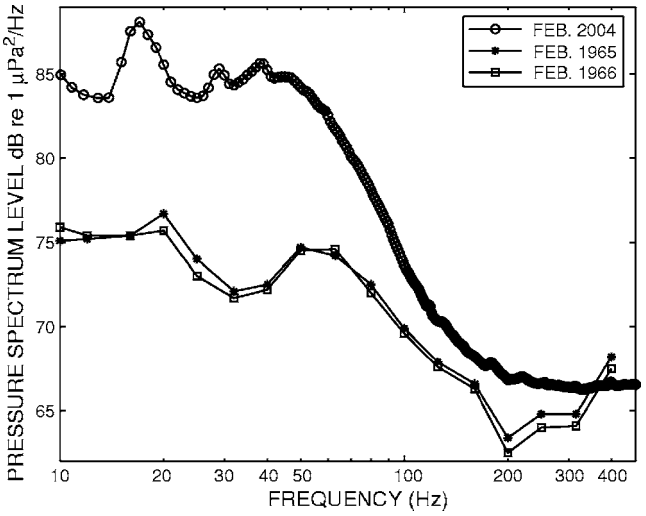

FIG. 3. Sound pressure spectrum levels (1 Hz bins) for the month of February 2004 compared to February 1965 and 1966. During February blue whales are absent from this site and the peak near 17 Hz in 2004 is from fin whale calls.

with the year to year variability of each months average level for the 30 months of data collected by Wenz. At 40 Hz, the standard deviation of the year to year comparison for each monthly average level in the Wenz data is 1.2 dB. Combining these two independent uncertainties as $\sqrt{(1.96*1.2)^2+1^2}=2.6$ dB as a 95% confidence interval on a one month average spectrum level. This approach is considered to provide a high estimate of actual uncertainty because it assumes a one month duration sample is required to provide an independent estimate of ambient noise. If only one week were required to produce an independent estimate of ambient noise, then the 1.2 dB would be divided by $\sqrt{4}$, four being the number of independent measurements in one month. Changes in weather may be the longest duration factor in determining what defines an independent measurement.

Seasonal differences in ocean ambient levels occur due to seasonal changes in wind driven waves, biological sound production, and shipping route changes. The strongest seasonal signal at the San Nicolas South site is due to blue whale singing (Burtenshaw *et al.*, 2004), which appears primarily as a broad peak near 20 Hz in the spectral data. Blue whales are known to be present at this site only from June through January, while fin whales are present year-round (Oleson, 2005). February through May there are no blue whales calls present, although fin whales calls are still evident (Fig. 3) in the 2003–2004 data. Fin whale calls produce a 3 dB peak of spectral energy near 16–18 Hz in the February 2004 data, but their calls are not obviously present in the February 1965 and 1966 data. Excluding the band of fin whale calling, the average February 2004 ambient pressure spectrum level is 10–14 dB higher than the February 1965 and 1966 levels over the 10–50 Hz band (Fig. 3). Above 100 Hz, there is only a 1–2 dB difference between the two sets of February noise data.

A comparison of recordings between November 2003 and November 1964 and 1965 reveals a strong blue whale presence (Fig. 4). Wenz (1969) reports as much as 18 dB of signal-to-noise for these whale calls in the spectral averages at the San Nicolas South site during 1964–1966. The blue whale call levels in peak season cannot be compared because 2003 data are not available during that time period, which occurs earlier in the fall (Burtenshaw *et al.*, 2004). Year to year variability is discussed in Burtenshaw *et al.* (2004), and it is obvious that blue whale call spectrum levels have increased substantially since 1964.

A long-term shift in the frequency of the blue whale calling is seen in the plot comparing November 2003 and 1964–1965 (Fig. 4). In 2003 the spectral energy peak due to blue whale calling is near 16 Hz, whereas in 1964–1965 the energy peak is near 22.5 Hz, corresponding to the dominant blue whale call frequency at that time (Thompson, 1965).

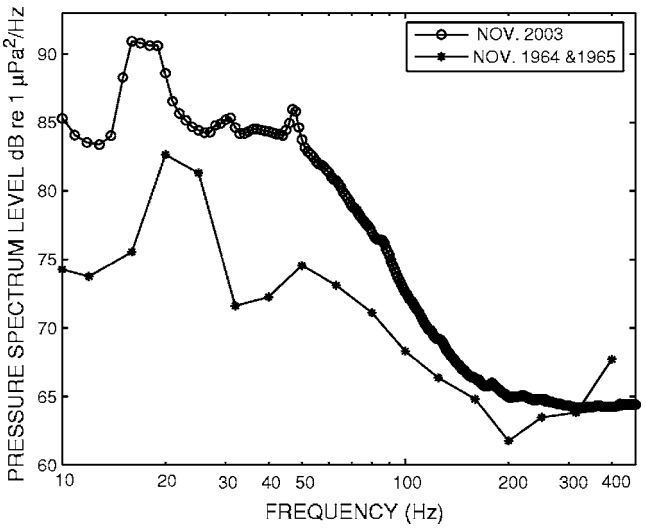

FIG. 4. Pressure spectrum level for November 2003 compared to November 1964–1965 in which blue whale calls are prominent near 16 Hz in 2003 and near 22.5 Hz in 1964–1965, illustrating a more than 30% the shift in call frequency over four decades.

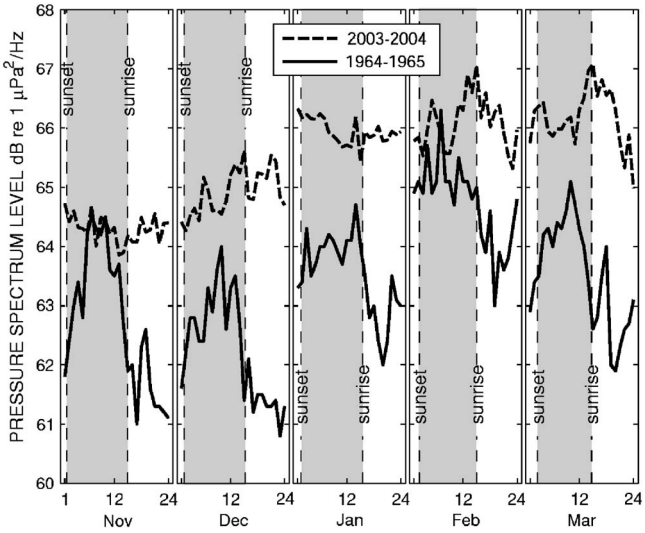

FIG. 5. Monthly averaged pressure spectrum levels at 315 Hz, plotted vs time of day (in GMT). The average band levels from 1964–1965 (solid line) are compared to 2003–2004 (dashed line) with band levels scaled as equivalent pressure spectrum levels. The hours from sunset to sunrise are shaded. Nightly chorusing, presumably from fish, is observed in 1964–1965 and is absent in 2003–2004.

Additional peaks at 32 and 48 Hz in the 2003 spectra are harmonics of the blue whale song fundamental and the 88 Hz peak is from an overtone within the blue whale song. Fin whale calls are not apparent in the average spectra when blue whale calling is as strong as occurs here in November even though from examination of the 2003–2004 data it is known that fin whale calls are present.

The 200–500 Hz frequency band displays a 2–4 dB diel variation in ambient noise for data from 1964–1966, which is absent in the 2003–2004 data (Fig. 5). In 1964–1966, higher sound pressure levels occur at night, typically with peak energy around midnight. There is no apparent seasonal change in the amount of diel variation in 1964–1966. No diel signal is observed in the 2003–2004 data. The ambient pressure spectrum level data above 200 Hz also have a seasonal increase of about 3 dB in overall level from November to January–February, both for the 1964–1966 and the 2003–2004 data sets (Fig. 5). These trends are likely related to changes in the average wind speeds with season.

Pressure spectrum levels for the San Nicolas South site in December 2003 are compared (Fig. 6) as cumulative distribution functions to the December 1965 data (Wenz, 1968a). These data for 2003 show a mean pressure spectrum level at 10–50 Hz of about 85 dB re 1 μPa^2/Hz, decreasing to about 65 dB re 1 μPa^2/Hz between 50–200 Hz, and remaining constant for 200–500 Hz. The spectrum level cumulative distributions are typically long tailed for higher values (Fig. 6). The ambient spectrum level 99th percentile is about 15 dB above the mean, whereas the first percentile is about 5 dB below the mean. Wenz (1968a)plotted cumulative distributions only for selected months and selected frequencies for the 1964–1966 ambient noise data, thus the distributions over the entire recording periods cannot be compared.

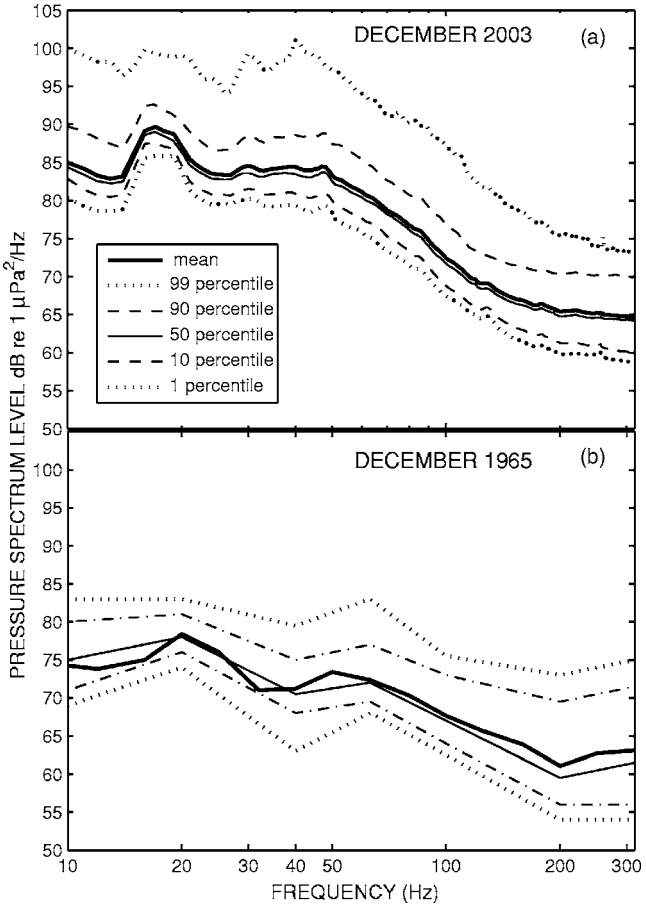

FIG. 6. (a) December 2003 cumulative distribution function for pressure spectrum levels at the San Nicolas South site. (b) December 1965 at the San Nicolas South site, after Wenz (1968a). Note the 50th percentile line does not closely track the mean because the mean was computed at 1/3 as many frequencies as the 50th percentile, each over a wider bandwidth.

IV. ANALYSIS

A. Shipping, 10–150 Hz

The 10–12 dB increase in ocean ambient pressure spectrum level in the 30–50 Hz band at this site may be representative of the entire Northeast Pacific, and is likely related to changes in commercial shipping. Vessel operation statistics indicate a steady growth in shipping traffic over the past few decades (Mazzuca, 2001). In addition to increases in the number of commercial vessels, the average gross tonnage and horsepower per vessel has increased. Lloyd's Register (1965, 2003) indicates that the world's commercial fleet approximately doubled during the past 38 years, from 41 865 vessels in 1965 to 89 899 vessels in 2003. Moreover, during the same period the gross tonnage (GT) of commercial vessels nearly quadrupled from 160 million GT in 1965 to 605 million GT in 2003 with a similar increase in propulsion power (Ross, 1993). Also, port turn-around time is faster today resulting in more days per year spent at sea by each ship.

A doubling of the number of ships alone would explain only 3 dB of the observed noise increase, since the noise from individual ships will combine incoherently [follow a 10*log(N) increase]. Higher sound levels from at least some of the vessels are needed to explain the additional 7–9 dB

increase in the 30–50 Hz band. Commercial vessel gross tonnage has been suggested as a proxy for shipping produced noise (National Research Council, 2003), but gross tonnage predicts noise increases from 1965 to 2003 of only 6 dB. Factors that can contribute to higher ship noise levels include greater average ship speeds, propulsion power, and propeller tip speeds (Ross, 1976).

B. Whales, 15–20 Hz

The long-term noise data presented here, together with other raw recordings of blue whales (Thompson, 1965; McDonald *et al.*, in press), show that the peak energy for blue whale call frequencies have shifted downward from about 22.5 Hz in 1964–1966 to near 16 Hz in 2003 (Fig. 4). In Wenz's data the blue whale dominant frequency occurs near the boundary between the third octave bins, thus both the 20 and 25 Hz bins show the signal. The monthly or yearly averaged noise data presented here sum large numbers of whale calls (~10 000–100 000), so that the observed frequency shift is an aggregate of calling for a large segment of these whale populations. It is tempting to see the blue whale call frequency shift as a response to increased shipping noise, for instance, as a means to decrease signal loss during propagation. However, there is little change in signal attenuation between 22 and 16 Hz, even for long-range (>10 km) propagation On the contrary, a lowered fundamental call frequency would result in lowered blue whale call source levels (Aroyan *et al.*, 2000), assuming a fixed air volume during call production. Decreased call source level is counter to the expectation that call source levels would increase to compensate for increased noise (the Lombard effect). Likewise, by shifting the fundamental call frequency from above 22 to 16 Hz, the change in background noise due to shipping is negligible so it seems unlikely that increased shipping noise is the dominant cause for blue whale call frequency shifts.

The blue whale population off California, however, has been increasing (Calambokidis and Barlow, 2004). An increased population density could lead to higher whale call peak energy levels in the long-term spectral averages. Increasing call source levels in the presence of increased noise (the Lombard effect) may be another factor explaining the higher (~10 dB) whale call peak energy in 2003 compared to 1964–1966 (Fig. 4). Note that these arguments apply to fin whales as well as blue whales, since blue whales are absent from the San Nicolas South site in the spring, and the energy peak observed near 17 Hz during 2004 (Fig. 3) is due to fin whale calls, although there is no obvious fin whale peak in the Wenz data.

C. Marine life, 40–500 Hz

Many biological sounds have diel variation, but the species responsible for each diel pattern is not always known. The character and seasonality of the sounds indicate whether the source is most likely made by crustacean, fish or whale (Fish, 1964; Edds-Walton, 1997). A 10–20 dB diel pattern, with higher intensities during the night at frequencies of 80–300 Hz, was reported west of San Clemente Island in 1963 (Wenz, 1942; 1964; Wenz *et al.*, 1965) in a water depth of 110 m (60 fathoms) in May through August. The diel pattern diminished during the fall and was absent in November and December. Observations at the same site in 1958–1959 reported biological sounds, but lacked a diel pattern. This change was attributed to changes in the abundance of sound producing fish. Fish chorusing is known to produce as much as 40 dB of seasonal change in background ambient noise at 325 Hz (Fish, 1964).

The 3 dB nightly chorus reported for the 1964–1966 San Nicolas South data is different from that reported for a similar setting along the continental shelf located farther north (Pacific Beach, Washington) in 1964–1966 (Wenz, 1968b). The Pacific Beach site has diel variation in the 40–100 Hz band with a peak level around 0800 local time (after sunrise) and a low around 2200 local time (just before midnight). The range of seasonal and geographic variations for diel patterns exhibited at the five stations off the west coast of the United States (Wenz, 1969) are not yet fully understood, but are likely related to the presence and relative abundance of different species of sound producing fishes and crustaceans.

Humpback whale calls and song are present at frequencies greater than 200 Hz in the 2003–2004 San Nicolas South recordings, but do not contribute significantly to the ambient pressure spectrum level when averaged over monthly or seasonal time periods as these calls are too sparse to have significant impact on such a long term average. Therefore, although humpback whales are known to produce diel chorusing (Au *et al.*, 2000), they are not a probable cause of diel variations in the 1964–1966 San Nicolas South data.

Snapping shrimp noise occurs predominantly at frequencies above 1 kHz (Albers, 1965; Au and Banks, 1998), above the frequencies analyzed in this study, but may have an impact on noise levels at the San Nicolas South site when wind speeds are low. Shrimp noise increases by as much as 9 dB during the night, showing a minimum at noon and peaks just before sunrise and just after sunset (Everest *et al.*, 1948). Snapping shrimp are believed to occupy waters depths less than 55 m (Everest *et al.*, 1948), thus their noise contribution to the San Nicolas South site would be the result of sound propagation from tens of kilometers distance, from sites farther up the continental shelf. Snapping shrimp presence in 1964–1965, therefore, seems unlikely to explain the 2–4 dB of diel variation observed.

Fish choruses have been recorded in deep water hundreds of kilometers from shallow water with diel variability of 10 dB at 480 Hz (Kelly *et al.*, 1985) and probable fish sounds have been recorded at 600 m depths where the water depth was 1600 m (Mann and Jarvis, 2004). Most studies of fish sound production have, not surprisingly, focused on shallow water species, but it may be that deep water fish species are responsible for the observed diel variation and increased average ambient levels observed by Wenz in 1964–1965, which were absent in 2003–2004 recordings.

D. Wind driven surface wave noise, 200–500 Hz

Wind driven wave noise is an important contributor to ocean ambient noise in the 200–500 Hz band (Ross, 1976).

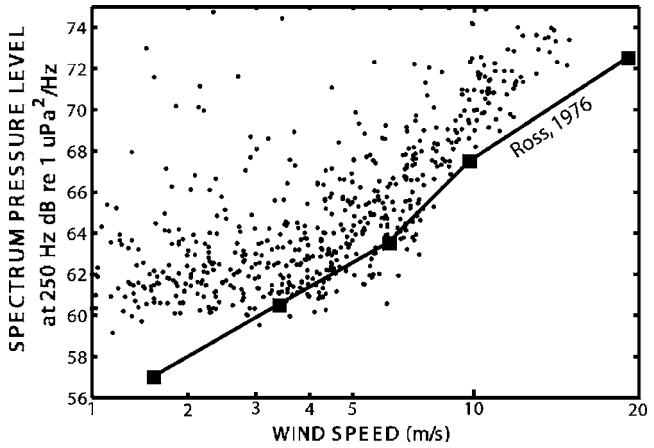

FIG. 7. Sound pressure level at 250 Hz for the San Nicolas South site vs hourly mean wind speed during November, 2003 at Tanner Bank (NDBC buoy 46047). The influence of wind driven wave noise is apparent above 6 m/s (11.7 kts). The Ross (1976) predicted mean ambient spectrum level at 250 Hz for sea surface agitation corresponding to wind speed is shown.

Wenz (1969) compared wind data for five northeast Pacific sites and suggested wind was the primary cause for differences in average ambient noise levels above 200 Hz. Assuming the observed increases in ambient noise are representative, the breakpoint between shipping and wind dominated noise has probably now moved well above 200 Hz. Wind data relevant to the San Nicolas South site are available from a National Data Buoy Center (NDBC) weather buoy on Tanner Bank (Fig. 1), approximately 110 km to the southeast (NDBC buoy 46047, 32.43 N 119.53 W). To test for dependence of ambient noise on wind, sound pressure levels at 250 Hz were plotted as a function of wind speed for the 2003–2004 San Nicolas South data (Fig. 7). The 110 km separation between the wind and the ambient noise recording sites may result in some error, but a correlation between wind speed and ambient noise is apparent above 6 m/s (11.7 kts). The wind related ambient noise levels from Ross (1976) are plotted in Fig. 7. A correlation between satellite derived wind speeds and ambient noise levels was previously reported for the San Nicolas South site (identified as site *f*) by Curtis *et al.* (1999).

In an attempt to understand the contribution of wind to the differences in ambient noise levels between 1964–1966 and 2003–2004, shown in Figs. 2–4, wind data from the two recording periods were compared. The mean wind speed reported from the Historical Wind Speed data base of the National Climatic Data Center from ship observations for the one degree grid block containing the San Nicolas South site was 7.0 m/s (13.7 kts) during November through March of 1963–1966. Wind data for 2003–2004 (from NDBC buoy 46047) show average wind speeds during the recording period of 5.7 m/s (11.0 kts). Wind speed during the recording period was lower than the 1991–2001 average wind speed of 6.4 m/s (12.5 kts) for November through March at NDBC buoy 46047. Although the 1964–1966 wind data come from different measurement methods and different locations, it appears the 2003–2004 recordings were made during a period of relatively low average winds. As an approximate correction Fig. 7 was examined, where a shift in wind speed from 5.7 to 7.0 m/s along a linear regression yields about 2.6 dB of increased ambient noise. This suggests that the observed increase in ambient noise at 250 Hz (1–3 dB) between 1964–1966 and 2003–2004 might have been significantly (~2.6 dB) greater if wind speeds had not been below average during the 2003–2004 recording period. A wind speed distribution analysis would be needed to more accurately predict the correction.

V. DISCUSSION

The noise level experienced at a particular site depends on the presence of noise sources such as whales, ships, and wind driven waves combined with the losses for sound propagation between the source locations and the site location. Owing to propagation complexities, shipping noise does not directly correspond to the distribution of ships. Ship or wave generated noise from the sea surface will contribute to ambient noise levels across the entire ocean basin if it is introduced into the deep sound channel. One pathway for shipping noise to enter the deep sound channel is at locations where the sound channel intersects bathymetric features such as the continental slope (Wagstaff, 1981; Dashen and Munk, 1984; Hodgkiss and Fisher, 1990). By a process commonly referred to as down-slope conversion, noise propagating down the continental slope can readily enter the deep sound channel. Therefore, shipping lanes that traverse the continental slope will be sites for efficient conversion of noise into the deep sound channel.

Another route for noise to enter the deep sound channel occurs at high latitudes, where the sound channel shoals to intersect the sea surface (Bannister, 1986). In this setting noise produced at the sea surface by shipping or waves will enter the deep sound channel and propagate efficiently to distant sites. Great circle vessel routes (the shortest distance) put most of the shipping traffic at high latitudes in the North Pacific, passing near the Aleutian Islands. The high latitude North Pacific is a major shipping route carrying the substantial vessel traffic between ports along the west coast of North America and Asia. Shipping noise that enters the deep sound channel at high latitude will then propagate to lower latitude sites, and become a component of the ambient noise.

The San Nicolas South site is relatively quiet when compared to other North Pacific sites with noise measurements made near the axis of the deep sound channel (Wenz, 1969). The major shipping lanes pass well north of the San Nicolas South site with vessels remaining over relatively shallow water until being far from this site. Downslope conversion of ship noise from these shipping lanes would take place off central California or points farther north. The relative proximity to major shipping lanes may explain why the noise levels at Point Sur were consistently 4–8 dB higher than those at San Nicolas South (Wenz, 1969). Noise measurements at San Nicolas South may be more broadly affected by shipping at high latitudes and by downslope conversion in the Western Pacific.

If it is assumed the San Nicolas South measurements are broadly representative of changes in the Northeast Pacific deep sound channel, ambient noise has been increasing at a

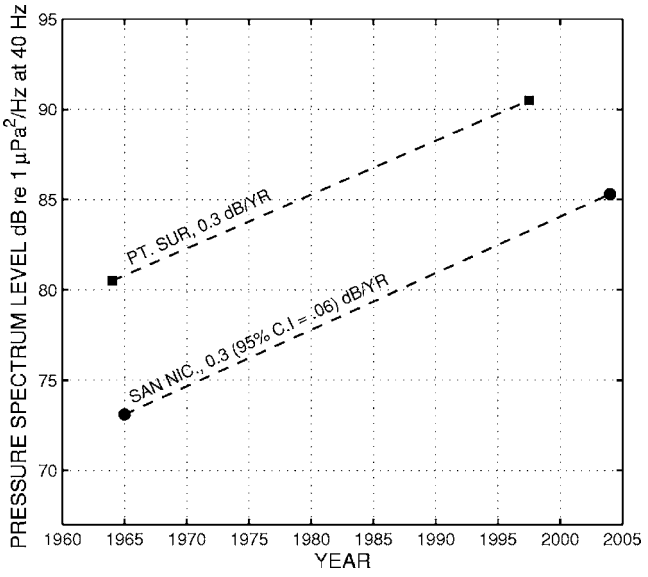

FIG. 8. North Pacific ambient noise measurements at low frequency (40 Hz) show an overall increase of about 3 dB per decade, based on repeat measurements at (●) San Nicolas South (this study) and (■) Point Sur (after Andrew *et al.*, 2002).

rate of 2.5–3 dB per decade over the past four decades in the 30–50 Hz band (Fig. 8). The repeated measurements at Point Sur, California from Andrew *et al.* (2002), and this study at the San Nicolas South site, although different in overall noise levels, have approximately the same trend for increasing ambient noise over the past few decades.

Ross (1976) argues that horsepower to the 4/3 power should be used as a rule of thumb for conversion to noise power. Ross (1976) further suggests that relatively few of the largest, and the fastest, vessels may be producing most of the noise. For instance, oil tankers and bulk dry transport vessels represent nearly 50% of the total gross tonnage, but less than 19% of the total number of vessels in the world's commercial fleet (data from Lloyd's register for 2001). Ross (1976) predicted 0.4 dB/yr noise increases (near 50 Hz) during the years 1950–1975 by adding the decibel increase due to the number of ships to 4/3 of the decibel increase in average horsepower per ship. Using these rules and further analyzing shipping data, it may be possible to match the observed increase in noise levels of about 12 dB near 40 Hz from 1964 to 2004.

Concerns have developed regarding the impacts of ocean ambient noise levels on marine mammals and other marine life (National Research Council, 2003, 2005). Characterization of the long-term changes in ocean ambient noise will require repeated measurements at multiple sites as present ship noise models may have large errors (Heitmeyer *et al.*, 2004), and will need to incorporate empirical measurements for validation (Etter, 2003). These measurements of ambient noise at a site west of San Nicolas Island, California, combined with studies by Andrew *et al.* (2002) and Ross (1976) suggest that low frequency ambient noise within the North Pacific deep sound channel has increased by at least 15 dB since 1950.

ACKNOWLEDGMENTS

The authors thank Rex Andrew, Orest Diachok, and Donald Ross for advice and comments on this manuscript. This work was supported by the US Navy CNO N45 and ONR, and the authors thank Frank Stone, Ernie Young, Jeff Simmons, Ellen Livingston, and Bob Gisiner.

Albers, V. M. (**1965**). *Underwater Acoustics Handbook II* (Pennsylvania State University Press, University Park, PA), p. 356.

Andrew, R. K., Howe, B. M., Mercer, J. A., and Dzieciuch, M. A. (**2002**). "Ocean ambient sound: Comparing the 1960's with the 1990s for a receiver off the California coast," ARLO **3**, 65–70.

Aroyan, J. L., McDonald, M. A., Webb, S. C., Hildebrand, J. A., Clark, D., Reidenberg, J. S., and Laitman, J. T. (**2000**). "Acoustic models of sound production and propagation," in *Hearing by Whales and Dolphins* Springer Handbook of Auditory Research 12 (Springer, New York) pp. 409–469.

Au, W. W. L., and Banks, K. (**1998**). "The acoustics of the snapping shrimp Synalpheus parneomeris in Kaneohe Bay," J. Acoust. Soc. Am. **103**, 41–47.

Au, W. W. L., Mobley, J., Burgess, W. C., Lammers, M. O., and Nachtigall, P. E. (**2000**). "Seasonal and diurnal trends of chorusing humpback whales wintering in waters off western Maui," Marine Mammal Sci. **16**, 530–544.

Bannister, R. W. (**1986**). "Deep sound channel noise from high latitude winds," J. Acoust. Soc. Am. **79**, 41–48.

Burtenshaw, J. C., Oleson, E. M., Hildebrand, J. A., McDonald, M. A., Andrew, R. K., Howe, B. M., and Mercer, J. A. (**2004**). "Acoustic and satellite remote sensing of blue whale seasonality and habitat in the Northeast Pacific," Deep-Sea Res., Part II **51**, 967–986.

Buskirk, R. E., Frohlich, C., Latham, C. V., Chen, A. T., and Lawton, J. (**1981**). "Evidence that biological activity affects ocean bottom seismograph recordings," Mar. Geophys. Res. **5**, 189–205.

Calambokidis, J., and Barlow, J. (**2004**). "Abundance of blue and humpback whales in the eastern north Pacific estimated by capture-recapture and line-transect methods," Marine Mammal Sci. **20**, 63–85.

Curtis, K. R., Howe, B. M., and Mercer, J. A. (**1999**). "Low-frequency ambient sound in the North Pacific: Long time series observations," J. Acoust. Soc. Am. **106**, 3189–3200.

Dashen, R., and Munk, W. (**1984**). "Three models of global ocean noise," J. Acoust. Soc. Am. **76**, 540–554.

Edds-Walton, P. L. (**1997**). "Acoustic communication signals of mysticete whales," Bioacoustics 8, 47–60.

Etter, P. C. (**2003**). *Underwater Acoustic Modeling and Simulation*, 3rd ed. (Spon, New York), p. 424.

Everest, F. A., Young, R. W., and Johnson, M. W. (**1948**). "Acoustical characteristics of noise produced by snapping shrimp," J. Acoust. Soc. Am. **20**, 137–142.

Fish, M. P. (**1964**). "Biological sources of sustained ambient sea noise," in *Marine Bio-Acoustics*, edited by W. N. Tavolga (Pergamon, New York), pp. 175–194.

Heitmeyer, R. M., Wales, S. C., and Pflug, L. A. (**2004**). "Shipping noise predictions: Capabilities and limitations," Mar. Technol. Soc. J. **37**, 54–65.

Hodgkiss, W. S., and Fisher, F. H. (**1990**). "Vertical directionality of ambient noise at 32°N as a function of longitude and wind speed," IEEE J. Ocean. Eng. **15**, 335–339.

Kelly, L. J., Kewley, D. J., and Burgess, A. S. (**1985**). "A biological chorus in deep water northwest of Australia," J. Acoust. Soc. Am. **77**, 508–511.

Lastinger, J. J. (**1982**). "Measurements on NORDA/DTAG AQ-1 hydrophones," USRD TM 6891, Underwater Sound Reference Detachment, Orlando, FL.

Mann, D. A., and Jarvis, S. M. (**2004**). "Potential sound production by a deep-sea fish," J. Acoust. Soc. Am. **115**, 2331–2333.

Mazzuca, L. L. (**2001**). "Potential effects of low frequency sound (LFS) from commercial vehicles on large whales," M.S. thesis, University of Washington, p. 70.

McDonald, M. A., Mesnick, S. L., and Hildebrand, J. A. (in press) "Biogeographic characterization of blue whale song worldwide: Using song to identify populations,"J. Cetacean Res. Manage..

National Research Council (**2003**). *Ocean Noise and Marine Mammals* (National Academies Press, Washington, DC), p. 204.

National Research Council (**2005**). *Marine Mammal Populations and Ocean*

Noise: Determining When Noise Causes Biologically Significant Effects (National Academy Press, Washington, DC), p. 142.
Oleson, E. M. (**2005**). "Calling behavior of blue and fin whales off California," Ph.D. dissertation, University of California, San Diego, p. 153.
Ross, D. (**1974**). "Ship sources of ambient noise," Proceedings of the International Workshop on Low Frequency Propagation and Noise, October; Reprinted in (**2005**). IEEE J. Ocean. Eng. **30**, 257–261.
Ross, D. (**1976**). *Mechanics of Underwater Noise* (Pergamon, New York), p. 375.
Ross, D. G. (**1993**). "On ocean underwater ambient noise," Acoust. Bull. **18**, 5–8.
Thompson, P. O. (1965). "Marine biological sound west of San Clemente Island," U.S. Navy Electronics Laboratory Report 1290, San Diego, CA, p. 42.
Wagstaff, R. A. (**1981**). "Low-frequency ambient noise in the deep sound channel—The missing component," J. Acoust. Soc. Am. **69**, 1009–1014.
Webb, S. C. (**1998**). "Broadband seismology and noise under the ocean," Rev. Geophys. **36**, 105–142.
Wenz, G. M. (**1962**). "Acoustic ambient noise in the ocean: Spectra and sources," J. Acoust. Soc. Am. **34**, 1936–1956.
Wenz, G. M. (**1964**). "Ambient noise measurements west of San Clemente Island," U.S. Navy Electronics Laboratory Report 1235, p. 46.
Wenz, G. M., Calderon, M. A., and Scanlan, T. F. (**1965**). "Underwater acoustic ambient-noise and transmission tests west of San Clemente Island, July 1963," U.S. Navy Electronics Laboratory Report 1260, p. 46.
Wenz, G. M. (**1968a**). "Properties of low-frequency, deep water ambient noise west of San Diego, California," Navy Undersea Warfare Center Technical Publication TP-39, recently declassified, p. 48.
Wenz, G. M. (**1968b**). "Properties of low-frequency, deep water ambient noise southwest of Pacific Beach, Washington," Navy Undersea Warfare Center Technical Publication TP-90, recently declassified, p. 38.
Wenz, G. M. (**1969**). "Low-frequency deep-water ambient noise along the Pacific coast of the United States," U.S. Navy J. Underwater Acoust. **19**, 423–444, recently declassified.
Wiggins, S. M. (**2003**). "Autonomous acoustic recording packages (ARPs) for long-term monitoring of whale sounds," Mar. Technol. Soc. J. **37**, 13–22.

A perturbation approach to acoustic scattering in dispersions

Valerie J. Pinfield[a] and Malcolm J. W. Povey
Procter Department of Food Science, University of Leeds, Leeds, LS2 9JT, United Kingdom

(Received 19 October 2005; revised 26 April 2006; accepted 26 April 2006)

Ultrasound spectroscopy has many applications in characterizing dispersions, emulsions, gels, and biomolecules. Interpreting measurements of sound speed and attenuation relies on a theoretical understanding of the relationship between system properties and their effect on sound waves. At its basis is the scattering of a sound wave by a single particle in a suspending medium. The problem has a well-established solution derived by expressing incident and scattered fields in terms of Rayleigh expansions. However, the solution is badly conditioned numerically. By definition, in the long-wavelength limit, the wavelength is much larger than the particle radius, and the scattered fields can then be expressed as perturbation series in the parameter *Ka* (wave number multiplied by particle radius), which is small in this limit. In addition, spherical Bessel and Hankel functions are avoided by using alternative series expansions. In a previous development of this perturbation method, thermal effects had been considered but viscous effects were excluded for simplicity. Here, viscous effects, giving rise to scattered shear waves, are included in the formulation. Accurate numerical correspondence is demonstrated with the established Rayleigh series method for an emulsion. This solution offers a practical computational approach to scattering which can be embodied in acoustic instrumentation.
[DOI: 10.1121/1.2206512]

PACS number(s): 43.35.Bf [RR] Pages: 719–732

I. INTRODUCTION

Ultrasound spectroscopy is a noninvasive technique suitable for use with a range of materials, such as emulsions, dispersions, gels, and solutions of biomolecules, with a wide range of particle sizes. In current instrumentation a frequency range of 0.1–200 MHz is used, and particle sizes over a wide range from 10 nm to 1 mm can be detected. The measured properties of the ultrasound signal, usually frequency-dependent velocity and attenuation, are related to the characteristics of the system, e.g., the particle size distribution, degree of aggregation, concentration, etc. A substantial review of the application and interpretation of ultrasound measurements can be found in Challis *et al.* (2005). In order to interpret such ultrasound measurements, it is necessary to relate the properties of the sound wave to the particle size and physical properties of the materials. At the basis of the relationship is the scattering characteristic of a single particle of given properties, and this is the subject of the present work. For an ensemble of such scatterers (such as an emulsion or dispersion), the combined effect on the sound wave is determined by multiple scattering theory.

The long-standing solution to the single-particle scattering problem uses partial wave expansions after Rayleigh (Strutt, 1896), expressing the sound fields as series of spherical harmonics. His solution was later extended for fluid particles by Epstein and Carhart (1953), and for solid particles by Allegra and Hawley (1972). Their solution is referred to as ECAH. The numerical solution of the resulting six boundary equations (for each partial wave order n) is badly conditioned, causing inaccuracy with the matrix inversion unless a high degree of machine precision is used. The spherical Bessel functions are also difficult to calculate at large complex arguments. These numerical difficulties are discussed by O'Neill *et al.* (2001) and Harlen *et al.*(2001), and such problems have limited the application of the method. The present work addresses these problems in the long-wavelength region, by the development of an alternative method of solution following Kleinman's method (Kleinman, 1965).

In a series of recent publications (Harlen *et al.*, 2001, 2003, Pinfield *et al.* 2005) the method which is valid in the long-wavelength region has been developed. In this limiting case, the wavelength of the incident sound wave is much larger than the particle radius, so that $Ka \ll 1$, where K is the wave number and a the radius of the particles. The sound fields have therefore been expanded as perturbation series in powers of Ka, after Kleinman (1965). Continuing the application of Kleinman's method, the radiation condition is satisfied by explicitly including exponential spherical sound-wave terms of the form e^{iKr}, thus avoiding the use of spherical Bessel and Hankel functions. The scattered field is then determined by solving a series of potential problems. The result is a much better conditioned solution to the boundary conditions which simplifies numerical calculation. It may be anticipated that such a method will lead to further developments concerning nonspherical scattering objects and multiple scattering.

The earlier work (Harlen *et al.*, 2001, 2003) applied to limited conditions within the long-wavelength region in which the thermal wavelength was either much larger or much smaller than the particle size. The most recent paper (Pinfield *et al.*, 2005) modified the method to be valid in the entire long-wavelength region, whatever the size of the thermal wavelength. However, viscous effects were neglected in

[a]Electronic mail: v.j.pinfield@leeds.ac.uk

all cases. For a viscous medium, shear waves (a transverse wave mode) are also produced at the particle surface. These shear waves were included in the ECAH method, and lead to a significant contribution to attenuation and velocity in some cases. In the work reported here the additional viscous effects are included in the previously documented method. Since the method itself has been detailed in the earlier paper (Pinfield *et al.*, 2005), it is only summarized here, with emphasis on the new contributions resulting from shear effects. In the next section, the principles of sound-wave propagation in fluids are summarized, and the problem of single-particle scattering is introduced. The ECAH forms for the sound waves are shown, together with the alternative perturbation expansion approach. Sections III and IV show how the wave potentials are defined inside and outside the particle, while Sec. V builds the solution by applying boundary conditions. Explicit results are shown for the lowest order coefficients. Section VI demonstrates the numerical agreement between the new method and the ECAH results for 20% v/v n-hexadecane oil-in-water emulsions in which the density difference between the continuous and dispersed phase is significant.

II. SOUND FIELDS IN A FLUID

The equations of motion for sound propagation in homogeneous fluids (including continuity, Navier-Stokes, energy) can be simplified by use of velocity potentials, such that

$$\mathbf{u} = -\nabla\phi + \nabla \times \boldsymbol{\chi}, \tag{1}$$

where $\mathbf{u}$ is the velocity of the fluid, ϕ is a scalar potential, and $\boldsymbol{\chi}$ is a vector potential satisfying the condition $\nabla \cdot \boldsymbol{\chi} = 0$. When viscous effects are neglected, such as in the earlier development of the method reported here (Pinfield *et al.*, 2005) the vector potential $\boldsymbol{\chi}$ is not included, and only scalar velocity potentials are required. Viscous effects were, however, included in the earlier ECAH method (Epstein and Carhart, 1953; and Allegra and Hawley, 1972).

Substituting Eq. (1) into the equations of motion results in three separate equations, two for scalar potentials and one for the vector potentials. The two scalar potentials correspond to longitudinal propagational and thermal wave modes, while the vector potential represents a transverse shear wave mode. The propagational mode is the "usual" mode by which sound travels in a fluid, while the thermal mode represents heat flow and the shear mode arises from viscous effects. Both the thermal and shear modes are dissipative and therefore highly localized.

The time dependence is defined by a factor $e^{-i\omega t}$, where ω is the angular frequency, so that each mode satisfies a Helmholtz equation,

$$(\nabla^2 + K^2)\varphi = 0 \quad (\nabla^2 + L^2)\psi = 0 \quad (\nabla^2 + S^2)\boldsymbol{\chi} = \mathbf{0}. \tag{2}$$

The total scalar potential is the sum of the propagational and thermal wave potentials.

The wave numbers, K for the propagational mode, L for the thermal mode, and S for the shear mode, are given to a very good approximation in fluids by

$$K = \frac{\omega}{v}\left(1 + i\frac{(\gamma-1)\sigma\omega}{2v^2}\right),$$

$$L = \left(\frac{\omega}{2\sigma}\right)^{1/2}(1+i), \tag{3}$$

$$S = \left(\frac{\omega}{2\nu}\right)^{1/2}(1+i),$$

where v is the speed of sound, γ is the ratio of specific heat capacities, σ the thermal diffusivity, such that $\sigma = \tau/\rho C_p$ where τ is the thermal conductivity, ρ is the density, and C_p is the specific heat capacity at constant pressure, and $\nu = \eta/\rho$ is the kinematic viscosity, where η is shear viscosity.

The wave number of the propagational mode is usually given in the form

$$K = \frac{\omega}{v} + i\alpha, \tag{4}$$

where α is the attenuation. It is appropriate to use the measured attenuation in (4) rather than the classical result (3) because of absorption effects which are not included in the classical equations.

The temperature fluctuations resulting from the wave modes are

$$T = \Gamma_c\varphi + \Gamma_t\psi, \tag{5}$$

where

$$\Gamma_c = \frac{-iK^2(\gamma-1)}{\beta(\omega + i\gamma\sigma K^2)}, \quad \Gamma_t = \frac{-iL^2(\gamma-1)}{\beta(\omega + i\gamma\sigma L^2)}, \tag{6}$$

where β is the thermal expansivity. Subscript c is used to denote the compressional (or propagational) mode and t the thermal mode. The shear mode does not contribute to the temperature fluctuation.

In the absence of viscous effects (Pinfield *et al.*, 2005), only the isotropic pressure needs to be considered, which results in stress terms in proportion to the density of the material. When both inertial and shear stress are included the stress terms are significantly more complicated, and cannot be expressed by a single factor. The relevant forms for the boundary conditions are given in the next section.

A useful thermodynamic relation is

$$\gamma - 1 = \frac{v^2\beta^2 T_0}{C_p}, \tag{7}$$

where T_0 is the temperature of the system, not the small temperature fluctuations caused by the wave motion.

A. Scattering of sound waves by particles

In order to determine the ultrasound propagation parameters for a dispersion of particles, we first consider a plane sound wave of angular frequency ω incident on a spherical particle of radius a. By combining the scattering properties of a number of such individual particles, it is possible to estimate the properties of an ensemble of particles. At the surface of the particle, waves of all modes are produced inside and outside the particle. Boundary conditions must be

satisfied at the particle surface, including the continuity of fluid velocity components, stress components, temperature, and heat flow. Viscous effects introduce requirements on the velocity component v_θ and the stress component $P_{r\theta}$. The axial symmetry of the incident plane wave reduces the vector potential $\boldsymbol{\chi}$ to a single component χ_ψ, and for simplicity this will be referred to simply as χ.

In terms of the wave potentials, the boundary conditions are given below. Primed quantities refer to the inside of the particle and φ_0 is the potential of the incident wave.

For the radial component of velocity v_r,

$$\frac{\partial}{\partial r}(\varphi_0+\varphi+\psi)-\frac{1}{r\sin\theta}\frac{\partial}{\partial\theta}(\chi\sin\theta)$$
$$=\frac{\partial}{\partial r}(\varphi'+\psi')-\frac{1}{r\sin\theta}\frac{\partial}{\partial\theta}(\chi'\sin\theta). \quad (8)$$

For the velocity component v_θ,

$$\frac{\partial}{r\partial\theta}(\varphi_0+\varphi+\psi)+\frac{1}{r}\frac{\partial}{\partial r}(r\chi)=\frac{\partial}{r\partial\theta}(\varphi'+\psi')+\frac{1}{r}\frac{\partial}{\partial r}(r\chi'). \quad (9)$$

In the absence of viscous effects, the continuity of stress reduced to a single equation representing the pressure inside and outside the particle. With viscous effects included, the stress components P_{rr} and $P_{r\theta}$ must be continuous across the boundary.

$$P_{rr}=P'_{rr} \quad (10)$$

and

$$P_{r\theta}=P'_{r\theta}. \quad (11)$$

The expressions relating the stress components to the wave potentials are as follows: For each compressional wave mode (the propagational and thermal modes)

$$P_{rr}=(i\omega\rho-2\eta k^2)\varphi-2\eta\frac{\partial^2\varphi}{\partial r^2}, \quad (12)$$

where k is the wave number for the mode,

$$P_{r\theta}=2\eta\frac{\partial}{\partial\theta}\left(\frac{\varphi}{r^2}-\frac{1}{r}\frac{\partial\varphi}{\partial r}\right). \quad (13)$$

Inside the particle, the physical properties for the particle should be used.

For the shear-wave mode, with axial symmetry (see the next section) the stress components are

$$P_{rr}=\frac{2\eta}{\sin\theta}\frac{\partial}{\partial\theta}\left[\sin\theta\left(-\frac{\chi}{r^2}+\frac{1}{r}\frac{\partial\chi}{\partial r}\right)\right], \quad (14)$$

$$P_{r\theta}=\eta\left[\left(\frac{2\chi}{r^2}-\frac{\partial^2\chi}{\partial r^2}\right)+\frac{1}{r^2}\frac{\partial}{\partial\theta}\left(\frac{1}{\sin\theta}\frac{\partial}{\partial\theta}(\chi\sin\theta)\right)\right], \quad (15)$$

where η is the shear viscosity. These equations for stress are appropriate for fluids. Further details on the stress relations are given by Povey (1997, pp. 106–109), and also by Epstein and Carhart (1953) and Allegra and Hawley (1972).

The thermal boundary conditions are unaffected by the shear waves and remain as in the previous work. The temperature continuity equation is

$$\Gamma_c\varphi_0+\Gamma_c\varphi+\Gamma_t\psi=\Gamma'_c\varphi'+\Gamma'_t\psi', \quad (16)$$

and the heat flux boundary condition

$$\Gamma_c\frac{\partial}{\partial r}(\varphi_0+\varphi)+\Gamma_t\frac{\partial\psi}{\partial r}=\hat{\tau}\left(\Gamma'_c\frac{\partial\varphi'}{\partial r}+\Gamma'_t\frac{\partial\psi'}{\partial r}\right), \quad (17)$$

where $\hat{\tau}=\tau'/\tau$ is the ratio of the thermal conductivities in each substance. When evaluating the boundary conditions, the following relations which were listed by Epstein and Carhart (1953) are useful:

$$-\frac{dP_n(\cos\theta)}{d\theta}=P_n^1(\cos\theta),$$

$$\frac{1}{\sin\theta}\frac{d}{d\theta}(\sin\theta P_n^1(\cos\theta))=n(n+1)P_n(\cos\theta).$$

The objective of the current work is to determine the scattered-wave amplitude for the system of a plane wave and spherical particle. The scattering amplitudes can be combined for an ensemble of particles to calculate the velocity and attenuation of a dispersion. To solve the scattering problem, the new general forms for each wave mode are proposed in Secs. III and IV, which satisfy the appropriate Helmholtz equation given in Sec. II, inside or outside the particle. Section V shows how the solution is constructed, applying the boundary conditions in Sec. V D in order to obtain the solution for scattered-wave amplitudes. Details of the method were given in a previous paper (Pinfield *et al.*, 2005), and are only summarized here. This paper is concerned with the additional effects introduced by the inclusion of viscous effects. First, the scattered waveforms for the ECAH method are shown.

B. ECAH method

In the ECAH method, the solution potentials were expressed as Rayleigh series, using the spherical harmonic functions. For the radial dependence, the Hankel function h_n is used outside the particle, whereas inside the particle the spherical Bessel function j_n function is appropriate. The angular dependence is defined by the Legendre polynomials (P_n) and associated Legendre polynomials (P_n^1). The vector potential in Epstein and Carhart (1953) used the symbol A; here, χ has been used to avoid confusion with the scattering coefficient A_n. ECAH took the forms for each wave potential to be as follows:

$$\varphi=\sum_{n=0}^{\infty}i^n(2n+1)A_nh_n(Kr)P_n(\cos\theta),$$

$$\psi=\sum_{n=0}^{\infty}i^n(2n+1)B_nh_n(Lr)P_n(\cos\theta),$$

$$\chi=\sum_{n=1}^{\infty}i^n(2n+1)C_nh_n(Sr)P_n^1(\cos\theta),$$

$$\varphi' = \sum_{n=0}^{\infty} i^n (2n+1) A'_n j_n(K'r) P_n(\cos\theta),$$

$$\psi' = \sum_{n=0}^{\infty} i^n (2n+1) B'_n j_n(L'r) P_n(\cos\theta),$$

$$\chi' = \sum_{n=1}^{\infty} i^n (2n+1) C'_n j_n(S'r) P_n^1(\cos\theta). \quad (18)$$

Similarly, the incident field (a plane wave) can be expressed as

$$\varphi_0 = \sum_{n=0}^{\infty} i^n (2n+1) j_n(Kr) P_n(\cos\theta). \quad (19)$$

The boundary conditions are applied by evaluating these functions and the appropriate derivatives at the particle surface $r=a$. The resulting set of equations is ill-conditioned numerically, and the Hankel and Bessel functions cause difficulties at some arguments. A full discussion of these difficulties is given by Harlen *et al.* (2001), showing that under some conditions the matrix becomes very nearly singular, which leads to inaccurate solution if insufficient computational accuracy is used. These problems led us to propose the construction of an alternative form of solution avoiding the use of Bessel functions and more appropriate to numerical solution.

C. Kleinman method and Poincaré series

Kleinman showed that a solution to scattering problems in the long-wavelength region $|Ka| \ll 1$ could be obtained by expanding the wave potentials as a perturbation series, thus

$$\phi = \sum_{m=0}^{\infty} (iKa)^m \phi_m, \quad (20)$$

where ϕ is one of the wave potentials. Thus, instead of solving for the total potential ϕ, each of a set of potentials ϕ_m must be found. This may appear to be more difficult, but in fact the series converges rapidly, so that a finite number of terms is required for a given accuracy. The solutions for potentials ϕ_m do not suffer from the numerical instability seen when solving for the overall potentials. Each of the wave potentials is expanded as a series in iKa, so that a set of potentials ϕ_m must be found for each wave type. The principles of the Kleinman method were described in previous work (Harlen *et al.*, 2001, 2003).

III. SOLUTION FORMS OUTSIDE THE PARTICLE

In the continuous phase outside the particle, the solutions of the Helmholtz equation must also satisfy the radiation condition according to Colton and Kress (1998, p. 21) and Kleinman (1965). Such solutions take the form

$$\phi = \frac{e^{ikr}}{r} \tilde{\phi} = \frac{e^{ikr}}{r} \sum_{l=0}^{\infty} \frac{f_l(\theta,\Omega)}{r^l}, \quad (21)$$

where f_l is the angular dependence (Harlen *et al.*, 2001).

The spherical Hankel function used in the ECAH method is one suitable solution, each $h_n(kr)$ including a factor e^{ikr}/r which represents a spherical outgoing wave. However, radiating solutions to the Helmholtz equation are not regular at infinity and it is the exponential part of the function which causes numerical difficulties at large arguments (for the thermal waves). The function $\tilde{\phi}$ does not suffer from the mathematical difficulties of the overall potential ϕ. Hence, the radiating terms of the wave potentials outside the particle have been explicitly included so that the boundary equations can work only with the remaining part of the potentials. So, applying Kleinman's method to each mode potential,

$$\varphi = e^{iK(r-a)} \tilde{\varphi}, \quad (22)$$

$$\psi = e^{iL(r-a)} \tilde{\psi}, \quad (23)$$

$$\chi = e^{iS(r-a)} \tilde{\chi}. \quad (24)$$

When applying boundary conditions for a spherical particle at $r=a$ the exponential factors do not contribute. The new potential functions are then expressed as series in iKa, using the Kleinman method, thus

$$(\tilde{\varphi}, \tilde{\psi}, \tilde{\chi}) = \sum_m (iKa)^m (\tilde{\varphi}_m, \tilde{\psi}_m, \tilde{\chi}_m). \quad (25)$$

Now, solution forms must be constructed for the partial potentials $\tilde{\varphi}_m$, etc., which satisfy the Helmholtz equation.

A. Propagational mode

The partial wave potentials for the propagational mode outside the particle are written as

$$\tilde{\varphi}_m = \sum_{n=0}^{\infty} \sum_{j=0} A_{nmj} \cdot \frac{r^j}{a^j} \cdot \frac{a^{n+1}}{r^{n+1}} \cdot P_n(\cos\theta). \quad (26)$$

The full wave potential can be constructed using Eqs. (25) and (22). Substitution into the Helmholtz Eq. (2) leads to the recurrence relation

$$A_{n,m,j} = -\frac{2(j-1-n)}{j(j-1-2n)} A_{n,m-1,j-1} \quad \text{for } j \geq 1. \quad (27)$$

Coefficients for order m are related to those of the previous order $m-1$ for all $j \geq 1$. The coefficient for $j=0$ remains to be solved from the boundary equations. The series is finite, terminating at $j=n$, since the recurrence relation shows that the coefficients are zero for $j=n+1$. The series often has even fewer terms, as will be seen when the boundary conditions are applied (Sec. V D).

B. Thermal mode

The thermal wave potential is based on the spherical Hankel function series expansion (see the Appendix and Pinfield *et al.*, 2005), so that the thermal wave potential takes the form

$$\tilde{\psi}_m = \sum_{n=0}^{\infty} \sum_{j=1}^{n+1} B_{nm} \cdot \frac{h_{nj}}{(Lr)^j} \cdot \frac{1}{S_{hL}} \cdot P_n(\cos\theta), \tag{28}$$

where

$$S_{hL} = \sum_{j=1}^{n+1} \frac{h_{nj}}{(La)^j} \tag{29}$$

is a normalizing factor which simplifies the boundary equations for numerical solution. This factor has no zeros, with the parameter La being of the type $\zeta(1+i)$. The coefficients h_{nj} are defined in the Appendix. The complete wave potential results from combining Eq. (28) with Eqs. (25) and (23).

C. Shear mode

In a similar way, the shear mode can also be expressed by the Hankel series expansion; thus

$$\tilde{\chi}_m = \sum_{n=0}^{\infty} \sum_{j=1}^{n+1} C_{nm} \cdot \frac{h_{nj}}{(Sr)^j} \cdot \frac{1}{S_{hS}} \cdot P_n(\cos\theta), \tag{30}$$

where

$$S_{hS} = \sum_{j=1}^{n+1} \frac{h_{nj}}{(Sa)^j}. \tag{31}$$

The complete wave potential results from combining Eq. (30) with Eqs. (25) and (24).

D. The incident wave

The incident plane wave was written in the ECAH method in terms of spherical harmonics, Eq. (19), but it can be expressed as a power series in (iKa) by expanding the spherical Bessel function, thus

$$\varphi_0 = \sum_{n=0}^{\infty} \sum_{s=0}^{\infty} (iKa)^{n+2s} \left(\frac{r}{a}\right)^{n+2s} F_n(s) P_n(\cos\theta), \tag{32}$$

where

$$F_n(s) = \frac{2^n (2n+1)(s+n)!}{s!(2s+2n+1)!}, \tag{33}$$

when n and s are non-negative integers (F is zero otherwise). See the Appendix for the numerical calculation of the function.

IV. SOLUTION FORMS INSIDE THE PARTICLE

Inside the particle, the solutions must satisfy the Helmholtz equation and be defined at the origin (taken as the center of the particle $r=0$). The spherical Bessel function j_n is one suitable solution, but evaluating it at large complex arguments causes difficulty, so alternative forms are again sought. The radiation condition is not relevant inside the particle.

A. Propagational mode

For the propagational mode inside the particle, the solution is defined by the perturbation series expansion

$$\varphi' = \sum_m (iKa)^m \varphi'_m, \tag{34}$$

and then expressing the potential as a series in powers of r

$$\varphi'_m = \sum_{n=0}^{\infty} \sum_{j=0} A'_{nmj} \cdot \frac{r^j}{a^j} \cdot \frac{r^n}{a^n} \cdot P_n(\cos\theta). \tag{35}$$

Substituting into the Helmholtz Eq. (2) results in the recurrence relation (36),

$$A'_{n,m,j} = \frac{\hat{c}}{j(2n+j+1)} A'_{n,m-2,j-2} \quad \text{for } j \geqslant 2,$$
$$A'_{n,m,j} = 0 \quad \text{for } j = 1 \text{ and all odd values of } j, \tag{36}$$

where

$$\hat{c} = \frac{K'^2}{K^2}, \tag{37}$$

which is frequency independent to a very good approximation.

Thus, coefficients for order m are related to those of a previous order $m-2$ for all even coefficients $j \geqslant 2$. The coefficient for $j=0$ remains to be solved from the boundary equations. In this case the limit of the series is determined by the number of nonzero coefficients for the previous order, producing an expanding triangle of coefficients. The solution of the boundary conditions shows that the first nonzero coefficient is for $n=m$, $j=0$, so that the limit of the series in j would be $j=m-n$, where $m>n$.

B. Thermal mode

For the thermal wave, a power series expansion of the function j_n would be inappropriate, because the argument of the function in the boundary equations could range from a very small value to a very large (complex) value depending on the frequency and radius, even in the long-wavelength region. Instead, the solution is expressed in terms of a sum of an incoming and outgoing wave,

$$\psi' = e^{iL'(r-a)} \tilde{\psi}'_+ - e^{-iL'(r-a)} \tilde{\psi}'_-. \tag{38}$$

Each of the new wave potentials is written as a perturbation series

$$\{\tilde{\psi}'_+, \tilde{\psi}'_-\} = \sum_m (iKa)^m \{\tilde{\psi}'_{+m}, \tilde{\psi}'_{-m}\}, \tag{39}$$

and each of the terms has the usual angular dependence; thus

$$\tilde{\psi}'_{+m} = \sum_{n=0}^{\infty} \sum_{l=1}^{n+1} B'_{nm} \cdot e^{2iL'a} \cdot \frac{j_{nl+}}{(L'r)^l} \cdot \frac{1}{S_{jL}} \cdot P_n(\cos\theta) \tag{40}$$

$$\tilde{\psi}'_{-m} = \sum_{n=0}^{\infty} \sum_{l=1}^{n+1} B'_{nm} \cdot \frac{j_{nl-}}{(L'r)^l} \cdot \frac{1}{S_{jL}} \cdot P_n(\cos\theta), \tag{41}$$

where

$$S_{jL} = \sum_{l=1}^{n+1} \frac{e^{2iL'a} j_{nl+} - j_{nl-}}{(L'a)^l}. \tag{42}$$

The coefficients j_{nl+} and j_{nl-} are defined in the Appendix. The factor $e^{2iL'a}$ results from the condition that the potential be defined at the origin. The normalizing factor S_{jL} has no zeros, since the zeros of the Bessel function $J_\nu(z)$ only occur for real arguments, for orders $\nu > -1$, whereas the parameter $L'a$ is complex, with the form $\zeta(1+i)$.

C. Shear mode

The shear mode inside the particle is constructed in a similar way to the thermal wave in the previous section; hence, the wave potential can be written

$$\chi' = e^{iS'(r-a)} \tilde{\chi}'_+ - e^{-iS'(r-a)} \tilde{\chi}'_- \tag{43}$$

$$\{\tilde{\chi}'_+, \tilde{\chi}'_-\} = \sum_m (iKa)^m \{\tilde{\chi}'_{+m}, \tilde{\chi}'_{-m}\}. \tag{44}$$

The shear-wave mode has angular dependence defined by the associated Legendre polynomials,

$$\tilde{\chi}'_{+m} = \sum_{n=0}^{\infty} \sum_{l=1}^{n+1} C'_{nm} \cdot e^{2iS'a} \cdot \frac{j_{nl+}}{(S'r)^l} \cdot \frac{1}{S_{jS}} \cdot P_n^1(\cos\theta) \tag{45}$$

$$\tilde{\chi}'_{-m} = \sum_{n=0}^{\infty} \sum_{l=1}^{n+1} C'_{nm} \cdot \frac{j_{nl-}}{(S'r)^l} \cdot \frac{1}{S_{jS}} \cdot P_n^1(\cos\theta), \tag{46}$$

where

$$S_{jS} = \sum_{l=1}^{n+1} \frac{e^{2iS'a} j_{nl+} - j_{nl-}}{(S'a)^l}. \tag{47}$$

The coefficients j_{nl+} and j_{nl-} are defined in the Appendix.

V. CONSTRUCTION OF THE SOLUTION

The analytical forms for the wave modes defined in the previous sections must be substituted into the boundary equations in order to determine the unknown coefficients for each mode. Terms in the same power of iKa are matched, as is the angular dependence. Factors appearing in the equations for the thermal and stress terms must therefore be appropriately expressed as powers of iKa. These are considered below.

A. Temperature factors

The temperature changes caused by the different waves were defined in Eq. (6). The relation

$$\left| \frac{K^2}{L^2} \right| \approx \frac{\omega\sigma}{v^2} \ll 1 \tag{48}$$

is true over a very wide frequency range (up to $\sim 10^{11}$ Hz for water at 30 °C). Thus, the thermal factors for the propagational mode can be simplified to

$$\Gamma_c = \frac{-iK^2(\gamma-1)}{\beta(\omega + i\gamma\sigma K^2)} \approx \frac{K^2(\gamma-1)}{\beta\sigma L^2} \tag{49}$$

and

$$\Gamma'_c = \frac{-iK'^2(\gamma'-1)}{\beta'(\omega + i\gamma'\sigma' K'^2)} \approx \frac{\hat{c}K'^2(\gamma'-1)}{\beta'\sigma' L'^2}. \tag{50}$$

The factors of (iKa) are of interest explicitly, so the thermal factors may be expressed in the form

$$\Gamma_c = (iKa)^2 g_c, \quad \Gamma'_c = (iKa)^2 g'_c. \tag{51}$$

For the thermal wave mode, the factors can also be simplified and are approximately independent of frequency,

$$\Gamma_t = \frac{-iL^2(\gamma-1)}{\beta(\omega + i\gamma\sigma L^2)} \approx -\frac{1}{\beta\sigma}, \tag{52}$$

and similarly in the dispersed phase.

It is also worth noting that the ratio of the temperature factors for the propagational and thermal modes is very small, showing that the temperature changes are dominated by the thermal mode,

$$\left| \frac{\Gamma_c}{\Gamma_t} \right| \approx \frac{K^2(\gamma-1)}{L^2}, \tag{53}$$

which is very small.

B. Stress

In the absence of viscous effects, the boundary equation for continuity of stress is simply related to the pressure inside and outside the particle surface (Pinfield *et al.*, 2005). The pressure relating to each wave mode was proportional to the frequency and the local density. With the inclusion of viscous stress, the P_{rr} component [Eq. (12)] includes terms in both $(Ka)^2$ and $(Sa)^2$ (through the ratio of $\omega\rho/\eta$) for the compressional modes (propagational and thermal). The relative magnitude of the contributions to the stress depends on frequency, or equivalently, on the magnitude of Sa. At low frequencies (known as the viscous limit), the viscous terms are dominant, whereas at high frequency (the inertial limit) the viscous terms are negligible and the motion is governed by the inertia of the particle. The $P_{r\theta}$ boundary contributions are proportional to the shear viscosity.

C. Definitions

The application of the boundary conditions leads to some complicated equations, which can be made simpler to read by using some further symbols to define collections of terms.

For the continuous phase

$$S_{hL} = \sum_{j=1}^{n+1} \frac{h_{nj}}{(La)^j}, \tag{54}$$

$$S_{dhL} = \sum_{j=1}^{n+1} \frac{(iLa - j)h_{nj}}{(La)^j}, \tag{55}$$

$$S_{d2hL} = \sum_{j=1}^{n+1} \frac{[-La^2 - 2iLaj + j(j+1)]h_{nj}}{(La)^j}, \quad (56)$$

and similar definitions for the shear wave factors S_{hS}, S_{dhS}, S_{d2hS}, replacing La by Sa in each case. In addition,

$$S_{d2hSS} = \frac{S_{d2hS}}{S_{hS}} - \{2 - n(n+1)\}. \quad (57)$$

For the dispersed phase

$$S_{jL} = \sum_{l=1}^{n+1} \frac{e^{2iL'a} j_{nl+} - j_{nl-}}{(L'a)^l}, \quad (58)$$

$$S_{djL} = \sum_{l=1}^{n+1} \frac{e^{2iL'a}(iL'a - l)j_{nl+} + (iL'a + l)j_{nl-}}{(L'a)^l}, \quad (59)$$

$$S_{d2jL} = \sum_{l=1}^{n+1} \{e^{2iL'a}[-L'a^2 - 2iL'al + l(l+1)]j_{nl+} + [L'a^2 - 2iL'al - l(l+1)]j_{nl-}\}/(L'a)^l, \quad (60)$$

and similar definitions for the shear-wave factors S_{jS}, etc., replacing $L'a$ by $S'a$ in each case, with an additional factor

$$S_{d2jSS} = \frac{S_{d2jS}}{S_{jS}} - \{2 - n(n+1)\}. \quad (61)$$

For the propagational mode, greater accuracy is achieved (avoiding subtraction of nearly equal terms) by using the recurrence relation (27) to write

$$S_{jA,m-s} = \sum_{j=0} A_{n,m-s,j} + \sum_{j=0}^{m-n} jA_{n,m-s+1,j} = \sum_{j=1}^{m-n} -\frac{j}{(j-2n)} A_{n,m-s,j} + \delta_{n0} A_{n,m-s,0}, \quad (62)$$

where δ_{n0} is a Kronecker delta such that $\delta_{nj}=1$ for $n=j$ and zero otherwise. Other factors are defined as follows:

$$S_{A,m-s} = \sum_{j=0}^{n} A_{n,m-s,j} \quad \text{for } s = 1,2,3 \quad S_{A,m} = \sum_{j=1}^{n} A_{n,m,j}, \quad (63)$$

$$S_{jA,m-s} = \sum_{j=1}^{n} -\frac{j}{(j-2n)} A_{n,m-s,j} + \delta_{n0} A_{n,m-s,0} \quad \text{for } s = 1,2,3, \quad (64)$$

$$S_{jjA,m-s} = \sum_{j=1}^{n} jA_{n,m-s,j} \quad \text{for } s = 0,1,2,3, \quad (65)$$

$$S_{j2A,m-s} = \sum_{j=1}^{n} j^2 A_{n,m-s,j} \quad \text{for } s = 0,1,2,3, \quad (66)$$

$$S_{A',m-s} = \sum_{j=0}^{m-n} A'_{n,m-s,j} \quad \text{for } s = 1,2,3 \quad S_{A',m} = \sum_{j=1}^{m-n} A'_{n,m,j}, \quad (67)$$

$$S_{jA',m-s} = \sum_{j=1}^{m-n} jA'_{n,m-s,j} \quad \text{for } s = 0,1,2, \quad (68)$$

$$S_{j2A',m-s} = \sum_{j=1}^{m-n} j^2 A'_{n,m-s,j} \quad \text{for } s = 0,1,2. \quad (69)$$

D. Boundary conditions

The boundary conditions [Eqs. (8)–(17)] are applied at the surface of the spherical particle $r=a$. Since both the Legendre polynomials and associated Legendre polynomials of different orders n are independent, the angular dependence in the boundary equations can only be satisfied if applied independently for each order n. In other words, there is a set of six boundary equations for each n. Each set must be solved independently for the coefficients of that order. The wave potentials have been defined as series in powers of iKa, so each boundary equation consists of summations over orders m. Terms in powers of (iKa) which may arise from various orders of m are matched on each side of the equation. If each order m is determined in turn, all coefficients for previous orders, e.g., $m-1$, are already known. In addition, the propagational mode coefficients for order m for $j \geqslant 1$ can be calculated from the previous order results [see Eqs. (27) and (36)]. Hence, the boundary equations for the n, mth order include six unknowns,

$$A_{nm0}, \quad A'_{nm0}, \quad B_{nm}, \quad B'_{nm}, \quad C_{nm}, \quad C'_{nm}.$$

Note that these coefficients do not have the same definition as in the previous work (Pinfield *et al.*, 2005) because of the inclusion of normalization factors which were not previously used, e.g., Eqs. (28) and (29). These normalizing factors help to condition the numerical matrix solution resulting from the boundary equations. The six boundary conditions (8)–(17) in the order $\{v_r, P_{rr}, v_\theta, P_{r\theta}, T, \text{heat flux}\}$ result in the equations below,

$$mF_n\left(\frac{m-n}{2}\right) - (n+1)[A_{nm0} + S_{A,m}] + S_{jA,m\_1} + \frac{S_{dhL}}{S_{hL}} B_{nm} - n(n+1)C_{nm} = n[A'_{nm0} + S_{A',m}] + S_{jA',m} + \frac{S_{djL}}{S_{jL}} B'_{nm} - n(n+1)C'_{nm}, \quad (70)$$

$$\{(Sa)^2 - 2m(m-1)\}F_n\left(\frac{m-n}{2}\right) + 2F_n\left(\frac{m-n-2}{2}\right) + \{(Sa)^2 - 2(n+1)(n+2)\}[A_{nm0} + S_{A,m}] - 2\{-(2n+3)S_{jjA,m} + S_{j2A,m} - 2(n+1)S_{A,m-1} + 2S_{jjA,m-1}\}$$

$$+\left\{(Sa)^2-2\frac{S_{d2hL}}{S_{hL}}\right\}B_{nm}+2B_{nm-2}$$
$$+2n(n+1)\left\{\frac{S_{dhS}}{S_{hS}}-1\right\}C_{nm}$$
$$=\hat{\eta}\{(S'a)^2-2n(n-1)\}[A'_{nm0}+S_{A',m}]$$
$$-2\hat{\eta}\{(2n-1)S_{jA',m}+S_{j2A',m}-S_{A',m-2}\}$$
$$+\hat{\eta}\left\{(S'a)^2-2\frac{S_{d2jL}}{S_{jL}}\right\}B'_{nm}+2\hat{\eta}B'_{nm-2}$$
$$+2n(n+1)\hat{\eta}\left\{\frac{S_{djS}}{S_{jS}}-1\right\}C'_{nm}, \tag{71}$$

$$F_n\left(\frac{m-n}{2}\right)+A_{nm0}+S_{A,m}+B_{nm}-\left\{\frac{S_{dhS}}{S_{hS}}+1\right\}C_{nm}$$
$$=A'_{nm0}+S_{A',m}+B'_{nm}-\left\{\frac{S_{djS}}{S_{jS}}+1\right\}C'_{nm}\Big\}, \tag{72}$$

$$2(m-1)F_n\left(\frac{m-n}{2}\right)-2(n+2)[A_{nm0}+S_{A,m}]+2S_{jAm\_1}$$
$$+2\left\{\frac{S_{dhL}}{S_{hL}}-1\right\}B_{nm}-\frac{S_{d2hSS}}{S_{hS}}C_{nm}$$
$$=2(n-1)\hat{\eta}[A'_{nm0}+S_{A',m}]+2\hat{\eta}S_{jA',m}$$
$$+2\hat{\eta}\left\{\frac{S_{djL}}{S_{jL}}-1\right\}B'_{nm}-\hat{\eta}\frac{S_{d2jSS}}{S_{jS}}C'_{nm}, \tag{73}$$

$$g_cF_n\left(\frac{m-n-2}{2}\right)+g_cS_{A,m-2}+\Gamma_tB_{nm}=g'_cS_{A',m-2}+\Gamma'_tB'_{nm}, \tag{74}$$

$$g_c(m-2)F_n\left(\frac{m-n-2}{2}\right)+g_c\{S_{jA,m-3}-(n+1)S_{A,m-2}\}$$
$$+\Gamma_t\frac{S_{dhL}}{S_{hL}}B_{nm}$$
$$=\hat{\tau}g'_c\{S_{jA',m-2}+nS_{A',m-2}\}+\hat{\tau}\Gamma'_t\frac{S_{djL}}{S_{jL}}B'_{nm}. \tag{75}$$

E. Solution

The solution proceeds by determining the coefficients for each order m in turn, starting at $m=0$. All coefficients are zero for $m<0$. Nonzero propagational mode coefficients for order m are calculated from the recurrence relations [Eqs. (27) and (36)]. The two thermal boundary conditions, Eqs. (74) and (75), for the n, mth order are unchanged by the addition of viscous effects. As before, since these equations include only the unknown thermal coefficients, other terms being from previous orders $m-2$ and $m-3$, Eqs. (74) and (75) can be solved for the thermal coefficients B_{nm} and B'_{nm} as follows:

$$B_{nm}=\left[-g_c\left(\hat{\tau}\frac{S_{djL}}{S_{jL}}-(m-2)\right)F_n\left(\frac{m-n-2}{2}\right)-g_c\left(\hat{\tau}\frac{S_{djL}}{S_{jL}}+(n+1)\right)S_{A,m-2}+g_cS_{jA,m-3}\right.$$
$$\left.+\hat{\tau}g'_c\left\{\left(\frac{S_{djL}}{S_{jL}}-n\right)S_{A',m-2}-S_{jA',m-2}\right\}\right]\Big/\Gamma_t\left(\hat{\tau}\frac{S_{djL}}{S_{jL}}-\frac{S_{dhL}}{S_{hL}}\right), \tag{76}$$

$$B'_{nm}=\left[-g_c\left(\frac{S_{dhL}}{S_{hL}}-(m-2)\right)F_n\left(\frac{m-n-2}{2}\right)-g_c\left(\frac{S_{dhL}}{S_{hL}}+(n+1)\right)S_{A,m-2}+g_cS_{jA,m-3}\right.$$
$$\left.+g'_c\left\{\left(\frac{S_{dhL}}{S_{hL}}-n\hat{\tau}\right)S_{A',m-2}-\hat{\tau}S_{jA',m-2}\right\}\right]\Big/\Gamma'_t\left(\hat{\tau}\frac{S_{djL}}{S_{jL}}-\frac{S_{dhL}}{S_{hL}}\right). \tag{77}$$

These coefficients can be substituted into the other boundary equations, (70)–(73), reducing the system of equations to four equations in four remaining unknown coefficients, A_{nm0}, A'_{nm0}, C_{nm}, C'_{nm} (for each order n, m).

For the case $n=0$, the boundary conditions in v_θ and $P_{r\theta}$ are identically satisfied, since $P_0^1(\cos\theta)=0$ [a factor of P_n^1 was canceled to obtain Eqs. (72) and (73)], and the shear wave contributions vanish in the v_r and P_{rr} equations. Thus, in this case, Eq. (70) gives

$$A_{0m0}=mF_0\left(\frac{m}{2}\right)+A_{0,m-1,0}-S_{jA'm}+\frac{S_{dhL}}{S_{hL}}B_{0m}-\frac{S_{djL}}{S_{jL}}B'_{0m}. \tag{78}$$

Viscous effects are seen only indirectly in the A_{0m0} coefficient through the coefficient from the previous order and the A'_{0mj} coefficients. No viscous contribution is present for the first nonzero coefficient, for $m=2$. The propagational coeffi-

cient inside the particle is more complicated, resulting from the contributions to stress from both inertial and viscous effects as follows:

$$\begin{aligned}\hat{\rho}(Sa)^2A'_{0m0} = {} & (m+1)\{(Sa)^2-2m\}F_0\left(\frac{m}{2}\right)+2F_0\left(\frac{m-2}{2}\right)\\ & +(Sa)^2\{A_{0,m-1,0}-\hat{\rho}S_{A',m}\}\\ & -\{(Sa)^2+2(\hat{\eta}-2)\}S_{jA',m}+2\hat{\eta}(S_{j2A'm}\\ & -S_{A',m-2})+\left\{(Sa)^2\left(\frac{S_{dhL}}{S_{hL}}+1\right)\right.\\ & \left.-2\left(\frac{S_{d2hL}}{S_{hL}}+2\frac{S_{dhL}}{S_{hL}}\right)\right\}B_{0m}+2B_{0,m-2}\\ & -\left\{(Sa)^2\left(\frac{S_{djL}}{S_{jL}}+\hat{\rho}\right)-2\left(2\frac{S_{djL}}{S_{jL}}+\hat{\eta}\frac{S_{d2jL}}{S_{jL}}\right)\right\}B'_{0m}\\ & -2\hat{\eta}B'_{0,m-2}, \end{aligned} \tag{79}$$

using the relation

$$\hat{\eta}(S'a)^2=\hat{\rho}(Sa)^2, \tag{80}$$

which arises from the definition of the shear wave numbers [Eq. (3)], where

$$\hat{\eta}=\eta'/\eta \text{ and } \hat{\rho}=\rho'/\rho.$$

For higher orders $n>0$ the four boundary equations (70)–(73) for order n, m, together with the solutions (76) and (77), can be solved by a matrix equation for the remaining unknown coefficients A_{nm0}, A'_{nm0}, C_{nm}, C'_{nm}. An analytical result could be obtained, but it is complicated and is only helpful for the lowest orders in m when further simplifications are possible. The matrix equation is as follows:

$$\underline{\underline{L}}=\begin{Bmatrix} n+1 & n(n+1) & n & -n(n+1)\\ (Sa)^2-2(n+1)(n+2) & 2n(n+1)\left(\frac{S_{dhS}}{S_{hS}}-1\right) & -\hat{\eta}\{(S'a)^2-2n(n-1)\} & -2\hat{\eta}n(n+1)\left(\frac{S_{djS}}{S_{jS}}-1\right)\\ 1 & -\left(\frac{S_{dhS}}{S_{hS}}+1\right) & -1 & \left(\frac{S_{djS}}{S_{jS}}+1\right)\\ -2(n+2) & -\frac{S_{d2hSS}}{S_{hS}} & -2\hat{\eta}(n-1) & \hat{\eta}\frac{S_{d2jSS}}{S_{jS}} \end{Bmatrix}, \tag{81}$$

$$\underline{\underline{R}}=\begin{Bmatrix} mF_n\left(\frac{m-n}{2}\right)-(n+1)S_{A,m}+S_{jA,m\_1}+\frac{S_{dhL}}{S_{hL}}B_{nm}-\frac{S_{djL}}{S_{jL}}B'_{nm}-nS_{A',m}-S_{jA',m}\\ \left[\begin{array}{l} -\{(Sa)^2-2m(m-1)\}F_n\left(\frac{m-n}{2}\right)-2F_n\left(\frac{m-n-2}{2}\right)\\ -\{(Sa)^2-2(n+1)(n+2)\}S_{A,m}\\ +2\{-(2n+3)S_{jjA,m}+S_{j2A,m}-2(n+1)S_{A,m-1}+2S_{jjA,m-1}\}\\ -\left\{(Sa)^2-2\frac{S_{d2hL}}{S_{hL}}\right\}B_{nm}-2B_{nm-2}+\hat{\eta}\left\{(S'a)^2-2\frac{S_{d2jL}}{S_{jL}}\right\}B'_{nm}+2\hat{\eta}B'_{nm-2}\\ +\hat{\eta}\{(S'a)^2-2n(n-1)\}S_{A',m}-2\hat{\eta}\{(2n-1)S_{jA',m}+S_{j2A',m}-S_{A',m-2}\} \end{array}\right]\\ -F_n\left(\frac{m-n}{2}\right)-S_{A,m}-B_{nm}+S_{A',m}+B'_{nm}\\ \left[\begin{array}{l} -2(m-1)F_n\left(\frac{m-n}{2}\right)+2\{(n+2)S_{A,m}-S_{jAm\_1}\}-2\left\{\frac{S_{dhL}}{S_{hL}}-1\right\}B_{nm}\\ +2\hat{\eta}\{(n-1)S_{A',m}+S_{jA',m}\}+2\hat{\eta}\left\{\frac{S_{djL}}{S_{jL}}-1\right\}B'_{nm} \end{array}\right] \end{Bmatrix}, \tag{82}$$

$$\underline{\underline{L}}\begin{Bmatrix} A_{nm0} \\ C_{nm} \\ A'_{nm0} \\ C'_{nm} \end{Bmatrix} = \underline{\underline{R}}. \tag{83}$$

The matrix equation is easily solved by numerical inversion. It is considerably better conditioned than the ECAH matrix equation as a result of the new formulation. Once the coefficients for the order n, m have been found, the process is repeated for the next order m, using the recurrence relations, then calculating the thermal coefficients, then solving the matrix equation as before. The complete calculation for all required orders m is repeated for each order n, corresponding to the partial wave order (the spherical harmonics).

By examining the boundary equations it is possible to deduce some general features of the solution. Since the lowest order (in m) contribution from the incident field for an order n is for $m=n$ [see Eq. (82)], the first nonzero coefficient will also be for $m=n$ for the nth-order partial wave. The power series expansion of the incident field [Eq. (32)] shows that the leading term for the nth order is indeed $(iKa)^n$, resulting in a corresponding factor in the scattered field. The thermal fields [see Eqs. (76) and (77)] are, however, two orders smaller, with a leading term of $(iKa)^{n+2}$.

If the first nonzero term for the propagational mode coefficient A_{nm0} is for $m=n$, then the application of the recurrence relation [Eq. (27)] shows that at order m, there will be nonzero coefficients for $j \leqslant m-n$ for $m>n$. However, the recurrence relation terminates the series at $j=n$. So, for each order n the maximum number of coefficients for the order m is

$$j_{\max} = \begin{cases} m-n & \text{for } n \leqslant m \leqslant 2n \\ n & \text{for } m > 2n. \end{cases} \tag{84}$$

Hence, there are nonzero coefficients for $j=n$ for all orders $m \geqslant 2n$. This is relevant in the far field as seen in the next section.

F. Multiple scattering

In practice, ultrasound measurements are made for a system or ensemble of particles in a dispersion. Usually, the ultrasound velocity (or speed) and/or attenuation is measured, often over a range of frequencies. To relate the single-particle scattering properties derived in the previous sections to the sound speed and attenuation in a dispersion, a multiple scattering theory is used. Such a theory evaluates the wave number of the dispersed system from the scattering coefficients of the individual particles.

In general, a limiting far-field solution can be written in the form

$$\varphi \rightarrow \frac{e^{iKr}}{r} f(\theta), \tag{85}$$

where the scattering amplitude $f(\theta)$ is written in terms of angular-dependent Legendre polynomials; thus

$$f(\theta) = \frac{1}{iK} \sum_{n=0}^{\infty} (2n+1) T_n P_n(\cos\theta), \tag{86}$$

where T_n is an element of the scattering matrix. These parameters are defined in the work of Waterman and Truell (1961), although other workers use slightly different definitions. The parameters can be related to the scattering amplitudes used in the previous sections by comparing Eqs. (85) and (86) with the solutions for the propagational mode, Eqs. (22), (25), and (26). Only coefficients for which $j=n$ contribute in the far field (leading to the $1/r$ dependence), and since the first nonzero coefficient for $j=n$ is for $m=2n$ (see Sec. V E), the far-field coefficient T_n is related to the coefficient A_{nmj} by

$$T_n = \frac{e^{-iKa}}{(2n+1)} \sum_{m=2n}^{\infty} (iKa)^{m+1} A_{nmn}. \tag{87}$$

The multiple scattering result for the wave number of the dispersion, B (Waterman and Truell, 1961, and Fikioris and Waterman, 1964; Lloyd and Berry, 1967)

$$\left(\frac{B}{K}\right)^2 = 1 + \frac{3\phi}{K^2 a^3} f(0) + \frac{9\phi^2}{4K^4 a^6}\left(f^2(\pi) - f^2(0) - \int_0^{\pi} d\theta \frac{1}{\sin(\theta/2)} \left(\frac{d}{d\theta} f^2(\theta) \right) \right), \tag{88}$$

which to second order gives

$$\left(\frac{B}{K}\right)^2 = 1 - \frac{3i\phi}{K^3 a^3} \sum_{n=0} (2n+1) T_n - \frac{27\phi^2}{K^6 a^6}\left(T_0 T_1 + \frac{10}{3} T_0 T_2 + 2T_1^2 + 11 T_1 T_2 + \frac{230}{21} T_2^2 + \cdots \right), \tag{89}$$

where multiple scattering has been included up to $n=2$. Note that here the symbol ϕ refers to the volume fraction of the dispersed particles.

Since the wave number is related to the velocity and attenuation by Eq. (4), the dominant contributions to velocity and attenuation scale as

$$\frac{T_n}{(Ka)^3} \tag{90}$$

[Equation (89)], so the leading term corresponds to $(Ka)^{2n-2}$. If velocity and attenuation are to be found to order $(Ka)^p$, spherical harmonics is required up to order

$$n = \left[\frac{(p+2)}{2} \right] \tag{91}$$

(where [ ] refers to the integer part), and orders up to

$$m = p + 2 \tag{92}$$

must be included. As an example, to obtain results for attenuation to order $(Ka)^2$, i.e., $p=2$, all coefficients up to and including $m=4$ and $n=2$ must be calculated. Note that this is only applicable for $p>0$. The leading-order terms for $p=0$ result from $n=0$ and $n=1$ up to order $m=2$.

G. Explicit solutions for low orders

Analytical results have been determined for the coefficients which contribute to attenuation up to order $(Ka)^0$. Those coefficients are A_{020} and A_{121}. The corresponding far-field coefficients are

$$T_0 = e^{-iKa}(iKa)^3 A_{020}, \quad T_1 = \frac{e^{-iKa}}{3}(iKa)^3 A_{121}, \quad T_2 = 0. \tag{93}$$

Substituting these coefficients into the equation for the wave number of the dispersion, B [Equation (89)] gives

$$\left(\frac{B}{K}\right)^2 = 1 - 3\phi e^{-iKa}(A_{020} + A_{121}) + 3\phi^2 e^{-2iKa}(3A_{020}A_{121} + 2A_{121}^2). \tag{94}$$

Higher order terms can be obtained by numerical inversion of the matrix form of the boundary equations as detailed in the earlier section. Here, the analytical forms of the two leading-order coefficients are determined. The process is given in detail by Pinfield *et al.* (2005) and only the changes introduced by including viscous effects are noted here.

The A_{020} coefficient is unchanged by the additional viscous effects, since it relates to a spherical partial wave and is dominated by the difference in compressibility and thermal properties. Thus,

$$A_{020} = \frac{(\hat{\rho} - \hat{c})}{3\hat{\rho}} + \frac{(g_c' - \hat{\rho}g_c)(\hat{\tau}\Gamma_t' - \Gamma_t)S_J S_H}{\hat{\rho}\Gamma_t\Gamma_t'(\hat{\tau}S_J - S_H)},$$

where

$$S_H = \frac{S_{dhL}}{S_{hL}} = (iLa - 1)$$

$$S_J = \frac{S_{djL}}{S_{jL}} = \frac{iL'a(e^{2iL'a} + 1)}{(e^{2iL'a} - 1)} - 1. \tag{95}$$

The viscous contribution does affect higher orders in m for $n=0$ through the stress contributions. The propagational mode coefficient A_{020}' inside the particle is, however, affected by viscous stress.

For the first-order partial wave $n=1$, the far-field coefficient results from A_{121} which is itself related by the recurrence relation [Eq. (27)] to A_{110} as follows:

$$A_{121} = -A_{110},$$

where the boundary equations lead to the result

$$A_{110} = (\hat{\rho} - 1)(Sa)^2 \Bigg/ \left\{ (2\hat{\rho} + 1)(Sa)^2 - 12 + \frac{6[(\hat{\eta}S_{j2S} - 2S_{j1S})(2S_{h1S} + \hat{\rho}(Sa)^2) - (S_{h2S} - 2S_{h1S})(2\hat{\eta}S_{j1S} + \hat{\rho}(Sa)^2)]}{(\hat{\eta}S_{h1S}S_{j2S} - S_{h2S}S_{j1S})} \right\}, \tag{96}$$

$$S_{h1S} = \frac{S_{dhS}}{S_{hS}} - 1 = \frac{((Sa)^2 + 3iSa - 3)}{(1 - iSa)}, \tag{97}$$

$$S_{h2S} = \frac{S_{d2hSS}}{S_{hS}} = \frac{(-i(Sa)^3 + 3(Sa)^2 + 6iSa - 6)}{(1 - iSa)}, \tag{98}$$

$$S_{j1S} = \frac{S_{djS}}{S_{jS}} - 1 = \frac{((S'a)^2 e_{-,+} + 3iS'a - 3e_{-,+})}{(-iS'a + e_{-,+})}, \tag{99}$$

$$S_{j2S} = \frac{S_{d2jSS}}{S_{jS}} = \frac{(-i(S'a)^3 + 3(S'a)^2 e_{-,+} + 6iS'a - 6e_{-,+})}{(-iS'a + e_{-,+})}, \tag{100}$$

$$e_{-,+} = \frac{(e^{2iS'a} - 1)}{(e^{2iS'a} + 1)}. \tag{101}$$

If only the first term in the denominator of Eq. (96) is used, the result reduces to that shown in the previous work (Pinfield *et al.*, 2005) in which the coefficient relates only to the density difference between the two phases. In that case, viscous effects were neglected so that only the effect of inertia is present in the $n=1$ (dipole) contribution. Here, the coefficient shows a contribution from both inertial and viscous effects, the relative magnitude of which is determined by the parameter Sa. For a given particle size, at low frequency (small Sa) the viscous effects dominate, whereas at high frequency (large Sa) the inertial terms are most important and the density difference becomes the only relevant parameter.

The ECAH method is not limited to the long-wavelength region in which $Ka \ll 1$, although the numerical calculation causes some difficulties. However, Epstein and Carhart (1953) did determine analytical solutions for the $n=0$ and $n=1$ coefficients which are valid in the limit $Ka \ll 1$ by considering the relative magnitude of the terms in the solution, and taking limiting forms of the functions. Our own solutions are equivalent to expanding the ECAH limiting solutions as series in powers of Ka and taking the first few terms,

TABLE I. Physical properties of n-hexadecane in water with 1% Tween20 at 20 °C (McClements and Coupland, 1996).

	Water+1% Tween20	n-hexadecane
Ultrasound velocity/m s^{-1}	1485.5	1357.9
Density/kg m^{-3}	999.5	773
Thermal expansivity/K^{-1}	0.000 22	0.000 91
Viscosity/Pa s	0.001 11	0.003 34
Specific heat capacity/J kg^{-1} K^{-1}	4182	2093
Thermal conductivity/W m^{-1} K^{-1}	0.59	0.14
Attenuation exponent p	2	2
Attenuation factor/Np m^{-1} MHz^{-p}	0.025	0.101

corresponding to the first orders in m. A full analytical comparison has not been carried out, but the numerical results shown in the next section show that the correspondence is accurate.

VI. NUMERICAL RESULTS

Numerical calculations have been carried out in MATLAB® for a model system of 20% (by volume) n-hexadecane in water at 20 °C with a particle diameter of 1 μm. The physical properties of the two components are given in Table I. The complete range of thermal and shear effects can be seen within the long-wavelength limit. Figures 1 and 2 show the velocity and attenuation as a function of frequency (by the parameter Ka) calculated by the ECAH method and the theoretical results presented here. Also shown are the results when viscous effects are neglected. Orders up to $n=2$ and $m=4$ were included, corresponding to effects in velocity and attenuation up to order $(Ka)^2$. Also shown are the results when shear effects are neglected.

The results for velocity and attenuation match closely those determined using the ECAH method up to around $Ka \sim 0.1$ as shown. Values of $|La|$ and $|Sa|$ are also shown on the plots, demonstrating that the most significant gradient in velocity and magnitude of attenuation occurs when either parameter is of order unity. At the limiting values of very small or very large $|La|$ or $|Sa|$ the velocity changes only slowly with frequency, and the attenuation is much lower. When $|Sa| \approx 1$ both inertial and viscous effects make a significant

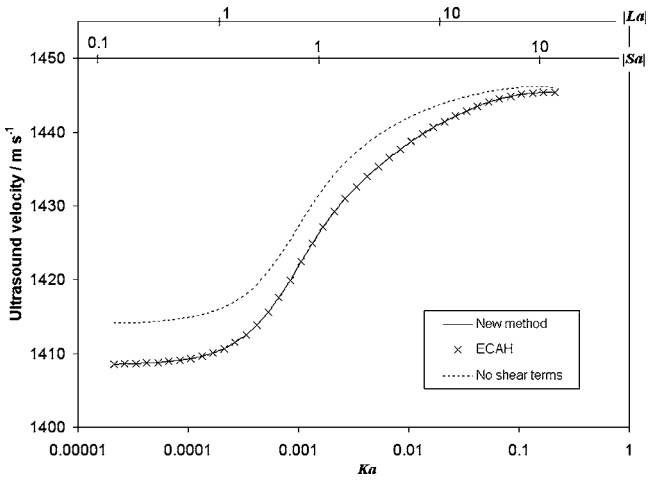

FIG. 1. Ultrasound velocity as a function of the parameter Ka for 20% hexadecane in water (with 1% Tween20) at 20 °C with a particle diameter of 1 μm. The new method is compared with the previous ECAH method (Epstein and Carhart, 1953) and in the absence of viscous/shear effects. The thermal parameter $|La|$ and shear parameter $|Sa|$ are shown above the plot. The parameters for the dispersed phase are $|L'a|=1.28|La|$, $|S'a|=0.52|Sa|$, and $K'a=1.09Ka$.

contribution and the attenuation is relatively high. Similarly the thermal scattering is greatest when the thermal wavelength is of similar order to the particle size ($|La| \approx 1$). In the case of water, $|La|$ and $|Sa|$ are of similar order to each other, causing both visco-inertial and thermal scattering to be significant in overlapping frequency ranges.

For the hexadecane in water system, shear effects make a significant contribution to the ultrasound velocity and attenuation, as can be seen in Figs. 1 and 2. In this case, the parameter $|Sa|$ is not applicable, since it tends to infinity, as the viscosity tends to zero. In the previous work (Pinfield *et al.*, 2005) a reasonable agreement was found with the ECAH method in spite of the neglect of viscous effects in that work. The system used for calculations in that case was sunflower oil in water emulsion, for which the density difference between the oil and water is small. The contribution of the visco-inertial scattering to velocity and attenuation is then much smaller. In the present case of a hexadecane in water dispersion, the density difference is much greater, and the visco-inertial effects are more significant.

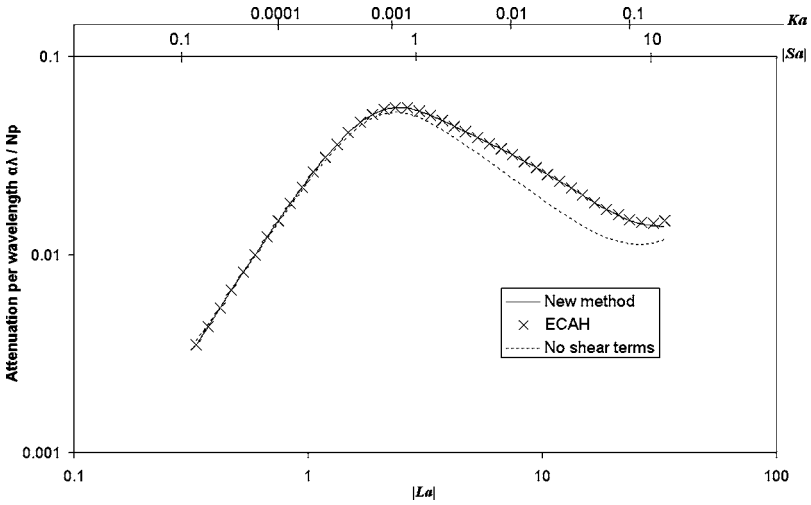

FIG. 2. Attenuation per wavelength as a function of the parameter $|La|$ for 20% hexadecane in water (with 1% Tween20) at 20 °C with a particle diameter of 1 μm. The new method is compared with the previous ECAH method (Epstein and Carhart, 1953) and in the absence of viscous/shear effects. The shear parameter $|Sa|$ scales in proportion to $|La|$ and is shown above the plot, along with the values of Ka. The parameters for the dispersed phase are $|L'a|=1.28|La|$, $|S'a|=0.52|Sa|$, and $K'a=1.09Ka$.

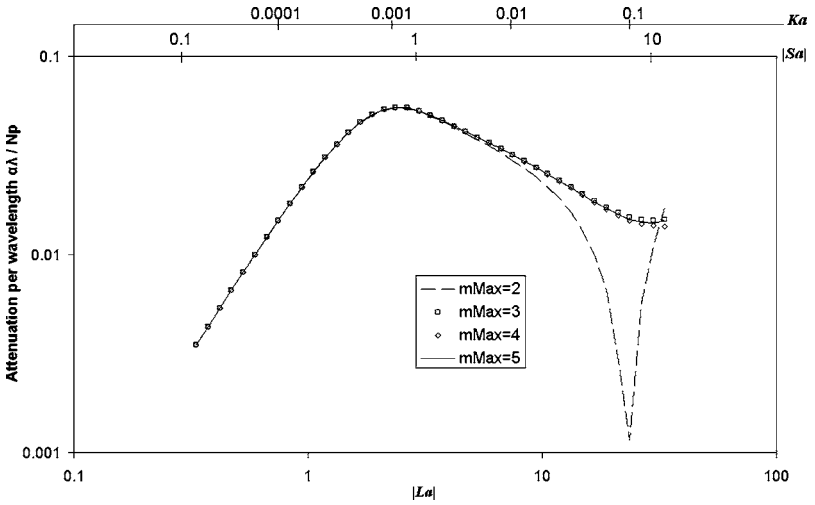

FIG. 3. Attenuation per wavelength as a function of the parameter $|La|$ for 20% hexadecane in water (with 1% Tween20) at 20 °C with a particle diameter of 1 μm. The plot shows the contribution of the first few orders in m, when the wave number is determined up to and including orders $n=2$. The shear parameter $|Sa|$ scales in proportion to $|La|$ and is shown above the plot, along with the values of Ka. The parameters for the dispersed phase are $|L'a|=1.28|La|$, $|S'a|=0.52|Sa|$, and $K'a=1.09Ka$.

Figures 1 and 2 show results calculated up to orders $n=2$ and $m=4$. These give good agreement with the ECAH method for $Ka \leqslant 0.1$. As Ka increases, higher order terms are needed to obtain an accurate result. Figure 3 shows the contribution of including these terms. The solution up to order $m=2$, corresponding to the zero order (in Ka) contribution to attenuation, is accurate for $Ka \leqslant 0.007$. However, at larger values of Ka, higher order terms must be included. The use of terms up to and including $m=4$, corresponding to terms in $(Ka)^2$ in attenuation produces a good result over a much wider range of values of Ka (within the condition $Ka \ll 1$).

VII. CONCLUSIONS

The method presented here enables the scattering properties of a spherical object to be calculated in the long-wavelength region, including the effects of heat fluctuations and viscous effects. The system configuration is identical to that solved by Epstein and Carhart (1953) and Allegra and Hawley (1972). However, the new method avoids the numerical problems associated with that well-established ECAH solution which uses Rayleigh expansions for the wave potentials and spherical Bessel and Hankel functions. These functions are difficult to calculate for large arguments and the matrix equation for the boundary conditions was numerically badly conditioned.

The results consist of a ladder of coefficients for each partial wave order, which when summed lead to the far-field scattering coefficient for that order. Recurrence relations [Eqs. (27) and (36)], followed by solution to the thermal boundary Eqs. (76) and (77) and then a matrix solution (81)–(83) produce coefficients which are then combined using Eq. (87) to obtain the far-field coefficient. This solution completes the application of Kleinman's method (Kleinman, 1965) to the acoustic scattering case, including thermal and shear effects. While this approach may appear more complicated than a direct solution to the boundary equations as in the ECAH method, it produces a numerically stable method, with no need for Bessel functions or a high-precision matrix inversion. The lowest partial wave orders can be obtained analytically as shown in Sec. V G and in fact in the long-wavelength region only the lowest orders are significant. These solutions are equivalent to a series expansion in Ka of the analytical results obtained by ECAH in the long-wavelength region. Although this has not been proven analytically, the numerical results demonstrate an accurate correspondence.

Although the results presented here can already be obtained by the ECAH solution, the new method was developed for several reasons. First, it was required to overcome the numerical difficulties with the ECAH solution, as has been stated. In addition, a more general method was sought to allow alternative particle shapes to be studied. At the current stage, the scattering potentials still use the partial wave expansions and a spherical particle shape, but future work may enable other shapes to be analyzed within this alternative approach. Kleinman (1965) developed his method in part to allow alternative shapes to be analyzed, without the requirement for special functions describing their geometry. His method was applied to single potential, whereas in the acoustical case propagational, thermal, and shear modes must be considered. A final intention of the development was to look at the problem of multiple scattering, having established a solution technique which would lend itself to the study of scattering at multiple centres. These items of study have yet to be achieved.

ACKNOWLEDGMENT

The research was supported by the U.K. Engineering and Physical Sciences Research Council (EPSRC), Grant GR/L/51034.

APPENDIX

For the incident field expansion in powers of Ka the function

$$F_n(s) = \frac{2^n(2n+1)(s+n)!}{s!(2s+2n+1)!} \tag{A1}$$

is used. In numerical calculations, the factorial functions suffer from overflow for all but very low orders (n,s). The

following recurrence relations can be used for accurate calculation:

$$F_0(0) = 1,$$

$$\frac{F_n(0)}{F_{n-1}(0)} = \frac{1}{(2n-1)} \text{ for } n \geqslant 1,$$

$$\frac{F_n(s)}{F_n(s-1)} = \frac{1}{2s(2n+2s+1)} \text{ for } s \geqslant 1. \tag{A2}$$

The thermal and shear wave solutions use expansions of the spherical Bessel functions which are not generally found in mathematical texts. The coefficients can be calculated for the order n by the formula below.

For the spherical Hankel function,

$$h_n(x) = e^{ix}\sum_{j=1}^{n+1} \frac{h_{nj}}{x^j}, \tag{A3}$$

$$h_{01} = -i \text{ for } n = 0,$$

for $n > 0$

$$h_{n,j} = \begin{cases} -ih_{n-1,j} & \text{for } j = 1 \\ -ih_{n-1,j} + (n+j-2)h_{n-1,j-1} & \text{for } 1 < j < n+1 \\ (2n-1)h_{n-1,j-1} & \text{for } j = n+1. \end{cases} \tag{A4}$$

Similarly, for the spherical Bessel function, this is defined in two parts, an outgoing and an ingoing traveling wave,

$$j_n(x) = e^{ix}\sum_{l=1}^{n+1} \frac{j_{nl+}}{x^l} - e^{-ix}\sum_{l=1}^{n+1} \frac{j_{nl-}}{x^l}, \tag{A5}$$

$j_{0,1+} = 1/2\text{i}$ for $n = 0$,

for $n > 0$

$$j_{n,l+} = \begin{cases} -ij_{n-1,l+} & \text{for } l = 1, \\ -ij_{n-1,l+} + (n+l-2)j_{n-1,l-1+} & \text{for } 1 < l < n+1, \\ (2n-1)j_{n-1,l-1+} & \text{for } l = n+1. \end{cases} \tag{A6}$$

$j_{0,1-} = 1/2i$ for $n = 0$,

for $n > 0$

$$j_{n,l-} = \begin{cases} ij_{n-1,l-} & \text{for } l = 1, \\ ij_{n-1,l-} + (n+l\text{-}2)j_{n-1,l-1-} & \text{for } 1 < l < n+1, \\ (2n-1)j_{n-1,l-1-} & \text{for } l = n+1. \end{cases} \tag{A7}$$

Allegra, J. R., and Hawley, S. A. (**1972**). "Attenuation of sound in suspensions and emulsions: Theory and experiments," J. Acoust. Soc. Am. **51**, 1545–1564.

Challis, R. E., Povey, M. J. W., Mather, M. L., and Holmes, A. K. (**2005**). "Ultrasound techniques for characterizing colloidal dispersions," Rep. Prog. Phys. **68**, 1541–1637.

Colton, D., and Kress, R. (**1988**). *Inverse Acoustic and Electromagnetic Scattering Theory*, 2nd ed. (Springer, Berlin).

Epstein, P. S., and Carhart, R. R. (**1953**). "The absorption of sound in suspensions and emulsions. I. Water fog in air," J. Acoust. Soc. Am. **25**, 553–565.

Fikioris, J. G., and Waterman, P. C. (**1964**). "Multiple scattering of waves. II. 'Hole correction' in the scalar case," J. Math. Phys. **5**, 1413–1420.

Harlen, O. G., Holmes, M. J., Povey, M. J. W., Qiu, Y., and Sleeman, B. D. (**2001**). "A low frequency potential scattering description of acoustic propagation in dispersions," SIAM J. Appl. Math. **61**, 1906–1931.

Harlen, O. G., Holmes, M. J., Povey, M. J. W., and Sleeman, B. D. (**2003**). "Acoustic propagation in dispersions and the geometric theory of diffraction," SIAM J. Appl. Math. **63**, 834–849.

Kleinman, R. E. (**1965**). "The Dirichlet problem for the Helmholtz equation," Arch. Ration. Mech. Anal. **18**, 205–229.

Lloyd, P., and Berry, M. V. (**1967**). "Wave propagation through an assembly of spheres. IV. Relations between different multiple scattering theories," Proc. Phys. Soc. London **91**, 678–688.

McClements, D. J., and Coupland, J. N. (**1996**). "Theory of droplet size distribution measurements in emulsions using ultrasonic spectroscopy," Colloids Surf., A **117**, 161–170.

O'Neill, T. J., Tebbutt, J. S., and Challis, R. E. (**2001**). "Convergence criteria for scattering models of ultrasonic wave propagation in suspensions of particles," IEEE Trans. Ultrason. Ferroelectr. Freq. Control **48**, 419–424.

Pinfield, V. J., Harlen, O. G., Povey, M. J. W., and Sleeman, B. D., (**2006**). "Acoustic propagation in dispersions in the long wavelength limit," SIAM J. Appl. Math., **66**, 489–509.

Povey, M. J. W. (**1997**). *Ultrasonic Techniques for Fluids Characterization* (Academic, San Diego).

Strutt, J. W. (Baron Rayleigh) (**1896**). *The Theory of Sound*, 2nd ed. (Macmillan, London).

Waterman, P. C., and Truell, R. (**1961**). "Multiple scattering of waves," J. Math. Phys. **2**, 512–537.

Surface wave modes in rails

D. Hesse and P. Cawley
Department of Mechanical Engineering, Imperial College London, London SW7 2AZ, United Kingdom

(Received 9 December 2005; revised 10 May 2006; accepted 15 May 2006)

Rail breaks caused by rolling contact fatigue defects are of growing concern to the railway industry. Very often critical defects cannot be detected reliably by conventional inspection methods. Low-frequency surface waves with a high penetration depth have the potential to overcome such difficulties. In this paper, the properties of surface wave modes in both new and worn rails are investigated and the implications for rail inspection are discussed. The dispersion curves of the dominant surface wave modes were determined up to a frequency of 350 kHz using a finite element model and show excellent agreement with experimental data. One surface wave mode was identified to be nondispersive and not significantly affected by cross-section changes due to wear at frequencies above 180 kHz. It exhibits a relatively homogeneous energy distribution in the upper half of the rail head and is therefore suitable for inspection purposes. The problem is that there exist several other surface modes with very similar propagation properties. The interference of these multiple modes, which may be generated either directly by the exciter or by mode conversion at defects, means that the received amplitude is position dependent. For this reason, accurate defect sizing will be difficult. [DOI: 10.1121/1.2211587]

PACS number(s): 43.35.Zc, 43.35.Cg, 43.40.Le [YHB] Pages: 733–740

I. INTRODUCTION

A major challenge for the maintenance of modern railways is the detection of critical surface cracks on the running surface of rails. Such defects are mainly induced by rolling contact fatigue (RCF), which has become a growing concern because of high traffic loads and increasing train speeds. In the recent past, rail breaks caused by RCF defects have led to severe or even fatal train accidents, such as the one in Hatfield (UK) in 2000.[1] Conventional inspection methods have proven not to be reliable enough in this context, which means that there is an urgent need for an alternative screening tool to detect critical defects in time. A promising candidate for this is the application of surface waves. They offer a high sensitivity to defects on or below the running surface of rails and allow screening of several meters of rail from a single inspection position.

Early publications on surface waves used on rails date back to the 1970s and focused on the high-frequency regime. Hall[2] performed time-of-flight measurements during fatigue testing (at 4.2 MHz) and Bray *et al.* investigated rail stress measurements[3,4] (at 0.5–2.0 MHz). However, the small penetration depth and therefore extremely high surface sensitivity of high-frequency surface waves used in time-of-flight measurements is a problem in the context of rail testing. The high density of features on the rail surface such as shallow RCF cracks would render the discrimination between critical (typically deeper than 5 mm) and noncritical defects impossible.

A better alternative are amplitude measurements of low-frequency surface waves with a high penetration depth and a reduced sensitivity to noncritical features at the rail surface. Recent publications tend to use such lower frequencies, sometimes as a result of the chosen excitation method. Broadband laser generation was utilized by Kenderian *et al.* (between 300 kHz and 2 MHz)[5] and Lanza di Scalea *et al.* (between 100 and 900 kHz)[6]. Dixon and co-workers used electromagnetic acoustic transducers (EMATs) for surface wave excitation in rails at frequencies between 150 and 500 kHz.[7,8] The authors of this paper investigated the excitation of surface waves in rails at frequencies around 200–250 kHz using a local immersion probe.[9,10] The frequency range was chosen to achieve a penetration depth into the rail of at least 10 mm. This is crucial to detect critical defects and distinguish them from shallow tolerable ones. It is in fact desirable to reduce the frequency even further and maximize the penetration depth, but to keep it above the frequency range where dispersion occurs. The wave length of such low-frequency surface waves is of the same order of magnitude as some radii of the rail curvature so that their character as guided waves has to be taken into account. Surface waves on various other types of waveguides have been extensively investigated in the context of surface acoustic wave (SAW) devices (see, for example, Refs. 11–15). However, these studies cannot be directly applied to establish a frequency range for low-frequency surface wave inspection of rails. Furthermore, knowledge about similar wave modes is vital to overcome multiple-mode excitation and interference problems which the authors reported in previous publications.[9,10] Complex signals caused by interference can lead to wrong interpretation when considered as a single Rayleigh wave arrival rather than a superposition of multiple surface wave modes. This issue has not been addressed in other publications on surface waves in rails. Finally, it is necessary to determine how the propagation and the mode shapes are affected by cross-section changes due to wear. In this paper, we therefore investigate the characteristics of surface modes in rails in detail and discuss the implications for rail inspection.

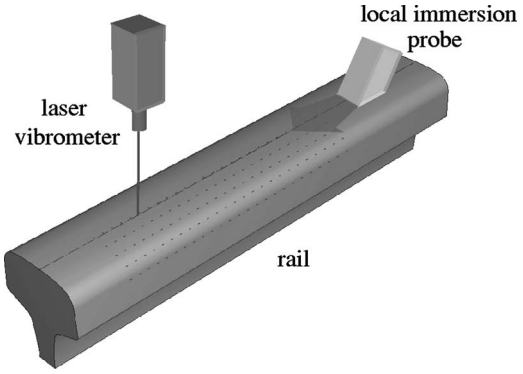

FIG. 1. Experimental setup for studying surface wave propagation in rail (only rail head and top of web shown).

II. THE PROBLEM OF MULTIPLE MODE EXCITATION

The concurrent existence of multiple surface wave modes in rails and their interfering behavior can be demonstrated with a very simple experiment. The idea is to excite surface waves using a standard setup and monitor the wave amplitude during propagation along the rail.

In our experimental setup, a local immersion probe angled at the Rayleigh wave angle (30°) was located centrally on the top surface of a BS113A type rail (see Fig. 1). The probe consisted of an immersion transducer with a center frequency of 250 kHz fixed in an aluminium casing which was filled with water. A coating of attenuative rubber dampened reverberations inside the casing. The water channel of the probe was sealed at the bottom with a rubber contact patch which matched the impedance of water, thus allowing easy handling of the probe. A few drops of water were sufficient to ensure good coupling between the 20-mm-wide, 25-mm-long contact patch and the rail surface. All measurements were carried out using a five-cycle Hanning windowed tone burst with a center frequency of 250 kHz. The excited and scattered wave fields in the rail were determined by moving a single-point laser vibrometer to different positions along the centerline of the rail and measuring the velocity component normal to the rail surface.

In Fig. 2 the maximum of the signal envelope as measured with the vibrometer is presented as a function of the distance between the probe and the vibrometer position. For

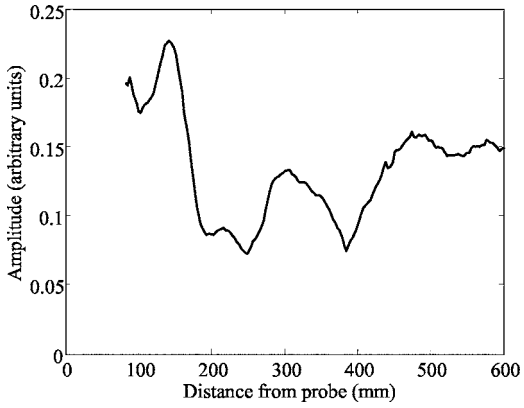

FIG. 2. Maximum of surface wave envelope as a function of the distance between probe and vibrometer.

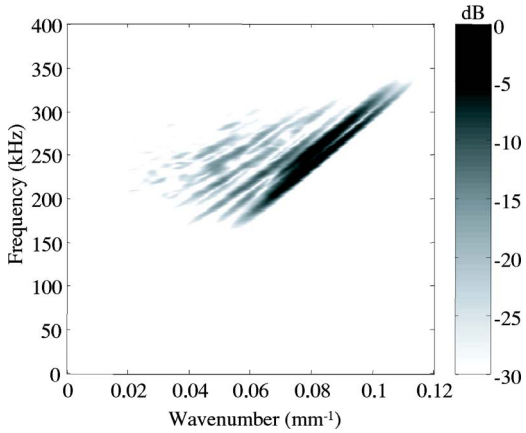

FIG. 3. Normalized modulus of 2D-FFT performed on centerline scan.

the single arrival of a Rayleigh wave one would expect the amplitude to decay gradually due to beam spreading. However, it is evident that in this case the amplitude of the signal is heavily modulated. Since the number of measurement points was very large (about 180) and the modulation is very consistent, the latter has to be caused by the interference of multiple wave modes rather than random noise. Different modes will have slightly different wavelengths and velocities and therefore cause the observed irregular pattern of constructive and destructive interference.

This was confirmed further by applying a two-dimensional fast Fourier transform (2D-FFT) to the data obtained from the vibrometer scan. (The 2D-FFT was carried out on the raw RF data, rather than the envelope shown in Fig. 2.) The normalized modulus of the result is plotted as a grayscale against wave number and frequency in Fig. 3. The gray patches correspond to different modes which are present in the signal and exhibit different dispersion relations between wave number and frequency. Due to resolution limits the regions overlap, so that it is not clear exactly how many modes are present.

The results clearly illustrate that the Rayleigh wave probe excited a large number of modes in the rail with different phase and group velocities, which explains the interference phenomenon of Fig. 2. Thus, any surface wave arrival at such low frequencies can potentially be an interfering group of guided wave modes in the rail cross section, rather than a single Rayleigh wave.

III. IDENTIFICATION OF SURFACE WAVE MODES

Having established the fact of multiple mode excitation, it was necessary to identify the mode shapes and dispersion curves of the relevant surface wave modes. These characteristics provide crucial information for choosing guided wave modes suitable for inspection purposes and optimizing their excitation.

A. Dispersion curves of guided wave modes in rails

The exact analytical analysis of wave propagation characteristics is only possible for wave guides with simple cross sections such as cylinders,[16] ellipses,[17] and rectangles with certain ratios of width to depth.[18] Under certain conditions it

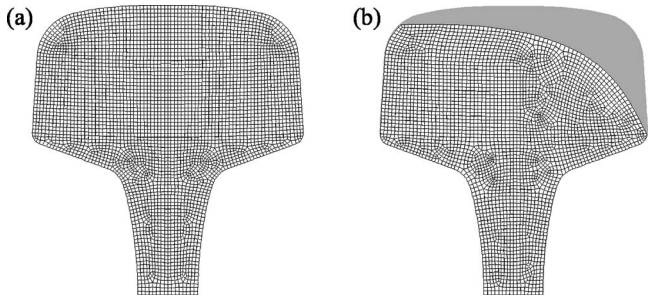

FIG. 4. Finite element meshes for generation of dispersion curves and mode shapes: (a) new rail and (b) extremely worn rail (gray area indicates removed part of cross section).

is possible to develop asymptotic analytical solutions for rods of arbitrary cross section, for example for short-wavelength high-frequency surface waves[14,15,19–22] and long-wavelength low-frequency waves.[19] However, in order to obtain dispersion curves over a wide range of frequencies and wave numbers, it is necessary to use numerical methods. Nigro[23] utilized the variational method of Ritz for bars with rectangular cross section. Fraser[24,25] obtained dispersion curves for bars with rectangular and elliptical cross section using the method of collocation. Elliptical and truncated elliptical cross sections were investigated by Nagaya[26] using a Fourier expansion collocation method. Lagasse[11] developed a semi-analytical finite element (FE) technique to calculate dispersion curves for topographic wave guides of arbitrary cross section used for SAW devices. Recently, an alternative approach for guided wave modes in bars using boundary element analysis was presented by Gunawan and Hirose.[27]

Gavrić was the first to employ a FE method to calculate dispersion curves and mode shapes for rails (up to a frequency of 6 kHz).[28] This method was adapted by Wilcox *et al.* for the use of standard FE software[29] and applied to rails for frequencies up to 50 kHz.[30] Similar FE methods were proposed for example by Gry,[31] Hayashi *et al.*,[32,33] and Damljanović and Weaver,[34] the latter even allowing for nonpropagating modes. Bartoli *et al.*[35] extended the semi-analytical FE technique to allow for viscoelastic material damping and applied it to rails. In all these publications, guided wave propagation in rails has been analyzed at relatively low frequencies ($\leqslant$100 kHz) and surface wave modes have not been discussed.

In this work, the method described by Wilcox *et al.*[29] is applied. Its basic concept is to consider a ring with very large diameter instead of a straight waveguide. This can be modeled using only a two-dimensional (2D) mesh and boundary conditions for cyclic symmetry which are often provided by standard FE software (in this case FINEL/FE77[36]). For a given cyclic order, the code generates a chosen number of eigenfrequencies and eigenvectors. The cyclic order corresponds to the number of wavelengths of a guided wave mode around the ring, with the eigenvector being its displacement distribution or mode shape at the corresponding (eigen-) frequency.

We considered cross sections of both new and extremely worn UIC60/CEN60E1 rails (see Fig. 4). The worn rail was assumed to have 5-mm vertical head loss and 9-mm lateral head loss at the gauge corner (measured 14 mm below the crown of the rail), which is close to the tolerated limits in the UK.[37] For the correct computation of mode shapes at higher frequencies it was necessary to set up fairly fine FE meshes. They consisted of about 4100 (3300 for the worn rail) linear four-node elements with a side length of approximately 1 mm. In order to overcome computer memory limitations, reduce computation time, and avoid solutions that are not relevant for railhead inspection (e.g., modes that are confined to the rail foot) only the upper half of the rail cross section has been modeled (see Fig. 4). As long as the strain energy density of a mode is negligibly low at this artificially introduced boundary, the mode shape and propagation characteristics can be considered identical to that of the full rail section.

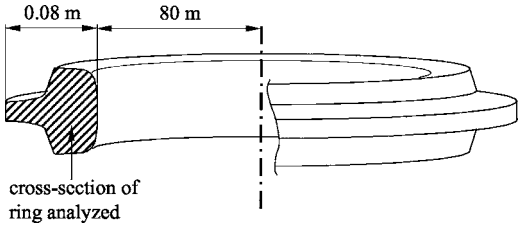

FIG. 5. Modeling of the rail waveguide as a ring with large radius (dimensions not to scale).

In order to avoid slightly asymmetric mode shapes at low frequencies due to curvature effects, we chose the symmetry axis of the ring to be perpendicular to the symmetry axis of the rail section (see Fig. 5). Restrictions in the FE software limited the model radius to 80 m, which is 100 times larger than the width of the ring cross section. Concerns regarding unwanted effects of curvature on the mode shapes are addressed in the Appendix, where it is shown that the results are not affected at all above 120 kHz.

Figure 6 shows the dispersion curves for the first 100 propagating modes of the new rail model [Fig. 4(a)], the highest cutoff frequency being at about 180 kHz. Not all these modes are relevant in the context of railhead inspection, therefore we discuss the extraction of relevant surface wave modes in the following section.

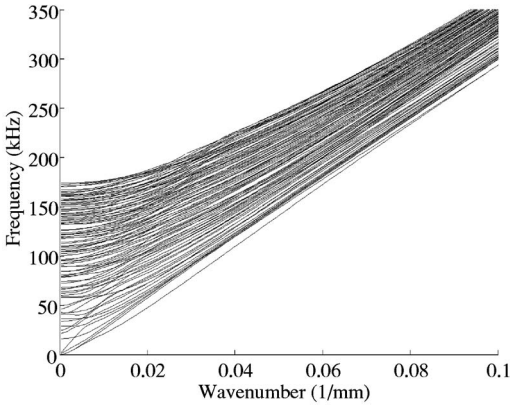

FIG. 6. Dispersion curves of the first 100 propagating modes of the FE model for the new rail.

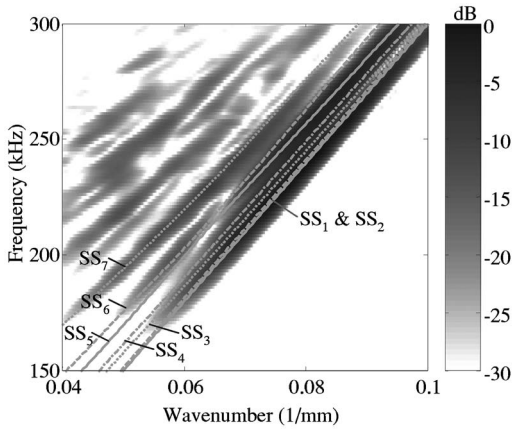

FIG. 7. Dispersion curves of the seven most significant symmetric surface modes superimposed on 2D-FFT of experimental data (magnified section of Fig. 3).

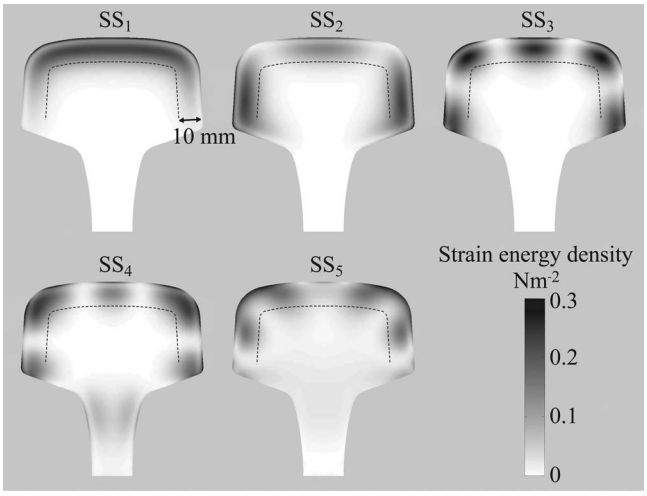

FIG. 8. Strain energy density of selected symmetric modes at 200 kHz.

B. Extraction of relevant surface wave modes

Surface wave modes can be identified within the large number of possible guided wave modes by comparing how efficiently they are excited by a probe located on the surface. Since the local immersion probe described in Sec. II applies a symmetric stress field normal to the rail surface, a reasonable first approximation for such a source is a single point force normal to the center of the rail surface. In that case, the normal displacement at the excitation point is proportional to the applied force. According to Wilcox *et al.*,[29,38] the proportionality factor can be defined as the excitability E:

$$E \propto u^2 f, \tag{1}$$

where f is the frequency and u is the displacement in the power normalized displacement mode shape at the location and direction of the applied force.

By calculating excitability values for all modes over a range of frequencies (here between 190 and 300 kHz) and comparing their maximum values, the seven most significant symmetric surface wave modes of the new rail section [Fig. 4(a)] were identified. ("Symmetric" refers to the vertical displacement field being symmetric with respect to the plane of symmetry of the cross section.) For simplicity they will be referred to in the following as SS_i $(i=1,\ldots,7)$.

The same procedure was applied to identify antisymmetric surface modes (AS_i) of the new rail, based on excitability values for a single point force 10 mm off the center line, and the surface modes WS_i of the worn rail [cross section shown in Fig. 4(b)].

C. Comparison of dispersion curves with experiment

To verify the modeling and surface wave mode extraction procedure, we superimposed the dispersion curves of SS_i $(i=1,\ldots,7)$ on the experimental data presented before (see Fig. 3). As Fig. 7 shows, the dispersion curves match very well the gray areas of the 2D-FFT, thus confirming the validity of the model and the identified modes. The dispersion curves of SS_1 to SS_4 are located close together within the dominant region in the 2D-FFT plot. Their influence cannot be separated due to resolution limits but they all seem to be significantly present in the excited signal. SS_5 appears to be present at frequencies above about 220 kHz, SS_6 mainly below that frequency, whereas SS_7 contributes over the whole bandwidth of the excitation signal. The additional gray areas in the 2D-FFT plot correspond to higher order modes. Since standard material properties have been assumed in the FE model, there is a slight mismatch to the rail steel properties in the experiment. For this reason, the group velocity of all surface modes shown, i.e., the slope of their dispersion curves in Fig. 7, appears to be marginally (about 1%) different from the experimental 2D-FFT data.

IV. STRAIN ENERGY DISTRIBUTIONS AND GROUP VELOCITIES OF SURFACE WAVE MODES

In order to assess the suitability of the identified surface wave modes for inspection purposes, it is necessary to analyze their strain energy densities and group velocity dispersion curves. The average strain energy density u_S allows us to determine in which areas of the cross section a mode is likely to have a high sensitivity to defects. It is defined as

$$u_S = \tfrac{1}{4}\mathbf{S}^*:\mathbf{c}:\mathbf{S}, \tag{2}$$

where $\mathbf{S}$ is the strain tensor and $\mathbf{c}$ is the stiffness tensor.

Figure 8 shows the strain energy density distributions

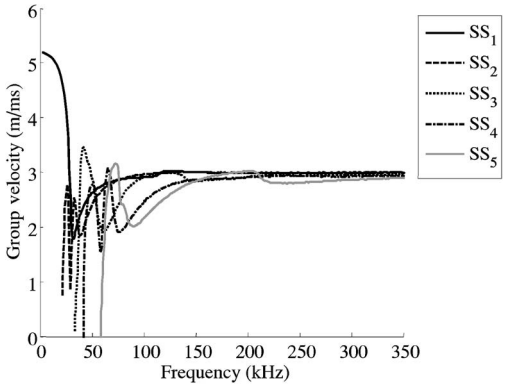

FIG. 9. Group velocity dispersion curves of the five most significant symmetric surface modes.

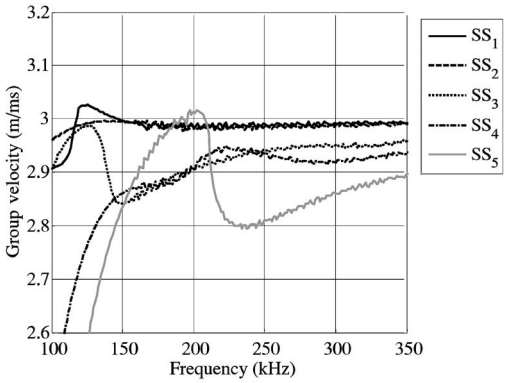

FIG. 10. Magnified section of Fig. 9, group velocity dispersion curves of the five most significant symmetric surface modes.

for the power normalized mode shapes of the symmetric modes SS_1 to SS_5 at a frequency of 200 kHz. The strain energy density at the bottom of the half rail sections shown is negligibly small. It can therefore be assumed that the mode shapes are identical to those of a full rail section. A penetration depth of at least 10 mm was desirable in order to obtain an increasing reflection coefficient with defect depth up to a depth of about 10 mm; this depth is shown in all the plots by a dashed line. All modes shown are confined to a region below about this depth, but they exhibit a different number of nodes and antinodes around the perimeter, with SS_1 being the lowest order mode. The energy density distribution normal to the surface is similar to that of a pure Rayleigh wave: the maximum value can be found at the surface (or "skin") and a second peak is located at a depth of about half the wavelength. Since the strain energy density of mode SS_1 is evenly distributed along the surface, it is best suited for inspection purposes.

The group velocities of SS_1 to SS_5 converge towards the Rayleigh wave velocity of about 3 m/ms at high frequencies, as can be seen in Fig. 9. However, the magnified plot in Fig. 10 of the frequency range between 100 and 350 kHz reveals a more complex situation. The group velocities of SS_1 and SS_2 converge to the same value of about 2990 m/s at around 150 kHz and stay essentially constant at frequencies higher than that, i.e., they are nondispersive. The dispersion curves of SS_3 and SS_4 are very similar and rise fairly

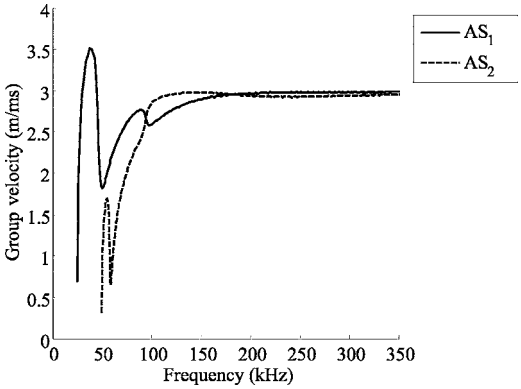

FIG. 11. Group velocity dispersion curves of the two most significant antisymmetric surface modes.

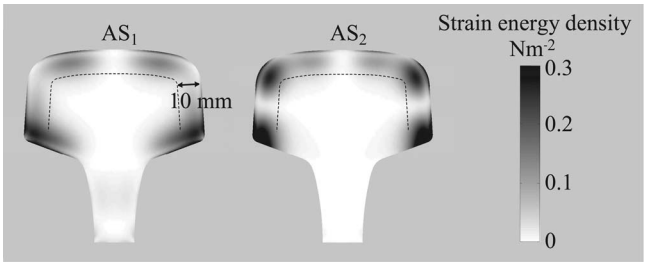

FIG. 12. Strain energy density of selected antisymmetric modes at 200 kHz.

monotonically from 150 kHz onwards. At 200 kHz their group velocity is still about 3% lower than that of SS_1 and SS_2 which reduces to about 1.5% at 350 kHz. The group velocity of SS_5 reaches a value of about 3 m/ms at 200 kHz, then drops to 2.8 m/ms around 230 kHz and converges towards the Rayleigh wave velocity even more slowly than SS_3 and SS_4. Note that the noise in the magnified dispersion curves is an artifact from the calculation of the group velocity.

The group velocities of the two most significant antisymmetric surface wave modes AS_1 and AS_2 converge to the Rayleigh wave velocity at high frequencies, too (see Fig. 11). It was found that the higher order modes are highly dispersive and are therefore not suitable for inspection purposes.

The strain energy density distributions of the two most significant antisymmetric modes are shown in Fig. 12. As expected, both AS_1 and AS_2 exhibit significant strain energy density towards the rail head corners, rather than along the symmetry axis of the cross section. Unfortunately, the strain energy density of both modes is high at the bottom corners of the rail head and fairly low close to the running surface. Therefore these modes do not seem very suitable for inspection purposes. However, they may be generated by mode conversion at defects and thus could interfere with symmetric mode signals.

An important issue for the use of surface wave modes as an inspection tool is the effect of cross-section changes due to wear on mode shapes and velocities. We therefore analyzed the cross section shown in Fig. 4(b) as a worst case scenario and matched up the extracted modes with those from the new rail. Figure 13 shows the strain energy distributions of the two most dominant surface modes in the worn rail for normal excitation on the center of the rail head. It is obvious that the mode denoted WS_1 is equivalent to the symmetric mode SS_1 in the new rail, whereas WS_2 corresponds to SS_3 (see Fig. 8 for comparison). Compared to SS_1, the

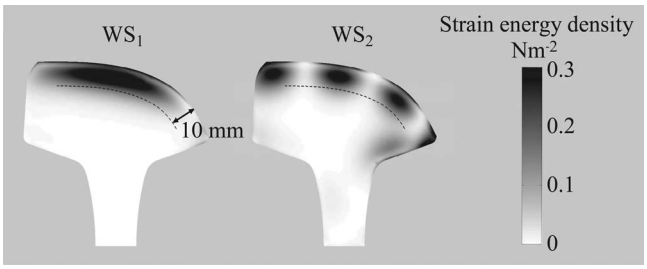

FIG. 13. Strain energy density of selected modes of an extremely worn rail at 200 kHz.

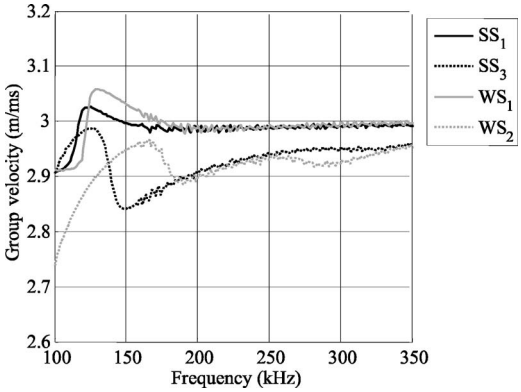

FIG. 14. Group velocity dispersion curves of the two most significant surface modes of the worn rail in comparison to the symmetric modes SS_1 and SS_3.

strain energy density of WS_1 is slightly more concentrated in the center of the railhead and decays marginally more towards the sides. However, despite the substantial change of cross section, there does not seem to be a significant qualitative difference between WS_1 and SS_1 in terms of sensitivity to defects in the gauge corner. The comparison of the dispersion curves of the corresponding modes in Fig. 14 shows that the group velocities of SS_1 and WS_1 are virtually identical above a frequency of about 180 kHz. This confirms the suitability of SS_1/WS_1 for inspection purposes.

The smaller radii of curvature of the analyzed worn rail section also support many other surface modes which are strongly confined to these corners. Such modes have been extensively discussed in the context of topographic wave guides for SAW devices (see, for example, Refs. 12, 13, and 15). However, they are not suitable for inspection purposes since they do not cover the cross-section area of interest and would depend strongly on the amount of wear.

V. DISCUSSION AND CONCLUSIONS

In this paper, we investigated the properties of surface wave modes in rails. The main aim was to determine the low-frequency limit at which there exists a nondispersive surface mode with a high penetration depth suitable for inspection purposes. Additionally, information on other surface modes with similar propagation is needed in order to avoid multiple mode excitation which can lead to wrong signal interpretation. We illustrated this issue using a relatively simple experiment and showed that signal arrivals at low frequencies around 250 kHz typically consist of a large number of concurrent interfering guided wave modes rather than a single Rayleigh wave as commonly assumed in other publications. We determined their dispersion curves using axisymmetric FE models for new and worn rail sections up to a frequency of 350 kHz and extracted the relevant symmetric and antisymmetric surface wave modes using excitability considerations. The dispersion curves showed excellent agreement with the 2D-FFT of the experimental data so that we can confidently assume that the reduced cross-section model of the rail head used here is a sufficiently accurate representation of a real rail.

It was found that the symmetric mode SS_1 has promising characteristics for inspection purposes, since it has an evenly distributed strain energy distribution at the surface and is essentially nondispersive. It maintains these qualities down to frequencies as low as 180 kHz, even if the rail is heavily worn. It appears therefore that this is the low-frequency limit at which a maximum penetration depth of the surface mode can be achieved without dispersion.

However, it will be a challenging task to separate SS_1 from the large number of other surface wave modes with very similar propagation characteristics, all of which are excitable from the railhead surface. Most of them are slightly or considerably dispersive, but at least one mode (SS_2) has the same group velocity as SS_1, thus making mode separation extremely difficult. Even if only one mode is excited, others will be generated by mode conversion at defects and all the modes will interfere, thus making the received amplitude position dependent, as shown in Fig. 2. The detection of critical defects seems therefore feasible, but defect sizing will be very difficult.

ACKNOWLEDGMENT

This project is funded by the EPSRC, UK.

APPENDIX: MODE SHAPE VERIFICATION USING FEM SIMULATIONS

As described in Sec. III A, the guided wave modes were obtained from an axisymmetric FE model which represents the rail as a curved rather than a straight waveguide. It was therefore necessary to verify that the model radius had been chosen to be large enough and thus the effect of curvature on the computed mode shapes is negligible. Since the effect would be significant only at high wavelength-to-radius ratios, it was only necessary to establish a low-frequency limit. For this purpose, the propagation of a pure surface wave mode was initiated and monitored in a three-dimensional straight FE model of the railhead using the mode shapes from the axisymmetric model.

A very efficient way to excite a pure mode in a FE model of a wave guide is to apply an appropriate displacement input at all nodes of the front cross section. However, since a tone burst signal has a finite frequency bandwidth, the change of the mode shape with frequency as well as position in the cross section has to be taken into account at each excitation node.[39] This so-called "exact mode shapes"[40] technique consists of three steps. First, a discretized frequency spectrum of the desired excitation waveform is calculated using a discrete Fourier transform. For all frequencies with significant amplitudes the power normalized displacement profiles (mode shapes) have to be available. Second, the frequency components of the signal are multiplied by the appropriate displacement profiles and finally summed up, thus generating a frequency spectrum for all three spatial directions at each node of the waveguide cross section. Third, an inverse Fourier transform is performed on all spectra to obtain time domain signals for each excitation node which can be applied as input displacement-time functions in the FE model.

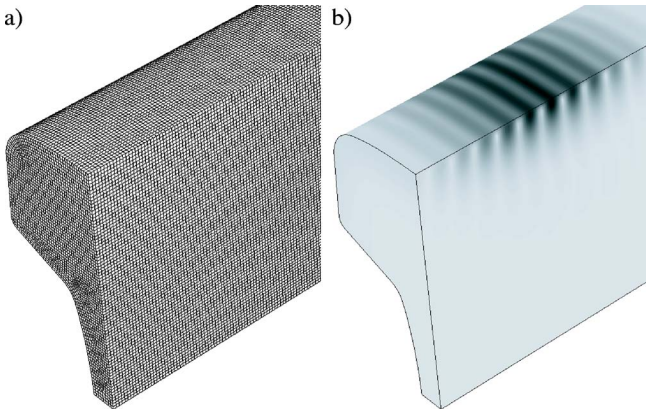

FIG. 15. Exact mode shape excitation of symmetric surface wave mode SS_1. (a) Mesh of FE model. (b) Snapshot of FE simulation after a propagation time of 40 μs. Displacement magnitude in linear gray scale (dark: maximum, light: zero).

The model was set up in the FE package ABAQUS utilizing its time marching "Explicit" solver and linear eight-node brick elements. Since we wanted to study the propagation of a symmetric mode, only half of a 400-mm-long railhead section was modeled and appropriate symmetry conditions were applied [see Fig. 15(a)]. The cross-section meshing was very similar to the one utilized in the axisymmetric 2D model presented above (see Fig. 4) with an element size of approximately 1 mm. For the excitation signal we used a Gaussian windowed tone burst at a center frequency of 200 kHz with a bandwidth of 20%, which has significant amplitude contributions (>-40 dB) between 120 and 280 kHz. As opposed to a Hanning windowed tone burst, this has the advantage of not exhibiting any side lobes in the frequency domain and therefore manipulation of only a limited bandwidth for the exact mode shape excitation does not introduce significant errors.

Figure 15(b) shows a snapshot of the model after a propagation time of 40 μs with the displacement magnitude plotted as a linear grayscale. The form of the displacement is very similar to the input with no sign of interference from other modes developing. The maximum signal envelope of the vertical displacement was monitored along the top edge of the symmetry plane and found to be constant within $\pm 2\%$. This confirms that the mode shapes generated with the axisymmetric model are not significantly affected by the curvature for frequencies above 120 kHz and can therefore be considered identical to those of a straight waveguide.

[1]Health & Safety Executive, UK, "Train derailment at Hatfield - 17 October 2000, Second HSE Interim report" (2001).
[2]K. G. Hall, "Crack depth measurement in rail steel by Rayleigh waves aided by photoelastic visualization," Non-Destruct. Testing **9**, 121–126 (1976).
[3]D. M. Egle and D. E. Bray, "Measurement of acoustoelastic and third-order elastic constants for rail steel," J. Acoust. Soc. Am. **60**, 741–744 (1976).
[4]D. E. Bray, M. E. Davis, and L. Reiter, "Rayleigh wave dispersion in the cold-worked layer of used railroad rail," J. Acoust. Soc. Am. **64**, 845–851 (1978).
[5]S. Kenderian, B. B. Djordjevic, and R. E. Green, "Sensitivity of point- and line-source laser-generated acoustic wave to surface flaws," IEEE Trans. Ultrason. Ferroelectr. Freq. Control **50**, 1057–1064 (2003).
[6]F. Lanza di Scalea, P. Rizzo, S. Coccia, I. Bartoli, M. Fateh, E. Viola, and G. Pascale, "Non-contact ultrasonic inspection of rails and signal processing for automatic defect detection and classification," Insight **47**, 346–353 (2005).
[7]S. Dixon and S. B. Palmer, "Wideband low frequency generation and detection of Lamb and Rayleigh waves using electromagnetic acoustic transducers (EMATs)," Ultrasonics **42**, 1129–1136 (2004).
[8]S. Dixon, R. S. Edwards, and X. Jian, "Inspection of rail track head surfaces using electromagnetic transducers (EMATs)," Insight **46**, 326–330 (2004).
[9]D. Hesse and P. Cawley, "The potential of ultrasonic surface waves for rail inspection," Rev. Prog. Quant. Nondestr. Eval. **24**, 227–234 (2005).
[10]D. Hesse and P. Cawley, "Excitation of surface wave modes in rails and their application for defect detection," Rev. Prog. Quant. Nondestr. Eval. **25**, 1593-1600 (2006).
[11]P. E. Lagasse, "Higher-order finite-element analysis of topographic guides supporting elastic surface waves," J. Acoust. Soc. Am. **53**, 1116–1122 (1973).
[12]A. A. Oliner, "Waveguides for acoustic surface waves: A review," Proc. IEEE **64**, 615–627 (1976).
[13]A. A. Oliner, *Acoustic Surface Waves*, Vol. **24** of *Topics in Applied Physics* (Springer-Verlag, Berlin, 1978).
[14]V. V. Krylov, "Rayleigh waves on smooth surfaces of arbitrary shape," Sov. Phys. Acoust. **25**, 425–428 (1979).
[15]V. V. Krylov, "Distinctive characteristics of guided surface-wave propagation in complex topographic structures," Sov. Phys. Acoust. **33**, 407–411 (1987).
[16]L. Pochhammer, "Ueber die Fortpflanzungsgeschwindigkeiten kleiner Schwingungen in einem unbegrenzten isotropen Kreiscylinder," J. Reine Angew. Math. **81**, 324–336 (1876).
[17]K. Sato, "Elastic wave propagation in an infinite bar of elliptical cross section," Bull. JSME **21**, 203–209 (1978).
[18]R. D. Mindlin and E. A. Fox, "Vibrations and waves in elastic bars of rectangular cross section," J. Appl. Mech. **27**, 152–158 (1966).
[19]G. Rosenfeld and J. B. Keller, "Wave propagation in elastic rods of arbitrary cross section," J. Acoust. Soc. Am. **55**, 555–561 (1974).
[20]J. A. Morrison, "Propagation of high frequency surface waves along cylinders of general cross section," J. Math. Phys. **16**, 1786–1794 (1975).
[21]L. O. Wilson and J. A. Morrison, "Propagation of high frequency elastic surface waves along cylinders of general cross section," J. Math. Phys. **16**, 1795–1805 (1975).
[22]J. A. Morrison, "High frequency approximations for elastic surface waves propagating along cylinders of general cross section," J. Math. Phys. **17**, 958–963 (1976).
[23]N. J. Nigro, "Steady-state wave propagation in infinite bars of noncircular cross section," J. Acoust. Soc. Am. **40**, 1501–1508 (1966).
[24]W. B. Fraser, "Stress wave propagation in rectangular bars," Int. J. Solids Struct. **5**, 379–397 (1969).
[25]W. B. Fraser, "Dispersion of elastic waves in elliptical bars," J. Sound Vib. **10**, 247–260 (1969).
[26]K. Nagaya, "Stress wave propagation in a bar of arbitrary cross section," J. Appl. Mech. **49**, 157–163 (1982).
[27]A. Gunawan and S. Hirose, "Boundary element analysis of guided waves in a bar with arbitrary cross-section," Eng. Anal. Boundary Elem. **29**, 913–924 (2005).
[28]L. Gavrić, "Computation of propagative waves in free rail using a finite element technique," J. Sound Vib. **185**, 531–543 (1995).
[29]P. Wilcox, M. Evans, O. Diligent, M. Lowe, and P. Cawley, "Dispersion and excitability of guided acoustic waves in isotropic beams with arbitrary cross section," Rev. Prog. Quant. Nondestr. Eval. **21A**, 203–210 (2002).
[30]P. Wilcox, B. Pavlakovic, M. Evans, K. Vine, P. Cawley, M. J. S. Lowe, and D. N. Alleyne, "Long range inspection of rail using guided waves," Rev. Prog. Quant. Nondestr. Eval. **22A**, 236–243 (2003).
[31]L. Gry, "Dynamic modeling of railway track based on wave propagation," J. Sound Vib. **195**, 477–505 (1996).
[32]T. Hayashi, W.-J. Song, and J. L. Rose, "Guided wave dispersion curves for a bar with an arbitrary cross-section, a rod and rail example," Ultrasonics **41**, 175–183 (2003).
[33]T. Hayashi, C. Tamayama, and M. Morimasa, "Wave structure analysis of guided waves in a bar with an arbitrary cross-section," Ultrasonics **44**, 17–24 (2006).
[34]V. Damljanović and R. L. Weaver, "Propagating and evanescent elasting waves in cylindrical waveguides of arbitrary cross section," J. Acoust. Soc. Am. **115**, 1572–1581 (2004).

[35]I. Bartoli, A. Marzani, F. Lanza di Scalea, and E. Viola, "Modeling wave propagation in damped waveguides of arbitrary cross-section," J. Sound Vib., in press, corrected proof available online 20 March 2006, http://www.sciencedirect.com/science/article/B6WM3–4JHMHXN-4/2/3/ea4b8d6623e6aea7d198e731bd757c5 (2006).
[36]D. Hitchings, *FE77 User Manual* (Imperial College of Science, Technology and Medicine, London, 1994).
[37]Railtrack plc, UK, "Railtrack line specification. Track maintenance requirements. RT/CE/S/104" (2000).
[38]P. Wilcox, M. J. S. Lowe, and P. Cawley, "The excitation and detection of lamb waves with planar coil electromagnetic acoustic transducers," IEEE Trans. Ultrason. Ferroelectr. Freq. Control **52**, 2370–2383 (2005).
[39]D. N. Alleyne, "The nondestructive testing of plates using ultrasonic lamb waves," Ph.D. thesis, Imperial College of Science, Technology and Medicine, 1991, http://www.imperial.ac.uk/ndt/public/publications/theses.htm.
[40]B. Pavlakovic, D. Alleyne, P. Cawley, and M. J. S. Lowe, "Simulation of lamb wave propagation using pure mode excitation," Rev. Prog. Quant. Nondestr. Eval. **17**, 1003–1010 (1998).

Beam pattern calculation for optimization of broadband array transducers

Qiongbo Wang, Ningqun Guo,[a] Hejun Du, and Weimin Huang
School of Mechanical and Aerospace Engineering, Nanyang Technological University, 50 Nanyang Avenue, Singapore 639798

(Received 11 October 2005; revised 18 May 2006; accepted 22 May 2006)

Broadband array transducers are widely used in medical imaging systems, and their beam patterns determine the imaging quality. The characteristics of the beam patterns such as mainlobe beamwidth and sidelobe levels are the major criteria for designing and optimizing sparse array systems. The spatial impulse response approach can be used to calculate the beam patterns rigorously in both near field and far field. However, it is time consuming due to the high sampling frequency required, and thus not suitable for array optimization. On the other hand, assuming the array elements to be omnidirectional point sources the field calculation can be much simplified and fast but at the expense of poor accuracy. This paper presents a modified model that has the accuracy comparable to that from the impulse response model while keeping the efficiency close to that of the simple point source model. The developed algorithm is particularly suitable for stochastic methods for two-dimensional (2D) sparse arrays design and optimization such as genetic algorithms (GA), in which the iterative beam pattern calculation dominates the optimization program running time.
 [DOI: 10.1121/1.2214149]

PACS number(s): 43.38.Hz [AJZ] Pages: 741–749

I. INTRODUCTION

Ultrasonic transducers used in diagnostic ultrasound imaging systems have evolved from single-element transducer to multielement array, and from one-dimensional array (1D), to two-dimensional array (2D). Two-dimensional array transducers make it possible for real time three-dimensional (3D) ultrasound imaging, which has received extensive research interest in recent years (Smith *et al.*, 1991), and fabrication of a prototype 2D dense phase array with 2500 elements was reported (Greenstein *et al.*, 1997). Real-time 3D imaging provides more detailed volumetric information to the system users than the 2D images, and is able to assist physicians to make more accurate and reliable diagnosis. The 3D system based on the 2D matrix transducer is also faster than the 3D reconstruction generated with joining successive 2D scan images. Commercial 3D ultrasound imaging systems employing 2D array transducers are now available from medical imaging vendors. For example, 2D matrix array with over 3000 elements is employed in a cardiograph ultrasound system (Peterson and Hutchins, 2004). They are made possible due to rapid technology advances in transducer material and design, interconnection design, integrated array electronics, data acquisition, imaging processing power, memory storage capability, as well as fast algorithms for beam calculation and beamforming, etc. (Savord and Solomon, 2003).

Most real-time 3D imaging systems developed so far have used 2D dense array transducers, where the array elements are fully populated or fully sampled in the matrix cells (Savord and Solomon, 2003; Eames *et al.*, 2005). There are many applications where a large aperture size or high frequency is required, which would result in increase in the number of array elements, as well as in the complexity of the array system. One of the possible alternatives to the dense arrays is to design and use sparse arrays which significantly reduce the number of elements but with acceptable performance (Yen *et al.*, 2000). Various methods have been reported to design and optimize sparse arrays including element layouts optimization and weighting function optimization, both for 1D and 2D arrays (Austeng and Holm, 2002a,b; Cardone *et al.*, 2002; Davidsen *et al.*, 1994; Holm *et al.*, 1997; Murino *et al.*, 1997; Schwartz and Steinberg, 1998). Apart from the optimization algorithm, the transducer pressure field response or the beam pattern is most important in determining the imaging quality (Angelsen, 2000). For optimization of sparse arrays which may have several thousand elements, the iterative procedure to calculate the beam pattern for each possible solution has to be used for hundreds of thousands of times, in particular for stochastic methods such as genetic algorithms (GA) where the beam pattern calculation dominates the optimization running time (Wang *et al.*, 2006). An efficient and accurate method in calculating the field response is therefore necessary.

In general, the beam pattern calculation methods can be divided into two categories. For the continuous wave (cw) case, the well-known diffraction theory (Gooodman, 1968) can be used to calculate the response in the frequency domain, while for pulse wave (pw) transducers the impulse response method is more suitable (Murino *et al.*, 1997). For narrow-band transducers, the temporal and spatial responses are completely separable. Furthermore, in the far field, it is well known that the response can be approximated by spatial Fourier transform, and if all elements are identical, the radiation pattern of the array can be computed by the product of the element factor and array factor, where the element factor is the radiation pattern of single element, and array factor is

[a]Electronic mail: mnqguo@ntu.edu.sg

the radiation pattern of an array (Steinberg, 1976). A semi-analytical method named the distributed point source method (DPSM) was developed (Piwakowski *et al.*, 1989), and used in some beam pattern simulators. By discretizing the transducer aperture into multiple point sources, it can be used to deal with the aperture with complicated shapes, and to calculate the nonhomogeneous field and scattered field, as well as the interactions between pairs of phased arrays (Placko and Kundu, 2003; Ahmad *et al.*, 2005).

The cw model can be used with pw ultrasonic transducers, but only applicable in the far-field and near-focusing region. With the above method, Lockwood *et al.* (1996) defined a new concept named effective aperture and proposed some sparse periodic arrays designs called Vernier array, both for 1D and 2D arrays. Pompei and Wooh (2002) optimized element shapes to obtain desired element factors in order to theoretically suppress grating lobes in phased array. However, the pw transducers used in medical imaging systems have broad bandwidths, and their transient pressure fields consist of a superposition of a wide spectrum of frequencies. This means computing using the above methods must be integrated over the bandwidth of the transducers, which will be very time consuming. On the other hand, in the near field the above method is also not applicable due to its far-field assumption. Finally, the pw transducers generate and receive short pulses, the steady-state response does not exist at all, and thus the method based on the time domain to analyze the transient response is preferred.

The impulse response method can be used to calculate the broadband radiation field rigorously in the time domain, with the assumption imposed by Rayleigh integral (Stepanishen, 1971), which removes the constraints of the far field. For the aperture with regular shape, the closed-form expression of the impulse response can be derived (Ullate and San Emeterio, 1992; Xue *et al.*, 1996). The field response can be achieved by the convolutions of the exciting signal with the electromechanical response of the transducer and the calculated spatial impulse response. The major problem of the impulse response approach is that it needs several gigahertz sampling frequency for computer simulations (Crombie *et al.*, 1997) to account for discontinuities in impulse responses, and hence it leads to very poor efficiency. Turnbull and Foster (1991), and Jensen and Svendsen (1992) have simplified this method by assuming that all impulse responses are in trapezoid shape in the far field, and able to deal with arbitrary shape of apertures (Jensen and Svendsen, 1992). However, the trapezoid assumption is not adequate in the near-axis region and rigorous impulse response method is still required for on axis calculations (Turnbull and Foster, 1991). For the above reasons, these approaches can only increase the calculation speed to some extent.

On the other hand, approximation methods are available and can be used by neglecting the lateral dimensions of the array elements (Cardone *et al.*, 2002), and the elements are thus treated as point sources. Then, the exact impulse response calculation procedures can be bypassed and computation efficiency is increased dramatically. However, this method is very poor in accuracy in the near field of the array or when the array steers off-axis. The failure of the point source model is because the elemental directivity cannot be simply ignored and the influence of element height on the radiation field also needs to be taken into account, especially in the near-field region.

With the above considerations, this paper develops a modified algorithm for beam pattern calculations which is used for array design and optimization. In Sec. II, the theories for the simple point source model and the rigorous impulse response method are briefly presented, and an efficient method which offers both fast calculation speed and comparable accuracy is presented. Section III presents the results using both 1D and 2D array examples for calculation of the field responses to demonstrate the advantages of the method in terms of the speed and accuracy.

II. THEORY

A. Impulse response method and point source model

It is well known that the radiation field from a rigid baffled plane vibration source to homogeneous isotropic and lossless medium can be calculated by Rayleigh integral over the whole source surface (Harris, 1981),

$$p(\vec{r},t)=\frac{\rho}{2\pi}\frac{\partial}{\partial t}\iint_S \frac{v\left(t-\frac{|\vec{r}-\vec{r}_s|}{c}\right)}{|\vec{r}-\vec{r}_s|}dS \tag{1}$$

where p is the pressure, v is the source velocity profile, ρ is the medium mass density, c is the sound velocity in the medium, S is the source surface, $\vec{r}$ is the spatial vector, and $\vec{r}_s$ is the vector in the source plane. For a soft baffle, an obliquity factor must be included, and the influence of this factor to the radiation field can be derived (Selfridge *et al.*, 1980). However, in this study, the following descriptions are all based on the rigid baffle.

Assume a linear array transducer consists of N elements with a coordinate system as shown in Fig. 1(a). Each element performs pistonlike vibration and the vibration profiles are uniform among all the elements, which is defined as $v_0(t)$. Using the Dirac delta function and convolution operator, one can obtain

$$p(\vec{r},t)=\frac{\rho}{2\pi}\frac{\partial v_0(t)}{\partial t} * \sum_{i=1}^{N} A_i \iint_{S_i} \frac{\delta\left(t-\frac{|\vec{r}-\vec{r}_s|}{c}-\tau_i\right)}{|\vec{r}-\vec{r}_s|}dS, \tag{2}$$

where A_i is the weighting coefficient, τ_i is the time delay to fulfill steering and focusing of the ith element, and sign * is the time convolution operator. If we define

$$h(\vec{r},t)=\sum_{i=1}^{N} A_i \iint_{S_i} \frac{\delta\left(t-\frac{|\vec{r}-\vec{r}_s|}{c}-\tau_i\right)}{2\pi|\vec{r}-\vec{r}_s|}dS \tag{3}$$

and

$$p_0(t)=\rho\frac{\partial v_0(t)}{\partial t}, \tag{4}$$

then

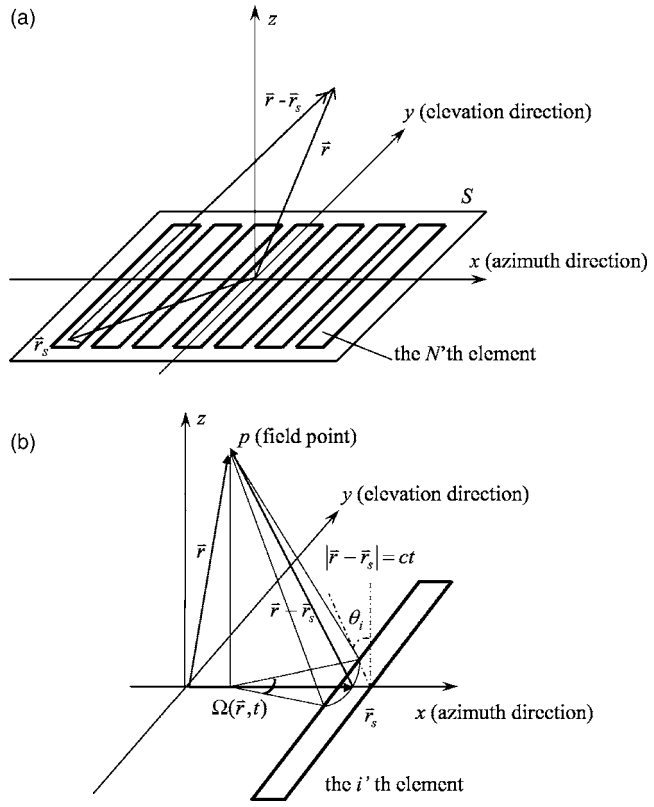

FIG. 1. The coordinate systems for 1D array radiation field calculation (a) for a 1D array and (b) for impulse response of single element.

$$p(\vec{r},t) = p_0(t) * h(\vec{r},t), \tag{5}$$

where $h(\vec{r},t)$ is termed as the array spatial impulse response. For linear array transducers, the array element has a narrow rectangular shape, and the closed-form analytical expression of Eq. (3) can thus be derived without any paraxial or far-field approximation (Ullate and San Emeterio, 1992). The response at any field point is a time-limited, amplitude-bounded, and piecewise continuous function.

The disadvantage of this method is that the existence of discontinuities requires very high sampling frequency for numerical calculation, especially for the paraxial points and small aperture size. The point source model simplifies the calculations by ignoring the element lateral dimension, and the pressure response is obtained as

$$p(\vec{r},t) = \sum_{i=1}^{N} \frac{A_i p_0\left(t - \frac{|\vec{r}-\vec{r}_i|}{c} - \tau_i\right)}{|\vec{r}-\vec{r}_i|}, \tag{6}$$

where $\vec{r}_i$ is the vector from the array center to the center of the ith element.

Equation (6) greatly simplifies the calculation procedure, but it also decreases the accuracy of the results. To show the difference and to compare, an example of the beam pattern of a linear 1D array is calculated. The array consists of 64 elements with an elemental pitch of 0.5λ, an aperture length L of 13.5 mm, and an element height of 10 mm. The excitation waveform $p_0(t)$, as shown in Fig. 2, is three periods of a 3.5-MHz sine wave weighted in a Hanning window, and of 65% in relative bandwidth (−6 dB). Beam patterns for the array focusing at $r=25$ mm and $\theta_F=30°$ are calculated using the impulse response model (Imp) and the point source model (PS), and are compared in Fig. 3(a). Clear deviation in the results from the two approaches can be observed, especially in the off-axis sidelobe region. Even as the distance r increases to the far field, the discrepancies between the two results still exist as shown in Fig. 3(b), where the array focus is at $r=125$ mm and $\theta_F=30°$.

The reason for the above discrepancies can be explained by the three assumptions implied in the point source model. The first is that the elemental directivity is uniform and independent of view angle θ_i, and the second is that the wave amplitude decreases proportionally with the propagation distance $|\vec{r}-\vec{r}_i|$. These two assumptions are not adequate for the linear array calculations. It can be shown that, even when the element width is at half-wavelength, the element cannot be treated as an omnidirectional point source. Furthermore, in the wave propagation direction, the wave amplitude varies more complicatedly than the spherical propagation assumption because of the influence of the elemental height. The third assumption is that the wave generated by each element keeps the same shape as that of $p_0(t)$, and only its amplitude varies at different field position. This assumption also fails in the near field due to the influence of the elemental height. The poor accuracy of the point source model is not reliable for array beam pattern calculation, the impulse response model is accurate but not suitable for optimization work due to its heavy computation burden, and an alternative, more efficient algorithm is described as follows.

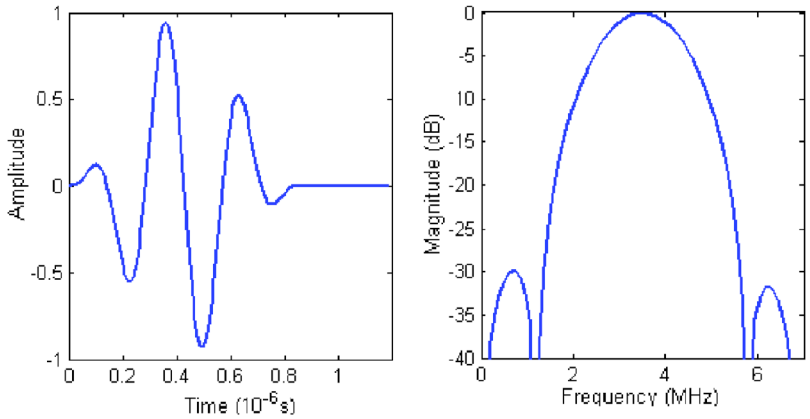

FIG. 2. (Color online) The waveform $p_0(t)$ and its spectrum at 3.5 MHz with bandwidth of 65%.

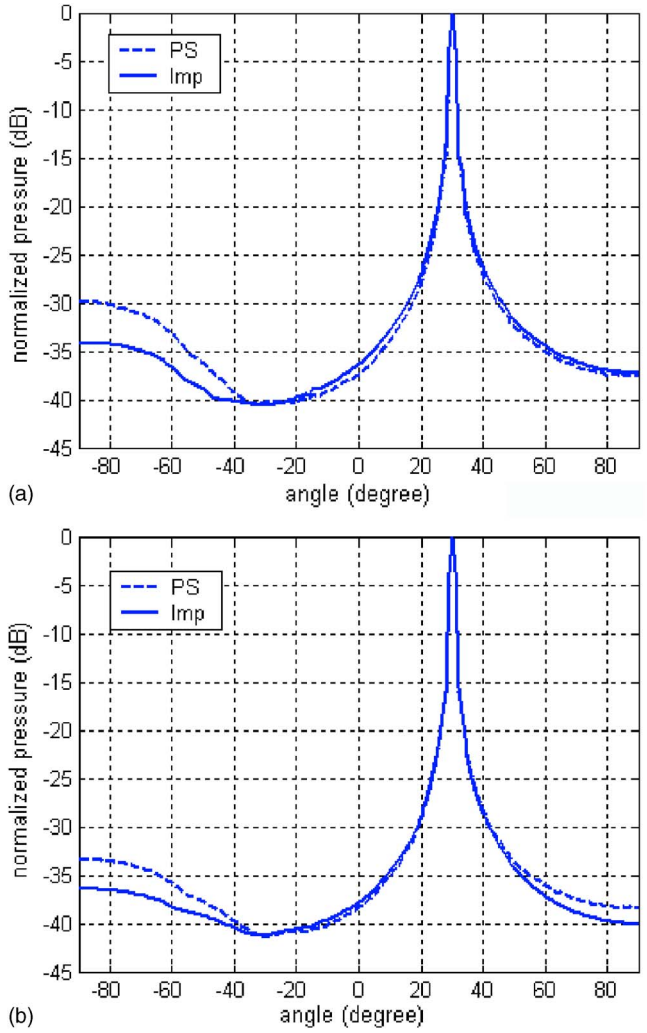

FIG. 3. (Color online) Beam patterns calculated by the point source model (dashed line) and the impulse response method (solid line) with the array focus at (a) $r=25$ mm, $\theta=30°$; (b) $r=125$ mm, $\theta=30°$.

B. Modified point source model for beam pattern calculation

1. Method 1: Modified point source model with the elemental directivity

The point source model has a few deficiencies due to its simplicity and assumptions, and the modifications can be made from its three implied assumptions. First, the elemental directivity can be corrected easily. Since the element width is assumed to be smaller than the wavelength, even for broadband signals, the directivity can be predicted with the narrow-band theory (Ullate and San Emeterio, 1992). This directivity is only angle dependent in far fields (for the single element, the far-field condition is easily satisfied), and can be calculated by the Fourier transform. For a line source, the Fourier transform results in a simple **sinc** function (Steinberg, 1976),

$$A(\theta_i) = \mathbf{sinc}\left[\frac{a}{\lambda}\mathbf{sin}(\theta_i)\right] \tag{7}$$

where a is the element width, θ_i is the viewing angle from field points, and a is the elemental width as shown in Fig. 1(b). Compared with the directivity result calculated by the impulse response method, the narrow-band prediction is accurate enough as shown in Fig. 4. Improvement for this approximation method can also be made through the Rayleigh-Sommerfeld diffraction formula (Selfridge *et al.*, 1980).

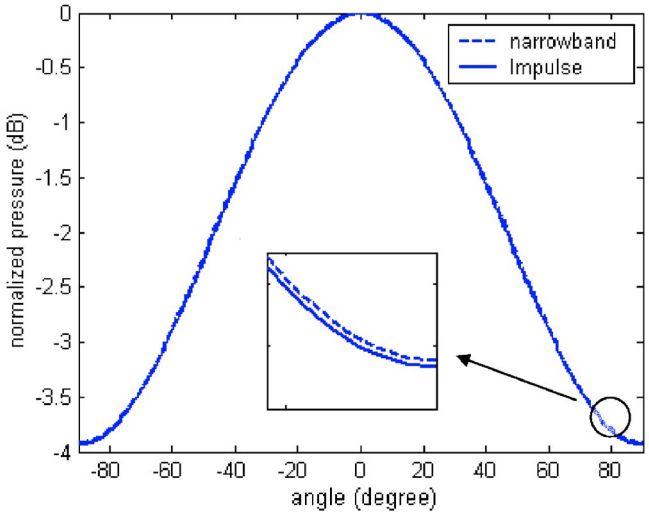

FIG. 4. (Color online) The element directivity predicted by the narrow-band theory (dashed line) and the impulse response method (solid line), with the inset showing a slight difference.

On the other hand, the amplitude of the pulse at any given point in the far field is inversely proportional to the propagation distance, and the amplitude due to the spherical propagation decay can be simplified to a factor $1/|\vec{r}-\vec{r}_i|$. The field pressure in Eq. (2) can be written as

$$p(\vec{r},t) = p_0(t) * \sum_{i=1}^{N} \frac{A_i \cdot \mathbf{sinc}\left[\frac{a}{\lambda}\mathbf{sin}(\theta_i)\right] \cdot \delta\left(t - \frac{|\vec{r}-\vec{r}_i|}{c} - \tau_i\right)}{2\pi \cdot |\vec{r}-\vec{r}_i|}. \tag{8}$$

Comparing Eq. (8) with (6), it can be found that the main difference is a correcting factor $A(\theta_i)$ as defined by Eq. (7). So, method 1 in Eq. (8) is in fact a modification of the point source model, and includes the element directivity to improve the accuracy of the simulation results.

2. Method 2: Based on single-element characteristics

The method can be further improved by incorporating the characteristics of the element, in particular, when the pressure wave transmitted from a single element is considered. Figures 5 and 6 show the impulse responses and corresponding radiation pressure waveforms from a single array element at the points where $r=25$ mm and varying angle of $\theta=0°$, 30°, 60°, and 90°, respectively. Figures 7 and 8 show the corresponding responses at $\theta=30°$ and varying distance of $r=25$, 40, 60, and 100 mm.

It can be seen from Fig. 6 that the waveforms at different angles vary little in terms of their shapes and time durations, and only the amplitude changes with the angle. This phenomenon can be explained by their impulse responses shown in Fig. 5. The amplitudes of these responses drop as the angle increases from 0° to 90°, but their shapes share the same feature, which is a high-amplitude spike followed by

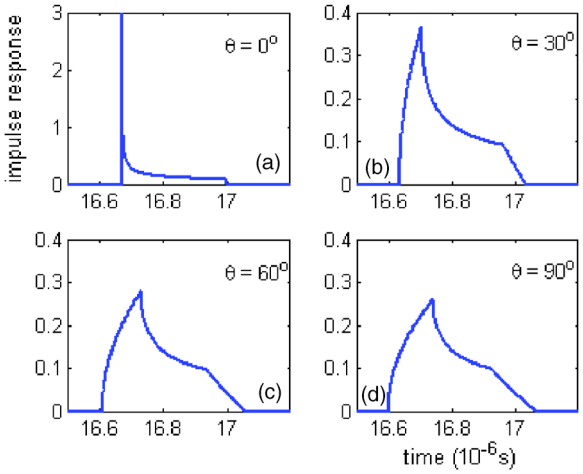

FIG. 5. (Color online) The impulse responses from single array element, at r=25 mm, (a) θ=0°; (b) θ=30°; (c) θ=60°; (d) θ=90°

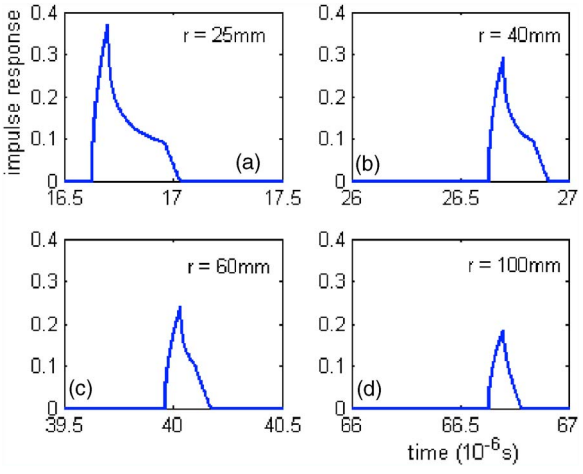

FIG. 7. (Color online) The impulse responses from a single array element at θ=30° and varying distance (a) r=25 mm; (b) r=40 mm; (c) r=60 mm; (d) r=100 mm.

an amplitude-decreasing part. Thus, the convolution to calculate the pressure results in some distortion from the original pressure wave $p_0(t)$ as shown in Fig. 2 and changes in amplitude. On the other hand, as the field distance r increases, the impulse response approaches ideal impulse as shown in Fig. 7, and the waveform shape becomes close to $p_0(t)$, as clearly shown in Fig. 8.

For the variation of the wave amplitude along the propagation direction, there is no explicit expression to describe it since it is greatly affected by the elemental height. It can be seen from Fig. 9 that the variation of the wave amplitude, calculated using the impulse response method, does not follow the spherical decay. However, despite the complexity, this variation is angle independent, which indicates that the variations are the same in any propagation direction.

Based on the above analysis on the single-element characteristics, the modified model to calculate radiation field from array transducers can be derived. The pressure from a single element can be simplified as

$$p_i(\vec{r},t) = p_{|\vec{r}-\vec{r}_i|}(t) * A_i \cdot A(\theta_i) \cdot A_r(|\vec{r}-\vec{r}_i|) \cdot \delta\left(t - \frac{|\vec{r}-\vec{r}_i|}{c} - \tau_i\right), \tag{9}$$

where $A_r(|\vec{r}-\vec{r}_i|)$ is the amplitude variation along the propagation distance $|\vec{r}-\vec{r}_i|$ for the ith element, and $p_{|\vec{r}-\vec{r}_i|}(t)$ denotes the waveform shape, which is at the distance of $|\vec{r}-\vec{r}_i|$ away from the element center. Clearly, $p_{|\vec{r}-\vec{r}_i|}(t)$ will be close to $p_0(t)$ as r increases; then, the array radiation field can be derived,

$$p(\vec{r},t) = \sum_{i=1}^{N} p_i(\vec{r},t). \tag{10}$$

Furthermore, in examining Fig. 8, one can find that the waveform $p_r(t)$ does not change dramatically with increasing distance r, especially the dominant cycles of $p_r(t)$, which have higher amplitude and almost keep intact. Thus, the waveform from the central element can be used to represent

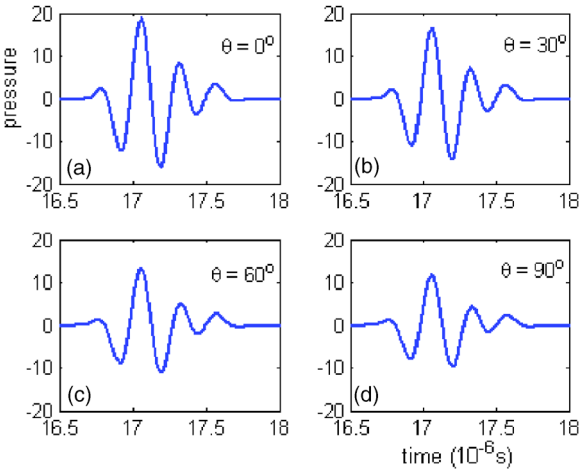

FIG. 6. (Color online) The pressure waveforms from single array element, at r=25 mm: (a) θ=0°; (b) θ=30°; (c) θ=60°; (d) θ=90°.

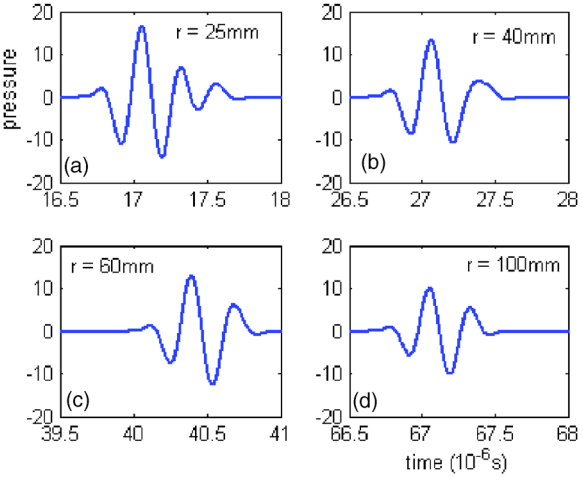

FIG. 8. (Color online) The pressure waveforms from a single array element at θ=30° and varying distance (a) r=25 mm; (b) r=40 mm; (c) r=60 mm; (d) r=100 mm.

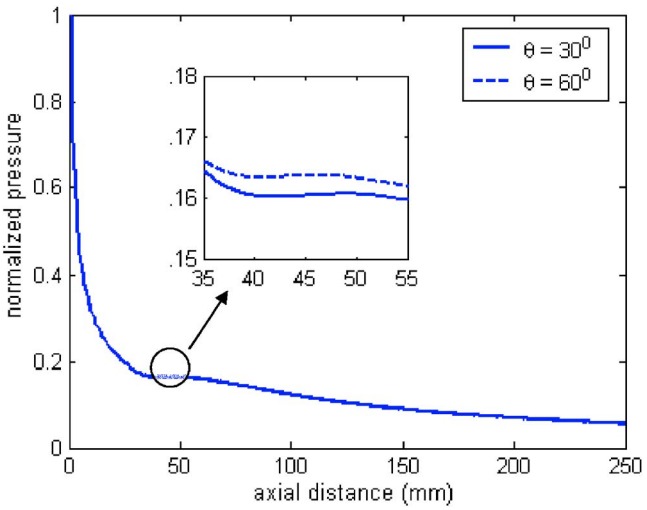

FIG. 9. (Color online) Variation of the pressure wave amplitude along the propagation direction at θ=30° (solid line) and θ=60° (dashed line).

waveforms from all other elements. Equation (10) can be further simplified to

$$p(\vec{r},t) = p_r(t) * \sum_{i=1}^{N} A_i \cdot A(\theta_i) \cdot A_r(|\vec{r}-\vec{r}_i|) \cdot \delta\left(t - \frac{|\vec{r}-\vec{r}_i|}{c} - \tau_i\right). \tag{11}$$

This equation separates the waveform transmitted by each element and the impulse response, which will facilitate the fast field calculations. For iterative field calculation procedures, many terms can be precalculated and stored on computer hard disk, such as $|\vec{r}-\vec{r}_i|, A(\theta_i)$, and $A_r(|\vec{r}-\vec{r}_i|)$. These data can be loaded in random memory before each field calculation, and greatly reduce the calculation time by the proposed method (method 2).

3. 2D array transducers

The algorithms derived in the above can be extended to 2D array transducers, where array elements are distributed in two dimensions in the transducer plane. In 2D arrays, the element is usually square in shape, and both element height and width are limited by the half-wavelength constraint to avoid grating lobes in the 3D radiation field. Due to the small size elements, the approximate method to calculate the radiation field can also be adopted. The coordinate system for 2D array calculations is shown in Fig. 10(a), where the array is located in the xy plane with the steering angle defined as θ in the azimuth plane (xz plane) and ϕ in the elevation plane (yz plane). The radiation fields of 2D arrays are five-dimensional data $p(r,\theta,\phi,t)$, but can be described by a 3D curved surface $p(\theta,\phi)$, after simplification to drop r by properly selecting the field point positions and remove t by the maximum projection (Holm, 1996).

With the assumptions that the array element height and width are $\lambda/2$ and an initial broadband pulse like $p_0(t)$ in Fig. 2 is used, it can be shown from the exact impulse response method that, even when the field points are very close to the element, the transient pressure waveforms obtained are almost identical to that initial pulse, and this is likely because

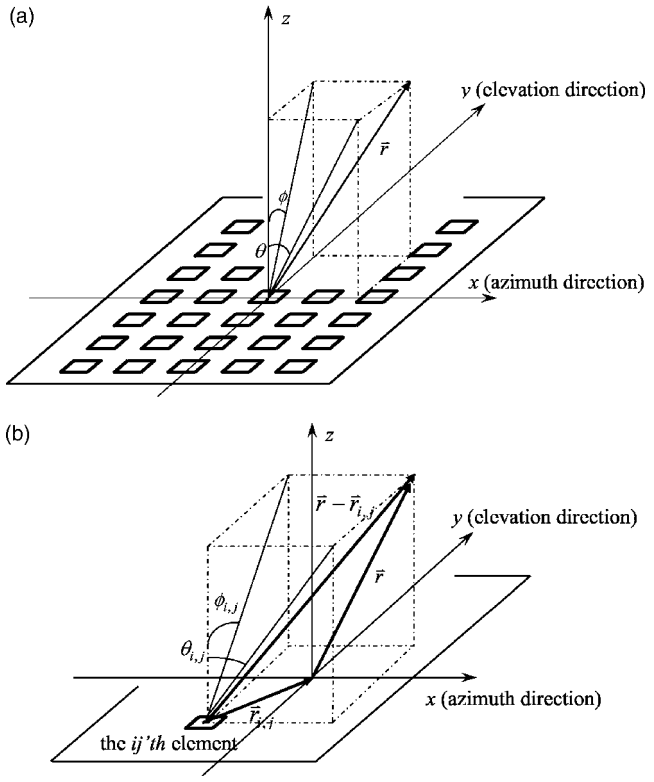

FIG. 10. (Color online) The coordinate system for 2D array radiation field calculation; $x-z$ plane is defined as the azimuth plane and the steering angle in this plane is θ. $y-z$ plane is the elevation plane, and the steering angle is ϕ (a) the coordinate system; (b) the viewing angle.

the small element size generates little distortion on the waveforms. Meanwhile, the far-field condition for the single element can be easily satisfied, so the amplitude variation along the wave propagation direction is inversely proportional to the distance at the given angles. This means that the calculation of the exact impulse response is not necessary for 2D arrays, and method 2 can be simplified further for the 2D case, where the amplitude variation factor $A_r(|\vec{r}-\vec{r}_i|)$ is no longer required. Function $p_0(t)$ can be used directly.

On the other hand, for the same reason as 1D arrays, the elemental directivity can be predicted by the narrow-band theory (Angelsen, 2000),

$$A(\theta,\phi) = \mathbf{sinc}\left[\frac{a}{\lambda}\cdot\mathbf{sin}(\theta)\right]\cdot\mathbf{sinc}\left[\frac{a}{\lambda}\cdot\mathbf{sin}(\phi)\right], \tag{12}$$

where a is the element dimension. Based on the above analysis, the spatial impulse response and the radiation field from 2D square arrays, which consist of $N\times N$ elements, can be approximately calculated by the following equations:

$$p(\vec{r},t) = p_0(t) * \sum_{i=1}^{N}\sum_{j=1}^{N} \frac{A_{i,j}\cdot A(\theta_{i,j},\phi_{i,j})}{2\pi|\vec{r}-\vec{r}_{i,j}|}\cdot\delta\left(t - \frac{|\vec{r}-\vec{r}_{i,j}|}{c} - \tau_{i,j}\right), \tag{13}$$

where the subscripts i,j represent the element lies in the ith row and jth column, respectively. $A_{i,j}$ is the apodization coefficient for this element, $\vec{r}_{i,j}$ is the element vector, and $\theta_{i,j},\phi_{i,j}$ are the viewing angles from the field point to the given element as shown in Fig. 10(b). It is evident that the

TABLE I. Times used to calculate a single field point pressure response by different methods (time unit: second).

	$r=25$ mm	$r=50$ mm	$r=100$ mm
Point source model	0.04	0.07	0.09
Method 1	0.04	0.07	0.09
Method 2	6.4	6.2	6.2
Method 2	0.05	0.07	0.09
Exact method	9.4	8.2	6.7

Excluding the time for calculation of the first single element.

above equation is the extension of method 1 to 2D arrays. However, the accuracy can be ensured for 2D arrays because the elements have small size in both lateral dimensions.

III. RESULTS

The approximate methods discussed in Sec. II B are tested with 1D and 2D array examples in this section to demonstrate the efficiency in terms of computation time and accuracy obtained, both of which are essential for design and optimization of the sparse array. The radiation field of the 1D array is calculated first by all four methods, including method 1, method 2, the simple point source model (PS), and exact impulse response method (Imp). It should be noted that all methods are implemented using MATLAB and run on the same PC; no optimization effort in programming is made so their efficiencies can be compared. The sampling frequency is 400 MHz for method 1, method 2, and point source model, and 4 GHz for the exact method.

The pressure waveforms for the on axis points where $\theta=0°$ and $r=25$, 50, and 100 mm are first calculated by all four methods to examine the transient pressure waveforms at the field points. The array focuses at $\theta=45°$, and all results are normalized to the amplitude at the focal point calculated by each method, respectively. Results in terms of corresponding computing time used are listed in Table I for comparison, and Table II lists the relative errors of different methods by comparing the maximum amplitude of their results with respect to that from the exact method.

It can be seen from Table I that the point source model and method 1 are the fastest, with the computation time at the order of tens of milliseconds for each point. Method 2 and the exact method are much slower, and they all need more than 6 s for each field point calculation. The exact method is the slowest because of the complicated calculation procedure and the high sampling frequency used. For the single field point calculation, method 2 also has no advantage on efficiency because almost all of the time is spent on the calculation of $A(\theta)$ and $A_r(|\vec{r}-\vec{r}_i|)$ of the single element using the exact method. However, it should be noted that method 2 allows the element characteristics such as $A(\theta)$ and $A_r(|\vec{r}-\vec{r}_i|)$ to be calculated separately. When $A(\theta)$ and $A_r(|\vec{r}-\vec{r}_i|)$ are precalculated, the time used by this method (denoted as method 2[a] in Table I) for subsequent calculation is also less than 10 milliseconds, which is on the same order as that with the point source model and method 1.

TABLE II. Amplitude errors (%) relative to the exact method.

	$r=25$ mm	$r=50$ mm	$r=100$ mm
Point source model	17.9	16.1	7.0
Method 1	8.4	5.8	4.1
Method 2	3.5	3.5	2.7

It is evident from Table II that the result by method 2 is a good approximation to that by the exact impulse response method. Even in the region close to the transducer, the accuracy is still very good, with the amplitude error at about 3%. Considering the gain in speed, this is a very good compromise unless the field point falls in the extreme near field. The pulse shapes are also accurate if compared with the exact method both in the near field and far field. This method is thus more suitable to calculate arrays beam patterns, in which the field points are all located with the same distance to the transducer center. Furthermore, the computing speed is of the same order as that by the point source model, and it takes about a few seconds to calculate one beam pattern ranges between −90° and 90°. Method 2 greatly improves the efficiency with sufficient accuracy, and is suitable for sparse array optimization where the beam pattern calculation may have to be carried over tens of thousands of times.

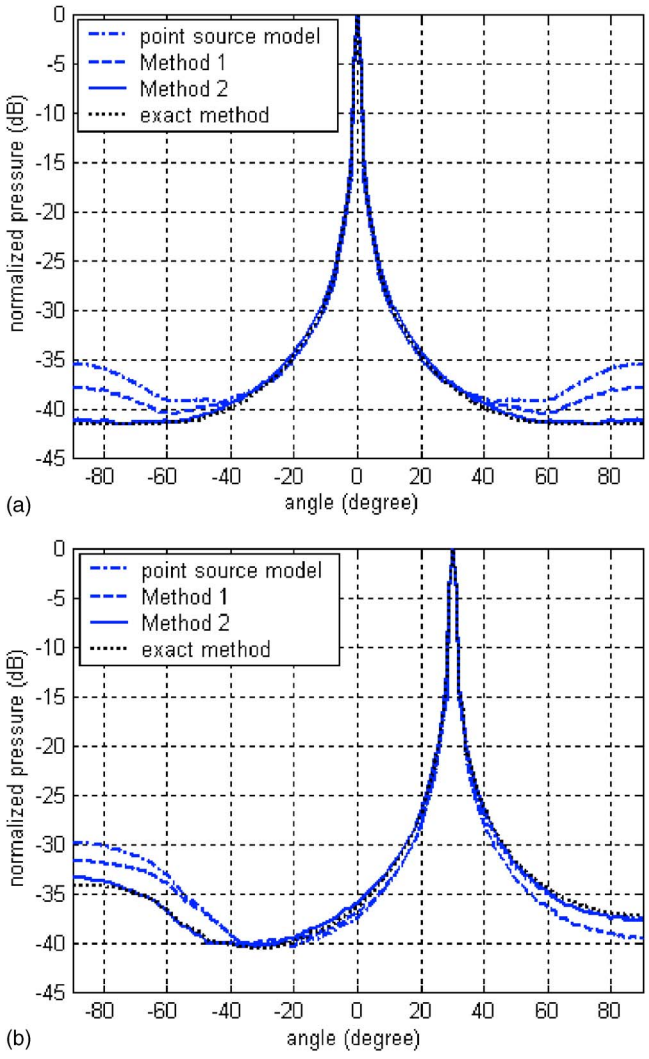

FIG. 11. (Color online) The beam patterns calculated by different methods with the array focusing at (a) $r=25$ mm, $\theta=0°$; (b) $r=25$ mm, $\theta=30°$.

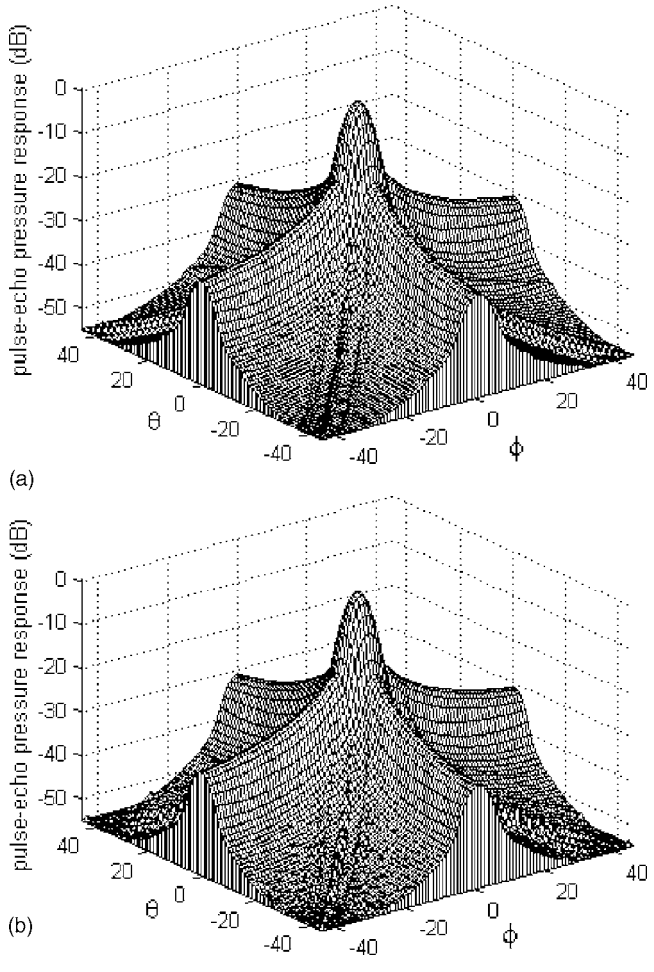

FIG. 12. Beam patterns of 2D array focusing at $r=40$ mm, θ, $\phi=0°$ calculated by (a) FIELD II and (b) the developed method.

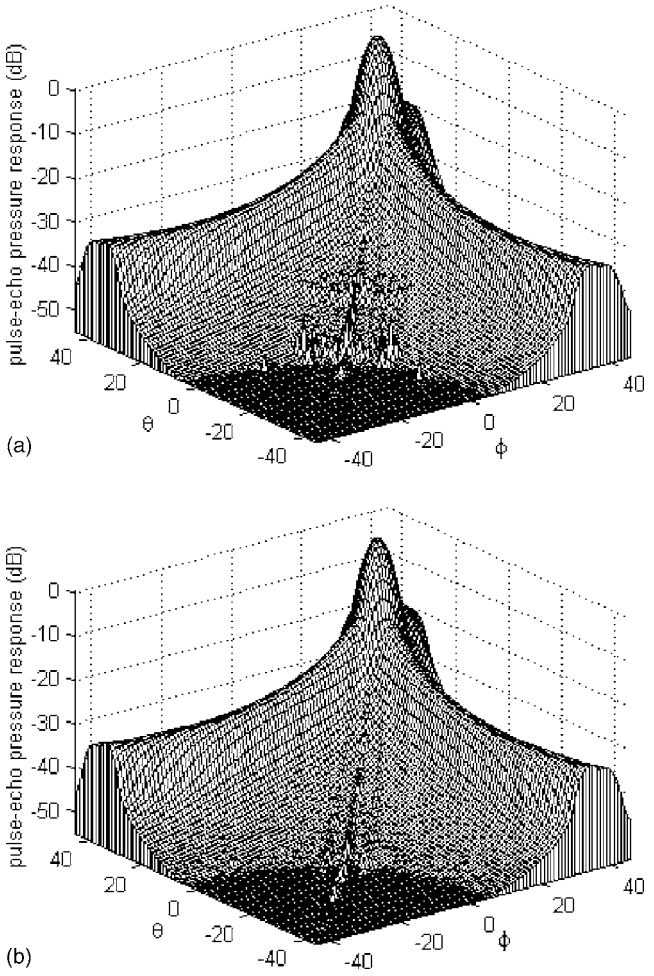

FIG. 13. Beam patterns of 2D array focusing at $r=40$ mm, θ, $\phi=30°$ calculated by (a) FIELD II; (b) the developed method.

Figure 11 show the beam patterns calculated by the above four methods, and the array focuses at $r=25$ mm, with $\theta=0°$ and 30°, respectively. It can be seen that all of the results are very close in the mainlobe region. As the angle increases, the results by the point source model and method 1 start to deviate from those by the exact method. However, the results by method 2 agree very well with those from the exact method, even in the full-field region. Once the performance of a single element is determined, method 2 has both very high efficiency and accuracy, and is thus more suitable for array design and optimization.

A 2D array is used as an example to compare the result using the proposed method with FIELD II, which used an approximate form of the impulse response and is programed in C (Jensen, 2001). The array consists of 20×20 square elements with an element pitch of 0.5λ, and the pressure input $p_0(t)$ shown in Fig. 2 is used. The sampling frequency used in FIELD II is 150 MHz, somewhat higher than the recommended value (100 MHz) to reduce the numerical noise level. For the method developed here the sampling frequency used is 400 MHz. Each array element is divided into 4×4 elements during simulation. A couple of the calculated cases are shown here, and the normalized mean-square errors between the results of these two methods are kept within 2%. Although the developed method uses higher sampling frequency than that of FIELD II, the computing time used is only about one-tenth of that used by FIELD II on average.

For the first case shown in Fig. 12, the array focuses on the axis θ, $\phi=0°$, while in the second case shown in Fig. 13 the array focuses off the axis, where θ, $\phi=30°$, $r=40$ mm, and the steering angles range is between ±45° for both cases. It can be seen that the results by the two methods match very well, though some numerical noise can be observed from the FIELD II result shown in Fig. 13(a). Further increase in the sampling frequency can reduce the noise, but at the expense of longer simulation time. In these cases the calculation time for each beam pattern is 8 to 10 s, while FIELD II needs more than 1 min with the same PC being used, demonstrating the efficiency of the method. Further improvement in efficiency can be obtained if the proposed method is implemented in more efficient C programming such as that used in FIELD II.

IV. CONCLUSIONS

An efficient method is presented to calculate the radiation pressure field for the design and optimization of broadband sparse arrays. The method, based on the point source model, incorporates the element directivity and element characteristics but avoids the calculation of the exact solution of the array impulse response. With the proposed method, the

accuracy increases dramatically compared with that from the point source model, and is comparable with that calculated by the exact impulse response method even in the near field. The calculation time using the proposed method is comparable to that using the point source model. This improved efficiency is possible since the array elements are usually smaller than 1 wavelength, and it is possible to use the precalculated characteristics of the single element in array calculations. For 2D arrays, since both sides of the array element are small, the method can be further simplified and only the element directivity is necessary to be used as the correction factor. Compared with the results of the widely used field simulator FIELD II, the calculating speed is increased by one order of magnitude on average with comparable accuracy. The model has been effectively applied in design and optimization of sparse arrays using genetic algorithms as reported elsewhere (Wang *et al.*, 2006).

Ahmad, R., Kundu, T., and Placko, D. (**2005**). "Modeling of phased array transducers," J. Acoust. Soc. Am. **117**(4), 1762–1776.

Angelsen, B. A. J. (**2000**). *Ultrasound Imaging* (Emantec AS, Trondheim, Norway).

Austeng, A., and Holm, S. (**2002a**). "Sparse 2-D arrays for 3-D phased array imaging—Design methods," IEEE Trans. Ultrason. Ferroelectr. Freq. Control **49**(8), 1073–1086.

Austeng, A., and Holm, S. (**2002b**). "Sparse 2-D arrays for 3-D phased array imaging—Experimental validation," IEEE Trans. Ultrason. Ferroelectr. Freq. Control **49**(8), 1087–1093.

Cardone, G., Cincotti, G., and Pappalardo, M. (**2002**). "Design of wide-band arrays for low side-lobe level beam patterns by simulated annealing," IEEE Trans. Ultrason. Ferroelectr. Freq. Control **49**(8), 1050–1059.

Crombie, P., Bascom, P. A. J., and Cobbold, R. S. C. (**1997**). "Calculating the pulsed response of linear arrays: Accuracy versus computational efficiency," IEEE Trans. Ultrason. Ferroelectr. Freq. Control **44**(5), 997–1009.

Davidsen, R. E., Jensen, J. A., and Smith, S. W. (**1994**). "Two-dimensional random arrays for real time volumetric imaging," Ultrason. Imaging **16**, 143–163.

Eames, M., Zhou, S., and Hossack, J. (**2005**). "High element count (3600), fully sampled, two dimensional transducer array," *Proceedings of IEEE Ultrason. Symposium*, Vol. **11**, pp. 2243–2246.

Goodman, J. W. (**1968**). *Introduction to Fourier Optics* (McGraw-Hill, San Francisco).

Greenstein, M., Lum, P., Yoshida, H., and Seyed-Bolorforosh, M. S. (**1997**). "A 2.5 MHz 2D array with *Z*-axis electrically conductive backing," IEEE Trans. Ultrason. Ferroelectr. Freq. Control **44**(5), 970–977.

Harris, G. R. (**1981**). "Review of transient field theory for a baffled planar piston," J. Acoust. Soc. Am. **70**, 10–20.

Holm, S. (**1996**). "Minimum sidelobe energy versus minimum peak sidelobe level for sparse array optimization," *Proc. NORSIG-96*, Helsinki, Finland.

Holm, S., Elgetun, B., and Dahl, G. (**1997**). "Properties of the beam pattern of weight- and layout-optimized sparse arrays," IEEE Trans. Ultrason. Ferroelectr. Freq. Control **44**(5), 983–991.

Jensen, J. A. (**2001**). Users' Guide For the FIELD II Program, Release 2.86.

Jensen, J. A., and Svendsen, N. B. (**1992**). "Calculation of pressure fields from arbitrarily shaped, apodized, and excited ultrasound transducers," IEEE Trans. Ultrason. Ferroelectr. Freq. Control **39**(2), 262–267.

Lockwood, G. R., Li, P. C., O'Donnell, M., and Foster, F. S. (**1996**). "Optimizing the radiation pattern of sparse periodic linear arrays," IEEE Trans. Ultrason. Ferroelectr. Freq. Control **43**(1), 7–14.

Murino, V., Trucco, A., and Tesei, A. (**1997**). "Beam pattern formulation and analysis for wide-band beamforming systems using sparse arrays," Signal Process. **56**(2), 177–183.

Peterson, R. B., and Hutchins, J. (**2004**). "The iE33 intelligent echocardiography system," Med. Mundi **48**(3), 45–48.

Piwakowski, B., and Delannoy, B. (**1989**). "Method for computing spatial pulse response: Time-domain approach," J. Acoust. Soc. Am. **86**(6), 2422–2432.

Placko, D., and Kundu, T. (**2003**). *Ultrasonic Nondestructive Evaluation: Engineering and Biological Material Characterization* (CRC Press, Boca Raton, FL), Chap. 2, pp. 143–202.

Pompei, F. J., and Wooh, S. (**2002**). "Phased array element shapes for suppressing grating lobes," J. Acoust. Soc. Am. **111**(5), 2040–2048.

Savord, B., and Solomon, R. (**2003**). "Fully sampled matrix transducer for real time 3D ultrasonic imaging," *Proceedings of IEEE Ultrason. Symposium*, **9**, pp. 945–953.

Schwartz, J. L., and Steinberg, B. D. (**1998**). "Ultrasparse, ultrawideband arrays," IEEE Trans. Ultrason. Ferroelectr. Freq. Control **45**(2), 376–393.

Selfridge, A. R., Kino, G. S., and Khuri-Yakub, B. T. (**1980**). "A theory for the radiation pattern of a narrow-strip acoustic transducer," Appl. Phys. Lett. **37**(1), 35–36.

Smith, S. W., Pavy, H. E., and Ramm, O. T. (**1991**). "High-speed ultrasound volumetric imaging system. I. Transducer design and beam steering," IEEE Trans. Ultrason. Ferroelectr. Freq. Control **38**(2), 100–108.

Steinberg, B. D. (**1976**). *Principles of Aperture and Array System Design* (Wiley-Interscience, New York).

Stepanishen, P. R. (**1971**). "The time-dependent force and radiation impedance on a piston in a rigid infinite planar baffle," J. Acoust. Soc. Am. **49**, 841–849.

Turnbull, D. H., and Foster, F. S. (**1991**). "Beam steering with pulsed two-dimensional transducer arrays," IEEE Trans. Ultrason. Ferroelectr. Freq. Control **38**(4), 320–333.

Ullate, L. G., and San Emeterio, J. L. (**1992**). "A new algorithm to calculate the transient near-field of ultrasonic phased arrays," IEEE Trans. Ultrason. Ferroelectr. Freq. Control **39**(6), 745–753.

Wang, Q. B., Guo, N. *et al.* (unpublished).

Xue, T., Lord, W., and Udpa, S. (**1996**). "Numerical analysis of the radiated fields of circular pistons and time-delay spherically focused arrays," IEEE Trans. Ultrason. Ferroelectr. Freq. Control **43**(1), 78–87.

Yen, J., Steinberg, J., and Smith, S. (**2000**). "Sparse 2-D array design for real time rectilinear volumetric imaging," IEEE Trans. Ultrason. Ferroelectr. Freq. Control **47**, 93–110.

Analytical modeling for bulk-micromachined condenser microphones

Chee Wee Tan[a] and Jianmin Miao[b]
Micromachines Centre, School of Mechanical and Aerospace Engineering, Nanyang Technological University, Singapore, 50 Nanyang Avenue, Singapore 639798, Singapore

(Received 11 April 2006; revised 24 May 2006; accepted 26 May 2006)

The advent of silicon micromachining technology has opened up numerous opportunities for the commercialization of many miniaturized sensors and one of the beneficiaries is the silicon condenser microphone. Simple analytical expressions, such as those formulated by Škvor/Starr for mechanical-thermal noise calculation, are used to describe the mechanical performance of a microelectromechanical system (MEMS) microphone. However, the location effect of acoustic holes is usually not considered on both frequency response and mechanical-thermal noise. In this paper, the theory of a condenser microphone is reviewed and a new analytical modeling method for the MEMS condenser microphones is proposed based on Zuckerwar's model. With reference to a B&K MEMS microphone, the theoretical results obtained by the modeling method are in very good agreements with those experimental ones reported. It is also concluded that there is an optimum location for acoustic holes in the backplate. Finally, a new design for MEMS microphone with a polarization voltage of 10 V is proposed, which has an open-circuit sensitivity of 2.1 mV/Pa (or −54 dB ref. 1 V/Pa), a bandwidth of 18 kHz, an *A*-weighted mechanical-thermal noise of 22 dB A, and a signal-to-noise ratio of 60 dB. This proposed microphone can be easily micromachined by using MEMS technology such as the deep reactive ion etching and wafer bonding technology.
 [DOI: 10.1121/1.2216561]

PACS number(s): 43.38.Kb, 43.38.Gy, 43.38.Ar, 43.58.Ta [AJZ] Pages: 750–761

I. INTRODUCTION

Coupled with matured silicon micromachining technology, capacitive microelectromechanical system (MEMS) microphones are very popular acoustic sensing devices because of their miniature size, cost effectiveness, and mass production capability. Microphones are electromechanical transducers that convert an incident pressure into a corresponding electrical output. There are many well established transduction principles[1] but the capacitive microphone stands out from the rest due to its high sensitivity, low power consumption, high immunity to external environment, excellent stability, and flat frequency response. An elastic diaphragm and a perforated rigid backplate constitute a pair of sensing electrodes, which behaves like a variable capacitor. The deformable diaphragm detects the pressure variations and converts the corresponding capacitance change into an output voltage by the application of a polarization voltage across the electrodes. Fine arrangement of perforated holes in the backplate weakens the air dampening effect, which ensures a flat frequency response at the desired operating bandwidth and reduces the mechanical-thermal noise[2,3] as well. A high microphone sensitivity is desired, which can be achieved by using corrugated,[4–6] spring-type,[6] and low stress PolySi[7] diaphragms.

In the design of earlier MEMS microphones,[7–12] only a small air gap could be implemented using the surface micromachining technology since the air gap is defined by the sacrificial layer, which is deposited by the thin film technology. The sticking of the thin diaphragm onto the backplate is a big problem during the release process by the wet etching of the sacrificial layer. Furthermore, numerous perforated holes in the backplate are necessary to ease the sacrificial layer etching and weaken the large air damping effect, which is introduced by the small air gap, and to optimize the bandwidth of the frequency response. In general, numerous perforated holes, which are of a few microns in diameter, are uniformly distributed over the entire backplate. Using reactive ion etch, holes are etched in the thin backplate of several microns, which can be either silicon nitride, polysilicon, or even polyimide. A thicker backplate is usually preferred since it can provide much better mechanical rigidity and stability. However, it is still a major challenge to etch small holes in a thick backplate, which is limited by the aspect ratio of the etched holes, by either dry or wet micromachining technologies. On the other hand, large holes would be very easy to etch, but the quantity of holes to be placed in the backplate will be limited. Another problem associated with the small quantity of large holes is the imminent increment of the mechanical-thermal noise.

MEMS microphones, which are fabricated with surface micromachining technology and with a thin, highly perforated backplate, have demonstrated its feasibility.[7–12] However, the traditional condenser microphones, with an acoustic slot around the circumference of the backplate and relatively fewer acoustic holes, have been widely accepted in the microphone industry because of their high performance, high reliability, and easy fabrication. Such design approach can also be adopted for MEMS microphones since the revolu-

[a]Electronic mail: cheewee@ntu.edu.sg
[b]Electronic mail: mjmmiao@ntu.edu.sg

tionary deep reactive ion etch (DRIE)[13–16] and other bulk micromachining technologies can be utilized to realize their fabrication. Recently, B&K developed a MEMS measurement microphone[17] with high sensitivity and low mechanical-thermal noise. For the fabrication, they adopted the bulk micromachining and wafer bonding technology. The low pressure chemical vapor deposition silicon nitride is used as the material for the diaphragm, which is subsequently formed by KOH wet etching to remove the silicon. For the silicon backplate, there are only four perforated holes with a slot around the circumference of the backplate, whose design is very similar to that of the traditional condenser microphone. The diaphragm and backplate wafers are then assembled together by the Au-Au thermocompression bonding technique. The air gap in the B&K MEMS microphone is quite large, which is about 20 μm, to ensure a very low level of mechanical-thermal noise since this microphone was designed for the sole purpose of acoustic measurement.

The microphone is a complex acoustical electromechanical system, which consists of tightly coupled acoustical, electrical, and mechanical elements. A common modeling approach to evaluate the performance of a microphone is the lumped-element method.[7–12,18] In this approach, through the use of simple analytical expressions, mass, compliance, and damping have their equivalent electrical counterparts in inductance, capacitance, and resistance, respectively. The lumped-element method, as exemplified by the analysis of Gabrielson,[2,3] has been very popularly used by the worldwide MEMS microphone research fraternity for more than one decade. Although the analytical expressions are easy to apply, they do have their inherent limitations. These expressions only emphasize the strong dependence on the total open area of holes, the number of holes, and the air gap thickness while the positional effect of holes and their locations on both frequency response and mechanical-thermal noise are not considered and properly addressed. In 1978, Zuckerwar[19,20] developed a comprehensive microphone model to simulate the traditional condenser microphones with a very good degree of accuracy. So far, to our knowledge, nobody has applied Zuckerwar's model to the simulation of any MEMS microphones. With the emergence of newer MEMS technologies, such as DRIE and wafer bonding, for the fabrication of microphones, it is very crucial to develop suitable microphone models to mirror such technological advancements.

In this paper, the theory of a condenser microphone by Zuckerwar[19] is reviewed. With reference to a B&K MEMS microphone,[17] the theoretical results based on Zuckerwar's model are compared, which demonstrate good agreements with those reported experimental ones. The positional effect of acoustic holes in the backplate and the impact of an acoustic slot around the circumference of the backplate on both frequency response and mechanical-thermal noise are presented and discussed. Finally, a new MEMS microphone design is proposed for nonmeasurement applications.

II. REVIEW OF CONDENSER MICROPHONE THEORY

The theory of the condenser microphone will be reviewed, which follows the analysis of Zuckerwar's model.[19]

TABLE I. Parameters of the B&K MEMS microphone.

Parameters	Symbol	Value
Diaphragm radius	a	1.95 mm
Diaphragm thickness	d	0.5 μm
Mass surface density of diaphragm	σ_M	0.0015 kg/m^2
Diaphragm tension	T	170 N/m
Backplate radius	b	1.4 mm
Unpolarized air gap	h	20 μm
Backchamber volume	V	7.6×10^{-8} m^3
Acoustic slot ($k=1$)		
Location of slot	a_1	1.675 mm
Slot width	r_1	0.55 mm
Slot depth	l_1	150 μm
Acoustic holes ($k=2$)		
Number of holes per radius ring	b_2	4
Location of radius ring	a_2	0.55 mm
Hole radius	r_2	40 μm
Hole depth	l_2	150 μm
Polarization voltage	E_0	200 V
Microphone capacitance	C_{mic}	3.5 pF
Preamplifier input capacitance	C_i	0.4 pF
Stray capacitance	C_s	5.1 pF

Approximated from the optical microscope photograph in Ref. 17.

The theoretical considerations are based on a circular diaphragm of radius a. Table I tabulates the parameters of the B&K MEMS microphone. Figure 1(a) illustrates the nomenclature of the B&K MEMS microphone while Fig. 1(b) illustrates the arrangement of acoustic slot and holes in the backplate.

A. Pull-in voltage

Assuming that the diaphragm tension dominates over its inertia, the critical pull-in voltage of the diaphragm, for a piston model and a rigid backplate, can be approximated by

$$V_{\text{in}} = \left(\frac{64Th^3}{27\epsilon_0 a^2}\right)^{1/2}, \tag{1}$$

where T is the diaphragm tension, h is the unpolarized air gap, and ε_0 is the dielectric permittivity of free air (8.85×10^{-12} F/m). If the diaphragm is very thin and has a high residual stress, then the pull-in voltage needs to be multiplied by a factor of 0.82, which is the optimum ratio between the diaphragm and the backplate area for maximum sensitivity.[1,21] A high pull-in voltage results from a high diaphragm tension, large air gap, and small diaphragm.

B. Electrical transfer function

The electrical transfer function of the microphone, with an acoustic slot around the circumference of the backplate, can be approximated by

$$M_e = \frac{E_0}{h_0}\left(1 - \frac{1}{2}\cdot\frac{S_{\text{bp}}}{S_{\text{dia}}}\right), \tag{2}$$

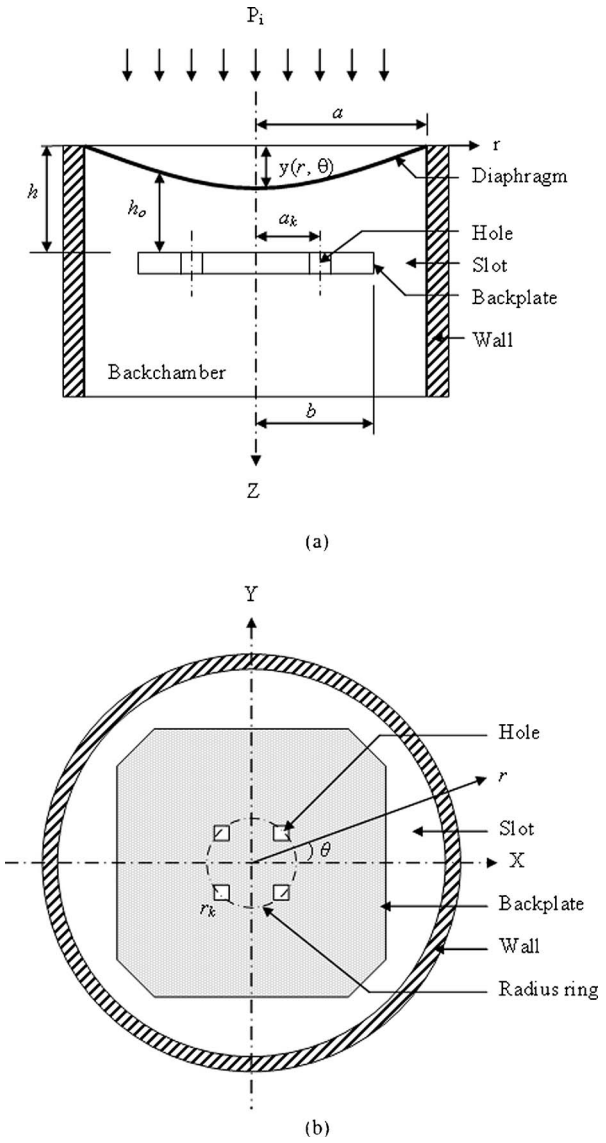

FIG. 1. B&K MEMS microphone: (a) Cross-sectional view and (b) arrangement of acoustic slot and holes in the backplate (Ref. 17) with the diaphragm removed.

where h_0 is the average air gap distance between the diaphragm and the backplate as a result of electrostatic deflection caused by the polarization voltage E_0, S_{dia} is the diaphragm area, and S_{bp} is the backplate area. For a circular diaphragm and backplate, the ratio of $S_{\text{bp}}/S_{\text{dia}}$ is simply $(b/a)^2$, where b is the backplate radius. This correction factor of $(1-b^2/2a^2)$ significantly enhances the electrical description of the circular microphone.[22] A high electrical sensitivity is favored by a high polarization voltage, small air gap, and large diaphragm to backplate area ratio.

C. Mechanical transfer function

The vibration motion of the system of coupled diaphragm and air layer is governed by the following four equations:[19]

(1) Equation of motion

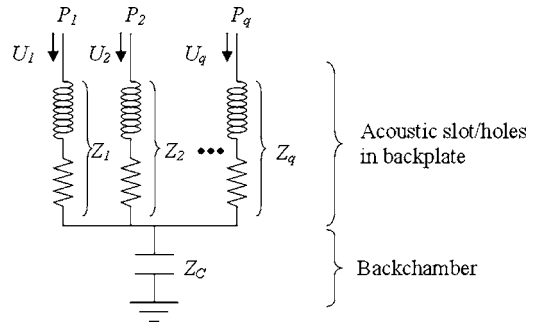

FIG. 2. Equivalent circuit of the acoustic slot and holes in the backplate.

$$\nabla^2 y(r,\theta) + K^2 y(r,\theta) = -\frac{p_i}{T} + \frac{p(r,\theta,0)}{T}, \tag{3}$$

(2) Navier-Stokes equation

$$j\omega\rho_0 \mathbf{v} = -\nabla p + \mu\left(\nabla^2 \mathbf{v} + \tfrac{1}{3}\nabla\nabla\cdot\mathbf{v}\right), \tag{4}$$

(3) Continuity equation

$$\rho_0 \nabla\cdot\mathbf{v} = -j\omega\rho, \tag{5}$$

(4) Equation of state

$$p = \rho c_{\text{T}}^2. \tag{6}$$

With reference to Figs. 1(a) and 1(b) and a cylindrical coordinate system (r,θ,Z), $y(r,\theta)$ is the deflection of the diaphragm, p_i is the incident acoustic pressure, $p(r,\theta,0)$ is the reaction pressure on the diaphragm, ω is the angular frequency of the incident acoustic pressure, $\mathbf{v}$ is the air particle velocity, ρ_0 is the static air density (1.205 kg/m^3), ρ is the time-varying air density, μ is the absolute viscosity of air (17.9×10^{-6} Ns/m^2), c_T is the isothermal speed of sound in air (290.2 m/s), and K is the wave number of sound in the diaphragm

$$K = \omega\left(\frac{\sigma_M}{T}\right)^{1/2}, \tag{7}$$

where σ_M is the mass surface density of the diaphragm.

Each acoustic hole in the backplate is assigned a number $(k=1,2,\ldots q)$ for identification where q is the total number of acoustic holes. If an acoustic slot is present around the circumference of the backplate, it is assigned as $k=1$. An equivalent circuit of the backplate and the backchamber is illustrated in Fig. 2. The equations of the impedance circuit can be written in a matrix form

$$\boldsymbol{P} = \boldsymbol{Z}\boldsymbol{U}, \tag{8}$$

where $\boldsymbol{P}$ is the $(q\times1)$ pressure matrix, $\boldsymbol{U}$ is the $(q\times1)$ volume velocity matrix, and $\boldsymbol{Z}$ is the $(q\times q)$ acoustic impedance matrix

$$\mathbf{P} = \begin{bmatrix} p_1 \\ p_2 \\ \cdot \\ \cdot \\ \cdot \\ p_q \end{bmatrix} \quad \mathbf{U} = \begin{bmatrix} U_1 \\ U_2 \\ \cdot \\ \cdot \\ \cdot \\ U_q \end{bmatrix},$$

$$\mathbf{Z} = \begin{bmatrix} Z_1 + Z_C & Z_C & \cdot & \cdot & Z_C & Z_C \\ Z_C & Z_2 + Z_C & & & \cdot & \cdot \\ \cdot & Z_C & & & \cdot & \cdot \\ \cdot & \cdot & & & \cdot & \cdot \\ \cdot & \cdot & & & Z_{q-1} + Z_C & Z_C \\ Z_C & \cdot & \cdot & \cdot & Z_C & Z_q + Z_C \end{bmatrix}. \quad (9)$$

The acoustic impedance of the backchamber, Z_C, can be modeled as

$$Z_C = \frac{\gamma \rho_0 c_T^2}{j\omega V}, \quad (10)$$

where γ is the specific heat ratio of air (1.403) and V is the volume of the backchamber. The acoustic impedance of the kth opening of the backplate can be modeled as

$$Z_k = \frac{(8\omega\rho_0\mu)^{1/2}}{\pi r_k^2}\left(1 + \frac{l_k}{2r_k}\right) + j\frac{\omega\rho_0(l_k + 1.7r_k)}{\pi r_k^2}, \quad (11)$$

where r_k is the radius of the kth hole. The acoustic impedance of the slot in the backplate can be modeled as

$$Z_1 = \frac{(2\omega\rho_0\mu)^{1/2}}{\pi a_1 r_1}\left(1 + \frac{l_1}{2r_1}\right) + j\frac{\omega\rho_0 l_1}{2a_1 r_1}, \quad (12)$$

where r_1 is the width of the slot.

Without going into the details of further mathematical derivations, of which can be found in Refs. 19 and 20, the deflection of the diaphragm, $y(r)$, independent of θ, can be written down as

$$y(r) = \frac{p_i}{TK^2} \cdot \frac{J_2(Ka)}{J_0(Ka) + D(\omega)}, \quad (13)$$

where $J_0(Ka)$ and $J_2(Ka)$ are the zero and second order Bessel functions of Ka, respectively and D is given by

$$D(\omega) = \frac{j4\omega\rho_0 J_0(Ka)}{\pi T J_2(Ka)} \times \sum_{m=0}^{\infty}\left[-j\omega\left(\frac{y_m}{y_0}\right) + \sum_{s=1}^{q}\left(\frac{f_s}{y_0}\right)s_s\Gamma_m J_0(\xi_m a_s)\right] \times \frac{1}{T_m J_0(\xi_m a)}\left\{\frac{J_2(Ka)\delta(m)}{4K^2a^2} + \frac{J_1(Ka)[1-\delta(m)]}{2Ka(K^2a^2 - \xi_m^2 a^2)}\right\}. \quad (14)$$

From Eq. (13), the mechanical sensitivity of the microphone is given by

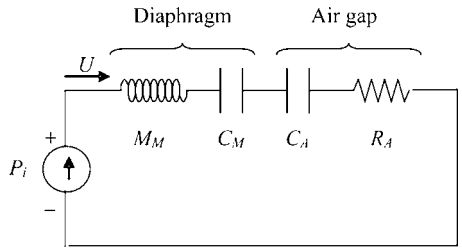

FIG. 3. Acoustical lumped-element equivalent circuit of the microphone.

$$M_m(\omega) = \frac{y(r)}{p_i} = \frac{1}{TK^2} \cdot \frac{J_2(Ka)}{J_0(Ka) + D(\omega)}. \quad (15)$$

At low frequencies, the mechanical sensitivity of Eq. (15) can be approximated by

$$M_m \approx \frac{a^2}{8T}. \quad (16)$$

Figure 3 illustrates the acoustical lumped-element equivalent circuit of the microphone. At frequencies that are well below the first resonant frequency of the diaphragm, the diaphragm mass, diaphragm compliance, air compliance, and air resistance can be expressed, respectively, as

$$M_M = \frac{4\sigma_M}{3\pi a^2}, \quad (17)$$

$$C_M = \frac{(\pi a^2)^2}{8\pi T}, \quad (18)$$

$$C_A(\omega) = \frac{(\pi a^2)^2}{8\pi T\,\mathrm{Re}(D)}, \quad (19)$$

$$R_A(\omega) = \frac{8\pi T\,\mathrm{Im}(D)}{\omega(\pi a^2)^2}. \quad (20)$$

The air resistance R_A accounts for the mechanical-thermal noise of the microphone, which is dependent on the air damping in the air gap and acoustic holes. The inherent miniaturized size of the microphone contributes to the mechanical-thermal noise as a result of molecular thermal agitation. This mechanical-thermal noise, together with other sources of background noise, establishes the lowest limit of acoustic pressure[23,24] that can be picked up by the microphone. This calls for a meticulous design of air gap, acoustic slot and holes in the backplate. A large air gap is necessary for a low mechanical-thermal noise microphone, but this is at the expense of low microphone sensitivity and narrow frequency bandwidth. To compensate for it, a large polarization voltage is required to enhance the sensitivity. Therefore, it is not a coincidence that commercial microphone measurement systems, which require a low level of noise, have polarization voltages of up to 200 V.

D. Microphone sensitivity

The open-circuit sensitivity of the microphone at low frequency can be expressed by

$$M_{\mathrm{oc}} = M_e M_m = \frac{E_0}{h_0}\left(1 - \frac{b^2}{2a^2}\right) \cdot \frac{a^2}{8T}. \tag{21}$$

The overall sensitivity of the microphone, including the preamplifier, is given by

$$M = M_{\mathrm{oc}} A_c A_v = \frac{E_0}{h_0}\left(1 - \frac{b^2}{2a^2}\right)\frac{a^2}{8T}\left(1 + \frac{C_i + C_s}{C_{to}}\right)^{-1}, \tag{22}$$

where C_{to} is the capacitance of the polarized microphone, C_i is the input capacitance of a preamplifier, C_s is the stray capacitance, A_c is the capacitive signal attenuation due to C_i and C_s, and A_v is the gain of the preamplifier, which is assumed to be one.

III. B&K MEMS MICROPHONE DESIGN

In the design of MEMS microphone, B&K adopted a design methodology[17] that is a reminiscence of their successful range of macro condenser microphones. For a MEMS microphone, its diaphragm is unusually large (∅ 3.9 mm). However, this is a necessary design consideration for a measurement microphone since a larger diaphragm has a higher sensitivity. The choice of silicon nitride as the thin and highly stressed diaphragm revolves around the compromise to achieve a low diaphragm tension (or mechanical-thermal noise) while avoiding designing an underdamped mechanical system. A thick rigid silicon backplate, with four KOH-etched holes, completes the pair of sensing electrodes. Silicon is chosen here as the backplate material to ease the fabrication process. The diaphragm and the backplate wafers are then bonded together using Au-Au thermocompression bonding at four anchor points, which paths the way for a large air gap and an acoustic slot. Any degradation of the microphone sensitivity, whether unintentionally by design or process, is compensated by a 200 V polarization voltage, which is made possible by a large air gap (20 μm). By no coincidence, this 200 V polarization voltage enables the microphone to be used in conjunction with an existing B&K Type 2670 low noise microphone preamplifier.[25] For packaging and testing purposes, the microphone is housed in a 1/4 in. microphone titanium body. Wet etching is also used to define an air channel above the diaphragm for maximum microphone sensitivity. The fabrication processes that are adopted by B&K involve many well established ones and mainly bulk micromachining, which is simple, inexpensive and, attractive for mass production.

IV. MECHANICAL-THERMAL NOISE ANALYSIS

The background noise level of a microphone is one of the most important design specifications because it imposes a restriction on the sensitivity of the microphone (i.e., it determines the lowest possible detectable acoustic pressure). The background noise consists of both external sources, such as power supply lines, radio frequency interference, and vibration, and internal generated ones such as mechanical-thermal noise,[2,3] electrical Johnson noise,[3,23,26] shot noise,[3,23,26] $1/f$ noise,[3,23,26,27] and preamplifier noise.[3,23] In the formulation[23] of the preamplifier noise, the effects of electrical Johnson noise, shot noise, and $1/f$ noise are clearly visible. In this section, only the mechanical-thermal noise is presented and discussed.

The movement of small movable mechanical components is adversely affected by molecular thermal agitation, which subsequently gives rise to mechanical-thermal noise. This mechanical-thermal noise can put a limiting factor on the performance of many small-sensor systems. For the capacitive microphone, one method of reducing the mechanical-thermal noise is to reduce the damping resistance through the meticulous design of the backplate and an optimum air gap. However, the resonant peak of the diaphragm increases as a result of a loss in the mechanical damping in the system.

In the approach of Zuckerwar,[19] the equivalent mechanical resistance due to the air gap and acoustic holes, which is frequency dependent, can be re-expressed as

$$R_A(f) = \frac{8\pi T\,\mathrm{Im}(D)}{2\pi f(\pi a^2)^2}. \tag{23}$$

The physical origin of the air resistance R_A lies in the viscous boundary layer losses in the air gap and more significantly, in the acoustic holes in the backplate. The pressure spectral density of the mechanical-thermal noise can then be expressed by

$$P_f = \sqrt{4k_B T R_A(f)}, \tag{24}$$

where k_B is the Boltzmann constant (1.38×10^{-23} J/K) and T is the absolute temperature (K).

For a comparison of modeling approaches, the mechanical-thermal noise analysis of Škvor[28] and Starr[29] is used. In this approach, the squeeze-film damping model—viscous loss that is associated with the squeezing of the fluid out from between two moving surfaces—is used in which, it dominates the dissipation mechanism for an air gap of several microns. For two parallel diaphragm and backplate, the equivalent mechanical resistance due to squeeze-film damping[29] is given by

$$R_{\mathrm{airgap}} = \frac{3\mu}{2\pi h^3}. \tag{25}$$

When acoustic holes are perforated in the backplate, the damping can be reduced significantly as the air has an alternative path to escape through the holes rather than being squeezed out from the edge of the backplate. The equivalent mechanical resistance due to acoustic holes[28] is given by

$$R_{\mathrm{hole}} = \frac{12\mu}{N\pi h^3} G(A), \tag{26}$$

where N is the number of holes in the backplate and $G(A)$ is given by

$$G(A) = \left[\frac{A}{2} - \frac{A^2}{8} - \frac{\ln A}{4} - \frac{3}{8}\right], \tag{27}$$

where A is the fraction of open area in the backplate. Notice how Eqs. (25) and (26) are heavily dependent on h and independent of frequency. For many applications, a good approximation of the total resultant mechanical resistance is

obtained by the parallel combination of Eqs. (25) and (26). The pressure spectral density of the mechanical-thermal noise is then given by

$$P_f = \sqrt{4k_B T(R_{\text{airgap}} // R_{\text{hole}})}. \tag{28}$$

The mechanical-thermal noise originates when thermally excited molecules impinge and collide into a mechanical barrier or structure. As in the case of squeeze-film damping, the probability and magnitude of such mechanical-thermal collisions can be increased by a reduction in the air gap thickness and/or an increase in the surface area of the diaphragm and the backplate other than the effect of temperature.

The approach of Škvor/Starr is relatively straightforward and it is suitable for any applications that have squeeze-film damping characteristics. Due to its simplicity, this form of approach, which depends significantly on both the air gap and the surface area of the plates, was popular with many authors.[7–12,18] It implies a constant air gap between two rigid parallel plates throughout the entire surface area of the plates during the squeeze-film damping operation. The radiation components of the plates are usually ignored for applications that operate at frequencies that are below a few tens of kilohertz. The analysis of Škvor/Starr places a huge emphasis on the air gap thickness (the equivalent mechanical resistance is inversely proportional to h^3) as indicated in Eqs. (25) and (26) and assumes that the equivalent mechanical resistance is independent of frequency. The next important parameter is the percentage of open area of acoustic holes in the backplate as indicated by $G(A)$ in Eq. (27). Thus, the approach of Škvor/Starr is based on the concepts of air gap thickness and plate area and it does not take into any considerations of the location of holes in the backplate, the thickness of the backplate, and the influence of the backchamber.

However, in the analysis of Zuckerwar, the microphone is the only targeted application, whereby the rigid backplate remains stationary in position while the edge of the deformable diaphragm is clamped at a fixed boundary. As a result, during normal sensing operation, there is no constant air gap between the two electrode plates throughout the entire surface area of the electrodes. Due to the clamped edge of the diaphragm, the "effective plate area" is smaller and the "effective air gap separation" is larger as compared to Starr's squeeze-film model. Moreover, the excited deflection profile of the diaphragm is taken into consideration by the use of a simple trial function for the diaphragm displacement $y(r)$ and the extensive usage of Bessel functions in Zuckerwar's formulation. Beside the air gap thickness and the total area of acoustic holes in the backplate, the analysis of Zuckerwar also emphasizes the dependency of R_A on the location of holes in the backplate, the thickness of the backplate, and the backchamber. The thickness of the backplate does play an important role in the damping characteristics of the microphone as a thicker backplate, compounded by small holes, poses a larger mechanical resistance to airflow. The omission of the location of holes in the backplate, the backplate thickness, and the backchamber in the analysis of Škvor/Starr probably explains why the approach of Zuckerwar yields a lower but more accurate R_A value than that of Škvor/Starr, a conclusion with which Gabrielson agrees. This will be illustrated numerically in the section that follows.

TABLE II. Theoretical and experimental results of the B&K MEMS microphone.

Parameters	Symbol	Theoretical	Experimental (Ref. 17)
Pull-in voltage	V_{in}	254 V	255–263 V
Open-circuit sensitivity	M_{oc}	23 mV/Pa	22 mV/Pa
		−33 dB ref. 1 V/Pa	−33 dB ref. 1 V/Pa
Overall sensitivity	M	9.4 mV/Pa	···
Bandwidth	BW	15 kHz	15 kHz
Membrane mass	M_M	167 kg/m^4	···
Membrane compliance	C_M	3.3×10^{-14} m^5/N	···
Air resistance	R_A	3.2×10^{8} Ns/m^5	···
Air compliance	C_A	5.4×10^{-13} m^5/N	···
Thermal noise	N	23 dB A	23 dB A
Signal-to-noise ratio	SNR	71 dB	···

Assume unity preamplifier gain.
Theoretical value at 250 Hz.
Theoretical value with reference to 1 Pa at 1 kHz.

The noise voltage spectral density of the mechanical-thermal noise can be expressed by

$$N_f = MP_f. \tag{29}$$

The background noise pressure level (A-weighted) of the mechanical-thermal noise can be expressed by

$$N = \sqrt{\int_{f_1}^{f_2} 4k_B T R_A A^2(f) df}, \tag{30}$$

where $A(f)$ is the function of the A-weighted filter, and f_1 and f_2 are 10 Hz and 20 kHz, respectively.

V. RESULTS AND DISCUSSIONS

Table II tabulates the theoretical results of the B&K MEMS microphone in which, the pull-in voltage, open-circuit sensitivity, bandwidth, and thermal noise demonstrate good agreements with those reported experimental ones found in Ref. 17. Figure 4 illustrates the normalized frequency response plot of the microphone, which again dem-

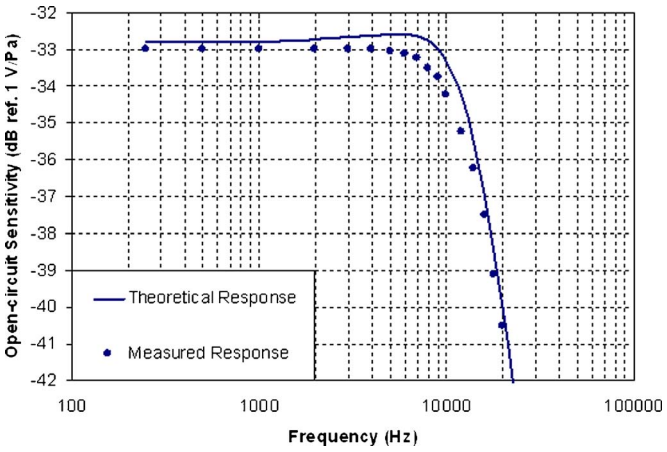

FIG. 4. (Color online) Normalized frequency response plot of the B&K MEMS microphone. Measured response is taken from Ref. 17.

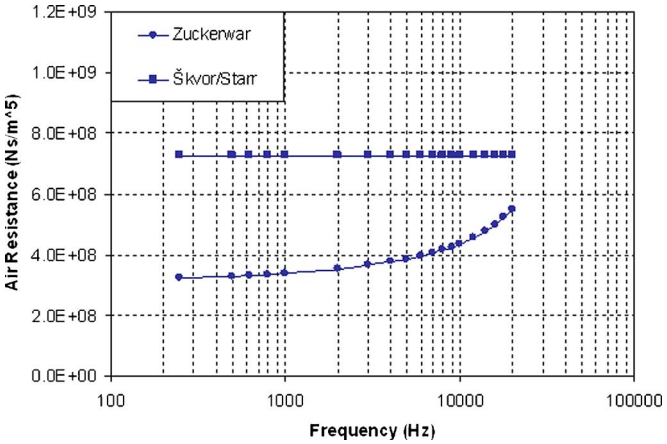

FIG. 5. (Color online) Comparison of approaches for the computation of air resistance R_A.

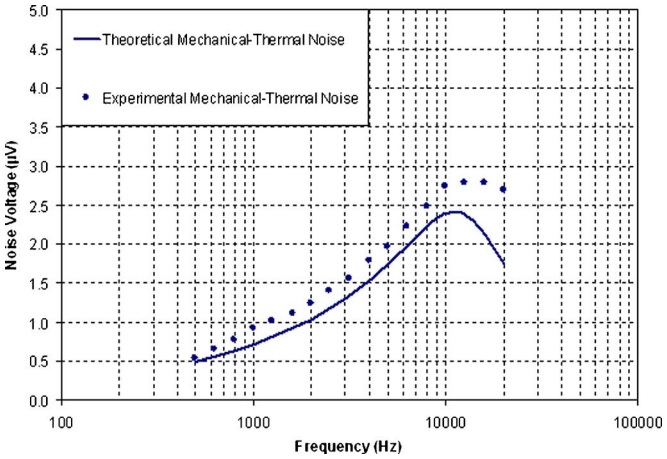

FIG. 6. (Color online) Theoretical and experimental mechanical-thermal noise spectrum of the B&K MEMS microphone. Experimental data are taken from Ref. 17 after the quadratic subtraction of the preamplifier noise from the total noise.

onstrates good agreement with the measured response. Using the same MEMS microphone, Fig. 5 highlights and validates the differing approaches of Zuckerwar and Škvor/Starr with respect to the computation of R_A. As expected, the approach of Zuckerwar yields a lower value and the frequency dependence nature of R_A is clearly seen. The calculated A-weighted mechanical-thermal noise of the microphone is 23 and 26 dB A for the approach of Zuckerwar and Škvor/Starr, respectively. The reported experimental value of 23 dB A agrees very well with the theoretical approach of Zuckerwar.

In the theoretical consideration of the mechanical-thermal noise, the analysis of Zuckerwar is used. For the noise analysis of the B&K MEMS microphone, only the preamplifier noise and the mechanical-thermal noise will be considered. The preamplifier noise dominates the total microphone noise below 500 Hz while the mechanical-thermal noise dominates from 500 Hz to 30 kHz. From Ref. 17, the preamplifier noise data points at 200 V polarization voltage are plotted until 400 Hz, curve fitted and then extrapolated from 500 Hz to 40 kHz. For curve fitting, a power curve is used (R^2=0.98). Next, the extrapolated preamplifier noise is quadratically subtracted from the experimental total noise at 200 V polarization voltage to attain the experimental mechanical-thermal noise spectrum. Figure 6 illustrates the mechanical-thermal noise spectrum of the microphone in which, the theoretical mechanical-thermal noise is in good agreement with the experimental one. Finally, the extrapolated preamplifier noise is quadratically added to the theoretical mechanical-thermal noise to yield the theoretical total noise spectrum. Figure 7 illustrates the total noise spectrum of the microphone in which, a good agreement is also observed between the theoretical and experimental results.

A. Effect of acoustic slot

There is an optimum size[20,22] for the backplate design, which states that the ratio of the backplate radius to the diaphragm radius is 0.82. This optimum size criterion implies an acoustic slot around the circumference of the backplate. The B&K design has a ratio of 0.72 and for comparison purpose, the slot is intentionally removed. Figures 8(a) and 8(b) illustrate the effect of a slot on the frequency response and the mechanical-thermal noise voltage spectrum density plots, respectively. For the frequency response plot, with a slot, the bandwidth is significantly larger. For the noise voltage spectrum density plot, with a slot, the mechanical-thermal noise drops significantly. With a slot, the surface area of the backplate is reduced. This reduction in surface area leads to a decrease in system damping and thus, a subsequent increase in bandwidth and a decrease in mechanical-thermal noise.

B. Effect of air gap thickness

Figures 9(a) and 9(b) illustrate the effect of air gap thickness on the frequency response and the mechanical-thermal noise voltage spectrum density plots, respectively. With reference to the B&K design of 20 μm, for an air gap thickness of 15 μm, a significant increase in microphone sensitivity and mechanical-thermal noise, and a significant decrease in bandwidth are observed. A high value of mechanical-thermal noise and a low value of bandwidth are not desirable for any microphone design. On the other hand,

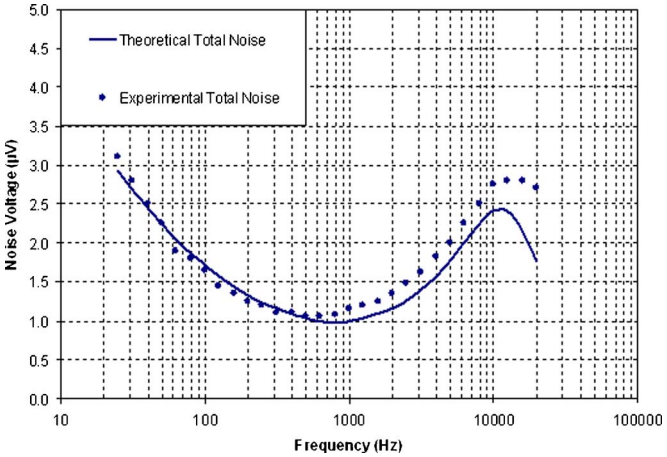

FIG. 7. (Color online) Theoretical and experimental total noise spectrum of the B&K MEMS microphone. Experimental data are taken from Ref. 17.

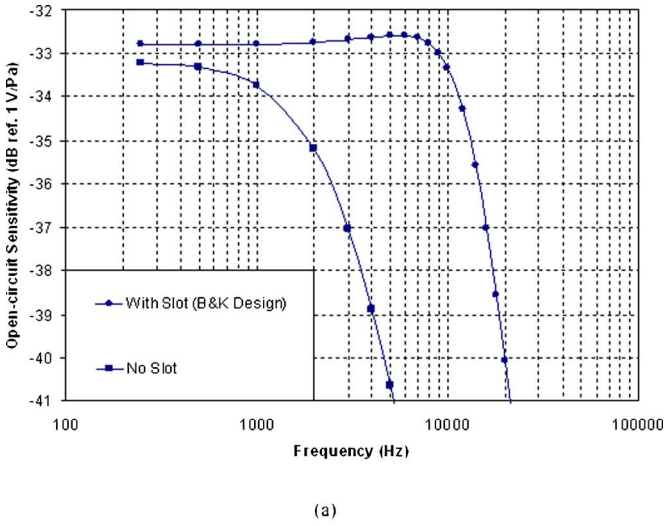

(a)

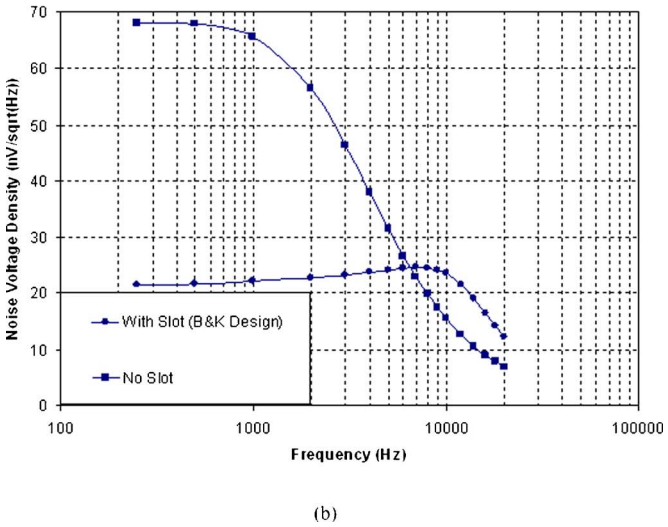

(b)

FIG. 8. (Color online) Effect of the acoustic slot on (a) the frequency response and (b) the mechanical-thermal noise voltage spectrum density plots.

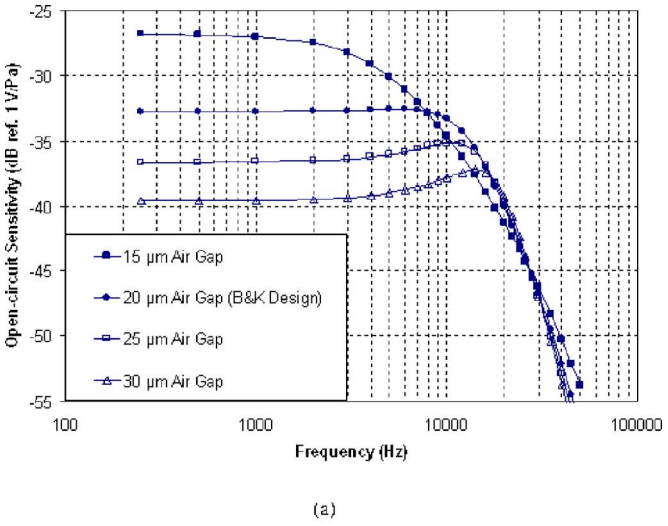

(a)

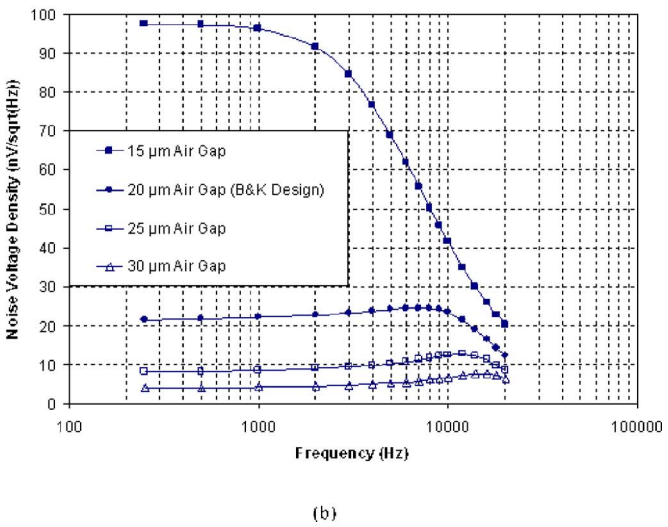

(b)

FIG. 9. (Color online) Effect of the air gap thickness on (a) the frequency response and (b) the mechanical-thermal noise voltage spectrum density plots.

for an air gap thickness of 25 and 30 μm, a significant decrease in microphone sensitivity is observed. Although there are significant enhancements in both bandwidth and mechanical-thermal noise, these improvements are at the expense of lower sensitivity. In addition, their frequency response curves show that they are transitioning towards underdamped systems as evidenced by the visible resonant peaks. A narrow air gap results in an increase in system damping, which leads to a lower bandwidth and a higher mechanical-thermal noise. The reverse is also true for a wider air gap. Therefore, the B&K design of 20 μm air gap thickness is a good compromise between sensitivity, bandwidth, and mechanical-thermal noise.

C. Effect of location of acoustic holes

Figures 10(a) and 10(b) illustrate the effect of location of acoustic holes on the frequency response and the mechanical-thermal noise voltage spectrum density plots, respectively. With reference to the B&K design of 0.55 mm, at a radius ring of 0.3 and 0.5 mm, there is an observable bandwidth reduction and mechanical-thermal noise increase due to an increase in damping property. At a radius ring of 0.6 and 0.8 mm, no significant deviations in bandwidth and mechanical-thermal noise are observed. The above results indicate that the location of holes does affect the performance of the microphone and there is an optimum location for the holes in the backplate. For this particular case, the optimum location for the holes is between 0.5 and 0.8 mm radius ring. However, with stricter tolerances at resonant frequency, the optimum location narrows down to between 0.5 and 0.6 mm radius ring, which is in the vicinity of the B&K design of 0.55 mm.

VI. PROPOSED NEW DESIGN FOR MEMS MICROPHONE

The design of the B&K MEMS microphone is strongly influenced by the requirement that it is to be used as a measurement microphone in conjunction with an existing B&K Type 2670 low noise microphone preamplifier.[25] For nonmeasurement applications, such as hearing aids, mobile phones, and etc., the polarization voltage of 200 V is simply

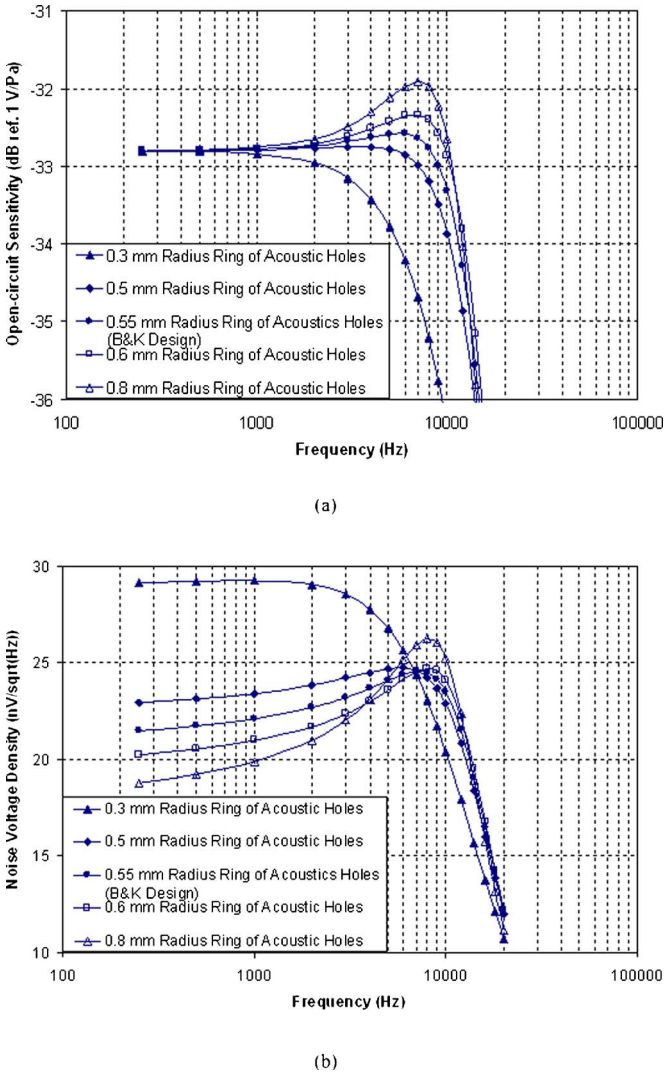

FIG. 10. (Color online) Effect of the location of acoustic holes on (a) the frequency response and (b) the mechanical-thermal noise voltage spectrum density plots.

too high and impossible to be used. For such applications, a much lower polarization voltage is used in the range of a few volts. To maintain a relatively high sensitivity, the air gap has to be reduced, however which will cause a higher mechanical-thermal noise. A typical signal-to-noise ratio of 55–60 dB is required for nonmeasurement microphone applications. Thus, there is no necessity to incorporate a large air gap since the mechanical-thermal noise requirement is less stringent as compared to a measurement microphone system. In proposing a new design for MEMS microphone for nonmeasurement applications, only the polarization voltage and the air gap thickness are reduced to 10 V and 10 μm, respectively, while all other parameters are maintained. After the reduction of the polarization voltage to 10 V and the air gap thickness to 10 μm, the open-circuit sensitivity of the microphone is reduced to 2.1 mV/Pa from the initial value of 22 mV/Pa. However, when the air gap thickness is reduced to 10 μm, the microphone design suffers from a low bandwidth and a high level of mechanical-thermal noise. To resolve these issues, additional acoustic

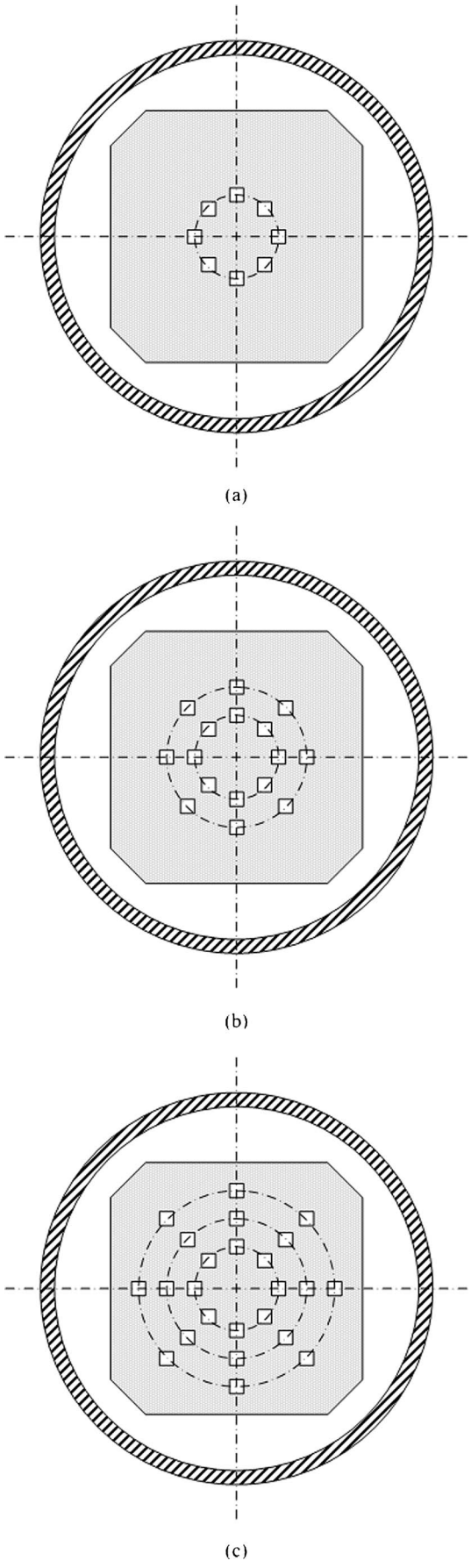

FIG. 11. Arrangement of acoustic slot and holes in the backplate of the proposed MEMS microphone: (a) eight-hole configuration, (b) 16-hole configuration, and (c) 24-hole configuration.

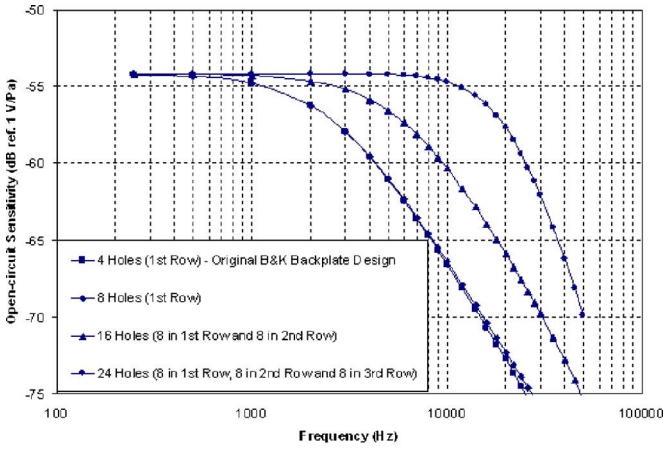

(a)

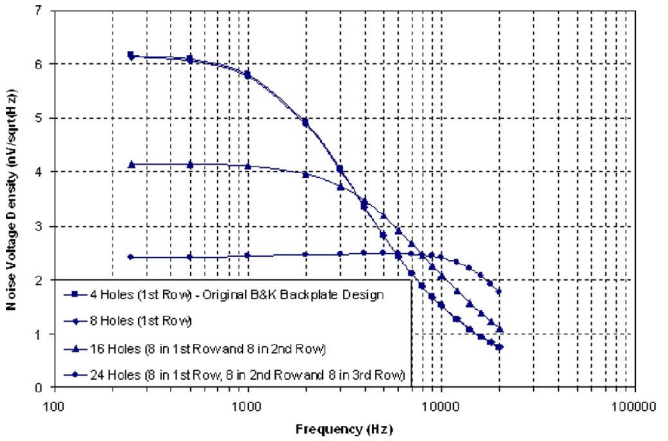

(b)

FIG. 12. (Color online) Effect of the number and the location of acoustic holes on (a) the frequency response and (b) the mechanical-thermal noise voltage spectrum density plots.

holes are required in the backplate to lower the air damping effect, which will enhance the bandwidth and lower the noise level.

Figure 11 illustrates three arrangements of acoustic slot and holes in the backplate of the proposed MEMS microphone, in which acoustic holes are distributed among three radius rings of 0.55 mm (first row), 0.8 mm (second row), and 1.1 mm (third row). Figures 12(a) and 12(b) illustrate the effect of both number and location of acoustic holes on the frequency response and the mechanical-thermal noise voltage spectral density plots, respectively. Based on our analytical model, there are no significant deviations between the original four-hole and eight-hole configurations when they are arranged in one ring. However, if additional acoustic holes are added to the second and third row, an observable enhancement in both the bandwidth and the mechanical-thermal noise can be easily seen. For an optimum bandwidth value, the 24-hole backplate configuration is selected for the proposed microphone design. From our analysis results, it can be concluded that the microphone frequency response, and especially the mechanical-thermal noise do not only depend on the number of acoustic holes, but also largely on the locations of the acoustic holes. The same conclusions cannot be drawn by using the widely used analytical model of Škvor/Starr.

TABLE III. Parameters of the proposed MEMS microphone.

Parameters	Symbol	Value
Diaphragm radius	a	1.95 mm
Diaphragm thickness	d	0.5 μm
Mass surface density of diaphragm	σ_M	0.0015 kg/m^2
Diaphragm tension	T	170 N/m
Backplate radius	b	1.4 mm
Unpolarized air gap	h	10 μm
Backchamber volume	V	7.6×10^{-8} m^3
Acoustic slot ($k=1$)		
Location of slot	a_1	1.675 mm
Slot width	r_1	0.55 mm
Slot depth	l_1	150 μm
Acoustic holes ($k=2,3,4$)		
Number of holes per radius ring	b_k	8, 8, 8
Location of radius ring	a_k	0.55, 0.8, 1.1 mm
Hole radius	r_k	40, 40, 40 μm
Hole depth	l_k	150, 150, 150 μm
Polarization voltage	E_0	10 V
Microphone capacitance	C_{mic}	6.9 pF
Preamplifier input capacitance	C_i	0.4 pF
Stray capacitance	C_s	5.1 pF

Assumed value.

The parameters of the proposed optimized MEMS microphone can be found in Table III. As tabulated in Table IV, this MEMS microphone design has an open-circuit sensitivity of 2.1 mV/Pa (or −54 dB ref. 1 V/Pa), a bandwidth of 18 kHz, an A-weighted mechanical-thermal noise of 22 dB A, and a signal-to-noise ratio of 60 dB. Figure 13 illustrates the theoretical noise voltage spectrum density plot of the proposed MEMS microphone with the preamplifier. Such performances are comparable with the traditional electret microphones and can meet the requirements of most applications.

For the B&K MEMS microphone, a thick silicon wafer is used as the rigid backplate wafer, in which four holes are etched anisotropically in KOH. The profile of the etched holes, as illustrated in Ref. 17, is that of a square opening

TABLE IV. Theoretical results of the proposed MEMS microphone.

Parameters	Symbol	Theoretical
Pull-in voltage	V_{in}	90 V
Open-circuit sensitivity	M_{oc}	2.1 mV/Pa −54 dB ref. 1 V/Pa
Overall sensitivity	M	1.2 mV/Pa
Bandwidth	BW	18 kHz
Membrane mass	M_M	167 kg/m^4
Membrane compliance	C_M	3.3×10^{-14} m^5/N
Air resistance	R_A	2.9×10^{8} Ns/m^5
Air compliance	C_A	5.4×10^{-13} m^5/N
Thermal noise	N	22 dB A
Signal-to-noise ratio	SNR	60 dB

Assume unity preamplifier gain.
Theoretical value at 250 Hz.
Theoretical value with reference to 1 Pa at 1 kHz.

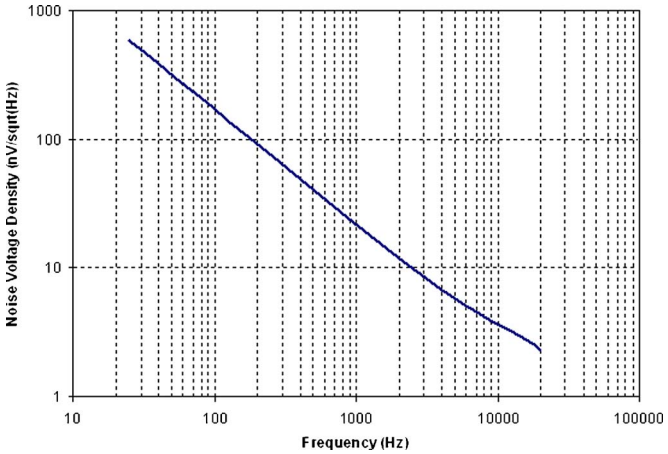

FIG. 13. (Color online) Calculated total noise voltage spectrum density of the proposed MEMS microphone with the preamplifier.

and a tapered cross section due to the nature of wet anisotropic etching of ⟨100⟩ silicon wafer. Thus, an increase of the hole density, if required by design, is limited by the anisotropically etched holes. As a result, DRIE is proposed here to replace the wet etching step in order to better control the cross sectional profile of the etched holes with the optimism of fabricating better performance microphones. Likewise, using the DRIE process, a higher density of high aspect ratio circular holes with vertical cross sectional profile can be realized in a thick silicon backplate wafer in order to cater for more acoustic holes in the backplate.

VII. CONCLUSION

The shift in the fabrication of MEMS microphones from surface to bulk micromachining, using deep reactive ion etching together with wafer bonding technology, necessitates a more accurate and reliable approach to microphone modeling. The theory of a condenser microphone, covering both the electrical and the mechanical transfer functions, is reviewed. The damping approach of Škvor/Starr is popular among many authors due to its simplicity. However, it is based on the concepts of air gap thickness, number of acoustic holes and plate area that do not take into any considerations of the location of acoustic holes in the backplate, the thickness of the backplate, and the influence of the backchamber. In this paper, we derived a new approach based on Zuckerwar's model to analyze the MEMS condenser microphone. With reference to a B&K MEMS microphone, the theoretical results obtained are in very good agreements with those reported experimental ones. An acoustic slot around the circumference of the backplate, which is absent from earlier MEMS microphones due to fabrication constraints, is essential for fabricating better performance microphones. It is also demonstrated that there is an optimum location for acoustic holes in the backplate. Finally, a new MEMS microphone design is proposed for nonmeasurement applications. The new design for the MEMS microphone just needs a polarization voltage of 10 V and it can achieve an open-circuit sensitivity of 2.1 mV/Pa (or −54 dB ref. 1 V/Pa), a bandwidth of 18 kHz, an *A*-weighted mechanical-thermal noise of 22 dB A, and a signal-to-noise ratio of 60 dB.

[1]P. R. Scheeper, A. G. H. van der Donk, W. Olthuis, and P. Bergveld, "A review of silicon microphones," Sens. Actuators, A **44**, 1–11 (1994).
[2]T. B. Gabrielson, "Mechanical-thermal noise in micromachined acoustic and vibration sensors," IEEE Trans. Electron Devices **40**, 903–909 (1993).
[3]T. B. Gabrielson, "Fundamental noise limits in miniature acoustic and vibration sensors," J. Vibr. Acoust. **117**, 405–410 (1995).
[4]X. Li, R. Lin, H. S. Kek, J. Miao, and Q. Zou, "Sensitivity-improved silicon condenser microphone with a novel single deeply corrugated diaphragm," Sens. Actuators, A **92**, 257–262 (2001).
[5]J. Miao, R. Lin, L. Chen, Q. Zou, S. Y. Lim, and S. H. Seah, "Design considerations in micromachined silicon microphones," Microelectron. J. **33**, 21–28 (2002).
[6]M. Füldner, A. Dehé, and R. Lerch, "Analytical analysis and finite element simulation of advanced membranes for silicon microphones," IEEE Sens. J. **5**, 857–863 (2005).
[7]P. C. Hsu, C. H. Mastrangelo, and K. D. Wise, "A high sensitivity polysilicon diaphragm condenser microphone," *Proc. 11th IEEE Workshop on MEMS '98*, Heidelberg, Germany, pp. 580–585, January 1998.
[8]P. R. Scheeper, A. G. H. van der Donk, W. Olthuis, and P. Bergveld, "Fabrication of silicon condenser microphones using single wafer technology," J. Microelectromech. Syst. **1**, 147–154 (1992).
[9]M. Pedersen, W. Olthuis, and P. Bergveld, "A silicon condenser microphone with polyimide diaphragm and backplate," Sens. Actuators, A **63**, 97–104 (1997).
[10]P. R. Scheeper, W. Olthuis, and P. Bergveld, "Improvement of the performance of microphones with a silicon nitride diaphragm and backplate," Sens. Actuators, A **40**, 179–186 (1994).
[11]M. Pedersen, W. Olthuis, and P. Bergveld, "High-performance condenser microphone with fully integrated CMOS amplifier and DC-DC voltage converter," J. Microelectromech. Syst. **7**, 387–394 (1998).
[12]S. Chowdhury, G. A. Jullien, M. A. Ahmadi, W. C. Miller, D. Keating, and N. Finch, "Acoustic and magnetic MEMS components for a hearing aid instrument," Proc. SPIE **4019**, 122–133 (2000).
[13]J. X. Gao, L. P. Yeo, M. B. Chan-Park, J. M. Miao, Y. H. Yan, J. B. Sun, Y. C. Lam, and C. Y. Yue, "Antistick postpassivation of high-aspect ratio silicon molds fabricated by deep-reactive ion etching," J. Microelectromech. Syst. **15**, 84–93 (2006).
[14]J. Miao, J. B. Sun, and M. Puech, "Fabrication of thick SiO_2 block with a dry-released underneath cavity in silicon for RF MEMS," Electron. Lett. **41**, 662–664 (2005).
[15]P. Dixit and J. Miao, "Aspect ratio dependent copper electrodeposition technique for very high aspect ratio through-hole plating," J. Electrochem. Soc. **153**, G552–G559 (2006).
[16]L. Fu, J. Miao, X. X. Li, and R. M. Lin, "Study of deep silicon etching for micro-gyroscope fabrication," Appl. Surf. Sci. **177**, 78–84 (2001).
[17]P. R. Scheeper, B. Nordstrand, J. O. Gulløv, B. Liu, T. Clausen, L. Midjord, and T. Storgaard-Larsen, "A new measurement microphone based on MEMS technology," J. Microelectromech. Syst. **12**, 880–891 (2003).
[18]R. Nadal-Guardia, A. M. Brosa, and A. Dehé, "AC transfer function of electrostatic capacitive sensors based on the 1-D equivalent model: Application to silicon microphones," J. Microelectromech. Syst. **12**, 972–978 (2003).
[19]A. J. Zuckerwar, "Theoretical response of condenser microphones," J. Acoust. Soc. Am. **64**, 1278–1285 (1978). The factor Γ_m is omitted from Eq. (21).
[20]A. J. Zuckerwar, "Principles of operation of condenser microphones," in *AIP Handbook of Condenser Microphone: Theory, Calibration and Measurements*, edited by George S. K. Wong and Tony F. W. Embleton (AIP, New York, 1995), Chap. 3, pp. 37–69. A factor 4 is omitted from Eq. (3.50).
[21]J. E. Warren, "Capacitance microphone static membrane deflections: Comments and further results," J. Acoust. Soc. Am. **58**, 733–740 (1975).
[22]M. S. Hawley, F. F. Romanow, and J. E. Warren, "The Western Electric 640AA capacitance microphone: Its history and theory of operation," in *AIP Handbook of Condenser Microphone: Theory, Calibration and Measurements*, edited by George S. K. Wong and Tony F. W. Embleton (AIP, New York, 1995), Chap. 2, pp. 8–34.
[23]V. Tarnow, "Thermal noise in microphones and preamplifiers," B&K Technical Review **3**, 3–14 (1972).
[24]V. Tarnow, "The lower limit of detectable sound pressure," J. Acoust. Soc. Am. **82**, 379–381 (1987).
[25]B&K Falcon Range 1/4 in. Type 2670 Microphone Preamplifier Product Data, B&K, Nærum, Denmark, 2003.

[26]A. J. Zuckerwar, T. R. Kuhn, and R. M. Serbyn, "Background noise in piezoresistive, electret condenser and ceramic microphones," J. Acoust. Soc. Am. **113**, 3179–3187 (2003).
[27]A. J. Zuckerwar and K. C. T. Ngo, "Measured $1/f$ noise in the membrane motion of condenser microphones," J. Acoust. Soc. Am. **95**, 1419–1425 (1994).
[28]Z. Škvor, "On the acoustical resistance due to viscous losses in the air gap of electrostatic transducers," Acustica **19**, 295–299 (1967).
[29]J. B. Starr, "Squeeze-film damping in solid-state accelerometers," *IEEE Workshop in Solid-State Sensor and Actuator 4th Technical Digest*, 1990, pp. 44–47.

Vibration and sound signatures of human footsteps in buildings[a)]

Alexander Ekimov[b)] and James M. Sabatier
The University of Mississippi, National Center for Physical Acoustics, 1 Coliseum Drive, University, Mississippi 38677

(Received 27 January 2006; revised 30 May 2006; accepted 1 June 2006)

The acoustic signature of a footstep is one of several signatures that can be exploited for human recognition. Early research showed the maximum value for the force of multiple footsteps to be in the frequency band of 1–4 Hz. This paper reports on the broadband frequency-dependent vibrations and sound pressure responses of human footsteps in buildings. Past studies have shown that the low-frequency band (below 500 Hz) is well known in the literature, and generated by the force normal to the ground/floor. The seismic particle velocity response to footsteps was shown to be site specific and the characteristic frequency band was 20–90 Hz. In this paper, the high-frequency band (above 500 Hz) is investigated. The high-frequency band of the vibration and sound of a human footstep is shown to be generated by the tangential force to the floor and the floor reaction, or friction force. The vibration signals, as a function of floor coverings and walking style, were studied in a broadband frequency range. Different walking styles result in different vibration signatures in the low-frequency range. However, for the walking styles tested, the magnitudes in the high-frequency range are comparable and independent of walking style. © *2006 Acoustical Society of America.* [DOI: 10.1121/1.2217371]

PACS number(s): 43.40.At, 43.60.Bf, 43.80.Jz [NX] Pages: 762–768

I. INTRODUCTION

Vibrations and sound produced by human activities are constituent parts in acoustic methods of human recognition. Early research of the acoustic signatures from human footsteps was conducted in the low-frequency range, typically below a few hundred Hertz. In the studies by Galbraith and Barton[1] and by Ebrahimpour *et al.*,[2] footsteps were measured on a force platform, where the of measurements did not exceed 200 Hz. It was shown that the maximum value for the force of multiple footsteps was in the frequency band of 1–4 Hz.[3]

Cress[4] investigated the seismic particle velocity response of outdoor ground sites to individuals that were crawling, walking, and running in distance range from 0 to 6 m. He showed that the same human activities had different vibration spectra at different outdoor sites due to changes in site characteristics. However, different activities (running, walking, or crawling) at the same site resulted in spectral responses that only differed by a constant amplitude-scaling factor. The spectra for different outdoor sites have maxima at different frequencies. He developed a model to explain and predict the ground vibration spectra from footsteps. Following this model, the seismic particle velocity response (vibration signature) $\hat{V}(\omega,R,t)$ at the frequency f ($\omega=2\pi f$) and at a distance R from the human activity results from multiplying a footstep force $\hat{F}(\omega,t)$ (force signature) and a site transfer function $\hat{T}(\omega,R)$ as denoted by

$$\hat{V}(\omega,R,t)=\hat{F}(\omega,t)\times\hat{T}(\omega,R). \tag{1}$$

The sign ^ denotes a complex function and t is time. The site transfer function $\hat{T}(\omega,R)$ describes the propagation of vibration between the location of the force and the location of the detector.

It was experimentally shown[4] that the transfer function $\hat{T}(\omega,R)$ is site specific and has an amplitude-frequency response similar to a band-pass filter with the maximum within the frequency band 20–90 Hz.

Li *et al.*[5] investigated the sound from human footsteps in a building as a function of a walker gender and certain anthropomorphic differences (weight, height, etc.). People being tested were walking in their own shoes with solid heels on a hardwood stage in a theater. The sound of four footsteps, at a distance within 1–3 m from the microphone, was recorded for each subject and digitized with a 12-bit digital converter at a sampling rate of 10 kHz. Analysis of a single footstep for 16 individual walkers showed the person-specific maximum in the Fourier spectra to be in the frequency band of 30 Hz–470 Hz.

Watters[6] measured the impact force value of a single hard-heeled female footstep on various floors (hardwood floor, concrete floor, or linoleum glued to hardwood floor) in a building. For the force measurements, he used a force sensor threaded into the heel of the shoe. Octave band analysis of the averaged force values for a number of footsteps showed the maximum in the first octave (the center frequency was 31.5 Hz). The force spectral amplitudes had negative slopes in the range of 30–50 dB from the first oc-

[a)]A portion of this work has been presented in James Sabatier and Alexander Ekimov, "Vibration signature of human footsteps on the ground and in buildings," J. Acoust. Soc. Am. **118**(3), 2021 (2005).

[b)]Electronic mail: aekimov@olemiss.edu

 0001-4966/2006/120(2)/762/7/$22.50

tave (the center frequency was 31.5 Hz) to the highest octave (the center frequency was 4000 Hz) depending on the floor type.

The footstep force applied to the ground/floor is due to two components: The normal force and the force tangential to the surface.[7] The magnitude of the normal force component depends on the human motion (walking, running, etc.) and on the person's weight. The normal force component is approximately equal to the person's weight for a typical walking style.[1,2] The tangential force is governed by the horizontal motion and is equal to the force of the ground/floor reaction, or friction force. The friction force is equal to the person's weight multiplied by a coefficient of friction.

Akay[8] presented an overview of the acoustics of friction. Friction is a result of sliding contacts between mechanical objects. Weak contacts between them produce a multiple-pulse excitation of these objects over a broad frequency spectrum. A well-known example of the sound from micro-contacts interaction is the random sound from rubbing pieces of sandpaper together.

This article presents the results of the acoustic measurements, using both microphones and accelerometers, of human footsteps in a broadband frequency range in a building. All vibration and sound measurements were conducted close to a walker at a distance of 1 m. The transfer function approach [Eq. (1)] for the vibration and sound can also be used for calculations of the vibration and sound responses at arbitrary distance R. In this case, the vibration particle velocity or sound pressure at the distance R from a walker results from multiplying the vibration particle velocity, or sound pressure, from a footstep measured at a distance of 1 m and the corresponding building transfer function for the vibration particle velocity or sound pressure.

Two characteristic frequency bands in the vibration and the sound responses from human footsteps were observed experimentally, and analyzed using Fourier transforms and dynamic spectra. The first-frequency band, generated by the force normal to the surface, is well known in the literature and is concentrated in a low-frequency range below 500 Hz. The second-frequency band is generated by the tangential force or friction force and is located in a higher-frequency range that extends to the ultrasonic frequencies.

II. SETUP FOR THE MEASUREMENT OF HUMAN FOOTSTEP VIBRATION AND SOUND RESPONSES IN A BUILDING

Previously reported footstep vibration measurements (force measurements) were conducted on force platforms.[1,2,7] These platforms have a flat frequency response in a frequency range of 0–0.1 kHz or higher.[9] The limitation for the upper frequencies is determined by the first natural resonance frequency of the platform. In this study, the vibration and the sound from footsteps were measured using a broadband three-axis accelerometer and a microphone. The accelerometer (PCB 356B18) was calibrated over the frequency range of 0.2 Hz–16.5 kHz, and had a sensitivity of 1 V/g. The microphone (B&K model 4188) measured the sound pressure of the footsteps, and was calibrated over the frequency range of 2 Hz–15 kHz. The accelerometer and the microphone had high-frequency rolloffs in sensitivities above 16.5 kHz and 15 kHz, respectively. Only the component of acceleration normal to the floor surface is presented and discussed in this article. Data recording and processing were conducted using a two-channel 16-bit data acquisition board (DAQ) (Echo Indigo IO) and software (Sound Technology, LAB432). In parallel to the acoustic signals acquisition, a digital camera (Fuji F10) operating at 30 frames per second made a video recording of footsteps.

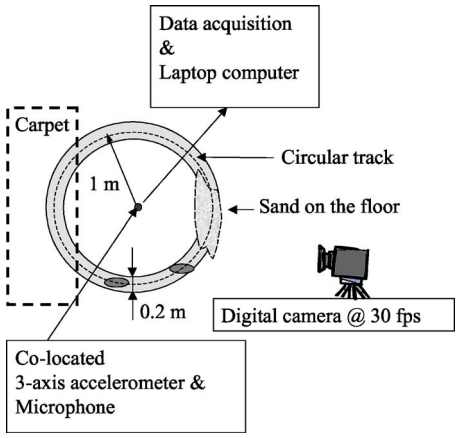

FIG. 1. Setup for the measurement of human footstep vibration and sound.

A test setup was constructed on a concrete floor covered by glued linoleum in an acoustic laboratory on the first floor of a modern university building, as shown in Fig. 1. The floor coverings were varied in the tests to modify the friction between the foot and the floor. In a few tests, the linoleum floor was partly covered by carpet and partly dusted with sand. These areas are marked in Fig. 1 by a dashed line.

In these experiments, the subjects walked within a circular track width 0.2 m, marked on the floor of the building. The median radius of the track was 1 m and, depending upon the length of a person's stride, 9–11 steps were required to complete a full circle. The vibration response of floor surface from the footsteps was measured by the accelerometer glued at the center of the circle. A microphone was co-located with the accelerometer and placed on thin (1 cm) foam.

III. FOOTSTEPS VIBRATION AND SOUND SIGNATURES: MULTIPLE FOOTSTEPS

Footstep signatures for the regular walking style for six people (three men and three women) were measured using the setup shown in Fig. 1. The floor covering was bare linoleum. A DAQ with a sampling rate of 44.1 kHz and 22.05 kHz antialiasing filter acquired signals from the accelerometer and the microphone. The dynamic spectra (spectrogram) of typical vibration and sound responses of the floor in the frequency band of 20 Hz–22 kHz for ten footsteps (full circle) are presented in Figs. 2(b) and 2(d), respectively. The fast Fourier transform (FFT) size is 4096; corresponding to 10.77 Hz in the spectral line resolution and 92.88 ms in the time resolution. Each Fourier spectral line resolution is equal to the sampling rate divided by the FFT size. The Fourier spectra of the acceleration and the sound pressure of footstep No. 6 [in Figs. 2(b) and 2(d)] are presented in Figs. 2(a) and

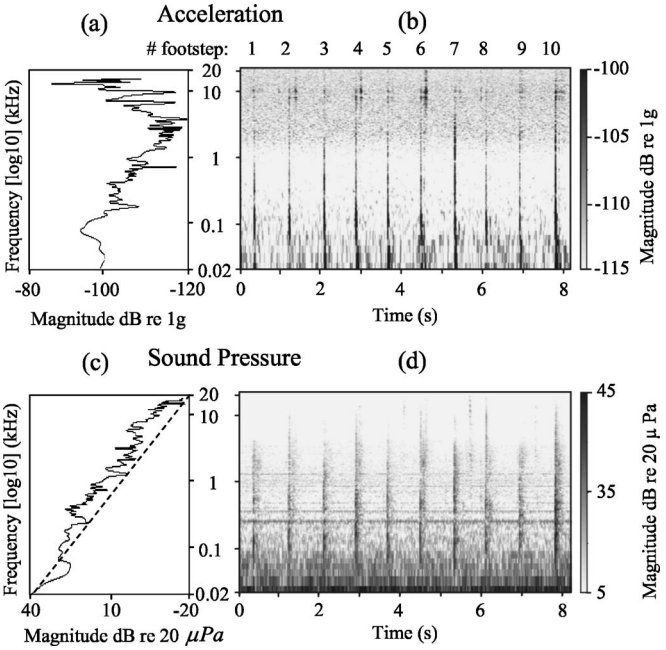

FIG. 2. Footstep signature: (a) Fourier spectra of single footstep No. 6 of the acceleration, (b) the spectrogram of ten footsteps for the acceleration, (c) Fourier spectra of single footstep No. 6 of the sound pressure (the dashed line corresponds the line $20\log_{10}P$ versus $-20\log_{10}f$), and (d) the spectrogram of ten footsteps for the sound pressure. The sampling rate was 44.1 kHz and the FFT size was 4096.

2(c). The time segments corresponding to footstep No. 6 (approximately within 150 ms) were extracted from the recorded signals of the acceleration and sound [shown in Figs. 2(b) and 2(d) as footstep No. 6], and then average spectra of these segments were computed (linear averaging with 50% overlap) and plotted in Figs. 2(a) and 2(c). The FFT size is 4096; corresponding to 10.77 Hz in the spectral line resolution.

Footstep signatures from the dynamic spectra analyses exhibit a broadband frequency response from low frequencies up to ultrasonic frequencies. The low-frequency (below 500 Hz) responses are well known from previous investigations.[1–6] In measurements previously reported in the literature,[4] geophones were used for the vibration measurements and these sensors naturally filter data above a few hundred Hertz. The vibration signal above 500 Hz [Figs. 2(a) and 2(b)] has a broadband frequency spectrum up to 22 kHz with high-frequency magnitudes comparable with the maxima of magnitudes at the low frequencies. The high-frequency vibration response up to 22 kHz is of particular interest in this article. The sound signal has a maximum value below 500 Hz, but also has components across an extended frequency range.

The comparison of vibration and sound spectra of a single footstep shown in Figs. 2(a) and 2(c) reveals quantitative differences in the dynamic ranges of the signals. The vibration signal (acceleration, A) has less dynamic range than the sound signal (sound pressure, P). A reasonable explanation for this difference lies in the physical nature of the measured signals. Sound pressure (P) is proportional to the vibration particle velocity (V) at the contacted point between the foot and the floor and can be represented by

$$\hat{P}_2(\omega,R) = \hat{Z}_{12}(\omega,R) \times \hat{V}_1(\omega), \tag{2}$$

where $\hat{P}_2(\omega,R)$ is the sound pressure measured by the microphone at Point 2 (center of the circle as shown in Fig. 1), $\hat{V}_1(\omega)$ is the vibration particle velocity at the contact point between the foot and the floor, and $\hat{Z}_{12}(\omega,R)$ is the transfer function (impedance) between the microphone location and the contact point. The distance between these two locations is $R=1$ m.

Acceleration is the derivative of a velocity. A Fourier spectrum of acceleration $A(\omega)$ is related to a velocity $V(\omega)$ spectrum by

$$A(\omega) = \omega \times V(\omega). \tag{3}$$

The acceleration measured at the center of the circle (point No. 2) can be related to the acceleration at the contact point between the foot and the floor (point No. 1) by

$$\hat{A}_2(\omega,R) = \hat{Y}_{12}(\omega,R) \times \hat{A}_1(\omega), \tag{4}$$

where $\hat{A}_2(\omega,R)$ and $\hat{A}_1(\omega)$ are the accelerations at the point Nos. 2 and 1, respectively, and $\hat{Y}_{12}(\omega,R)$ is the transfer function for the acceleration between point Nos. 1 and 2. Combining Eqs. (2)–(4) shows that the sound pressure and acceleration are related by

$$P_2(\omega,R) = \frac{A_2(\omega,R)}{\omega} \times \frac{Z_{12}(\omega,R)}{Y_{12}(\omega,R)}. \tag{5}$$

If $Z_{12}(\omega,R)$ and $Y_{12}(\omega,R)$ have the same frequency dependence, then it follows from Eq. (5) that sound pressure $P_2(\omega,R)$ has an additional 6 dB per octave slope $[P_2(\omega,R) \sim 1/\omega]$ compared with the acceleration $A_2(\omega,R)$. Corresponding to this slope (6 dB per octave) the line $P(f)$ versus $(f)^{-1}$, or in the logarithmic scale $20\log_{10}P(f)$ versus $-20\log_{10}f$, is plotted (dashed line) in Fig. 2(c). This line is in a good agreement with the experimental data trend for the sound pressure. Certainly, the transfers functions $Z_{12}(\omega,R)$ and $Y_{12}(\omega,R)$ [Eq. (5)] have the potential to change the relative difference between the sound pressure and acceleration in an arbitrary case of environmental conditions.

The effect of the reduced dynamic range for the acceleration versus the sound pressure in the footstep signal helps to detect and identify the high-frequency band in the footstep signature, and results in a preference in measurement of acceleration versus the sound pressure in the broadband frequency range.

IV. SOURCE OF THE HIGH-FREQUENCY BAND IN HUMAN FOOTSTEPS

Additional measurements were conducted to study the high-frequency source in the human footstep vibration signature. It is known that the sliding contacts between mechanical objects produced a broadband friction response. The spectrum of this response depends on the contact conditions and object's elastic properties.[8,10] Changing the floor coverings or footwear type modifies the contact conditions and friction coefficient between the foot and the floor. Since the

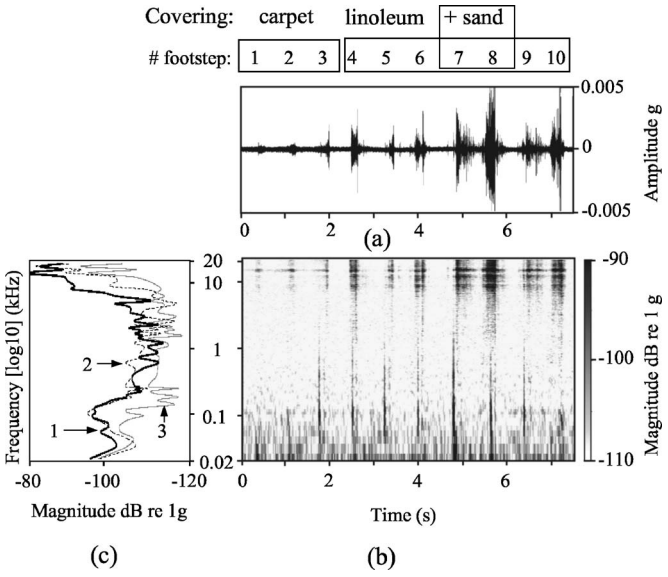

FIG. 3. Footsteps vibration signatures on the different floor coverings (carpet, linoleum, and linoleum with sand): (a) The signal in the time domain, (b) the spectrogram of ten footsteps, and (c) Fourier spectra of a single footstep on the carpet (3), linoleum (2), and on the linoleum with sand (1). The sampling rate was 44.1 kHz and the FFT size was 4096.

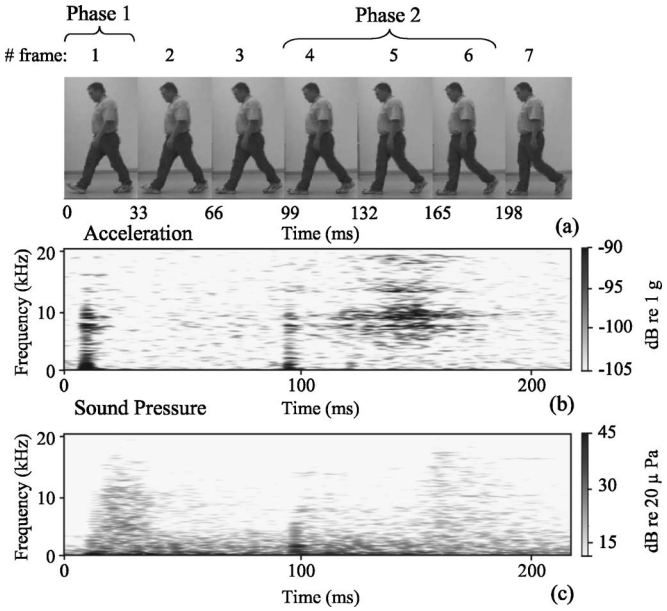

FIG. 4. Two phases of a foot motion in a single footstep: (a) Serial frames of the video record of a single footstep, and (b) and (c) are corresponding them the spectrograms of the acceleration and the sound pressure. Phase 1 (heel strike): The deceleration stage of the first foot (the signal is in the time range of 0–33 ms). Phase 2 (toe slap and weight transfer): The deceleration stage (toe slap) of the first foot (the signal is in the time range of 99–132 ms) and the acceleration stage (weight transfer from one leg to the other) of the second foot (the signal is in the time range of 132–198 ms). The sampling rate was 44.1 kHz and the FFT size was 512.

friction force is equal to the person's weight multiplied by the friction coefficient, a change in floor covering or footwear type should modify the spectrum of the footstep vibration response. Tests were conducted on the setup shown in Fig. 1, where the linoleum floor was partly covered by carpet, partly dusted with sand, and was partly bare. The different floor conditions should represent three separate values for the friction coefficient. Figures 3(a)–3(c) present the test results of the floor vibration response for ten regular footsteps (full circle) of a walking man. The sampling rate was 44.1 kHz and the FFT size was 4096. The first three footsteps were on the carpet [Footsteps 1–3 in Figs. 3(a) and 3(b)], the next three were on the linoleum floor [Footsteps 4–6 in Figs. 3(a) and 3(b)], the next two were on the linoleum floor dusted with sand [Footsteps 7 and 8 in Figs. 3(a) and 3(b)], and the last two footsteps were on the bare linoleum floor [Footsteps 9 and 10 in Figs. 3(a) and 3(b)]. A comparison of the Fourier spectra in Fig. 3(c) of a single footstep on the linoleum floor (curve 2) and on the linoleum floor dusted with sand (curve 1), as well as the spectrogram in Fig. 3(b), shows that changing the friction value mainly modified the high-frequency vibrations. The low-frequency magnitudes of vibrations (below 500 Hz) were changed less in comparison with the high-frequency vibrations. One of the possible explanations is the walker awareness of the sand dusted on the floor that results in the variation of the normal force component. The carpet covering modified the elasticity as well as the friction coefficient of the surface contact [curve 3 in Fig. 3(c)] and, therefore, decreased the low- and the high-frequency vibrations of the footstep. The last two footsteps [9 and 10 in Figs. 3(a) and 3(b)] were on the bare linoleum floor. Sand on the walker's shoes, due to the previous two footsteps on the sandy floor, increased the friction and the high-frequency vibrations as compared to Footsteps 4–6 on the bare linoleum floor. These measurements support the idea that the high-frequency vibrations were produced by friction. The friction response had a broadband vibration spectrum with a maximum in the frequency range of 10–15 kHz [Figs. 3(b) and 3(c)].

V. SINGLE FOOTSTEP ACOUSTIC SIGNATURE ANALYSES

Li *et al.*[5] observed two rapid oscillations at the beginning and at the end of a footstep in the sound waveform, and explained them as the heel and the toe strikes. Human footsteps are the repeatable cycles of the acceleration, and the deceleration of the foot motions in the horizontal and vertical directions. In the acceleration stage, the speed of a foot increases from zero to a speed; exceeding the total speed of the human body motion. In the deceleration stage, the speed of the foot decreases to zero.

Detailed analysis of vibration and sound signatures for a single footstep was conducted using the synchronized record of signals from an accelerometer and a microphone (setup is shown in Fig. 1 with the floor covered by bare linoleum) and a video record at 33 ms of time resolution. The serial frames of the video record of a single typical footstep, the dynamic spectra of the acceleration and the sound pressure, aligned in time, are shown in Figs. 4(a)–4(c). The sampling rate was 44.1 kHz and the FFT size was 512, that correspond to 86.13 Hz in the spectral line resolution and 11.6 ms in the time resolution. Two phases of foot motion provided the major contribution to the human footstep vibration and sound signatures in a single footstep. The first phase (heel strike) corresponded to the motion when the heel of the leading foot

TABLE I. Walking styles.

n	Walking style	Leg profile at the first contact the floor	Leg-spring stiffness
1	Regular	A straight knee. The heel contacted the floor.	Maximum
2	Soft	A curved knee. The heel/foot contacted the floor.	Moderate
3	Stealthy	A curved knee. The toe contacted the floor.	Minimum

contacted the floor in the deceleration stage [first frame in Fig. 4(a)]. The second phase (toe slap and weight transfer from one leg to the other) [Frames 4–6 in Fig. 4(a)] corresponded to the contact of the toe of the leading foot (deceleration stage) and the pushing motion of the trailing foot (acceleration stage) as shown in Fig. 4(a).

The time between these two phases was in the range of 100 ms for the regular walking style. The time for the first phase was shorter than the time for the second phase. Spectrograms of the first and the second phases were different, as shown in the data in Figs. 4(b) and 4(c). The first phase (heel strike) response included the deceleration stage of the leading foot [the signal is in the time range of 0–33 ms in Figs. 4(b) and 4(c)]. The second phase (toe slap and weight transfer) showed two separate responses: The first one (toe slap) resulted from the deceleration stage of the leading foot (the signal was in the time range of 99–132 ms), and the second response (weight transfer) resulted from the acceleration stage of the trailing foot (the signal was in the time range of 132–198 ms), as shown in Figs. 4(b) and 4(c). The single footstep motion phases had broadband frequency vibration and sound responses.

VI. WALKING STYLE ANALYSES

Houston and McGaffigan[11] extracted and investigated two styles of walking (standard and stealthy) at an outdoor facility in the frequency range below 100 Hz. They showed that the vibration response of the ground to footsteps depends on the walking style. The seismic response of the ground for stealthy walking was less than for standard (regular) walking.

Walker *et al.*[12] used a mass-spring model for the calculation of a running man's leg stiffness. It was experimentally shown that leg stiffness is a function of running speed. In this study, the first natural frequency f_0 of the mass-spring system is given by

$$f_0 = \frac{1}{2\pi}\sqrt{\frac{K}{M}}, \tag{6}$$

where K is an effective vertical stiffness of a leg spring and M is a body mass.

They found that the first natural frequency f_0 was below 4 Hz. Their model did not include the effects of controlled leg-spring stiffness K for a constant speed of walking/running.

These results were used to develop a model of a walking person as a mechanical system with controlled leg-spring stiffness K. It was proposed that K is a function of walking style for a constant speed of motion. A dynamic force applied from a human to the ground/floor is defined from theory of vibration isolation,[13] as

$$F_s = \frac{F}{B(\omega)}, \tag{7}$$

where $B(\omega)$ is the force transfer coefficient, F is the force applied to the vibration isolator from the vibrated system, F_s is the force applied from the vibration isolator to the supported system foundation. The force transfer coefficient $B(\omega)$ quantifies the force reduction efficiency by the vibration isolator.

For the simple mass-spring system, at frequencies f much higher than the resonance frequency (f_0) of a system installed on a vibration isolator (in our particular case $f_0 < 4$ Hz), the force transfer coefficient defines:[13]

$$B(\omega) = \frac{f^2}{f_0^2}, \tag{8}$$

where f_0 is the resonance frequency of a mass-spring system calculated from Eq. (6), K is the stiffness of the isolator, and M is the mass of system mounted on the isolator.

Substitution of $B(\omega)$ from Eq. (8) into Eq. (7), and f_0 from Eq. (6), gives

$$F_s = \frac{F}{f^2} \times \frac{K}{4\pi^2 M}. \tag{9}$$

From the human mass-spring model, Eq. (9), it follows that the force applied to the ground/floor is proportional to an individual leg stiffness K. On the basis of previous research,[1] it is possible to make an assumption that F is constant for a constant speed of walking.

Substituting for the force F_s from Eq. (9) into Eq. (1) gives, for the vibration magnitude,

$$V_2(\omega,R,t) = T_{12}(\omega,R) \times \frac{F(\omega,t) \times K}{4\pi^2 M \times f^2}, \tag{10}$$

where $V_2(\omega,R,t)$ is the vibration at the detector location (Point 2), and $T_{12}(\omega,R)$ is the transfer function (admittance) between the force (Point 1) and detector locations (Point 2).

From Eq. (10), the vibration $V_2(\omega,R,t)$ from footsteps is proportional to the leg stiffness K of the walker. Equation (10) may be written for the acceleration. In this case, $T_{12}(\omega,R)$ is the transfer function defined for the acceleration.

This mass-spring model was tested under the laboratory conditions using the setup presented in Fig. 1 (bare linoleum). Three variations of leg-spring stiffness and corresponding walking styles are presented in Table I. The values of the leg stiffness are qualitatively indicated from the leg

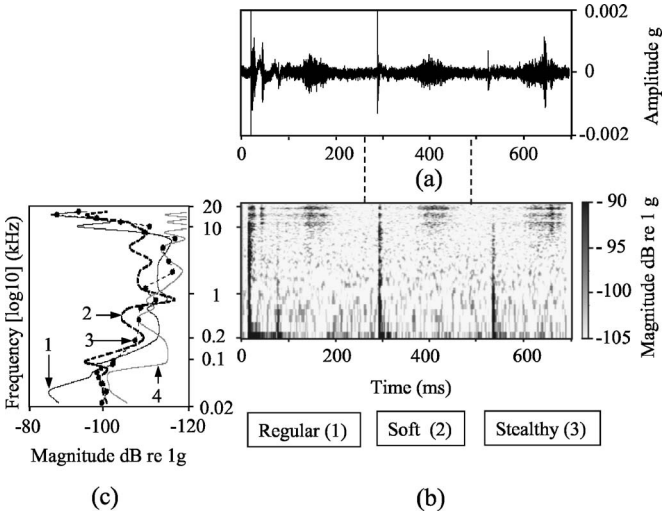

FIG. 5. (a) Time domain signal and (b) spectrogram of a single footstep for regular (1), soft (2), and stealthy (3) styles of walking (the sampling rate was 44.1 kHz and the FFT size was 512). (c) Spectra of a single footstep for regular (1), soft (2), and stealthy (3) styles of walking, and the background noise floor (4) (the sampling rate was 44.1 kHz and the FFT size was 4096).

profile. Each of the three distinct styles of walking (regular, soft, and stealthy, as shown in Table I) occurred at the same speed of walking. All tests were conducted with the same subject to exclude the personal difference parameter from the inquiry.

The vibration data for a single step were taken from the circular track data of 9–11 footsteps for each walking style, and were spliced together, as shown in Figs. 5(a) and 5(b). The sampling rate was 44.1 kHz. The FFT size was 512 in the spectrogram [Fig. 5(b)], and 4096 in the spectra [Fig. 5(c)]. In Fig. 5(c), the spectra of vibration responses from these footsteps in the frequency range of 20 Hz–16.5 kHz are presented with a comparison to the ambient noise floor.

The maximum vibration response for the footstep in the low-frequency range (below 500 Hz) was near 40 Hz for the regular walking style (A_1), and approximately 15 dB less (near the noise floor at the same frequency) for the soft (A_2) and stealthy styles (A_3) [Fig. 5(c)]. A_n is the magnitude of acceleration; $n=1$, 2, 3 is a number corresponding to the different walking styles from Table I.

In this experimental setup, $T_{12}(\omega,R)$ was the constant building transfer function for acceleration for all tested styles of walking. Equation (10) shows that the vibration response difference, for the footsteps in the frequency band near 40 Hz of the soft and stealthy styles versus regular style of walking ($A_1>A_2,A_3$), was due to the leg's reduced stiffness ($K_1>K_2,K_3$). This is experimental confirmation of the possibility of the walker controlling leg stiffness in order to walk stealthily.

The frequency responses for the high-frequency range (near 15 kHz) and the low-frequency range (below 500 Hz) had comparable magnitudes, as shown in Figs. 5(b) and 5(c) for the regular walking style only. Soft and stealthy styles had reduced low-frequency magnitudes. All tested styles of walking had comparable magnitudes in the high-frequency range [Figs. 5(b) and 5(c)] of 10–15 kHz.

Furthermore, the high-frequency vibration responses to the footstep have higher signal-to-noise ratios because the noise floor was less at the high frequencies than at the low frequencies [see Fig. 5(c)]. Typically, ambient noise floor rolls off from low to high frequencies even in industrial environments.[14] The high-frequency vibrations also had broader frequency responses than the low-frequency vibrations. Consequently, greater potential existed at high frequencies for extracting the footstep signature from the ambient noise for all styles of walking.

The mass-spring model, with the element of stiffness control and the tests results, explain the vertical force and resulting vibration reductions for footsteps in the low-frequency range and this occurred from changes in the walker's leg stiffness. Although walking styles resulted in different vibration signatures in the low-frequency range (below 500 Hz), comparable vibration magnitudes were observed in the high-frequency range.

VII. CONCLUSIONS

Two characteristic frequency bands in the vibration and the sound responses from human footsteps were observed experimentally in a building. The first frequency band was generated by a force normal to the surface, is well known in the literature, and was concentrated in the low-frequency range below 500 Hz. The second frequency band was generated by the tangential force to the floor and floor reaction, or friction force, and is located in the high-frequency range.

A detailed analysis of a single footstep shows two phases in a footstep. These phases resulted in differences in the time and spectral domains, and provided striking and sliding contacts between the foot and the floor.

Three distinct types of walking styles (regular, soft, and stealthy) with the same speed of motion were described and investigated. These styles resulted in different vibration magnitudes in the low-frequency range (below 500 Hz) due to differences in the walker's leg stiffness; but, all styles had comparable vibration magnitudes in the high-frequency range because of friction.

ACKNOWLEDGMENTS

The authors thank Craig Hickey for helpful comments. This work was supported by the Department of the Army, Army Research Office, under Contract No. W911NF-04-1-0190. Any opinions, findings and conclusions, or recommendations expressed in this material are those of the author and do not necessarily reflect the views of the sponsor.

[1]F. W. Galbraith and M. V. Barton, "Ground loading from footsteps," J. Acoust. Soc. Am. **48**, 1288–1292 (1970).
[2]A. Ebrahimpour, A. Hamam, R. L. Sack, and W. N. Patten, "Measuring and modeling dynamic loads imposed by moving crowds," J. Struct. Eng. **122**, 1468–1474 (1996).
[3]S. Mouring, "Dynamic response of floor systems to building occupant activities," Ph.D. dissertation, The Johns Hopkins University, MD, (1992).
[4]D. H. Cress, "Terrain considerations and data base development for the design and testing of devices to detect intruder-induced ground motion," U.S. Waterways Experimental Station, Technical Report No. M-78-1 U.S. Army Engineer Waterways Experiment Station, Vicksburg, MS (1978).
[5]X. Li, R. J. Logan, and R. E. Pastore, "Perception of acoustic source characteristics: Walking sounds," J. Acoust. Soc. Am. **90**, 3036–3049

(1991).
[6]B. G. Watters, "Impact-noise characteristics of female hard-heeled foot traffic," J. Acoust. Soc. Am. **37**, 619–630 (1965).
[7]M. Kohle and D. Merkl, "Analyzing human gait patterns for malfunction detection," SAC 2000, *Proceedings of the 2000 ACM symposium on Applied Computing*, Como, Italy, Vol. **1**, pp. 41–45 (2000).
[8]A. Akay, "Acoustics of friction," J. Acoust. Soc. Am. **111**, 1525–1548 (2002).
[9]Biomechanics Force Platform, AMT Inc., Watertown, MA (2005).
[10]R. B. Abbott, "Response measurement and harmonic analysis of violin tones," J. Acoust. Soc. Am. **7**, 111–116 (1935).
[11]K. M. Houston and D. P. McGaffigan, "Spectrum analysis techniques for personnel detection using seismic sensors," Proc. SPIE **5090**, 162–173 (2003).
[12]C. A. Walker and R. Blair, "Leg stiffness and damping factors as a function of running speed," Sports Eng. **5**, 129–139 (2002).
[13]E. Skudrzyk, *Simple and Complex Vibratory Systems* (University Park, Pennsylvania State University Press, 1968).
[14]H. E. Bass and L. N. Bolen, "Ultrasonic background noise in industrial environments," J. Acoust. Soc. Am. **78**, 2013–2016 (1985).

Vibroacoustic analysis of rectangular plates with elastic rotational edge restraints

W. L. Li[a)]
Department of Mechanical Engineering, Mississippi State University, Mississippi State, Mississippi 39762

(Received 14 January 2005; revised 12 April 2006; accepted 12 May 2006)

This investigation deals with the vibration of and the acoustic radiation from a simply supported rectangular plate with elastic restraints against edge rotations. The displacement of the plate is first sought as a series expansion in terms of the beam functions. Each of the beam functions is then expressed as the linear combination of a Fourier sine series and a complementary sufficiently smooth function that is introduced to ensure and improve the convergence of the Fourier series expansion. To facilitate the acoustic analysis, the plate displacement is eventually simplified to a standard Fourier sine series. The modal and acoustic characteristics of square plates are studied for different restraining stiffnesses and configurations. It is shown that the modes of the restrained plates can be considerably different from those in the simply supported case, so are the corresponding modal radiation efficiencies. The proposed method is generally applicable to rectangular plates elastically restrained along any edge(s), and the acoustic calculations are valid for an arbitrary acoustic or structural (modal) wave number. © *2006 Acoustical Society of America.*
[DOI: 10.1121/1.2211567]

PACS number(s): 43.40.-r, 43.40.Dx, 43.40.Rj [JGM] Pages: 769–779

I. INTRODUCTION

Sound radiation from simple plates or plates with various complicating features is of practical importance to noise control, and has been an active research subject for many years. Although sound radiation from a simply supported rectangular plate is a classical problem in structural acoustics, it is widely believed that its analytical solution is generally not available for an arbitrary (moderate) acoustic wave number. So some kind of numerical technique is often used to determine the modal radiation resistances of a plate, which is typically the most time-consuming part of the acoustic analysis. In order to alleviate the computational burden, researchers have developed various approximate or asymptotic solutions which are usually valid only for extreme acoustic/structural wave numbers.[1–6] For large wave numbers, the sound radiation from a plate is primarily dictated by (the mean behaviors of) a group of resonant modes, and the statistical energy analysis methods become particularly useful.[1,7,8] However, the deterministic methods are generally necessary for small to moderate wave numbers.

By expanding the Green's function into a MacLaurin series, Williams[4] expressed the radiated sound power in the form of power series of the acoustic wave number. An alternative expansion was also derived in terms of the Fourier transformed velocity and its derivatives in the wave number space. The concept of expanding the Green's function into a power series was recently adopted by Li[9] in deriving a set of analytical formulas for calculating the self and mutual radiation resistances of a simply supported plate. The results, based on the simplified Kirchhoff plate theories and the Helmholtz wave equation for the acoustic medium, are exact for any acoustic wave number, including the moderate wave numbers which are often of primary concern in an acoustic analysis.

Most investigations in the literature have been focused on the self-radiation resistance of an individual mode, and the radiated sound power is simply calculated by adding up the self-powers independently radiated by each mode. Although the potential error associated with this simplification has long been realized, the mutual radiation resistances are still routinely ignored in the sound power calculation probably because of the common belief that the determination of the mutual radiation resistances is an enormous burden computationally. Based on William's results, Snyder and Tanaka[10] derived a set of simple formulas for calculating the mutual radiation resistances directly from the self terms for small wave numbers. Li and Gibeling[11] developed an algorithm for an easy and accurate determination of the mutual radiation resistances, and demonstrated that the cross-modal couplings could have a meaningful impact on the radiated sound power, even at a resonant frequency. The consideration of the mutual radiation resistances is also of significance to other more complicated problems in which the plates may be loaded with features such as springs, masses, or ribs. In such a case, as shown by Li and Gibeling,[12] it is still possible to express the displacement function as a linear superposition of the modes for the unloaded plate, and the sound power radiation can be readily determined from the self and mutual radiation resistances of the unloaded plate.

Another important factor that can have a significant impact on sound radiation is the plate boundary conditions. Gomperts[13,14] investigated the sound radiation under general boundary conditions, and observed that the radiation efficiency of a plate with greater edge constraints is not necessarily higher than that for a plate with less edge restraints. On the other hand, it is widely believed that adding rotational

[a)]Electronic mail: li@me.msstate.edu

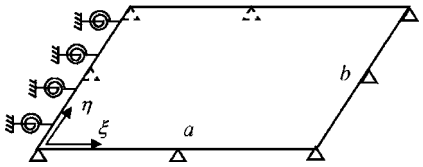

FIG. 1. A simply supported rectangular plate with an elastically restrained edge.

restraints to a simply supported edge will increase the radiation efficiency of the plate. In particular, a 3-dB correction is often applied to a clamped plate for frequencies up to half of the critical frequency,[15,16] and is then progressively reduced to unity at the critical frequency. Leppington *et al.*[17] also predicted this trend for high modal numbers through studying a semi-infinite plate with an elastic edge restraint against rotation. A correction factor was used to relate the radiation efficiency of a restrained plate to that of a simply supported plate. These calculations, however, cannot be easily extended to the so-called corner modes because of the nonseparable nature of the plate problem. The analytical results of Leppington *et al.*[17] were employed by Ohlrich and Hugin[18] to calculate the modal-averaged correction factors of the edge modes for the influence of the boundary constraints as well as the angle of the baffle.

In this investigation, a Fourier series method recently developed by Li[19] will be extended to the vibrations of simply supported rectangular plates with elastically restrained edges. The transverse displacement is eventually expressed as a simple Fourier sine series, thus allowing a direct use of the acoustic solutions currently available for a simply supported plate. This method is generally applicable to each mode, and good for any acoustic or structural (modal) wave number. Numerical results are presented for several different edge restraining stiffnesses and configurations.

II. THE VIBRATION OF A PLATE WITH ROTATIONAL EDGE RESTRAINTS

Figure 1 shows a simply supported rectangular plate with rotational elastic restraint at $x=0$. It should be noted that the plate is here allowed to be elastically restrained along any edge(s). The vibration of the plate is governed by the plate equation

$$D\nabla^4 w(x,y) - \rho h\omega^2 w(x,y) = f(x,y), \tag{1}$$

where $\nabla^4 = \partial^4/\partial x^4 + 2\partial^4/\partial x^2\partial y^2 + \partial^4/\partial y^4$, $w(x,y)$ is the flexural displacement, and ω is the angular frequency; D, ρ, and h are, respectively, the bending rigidity, the mass density, and the thickness of the plate; $f(x,y)$ is the distributed load acting on the plate.

The plate is assumed to be simply supported at each edge. In addition, each of the edges is elastically restrained against rotation, that is,

$$K_{x0}\partial w/\partial x = D\left(\frac{\partial^2 w}{\partial x^2} + \nu\frac{\partial^2 w}{\partial y^2}\right) \quad \text{at } x = 0, \tag{2}$$

$$K_{x1}\partial w/\partial x = -D\left(\frac{\partial^2 w}{\partial x^2} + \nu\frac{\partial^2 w}{\partial y^2}\right) \quad \text{at } x = a, \tag{3}$$

$$K_{y0}\partial w/\partial y = D\left(\frac{\partial^2 w}{\partial y^2} + \nu\frac{\partial^2 w}{\partial x^2}\right) \quad \text{at } y = 0, \tag{4}$$

$$K_{y1}\partial w/\partial y = -D\left(\frac{\partial^2 w}{\partial y^2} + \nu\frac{\partial^2 w}{\partial x^2}\right) \quad \text{at } y = b \tag{5}$$

where ν is Poisson ratio, and K_{x0} and K_{x1} (K_{y0} and K_{y1}) are the stiffnesses of the rotational springs at $x=0$ and $x=a$ ($y=0$ and $y=b$), respectively. When an edge such as $x=0$ is simply supported regardless of whether it is elastically restrained against rotation, the displacement function $w(0,y)$ and its derivatives with respect to y are identically equal to zero. Thus, all the v-related terms will vanish in Eqs. (2)–(5).

In terms of the nondimensional variables, $\xi = x/a$, $\eta = y/b$, Eqs. (1)–(5) can be rewritten as

$$D\left(\frac{\partial^4}{\partial\xi^4} + 2\frac{\partial^4}{\sigma^2\partial\xi^2\partial\eta^2} + \frac{\partial^4}{\sigma^4\partial\eta^4}\right)w(\xi,\eta) - \rho h a^4\omega^2 w(\xi,\eta) = f(\xi,\eta), \tag{6}$$

$$K_{\xi 0}\frac{\partial w}{\partial\xi} - \frac{\partial^2 w}{\partial\xi^2} = 0 \quad \text{at } \xi = 0, \tag{7}$$

$$K_{\xi 1}\frac{\partial w}{\partial\xi} + \frac{\partial^2 w}{\partial\xi^2} = 0 \quad \text{at } \xi = 1, \tag{8}$$

$$K_{\eta 0}\frac{\partial w}{\partial\eta} - \frac{\partial^2 w}{\partial\eta^2} = 0 \quad \text{at } \eta = 0, \tag{9}$$

$$K_{\eta 1}\frac{\partial w}{\partial\eta} + \frac{\partial^2 w}{\partial\eta^2} = 0 \quad \text{at } \eta = 1, \tag{10}$$

where $\sigma = b/a$, and

$$K_{\xi j} = aK_{xj}/D,$$

$$K_{\eta j} = bK_{yj}/D \tag{11}$$

$$(j = 0,1). \tag{12}$$

In this study, the plate displacement will be sought as a series expansion

$$w(\xi,\eta) = \sum_{m,n=1} A_{mn}X_m(\xi)Y_n(\eta), \tag{13}$$

where $X_m(\xi)$ and $Y_m(\eta)$ are the characteristic functions for a beam that has the same boundary conditions in the x and y direction, respectively.

Although beam functions can be generally expressed as a linear combination of trigonometric and hyperbolic functions, they include some unknown parameters that have to be determined from the boundary conditions. As a consequence, each boundary condition will typically require a different set of beam functions. In real calculations, this is not only inconvenient, but also tedious and difficult when elastic supports are involved.

In order to avoid this difficulty, an improved Fourier series method[19] will be employed here in which the characteristic function is expressed as

$$X(\xi) = \sum_{m=1}^{\infty} a_m \sin \lambda_m \xi + p(\xi) \quad (\lambda_m = m\pi), \quad 0 \leqslant \xi \leqslant 1, \tag{14}$$

where $p(\xi)$ denotes a sufficiently smooth function which, regardless of the boundary conditions, is required to satisfy, in addition to $p(0)=p(1)=0$, the following conditions:

$$\frac{\partial^2 p}{\partial \xi^2} = \frac{\partial^2 w}{\partial \xi^2} = \beta_{\xi 0} \quad \text{at } \xi = 0, \tag{15}$$

$$\frac{\partial^2 p}{\partial \xi^2} = \frac{\partial^2 w}{\partial \xi^2} = \beta_{\xi 1} \quad \text{at } \xi = 1. \tag{16}$$

As discussed in the previous papers,[19,20] the introduction of such a complimentary function $p(\xi)$ has two primary benefits: (1) the Fourier series solution is now applicable to any boundary conditions, and (2) the accuracy and convergence of the Fourier series expansion have been improved considerably.

Thus far, $p(\xi)$ has only been identified as a continuous function defined over [0,1]. Theoretically, there are an infinite number of possible choices for it. As an illustration, $p(\xi)$ is here chosen as a polynomial function in the form of

$$p(\xi) = \zeta^T(\xi)\beta_\xi, \tag{17}$$

where

$$\beta_\xi = \begin{Bmatrix} \beta_{\xi 0} \\ \beta_{\xi 1} \end{Bmatrix}, \tag{18}$$

$$\zeta(\xi) = \begin{Bmatrix} -\xi(2 - 3\xi + \xi^2)/6 \\ \xi(\xi^2 - 1)/6 \end{Bmatrix}. \tag{19}$$

It is easy to verify that such a polynomial will automatically satisfy Eqs. (15) and (16).

By substituting Eqs. (14) and (17). into the boundary conditions, Eqs. (7) and (8), one will be able to determine the unknown coefficients in terms of the Fourier coefficients, that is,

$$\beta_\xi = \sum_{m=1}^{\infty} a_m \tilde{\beta}_{\xi m}, \tag{20}$$

where

$$\tilde{\beta}_{\xi m} = \begin{Bmatrix} \dfrac{2K_{\xi 0}\lambda_m[6 + (2 + (-1)^m)K_{\xi 1}]}{(12 + 4(K_{\xi 1} + K_{\xi 0}) + K_{\xi 0}K_{\xi 1})} \\ -\dfrac{2K_{\xi 1}\lambda_m[6(-1)^m + (1 + 2(-1)^m)K_{\xi 0}]}{(12 + 4(K_{\xi 1} + K_{\xi 0}) + K_{\xi 0}K_{\xi 1})} \end{Bmatrix}. \tag{21}$$

Accordingly, Eq. (14) can be rewritten as

$$X(\xi) = \sum_{m=1}^{\infty} a_m[\sin \lambda_m \xi + \varphi_{\xi m}(\xi)], \quad 0 \leqslant \xi \leqslant 1, \tag{22}$$

where

$$\varphi_{\xi m}(\xi) = -\frac{\xi(\xi - 1)\lambda_m}{3(12 + 4(K_{\xi 1} + K_{\xi 0}) + K_{\xi 0}K_{\xi 1})} \times \{K_{\xi 0}[6 + (2 + (-1)^m)K_{\xi 1}](\xi - 2) + K_{\xi 1}[6(-1)^m + (1 + 2(-1)^m)K_{\xi 0}](\xi + 1)\}. \tag{23}$$

The beam function $Y(\eta)$ can be directly obtained from Eqs. (22) and (23) by simply replacing ξ and $K_{\xi i}$ with η and $K_{\eta i}$, respectively.

Thus, the plate displacement, the two-dimensional version of Eq. (22), can be expressed as

$$w(\xi, \eta) = \sum_{m,n=1}^{\infty} A_{mn}(\sin \lambda_m \xi + \varphi_{\xi m}(\xi))(\sin \lambda_n \eta + \varphi_{\eta n}(\eta)), \quad 0 \leqslant \xi, \eta \leqslant 1. \tag{24}$$

The expansion coefficients, A_{mn}, will be determined from the governing equation by using, for instance, the Galerkin's method. The final equation can be written as

$$(\mathbf{K} - (\rho h a^4/D)\omega^2 \mathbf{M})\mathbf{A} = \mathbf{f}, \tag{25}$$

where

$$\mathbf{A} = \{A_{11}, A_{12}, \ldots, A_{m1}, \ldots, A_{mn}, \ldots\}^T, \tag{26}$$

$$K_{mn,m'n'} = \lambda_{m'}^4(\delta_{mm'} + S_{m'm}^{\xi})(\delta_{nn'} + S_{nn'}^{\eta} + S_{n'n}^{\eta} + Z_{nn'}^{\eta}) + \sigma^{-4}\lambda_{n'}^4(\delta_{mm'} + S_{mm'}^{\xi} + S_{m'm}^{\xi} + Z_{mm'}^{\xi})(\delta_{nn'} + S_{n'n}^{\eta}) + 2\sigma^{-2}(-\lambda_{m'}^2\delta_{mm'} - \lambda_{m'}^2 S_{m'm}^{\xi} + \hat{S}_{mm'}^{\xi} + \hat{Z}_{m'm}^{\xi})(-\lambda_{n'}^2\delta_{nn'} - \lambda_{n'}^2 S_{n'n}^{\eta} + \hat{S}_{nn'}^{\eta} + \hat{Z}_{n'n}^{\eta}), \tag{27}$$

$$M_{mn,m'n'} = (\delta_{mml} + S_{mml}^{\xi} + S_{m'm}^{\xi} + Z_{mml}^{\xi})(\delta_{nn'} + S_{nn'}^{\eta} + S_{n'n}^{\eta} + Z_{nn'}^{\eta}), \tag{28}$$

and

$$f_{mn} = 2\int_0^1 f(\xi, \eta)(\sin \lambda_m \xi + \varphi_{\xi m}(\xi))(\sin \lambda_n \eta + \varphi_{\eta n}(\eta))d\xi d\eta. \tag{29}$$

For conciseness, the new matrices in Eqs. (26)–(28) are defined in the Appendix.

For a given force, Eq. (25) can be directly solved for the expansion coefficients, and hence the plate displacement. By setting the force vector on the right-hand side to zero, Eq. (25) will reduce to a standard characteristic equation from which the modal properties of the restrained plate can be readily calculated.

III. THE ACOUSTIC RADIATION FROM AN ELASTICALLY RESTRAINED PLATE

The acoustic power radiated from a baffled simply supported plate can be calculated from[1]

$$W = \tfrac{1}{2} ab\rho_0 c\omega^2 \mathbf{A}^H \Xi \mathbf{A}, \tag{30}$$

where c is the speed of sound, ρ_0 is the density of the acoustic medium, and the superscript H denotes the Hermitian operation. The symbol Ξ in Eq. (30) designates the specific radiation resistance matrix defined as[9]

$$\zeta_{mn,m'n'} = \frac{2kab}{\pi} \int_0^1 \int_0^1 \int_0^1 \int_0^1 \sin \lambda_m \xi \sin \lambda_n \eta \sin \lambda_{m'} \xi' \sin \lambda_{n'} \eta' \frac{\sin \bar{k}\sqrt{(\xi-\xi')^2 + \sigma^2(\eta-\eta')^2}}{\sqrt{(\xi-\xi')^2 + \sigma^2(\eta-\eta')^2}} d\xi' d\eta' d\xi d\eta, \tag{31}$$

where $k = \omega/c$ and $\bar{k} = ka$.

The major diagonal elements of the radiation resistance matrix Ξ are often referred to as the self radiation resistances and all the others as the mutual radiation resistances. It is well known that the cross-modal coupling exists only between a pair of modes which have the same parity indices in both ξ and η direction. Hence, only about a quarter of the off-diagonal elements are not identically equal to zero.

To investigate the modal radiation characteristics of the restrained plate, let A^l_{mn} be the (m,n)th component of the lth eigenvector. Then the corresponding mode shape is simply obtained from

$$\Phi^l(\xi,\eta) = \sum_{m,n=1}^{\infty} A^l_{mn} (\sin \lambda_m \xi + \varphi_{\xi m}(\xi))(\sin \lambda_n \eta + \varphi_{\eta m}(\eta)). \tag{32}$$

Equation (32) can be further simplified by making use of the following Fourier expansion:

$$\varphi_{\xi m}(\xi) = \sum_{n=1}^{\infty} S^{\xi}_{nm} \sin \lambda_n \xi. \tag{33}$$

In light of Eq. (33), Eq. (32) can be eventually written as

$$\Phi^l(\xi,\eta) = \sum_{m,n=1}^{\infty} \bar{A}^l_{mn} \sin \lambda_m \xi \sin \lambda_n \eta, \tag{34}$$

where

$$\bar{A}^l_{mn} = \sum_{m',n'=1}^{\infty} (\delta_{mm'}\delta_{nn'} + \delta_{mm'} S^{\eta}_{nn'} + \delta_{nn'} S^{\xi}_{mm'} + S^{\xi}_{mm'} S^{\eta}_{nn'}) A^l_{m'n'}, \tag{35}$$

and

$$\sum_{m,n=1}^{\infty} \bar{A}^l_{mn} \bar{A}^l_{mn} = 1. \tag{36}$$

Theoretically, the validity of Eq. (34) is directly dependent upon that of the Fourier series expansion, Eq. (33). Fortunately, as shown already, the series expansion will be converging according to[20]

$$\varphi_{\xi m}(\xi) \sim \sum_{n=1}^{N} S^{\xi}_{nm} \sin \lambda_n \xi + O(\lambda_{N+1}^{-3}). \tag{37}$$

Although an excellent convergence of Eq. (34) has been ensured by Eq. (37), its truncated version may not exactly satisfy the plate boundary conditions in actual numerical calculations because the second-order derivatives approach zero. However, since this expansion is only introduced to facilitate the acoustic calculations, its effects on sound radiation will be primarily due to the possible distortion to the second derivatives (of the displacement) over the infinitely narrow areas adjacent to the edges. Thus, the accompanying effects, if any, are expected to be of higher order.

From Eqs. (34) and (36), the modal radiation efficiency of the lth mode can be calculated from

$$\sigma^l = (\bar{\mathrm{A}}^l)^{\mathrm{H}} \Xi \bar{\mathrm{A}}^l. \tag{38}$$

It can be verified that the self radiation resistances do not necessarily have numerical dominance over the mutual radiation resistances. Therefore, the contributions of the mutual radiation resistances will generally need to be included in the acoustic calculations, especially in the current cases.

In essence, Eq. (34) has effectively converted the vibroacoustic analysis of an elastically restrained plate into that of a simply supported plate. As a result, many of the existing formulas or techniques can be readily applied to the restrained plate.

For an arbitrary acoustic wave number, the integral in Eq. (31) is traditionally calculated through numerical integrations, which is usually a computing intensive task. To overcome this problem, the analytical formulas previously derived by Li[9] will be used here:

$$\zeta_{mn,mn} = \frac{2}{\pi} \sum_{p=0}^{\infty} \sum_{q=0}^{p} \binom{p}{q} \frac{(-1)^p \bar{k}^{2p+2} \sigma^{2q+1}}{(2p+1)!} T^m_{2p-2q} T^n_{2q}, \tag{39}$$

$$\zeta_{mn,m'n'} = \frac{2}{\pi} \sum_{p=0}^{\infty} \sum_{q=0}^{p} \binom{p}{q} \frac{(-1)^p \bar{k}^{2p+2} \sigma^{2q+1}}{(2p+1)!} U^{mm'}_{2p-2q} U^{nn'}_{2q}, \tag{40}$$

$$\zeta_{mn,m'n} = \frac{2}{\pi}\sum_{p=0}^{\infty}\sum_{q=0}^{p}\binom{p}{q}\frac{(-1)^p\bar{k}^{2p+2}\sigma^{2q+1}}{(2p+1)!}U_{2p-2q}^{mm'}T_{2q}^{n}, \quad (41)$$

and

$$\zeta_{mn,mn'} = \frac{2}{\pi}\sum_{p=0}^{\infty}\sum_{q=0}^{p}\binom{p}{q}\frac{(-1)^p\bar{k}^{2p+2}\sigma^{2q+1}}{(2p+1)!}T_{2p-2q}^{m}U_{2q}^{nn'}. \quad (42)$$

It has been shown that by making use of this set of formulas, the computing time spent on calculating the radiation resistance matrix can be reduced by orders of magnitude as compared with the traditional numerical integration techniques[9].

IV. RESULTS AND DISCUSSIONS

A. Modal radiation efficiencies for plates uniformly restrained at edges

As an example, consider a square plate with a uniform rotational restraint along each of its edges. Plotted in Fig. 2 are the radiation efficiencies of the several lowest modes for a few different stiffness values, $K_\xi=0,1,10,\infty$ ($K_\xi=0$ and $K_\xi=\infty$ actually represent the simply supported and clamped boundary condition, respectively). The abscissa for each curve is the acoustic wave number normalized by the modal (or bending) wave number for the corresponding mode. Unlike for a simply supported plate, the modal wave number for the elastically restrained plate (if it is still a valid term) can no longer be generally determined from the pattern of the nodal lines; instead they are nominally determined as $k_p=(\omega_n^2\rho h/D)^{1/4}$. It is seen from Fig. 2 that the plate with rotational restraints tends to become a more effective sound radiator than the less restrained simply supported plate. In addition, the elastic restraints appear to have a greater impact on the radiation efficiencies of the higher-order modes. As seen in Fig. 2(g), the modal radiation efficiency can be increased by as much as 3 db at or near $k/k_p=0.5$. It is also observed that the restraints will generally have a negligible impact at, near, and above the critical frequencies.

It should be noted that while many modes of the restrained plates still look similar to their counterparts in the simply supported case, the original modes (3, 1) and (1, 3) ($\omega_{1,3}a^2\sqrt{\rho h/D}=\omega_{3,1}a^2\sqrt{\rho h/D}=98.7$) are now replaced by two new modes ($\omega_5 a^2\sqrt{\rho h/D}=131.6, \omega_6 a^2\sqrt{\rho h/D}=132.2$), as plotted in Fig. 3. Although these two modes have very close natural frequencies, they are quite different in terms of mode shapes. The familiar sinusoidal wave forms (in the x and y directions) for a simply supported plate have been destroyed or disturbed by the rotational restraints even when they are symmetrically applied to the plate. As a result, the corresponding modes can no longer be conveniently identified by the modal wave numbers. Mathematically, this stems from the fact that the plate equation is not separable in general under the current boundary conditions[17]. These changes are clearly reflected in the corresponding modal radiation efficiency curves given in Figs. 2(d) and 2(e). Taking a close look at the fifth mode in Fig. 3(a), one will notice its similarity to mode (2, 2) in terms of its spatial distribution, which explains the resemblance of their modal radiation efficiency curves in Figs. 2(c) and 2(d). Interestingly, despite the significant difference in the mode shapes and in the radiation efficiencies below $k/k_p=0.5$, the modal radiation efficiency curves again become converged near and above the critical frequencies.

B. Radiation efficiencies for plates with different restraining configurations

To better understand the effects of the rotational restraints, we will look at a few more cases involving different restraining configurations. The first one concerns a plate restrained only at $x=0$. For all the stiffness values, the first ten modes under consideration are basically unaffected regarding both the mode shape and the modal order or sequence. Referring to Fig. 4, the edge restraint manifests itself primarily in distorting and widening the first lobe. Acoustically, these modifications tend to amplify the so-called edge or corner effects, and hence to increase the radiation efficiencies of the corresponding modes, as illustrated in Fig. 5. It should be pointed out that the radiation efficiencies for the rest of the first ten modes are barely affected by the rotational restraint. This is because the restraint added to $x=0$ will primarily modify the first (row of) lobe(s), and enhance the acoustic radiation if the edge effect happens to result from the restrained edge. Take mode (1, 3) for example. The edge effect is specifically attributed to the two edges parallel to the x axis. So it can be expected that the restraint at $x=0$ will primarily push the active zones or lobes away toward the opposite edge, and thus will not have a significant impact on the corresponding modal radiation efficiency which is dictated by (the effects of) the edges at $y=0$ and $y=b$. If the rotational restraints are simultaneously applied at $x=0$ and $x=a$, the acoustic effects can be enhanced by both the edges for certain modes. This is manifested in the approximate doubling of the corrections to the corresponding modal radiation efficiencies for the one-edge restrained plate.

When the plate is restrained along two adjacent edges such as at $x=0$ and $y=0$, many of its modes will be considerably different from the familiar ones for the simply supported boundary condition. As seen from Fig. 6, the modes now become more complicated, and the modal lines are no longer parallel to the x and y axes. Although not plotted here, modes 3, 8, 10 are actually very similar to modes 2, 7 and 9 with a 90° rotation, respectively. The radiation efficiencies for the ninth and tenth modes are compared in Fig. 7. Although there is no clear difference, other than a 90° rotation, between the ninth and tenth modes, their radiation efficiencies are noticeably different at small wave numbers. A similar comparison is also observed between the radiation efficiencies for the second and third modes. It is also interesting to point out that although many modes, such as the seventh and ninth modes, look considerably different from their simply supported counterparts, this disparity may not be proportionally reflected in the corresponding radiation efficiency curves, as illustrated in Fig. 7.

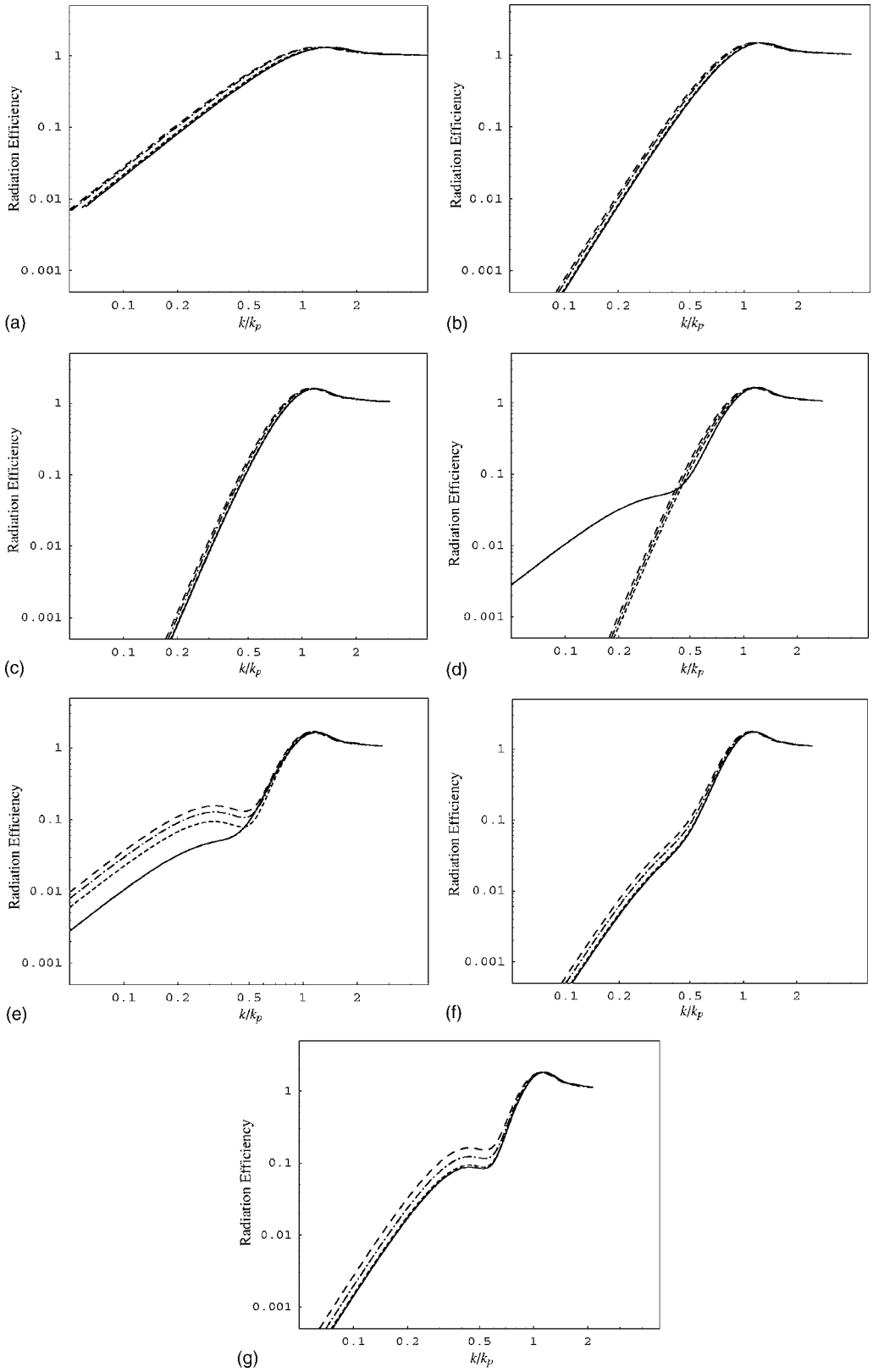

FIG. 2. Modal radiation efficiencies: (a) the first mode, (b) the second and third modes, (c) the fourth mode, (d) the fifth mode, (e) the sixth mode, (f) the seventh and eighth modes, and (g) the ninth and tenth modes; (—) $K_\xi=0$, (---) $K_\xi=1$, (-·-), $K_\xi=10$, (——) $K_\xi=\infty$.

For the plate restrained, for instance, at $x=0$, $x=a$, and $y=0$, most modes will resume the original wave shapes as in the simply supported case. In Fig. 8, the radiation efficiencies are plotted for a pair of representative modes, the fifth and sixth modes. It is seen that the effect of the elastic restraints on the sixth modes, (3,1), is about twice higher than that on the fifth mode, (1,3). This is because there are two distorted lobes in mode (3, 1) as compared with only one in

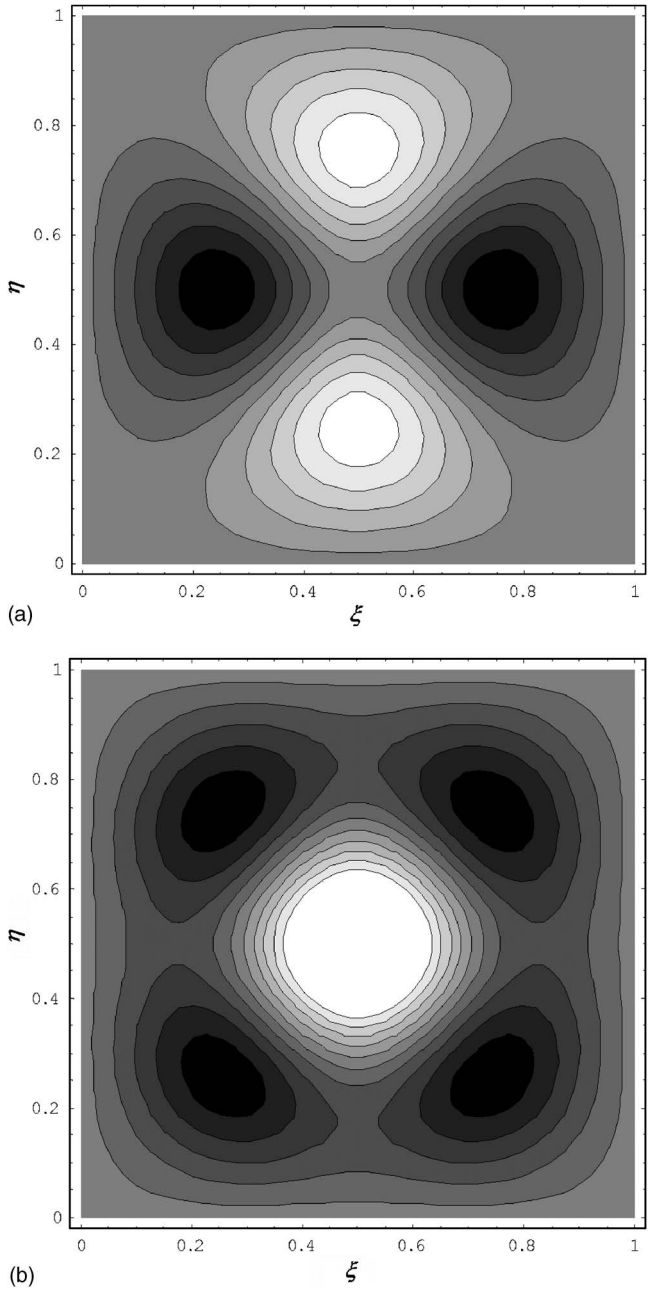

FIG. 3. Mode shapes of a uniformly restrained plate: (a) the fifth mode, and (b) the sixth mode.

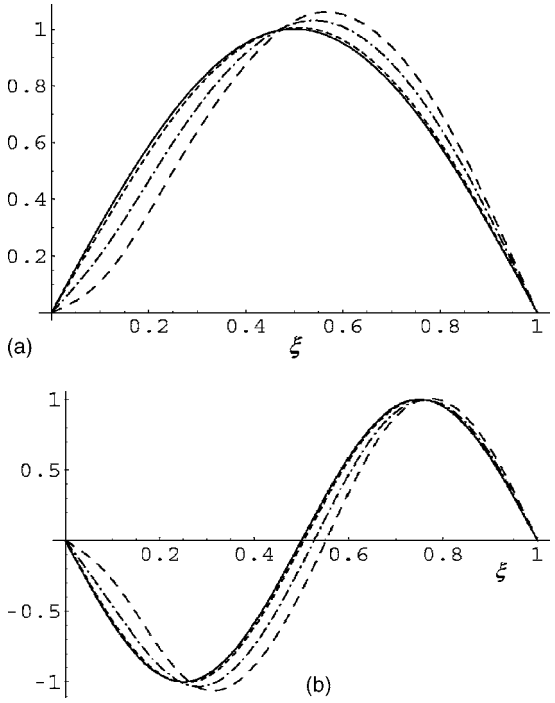

FIG. 4. Mode shapes of a plate restrained at $x=0$: (a) the first mode, (b) the third mode.

mode (1, 3). Based on the same argument, one could expect that the radiation efficiency for the fifth mode is close to that previously given in Fig. 5(c) for the one-edge restrained plate. A careful comparison will reveal that the modal radiation efficiency in this case is slightly smaller, probably because the length of the distorted lobe, or the effective length of the edge at $y=0$, is actually reduced due to the extra restraints at $x=0$ and $x=a$.

While the current method can be generally employed to study the sound radiation from any plate mode, one may be interested in applying it specifically to "edge modes" for a comparison with an existing solution. For this purpose, Fig. 9 shows the correction factors calculated for mode (10, 1) of a square plate with a clamped edge at $x=0$. The correction factor was previously used by Leppington *et al.*[17] to measure the contributions arising from the extra boundary restraint with reference to the simply supported case. The dashed line in Fig. 9 is obtained from their asymptotic formula for an edge mode by accordingly setting the plate wave numbers as $k_x=10\pi/a$ and $k_y=\pi/b$. A significant difference is observed between these two estimates, which is, however, predictable in view of the fact that the asymptotic formula is essentially derived for a semi-infinite plate with a rotational restraint. When three additional edges are present for a finite plate, the adjacent areas will become the active zones in radiating sound and their contributions tend to remain the same regardless of whether the edge $x=0$ is clamped or not. Thus, the relative change in modal radiation efficiency resulting from the extra edge restraint will appear smaller for a finite plate (as compared with a semi-infinite plate) even though the structural wave numbers are kept the same in both directions. It is not difficult to understand that the contributions from the edges parallel to the x axis is in inverse proportion to the (modal) wave number in the x direction; indeed, the correction factor for mode (12, 1) shifts by about 15% toward the asymptotic estimate. While the modal index in the y direction seems to have insignificant effect on the level of the correction factor, its increase can make the waviness of the correction factor curve quickly disappear (approaching the smoothness of the asymptotic solution). From the above discussions, one should be able to conclude that an asymptotic solution derived from a semi-infinite plate model can overestimate the effects of an edge restraint on the acoustic radiation from a finite plate, even though it is dictated by edge modes.

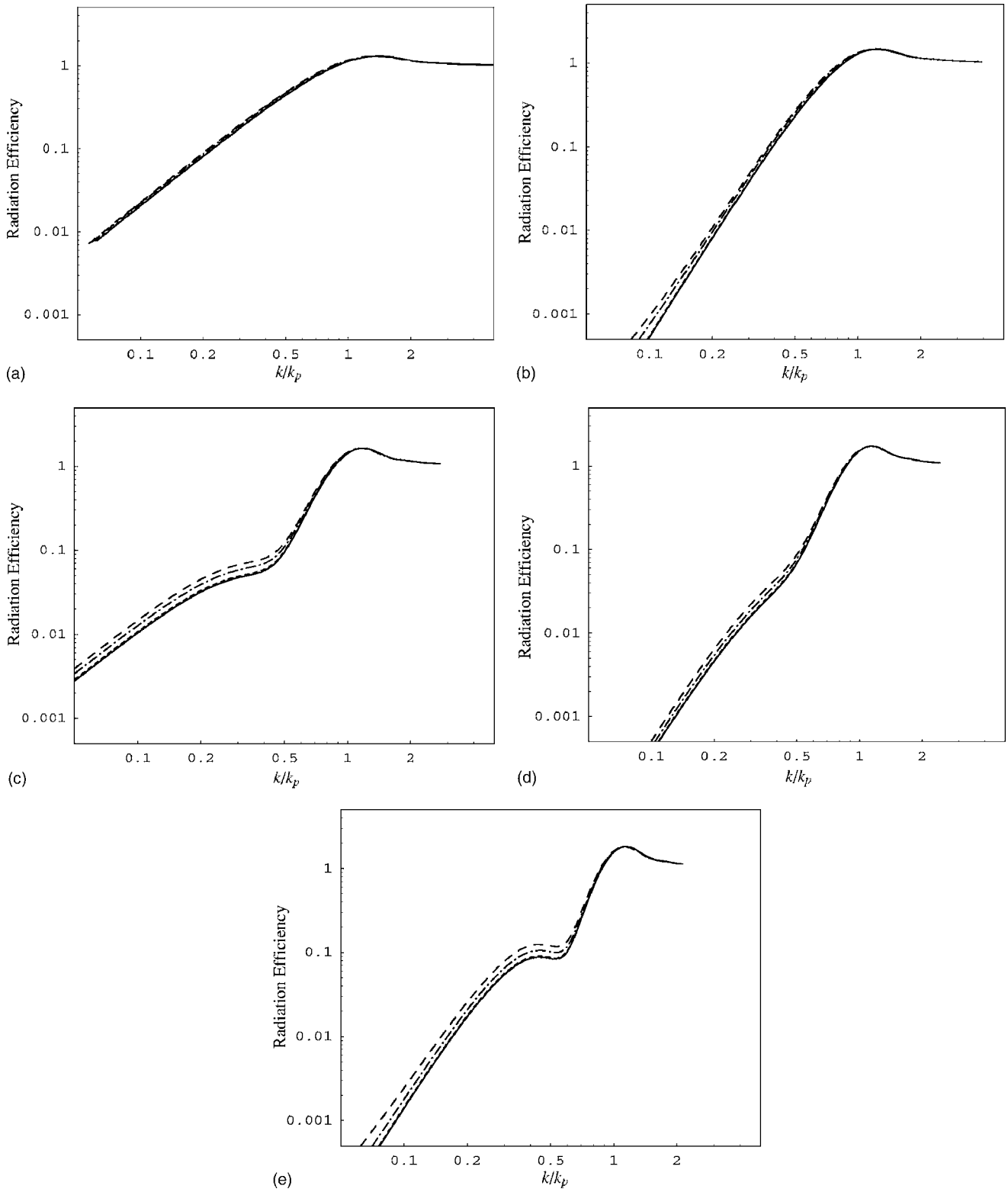

FIG. 5. Modal radiation efficiencies: (a) the first mode, (b) the third mode, (c) the sixth mode, (d) the eighth mode, and (e) the tenth mode; (—) $K_\xi=0$, (---) $K_\xi=1$, (--·-) $K_\xi=10$, (——) $K_\xi=\infty$.

V. CONCLUSIONS

An analysis method has been presented for the vibroacoustic study of a rectangular plate elastically restrained at an edge against rotation. The transverse displacement of the plate is expressed as a general series expansion, and the expansion coefficients are determined by using the familiar Galerkin's method. Further it is shown that the plate displacement and modes can be eventually simplified to a Fourier sine series, which allows many existing formulas or techniques to be directly used for the acoustic analysis of the restrained plate. This method is theoretically accurate for any acoustic or structural (modal) wave number.

For the modes whose shapes are not significantly modified by the rotational restraint(s), the added edge restraint(s)

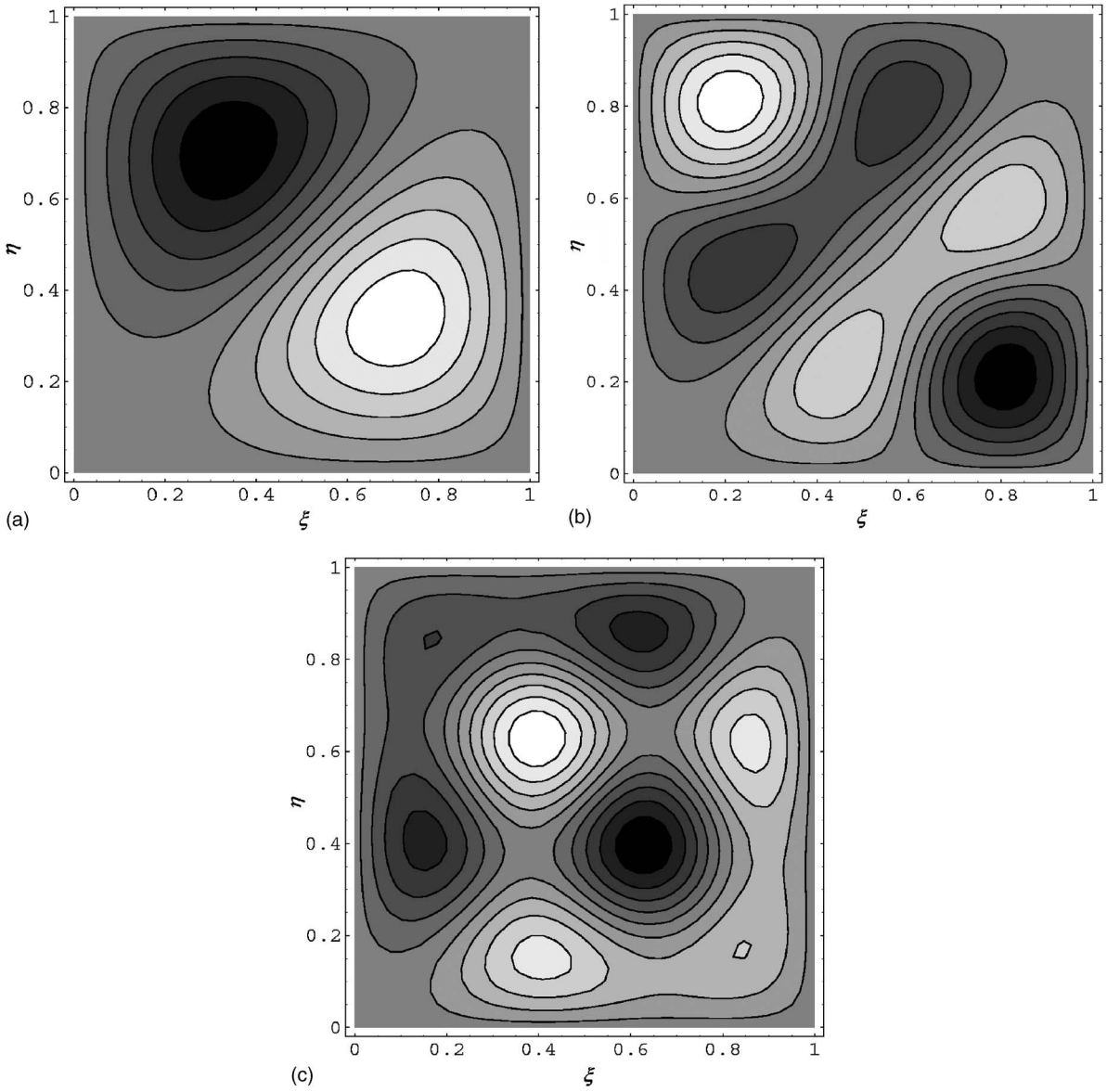

FIG. 6. Mode shapes of a plate restrained at $x=0$ and $y=0$: (a) the second mode, (b) the seventh mode, and (c) the ninth mode.

tends to have an enhancement effect on the radiation efficiencies. The correction to the modal radiation efficiency for an edge mode will depend upon the number of "relevant" edges actually restrained, and can be up to 3 dB as often quoted in the literature. However, since many modes may be substantially different from their simply supported counterparts and can no longer be generally identified by the wave number components, then it is not always possible, or even meaningful, to directly correlate or compare the modal radiation efficiencies with those for the unrestrained plate. In addition, because the sound radiation from a plate is usually dictated by the resonant mode(s) at a given frequency, the plate with a greater edge restraint does not necessarily have higher radiation efficiency than a less restrained (simply supported) plate. In other words, it cannot be generally concluded that an extra edge restraint will have an enhancing effect on the sound radiation from a plate.

APPENDIX

The new variables in Eqs. (27) and (28) are defined as follows:

$$S_{mn}^{\xi} = 2\int_0^1 \varphi_{\xi n}(\xi)\sin\lambda_m \xi d\xi$$

$$= \frac{-4\lambda_n}{[12+4(K_{\xi 1}+K_{\xi 0})+K_{\xi 0}K_{\xi 1}]\lambda_m^3}\{6(-1)^{m+n}K_{\xi 1}+K_{\xi 0}[6 + (2+(-1)^m+(-1)^n+2(-1)^{m+n})K_{\xi 1}]\}, \quad \text{(A1)}$$

$$\hat{S}_{mn}^{\xi} = 2\int_0^1 \frac{d^2\varphi_{\xi n}(\xi)}{d\xi^2}\sin\lambda_m \xi d\xi = -\lambda_m^2 S_{mn}, \quad \text{(A2)}$$

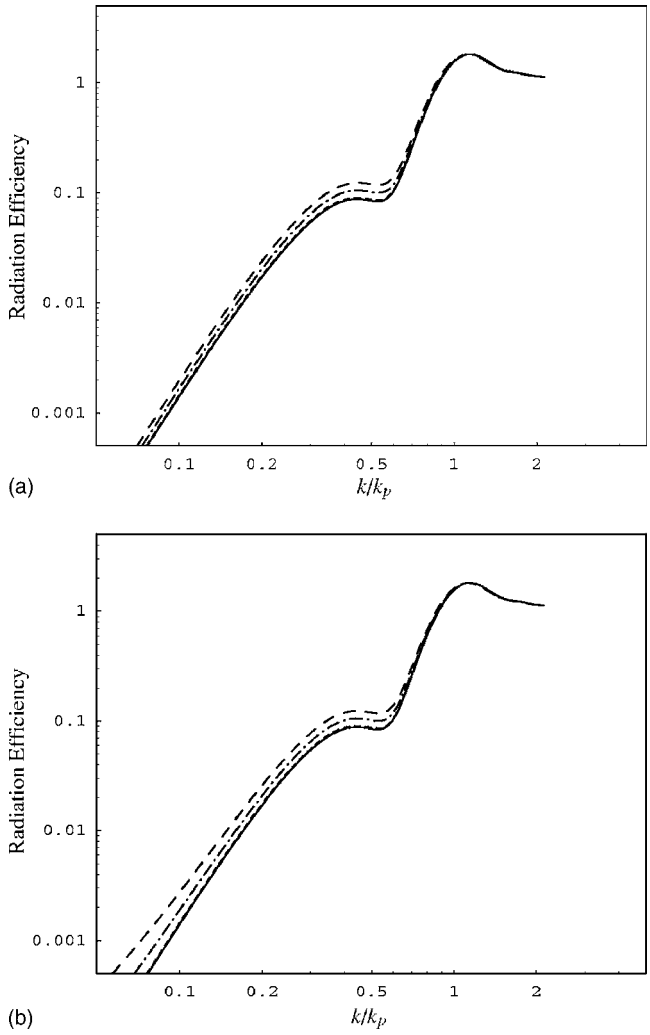

FIG. 7. Modal radiation efficiencies: (a) the ninth mode, and (b) the tenth mode; (—) $K_\xi=0$, (---) $K_\xi=1$, (-·-) $K_\xi=10$, (——) $K_\xi=\infty$.

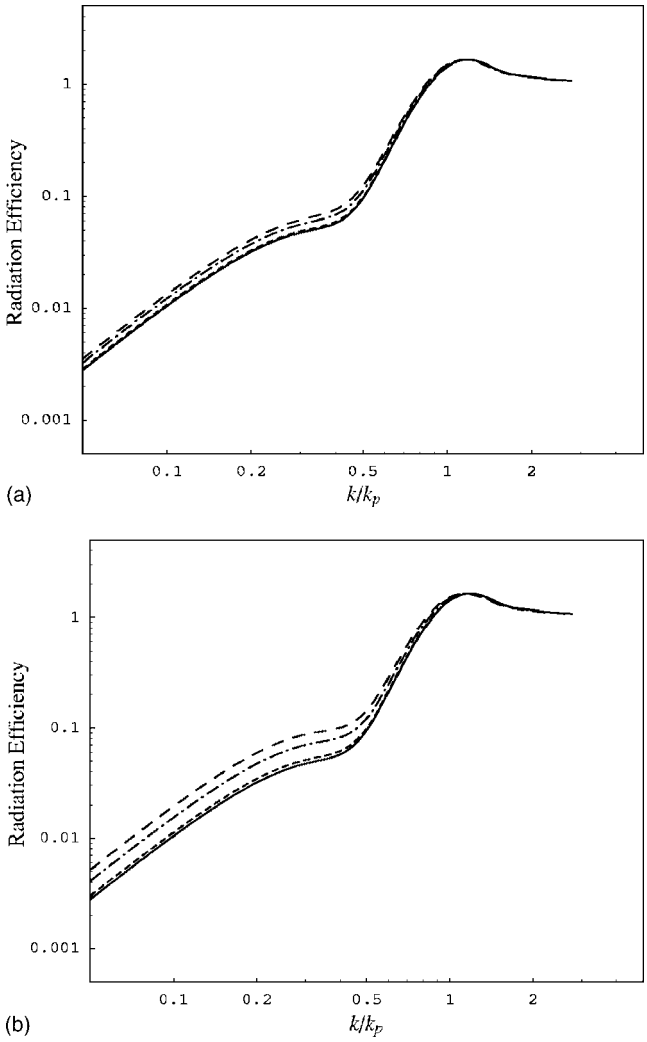

FIG. 8. Modal radiation efficiencies: (a) the fifth mode, and (b) the sixth mode; (—) $K_\xi=0$, (---) $K_\xi=1$, (-·-) $K_\xi=10$, (——) $K_\xi=\infty$.

$$Z_{mn}^{\xi}=2\int_0^1 \varphi_{\xi m}(\xi)\varphi_{\xi n}(\xi)d\xi$$

$$=\frac{\lambda_m\lambda_n}{210[12+4(K_{\xi 1}+K_{\xi 0})+K_{\xi 0}K_{\xi 1}]^2}\{128(-1)^{m+n}K_{\xi 1}^2$$
$$-4K_{\xi 0}K_{\xi 1}[31((-1)^m+(-1)^n)$$
$$+(5(-1)^m+5(-1)^n-11(-1)^{m+n})K_{\xi 1}]$$
$$+K_{\xi 0}^2[128-4K_{\xi 1}(5(-1)^m+5(-1)^n-11)$$
$$+K_{\xi 1}^2(4-3(-1)^m-3(-1)^n+4(-1)^{m+n}\ ]\}\qquad \text{(A3)}$$

and

$$\hat{Z}_{mn}^{\xi}=2\int_0^1 \varphi_{\xi m}(\xi)\frac{d^2}{d\xi^2}\varphi_{\xi n}(\xi)d\xi$$

$$=\frac{-\lambda_m\lambda_n}{15[12+4(K_{\xi 1}+K_{\xi 0})+K_{\xi 0}K_{\xi 1}]^2}\{96(-1)^{m+n}K_{\xi 1}^2$$
$$-12K_{\xi 0}K_{\xi 1}[7((-1)^m+(-1)^n)+((-1)^m+(-1)^n$$
$$-3(-1)^{m+n})K_{\xi 1}]+K_{\xi 0}^2[96-12K_{\xi 1}((-1)^m+(-1)^n-3)$$
$$+K_{\xi 1}^2(4-(-1)^m-(-1)^n+4(-1)^{m+n}\ ]\}.\qquad \text{(A4)}$$

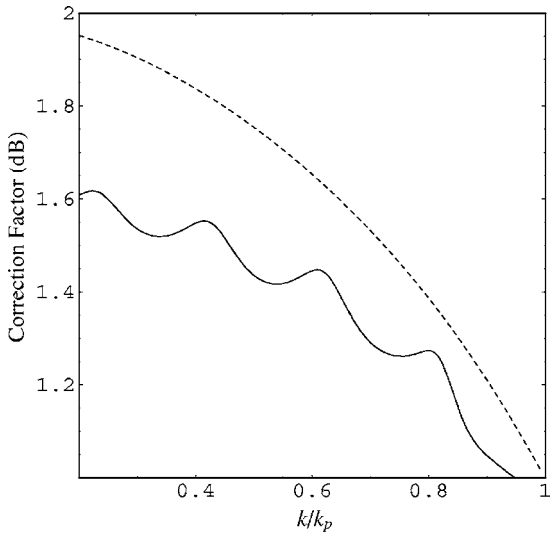

FIG. 9. The estimated correction factors for mode (10, 1) of a square plate with one edge clamped at $x=0$; (—) current solution, (---) asymptotic estimate (Ref. 17).

The similar variables corresponding to the η direction can be directly obtained by simply replacing $K_{\xi i}$ with $K_{\eta i}$ in Eqs. (A1)–(A4).

[1]G. Maidanik, "Response of ribbed panels to reverberant acoustic fields," J. Acoust. Soc. Am. **34**, 809–826 (1962).
[2]C. E. Wallace, "Radiation resistance of a rectangular panel," J. Acoust. Soc. Am. **51**, 946–952 (1972).
[3]H. G. Davies, "Sound from turbulent-boundary-layer-excited panels," J. Acoust. Soc. Am. **49**, 878–889 (1971).
[4]E. G. Williams, "A series expansion of the acoustic power radiated from planar sources," J. Acoust. Soc. Am. **73**, 1520–1524 (1983).
[5]H. Levine, "On the short wave acoustic radiation from planar panels or beams of rectangular shape," J. Acoust. Soc. Am. **76**, 608–615 (1984).
[6]F. G. Leppington, E. G. Broadbent, and K. H. Heron, "The acoustic radiation efficiency of rectangular panels," Proc. R. Soc. London, Ser. A **382**, 245–271 (1982).
[7]G. Xie, D. J. Thompson, and D. J. C. Jones, "The radiation efficiency of baffled plates and strips," J. Sound Vib. **280**, 181–209 (2005).
[8]R. H. Lyon and R. G. DeJong, *Theory and Applications of Statistical Energy Analysis* (Butterworth-Heinemann, Boston, 1995).
[9]W. L. Li, "An analytical solution for the self and mutual radiation resistances of a rectangular plate," J. Sound Vib. **245**, 1–16 (2001).
[10]S. Snyder and N. Tanaka, "Calculating total acoustic power output using modal radiation efficiencies," J. Acoust. Soc. Am. **97**, 1702–1709 (1995).
[11]W. L. Li and H. J. Gibeling, "Determination of the mutual radiation resistances of a rectangular plate and their impact on the radiated sound power," J. Sound Vib. **229**, 1213–1233 (2000).
[12]W. L. Li and H. J. Gibeling, "Acoustic radiation from a rectangular plate reinforced by finite springs at arbitrary locations," J. Sound Vib. **220**, 117–133 (1999).
[13]M. C. Gomperts, "Sound radiation from baffled, thin, rectangular plates with general boundary conditions," Acustica **30**, 320–327 (1974).
[14]M. C. Gomperts, "Sound radiation from baffled, thin, rectangular plates," Acustica **37**, 93–102 (1977).
[15]G. Maidanik, "Radiation efficiency of panels," J. Acoust. Soc. Am. **35**, 115 (1963).
[16]F. J. Fahy, "Vibration of containing structures by sound in the contained fluid," J. Sound Vib. **10**, 490–512 (1969).
[17]F. G. Leppington, E. G. Broadbent, and K. H. Heron, "The acoustic radiation from rectangular panels with constrained edges," Proc. R. Soc. London, Ser. A **393**, 67–84 (1984).
[18]M. Ohlrich and C. T. Hugin, "On the influence of boundary constraints and angled baffle arrangements on sound radiation from rectangular plates," J. Sound Vib. **277**, 405–418 (2004).
[19]W. L. Li, "Free vibrations of beams with general boundary conditions," J. Sound Vib. **237**, 709–725 (2000).
[20]W. L. Li, "Comparison of Fourier sine and cosine expansions for beams with arbitrary boundary conditions," J. Sound Vib. **255**, 185–194 (2002).

On tuning a reactive silencer by varying the position of an internal membrane[a)]

Jane B. Lawrie[b)] and Idil M. M. Guled
School of Information Systems, Computing and Mathematics, Mathematical Sciences, Brunel University, Uxbridge UB8 3PH, United Kingdom

(Received 7 August 2005; revised 4 April 2006; accepted 19 May 2006)

A mode-matching method is used to investigate the performance of a two-dimensional, modified reactive silencer. The modification takes the form of a membrane which is attached to the internal walls of the expansion chamber parallel to the axis of the inlet/outlet ducts. The height of the membrane above the level of the inlet/outlet ducts can be varied and, by this means, the device is tuned. It is shown that the stopband produced by the silencer can be broadened and/or shifted depending upon the height to which the membrane is raised. Attention is focused on the efficiency of the device at low-frequencies—the regime where dissipative silencers are usually least effective. The potential use of the device as a component in a hybrid silencer for heating ventilation and air-conditioning (HVAC) ducting systems is discussed. © *2006 Acoustical Society of America.*
[DOI: 10.1121/1.2213571]

PACS number(s): 43.50.Gf, 43.20.Mv, 43.40.Dx [DKW] Pages: 780–790

I. INTRODUCTION

Ducted fan noise is an issue that affects a diverse range of industrial applications: the generation of "buzz-saw" noise in aero-engines;[1] noise emission from chimney stacks of power stations;[2] and heating ventilation and air-conditioning (HVAC) systems.[3] Dissipative devices such as acoustic linings or silencers are often used to reduce the noise levels. These work well in the mid- and high-frequency range but are less effective for low-frequency noise. In many applications, therefore, it is the low-frequency tonal fan noise that is the most pervasive.

Tonal fan noise tends to be in the range 100–500 Hz and restricted to a narrow band which, depending on the application, can be as large as 50 Hz (Ref. 2) or as little as 6 Hz.[4] In recent years much research has been carried out on ways of reducing such noise. Passive devices that perform at low frequencies include expansion chambers and Helmholtz resonators. Both, however, are of limited value in practical situations, such as HVAC installations, where constraints on space rule out the use of bulky devices. Further, in the case of the Helmholtz resonator, the transmission loss is modest, typically in the region of 6 dB,[5] and the frequency range over which it is effective is narrow. The latter point has been addressed and various designs for an adaptive Helmholtz resonator have been proposed; see for example de Bedout *et al.*[6] While Helmholtz resonators, both adaptive and standard, have found application in a range of industries,[5,7] they are not, to the authors's knowledge, extensively used in HVAC systems.

An alternative to passive noise control is offered by active devices which aim at cancellation of the noise. This is a fast-growing area of research and it is clear that impressive levels of noise reduction are possible for a wide range of applications.[3,2,4] Such devices are, however, not without potential problems. They all require additional energy (and thus additional expense) to achieve noise reduction and, further, the loudspeakers may occupy space in the region exterior to the duct. For example, the housing for the active silencer cassette in the configuration considered by Krüger[3] is spacewise equivalent to a rather bulky expansion chamber. In situations where space is limited, this extra height would be undesirable. Furthermore, in all such devices there is the possibility of creating more noise should the control algorithm fail.

In this paper a generalization of the reactive silencer recently investigated by Huang[8–10] is considered with a view to assessing its potential as a means of reducing tonal fan noise in HVAC systems. The device comprises a two-dimensional reactive silencer in which a membrane is attached to the internal walls of the expansion chamber parallel to the axis of the inlet/outlet ducts. The height of the membrane above the level of the inlet/outlet ducts can be varied, and the device is tuned by selecting the membrane height that gives the widest stopband for a specified frequency. The concept of utilizing flexible panels as a means of controlling low-frequency noise is by no means new. As long ago as 1963 Dowell and Voss[11] studied the vibrations of a cavity-backed panel in the presence of flow. More recently, and in the context of architectural acoustics, Kang and Fuchs[12] have investigated the effectiveness of cavity-backed microperforated membranes as an acoustic absorber.

The model problem is solved using a mode-matching technique. The fluid velocity potentials in the inlet and outlet ducts are expressed in the form of standard Fourier cosine series. In contrast, due to the presence of high-order spacial

[a)]Portions of this work were presented in Mohamed-Guled and Lawrie, "A parametric investigation of the acoustic power in a two-dimensional waveguide with membrane bounded cavity," in *Proceedings of IUTAM 2002/4*, edited by A. B. Movchan (Kluwer, Dordrecht, 2004). Liverpool, U.K July 2002.

[b)]Author to whom correspondence should be addressed. Electronic mail: jane.lawrie@brunel.ac.uk

derivatives in the membrane boundary condition, the eigensystem of the silencer region is non-Sturm-Liouville. Further, the eigenfunctions are piecewise continuous. Nevertheless, the system satisfies a known orthogonality relation.[13,14] This, together with the usual orthogonality property for $\{\cos(n\pi y/a)|n=0,1,2,\ldots\}$, enables continuity of pressure/normal velocity to be imposed at the mouths of the inlet/outlet ducts, and appropriate edge conditions to be applied where the membrane joins the structure. The two resulting systems of algebraic equations, formulated in terms of the amplitudes of the reflected and transmitted waves, are truncated and solved numerically. In this article the roots of the characteristic function for the modified expansion chamber are determined numerically before the mode-matching equations are truncated and inverted. For a nondissipative system, such as this, root finding usually presents few problems. It is worthwhile mentioning, however, that the boundary value problem for the model problem falls within the class whereby the mode-matching equations can be recast into root-free form,[15] which bypasses the root-finding process.

In contrast, the method employed by Huang[8,9] automatically avoids the need for root finding. He employs a technique whereby the sound fields within the duct and cavity are represented by an infinite sum of Fourier integrals, each one forced by a velocity distribution $\sin[n\pi(x+\ell)/(2\ell)]$ on the duct surface for $-\ell \leqslant x \leqslant \ell$. The Fourier coefficients of the pressure field are then determined by substituting an evaluated form of the Fourier integrals into the membrane condition. This works well for the case in which the membrane lies at the mouth of the expansion chamber in line with the upper boundary of the inlet/outlet ducts. The method cannot, however, be extended to the more general situation in which the membrane lies above or below this level.

The aims of this article are to investigate the effects of varying the height of the membrane within the expansion chamber; to discuss the the potential for using this device as a component of a hybrid silencer for HVAC ducting systems; to compare Huang's solution method with the mode-matching method, and to discuss the relative merits of the two approaches. In Sec. II the traveling wave forms for the expansion chamber region are discussed and the appropriate orthogonality relation is stated. This is used in Sec. III, where the boundary value problem corresponding to acoustic transmission through the modified reactive silencer is stated and solved using the mode-matching technique outlined above. Section IV is concerned with the derivation of a low-frequency approximation to the solution. This proves to be surprisingly accurate and is a useful tool in terms of verifying the results obtained via mode matching. In Sec. V numerical results are presented. Of particular interest are those showing transmission loss against frequency for silencers with low aspect ratio (i.e., those in which the ratio of silencer length to expansion chamber height is less than three). It is found that such silencers exhibit only modest stopbands when the membrane is positioned at the mouth of the expansion chamber; however, by altering the position of the membrane they can be tuned and the width of the stopband can be increased by up to 38%. Finally, Sec. VI presents a discussion of the results and potential extensions to the theory.

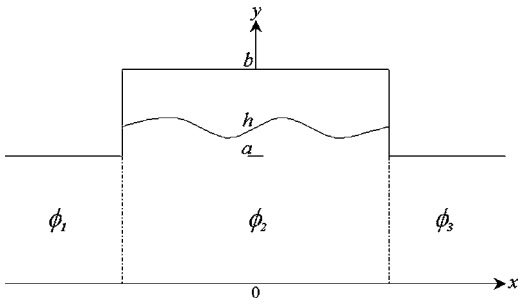

FIG. 1. Silencer geometry.

II. TRAVELING WAVE SOLUTIONS

In this section a detailed discussion of the traveling wave forms of the silencer region (see Fig. 1) is presented. It is appropriate, therefore, to consider the unforced boundary value problem governing the fluid velocity potential within an infinite rigid duct, of height $\bar{b}$, in which a horizontal membrane is situated along $\bar{y}=\bar{h}$, $-\infty<\bar{x}<\infty$, with $0<\bar{h}<\bar{b}$. Harmonic time dependence, $e^{-i\omega\bar{t}}$, where ω is the radian frequency, is assumed. Thus, the time-dependent fluid velocity potential, $\bar{\Phi}$, can be expressed as $\bar{\Phi}(\bar{x},\bar{y},\bar{t})=\bar{\phi}(\bar{x},\bar{y})e^{-i\omega\bar{t}}$ and, henceforth, the time-independent potential $\bar{\phi}$ will be used. It is convenient to nondimensionalize the boundary value problem using typical length and time scales k^{-1} and ω^{-1}, where $k=\omega/c$. Thus, the nondimensional quantities x, y, etc. will henceforth be used. These are related to their dimensional counterparts by $x=k\bar{x}$, $y=k\bar{y}$, etc.

The velocity potential satisfies Helmholtz's equation with unit wave number, that is

$$(\nabla^2+1)\phi=0. \tag{1}$$

At the rigid walls the normal component of velocity potential is zero,

$$\frac{\partial\phi}{\partial y}=0, \quad y=0,b, \quad -\infty<x<\infty. \tag{2}$$

The membrane at $y=h$, $-\infty<x<\infty$, is described by the condition

$$\left(\frac{\partial^2}{\partial x^2}+\mu^2\right)\frac{\partial\phi}{\partial y}-\alpha[\phi(x,y)]_{h^-}^{h^+}=0, \quad y=h, \tag{3}$$

where μ and α are the nondimensional *in vacuo* membrane wave number and the nondimensional fluid loading parameter, respectively. These quantities are defined by $\mu=c/c_m$ and $\alpha=c^2\rho/(kT)$, where $c_m=(T/\rho_m)^{1/2}$ is the *in vacuo* speed of waves on the membrane, T is the membrane tension, and ρ_m is the mass per unit area of the membrane.

On using the usual process of separation of variables, it is found that the eigenmodes for the silencer region are

$$\phi_n=Y_n(y)e^{\pm i\nu_n x}, \quad 0\leqslant y\leqslant b, \tag{4}$$

where

$$Y_n(y)=\begin{cases}\cosh(\gamma_n y), & 0\leqslant y\leqslant h\\ \xi_n\cosh[\gamma_n(b-y)], & h<y\leqslant b\end{cases}, \tag{5}$$

and

$$\xi_n = \begin{cases} -\dfrac{\sinh(\gamma_n h)}{\sinh[\gamma_n(b-h)]}, & n \neq 1 \text{ and } \gamma_n \neq \dfrac{ij\pi q}{ph} \\ 1, & n = 1 \\ (-1)^j, & n \neq 1 \text{ and } \gamma_n = \dfrac{ij\pi q}{ph} \end{cases} \tag{6}$$

with $\gamma_n^2 - \nu_n^2 + 1 = 0$. This expression encompasses both fluid-membrane coupled waves and uncoupled modes. For the coupled modes, the eigenvalues, γ_n^c, $n=0,1,2,\ldots$, are the roots of the characteristic equation

$$K(\gamma) = (\gamma^2 + 1 - \mu^2)\gamma \sinh(\gamma h) - \alpha \frac{\sinh(\gamma b)}{\sinh[\gamma(b-h)]} = 0. \tag{7}$$

Note that $K(\gamma)$ is an even function of γ. It is convenient, therefore, to denote the roots of (7) by $\pm\gamma_n^c$, $n=0,1,2,\ldots$ and discuss only the positive roots (i.e., those lying in the upper half of the complex gamma plane axes, which is deemed to include the positive real axis). It is found that there is always one real root, $\gamma_0^c > 0$, and an infinite number of imaginary roots, γ_n^c, $n=1,2,3,\ldots$, which are labeled with increasing distance up the imaginary axis. In addition to the fluid membrane modes there are other possible waveforms for the silencer region. First is the plane acoustic wave e^{ix}. This is a trivial solution to (3) and it follows that this mode can always exist without interaction with the membrane. Other uncoupled modes exist only if the silencer height b can be expressed in the form $b=ph/q$, for integer values of p and q. The modes of interest are a subset of the usual rigid duct modes: those that have zero velocity normal to the membrane at $y=h$. Thus, admissible wave numbers for the uncoupled modes are defined by $\gamma_1^\mu = 0$ (always present) and $\gamma_j^\mu = ij\pi q/(ph)$, $j=p,2p,3p,\ldots$ (present only for $b=ph/q$). Note that these wave numbers are *not* roots to the characteristic equation (7).

The set of all admissible wave numbers is the union of those for the coupled and uncoupled modes, that is, $\{\gamma_n | n=0,1,2\ldots\} = \{\gamma_m^c | m=0,1,2,\ldots\} \cup \{\gamma_j^\mu | j=1,p,2p,\ldots\}$. They are ordered $\gamma_0 = \gamma_0^c$, $\gamma_1 = \gamma_1^\mu$ and then by increasing imaginary part. The functions $Y_n(y)$ defined by (5) and (6) satisfy the following orthogonality relation:[14]

$$Y_n'(h)Y_m'(h) + \alpha \int_0^b Y_n(y)Y_m(y)dy = E_n \delta_{mn}, \tag{8}$$

where the prime indicates differentiation with respect to y and δ_{mn} is the usual Kronecker delta. For fluid-coupled modes the quantity E_n is given by

$$E_n = \frac{Y_n'(h)}{2\gamma_n} \frac{d}{d\gamma} K(\gamma)\bigg|_{\gamma=\gamma_n}, \tag{9}$$

whereas for the uncoupled modes

$$E_n = \frac{\alpha b}{2} \varepsilon_{n-1}, \tag{10}$$

where $\varepsilon_n = 2$ for $n=0$ and 1 otherwise. Equations (9) and (10) can be rearranged for the general case as

$$E_n = \frac{\alpha}{2}[e_n(h) + \xi_n^2 e_n(b-h)], \tag{11}$$

where

$$e_n(x) = x + \frac{(3\gamma_n^2 + 1 - \mu^2)}{2\gamma_n(\gamma_n^2 + 1 - \mu^2)} \sinh(2\gamma_n x). \tag{12}$$

III. THE BOUNDARY VALUE PROBLEM

The mode-matching solution for acoustic transmission through the modified silencer is presented in this section. The model comprises rigid inlet and outlet ducts occupying the regions $0 \leqslant y \leqslant a$, $|x| > \ell$ of a Cartesian frame of reference, together with a finite duct of height $b > a$ in the gap $|x| \leqslant \ell$. The structure is closed by two vertical rigid surfaces at $x = \pm\ell$, $a \leqslant y \leqslant b$, forming a rectangular expansion chamber. The interior region of the duct contains a compressible fluid of sound speed c and density ρ. The fluid in the expansion chamber is separated into two regions by a horizontal membrane which lies along $y=h$, $h \geqslant a$, $|x| \leqslant \ell$; see Fig. 1.

A multimodal incident field, with harmonic time dependence, is incident in the positive x direction towards $x=-\ell$ where it is scattered. It is convenient to split the velocity potential into three parts corresponding to the inlet duct, the expansion chamber, and the outlet duct, respectively. The time-independent fluid velocity potentials for each duct region are thus $\phi_1(x,y)$, $x<0$; $\phi_2(x,y)$, $0<x<2\ell$, and $\phi_3(x,y)$, $x>2\ell$. The velocity potentials, ϕ_j, $j=1,3$, satisfy the nondimensionalized Helmholtz's equation (1) with boundary conditions

$$\frac{\partial \phi_1}{\partial y} = 0, \quad y = 0, a, \quad -\infty < x \leqslant -\ell, \tag{13}$$

$$\frac{\partial \phi_3}{\partial y} = 0, \quad y = 0, a, \quad \ell \leqslant x < \infty, \tag{14}$$

whereas the potential ϕ_2 satisfies Eqs. (1)–(3) together with

$$\frac{\partial \phi_2}{\partial x} = 0, \quad x = \pm\ell, \quad a < y \leqslant b, \tag{15}$$

and the edge condition

$$\phi_{2y}(\pm\ell, h) = 0, \tag{16}$$

where the subscript y indicates differentiation with respect to that variable. The eigenfunction expansions for ϕ_j, $j=1,2,3$ are

$$\phi_1 = \sum_{n=0}^{\infty} F_n \cos\left(\frac{n\pi y}{a}\right) e^{i\eta_n(x+\ell)} + \sum_{n=0}^{\infty} A_n \cos\left(\frac{n\pi y}{a}\right) e^{-i\eta_n(x+\ell)}, \tag{17}$$

$$\phi_2 = \sum_{n=0}^{\infty} (B_n e^{i\nu_n x} + C_n e^{-i\nu_n x}) Y_n(y), \tag{18}$$

$$\phi_3 = \sum_{n=0}^{\infty} D_n \cos\left(\frac{n\pi y}{a}\right) e^{i\eta_n(x-\ell)}, \tag{19}$$

where $Y_n(y)$ is given by (5). Here, F_n are the amplitudes of the incident modes while A_n, D_n are the complex amplitudes of the nth reflected, transmitted modes, respectively and B_n, C_n are the amplitudes of the modes in the silencer region. Note that $\eta_n=(1-n^2\pi^2/a^2)^{1/2}$ and $\nu_n=(\gamma_n^2+1)^{1/2}$, $n=0,1,2,\ldots$. The focus of this article is on transmission loss at low frequencies and, as such, plane-wave forcing is of primary interest. To broaden the applicability of the article, however, the model problem has been formulated for a multimodal incident field. For plane-wave forcing $F_n=\delta_{n0}$, $n=0,1,2,\ldots$, whereas the appropriate form of the modal amplitudes in the case of, for example, equal modal energy density, are given by Mechel.[16]

The coefficients A_n, B_n, C_n, and D_n are determined by matching the fluid pressure and the normal velocity at the interfaces $x=\pm\ell$, $0\leqslant y\leqslant a$. Continuity of pressure is expressed as

$$\phi_1(-\ell,y) = \phi_2(-\ell,y), \quad 0\leqslant y\leqslant a, \tag{20}$$

and

$$\phi_2(\ell,y) = \phi_3(\ell,y), \quad 0\leqslant y\leqslant a. \tag{21}$$

Similarly, continuity of normal velocity gives

$$\frac{\partial\phi_2}{\partial x}(-\ell,y) = \begin{cases} \dfrac{\partial\phi_1}{\partial x}(-\ell,y), & 0\leqslant y\leqslant a \\ 0, & a<y\leqslant b \end{cases}, \tag{22}$$

and

$$\frac{\partial\phi_2}{\partial x}(\ell,y) = \begin{cases} \dfrac{\partial\phi_3}{\partial x}(\ell,y), & 0\leqslant y\leqslant a \\ 0, & a<y\leqslant b \end{cases}. \tag{23}$$

On substituting (17)–(19) into (20) and (21) and making use of the orthogonality relation for $\{\cos(n\pi y/a)\}$, it is found that

$$A_n + F_n = \frac{2}{a\epsilon_n}\sum_{m=0}^{\infty}(B_m e^{-i\nu_m\ell} + C_m e^{i\nu_m\ell})R_{nm} \tag{24}$$

and

$$D_n = \frac{2}{a\epsilon_n}\sum_{m=0}^{\infty}(B_m e^{i\nu_m\ell} + C_m e^{-i\nu_m\ell})R_{nm}, \tag{25}$$

where

$$R_{nm} = \int_0^a \cos\left(\frac{n\pi y}{a}\right) Y_m(y)\,dy. \tag{26}$$

This is easily evaluated to obtain

$$R_{nm} = \begin{cases} \dfrac{(-1)^n\gamma_m\sinh(\gamma_m a)}{\gamma_m^2 + \dfrac{n^2\pi^2}{a^2}}, & h\geqslant a \\ P_{mn} + \xi_n Q_{mn}, & h<a, \end{cases} \tag{27}$$

where

$$P_{mn} = \frac{\dfrac{m\pi}{a}\sin\left(\dfrac{m\pi h}{a}\right)\cosh(\gamma_n h) + \gamma_n\sinh(\gamma_n h)\cos\left(\dfrac{m\pi h}{a}\right)}{\dfrac{m^2\pi^2}{a^2}+\gamma_n^2} \tag{28}$$

and

$$Q_{mn} = \frac{\cos\left(\dfrac{m\pi h}{a}\right)\gamma_n\sinh(\gamma_n d) - \dfrac{m\pi}{a}\sin\left(\dfrac{m\pi h}{a}\right)\cosh(\gamma_n d) - (-1)^m\gamma_n\sinh(\gamma_n d)}{\dfrac{m^2\pi^2}{a^2}+\gamma_n^2}, \tag{29}$$

with $d=b-h$.

On substituting (17)–(19) into (22) and (23) and using the orthogonality relation (8) it is found, after a little rearrangement, that

$$B_n + C_n = \frac{1}{2E_n\nu_n\sin(\nu_n\ell)} \times\left[JY_n'(h) + i\alpha\sum_{m=0}^{\infty}(F_m - A_m - D_m)\eta_m R_{mn}\right] \tag{30}$$

and

$$B_n - C_n = \frac{1}{2E_n\nu_n\cos(\nu_n\ell)} \times\left[-iHY_n'(h) + \alpha\sum_{m=0}^{\infty}(F_m - A_m + D_m)\eta_m R_{mn}\right]. \tag{31}$$

It is straightforward to use (30) and (31) to eliminate B_m and C_m from (24) and (25). It is found that

$$\psi_n = -F_n - \frac{2H}{\alpha\epsilon_n}\Theta_n - \frac{2i\alpha}{\epsilon_n\alpha}\sum_{m=0}^{\infty}(F_m - \psi_m)\eta_m\Lambda_{nm} \tag{32}$$

and

$$\chi_n = -F_n + \frac{2J}{a\epsilon_n}\Upsilon_n + \frac{2i\alpha}{\epsilon_n a}\sum_{m=0}^{\infty}(F_m - \chi_m)\eta_m\Omega_{nm}, \tag{33}$$

where $\psi_n=(A_n-D_n)$, $\chi_n=(A_n+D_n)$, and

$$\Lambda_{nm} = \sum_{j=0}^{\infty}\frac{\tan(\nu_j\ell)}{\nu_j E_j}R_{nj}R_{mj}; \tag{34}$$

$$\Theta_n = \sum_{j=0}^{\infty}\frac{\tan(\nu_j\ell)}{\nu_j E_j}R_{nj}Y_j'(h). \tag{35}$$

Note that Ω_{nm} and Υ_n are given by (34) and (35), respectively, with $\tan(\nu_j\ell)$ replaced by $\cot(\nu_j\ell)$.

The constants H and J are determined via the edge conditions (16). It is found that

$$H = i\alpha\frac{\Sigma_{n=0}^{\infty}(\psi_n - F_n)\Theta_n\eta_n}{\Delta_H} \tag{36}$$

and

$$J = i\alpha\frac{\Sigma_{n=0}^{\infty}(\chi_n - F_n)\Upsilon_n\eta_n}{\Delta_J}, \tag{37}$$

where

$$\Delta_H = \sum_{m=0}^{\infty}\frac{\tan(\nu_m\ell)[Y_m'(h)]^2}{\nu_m E_m}, \tag{38}$$

and Δ_J is given by (38) with $\tan(\nu_m\ell)$ replaced by $\cot(\nu_m\ell)$. Equations (32) and (33) can be solved by truncation and numerical inversion of the matrix.

IV. A LOW-FREQUENCY APPROXIMATION

In the previous section the boundary value problem was stated and reduced, using a mode-matching procedure, to a system of equations that must be truncated and solved numerically. It is useful to be able to verify the results obtained via this approach and, for this purpose, an approximate solution is now derived under the assumption $k\bar{a}\ll 1$. The usual low-frequency approximation, see (51), for an unmodified expansion chamber (i.e., without a membrane) is derived by approximating the velocity potentials ϕ_j, $j=0,1,2\ldots$ by just one duct mode—the fundamental plane-wave mode. For the current problem such an approximation is valid only for the inlet and outlet ducts, that is, for ϕ_1 and ϕ_3. To adequately describe the presence of the membrane in the expansion chamber three duct modes are required. In Sec. II it was shown that, for all frequencies, both the first coupled mode and the plane-wave mode will always propagate. An additional mode is needed, however, in order to enforce the membrane edge condition.

It is convenient to make use of the symmetry of the duct geometry and consider the symmetric and antisymmetric subproblems separately. In both cases only the left-hand side of the system need be considered, and the conditions $\phi_{2x}^s(0,y)=0$ or $\phi_2^a(0,y)=0$ are applied along the line of symmetry for the symmetric and antisymmetric cases, respectively. For the symmetric subproblem the potential in the inlet duct is approximated as

$$\phi_1^s(x) \approx e^{ix} + A_0^s e^{-ix}, \tag{39}$$

while

$$\phi_2^s(x,y) \approx B_0^s\cos(\nu_0 x)Y_0(y) + B_1^s\cos(x) + B_2^s\cos(\nu_2 x)Y_2(y), \tag{40}$$

where the duct modes $Y_0(y)$ and $Y_2(y)$ are given by (5). There are four unknown coefficients, that is, A_0^s, B_0^s, B_1^s, and B_2^s and, thus, four conditions are required. An obvious choice is the membrane edge condition,

$$\left.\frac{\partial\phi_2^s}{\partial y}\right|_{x=-\ell,y=h} = 0, \tag{41}$$

which relates B_2^s to B_0^s. In addition, the velocity flux across $x=-\ell$, $h<y\leqslant b$ must also be zero,

$$\int_h^b \left.\frac{\partial\phi_2^s}{\partial x}\right|_{x=-\ell} dy = 0. \tag{42}$$

It should be noted that this does not enforce zero normal velocity at the surface; instead, it implies that the average normal velocity is zero. Continuity of average pressure is applied at $x=-\ell$, $0\leqslant y<a$,

$$\frac{1}{a}\int_0^a \phi_2^s|_{x=-\ell}dy = \phi_1^s(-\ell), \tag{43}$$

and, finally, it is assumed that the velocity flux at the mouth of the inlet duct is equal to that across the surface $x=-\ell$, $0\leqslant y<h$ within the expansion chamber,

$$\int_0^h \left.\frac{\partial\phi_2^s}{\partial x}\right|_{x=-\ell} dy = a\left.\frac{\partial\phi_1^s}{\partial x}\right|_{x=-\ell}. \tag{44}$$

Although this does not accommodate the condition of zero normal velocity at the surface $x=-\ell$, $a\leqslant y\leqslant h$ when $h>a$, nor model the singularity in the fluid velocity at the corner, $x=-\ell$, $y=a$, this type of approximation is well accepted for low frequencies.[17]

The coefficient of interest is A_0^s and, after some algebraic manipulation, it is found that

$$A_0^s e^{2i\ell} = -\frac{\Delta^s}{(\Delta^s)^*}, \tag{45}$$

where the asterisk indicates the complex conjugate,

$$\Delta^s = [\gamma_2^2\nu_0\tan(\nu_0\ell) - \gamma_0^2\nu_2\tan(\nu_2\ell)][b - ia\cot(\ell)] - i(b-h)\tau, \tag{46}$$

and

$$\tau = \frac{\gamma_2^2\sinh(\gamma_0 a)}{\sinh(\gamma_0 h)} - \frac{\gamma_0^2\sinh(\gamma_2 a)}{\sinh(\gamma_2 h)}. \tag{47}$$

For the antisymmetric problem it is found that

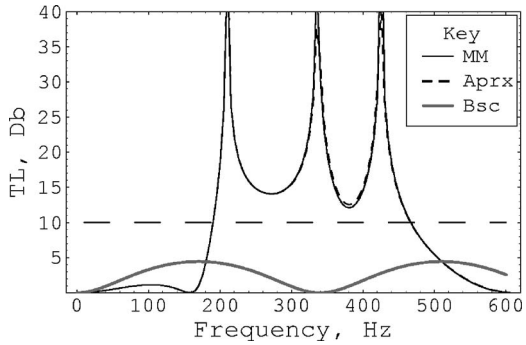

FIG. 2. Transmission loss against frequency for $\bar{a}=\bar{h}=0.05$ m, $\bar{b}=0.15$ m, $\bar{\ell}=0.25$ m, $\rho_m=0.1715$ kg m^{-2}, and $T=7500$ N m^{-2}.

$$A_0^a e^{2i\ell} = -\frac{\Delta^a}{(\Delta^a)^*}, \tag{48}$$

where

$$\Delta^a = [\gamma_2^2 \nu_0 \cot(\nu_0 \ell) - \gamma_0^2 \nu_2 \cot(\nu_2 \ell)][b + ia \tan(\ell)] + i(b-h)\tau. \tag{49}$$

The approximate solution to the full problem is obtained from the symmetric and antisymmetric subproblems simply by noting that the reflection and transmission coefficients for the fundamental modes are given by $A_0=(A_0^s+A_0^a)/2$ and $D_0=(A_0^s-A_0^a)/2$, respectively.

Although this is essentially a low-frequency approximation, it is found that transmission loss predictions have very good accuracy for situations in which $h=a$, $k\bar{a}<1$, and no more than three modes propagate in the expansion chamber. Although still good for low frequencies, the accuracy reduces as $h-a$ increases. A minor disadvantage is that the approximate solution does require numerical evaluation of the first two roots of (7).

V. NUMERICAL RESULTS

The usual measure of performance for an HVAC silencer is transmission loss, that is, $\mathcal{L}=-10\log_{10}(P_{\text{trans}}/P_{\text{inc}})$, where

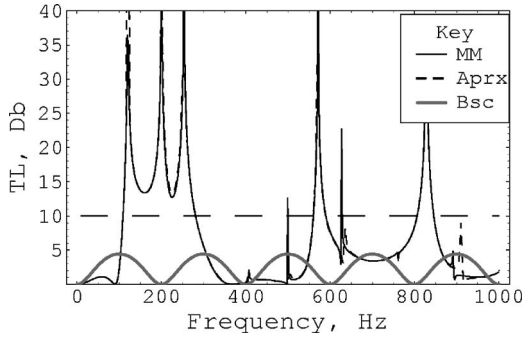

FIG. 3. Transmission loss against frequency for $\bar{a}=\bar{h}=0.085$ m, $\bar{b}=0.255$ m, $\bar{\ell}=0.425$ m, $\rho_m=0.208\,25$ kg m^{-2}, and $T=11\,435$ N m^{-2}.

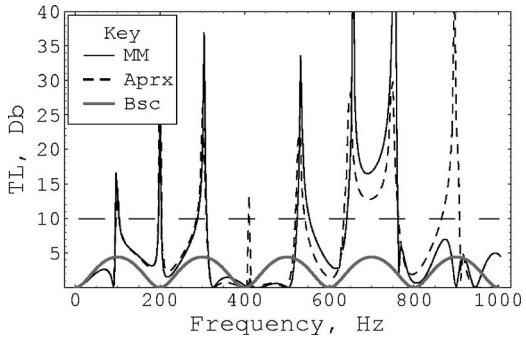

FIG. 4. Transmission loss against frequency for $\bar{a}=0.085$ m, $\bar{h}=0.17$ m, $\bar{b}=0.255$ m, $\bar{\ell}=0.425$ m, $\rho_m=0.208\,25$ kg m^{-2}, and $T=11\,435$ N m^{-2}.

$$P_{\text{trans}} = \Re\left\{\frac{1}{2}\sum_{n=0}^{\infty} |D_n|^2 \eta_n^* \varepsilon_n\right\}, \tag{50}$$

and the incident power is $P_{\text{inc}}=1$. In this section numerical results are presented in terms of transmission loss and, where appropriate, in terms of P_{trans}. In Figs. 2–15 the solid line (*MM*) is calculated by truncating and inverting the mode-matching solution (using 20 terms). The short-dashed (Aprx) curve is obtained using the low-frequency approximation of Sec. IV. Comparison is made with the approximate transmission loss for the expansion chamber in the absence of the membrane. This solution, referred to as basic (Bsc), is plotted using the low-frequency approximate formula,[17]

$$\mathcal{L} = 10\log_{10}\left\{1 + \frac{1}{4}\left(\frac{\mathcal{A}_1}{\mathcal{A}_2} - \frac{\mathcal{A}_2}{\mathcal{A}_1}\right)^2 \sin^2(2k\bar{\ell})\right\}, \tag{51}$$

where $\mathcal{A}_1$ and $\mathcal{A}_2$ are the cross-sectional areas of the inlet/outlet duct and the expansion chamber, respectively. Note that, for the two-dimensional silencer considered here, $\mathcal{A}_1=\bar{a}$ and $\mathcal{A}_2=\bar{b}$. For the silencer geometries considered here the basic model achieves, at best, a transmission loss in the region of 5 dB. The horizontal line shown on the transmission loss graphs indicates 10 dB. For the purposes of this investigation, a stopband is classified as a range of frequency for which the transmission loss exceeds 10 dB.

It is convenient to revert to dimensional variables in order to describe the silencer parameters. The first three graphs, Figs. 2–4, deal with two silencers studied by Huang[9]

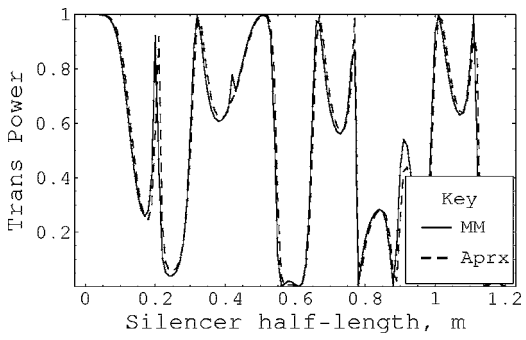

FIG. 5. Transmitted power flux against silencer half-length for $\bar{a}=\bar{h}=0.15$ m, $\bar{b}=0.45$ m, $\rho_m=0.2$ kg m^{-2}, $T=3250$ N m^{-2}, and $f=200$ Hz.

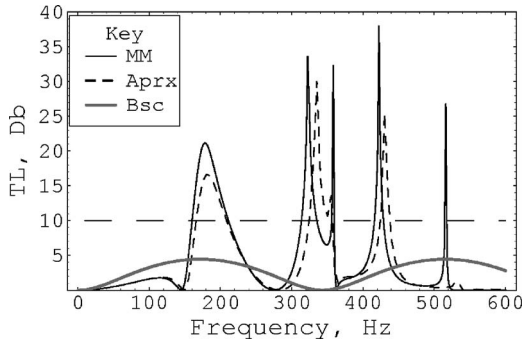

FIG. 6. Transmission loss against frequency for $\bar{a}=\bar{h}=0.15$ m, $\bar{b}=0.45$ m, $\bar{\ell}=0.25$ m, $\rho_m=0.2$ kg m^{-2}, and $T=3250$ N m^{-2}.

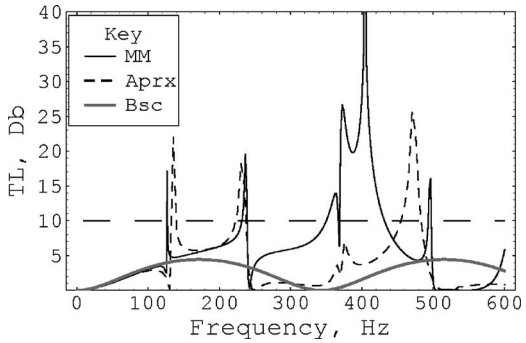

FIG. 8. Transmission loss against frequency for $\bar{a}=0.15$ m, $\bar{h}=0.385$ m, $\bar{b}=0.45$ m, $\bar{\ell}=0.25$ m, $\rho_m=0.2$ kg m^{-2}, and $T=3250$ N m^{-2}.

and Haung and Choy.[18] The two configurations both involve small inlet ducts and comparatively long membranes with high tensions. These graphs are obtained using sound speed 340 ms^{-1} and fluid density 1.225 kg m^{-3}, whereas for all remaining graphs these quantities are taken as 343.5 ms^{-1} and 1.2043 kg m^{-3}, respectively.

In Fig. 2 the inlet and outlet ducts are 0.05 m high and the expansion chamber is of height 0.15 m; the silencer half-length is 0.25 m, while the membrane mass and tension are $\rho_m=0.1715$ kg m^{-2} and $T=7500$ N m^{-2}, respectively. Clearly there is excellent agreement between the the mode-matching and low-frequency approximate solutions. The parameters used here are thought to be the same as that used by Huang and Choy,[18] and the transmission loss curves presented in Fig. 2 agree well with the equivalent curves presented in that article.

Figure 3 shows transmission loss against frequency for a silencer with inlet/outlet ducts of height 0.085 m and expansion chamber of height 0.1225 m. The membrane mass and tension are 0.208 25 kg m^{-2} and 11 435 N m^{-2}. The parameters chosen for this silencer configuration are identical to those used by Huang[9] and, again, the curves presented here are in agreement with those of that article. Although the transmission loss is comparatively low for the frequency range 550–850 Hz, the general shape of the curve is reminiscent of a stopband and, indeed, it proves relatively easy to adjust the membrane height in order to "extract" one. This is shown in Fig. 4, where the silencer has exactly the same physical dimensions and membrane properties as for Fig. 3 other than the membrane being located within the expansion chamber so that $\bar{h}=0.17$ m. The stopband which is evident in Fig. 3 for the frequency range 109–280 Hz has now diminished while a new stopband has emerged for 642–760 Hz. For both Figs. 3 and 4 there is clearly a passband in the frequency range 400–500 Hz and the membrane height could not be adjusted to significantly improve transmission loss for this range. The mode-matching curves in Figs. 3 and 4 are validated by their close agreement with the low-frequency approximate solution.

Both the silencer configurations considered so far have in common an aspect ratio of $\mathcal{R}=5$, where $\mathcal{R}=2\ell/(b-a)$. Huang[10] has shown that high aspect ratios tend to produce wide stopbands, but that if $\mathcal{R}$ is too large the troughs between resonant peaks in the stopband tend to drop below 10 dB. In contrast, low aspect ratios tend to produce high but narrow stop bands. The value $\mathcal{R}=5$ is close to optimum but is impractical for the application considered here. Furthermore, it is felt that tensions as high those used for Figs. 2–4 might be difficult to sustain in practice. To be of practical use in an HVAC system the expansion chamber must ideally be low and only moderately long or, if tall, short in comparison to its height. For these reasons attention is now directed towards bigger ducts with lower aspect ratios and membranes with lower tensions. We restrict our attention to a stainless-steel membrane of thickness 0.025 mm (thus $\rho_m=8050\times0.025\times10^{-3}\approx0.2$ kg m^{-2}) and tension 3250 N m^{-2}.

The issue of how to design an appropriate expansion chamber must be considered. With so many parameters involved this is not a trivial procedure. The approach taken here is to decide first on the frequency range that is to be

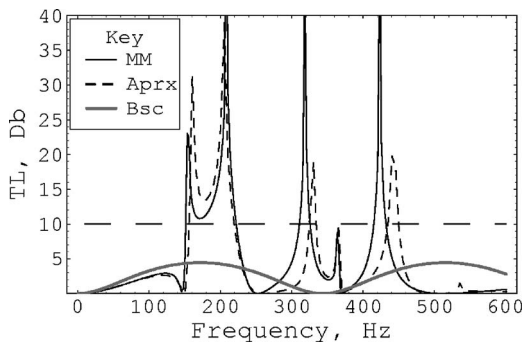

FIG. 7. Transmission loss against frequency for $\bar{a}=0.15$ m, $\bar{h}=0.24$ m, $\bar{b}=0.45$ m, $\bar{\ell}=0.25$ m, $\rho_m=0.2$ kg m^{-2}, and $T=3250$ N m^{-2}.

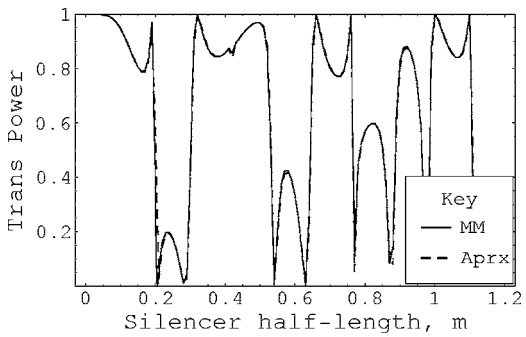

FIG. 9. Transmitted power flux against silencer half-length for $\bar{a}=\bar{h}=0.15$ m, $\bar{b}=0.3$ m, $\rho_m=0.2$ kg m^{-2}, $T=3250$ N m^{-2}, and $f=200$ Hz.

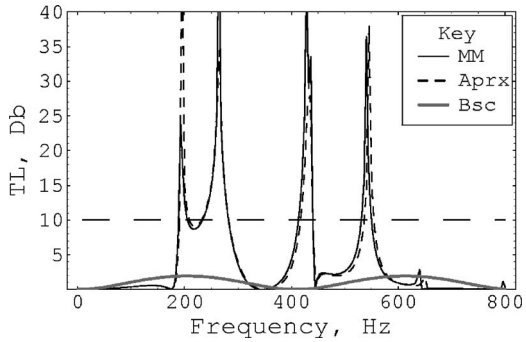

FIG. 10. Transmission loss against frequency for $\bar{a}=\bar{h}=0.15$ m, $\bar{b}=0.3$ m, $\bar{\ell}=0.21$ m, $\rho_m=0.2$ kg m^{-2}, and $T=3250$ N m^{-2}.

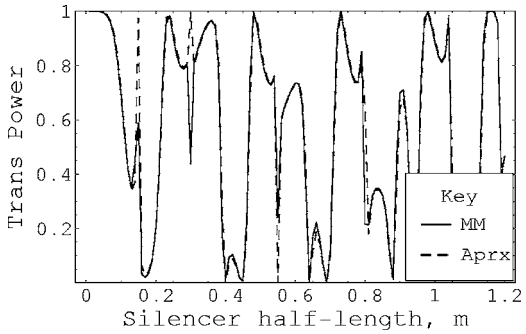

FIG. 12. Transmitted power flux against silencer half-length for $\bar{a}=\bar{h}=0.15$ m, $\bar{b}=0.3$ m, $\rho_m=0.2$ kg m^{-2}, $T=3250$ N m^{-2}, and $f=300$ Hz.

stopped, say 180–220 Hz. Then, choose the heights for the inlet/outlet ducts and expansions chamber. In Figs. 5–8 the heights for the inlet/outlet ducts and expansion chamber are 0.15 and 0.45 m, respectively. The height of a typical HVAC duct is in the range 0.3–0.45 m and thus the device is an appropriate size to form a component of a hybrid silencer. It is envisaged that such a component would lie within the HVAC duct, sandwiched between panels of porous material. Length is thus an important issue—to be of practical use the device must not be long. The membrane mass and tension have already been selected so, in order to select the appropriate silencer length, the proportion of transmitted power, given by (50), is plotted with $\bar{h}=\bar{a}$ against silencer half-length for a frequency of 200 Hz. It is clear from Fig. 5 that the transmitted power is low when $\bar{\ell}\approx 0.25$ m and near zero when $\bar{\ell}=0.6$ m. The shorter length, which gives an aspect ratio $\mathcal{R}=1.67$, is selected for Figs. 6–8.

Figure 6 shows transmission loss against frequency for $\bar{h}=\bar{a}$. Although the transmission loss is reasonably good in the range 160–210 Hz, the curve does not have the same characteristic shape of the stopbands formed between two or three resonant frequencies (see Figs. 2–4). This is due to the fact that at the selected length the transmitted power flux, although small, was not close to zero (see Fig. 5). Figure 7 shows the effect altering the position of the membrane. In this case $\bar{h}=0.24$ m and the stopband is more clearly defined and is wider, now covering the frequency range 153–220 Hz, which is an increase of 34%. The stopband can be broadened further by increasing $\bar{h}$ to 0.25 m; however, this is at the cost of a small reduction in transmission loss at the center of the stopband. In both Figs. 6 and 7 the possibility of a stopband in the region 300–450 Hz is suggested by the shape of the curve. This stopband is extracted by moving the membrane higher into the expansion chamber so that $\bar{h}=0.385$ m. The new stopband, shown in Fig. 8, embraces the frequencies 370–434 Hz but, of course, the emergence of this stopband is at the expense of the first. It is clear, however, that the overall performance of the silencer with the membrane raised to this higher level is significantly better than that achieved by the basic model (i.e., the expansion chamber without membrane) for frequencies in the range 260–460 Hz.

In the next three figures the height of the inlet duct, the membrane mass, and membrane tension are as for Figs. 5–8. The height of the expansion chamber, however, is reduced to 0.3 m. Figure 9 shows the proportion of transmitted power against silencer half-length for a frequency of 200 Hz. The transmitted power is near zero when $\bar{\ell}\approx 0.21$ m, and this value is used for Figs. 10 and 11. The resulting silencer has an aspect ratio of $\mathcal{R}=2.8$ and transmission loss against frequency is shown, for the case $\bar{h}=\bar{a}$, in Fig. 10. Although there is a clear spike in transmission loss at 200 Hz (as predicted by Fig. 9), the stopband falls below 10 dB in the region 210–230 Hz. The membrane height cannot be adjusted to improve this since raising the membrane causes the transmission loss in this region to drop further. It is interesting to note that the length chosen for this silencer was such that the frequency 200 Hz is close to a resonant value, whereas for

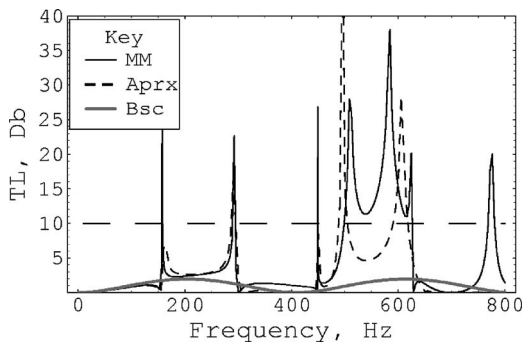

FIG. 11. Transmission loss against frequency for $\bar{a}=0.15$ m, $\bar{h}=0.25$ m, $\bar{b}=0.3$ m, $\bar{\ell}=0.21$ m, $\rho_m=0.2$ kg m^{-2}, and $T=3250$ N m^{-2}.

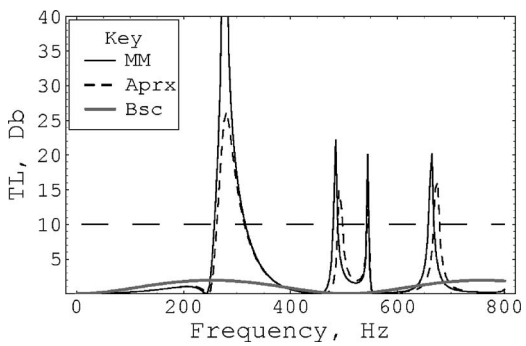

FIG. 13. Transmission loss against frequency for $\bar{a}=\bar{h}=0.15$ m, $\bar{b}=0.3$ m, $\bar{\ell}=0.17$ m, $\rho_m=0.2$ kg m^{-2}, and $T=3250$ N m^{-2}.

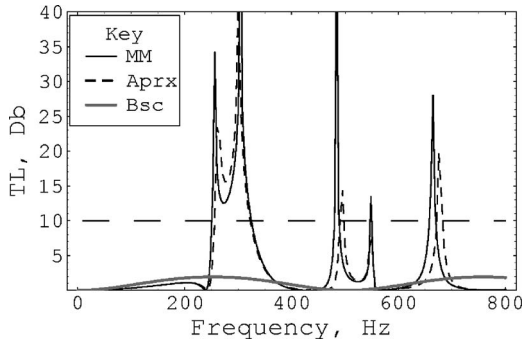

FIG. 14. Transmission loss against frequency for $\bar{a}=0.15$ m, $\bar{h}=0.17$ m, $\bar{b}=0.3$ m, $\bar{\ell}=0.17$ m, $\rho_m=0.2$ kg m^{-2}, and $T=3250$ N m^{-2}.

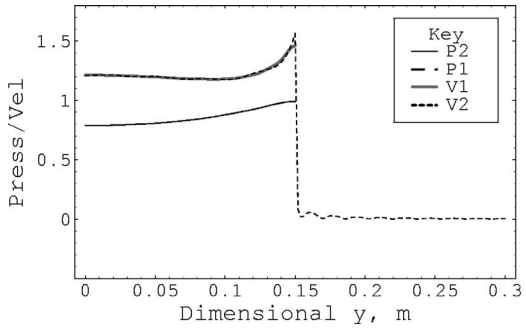

FIG. 16. Absolute value of nondimensional pressure and normal velocity against $\bar{y}$, $0\leqslant\bar{y}\leqslant\bar{a}$. Silencer parameters are $\bar{a}=\bar{h}=0.15$ m, $\bar{b}=0.3$ m, $\bar{\ell}=0.17$ m, $\rho_m=0.2$ kg m^{-2}, and $T=3250$ N m^{-2} and $f=620$ Hz.

Figs. 6–8 this was not the case. Figure 11 shows that, on raising the membrane further, to a height of 0.25 m, a new stopband is formed in the frequency range 500–624 Hz.

Figure 12 shows the proportion of transmitted power against silencer half-length for a frequency of 300 Hz; the values of all other parameters are the same as for Fig. 9. In this case the curve shows two nonresonant minima. The value of ℓ is chosen to be 0.17 m, corresponding with the lower of the two minima, and the resulting silencer has an aspect ratio of $\mathcal{R}=2.27$. Figure 13 shows the transmission loss for $\bar{h}=\bar{a}$. The shape of the stopband around 300 Hz is very high and narrow with a range of 260–312 Hz. Moving the membrane up a short distance into the expansion chamber, so that $\bar{h}=0.17$ m, the shopband is broadened by approximately 38%. This is shown in Fig. 14. Moving the membrane further into the expansion chamber, see Fig. 15, the stopband is shifted and broadened, now encompassing all frequencies in the range 560–686 Hz.

The final two figures are presented as a means of validating the mode-matching method for the cases $\bar{h}=\bar{a}$ and $\bar{h}\neq\bar{a}$, respectively. The accuracy of a mode-matching solution is assessed by how well the matching conditions, i.e., Eqs. (20)–(23), are satisfied. Figures 16 and 17 show the absolute value of the nondimensional pressure and normal velocity at $\bar{x}=\ell$ for exactly the same silencer parameters as in Figs. 13 and 15, respectively. The velocity $\phi_{2x}(-\ell,y)$ is plotted for $0\leqslant\bar{y}\leqslant\bar{b}$, while the other quantities are plotted for $0\leqslant\bar{y}\leqslant\bar{a}$. The frequency at which this comparison is made is 620 Hz. This value was chosen because it lies in the middle of a range where, for Fig. 15, the low-frequency approximation and the mode-matching solution show poor agreement. In Fig. 16, where $h=a$, the pressure and normal velocity show excellent agreement [both pairs of curves overlie for $0\leqslant y\leqslant a$ and $\phi_{2x}(-\ell,y)=0$ for $a\leqslant y\leqslant b$]. Thus, conditions (20)–(23) are fully satisfied. This is true at all relevant frequencies and, further, the matching conditions at $x=\ell$ are met to the same accuracy. In Fig. 17 the nondimensional pressures, that is $\phi_1(-\ell,y)$ and $\phi_2(-\ell,y)$, overlie, indicating excellent agreement. Furthermore, the normal velocity $\phi_{2x}(-\ell,y)$ is zero for $h\leqslant y\leqslant b$ and tends rapidly to zero in the region $a\leqslant y\leqslant h$. For $0\leqslant y\leqslant a$ the normal velocities, $\phi_{1x}(-\ell,y)$ and $\phi_{2x}(-\ell,y)$, are not in close agreement. Although the two curves oscillate around their mean value and the amplitude of oscillation reduces significantly as $y\to 0$, close to the corner $(y=a)$ the solutions diverge. As expected from the singular nature of the corner flow, this situation is not improved by increasing the number of terms used when truncating and inverting the mode-matching equations (20 terms were used here). Nevertheless, the normal velocities show a satisfactory level of agreement. Altering the frequency at which these comparisons are made does not significantly alter the accuracy. Furthermore, the same level of accuracy is observed at the outlet interface, that is at $x=\ell$.

To summarize, for $h\geqslant a$, the mode-matching solution satisfies (20) and (21) and, also,

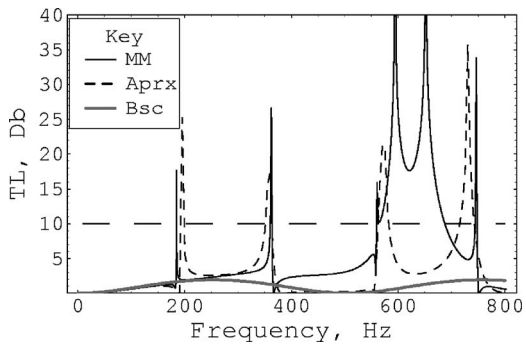

FIG. 15. Transmission loss against frequency for $\bar{a}=0.15$ m, $\bar{h}=0.275$ m, $\bar{b}=0.3$ m, $\bar{\ell}=0.17$ m, $\rho_m=0.2$ kg m^{-2}, and $T=3250$ N m^{-2}.

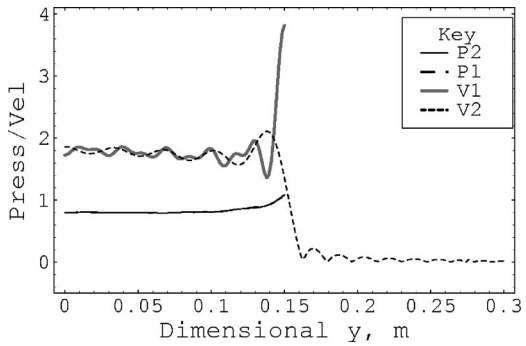

FIG. 17. Absolute value of nondimensional pressure and normal velocity against $\bar{y}$, $0\leqslant\bar{y}\leqslant\bar{a}$. Silencer parameters are $\bar{a}=0.15$ m, $\bar{h}=0.275$ m, $\bar{b}=0.3$ m, $\bar{\ell}=0.17$ m, $\rho_m=0.2$ kg m^{-2}, and $T=3250$ N m^{-2} and $f=620$ Hz.

$$\phi_{2x}(\pm\ell, y) = 0, \quad h \leqslant y \leqslant b. \tag{52}$$

The normal velocities, however, are not in exact agreement for $0 \leqslant y \leqslant a$ because a Fourier cosine series cannot accurately represent an integrable singularity of the type present in the fluid velocity at $x = \pm\ell$, $y = a$. In view of the fact that the systems of equations derived by mode-matching automatically conserve power,[15,14] it is worthwhile asking what global condition the normal velocities satisfy at $x = \pm\ell$ when $h > a$. For the parameters and frequency ranges considered herein, it has been verified numerically that the mode-matching solution satisfies (52) and

$$\int_0^h \left.\frac{\partial\phi_2}{\partial x}\right|_{x=\pm\ell} dy = \int_0^a \left.\frac{\partial\phi_1}{\partial x}\right|_{x=\pm\ell} dy. \tag{53}$$

(For the parameters of Fig. 15, this condition is satisfied to five decimal places for frequencies up to 800 Hz, reducing to three decimal places at 1800 Hz.) This, of course, is simply continuity of velocity flux and is a weaker condition than (22) and (23). That is, if (22) and (23) are satisfied then (53) must be, but the converse is not true. Nevertheless (53) is a necessary physical condition for the problem, and it is gratifying that the mode-matching solution satisfies this for $h > a$—even though such a condition is not explicitly built into the model.

VI. DISCUSSION

It is well established[8,9,18] that a membrane attached across the mouth of an expansion chamber can dramatically reduce the transmission of low-frequency noise along a ducting system. This article has investigated the effects of altering the height of the membrane so that it lies within the expansion chamber. Attention has been restricted to silencers with low aspect ratio and subject to low-frequency incident sound. Silencers with low aspect ratio tend to produce narrow, high stopbands when the membrane lies across the mouth of the expansion chamber,[10] and it has been shown that such silencers can be "tuned" by altering the membrane position. Raising the membrane a short distance into the chamber tends to broaden the stopband; increases in stopband width of up to 38% have been observed. If the membrane is raised higher into the cavity, the frequency range of the stopband is shifted, by approximately one octave, and broadened. It has, however, also been noted that passbands exist and that these cannot be eliminated by altering the membrane position.

One of the aims of this paper was to investigate this device with a view to its use as a component in a hybrid silencer[7] for HVAC ducting systems. Although there is much work to be done on this subject, the initial findings are interesting. The heights of the silencers considered in this article were consistent with dimensions of a typical HVAC duct and the half-lengths were, at most, 0.25 m. Yet stopbands of up to 72 Hz were achieved at low frequencies. There are, of course, potential drawbacks to the device. As the membrane is moved up into the expansion chamber a corner is formed at the junction of the inlet duct and chamber. For low-frequency situations, such as those considered here, this does not significantly effect the results but it is potentially more problematic for high frequencies. Also, it remains to be seen whether transmission loss remains high with the inclusion of flow—particularly as the exposed corner is a potential source of turbulence once flow is introduced. Such a device, however, has been considered with a view to incorporation inside an HVAC duct between panels of absorbent material. Judicious positioning of the absorbent panels could well eliminate problems due the the corner of the expansion chamber.

The results presented herein are closely related to the work of Huang.[8–10,18] The method by which the model problem is solved, however, is quite different and lends itself to a wide range of extensions to the theory. First, although the zero displacement edge condition is used here, see (16), it is equally straightforward (if less practical) to apply the condition of zero gradient. Further, the membrane can be replaced by an elastic plate, in which case any appropriate set of edge conditions (for example, clamped, pin-jointed, or free) can be enforced. In contrast, the membrane edge condition is built into Haung's method and cannot be altered. Although the latter point is not significant for a membrane, it becomes relevant should the membrane be replaced by an elastic plate, in which case the analysis is straightforward *only* for the case in which the plate edges are pin-jointed.[19] Finally, Kang and Fuchs[12] have suggested, in the context of architectural acoustics, that two membranes, one positioned at the mouth of the cavity and one within, yield a broader spectrum of noise reduction. While the application of their work is quite different from that considered here, the concept of using two membranes is intriguing. Although it is impossible to comment on any potential advantages in terms of tuning the device, problems due to the corner singularity would certainly be eliminated. The mode-matching method propounded herein is a highly appropriate method by which to study such a device, whereas the method used by Huang cannot easily deal with the internal membrane.

[1] A. McAlpine and M. J. Fisher, "On the prediction of 'buzz-saw' noise in acoustically lined aero-engine inlet ducts," J. Sound Vib. **265**(1), 175–200 (2003).

[2] S. Laugesen, "Active control of multi-modal propagation of tonal noise in ducts," J. Sound Vib. **195**(1), 33–56 (1996).

[3] J. K. Krüger, "The calculation of actively absorbing silencers in rectangular ducts," J. Sound Vib. **257**(5), 887–902 (2002).

[4] J.-D. Wu and M. R. Bai, "Application of feedforward adaptive active-noise control for reducing blade passing noise in centrifugal fans," J. Sound Vib. **239**(5), 1051–1062 (2001).

[5] S. J. Estève and M. E. Johnson, "Development of an adaptive Helmholtz resonator for broadband noise control," in Proceedings of IMECE2004, Anaheim, CA (2004).

[6] J. M. de Bedout, M. A. Franchek, R. J. Bernhard, and L. Mongeau, "Adaptive-passive noise control with self-tuning Helmholtz resonators," J. Sound Vib. **202**, 109–123 (1997).

[7] A. Selemet, I. J. Lee, and N. T. Huff, "Acoustic attenuation of hybrid silencers," J. Sound Vib. **262**, 509–527 (2003).

[8] L. Huang, "A theoretical study of duct noise control by flexible panels," J. Acoust. Soc. Am. **106**, 1801–1809 (1999).

[9] L. Huang, "Modal analysis of a drumlike silencer," J. Acoust. Soc. Am. **112**, 2014–2025 (2002).

[10] L. Huang, "Parametric study of a drumlike silencer," J. Sound Vib. **269**, 467–488 (2004).

[11] E. H. Dowell and H. M. Voss, "The effect of a cavity on panel vibrations," AIAA J. **1**, 476–477 (1963).

[12] J. Kang and H. V. Fuchs, "Predicting the absorption of open weave textiles and microperforated membranes backed by an air-space," J. Sound Vib.

220(5), 905–920 (1999).
[13]J. B. Lawrie and I. D. Abrahams, "An orthogonality condition for a class of problems with high order boundary conditions; applications in sound/structure interaction," Q. J. Mech. Appl. Math. **52**(2), 161–181 (1999).
[14]D. P. Warren, J. B. Lawrie, and I. M. Mohamed, "Acoustic scattering in waveguides that are discontinuous in geometry and material property," Wave Motion **36**(2), 119–142 (2002).
[15]J. B. Lawrie and R. Kirby, "Mode-matching without root-finding: Application to a dissipative silencer," J. Acoust. Soc. Am. **119**, 2050–2061 (2006).
[16]F. P. Mechel, "Theory of baffle-type silencers," Acustica **70**, 93–111 (1990).
[17]A. P. Dowling and J. E. Ffowcs Williams, *Sound and Sources of Sound* (Ellis Horwood, London, U.K., 1983).
[18]L. Huang and Y. S. Choy, "Vibroacoustics of three-dimensional drum silencer," J. Acoust. Soc. Am. **118**, 2313–2320 (2005).
[19]L. Huang, "Broadband sound reflection by plates covering side-branch cavities in a duct," J. Acoust. Soc. Am. **119**, 2628–2638 (2006).

Spatial sampling for night levels estimation in urban environments

J. Romeu, S. Jiménez, M. Genescà, T. Pàmies, and R. Capdevila
Laboratory of Acoustics and Mechanical Engineering (LEAM),
Technical University of Catalonia C/ Colom 11, 08222 Terrassa, Spain

(Received 27 January 2006; revised 25 May 2006; accepted 26 May 2006)

The procedure for spatial sampling in order to find out the relation between L_{day} and L_{night} for urban noise is presented. From that data, other parameters like L_{dn} or L_{den} can be easily obtained from L_{day} values. To this end, a long-term measuring campaign was carried out in eight cities of different types and sizes in northeastern Spain. The statistical treatment of the measures was based on a characterization of the streets in view of their type, including factors such as traffic and land use, which enabled a final classification of six types of streets. The results show that streets of the same type located in different cities do not have the same value for L_{day}-L_{night}, due to socioeconomic factors, but analyzed city by city have a close to normal (or *t*-Student) distribution. Under this behavior, it is demonstrated that a sample of between 14 and 25 points, depending on the city characteristics, is needed in order to calculate L_{day}-L_{night}, with a confidence level of 95% and a margin of error of ±1 dB(A). © *2006 Acoustical Society of America.* [DOI: 10.1121/1.2215219]

PACS number(s): 43.50.Rq [KA] Pages: 791–800

I. INTRODUCTION

Nowadays most of the environmental noise indicators[1] tend to include night values, in form of L_{night}, L_{den}, or L_{dn}. The method to calculate them can be by both measurements and simulation. At present, it is not possible to ascertain which method is more accurate[2] in general terms. In any event, the sampling conditions will have a decisive effect on any attempt to attain representative results—whatever method is used. In one method, the acoustic measurement point must be selected, and in the other the point at which vehicles will be counted. With regard to sampling, both the spatial aspect (the number and location of the noise-measuring or vehicle-counting points) and the timeframe (the number of measurements that are taken over the year at each point) must be considered, with the aim of ensuring that the results are representative of year-round conditions.[3–5] Thus, traffic measurements can be treated as noise measurements and, in this paper, no distinction will be made, although the results will be derived from noise measurements.

The procedure for carrying out studies of environmental noise in cities from direct noise measurements is not well stabilized. A typical procedure is to carry out short-term measurements of varying duration (from 2 min to 2 h) at different intervals during the day and night. This procedure was followed in pioneering experiences in the field of environmental studies[6] and has continued to be standard practice.[7–9] More recently, 24-h measurements have been carried out in some works[10–14] but not with the aim of studying night-time behavior. Also ignoring night-time effects, some other studies have expanded the duration of short-term measurements continuous up to 8 h.[14–16] The estimation of L_n or L_{den} requires knowledge of what happens throughout the night-time period because, in contrast to the daytime period, during which noise levels remain more or less constant,[7,11,12,17,18] during the night they vary greatly. Therefore, during this period noise measurements must be taken directly; alternatively, realistic traffic data are required (traffic flow per hour, percentage of heavy vehicles, and speed).[19]

For direct noise readings, short-term measurements may be taken at various intervals during the night or continuous measurements may be taken over 24 h or more. Whichever the procedure, it will incur high costs in terms of manpower and equipment. Furthermore, it is also unlikely that cities will have traffic data that are sufficiently representative of all the streets in the city and all the time periods.[20,21] Data are generally available for main roads only, which can mean that the maps are biased, in that they give prominence to noisier streets,[9] or that the characterization of streets with less traffic is not entirely realistic. Therefore, one may conclude that the sampling procedure is an extremely important stage in the drawing up of noise maps (and in environmental noise studies in general), both from the standpoint of rigor and representativity, and in terms of the financial costs that may be incurred.

The noise on a street depends on the types of noise sources (activity or traffic) and on the conditions of the street itself, such as its geometry, the presence of obstacles in the sound propagation path, and the types of paving and materials in general. The relationship between daytime and night-time levels, which may be represented by the L_{day}-L_{night} parameter, on the other hand, depends exclusively on the conditions that define the noise source: activity or traffic. The fact that fewer factors influence the L_{day}-L_{night} parameter with respect to those that determine the L_{day} value suggests that the variability of L_{day}-L_{night} will be less than that of L_{day}. Therefore, the size of the spatial sample used to determine the difference between daytime and night-time behavior should be smaller than that which is needed to determine the values for L_{day} with a certain degree of accuracy.

The aim of this work is to determine whether it is possible to establish a spatial sampling strategy that allows the

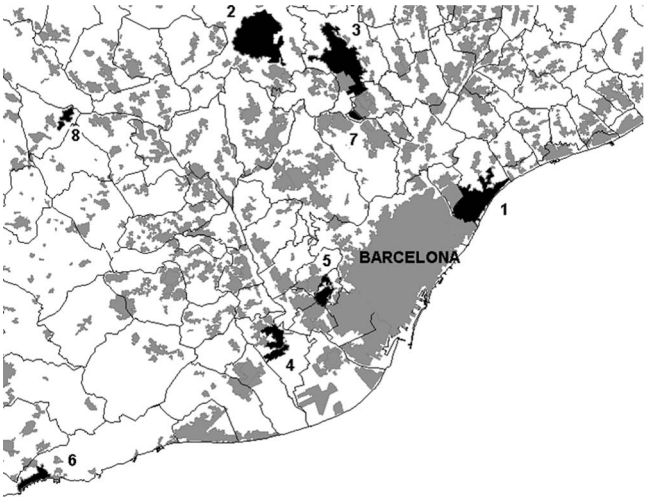

FIG. 1. Cities around metropolitan area of Barcelona. In black, cities studied in this work. Distance between cities 1 and 2 is about 25 km.

L_{day}-L_{night} and, therefore, L_{den}-L_{day} parameters to be quantified, which would enable the values for L_{den} or L_{night} (or even L_{dn}, for example) to be calculated from L_{day} values, something which is only hinted at in other works.[T1–14] This would significantly simplify the method for drawing up noise maps, with no loss of rigor, because L_{day} values can be obtained from short-term measurements during representative periods,[22] while L_{den} and L_{night} values could be determined from fewer long-term measurements. This work is based on an analysis of the results obtained in a measuring campaign in eight Catalan cities of different sizes and varying socioeconomic conditions. The behavior of noise indicators (L_{day}, L_{night}, and L_{den}) is analyzed in view of each city's main characteristics.

II. DESCRIPTION OF THE CITIES STUDIED

All of the cities studied are located around the great urban hub that is the city of Barcelona, in northeastern Spain. Barcelona has a population of around 1.5 million people and is the political, commercial, and financial center of Catalonia (Fig. 1). A number of smaller cities are adjacent to Barcelona and to each other, and they practically make up one agglomeration. This is what is referred to as the metropolitan area. Many of these smaller cities share public services with Barcelona, and the movement of vehicles and citizens generally occurs between these cities and Barcelona, and not between the cities themselves. At about 25 km from Barcelona, one finds what is referred to as the second metropolitan belt, which comprises cities that are already a center of influence in their respective areas but that have close ties with Barcelona.

This study includes three cities from the metropolitan area, namely Badalona (city 1), Sant Boi (city 4), and Esplugues (city 5), in decreasing order referring to the number of inhabitants. The main activities are, in all cases, industry, commerce, and business (see Table I). Also three cities located in the second belt are also taken into account: Terrassa (city 2) and Sabadell (city 3), which are similar regarding the number of inhabitants and registered vehicles, but the first one is more of an industrial type while the latter of a commercial one, and a third one, Badia (city 7), which is a dormitory town mainly for people who work in Barcelona or the metropolitan area. Away from the influence of Barcelona, there are Sitges (city 6), a touristy site, and Masquefa (city 8), which is a small town rather than a city, and its main activities are agriculture and industry.

III. MEASUREMENT METHOD

A. Selection of sampling points

In general terms, different strategies may be employed to study environmental noise in a city, depending on the methods for selecting the sampling points:[6]

(i) Random sampling: point measurements are selected by means of a rectilinear grid, the size of which depends on the city.
(ii) Sampling by land use: measurement points are located depending on the land use characteristics, according to city planning categories[7] such as commercial use, residential use, etc. The points are chosen randomly or arbitrarily, by looking for values that are representative of the area that is being surveyed. Although research[6] shows that patterns and levels of noise are likely to be similar in each land use category—because noise levels are highly dependent on the volume of traffic, which is not necessarily different for different types of land use—this methodology is still used,[15] although it might seem more appropriate to large scale sampling on a supramunicipal scale.[12,23]

TABLE I. Characteristics of the cities (industry includes agriculture).

					Activity (%)		No. of cars (%)		
City	Inhabitants	Density (hab/km^2)	Vehicles	Activities	Industry	Services	Cars	Motorbike	Heavies
1	214.874	28.649	108.705	12.910	17	83	77	7.2	16.8
2	189.212	19.112	114.231	10.473	27	73	82.0	7.7	10.3
3	193.338	19.372	115.116	15.801	23	77	83.0	6.8	10.2
4	80.636	29.215	43.993	5.118	23	77	77.6	6.3	16.1
5	45.915	16.281	27.022	3.597	23	77	76.7	10.7	12.6
6	23.172	5.149	13.144	2.670	18	82	67.7	17.7	14.6
7	14.313	28.626	19.494	417	21	79	84.2	4.1	11.7
8	7.250	3.468	4.071	471	40	60	73.0	7.0	20.0

(iii) Receiver-oriented sampling: measurements are taken by considering only the population and focusing on dwellings or schools, for example. This method could be employed to estimate the population's exposure to noise, but it would not be the best method for collecting the data needed to design and apply correction plans.
(iv) Source-oriented sampling: it could be the best method to design actions plans, because it should allow us to know the noise source. Nonetheless, the other methods could be adapted, not without difficulty, to enable the sources to be differentiated. All works carried out using simulation employ this technique, but it also appears to have prevailed in more recent works on environmental noise.[24]

As a summary of the aforementioned sampling methods, it should be considered that measurement sites within an area can be selected either randomly or deterministically. Random sampling can be carried out by laying a grid over a map of the area and measuring at the intersections of the lines or at specific points on the grid. Deterministic selection requires detailed knowledge of the area being surveyed in which measurement sites are chosen on the basis of known characteristics. If simulation techniques are to be employed, then random traffic measurements are inappropriate. If experimental sound measurements are preferred, the grid should be small enough to ensure the characterization of noise sources and the estimation of environmental parameters such as population exposed to different noise levels.[6]

For the present work, a sampling technique that focuses on the source of noise (disaggregation, as defined by Brown[6]) is applied. This means that streets were grouped according to their predominant traffic characteristics, with the aim of ascertaining whether trends common to each group could be identified. That is to say, with reference to the noise made by vehicles, we identified various types of roads that we wished to characterize.[8,9] These types, however, must be viewed in the light of land use and also perhaps population density,[25] which may alter, or not, the acoustic behavior of a road that crosses different types of land, as classified in urban planning laws. Hence, a combination of land use sampling and source sampling was applied; measurement points were selected depending on both characteristics. In keeping with this strategy, the roads were classified into five groups (see Fig. 2):

(i) *Access roads*: roads leading into the city.
(ii) *Ring roads*: major roads that distribute traffic between the various entry points to the city and that encircle the city but are located in or next to urban areas. They generally have few or no traffic lights and the speed limit or average speed of traffic is around 80 km/h.
(iii) *Distribution roads*: trunk roads that distribute traffic to different zones, but within the city. Although they are priority roads, they have traffic lights and the average speed is low (maximum 50 km/h).
(iv) *Common streets*: streets in the urban grid that take people to their final destination, which is usually their home, a commercial outlet, or other kinds of services.
(v) *Pedestrian streets*: streets for pedestrians, with occasional traffic comprising vehicles loading and unloading goods or vehicles belonging to residents in the area.
(vi) *Streets affected by infrastructure*: streets close to large-scale infrastructures that cross the city, which are not used by the inhabitants themselves or are predominantly used by vehicles that are passing through. They usually run alongside motorways, and the noise source is the infrastructure (motorway), and not the street itself.

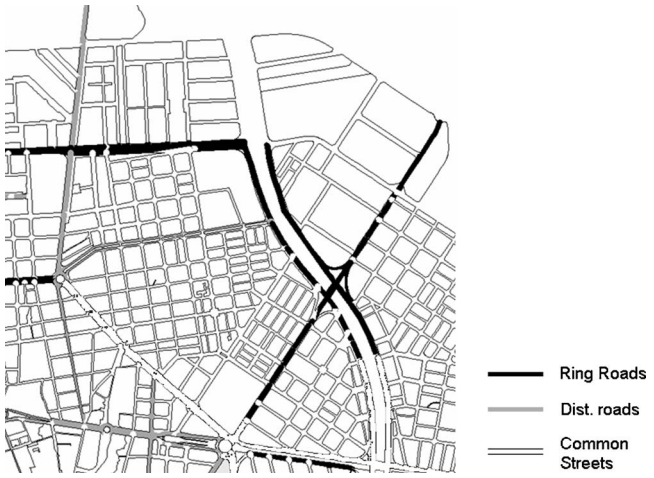

FIG. 2. An example of street typologies considered for city 2. Access roads tend to behave like ring roads or main roads, depending on the traffic flow.

With respect to land use, one must bear in mind that the typology of Spanish cities is generally in keeping with the concept of the compact city, in which the city center contains all the types of land use, which gives rise to vague, complex boundaries. For example, one cannot generally speak of school or hospital areas, because these facilities are usually integrated into the urban landscape and do not form a differentiated area that is separate from areas involving other types of land use. With this in mind, the types of land use initially considered were as follows:

(i) *Residential*
(ii) *Industrial*: even though in recent years all heavy industry has been moved to industrial estates outside the city center, in some cities industrial activity still occurs within the city limits.
(iii) *Entertainment activities*: these activities can take place at night, and there is a tendency to group them in specific areas of the city.
(iv) *Commercial*: where most of the activity is during the daytime.

Once road types and their uses have been determined, one must decide on the location of the measurement point. Therefore, if different road segments have different uses, data on each of these segments are needed. If the data exclusively concern traffic (for the simulation method), in addition

to land use one also needs to determine beforehand whether there are significant changes in the characteristics of the traffic (flow, speed, and composition). If the purpose of the method is measuring, one must also take into account the transverse profile and the existence of slopes. The segmentation of the streets according to these parameters will give the total number of segments to be studied (whose L_{den}, L_{night}, or L_{dn} has to be assessed).

Once the segments to be studied have been defined, the sampling points are selected in a random manner; nevertheless, they should be located at least 200 m away from traffic lights, to avoid the potential influence of the latter.[26] Placing the measurement points at singularities that are not representative of the street—such squares attached to streets with a predominantly transverse U profile—must also be avoided and studied in detail.

B. Long-term measurements

Sound level meters were generally placed on the first floor of buildings and at least 1.5 m from the facade. As far as measurements have been done in streets and far away from intersections and squares, noises measured have been always coming from near sources, and only in these streets with comparatively low noise, noise measured can be affected for background noise coming from the rest of the city. No corrections were applied in order to avoid the effect of noise reflections in facades, because measurements were to be representative of environmental noise in the streets and the work was focused on differences between day and night levels. Thus, the behavior of the street's transversal profile was not taken into account. $L_{A,eq}$ values were stored every 15 min for periods of more than 48 h. After ascertaining that there were no atypical measurements, the results were grouped into $L_{A,eq}$ values of 60 min, in order to obtain the following parameters:

L_{day}: $L_{A,eq}$ between 7:00 a.m. and 7:00 p.m.
$L_{evening}$: $L_{A,eq}$ between 7:00 p.m. and 11:00 p.m.
L_{night}: $L_{A,eq}$ between 11:00 p.m. and 7:00 a.m.
L_{den}, according to the following formula:

$$L_{den} = 10 \lg \frac{1}{24}(12 \times 10^{L_{day}/10} + 4 \times 10^{L_{(evening+5)/10}} + 8 \times 10^{(L_{night}+10)/10}).$$

The European Directive[1] allows different time intervals to be used, particularly in Mediterranean countries, where the evening period may begin at 9 p.m. and last for just two hours. In general, using one expression or another resulted in negligible differences of around 0.5 dBA.[27]

The measurements were taken on working days from September to June, thus avoiding the singularities that may occur on bank holidays or at Christmas. If these specific effects are avoided and it is ensured that no significant changes occur in the streets,[25] noise levels remain constant throughout the year.[28] The measurements can be considered to be representative of these conditions, because the only significant variations occur at the weekend and in the summer, and even then their effects on the annual values are limited.[29]

TABLE II. Sampling points per city.

City	1	2	3	4	5	6	7	8
No. of 24 h measurements	36	31	32	18	19	13	9	19

Table II shows the number of measurements taken in each city. The number of measurements depends on the type of street, land use, and the number of existing segments (statistical population) in each city, but there is obviously a relationship between the size of the city and the number of measurements taken, except in the cases of cities 7 and 8. City 7, despite having a larger population than city 8, required fewer measurement points because the city is highly uniform with strong predominance of large blocks of flats, in that it is a dormitory town that does not have a great number of services or activities (see Table I).

IV. RESULTS AND DISCUSSION

In Sec. III A, in which the experiment is outlined, streets are classed into six types. The streets may in turn be influenced by land use, of which there are four categories. This gives rise to a total of 24 possible combinations of street type/land use, although some of these are highly improbable (pedestrian streets designed for industrial use, for example) and others in which the street type predominates over the land use, meaning that the influence of the latter may be negligible (traffic on ring roads or large infrastructures predominates over the use made of the land they pass through, for example). Eliminating unlikely combinations, together with the experimental results obtained regarding the streets' daytime-afternoon-night-time behavior, sampled in accordance with the segmentation described in Sec. III, show that these 24 combinations may be simplified basically into six categories:

(i) Ring roads: includes roads that encircle the city and some of the roads classified as access roads.
(ii) Main roads: arterial roads that distribute the traffic within the city (distribution roads) and some roads classified as access roads.
(iii) Common streets: destination streets of residential or commercial use.
(iv) Pedestrian streets: includes commercial, residential, and recreational streets.
(v) Industrial areas: industrial sectors located within the city limits.
(vi) Streets influenced by infrastructures: streets located close to large infrastructures that cross the city (not ring roads).

The land use, except for industrial activities, does not seem to have any significant effect on 24-h behavior of streets with traffic, whether these are access roads, distribution roads, or common streets. In some cases, intensive commercial activities on entertainment activities tend to be pe-

TABLE III. Summary of mean and variance results for L_{day}, $L_{evening}$, L_{night}, L_{day}-L_{night}, and L_{den}-L_{day}.

		L_{day}		$L_{evening}$		L_{night}		L_{day}-L_{night}		L_{den}-L_{day}	
	City	Mean	S^2	Mean	S^2	Mean	S^2	Mean	S^2	Mean	S^2
Ring-roads	2	72.2	2.9	71.7	6.2	65.7	5.5	6.5	0.63	2	0.2
	3	72.2	19.0	70.8	14.5	67.6	20.2	4.7	0.67	3.1	0.36
	1	70.3	14.4	65.7	25.1	63.8	11.4	6.6	0.87	2	0.26
Main roads	2	69.3	5.1	68	5.5	61.3	6.5	8	0.52	1.3	0.13
	3	71.3	2.7	69.9	2.1	64	2.4	7.3	0.64	1.8	0.21
	5	65.6	13.9	64.5	13	59.6	14.3	5.9	0.37	2.1	0.14
	7	63.7	32	62.2	24	57.4	36.7	6.3	0.39	2	0.10
	4	67	9.1	67	10.1	61.2	11.7	5.8	0.57	2.4	0.16
	1	68.5	11	64.9	29.5	60.4	10.5	8.1	0.27	1.2	0.09
Common streets	2	65.9	22.8	65.2	28.1	55	26.3	10.9	2.75	0.5	0.46
	3	67	8.9	66.4	11.6	65	9.5	8.7	2.15	1.6	0.77
	5	64.4	3.6	65.3	4.9	55.9	5.5	8.5	0.22	1.5	0.25
	4	64.5	5.4	65.3	2.9	56.6	4.3	7.9	0.33	1.6	0.09
	8	57.3	67.9	55.7	57.8	47.7	81.8	9.6	1.56	1.4	0.19
	1	63.1	13.4	54.7	16.3	53.4	13.4	9.3	1.54	0.8	0.56
Pedestrian	2	60.5	31.8	59.4	20.1	50.1	18.8	10.4	1.5	0.4	0.37
	4	62.9	21.6	62.9	26.2	56.5	8.8	6.5	7.51	2.5	1.22
	1	62.8	1.7	52	14.4	59.6	14.4	10.8	5.6	0.9	0.35
	8	63.5	96.8	63.1	115	49.6	41.1	13.9	9.68	0.7	1.6
	6	64.1	7.5	59.1	8.8	56.1	6.6	7.9	10.2	1.4	2.31
Industrial	2	63	2.4	58.6	23.1	58.4	0	4.6	1.21	2.8	0.42
	5	61.9	6.7	60.1	1.3	54.8	2.9	7.2	0.58	1.5	0.26
	1	64.3	11.5	58.9	4.5	58.9	4.5	5.4	1.64	2.3	0.51
Affected by infrastructure	5	68.8	15.8	67.6	16.8	63.2	15.5	5.6	0.06	2.2	0.02
	7	76.5	11.5	73.9	11.5	70.6	14.0	5.1	0.06	2.6	0.02
	1	81.1	0.3	70.5	63.9	70.7	58.5	5.6	0	2.2	0

destrian only, which means that the pedestrian street type tends to coincide with commercial land use, for which the principal source of noise is human activity. Acoustic conditions of streets affected by industrial use are different to the rest. There are two types of industrial use: the first, in which heavy industry that is continuously in operation predominates, and the second, in which there is a predominance of small workshops that only operate during the day. In the case of the latter, the predominant noise source, both during the day and at night, is the traffic on the streets themselves, which enables them to be characterized according to the type of street (generally a distribution road or common street) and not by its activity. If there is a predominance of heavy industry, the noise it generates continues at night, which means that the difference between L_{day} and L_{night} is relatively small compared to other streets for which traffic conditions are similar. The industrial areas mentioned in this work only refer to those affected by heavy industry.

A. Summary and justification of results

Table III summarizes the mean values and variance for L_{day}, L_{night}, and $L_{evening}$, as well as for the differences between L_{day} and the rest of the values (L_{day}-L_{night} and L_{den}-L_{day}, respectively) for all the categories found. First, the most noticeable difference found was that the results generally showed very high variation values for the L_{day}, L_{night}, and $L_{evening}$ parameters, which were much less significant for the L_{day}-L_{night} and L_{den}-L_{day} parameters. This would seem to suggest that the classification of streets by type is more appropriate from the point of view of the difference between L_{day} and L_{night}, more so than for L_{day} and L_{night} values. These results also confirm the initial hypothesis that the L_{day}, L_{night}, and $L_{evening}$ values are more variable than the relationship between them.

Focusing on the analysis of the L_{day}-L_{night} parameter, which tells us about the reduction in sound levels that occurs at night with respect to the daytime period, we can see that, other than in a few, specific cases, the value obtained is far from the 10 dBA or more that is generally thought of as a standard or reference value in many regulations,[30,31] as it has been presented in previous works.[7,12,17] There is a clear relationship between streets of the same type and between the

results for L_{day}-L_{night} and the socioeconomic conditions of the cities. In general, streets affected by traffic noise tend to behavior in a similar form for all the cities studied. This is not the case for pedestrian streets: values for L_{day}-L_{night} of between 6.5 and 13.9 dBA were found, and the variance results obtained for each city are also high. This proves that there are significant differences within each city, which are the result of the activities that are carried out in these streets and cause different acoustic behavior, particularly at night. It is possible that various subtypes could be included as pedestrian streets, but, at present, the number of pedestrian streets studied is not large enough to enable trends to be identified.

The results obtained for the L_{day}-L_{night} parameter for streets affected by industrial activities do not show much variability. The reason could be that the types of industry found in these cities are relatively similar and there are no large industrial estates. In any case, an analysis of the scenarios observed requires, first of all, a specific study of the location of the activities that generate a great deal of noise and, secondly, a specific acoustic characterization of the source.

In the streets with a predominance of traffic noise, the distinction between the streets that serve the city itself (ring roads, distribution roads, and common streets) and those that are affected by infrastructures can be made. The daytime-night-time behavior of the latter is very similar within the cities (negligible variance), as well as between the various cities characterized. Average L_{day}-L_{night} values are between 4.2 and 5.6 dBA, the lowest of all the types considered. The reason may reside in the fact that infrastructures are supramunicipal and that there is no direct relationship between the city and these infrastructures, which means that their acoustic behavior is independent of the city and also of the area of the city. The L_{day} values, on the other hand, show acute differences, with particularly significant variations in cities 5 and 7. The reason for this is that levels depend on the transverse profile (the infrastructures may be elevated or depressed, for example), on the distance between the infrastructure and the streets, and the presence of barriers or other obstacles.

For streets in which there is a predominance of traffic noise, that is, most of the streets in a city, it is possible to identify some trends in their behavior, which are listed below.

(i) The general tendency is for the L_{day}-L_{night} parameter to decrease as the values of the daytime level L_{day} increase. This suggests that there is a significant correlation between the L_{day}-L_{night} parameter and the L_{day} value (and traffic flow, therefore). Specifically, from the Table III one can see that for the streets typified as ring roads, daytime levels are around 70 to 72 dBA, and the L_{day}-L_{night} parameter is between 4.7 and 6.6 dBA, while for the type of street with lower L_{day} values (common streets), the L_{day}-L_{night} difference is between 7.9 and 10.9 dBA.

(ii) Access roads or their prolongation into the city can be classified as external ring roads or distribution roads. The roads that connect the cities to communication hubs or large cities tend to exhibit behavior that is very similar to that of ring roads. The roads that connect the cities to small towns tend to exhibit behavior that is very similar to that of internal distribution roads, because, in many cases, the internal distribution roads are old roads that have been absorbed by urban sprawl.

(iii) The variance of ring roads and main roads shows similar values for both types, which is consistent with previous studies that showed that, for a flow of traffic of more than 200 vehicles/h, the variability of noise levels does not change.[32] It must be borne in mind that both types show traffic flows that are considerably above this value.

(iv) The variance of common streets increases significantly with respect to the previous types, which is also consistent with previous studies carried out solely with daytime L_{Aeq} values,[8] even though the values obtained for the L_{day}-L_{night} parameter are clearly lower than those from daytime L_{Aeq}. This is to be expected, because within this type there may be streets with more commercial or service activities than others, or streets in which the characteristics of the traffic are different (heavy vehicles or motorcycles, for example), the consequences of which are a greater variability in the value of the L_{day}-L_{night} parameter. They also have less traffic than ring roads or main roads, which has been shown to be a cause of an increase in the variance.[33] A further cause may be that background noise from nearby streets could have significant influence in streets with relatively little traffic.

As shown in Table III, the L_{day}-L_{night} values for the same type of street are different for each city. This suggests that, although it seems possible to group the streets in a city according to the classification proposed, it is not possible to extrapolate the results for a given street type to different cities. This means that each city has different values for the L_{day}-L_{night} parameter for its streets, which will be a function of socioeconomic variables within the city. We found justifiable differences in the L_{day}-L_{night} parameter for each type of street and for different cities:

(a) Ring roads: from Table III it comes out that the difference between the equivalent daytime and night-time levels in cities acting as a local capital is lower because night-time activity concentrates in them while surrounding cities are still quiet. City 1 is too near Barcelona to develop the role of a local capital and city 2, in spite of sharing this role with city 3, is exceeded by the latter with regard to commerce, leisure activities, and night-time activities.

(b) Main roads: in general, the L_{day}-L_{night} parameter for main roads is about 1.5 dBA higher than for ring roads with some exceptions. In cities with an absence of ring roads (cities 4 and 5), main roads are used in its place. Thus, the L_{day}-L_{night} parameter is lower and similar to that of the ring roads. Finally, cities away from Barcelona (city 7), with limited

transport activity and relatively small size, have a low L_{day}-L_{night} value due to the lack of activity in both day and night periods.

(c) Common streets: these streets have the L_{day}-L_{night} values that are closest (in some cases even equal) to 10 dBA, the level contemplated in most legislation, but variance seems to increase with the number of inhabitants when talking about cities (not the case of towns).

The L_{den}-L_{day} parameter mimics the results listed for the L_{day}-L_{night} parameter, although the values are much smaller and the variance is much lower. As a main conclusion, it seems that the estimation of the L_{night} (or L_{den} or L_{dn}) parameter from L_{day} (obtained by short term measurements) can be done with a relatively small sample and with a sufficiently small margin of error. The classification of streets by type leads to a significant decrease in the variance values with respect to the random sampling in that no street types are distinguished.[11] This suggests that it may be possible to predict the number of sampling points that will ensure the reliability of the noise map, at least for streets in which there is a predominance of noise from traffic. Pedestrian streets and those with a predominance of heavy industry need to be characterized deliberately, even though the results obtained in this work may serve as a guide.

B. Statistical analysis for streets with traffic noise

This analysis in only addressed to streets with a predominance of traffic noise, because the amount of data for pedestrian and industrial streets is not enough to carry out predictions.

Let us suppose that all the streets in a city that are of a certain type (ring roads, distribution roads, or urban streets) make up a statistical population of size N, and that the random variables to be studied are L_{day}-L_{night} and L_{den}-L_{day} on these streets. The issue that arises is whether the estimation of $\overline{L_{day}-L_{night}}$ or $\overline{L_{den}-L_{day}}$ can be determined, with a high degree of precision from a relatively small sample (n) of population. According to the central limit theorem, n can be calculated as follows if $n \geqslant 30$ is expected:

$$n = \frac{N * Z_\alpha^2 * \sigma^2}{d^2 * (N-1) + Z_\alpha^2 * \sigma^2}, \tag{1}$$

where Z_α^2 is the value of the standard normal distribution N(0,1) (which has a mean of 0 and a standard deviation of 1) for a confidence interval of 1-α, N is the total population, $\pm d$ is the estimation error, and σ^2 is the variance of the population.

In our case, to take at least 30 long-term measures (which allow us to ascertain $\overline{L_{day}-L_{night}}$ or $\overline{L_{den}-L_{day}}$) for each street type considered is too expensive, so n should always be less. In cases with a small number of samples n, a variant of Eq. (1) can be used provided that distribution of L_{day}-L_{night} and L_{den}-L_{day} is reasonably close to a normal distribution:[34,35]

TABLE IV. Comparison between correlation values of the normal probability plot and the minimum value to assume normal distribution (here called boundary). Bold numbers show results under minimum value.

	City	Boundary	L_{day}-L_{night}	L_{den}- L_{day}
Ring-roads	2	0.879	0.9505	0.983
	3	0.905	0.9473	0.9067
	1	0.89	0.926	0.8948
Main roads	2	0.934	0.9548	0.9424
	3	0.922	0.9303	0.9373
	5	0.899	0.9089	0.9055
	7	0.868	0.9584	0.9526
	4	0.917	**0.9117**	0.9162
	1	0.89	0.9536	0.9153
Common streets	2	0.905	0.9425	0.9536
	3	0.926	**0.9233**	0.9116
	5	0.868	0.9845	0.8781
	4	0.879	0.8922	0.9643
	8	0.917	0.9427	0.9266
	1	0.922	0.9862	0.9225

$$n = \frac{N * t_{n_o-1,\alpha}^2 * S^2}{d^2 * (N-1) + t_{n_o-1,\alpha}^2 * S^2}, \tag{2}$$

where $t_{n_o-1,\alpha}$ is the value of a Student distribution for a confidence interval of 1-α and ν-parameter of $n-1$.

To be able to decide whether the L_{day}-L_{night} and L_{den}-L_{day} variables have an approximately normal distribution, we used a normal probability plot and calculated the correlation coefficient, which was compared to threshold values for a significance level of 5%.[36] Table IV shows the results for each of the cities and street types considered. As can be seen, the values are very close to the threshold value in all the cases. This does not enable us to assert that a normal distribution best characterizes the distribution of L_{day}-L_{night} or of L_{den}-L_{day}, although it may be said that the normal distribution is a reasonable approximation. To ratify this conclusion, we calculated the skewness and kurtosis values for each sample, and compared these to the expected skewness and kurtosis values for the case of a normal distribution for a confidence interval of 95%.[37] Table V shows the results obtained in these calculations. As all the values in this table clearly fall within admissible limits, we can corroborate that the L_{day}-L_{night} and L_{den}-L_{day} distributions behave in a close to normal manner.

This therefore justifies using Eq. (2) to calculate the size of the sample. By considering that equation, one may deduce that the size of the population (N) is not an influential factor if $N-1 \gg t_{n_o-1,\alpha}^2 * S^2$, because N appears in the numerator and denominator of the fraction. In most cases, the size of the population (N), as defined in this work, is much greater than the product $t_\alpha^2 * S^2$ (as an example, see Table VI). As a result, one can estimate the number of long-term measures that should be carried out independently of the size (quantity of segments) of each city, because Eq. (2) is simplified into Eq. (3):

TABLE V. Comparison of skewness and kurtosis values and boundary values to accomplish in order to assume normal distribution.

		Skewness			Kurtosis			
Streets	City	L_{day}-L_{night}	L_{den}-L_{day}	Boundaries	L_{day}-L_{night}	L_{den}-L_{day}	Boundaries	
Ring-roads	2	0.31	0.15	±2.19	1.71	2.02	−1.40	7.40
	3	0.51	−0.97	±1.73	2.22	2.29	−0.50	6.50
	1	−0.73	1.42	±2.00	2.26	3.51	−1.00	7.00
Main roads	2	0.09	−0.45	±1.31	1.50	2.04	0.40	5.60
	3	1.09	−0.70	±1.48	3.14	3.58	0.00	6.00
	5	−0.82	0.72	±1.85	2.76	2.41	−0.70	6.70
	7	0.39	−0.36	±2.45	1.97	1.57	−1.90	7.90
	4	−0.84	0.77	±1.55	2.60	2.58	−0.10	6.10
	1	−0.46	−0.50	±2.00	2.29	2.74	−1.00	7.00
Common streets	2	0.52	−0.23	±1.85	1.89	1.83	−0.70	6.70
	3	−1.08	1.46	±1.41	4.02	4.44	0.20	5.80
	5	−0.31	0.79	±2.45	1.78	2.00	−1.90	7.90
	4	0.71	0.38	±2.83	1.50	1.50	−2.70	8.70
	8	0.08	−0.57	±1.55	1.83	1.97	−0.10	6.10
	1	0.18	0.79	±1.48	2.01	2.61	0.00	6.0

$$n = t_{\alpha}^2 * S^2. \quad (3)$$

Table VII shows the number of sampling points for long-term measures (traffic counts), which according to Eq. (3) would be needed to estimate $\overline{L_{day}-L_{night}}$ or $L_{den}-L_{day}$ for the different street types and cities considered in this work. We considered a confidence level of 95% and a margin of error of ±1 dBA,[2,23] with the data of $t^2_{n_o-1,\alpha}$ and S^2 corresponding to the study of each street type and city. From the table it comes out that five to six measurements are enough to estimate $\overline{L_{day}-L_{night}}$ for ring roads, while only two measurements are needed to estimate $L_{den}-L_{day}$. In the case of main roads, two to four measurements are required to estimate $\overline{L_{day}-L_{night}}$, and one measurement to asses, $L_{den}-L_{day}$. Finally, regarding to common streets, 7 to 15 and 1 to 4 measurements are needed to estimate $\overline{L_{day}-L_{night}}$ and $L_{den}-L_{day}$ in the order given. In all cases we need fewer measurements to estimate $L_{den}-L_{day}$ than $\overline{L_{day}-L_{night}}$, but since we want to estimate both parameters, $\overline{L_{day}-L_{night}}$ would set the minimum number of measurements to be made.

In all cities, few and similar number of measurements are required for parameter estimation related to ring roads and main roads. Common streets generally require a larger sample, and greater differences were found between cities. In any case, in order to draw general conclusions, it seems advisable to disregard the small sample size of city 5, which can be due to its characteristics. As a final comment, in all cities the size of the sample was smaller than that of the real sample taken in each city (Table II), which validates the procedure followed.

TABLE VI. N and $t^2_{n_o-1,\alpha} * S^2$ values for city 2.

	N	$t^2_{n_o-1,\alpha} * S^2$
Ring-roads	55	5
Main roads	40	2
Common streets	833	15

C. Estimation of L_{night} and L_{den} from L_{day} values

According to the procedure followed and the results obtained, a method may be proposed for estimating the values of $\overline{L_{day}-L_{night}}$ and $L_{den}-L_{day}$ for any city, with predetermined confidence and error levels. In a theoretical case, the steps to be taken are as follows:

(1) Divide the streets into segments as a function of vari-

TABLE VII. Number of samples for an estimation of $\overline{L_{day}-L_{night}}$ and $L_{den}-L_{day}$ with a confidence level of 95% and a margin of error of ±1 dBA.

Streets	City	Sampling points for L_{day}-L_{night}	Sampling points for L_{den}-L_{day}
Ring-roads	2	5	2
	3	4	2
	1	6	2
Main roads	2	2	1
	3	3	1
	5	2	1
	7	4	1
	4	3	1
	1	2	1
Common streets	2	15	3
	3	10	4
	5	2	3
	4	7	2
	8	8	1
	1	8	3

ables that have an effect on the resulting noise levels and classify them according to the types described in Sec. IV of this paper. It has been demonstrated that access roads may exhibit the behavior of ring roads or main roads. Given that the statistical behavior of both types is very similar, we propose grouping temporally all the streets that fall into the types of ring roads, main roads, and access roads into a single typology of *major roads.* Final grouping into two main types (ring roads and main roads, according to this text) will depend on the results.

(2) Use the values in Table VII as a guide in order to determine the sample size. If main roads and access roads are initially classed as one type, the sample needed to estimate L_{night} for this type should be between seven and ten measures, while for common streets the sample should involve between 7 and 15 measures (having ignored the result for city 5). To choose one value or another is not exactly a function of the size of the city (population), but rather of the degree of uniformity (the more uniform the city is, the fewer measurement points required). Usually, the larger the city, the less uniform it is, because it will have a central area, residential areas, suburban areas, and different types of land use, none of which are different enough to warrant establishing new categories but which do increase the variability of the results.

(3) Ascertain whether the variance of the results in the major roads is high and analyze whether it will be reduced by distinguishing between ring-road and main-road types.

(4) Determine whether the results for the variance of the types obtained are in the order of the types presented in this work. If this is not the case, it would be advisable to increase the number of measures of the types that show high variance, according to Eq. (3).

The variance of the streets affected by infrastructures is so low that a measure (traffic count) of 24 h per infrastructure may be enough to assess the L_{night} and L_{den} parameters correctly.

V. CONCLUSIONS

This paper shows that the parameters $L_{day}-L_{night}$ and L_{den}-L_{day} may be treated as a close to normal distribution in terms of the spatial variation of an urban area. This enables us to determine the values of $L_{day}-L_{night}$ or $L_{den}-L_{day}$ from a small sample of long-term measurements or counts, without compromising the validity of the results. These parameters enable the L_{night}, L_{den}, or L_{dn} parameters to be estimated from L_{day} values, which are easier to obtain.

The L_{day}-L_{night} and L_{den}-L_{day} values vary significantly between cities and they are not related with city size (in population or density) or total amount of traffic. Therefore, it is not advisable to choose an average value for each street type from the values found in this work. On the contrary, the results highlight the need to carry out the study city by city, with an appropriate sampling campaign.

For an optimal estimation of the parameters of $L_{day}-L_{night}$ or $L_{den}-L_{day}$, with the smallest possible number of samples, it has been demonstrated that the categorization of streets, differentiated according to the types described, give very low variance values, which also enable very small samples to be used. It has been shown that the number of samples does not directly depend on the number of inhabitants or of streets, but rather on the degree of uniformity of the city that is being assessed. In any case, the number of measurement or traffic counting points for streets in which the main source of noise is traffic ranges between 14 and 25, for all street types, which would incur costs that can be met by the city authorities.

The current sample of pedestrian streets is not sufficient, although the variance values found are very high. Thus, many measurement points would be required for the correct estimation of $L_{day}-L_{night}$ or $L_{den}-L_{day}$. It is possible that the pedestrian streets may be divided up depending on their use, which would reduce the variance and, as a result, the number of samples. In any case, there are not many of these types of streets and a detailed study could be carried out of their acoustic behavior. In fact, the results show that a study of this type is necessary in assessing environmental noise, because averages for L_{night} as high as 60 dBA were found for certain cities, which represents noise levels equivalent to those found on main roads.

[1]Directive 2002/49/EC, Journal of the European Communities 18.07.2002.
[2]T. T. Wolde, "The EU noise policy and the related research needs," Acta. Acust. Acust. **89**, 735–742 (2003).
[3]W. A. Utley, "Temporal sampling techniques for the measurement of environmental noise," Appl. Acoust. **15**, 191–203 (1982).
[4]E. Gaja, A. Gimenez, S. Sancho, and A. Reig, "Sampling techniques for the estimation of the annual equivalent noise level under urban traffic conditions," Appl. Acoust. **64**, 43–53 (2003).
[5]H. B. Safeer, "Community noise levels-a statistical phenomenon," J. Sound Vib. **26**, 489–502 (1973).
[6]A. L. Brown and K. C. Lam, "Urban noise surveys," Appl. Acoust. **20**, 23–39 (1987).
[7]M. Omiya, K. Kuno, Y. Mishina, Y. Oishi, and A. Hayashi, "Comparison of community noise ratings by L50 and LAeq," J. Sound Vib. **205**, 545–554 (1997).
[8]J. M. Barrigón, V. Gómez, J. Méndez, R. Vílchez, and J. Trujillo "An environmental noise study in the city of Cáceres, Spain," Appl. Acoust. **63**, 1061–1070 (2002).
[9]J. M. Barrigón, V. Gómez, J. Méndez, R. Vilchez, J. Vaquero, and J. Trujillo, "A categorization method applied to the study of urban road traffic noise," J. Acoust. Soc. Am. **117**, 2844–2852 (2005).
[10]M. U. Onuu, "Road traffic noise in Nigeria: measurements, analysis and evaluation of nuisance," J. Sound Vib. **233**, 391–405 (2000).
[11]A. Garcia and J. Garrigues, "24-Hour continuous sound-level measurements conducted in Spanish urban areas," Noise Control Eng. J. **46**, 159–166 (1998).
[12]C. J. Skinner and C. J. Grimwood, "The UK noise climate 1990-2001: population exposure and attitudes to environmental noise," Appl. Acoust. **66**, 231–243 (2005).
[13]T. Kihlman and S. AbuKhader, "Long-term noise abatement planning-case studies in Göteborg, Sweden," *Proc. Internoise 2001*, The Hague, 2001.
[14]D. Chakrabarty, S. Santra, A. Mukherjee, B. Roy, and P. Das, "Status of road traffic noise in Calcutta metropolis," J. Acoust. Soc. Am. **101**, 943–949 (1997).
[15]P. Trombetta, F. Belisario, and W. Alves, "Environmental noise pollution in the city of Curitiba, Brazil," Appl. Acoust. **63**, 351–358 (2002).
[16]W. M. To, R. Ip, G. Lam, and C. Yau, "A multiple regression model for urban traffic noise in Hong Kong," J. Acoust. Soc. Am. **112**, 551–556 (2002).
[17]E. A. Shaw, "Noise environments outdoors and the effects of community

noise exposure," Noise Control Eng. J. **44**, 109–119 (1996).
[18]W. A. Utley, "Temporal sampling techniques for the measurement of environmental noise," Appl. Acoust. **15**, 191–203 (1982).
[19]European Commission Working Group Assessment of Exposure to Noise, "Good Practice Guide in Strategic Noise Mapping and the Production of Associated Data on Noise Exposure," December 2003.
[20]DEFRA, Noise Mapping England. The London Road Traffic Noise Map, 2004.
[21]NiedersächsischesLandesamt für Ökologie, "Development of a digital model for computing a noise map for the Brussels area," 2002.
[22]H. B. Safeer, J. E. Wesler, and E. J. Rickley, "Errors due to sampling in community noise level distributions," J. Sound Vib. **24**, 365–376 (1972).
[23]K. Attengorough, S. Clark, and W. A. Utley, "Background noise levels in the United Kingdom," J. Sound Vib. **48**, 359–375 (1976).
[24]B. Li, S. Tao, and R. W. Dawson, "Evaluation and analysis of traffic noise from the main urban roads in Beijing," Appl. Acoust. **63**, 1137–1142 (2002).
[25]H. B. Safeer, "Community noise levels-a statistical phenomenon," J. Sound Vib. **26**, 489–502 (1973).
[26]B. Favre, "Noise at the approach to traffic lights: result of a simulation programme," J. Sound Vib. **58**(4), 563–578 (1978).
[27]S. Jiménez, R. Alsina, P. Perera, and J. M. Arriaga, "The European directive on assessment and management of environmental noise. Variability in the noise indicators," *Proceedings of Forum Acusticum 02*, Sevilla, Spain, 2002.
[28]I. D. Griffiths, F. J. Langdon, and M. A. Swan, "Subjective effects of traffic noise exposure: reliability and seasonal effects," J. Sound Vib. **71**, 227–240 (1980).
[29]J. Romeu, S. Jimenez, T. Pamies, and M. Genesca, "L_{den} assessment methodology for acoustic maps: simulation or measurements?," *Proceedings of Internoise 2003*, Jeju, Korea, 2003.
[30]Department of Environmental Protection, Noise code. New York City, March 1998.
[31]World Health Organization Regional Office for Europe, Noise and Health, "Local authorities, health and environment briefing pamphlet series 35," 2000.
[32]D. Gilbert, "Noise from road traffic (interrupted flow)," J. Sound Vib. **51**, 171–181 (1977).
[33]D. J. Fisk, "Statistical sampling in community noise measurement," J. Sound Vib. **30**, 221–236 (1973).
[34]R. Peck, C. Olsen, and J. Devore, *Introduction to Statistics and Data Analysis* (Duxbury, Pacific Grove, 2001).
[35]J. Santiago and R. Escuder, *Estadística aplicada. Inferéncia estadísitica* (Applied statistics. Statistical inference) (Tirant lo Blanch, València, 1994).
[36]J. J. Filiben, "The probability plot correlation coefficient test for normality," Technometrics **17**, 111–117 (1975).
[37]A. Stuart and J. K. Ord, *Kendall's Advanced Theory of Statistics. Volume 1: Distribution Theory*, 6th ed. (Edward Arnold, London, 1994).

Auralization study of optimum reverberation times for speech intelligibility for normal and hearing-impaired listeners in classrooms with diffuse sound fields

Wonyoung Yang and Murray Hodgson
Acoustics and Noise Research Group, School of Occupational and Environmental Hygiene, University of British Columbia, 2206 East Mall, Vancouver, BC V6T 1Z3, Canada

(Received 3 February 2006; revised 25 May 2006; accepted 30 May 2006)

Speech-intelligibility tests auralized in a virtual classroom were used to investigate the optimal reverberation times for verbal communication for normal-hearing and hearing-impaired adults. The idealized classroom had simple geometry, uniform surface absorption, and an approximately diffuse sound field. It contained a speech source, a listener at a receiver position, and a noise source located at one of two positions. The relative output levels of the speech and noise sources were varied, along with the surface absorption and the corresponding reverberation time. The binaural impulse responses of the speech and noise sources in each classroom configuration were convolved with Modified Rhyme Test (MRT) and babble-noise signals. The resulting signals were presented to normal-hearing and hearing-impaired adult subjects to identify the configurations that gave the highest speech intelligibilities for the two groups. For both subject groups, when the speech source was closer to the listener than the noise source, the optimal reverberation time was zero. When the noise source was closer to the listener than the speech source, the optimal reverberation time included both zero and nonzero values. The results generally support previous theoretical results.
 [DOI: 10.1121/1.2216768]

PACS number(s): 43.55.Hy, 43.55.Ka [NX] Pages: 801–807

I. INTRODUCTION

Verbal communication is one of the most important acoustical activities in many rooms. Rooms vary from small meeting rooms and classrooms to larger auditoria and conference rooms. The acoustical designs of such rooms should achieve a high degree of speech intelligibility for listeners in the rooms. Speech intelligibility is directly related to speech-to-noise level difference and is inversely related to reverberation time.[1] However, in rooms the situation is complicated by the fact that reverberation and steady-state levels interact. Increased reverberation increases speech and noise levels by increasing the reverberant sound energy; this increases or decreases the speech-to-noise level difference at a listener position depending on the listener's relative distances to the speech and noise sources. Here, we consider rooms with approximately diffuse sound fields, for which reverberation can be accurately described by the reverberation time (RT), so that the results can be related to previous experimental research.

The literature reports a number of experimental and theoretical studies which investigated the relationship between the prevailing acoustical conditions and resulting speech intelligibility. These studies accounted for noise, and the interaction between reverberation and speech-to-noise level difference, with varying degrees of realism. A brief overview of the literature is presented here—see Ref. 2 for a full review and discussion.

Nabelek and Robinson[3] showed that, in the absence of noise, speech intelligibility was inversely related to reverberation time—that is, the optimal reverberation time for speech intelligibility was zero. Nabelek and Pickett[4,5] and Finitzo-Hieber and Tillman[6] performed speech-intelligibility tests with normal-hearing and hearing-impaired subjects, for various fixed speech-to-noise level differences in rooms with various fixed reverberation times, again finding that speech intelligibility decreased with increased reverberation time. Hearing-impaired people were more sensitive to reverberation than normal-hearing people. These experimental studies were unrealistic in effectively assuming a diffuse sound field by involving exponential sound decays, and in not accounting for the interaction between reverberation and sound levels. The theoretical studies, on the other hand, were based on speech-intelligibility metrics which are considered to be good predictors of speech intelligibility, and which account for the interaction. Bradley,[1] using both subjective test results and theoretical prediction of the U_{50} useful-to-detrimental energy metric in diffuse sound fields, found optimum reverberation times of 0.4 to 0.5 s for classrooms with a uniform background-noise level of 30 dBA. Houtgast *et al.*[7] used a numerical model to find nonzero optimum reverberation times for a variety of rooms with nondiffuse sound fields, and for various speech-to-noise level differences. The effects of reverberation on noise were incorporated by considering the audience as a collection of individual noise sources. Bistafa and Bradley[8] used a theoretical model to predict nonzero optimal reverberation times in diffuse sound fields using a number of metrics. They found that increased reverberation increased early energy and intelligibility—too much reverberation decreased intelligibility. However, noise levels were again unrealistically assumed to be uniform throughout the room. Hodgson and Nosal[2] incorporated noise into a theoretical model in a realistic manner, by in-

cluding noise sources in the rooms, which had diffuse sound fields. Predicted optimum reverberation times depended on the source directivities, the speech-to-noise level difference at the listener's position, the positions and orientations of the speaker and the noise source, and the number of noise sources. They found that, if the speech source was farther from the listener than the noise source, then speech levels increased more with reverberation than did noise levels, and the level difference increased with reverberation, tending to increase intelligibility. If, on the other hand, the noise source was farther from the listener than the speech source, then noise levels increased more with reverberation than did speech levels, tending to decrease intelligibility. Thus, the effect of reverberation on intelligibility depended on the relative distances from the listener to the speech and the noise sources. The effect increases with source/receiver distance and, therefore, is greater when source/receiver distances are larger than the reverberation radius (or critical distance).

In this paper, auralization techniques are used to identify optimal reverberation times in an idealized classroom with speech and babble-noise sources and an approximately diffuse sound field, in order to validate theoretical prediction. Considering individual speech and noise sources is more realistic. Subjective tests have the potential to be more accurate than theoretical prediction. Optimal reverberation times are found by performing speech-intelligibility tests with normal-hearing and hearing-impaired adult subjects. Considering the U_t speech-intelligibility metric that has been shown to be well-suited to the prediction of speech intelligibility in classrooms,[1] the early/late energy time t that best predicts speech intelligibility is found for both subject groups. Involving both normal- and hearing-impaired subjects allows similarities and differences between these two subject groups to be determined.

II. THEORETICAL CONSIDERATIONS

U_t is a metric based on the useful-to-detrimental energy-ratio concept. This concept divides acoustical energy received after the arrival of the direct sound into useful and detrimental parts. The useful part consists of the direct energy from the speaker, E_d, and the early-arriving, reflected energy from the speaker, E_e. The remaining reflected, or late-arriving, energy, E_l, is considered detrimental. In addition to the late-arriving reflected energy, noise energy, E_n, is detrimental. Thus, the measured useful-to-detrimental ratio calculated from measured data is defined as

$$U_{t,m} = 10 \log\left\{\frac{E_d + E_{e,t}}{E_{l,t} + E_n}\right\} \text{dB}. \tag{1}$$

The U_t useful-to-detrimental ratio can also be predicted based on diffuse-field theory,[2]

$$U_{t,p} = 10 \log\left\{\frac{(r_{h_s}^2/r_s^2) + 1 - e^{-kt}}{e^{-kt} + 10^{(L_{nf1}-L_{sf1})/10}(r_{h_s}^2/r_n^2 + q_s/q_n)}\right\} \text{dB}, \tag{2}$$

The subscripts "m" and "p" refer to measured and predicted data, respectively. Here, $k = \ln(10^6)/\text{RT}$, where RT is the reverberation time, r_s is the distance from the speech source to the listener, r_n is the distance from the noise source to the listener, and r_{h_s} is the reverberation radius (or critical distance) associated with the speech source. L_{sf1} and L_{nf1} are the long-term anechoic levels at 1 m directly in front of the speech and noise sources, in a free field, respectively; q_s and q_n are their directivity indices.

III. EXPERIMENTAL METHODOLOGY

A. Classroom and sound-field simulation procedures

In this study, the objective was to model an idealized room with an approximately diffuse sound field and exponential sound decay. Thus, the design was based on previous research into the factors that relate to a diffuse sound field.[9] The virtual classroom was based on a real 95-seat classroom of simple, rectangular geometry. It was 11 m long, 7 m wide, and 4 m high (volume=385 m^3). Predictions were made in octave bands from 125 to 4000 Hz. The same absorption coefficients were used for all octave bands and for all surfaces. The absorption coefficient was varied to achieve different reverberation times. Values of 1.0, 0.68, 0.40, and 0.21 were used, respectively, to obtain reverberation times of 0.0, 0.2, 0.4, and 0.8 s. The corresponding reverberation radii varied from 3 to 1 m. In order to avoid strong specular reflections from the surfaces, and to promote diffuse fields with exponential sound decays, all surfaces were defined to be 30% diffusely reflecting.[10] CATT-ACOUSTIC v8.0[11] was used to predict and auralize the sound fields. The number of rays and the truncation time were 10 088 and 1.0 s, respectively, for both prediction and auralization. In order to verify the diffusiveness of the simulated sound fields, predicted early-decay times and RTs were compared; these should be very similar in a diffuse sound field with an exponential sound decay. The differences were always less than 0.05 s at mid frequencies (500, 1000, and 2000 Hz).

The classroom contained a speech source, a noise source, and a virtual listener, all located at least 2 m from surfaces. Two noise-source positions were considered—one between the speech source and the listener, such that the noise source was closer to the listener than the speech source (noise 1), and one farther from the speech source than the listener (noise 2). Figure 1 shows the floor plan of the virtual room, with the relative positions of the listener, the speaker, and the noise sources. The speech source had humanlike directivity; the noise source was omnidirectional. The listener and the speech source faced each other. The relative output power levels of the speech and noise sources were chosen to give differences (SNS) of 0 and 5 dB. Note that SNS is different from the difference in the speech and noise levels at a receiver location (SNR). The values of SNS and RT were selected on the basis of preliminary listening tests. These covered a wide range of SNS and RT values and allowed the more limited ranges, resulting in realistic SNR values and expected to contain the optimal RT values, which were used here to be identified. The test RT values were additionally chosen to cover the range including zero and the optimal values specified in classroom standards.[1]

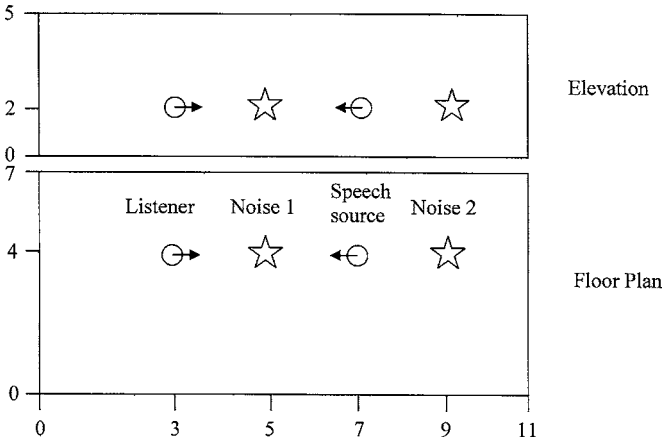

FIG. 1. Floor-plan and elevation of the virtual classroom, showing the speaker, listener, and noise-source positions. All coordinates are in meters.

Binaural impulse responses between the listener and the speech and noise sources were predicted. In order to take into account the effects of the head, shoulder, and external auditory systems of the virtual listener, the head-related transfer functions (HRTFs) provided with the CATT-ACOUSTIC system were used. Headphone playback without equalization, and diffuse-field HRTF data, were used in this work.

The resulting sound fields were auralized using the CATT-ACOUSTIC software. The speech-signal level was chosen to approximate typical classroom levels. The noise-source levels were set relative to the input speech level to achieve the two test SNS values. A total of 16 different sound-field configurations was created, consisting of all combinations of the two speech- and noise-source relative output levels (SNS =0 and 5 dB), the four reverberation times (RT=0, 0.2, 0.4, and 0.8 s), and the two positions of the noise source (noise 1 and noise 2). As shown in Table I, the speech-to-noise level differences received at the listener position (SNR), corresponding to the two SNS values, varied in the various configurations from −6 to +8.5 dB.

The Modified Rhyme Test (MRT) (Ref. 12) was used as the speech-intelligibility test method. Twelve 50-word MRT word lists recorded by a male, native-Canadian talker in an anechoic chamber were combined through the CATT-ACOUSTIC system with four-talker babble noise (available from AUDITECH[13]). The MRT-speech and babble-noise signals for each test configuration were mixed together using the GOLDWAVE v5.1 sound-editing program,[14] at levels corresponding to the predicted sound-pressure levels at the listener position. The resulting, final auralization test materials were transferred to a compact disc for presentation to subjects using a CD player. The test material was replayed through Sony MDR V600 headphones in a soundproof room. Each subject was tested individually. Each listened to a complete list of 50 words for each of the 16 different sound-field configurations. In order to avoid score inflation caused by the closed-set method used here, subjects were instructed not to guess the answer. The tests were presented in randomized order. The presentation levels were set by the predicted levels of the sound-field configurations, and used for both normal and hearing-impaired groups.

TABLE I. Received speech-to-noise level differences (SNR in dB) for all test sound-field configurations.

	SNS=0 dB		SNS=5 dB	
RT(s)	Noise 1	Noise 2	Noise 1	Noise 2
0.0	−6.0	3.5	−1.0	8.5
0.2	−4.5	2.1	0.4	7.2
0.4	−2.8	1.2	2.1	6.2
0.8	−1.5	0.6	3.3	5.7

B. Subjects

Hearing-screening tests were done prior to the speech-intelligibility testing, to identify the hearing categories of the subjects. Subject groups for the study were normal-hearing adults, and hearing-impaired adults with a mild to moderate sensorineural hearing loss, whose first language was English. The hearing-loss criteria for the hearing-impaired subjects were lower than 25 dB HL (HL=hearing loss) between 250 Hz and 1 kHz, and between 30 and 55 dB HL from 2 to 8 kHz, with no more than 15-dB difference between the two ears at any two frequencies. This represents a typical frequency response for sensorineural hearing loss.[15] The hearing-impaired subjects in this work did not use hearing aids in their everyday lives.

Data collection was done at two different sites: the University of British Columbia, Vancouver, BC (UBC) and Central West Health, Grand Falls-Windsor, NL (CWH). Forty-three normal-hearing and 28 hearing-impaired subjects, with mean ages of 26 and 48 years, respectively, completed the tests. For the normal-hearing subjects, the difference between the UBC and CWH groups was not statistically significant. For the hearing-impaired subjects, the difference was statistically significant ($p<0.05$), with the CWH hearing-impaired group showing a lower average MRT score than the UBC group. However, the subject groups at the two locations showed similar variations of scores with the different test configuration (i.e., for different SNS and RT); thus, the results for the two groups were combined. The exact reason for the difference in the results for the hearing-impaired subjects at the two test sites is not known.

IV. RESULTS

A. Speech intelligibility

Mean speech-intelligibility scores for the 16 sound-field configurations were calculated separately for the normal-hearing and hearing-impaired subject groups. Results are presented as the percentage of correct responses. Figure 2 shows the variations of the mean speech-intelligibility score (with 95% confidence interval) with reverberation time and noise-source position.

For normal-hearing subjects, when the noise source was farther from the listener than the speaker (noise 2), with either SNS=5 or 0 dB, the mean speech-intelligibility scores exceeded 85% for all reverberation times. Analysis of variance (ANOVA) was employed to compare the sensitivity of the scores to variations in the speech- and noise-source output-level difference (SNS) and reverberation time (RT).

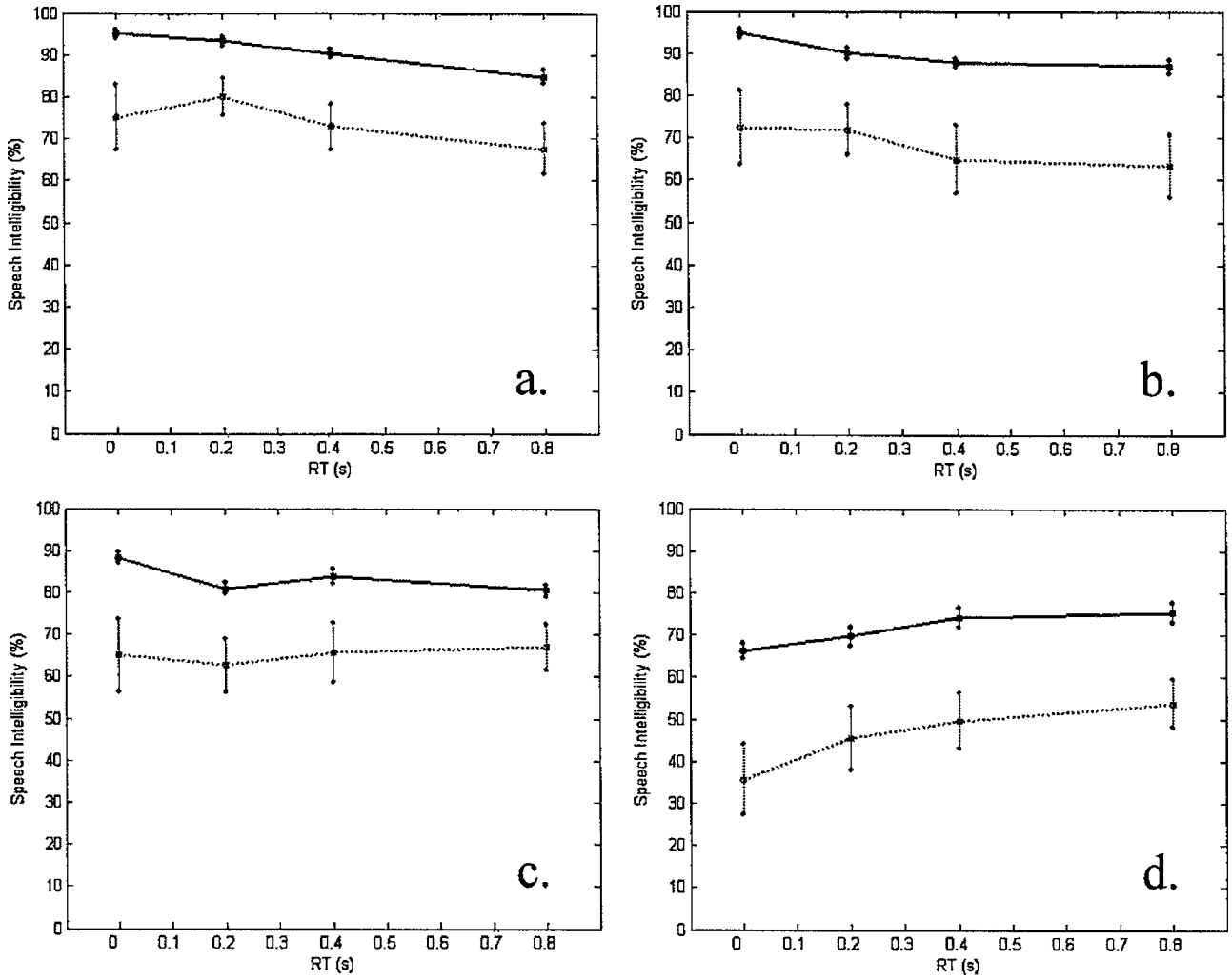

FIG. 2. Variation of mean speech-intelligibility score, and 95% confidence interval, with RT: (a) SNS=5 dB, noise 2; (b) SNS=0 dB, noise 2; (c) SNS =5 dB, noise 1; (d) SNS=0 dB, noise 1). (——) normal-hearing; (·····) hearing-impaired.

The mean scores for the four different RTs were found to be statistically different ($p<0.0005$). The mean scores at each RT were ranked using Tukey's paired comparison test[16] ($\alpha=0.05$). The rank orders by the mean speech-intelligibility scores varied in inverse relation to the RT, except for two pairs for which scores were not statistically different: RT =0.0 and 0.2 s with SNS=5 dB, and RT=0.4 and 0.8 s with SNS=0 dB. With SNS=5 dB, for RTs of 0.2 and 0.4 s, the mean speech-intelligibility scores were significantly higher than those with SNS=0 dB ($p<0.001$). However, the difference at RT=0.8 s was not significant, although the mean speech-intelligibility scores with SNS=5 dB were lower than those with SNS=0 dB. When RT was 0.0 s there was no statistical difference between SNS=5 dB and SNS=0 dB ($p=0.554$).

For hearing-impaired subjects, with noise 2, the mean speech-intelligibility scores were between 68.3% and 80.0% with SNS=5 dB, and between 64.3% and 72.5% with SNS =0 dB. The differences between the scores for the normal-hearing and hearing-impaired subjects were 13.3% to 19.5% with SNS=5 dB, increasing to 17.8% to 22.7% with SNS =0 dB. The ANOVA results for the difference in the mean speech-intelligibility test scores between the normal-hearing and hearing-impaired subjects indicated a statistically significant difference ($p<0.0005$). For the hearing-impaired subjects in this case, the 95% confidence intervals overlapped at the different RTs; therefore, statistical confidence in the rank order was lower. With SNS=5 dB, the peak (i.e., the locally highest value, possibly not statistically significant) occurred at RT=0.2 s and its confidence interval was relatively narrow; with SNS=0 dB, the highest mean speech-intelligibility score was at RT=0.0 s. For the four RTs tested, there were no significant differences between the scores with SNS=5 dB and 0 dB, except in the case of RT=0.2 s ($p<0.05$).

For normal-hearing subjects, when the noise source was positioned between the listener and the speaker (noise 1), with SNS=5 dB, mean speech-intelligibility scores varied from 80.4% to 88.3%. There were two peaks in the score, at RT=0.0 and 0.4 s; the difference was not statistically significant according to their rank order by Tukey's pairwise comparison test ($\alpha=0.05$). For the hearing-impaired subjects in the same conditions, mean speech-intelligibility scores varied from 61.7% to 67.6%. Of the values tested, the highest score occurred at RT=0.8 s. The differences between the

TABLE II. Adjusted coefficients of determination (R^2) associated with third-order-polynomial regression fits for each U_t value, for both normal-hearing and hearing-impaired subjects. The highest values are in bold.

	Normal-hearing		Hearing-impaired	
U_t	Measured	Predicted	Measured	Predicted
U_{20}	74.7	72.6	70.2	66.4
U_{30}	81.1	80.0	81.4	78.6
U_{40}	83.8	84.3	88.6	86.6
U_{50}	**85.2**	86.0	92.6	91.0
U_{60}	84.7	**86.4**	93.9	93.3
U_{70}	83.9	86.2	**94.5**	94.5
U_{80}	83.2	85.7	**94.5**	95.0
U_{90}	82.4	85.1	**94.5**	**95.3**
U_{100}	81.9	84.4	94.4	**95.3**
U_{110}	81.3	83.8	94.3	95.2
U_{120}	80.8	83.3	94.1	95.1

scores for the normal-hearing and hearing-impaired subjects varied from 12.8% to 22.3% with SNS=5 dB, and the differences were statistically significant.

In the case of noise 1, with SNS=0 dB, mean speech-intelligibility scores increased with increasing reverberation time for both normal- and hearing-impaired groups. Of the RTs tested, the mean speech-intelligibility score had its highest value at RT=0.8 s for both subject groups. The mean scores for the four RTs were again ranked using Tukey's paired comparison test (α=0.05), and were found to vary directly with RT, with 99.9% confidence. The lowest mean speech-intelligibility scores measured in the various test configurations varied between 66.2% and 75.3% for normal-hearing subjects, and between 36.7% and 55.1% for hearing-impaired subjects. The differences between the scores for the two subject groups varied from 20.2% to 29.5%, the biggest differences seen in the four cases. The difference between the results for SNS=0 and 5 dB was statistically significant ($p < 0.0005$) for both subject groups.

B. Best predicting early-time limit

For each sound-field configuration, useful-to-detrimental ratios were calculated from the predicted impulse responses and the applicable speech and noise levels, according to Eq. (1). They were also predicted using Eq. (2) for comparison with theory. Early-time limits of $t=20, 30, \ldots, 120$ ms were used. In order to identify the early-time limits which best predicted the measured speech intelligibility, regression analyses were performed on the mean speech-intelligibility scores for each sound-field configuration. Since the relationships were clearly not linear or quadratic, and following Bradley,[17] third-order polynomials were fit. Table II shows the strengths of the relationships—quantified by the goodness-of-fit measure, R^2—between each measure and speech intelligibility, for both the normal- and hearing-impaired results.

Since the form of the trendline and the number of data points was the same in every case, the success of each measure can be compared by comparing the corresponding R^2 values. In both calculation and prediction results, the trends were similar. $U_{50,m}$ and $U_{60,p}$ were most accurate at predicting the speech-intelligibility results for the normal-hearing subjects. However, for the hearing-impaired subjects, $U_{70,m}$,$U_{80,m}$, and $U_{90,m}$ and $U_{90,p}$ and $U_{100,p}$ predicted the results best; that is, with early-time limits 20–40 ms higher than for the normal-hearing group. That the limit was higher in prediction than in measurement may be due to the fact that the sound fields in the virtual rooms were not perfectly diffuse as assumed in prediction. The $U_{50,m}$ (for normal hearing, "NH") and $U_{80,m}$ (for hearing-impaired, "HoH") regression curves are shown in Fig. 3. The corresponding equations are as follows:

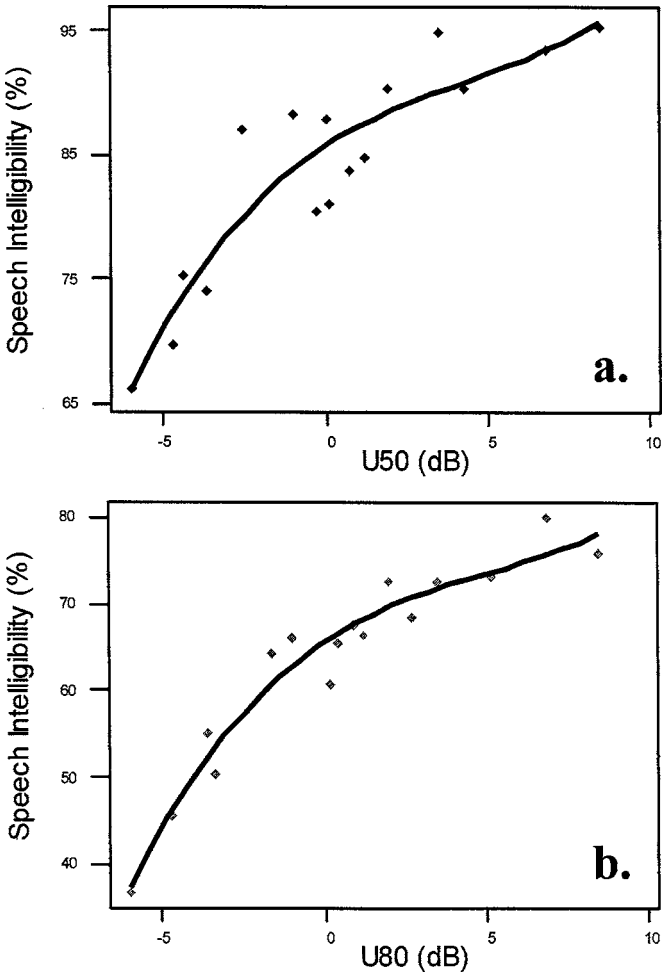

FIG. 3. Variation of mean speech-intelligibility score with useful-to-detrimental ratio using the best-fit early-time limit for all sound-field configurations and the best-fit third-order polynomial regression curves: (a) normal-hearing, $U_{50,m}$; (b) hearing-impaired, $U_{80,m}$.

Normal hearing:

$$\mathrm{SI}_{\mathrm{NH},m} = 85.2 + 1.94 \cdot U_{50,m} - 0.167 \cdot U_{50,m}{}^2 + 0.009 \cdot U_{50,m}{}^3 \quad R^2 = 85.2\%$$

$$\mathrm{SI}_{\mathrm{NH},p} = 85.6 + 1.77 \cdot U_{60,p} - 0.176 \cdot U_{60,p}{}^2 - 0.012 \cdot U_{60,p}{}^3 \quad R^2 = 86.4\%$$

Hearing-impaired:

$$SI_{HoH,m} = 64.1 + 2.86 \cdot U_{80,m} - 0.232 \cdot U_{80,m}{}^2 + 0.010 \cdot U_{80,m}{}^3 \quad R^2 = 94.5\%$$

$$SI_{HoH,p} = 64.7 + 2.66 \cdot U_{100,p} - 0.245 \cdot U_{100,p}{}^2 - 0.013 \cdot U_{100,p}{}^3 \quad R^2 = 95.3\%$$

V. DISCUSSION

The speech-intelligibility results for the normal-hearing and hearing-impaired subjects obtained with the Modified Rhyme Tests revealed some basic differences in perception by the two groups, and also some similarities.

Normal-hearing subjects in our study generally showed decreased speech intelligibility with increased reverberation time when the speech source was closer to the listener than the noise source (noise 2). When the noise source was between the speech source and the listener (noise 1), of the RTs tested, the optimal reverberation time varied from 0.4 to 0.8 s when the SNS varied from 5 to 0 dB, except for normal-hearing subjects with SNS=5 dB, for which the highest score was obtained with RT=0 s. Except for this result, the results generally support those of Hodgson and Nosal[2] (who also proposed a detailed explanation for their results).

In general, hearing-impaired subjects in our study showed similar trends to the normal-hearing subjects. This is consistent with recent work by Bradley, Sato, and Picard.[18] Of course, the hearing-impaired listeners were more adversely affected by reduced speech-to-noise level difference. Increased reverberation time generally resulted in increased speech intelligibility when the noise source was closer than the speech source to the listener (noise 1). Increased reverberation time above RT=0 or 0.2 s decreased speech intelligibility when the speech source was closer to the listener than the noise source (noise 2). When the noise source was farther from the listener than the speech source, the optimal reverberation time included zero and low, nonzero values. The results for the hearing-impaired subjects had relatively large standard deviations on their mean speech-intelligibility scores. The greatest standard deviations always occurred at RT=0 s among the four reverberation times. The smallest standard deviations always occurred at the RTs resulting in the peak mean speech intelligibility scores—i.e., at the optimal reverberation times.

When the noise source was farther from the listener than the speech source, the difference in score resulting from the two different speech- and noise-source output level differences (SNS) was smaller than those when the noise was between the speech source and the listener, for both the normal- and hearing-impaired subject groups.

VI. CONCLUSION

The results of this work generally support previous theoretical predictions.[2] With the noise source incorporated in a realistic manner, the optimal reverberation times were dependent on its positions relative to the speaker and the listener in a room. The optimal reverberation time was zero or near zero when the noise source was farther than the speaker; zero and higher nonzero reverberation times were found to be optimal when the noise source was between the listener and the speaker. If the speech-to-noise level difference is adverse for a subject group, some reverberation is required to increase the speech signal. The best early-time limit in the useful-to-detrimental energy ratio was 50–60 ms for normal-hearing subjects. U_{70}, U_{80}, or U_{90} were the most accurate predictors of the mean speech-intelligibility score. Hearing-impaired subjects apparently require more early energy than normal-hearing subjects with this range of the speech-to-noise level difference.

In this study, a simple, idealized classroom with approximately diffuse sound field and exponential sound decay was studied, as was the case in previous experimental work reported in the literature. Thus, the results depended on the overall reverberation in the room. They also depended on the source and receiver locations involved; Ref. 2 contains further discussion of the effect of varying these parameters. Ignored in this study is the influence of detailed room-acoustical factors such as individual reflections from the wall, floor, or ceiling; these relate to the exact room geometry and surface-absorption distribution, and exist in realistic rooms. It would be interesting to repeat the study using a more realistic model of a classroom, to improve the current work. The optimal reverberation might be found to vary from room to room depending, for example, on details of the arrival of reflections at the receiver. It would also be interesting to include replay-headphone equalization and angularly varying HRTF data in the simulations, though the relatively small standard deviations of the mean speech-intelligibility scores among the normal-hearing subjects suggests that considering differences in the subjects' HRTFs may not be necessary, and that the effect of headphone distortion is negligible.

ACKNOWLEDGMENTS

The authors gratefully acknowledge the collaboration of Maki Uemae for performing the CWH tests, and of Mark Bliss for creating the MRT recordings for this study.

[1] J. S. Bradley, "Speech intelligibility studies in classrooms," J. Acoust. Soc. Am. **80**(3), 846–854 (1986).
[2] M. R. Hodgson and E.-M. Nosal, "Effect of noise and occupancy on optimal reverberation times for speech intelligibility in classrooms," J. Acoust. Soc. Am. **111**(2), 931–939 (2002).
[3] A. K. Nabelek and P. K. Robinson, "Monaural and binaural speech perception in reverberation for listeners of various ages," J. Acoust. Soc. Am. **71**(5), 1242–1248 (1982).
[4] A. K. Nabeleck and J. M. Pickett, "Monaural and binaural speech perception through hearing aids under noise and reverberation with normal and hearing-impaired listeners," J. Speech Hear. Res. **17**, 724–739 (1974).
[5] A. K. Nabelek and J. M. Pickett, "Reception of consonants in a classroom as affected by monaural and binaural listening, noise, reverberation, and hearing aids," J. Acoust. Soc. Am. **56**(2), 628–639 (1974).
[6] T. Finitzo-Hieber and T. W. Tillman, "Room acoustics effects on monosyllabic word discrimination ability for normal and hearing-impaired children," J. Speech Hear. Res. **21**, 441–458 (1978).
[7] T. Houtgast, H. J. M. Steeneken, and R. Plomp, "Predicting speech intelligibility in rooms from the modulation transfer function: II. Mirror image computer model applied to rectangular rooms," Acustica **46**, 73–81 (1980).

[8]S. R. Bistafa and J. S. Bradley, "Reverberation time and maximum background-noise level for classrooms from a comparative study of speech intelligibility metrics," J. Acoust. Soc. Am. **107**(2), 861–875 (2000).
[9]M. R. Hodgson, "When is diffuse-field theory applicable?," Appl. Acoust. **49**(3), 197–207 (1996).
[10]M. Hodgson, "Evidence of diffuse surface reflections in rooms," J. Acoust. Soc. Am. **89**(2), 765–771 (1991).
[11]http://www.catt.se
[12]E. J. Kreul, J. C. Nixon, K. D. Kryter, D. W. Bell, J. S. Lang, and E. D. Schubert, "A proposed clinical test of speech discrimination," J. Speech Hear. Res. **11**(3), 536–552 (1968).
[13]http://www.auditec.com
[14]http://www.goldwave.com
[15]D. Henderson, R. J. Salvi, F. A. Boettcher, and A. E. Clock, "Neurophysiologic correlates of sensory-neural hearing loss," in *Handbook of Clinical Audiology*, 4th ed., edited by J. Katz (Williams & Wilkins, Baltimore, 1994), Chap. 4.
[16]W. Mendenhall, R. J. Beaver, and B. M. Beaver, *Introduction to Probability and Statistics*, 10th ed. (Duxbury Press, Belmont, CA, 1999).
[17]J. S. Bradley, "Predictors of speech intelligibility in rooms," J. Acoust. Soc. Am. **80**(3), 837–845 (1986).
[18]J. S. Bradley, H. Sato, and M. Picard, "On the importance of early reflections for speech in rooms," J. Acoust. Soc. Am. **113**(6), 3233–3244 (2003).

Experimental evaluation of radiosity for room sound-field prediction

Murray Hodgson
School of Occupational and Environmental Hygiene and Department of Mechanical Engineering, University of British Columbia, 2206 East Mall, Vancouver, BC, V6T 1Z3, Canada

Eva-Marie Nosal[a)]
Department of Mathematics, University of British Columbia, 1984 Mathematics Road, Vancouver, BC, V6T 1Z2, Canada

(Received 8 November 2005; revised 13 April 2006; accepted 25 May 2006)

An acoustical radiosity model was evaluated for how it performs in predicting real room sound fields. This was done by comparing radiosity predictions with experimental results for three existing rooms—a squash court, a classroom, and an office. Radiosity predictions were also compared with those by ray tracing—a "reference" prediction model—for both specular and diffuse surface reflection. Comparisons were made for detailed and discretized echograms, sound-decay curves, sound-propagation curves, and the variations with frequency of four room-acoustical parameters—EDT, RT, D_{50}, and C_{80}. In general, radiosity and diffuse ray tracing gave very similar predictions. Predictions by specular ray tracing were often very different. Radiosity agreed well with experiment in some cases, less well in others. Definitive conclusions regarding the accuracy with which the rooms were modeled, or the accuracy of the radiosity approach, were difficult to draw. The results suggest that radiosity predicts room sound fields with some accuracy, at least as well as diffuse ray tracing and, in general, better than specular ray tracing. The predictions of detailed echograms are less accurate, those of derived room-acoustical parameters more accurate. The results underline the need to develop experimental methods for accurately characterizing the absorptive and reflective characteristics of room surfaces, possible including phase.
[DOI: 10.1121/1.2216559]

PACS number(s): 43.55.Ka [NX] Pages: 808–819

I. INTRODUCTION

Acoustical radiosity is a geometrical sound-field prediction method that assumes diffusely reflecting boundaries. It was first developed in illumination engineering[1] as radiative transfer theory, and later in the thermal-engineering community, as the theory of radiation heat transfer.[2,3] Efficient methods have been developed to implement radiosity in computer graphics.[4,5] For an application to acoustics, to account for the finite speed of sound, Kuttruff developed the time-dependent integral equation.[6,7] Acoustical radiosity has seen much development since that time.[8–26]In particular, in a recent paper,[19] theory and methods relating to the application of acoustical radiosity to the room sound-field prediction were presented and validated in comparison with analytical solutions. In a subsequent paper,[20] the influences of various discretization parameters on the radiosity prediction accuracy were studied. Moreover, acoustical-radiosity methods were validated numerically by predicting the sound fields in cubic enclosures, and by comparing the results with ray-tracing predictions. Of primary interest here is the experimental evaluation of the accuracy of acoustical-radiosity predictions.

Various researchers have compared the characteristics of room sound fields predicted assuming diffuse, specular, or mixed specular/diffuse reflection.[21–24] Radiosity has been used to elucidate the characteristics of sound fields in rooms with diffusely reflecting surfaces.[21,24] Lam[23] showed that different ways of implementing mixed specular/diffuse reflection (none involving radiosity) can give somewhat different prediction results. Specular ray tracing (i.e., ray tracing assuming specular surface reflection) and radiosity have been shown to give significantly different predictions, as expected for diffusely versus specularly reflecting boundaries. The difference in parameter predictions is especially pronounced in disproportionate rooms, or those with nonuniform absorption distributions. Most notably, the assumption of diffuse reflection leads to lower reverberation times, lower steady-state levels at positions not close to a source, and to lower early energy and, therefore, early-to-late energy fractions due to the temporal "smearing" of individual early specular reflections to larger times. Diffuse ray tracing makes the same physical assumptions as radiosity—energy superposition and diffuse reflection—and it has been shown that they are equivalent in their limiting cases.[25] In practical cases (finite number of rays/patches in ray tracing/radiosity, and so on), predicted room parameters are very similar,[19,25] but the details of the echograms may differ.[20]

Comparisons between radiosity predictions and measurement in rooms have been limited to sound-pressure lev-

[a)]Current affiliation: School of Ocean and Earth Sciences and Technology, Department of Geology and Geophysics, University of Hawaii at Manoa, 1680 East-West Road POST 813, Honolulu, HI, 96822. Electronic mail: nosal@hawaii.edu

els and reverberation times for which, in general, good agreement is found. Kang[23] reports comparing radiosity predictions with scale-model results, obtaining good agreement. Shi *et al.*[26] report predicting reverberation times to within 1% of the measured values in two enclosures. Of course, the reverberation time and steady-state level do not fully characterize the acoustical characteristics of a room. Objective measures that depend on the early and late parts of the impulse response are needed to more fully quantify the listener perception of a sound field. These include early-decay time, clarity, and definition.[21] It is also of interest to compare the details of predicted and measured echograms and corresponding sound-decay curves.

Our primary objective in the present paper is to investigate how acoustical radiosity performs in predicting real room sound fields. This was done by comparing radiosity predictions with experimental results in three existing rectangular rooms. The rooms were chosen to have increasing nonuniformity in their geometry and surface-absorption distribution—both associated with increasingly nondiffuse sound fields—and different surface-reflection properties. Radiosity predictions were also compared with those by ray tracing, though this was a secondary objective. Ray-tracing can be considered to represent numerical experimentation,[21] and has been shown to be capable of predicting room sound fields accurately.[27] It was, therefore, used here as a "reference" prediction method.

II. PREDICTION APPROACHES

The underlying concept behind acoustical radiosity is quite simple. The enclosure is divided into elements (infinitesimally small in theory, finite in size in practical applications). Each element is considered as both a receiver and a secondary source. Considered as a receiver, the energy incident on an element is just the total energy arriving from all sources (both primary and secondary) in the enclosure. When acting as a secondary source, the element is treated as a diffuse reflector; energy leaving the element is proportional to the energy incident (according to the absorption coefficient of the element)—it does not depend on the angle of incidence, and it obeys Lambert's cosine law. In numerical implementations, form factors that give the fraction of energy leaving one element that is incident on another, are precomputed for a given environment, and stored in a look-up table. This initial "rendering" of the environment is the most computationally demanding step, after which the calculation of the sound field at any given receiver position can be done in real time.

Ray tracing involves modeling the workshop geometry and the acoustical properties (absorption and diffuse-reflection coefficients) of the surfaces, the source sound-power levels and positions, the receiver positions, and air absorption. Prediction involves tracing rays from the source as they reflect around the room, respecting the assumed reflection laws, and accounting for their energies and times of arrival when they reach the receiver position. The ray-tracing algorithm used here was the Monte-Carlo approach of Ondet and Barbry,[28] developed for predicting steady-state levels in industrial workshops. It was modified to allow individual room surfaces to reflect an arbitrary proportion of incident energy diffusely (according to Lambert's law) with the remainder reflecting specularly, as well as to predict room echograms (the pressure-squared time response at a receiver position, which results from the radiation of an energy impulse by a source). Note that this is apparently the model that Lam[23] referred to as "the secondary randomized diffuse rays model." Of course, both radiosity and ray tracing are energy-based prediction approaches that ignore the wave phase and, therefore, modal effects caused by wave interference. Thus, they would be expected to be less accurate at lower frequencies.

III. TEST ROOMS

This investigation involved three real rooms—a squash court, a classroom, and an office—of simple, rectangular geometry, which are very different from the long rooms, industrial workshops, and concert halls involved in previous studies.[22–24] Following are their descriptions.

A. Squash Court

The first test room was a regulation squash court with length=9.70 m, width=6.40 m, and height=6.15 m. The walls and ceiling were of painted concrete, and the floor was of varnished hardwood. A small door allowing access into the court was located in the center of the front wall. The court had a glass window along the top 2 m of the front wall. The Squash Court was chosen for its relatively uniform geometry (length, width, and height are similar) and because all walls had similar acoustical properties. With its quasicubic geometry and low, uniformly distributed surface absorption, the Squash Court would be expected to contain a highly diffuse sound field, even if the hard, flat surfaces are substantially specularly reflecting.[21,29]

B. Classroom

As shown in Fig. 1, the second test room was an empty, medium-sized classroom with length=13.70 m, width =7.80 m, and height=2.60 m. It had walls of painted concrete, blackboards on the front and sidewalls, a short length of curtain on one sidewall, a floor of linoleum tiles on concrete, and a ceiling of acoustical tiles glued to concrete. Two doors were located on one sidewall. The Classroom was chosen because it had one dimension (the length) that is much longer than the others, and because it had a nonuniform surface-absorption distribution (the ceiling is more absorbent than the other surfaces). Thus, the contained sound field would be expected to be somewhat nondiffuse,[21,29] despite the fact that some of the Classroom surfaces are sound absorbing or of panel construction, likely resulting in diffuse reflection.

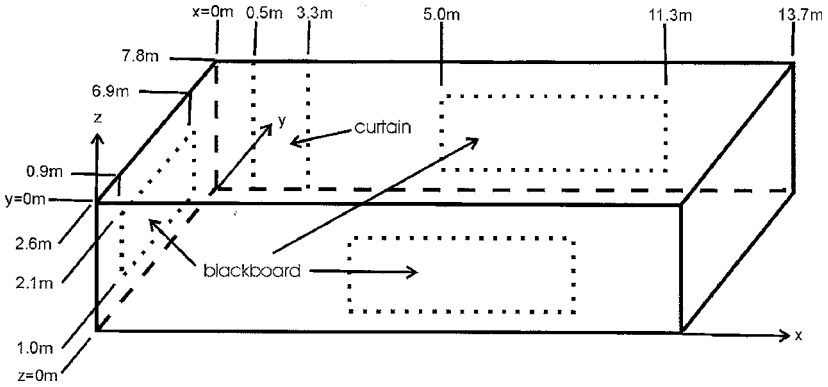

FIG. 1. Wireframe drawing of the Classroom.

C. Office

The third test room was a small, empty office, with dimensions of 5.36 m long, 3.94 m wide, and 2.71 m high. It had a floor of vinyl tile on concrete, four walls of drywall on 100 mm studs, and a suspended acoustical-tile ceiling. The Office was chosen because it was small—with relatively uniform geometry—but with a nonuniform absorption distribution (again, the ceiling is more absorbent than the other surfaces). Thus, like the Classroom, it would be expected to have a somewhat nondiffuse sound field and partially diffusely reflecting surfaces.

IV. EXPERIMENTATION

In each room, measurements were made of room impulse responses between an omnidirectional loudspeaker-array source and a receiver, using the Maximum Length Sequence System Analyzer (MLSSA). The maximum-length-sequence signal from MLSSA passed through a QSC Audio USA 370 power amplifier to the speaker array in the room. A Rion NA-29E Octave-Band Analyzer converted the acoustic signal at the receiver position into an electrical signal that was transmitted back to MLSSA for analysis.

Measurements were made for source and receiver positions located along the main horizontal axis of each of the rooms. In the Squash Court the source was 1.50 m from one wall and 1.30 m high; in the Classroom it was 2.00 m from one wall and 1.30 m high; in the Office it was 0.75 m from one wall and 1.35 m high. Receiver positions were 1.3 m high, and located at 0.5, 1.0, 2.0, 3.0 m from the source, as appropriate given the room size. For the Classroom and Office, a measurement bandwidth of 12 kHz was used, allowing results in octave bands from 125 to 8000 Hz to be obtained; measured impulse responses were 1.82 s long. Because of longer reverberation times in the Squash Court, longer impulse responses were needed to obtain accurate results. Thus, the bandwidth was decreased to 6 kHz, resulting in 3.64 s long responses, providing results from 125 to 4000 Hz. Before measurements were made, the omnidirectional loudspeaker array was calibrated with respect to the radiated acoustical power for the two MLSSA bandwidths used in the tests.

MLSSA analyzed the received signal from the microphone, and calculated the cross-correlation between the received response and the original signal, to find the impulse response and the corresponding echogram. From this, steady-state sound-pressure levels, and the values of room-acoustical parameters of interest—steady-state sound-pressure level L_p, early-decay time EDT, reverberation time RT, definition D_{50}, and clarity C_{80}—were calculated. The (unfiltered) impulse responses were then filtered in octave bands by the MLSSA filtering algorithms, and octave-band sound-decay curves calculated. The filtered echograms and sound-decay curves were subsequently used for comparison with predicted impulse responses, echograms, and decay

TABLE I. Air-absorption exponents and surface absorption coefficients used in the predictions.

			Frequency band (Hz)						
Room	Surface	Area	125	250	500	1000	2000	4000	8000
Air-absorption exponent (10^{-3} Np/m)			0.095	0.305	0.699	1.20	2.29	6.24	21.5
Squash Court	**All**	415.0	0.106	0.057	0.042	0.036	0.038	0.031	–
Classroom	**Room average**		0.101	0.102	0.110	0.113	0.131	0.128	0.086
	Blackboard	22.0	0.010	0.010	0.010	0.010	0.030	0.040	0.020
	Walls	82.2	0.020	0.010	0.030	0.030	0.030	0.040	0.020
	Ceiling	106.2	0.270	0.280	0.290	0.300	0.350	0.340	0.230
	Floor	106.2	0.020	0.020	0.020	0.020	0.020	0.010	0.010
	Curtain	7.3	0.010	0.010	0.010	0.010	0.020	0.030	0.020
Office	**Room average**		0.081	0.061	0.055	0.052	0.080	0.095	0.087
	Ceiling	21.1	0.200	0.140	0.160	0.170	0.270	0.300	0.300
	Floor	21.1	0.010	0.010	0.010	0.010	0.010	0.020	0.010
	Walls	50.4	0.060	0.050	0.030	0.020	0.030	0.040	0.030

TABLE II. Numerical parameters used in the radiosity predictions.

	Squash Court	Classroom	Office
Echogram length (s)	5.03	1.14	2.5
Echogram resolution (s)	1/8000	1/12000	1/12000
t_{max} (s)^2	4.0	1.0	2.0
t_{final} (s)^2	5.0	1.1	2.5

curves. Octave-band-filtered, steady-state sound-pressure levels and other room-acoustical parameters were read directly from the MLSSA output display.

All measurements were done twice by two different experimenters, the two results being virtually identical, confirming the high quality of the experimental results.

V. PREDICTION

For each of the three test rooms, predictions were made of echograms, sound-decay curves, L_p, EDT, RT, D_{50}, and C_{80} using radiosity and ray tracing. To model the test rooms, their dimensions, and the same source and receiver positions as used in the experimental work, were input. The sound-power levels of the omnidirectional loudspeaker array used in the testing were used in the predictions. Results were obtained in octave bands from 125 to 8000 Hz (4000 Hz for the Squash Court), for all source and receiver positions in the rooms. Echograms and sound-decay curves are only presented for the receiver position at 3 m from the source, and for the 1000 Hz octave band. Sound-propagation curves—SP(r), showing the variation with distance r of steady-state levels normalized to the source sound-power level: SP(r) $=L_p(r)-L_w$—are presented at 250, 1000, and 4000 Hz. Presented here are octave-band values, at the 3 m receiver position, of EDT, RT, D_{50}, and C_{80}, determined as follows.

(i) EDT and RT were determined, respectively, from the 0 to −10 dB and −5 to −35 dB parts of the sound-decay curves.

(ii) D_{50} and C_{80} were calculated from the echogram $E(t)$, with time $t=0$ reset to the arrival time of the direct sound, as follows:[21]

$$D_{50} = \frac{\int_0^{50\ \mathrm{ms}} E(t)dt}{\int_0^T E(t)dt}\ \%\ , \tag{1}$$

$$C_{80} = 10\log\left(\frac{\int_0^{80\ \mathrm{ms}} E(t)dt}{\int_{80\ \mathrm{ms}}^T E(t)dt}\right)\ \mathrm{dB}, \tag{2}$$

in which T is the maximum time to which the echogram was measured or predicted.

Regarding air absorption, environmental conditions in all rooms were typically 23 °C and 50% relative humidity under standard atmospheric pressure. Corresponding air-absorption exponents were found using the formulas of Bass *et al.*,[30] and are listed in Table I.

A difficult parameter to estimate accurately for use in prediction is the room surface-absorption coefficient, which, of course, can vary from surface to surface, and with frequency. While methods exist for measuring the acoustical properties of individual room surfaces accurately *in situ*,[31] their application here was beyond the scope of the present study. Therefore, following other researchers, absorption coefficients $\bar{\alpha}$ were estimated from measured reverberation times, by the following empirical method. First, the average octave-band surface-absorption coefficients $\bar{\alpha}$ were found

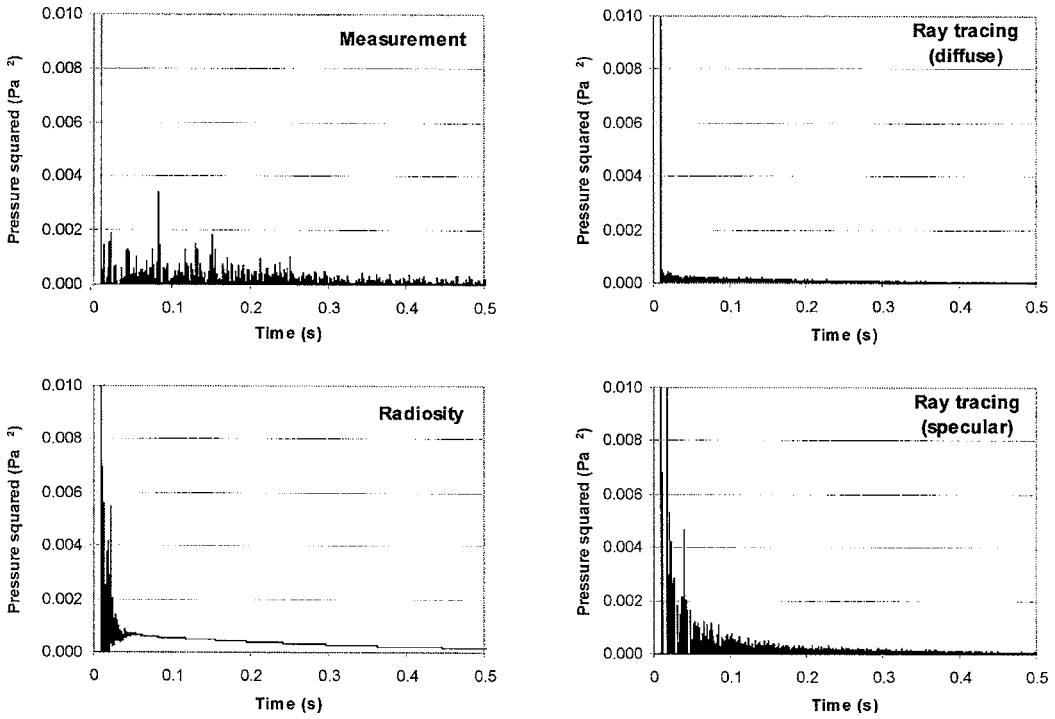

FIG. 2. Measured and predicted echograms in the Squash Court at $r=3$ m and 1000 Hz. Note that the amplitudes of the direct-sound and some first-reflection peaks exceed the plotted range of the abscissa.

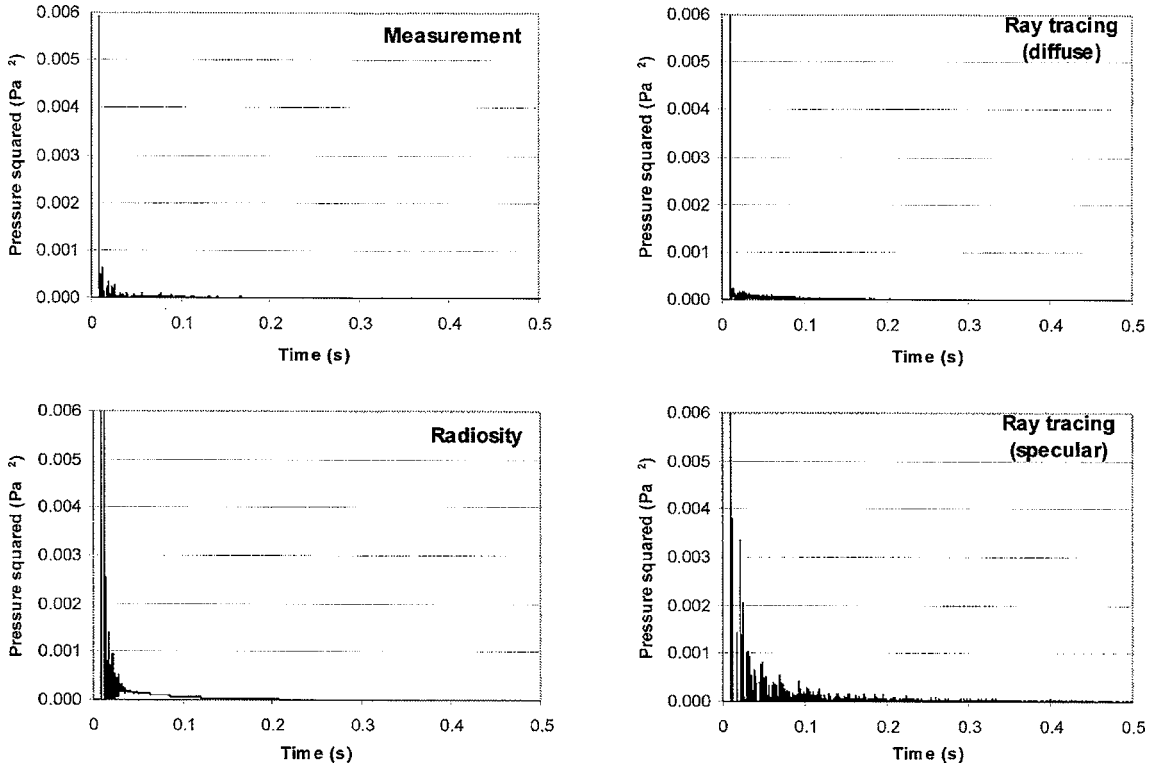

FIG. 3. Measured and predicted echograms in the Classroom at $r=3$ m and 1000 Hz. Note that the amplitudes of the direct-sound and some first-reflection peaks exceed the plotted range of the abscissa.

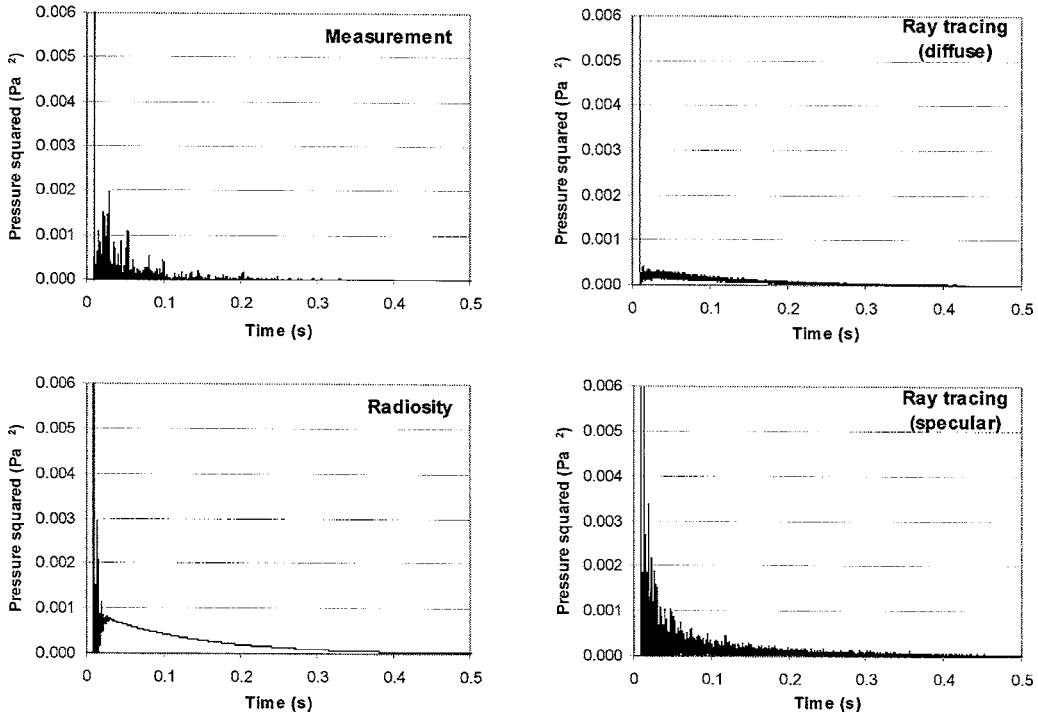

FIG. 4. Measured and predicted echograms in the Office at $r=3$ m and 1000 Hz. Note that the amplitudes of the direct-sound and some first-reflection peaks exceed the range of the abscissa.

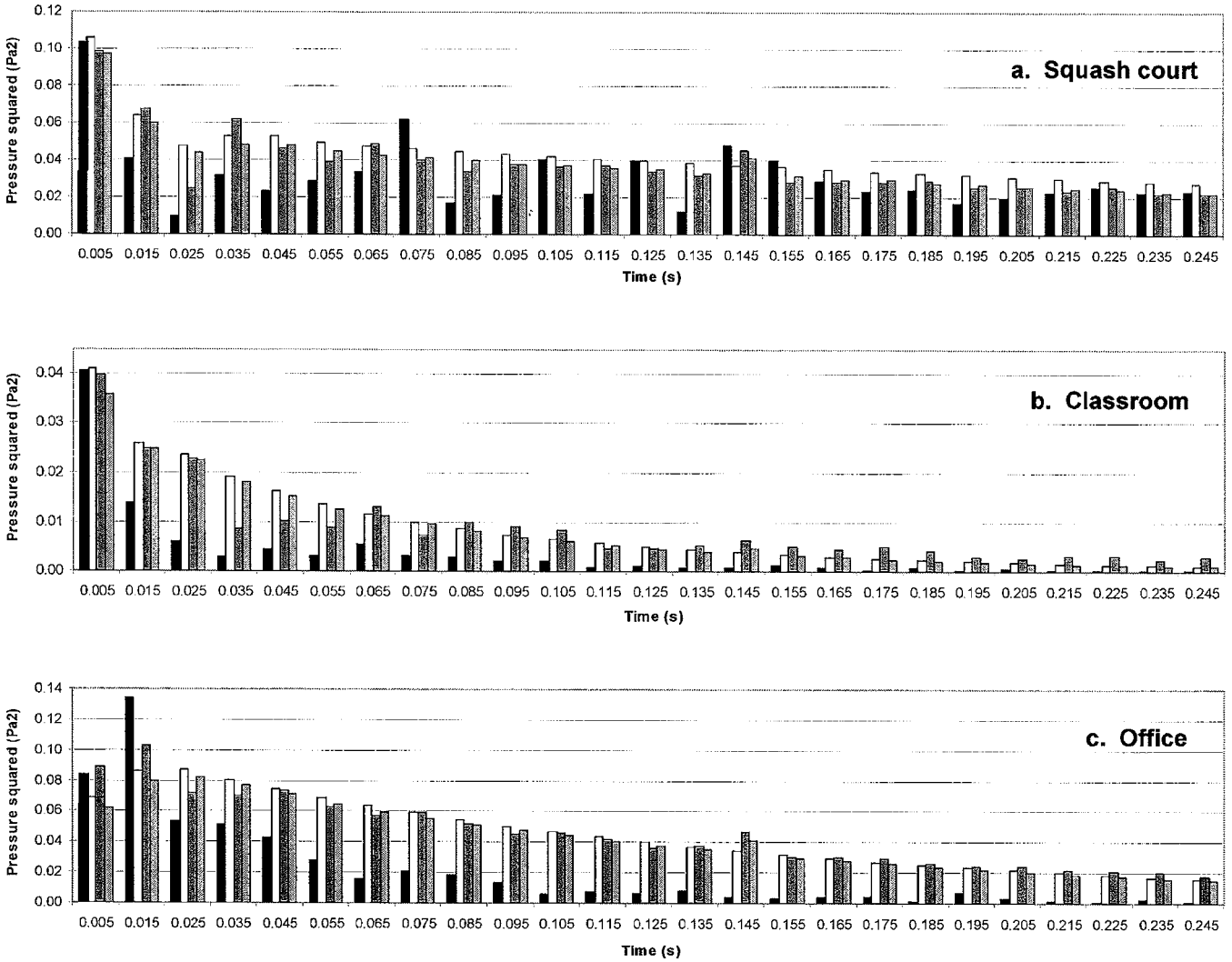

FIG. 5. Measured and predicted discretized echograms at $r=3$ m and 1000 Hz: ■, measured; □, radiosity; ■, ray tracing (specular); ■ ray-tracing (diffuse).

from the room-average, octave-band, measured reverberation times RT using diffuse-field theory:

$$\bar{\alpha} = 1 - \exp\left[\frac{V}{S}\left(4m - \frac{24 \ln 10}{c\,\mathrm{RT}}\right)\right], \tag{3}$$

where V is the room volume in m^3, S is the surface area of the room in m^2, m is the air-absorption exponent in m^{-1}, and c is the sound speed in m/s. Second, absorption was distributed over the room surfaces based on physical considerations, and in such a way that the assigned absorption coefficients combined to give the average absorption coefficients found in the first step. The absorption coefficients for the rooms found by this method are given in Table I.

In order to investigate the influence of absorption distribution on radiosity prediction, absorption coefficients of surfaces in the squash court and office were varied first by 10%, then by 50%, keeping the same average values. Small changes in the predicted echograms resulted, but predicted values of the other acoustical parameters did not change. Thus, for example, the coefficients of the glued-tile ceiling in the Classroom, which were likely too high at low frequency, do not significantly affect the results, except possibly in the case of specular ray tracing.

Ray-tracing predictions were done for the cases of fully specular and fully diffuse reflection, as described in more detail below. To ensure results were statistically meaningful, representing ensemble averages, echograms averaged from those predicted for 32 different values of the integer used to initialize the random-number generator in the ray-tracing algorithm are presented.

Ray tracing was run with 10^6 rays traced for 500 reflections. The receiver was a cubic cell with a side length of 0.1 m. Echograms were predicted to 0.5 s with a resolution of 1/1000 s in the Squash Court, and to 1 s with a resolution of 1/36 000 s in the other two rooms. In the radiosity predictions, the surfaces of the Squash Court were divided into 291 patches, while the classroom and office had 256 patches. These subdivisions were deemed sufficient for an accurate prediction, based on previous discretization investigations[20] and on several exploratory predictions that showed insignificant variation from the results of predictions with finer meshing. Different time-discretization periods and time limits

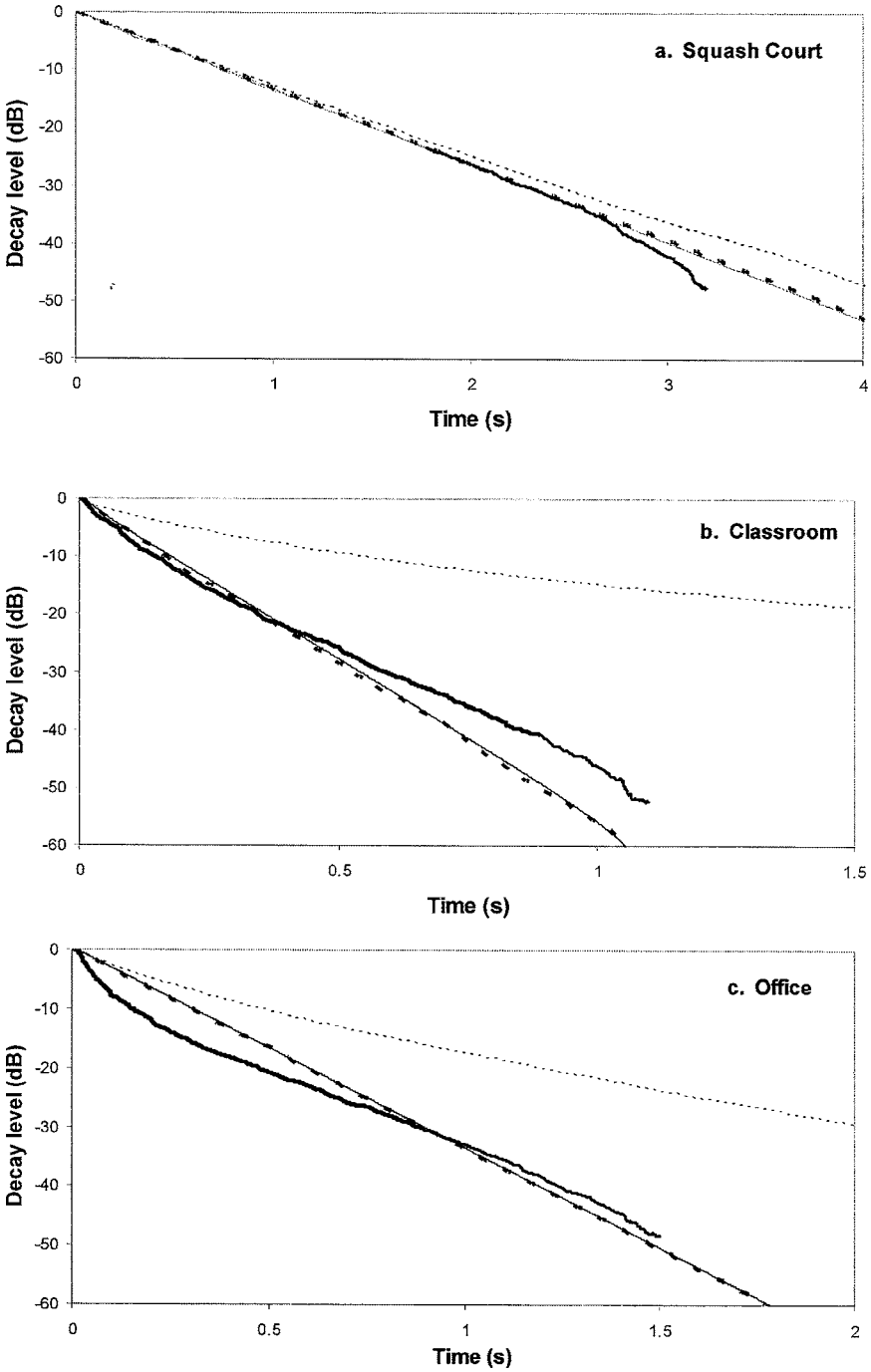

FIG. 6. Measured and predicted sound-decay curves at $r=3$ m and 1000 Hz: (—) measured; (—) radiosity; (···) ray tracing (specular); (– – –) ray tracing (diffuse).

were used for different sets of predictions, as indicated in Table II, which also shows the maximum times to which echograms were predicted.

VI. RESULTS

We now compare the predictions by the three models, keeping in mind the different ways they modeled surface reflection. Recall that the main objective was to evaluate the accuracy of the radiosity approach. Secondary aims were to confirm what is known about the accuracies of different prediction approaches, and the effect of different surface-reflection assumptions. In particular, we compare prediction with experiment, to evaluate the accuracy of the prediction approaches and possibly draw conclusions about the acoustical characteristics—e.g., the surface absorption and reflection properties—of the rooms.

A. Echograms

Figure 2 shows the first 50 ms of the 1 kHz echograms at $r=3$ m in the Squash Court obtained from measurement, from prediction by radiosity, as well as by ray tracing for both diffuse and specular reflection. Figures 3 and 4, respectively, show the corresponding echograms for the Classroom and the Office.

In all cases, the measured and predicted echograms look somewhat different—especially in the Squash Court. In particular, radiosity, and diffuse ray-tracing are different. The

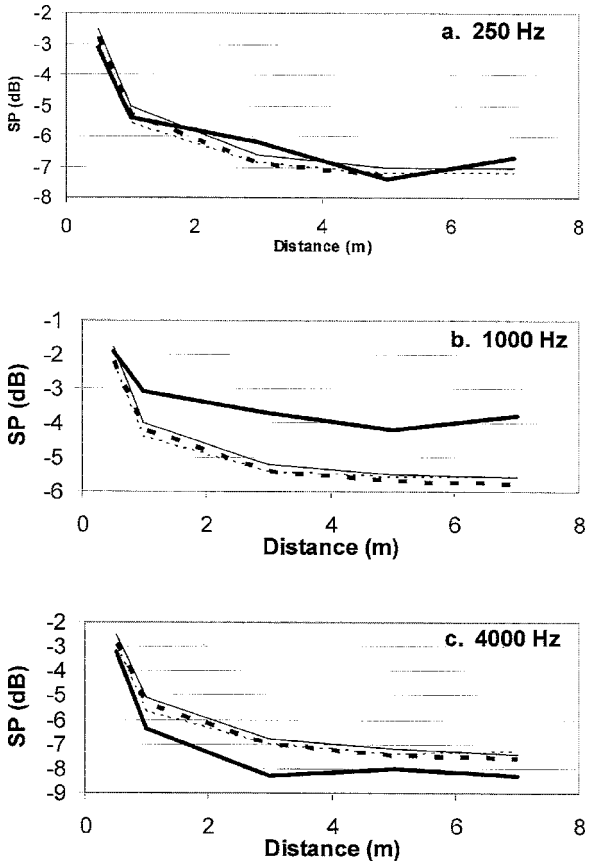

FIG. 7. Sound-propagation curves in the Squash Court: (—) measured; (—) radiosity; (···) ray-tracing (specular); (– – –) ray tracing (diffuse).

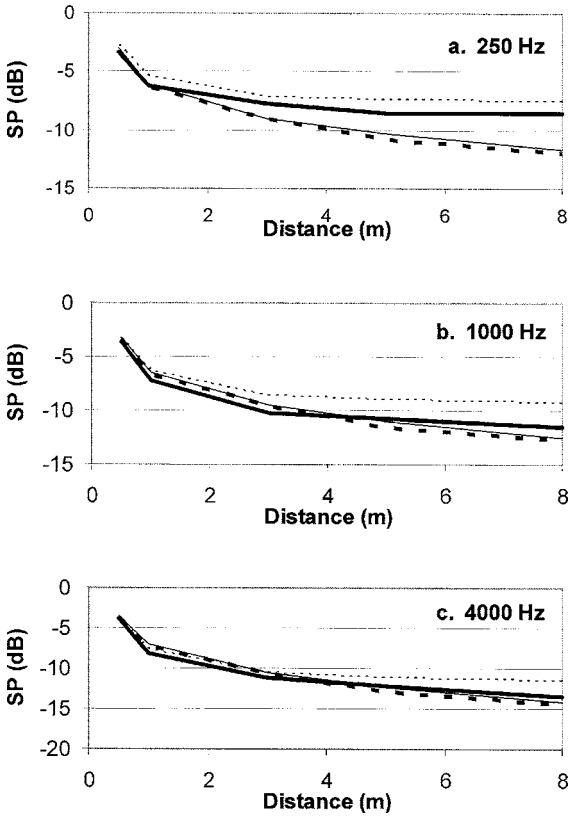

FIG. 8. Sound-propagation curves in the Classroom: (—) measured; (—) radiosity; (···) ray-tracing (specular); (– – –) ray-tracing (diffuse).

differences between the echograms predicted by radiosity and by ray-tracing are similar to those discussed in Ref. 20. The measured, radiosity, and specular ray-tracing echograms contain distinct early-reflection peaks; these are not apparent with diffuse ray tracing, which apparently smears out individual reflections. It is interesting that this does not occur with radiosity. The echogram predicted by diffuse ray tracing apparently has the least energy in the first 100 ms, that by specular ray-tracing the most, and that by radiosity an intermediate amount. In the Squash Court, the echogram predicted by specular ray-tracing apparently agrees best, though not very well, with experiment. This suggests that the Squash Court surfaces were specularly reflecting, as might be expected given its hard, flat surfaces. In the Classroom, agreement appears closest with diffuse ray tracing (and, possibly, radiosity), consistent with the occurrence of diffuse reflection. In the Office, radiosity and, surprisingly, specular ray tracing gave the closest agreement.

B. Discretized echograms

The same data that was used to create the echograms in the previous section were used to calculate the discretized echograms for the three rooms. The time resolution used to obtain these figures was 10 ms. The first 250 ms of these echograms are shown in Fig. 5. In general, radiosity and diffuse ray tracing predicted similar results, both predicting—because of the temporal smearing that results from diffuse reflection—fairly smooth variations of amplitude with time, with radiosity predicting slightly higher amplitudes. At larger times, specular ray tracing is similar; however, at shorter times, specular ray-tracing differs, predicting significant local fluctuations of energy with time, associated with individual specular reflections. None of the prediction methods accurately predicted the measured distribution of energy with time. The measured discretized echograms show fairly smooth variations of amplitude with time in the Classroom and Office, as predicted by radiosity and diffuse ray-tracing, and consistent with diffuse reflection. In the case of the Squash Court, the measured discretized echograms show significant local fluctuations of energy with time, similar to those predicted by specular ray tracing, at least at shorter times; again, this is consistent with specular reflection. In general, predicted levels are higher than those measured.

C. Sound-decay curves

Figure 6 shows the measured and predicted 1000 Hz sound-decay curves at $r=3$ m in the three rooms. As expected from previous research, the curves predicted by radiosity and diffuse ray tracing are very similar in all cases. Those predicted by specular ray tracing have lower rates of decay, particularly in the Classroom and Office. Radiosity and diffuse ray tracing gave good general agreement with measurement, while specular ray tracing underestimated the rate of decay. Assuming that surface absorption was accurately modeled, these results suggest that the surfaces of all three rooms—especially the Classroom and Office—were somewhat diffusely reflecting at 1000 Hz.

In the Squash Court, radiosity and diffuse ray tracing accurately predicted the complete measured sound-decay curve, while specular ray tracing underestimated the decay rate slightly. This is consistent with surface absorption being well modeled, and the occurrence of diffuse surface reflection. In the Classroom, radiosity and diffuse ray tracing only predicted the initial part of the decay curves well. This could indicate that, while the absorption of surfaces close to the source was correctly modeled, that on more distant surfaces was overestimated. In the Office, radiosity and diffuse ray tracing only predicted the final part of the decay curves well, possibly indicating that, while the absorption of surfaces far from the source was correctly modeled, that on closer surfaces was underestimated.

D. Sound-propagation curves

Figure 7 shows the measured and predicted sound-propagation curves at 1 kHz in the Squash Court at 250, 1000, and 4000 Hz. Figures 8 and 9 show the corresponding results for the Classroom and Office. In all cases, the measured and predicted levels at short distances were similar, indicating that the output powers of the experimental sound source had been accurately determined. Levels predicted by radiosity and diffuse ray tracing were very similar in all three rooms and frequencies, and at all distances. Specular ray tracing predicted similar levels in the Squash Court, confirming that the type of surface reflection has little effect on steady-state levels in rooms that already have diffuse sound fields because of their proportionate geometries and uniform absorption distributions[29]—and in the Office at 250 Hz. However, levels were higher in the Classroom, and in the Office at 1000 and 4000 Hz.

In the Squash Court, prediction agreed well with measurement at 250 Hz, was as much as 2 dB high at 1000 Hz, and was about 1 dB low at 4000 Hz. These differences are surprisingly large given the short source/receiver distances involved. They suggest that the surface absorption used in prediction was too high at 1000 Hz and too low at 4000 Hz, and may partially be due to modal effects. In the Classroom, specular ray-tracing agreed best with the measurement at 250 Hz, with radiosity and diffuse ray tracing agreeing best at higher frequencies. These results are consistent with specular reflection and correctly predicted absorption, or with diffuse reflection and underestimated absorption, at 250 Hz. At higher frequencies, the results suggest that the room surfaces were diffusely reflecting and that the absorption assumed in prediction was correct. In the Office, levels predicted by all three methods were generally higher than those measured, particularly at 4000 Hz. At 250 and 1000 Hz, the measured curves show local level variations that are likely due to modal effects, and that are not pre-

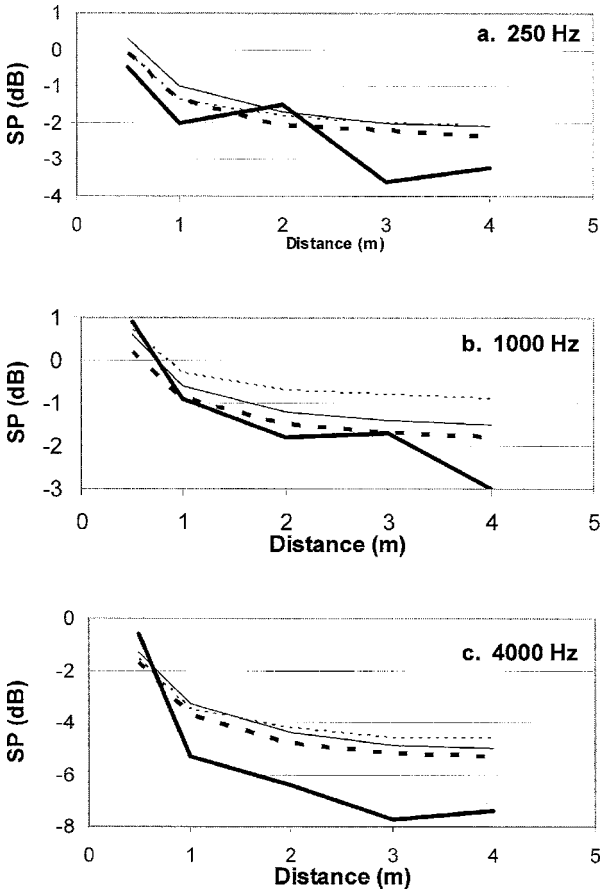

FIG. 9. Sound-propagation curves in the Office: (—) measured; (—) radiosity; (···) ray-tracing (specular); (– – –) ray tracing (diffuse).

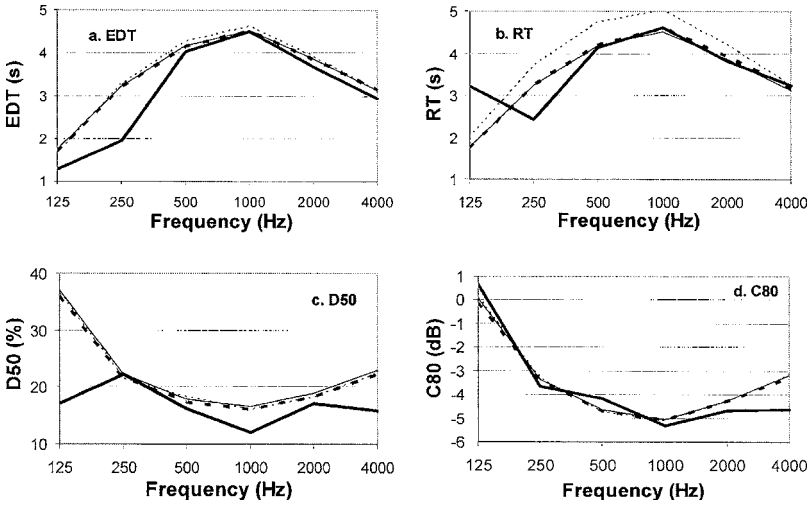

FIG. 10. Parameter values in the Squash Court at $r = 3$ m: (—) measured; (—) radiosity; (···) ray tracing (specular); (– – –) ray tracing (diffuse).

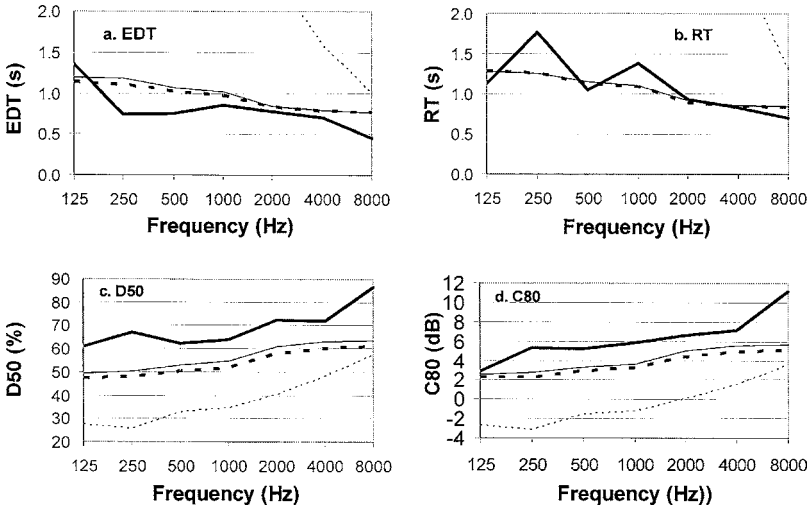

FIG. 11. Parameter values in the Classroom at $r=3$ m: (—) measured; (—) radiosity; (···) ray-tracing (specular); (– – –) ray tracing (diffuse). Note that many of the measured RT values exceed the plotted range of the abscissa.

dicted. The results suggest that surface absorption at these frequencies was underestimated; conclusions regarding surface diffusion cannot be drawn.

E. Room-acoustical parameters

Figure 10 shows the variations with frequency of EDT, RT, D_{50}, and C_{80} at $r=3$ m for the Squash Court. Figures 11 and 12 show the corresponding results for the Classroom and Office. In all cases, predictions by radiosity and diffuse ray tracing were very similar.

In the Squash Court, specular ray-tracing agreed well with the other two prediction approaches, except in the case of RT, for which it predicted slightly higher values due to the slightly concave sound-decay curves [see Fig. 6(a)]. Prediction generally agreed well with experiment, except at low frequencies—at which the predicted EDT's and D_{50}'s were high, at which predicted RT's were low at 125 Hz and high at 250 Hz, and for C_{80} at 4000 Hz—at which the prediction was high. The worse agreement at low frequencies is likely due to surface-panel-vibration and modal effects which are not predicted.

In the Classroom, the prediction by radiosity and diffuse ray tracing generally agreed well with experiment, with a slightly tendency for EDT to be overestimated, RT underestimated, and D_{50} and C_{80} underestimated. As expected from the disproportionate geometry and nonuniform absorption distribution, the prediction by specular ray tracing agreed poorly with experiment, massively overestimating EDT and RT, and underestimating D_{50} and C_{80}. In other words, the prediction underestimated the early energy relative to the late energy. At low frequency, this may, in part, be due to the excessive absorption assumed for the relatively near ceiling surface.

In the Office, similar trends occurred. Specular ray tracing again overestimated EDT and RT and underestimated D_{50} and C_{80}. Radiosity and diffuse ray tracing gave better agreement with experiment, especially for RT, but still overestimated EDT and underestimated D_{50} and C_{80}.

F. Discussion

Radiosity and diffuse ray tracing generally agreed closely. This is not surprising, since these are alternative energy-based prediction approaches that assume diffuse surface reflection. The one exception was in the prediction of the detailed echograms—radiosity predicted somewhat discrete early reflections, whereas diffuse ray tracing did not. In any case, this clearly did not affect derived acoustical parameters, which are predicted to be virtually identical by the two

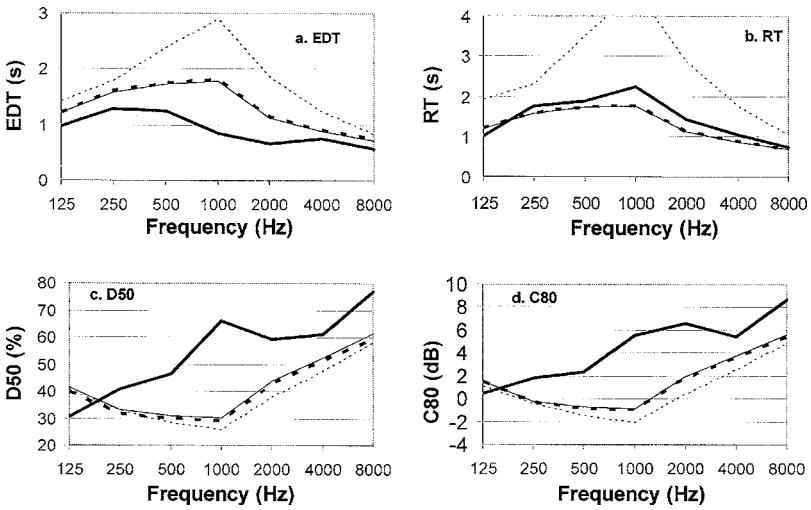

FIG. 12. Parameter values in the Office at $r=3$ m: (—) measure d; (—) radiosity; (···) ray-tracing (specular); (– – –) ray tracing (diffuse).

methods. Specular ray tracing can give very different results from radiosity and diffuse ray tracing. This is particularly evident in rooms, such as the Classroom and Office, that have inherently nondiffuse sound fields and somewhat diffusely reflecting surfaces.

The results demonstrate that it is hard to draw definitive conclusions about the accuracy of the different models, or the acoustical characteristics of rooms assumed in prediction, from comparisons of prediction with experiment—even in the case of simple, rectangular rooms. If it is known that a room is accurately modeled, conclusions can be drawn about the inherent accuracy of the prediction models. If it is known that the predictions models are accurate, conclusions can be drawn about the accuracy of the room characteristics assumed in the room model. The situation is complicated by the fact that a room model includes information about both the absorption and the diffusion of the room surfaces. These have different effects on different prediction parameters; sometimes they have similar effects on a particular parameter, so that the same prediction results—and the same agreement with experimental results—can be obtained by increasing (decreasing) one of the factors and decreasing (increasing) the other. More accurate methods are needed for characterizing the absorptive and reflective properties of room surfaces, especially *in situ* and possibly including phase effects. The results for different parameters have somewhat different implications regarding the apparent accuracy of the room models. In other words, different values of the prediction parameters describing the rooms may be needed to predict different room-acoustical parameters; this is dissatisfying, as noted by Lam.[23] Note also that only completely specular and completely diffuse reflection (modeled by Lambert's Law) were studied here. In reality, partially specular and partially diffuse reflection may have occurred at the test-room surfaces. The low-frequency results may also be indicative of the inherent limitations of energy-based models. The large differences between the measured and predicted 1000 Hz impulse responses may call into question the MLSSA system's octave-band filtering algorithms.

Radiosity predicted detailed and discretized echograms poorly in the Squash Court, and fairly well in the Classroom and Office. In the latter two cases, it predicted some characteristics of the echograms (e.g., their lack of strong local variations) very well. It predicted sound-decay curves quite well. Sound-propagation curves were predicted well in some cases, less well in others. As this was also true of the other models, definitive conclusions regarding the accuracy of radiosity are difficult to draw. The same is true with respect to prediction of the other room-acoustical parameters. Certainly, radiosity tended to overestimate early-decay times, and underestimate early-to-late energy fractions.

VII. CONCLUSION

In order to evaluate the accuracy of radiosity for room sound-field prediction, radiosity predictions were compared with ray-tracing predictions and measurements made in three rooms—a Squash Court, a Classroom, and an Office. Ray-tracing predictions were also made for the cases of completely specular and completely diffuse surface reflection for comparison with a "reference" prediction model. Radiosity and diffuse ray-tracing predictions often agreed closely, but were quite different from specular ray tracing. Radiosity showed reasonable agreement with experiment in some, but not all, cases. This was particularly true in the Classroom and Office, which likely had somewhat diffusely reflecting surfaces—radiosity assumes diffuse reflection. The results suggest that an assumption of purely diffuse reflection—as made by radiosity—is less limiting than an assumption of purely specular reflection.

In summary, the results of this work show that radiosity can predict room sound fields with some accuracy, at least as well as one other energy-based approach (diffuse ray tracing) and, in general, better than another energy-based approach (specular ray tracing). Predictions of detailed echograms—required, for example, for accurate auralization—are less accurate, those of derived room-acoustical parameters—used to evaluate the acoustical environments in the room—are more accurate. Radiosity prediction is most accurate in rooms with surfaces that—for example, because they are sound absorbing and/or of panel constructions—reflect sound somewhat diffusely. The results of this study highlight the difficulties in comparing the prediction to measurement in rooms, and the importance of developing improved methods for accurately characterizing the absorptive and reflective properties of room surfaces.

[1]Z. Yamauti, "The light flux distribution of a system of inter-reflecting surfaces," J. Opt. Soc. Am. **13**, 561–571 (1926).
[2]E. Sparrow and R. Cess, *Radiation Heat Transfer* (Hemisphere, Washington, DC, 1978).
[3]R. Siegel and J. Howell, *Thermal Radiation Heat Transfer*, 3rd ed. (Hemisphere, Washington, DC, 1981).
[4]M. F. Cohen and J. R. Wallace, *Radiosity and Realistic Image Synthesis* (Academic, Boston, 1993).
[5]F. X. Sillion and C. Puech, *Radiosity and Global Illumination* (Morgan Kaufmann, San Fransisco, 1994).
[6]H. Kuttruff, "Simulierte Nachhallkurven in Rechteckräumen mit diffusem Schallfeld," Acustica **25**, 333–342 (1971).
[7]H. Kuttruff, "Nachhall und effective Absorption in Räumen mit diffuser wandreflexion," Acustica **35**, 141–153 (1976).
[8]M. M. Carroll and C. F. Chien, "Decay of reverberant sound in a spherical enclosure," J. Acoust. Soc. Am. **62**, 1442–1446 (1977).
[9]M. M. Carroll and R. N. Miles, "Steady-state sound in an enclosure with diffusely reflecting boundary," J. Acoust. Soc. Am. **64**, 1424–1428 (1978).
[10]W. B. Joyce, "Exact effect of surface roughness on the reverberation time of a uniformly absorbing spherical enclosure," J. Acoust. Soc. Am. **64**, 1429–1436 (1978).
[11]E. N. Gilbert, "An iterative calculation of reverberation time," J. Acoust. Soc. Am. **69**, 178–184 (1981).
[12]M. R. Schroeder and D. Hackman, "Iterative calculation of reverberation time," Acustica **45**, 269–273 (1980).
[13]H. Kuttruff, "Stationäre Schallausbreitung in Flachrämen," Acustica **57**, 62–70 (1985).
[14]H. Kuttruff, "A simple iteration scheme for the computation of decay constants in enclosures with diffusely reflecting boundaries,"J. Acoust. Soc. Am. **98**, 288–293 (1995).
[15]H. Kuttruff, "Energetic sound propagation in rooms," Acust. Acta Acust. 83, 622–628 (1997).
[16]R. N. Miles, "Sound field in a rectangular enclosure with diffusely reflecting boundaries," J. Sound Vib. **922**, 203–226 (1984).
[17]T. Lewers, "A combined beam tracing and radiant exchange computer model of room acoustics," Appl. Acoust. **38**, 161–178 (1993).
[18]L. P. Franzoni, D. B. Bliss, and J. W. Rouse, "An acoustic boundary element method based on energy and intensity variables for prediction of

high-frequency broadband sound fields," J. Acoust. Soc. Am. **110**, 3071–3080 (2001).
[19]E.-M. Nosal, M. R. Hodgson, and I. Ashdown, "Improved algorithms and methods for room sound-field prediction by acoustic radiosity in arbitrary polyhedra," J. Acoust. Soc. Am. **116**, 970–980 (2004).
[20]E.-M. Nosal, M. R. Hodgson, and I. Ashdown, "Investigation of the validity of radiosity for sound field prediction in cubic rooms," J. Acoust. Soc. Am. **116**, 3505–3514 (2004).
[21]H. Kuttruff, *Room Acoustics*, 4th ed. (Spon Press, London, 2000).
[22]M. R. Hodgson, "Evidence of diffuse surface reflections in rooms," J. Acoust. Soc. Am. **89**, 765–771 (1991).
[23]Y. M. Lam, "A comparison of three diffuse reflection modeling methods used in room acoustics computer models," J. Acoust. Soc. Am. **100**, 2181–2191 (1996).
[24]J. Kang, "Reverberation in rectangular long enclosures with diffusely reflecting boundaries," Acta. Acust. Acust. **88**, 77–87 (2002).
[25]A. LeBot and A. Bocquillet, "Comparison of an integral equation on energy and the ray-tracing technique in room acoustics," J. Acoust. Soc. Am. **108**, 1732–1740 (2000).
[26]J. Shi, A. Zhang, J. Encarnação, and M. Göbel, "A modified radiosity algorithm for integrated visual and auditory rendering," Comput. Graphics **17**, 633–642 (1993).
[27]M. R. Hodgson, "On the accuracy of models for predicting sound propagation in fitted rooms," J. Acoust. Soc. Am. **88**, 871–878 (1989).
[28]A. M. Ondet and J. L. Barbry, "Modelling of sound propagation in workshops using ray-tracing," J. Acoust. Soc. Am. **85**, 29–46 (1987).
[29]M. R. Hodgson, "When is diffuse-field theory applicable," Appl. Acoust. **49**, 197–207 (1996).
[30]H. E. Bass, L. C. Sutherland, A. J. Zuckerwar, D. T. Blackstock, and D. M. Hester, "Atmospheric absorption of sound: further developments," J. Acoust. Soc. Am. **97**, 680–683 (1995).
[31]J.-F. Li and M. R. Hodgson, "*In situ* experimental determination of surface impedance at oblique incidence using pseudo-random sequences and a single microphone," J. Acoust. Soc. Am. **102**, 2200–2210 (1997).

On the qualification of anechoic chambers; Issues related to signals and bandwidth

Kenneth A. Cunefare[a] and Jeff Badertscher
The Woodruff School of Mechanical Engineering, The Georgia Institute of Technology, Atlanta, Georgia 30332

Volker Wittstock[b]
Department 1.7 (Applied Acoustics), Physikalisch-Technische Bundesanstalt, Bundesallee 100, 38116 Braunschweig, Germany

(Received 25 August 2005; revised 10 May 2006; accepted 10 May 2006)

The qualification of anechoic and hemianechoic chambers requires selection of signal type and acquisition bandwidth to be used. This work demonstrates that, while a broadband random source may be used, the signal at points removed from the source are not composed of random combinations of direct and reflected waves, except in the limit of infinite bandwidth. It is shown that chamber qualification may be represented as finding the ratio of two transfer functions, where one includes the reflected waves, and the other is the free-field transfer function between the source and receiver. Consideration of this approach leads to a generic representation for the deviation from free-field performance where bandwidth is demonstrated to suppress the dominant modulation contributions of reflections. It is demonstrated that pure-tone qualifications will always exhibit a higher deviation from free-field performance than a broadband qualification. Finally, it is shown that the use of an incoherent source model in method-of-images simulations for the broadband performance of anechoic chambers is fundamentally flawed.
[DOI: 10.1121/1.2211467]

PACS number(s): 43.55.Pe, 43.58.Vb [AJZ] Pages: 820–829

I. INTRODUCTION

Qualification of anechoic chambers continues to be an issue of significant interest, and some concern, as to the proper method for characterizing the performance of these rather common facilities in academic, industrial, and government laboratories. Of interest here is the commonly employed method of inverse-square law traversing, as embodied in Annex A of ISO 3745,[1] where issues of concern include the merits of continuous vs discrete point measurement traverses, and the use of broadband vs pure-tone excitation signals. The merits of continuous vs discrete were taken up by Luykx and Vercammen[2] in 2001 and Cunefare *et al.*[3,4] Broadband vs pure-tone test signals have been considered by Cunefare *et al.*[3,4] and Wittstock and Bethke.[5] Of principal concern to the work presented here is the choice of the test signal to be used in qualifying a chamber and the impact of the bandwidth employed in the chamber excitation and data acquisition. Specifically, the key objective of this work is to demonstrate that the bandwidth of excitation and acquisition critically impacts the results of qualification programs. Related issues of interest include the demonstration that chamber qualification may be represented as the measurement of transfer functions, and demonstration that the use of an incoherent source model for method-of-images simulations of anechoic chambers[6,7] is fundamentally flawed.

Recently, Wittstock and Bethke,[5] considering the case of reflection from a single plane surface and employing the method of images, demonstrated that the measurement bandwidth will have a strong influence, concluding that the larger the bandwidth, the lesser the contribution of reflections observed in the response. Additionally, they demonstrated through experiment that the qualitative implication of their analytical development is observable in real chambers. This qualitative bandwidth-dependency implication may also be observed in the experimental data presented by Cunefare *et al.*,[3,4] though that work did not explicitly address bandwidth issues. While the work of Wittstock and Bethke was explicitly derived considering but a single reflective surface, the basic methodology may be used in a more general derivation to elucidate the impact of measurement bandwidth upon the results obtained from broadband qualification of anechoic and hemianechoic chambers; this elucidation is the key focus of the present work. A key contribution of the work is a generalization and extension of the development initially presented by Wittstock and Bethke.[5]

The work of Wittstock and Bethke, and the key development of this paper, also have implications for a common modeling scheme applied to anechoic and hemianechoic chambers. Duda[7] and Wang and Cai[6] used the method of images as a means to model the performance of anechoic and hemianechoic chambers. In addition to simulations of pure-tone behavior, such work has also considered the broadband performance of chambers. In the broadband simulations, the assumption was used that the source and its images were incoherent, such that the rms pressure squared at an observa-

[a]Electronic mail: ken.cunefare@me.gatech.edu
[b]Electronic mail: volker.wittstock@ptb.de

tion point is just the sum of the rms pressure squared from the source and its images. The analysis employed by Wittstock and Bethke, as extended here, demonstrates that this assumption is valid only in the limit of infinite bandwidth, and is fundamentally incorrect for finite-bandwidth analyses.

Of some historical note to the issues of interest in this paper, in 1959 Stroh[8] developed a time-domain method to measure the "acoustic ratio," that is, the ratio between the direct and indirect energy at an observation point in a room, a task not unlike that performed in chamber qualification. The method considered the ratio of the energy along the direct and image-source paths between an input sound source and a receiver, expressed in terms of auto- and cross-correlation functions. The method assumed the signal along the direct path to be incoherent with respect to the "noise" due to transmission along the indirect paths. To enforce this assumption, which required suppression of cross-correlation terms between the input and response, Stroh employed an input noise signal that spanned three and a half octaves. Stroh's approach is merely the time-domain analog of the frequency-domain analyses considered here.

At present, the most commonly employed methodology for qualification of anechoic and hemianechoic chambers is detailed in Annex A of ISO 3745:2003.[1] In ISO 3745, the signal to be used for qualification is specified to be random noise; pure-tone qualifications are recommended only in the case where test articles are expected to exhibit pure tones. Further, Annex A specifies that measurements are to be made at either a minimum of 10 discrete points at no greater than 0.1-m spacing, or, with a microphone in continuous motion.

The following first develops some basic material related to the time-domain and frequency-domain representations of signals contaminated by an echo. The paper then demonstrates that chamber qualification may be considered to be a process of measuring the ratio of two transfer functions: that corresponding to direct radiation between a source and receiver, and that representing the total radiation including all reflections. Next, the developments are made specific for sound fields in chambers, and the resulting predictions are validated experimentally. Finally, the paper then takes up the question of the validity of the incoherent-source method-of-images broadband model.

II. SIGNALS, ECHOES, AND BANDWIDTH CONSIDERATIONS

This section develops some basic material that will assist in formulating and interpreting the signals that are obtained and assessed in the course of a chamber qualification. Furthermore, this section explores general implications of bandwidth on band averages of signals contaminated by echoes, with implications brought out through consideration of a simple example.

Consider a time-domain signal x contaminated by its attenuated, time-delayed echo,[9]

$$y(t) = x(t) + ax(t-\tau). \tag{1}$$

In the context of chamber qualification, x is the signal that would have existed in the absence of reflections, while y is the signal that is actually present in the chamber. In Eq. (1), a is an attenuation factor, which may be interpreted, for example, as a reflection coefficient, and where t is time and τ is a time delay. The Fourier transform of y is

$$Y(f) = (1 + ae^{j2\pi f\tau})X(f), \tag{2}$$

where f represents frequency. The ratio of the squared magnitude of Y to that of X is

$$|Y(f)|^2/|X(f)|^2 = 1 + a^2 + 2a\cos(2\pi f\tau). \tag{3}$$

The effect of the echo in the frequency domain is to introduce a bias and a modulation as compared to $|X(f)|^2$ alone. The bias is represented by the second term in Eq. (3) while the modulation is the third term in Eq. (3). If the attenuation factor a is less than unity, then Eq. (3) indicates that the amplitude of the modulation term, $2a$, will always be larger than the magnitude of the bias term, a^2; the phase component of the modulation term then determines the relative contribution of the modulation term vs that of the bias term.

The decibel deviation between the echo-free signal X and the with-echo signal Y, and an upper bound on that deviation, may be obtained from Eq. (3) as

$$\Delta L_{\mathrm{PT}} = 10\log(1 + a^2 + 2a\cos(2\pi f\tau)) \le 20\log(1+a), \tag{4}$$

where the subscript PT indicates that the deviation is applicable to a pure tone. Note that the bound on the deviation, $20\log(1+a)$, is not directly a function of frequency, though the bound does not preclude the attenuation factor a from being a function of frequency.

Turning now to the case where the signal x spans some finite bandwidth, the ratio of the energy of Y to that of X within a band of frequencies $B=f_2-f_1$, and the upper bound on that ratio, is

$$|Y|^2/|X|^2_{\mathrm{band}} = 1 + a^2 + 2a\cos(2\pi f_c\tau)\mathrm{sinc}(\pi B\tau) \le 1 + a^2 + \frac{2a}{\pi B\tau}, \tag{5}$$

where $\mathrm{sinc}(z)=\sin(z)/z$ and f_c is the arithmetic (not geometric) center frequency of the band, $f_c=(f_2+f_1)/2$. Equation (5) assumes that the attenuation factor a is not a function of frequency, and that $X(f)$ is flat across the bandwidth of integration. The bound in Eq. (5) is valid for large values of the argument $\pi B\tau$; the small argument bound corresponds to that for pure tones, Eq. (4). If the attenuation factor a is a function of frequency, then the ratio in Eq. (5) still may be bounded by

$$|Y|^2/|X|^2_{\mathrm{band}} \le 1 + a^2_{\max} + \frac{2a_{\max}}{\pi B\tau}, \tag{6}$$

where $a_{\max}$ the maximum value of a within the band. As with the pure-tone expression, Eq. (3), the second term of Eqs. (5) and (6) represents a bias contribution due to the echo, while the third term represents an echo modulation contribution; these two terms account for the additional energy in the band as compared to the echo-free signal. If the echo was uncorrelated with the signal, then only the first and second terms of Eqs. (3), (5), and (6) would be

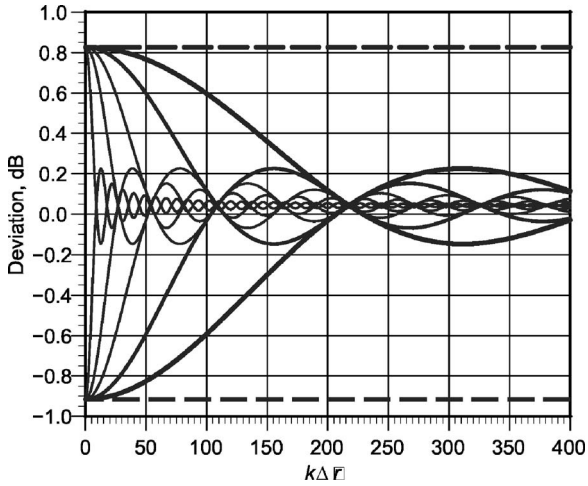

FIG. 1. Envelopes of dB difference between a signal and signal contaminated by an echo with attenuation $a=0.1$, for different bandwidths: Dashed lines are limiting bounds for pure-tone signals. Thick to thin lines correspond to 1/1, 1/3, 1/6, 1/12, and 1/24-octave bandwidths.

nonzero, as would be the case for the combination of incoherent signals; but, if the echo was uncorrelated with its originating signal, then it is not a time-delayed version of that originating signal, and hence it is not an echo.

As with the pure-tone case, if the parameter of interest is the relative deviation in the band-integrated level, then such is found through the decibel value of Eq. (5), i.e.,

$$\Delta L_{\text{band}} = 10 \log(1 + a^2 + 2a \cos(2\pi f_c \tau)\text{sinc}(\pi B \tau)), \quad (7)$$

with a bound of

$$\Delta L_{\text{band}} \leq 10 \log\left(1 + a_{\max}^2 + \frac{2a_{\max}}{\pi B \tau}\right), \quad (8)$$

where $a_{\max}$ is construed here to include the case of frequency-independent a as well. Equation (8) clearly indicates that the deviation associated with the presence of echoes decreases with increasing bandwidth B, that is, a significant implication of the third term of Eq. (8) is that the wider the bandwidth, the lesser the contribution of the echo-induced modulation in relation to the direct contribution.

Additional insight may be gained from the developments of this section by assuming that the time delay τ is due to a path-length difference between the signal and its echo of Δr, for a signal propagating at a speed c. This permits Eq. (4) to be expressed as

$$\Delta L_{\text{PT}} = 10 \log(1 + a^2 + 2a \cos(k\Delta r)) \quad (9)$$

for pure-tone signals and Eq. (7) to be expressed as

$$\Delta L_{\text{band}} = 10 \log(1 + a^2 + 2a \cos(k\Delta r)\text{sinc}(bk\Delta r/2)) \quad (10)$$

for broadband signals. In Eq. (10), b is the proportionality constant for proportional frequency bands, such that $B=bf_c$. Consider Fig. 1, which depicts the limiting bounds of Eq. (9) for pure-tone signals and the envelope of Eq. (10) for broadband signals and over a range of $k\Delta r$, for an attenuation factor of $a=0.1$ and for bandwidths of 1/1, 1/3, 1/6, 1/12, and 1/24 octave. The envelope of Eq. (10) is

$$\Delta L_{\text{band,envelope}} = 10 \log(1 + a^2 \pm 2a \text{ sinc}(bk\Delta r/2)). \quad (11)$$

A different value of the attenuation factor a does not alter the shapes of the curves in Fig. 1, rather, it alters their amplitudes. The significance of Fig. 1 is that it clearly demonstrates, for fixed $k\Delta r$, the larger the bandwidth, the lesser the deviation between the energy in a signal and the energy in the signal contaminated with its echo. Similarly, for a given proportional bandwidth, the larger $k\Delta r$, the lesser the deviation between the signal and its signal-with-echo counterpart. The fact that these considerations have bearing upon anechoic chamber qualification, and physical implications for such, will be addressed further in Sec. VI.

III. QUALIFICATION AS MEASUREMENT OF TRANSFER FUNCTIONS

This section considers in a general manner the sound field that exists within a chamber, and demonstrates that chamber qualification as commonly practiced is equivalent to the measurement of the ratios of transfer functions. This equivalence is then explored with respect to the nature of signals that are commonly employed in chamber qualification.

Consider the signal received at an observer point within a chamber; the signal will be comprised of the direct-radiation component from the sound source, as well as the superposition of all reflected sound energy arriving at that observation point. There is nothing random about the reflections; for fixed source and receiver positions, the energy that leaves the source in a given direction travels by the same paths to the receiver every time. The transmission between the source and receiver is linear and time invariant. Note that Kutruff and Bruchmuller's[10] work for estimation of the apparent reflection coefficient of an anechoic chamber through matching of the statistical distribution of sound-pressure levels at fixed distance from a sound source to the distribution obtained from a method-of-images model also presumes that the propagation between source and receiver is deterministic, not random. In light of these considerations, it is evident that the sound pressure at the observation point is comprised of signals that arrive at various time lags relative to the direct arrival, but those time lags are fixed, not random, for any particular travel path. In consequence, for an observation point at a distance r_1 from a sound source of strength q, the total pressure is

$$p_1(r_1,t) = q(t-\tau)h_{\text{direct}}(t-\tau) + \int_{-\infty}^{t} q(t-\tau')h_{\text{reflections}}(t-\tau')d\tau', \quad (12)$$

where h_{direct} is the impulse response function between the source and receiver for direct radiation, and $h_{\text{reflections}}$ is the impulse response function for all nondirect paths from the source to the receiver. Recognize that h_{direct} just the time-domain free-space Green's function for three-dimensional radiation. In contrast, $h_{\text{reflections}}$ is generally acknowledged to be too complex to model analytically; nonetheless, it is deterministic, not random. A common approximation for $h_{\text{reflections}}$ in anechoic chamber modeling is the

method-of-images.[10,11,6,7] Note that Eq. (12) may be considered to be an extended form of Eq. (1), that is, a signal combined with its attenuated, time-delayed echo.

In light of Eq. (12), even if the source strength q is random in time, the pressure at the receiver point is not strictly random. If q is broadband random, its autocorrelation function will be zero for all nonzero time delays. But, the autocorrelation of p_1 will clearly not be zero for nonzero time delays, due to the presence of the echo. Indeed, Eq. (12) may be understood to represent the time-domain response of a linear time-invariant system subjected to an input q.

Given that the pressure response at a fixed observation point is that of linear time-invariant system, then there exists an equivalent frequency-domain transfer function representation for the pressure at the observation point, expressed as

$$P_1(f) = Q(f)H_{\text{direct}}(f) + Q(f)H_{\text{reflections}}(f), \tag{13}$$

where P, Q, and H are the Fourier transforms of the functions in Eq. (12). In chamber qualification, the metric of interest is the deviation between the observed pressure magnitude and the pressure magnitude that would have been obtained in a free field, where the free-field pressure may be represented as

$$P_0(f) = Q(f)H_{\text{direct}}(f), \tag{14}$$

such that the desired deviation is

$$\frac{|P_1(f)|^2}{|P_0(f)|^2} = 1 + \frac{|H_{\text{reflections}}(f)|^2}{|H_{\text{direct}}(f)|^2} + 2\,\text{Re}\left(\frac{H_{\text{reflections}}(f)}{H_{\text{direct}}(f)}\right). \tag{15}$$

In light of Eq. (3), recognize that

$$\frac{|H_{\text{reflections}}(f)|}{|H_{\text{direct}}(f)|} = |a(f)| \tag{16}$$

and

$$\text{Re}\left(\frac{H_{\text{reflections}}(f)}{H_{\text{direct}}(f)}\right) = a(f)\cos(2\pi f\tau). \tag{17}$$

The implication of Eq. (15) is that chamber qualification as considered here is actually a process of determining the ratio of the transfer functions for the direct and reflected wave components in a chamber. Note that this may also be inferred from Nobile's work concerning the use of a hemianechoic chamber for the measurement of the acoustic absorption of materials.[12]

For measurements over a band of frequencies

$$|P_1(f)|^2_{\text{band}} = \int_{f_1}^{f_2} |Q(f)H_{\text{direct}}(f) + Q(f)H_{\text{reflections}}(f)|^2 df \tag{18}$$

and

$$|P_0(f)|^2_{\text{band}} = \int_{f_1}^{f_2} |Q(f)H_{\text{direct}}(f)|^2 df, \tag{19}$$

and the deviation from free-field performance is the ratio of the resultants of Eqs. (18) and (19). A significant implication of the development above is that the result of a broadband qualification test will critically depend on the spectrum shape and frequency content within the band of interest.

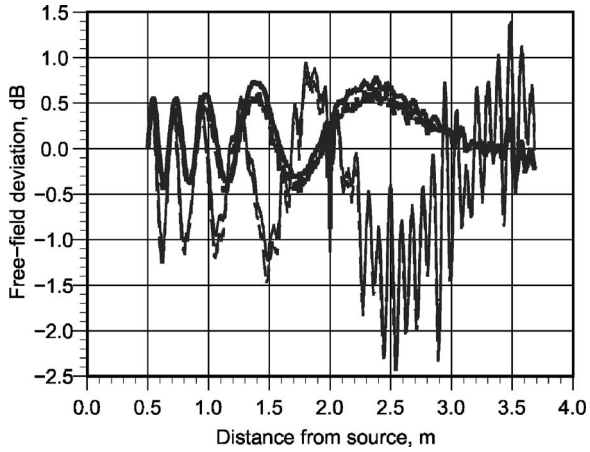

FIG. 2. Comparison of traverses performed in PTB's hemianechoic chamber excited by 2000 Hz pure tone and excited by broadband signals approximately spanning at 2000-Hz 1/3-octave band. ——— pure tone at 2000 Hz, - - - - broadband noise excitation narrow-band filtered (15.625 Hz bandwidth) at 2000 Hz, - - - - 31 tones approximately spanning 2000 Hz 1/3 octave, - - - - 2000-Hz 1/3-octave band noise.

Beyond spectrum shape considerations though, Eqs. (18) and (19) have implications for the nature of signals used in chamber qualification. Different results will be obtained, for example, for broadband measurements employing pink-noise and white-noise sources, as Eqs. (18) and (19) indicate that such will have different spectral weighting applied to the transfer functions. Further, Eqs. (18) and (19) indicate that the results obtained from two different signals Q will be the same if the signals have the same spectral content. For example, the traverse results obtained through the use of a signal comprised of multiple equal-amplitude pure-tone components should converge to that obtained using a white-noise signal over a band as the number of tones within the band is increased. Finally, Eqs. (18) and (19) indicate that traverses performed using a pure-tone excitation and broadband noise narrow-band filtered at the pure tone's frequency will theoretically yield the same result. The only consideration of the use of one type of signal vs another (e.g., pure tone, multitone, pink noise, white noise, etc.) reduces to the proper selection of an averaging interval appropriate to the nature of the signal.

The results from two particular experiments of Wittstock and Bethke,[5] described by them as "interesting," may be interpreted in light of the above. Wittstock and Bethke performed traverses in a hemianechoic chamber at Physikalisch-Technische Bundesanstalt, Braunschweig, Germany (PTB). A planar reflective surface of 2 m^2 was intentionally introduced into the chamber to produce a significantly observable deviation from free-field performance. Traverses were performed using pure-tone and broadband signals, as well as signals comprising multiple pure tones. Sound-pressure levels were recorded as a function of distance from a sound source, and the inverse-square law decay was subtracted from the result, yielding an estimate of the deviation from free-field performance. Figure 2 depicts an example of the

data obtained for pure-tone signals at 2000 Hz, and broadband signals spanning the 2000-Hz 1/3-octave band.

The first result of interest is that, when random noise was used to excite the subject chamber, but the response was narrow-band filtered, the resulting deviation tracked quite closely to the results obtained when a pure-tone excitation was used to excite the chamber, as is evident in Fig. 2 for the traverse data for these two cases. This result validates the stated implications of Eqs. (18) and (19) concerning narrow-band filtered noise and single pure-tone excitations. The second result of interest is that, when simultaneous tones were used to excite the chamber, with those tones spanning the same band as a companion random noise test, the resulting deviation for the multitone test was almost indistinguishable from that obtained using random excitation, also depicted in Fig. 2. This result is also predicted by Eqs. (18) and (19), in that it is the frequency content within the bandwidth of measurement that is significant, and not whether or nor the signal is comprised of pure tones or random noise. The results presented in Wittstock and Bethke's paper, as well as those in Fig. 2, are in clear accord with the development above, as it is well established that transfer functions may be obtained using pure-tone and random excitations (among other signal types), and, as is seen above, chamber qualification testing as considered here is nothing more than determining the ratio of two transfer functions.

IV. CONSIDERATION OF REFLECTIONS AND BANDWIDTH IN CHAMBER QUALIFICATION

The following repeats in outline some of the developments of the prior sections, but applies physical interpretations and approximations appropriate to the situation that pertains for a chamber qualification. Consider a point source at some position within an anechoic chamber. The free-field pressure produced by a source of unit amplitude at an observation point at distance r_1 from the source is

$$p_1(r_1,t) = \frac{e^{j(\omega t - kr_1)}}{r_1}, \tag{20}$$

where ω is the circular frequency, c is the speed of sound, and $k=\omega/c$ is the wave number.

The contribution from all reflections at the observation point may be represented as

$$p_2(t) = ae^{j(\omega t - \phi)}, \tag{21}$$

where a is an attenuation factor with the same significance as in Eqs. (1) and (2), and the phase shift ϕ is equivalent to $2\pi f\tau$ as in Eq. (2). Equation (21) follows from the fact that the superposition of any number of sinusoids may be represented as a single equivalent sinusoid. Further, Eq. (21) may be considered to be the resultant of the Fourier transform of the second term in Eq. (12), that is, it represents $QH_{\text{reflections}}$. Proceeding, the total pressure at r_1 is the sum of p_1 and p_2,

$$p_{\text{tot}} = p_1 + p_2 = \frac{1}{r_1}e^{j(\omega t - kr_1)} + ae^{j(\omega t - \phi)}, \tag{22}$$

and considering Eqs. (1) and (2), recognize that Eq. (22) is in the form of a signal and its echo. With the form of the pressure due to reflections in Eq. (21) and its combination with the direct radiation in Eq. (20), all of the developments in Sec. II concerning bandwidth considerations apply to the signals encountered in anechoic chamber qualification. Of particular interest to the objective of this paper, the implication of Eq. (8) that the greater the bandwidth employed, the lesser the contribution of the echo modulation term to the deviation from free-field performance applies to the sound field that exists at an observation point within an anechoic chamber.

While Eq. (21) is strictly valid for representing the resultant of all reflections at a particular observation point, it does not provide a ready means for physical interpretation relevant to the parameters of interest in anechoic chamber qualification. An alternative representation which does provide such a basis is found by expressing the contribution due to all reflections as

$$p_2(r_2,t) = \frac{|R_{\text{eq}}|}{r_2}e^{j(\omega t - kr_2 + \phi)}, \tag{23}$$

where R_{eq} is an equivalent reflection coefficient, r_2 is an equivalent distance, and ϕ is the phase angle of the equivalent reflection coefficient. The physical interpretation of Eq. (23) is that the resultant of all reflections may be expressed as the contribution due to radiation from the source spherically spreading through a distance r_2 and experiencing additional attenuation beyond spherical spreading characterized by the equivalent reflection coefficient R_{eq}; note that R_{eq} may be a function of both position and frequency. While Eq. (23) is a convenient representation for the combined contributions of reflections, it is not mathematically unique; the magnitude of R_{eq} and r_2 may be chosen arbitrarily so that their ratio yields the magnitude of p_2. Specifying either R_{eq} or r_2 permits the other parameter to be determined, assuming that the magnitude of p_2 is known.

While it is tempting to fix the value of R_{eq} to be equal to the normal-incidence reflection coefficient of the wall treatment, such is probably not justifiable due to the following considerations. First, consider that the normal-incidence reflection coefficient R is obtained under conditions of normal incidence, and where the incident and reflected waves have diametrically opposed propagation directions. In an anechoic chamber, spherically spreading waves are incident upon the wall treatments at other than normal incidence and the angle of incidence is not constant everywhere on the walls of the chamber. Second, the sound energy that arrives at the observation point does so for propagation directions that encompass the entire 4π solid angle surrounding the observation point. A simple thought experiment will demonstrate that R_{eq}, as considered here, can vary from a minimum of zero to some unknown multiple of the normal incidence reflection coefficient. Consider N reflections of equal strength and equal phase arriving at the observation point. Assume that their propagation distances are on the same order as that of the direct radiation, and that their reflection strength may be characterized by the normal incidence reflection coefficient. In this instance, the equivalent reflection would be $R_{\text{eq}} \approx NR$. If the reflections arrived such that their amplitudes and phases completely cancel, then $R_{\text{eq}}=0$. This thought ex-

periment leads to the conclusion that fixing R_{eq} as equal to the normal incidence reflection coefficient is not well justified on physical grounds. For our purposes here, though, the exact value of R_{eq} is not significant.

If R_{eq} cannot be specified, then the question becomes how to specify r_2 on physically defensible grounds. Assuming that an anechoic chamber has a uniformly performing wall treatment, such that there are no localized regions of significantly different reflection properties, then those portions of the chamber's walls that are closest to the observation point should have the strongest impact to the resultant pressure at the observation point. Therefore, a reasonable choice for r_2 is the minimum ray-acoustics distance from the source to the observation point via reflection off the walls. Of course, the validity of this choice for r_2 can only be verified if the predictions obtained through the consequent developments are borne out in practice; such verification is provided in Sec. V.

Given the representation for the reflections in Eq. (23), then the total pressure at the observation point is

$$p_{tot} = p_1 + p_2 = \frac{1}{r_1} e^{j(\omega t - kr_1)} + \frac{|R_{eq}|}{r_2} e^{j(\omega t - kr_2 + \phi)}. \tag{24}$$

Following the developments of Sec. II, the ratio of sound energy in the free-field (direct field) to that in the anechoic chamber (direct field plus echoes) is

$$\frac{p_{tot,rms}^2}{p_{1,rms}^2} = 1 + \left(\frac{r_1|R_{eq}|}{r_2}\right)^2 + \frac{2r_1|R_{eq}|}{r_2}\cos(\phi - k\Delta r), \tag{25}$$

where $\Delta r = (r_2 - r_1)$ is the incremental propagation distance along the ray-acoustics path defined by r_2 as compared to the direct path r_1. The term $k\Delta r$ is the spatial phase associated with the incremental propagation distance.

Equation (25) is in the same form as Eq. (3), such that the attenuation factor as used in the developments of Sec. II may be identified as

$$a = |R_{eq}| r_1 / r_2. \tag{26}$$

The decibel deviation from free-field performance is then

$$\Delta L_{PT} = 10\log\left(1 + \left(\frac{|R_{eq}|}{r_2/r_1}\right)^2 + 2\frac{|R_{eq}|}{r_2/r_1}\cos(\phi - k\Delta r)\right), \tag{27}$$

where the subscript PT indicates a pure-tone result. The deviation is bounded by

$$\Delta L_{PT} \le 10\log\left(1 + \left(\frac{|R_{eq}|}{r_2/r_1}\right)^2 + 2\frac{|R_{eq}|}{r_2/r_1}\right). \tag{28}$$

For a finite bandwidth, the ratio of the total rms-pressure squared to the free-field rms pressure squared within a band $B = (f_2 - f_1) = c(k_2 - k_1)/2\pi$ is

$$\frac{p_{tot,rms,B}^2}{p_{1,rms,B}^2} = 1 + \left(\frac{|R_{eq}|}{r_2/r_1}\right)^2 + \frac{c|R_{eq}|}{B\Delta r r_2/r_1}(\sin(\phi - k_1\Delta r) - \sin(\phi - k_2\Delta r)). \tag{29}$$

Implicit in Eq. (29) is an assumption that the equivalent absorption is not a function of frequency, which may not be the case. Defining the relative bandwidth b as $b = B/f$, and with some rearrangement and grouping of terms, Eq. (29) becomes

$$\frac{p_{tot,rms,B}^2}{p_{1,rms,B}^2} = 1 + \left(\frac{|R_{eq}|}{r_2/r_1}\right)^2 + 2\frac{|R_{eq}|}{r_2/r_1} \times \cos(\phi - k\Delta r)\mathrm{sinc}(bk\Delta r/2). \tag{30}$$

The decibel deviation from free-field performance is then

$$\Delta L_B = 10\log\left(1 + \left(\frac{|R_{eq}|}{r_2/r_1}\right)^2 + 2\frac{|R_{eq}|}{r_2/r_1} \times \cos(\phi - k\Delta r)\mathrm{sinc}(bk\Delta r/2)\right), \tag{31}$$

where the subscript B indicates a deviation over a bandwidth B. The deviation is bounded by

$$\Delta L_B \le 10\log\left(1 + \left(\frac{|R_{eq}|}{r_2/r_1}\right)^2 + 2\frac{|R_{eq}|}{r_2/r_1}|\mathrm{sinc}(bk\Delta r/2)|\right). \tag{32}$$

Note that the pure-tone result, Eq. (27), may be obtained from Eq. (31) in the limit of b approaching zero. Finally, note that Eqs. (27) and (31) are equivalent to Eqs. (9) and (10) in Sec. II, and therefore the implications of Fig. 1 are applicable here.

Comparing Eqs. (27) and (31), the sole significant difference between the pure tone and broadband relationships is the sinc function operating on the third term of the right-hand side of Eq. (31). The first two terms in Eqs. (27) and (31) result if the source and its echo are incoherent; the third term is the modulation component between the signal and its echo, as developed in Sec. II. The sinc function in Eq. (31) is critically important with respect to broadband tests, as once its argument becomes sufficiently large, the sinc function becomes small and thereby suppresses the modulation component introduced by the echoes.

The influence of the sinc function in Eq. (31) on the outcome of a measurement may best be elucidated by considering two limiting cases corresponding to small and large arguments. Underpinning these limiting cases are constraints upon the values that the distance Δr and the wave number k can exhibit. Specifically, since r_2 is defined to be the minimum ray-acoustics distance between the source and observation position, and assuming a rectangular chamber of dimensions $A \times B \times C$ with a source positioned at its center, then geometric considerations constrain Δr to have a maximum possible value equal to the minimum dimension of the chamber. That is, if $A > B > C$, then $\Delta r_{max} = C$. Geometric considerations further dictate that Δr has its maximum value at the position of the source, and declines to its minimum value of zero at the point where the traverse intersects the walls. As for the wave number k, given the typical frequencies considered in qualifying anechoic chambers, k will vary from approximately 1.1 (~63 Hz) up to 180 (~10 kHz). The contour map of Fig. 3 provides an illustration of the issues raised in the consideration of small and large arguments developed below. Figure 3 presents the envelope of dB difference be-

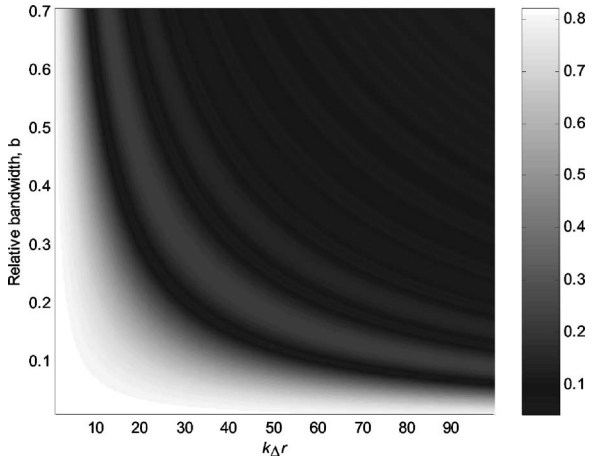

FIG. 3. Contour map of the magnitude of the envelope of dB difference between a signal and signal contaminated by an echo with attenuation $a=0.1$, for different bandwidths as function of $k\Delta r$. The positive values in Fig. 1 may be considered to be horizontal slices through this map.

tween a signal and its echo-contaminated counterpart for an attenuation coefficient $a=0.1$ as function of $k\Delta r$ and relative bandwidth b.

For the small argument case, $bk\Delta r/2 \ll 1$, $\mathrm{sinc}(bk\Delta r/2) \cong 1$, and Eq. (31) reduces to Eq. (27); such that a broadband measurement would yield the same result as the pure-tone measurement. The argument $bk\Delta r/2$ may be made very small by: (i) narrow-bandwidth analysis such that $b \ll 1$; (ii) low frequency, $k \ll 1$; and (iii) small values for the difference in propagation distances, $\Delta r \ll 1$. These cases are clearly evident in Fig. 3, as the regions of large deviation from free-field performance occur near the axes of the plot, where the values of the product $bk\Delta r$ are "small," and hence this "small argument" case discussion applies. The indication that narrow bandwidth recovers the pure-tone measurement is evident from the prior discussion pertaining to the transfer-function representation of chamber qualification, and the experimental results of Wittstock and Bethke.[5] Given the typical range of k that pertains for chamber qualification, it is evident that condition (ii) cannot be met. The remaining term of interest, then, is $\Delta r \ll 1$, which from the geometric constraints discussed previously occurs only when the observation point is very close to a reflecting surface. Therefore, the broadband measurement recovers the information obtained through a pure-tone measurement only in the cases of a narrow-band analysis (e.g., broadband noise source but narrow-band data acquisition), or, for measurement locations physically close to a reflecting surface. An implication of this last point is that the small argument condition applies toward the end of a chamber traverse, on approach to the walls.

For large argument, $bk\Delta r/2 > 1, |\mathrm{sinc}| < 1$, and hence the sinc function rapidly attenuates the third term of Eq. (31), and the deviation from free-field performance is suppressed. For example, when the argument is greater than 10, the magnitude of the sinc function is less than 0.1. The argument $bk\Delta r/2$ may be made large by $k \gg 1$, by $\Delta r \gg 1$, and by their product $k\Delta r \gg 1$. In Fig. 3, the large argument case applies to those regions moving away from the axes. For third-octave bands, $b=0.232$, and for full octave bands $b=0.707$; b cannot directly lead to a large argument. However, if the criterion for "large" is set at some fixed value, then b impacts what values of k and Δr will satisfy the criterion. Clearly, higher frequencies lead to large values of the argument. Also, observation locations closer to the source than to the walls will lead to large values of Δr in all but the smallest useful chamber. The combination of these conditions leads to the conclusion that the large argument case applies at the start of a traverse, closest to the test source. A further implication of this case is that, for typical chamber sizes, in the region extending some few meters from a source, and for higher frequency bands, the use of a broadband measurement substantially suppresses the modulation of the reflection contribution as compared to a pure-tone measurement.

This begs the question, by how much do the results from a pure-tone test and from a broadband test differ? Figure 3 provides some insight into this question, and also illustrates that the answer cannot be reduced to a single guideline. First, it is evident from the developments hitherto that $\Delta L_{\mathrm{PT}} \geq \Delta L_{\mathrm{B}}$, that is, the deviation observed in a narrow-band test will always be greater than that observed in a broadband test for the same frequency range of interest. Further, the qualitative implications Fig. 3 are that, if one is using a broadband measurement, there is more likelihood that the large argument case will apply than the alternative; and for the small argument case, the deviation from free-field performance is much smaller, and approaching negligibly small values, than the alternative large argument case. This last observation is based on the relative dominance of regions of low deviation from free-field performance evident in Fig. 3. Therefore, a broadband traverse will always have a greater tendency to "qualify" as compared to a pure-tone traverse. This observation has been validated by the experimental data in the prior publications of Wittstock and Bethke[5] and Cunefare *et al.*[4] In the following, we provide further validation of these issues, as well as the signal content implications of Sec. III.

V. EXPERIMENTAL VALIDATION

For the purposes of validating the physical implications of bandwidth on traverse measurements developed in the previous sections, pure-tone and broadband traverses were performed in an anechoic chamber and a hemianechoic chamber at the Georgia Institute of Technology (GT). The traverses employed signals of increasing bandwidth, and spanned from near the test source to near the walls of the chambers.

The anechoic chamber has an interior clear dimension of $5.1 \times 5.1 \times 3.9$ m. Its wall treatment is an Industrial Acoustics Company "Metadyne" wedge system. The anechoic chamber has a design cutoff 80 Hz. The hemiaechoic room has an interior clear dimension of $7.5 \times 5.9 \times 4.3$ m, and has a melamine foam wedge treatment, again with a design cutoff frequency of 80 Hz.

The main elements of the traversing system used to acquire sound-pressure level data along radial lines extending from near the center of each chamber to near the walls comprised a sound generation system, a motion control system, a reference and traverse microphone, and a data acquisition

system. The sound generation system comprised a signal generator, power amplifier, and sound source. The motion control system comprised fixed guide wires and pulley system in the chamber, a microphone carriage, and a computer-controlled motor. The microphone carriage was pulled up the guide wires via Kevlar take-up line routed through quiet pulleys to the motor located outside the chamber. The traverse microphone was attached to the carriage. The reference microphone was located at a fixed position within the chamber, and served as a means to monitor the sound-source stability over the duration of the traverse. The data acquisition system included the microphone signal conditioning and a PC-based data acquisition card. The data acquisition system also integrated the motion control system, permitting synchronization of these functions. The traverse data acquired with this system was postprocessed following the protocol described in the ISO 3745 standard.[1] In brief, this processing yields a measurement of the deviation from free-field performance as a function of distance from the sound source. More detailed descriptions of the traverse system and data processing may be found in the publication by Cunefare *et al.*[4]

Radial traverses were performed starting near the center of each chamber, and extending toward a corner. Traverses were performed using a pure-tone signal as well as finite-bandwidth signals spanning 1/12, 1/6, and 1/3 octaves around the center frequency of interest. Multitone signals were constructed spanning the bandwidths of interest, as permitted by the developments of Sec. III regarding the transfer-function interpretation of chamber qualification. Traverses were also performed using pink-noise excitation at 1/3-octave bandwidth as a means to validate the multitone signal tests. The use of the multitone signals permitted more time-efficient traversing, as the use of tones affords shorter traverse durations with less sample-to-sample variation as compared to traverses with noise signals. For all traverses the bandwidth of the data acquisition was matched to the bandwidth of the source signal.

Figure 4 presents the results for traverses at 1 kHz into a corner of the anechoic chamber. The plot is structured such that the pure-tone deviation is at the top, while each subsequent curve proceeding down the plot is the deviation for an increasing bandwidth, ending with 1/3-octave bandwidth at the bottom. The bottom two deviation plots are both for 1/3-octave bandwidths, with the upper acquired using a multitone signal, and the lower acquired using pink noise. The bottom two deviation lines demonstrate that the multitone signal provides the same information as the noise traverse, as the development in Sec. III predicts. It is also evident that the deviation data obtained using the noise signal have greater sample-to-sample variation as compared to the multitone traverse over the same bandwidth. Certainly, the noise traverse could have been made "smoother" by increasing the averaging time at each spatial point; however, the noise traverse already required some 15 min to acquire, and increasing the averaging time would have proportionally increased the time for a traverse; the pure-tone traverse required some 4 min to acquire, while the longest duration multitone traverse required approximately 8 min.

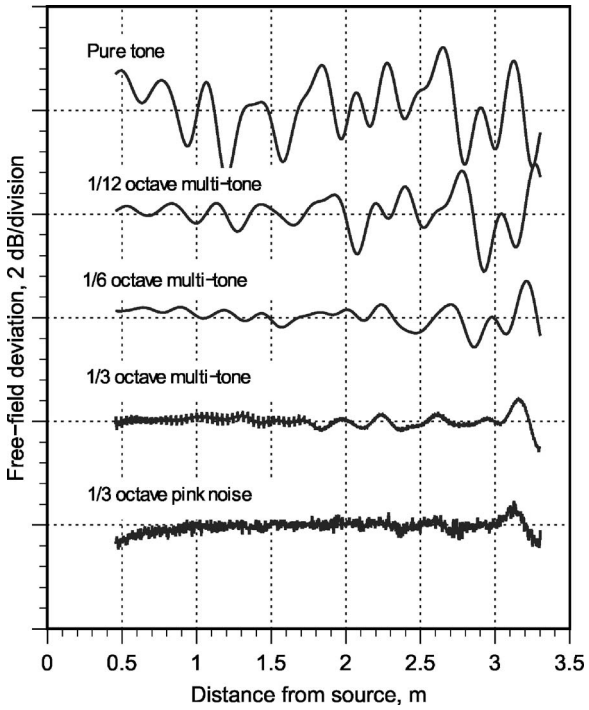

FIG. 4. Deviation from free-field performance at 1000 Hz recorded in the GT full anechoic chamber, for pure-tone and increasing bandwidth signals and measurements. Pure-tone traverse at the top of the plot, with traverses spanning increasing bandwidths toward bottom. Bottom two plots are both 1/3 octave, with the upper using a multitone excitation signal and the lower using pink noise.

The developments of Secs. III and IV lead to the prediction that (i) increasing the bandwidth for the signal and data acquisition reduces the spatial variation as compared to a pure-tone traverse with the same center frequency; and (ii) the deviation from free-field performance using a broadband signal increases with increasing distance from the source, with the magnitude increasing toward the walls. Clearly, the deviation plots in Fig. 4 substantiate each of these points.

Figure 5 presents a similar sequence of deviation curves as Fig. 6, but for a center frequency of 2 kHz, one octave higher. With the higher center frequency, k is greater, such that the developments of Secs. III and IV predict that the deviation from free-field performance should be even less than that observed at 1 kHz, and that the observed deviation should be pushed even further toward the walls. These characteristics are observed in the deviation data in Fig. 5 in comparison to Fig. 4.

Finally, Fig. 6 presents the results obtained at 1 kHz in the GT hemianechoic chamber, to demonstrate that the results obtained in the anechoic chamber are not somehow unique to that chamber; the same qualitative behavior observed in the anechoic room is also observed in the hemianechoic room.

VI. THE "BROADBAND" METHOD-OF-IMAGES MODEL

A final issue of relevance to the developments of this paper is the validity of the "broadband" model used in some method-of-images simulations of anechoic chambers.[6,7] The model as used by Wang[6] and Duda[7] assumes that, since the

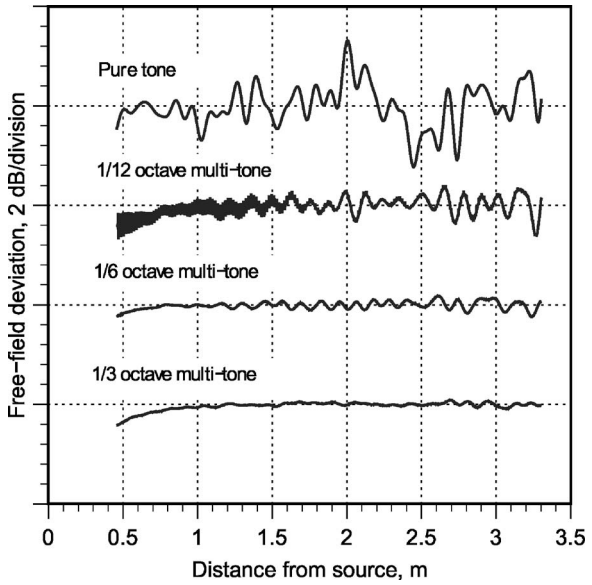

FIG. 5. Deviation from free-field performance at 2000 Hz recorded in the GT full anechoic chamber, for pure-tone and increasing bandwidth signals and measurements. Pure-tone traverse at the top of the plot, with traverses spanning increasing bandwidths toward bottom.

source signal is random, the combination of the direct and reflected waves at a receiver point will be incoherent, such that the total rms pressure squared is merely the sum of the rms pressure squared for each image source. As noted in the previous section, treating a signal and its echo as incoherent is equivalent to neglecting the echo modulation term of Eq. (3). However, this assumption is erroneous for the signals that exist in anechoic and hemianechoic chambers, as will be demonstrated in consequence of the following development.

In method-of-images modeling of anechoic chamber performance, $H_{\text{reflection}}$ is replaced by the direct-radiation transfer function for the image sources, such that Eq. (15) may be rewritten as

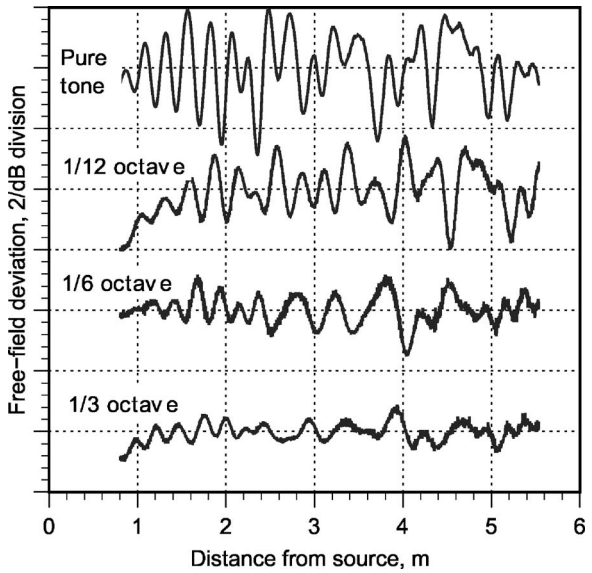

FIG. 6. Deviation from free-field performance at 1000 Hz recorded in the GT hemianechoic chamber, for pure-tone and increasing bandwidth signals and measurements. Pure-tone traverse at the top of the plot, with traverses spanning increasing bandwidths toward bottom.

$$\frac{|P_1(f)|^2}{|P_0(f)|^2} = 1 + \frac{|H_{\text{direct,images}}(f)|^2}{|H_{\text{direct}}(f)|^2} + 2\,\text{Re}\left(\frac{H_{\text{direct,images}}(f)}{H_{\text{direct}}(f)}\right). \tag{33}$$

However, when considering random noise excitation modeling of a chamber,[6,7] the third term of Eq. (33) has been neglected, with the assertion that the sound field at the receiver is uncorrelated with the source, such that

$$\frac{|P_1(f)|^2}{|P_0(f)|^2} = 1 + \frac{|H_{\text{direct,images}}(f)|^2}{|H_{\text{direct}}(f)|^2}. \tag{34}$$

However, as implied by Eq. (5), Eq. (34) is only valid in the limit of infinite bandwidth, B; for finite bandwidth, the third term in Eq. (33) must be retained, or at the least, shown to be negligible as compared to the other terms in the expression for the chosen bandwidth of analysis, which has not been done to date. The problem with the broadband approximation model for anechoic chamber performance is that the underlying assumption that the source and its reflections are incoherent is incorrect; the reflections are merely time-delayed and attenuated echoes of the source itself, where the time delay and attenuation is deterministic, not random. Chambers are not qualified using infinite-bandwidth measurements, regardless of the nature of the source; quite to the contrary, they are typically qualified using narrow bands, 1/3-octave bands, and full-octave measurement bands.

VII. CONCLUSIONS

The work presented here clearly indicates that the use of a bandlimited broadband traverse, as indicated in ISO 3745, will display less deviation from free-field performance as compared to a pure-tone traverse due to the effect of the bandwidth in suppressing modulation due to echoes. Further, the developments indicate that the suppression of modulation is greatest toward the center of an anechoic chamber; the impact of the echo modulation increases as one approaches the walls. These predictions have been experimentally validated.

Consideration of the signals acquired in the course of chamber qualification reveals that chamber qualification is nothing more than a transfer function measurement. In that light, while the results of broadband chamber qualification are affected by the excitation signal spectral content, the gross differences between pure-tone and broadband traverses arise, as demonstrated here, due to the acquisition bandwidth.

A fundamental implication of the work presented here is that bandlimited measurements in an anechoic or hemianechoic chamber will always have some error due to the chamber, with that error being reduced by the use of large-bandwidth measurements; however, that practice would reduce the frequency discrimination of such measurements accordingly. There is no such thing as an "incoherent" source in a chamber if bandlimited measurements are performed.

Finally, this work demonstrates that the use of an "incoherent image-source" method-of-images model for simulation of broadband performance of anechoic and hemianechoic chambers is fundamentally flawed.

[1]ISO 3745-2003 "Acoustics-Determination of sound power levels of noise sources - Precision methods for anechoic and semi-anechoic rooms," (International Organization for Standardization, Geneva, Switzerland).
[2]M. P. M. Luykx and M. L. S. Vercammen, "Reflections in anechoic rooms," in *Proceedings of Inter-Noise 2001*, The Hague, The Netherlands, CD Proceedings available through The Acoustical Society of the Netherlands, www.internoise2001.nl, pp. 2187–2191 (2001).
[3]K. A. Cunefare, V. B. Biesel, A.-M. Albanese, M. Holdhusen, A. Graf, R. Rye, and J. Tran, "Anechoic chamber qualification per ISO 3745 and ASA/ANSI S12.35," in *Proceedings of 17th International Congress of Acoustics*, Rome, Italy, CD Proceedings, paper 6B.05.03 (2001).
[4]K. A. Cunefare, V. B. Biesel, J. Tran, R. Rye, A. Graf, M. Holdhusen, and A.-M. Albanese, "Anechoic chamber qualification: Traverse method, inverse square law analysis method, and nature of test signal," J. Acoust. Soc. Am. **113**, 881–892 (2003).
[5]V. Wittstock and C. Bethke, "The influence of bandwidth on the qualification of anechoic and hemianechoic rooms," in *Proceedings of The 33rd International Congress and Exposition on Noise Control Engineering*, Prague, Czech Republic, CD Proceedings available through INCE-USA, www.inceusa.org (2004).
[6]J.-Q. Wang and B. Cai, "Calculation of free-field deviation in an anechoic room," J. Acoust. Soc. Am. **85**, 1206–1212 (1989).
[7]J. Duda, "Inverse square law measurements in anechoic rooms," Sound Vib. **32**(12), 20–25 (1998).
[8]W. R. Stroh, "Direct measurement of the acoustic ratio," J. Acoust. Soc. Am. **31**, 234–238 (1959).
[9]Fundamentals of Noise and Vibration, edited by F. Fahy and J. Walker (E & FN Spon, London, 1998).
[10]H. Kuttruff and H. G. Bruchmuller, "On measuring techniques for the examination of anechoic rooms," Acustica **30**, 342–349 (1974).
[11]M. E. Delany and E. N. Bazley, "The high frequency performance of wedge-lined free field rooms," J. Sound Vib. **55**, 195–214 (1977).
[12]M. A. Nobile, "Measurement of the spherical wave absorption coefficient at oblique incidence using the two-microphone transfer function method," in *Proceedings of Inter-Noise 89*, Newport Beach, CA, Institute of Noise Control Engineering, pp. 1067–1072 (1989).

A note on the calibration of pressure-velocity sound intensity probes[a)]

Finn Jacobsen[b)] and Virginie Jaud[c)]
Acoustic Technology, Ørsted-DTU, Technical University of Denmark, Building 352, Ørsteds Plads, DK-2800 Kgs. Lyngby, Denmark

(Received 20 January 2006; revised 18 May 2006; accepted 20 May 2006)

A pressure-velocity sound intensity probe is a device that combines a pressure microphone with a particle velocity transducer. Various methods of calibrating such sound intensity probes are examined: a far field method that requires an anechoic room, a near field method that involves sound emitted from a small hole in a plane baffle, a near field method where the sound is emitted from a hole in a spherical baffle, and a method that involves an impedance tube. The performance of the two near field methods is examined both in an anechoic room and in various ordinary rooms. It is shown that whereas reflections from the edges from a plane baffle disturb the calibration, the method based on a spherical baffle gives acceptable results in a wide frequency range even when the calibration is carried out in a small office, provided that the distance between the hole and the device under test is about 5 cm. © *2006 Acoustical Society of America.* [DOI: 10.1121/1.2214144]

PACS number(s): 43.58.Vb, 43.58.Fm, 43.20.Ye [AJZ] Pages: 830–837

I. INTRODUCTION

Until recently direct measurement of the acoustic particle velocity in air was almost impossible. However, a pressure-velocity ("*p-u*") sound intensity probe based on a particle velocity transducer called the "Microflown" combined with a small pressure microphone has now been available for some years,[1,2] and recent results seem to indicate that it is viable.[3] The potential applications of such a device include the applications of the conventional, standardized sound intensity measurement technique based on pairs of matched condenser microphones (the "*p-p* method"),[4,5] that is, measurement of sound power, identification and ranking of sources, visualization of sound fields, measurement of transmission loss, identification of transmission paths, etc.[6] However, there seem to be additional potential applications, for instance measurement of sound absorption,[7,8] and near field acoustic holography[9] and other inverse source identification techniques.[10,11] It is also potentially useful that a particle velocity transducer placed close to a vibrating surface is less affected by background noise than a pressure microphone.[12,13] Most of these applications rely on accurate calibration of the two transducers of the *p-u* intensity probe, and for some applications the phase calibration has been shown to be of critical importance.[3,8] However, whereas calibration of the pressure microphones of a *p-p* sound intensity probe is fairly simple and unproblematic,[4–6] there is no established method of calibrating a *p-u* probe.[6] The two transducers are completely different and cannot be expected to have the same amplitude and phase response, and therefore it is necessary to determine a correction of one of them relative to the other. Since condenser microphones are well behaved and easy to calibrate with a reference microphone the obvious choice is to calibrate the particle velocity transducer relative to the pressure transducer of the *p-u* probe.[6]

Calibration of a *p-u* intensity probe involves exposing it to a sound field with a known relationship between the sound pressure and the particle velocity. A number of methods have been described in the literature. In the underwater acoustics community, where the *p-u* intensity measurement principle is more established than in air-borne sound, a common calibration technique involves the use of a vertical water-filled tube in which the water-air interface provides an almost perfect pressure-release termination and thus a known relation between the pressure and the velocity in the sound field in the tube.[14–16] A similar method can be used in air with a rigidly terminated tube,[1,2] but since modes of higher order must be avoided the frequency range is limited to a few kilohertz. One can also calibrate in a large anechoic room.[3] However, there is obviously a need for a calibration technique that covers a substantial part of the audible frequency range and can be used *in the field*. One possible such field calibration method involves measuring relatively near a small loudspeaker in an ordinary room and removing the influence of room reflections using a time-selective technique.[7] However, because of the resulting truncation of the impulse response this method is not accurate at low frequencies.[7]

If the measurement takes place very close to a source then reflections from the surroundings can perhaps be ignored. The purpose of this paper is to examine various methods of calibrating *p-u* sound intensity probes, including two near field techniques that might work also in ordinary rooms.

[a)]Portions of this work were presented in "Measurement of sound intensity: *p-u* probes versus *p-p* probes," Proceedings of Noise and Vibration Emerging Methods 2005, Saint Raphaël, France, April 2005, and in "Calibration of *p-u* intensity probes," Proceedings of Euronoise 2006, Tampere, Finland, May 2006.

[b)]Author to whom correspondence should be addressed; Electronic mail: fja@oersted.dtu.dk
[c)]Electronic mail: virginie.jaud@gmail.com

II. OUTLINE OF THEORY

The complex sound intensity can be expressed in terms of the cross spectrum between the sound pressure and the particle velocity,[3,6]

$$I_r + jJ_r = S_{pu}, \tag{1}$$

where I_r is the active intensity, J_r is the reactive intensity, and S_{pu} is the cross spectrum. However, the "true" particle velocity is not directly available; therefore the available signal from the particle velocity transducer must be corrected in phase and in amplitude by multiplying with a complex transfer function, $H_{\hat{u}u}$. This function can be determined by exposing the *p-u* intensity probe to sound field conditions where the specific acoustic impedance is known. The ratio of the "true" specific acoustic admittance in the sound field at the position where the *p-u* intensity probe is placed during calibration, H_{pu}, to the corresponding measured frequency response between the signals from the probe, $H_{p\hat{u}}$, provides the correction of the particle velocity signal relative to the pressure signal, to be used in subsequent measurements of the complex sound intensity as follows:[3,6]

$$S_{p\hat{u}}H_{\hat{u}u} = S_{p\hat{u}}\frac{H_{pu}}{H_{p\hat{u}}} = S_{pu} = I_r + jJ_r, \tag{2}$$

where $S_{p\hat{u}}$ is the measured cross spectrum between the sound pressure and the particle velocity.

A. Far field calibration in an anechoic room

The simplest solution would be to expose the device under test to a propagating plane wave in which the specific acoustic admittance equals the reciprocal of the characteristic impedance of the medium,

$$H_{pu}^{(1)} = \frac{1}{\rho c}. \tag{3}$$

However, one cannot obtain plane wave conditions at low frequencies even in the largest room, but must correct for the change in phase and amplitude associated with a finite distance to the source.[3] If the source can be assumed to be a monopole a distance of r from the observation point then Eq. (3) becomes

$$H_{pu}^{(2)} = \frac{1}{\rho c}\left(1 + \frac{1}{jkr}\right), \tag{4}$$

where k is the wave number. (Note that the $e^{j\omega t}$ convention is used in this paper.) Figure 1, which shows the ratio of $H_{pu}^{(2)}$ to $H_{pu}^{(1)}$, demonstrates that the phase shift associated with the finite distance cannot be neglected below a few hundred hertz even at a distance of 4 m. No ordinary loudspeaker resembles a monopole in its near field, and therefore a distance of several meters is needed. Thus a very special source or a large anechoic room of high quality is required.

B. A monopole on a rigid plane baffle

If the sound field could be generated by a real monopole one might use Eq. (4) also very near the source, perhaps even without an anechoic room. Unfortunately it is very difficult to construct a "real monopole," that is, an omnidirectional source that can cover a wide frequency range. On the other hand, a small circular hole in a large plane baffle, driven by an enclosed loudspeaker on the other side of the baffle, might approximate a monopole on a baffle and thus generate a simple spherical sound field in the half-space in front of the baffle. In principle the hole should be as small as possible, and the *p-u* intensity probe should be placed very near the hole. However, in practice the dramatic increase of the particle velocity level relative to the sound pressure level very near a monopole, the need for a well-defined distance between the hole and the transducer, the influence of scattering caused by the transducer, and the influence of reflections from the edges of the baffle call for a compromise. Figure 2 shows the ratio of $H_{pu}^{(2)}$ to $H_{pu}^{(1)}$ in the near field of a monopole on a baffle.

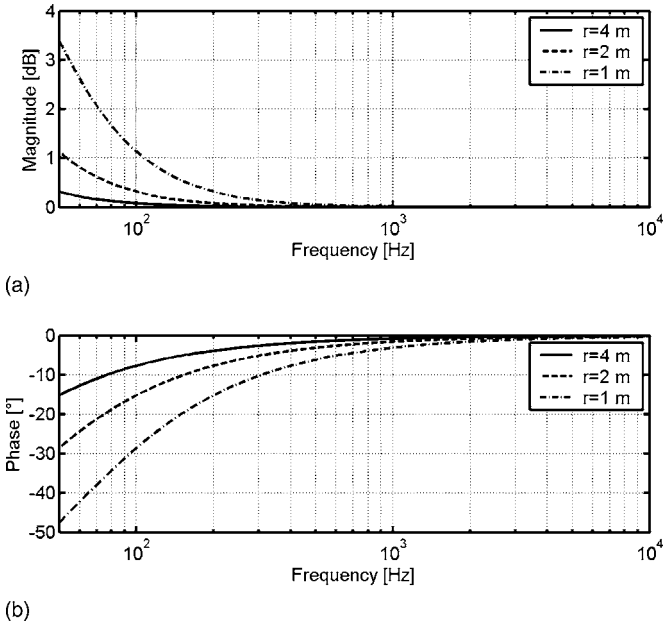

FIG. 1. Magnitude (a) and phase (b) of the normalized specific acoustic admittance at three different distances in the far field of a monopole.

If the hole is small compared with the wavelength then the sound field inside the hole is one-dimensional, and one can improve Eq. (4) by regarding the resulting source as a piston on a baffle. At a distance of r from a baffled, circular piston of radius b the specific acoustic admittance is[17]

$$H_{pu}^{(3)} = \frac{1}{2\rho c}\left(1 + \frac{r}{\sqrt{r^2+b^2}} - j\left(1 - \frac{r}{\sqrt{r^2+b^2}}\right) \times \cot\left(\frac{k}{2}[\sqrt{r^2+b^2} - r]\right)\right) \tag{5}$$

on the axis of the piston. Figure 3 shows the ratio of $H_{pu}^{(3)}$ to $H_{pu}^{(2)}$ at a distance of 5 cm from the baffle. It can be seen that the influence of a finite radius is fairly small except when the distance r is comparable to the diameter $2b$. Note that the magnitude of the specific acoustic impedance is reduced by a finite source, in agreement with the fact that the acoustic center of a piston on a baffle is behind the actual surface.[18]

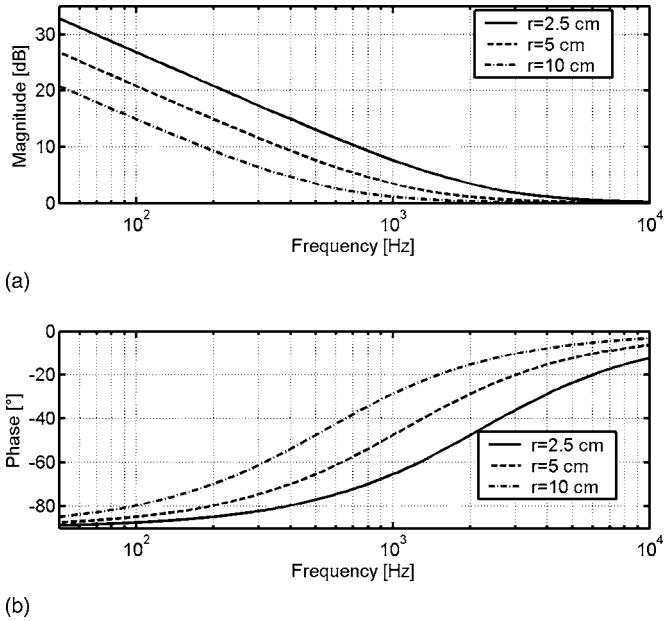

FIG. 2. Magnitude (a) and phase (b) of the normalized specific acoustic admittance at three different distances in the near field of a monopole on a plane baffle.

C. A monopole on a rigid spherical baffle

In practice a plane baffle must obviously be finite, and thus there will inevitably be reflections from the edges. Vibrations caused by the loudspeaker reaction might also be a problem. On the other hand a spherical baffle has no edges and can easily be made very stiff. Thus another solution might be to let the source be a small hole in a hollow rigid sphere driven by a loudspeaker inside the sphere. In the sound field generated by a point source on a rigid sphere the specific acoustic admittance on the axis has the value[19]

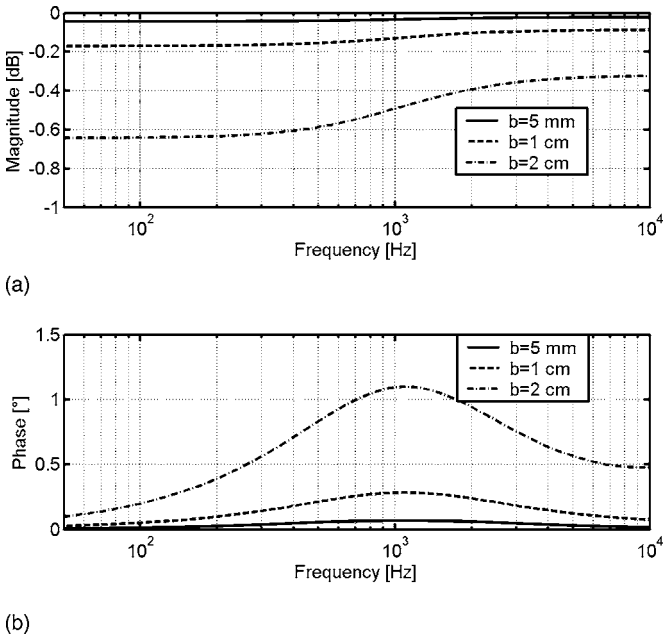

FIG. 3. The effect of the radius of a circular piston, b, on a plane baffle on the (a) magnitude and (b) phase of the specific acoustic admittance at a position 5 cm from the piston.

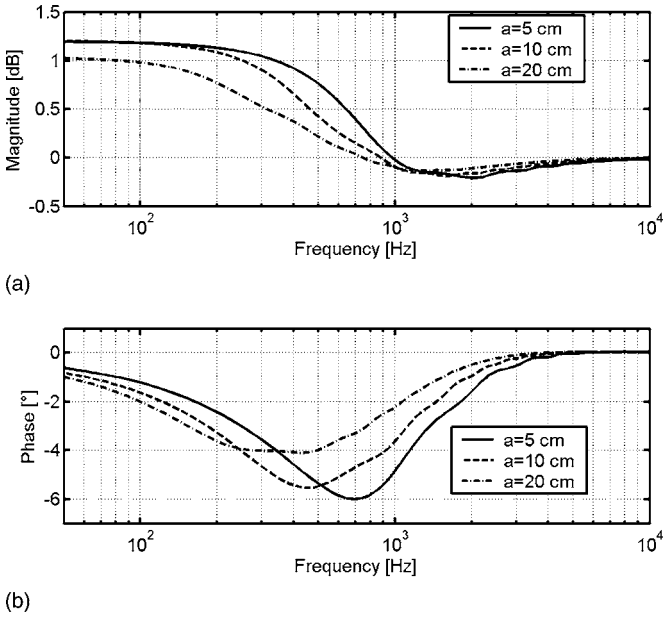

FIG. 4. Magnitude (a) and phase (b) of the ratio of the specific acoustic admittance 5 cm from a monopole on a rigid sphere of radius a to the specific acoustic admittance 5 cm from a monopole on a plane baffle.

$$H_{pu}^{(4)} = \frac{j}{\rho c} \frac{\sum_{m=0}^{\infty} \left(m + \frac{1}{2} \right) \frac{h_m'(kr)}{h_m'(ka)}}{\sum_{m=0}^{\infty} \left(m + \frac{1}{2} \right) \frac{h_m(kr)}{h_m'(ka)}}, \tag{6}$$

where a is the radius of the sphere, r is the distance from the observation point to the center of the sphere, h_m is the spherical Hankel function of the second kind and order m, and h_m' is its derivative.

Figure 4 shows the ratio of the specific acoustic impedance in front of a monopole on a spherical baffle, $H_{pu}^{(4)}$, to the specific acoustic admittance in front of a monopole on a planar baffle, $H_{pu}^{(2)}$, at a distance of 5 cm. This ratio is close to unity, indicating that the two admittances are similar. Note that the specific acoustic admittance at a given position in front of a monopole on a sphere at low frequencies is larger than the specific acoustic admittance in front of a monopole on a plane baffle, in agreement with the fact that the acoustic center of a monopole on a sphere is in front of the physical source whereas the acoustic center of a monopole on a plane baffle coincides with the source.[18] Note also the small irregularities between 1 and 5 kHz; they are due to interference between the direct wave and a wave that has traveled around the sphere. In the limit of $a \to 0$ and $a \to \infty$ Eq. (6) approaches Eq. (4).

Since the hole in the sphere cannot be infinitely small one might regard it as a small piston of radius b rather than a point source. In this case the specific acoustic admittance becomes[19]

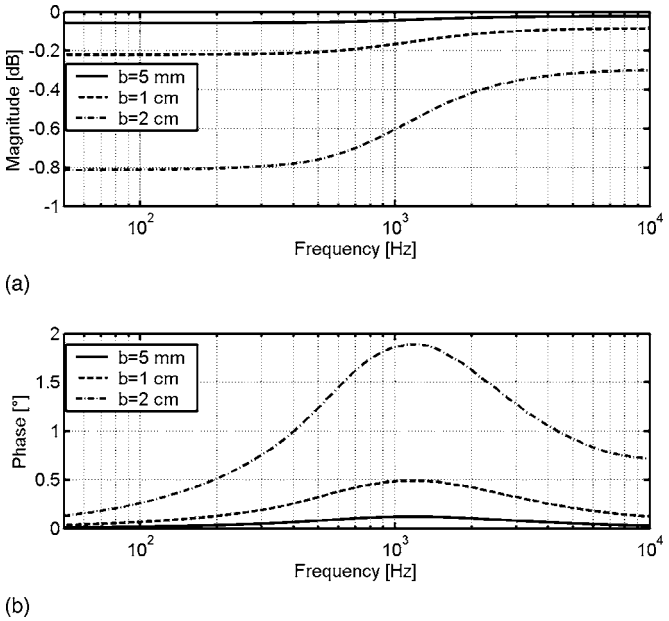

FIG. 5. The effect of the radius of a circular piston, b, on a rigid sphere with a radius of 10 cm on the magnitude (a) and phase (b) of the specific acoustic admittance at a position 5 cm from the piston.

$$H_{pu}^{(5)} = \frac{j}{\rho c} \frac{\sum_{m=0}^{\infty} (P_{m-1}(\cos\alpha) - P_{m+1}(\cos\alpha)) \frac{h_m'(kr)}{h_m'(ka)}}{\sum_{m=0}^{\infty} (P_{m-1}(\cos\alpha) - P_{m+1}(\cos\alpha)) \frac{h_m(kr)}{h_m'(ka)}}, \quad (7)$$

where $\alpha = \arcsin(b/a)$ and P_m is the Legendre function of order m.

The ratio of $H_{pu}^{(5)}$ to $H_{pu}^{(4)}$ is shown in Fig. 5. As can be seen the effect of a finite size of the piston on a sphere is similar to but somewhat larger than the effect of a finite piston on a plane baffle.

D. Two methods based on an impedance tube

Yet another possibility is to use a standing wave tube with a rigid termination. Under such conditions the specific acoustic admittance is

$$H_{pu}^{(6)} = \frac{j \tan(kl)}{\rho c}, \quad (8)$$

where l is the distance between the transducer and the rigid termination. Obviously this method breaks down when this distance is a multiple of a quarter of a wavelength. Moreover, viscothermal losses must be taken into account unless the distance is relatively short,[20] which suggests that l should be less than a quarter of a wavelength at the highest frequency at which the underlying assumption of plane waves holds good. It is not possible to cover the entire frequency range of interest with the tube method.

Alternatively one might measure the frequency response between the particle velocity signal and the sound pressure at the rigid termination using a reference microphone at the termination, and then compensate for the difference between the pressure channel of the p-u probe and the reference microphone by placing the p-u probe next to the reference microphone at the termination in a subsequent measurement. The ratio of the particle velocity to the pressure at the termination is

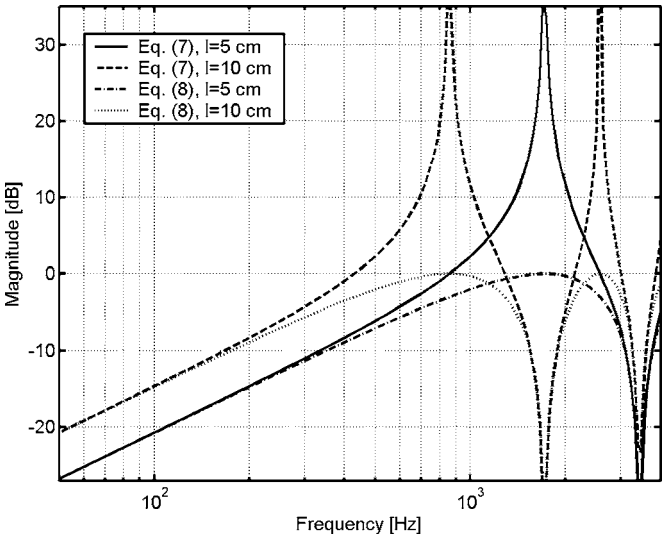

FIG. 6. Magnitude of the normalized specific acoustic admittance at two different positions in a tube with a rigid termination, and magnitude of the normalized ratio of the particle velocity at the same positions to the pressure at the rigid termination.

$$H_{pu}^{(7)} = \frac{j \sin(kl)}{\rho c}, \quad (9)$$

and this expression gives useful results an octave above Eq. (8) as can be seen in Fig. 6. Equations (8) and (9) can easily be extended to take account of viscous and thermal propagation losses in the tube and thermal losses at the rigid termination,[20] and this has also been tried. However, with the tube dimensions used in the investigation described in what follows the effect of such losses is completely negligible.

III. EXPERIMENTAL RESULTS

The two near field methods described in Sec. II have been examined both in a large anechoic room that provides a good approximation to free-field conditions down to 50 Hz,[21] in an ordinary room of about 180 m^3 and a reverberation time of about 0.5 s, and in a small office. In the anechoic room the far field method was also applied since, presumably, this method is the most accurate one. In all cases a Brüel and Kjær (B&K) "Pulse" analyzer of type 3560 in one-twelfth octave mode was used (although the results presented in what follows are plotted in one-third octave bands). The device under test was a Microflown $\frac{1}{2}$ inch p-u sound intensity probe. Three sources were used in these experiments. In the far field measurements the source was a 60 mm diameter two-way "coincident-source" loudspeaker unit produced by KEF, mounted in a rigid plastic sphere with a diameter of 270 mm. The "monopole on an infinite baffle" was a wooden IEC baffle for loudspeaker testing with dimensions 1.35×1.65 m with a 20 mm diameter hole (with a brass ring so as to reduce flow noise caused by the high air velocity) driven by a conventional small enclosed loudspeaker unit

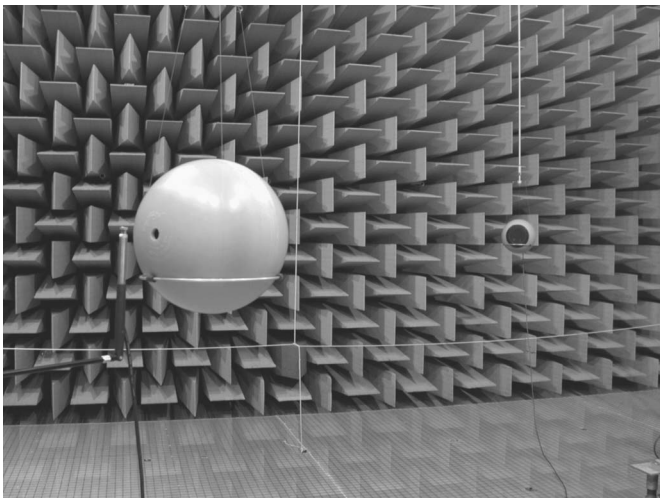

FIG. 7. The Microflown *p-u* probe close to the experimental "monopole on a sphere" in the anechoic room. In the background the experimental "piston on a sphere" can be seen.

produced by VIFA behind the baffle. The "monopole on a sphere" was 90 mm VIFA unit mounted inside a rigid plastic sphere with a diameter of 270 mm with a 20 mm diameter hole in front of the loudspeaker. Figure 7 shows the Microflown *p-u* intensity probe close to the "monopole on a sphere" in the anechoic room. In the background the KEF loudspeaker mounted in a sphere can be seen.

All loudspeakers were driven with signals generated by the "Pulse" analyzer and passed through a one-third octave band equalizer (GE27, produced by Rane). Before each measurement the equalizer was adjusted so as to get the flattest possible response of the sound pressure and particle velocity signals. The "frequency-band coherence" between these two signals[22] turned out to be useful for finding the best setting of the equalizer; the best results were obtained with a frequency-band coherence of unity in the entire frequency range.

Figure 8 shows the amplitude and phase correction of the *p-u* probe measured with the KEF loudspeaker in the anechoic room at four different distances from 27 cm to 7.2 m. The measured frequency responses have been processed using Eq. (7), that is, assuming that the source can be modeled as a piston on a sphere. The strange behavior of the phase at 8 and 10 kHz is probably due to the irregular pressure response of the *p-u* probe in this frequency range.[3] Close examination reveals some small irregularities in the amplitude and phase determined at the longest distance where the source has probably been too close to the wedges of the anechoic room, but on the whole the results agree within ±0.3 dB and ±1° above 100 Hz, as can be seen in Fig. 9, which shows the same data as Fig. 8, but normalized with the correction determined at 70 cm distance. The data have also been processed using Eq. (4), that is, assuming that the loudspeaker can be modeled as a monopole. The results (not shown) are very similar, but the agreement is slightly better with the piston-on-a-sphere model [Eq. (7)], in particular at the shortest distance. Accordingly, the correction based on this model and data obtained at a distance of 70 cm are used as a reference in what follows. It should be mentioned that

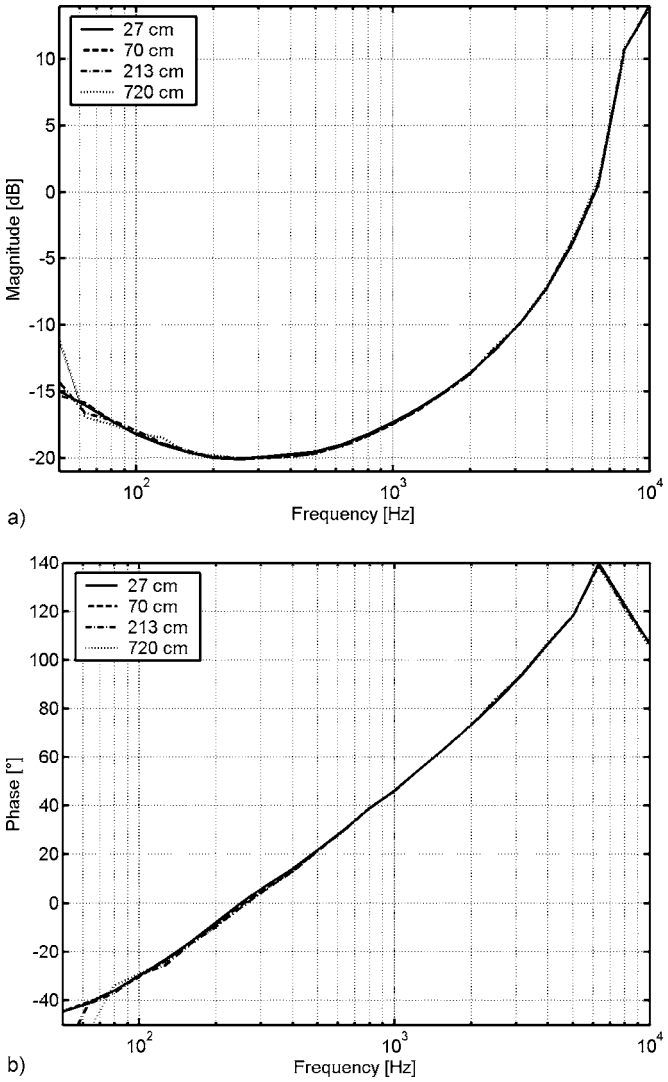

FIG. 8. Amplitude (a) and phase (b) calibration of the Microflown *p-u* probe determined at four different distances from the KEF loudspeaker mounted in a sphere in the anechoic room.

similar corrections determined in the same anechoic room at different distances from a more conventional two-way loudspeaker (Rogers LS3/5A "Monitor Loudspeaker") did not agree nearly as well at low frequencies,[3] confirming that a "coincident source" loudspeaker mounted in a sphere approximates a monopole (and, of course, a piston on a sphere) far better than an ordinary loudspeaker in a rectangular box.

Figure 10 shows the amplitude and phase correction determined at three different distances from the "monopole on a sphere" in the anechoic room, normalized with the reference calibration. Although it hardly matters the expression that takes account of the finite size of the hole [Eq. (7)] was used in processing the measured data. Between 63 Hz and 1.6 kHz the results agree with the reference measurement within ±0.5 dB and ±2°. The agreement is less perfect but still quite good between 2 and 8 kHz.

Figure 11 shows the results of similar measurements at two different distances from the "monopole on a sphere" in the ordinary room. Above 100 Hz the results are similar to the results obtained with the same source in the anechoic room, although there are more erratic (small) variations with

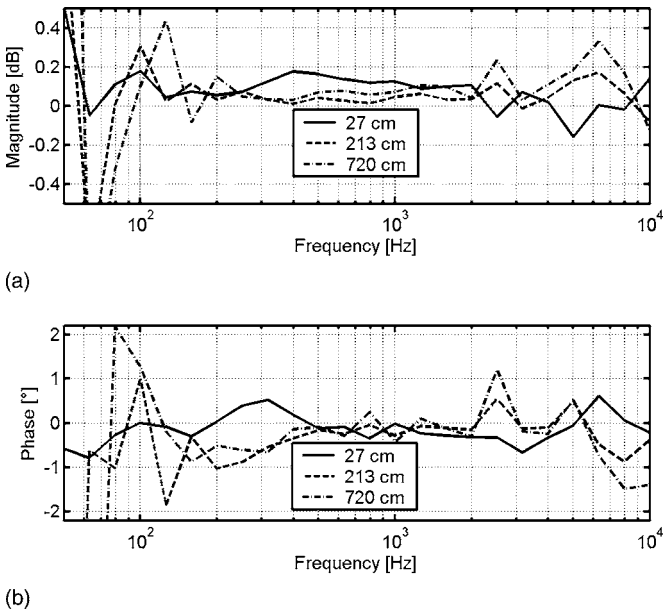

FIG. 9. Amplitude (a) and phase (b) calibration determined at three different distances from the KEF loudspeaker in the anechoic room relative to the calibration determined at a distance of 70 cm.

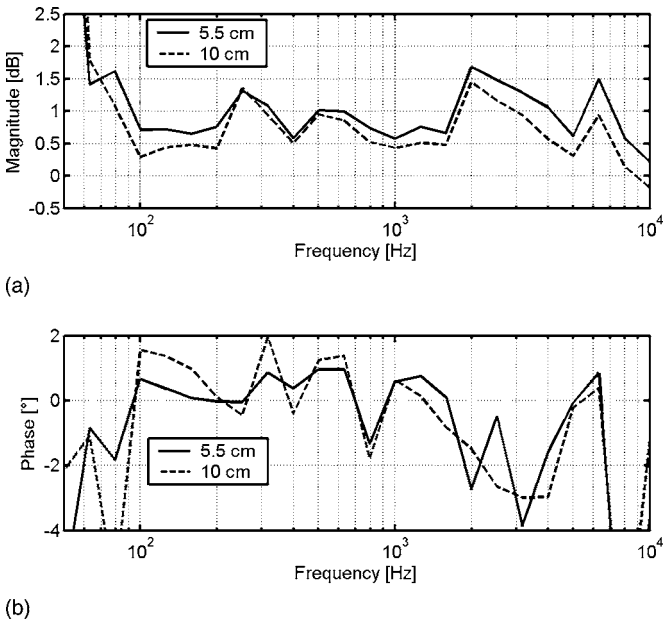

FIG. 11. Amplitude (a) and phase (b) calibration determined at two different distances from the "monopole on a sphere" in an ordinary room relative to the reference calibration.

the frequency, but for some reason the amplitude seems to have been shifted about 0.7 dB. Results obtained at other positions in the same room and in the small office (not shown) were very similar except below 100 Hz.

Figure 12 shows the results of the measurements close to the "monopole on a plane baffle" in the anechoic room. Also in this case the presumably most accurate expression that takes account of the finite dimension of the hole [Eq. (5)] was used. In this case somewhat larger systematic deviations (within ±4°) between the phase and the reference phase occur. These deviations, which could also be seen in similar measurements carried out in the ordinary room (not shown), are undoubtedly caused by reflections from the edges of the baffle. The same inexplicable tendency to overestimation of the amplitude correction by about 0.7 dB as observed in Fig. 11 can also be seen here.

Figure 13 shows a tube with a reference microphone (a B&K microphone of type 4192) at the rigid termination. The tube is driven by a loudspeaker at the other end, and the resonances are damped by absorbing material placed in front of the loudspeaker. The holes for the transducers are tightened with rubber rings, and holes not used are blocked by solid brass plugs. The distance l is 5 cm, so in principle the

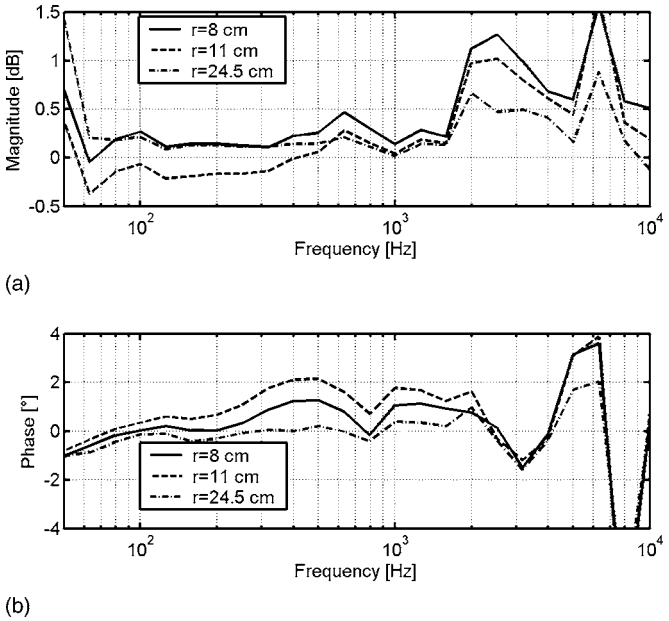

FIG. 10. Amplitude (a) and phase (b) calibration determined at three different distances from the "monopole on a sphere" in the anechoic room relative to the reference calibration.

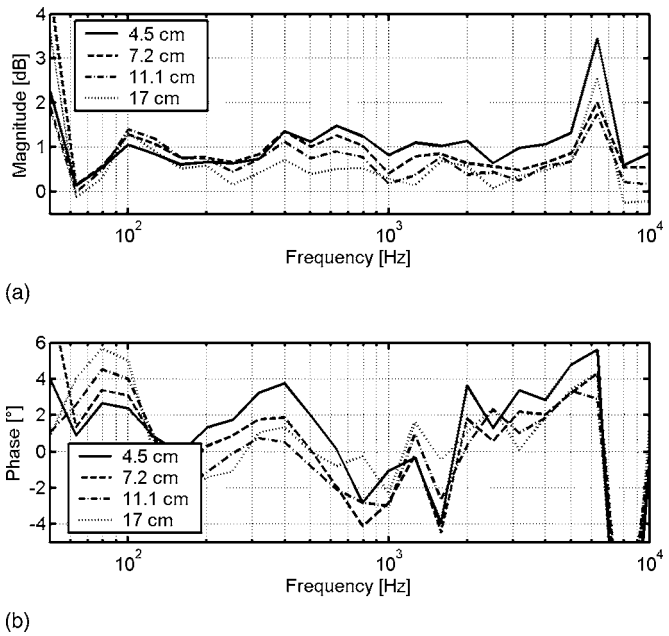

FIG. 12. Amplitude (a) and phase (b) calibration determined at four different distances from the "monopole on a plane baffle" in the anechoic room relative to the reference calibration.

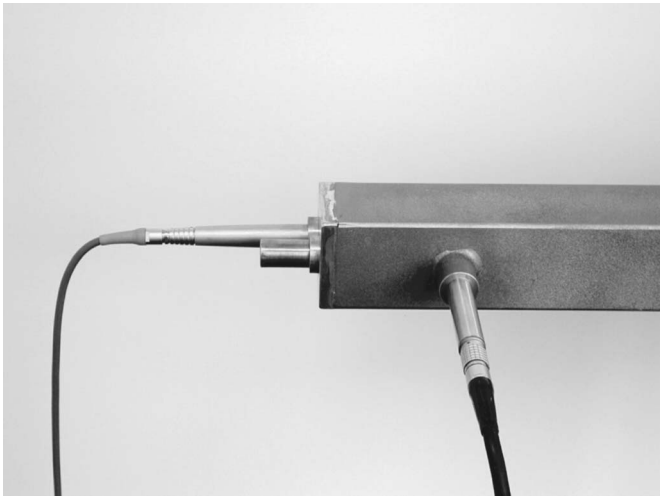

FIG. 13. Tube with the Microflown *p-u* probe mounted 5 cm from the rigid termination and a B&K microphone mounted at the termination.

device should work up to 1.7 kHz if the "direct" method based on Eq. (8) is used and up to 3.4 kHz if the alternative method involving a reference microphone is used (cf. Fig. 6). In this case the "Pulse" analyzer was used in the FFT mode with a spectral resolution of 1 Hz. Figure 14 shows a comparison of the resulting amplitude and phase corrections with the reference measurement from the anechoic room. The two amplitude corrections agree with the reference within 1 dB, and the two phase corrections agree with the reference within 4° except above 1.5 kHz. There is no obvious explanation for the systematic underestimation of the amplitude seen between 200 and 400 Hz and the systematic overestimation of the phase beween 300 and 600 Hz.

IV. DISCUSSION

It seems clear that the most accurate calibration method requires a large anechoic room. However, from a practical point of view the near field method based on a "monopole on a sphere" is more interesting. The most obvious contribution to the measurement uncertainty with this method is associated with determining the physical distance r in Eq. (6) [or Eq. (7)]. If the uncertainty on a "true" distance of 5 cm amounts to, say, 1 mm, then the resulting uncertainty will take values up to 0.2 dB and 0.6°. On the other hand, increasing the distance inevitably increases the influence of deviations from perfect free-field conditions. Reflections of extraneous noise from the sphere may disturb the weak pressure signal (cf. Fig. 2), and this problem is probably most serious if the transducer is very close to the sphere. A distance of 5 cm seems a good compromise. However, it is clear from the experimental results that there are other contributions to the resulting uncertainty than the uncertainty on the distance.

The small but apparently systematic deviations seen in Fig. 10(a) between 2 and 6.3 kHz, the small but systematic overestimation seen in Figs. 11(a) and 12(a), and the small deviations seen in Figs. 14(a) and 14(b) may *perhaps* be due to the transducer under test rather than the calibration procedures. It is apparent from Figs. 1, 2, and 6 that the specific

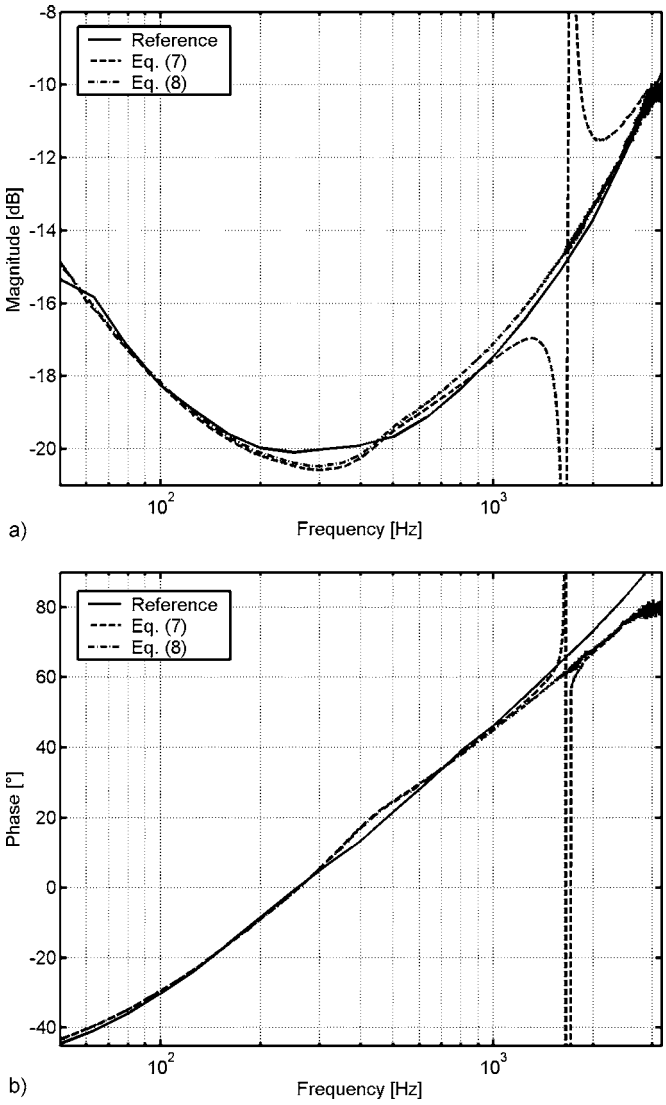

FIG. 14. Amplitude (a) and phase (b) calibration determined in the tube using the methods based on Eq. (8) and Eq. (9). The reference calibration determined in the anechoic room is also shown.

acoustic admittance takes values that vary over an interval of 40 dB, and *perhaps* the particle velocity transducer is not perfectly linear.

The required accuracy of the calibration depends, of course, on the application of the *p-u* intensity probe. In Ref. 8 it was concluded that reliable measurement of absorption coefficients with such a device calls for calibration errors within 0.5 dB and 2° unless the sample under test is highly absorbing, in which case somewhat larger errors can be tolerated. The results presented in the foregoing indicate that this accuracy can be achieved in a large anechoic room of good quality. However, it seems that it is only just possible to satisfy this requirement with the "monopole on a sphere" in an ordinary room.

The analysis presented in Ref. 3 showed that the required accuracy of the phase calibration of a *p-u* intensity probe used in sound power measurements depends on whether the measurements take place in the reactive near field of the source under test or not. If near fields are avoided then fairly large phase errors, say ±10°, can be tolerated.

However, if the measurement surface is close to a source the ratio of the reactive to the active intensity may well take values of up to 10 dB at low frequencies,[3,23] and then even a phase error of ±2.5° is unacceptable (the resulting error in the estimated sound power would be 1.6 dB/−2.5 dB). With *extremely* reactive sound field conditions, as in the experiments with the loudspeaker dipole described in Ref. 3, only a very good calibration carried out in a large anechoic room will be good enough. If an anechoic room of adequate quality is not available then the only way of obtaining a phase correction of satisfactory accuracy seems to be to use the phase adjustment technique described in Ref. 3.

The investigation presented here has concentrated on calibrating the particle velocity transducer relative to the pressure microphone of the *p-u* intensity probe. However, it is perhaps worth mentioning that absolute calibration of a particle velocity transducer may be possible with the "monopole on a sphere" using the sound pressure behind the loudspeaker inside the sphere as a reference. This pressure, which can be measured with a calibrated condenser microphone, is proportional to the volume displacement.

V. CONCLUSIONS

A number of methods of calibrating a *p-u* sound intensity probe have been examined. The most accurate method requires an anechoic room of good quality and a "coincident source" loudspeaker mounted in a sphere. If the anechoic room is sufficiently large then an ordinary loudspeaker placed far from the transducer under test can be used instead. A near field method involving sound emitted from a hole in a hollow rigid sphere gives slightly less accurate results, but has the significant advantage that it can be used in the field. Alternatively, a similar near field method with a plane baffle can be used, also in the field, but this method is less accurate than the method based on a sphere since reflections from the edges of the baffle cannot be avoided. Finally, it is possible to calibrate in an impedance tube, although only in a limited frequency range.

ACKNOWLEDGMENTS

The authors would like to thank Microflown for lending us a *p-u* intensity probe. The authors would also like to thank Vicente Cutanda for the idea of using a spherical baffle.

[1]H.-E. de Bree, "The Microflown: An acoustic particle velocity sensor," Acoust. Aust. **31**, 91–94 (2003).
[2]R. Raangs, W. F. Druyvesteyn, and H.-E. de Bree, "A low-cost intensity probe," J. Audio Eng. Soc. **51**, 344–357 (2003).
[3]F. Jacobsen and H. E. de Bree, "A comparison of two different sound intensity measurement principles," J. Acoust. Soc. Am. **118**, 1510–1517 (2005).
[4]IEC Publication 61043, *Instruments for the Measurement of Sound Intensity—Measurements with Pairs of Pressure Sensing Microphones* (International Electrotechnical Commission, Geneva, Switzerland, 1993).
[5]American National Standard ANSI S1.9-1996, *Instruments for the Measurement of Sound Intensity* (American National Standards Institute, New York, 1996).
[6]F. J. Fahy, *Sound Intensity*, 2nd ed. (E & FN Spon, London, 1995).
[7]H.-E. de Bree, R. Lanoye, S. de Cock, and J. van Heck, In situ, broad band method to determine the normal and oblique reflection coefficient of acoustic materials, SAE technical paper 2005-01-2443, SAE noise and vibration conference and exhibition, Grand Traverse, MI, USA, 2005.
[8]Y. Liu and F. Jacobsen, "Measurement of absorption with a *p-u* sound intensity probe in an impedance tube," J. Acoust. Soc. Am. **118**, 2117–2120 (2005).
[9]F. Jacobsen and Y. Liu, "Near field acoustic holography with particle velocity transducers," J. Acoust. Soc. Am. **118**, 3139–3144 (2005).
[10]R. Visser, "Acoustic source localization based on pressure and particle velocity measurements," Proceedings of Inter-Noise 2003, Jeju, Korea, 2003, pp. 665–670.
[11]R. Visser, A boundary element approach to acoustic radiation and source identification, Ph.D. thesis, University of Twente, The Netherlands, 2004.
[12]O. Wolff and R. Sottek, Panel contribution analysis—An alternative window method, SAE technical paper 2005-01-2273, SAE noise and vibration conference and exhibition, Grand Traverse, MI, USA, 2005.
[13]H.-E. de Bree and W. F. Druyvesteyn, A particle velocity sensor to measure the sound from a structure in the presence of background noise, Proceedings of forum acusticum 2005, Budapest, Hungary, 2005.
[14]T. B. Gabrielson, D. L. Gardner, and S. L. Garret, "A simple neutrally buoyant sensor for direct measurement of particle velocity and intensity in water," J. Acoust. Soc. Am. **97**, 2227–2237 (1995).
[15]K. Kim, T. B. Gabrielson, and G. C. Lauchle, "Development of an accelerometer-based underwater acoustic intensity sensor," J. Acoust. Soc. Am. **116**, 3384–3392 (2004).
[16]K. J. Bastyr, G. Lauchle, and J. A. McConnel, "Development of a velocity gradient underwater acoustic intensity sensor," J. Acoust. Soc. Am. **106**, 3178–3188 (1999).
[17]K. Beissner, "On the plane-wave approximation of acoustic intensity," J. Acoust. Soc. Am. **71**, 1406–1411 (1982).
[18]F. Jacobsen, S. Barrera Figueroa, and K. Rasmussen, "A note on the concept of acoustic center," J. Acoust. Soc. Am. **115**, 1468–1473 (2004).
[19]E. G. Williams, *Fourier Acoustics. Sound Radiation and Nearfield Acoustical Holography* (Academic Press, London, 1999).
[20]S. W. Rienstra and A. Hirschberg, An introduction to acoustics, Technische Universiteit Eindhoven, 1999.
[21]F. Ingerslev, O. J. Pedersen, P. K. Møller, and J. Kristensen, "New rooms for acoustic measurements at the Danish Technical University," Acustica **19**, 185–199 (1968).
[22]F. Jacobsen, "Active and reactive, coherent and incoherent sound fields," J. Sound Vib. **130**, 493–507 (1989).
[23]F. Jacobsen and H.-E. de Bree, Intensity-based sound power determination under adverse sound field conditions: *p-p* probes versus *p-u* probes, Proceedings of Twelfth International Congress on acoustics and vibration, Lisbon, Portugal, 2005.

Wideband multichannel time-reversal processing for acoustic communications in highly reverberant environments

James V. Candy,[a] David H. Chambers, Christopher L. Robbins, Brian L. Guidry, Andrew J. Poggio, Farid Dowla, and Claudia A. Hertzog
University of California, Lawrence Livermore National Laboratory, P.O. Box 808, Livermore, California 94551

(Received 15 January 2006; revised 15 May 2006; accepted 16 May 2006)

The development of multichannel time-reversal (T/R) processing techniques continues to progress rapidly especially when the need to communicate in a reverberant environment is critical. The underlying T/R concept is based on time-reversing the Green's function characterizing the uncertain communications channel mitigating the deleterious dispersion and multipath effects. In this paper, attention is focused on two major objectives: (1) wideband communications leading to a time-reference modulation technique; and (2) multichannel acoustic communications in two waveguides: a stairwell and building corridors with many obstructions, multipath returns, severe background noise, disturbances, and long propagation paths (~180 ft) including disruptions (bends). It is shown that T/R receivers are easily extended to wideband designs. Acoustic information signals are transmitted with an eight-element array to two receivers with a significant loss in signal levels due to the propagation environment. The results of the new wideband T/R processor and modulation scheme demonstrate that the overall performance for both high (24-bit) and low (1-bit) bit level analog-to-digital converter designs. These results are validated by performing proof-of-principle acoustic communications experiments in *air*. It is shown that the resulting T/R receivers are capable of extracting the transmitted coded sequence from noisy microphone array measurements with zero-bit error.
 [DOI: 10.1121/1.2211588]

PACS number(s): 43.60.Dh, 43.28.We, 43.28.Tc [ES] Pages: 838–851

I. INTRODUCTION

Complex reverberant environments, especially enclosed waveguide structures, offer a distinct challenge to communications systems. Because of the enclosure, short reverberation paths evolve that can rapidly deteriorate the communications medium creating distortion and loss of signal levels due to destructive interference.[1,2] The need to communicate in such environments prove important for a variety of applications based on military operations in caves and underground structures, a maze of buried pipes where systems attempt to communicate critical information about chemical anomalies jeopardizing a city or even the autonomous operations of independent robots servicing hazardous waste facilities in the future. In all of these cases, inherent obstructions cause transmitted signals to reflect, refract, and disperse in a multitude of directions distorting both their shape and arrival times at network receiver locations. Thus, this creates a problem in transmitting information in the form of waves throughout a complex environment. Waves are susceptible to *multiple paths* and *distortions* created by a variety of possible obstructions present in complex waveguide environments. This is precisely the communications problem we solve using the physics of wave propagation to not only mitigate the noxious effects created by the medium, but also to utilize it in a constructive manner enabling a huge benefit in communications. We use *time-reversal*[3,4] (T/R) preprocessing coupled with a wideband receiver design to accomplish this task.

Time-reversal is applied to reconstruct transmitted communication signals by *retracing* all of the multiple paths that originally distorted the transmitted signals. Contrary to intuitive notions, multipath propagation in a communications channel residing in such an environment can be considered a potential advantage by increasing the overall signal-to-noise ratio (SNR)—when utilized properly. T/R communications is based on taking advantage of the multipath arrivals and multiple scatters to enhance SNR. The basic communications problem is to transmit coded information through the environment or medium and receive it at desired receiver or client-station. These client-stations can also broadcast through the medium characterized by unique Green's function paths to create a two-way communication link as depicted in Fig. 1. Here we investigate the performance of wideband communication systems employing sensor arrays using multichannel processors in a reverberant multipath/multiple scatterer environment.

The basic idea in wideband processing for communications is to transmit a short-time information pulse capable of carrying coded information while simultaneously interrogating the medium to extract a set of Green's functions for transmitter-receiver pairs. Many applications simply transmit a sharp, short-time pulse to approximate an impulse from the

[a]Currently on sabbatical leave at the University of Cambridge, Department of Engineering, Signal Processing Group, Trumpington Rd, Cambridge CB2 1PZ, U.K.; electronic mail: tsoftware@aol.com

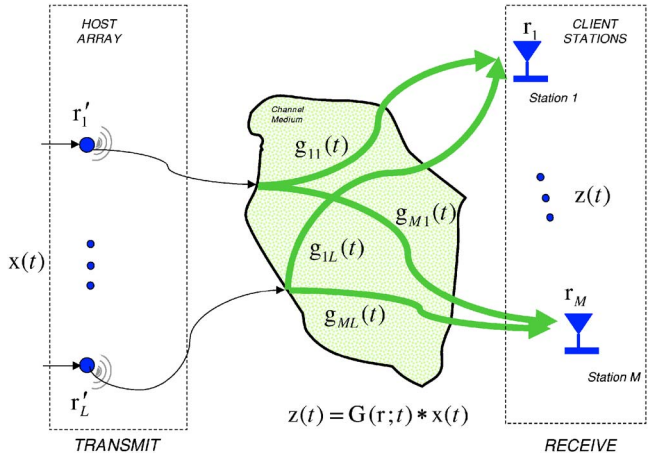

FIG. 1. (Color online) The basic communications problem: Host array transmission to client receiver stations through propagation channel (medium). The basic environment including the host transmitter/receiver, hostile medium along with the corresponding sets of Green's functions transmitter-receiver pairs from host array to client receiver stations in the communications network array.

host-station thereby providing the Green's function response directly to the client-station and then follow it with the coded information message.[1,2] Here we define the *host-station* as the transmitting array and the *client-station* as the receiving stations. Note, however, *both* transmit and receive while communicating. This is the approach we take in this paper simultaneously estimating the channel response and transmitting coded information. We use a correlation-based receiver design coupled with T/R processing to extract the codes from noisy, reverberant data.

T/R communications evolved from the work of Parvulescu[5] where the underlying Green's function of the ocean was first estimated using a pilot signal or probe pulse, time reversed and retransmitted through the medium to focus and achieve a high SNR gain. The realization of multichannel T/R receivers is described by a sequence of papers developing the theory.[6,7] Receiver realizations discussed in this case are equivalent to postprocessing the received data with the estimated Green's functions, this work was followed by equivalent model-based methods.[8,9] Subsequent experiments to demonstrate the performance of T/R in the ocean channel followed.[10–13] Schemes related to that of this paper using a passive approach and correlation-based designs for incoherent communications in underwater acoustics[14–16] were recently developed. Exclusive T/R designs demonstrated the effectiveness of a variety of T/R receiver realizations in a highly reverberant environment for point-to-point and array-to-point communications.[17,18] The work we present in this paper extends these results to the wideband case for both multibit resolution [24-bit analog-to-digital (A/D) conversion] and the minimal resolution "1-bit" T/R receiver designs.[18] The realizations of various 1-bit T/R receivers are discussed and applied to noisy microphone array measurements in these reverberant environments.

In Sec. II, the underlying T/R theory relative to the multichannel communication problem is briefly discussed including the development of the wideband time-reference (TRef) receivers and other essential components of an acoustics communications system. We also include the corresponding 1-bit realization to compare them with the narrowband designs in the well-known stairwell environment.[17,18] The development of a suite of wideband experiments to assess the feasibility and performance of the T/R receivers is described in Sec. III along with the associated signal processing. Finally, we summarize these results and discuss future efforts.

II. T/R COMMUNICATIONS: A BRIEF REVIEW

In this section we briefly discuss the suite of "wideband" multichannel time-reversal receivers used to recover a transmitted information sequence or code from a set of receiver measurements in reverberant, temporally stationary environments. The emphasis is on the processing provided by the various realizations to extract the information signal and characterize receiver performance. Subsequent experiments are performed to demonstrate the feasibility of using wideband time-reversal designs to extract the coded information sequence.

A. Time-reversal background

The extraction of a transmitted information sequence can be transformed to the problem of maximizing the output signal-to-noise ratio, $\mathrm{SNR}_{\mathrm{out}}$, at the receiver of a communications system.[1,2] This problem is termed the matched-filter problem and for time-reversal is identical to the classical problem with a "known" Green's function of the medium replacing the known replicant with the filtering operation simply the cross correlation of the Green's function with the received measurement.[3,4] The Green's function, $g(r,r_0;t)$, is the result of a point-to-point communications link between a *host*-station (transmitter) at r_0 to a *client*-station (receiver) at r. In the T/R case, the matched-filter solution is again found by maximizing the output SNR leading to $f(t)=g(r,r_0;T-t)$. Thus, for T/R, the optimal matched-filter solution is the time-reversed Green's function from the host-station to client-station or vice versa. Since T/R theory requires reciprocity,[3,4] this result is valid for *both* transmission and reception, that is, $g(r,r_0;T-t)\leftrightarrow g(r_0,r;T-t)$. Note also that when an array is included to sample the spatial field or transmit a wave, then a solution evolves with *sets* of Green's function transmitter-receiver pairs. These results include the focus at the client-station position, r_0, yielding the optimal, *spatiotemporal* matched-filter solution,[3,4] $g(\mathbf{r}_\ell,\mathbf{r}_0;T-t)$ at sensor position, $\mathbf{r}_\ell$.

B. Multichannel T/R receivers

In this section, we briefly review the multichannel communications problem from the signal processing perspective[17,18] and discuss the time-reversal solutions.

Define the field received at the mth station spatially located at $\mathbf{r}_m$ and at time t by the spatiotemporal signal, $z(\mathbf{r}_m;t)$ and the excitation signal transmitted from the ℓth array element spatially located at $\mathbf{r}'_\ell$ and t by $x(\mathbf{r}'_\ell;t)$. The transmitted signal propagates through the time invariant medium characterized by its impulse response or Green's function,

$g(\mathbf{r}_m, \mathbf{r}'_\ell; t)$, representing the propagation medium from the host-station transmitted signal (array sensor) to the client-station received signal. This *spatiotemporal propagation* relation can be written compactly as

$$\mathbf{z}(t) = \mathbf{G}(\mathbf{r}; t) * \mathbf{x}(t), \tag{1}$$

where $\mathbf{z} \in \mathbf{C}^{M\times 1}$ is the received signal at all of the M stations, $\mathbf{x} \in \mathbf{C}^{L\times 1}$ is the information or message signal transmitted by the array into the medium represented by its transfer (impulse response) matrix, $\mathbf{G} \in \mathbf{C}^{M\times L}$, consisting of the channel impulse responses or Green's function, $g(\mathbf{r}_m, \mathbf{r}'_\ell; t)$, from the ℓth-transmit array sensor element to the mth-receiver station. More compactly, if we define

$$g_{m\ell}(t) \equiv g(\mathbf{r}_m, \mathbf{r}'_\ell; t), \tag{2}$$

then the propagation relation can be rewritten in the standard vector-matrix format where the indices identify the spatial path vector locations, that is, $(\mathbf{r}_m, \mathbf{r}'_\ell) \rightarrow (m, \ell)$ as depicted in Fig. 1. Recall, we define the *host-station* as the transmitting array and the *client-station* as the receiver, but both transmit and receive when communicating. The spatiotemporal propagation of Eq. (1) can now be expressed in terms of L-dimensional row vectors with the convolution operator replacing the usual vector-matrix multiplication operator to give

$$\mathbf{z}(t) = \begin{bmatrix} \mathbf{g}_1^T(t) \\ \vdots \\ \mathbf{g}_M^T(t) \end{bmatrix} * \mathbf{x}(t) = \begin{bmatrix} \mathbf{g}_1^T(t) * \mathbf{x}(t) \\ \vdots \\ \mathbf{g}_M^T(t) * \mathbf{x}(t) \end{bmatrix}, \tag{3}$$

where the set of row vectors, $\mathbf{g}_m^T(t)$, define the propagation path of the transmitted signals from the array to the mth client-station as in Fig. 1. At this station the data received from the transmit array is therefore

$$z_m(t) = \mathbf{g}_m^T(t) * \mathbf{x}(t) = \sum_{\ell=1}^{L} g_{m\ell}(t) * x_\ell(t). \tag{4}$$

Note that we must first estimate the Green's function denoted by $\hat{g}(r;t)$ from measured pilot data in order to implement these designs. In signal processing this is called the system identification or equivalently parameter estimation problem and is readily solved using the well-known Wiener filter design techniques.[19,20]

1. T/R receiver I

The T/R I receiver realization is based on transmitting the time reversed, estimated Green's functions convolved on each array sensor channel with the information signal to the mth client-station. In this realization the transmitted code is given by

$$\mathbf{x}(t) = \hat{\mathbf{g}}_m(-t) \otimes i(t) = \begin{bmatrix} \hat{g}_{m1}(-t) * i(t) \\ \vdots \\ \hat{g}_{mL}(-t) * i(t) \end{bmatrix}, \tag{5}$$

where $\otimes$ is defined as the Kronecker convolution operator (element-by-element multiply) yielding an $L\times 1$ complex vector. Therefore from Eq. (1) we have that the wave propagated from the transmit array through the medium is

$$\mathbf{z}_{i\hat{g}_m X}(t) = \mathbf{G}(\mathbf{r}; t) * \mathbf{x}(t) = \mathbf{G}(\mathbf{r}; t) * (\hat{\mathbf{g}}_m(-t) \otimes i(t)), \tag{6}$$

with the subscript representing the information signal (i) convolved with the estimated Green's functions ($\hat{\mathbf{g}}_m$) corresponding to the mth client-station on transmission (X). This expression can be written as and shown to be[18]

$$\mathbf{z}_{i\hat{g}_m X}(t) = \begin{bmatrix} \mathbf{g}_1^T(t) \\ \vdots \\ \mathbf{g}_M^T(t) \end{bmatrix} * (\hat{\mathbf{g}}_m(-t) \otimes i(t)) = \begin{bmatrix} \bar{C}_{g_1\hat{g}_m}(t) \\ \vdots \\ \bar{C}_{g_M\hat{g}_m}(t) \end{bmatrix} \otimes i(t), \tag{7}$$

where the cross-correlations (matched filtering) are defined by

$$\bar{C}_{g_k\hat{g}_m}(t) \equiv \sum_{\ell=1}^{L} C_{g_k\hat{g}_m}(\ell; t) \text{ for } C_{g_k\hat{g}_m}(\ell; t) \equiv g_{k\ell}(t) * \hat{g}_{m\ell}(-t),\ k = 1, \ldots, M.$$

Therefore at the kth client-station, we have

$$z_k(t) \equiv z_{i\hat{g}_m X}(k; t) = \bar{C}_{g_k\hat{g}_m}(t) * i(t), \tag{8}$$

where that maximum correlation (coherence) occurs when $k=m$, matching the set of Green's functions to the appropriate client-station. This is true, since the auto rather than cross correlation is achieved demonstrating that the transmitted wave field satisfies the time-reversal focusing principle.[3,4] The output of this realization, T/R I, at the receivers is simply, $\mathbf{R}_{i\hat{g}_m X}(t) = \mathbf{z}_{i\hat{g}_m X}(t)$ and over the entire communications network (M client-station receivers) or at the kth client-station as $R_{i\hat{g}_m X}(k;t) = z_{i\hat{g}_m X}(k;t) = z_k(t)$.

2. T/R receiver II

This realization is identical to that of T/R I replacing the reversed Green's function with a reversed pilot measurement, $z_p(-t) \rightarrow \mathbf{g}_m^T(-t)$ on transmission where $\mathbf{z}_p(t) = \mathbf{g}_m^T(t) * \mathbf{p}(t)$ for the mth client-station and $\mathbf{p}(t)$ the known pilot. On reception at the client-station, we have

$$R_{ipX}(t) = z_{ipX}(t) * p_m(t) = \bar{C}_{g_m g_m}(t) * C_{p_m p_m}(t) * i(t). \tag{9}$$

3. T/R receiver III

The realization for this receiver is also similar to that of T/R Receiver I; however, the reversed client-station set of Green's functions is performed on *reception* rather than transmission. Starting with the receiver input from the transmitted wave field of Eq. (8) as

$$z_m(t) = \mathbf{g}_m^T(t) * \mathbf{i}(t), \tag{10}$$

and convolving it with the estimated reversed Green's functions, we obtain

$$\mathbf{R}_{i\hat{g}_m R}(t) = z_m(t) * \hat{\mathbf{g}}_m(-t) = (\mathbf{g}_m^T(t) * \hat{\mathbf{g}}_m(-t)) * \mathbf{i}(t), \tag{11}$$

where $\mathbf{R}_{i\hat{g}_m R}(t) \in \mathrm{R}^{L\times 1}$, $\mathbf{i}(t) = \mathbf{1} \cdot i(t)$ for $\mathbf{1} \in \mathrm{R}^{L\times 1}$, a vector of ones. Rearranging this expression we have

$$\mathbf{R}_{i\hat{g}_m R}(t) = \hat{\mathbf{g}}_m(-t) * z_m(t) = (\hat{\mathbf{g}}_m(-t) * \mathbf{g}_m^T(t)) * \mathbf{i}(t)$$
$$= \mathbf{C}_m(t) * \mathbf{i}(t) = \sum_{\ell=1}^{L} C_{\hat{g}_\ell g_\ell}(m;t) * i(t), \quad (12)$$

for $\mathbf{C_m}(t) \in \mathrm{R}^{L\times L}$, a *correlation matrix* with its cross-correlation components

$$C_{\hat{g}_k g_\ell}(m;t) \equiv \hat{g}_{mk}(-t) * g_{m\ell}(t) \quad \text{for } k = 1, \ldots, L; \quad \ell = 1, \ldots, L.$$

4. T/R receiver IV

This realization is similar to that of T/R II where the reversed pilot measurement, $z_p(-t)$ and the pilot $p_m(t)$ for the mth client-station are performed on reception to give

$$R_{ip_m X}(t) = z_{p_m}(-t) * z_m(t) * p_m(t)$$
$$= \sum_{\ell=1}^{L} C_{g_\ell g_\ell}(m;t) * C_{p_m p_m}(t) * i(t). \quad (13)$$

C. Green's function estimation

The Green's function is an integral part of T/R receiver realizations. It can be estimated from a pilot signal measurement and is similar to the operations used for equalization,[1,2] but is much better conditioned numerically for solution, since the forward, $g(r;t)$, rather than the inverse, $g^{-1}(r;t)$, is required for T/R. The estimated Green's function is used in the realizations to mitigate the distortion effects created by the medium and unknown transfer characteristics of the measurement system. For the multichannel case, we assume that the Green's functions can be estimated in transmitter-receiver pairs by transmitting the pilot signal from host-station sensor to the client-station receiver, individually. We use the Wiener solutions[19,20] for this wide-band design. However, we could have just made the assumption that the short-time pulse is an impulse and use the measured responses directly.

D. 1-bit T/R receiver implementation

Since the spatial information in the transmitted signal is essentially described by the *phase* portion of the propagating wave $[g(\mathbf{r};t)]$, the amplitude information is not as critical in utilizing the multipath. We use a receiver that exploits the phase of reversed signals.[21] This is accomplished by recording the corresponding zero-crossings of the time-reversed signals quantized between ±1 amplitudes establishing the 1 -bit T/R receiver realizations.[18] This two-state system is commonly referred to as binary phase shift keying (BPSK) in the communications literature. The major advantage of such an implementation is that instead of requiring an expensive A/D converter (e.g., 24 bits), a simple threshold switch can be used instead, since all that is required is to detect the zero-crossings. The disadvantage of this approach is increased quantization error and noise. That is, the noise will also be quantized to the ±1 amplitudes and its inherent high frequency zero-crossings as well.

Although the 1-bit receiver design is simple in concept, it does introduce uncertainty into the processed data. Since 1-bit quantization is a *nonlinear* process, it is identical to a switch or relay in a physical system. The crudeness of 1-bit sampling introduces large quantization errors relative to the amplitude sampling. In fact the lower bound on quantization error indicates that the 1-bit design introduces seven orders of magnitude larger deviations (errors) than the 24-bit design.[1,2] This error translates into an equivalent measurement noise decreasing the "in-band" (signal frequency bandwidth) SNR. The 1-bit quantization also acts as a strong amplifier of low amplitude data (usually noise) thereby reducing the overall SNR. From the time-reversal perspective, it does offer a cost effective solution to phase sampling high frequency signals (EM, ultrasound) providing a mechanism to use T/R processing thereby increasing the overall spatial gain and coherence available at the receiver. This completes the discussion of the T/R receiver designs used as a compliment to preprocess the input for our time-reference modulation scheme to follow.

III. WIDEBAND T/R COMMUNICATIONS

In this section we discuss the development of a wideband T/R receiver design based on the concept of ultrawideband communications systems and the special modulation schemes associated with them. A communications system is deemed "wideband" based on its *fractional bandwidth*[22–24] that is defined as the ratio of its bandwidth and center frequency both specified by its high and low cutoff frequencies, that is,

$$\mathrm{BW}_{\mathrm{fractional}} \equiv \frac{\mathrm{BW}}{f_{\mathrm{center}}} \times 100(\%), \quad (14)$$

where $\mathrm{BW}=f_{\mathrm{hi}}-f_{\mathrm{lo}}$ is the transmission bandwidth and $f_{\mathrm{center}}=(f_{\mathrm{hi}}+f_{\mathrm{lo}})/2$ is the center (average) frequency with f_{hi}, f_{lo} the respective upper and lower −10 dB emission point frequencies. In standard ultrawideband radio (electromagnetic transmissions) with typical center frequencies of $f_{\mathrm{center}} > 2.5$ GHz need to have a −10 dB bandwidth of at least 500 MHz, while systems with $f_{\mathrm{center}} < 2.5$ GHz need to have a fractional bandwidth of at least 20%. Such systems rely on short pulse wave forms that do *not* require sinusoidal carriers, since they can operate at baseband frequencies. In electromagnetics wideband transmissions have distinct advantages in communications.[22–24]

Here we concentrate on taking advantage of the "carrier-free" modulation scheme called *time-reference modulation* that is based on transmitting short-time, modulating pulses and investigating the polarity of the resulting correlations. This scheme is closely related to the usual time-reversal procedures, since the autocorrelation process involves convolving the signal with its time-reversed replicant. Let us investigate the usual time-reference (TRef) modulation scheme first and incorporate the complimentary T/R receiver. The TRef design is basically a correlation-based receiver[22–24] that uses a pair of pulses per symbol: the first a pilot and the second the symbol. Since we are using a BPSK coding scheme, our symbol is the pulse multiplied by a ±1 either

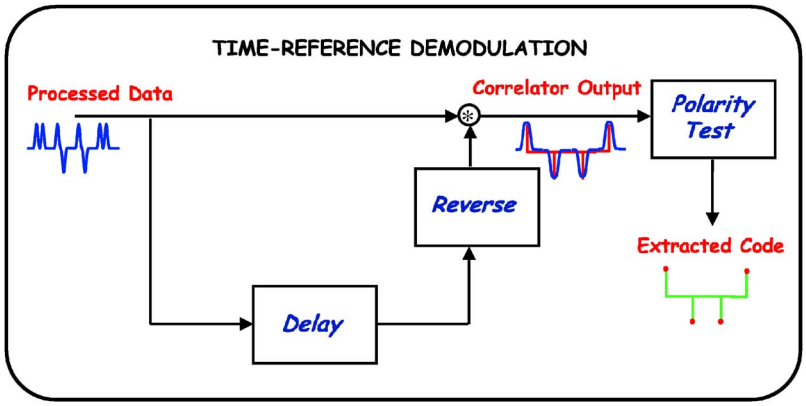

FIG. 2. (Color online) Time-reference receiver: reception (raw or processed data); inter-pulse delay (τ_P), reversal, correlation, and polarity (sign) test for code extraction.

preserving or inverting the pilot. Thus, the decoding process requires locating the pulse by *synchronizing* the receiver and using *a priori* knowledge of the interpulse timing intervals. The operations and timing of the TRef receiver are illustrated in Fig. 2. Here the received signal is delayed and correlated at the prespecified *interpulse delay*, τ_P, within the *symbol time interval* (time segment) defined by τ_S ($\tau_S > \tau_P$) and then followed by a *polarity test* to determine the *sign*, σ. Consider the information signal (pulse pair), $i(t)$,

$$i(t) = p(t) + \sigma_k p(t - \tau_p) \quad \text{for } \sigma_k = \pm 1 \text{ and } k\tau_S < t \leqslant (k+1)\tau_S \text{ with } k = 0, \ldots, K, \tag{15}$$

where $p(t)$ is the designed pulse (Gaussian-windowed chirp in our application) along with its delayed counterpart (see Fig. 2)

$$i(t - \tau_P) = p(t - \tau_P) + \sigma_k p(t - 2\tau_P),$$

then the correlator output at τ_P for t in the kth interval is

$$C_{\text{ii}}(\tau_P) = \int_{t-\tau_P}^{t} i(\alpha) i(\alpha - \tau_P) d\alpha \quad \text{for } k\tau_S \leqslant t \leqslant (k+1)\tau_S, \tag{16}$$

followed by the polarity test

$$\hat{\sigma}_k = \text{signum}[C_{\text{ii}}(\tau_P)]. \tag{17}$$

The key to understanding the time-reference modulation operation is realizing that both the interpulse and symbol delays, $\{\tau_P, \tau_S\}$, are known *a priori* by the host-station and the clients; therefore, the received signal is delayed by τ_P and polarity tested over each subsequent τ_S-interval to extract each ± 1 bit. To see this confine the operation to an τ_S-interval so that Eq. (15) holds, then (1) perform the multiplication:

$$\begin{aligned} i(t)i(t - \tau_P) = {} & p(t)p(t - \tau_P) \\ & + \sigma_k p(t - \tau_P)p(t - \tau_P) + \sigma_k p(t)p \\ & \times (t - 2\tau_P) + \sigma_k^2 p(t - \tau_P)p \\ & \times (t - 2\tau_P), \quad \text{such that} \\ & k\tau_S < t \leqslant (k+1)\tau_S, \quad k = 0, \ldots, K; \end{aligned} \tag{18}$$

(2) perform the expectation to obtain:

$$\begin{aligned} C_{\text{ii}}(\tau_P) = E\{i(t)i(t - \tau_P)\} = {} & \sigma_k C_{PP}(0) + (1 + \sigma_k^2) C_{PP}(\tau_P) \\ & + \sigma_k C_{PP}(2\tau_P), \end{aligned} \tag{19}$$

and finally (3) test the polarity of $C_{ss}(\tau_P)$ for a $+1$ or -1. If we assume that an impulse is selected for the pulse shape, then clearly the product of Eq. (18) is

$$\begin{aligned} C_{\text{ii}}(\tau_P) = E\{ & \delta(t)\delta(t - \tau_P) + \sigma_k \delta(t - \tau_P)\delta(t - \tau_P) \\ & + \sigma_k \delta(t)\delta(t - 2\tau_P) + \sigma_k^2 \delta(t - \tau_P)\delta(t - 2\tau_P)\}, \end{aligned}$$

this gives

$$C_{\text{ii}}(\tau_P) = E\{\sigma_k \delta(t - \tau_P)\delta(t - \tau_P)\} = \int_{t-\tau_S}^{t} \sigma_k dt = \sigma_k \tau_S. \tag{20}$$

So we see in the impulsive case, the receiver estimates the sign bit directly. In Fig. 3 we show the results for a Gaussian pulse shape and code $(+1, -1, -1, +1)$ with its recovery using the TRef receiver. Here in Fig. 3(a) we show the modulated code along with its delayed replicant in (b) and observe the correlation output with extracted code (point or impulse) used to determine the sign bit in (c). Note that it is only necessary to estimate the correlation value at τ_P within the τ_S-interval and determine its sign. We show the entire correlation function for completeness.

In the general case, the code is propagated through a medium causing a *propagation delay*, τ_M, as well; therefore, we model the *transmitted information sequence* (pulse train) as

$$\begin{aligned} i(t) = {} & \sum_{k=0}^{K} p(t - \tau_M - k\tau_S) + \sigma_k p(t - \tau_M - \tau_P - k\tau_S) \\ & \text{for } k\tau_S < t \leqslant (k+1)\tau_S. \end{aligned} \tag{21}$$

Note also from this model the *synchronization* problem becomes that of estimating the propagation delay, $\hat{\tau}_M$, from a controlled data set using the matched-filter approach.[1,2]

Unfortunately, the complex medium also distorts the information sequence in both amplitude and phase, that is, the received signal is

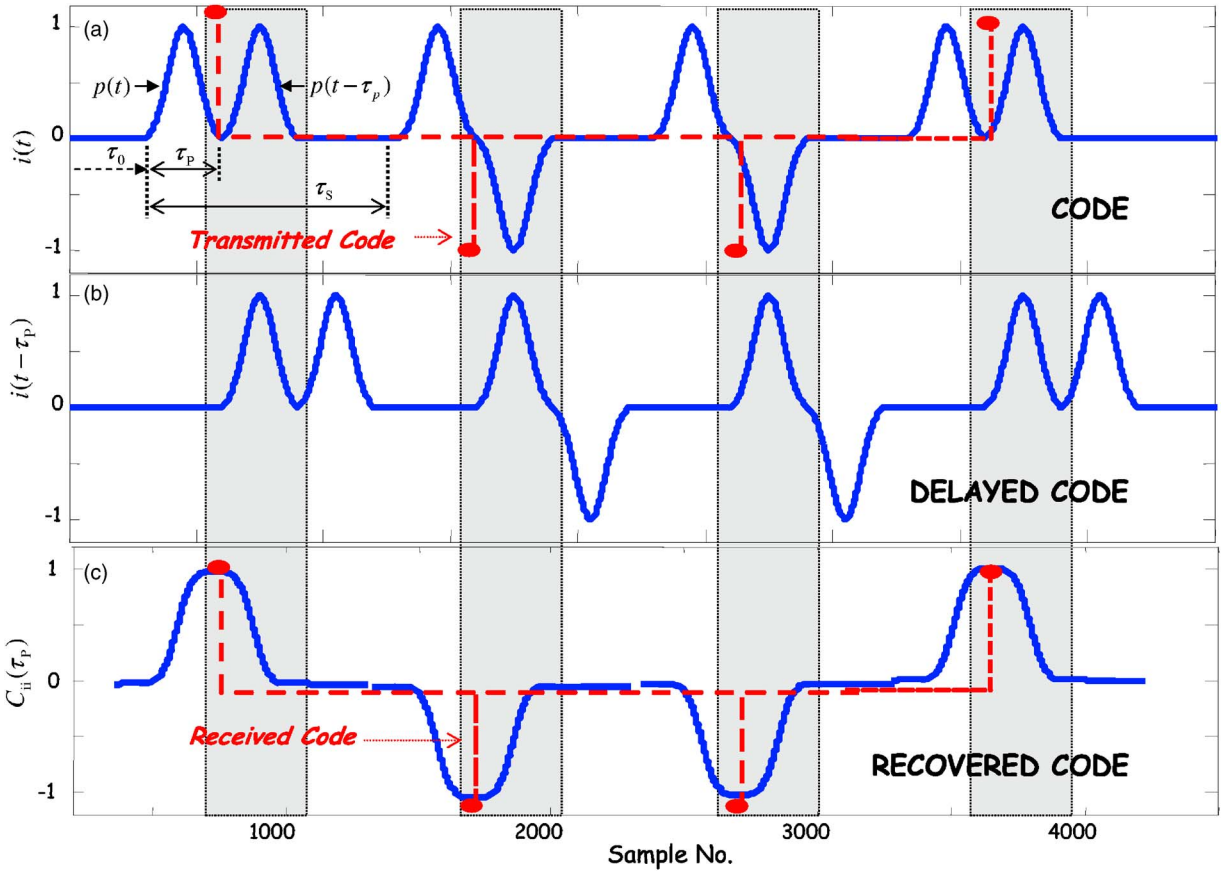

FIG. 3. (Color online) Time-reference receiver demodulation: (a) transmitted Gaussian pulse coded pairs. (b) Interpulse delayed, τ_P, sequence. (c) Correlation output with recovered sign bits (dashed impulses) from polarity testing.

$$z(t) = g(\mathbf{r};t) * i(t) \tag{22}$$

for $g(\mathbf{r};t)$ the spatiotemporal Greens function characterizing the medium as before. In this more realistic case, we see that the TRef output is therefore

$$C_{zz}(t) = [g(\mathbf{r};t) * i(t)] * [g(\mathbf{r};\tau_P - t) * i(\tau_P - t)], \tag{23}$$

which can be expressed as

$$\begin{aligned} C_{zz}(t) &= [g(\mathbf{r};t) * g(\mathbf{r};\tau_P - t)] * [i(t) * i(\tau_P - t)] \\ &= C_{gg}(\tau_P - t) * C_{\mathrm{ii}}(\tau_P - t), \end{aligned} \tag{24}$$

from the commutivity property of the convolution operator. Clearly, the maximum is achieved at $t=\tau_P$ giving the desired result. So we see that instead of observing the autocorrelation of the transmitted information sequence, we observe a distorted version resulting in the smearing of the code with the correlation function of the medium. Of course, noise contaminates this result as well.[17,18]

One approach to remove these adverse effects is to use the T/R receiver in conjunction with the TRef modulation-technique thereby mitigating the medium distortion and enhancing the information sequence for improved reception. This can be accomplished by focusing on-transmit via T/R I and II or passively on-receive via T/R III and IV. On transmission or reception the effect of time-reversal is to provide a processed input to the TRef receiver, that is,

$$z_{\mathrm{T/R}}(t) = z(t) * \hat{g}(\mathbf{r};-t) = C_{g\hat{g}}(t) * i(t). \tag{25}$$

A typical result for a Gaussian-windowed chirp pulse sequence is shown in Fig. 4. Here we see the result of propagating the sequence that was designed to match the information bandwidth[17,18] through the highly reverberant medium. In Fig. 4(a) the transmitted pulse pair code sequence is shown along with the distorted received signal in (b). The result of the T/R preprocessing is shown in Fig. 4(c) along with an expanded Gaussian-windowed pulse. The TRef receiver then processes these data instead of the raw data increasing its performance to extract the code.

The basic operation of the overall T/R, TRef receiver design is illustrated in Fig. 5 where we observe the raw multichannel array input data preprocessed by the T/R receiver. Synchronization is accomplished using the classical matched-filter with transmitted pulse replicant to estimate the propagation delay, τ_M. Once synchronized, the TRef receiver locates the code and quantizes to extract the sign bit of the BPSK sequence.

It is interesting to note that just as in classical detection theory,[19] the value of the threshold is also selected for the receivers based on some performance criterion. We use a *symbol error criterion* to evaluate the performance of each of the receiver realizations in this paper. *Symbol error* is defined as the percentage of symbols missed over the total transmitted. In our application, since a symbol is represented by one bit, symbol error is synonymous to bit error.

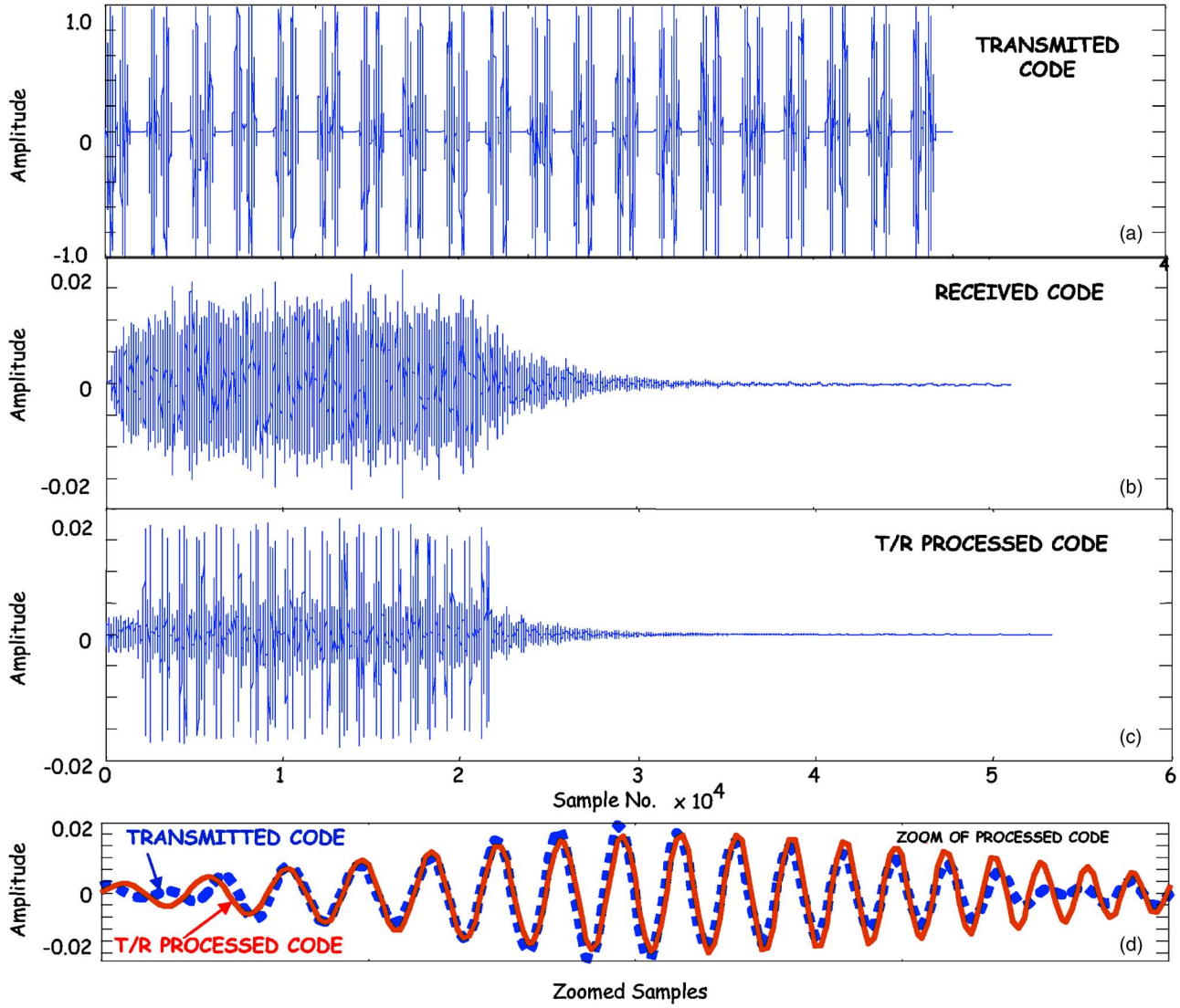

FIG. 4. (Color online) T/R preprocessing for Gaussian-windowed chirp in a reverberative stairwell medium: (a) Transmitted pulse pair (code) sequence. (b) Raw received data. (c) T/R preprocessed data for input to TRef demodulator. (d) Zoomed Gaussian-window chirp pulse estimation (transmitted and recovered).

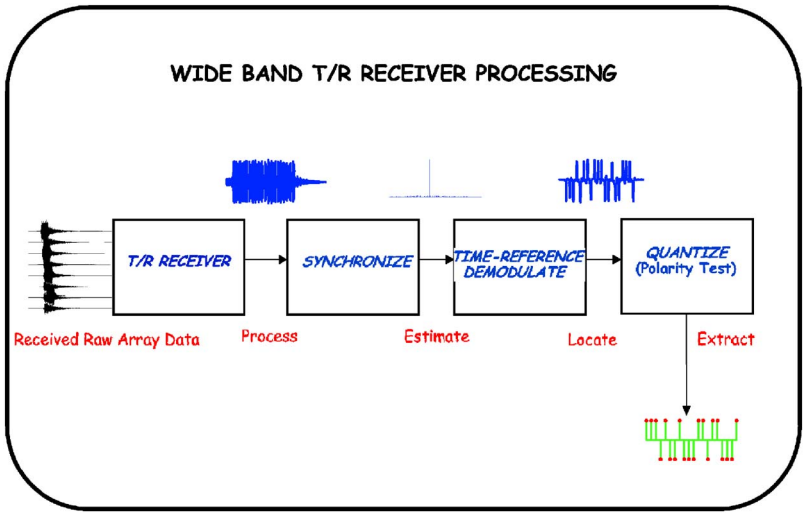

FIG. 5. (Color online) TRef receiver with complimentary T/R processing: raw multichannel array input data, T/R preprocessor, matched-filter synchronizer, TRef demodulator and quantizer to extract the code.

IV. EXPERIMENTS

In this section we describe a variety of proof-of-principle experiments executed to evaluate the performance of the wideband designs. We investigate the performance of the various T/R receiver realizations (I–IV) used as preprocessors coupled to the TRef demodulation scheme. We discuss the results of the experiments demonstrating the performance of multichannel communications systems for both the 24- and 1-bit designs discussed in Sec. II D. As mentioned previously, we estimate the set of Green's functions of the environment for each transmitter-receiver pair. Using these Green's functions, we developed an experimental computer simulation for design and implementation of the various receivers.

We selected three experimental environments: (1) *stairwell*; (2) *short* waveguide; and (3) *long* waveguide. For comparative purposes, the stairwell is that used in narrowband designs[17,18] but now using the wideband T/R design, while the short and long waveguide experiments were selected to investigate the wideband receiver designs in a highly reverberant environment that has a variety of applications including robot communications in a confined environment, military operations in caves and waveguides as well as mapping.

With this motivation in mind, we discuss the experimental environment and processing to gather the data from the TRef receiver using the T/R preprocessor. We have already addressed the steps required to extract the coded information sequence using the various T/R receiver realizations coupled to the TRef modulation scheme in the previous section.

The basic experimental approach is summarized (see Fig. 5):

1. *transmit* the pilot signal, that is, excite the medium with a Gaussian-windowed chirp pulse (pilot) signal to estimate the set of Green's functions;
2. *transmit* the pulse-pair coded information signals from the host-station array (speakers) along with the required Green's functions (T/R I and II), measured pilot signal, etc., through the reverberant medium to the microphone receiver;
3. *receive* (client-station microphone) the noisy, reverberant signal and digitize;
4. *preprocess* the raw data with the T/R receiver realizations (software);
5. *synchronize* the processed data using a matched-filter processor to estimate the temporal onset of the code (propagation delay);
6. *locate* the code by demodulating it with the TRef receiver; and
7. *quantize* the code using the polarity test and extracting it from the demodulated data for performance analysis.

We used the identical equipment for each of the subsequent experiments with time-reference (correlation-based) modulation for the wideband case and compared the results to the previous narrowband amplitude modulated designs.[17,18] The array-to-point (host-station to client-station) experiments were performed using Meyer Sound, MM-4, 4-in. single element speakers configured in an eight-element vertical array with a 6-in. pitch powered by a Crown Audio CTS 8200, 8-channel, 150 W amplifier and a Data Physics, DP-703 arbitrary wave form generator/digitizer for transmitting both the Gaussian-windowed (23.4-ms duration) chirp pulse (pilot) swept from 0.6 to 1.8 kHz corresponding to a 50% fractional bandwidth. The corresponding signed BPSK code pulse with an interpulse spacing of 23.4 ms (τ_P) was designed to ensure nonoverlapping code pulses while the symbol period (τ_S) associated with the transmission of 78.1 ms ensured adequate temporal symbol separation and integration time for the polarity tests. On reception, B&K 4935, $\frac{1}{4}$ in.-microphones are used in an eight-element receiver array along with the 24-bit Data Physics digitizer sampling at 12.8 kHz. We use two, eight-element, linearly spaced (6-in. pitch), vertical arrays to construct the host-station array: one for transmission consisting of the eight speakers and one for reception consisting of the eight microphone receivers. Individual speakers and microphones are positioned at each client-station in the reverberant environment. The experiment is controlled using a laptop computer. The transmitted code, the Gaussian-windowed chirp of Fig. 4, was received on a client-station microphone. As observed in the figure, the measurement is dominated by a long reverberation response and noise.

For our receiver performance analysis, we use the symbol (bit) error criterion.[17] We determine the symbol error by varying the threshold at the processed receiver output and determine the number of symbols missed at that threshold. The performance function (% symbol error versus threshold) is "U-shaped" with the base of the "U" residing in the *zero-symbol error* region (e.g., see Fig. 6 for TRef I). Of particular interest is the percentage of the threshold interval corresponding to the zero-symbol error region *relative* to the *total* threshold interval (−1 to +1) evaluated. We use this threshold interval percentage to provide a metric for evaluating the robustness of the particular receiver design. The *higher* the percentage, the larger the threshold interval corresponding to zero-symbol error and therefore the more robust the design. We compared all of the receiver designs and a bar chart with these percentages listed in the figures to follow is illustrated in Figs. 12–14. We also calculated the percentage threshold intervals for each realization using both 24- and 1-bit designs.

A. Stairwell experiments and results

The first set of experiments was performed in a stairway located between two floors consisting of three landings, high ceilings of corrugated steel, pipes, handrails and other non-sound absorbing protrusions as well as ambient building noise.[17,18] Geometrically, the L-shaped stairwell is approximately 20 ft high with the second (middle) landing, a 5 ft $\times$5 ft square pad, centered at 12.5 ft from the first (entry) landing. After the 90° downward turn, the stairs proceed to the third (bottom) landing 22.5 ft from the second landing on center. The width is 4 ft with the ceiling at varying heights relative to the steps. It is completely enclosed establishing a highly reverberant waveguide.

For the stairwell, client-station No. 1 is located at the

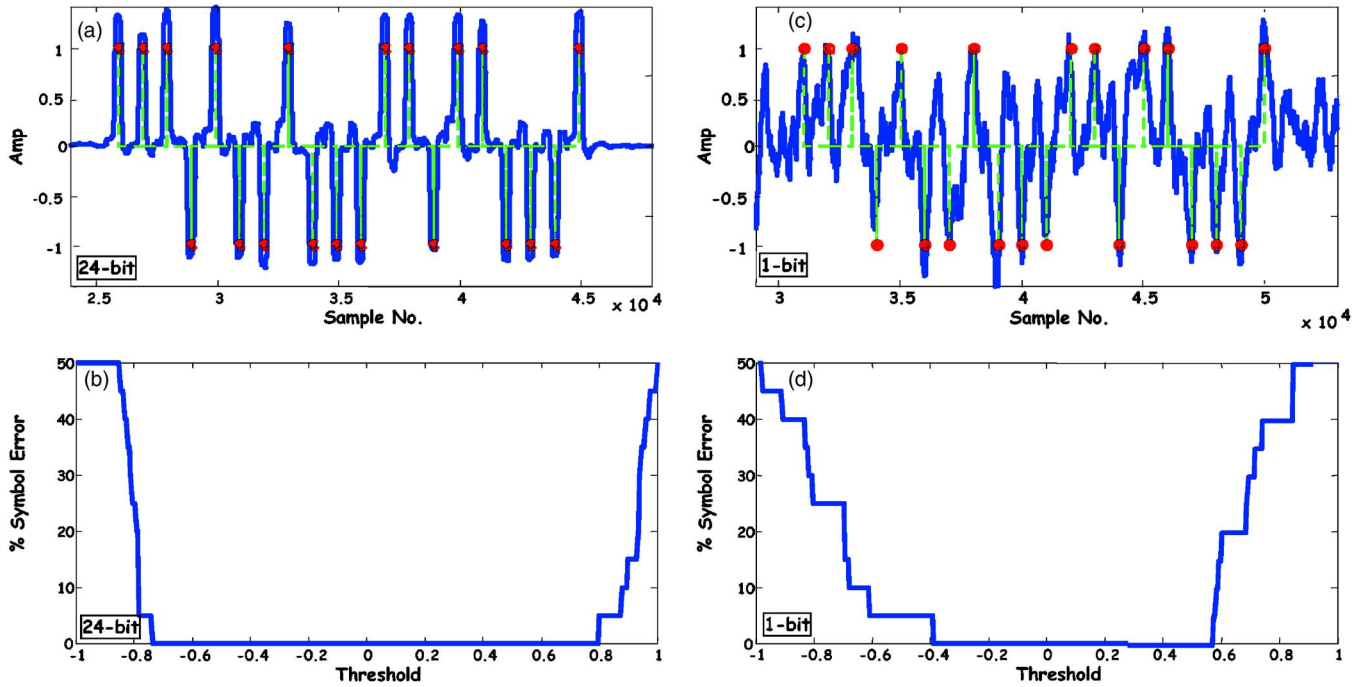

FIG. 6. (Color online) Multichannel TRef I receiver output coded estimates (solid line) using the T/R I preprocessor in *stairwell*: Coded estimates (solid line) along with true BPSK code sequence (solid line) for 24-bit (a) and 1-bit (c) designs at each client receiver for true symbols (*) and estimated symbols (○) yielding a zero-bit error performance for the selected threshold. Performance U curves for focusing at client one using 24-bit (b) (73% zero-symbol error threshold interval) and 1-bit (d) (43% threshold interval) designs. The degradation of the 1-bit design is 30% threshold interval.

second landing, while client-station No. 2 is at the first (entry) landing. Note that client-station No. 1 has a higher SNR than that at client-station No. 2 due to the direct path with the transmitter located at the bottom landing. After obtaining the set of Green's functions for each client-station receiver, we investigate the following cases: (1) focused transmission to each client-station receiver, *individually* and checked the other (nonfocused) client-station receiver station for leakage of the cross-correlation functions; and (2) repeated experiments for 1-bit realization. Each of the T/R I and II receivers (focus on transmit), was focused on the individual client-station receivers and their performance evaluated, while T/R

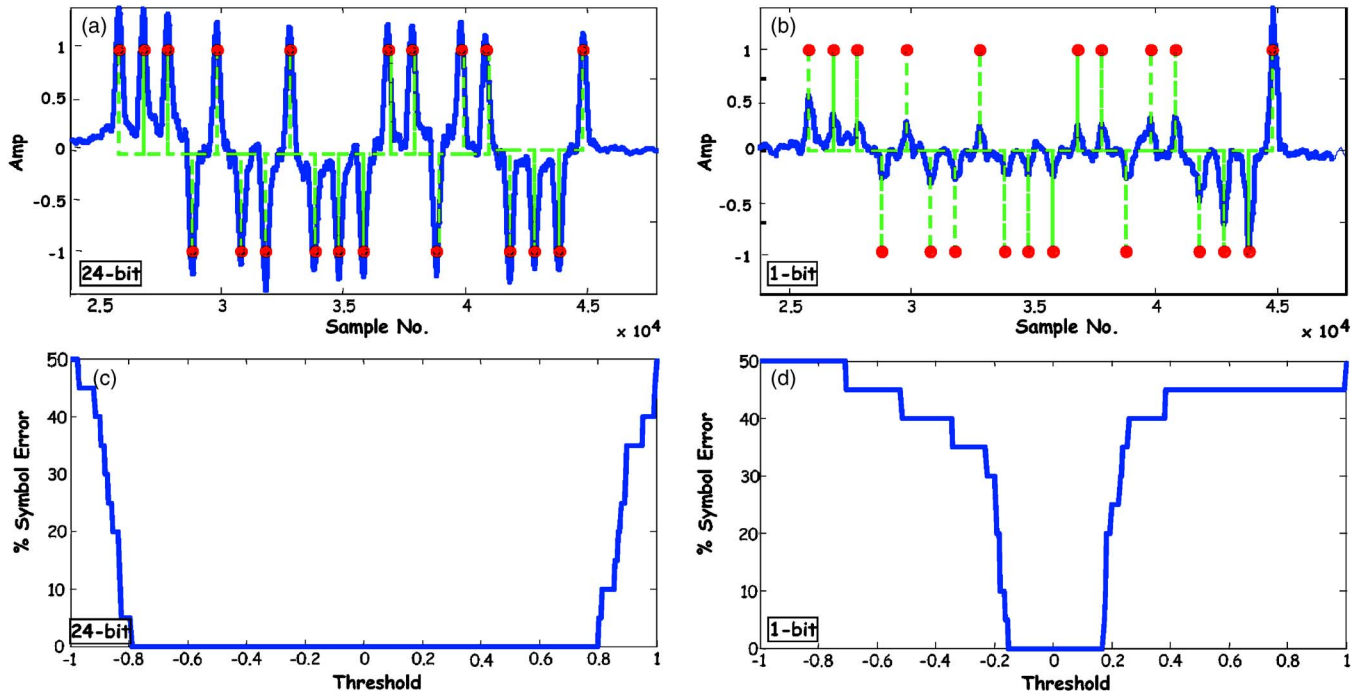

FIG. 7. (Color online) Multichannel TRef III receiver output coded estimates (solid line) using the T/R III preprocessor in *stairwell*: Coded estimates (solid line) along with true BPSK code sequence (solid line) for 24-bit (a) and 1-bit (c) designs at each client receiver for true symbols (*) and estimated symbols (○) yielding a zero-bit error performance for the selected threshold. Performance U curves for focusing at client one using 24-bit (b) (80% zero-symbol error threshold interval) and 1-bit (d) (20% threshold interval) designs. The degradation of the 1-bit design is 60% threshold interval.

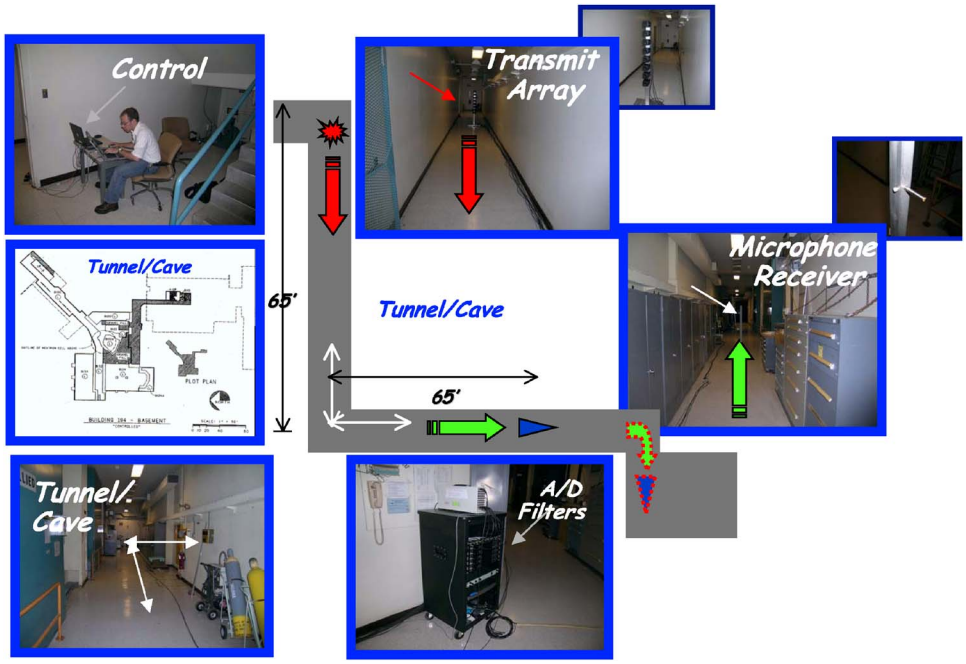

FIG. 8. (Color online) Experimental environment and setup for T/R communications testing: waveguide layout with blind hallways and high corrugated steel ceilings (10–20 ft) along with the equipment setup for array-to-point communications. Note that a schematic map demonstrates the waveguide communications path with the client receiver is approximately 180 ft from host array.

III and IV receivers (focus on receive) were also investigated.

1. TRef I receiver performance

The realization of this TRef I receiver (see Fig. 2) uses the estimated set of Green's functions from the array sensors convolved with the code *transmitted* into the stairwell.[17,18] This is a common realization that has been applied in the literature.[5–16] After T/R preprocessing, synchronization, and demodulation, we see the corresponding information code estimates produced from the output of the TRef I receiver in Fig. 6. For each client-station receiver the 24- and 1-bit de-

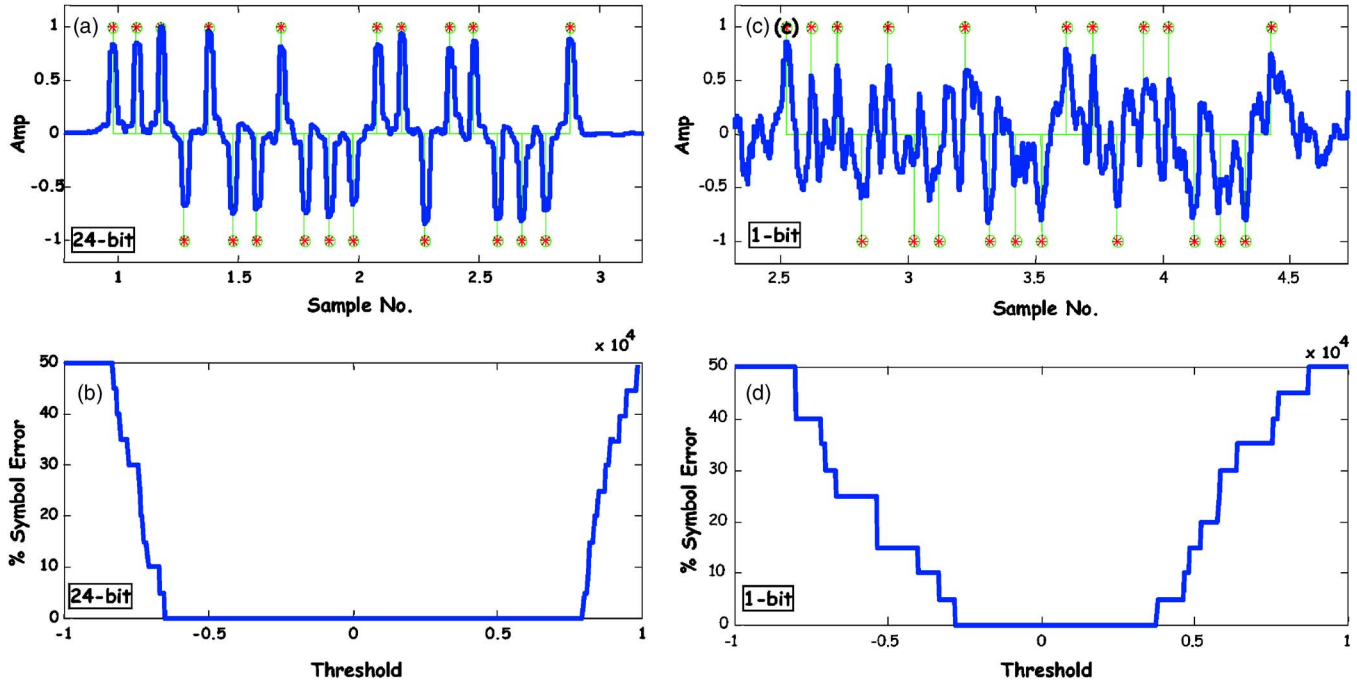

FIG. 9. (Color online) Multichannel TRef I receiver output coded estimates (solid line) using the T/R I preprocessor in *short waveguide* (~130 ft): Coded estimates (solid line) along with true BPSK code sequence (solid line) for 24-bit (a) and 1-bit (c) designs at each client receiver for true symbols (*) and estimated symbols (○) yielding a zero-bit error performance for the selected threshold. Performance U curves for focusing at client one using 24-bit (b) (73% zero-symbol error threshold interval) and 1-bit (d) (33% threshold interval) designs. The degradation of the 1-bit design is 40% threshold interval.

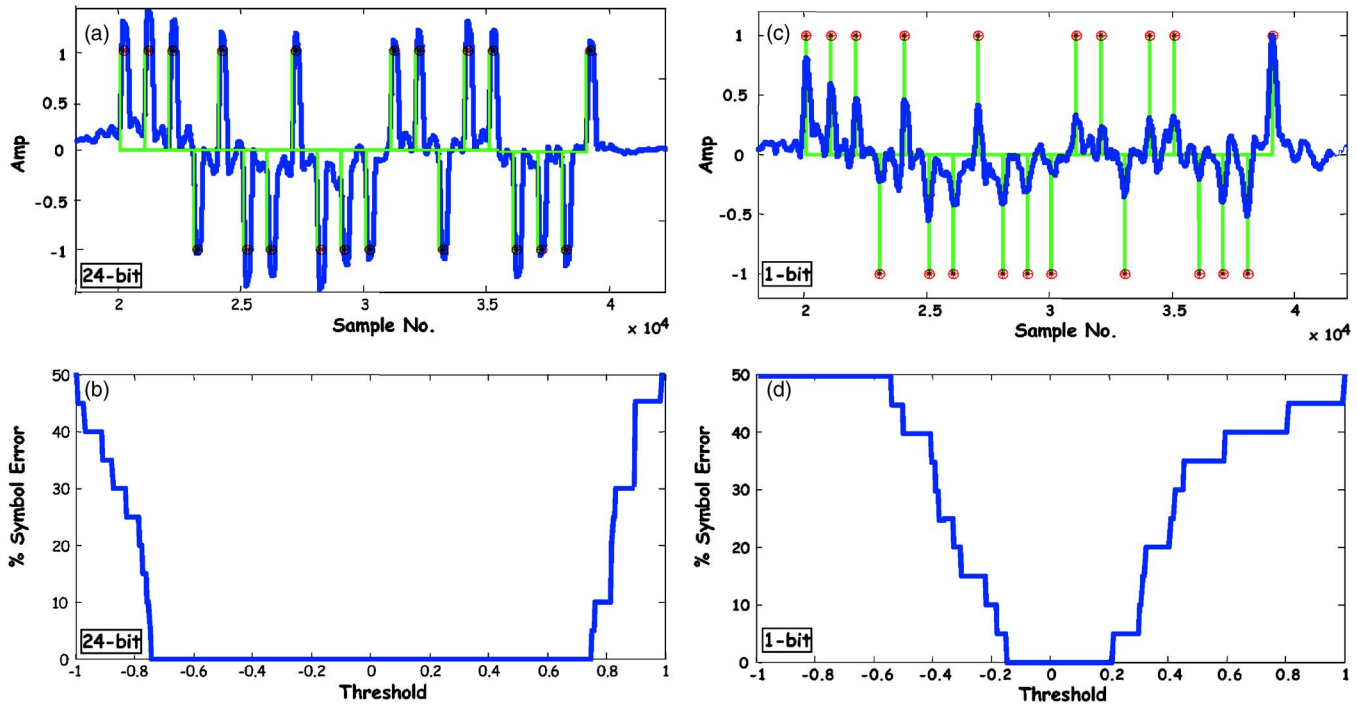

FIG. 10. (Color online) Multichannel TRef III receiver output coded estimates (solid line) using the T/R III preprocessor in *short waveguide* (~130 ft): Coded estimates (solid line) along with true BPSK code sequence (solid line) for 24-bit (a) and 1-bit (c) designs at each client receiver for true symbols (*) and estimated symbols (○) yielding a zero-bit error performance for the selected threshold. Performance U curves for focusing at client one using 24-bit (b) (75% zero-symbol error threshold interval) and 1-bit (d) (9% threshold interval) designs. The degradation of the 1-bit design is 66% threshold interval.

signs (upper row) are illustrated using solid lines. This code estimate is down-sampled to the symbol rate and then quantized based on a selected threshold. Each estimated symbol (○) is then compared to the true transmitted symbol (*) that is overlaid in the figure for illustrative purposes. For TRef I, it is clear that raw coded information pulses are discernible at the receiver output data (solid line) and that the preprocessed data tracks the "true" code. Since all of the symbols estimated by TRef I quantizer perfectly match those transmitted, the BPSK information code is captured with zero-symbol

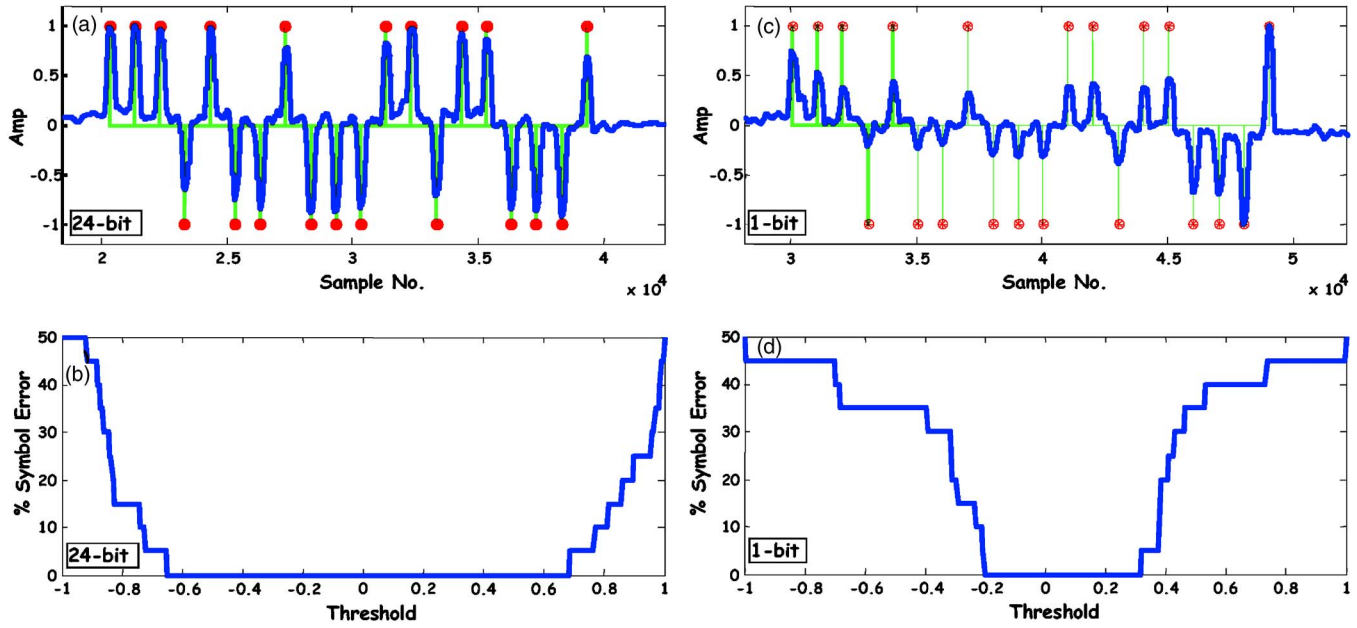

FIG. 11. (Color online) Multichannel TRef III receiver output coded estimates (solid line) using the T/R III preprocessor in *long waveguide* (~180 ft): Coded estimates (solid line) along with true BPSK code sequence (solid line) for 24-bit (a) and 1-bit (c) designs at each client receiver for true symbols (*) and estimated symbols (○) yielding a zero-bit error performance for the selected threshold. Performance U curves for focusing at client one using 24-bit (b) (68% zero-symbol error threshold interval) and 1-bit (d) (25% threshold interval) designs. The degradation of the 1-bit design is 43% threshold interval.

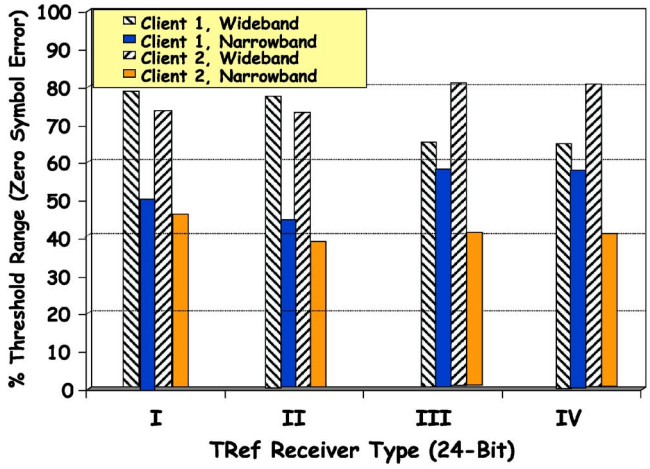

FIG. 12. (Color online) TRef I–IV wideband receiver overall performance in *stairwell* using T/R preprocessor based on the threshold range (% of total) for zero-symbol error threshold interval performance at both client stations for 24-bit designs. The narrowband designs from previous work (Ref. 18) are included for comparison.

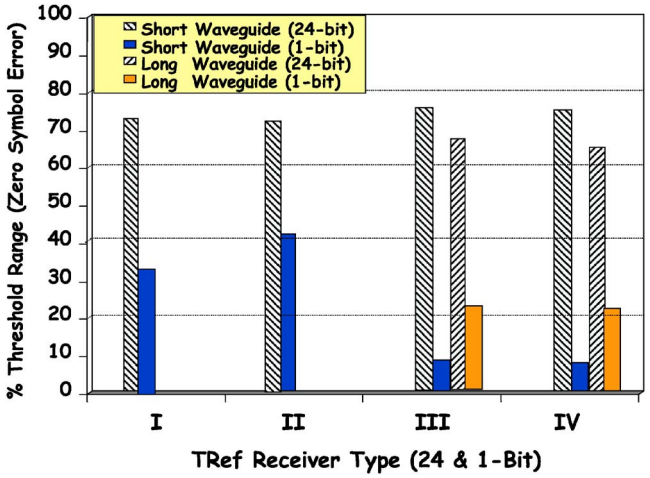

FIG. 14. (Color online) TRef III–IV receiver performance in *short* (~130 ft) and *long waveguides* (~180 ft) using T/R preprocessor based on the threshold range (% of total) for zero-symbol error threshold interval performance at both client stations for both 24- and 1-bit designs.

error for the selected threshold. Note also the high SNR achieved through T/R focusing and inherent array gain compared to the previous narrowband experiments reported on previously.[17,18] It is also interesting to note that the 1-bit designs at each client-station have deteriorated compared to the 24-bit design. This performance is expected due to increased quantization noise.

By varying the threshold over the entire T/R receiver estimate, the performance U curve (% symbol error versus threshold) is generated as shown in Fig. 6 (lower row). This curve plays a role similar to the operating characteristic curve[19] in classical detection theory—thresholds can be selected to minimize symbol error. As mentioned previously, the length or range of the threshold interval yielding zero-symbol error compared to the total range gives an indication of the performance capability of the receiver. Each receiver is compared in the bar charts of Figs. 12–14. The interesting property is that it is possible to find a threshold interval

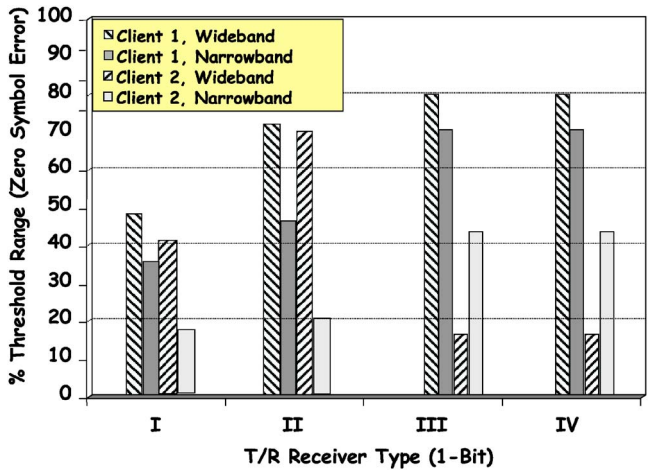

FIG. 13. (Color online) TRef I–IV wideband receiver overall performance in *stairwell* using T/R preprocessor based on the threshold range (% of total) for zero-symbol error threshold interval performance at both client stations for 1-bit designs. The narrowband designs from previous work (Ref. 18) are included for comparison.

yielding zero-symbol error indicating the robustness of the receiver, that is, the larger the interval, the more threshold values can be selected to yield zero-symbol error. The performance on these data is as expected, some robustness is sacrificed as the cost of simplicity using the 1-bit designs. Examining the U curves, we see that the receiver is able to achieve approximately a 72% threshold interval using the 24-bit design, while the interval decreases significantly to 43% using the 1-bit design. The 1-bit design captures the spatial information by using the zero-crossings of *both* signal and noise eliminating the amplitude information. When noise only is quantized, it has an amplitude level of ±1. The inherent in-band signal and noise have now also been quantized to the *same* level thereby causing the observed performance degradation.

2. TRef III receiver performance

This TRef III receiver uses the estimated set of Green's functions convolved with the raw received code data on *reception*. The results of the performance of this realization are shown in Fig. 7. After the T/R preprocessing, the experimental results track the transmitted code as before. For the selected threshold, zero-symbol error is achieved with perfect code recovery. In the figure we observe the outstanding performance of the 24-bit (80% zero-symbol error threshold interval) and the degraded performance of the 1-bit (20% threshold interval) designs (upper row). The overall performance is also shown in the lower row of the figure where we observe the U-shaped symbol error curves. The performance of this receiver is quite good; however, we note the significant performance degradation in the 1-bit design due to the inherent quantization errors.

3. Overall stairwell performance

Next we compare the overall robustness performance of each design at the individual client-stations for both 24- and 1-bit designs shown in Figs. 12 and 13. We illustrate the performance by bar charts with the height of the bar deter-

mined by the % threshold range occupied by zero-symbol error of the corresponding U curve. In Fig. 12 the 24-bit design chart shows a significant performance improvement over previous point designs[6,7] with the average wideband range over 72% (client-station 1) and 77% (client-station 2) of the total threshold interval for zero-symbol error compared to the narrowband designs[18] with just over 48% (client-station 1) and 44% (client-station 2) illustrating that the TRef design coupled with the T/R preprocessor is quite capable of operating effectively in a highly reverberant environment with improved performance. This improvement appears to be true for the 1-bit realizations except for client-station 2 using T/R III and IV preprocessing. The average wideband range has degraded somewhat to 70% for client-station 1 and severely to 34% for client-station 2, while the narrowband realizations were at 56% and 32%, respectively.[18] Even though the wideband realizations are an improvement over the narrowband for the 1-bit receivers on average, the poor individual performances of TRef III and IV are troublesome. The cause in the 1-bit case is usually a significant loss in signal levels creating higher quantization errors. However, it still appears reasonable to conclude that the wideband designs using the TRef receiver with the T/R preprocessors demonstrate an improved overall performance over the narrowband designs.

B. Waveguide experiments and results

The second set of experiments was performed in the building corridors shown in Fig. 8 where we see the structure that is actually part of an underground accelerator complex located at the Lawrence Livermore National Laboratory. It consists of a series of bends, corners, and turns with ancillary equipment and racks as well as varying ceiling heights throughout. Large concrete and steel doors are present for radiation protection when the accelerator is activated. The *short* waveguide consists of 130-ft-long run stretch with major bends and severe 90° turn while the *long* waveguide consists of the short waveguide extended for an overall length of 180 ft with the receiver located in a heavily shielded laboratory including large and noisy equipment (generators, coolers, air conditioners, fans, etc.) with concrete walls and the large concrete/steel door for radiation isolation. All of these obstructions contribute significantly creating a highly reverberant environment. The figure illustrates the various parts of the waveguide environment along the communications path.

The TRef receivers I and III were implemented using the T/R processor as before under the same propagation and transmission/reception conditions used in the stairwell (τ_P, τ_S), Gaussian-windowed chirp, etc. The *short* waveguide results are shown in Figs. 9 and 10 TRef I performance is illustrated in Fig. 9 yielding a 73% zero-symbol error threshold interval with the 24-bit scheme, similar to the *stairwell* performance, with the 1-bit design deteriorating to a 38% threshold interval indicating the sensitivity of the design to quantization errors contributed to the significant loss in SNR created by the obstructions and the length of the propagation paths.

The *short* waveguide results for TRef III are shown in Fig. 10 where we observe a 73% threshold interval for the 24-bit design with a severe deterioration of performance for the 1-bit design of 9% threshold interval. It appears that the wideband design suffers more significant degradation for the 1-bit designs than the narrowband case due to the decreased signal levels created by propagation losses and therefore increased quantization errors. Also the amount of in band noise is intrinsically larger for the wide band case.

The final set of experiments is shown in Fig. 11 for the *long* waveguide designs of TRef III. Here we again observe degradation in overall performance to 68% for the 24-bit design and a 26% zero-symbol error threshold interval for the 1-bit design. Again this is not unexpected due to the propagation losses and ensuing quantization errors.

These results imply that the longer the waveguide, the more propagation losses contribute to a significant decrease in SNR at the receiver. Therefore, the robust performance of the receivers suffers degradations especially for the 1-bit designs, that is, the zero-symbol error threshold intervals decrease significantly. As demonstrated, the 1-bit designs are much more sensitive to these losses than in previous studies.[18] This follows since decreasing signal levels increases the in-band noise and uncertainty leading to much larger quantization errors and therefore severe deterioration of the receiver performance even using the T/R preprocessing for enhancement.

Overall waveguide performance. The overall performance of the wideband TRef processor for both the *short* and *long* waveguide environments is shown in the bar chart of Fig. 14 with the % zero-symbol error threshold range shown as before for the stairwell. The chart displays both the 24- and 1-bit realizations. The 24-bit *short* and *long* waveguide experimental results are quite good with an average threshold range of 75% and 67%, respectively. This slight decrease in the long waveguide is expected because of the lower SNR due to propagation losses caused by its extended length and obstructions. However, the 1-bit results are somewhat disappointing with an average threshold range of less than 10% for the short waveguide and 25% for the long. Again TRef III and IV demonstrate poor individual performance. Overall the 24-bit TRef receiver performance is quite good for both waveguide experiments, while the 1-bit realizations are just marginal comparatively. It is interesting to note that the 1 -bit performance is better for longer waveguide than the shorter waveguide. This might be caused by a decrease in ambient noise at the position of the microphone for the long waveguide.

V. CONCLUSIONS

In this paper we have discussed the development of a multichannel wideband time-reference (TRef) or correlation-based receiver using a time-reversal (T/R) preprocessor to enhance and extract an information sequence transmitted through highly reverberant media. We have evaluated the performance of this design in a well-known stairwell that was used for narrowband designs previously[17,18] and compared the overall results. This effort, therefore, extends the

previous narrowband results to the wideband case and explores communications in waveguide structures that are important in a variety of applications.

We discussed the performance of the multichannel, wideband receiver designs in the highly reverberant stairwell demonstrating that the performance was comparable by achieving the same level of performance using the % zero-symbol error metric. We also showed that the wideband receiver designs could be deployed effectively in a waveguide environment of an accelerator facility at the Lawrence Livermore National Laboratory. Again the performance was quite comparable to that expected of a narrowband system, but somewhat surprisingly the 1-bit receiver realizations degraded significantly over the past work.[17,18] It was conjectured that the elongated acoustic propagation paths causing large signal attenuation was the underlying catalyst increasing the significance of the 1-bit quantization errors.

More specifically, the wideband TRef receiver realization with the T/R preprocessor demonstrated superior performance to the previous narrowband designs in all of the 24-bit experiments; however, the 1-bit wideband designs were just marginally better or equivalent to the narrowband case. From these results we conclude that coupling the T/R preprocessor to a wideband TRef modulation receiver not only simplifies the synchronization problem, but clearly improves the overall communication system performance in a highly reverberant environment. We also conclude that the TRef processor is capable of performing well in complex waveguide environments providing an effective method of communication in air.

Future work in this area is based on applying these results especially the 1-bit realizations to the electromagnetic case for wireless communications.

ACKNOWLEDGMENTS

This work was performed under the auspices of the U. S. Department of Energy contract by the Lawrence Livermore National Laboratory under Contract No. W-7405-Eng-48. The thorough review and excellent comments by the anonymous reviewers led to a much better manuscript.

[1]J. G. Proakis, *Digital Communications* (McGraw-Hill, New York, 1995).
[2]S. Haykin, *Communication Systems* (Wiley, New York, 2001).
[3]M. Fink, "Time reversal in acoustics," Contemp. Phys. **37**, 95–109 (1996).
[4]D. H. Chambers, J. V. Candy, S. K. Lehman, J. S. Kallman, A. J. Poggio, and A. W. Meyer, "Time-reversal and the spatio-temporal matched-filter," J. Acoust. Soc. Am. **116**, 1348–1350 (2004).
[5]A. Parvulescu, "Matched-signal (MESS) processing by the ocean," J. Acoust. Soc. Am. **98**, 943–960 (1995).
[6]D. R. Jackson and D. R. Dowling, "Phase conjugation in underwater acoustics," J. Acoust. Soc. Am. **89**, 171–181 (1991).
[7]D. R. Dowling, "Acoustic pulse compression using passive phase-conjugate processing," J. Acoust. Soc. Am. **95**, 1450–1458 (1994).
[8]J.-P. Hermand and W. Roderick, "Acoustic model-based matched filter processing for fading time-dispersive ocean channels: Theory and experiment," IEEE J. Ocean. Eng. **18**, 447–465 (1993).
[9]R. K. Brienzo and W. S. Hodgkiss, "Broadband matched-field processing," J. Acoust. Soc. Am. **94**, 2821–2831 (1993).
[10]W. A. Kuperman, W. S. Hodgkiss, and H. C. Song, "Phase conjugation in the ocean: Experimental demonstration of an acoustic time-reversal mirror," J. Acoust. Soc. Am. **103**, 25–40 (1998).
[11]J.-P. Hermand, "Broad-band geoacoustic inversion in shallow water from waveguide impulse response measurements on a single hydrophone: Theory and experimental results," IEEE J. Ocean. Eng. **24**, 41–66 (1999).
[12]W. S. Hodgkiss, H. C. Song, W. A. Kuperman, T. Akal, C. Ferla, and D. R. Jackson, "A long range and variable focus phase-conjugation experiment in shallow water," J. Acoust. Soc. Am. **105**, 1597–1604 (1999).
[13]G. Edelmann, T. Akal, W. S. Hodgkiss, S. Kim, W. A. Kuperman, and H. C. Song, "An initial demonstration of underwater acoustic communication using time reversal," IEEE J. Ocean. Eng. **27**, 602–609 (2002).
[14]D. Rouseff, D. R. Jackson, W. L. Fox, C. D. Jones, J. A. Ritcey, and D. R. Dowling, "Underwater acoustic communication by passive-phase conjugation: Theory and experiment," IEEE J. Ocean. Eng. **26**, 821–831 (2001).
[15]K. B. Smith, A. M. Abrantes, and A. Larraza, "Examination of time-reversal acoustics in shallow water and applications to noncoherent underwater communications," J. Acoust. Soc. Am. **113**, 3095–3110 (2003).
[16]M. Heinemann, A. Larraza, and K. B. Smith, "Experimental studies of applications of time-reversal acoustics to noncoherent underwater communications," J. Acoust. Soc. Am. **113**, 3111–3116 (2003).
[17]J. V. Candy, A. W. Meyer, A. J. Poggio, and B. L. Guidry, "Time-reversal processing for an acoustic communications experiment in a highly reverberant environment," J. Acoust. Soc. Am. **115**, 1621–1631 (2004).
[18]J. V. Candy, A. J. Poggio, D. H. Chambers, B. L. Guidry, C. L. Robbins, and C. A. Kent, "Multichannel time-reversal processing for acoustic communications in a highly reverberant environment," J. Acoust. Soc. Am. **118**, 2339–2354 (2005).
[19]D. H. Johnson and D. E. Dudgeon, *Array Signal Processing: Concepts and Techniques* (Prentice-Hall, Engelwood Cliffs, NJ, 1993).
[20]J. V. Candy, *Model-Based Signal Processing* (Wiley/IEEE Press, Hoboken, NJ, 2006).
[21]A. Derode, A. Tourin, and M. Fink, "Ultrasonic pulse compression with one-bit time reversal through multiple scattering," J. Appl. Phys. **85**, 6343.
[22]L. Yang and G. B. Giannakis, "Ultra-wideband communications," IEEE Signal Process. Mag. **21**, 26–54 (2004).
[23]A. F. Naguib, N. Seshadri, and A. R. Calderbank, "Space-time coding and signal processing for high data rate wireless communications," IEEE Signal Process. Mag. **17**, 76–92 (2000).
[24]A. J. Paulraj and C. B. Papadias, "Space-time processing for wireless communications," IEEE Signal Process. Mag. **14**, 49–83 (1997).

Efficient array beam forming by spatial filtering for ultrasound B-mode imaging

Kang-Sik Kim, Jie Liu, and Michael F. Insana
Department of Bioengineering and Beckman Institute for Advanced Science and Engineering, University of Illinois at Urbana-Champaign, 3120 DCL, MC-278 1304 W. Springfield Avenue, Urbana, Illinois 61801

(Received 30 January 2006; revised 22 May 2006; accepted 24 May 2006)

This paper proposes an efficient array beam-forming method using spatial matched filtering (SMF) for ultrasonic imaging. In the proposed method, ultrasonic waves are transmitted from an array subaperture with fixed transmit focus as in conventional array imaging. At receive, radio frequency echo signals from each receive channel are passed through a spatial matched filter that is constructed based on the system transmit-receive spatial impulse response. The filtered echo signals are then summed without time delays. The filter concentrates and spatially registers the echo energy from each element so that the pulse-echo impulse response of the summed output is focused with acceptably low side lobes. Analytical beam pattern analysis and simulation results using a linear array show that this spatial filtering method can improve lateral resolution and contrast-to-noise ratio as compared with conventional dynamic receive focusing (DRF) methods. Experimental results with a linear array are consistent but point out the need to address additional practical issues. Spatial filtering is equivalent to synthetic aperture methods that dynamically focus on both transmit and receive throughout the field of view. In one common example of phase aberrations, the SMF method was degraded to a degree comparable to conventional DRF methods.
 [DOI: 10.1121/1.2214393]

PACS number(s): 43.60.Fg, 43.35.Yb [TDM] Pages: 852–861

I. INTRODUCTION

The goal of ultrasonic pulse-echo beam forming is to focus all the available acoustic energy at each point in the imaging field.[1] Conventional beam formers currently used in array systems apply separate focusing methods during pulse transmission and echo reception. The focal length and aperture size during transmission generate point spread functions that vary with tissue depth. Launching M pulses for each line of site allows focusing at M depths at the cost of a proportional reduction in frame rate. To keep frame rates high, the transmission f number (ratio of focal length to aperture size) is often set relatively large to maximize the depth of focus.

Conversely, on receive, the focal length and active aperture size are varied dynamically (dynamic-receive focusing[2] or DRF) to focus the received beam at each depth with a relatively constant f number. The pulse-echo cross-range resolution, however, is determined by the product of the transmitted and received beamwidths, so the pulse-echo point spread function from DRF beam forming is most compact near the transmit focal length and thus remains time varying for real-time imaging. Ideal improvements in beam forming require methods able to uniformly focus both transmit and receive beams at all depths without significantly lowering frame rate or echo signal-to-noise ratio (eSNR).

One solution is synthetic aperture (SA) imaging.[3,4] SA imaging is a label that defines a family of techniques each designed to provide uniformly high spatial resolution, but frequently at the cost of side-lobe growth, reduced eSNR, and/or frame rate. For example, pulses can be transmitted from a source element smaller than the wavelength that is scanned across the large aperture area to be synthesized. Following transmission, echoes are recorded, time delayed, and coherently summed. The pulse-echo point spread function from this SA method in effect corresponds to focusing on both transmit and receive. Unfortunately, tissue or transducer movements occurring during SA acquisition generate phase distortions, thus producing beam-forming errors that widen the beam and degrade image quality. Receive aperture sizes can be varied to speed acquisition time and reduce system complexity but with diminished performance.[5] Alternatively motion compensation has been applied,[6,7] but at the costs of greater computational load and lower frame rate.

Another beam-forming solution involves spatial filtering of the echo signals. In one technique, transmit and receive foci are both fixed. Focusing is achieved by Wiener filtering the beam-formed rf echo signals in two dimensions, where the filter is constructed from prior knowledge of the pulse-echo point spread function and noise properties.[8] Under limited conditions, this approach is ideal for detecting large, low-contrast targets provided the impulse response and noise properties are known.[9] Spatial filtering has also been applied in SA methods for deconvolving finite-sized subapertures to improve spatial resolution, sensitivity, and frame rate,[10] and to design voltage signals applied to array elements during transmission that improve focusing in aberrating media.[11] Still others have suggested echo filtering methods for beam forming in combination with coded-pulse transmission or SA-type acquisition schemes.[12,13]

In this context, our goal is to explore beam-forming strategies that are efficient in terms of computational and hardware requirements and robust, and to evaluate them through comparison with conventional methods. We propose

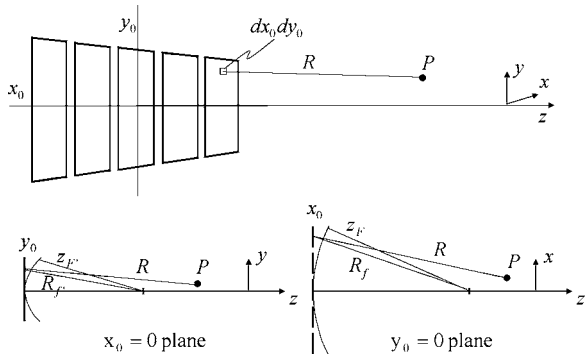

FIG. 1. The geometry of the beam pattern analysis is illustrated.

a large-aperture, fixed-focus technique for pulse transmission in which rf echo signals are matched filtered by the pulse-echo point spread function and summed. This spatial matched filtering (SMF) approach to beam forming yields a lateral resolution equivalent to common SA methods for one-dimensional (1D) arrays. In addition, eSNR is superior to conventional DRF methods although axial resolution is somewhat compromised. We show that spatial matched filtering of individual receive-element signals has the potential to generate significantly lower side lobes than does filtering beam-formed echo signals, although practical issues for 1D arrays lead us to prefer filtering of beam-formed echoes. Also the effects of phase aberrations on lesion visibility appear no worse than those for DRF methods at least for one situation. Spatial filtering offers the additional advantage of not requiring delay circuits in the beam former, which simplifies the stringent hardware requirements for imaging with arrays particularly at high frequencies. Conditions under which the SMF method offers an efficient beam-forming solution are discussed.

This paper is organized as follows. Section II describes SMF beam forming in the context of classical Fourier optics. Section III summarizes our simulation results using linear array transducer and Field II to verify predicted performance. Also, experimental results using Siemens Antares scanner and phantom are presented. Finally, the paper concludes in Sec. IV.

II. METHODS AND ANALYSIS

A. Continuous-wave fields

To compare the proposed SMF method with the conventional DRF beam former, we briefly review standard expressions for complex fields from a continuous-wave (CW) radiator that guide focusing strategies.

Figure 1 illustrates a standard 3D geometry for describing pressure profiles from a planar, rectangular aperture of a 1D array transducer. The coordinates on the array surface are (x_0,y_0) while those in the measurement field are (x,y,z), such that $R=\sqrt{(x-x_0)^2+(y-y_0)^2+z^2}$ is the distance from the transmit aperture surface $a_t(x_0,y_0)$ to the field point P. The Rayleigh-Sommerfeld diffraction formula at wavelength λ and wave-number $k=2\pi/\lambda$ gives the following expression for the complex field[14] transmitted at radial temporal frequency $\omega=kc$, where c is the speed of sound

$$\varphi_\omega(P)=\frac{1}{j\lambda}\int_{-\infty}^{+\infty}dy_0\int_{-\infty}^{+\infty}dx_0a_t(x_0,y_0)\frac{e^{jkR}}{R}\frac{z}{R}. \tag{1a}$$

CW pressure p_ω is related to the complex field φ_ω via

$$p_\omega(P,t)=\mathrm{Re}\{Q(\omega)\varphi_\omega(P)e^{-j\omega t}\}, \tag{1b}$$

where $\mathrm{Re}\{\cdot\}$ is the real part of the argument and $Q(\omega)$ is the complex pressure amplitude. The subscript ω indicates that the function applies to a single frequency value.

Factors e^{jkR}/R and z/R in Eq. (1a) are the Green's function and obliquity factor, respectively.[14] Limiting our attention to field points near the z axis, we approximate

$$\frac{z}{R^2}\approx\frac{1}{z}\quad\text{and}\quad jkR\approx jk\left[z+\frac{x_0^2}{2z}+\frac{y_0^2}{2z}-\frac{xx_0}{z}-\frac{yy_0}{z}\right], \tag{2}$$

which allows us to expand and simplify Eq. (1a)

$$\varphi_\omega(P)=\frac{e^{jkz}}{j\lambda z}\int_{-\infty}^{+\infty}dy_0e^{-jkyy_0/z}\times\int_{-\infty}^{+\infty}dx_0e^{-jkxx_0/z}a_t(x_0,y_0)e^{jk(x_0^2+y_0^2)/2z}. \tag{3}$$

It is well known that the objective of focusing when imaging under the Fresnel approximation is to eliminate the quadratic phase factor $\exp[jk(x_0^2+y_0^2)/2z]$ in Eq. (3). Success achieves diffraction-limited cross-range resolution,[15] where the field pattern is given by the spatial Fourier transform of the transmit aperture function.

A conventional delay-and-sum beam former[1] uses the geometry of Eq. (3) to calculate the time delays that focus the CW field. Focusing is equivalent to multiplying by the phase factor $\exp[-jk(R_f-z_F+R_{f'}-z_{F'})]$, where z_F (see Fig. 1) and $z_{F'}$ are the radii of curvature along the lateral x_0 and elevational y_0 axes, respectively. Also $R_f^2=x_0^2+z_F^2$ and $R_{f'}^2=y_0^2+z_{F'}^2$ are the distances from points on the aperture to the corresponding radius of curvature in the $y_0=0$ and $x_0=0$ planes, respectively. Applying the paraxial approximation to the focusing phase factor, as in Eq. (2), yields $\exp[-jk(R_f-z_F+R_{f'}-z_{F'})]\cong\exp[-jk(x_0^2/2z_F+y_0^2/2z_{F'})]$, so that Eq. (3) becomes

$$\varphi_\omega(P)=\frac{e^{jkz}}{j\lambda z}\int_{-\infty}^{+\infty}dy_0a_t(y_0)e^{-jkyy_0/z}e^{jk\beta'y_0^2}\times\int_{-\infty}^{+\infty}dx_0a_t(x_0)e^{-jkxx_0/z}e^{jk\beta x_0^2}, \tag{4}$$

where $\beta=1/2z-1/2z_F$ and $\beta'=1/2z-1/2z_{F'}$. We also assumed separability of the transmit aperture function to write $a_t(x_0,y_0)=a_t(x_0)a_t(y_0)$.

B-mode imaging for 1D arrays occurs in the x,z plane at $y=0$. Consequently

$$\varphi_\omega(x,z) = C_\omega(z)\int_{-\infty}^{\infty} dx_0 a_t(x_0) e^{-jkx/zx_0} e^{jk\beta x_0^2},$$

$$\text{where } C_\omega(z) = e^{jkz}/j\lambda z \int_{-\infty}^{\infty} dy_0 a_t(y_0) e^{jk\beta' y_0^2}. \tag{5}$$

The z dependence of C_ω reminds us that a fixed elevational focus from a 1D linear array gives a depth dependent point spread function regardless of scan plane focusing. In the focal region, $z \cong z_F$ implies $\beta \cong 0$ and therefore the field in Eq. (5) is simply the spatial Fourier transform of the aperture function

$$\varphi_\omega(x,z_F) = C_\omega(z_F) A_t(u_x), \tag{6}$$

where $A_t(u_x) = \Im\{a_t(x_0)\}_{u_x = x/\lambda z}$ is shorthand for the spatial Fourier transform of the transmit aperture function a_t. It is evaluated at spatial frequency u_x, which is a function of lateral field position x. Finally, from Eq. (1b), a band-limited pressure pulse in the scan plane with bandwidth Ω is given by

$$p(x,z,t) = \frac{1}{2\pi}\,\mathrm{Re}\left\{\int_\Omega d\omega Q(\omega)\varphi_\omega(x,z)e^{-j\omega t}\right\}. \tag{7}$$

B. Conventional delay-and-sum beam forming

Assume we transmit a broadband, focused acoustic pulse at one focal length. We then receive echoes on each array element that are delayed and summed assuming an ideal, in-plane, dynamic-receive focusing (DRF) technique with fixed f number. This focusing is ideal in the sense that the in-plane radius of curvature $z_F(z)$ and in-plane receive aperture $a_r(x_0,z)$ are continuously varied such that $a_r(x_0,z)/z_F(z)$ and the received field are both relatively constant with depth. Equation (5) applies to both transmit and receive apertures because of the principle of reciprocity.[16] The pulse-echo field at frequency ω, ψ_ω, is the product of the transmitted φ_ω and received φ'_ω fields. For a conventional beam former, we find from Eqs. (5) and (6) that

$$\psi_{\omega,C}(x,z) = \varphi'_\omega(x,z)\varphi_\omega(x,z)$$
$$= C_\omega^2(z) A_r(u_x,z)\left[\int_{-\infty}^{\infty} dx_0 a_t(x_0) e^{-jkx/zx_0} e^{jk\beta x_0^2}\right], \tag{8}$$

where $A_r(u_x,z) = \Im\{a_r(x_0,z)\}_{u_x = x/\lambda z}$ is the spatial Fourier transform of the receive aperture function that varies with depth. Equation (8) is the narrowband pulse-echo field at $y=0$ for a conventional beam former; it is our standard for comparison. If the transmit-receive apertures have equal length in the scan plane $a_t(x_0) = a_r(x_0) = a(x_0)$, and the transducer is weakly focused in elevation, e.g., $a(y_0)/z_{F'}$ for a f number of 4, the best lateral resolution is obtained at the transmit focal length $z = z_F$, where $\beta = 0$. From Eq. (8) we see that

$$\psi_{\omega,C}(x,z_F) = C_\omega^2(z_F) A^2(u_x,z_F). \tag{9}$$

The goal of the SMF beam former is to efficiently obtain the field in Eq. (9) for all z while compromising eSNR and contrast resolution as little as possible.

C. Spatial matched filtering (SMF)

1. Filtering before summing

The above equations and Fig. 1 may also be used to explain and analyze the SMF beam former. In this section, we filter receive-channel echoes individually before summation. A focused array aperture $a_t(x_0,y_0)$ transmits sinusoids at frequency ω. Echoes are received by individual array elements located at $x_0 = x_r$. If the element width along x is smaller than the wavelength, each receive aperture may be approximated by $a_r(x_0,y_0) = \delta(x_0 - x_r)a_r(y_0)$. From Eq. (5), the pulse-echo field from the array element at x_r becomes

$$\psi_\omega(x,z;x_r) = \varphi'_\omega(x,z;x_r)\varphi_\omega(x,z)$$
$$= C_\omega^2(z) e^{jk\beta x_r^2} e^{-jkx/zx_r} \int_{-\infty}^{\infty} dx_0 a_t(x_0) e^{jk\beta x_0^2} e^{-jkx/zx_0}. \tag{10}$$

We now matched filter the receive fields along the x axis with Eq. (10) evaluated at the corresponding value of x_r. The corresponding pulse-echo point spread function for this SMF beam former is the convolution of ψ_ω with its complex conjugate ψ_ω^* along the x axis

$$\psi'_\omega(x,z;x_r) = \psi_\omega(x,z;x_r)^* \psi_\omega^*(-x,z;x_r) = C_\omega^4(z)\int_{-\infty}^{\infty} d\tau\left[e^{jk\beta x_r^2} e^{-jk\tau/zx_r}\int_{-\infty}^{\infty} dx_0 a_t(x_0) e^{jk\beta x_0^2} e^{-jk\tau/zx_0}\right]$$
$$\times\left[e^{-jk\beta x_r^2} e^{jk(\tau-x)/zx_r}\int_{-\infty}^{\infty} dx_1 a_t(x_1) e^{-jk\beta x_1^2} e^{jk(\tau-x)/zx_1}\right]$$
$$= C_\omega^4(z) e^{-jkx/zx_r}\int_{-\infty}^{\infty} dx_1 \int_{-\infty}^{\infty} dx_0 a_t(x_0) a_t(x_1) e^{jk\beta(x_0^2 - x^2)} e^{-jkx/zx_1}\int_{-\infty}^{\infty} d\tau e^{-jk\tau/z(x_0 - x_1)}$$
$$= \frac{4\pi^2 z}{k} C_\omega^4(z) e^{-jkx/zx_r}\int_{-\infty}^{\infty} dx_1 a_t^2(x_1) e^{-jkx/zx_1}$$
$$= \frac{4\pi^2 z}{k} C_\omega^4(z) e^{-jkx/zx_r} A_{(2)t}(u_x), \tag{11}$$

where $A_{(2),t}(u_x)=\Im\{a_t^2(x_1)\}_{u_x=x/\lambda z}$ represents the spatial Fourier transform of the *squared* transmit aperture function. Equation (11) clearly shows that spatial matched filtering eliminates the quadratic phase factor from the transmit aperture, and therefore it is a method for focusing the transmitted beam at all depth if we know ψ_ω accurately.

The final step is to sum the outputs of the filtered fields weighted by the square of the receive aperture

$$\begin{aligned}\bar{\psi}_{\omega,S}(x,z) &= \int_{-\infty}^{+\infty} dx_r a_r^2(x_r,z)\psi'_\omega(x,z;x_r)\\ &= C_\omega^4(z)A_{(2),t}(u_x)\int_{-\infty}^{\infty} dx_r a_r^2(x_r,z)e^{-jkxx_r/z}\\ &= \frac{4\pi^2 z}{k}C_\omega^4(z)A_{(2)}^2(u_x),\end{aligned} \tag{12}$$

where we have set $a_t(x)=a_r(x,z)=a(x)$. $\bar{\psi}_{\omega,S}$ is the pulse-echo field for the SMF beam former where the echoes are filtered before being summed.

Examination of Eqs. (8) and (12) allows us to compare conventional DRF and SMF beam formers. SMF is able to focus at all depths and not just at the transmit focal length. Also SMF does not require application of echo delays before summing. However, both advantages are only realized if the shift-varying point spread functions $\psi_\omega(x,z;x_r)$ are known accurately for all depths z and for each receive array element at x_r. Similarly, the focusing geometry that applies to the DRF beam former must also be known. Geometric or filtering errors will increase side lobes energy and the main lobe width in either beam former. Consequently Eqs. (8) and (12) are both idealizations that require experimentation to evaluate relative performances under realistic conditions.

2. Filtering after summing

Implementation of the SMF method is much simpler if it is possible to filter just once after summing all the receiver channel outputs. From Eq. (5), where we assume a fixed focal geometry that is equal on transmission and reception, we have

If we now spatially matched filter Eq. (13) in the manner of Eq. (11) we find

$$\begin{aligned}\bar{\bar{\psi}}_{\omega,S}(x,z) &= \bar{\psi}_\omega(x,z) * \bar{\psi}_\omega^*(-x,z)\\ &= C_\omega^4(z)\int_{-\infty}^{+\infty} dx_0[a^2(x_0)e^{-jkxx_0/z}]^2\\ &= \left(\frac{4\pi^2 z}{k}\right)^2 C_\omega^4(z)A_{(4)}(2u_x),\end{aligned} \tag{14}$$

where $\bar{\bar{\psi}}_{\omega,S}$ is the pulse-echo field for the SMF beam former where the echoes are filtered after being summed, and $A_{(4)}(2u_x)=\Im\{a^4(x)\}_{2u_x=2x/\lambda z}$ is the spatial Fourier transform of the fourth power of the aperture function. Let us compare Eqs. (9), (12), and (14). It is significant that the spatial frequency in Eq. (14) is scaled by a factor of 2 compared with Eqs. (9) and (12). The factor of 2 means that the SMF applied to beam-formed echo data Eq. (14) has a narrower main lobe, like synthetic aperture focusing techniques.[5] However it also produces relatively higher-amplitude side-lobe levels because the pulse-echo point spread function depends on the one-way focused beam pattern; i.e., A is to the first power in Eq. (14) and it is squared in Eqs. (9) and (12). These feature combinations may be considered strengths or weaknesses depending on if the application is resolution or contrast limited.

Finally, introducing a linear-array aperture function we obtain results that permit comparisons with other techniques found in the literature.[5] For rectangular transmit-receive apertures of equal area and unit amplitude, where the array has $2N+1$ elements each of area $w_x\times w_y$ that are separated by a distance d along the x axis, we have

$$a(x_0,y_0)=\mathrm{rect}\left(\frac{y_0}{w_y}\right)\times\sum_{n=-N}^{N}\mathrm{rect}\left(\frac{x_0-nd}{w_x}\right). \tag{15}$$

From Eq. (12), the lateral pulse-echo point spread function for SMF before summing is

$$\begin{aligned}\bar{\psi}_{\omega,S}(x,z) &= \frac{4\pi^2 z}{k}w_x w_y C_\omega^4(z)\mathrm{sinc}^2\left(\frac{w_x}{\lambda z}x\right)\\ &\times\left[\frac{\sin\left(kd\frac{2N+1}{2z}x\right)}{\sin\left(kd\frac{1}{2z}x\right)}\right]^2,\end{aligned} \tag{16}$$

where $\mathrm{sinc}(x)=\sin(\pi x)/\pi x$. The methods can be compared at the transmit focal length as follows. From Eq. (9), we find $\psi_{\omega,C}(x,z_F)$ for the DRF method is also given by Eq. (16) except that $C_\omega^4(z)4\pi^2 z/k$ is replaced by $C_\omega^2(z_F)$. Applying the same rectangular array of Eq. (15) to (14) also results in Eq. (16) for $\bar{\bar{\psi}}_{\omega,S}(x,z)$, except that the squared terms are to the first power on the right side of the equation and x is replaced by $2x$.

To simplify the equations and concentrate on lateral resolution assessment, the main results summarized in Eqs. (8), (12), and (14) are expressed as narrow-band complex fields, which are not directly measurable. Conversions from complex fields to broadband echo signal voltages[1,17] involve computation of the time-varying force on the transducer aperture surface from the pressure field Eq. (1b) scattered from a point reflector followed by a weighted integration over the transducer bandpass. The process produces a product of the transmit-receive lateral field patterns as shown in Eq. (8) and a convolution in time, which means the pulse-echo impulse response is longer in duration than the transmitted pulse. To form a beam using a frame of echo signals, we apply a 2D spatiotemporal matched filter.[18] For example, if $g(t,x)$ is the broadband rf echo signal from a scattering medium using a system with impulse response $h(t,x)$ and $y(t,x)$ is echo signal output from the spatiotemporal filter, we have $y(t,x)=h(-t,-x)*g(t,x)$. Although the filter focuses the beam along the x axis as shown in Eqs. (12) and (14) above, it also lengthens the duration of the temporal impulse response. For a Gaussian-shaped pulse, axial resolution is reduced because the effective pulse length increases by a factor of $\sqrt{2}$ using

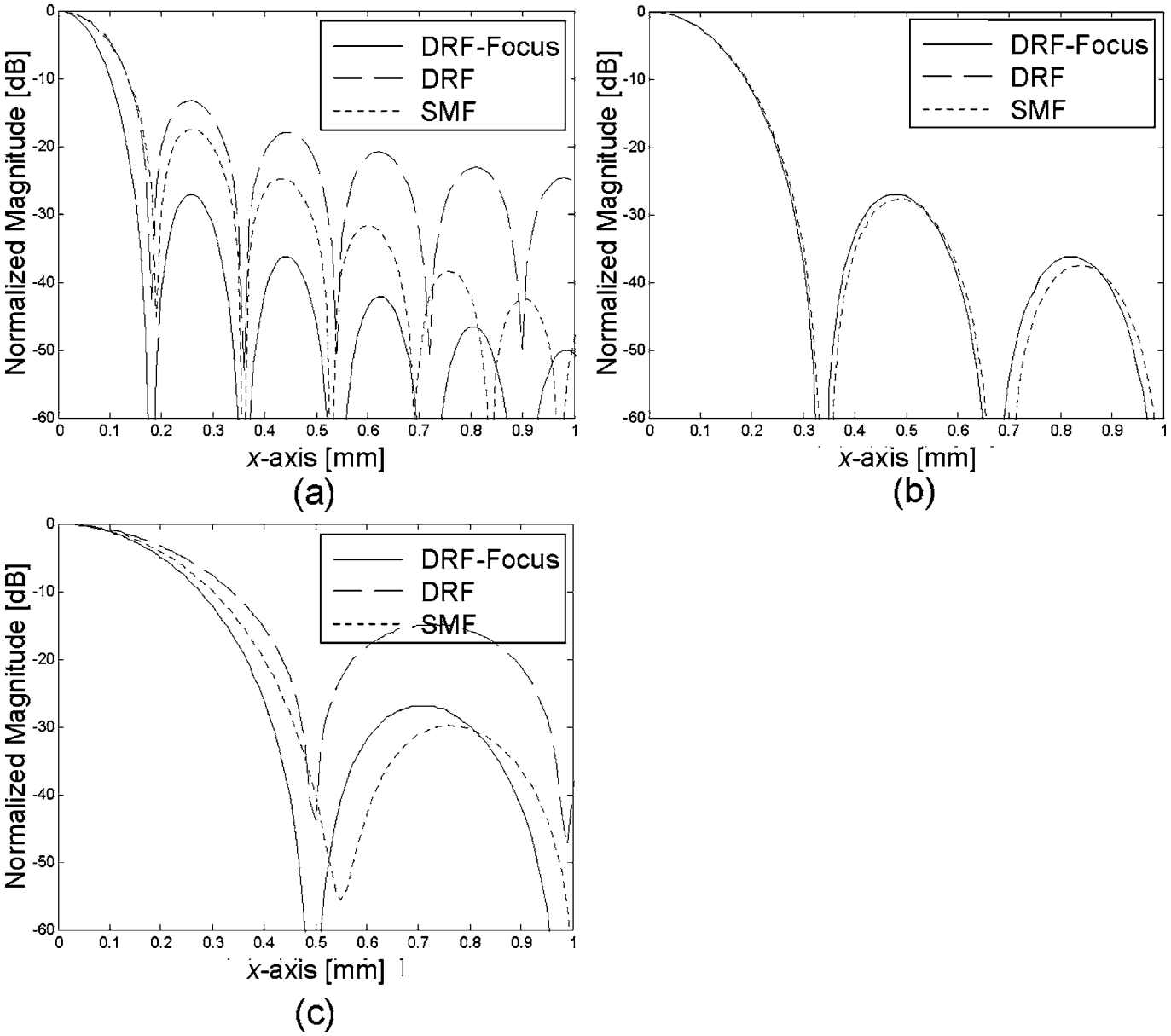

FIG. 2. Comparison of CW, transmit receive, lateral beam patterns for the DRF-focus, DRF, and SMF beam formers for a point reflector placed on axis at (a) 20 mm depth, (b) 40 mm depth, and (c) 60 mm depth. The transmit focus is fixed at 40 mm for the DRF and SMF methods and is refocused at each depth for the DRF-focus method.

filtering as compared with conventional DRF methods.

III. SIMULATION AND EXPERIMENTAL RESULTS

The above predictions of beam-former performances were validated using rf echo simulations from Field II (Ref. 19) for a broadband linear array transducer. The center frequency of the Gabor pulse transmitted was 10 MHz, and the −6 dB bandwidth was 7 MHz. The array element pitch was chosen to be $d=0.20$ mm, elements were $w_y=5$ mm long in elevation, and the transmit foci are fixed at $z_F=40$ mm and $z_F'=18$ mm for all data processed with DRF and SMF techniques. Ninety-six transmit-receive channels were used so that the apertures were fixed in area (no aperture growth) and equal to 19.2 mm × 5 mm.

In the following results, "DRF-focus" beam plots describe patterns obtained when transmit and receive apertures are both focused at the center of the image field, either 20, 40, or 60 mm. "DRF" plots describe results for a fixed 40-mm in-plane focal length on transmit; the receive beam is dynamically focused. "SMF" results are from Eq. (12) where $z_F=40$ mm for the fixed transmit and fixed receive focal lengths unless otherwise noted.

Figure 2 shows CW transmit-receive beam patterns for the DRF-focus, DRF, and SMF beam formers when a point reflector is positioned on axis at 20, 40, and 60 mm depths. These distances are proximal to, at, and distal to the fixed 40-mm transmit focal length of the DRF and SMF methods. For these data, SMF results are from a lD spatial filter applied along the x_0 axis. The three methods have very similar lateral profiles at the transmit focal length [Fig. 2(b)]. The DRF-focus method generates diffraction-limited sinc^2 beam patterns at all depths because the beam is focused on both

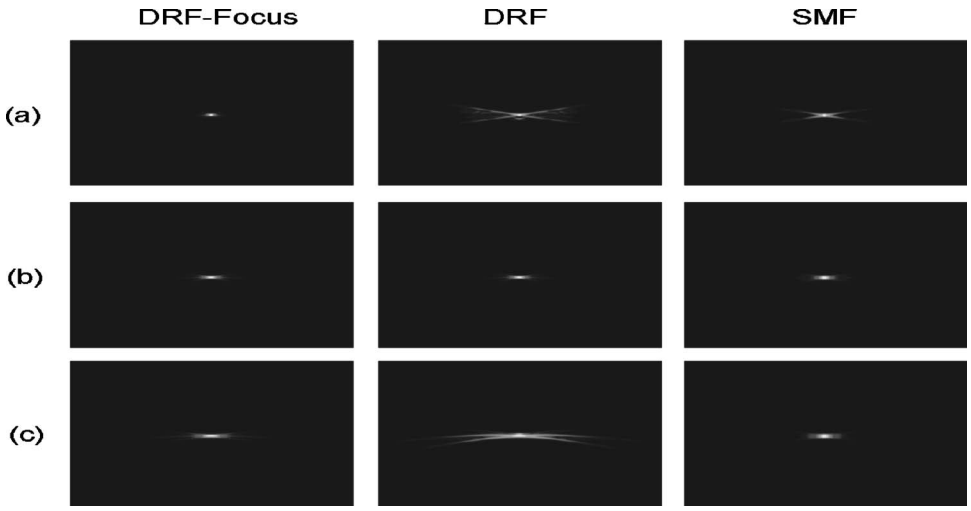

FIG. 3. Comparison of broadband, pulse echo, 2D point spread functions for the DRF-focus, DRF, and SMF beam formers at (a) 20 mm depth, (b) 40 mm depth, and (c) 60 mm depth. The transmit focus is fixed at 40 mm for the DRF and SMF methods and is refocused at each depth for the DRF-focus method. Images are normalized to the individual peak values and displayed with 60 dB dynamic range.

transmit and receive—it is a gold standard for beam forming. Although SMF widens the main lobe and spreads the nulls compared with the DRF-focus [Figs. 2(a) and 2(c)], it also generates side lobes that are lower than those of conventional DRF methods.

Figure 3 shows broadband, 2D, in-plane, pulse-echo point spread functions for each method. After beam formation, the point spread functions are envelope detected, the amplitudes are normalized to the peak values, log compressed with a dynamic range of 60 dB, and scan converted for display. The SMF results are from a 2D spatial matched filter applied in the x-z plane. Figure 4 shows corresponding lateral beam patterns; however they are not necessarily amplitude values plotted along the x axis for constant z as in Fig. 2. Instead we plot peak amplitude values found at any depth along each axial scan line. Figure 3(a) shows that DRF-focus provides the best broadband lateral resolution in the near field (20 mm) despite the claim of Eq. (12) for narrow band CW beams that diffraction limited resolution is obtained. In the near field, the paraxial approximation breaks down so that Eq. (12) is an optimistic predictor of beamwidth. Nevertheless the broadband pulse energy is more spatially compact with the SMF method compared to the DRF method in the near field. At the transmit focal depth of 40 mm, all lateral beamwidths are comparable and yet there is some loss of axial resolution for the SMF method as expected from 2D filtering. In the far-field (60 mm), the broadband beamwidth for the 2D SMF method is narrowest, unlike the narrow band beam patterns of Fig. 2. It is not that SMF surpasses the diffraction limit; rather the broadband results are not accurately predicted by the simple narrow band equations above. Beam simulations provide more accurate results for comparing broadband beam-forming strategies.

Further insights into the SMF method can be obtained from Figs. 5 and 6. Figures 5(a) and 5(b) show images of a point reflector placed on the beam axis at 60 mm. The full transmit aperture is activated and focused at 40 mm, but only the center element of the receive aperture is activated. In Fig. 5(a), a B-mode image was formed from the echo signal [Eq. (10)], and in Fig. 5(b), the echo was matched filtered before creating the image [Eq. (11)]. That is, Fig. 5(b) is a 2D autocorrelation of the rf echo signal corresponding to the image in Fig. 5(a). Clearly two effects of filtering are to condense the pulse energy and straighten the phase front. Consequently, when echoes from other receiver elements are also filtered and then summed to form a receive aperture, Eq. (12), the resulting pulse is more focused than a delay-and-sum strategy without filtering. Also, because filtering concentrates echo energy, eSNR is greater for SMF than DRF. Even when the transmit focus is moved from 40 mm to the scatterer position at 60 mm [Fig. 5(c)], the 2D SMF method [Fig. 5(b)] is better able to focus the beam. The effects are more clearly seen using the beam profiles in Fig. 6 that are taken from the data in Fig. 5.

Complete comparisons must extend beyond point reflectors to include scattering fields that generate speckle and have low-contrast targets. Such fields were simulated with Field II for a 2D anechoic target; the results are shown in Fig. 7. Also included are images formed using the spatial matched filter applied after summing receive elements, Eq. (14); these are labeled "SMF-BF." SMF-BF and DRF images appear to provide comparable target visibility. The SMF (filtering before summing) results are comparable to the gold-standard DRF-focus method at and beyond the focal length. The SMF contrast is degraded in the near field relative to DRF-focus and yet is superior to DRF. Results are consistent with the lateral beam profiles of Fig. 4(a). Contrast-to-noise ratio (CNR) values for the SMF images are superior to DRF everywhere but at the focus where all four methods are comparable. For these conditions, filters constructed from the impulse response at the vertical center of the imaging field apply reasonably well over a depth of focus of approximately 10 mm.

The SMF beam former was implemented experimentally on a standard Siemens Antares system with the ultrasound research interface (URI) feature to acquire beam-formed rf data. Also we applied special software from the manufacturer to control features of the transmit/receive apertures. The sound speed used by the system for beam forming was adjusted to match the ATS™ phantom (Model 539) scanned. RF data were recorded individually from each of the 192 receive channels, and B-mode images were formed and displayed offline (Fig. 8).

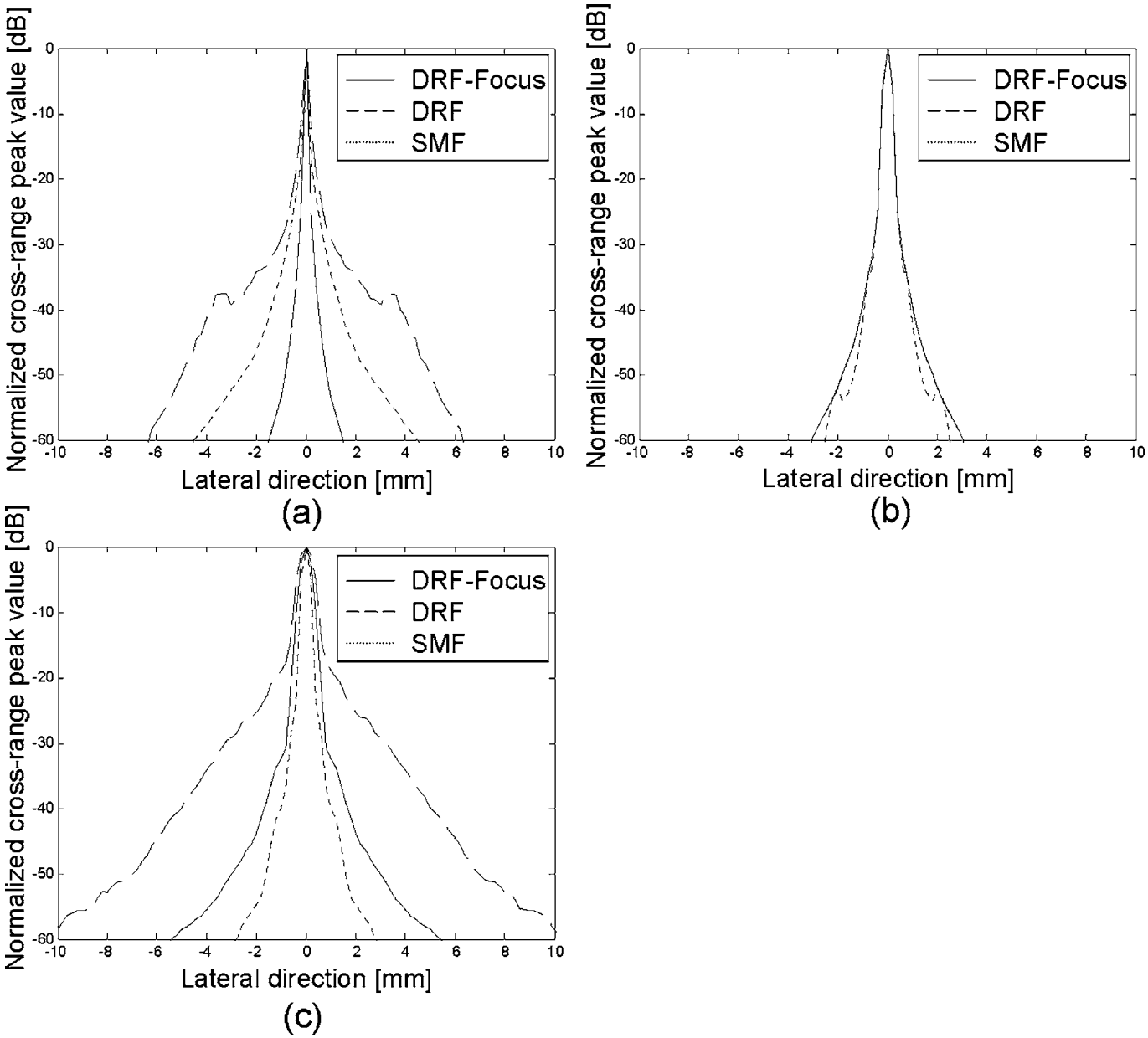

FIG. 4. Lateral beam patterns from the broadband pulse-echo point spread functions in Fig. 3.

The transducer was a 10 MHz (VF10-5) linear array with 0.2 mm element spacing. The lateral image line density was about 10/mm and the transmit focus was fixed at $f/2$. Figure 8 displays phantom images for the DRF-focus, DRF, SMF-BF, and SMF beam formers when the center of the anechoic region was positioned at 10, 20, and 30 mm depths. The speckle pattern and brightness of the SMF method is nonuniform in this initial experiment because the size and phase steering of the transmit aperture scanned across the array was varied in a way we could not control. Our matched filter only accounted for an axially varying impulse response. In spite of speckle heterogeneities caused by our limited control of the transmit aperture, image contrast for the spatial

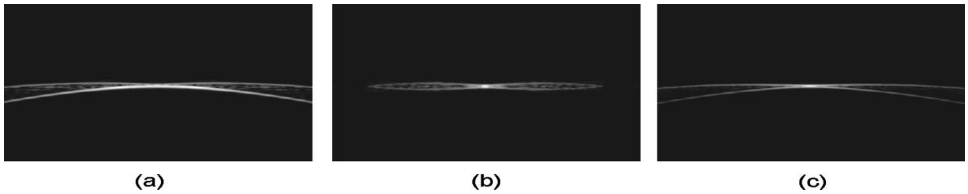

FIG. 5. B-mode images of a point target placed on the z axis at 60 mm. The full transmit aperture was applied with a fixed, 40-mm focal length but only the center transducer element was used to receive echoes (a). Applying a 2D matched filter to the rf echo signal in (a) results in the image of (b). (c) is the image constructed also from center receive element but where the transmit focus was moved to 60 mm (DRF-focus result).

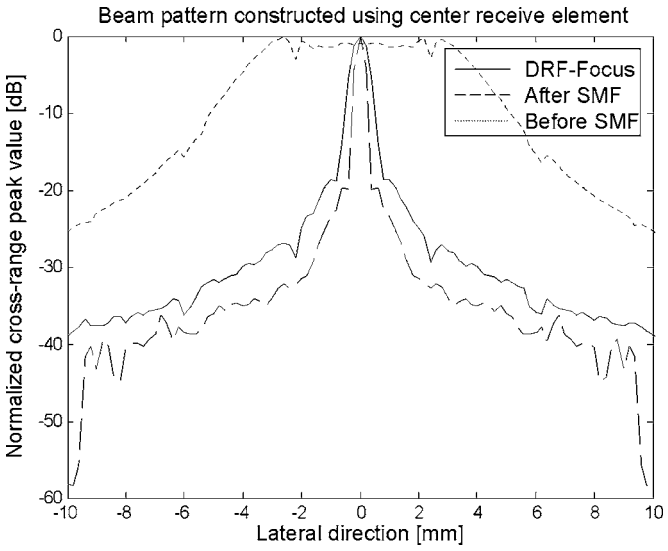

FIG. 6. Lateral beam patterns from the broadband pulse echo point spread functions in Fig. 5.

matched filter applied before or after receive-signal summation was superior to conventional DRF methods.

We tested the robustness of SMF relative to DRF in the presence of phase aberrations using Field II simulations for one specific situation. A random phase screen was placed at the aperture surface with a correlation length of 3.6 mm in-plane and aberration strength of 34 ns. These parameters are considered typical values for breast tissue.[20] Other conditions were set to be the same as those of Fig. 7. The images of Fig. 9 may be directly compared to those in the right two columns of Fig. 7 except the images of Fig. 9 were acquired through the phase screen. Targets imaged through the screen are degraded for both beam formers, more in the far field than in the near field. However, for this specific situation, aberrations do not appear to affect the SMF method any more or less than the DRF method; specifically, SMF continues to provide somewhat better CNR values at all depths.

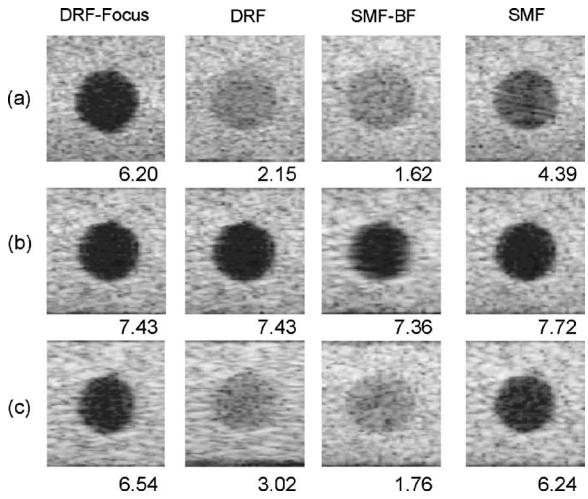

FIG. 7. The images are from echo simulations of a cyst phantom that were processed using DRF-focus (left panel), DRF (center panel), and SMF (right panel) beam formers. The transmit focus is set to 40 mm for DRF and SMF and is refocused at each depth for the DRF-focus method. The cyst diameter is 4 mm and the medium has a constant speed of sound. All images are displayed with 60 dB dynamic range. Cyst centers are placed at depths of (a) 20 mm, (b) 40 mm, and (c) 60 mm. CNR values appearing in each image are computed using $\mathrm{CNR}=|\langle S_i\rangle-\langle S_o\rangle|/\sqrt{\sigma_o^2+\sigma_i^2}$, where $\langle S_{i,o}\rangle$ and $\sigma_{i,o}^2$ are the mean and variance of image pixels inside and outside the target.

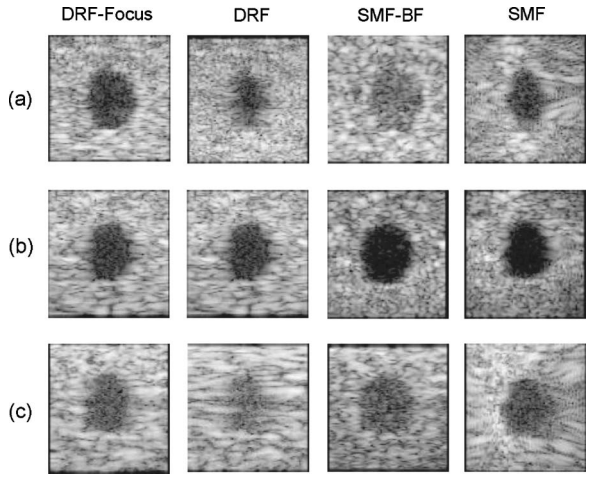

FIG. 8. The images are from pulse-echo experiments of a cyst phantom that were processed using DRF-focus (left column), DRF (center-left column), SMF-BF (center-right column), and SMF (right column) beam formers. The transmit focus is fixed at 20 mm for the DRF SMF-BF, and SMF images. However the transmit beam is repositioned at each depth for the DRF-focus method. The cyst diameter is 4 mm, and all images are logarithmically compressed and displayed with 50 dB dynamic range. Cyst centers are placed at depths of (a) 10 mm, (b) 20 mm, and (c) 30 mm.

Table I lists the relative eSNR values for each beamforming method at three depths. eSNR is defined in the scan plane (fixed y) and at a fixed depth z for random point-scattering media and white Gaussian noise as

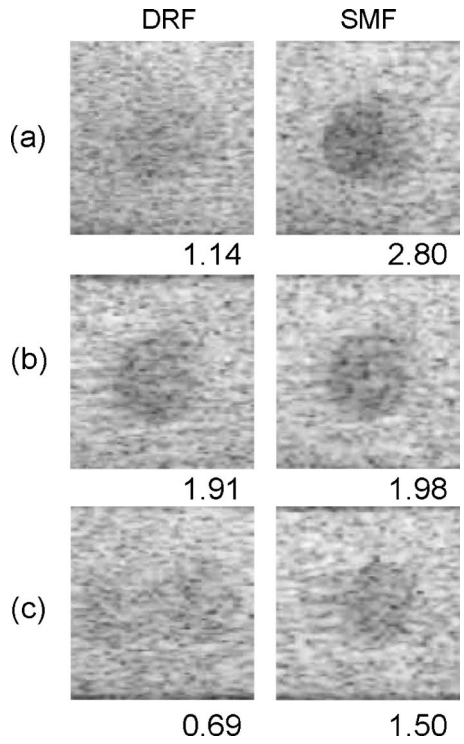

FIG. 9. The effects of phase aberration. These images are the same as those in the right two columns of Fig. 7 except that a random phase screen was placed in a plane at the aperture surface. The correlation length of the random phase distortion in the x,y plane is 3.6 mm and the aberration strength is 34 ns.

TABLE I. Echo signal-to-noise ratio values (eSNR in decibels) for each beam-forming method. The results are relative to the DRF-focus beam former at 20 mm depth.

	Focus	DRF	SMF-BF	SMF
20 mm	0	−14.43	−7.52	+7.91
40 mm	−24.30	−24.30	−15.11	−14.26
60 mm	−43.22	−52.10	−38.59	−33.03

$$\mathrm{eSNR}(y,z) = \frac{\sigma_f^2}{T\sigma_n^2}\int_0^T dt \int_{-\infty}^{\infty} dx h^2(t,x,y,z), \tag{17}$$

where σ_f^2 and σ_n^2 are the object and noise variances, T is the duration of the time series, and $h(t,x,y,z)$ is the spatiotemporal pulse-echo point spread function.[17] We fixed the depth at $z=20$ mm, computed the integrals in Eq. (17), and then selected a value for $T\sigma_n^2/\sigma_f^2$ of 0.311×10^{-7}, which gave us an in-plane $\mathrm{eSNR}(y,z)=10^4$(40 dB). Assuming $\sigma_f^2=1$, we computed σ_n^2 for these conditions and added the corresponding noise to the simulated rf echo data. Table I gives the measured eSNR values resulting from images simulated for each method. Values in the table are normalized by the value of the DRF-focus beam former at $z=20$ mm.

IV. DISCUSSION AND CONCLUSIONS

As with synthetic aperture methods, SMF effectively focuses both transmit and receive beams. The resulting pulse-echo point spread function yields superior lateral resolution compared to conventional DRF except near the transmit focal length where they are comparable. Table I clearly shows that one advantage of the SMF beam former over the DRF method is a significant increase in eSNR ratio at all depths. The improvement in eSNR results from more effective use of the signal energy by the SMF method.[8] Details of each process affect eSNR and relative side lobe energy in addition to spatial resolution, and so the merits of each technique depend on the application.

Also, in terms of implementation, another important difference between conventional delay-sum beam formers and SMF beam formers is that SMF needs shift variant 2D finite impulse response (FIR) filters instead of digital delay circuits. It is well known that current commercial ultrasound systems employ different kinds of (receive) beam-forming methods, for example, interpolation beam former, phase rotator, and partial beam former. These beam formers are implemented efficiently in terms of cost and hardware complexity in different manners by companies. Like conventional delay-sum beam formers, therefore, SMF can also be implemented in many different ways such as in time domain or frequency domain, which are being investigated by the authors.

Other implementation effects are seen by comparing the SMF-BF and SMF results for the simulation in Fig. 7 and the phantom experiment in Fig. 8. As is typically the case in commercial systems, beam properties vary as the aperture scans across the linear array. These effects are not part of the simulations, so it is accurate to assume shift invariance laterally. When impulse response functions used to filter echo data are exact, it is better to filter each receive signal before summing (column SMF in Fig. 7) than to filter echoes summed over the receive aperture (column SMF-BF in Fig. 7). However, when the impulse responses are only known approximately, then it is better to filter echoes after summation (column SMF-BF in Fig. 8) than before summation (column SMF in Fig. 8). Summing before filtering concentrates the acoustic energy so that filter errors are less important. The alternative is to extend the filter bank to form match filters that vary with lateral position as well as axial position, thus increasing the computational load.

We summarize for comparison of beam-forming methods several important imaging features in Table II. Features include the beam width parameter λz_F/aperture length, maximum side lobe height, and eSNR. For the DRF-focus and SMF methods, there are $N'=2N+1$ elements that make up the active aperture of the 1D array. We compare these results to those for a synthetic aperture focusing (SAF) method,[5] where the single element used to transmit and receive wave forms is scanned sequentially along the x_0 axis for the N'-elements aperture. We also include results for a multielement synthetic phased array (M-SPA) method,[5] where a single element is used to transmit while all N' elements are used on receive. Note that eSNR for the SA and M-SPA methods can vary widely depending on the use of defocusing and coded pulse excitation techniques.[5,21]

Compared to the DRF-focus standard method, the M-SPA and SMF [before summing, Eq. (12)] methods provide equivalent beam properties but over the entire depth of field and with greater eSNR. Lateral resolution is improved with SAF and SMF-BF [after summing, Eq. (14)] but at the

TABLE II. Performance comparisons for various beam-forming methods.

Methods		Lateral beam width	Main lobe width ($\times\lambda z_F$)	Max side lobe height (dB)	eSNR (dB)
DRF	DRF-focus	$\frac{\sin^2(kdN'x/2z)}{\sin^2(kdx/2z)}$	$\frac{1}{N'd}$	−26	0
SA	SAF	$\frac{\sin(kdN'x/z)}{\sin(kdx/z)}$	$\frac{1}{2N'd}$	−13	-
	M-SPA	$\frac{\sin^2(kdN'x/2z)}{\sin^2(kdx/2z)}$	$\frac{1}{N'd}$	−26	-
	SMF-BF	$\frac{\sin(kdN'x/z)}{\sin(kdx/z)}$	$\frac{1}{2N'd}$	−13	13.35
	SMF	$\frac{\sin^2(kdN'x/2z)}{\sin^2(kdx/2z)}$	$\frac{1}{N'd}$	−26	20.63

cost of higher amplitude side lobes and relatively lower eSNR. The best choice of method depends on the application. For example, to view small, high contrast targets such as calcified plaques or microcalcifications, high lateral resolution methods are desired for spatial-resolution-limited conditions. Conversely, to differentiate cystic voids from hypoechoic tumors, low side lobes and high eSNR are desired for these contrast-resolution-limited conditions. SMF methods have an advantage over SA techniques in that the data are acquired in parallel, thus minimizing motion artifacts.

Finally we point out that Table II results are for SMF methods that assume a rectangular aperture without apodization. For shift-varying point spread functions the single match filter is replaced by a filter bank to account for depth dependence and minimize side lobes from mismatched filters. To minimize the number of filters in the bank or to reduce aberrating effects, one might be tempted to minimize side lobes by apodization. However, Eqs. (12) and (14) show that apodization will also significantly reduce lateral resolution because the beam profile is given by the aperture function raised to a power.

Above all, to maximize the performance of SMF beamformers, we should be able to estimate system transmit-receive spatial impulse response in different media to form filters. There are various factors affecting filter design such as wave-front distortions (amplitude and phase), frequency dependent attenuation, and nonlinear propagation. These characteristics have been widely studied in the context of beamforming. The performance of SMF beamformers will improve as our ability to adaptively form beams advances.

ACKNOWLEDGMENT

This project was supported in part by the National Institutes of Health, R01 CA082497.

[1]A. Macovski, *Medical Imaging Systems* (Prentice-Hall, Englewood Cliffs, NJ, 1983).
[2]B. A. J. Angelsen, *Ultrasonic Imaging: Waves, Signals, and Signal Processing* (Emantec AS, Trondheim, Norway, 2000).
[3]C. B. Burckhardt, P-A. Grandchamp, and H. Hoffmann, "An experimental 2 MHz synthetic aperture sonar system intended for medical use," IEEE Trans. Sonics Ultrason. **SU–21**, 1–6 (1974).
[4]B. D. Steinberg, *Principles of Aperture and Array System Design: Including Random and Adaptive Arrays* (Wiley, NY, 1976).
[5]M. Karaman, P-C. Li, and M. O'Donnell, "Synthetic aperture imaging for small scale systems," IEEE Trans. Ultrason. Ferroelectr. Freq. Control **42**, 429–442 (1995).
[6]G. E. Trahey and L. F. Nock, "Synthetic receive aperture imaging with phase correction for motion and for tissue inhomogeneities. Part I: Basic principles," IEEE Trans. Ultrason. Ferroelectr. Freq. Control **39**, 489–495 (1992).
[7]Y. M. Kadah, A. E.-M. El-Sharkawy, and A-B. M. Youssef, "Navigator echo motion artifact suppression in synthetic aperture ultrasound imaging," IEEE Trans. Biomed. Eng. **52**, 127–131 (2005).
[8]R. J. Zemp and M. F. Insana, "Nearfield coding and spatial processing for ultrasonic imaging," Proc.-IEEE Ultrason. Symp. 1258–1261 (2004).
[9]R. J. Zemp, M. D. Parry, C. K. Abbey, and M. F. Insana, "Detection performance theory for ultrasound imaging systems," IEEE Trans. Med. Imaging **24**, 300–310 (2005).
[10]Fredrik Lingvall, Tomas Olofsson, and Tadeusz Stepinski, "Synthetic aperture imaging using sources with finite aperture: Deconvolution of the spatial impulse response," J. Acoust. Soc. Am. **114**, 225–234 (2003).
[11]M. Tanter, J.-F. Aubry, J. Gerber, J.-L. Thomas, and M. Fink, "Optimal focusing by spatio-temporal inverse filter. I. Basic principles," J. Acoust. Soc. Am. **110**, 37–47 (2001).
[12]J. A. Jensen and P. Gori, "Spatial filters for focusing ultrasound images," Proc.-IEEE Ultrason. Symp. 1507–1511 (2001).
[13]M. L. Li and P. C. Li, "Filter based synthetic transmit and receive focusing," Ultrason. Imaging **23**, 73–89 (2001).
[14]J. W. Goodman, *Introduction to Fourier Optics*, 2nd ed. (McGraw-Hill, NY, 1996).
[15]Cross-range spatial resolutions are labeled in rectangular coordinates as lateral (x_0) and elevational (y_0).
[16]A. D. Pierce, *Acoustics: An Introduction to Its Physical Principles and Applications* (McGraw-Hill, NY, 1981).
[17]R. J. Zemp, C. K. Abbey, and M. F. Insana, "Linear system models for ultrasonic imaging: Application to signal statistics," IEEE Trans. Ultrason. Ferroelectr. Freq. Control **50**, 642–654 (2003).
[18]J. Liu, K-S. Kim, and M. F. Insana, "Beamforming using spatio-temporal filtering," Proc.-IEEE Ultrason. Symp. (2005).
[19]J. A. Jensen and N. B. Svendsen, "Calculation of pressure fields from arbitrarily shaped, apodized, and excited ultrasound transducers," IEEE Trans. Ultrason. Ferroelectr. Freq. Control **39**, 262–267 (1992).
[20]J. J. Dahl, D. A. Guenther, and G. E. Trahey, "Adaptive imaging and spatial compounding in the presence of aberration," IEEE Trans. Ultrason. Ferroelectr. Freq. Control **52**, 1131–1144 (2005).
[21]K. L. Gammelmark and J. A. Jensen, "Multielement synthetic transmit aperture imaging using temporal encoding," IEEE Trans. Med. Imaging **22**, 552–563 (2003).

Adaptive sparse representations of ultrasonic signals for acoustic microimaging

Guang-Ming Zhang and David M. Harvey
General Engineering Research Institute, Liverpool John Moores University, Byrom Street, Liverpool, L3 3AF, United Kingdom

Derek R. Braden
Delphi Electronics & Safety, Kirkby, Liverpool, L33 7XL, United Kingdom

(Received 6 March 2006; revised 26 May 2006; accepted 26 May 2006)

Acoustic microimaging (AMI) is a common nondestructive tool for failure analysis of microelectronic packages. Accurate estimation of the reflected ultrasonic echoes is essential for detection and location of defects inside the microelectronic packages. In this paper, an advanced AMI technique based on adaptive sparse representations is proposed to estimate the ultrasonic echoes and recover the reflectivity function. An adapted overcomplete dictionary capable of concise expression of ultrasonic signals is first learned by the focal underdetermined system solver-based column normalized dictionary learning algorithm. The ultrasonic A-scans generated by an AMI system are then decomposed into adaptive sparse representations over the learned dictionary using a sparse basis selection algorithm. Echo selection and echo estimation are further performed from the resulting adaptive sparse representations. The proposed technique offers a solution to the blind source separation problem for restoration of the reflectivity function and can separate closely spaced overlapping echoes beyond the resolution of the AMI system. Experimental verifications are carried out using both synthetic and measured data. The results show the proposed technique produces high resolution and accurate estimates for ultrasonic echoes. © *2006 Acoustical Society of America.*
[DOI: 10.1121/1.2215407]

PACS number(s): 43.60.Hj, 43.60.Lq, 43.60.Np [EJS] Pages: 862–869

I. INTRODUCTION

As advanced microelectronic packages such as BGA, Flip-Chip, and 3D packages are continually being shrunk, location and detection of internal features and defects in the package have approached and are even beyond the resolution limits of conventional acoustic microimaging (AMI) methods. Novel techniques to solve this problem are required.

AMI signals recorded from microelectronic packages are a class of special signals comprised of a few echoes reflected from limited interfaces/defects. Generally, an AMI signal can be assumed to have a very sparse representation in a proper signal dictionary. Ultrasonic echo separation and echo estimation can be accomplished from the sparse signal representation of the AMI signal, even when the reflected echoes are overlapped in the time and/or frequency domains, thus resulting in a super-resolution.[1–3] Recently inferring sparse signal representations in overcomplete dictionaries has become a hot research area because overcomplete representations are more flexible in terms of how the signal is represented.[4–7]

Several advanced AMI techniques have been proposed in our recent research,[1–3] including acoustic time-frequency domain imaging (TFAMI),[3] sparse signal representation based AMI (SSRAMI),[1] and learning overcomplete representation based AMI (LORAMI).[2] These methods improved the axial resolution and robustness of traditional AMI systems by employing acoustical time-frequency domain imaging with sparse representations of ultrasonic signals. The performance of LORAMI was further improved by using a learned dictionary instead of the nonadapted dictionary as used in SSRAMI because the basis vectors in the learned dictionary matched the ultrasonic echoes better than those from the nonadapted dictionary.[7] However, several issues were raised for LORAMI. Firstly, the higher overcomplete dictionary did not show greater performance than the less overcomplete dictionary. For example, the 3×-overcomplete and 4×-overcomplete dictionaries were poorer than the 2×-overcomplete dictionary although they all were better than the complete dictionary. Secondly, the amplitudes of recovered echoes from the adaptive sparse representations were far lower than their original amplitudes. These issues are addressed in this paper, and a new LORAMI technique is proposed and investigated.

II. ADAPTIVE SPARSE REPRESENTATIONS OF ULTRASONIC SIGNALS

A. Basic theory

According to Refs. 2 and 3, the received ultrasonic radio-frequency A-scan y from microelectronic package inspection by an AMI system can be modeled as

$$y(t) = \sum_{i=1}^{M} c_i x_i(t) + \xi(t), \tag{1}$$

where $x_i(t)$ is the "quasi" ultrasonic incident pulse impinged to the ith interface, and c_i is the reflection coefficient at the interface. Giving the observed A-scan y, the problem of ultrasonic signal representation is then formulated as the prob-

lem of *blind source separation* that infers both c_i and x_i.

The sparse representation of an ultrasonic signal is that of representing the observed ultrasonic A-scan $y \in R^N$ using a small number of nonzero components in the reflectivity function $c \in R^L$ under the linear model

$$y = \Phi c + \xi, \tag{2}$$

where the dictionary Φ is a matrix of size $N \times L$, whose columns are the overcomplete basis vectors $\{\phi_i\}_{i=1}^L$, and $L > N$. Each basis vector ϕ_i represents the activity of a possible ultrasonic incident pulse. The additive noise ξ is assumed to be Gaussian, $p_\xi = N(0, \sigma^2 I)$, where I is an identity matrix. Assume also that the prior distribution of the reflectivity function c is a generalized exponential of the form,

$$p(c) \sim \exp\left(-\sum_{i=1}^{L} |c_i|^p\right), \tag{3}$$

where $p \in (0, 1]$. Such a prior has been shown to encourage sparsity in many situations because of the heavy tails and sharp peak at zero. When $p \to 0$, the exponent of this prior approaches an l_0 norm, i.e., a count of the number of nonzero elements in c. Given this prior, *maximum a posteriori* solution to Eq. (2) is formulated as

$$\begin{aligned} \hat{c} &= \arg\max_c [\log p(y|\Phi, c) + \log p(c)] \\ &= \arg\min_c \|y - \Phi c\|^2 + \lambda \sum_{i=1}^{L} |c_i|^p, \end{aligned} \tag{4}$$

where we have assumed a Gaussian likelihood model, and λ represents a trade-off parameter balancing sparsity with quality of fit.[1,6]

To obtain the adaptive sparse representations of ultrasonic signals, it is required to learn the dictionary Φ from an adequate and representative set of training data for a practical application. Our earlier work[2] showed that the learned basis vectors can represent the activities of incident pulses x_i in Eq. (1) much closer than the existing model, and then the reflection coefficients c_i can be inferred more accurately.

Several algorithms have been developed to learn the overcomplete dictionary, including overcomplete Independent Component Analysis (overcomplete ICA)[7] and FOCal Underdetermined System Solver-based Column Normalized Dictionary Learning algorithm (FOCUSS-CNDL).[6]

B. Overcomplete independent component analysis

The overcomplete ICA dictionary learning algorithm contains two major parts, inferring the sources and learning dictionary.[7] By assuming a Laplacian prior on c and that c_i are mutually independent, the sources c are estimated using a modified conjugate gradient optimization of a cost function closely related to Eq. (4) that uses the l_1 norm. The dictionary Φ is updated by gradient ascent on the likelihood using a Gaussian approximation. So, each iteration consists of the computation of $\hat{c}$, followed by a dictionary update.

C. Focal underdetermined system solver-based column normalized dictionary learning

Similarly to the overcomplete ICA, each iteration of the FOCUSS-CNDL algorithm also includes two major steps: a sparse basis selection step and a dictionary learning step. The sparse basis selection is done by FOCUSS,[8] and the dictionary learning Φ-update step uses gradient descent. The algorithm is summarized as follows. Giving a set of training data $Y = (y_1, \ldots, y_K)$, for each vector y_k the corresponding sparse source vector c_k is updated using one iteration of the FOCUSS algorithm:

$$\hat{c}_k = \Pi^{-1}(\hat{c}_k)\hat{\Phi}^T(\lambda_k I + \hat{\Phi}\Pi^{-1}(\hat{c}_k)\hat{\Phi}^T)^{-1} y_k, \tag{5}$$

where $\Pi^{-1}(\hat{c}_k) = \mathrm{diag}(|\hat{c}_k[i]|^{2-p})$ and $\lambda_k = \beta(\hat{c}_k)$ is the regulation parameter. After updating the K source vectors c_k, $k = 1, \ldots, K$, the dictionary $\hat{\Phi}$ is reestimated by

$$\hat{\Phi} = \hat{\Phi} - \gamma(\delta\hat{\Phi} - \mathrm{tr}(\hat{\Phi}^T \delta\hat{\Phi})\hat{\Phi}), \tag{6}$$

where $\delta\hat{\Phi} = \hat{\Phi}\Sigma_{\hat{c}\hat{c}} - \Sigma_{y\hat{c}}$, $\Sigma_{\hat{c}\hat{c}} = \frac{1}{K}\sum_{k=1}^K \hat{c}_k \hat{c}_k^T$, $\Sigma_{y\hat{c}} = \frac{1}{K}\sum_{k=1}^K y_k \hat{c}_k^T$, and $\gamma > 0$ is the learning rate parameter. After each update of the dictionary $\hat{\Phi}$, each basis vector ϕ_i is renormalized to $\phi_i = \phi_i / (\sqrt{L}\|\phi_i\|)$. Notice that unlike overcomplete ICA that assumes $p = 1$ in Eq. (3), in this FOCUSS-CNDL algorithm p can be set to any value within the interval $(0, 1]$, i.e., $0 < p \leqslant 1$.

III. THE PROPOSED LORAMI TECHNIQUE

A novel acoustic microimaging method called LORAMI was proposed in our earlier work.[2] The LORAMI method consisted of four major steps: *dictionary learning*, *dictionary preprocessing*, *echo separation*, and *echo selection and image generation*. It was based on the adaptive sparse representations of ultrasonic signals. The overcomplete dictionary was learned by the overcomplete ICA dictionary learning algorithm. However, the coefficient distribution of an ultrasonic A-scan acquired from a flip-chip package is much sparser than that of the Laplacian [i.e., $p = 1$ in Eq. (3)] assumed by the overcomplete ICA algorithm. Because of the flexibility in setting the sparse prior, FOCUSS-CNDL is a good alternative to overcomplete ICA, so a new LORAMI technique is proposed to improve the LORAMI performance in this paper.

The proposed technique is a modified form of the old LORAMI method, where the adapted dictionary is first learned by FOCUSS-CNDL, instead of by overcomplete ICA. Once a dictionary has been learned, the second step, *dictionary preprocessing*, is performed as follows: (1) each basis vector in the dictionary is normalized with $\|\phi_i\| = 1$; (2) we go through the dictionary to calculate the Heisenberg cell of each basis vector, i.e., its centers and widths in the time and frequency domains. The third step, *echo separation*, is carried out by inferring the adaptive sparse representations of ultrasonic A-scans using the FOCUSS algorithm. The adaptive sparse representation can be displayed in the phase plane, and each basis vector is represented by its Heisenberg cell.[9,10] The fourth step, *echo selection and image generation*, is summarized as follows:[1] First, a time-frequency win-

dow is determined in terms of the frequency of transducer and the interface to be investigated in the microelectronic package. Second, in the given time-frequency window we search for the time-frequency atoms whose centers are lying in the window, and among them pick up the one with the biggest decomposed coefficient. The selected time-frequency atom and its coefficient AMI is used as the approximation of the expected incident pulse x_i and reflection coefficient c_i. Finally, reflection coefficient AMI is carried out by directly displaying these selected coefficients at their corresponding position of the C-scan image. Amplitude-polarity AMI can also be carried out by reconstructing the reflected echoes $s_i(t)$ using x_i and c_i. The peak intensity value and polarity of the reconstructed echo is displayed at the corresponding position of the C-scan image.

IV. SIMULATION STUDY

A. Simulation of ultrasonic A-scans

To evaluate the adaptive sparse representations of ultrasonic signals and test the proposed LORAMI technique, simulation data were created by the following method. Ultrasonic A-scans were produced according to the AMI signal model of Eq. (1), where the incident pulses x_i were simulated by three measured ultrasonic pulses obtained from a planar reflector in a water tank using, respectively, 230-, 50-, and 30-MHz transducers on a commercial AMI system. To reduce the signal length, each the measured pulse was downsampled by a scale 2, truncated to a length of 61 samples, and then normalized to $\|x_i\|=1$.

Each echo s_i ($s_i=c_i x_i$) in an A-scan was then generated, where the reflection coefficient that determined the amplitude of each echo was changed to simulate different reflectivity properties of the interrogated interfaces/features. Each echo was translated along the time axis to various time positions to simulate a wide diversity of interfaces at different depths. The simulated A-scan was the superposition of several echoes according to Eq. (1).

B. Dictionary learning

A training data set consisting of 43 200 simulated A-scans was generated by the following steps:

(1) Each A-scan was set to 144 samples in length, and it was assumed that two ultrasonic echoes were present in an A-scan.
(2) A random time position was set for each echo within the A-scan.
(3) Randomly pick up two from the three simulated ultrasonic pulses described in Sec. IV A. Then translate each pulse along the time axis so that its center was located in the setting position of step 2.
(4) Superpose the two translated pulses, resulting in an A-scan.
(5) Subtract the mean of the resulting A-scan and normalize it.
(6) Repeat steps 1–5 until all A-scans had been generated.

From the training data set, a number of dictionaries were learned by overcomplete ICA and FOCUSS-CNDL with different prior distributions (i.e., different p) and different degrees of overcompleteness. The dictionaries were initialized by Gaussian-modulated random vectors during the learning process.

C. Effect of the reflection coefficient prior distribution

Previous research has revealed that there are some limitations when the overcomplete ICA algorithm is applied to acoustic microimaging of microelectronic packages. One possible reason is that the Laplacian prior assumption for the reflectivity function c is inaccurate, and thus different priors could be used to improve the efficiency of adaptive sparse representations of ultrasonic signals. This experiment was carried out to investigate this effect of the prior distribution of reflection coefficients on ultrasonic echo separation and echo estimation. Echo separation and echo estimation were accomplished by the proposed LORAMI technique. An appropriate time-frequency atom (i.e., a basis vector) was selected by a given time-frequency window. The selected basis vector and its coefficient were used as the approximation of the expected incident pulse x_i and reflection coefficient c_i, respectively. From x_i and c_i, the expected ultrasonic echo was recovered directly according to Eq. (1).

Four 2×-overcomplete (288 basis vectors) dictionaries learned by the FOCUSS-CNDL algorithm with different sparse priors, $p=1$, 0.7, 0.4, 0.1, respectively, were used in the experiment. A large number of test A-scans were generated using the method described in Sec. IV A, and each A-scan contained two echoes with different reflection coefficients and different degrees of overlap in the time and frequency domain. The overlap degree in the frequency domain was adjusted by combining the simulated incident pulses (230-, 50-, and 30-MHz ultrasonic pulses) in different order. The overlap degree in the time domain was tuned by translating these pulses along the time axis. The test A-scans were decomposed into sparse representations by FOCUSS over these learned dictionaries. The time-frequency window was set to the Heisenberg cell of the first echo. The performance of ultrasonic echo separation and echo estimation was measured by the energy error, E_{err}, which was defined as

$$E_{\mathrm{err}}=\frac{\|\tilde{s}_i-s_i\|_2}{\|s_i\|_2}\times 100\,\%\,, \tag{7}$$

where s_i is the original echo and $\tilde{s}_i$ is the recovered echo.

Table I tabulates some results for recovering the first echo from the test A-scans using the proposed LORAMI technique. The experimental results show that the assumed prior distribution of reflection coefficients does affect the LORAMI performance, and the prior $p=0.4$ are slightly better than the other three priors on average. Theoretically, producing such results might be explained as follows: two errors would occur when learning Φ and inferring c with the FOCUSS-CNDL algorithm, namely, convergence error (i.e., convergence to a standard local minimum) and structure error (i.e., convergence to a minimum/possibly global that is not maximally sparse yet has a lower cost function value

TABLE I. Effect of the prior distribution of reflection coefficients.

	E_{err} (%)			
A-scan no.	$P=1$	$P=0.7$	$P=0.4$	$P=0.1$
1	47.4	59.6	61.9	60.6
2	52.6	74.0	72.3	58.7
3	51.8	46.7	47.5	55.8
4	73.3	40.0	49.8	57.5
5	41.5	66.5	42.2	66.4
6	74.5	75.7	33.7	57.0
7	64.6	63.8	35.6	11.6
8	44.3	38.4	45.5	57.6
9	48.1	37.6	30.6	55.7
Average	55.3	55.8	46.6	53.4

than the generating solution).[5] The assumed prior of c with $p=0.1$ was closer to the actual distribution of reflection coefficients, and thus we expected less structure error but were frequently trapped by local minima, resulting in large convergence error. As p became larger, the structure error went up but the convergence error descended. The final performance was controlled by the combined error.

D. Effect of the overcompleteness degrees of learned dictionaries

Research work has shown that the decomposition of a signal in an overcomplete dictionary can offer many advantages.[8,11,12] These advantages can lead to greater performance in relevant applications, for example sparse coding and acoustic micro imaging. In the previous research[2,7] a higher overcomplete dictionary, however, did not show greater performance than a less overcomplete dictionary.

This simulation was performed to examine the effect of overcompleteness degrees of learned dictionaries on the performance of the proposed LORAMI technique. The test A-scans were decomposed into sparse representations over the dictionaries learned by FOCUSS-CNDL with different overcompleteness degrees. The first echo of each test A-scan was estimated using the proposed LORAMI technique, where the time-frequency window was set to the Heisenberg cell of the first echo. The energy error in Eq. (7) was presented to evaluate the efficiency of overcomplete representations. The results for nine A-scans are listed in Table II. From the table, it is observed that overall the $3\times$-overcomplete dictionaries achieve the peak performance, and then the performance goes into a descent after that. One possible reason for such results is that in the FOCUSS-CNDL dictionary learning algorithm, the dictionary Φ, and the elements of the set c are assumed to be mutually independent. In fact, this assumption is difficult to be met for our AMI signals, particularly when two ultrasonic echoes are closely overlapped.

E. Comparison of two LORAMI techniques

1. Ultrasonic echo estimation

This experiment was carried out to compare the performance of the proposed LORAMI (referred to as LORAMI-II hereafter) with the previous one (referred to as LORAMI-I), where two performance criteria, amplitude error and normalized energy error, were used. The amplitude error, A_{err}, was defined as

$$A_{\text{err}} = \frac{(\tilde{A}_i - A_i)}{A_i} \times 100\,\%\,, \tag{8}$$

where $\tilde{A}_i$ is the peak intensity value of the recovered echo by LORAMI from a gated A-scan, and A_i is the peak intensity of the original echo. The normalized energy error, nE_{err}, which measures the waveform of the estimated echo, was defined as

$$nE_{\text{err}} = \frac{\|n\tilde{s}_i - ns_i\|_2}{\|ns_i\|_2} \times 100\,\%\,, \tag{9}$$

where ns_i is the normalized original echo ($\|ns_i\|_2=1$) and $n\tilde{s}_i$ is the normalized recovered echo ($\|n\tilde{s}_i\|_2=1$).

Two LORAMI techniques were performed on both noninterfering A-scans and overlapping A-scans. Three $2\times$-overcomplete dictionaries were used. One was learned by overcomplete ICA, and the other two were learned by FOCUSS-CNDL with the parameter $p=1$ and 0.4, respectively. The time-frequency window was set to the Heisenberg cell of the first echo. Some results are listed in Table III, from which it is observed that LORAMI-II outperforms

TABLE II. Effect of the overcompleteness degree of learned dictionaries.

	E_{err} (%)					
	$P=1$			$P=0.4$		
A-scan no.	$2\times$ Overcomp.	$3\times$ Overcomp.	$4\times$ Overcomp.	$2\times$ Overcomp.	$3\times$ Overcomp.	$4\times$ Overcomp.
1	48.2	47.7	21.2	41.8	5.3	4.7
2	49.4	52.9	38.1	46.0	38.1	52.4
3	61.1	65.1	50.7	68.6	71.4	75.7
4	50.7	78.3	74.1	64.9	71.3	56.2
5	73.3	32.4	61.9	49.8	47.3	58.3
6	41.5	72.3	41.6	42.2	64.6	62.6
7	74.5	20.8	71.5	33.7	42.5	69.9
8	39.9	35.3	57.8	59.6	40.9	45.8
9	55.5	28.2	47.9	39.9	24.3	56.4
Average	54.9	48.1	51.6	49.6	45.1	53.6

TABLE III. Performance comparison of two LORAMI techniques in terms of the amplitude error A_{err} and the normalized energy error nE_{err}.

		A_{err} (%)			nE_{err} (%)		
		LORAMI-I	LORAMI-II		LORAMI-I	LORAMI-II	
	A-scan no.		$P=1$	$P=0.4$		$P=1$	$P=0.4$
Noninterfering	1	−55.9	−3.3	−30.2	43.1	3.7	32.7
	2	−64.3	−3.9	−26.4	28.7	13.1	55.5
	3	−63.8	−17.0	−22.2	26.5	33.3	37.1
Overlapping	4	−60.7	−1.9	−10.1	87.9	4.0	16.4
	5	−68.3	−42.5	−7.6	55.7	45.1	48.4
	6	−47.5	−1.8	−1.0	33.6	4.7	7.0
	7	−66.0	−74.7	−36.1	51.9	37.3	54.0
	8	−78.8	−54.9	−51.4	44.0	43.9	57.9
	9	−75.3	−56.9	−61.9	24.4	18.7	46.8
	Average	−64.5	−28.5	−27.4	43.9	22.6	39.5

LORAMI-I significantly in terms of the amplitude error and the normalized energy error. In addition, it is worth noting that the prior $p=1$ performs better than $p=0.4$ in terms of nE_{err}. This conflicts with the above conclusion obtained in terms of E_{err}. Its explanation requires further work.

Obviously, from Table III we can also conclude that LORAMI-II is more flexible and accurate in learning the patterns of ultrasonic echoes and representing ultrasonic signals than LORAMI-I for microelectronic package characterization. This is demonstrated in Fig. 1. The test A-scan no. 4 in Table III is plotted in Fig. 1(a), where two echoes are overlapped. Figures 1(b)–1(d) display its sparse representations obtained by LORAMI-I and LORAMI-II with $p=1$ and 0.4, where the darkness of the time-frequency image increases with the energy value, and each time-frequency atom selected by LORAMI is represented by a Heisenberg box. It can be seen that although two overlapped echoes cannot be resolved in the time domain, they are clearly separated in the time-frequency domain. Figure 1(e) shows the original first echo in Fig. 1(a). The recovered corresponding echoes are plotted in Figs. 1(f)–1(h). It is clearly observed that both amplitudes and waveforms of the recovered echoes by LORAMI-II are much closer to the original echo than LORAMI-I.

2. Ultrasonic echo location

A further experiment was carried out to examine the performance of the proposed techniques on echo location, which is important for defect location and thin layer thickness measurement. In this experiment, test A-scans were created to contain only one ultrasonic echo. The location error was measured by the arrival time error and center frequency error of the recovered echo obtained from the adaptive sparse

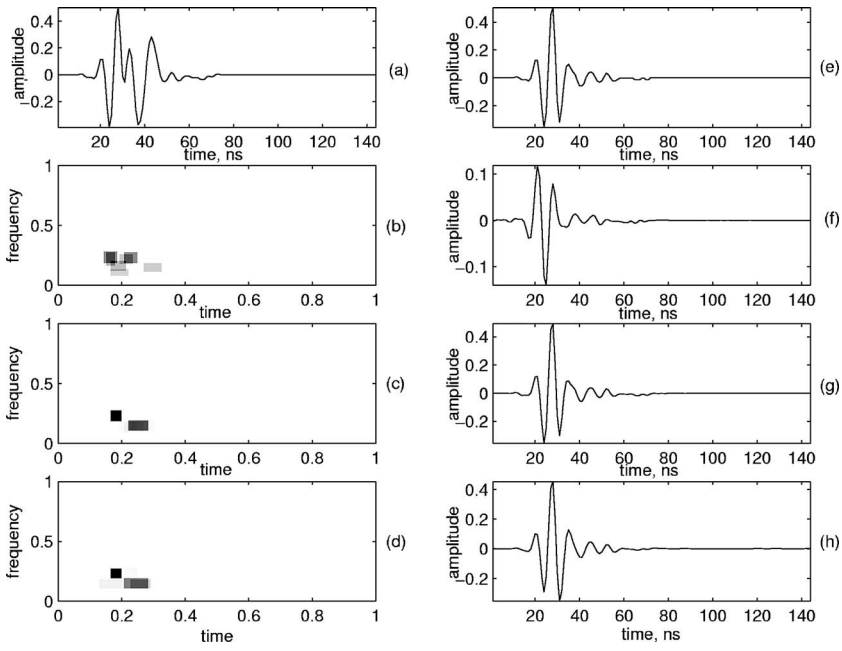

FIG. 1. Adaptive sparse representations and ultrasonic echo estimation. (a) A simulated A-scan. The adaptive sparse representations inferred (b) by LORAMI-I, (c) by LORAMI-II with $p=1$, and (d) by LORAMI-II with $p=0.4$. (e) The original echo (first echo) in (a). The recovered echo (f) by LORAMI-I, (g) by LORAMI-II with $p=1$, and (h) by LORAMI-II with $p=0.4$.

TABLE IV. Comparison of two LORAMI techniques in terms of the location error.

	Arrival time error (in sample number)			Centre frequency error (MHz)		
		LORAMI-II			LORAMI-II	
	LORAMI-I	$P=1$	$P=0.4$	LORAMI-I	$P=1$	$P=0.4$
1	−2	−2	−2	−3.47	−3.47	0
2	−1	−1	0	17.36	0	0
3	0	−1	−2	3.47	3.47	3.47
4	−4	2	−2	0	−3.47	−3.47
5	5	4	−1	−6.94	0	0
6	−1	0	−1	0	3.47	3.47
7	2	−2	−1	0	0	−3.47
8	4	0	−1	6.94	0	−3.47
9	−2	−1	−3	6.94	3.47	3.47

representations using LORAMI. Some results are listed in Table IV, from which it can be seen that LORAMI-II slightly surpasses LORAMI-I on echo location.

F. The LORAMI performance for C-scan imaging

In this subsection, an experiment was carried out to evaluate the LORAMI performance for C-scan imaging. Since the used AMI system could not provide 3D rf data, it was impossible to generate C-scan images of microelectronic packages using the LORAMI techniques. However, the performance of the LORAMI techniques can be quantitatively verified by the experiment elaborated in Ref. 2. Although that experiment was based on 1D ultrasonic A-scan signals, the AMI error criteria used in Ref. 2 can genuinely evaluate the imaging performance such as axial resolution. As a C-scan image is generated by x-y scanning, and at each x-y position the processing of the gated A-scan signal results in a pixel in the C scan, the imaging error caused by echo overlap is mainly produced in the stage of generating a pixel value from a gated A-scan. This imaging error was measured in the experiment.

The experiment in Sec. V E of Ref. 2 was repeated in this work. The proposed LORAMI-II was added to the experiment, where the learned 2×-overcomplete dictionary with $p=0.4$ was used. Its performance was measured using the same AMI error defined in Eq. (10) of Ref. 2. Results for eight A-scans are presented in Table V, where parameters $A1$ and $A2$ are the amplitudes of two echoes separately, $v2-v1$ is the frequency separation of two echoes, and $u2-u1$ is the time separation (in sample number) of two echoes. The interface for C-scan imaging was set to the first echo by choosing gates as follows: for conventional time domain AMI (TDAMI), the gate was chosen to center at $u1$, with width equal to 20 samples, which is the narrowest gate available in our commercial AMI system. The time-frequency window was set to the Heisenberg box of the first echo. The experimental results demonstrate that significant improvement in imaging performance has been achieved by LORAMI-II.

V. EXPERIMENT WITH MEASURED DATA

The proposed technique was further validated by experiments with measured data. Several circuit boards used in automotive applications and fabricated using ceramic thick film hybrid circuit technology were used as test boards. For the thick film hybrid circuitry, multiple layers (tracks, conductors, dielectric layers, etc.) were printed onto a ceramic substrate or dielectric and fired. This work focused on the quality and reliability testing of flip-chip solder joints, and ultrasonic A-scans were acquired from various flip-chip packages mounted on these boards. On each package, 16 A-scans from different positions were stored. Selected position points were the representatives of typical structures such as solder joints, with and without defects, and the nonsolder joint area. At each point we captured A-scans starting from the package top with a signal length of 512 samples using both 230- and 50-MHz transducers.

A training data set was made to consist of AMI segments. Each AMI segment was randomly extracted from the acquired A-scans, having 144 samples in length. The mean value of a segment was subtracted from it for each segment. These resulting segments were then normalized. In order that each learned basis vector only models a single echo pattern, extracting segments randomly is very important. Otherwise, the learned basis vector might be a pattern with multiple echoes inside.[2]

Two training data sets were constructed in the experiment. One is for the 50-MHz transducer, and the other one is for the 230-MHz transducer. Each training data set was comprised of 25 200 segments. For each transducer, a 2×-overcomplete dictionary with $p=0.4$ was learned using

TABLE V. The LORAMI performance for C-scan imaging.

	Parameters			AMI error (%)			
A-scan no.	A1/A2	$u2$-$u1$ (Sample no.)	$v2$-$v1$ (MHz)	LORAMI-I	LORAMI-II	Conventional TDAMI	LORAMI-II (SBL)
1	1	22	39.06	1.27	−0.97	0	−7.38
2	0.8	12	39.06	2.39	−5.41	3.23	5.03
3	0.5	12	39.06	15.99	−4.67	93.37	5.72
4	1	6	39.06	−14.76	−5.73	31.08	−9.51
5	1	31	21.48	−5.76	−5.38	0	0.24
6	1/1.5	11	21.48	−8.15	2.10	−7.10	−15.48
7	1	20	17.58	−0.48	7.61	0	−13.78
8	0.8	10	17.58	17.86	6.81	52.85	3.56

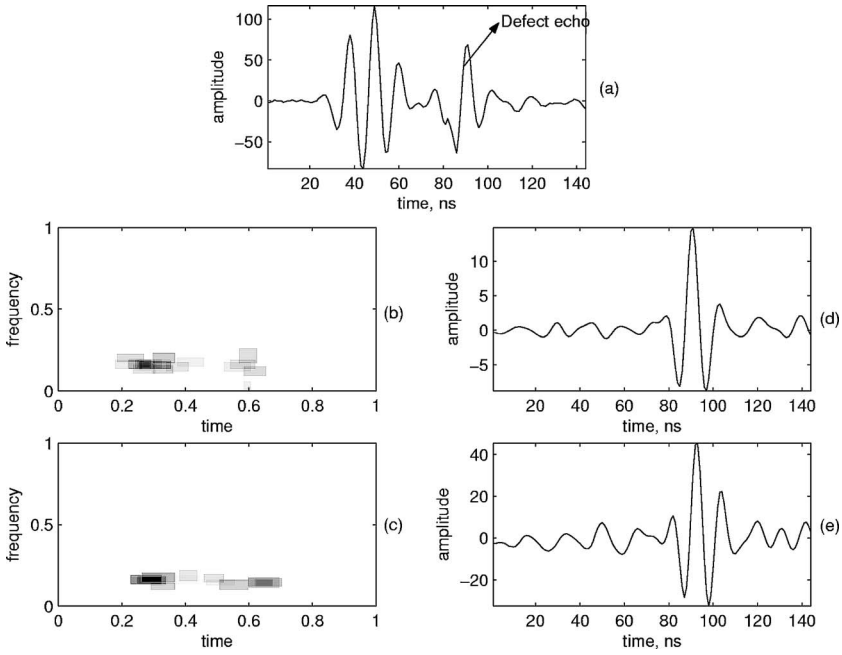

FIG. 2. (a) An A-scan acquired by the 230-MHz transducer. The adaptive sparse representation of (a) inferred (b) by LORAMI-I and (c) by LORAMI-II. The recovered defect echo (c) by LORAMI-I and (d) by LORAMI-II.

the FOCUSS-CNDL algorithm, and another 2×-overcomplete dictionary was learned using the overcomplete ICA algorithm. Both dictionaries were initialized by Gaussian-modulated random vectors during the learning process.

Figure 2(a) shows an A-scan acquired by the 230-MHz transducer from a defective solder joint, in which the first echo is from the die-solder joint interface, and the second echo is reflected from the defect. At the same point, the measured A-scan using the 50-MHz transducer is plotted in Fig. 3(a), where two echoes cannot be resolved due to the lower axial resolution of the 50-MHz transducer. Figures 2(b) and 2(c) display the adaptive sparse representations of the A-scan in Fig. 2(a) obtained by LORAMI-I and LORAMI-II, respectively. The defect echoes recovered from the sparse representations are displayed in Figs. 2(d) and 2(e). Similarly, the processing results of Fig. 3(a) are displayed in Figs. 3(b)–3(e). Comparing Figs. 2 and 3, it is observed that both LORAMI techniques resolve the overlapped echoes, even in the low resolution 50-MHz A-scan. It is also seen that the amplitude error is largely reduced by LORAMI-II.

VI. DISCUSSION

Although the experimental results have demonstrated the advantages of the proposed technique, how to choose the optimal prior parameter p from the measured data for a certain application is a challenge.

Recently the sparse Bayesian learning (SBL)[13] algorithm has been adapted to the problem of finding sparse signal representations from an overcomplete dictionary. In contrast to FOCUSS and overcomplete ICA, which assume a fixed prior, SBL estimates a parametrized Gaussian prior,

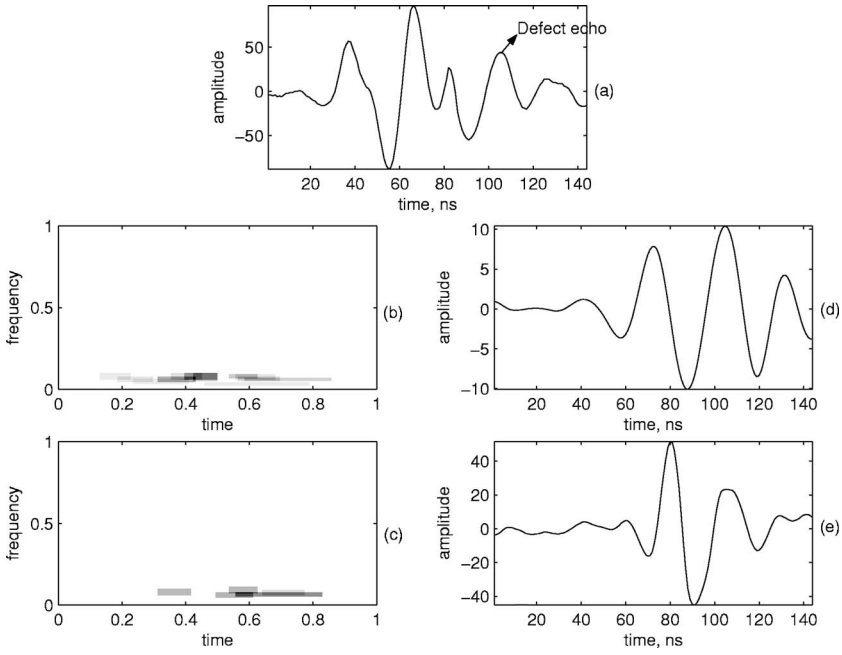

FIG. 3. (a) An A-scan acquired by the 50-MHz transducer from the same sample and same x-y position as Fig. 2. The adaptive sparse representation of (a) inferred (b) by LORAMI-I and (c) by LORAMI-II. The recovered defect echo (c) by LORAMI-I and (d) by LORAMI-II.

$$p(c) = p(c|\alpha) = \prod_{i=0}^{L} N(c_i|0, \alpha_i^{-1}), \tag{10}$$

where α is a vector of L hyperparameters controlling the prior variance of each element c_i. These hyperparameters are estimated from the observed data by marginalizing over the coefficients c_i and then performing maximum likelihood optimization.[5]

Moreover, it is worth noting that once a dictionary has been learned for a specific application, a different sparse basis selection algorithm can be used to infer the reflectivity function c. As it estimates a parametrized prior of the reflection coefficients c from the decomposed A-scan, SBL could be a good alternative to FOCUSS to avoid the selection of prior parameter p in some applications.

Some experimental results using SBL instead of FOCUSS in the proposed LORAMI-II technique are presented in the last column of Table V. It can be seen that good imaging performance is achieved by SBL although it is not as good as the FOCUSS in this experiment. Further research will be performed in the future.

In addition, in the numerical simulation described in Sec. IV, the trade-off parameter λ in Eq. (4) was determined by trial and error for each LORAMI technique, separately. In order to have most accurate performance comparison, the trade-off parameter and other parameters used in the two LORAMI algorithms were kept fixed throughout these comparison experiments.

VII. CONCLUSION

In this paper, a new LORAMI technique has been presented in which dictionary learning is accomplished by FOCUSS-CNDL and sparse representations are inferred by the FOCUSS basis selection algorithm. The adaptive sparse representations of AMI signals were significantly improved by the proposed technique. The efficiency of ultrasonic signal representations led to the further improvement of LORAMI performance for ultrasonic echo separation, echo estimation, echo location, and C-scan imaging. Several issues raised in the previous LORAMI technique have been addressed and partly solved in this paper.

ACKNOWLEDGMENT

This work has been supported by The Engineering and Physical Sciences Research Council (EPSRC) of UK.

[1]G.-M. Zhang, D. M. Harvey, and D. R. Braden, "Advanced acoustic micro imaging using sparse signal representation for the evaluation of microelectronic packages," IEEE Trans. Adv. Packag. **29**(2), 271–283 (2006).
[2]G.-M. Zhang, D. M. Harvey, and D. R. Braden, "An improved acoustic microimaging technique with learning overcomplete representation," J. Acoust. Soc. Am. **118**, 3706–3720 (2005).
[3]G.-M. Zhang, D. M. Harvey, and D. R. Braden, "Resolution improvement of acoustic micro imaging by continuous wavelet transform for semiconductor inspection," Microelectron. Reliab. **46**(5-6), 811–821 (2006).
[4]M. Davies, "Simple mixture model for sparse overcomplete ICA," IEE Proc. Vision Image Signal Process. **15**(1), 35–43 (2004).
[5]D. P. Wipf and B. D. Rao, "Sparse Bayesian learning for basis selection," IEEE Trans. Signal Process. **52**(8), 2153–2164 (2004).
[6]K. Kreurz-Delgado, J. F. Murray, and B. D. Rao, "Dictionary learning algorithms for sparse representation," Neural Comput. **15**, 349–396 (2003).
[7]M. S. Lewicki and T. J. Sejnowski, "Learning overcomplete representations," Neural Comput. **12**, 337–365 (2000).
[8]B. D. Rao and K. Kreurz-Delgado, "An affine scaling methodology for best basis selection," IEEE Trans. Signal Process. **47**(1), 187–200 (1999).
[9]I. Daubechies, "The wavelet transform, time-frequency localization and signal analysis," IEEE Trans. Inf. Theory **36**(5), 961–1005 (1990).
[10]S. G. Mallat and Z. Zhang, "Matching pursuit with time-frequency dictionaries," IEEE Trans. Signal Process. **41**(12), 3397–3415 (1993).
[11]M. S. Lewicki and B. A. Olshausen, "Probabilistic framework for the adaptation and comparison of image codes," J. Opt. Soc. Am. A **16**(7), 1587–1601 (1999).
[12]B. A. Olshausen and D. J. Field, "Emergence of simple-cell receptive field properties by learning a sparse code for natural images," Nature (London) **381**, 607–609 (1996).
[13]M. E. Tipping, "Sparse Bayesian Learning and the Relevance Vector Machine," J. Mach. Learn. Res. **1**, 211–244 (2001).

Source localization in the presence of gross sediment uncertainties

Ralph N. Baer and Michael D. Collins
Naval Research Laboratory, Washington, DC 20375

(Received 31 January 2006; revised 16 May 2006; accepted 17 May 2006)

The possibility of determining the location of an acoustic source in the presence of gross sediment uncertainties is investigated. Promising results are obtained using focalization, which involves constructing ambiguity surfaces corresponding to randomly selected realizations of the sediment parameters. Due to a parameter hierarchy in which the source location is more important than environmental parameters, it is often possible to reliably determine the source position without determining the correct sediment parameters. The examples involve multiple sediment layers, with sound speeds and range-dependent thicknesses that are unknown. An example that includes both sediment uncertainties and internal waves is also included.
[DOI: 10.1121/1.2213523]

PACS number(s): 43.60.Kx, 43.30.Wi [AIT] Pages: 870–874

I. INTRODUCTION

Matched-field processing is a generalization of beamforming for determining the location of an acoustic source in the ocean.[1–3] Data are compared with plane waves in order to estimate the bearing of a source in beamforming. Data are compared with solutions of the wave equation in matched-field processing, which is a much harder problem since the coefficients of the wave equation (sound speed, bathymetry, etc.) are required as inputs. Matched-field processing can fail when there are relatively small uncertainties in these parameters,[4–7] which are exceedingly difficult to obtain in many ocean environments.

By exploiting a parameter hierarchy, it is often possible to localize a source with limited knowledge of the environmental parameters.[8] The combined inverse problem for the source and the environment tends to have a highly nonunique solution. The solution of the wave equation tends to be much more sensitive to source location than to environmental parameters, and it is often possible to determine the source location without determining the true environmental parameters. Focalization is the process of adjusting the environmental parameters until the source location comes into focus.[8]

Perhaps the most dreaded types of environmental uncertainty are those that are associated with sound speed fluctuations due to internal waves and heterogeneity in the sediment. It is usually impractical to eliminate these uncertainties even in the smallest regions of interest in applications of matched-field processing. Both types of uncertainty are highly complex, internal waves vary with time, and the sediment is much harder to access than the water column. Focalization has recently been applied to localize a source in the presence of internal waves.[9] It was found that internal waves ultimately become a serious limiting factor for distant sources but that localization can be improved by including internal waves in the parameter space. In this paper, we show that focalization can also be effective in the presence of gross sediment uncertainties. We also consider a problem involving both sediment uncertainties and internal waves.

II. SEDIMENT UNCERTAINTIES

Matched-field processing is very effective under ideal conditions: the data is of high quality, the ocean waveguide supports a sufficient number of modes, the array of hydrophones has sufficient aperture, the signal-to-noise ratio is high, and the environmental parameters are known precisely. The first three requirements can be met by using appropriate experimental techniques and considering appropriate frequencies. It is much harder to meet the other requirements. Low signal-to-noise ratio can be handled by including an estimate of the covariance of the noise in the processing.[10] In this paper, we are concerned with the issue of uncertain sediment parameters. Since small amounts of uncertainty can cause matched-field processing to fail and there are usually gross uncertainties in the sediment, it was not obvious that focalization would work for this problem before we actually tried it.

We consider a sediment model that consists of homogeneous layers of variable thickness. The uncertain parameters are the thicknesses of the layers as a function of range and the sound speeds in the layers. We fix the densities and attenuations at constant values since these parameters tend to be less important than sound speed. We ignore sound speed gradients within layers for the same reason. The complexity of the model could be increased, but this simple model includes gross uncertainties and should suffice to illustrate the main idea.

We apply the approach used in Ref. 9 to solve the focalization problem. This involves randomly selecting realizations of the environment, constructing ambiguity surfaces by the method of phase conjugation and back propagation, and constructing histograms of the locations of the main peaks in the ambiguity surfaces. For any given realization of the environment, the main peak may occur at a spurious location.

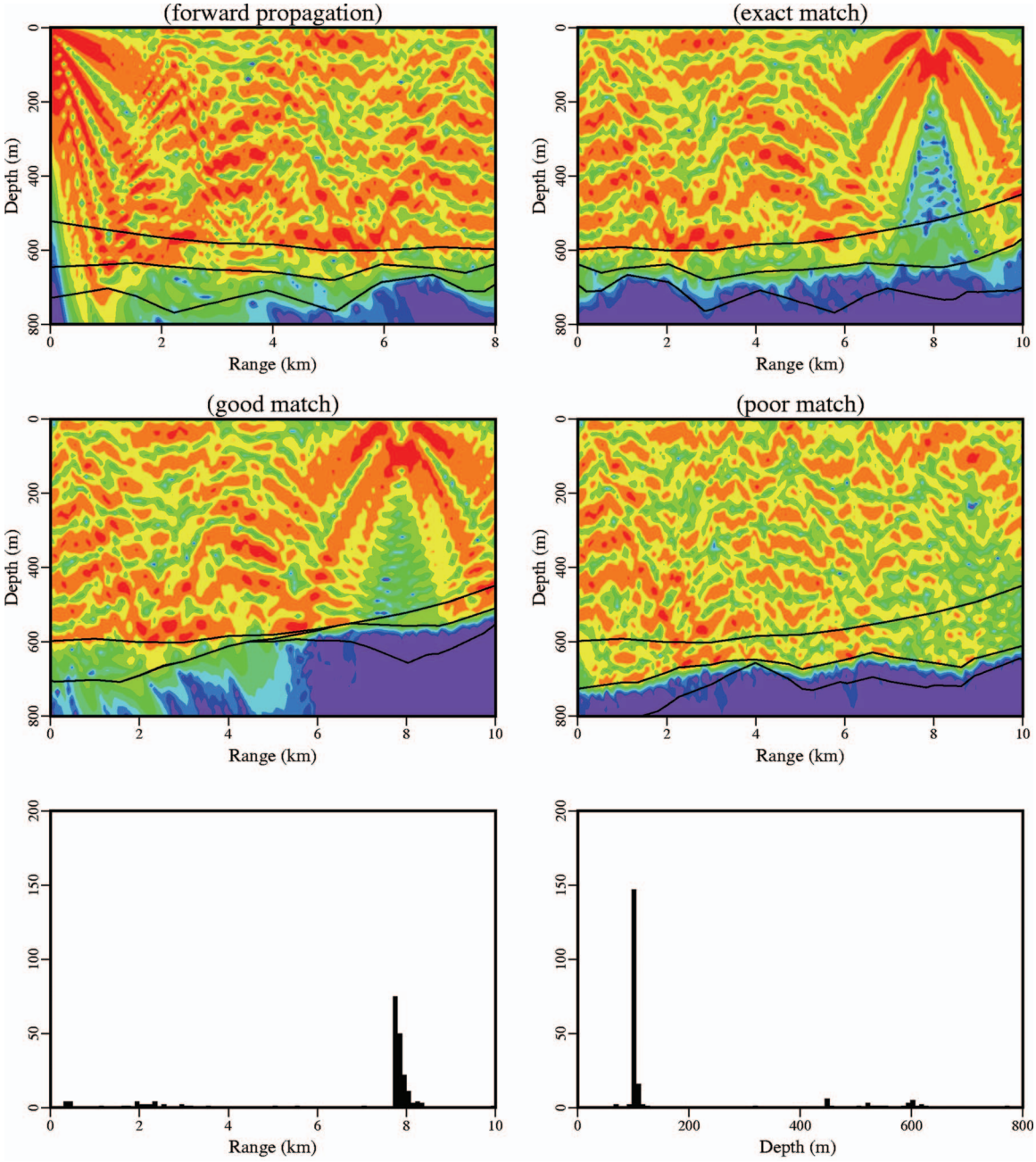

FIG. 1. Results for example A, which involves a 50-Hz source located 8 km from the array and 102 m below the surface. The forward propagation from the source exhibits significant interaction with the sediment layers. The ambiguity surface corresponding to the exact environment contains a strong peak at the source location. Random realizations of the sediment provide good matches in some cases and poor matches in other cases. As the histograms indicate, the good matches outnumber the poor matches for this case. Some of the peaks in the histogram occur far from the source.

Focalization provides a reliable estimate of the source location when the main peak occurs near the source location more frequently than at any other location.

We use the same sediment parameters for each of the examples. In the top layer, the sound speed is 1600 m/s, the density is 1.2 g/cm^3, and the attenuation is 0.1 dB/λ. In the middle layer, the sound speed is 1850 m/s, the density is 1.4 g/cm^3, and the attenuation is 0.2 dB/λ. In the half space, the sound speed is 2000 m/s, the density is 1.7 g/cm^3, and the attenuation is 0.4 dB/λ. During focalization, we construct realizations of the sediment by selecting sound speeds from uniform distributions. Values are selected between 1395 and 2325 m/s in the top layer, 1495 and 2425 m/s in the middle layer, and 1595 and 2525 m/s in the half space. Realizations of the layer thicknesses are selected as functions of range with the requirement that 200 m is the maximum thickness and that 2.86 deg is the maximum slope. Values for the thicknesses are selected uniformly between −40 and 200 m, with negative values truncated to zero in order to allow a finite probability that a layer tapers to zero thickness. The interfaces between layers are piece-wise linear, with the horizontal distances between nodes selected randomly between upper and lower bounds (which are given for each example). In the water column, we use the canonical profile[11] that was used in Ref. 9 for each of the examples. We work in

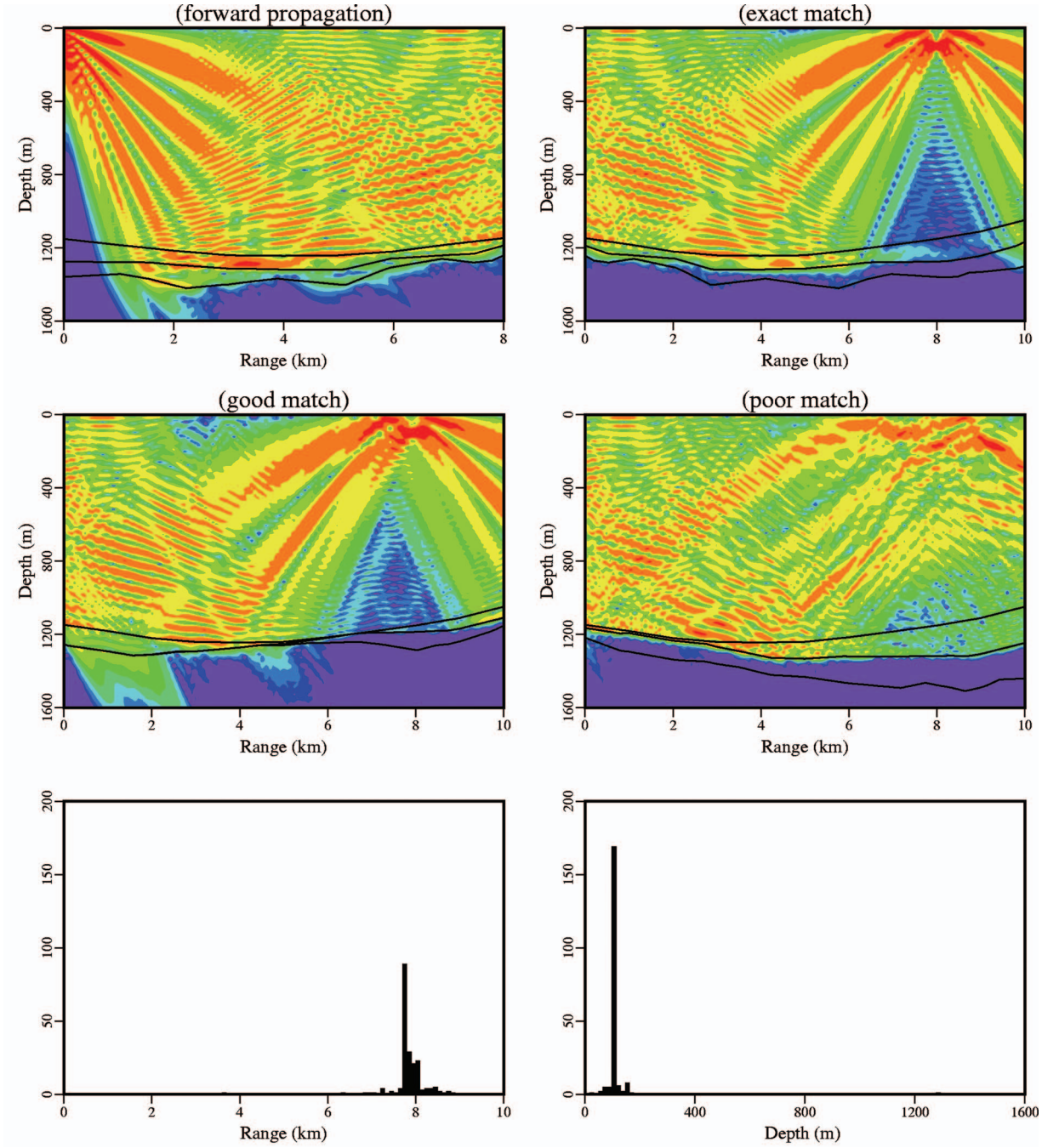

FIG. 2. Results for example B, which involves deeper water than example A. There is less bottom interaction than in example A, and focalization performs slightly better. There are no peaks in the histograms located far from the source location.

cylindrical coordinates, where the range r is the horizontal distance from a vertical array of hydrophones and z is the depth below the ocean surface.

For example A, there is a 50-Hz source at $r=8$ km and $z=104$ m in an environment in which the bathymetry varies between approximately 450 and 600 m. The spacings between the nodes for the interfaces are chosen between 100 and 2000 m for this case. Results for example A appear in Fig. 1. The plot of the forward propagating field illustrates that there is significant interaction with the sediment layers. In the ambiguity surface corresponding to the true environment, a strong peak appears at the source location. Also appearing in Fig. 1 are two of the ambiguity surfaces that were generated from 200 realizations of the sediment. There is a strong peak at the source location in one of these surfaces but not in the other. The histograms appearing in Fig. 1 indicate that the source location is reliably obtained, but there are some small peaks far from the source location.

Example B is similar to example A, with the exception that the bathymetry varies between approximately 1050 and 1235 m/s. Results for example B appear in Fig. 2. For this case, there is less interaction with the bottom. In contrast to example A, there is no evidence in the histograms of peaks far from the source location, but some of the ambiguity surfaces (such as the one shown in Fig. 2) do not have a dominant peak near the source location.

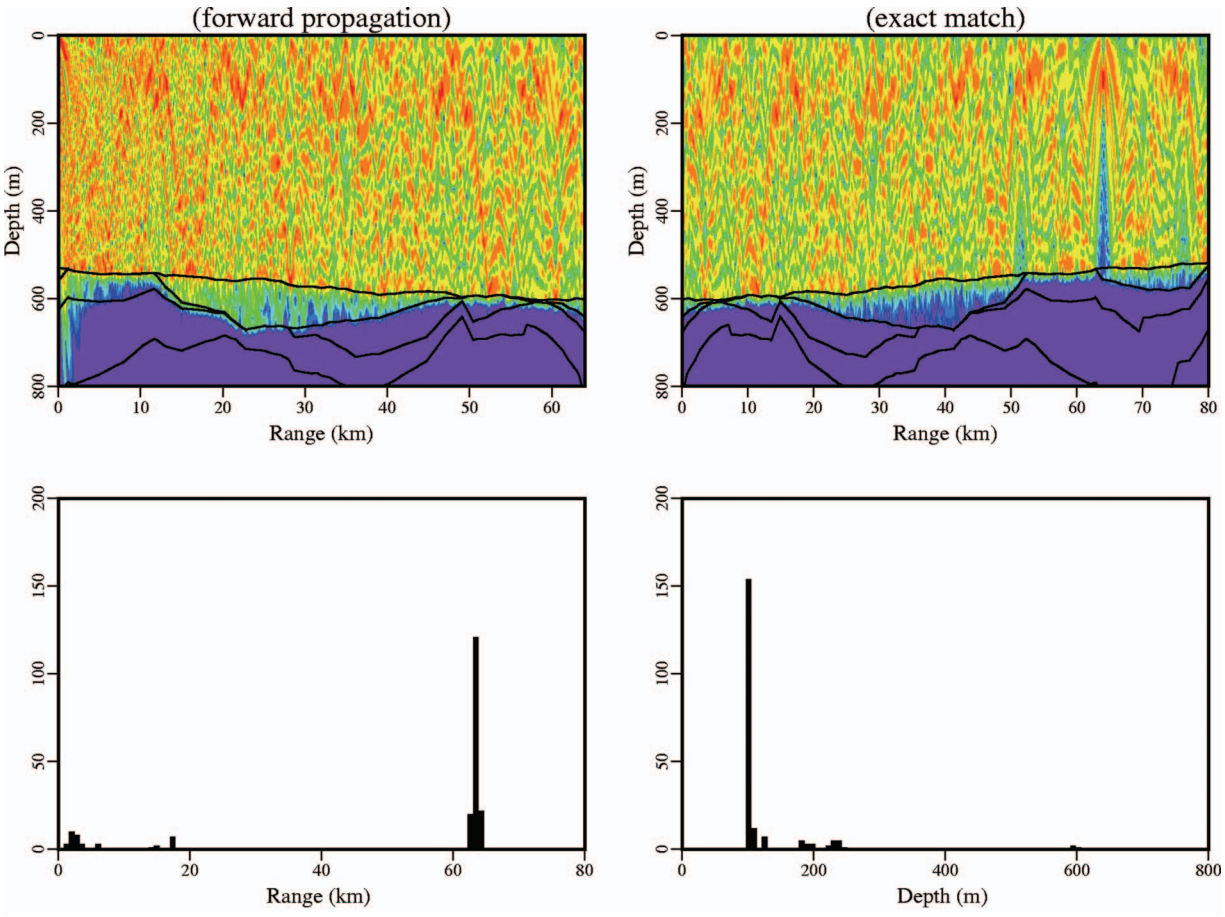

FIG. 3. Results for the case without internal waves of example C, which involves longer range than example A: a 75 Hz source 64 km from the array and 102 m below the surface. The results are similar to the results for the previous examples at much smaller ranges.

III. SEDIMENT UNCERTAINTIES AND INTERNAL WAVES

In this section, we consider a problem involving both sediment uncertainties and internal waves. Internal waves are more important at higher frequencies. Sediment uncertainties tend to be more important at lower frequencies. Both effects are important for some problems. Internal waves are more important at longer ranges. The effects of sediment uncertainties tend not to accumulate as rapidly with range since energy that interacts with the sediment is attenuated. We use the model that is discussed in Ref. 9 to generate realizations of the internal wave field.

Example C is similar to example A, with the exception that the source range is 64 km and the bathymetry varies between approximately 500 and 600 m. We consider 70- and 75-Hz cases, which are more sensitive to internal waves than the 50-Hz cases in the previous examples. The spacings between the nodes for the interfaces are chosen between 250 and 10 000 m for this case. Appearing in Fig. 3 are results for the case without internal waves, which serve to illustrate the effects of sediment uncertainties at longer range and as a base case before adding the internal waves. The performance is similar to the previous examples, which involved much smaller ranges. Appearing in Fig. 4 are histograms for the case with internal waves. The depth is recovered reliably for both frequencies, but the range is ambiguous. There are strong peaks near $r=64$ km for both frequencies. There are also strong peaks at other ranges, but they can be discounted since they occur at different ranges for the two frequencies.

IV. CONCLUSION

Focalization appears to be a promising approach for localizing a source in an environment with gross sediment uncertainties. In simulations, sources were successfully localized by searching over a parameter space that includes a wide range of environments. An implementation based on histograms is effective for this problem. As in previous studies of focalization, the key to the performance is a parameter hierarchy in which source location is much more important than environmental parameters. It is often possible to localize the source without determining correct values for the environmental parameters. The approach also performs well for a case involving both sediment uncertainties and internal waves.

ACKNOWLEDGMENTS

This work was supported by the Office of Naval Research.

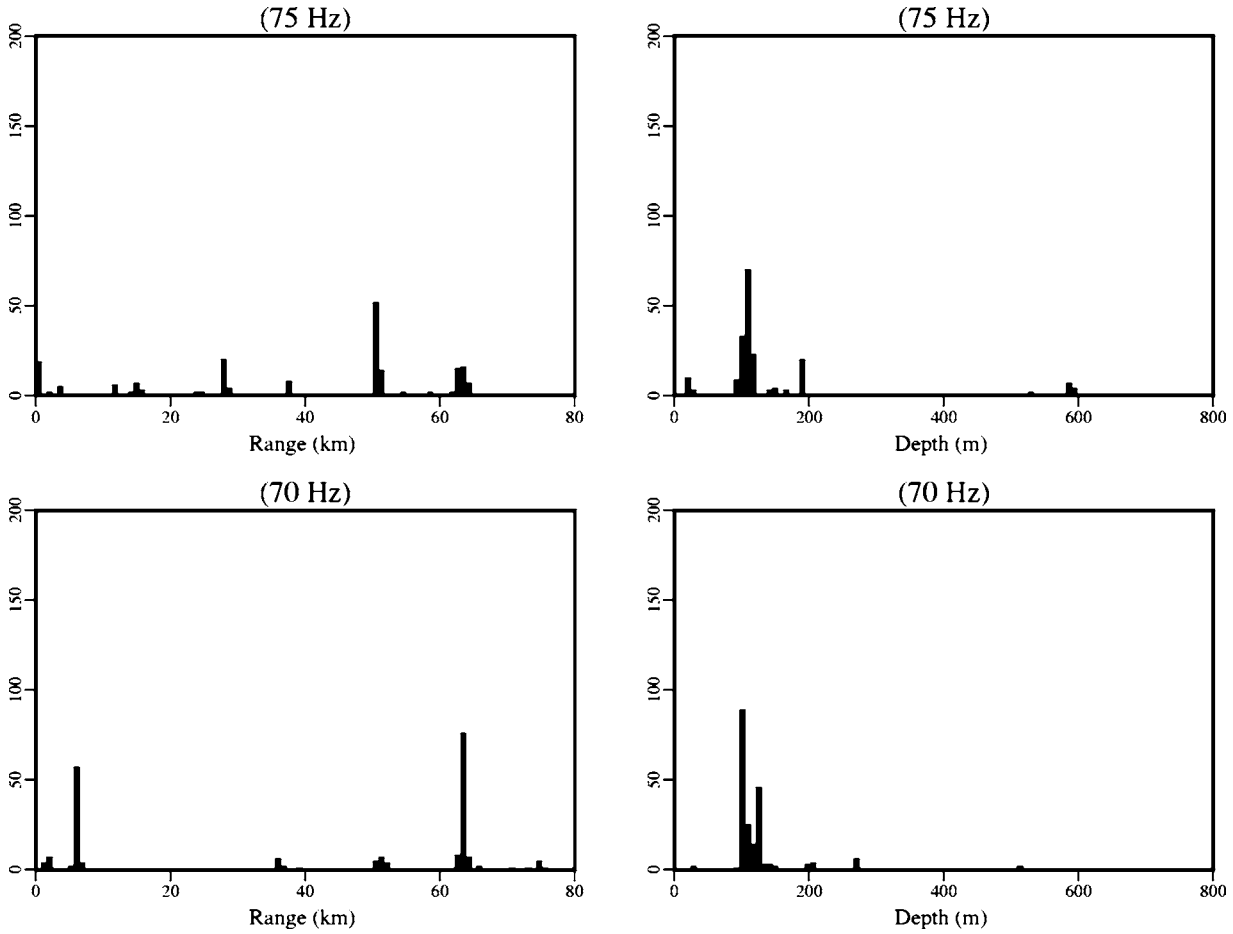

FIG. 4. Results for the case with internal waves of example C, which involves longer range than example A: a narrowband source is located 64 km from the array and 102 m below the surface. The main peaks are at the correct location in the depth histograms at 70 and 75 Hz. Although there are large false peaks in the range histograms for both frequencies, the false peaks can be ruled out since they occur at different positions for the two frequencies.

[1]H. P. Bucker, "Use of calculated sound fields and matched-field detection to locate sound sources in shallow water," J. Acoust. Soc. Am. **59**, 368–373 (1976).
[2]A. B. Baggeroer, W. A. Kuperman, and H. Schmidt, "Matched field processing: Source localization in correlated noise as an optimum parameter estimation problem," J. Acoust. Soc. Am. **83**, 571–587 (1988).
[3]A. B. Baggeroer, W. A. Kuperman, and P. N. Mikhalevsky, "An overview of matched field methods in ocean acoustics," IEEE J. Ocean. Eng. **18**, 401–424 (1993).
[4]M. B. Porter, R. L. Dicus, and R. G. Fizell, "Simulations of matched-field processing in a deep water Pacific environment," IEEE J. Ocean. Eng. **12**, 173–181 (1987).
[5]A. Tolstoy, "Sensitivity of matched field processing to sound-speed profile mismatch for vertical arrays in a deep water Pacific environment," J. Acoust. Soc. Am. **85**, 2394–2404 (1989).
[6]R. M. Hamson and R. M. Heitmeyer, "Environmental and system effects on source localization in shallow water by the matched-field processing of a vertical array," J. Acoust. Soc. Am. **86**, 1950–1959 (1989).
[7]D. F. Gingras, "Methods for predicting the sensitivity of matched-field processors to mismatch," J. Acoust. Soc. Am. **88**, 423–433 (1990).
[8]M. D. Collins and W. A. Kuperman, "Focalization: Environmental focusing and source localization," J. Acoust. Soc. Am. **90**, 1410–1422 (1991).
[9]R. N. Baer and M. D. Collins, "Source localization in the presence of internal waves," J. Acoust. Soc. Am. **118**, 3117–3121 (2005).
[10]L. T. Fialkowski, M. D. Collins, J. S. Perkins, and W. A. Kuperman, "Source localization in noisy and uncertain ocean environments," J. Acoust. Soc. Am. **101**, 3539–3545 (1997).
[11]W. H. Munk, "Sound channel in an exponentially stratified ocean with applications to SOFAR," J. Acoust. Soc. Am. **55**, 220–226 (1974).

Multiple scattering between two elastic cylinders and invariants of the time-reversal operator: Theory and experiment

Jean-Gabriel Minonzio,[a] Claire Prada, Alexandre Aubry, and Mathias Fink
Laboratoire Ondes et Acoustique, Université Paris 7 Denis Diderot, UMR CNRS 7587, ESPCI, 10 rue Vauquelin, 75231 Paris Cedex 05, France

(Received 18 October 2005; revised 31 May 2006; accepted 1 June 2006)

The decomposition-of-the-time-reversal-operator method is an ultrasonic method based on the analysis of the array response matrix used for detection and characterization. The eigenvalues and the eigenvectors of the time-reversal operator (equivalent to the singular values and the singular vectors of the array response matrix) provide information on the localization and nature of scatterers in the insonified medium. Here, the eigenmodes of the time-reversal operator are studied for two elastic cylinders: The effects of multiple scattering and anisotropic scattering are considered. Analytical expressions for the singular values are established within the isotropic scattering approximation. Then, the comparison with a complete model is presented, putting in evidence the importance of the anisotropy of the scattering. Experiments, carried out at central frequency 1.5 MHz on 0.25 mm diameter nylon and copper cylinders embedded in water, confirm the theory. In particular, the small cylinder limit and the effect of the dominant quadrupolar normal mode of nylon are discussed. © *2006 Acoustical Society of America.* [DOI: 10.1121/1.2217128]

PACS number(s): 43.60.Pt, 43.28.We, 43.20.Fn [DRD] Pages: 875–883

I. INTRODUCTION

The analysis of acoustic scattering is an important tool for imaging and object identification. It has applications among nondestructive evaluation, medical imaging, or underwater acoustics. The decomposition-of-the-time-reversal-operator (DORT) method is an original approach to scattering analysis which has been developed since 1994. It was derived from the theoretical analysis of acoustic time-reversal mirrors used in pulse echo mode. DORT is the French acronym for Décomposition de l'Opérateur de Retournement Temporel. It consists of the determination of the invariants of the time-reversal operator obtained by singular value decomposition of the array response matrix **K**. It was applied to detection and selective focusing through nonhomogeneous media containing multiple targets.[1] It has also been applied to nondestructive evaluation[2] and characterization of a cylindrical shell through the analysis of the circumferential Lamb waves.[3] Besides, the DORT method has shown potential for highly resolved detection in a water waveguide, experimentally[4–6] and theoretically.[7,8] This method is general and applies to all types of linear waves, thus it is also studied for electromagnetic applications.[9,10]

The first study of the invariants of the time-reversal operator for two scatterers was presented in 1996 by Prada *et al.*[11] Considering isotropic scatterers and single scattering, the eigenproblem was solved. Recently, that point of view was used by Lehman and Devaney,[12] to achieve time-reversal imaging. The effect of multiple scattering was first addressed in subwavelength localization experiments, by Prada and Thomas.[13] It was shown that, for closely spaced scatterers, multiple scattering becomes significant and affects the singular values of the array response matrix, however leaving the rank of this matrix unchanged. A rough model assuming isotropic scattering was used but not described in this paper. Recently, Devaney *et al.*[14] provided a theoretical framework that takes into account multiple isotropic scattering to achieve high-resolution time-reversal imaging. In Refs. 11–14, the scattering was always supposed to be isotropic, but recent analysis on elastic spheres[15] and cylinders[16] showed that, even for a single small scatterer, the anisotropy of the scattering leads to multiple singular values and singular vectors. Consequently, anisotropy has to be taken into account for an accurate calculation of the invariants of the time-reversal operator for two elastic cylinders.

The scattering of two parallel elastic cylinders was first described by Twersky in 1952,[17] in terms of multiple scattering between two anisotropic scatterers. The isotropic scattering approximation and small cylinder limit were presented. That model, valuable for a large separation compared to the wavelength, was then completed in various papers. Among them, there was a clear description provided by Young and Bertrand in 1975,[18] which is used in the present paper to calculate the array response matrix.

Here, the effect of both multiple scattering and anisotropic scattering on the singular values of the two elastic cylinders problem is analyzed. First, generalities about the DORT method, the scattering of a single elastic cylinder, and the isotropic scattering approximation are briefly recalled in Sec. II. Then, a complete model for two elastic cylinders is presented in Sec. III, taking into account all significant normal modes of scattering. The rank of the array response matrix **K** is discussed. Then, **K** is written within the isotropic scattering approximation, taking into account the monopolar normal modes. Within that approximation, analytical expressions of the singular values and singular vectors, for two identical cylinders in symmetrical positions, are provided. These expressions bring an overall physical understanding of

[a]Electronic mail: jean-gabriel.minonzio@espci.fr

the role of multiple scattering. In order to improve the description, a correction to the isotropic model using the values of back- and sidescattering is proposed. Approximations and the complete model are then discussed. Finally, in Sec. IV, experimental results on 0.25 mm diameter copper and nylon cylinders are presented, and compared to the complete model.

II. GENERALITIES

In this part, some well known results are briefly recalled to set the framework of the analysis. An array of N transmit-receive transducers, used in a time-invariant scattering medium, is characterized at each frequency ω by the array response matrix $\mathbf{K}(\omega)$,[1] the elements of which are the Fourier transform at frequency ω of the $N\times N$ interelement impulse responses. The receive vector $\mathbf{R}(\omega)$ is related to the transmit vector $\mathbf{E}(\omega)$ through the equation $\mathbf{R}(\omega)=\mathbf{K}(\omega)\mathbf{E}(\omega)$. The time-reversal operator ${}^t\mathbf{K}^*\mathbf{K}$ is diagonalizable (the notation * and ^{t} mean complex conjugate and transpose operations), and its eigenvectors can be interpreted as invariants of the time-reversal process. In fact, the eigenvectors of ${}^t\mathbf{K}^*\mathbf{K}$ and $\mathbf{K}{}^t\mathbf{K}^*$ are the singular vectors of the array response matrix $\mathbf{K}$, while the eigenvalues are the square of the singular values of $\mathbf{K}$.[1] Consequently, the DORT method, which consists of the analysis of the invariants of the time-reversal operator, requires the singular value decomposition (SVD) of the array response matrix $\mathbf{K}$. The SVD is written $\mathbf{K}=\mathbf{U}\mathbf{\Sigma}{}^t\mathbf{V}^*$, where $\mathbf{\Sigma}$ is a real positive diagonal matrix of singular values σ_j, $\mathbf{U}$ and $\mathbf{V}$ are unitary matrices—the column of which are the singular vectors $\mathbf{U}_j$ and $\mathbf{V}_j$, with $1\leqslant j\leqslant N$. Thanks to reciprocity, $\mathbf{K}$ is a symmetrical matrix, and it is straightforward to show that $\mathbf{U}_j$ is the conjugate of $\mathbf{V}_j$ multiplied by an undetermined phase term ϕ_j: $\mathbf{U}_j=\mathbf{V}_j{}^* e^{i\phi_j}$. In the following, for simplicity and uniqueness, $\mathbf{U}_j$ is chosen equal to $\mathbf{V}_j{}^*$ (i.e., $\phi_j=0$). In that case, the SVD is written $\mathbf{K}=\mathbf{U}\mathbf{\Sigma}{}^t\mathbf{U}$.

A. The case of a single elastic cylinder

A single elastic cylinder (number 1) of radius a_1, perpendicular to a linear array of transducers, is placed at a distance $F\gg a_1$ from the array plane and at a distance dy_1 from the array axis (Fig. 1). The transducers are supposed to be long rectangles so that the problem can be considered as two dimensional (2D). The response from transducer number j to the scatterer is written H_{1j}. The Green function is approximated by the 2D far-field Hankel function of the first kind $H_0^{(1)}(k_0 r_{1j})$. Taking into account the aperture function of the transducer, $O_{1j}=\mathrm{sinc}[A(y_j-dy_1)/r_{1j}]$, the response is written as

$$H_{1j}=O_{1j}\sqrt{\frac{2}{i\pi k_0 r_{1j}}}e^{ik_o r_{1j}},\quad 1\leqslant j\leqslant N, \tag{1}$$

where k_0 is the wave number in water and r_{1j} is the distance between the jth transducer and cylinder 1, $r_{1j}=\sqrt{F^2+(y_j-dy_1)^2}$. The $1\times N$ vector of components H_{1j}, denoted $\mathbf{H}_1$, describes the propagation from the N transducers to the scatterer. Due to the reciprocity principle, the backpropagation, from the scatterer to the transducers, is described by ${}^t\mathbf{H}$. The scattered pressure by an elastic cylinder is a sum of normal modes.[21] Hence, the expression of the array response matrix $\mathbf{K}$ is ${}^t\mathbf{H}_1\tilde{\mathbf{C}}_1\mathbf{H}_1$, where the $N\times N$ scattering matrix $\tilde{\mathbf{C}}_1$ has the following components:[16]

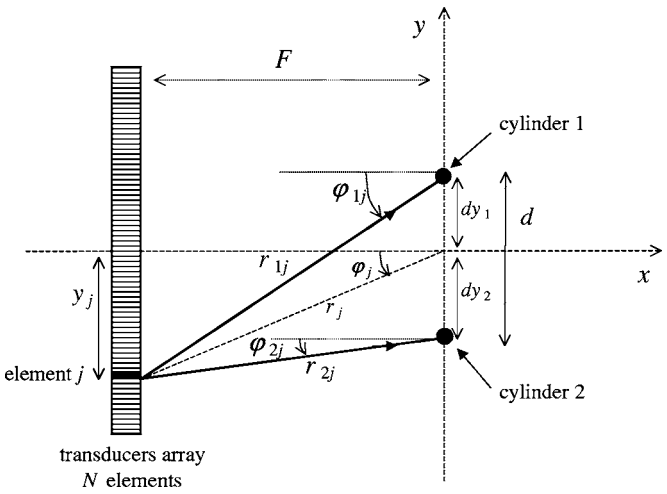

FIG. 1. Geometry of the experiment: Two elastic cylinders, located at positions dy_1 and dy_2, are placed at a distance F from the array. The distance between the cylinders is denoted by d. Every transducer position is denoted by y_j (with j ranging from 1 to N). The problem is considered as 2D.

$$\tilde{C}_{1ij}=\sum_{n=-\infty}^{\infty} R_{1,n}(-1)^n e^{in\varphi_{1ij}}. \tag{2}$$

The terms $R_{1,n}$ are the scattering coefficients given by Flax *et al.*[21] They are functions of the density ρ_1, the radius a_1, and the transverse and longitudinal wave speeds (c_{T1} and c_{L1}) of cylinder 1, and the density ρ_0 and wave speed c_0 of the surrounding fluid. The angle between emission and reception directions is φ_{1ij} equal to $\varphi_{1j}-\varphi_{1i}$ (Fig. 1). That sum is formally infinite, though the terms for which $n\gg k_0 a$ are negligible. If m denotes the highest normal mode order taken into account, the rank of $\tilde{\mathbf{C}}_1$ is less or equal to $2m+1$, the number of normal modes. Within the small cylinder limit ($k_0 a<0.5$) $m=1$, so that the rank is 3.[16] Furthermore, the rank of $\mathbf{K}$ is equal to the rank of $\tilde{\mathbf{C}}_1$, since it is less than N. The singular vectors are combinations of the projections of the normal modes onto the array.[16]

B. Isotropic scattering approximation

Within the isotropic approximation, the scattered pressure expression is reduced to one normal mode: The monopolar one.[16] The scattering matrix $\tilde{\mathbf{C}}_1$ reduces to the complex term $R_{1,0}$. Denote by $R_{1,0}=|R_{1,0}|e^{i\phi_{1,0}}$, with $|R_{1,0}|$ as the modulus of the scattering coefficient and $\phi_{1,0}$ as the scattering phase shift. Let $\|\mathbf{H}_1\|$ be the norm of the vector $\mathbf{H}_1$. The expression of the array response matrix $\mathbf{K}$ is then $\mathbf{K}={}^t\mathbf{H}_1 R_{1,0}\mathbf{H}_1$. The matrix $\mathbf{K}$ is rank 1 by construction, so that the SVD is written as $\mathbf{K}=\tilde{\mathbf{U}}_1\tilde{\sigma}_1{}^t\tilde{\mathbf{U}}_1$, where $\tilde{\sigma}_1$ is the real positive singular value and $\tilde{\mathbf{U}}_1$ is the normalized singular vector. The singular value is expressed as

$$\tilde{\sigma}_1=|R_{1,0}|\,\|\mathbf{H}_1\|^2, \tag{3}$$

and the $N\times 1$ singular vector is

$$\tilde{\mathbf{U}}_1 = \frac{{}^t\mathbf{H}_1 e^{i\phi_{1,0}/2}}{\|\mathbf{H}_1\|}. \quad (4)$$

With that convention, the phase of a singular vector corresponds to the phase shift due to the propagation from the array to the scatterer plus one-half of the scattering phase shift.

III. THEORY

Two elastic cylinders, noted 1 and 2, are placed at a distance F from the array (Fig. 1). The distance between the cylinder axes is denoted by d. To apprehend the effect of multiple scattering and anisotropic scattering on the singular values, the array response matrix is first expressed using a complete model, then different approximations are proposed.

A. General case: Two elastic cylinders complete model

The expression of the array response matrix $\mathbf{K}$ is derived from Eq. (21) of Young and Bertrand.[18] The vectors $\mathbf{H}_1$ and $\mathbf{H}_2$ are defined as in Sec. II, as the responses from the array to the centers of the cylinders [Eq. (1)]. $\mathbf{K}$ is written as the sum of four terms: Two terms with the same propagation vectors $\mathbf{H}_j$ $(j=1, 2)$, and two terms coupling vectors $\mathbf{H}_1$ and $\mathbf{H}_2$:

$$\mathbf{K} = {}^t\mathbf{H}_1\mathbf{C}_1\mathbf{H}_1 + {}^t\mathbf{H}_2\mathbf{C}_2\mathbf{H}_2 + {}^t\mathbf{H}_1\mathbf{C}_{1\text{-}2}\mathbf{H}_2 + {}^t\mathbf{H}_2\mathbf{C}_{2\text{-}1}\mathbf{H}_1. \quad (5)$$

For a distance d, small compared to F, the far-field approximation made in Ref. 18 leads to $\varphi_{1j} \approx \varphi_{2j} \approx \varphi_j$, with $1 \leqslant j \leqslant N$, where φ_j is the angle with the reference axis (Fig. 1). The elements of the $N \times N$ scattering matrices $\mathbf{C}$ are then written as

$$C_{1ij} = \sum_{n=-\infty}^{+\infty} i^{-n} W_n^- e^{in\varphi_{ij}}, \quad (6a)$$

$$C_{2ij} = \sum_{n=-\infty}^{+\infty} i^{n} W_{-n}^+ e^{in\varphi_{ij}}, \quad (6b)$$

$$C_{1-2ij} = \sum_{n=-\infty}^{+\infty} i^{n} X_{-n}^- e^{in\varphi_{ij}}, \quad (6c)$$

$$C_{2-1ij} = \sum_{n=-\infty}^{+\infty} i^{-n} X_{n}^+ e^{in\varphi_{ij}}, \quad (6d)$$

where coefficients $X_n^{\pm}$ and $W_n^{\pm}$ are functions of the scattering coefficients of each cylinder $R_{1,n}$, $R_{2,n}$ and of the Hankel functions $H_n^{(1)}(k_0 d)$ describing the propagation between the two cylinders. As in the case of a single elastic cylinder, m denotes the highest normal mode order taken into account. In Appendix A, it is shown that the rank of $\mathbf{K}$ is less than or equal to $2(2m+1)$, which is the sum of the rank of $\tilde{\mathbf{C}}_1$ and $\tilde{\mathbf{C}}_2$ (Sec. II A). This means that multiple scattering leaves the rank unchanged. The expressions for $X_n^{\pm}$ and $W_n^{\pm}$ are given in Ref. 18 for two perfectly rigid cylinders. In order to compare with experimental results in Sec. IV, the coefficients of $\mathbf{K}$ using the exact scattering coefficients of each copper or nylon cylinder will be calculated, as described by Decanini *et al.*[19] Before, in Sec. III B, the analytic expression of the array response matrix using the isotropic scattering approximation as in Twersky[17] is given.

B. Isotropic scattering approximation

In this section, the singular values of the two cylinder problem are studied; writing the array response matrix $\mathbf{K}$ within the isotropic scattering approximation. Then, the SVD equation is projected in order to reduce the N-dimensional problem to a 2D problem. Finally, the analytic expressions of the singular values for two identical cylinders in symmetrical positions are established and discussed.

1. Expressions of the array response matrix K

The isotropic scattering approximation means that the scattering sum C_{ij} [Eq. (6)] is limited to monopolar terms, $n=0$. The coefficients $X_0^{\pm}$ and $W_0^{\pm}$ depend on the scattering coefficients $R_{j,0}$ $(j=1, 2)$ and on the Hankel function of the first kind $H_0^{(1)}(k_0 d)$, denoted h. Their expressions are

$$W_0^- = \frac{R_{1,0}}{1 - R_{1,0}R_{2,0}h^2}, \quad (7a)$$

$$W_0^+ = \frac{R_{2,0}}{1 - R_{1,0}R_{2,0}h^2}, \quad (7b)$$

$$X_0^- = X_0^+ = \frac{R_{1,0}R_{2,0}h}{1 - R_{1,0}R_{2,0}h^2}. \quad (7c)$$

Using these expressions, the array response matrix $\mathbf{K}$ can be written as

$$\mathbf{K} = (\mathbf{K}^{(1)} + \mathbf{K}^{(2)})\frac{1}{1 - R_{1,0}R_{2,0}h^2}. \quad (8)$$

An interpretation of each term in Eq. (8) is now given. First, single scattering is considered, and only the direct scattering between the array and the cylinders are taken into account.[11,13] This is the distorted wave Born approximation described in Refs. 12 and 14. In that case, the array response matrix, noted $\mathbf{K}^{(1)}$ for a single scattering contribution, is the sum of two array response matrices [Fig. 2(a)], each one corresponding to a single isotropic cylinder as described in Sec. II B:

$$\mathbf{K}^{(1)} = {}^t\mathbf{H}_1 R_{1,0}\mathbf{H}_1 + {}^t\mathbf{H}_2 R_{2,0}\mathbf{H}_2. \quad (9)$$

Likewise, the double scattering corresponds to the paths described in Fig. 2(b). Thus, the double scattering contribution noted $\mathbf{K}^{(2)}$ is written as

$$\mathbf{K}^{(2)} = {}^t\mathbf{H}_2 R_{2,0} h R_{1,0}\mathbf{H}_1 + {}^t\mathbf{H}_1 R_{1,0} h R_{2,0}\mathbf{H}_2. \quad (10)$$

Multiple scattering between the cylinders is also taken into account. Two cases are distinguished depending on the parity of the number of scatterings. If that number is odd, the propagation vectors $\mathbf{H}_j$ $(j=1, 2)$, from the array and back to the array, are the same [Fig. 3(a)]. On the contrary, in the even case, the propagation vectors are different [Fig. 3(b)].

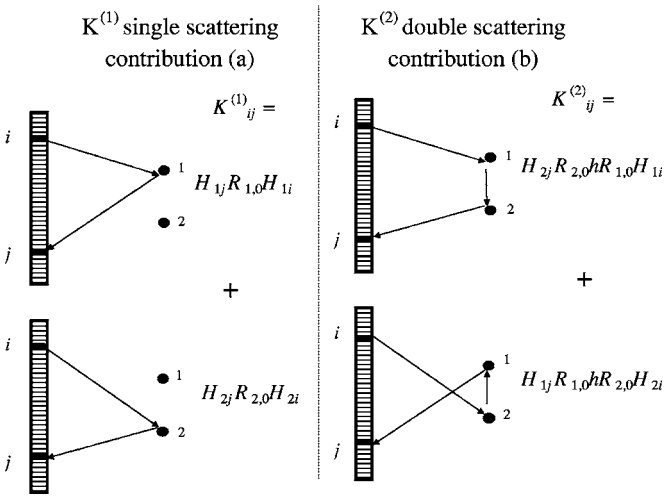

FIG. 2. Expressions of the single scattering contribution $\mathbf{K}^{(1)}$ (a), and double scattering contribution $\mathbf{K}^{(2)}$ (b). A element $K_{ij}^{(1)}$ is a sum of two terms, each one corresponds to a single scattering on the cylinder 1 ($H_{1j}R_{1,0}H_{1i}$) or 2 ($H_{2j}R_{2,0}H_{2i}$). A element $K_{ij}^{(2)}$ is also a sum of two terms. The first one corresponds to the scattering on the cylinder 1 then on the cylinder 2: $H_{2j}R_{2,0}hR_{1,0}H_{1i}$. The second one corresponds to the scattering on the cylinder 2, then the cylinder 1: $H_{1j}R_{1,0}hR_{2,0}H_{2i}$. The propagation term between the two scatterers is denoted h.

The term $R_{1,0}R_{2,0}h^2$ corresponds to the weight of a round trip between the cylinders with two scatterings. Hence, the third scattering order contribution $\mathbf{K}^{(3)}$ is equal to $R_{1,0}R_{2,0}h^2\mathbf{K}^{(1)}$. Similarly, $\mathbf{K}^{(4)}=R_{1,0}R_{2,0}h^2\mathbf{K}^{(2)}$, $\mathbf{K}^{(5)}=(R_{1,0}R_{2,0}h^2)^2\mathbf{K}^{(1)}$, and so on. Therefore, the asymptotic value of the array response matrix $\mathbf{K}$ corresponds to Eq. (8): The sum of the single and double scattering contributions $\mathbf{K}^{(1)}+\mathbf{K}^{(2)}$ multiplied by the asymptotic value of the geometric sum of the ratio $R_{1,0}R_{2,0}h^2$.

2. Projected array response matrix S

The single scattering contribution $\mathbf{K}^{(1)}$ [Eq. (9)] is expressed as

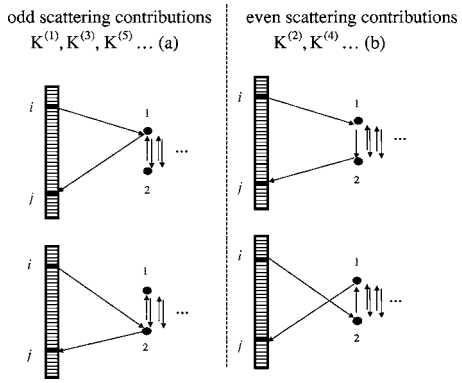

FIG. 3. Expression of the nth scattering order contribution $\mathbf{K}^{(n)}$ as function of the parity of the number of scatterings. The term corresponding to two propagations between the cylinders and two scatterings is equal to $R_{1,0}R_{2,0}h^2$. For odd contribution (a), $\mathbf{K}^{(2n+1)}$ is equal to $(R_{1,0}R_{2,0}h^2)^n\mathbf{K}^{(1)}$. For even contribution (b), $\mathbf{K}^{(2n)}$ is equal to $(R_{1,0}R_{2,0}h^2)^n\mathbf{K}^{(2)}$.

$$\mathbf{K}^{(1)}=\tilde{\mathbf{U}}_1\tilde{\sigma}_1{}^t\tilde{\mathbf{U}}_1+\tilde{\mathbf{U}}_2\tilde{\sigma}_2{}^t\tilde{\mathbf{U}}_2, \tag{11}$$

where $\tilde{\sigma}_j$ and $\tilde{\mathbf{U}}_j$ ($j=1, 2$) are the singular values and vectors if each scatterer is alone [Eqs. (3) and (4)]. In general, they are not singular vectors anymore as $\tilde{\mathbf{U}}_1$ and $\tilde{\mathbf{U}}_2$ are not orthogonal. By analogy $\tilde{\sigma}_{12}$ denotes the weight of the double scattering interaction:

$$\tilde{\sigma}_{12}=he^{i/2(\phi_{1,0}+\phi_{2,0})}|R_{1,0}|\,|R_{2,0}|\,\|\mathbf{H}_1\|\,\|\mathbf{H}_2\|. \tag{12}$$

The $\tilde{\sigma}_{12}$ term is complex, whereas the singular values $\tilde{\sigma}_j$ are real positive. Thus, the double scattering contribution $\mathbf{K}^{(2)}$ [Eq. (10)] is written as

$$\mathbf{K}^{(2)}=\tilde{\mathbf{U}}_1\tilde{\sigma}_{12}{}^t\tilde{\mathbf{U}}_2+\tilde{\mathbf{U}}_2\tilde{\sigma}_{12}{}^t\tilde{\mathbf{U}}_1. \tag{13}$$

The matrix $\mathbf{K}$ is a linear combination of $\tilde{\mathbf{U}}_1$ and $\tilde{\mathbf{U}}_2$ [Eq. (8)], hence it is rank 2. This is in agreement with Devaney *et al.*[14] Thus, the singular value decomposition of $\mathbf{K}$ is written as

$$\mathbf{K}=\mathbf{U}_1\sigma_1{}^t\mathbf{U}_1+\mathbf{U}_2\sigma_2{}^t\mathbf{U}_2, \tag{14}$$

where σ_j and $\mathbf{U}_j$ ($j=1, 2$) are the singular values and vectors of the two cylinder problem. The singular vector $\mathbf{U}_j$ is expressed as a linear combination of the vectors $\tilde{\mathbf{U}}_1$ and $\tilde{\mathbf{U}}_2$

$$\mathbf{U}_j=\chi_{1j}\tilde{\mathbf{U}}_1+\chi_{2j}\tilde{\mathbf{U}}_2,\quad j=1,2. \tag{15}$$

The χ_{ij} terms are complex. The term $\boldsymbol{\chi}_j$ denotes the 2×1 vector containing the term χ_{1j} and χ_{2j}. Expressing $\mathbf{K}$ and $\mathbf{U}_j$ as functions of $\tilde{\mathbf{U}}_j$, the N-dimensional problem can be reduced to a 2D problem. The relation $\mathbf{K}\mathbf{U}_j{}^*=\sigma_j\mathbf{U}_j$ is expressed as $\mathbf{S}\boldsymbol{\chi}_j{}^*=\sigma_j\boldsymbol{\chi}_j$, where $\mathbf{S}$ is the a matrix of dimension 2 and corresponds to the projection of the array response matrix on the subspace Span $\{\tilde{\mathbf{U}}_1,\tilde{\mathbf{U}}_2\}$ (Appendix B). Accordingly, it leads to $\mathbf{S}\mathbf{S}^*\boldsymbol{\chi}_j=\sigma_j^2\boldsymbol{\chi}_j$. That is to say σ_j^2 and $\boldsymbol{\chi}_j$ are, respectively, the eigenvalues and eigenvectors of $\mathbf{S}\mathbf{S}^*$, which corresponds to the projection of the time-reversal operator $\mathbf{K}\mathbf{K}^*$ on the subspace Span $\{\tilde{\mathbf{U}}_1,\tilde{\mathbf{U}}_2\}$.

3. Resolution for two identical cylinders in symmetrical positions

The calculations of the singular values and vectors for two identical cylinders in symmetrical positions are explained in Appendix C. Denote by w_{12} as the hermitian scalar cross product ${}^t\tilde{\mathbf{U}}_1^*.\tilde{\mathbf{U}}_2$, which is real in the symmetrical case. Denote by $\tilde{\sigma}$ as the singular value for a single cylinder of monopolar term R_0. In that case, the singular values are

$$\sigma_+=\tilde{\sigma}(1+w_{12})\left|\frac{1}{1-R_0h}\right|, \tag{16a}$$

$$\sigma_-=\tilde{\sigma}(1-w_{12})\left|\frac{1}{1+R_0h}\right|, \tag{16b}$$

associated with the singular vectors

$$\mathbf{U}_+\propto(\tilde{\mathbf{U}}_1+\tilde{\mathbf{U}}_2)/\|\tilde{\mathbf{U}}_1+\tilde{\mathbf{U}}_2\|, \tag{17a}$$

$$\mathbf{U}_-\propto(\tilde{\mathbf{U}}_1-\tilde{\mathbf{U}}_2)/\|\tilde{\mathbf{U}}_1-\tilde{\mathbf{U}}_2\|. \tag{17b}$$

C. Back- and sidescattering approximation

In this section, a correction to the isotropic scattering approximation using only two values of the anisotropic scattering values is proposed: The backscattering amplitude ($\varphi = 0°$) and the sidescattering amplitude ($\varphi = 90°$). Denote by C_0 and C_{90}, the values of the scattering amplitude at those angles [Eq. (2)]. That approximation assumes that the back- and sidescattering are constant within the array aperture; hence, the singular values calculation is similar to the isotropic scattering calculation (Appendix D). The singular values are then

$$\sigma_+ = \tilde{\sigma}(1 + w_{12}) \left| 1 + h \frac{C_{90}^2}{C_0} \frac{1}{1 - C_0 h} \right|, \tag{18a}$$

$$\sigma_- = \tilde{\sigma}(1 - w_{12}) \left| 1 - h \frac{C_{90}^2}{C_0} \frac{1}{1 + C_0 h} \right|. \tag{18b}$$

To provide an analytical expressions for C_0 and C_{90}, the small cylinder limit is used, valid for $k_0 a < 0.5$, described by Minonzio *et al.*[16] and Twersky.[17] In that case, the scattering is the sum of two normal modes (monopole and dipole). It depends on the compressibility contrast α, the density contrast β and on a scattering coefficient c, which are written[20]

$$\alpha = 1 - \frac{\rho_0 c_0^2}{\rho_1 (c_L^2 - c_T^2)}, \tag{19a}$$

$$\beta = 2 \frac{\rho_1 - \rho_0}{\rho_1 + \rho_0}, \tag{19b}$$

$$c = -i \pi k_0^2 a^2 / 4. \tag{19c}$$

The weight of the monopolar mode is $R_0 = \alpha c$, and the weight of the dipolar mode is $-2R_1 = \beta c$. Thus, the backscattering coefficient is $C_0 = (\alpha + \beta)c$, and the sidescattering coefficient is $C_{90} = \alpha c$. In both cases, the scattering phase shift is $\phi = -\pi/2$.

D. Comparison of the three models

In Fig. 4, results given by the three models are compared: Isotropic scattering approximation [Eq. (16)], back- and sidescattering approximation [Eq. (18)], and the complete model. The normalized singular values are shown for two identical cylinders, at a single frequency, versus the distance d between the two cylinders. The diameters are equal to 0.25 mm and the frequency is 1.5 MHz, hence $k_0 a = 0.8$. Separation d ranges from contact ($d = 2a$) to 3 mm. Figure 4(a) shows the copper case, and Fig. 4(b) shows the nylon case. Physical parameters taken into account for calculations are given in Table I.

The isotropic and the back- and sidescattering approximations give the same expression for the singular values for single scattering, keeping only the first-order term: $\sigma_\pm^{(1)} = \tilde{\sigma}(1 \pm w_{12})$. As in Sec. III B, superscript (1) is used for single scattering. That expression is equivalent to Eq. (25) of Prada *et al.*[11] Single scattering singular values are shown as a dashed line (Fig. 4). If d is small compared to the resolution cell, the nonresolved case, w_{12} is close to 1: $\sigma_+^{(1)} \approx 2\tilde{\sigma}$ and

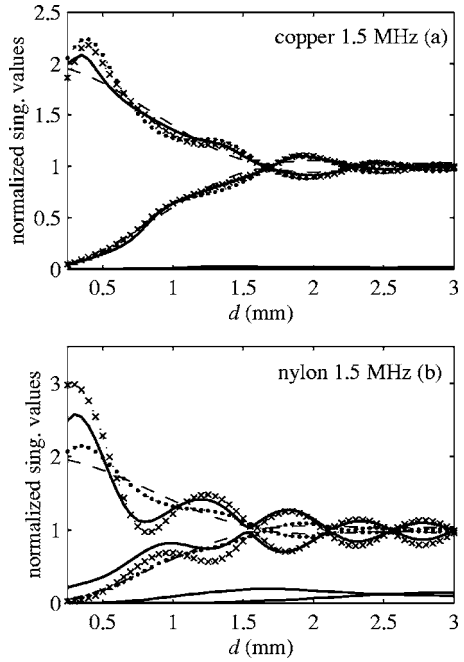

FIG. 4. Normalized singular values versus separation d, for two 0.25 mm diameter cylinders, at 1.5 MHz, copper (a) and nylon (b): Single scattering (dashed line), isotropic scattering approximation (•), back- and sidescattering approximation (×) and complete model (solid line).

$\sigma_-^{(1)} \approx 0$. On the contrary, if d is large compared to the resolution cell, the well-resolved case, w_{12} is close to 0: $\sigma_+^{(1)} \approx \sigma_-^{(1)} \approx \tilde{\sigma}$.[11–13] Note that the SVD gives the singular values in order of importance, i.e., $\sigma_1 \geqslant \sigma_2$. On the contrary, the previous equation gives $\sigma_+^{(1)}$ inferior to $\sigma_-^{(1)}$ when w_{12} is negative.

For the three models, the singular values $\sigma_\pm$ present oscillations compared with the single scattering singular value $\sigma_\pm^{(1)}$ (Fig. 4). For $d < 0.6$ and $d > 1.1$, σ_+ is larger than $\sigma_+^{(1)}$, whereas for $0.6 < d < 1.1$, σ_+ is smaller than $\sigma_+^{(1)}$. The second singular value σ_- presents opposite variations compared with $\sigma_-^{(1)}$. It is possible to explain these oscillations looking at the expression for the singular values [Eqs. (16) and (18)]. In both cases, the singular values can be written as a second-order Taylor expansion:

$$\sigma_\pm \approx \tilde{\sigma}(1 \pm w_{12})\{1 \pm |x||h| \cos(k_0 d - \pi/4 + \phi_x) + o(h^2)\}, \tag{20}$$

where x is equal to R_0 or C_{90}^2/C_0 and ϕ_x is the phase of x. The phase of h is equal to $k_0 d - \pi/4$, because h reduces to $e^{ik_0 d}\sqrt{2/i\pi k_0 d}$ for large arguments (valid for $k_0 d > 2$ or $d > 0.3\lambda$). With $\phi_x = -\pi/2$, the oscillations given by the Taylor expansion are in good agreement with the complete model singular values shown in Fig. 4. The two first zeros of the cosine correspond to $k_0 d = 5\pi/4$ and $9\pi/4$ ($d = 0.6$

TABLE I. Physical parameters of copper and nylon.

	ρ (g cm^{-3})	c_L (mm μs^{-1})	c_T (mm μs^{-1})	α	β
Copper	8.9	5.0	2.3	0.99	1.6
Nylon	1.15	2.5	1.0	0.62	0.14
Water	1	1.48			

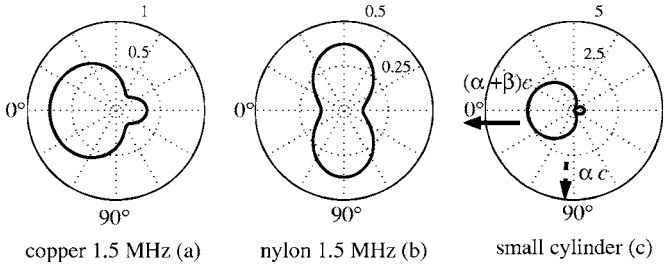

FIG. 5. Scattering patterns $|\tilde{C}(\varphi)|$: 0.25 mm diameter copper (a), nylon (b) at 1.5 MHz and small cylinder limit (c). Patterns (a) and (b) have been calculated with Eq. (2). Pattern (c) is equal to $|\alpha+\beta\cos(\varphi)|$, where α and β are the compressibility and density contrasts of copper (Table I).

and 1.1 mm). Likewise, the extrema are located at $k_0 d = 3\pi/4$ and $7\pi/4$ (d=0.4 and 0.9 mm). Accordingly, the small cylinder limit scattering phase shift ($-\pi/2$) is correct in that case [Eq. (19c)]. The cosine positive domain corresponds to constructive inferences between single and multiple scattering. On the contrary, the negative domain corresponds to destructive interferences.

However, the amplitude of the singular values given by the isotropic scattering approximation (•) differs from those given by the complete model (solid line). That difference can be explained by the scattering patterns shown in Fig. 5(a) for copper and Fig. 5(b) for nylon. For copper, $|C_{90}|$ is less than $|C_0|$. This is why the complete model oscillations are smaller than the oscillations given by the isotropic scattering approximation [Fig. 4(a)]. On the contrary, for nylon, $|C_{90}|$ is larger than $|C_0|$; so that the complete model oscillations are larger than the isotropic ones [Fig. 4(b)]. The back- and side-descattering approximation (×) compensates for part of that difference, and agrees really well for large values of d. Furthermore, for metals, as the quadrupolar term R_2 is small, for $k_0 a < 1$, the small cylinder limit [Eq. (19)] is a good approximation. The small cylinder limit scattering pattern [Fig. 5(c)] is close to the copper one [Fig. 5(a)].

Furthermore for nylon, the complete model does not show similar oscillations for the lower pair of singular values σ_3 and σ_4. In the copper case, these singular values are due to the antisymmetric dipolar normal modes, which are maximum for 90° scattering angles, as described by Minonzio *et al.*[16] On the contrary, for nylon, the second pair of singular values seems to be weakly affected by multiple scattering. In that case, these singular values are due to the antisymmetric quadrupolar normal modes.[16] Actually, the nylon dipolar mode is small because of the weak density contrast. For 90° scattering angles, the antisymmetric quadrupolar modes are null, so that for nylon the effect of multiple scattering is weak for those singular values.

IV. EXPERIMENTAL RESULTS AND DISCUSSIONS

A. Experimental setup

In a water tank a 96 element linear array—with 1.5 MHz central frequency and 0.5 mm pitch—is used. The two cylinders are identical, but their positions are not symmetrical. One cylinder is fixed, whereas the second one is connected to a motor. The distance d between the two cylinders is incremented from contact ($d=2a$) to 3 mm. The distance from the array is $F=50$ mm. Experiments have been carried out for two materials: Copper and nylon. In both cases, the diameters were taken equal to 0.25 mm. With that array, the parameter A of the aperture function does not depend on frequency [Eq. (1)]. It has been experimentally measured and is equal to 1.6. A reception level correction law is used as described by Minonzio *et al.*[16] As the wave backscattered by such small objects is very weak, the Hadamard-Walsh basis with chirps is used to acquire the array response matrix so as to optimize the signal-to-noise ratio in the whole bandwidth (1–2 MHz).[8]

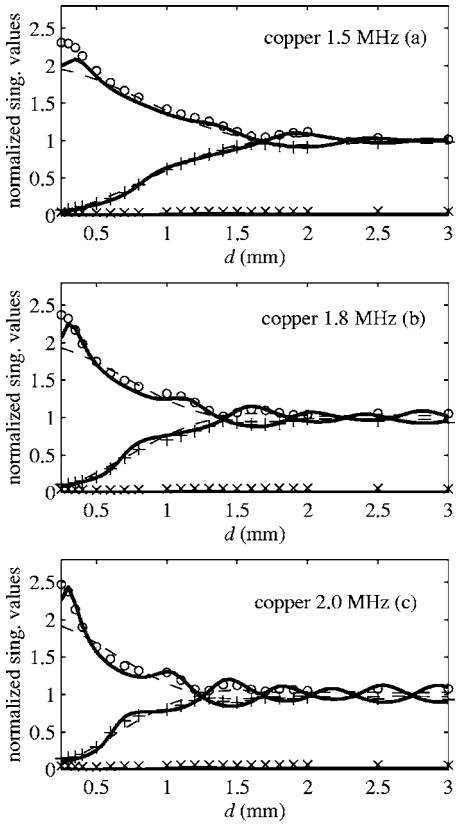

FIG. 6. Two 0.25 mm diameter copper cylinders: Experimental and complete model normalized singular values versus the separation d. Three frequencies are shown: 1.5 MHZ (a), 1.8 MHz (b), and 2 MHz (c), single scattering (dashed line), complete model (solid line), and experimental values (o, +, ×).

B. Two copper cylinders

The first experiment was carried out on two 0.25 mm diameter copper cylinders. Physical parameters, given in Table I, are taken into account for the complete model calculations. Figures 6(a)–6(c) show the normalized singular values versus the distance for three frequencies, 1.5, 1.8, and 2 MHz. There is good agreement between experimental and theoretical values (complete model). For copper, as already observed in Sec. III D, the small cylinder limit gives good results. Therefore, Eqs. (18) and (19) are sufficient to describe the multiple scattering between two small metallic cylinders. Experimental results are similar to those presented by Prada and Thomas;[13] however, the multiple scattering model was not described.

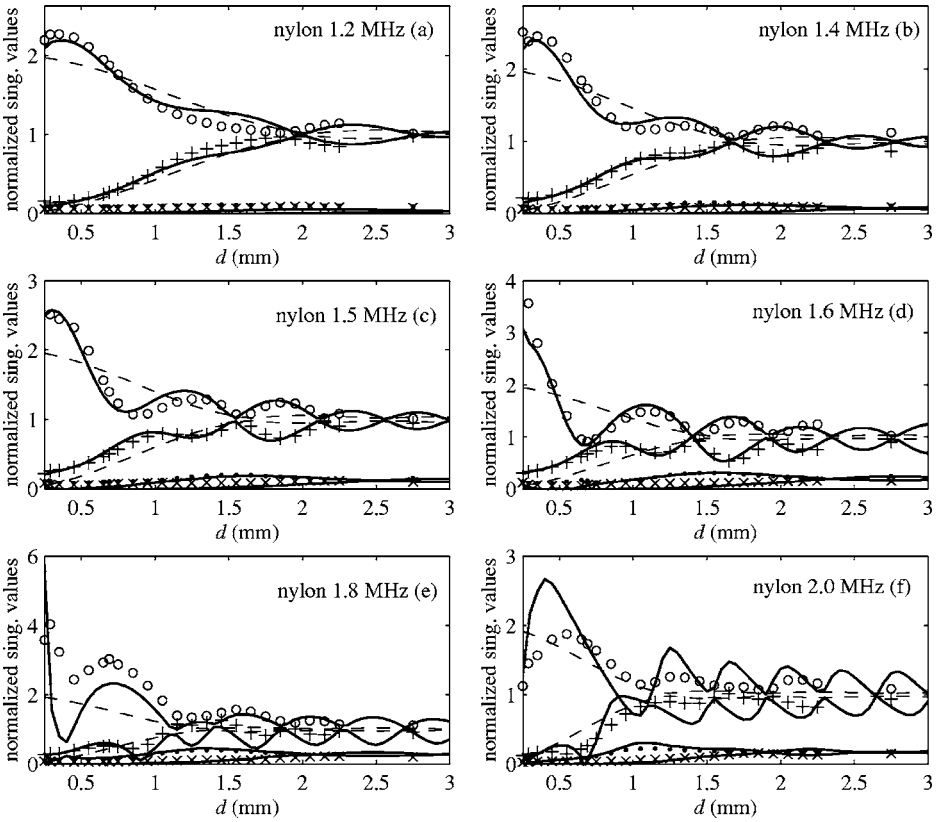

FIG. 7. Two 0.25 mm diameter nylon cylinders: Experimental and complete model normalized singular values versus the separation d. Six frequencies, from 1.2 to 2 MHz are shown, single scattering (dashed line), complete model (solid line), and experimental values ($o, +, \bullet, \times$). The singular values $\boldsymbol{\sigma}_3$ ($\bullet$) and $\boldsymbol{\sigma}_4$ ($\times$) are weakly affected by multiple scattering.

C. Two nylon cylinders

The second experiment was carried out on two 0.25 mm diameter nylon cylinders. Physical parameters, given in Table I, are taken into account for the complete model calculations. Figures 7(a)–7(f) show the singular values versus the distance for six frequencies between 1.2 and 2 MHz. There is a good agreement between experimental and theoretical values (complete model). The frequency 2 MHz corresponds to the peak of the quadrupolar term R_2 described in Ref. 16. For that frequency, the scattering pattern is a quadrupole with a scattering phase shift equal to $-\pi$, instead of $-\pi/2$, for the small cylinder limit. Thus the maximum interaction appears for $k_0 d$ equal to $5\pi/4$ (d=0.5 mm), instead of $3\pi/4$. It clearly appears that the small cylinder limit, which does not take the quadrupolar mode into account, is not valid for the nylon cylinders.

Furthermore, the lower-order singular values σ_3 and σ_4 are not negligible, as in the copper case. They are clearly measured for frequencies beyond 1.5 MHz [Figs. 7(c)–7(f)]. As noticed in Sec. III D, the effect of multiple scattering seems to be small for those singular values.

V. CONCLUSION

In order to describe how multiple scattering between two elastic cylinders affects the singular values of the interelement array-response matrix $\mathbf{K}$, three points of view have been proposed: Isotropic scattering, back- and sidescattering, and a complete model. The rank of $\mathbf{K}$ was specified as a function of the number of normal modes taken into account: All the significant ones for the complete model, only the monopolar ones for the isotropic scattering approximation. Within that approximation, for two identical cylinders in symmetrical position, analytical expressions for the singular values $\sigma_\pm$ have been given [Eq. (16)] which, explain overall the oscillations given by the complete model. A correction to the isotropic model is proposed using the back- and sidescattering amplitudes [Eq. (18)]: It compensates for part of the difference between isotropic and complete models. Within the small cylinder limit, back- and sidescattering amplitudes are expressed as a function of the compressibility and density contrasts α and β [Eq. (19)]. For metal cylinders, for $k_0 a < 1$, that expression is sufficient to describe the multiple scattering problem. Experimental results confirm the validity of the model for 0.25 mm diameters nylon and copper cylinders, for frequencies between 1.2 and 2 MHz. The effect of the interaction between the two cylinders is clearly shown. For nylon, the two following singular values σ_3 and σ_4 are weakly affected by multiple scattering because of the predominance of the quadrupolar normal mode.

APPENDIX A: RANK OF K

Let us denote by m the highest normal mode order taken into account in Eq. (6). Let us define four $(2m+1)\times(2m+1)$ diagonal square matrices $\mathbf{W}^{\pm}$ and $\mathbf{X}^{\pm}$:

$$\mathbf{W}^{-} = \mathrm{diag}(i^{-n} W_n^{-}), \tag{A1a}$$

$$\mathbf{W}^{+} = \mathrm{diag}(i^{n} W_{-n}^{+}), \tag{A1b}$$

$$\mathbf{X}^{-} = \mathrm{diag}(i^{-n} X_n^{-}), \tag{A1c}$$

$$\mathbf{X}^{+} = \mathrm{diag}(i^{n} X^{-}_{-n}), \tag{A1d}$$

with $-m \leqslant n \leqslant m$. Let also define $\mathbf{E}$ as a $(2m+1) \times N$ matrix of coefficients $E_{jn} = e^{in\varphi_j}$. Using $\varphi_{ij} = \varphi_j - \varphi_i$, Eq. (5) can be written as

$$\begin{aligned}\mathbf{K} = {}^{t}(\mathbf{E}\mathbf{H}_1)\mathbf{W}^{-}\mathbf{E}^{*}\mathbf{H}_1 + {}^{t}(\mathbf{E}\mathbf{H}_2)\mathbf{W}^{+}\mathbf{E}^{*}\mathbf{H}_2 \\ + {}^{t}(\mathbf{E}\mathbf{H}_1)\mathbf{X}^{-}\mathbf{E}^{*}\mathbf{H}_2 + {}^{t}(\mathbf{E}\mathbf{H}_2)\mathbf{X}^{+}\mathbf{E}^{*}\mathbf{H}_1,\end{aligned} \tag{A2}$$

where $\mathbf{K}$ appears to be the product of three larger matrices, such that

$$\mathbf{K} = {}^{t}\begin{bmatrix}\mathbf{E}\mathbf{H}_1 \\ \mathbf{E}\mathbf{H}_2\end{bmatrix}\begin{bmatrix}\mathbf{W}^{-} & \mathbf{X}^{-} \\ \mathbf{X}^{+} & \mathbf{W}^{+}\end{bmatrix}\begin{bmatrix}\mathbf{E}^{*}\mathbf{H}_1 \\ \mathbf{E}^{*}\mathbf{H}_2\end{bmatrix}. \tag{A3}$$

The dimension of the square matrix in the center is $2(2m+1)$, so that the rank of $\mathbf{K}$ is necessarily lower than $2(2m+1)$ since it is less than N.

APPENDIX B: EXPRESSION OF THE PROJECTED ARRAY RESPONSE MATRIX S

For two elastic cylinders, within the isotropic scattering approximation, the matrix $\mathbf{S}$ is expressed as

$$\mathbf{S} = (\tilde{\boldsymbol{\Sigma}}\mathbf{W}_1 + \tilde{\sigma}_{12}\mathbf{W}_2)\frac{1}{1 - R_{1,0}R_{2,0}h^2}, \tag{B1}$$

where $\tilde{\boldsymbol{\Sigma}}$, $\mathbf{W}_1$, and $\mathbf{W}_2$ are 2×2 matrices. $\tilde{\boldsymbol{\Sigma}}$ is diagonal and contains the single cylinder singular values $\tilde{\sigma}_j$ equal to $|R_{j,0}|\,\|\mathbf{H}_j\|^2$ [Eq. (3)]. Let us denote by w_{ij} $(i, j=1, 2)$ the hermitian scalar product equal to ${}^{t}\mathbf{U}^{*}.\tilde{\mathbf{U}}_j$. As the $\tilde{\mathbf{U}}_j$ are normalized [Eq. (4)], w_{ii} is equal to 1. In general, that product is complex and w_{ji} is equal to w_{ij}^{*}. The modulus $|w_{ij}|$ ranges from 0 to 1. It corresponds to the normalized acoustic field on the second scatterer when the field is focused on the first one.[11] The matrices $\mathbf{W}_j$ contain the w_{ij} terms. The matrices are written as

$$\tilde{\boldsymbol{\Sigma}} = \begin{pmatrix}\tilde{\sigma}_1 & 0 \\ 0 & \tilde{\sigma}_2\end{pmatrix}, \tag{B2}$$

$$\mathbf{W}_1 = \begin{pmatrix}1 & w_{12}^{*} \\ w_{12} & 1\end{pmatrix},$$

$$\mathbf{W}_2 = \begin{pmatrix}w_{12} & 1 \\ 1 & w_{12}^{*}\end{pmatrix}.$$

The matrix product $\tilde{\boldsymbol{\Sigma}}\mathbf{W}_1$ is the single scattering projected matrix. It corresponds to the matrix $\mathbf{S}'$ presented in the Appendix of Ref. 11.

APPENDIX C: RESOLUTION FOR TWO IDENTICAL CYLINDERS IN SYMMETRICAL POSITIONS

The two cylinders are now considered as identical in a symmetrical geometry with respect to the array axis (x axis, Fig. 1), i.e., $dy_1 = -dy_2$. If the cylinders are identical, $R_{1,0}$ is equal to $R_{2,0}$: The weight of the monopolar normal modes is denoted R_0. Furthermore, if the positions are symmetrical, the norms $\|\mathbf{H}_j\|$ are also equal. So the $\tilde{\sigma}_j$ coefficients are equal: They are denoted $\tilde{\sigma}$. Likewise, the weight of the double scattering interaction $\tilde{\sigma}_{12}$ is equal to $R_0 h\tilde{\sigma}$ [Eq. (12)], and the round trip interaction term $R_{1,0}R_{2,0}h^2$ is equal to $(R_0 h)^2$. For symmetrical positions, the crossed scalar product w_{12} and w_{21} are real and equal. Thus, the symmetrical case simplifies the matrices product $\mathbf{W}_i\mathbf{W}_j$ $(i, j=1, 2)$ as

$$\mathbf{W}_1^2 = \mathbf{W}_2^2 = \begin{pmatrix}1 + w_{12}^2 & 2w_{12} \\ 2w_{12} & 1 + w_{12}^2\end{pmatrix}, \tag{C1}$$

$$\mathbf{W}_1\mathbf{W}_2 = \mathbf{W}_2\mathbf{W}_1 = \begin{pmatrix}2w_{12} & 1 + w_{12}^2 \\ 1 + w_{12}^2 & 2w_{12}\end{pmatrix}. \tag{C2}$$

Therefore, the expression of $\mathbf{S}\mathbf{S}^{*}$ is

$$\begin{aligned}\mathbf{S}\mathbf{S}^{*} = \tilde{\sigma}^2[(1 + |R_0 h|^2)\mathbf{W}_1^2 \\ + (R_0 h + (R_0 h)^{*})\mathbf{W}_1\mathbf{W}_2]\frac{1}{|1 - (R_0 h)^2|^2}.\end{aligned} \tag{C3}$$

The expression of the $\mathbf{S}\mathbf{S}^{*}$ matrix is symmetrical, in $\begin{pmatrix}a & b \\ b & a\end{pmatrix}$ form. Thus, the two eigenvalues $\sigma_{\pm}^2$ are written $a+b$ and $a-b$, associated with the eigenvectors $1/\sqrt{2}\,{}^{t}(1\ \ 1)$ and $1/\sqrt{2}\,{}^{t}(1\ \ -1)$. The singular values of $\mathbf{K}$ [Eq. (16)] are the square roots of the eigenvalues of $\mathbf{S}\mathbf{S}^{*}$. The singular vectors are given in Eq. (17).

APPENDIX D: BACK-AND SIDESCATTERING APPROXIMATION

Let us denote by C_0 the value of the backscattering; and C_{90}, the value of the sidescattering [Eq. (2)]: C_0 is equal to $R_0 - 2R_1 + 2R_2 + \ldots$ and C_{90} to $R_0 - 2R_2 + \ldots$ With those notations, the singular value $\tilde{\sigma}$ is equal to $|C_0|\,\|\mathbf{H}_1\|^2$ for a single scatterer, the weight of the double scattering interaction $\tilde{\sigma}_{12}$ [Eq. (12)] is equal to $\tilde{\sigma}C_{90}^2 h/C_0$ and the round trip interaction term is equal to $(C_0 h)^2$. Accordingly, the expression of the projected array response matrix $\mathbf{S}$ is

$$\mathbf{S} = \tilde{\boldsymbol{\sigma}}\left(\mathbf{W}_1 + h\frac{C_{90}^2}{C_0}(\mathbf{W}_2 + C_0 h\mathbf{W}_1)\frac{1}{1 - (C_0 h)^2}\right). \tag{D1}$$

Calculations are similar to those in Appendix C. The singular vectors are the same as before [Eq. (17)]. The singular values are given in Eq. (18).

[1] C. Prada and M. Fink, "Eigenmodes of the time reversal operator: a solution to selective focusing in multiple-target media," Wave Motion **20**, 151–163 (1994).

[2] E. Kerbrat, C. Prada, D. Cassereau, R. K. Ing, and M. Fink, "Detection and imaging in complex media with the DORT method," Proc.-IEEE Ultrason. Symp., 779–783 (2000).

[3] C. Prada and M. Fink, "Separation of interfering acoustic scattered signals using the invariant of the time-reversal operator. Application to Lamb waves characterization," J. Acoust. Soc. Am. **104**, 801–807 (1998).

[4] D. R. Jackson and D. R. Dowling, "Phase conjugation in underwater acoustics," J. Acoust. Soc. Am. **89**, 171–181 (1991).

[5] W. A. Kuperman, W. S. Hodgkiss, H. C. Song, T. Akal, C. Ferla, and D. R. Jackson, "Phase conjugation in the ocean: Experimental demonstration of an acoustic time-reversal mirror," J. Acoust. Soc. Am. **103**, 25–40 (1998).

[6] C. F. Gaumond, D. M. Fromm, J. F. Lingevitch, R. Menis, G. F. Edelmann, D. C. Calvo, and E. Kim, "Demonstration at sea of the decomposition-of-the-time-reversal-operator technique," J. Acoust. Soc. Am. **119**, 976–990 (2006).

[7] N. Mordant, C. Prada, and M. Fink, "Highly resolved detection and selective focusing in a waveguide using the D.O.R.T. method," J. Acoust. Soc.

Am. **105**, 2634–2642 (1999).
[8]T. Folégot, C. Prada, and M. Fink, "Resolution enhancement and separation of reverberation from target echo with the time reversal operator decomposition," J. Acoust. Soc. Am. **113**, 3155–5160 (2003).
[9]H. Tortel, G. Micolau, and M. Saillard, "Decomposition of the time reversal operator for electromagnetic scattering," J. Electromagn. Waves Appl. **13**, 687–719 (1999).
[10]D. H. Chambers and J. G. Berryman, "Time-reversal analysis for scatterer characterization," Phys. Rev. Lett. **92**, 023902 (2004).
[11]C. Prada, S. Manneville, D. Spoliansky, and M. Fink, "Decomposition of the time reversal operator: Application to detection and selective focusing on two scatterers," J. Acoust. Soc. Am. **99**, 2067–2076 (1996).
[12]S. K. Lehman and A. J. Devaney, "Transmission mode time-reversal super-resolution imaging," J. Acoust. Soc. Am. **113**, 2742–2753 (2003).
[13]C. Prada and J. L. Thomas, "Experimental subwavelength localization of scatterers by decomposition of the time reversal operator interpreted as a covariance matrix," J. Acoust. Soc. Am. **114**, 235–243 (2003).
[14]A. J. Devaney, E. A. Marengo, and F. K. Gruber, "Time-reversal-based imaging and inverse scattering of multiply scattering point targets," J. Acoust. Soc. Am. **118**, 3129–3138 (2005).
[15]D. H. Chambers and A. K. Gautesen, "Time reversal for a single spherical scatterer," J. Acoust. Soc. Am. **109**, 2616–2624 (2001).
[16]J. G. Minonzio, C. Prada, D. Chambers, D. Clorennec, and M. Fink, "Characterization of subwavelength elastic cylinders with the decomposition of the time-reversal operator: Theory and experiment," J. Acoust. Soc. Am. **117**, 789–798 (2005).
[17]V. Twersky, "Multiple scattering of radiation by an arbitrary planar configuration of parallel cylinders and by two parallel cylinders," J. Appl. Phys. **23**, 407–414 (1952).
[18]J. W. Young and J. C. Bertrand, "Multiple scattering by two cylinders," J. Acoust. Soc. Am. **58**, 1190–1195 (1976).
[19]Y. Decanini, A. Folacci, E. Fournier, and P. Gabrielli, "Exact S-matrix for N-disc systems and various boundary conditions: I. Generalization of the Korringa–Kohn–Rostoker–Berry method," J. Phys. A **31**, 7865–7889 (1998).
[20]R. Doolittle and H. Überall, "Sound scattering by elastic cylindrical shells," J. Acoust. Soc. Am. **39**, 272–275 (1966).
[21]L. Flax, G. Gaunard, and H. Überall, "Theory of resonance scattering," *Physical Acoustics*, edited by W. Mason and R. Thurston (Academic, New York, 1976), Vol. **XV**, pp. 191–294.

Distortion-product otoacoustic emission suppression growth in normal and noise-exposed rabbits

Christopher A. Porter
School of Medicine, University of Colorado Health Sciences Center, Denver, Colorado 80203

Glen K. Martin[a] and Barden B. Stagner
Jerry Pettis Memorial Veterans Medical Center, Research Service (151), 11201 Benton Street, Loma Linda, California 92357

Brenda L. Lonsbury-Martin
Division of Otolaryngology–Head & Neck Surgery, Department of Surgery, Loma Linda University School of Medicine, Loma Linda, California 92354

(Received 3 December 2005; revised 2 May 2006; accepted 8 May 2006)

This study investigated noise-induced changes in suppression growth (SG) of distortion product otoacoustic emissions (DPOAEs). Detailed measurements of SG were obtained in rabbits as a function of f_2 frequencies at four primary-tone levels. SG measures were produced by using suppressor tones (STs) presented at two fixed distances from f_2. The magnitude of suppression was calculated for each ST level and depicted as contour plots showing the amount of suppression as a function of the f_2 frequency. At each f_2, SG indices included slope, suppression threshold, and an estimate of the tip-to-tail value. All suppression measures were obtained before and after producing a cochlear dysfunction using a monaural exposure to a 2-h, 110-dB SPL octave-band noise centered at 2 kHz. The noise exposure produced varying amounts of cochlear damage as revealed by changes in DP-grams and auditory brainstem responses. However, average measures of SG slopes, suppression thresholds, and tip-to-tail values failed to mirror the mean DP-gram loss patterns. When suppression-based parameters were correlated with the amount of DPOAE loss, small but significant correlations were observed for some measures. Overall, the findings suggest that measures derived from DPOAE SG are limited in their ability to detect noise-induced cochlear damage. © *2006 Acoustical Society of America.* [DOI: 10.1121/1.2211407]

PACS number(s): 43.64.Jb, 43.64.Bt, 43.64.Kc, 43.64.Ri [APS] Pages: 884–900

I. INTRODUCTION

It is well known that distortion-product otoacoustic emissions (DPOAEs) are produced when two pure tones are presented simultaneously to the ear (Kemp, 1979), and that the introduction of a third suppressor tone (ST) in addition to the two primary tones can result in suppression of the measured DPOAE (Brown and Kemp, 1984). By keeping the level of the primary tones constant and sweeping the ST in frequency and level to produce a criterion amount of DPOAE suppression, DPOAE suppression tuning curves (STCs) can be constructed (Brown and Kemp, 1984). Depending on the collection protocol, a number of features can be extracted from DPOAE STC measurements including STC characteristic frequency, STC tip threshold, Q_{10dB} estimates of tuning sharpness, measures of cochlear-amplifier gain in the form of tip-to-tail differences, and functions describing suppression growth (SG) and the associated SG slopes.

Because SG functions share many similarities to other psychoacoustical and physiological measures of cochlear-response growth, SG has recently received considerable attention in both normal and abnormal human ears (e.g., Abdala and Chatterjee, 2003; Abdala and Fitzgerald, 2003; Gorga *et al.*, 2003; Abdala, 2004). SG or the slope of the function describing DPOAE suppression as a function of ST level can be measured for STs placed at various frequencies, either above or below the f_2 primary tone used to evoke the DPOAE. In studies of SG, the f_2 primary can be regarded as the "probe," because it is presumably at or near the site of DPOAE generation, and the ST can be considered the equivalent of the "masker" typically employed in psychoacoustical studies (see Gorga *et al.*, 2002; Abdala and Chatterjee, 2003).

To better understand the intricacies of DPOAE suppression and its relationship to both normal and abnormal cochlear function, a number of human studies have focused on DPOAE STCs and related measures including SG either during development (Abdala, 1998, 2000, 2001a, b, 2004; Abdala and Chatterjee, 2003; Abdala *et al.*, 1996), or in normal as compared to ears with sensorineural hearing loss (SNHL) (Abdala and Fitzgerald, 2003; Gorga *et al.*, 2003). In addition, to examine DPOAE-suppression characteristics under more controlled conditions, animal studies have been performed in which cochlear function was deliberately altered in ways known to adversely affect single auditory-nerve fiber responses to assess the sensitivity of DPOAE STC measures to these insults (Martin *et al.*, 1998a; Howard *et al.*, 2002, 2003).

[a]Author to whom correspondence should be addressed. Electronic mail: glen.martin2@med.va.gov

 0001-4966/2006/120(2)/884/17/$22.50

During human development, premature neonates have been shown to have narrower STCs than adults at f_2=1.5 and 6 kHz and shallower SGs for STs lower in frequency than f_2 (Abdala, 1998, 2001b; Abdala and Chatterjee, 2003). These latter effects were strongest and most reliable at 6 kHz and were interpreted as reflecting immaturities in cochlear function at higher frequencies prior to birth. Term neonates had adultlike suppression tuning at f_2=1.5 kHz, but narrower and sharper STCs than adults at 6 kHz (Abdala *et al.*, 1996; Abdala, 1998). Term neonates also showed considerably shallower SGs for low-frequency STs at both 1.5 and 6 kHz. Together, these results suggest that several DPOAE-suppression characteristics were reliably influenced by the degree of cochlear maturity.

Recently, Gorga *et al.* (2003) examined STCs with an f_2 at 4 kHz in both normal-hearing subjects and patients with mild-to-moderate SNHL. They observed few differences in tuning properties between the two groups as measured by DPOAE STCs, although Q_{10dB} and Q_{ERB} (best frequency divided by the equivalent rectangular bandwidth) were slightly larger (i.e., sharper tuned) in impaired ears, regardless if comparisons were made at equal SPL or equal sensation levels (SLs). Impaired ears also tended to show sharper tuning at the STC tip and less steep SG functions for lower-frequency suppressors, along with steeper SG functions for higher-frequency suppressors. In addition, larger tip-to-tail differences of about 5–6 dB were noted in normal ears as compared to comparable tip-to-tail differences computed for impaired ears at either equivalent SPL or SL. However, comparisons made at equivalent SLs showed the largest effects. Although the variability in these measures was great, the tip-to-tail differences were one of the most significant findings that could be derived from suppression measurements in the Gorga *et al.* (2003) study.

Martin and colleagues (Martin *et al.*, 1998a; Howard *et al.*, 2002, 2003) examined the effects of diuretics and reversible noise exposures in rabbits on the characteristics of DPOAE STCs at 2.8 and 4 kHz, along with the effects of permanent noise damage on STCs obtained from 1.4 to 11.3 kHz in $\frac{1}{2}$-oct steps. Typically, measures of STC tip parameters including threshold, characteristic frequency, and Q_{10dB} were relatively unchanged, even when administration of loop diuretics or noise exposure produced substantial changes in DPOAE levels. However, like that observed in the above-noted human studies, there was an overall tendency for STCs in damaged ears to exhibit sharper tuning. For example, following diuretic administration, there were small increases in STC tip thresholds while, after mild noise exposure, STC tip thresholds tended to decrease. More severe noise exposure resulting in permanent cochlear damage did not reliably alter this outcome. None of the above-described rabbit studies performed by Martin and colleagues quantified SG, although examination of the spacing of the contour lines in rabbit suppression-response areas following various cochlear insults suggested that SG slopes, if measured, would tend to be shallower than their baseline counterparts. Moreover, in contrast to the Gorga *et al.* (2003) findings in humans, Howard *et al.* (2003) did not observe any significant tip-to-tail changes in rabbits with permanent noise-induced cochlear dysfunction.

A major shortcoming of human DPOAE STC studies that have extracted SG data from STC responses is that SGs can only be examined at a few f_2 frequencies, because of the time-consuming procedures required to obtain DPOAE STCs. Consequently, in most studies performed to date, SGs have not been easily related to the corresponding pattern of hearing loss, thus limiting our knowledge of how this measure is correlated with abnormal cochlear activity. Also, because of the ethical limitations of human research, SGs have not been measured before and after the administration of controlled cochlear insults.

The present study performed in rabbits was designed to circumvent some of these shortcomings by collecting detailed measures of SG as a function of f_2 frequency similar to activity depicted by traditional DP-grams. Selected slices of DPOAE STCs were isolated by placing ST frequencies at constant distances with respect to f_2, while the level of the ST was varied to obtain SG for a particular ST frequency. The amount of suppression as a function of the f_2 frequency was then plotted as 3-dB iso-suppression contours and SG slopes were computed from these functions for each ST frequency. This approach produced high-resolution "images" of SG as a function of f_2 frequency for four f_2 levels that could be compared to those obtained before and after noise exposures designed to produce permanent alterations in cochlear function. From these measures, it was also possible to extract estimates of STC tip thresholds and tip-to-tail estimates of cochlear-amplifier gain across the identical frequency span.

II. METHODS

A. Subjects

Subjects were eight young female albino rabbits weighing 3–4 kg. Prior to experimental procedures, each rabbit was determined to have normal DPOAEs in both ears as compared to an extensive database of rabbit DPOAEs from our laboratory. Testing was performed in unanesthetized animals that had been habituated to being confined by a standard plexiglass rabbit restrainer and having their heads further stabilized by a Velcro chinstrap. Throughout the course of the study, rabbits were housed within a standard laboratory animal-care facility, maintained on a routine 12-h light/dark cycle (lights on at 7 a.m., off at 7 p.m.), and provided with food and water *ad lib* in their cages. All experimental protocols were reviewed and approved by the Institutional Animal Care and Use Committee of the University of Colorado Health Sciences Center.

B. Baseline DP-gram measurement procedures

DPOAE levels were collected as a function of f_2 frequency in the form of "DP-grams" with f_2 ranging from 1.6 to 20.55 kHz in $\frac{1}{10}$-oct steps. Equilevel DP-grams were collected at seven different primary-tone levels in 5-dB steps from 45 to 75 dB SPL. Additionally, four unequal level DP-grams were obtained and analyzed (L_1, L_2 =60,55;55,45;50,35;45,25 dB SPL) along a function de-

signed to maximize DPOAE levels and optimize sensitivity to cochlear damage (Whitehead *et al.*, 1995). DP-grams were obtained for both the exposed and nonexposed ears prior to noise exposure and at 3–4 weeks postexposure, when the effects of noise overexposure were clearly permanent. These detailed DP-gram measures were used to determine if the rabbit's ears were normal according to our database of normal rabbit DPOAEs, and to provide a detailed assessment of the effects of noise exposure for comparison to auditory brainstem response (ABR) measures.

Primary tones were produced by two digital-to-analog (D/A) channels of a digital-signal processing (DSP) board (Digidesign, Audiomedia), mounted in a microcomputer (Apple, Macintosh Quadra 700). The f_1 and f_2 ($f_2/f_1 = 1.25$) signals were presented using two ear-speakers (Etymotic Research, ER-2) and the level of the ear-canal sound pressure was measured using a low-noise microphone assembly (Etymotic Research, ER-10A). The ear-canal signal was synchronously sampled at 44 100 kHz and averaged ($n=4$) by an analog-to-digital (A/D) channel of the DSP board. A 4096-point fast Fourier transform (FFT) of the time sample was performed by customized software. The $2f_1-f_2$ DPOAE and associated noise-floor (NF) levels were extracted from the FFT. The NF was based upon the average of eight frequency bins on either side of the DPOAE frequency bin, excluding the first bin on either side of the DPOAE frequency. All data were collected with the restrained rabbit positioned in a double-wall sound-treated booth (Acoustic Systems). For DPOAE suppression measures, the ST was digitally mixed with f_1 and presented on the f_1 channel. The ST was rotated in phase by 90° over the four presentations, and then time averaged to eliminate the majority of emission components produced by the ST.

C. Auditory brainstem response (ABR) correlations with DPOAEs

ABRs were collected at $\frac{1}{2}$-oct intervals from 1.4 to 22.6 kHz in the exposed and nonexposed ears. Permanent ABR threshold shifts were calculated as differences from thresholds in the nonexposed ear and were measured from 9 to 21 weeks postexposure. Eliciting stimuli were 3-ms tone pips with 1-ms rise/fall times that were digitally generated with a commercially available signal-generation device [Tucker Davis Technologies (TDT), SigGen] and presented at a rate of 21/s using associated signal-presentation hardware (TDT System II, BioSig). Active ABR electrodes were placed at the vertex and mastoid of the test ear, while the hind foot served as the ground. Signals were amplified with a gain of 200 k and average waveforms were based on 260 stimulus presentations. Tone pips were decreased in level from 80 to 15 dB SPL in 5-dB steps. Waveforms were subsequently printed out and scored by six blinded observers for determining thresholds for each frequency. Threshold was defined as a just-detectable response in the ABR waveform. Final ABR thresholds were based on the average of the six-observer threshold determinations. DPOAE losses and ABR threshold shifts were calculated in $\frac{1}{2}$-oct steps from 2.8 to 16 kHz based upon differences between the nonexposed control ear and the noise-exposed experimental ear. For DPOAEs, the f_2 frequency nearest the actual ABR test frequency was used for computing the difference score. At each primary-tone level, using linear regression, correlations between DPOAE changes and ABR threshold shifts were calculated based upon the six scores contributed by each rabbit at this test level.

D. Noise exposure

Rabbits were anesthetized prior to noise exposure using a xylazine (20 mg/kg) and ketamine (80 mg/kg) anesthetic cocktail and then placed in the restrainer using the chinstrap to secure the head. For noise exposure, the ER-2 speaker used for f_1 generation was replaced by an insert ear-speaker (Etymotic Research, ER-3) to obtain higher sound pressure levels. The 2-h, 2-kHz, 110-dB SPL octave band noise (OBN) exposure stimulus was generated by band-pass filtering the output of a broadband noise source, amplified by a stereo receiver (Denon, DRA-295) and presented monaurally to the ear canal of the experimental ear, which was randomly selected. The OBN was delivered to the ear canal with a 10-cm piece of speaker tubing (Etymotic Research) inserted into a hole in an E-A-R (Aearo Co.) foam hearing protector that was sealed in the rabbit's outer ear canal. This closed-field noise-exposure procedure resulted in DP-gram loss patterns that were very similar to those produced in awake rabbits by free-field exposures to a 2-kHz OBN presented for 6 h per day for 2 days (Franklin *et al.*, 1991; Howard *et al.*, 2003). And, the monaural-exposure strategy reserved the unexposed ear as a control for comparison measures made in the noise-exposed ear.

E. Suppression growth as a function of f_2 frequency

Initially, a "control" DP-gram ($f_2=1.4-22.6$ kHz in $\frac{1}{5}$-oct steps) was collected at one of four primary-tone levels ($L_1,L_2=70,70;65,65;60,55;55,45$ dB SPL). Next, DP-grams were obtained with an ST fixed in frequency with respect to f_2 or f_1 (i.e., f_2-30 Hz, $f_2-\frac{1}{2}$ oct, f_2-1 oct, $f_1+\frac{1}{2}$ oct, f_1+1 oct). Of the conditions with the ST below the f_2 frequency, only the f_2-30 Hz and the f_2-1 oct SG-slope results are described here, because the $f_2-\frac{1}{2}$ oct condition did not reveal any fundamental differences from the other two ST frequencies. ST frequencies above f_2 were not analyzed because of the complexities of suppression above the f_2 in rabbits (see Martin *et al.*, 1999; Howard *et al.*, 2003). The suppressor was incremented in 2-dB steps from 35 to 85 dB SPL to produce 25 DP-grams that reflected the influence of the ST. The control DP-gram magnitudes were subtracted from each ST-associated DP-gram to obtain the amount of suppression as a function of the f_2 frequency. These values were plotted as contour plots with f_2 frequency on the abscissa and ST level on the ordinate, and with the amount of suppression represented as 3-dB iso-suppression contours. One suppressor condition (e.g., f_2-30 Hz or f_2-1 oct) was equivalent to one slice through a suppression response area that was used to construct a STC. Unlike the

ABR versus DPOAE correlations, suppression measures were sampled before and after noise exposure in the same ear.

F. Suppression growth slope calculations

SG slopes were calculated in a manner similar to that described by Gorga *et al.* (2002). That is, the amount of suppression was expressed as a decrement in dB from the control value in the absence of the ST and plotted as a function of suppressor level. Data were transformed by the equation $D = 10\log(10^{decr/10} - 1)$ of Gorga *et al.* (2002) to linearize the decrement functions. SG slopes were computed from these functions. Points within +1 standard deviation (SD) of the NF were not included in the calculations, and the curve was truncated once the NF was reached. Slopes were computed for decrements encompassing 1–15 dB, plotted for each f_2 frequency, and compared to the corresponding DPOAE levels and NFs before and after the noise-exposure session.

G. Suppression-threshold and tip-to-tail measurements

Suppression thresholds were computed by extrapolating the decrement functions to determine the ST level that produced 3 dB of suppression, and these values were plotted as a function of f_2 frequency. Tip-to-tail differences were computed by subtracting thresholds at $f_2 - 30$ Hz from thresholds at $f_2 - 1$ oct and these values were displayed as a function of the f_2 frequency.

H. Statistical analysis

Average values were computed from individual scores for measures of DPOAE level, $f_2 - 30$ Hz slope, $f_2 - 1$ oct slope, corresponding thresholds, and tip-to-tail values. Paired Student's t tests were also calculated at each f_2 for these measures obtained both before and after noise exposure to determine significant differences at each frequency. Because of the large number of f_2 comparisons (17 for each variable and across four primary-tone levels, i.e., 68 values for each f_2), only significance levels of $p < 0.01$ and $p < 0.001$ using Bonferroni corrections ranging from 5 (0.01) to 50 (0.001) comparisons were noted as indicators of reliable differences.

Linear regression was used to compute correlations between the amount of DPOAE change (postexposure minus preexposure values), and the exposure-induced alterations to each of the above measures were derived from DPOAE suppression measures. These analyses were restricted to measures obtained between 2 and 13.5 kHz, because inspection of the SG-contour plots suggested that outside of this range extreme scores were likely to be encountered, probably due to poor signal-to-noise ratios below 2 kHz and possible calibration difficulties above 15 kHz. For these correlations, $p < 0.05$ was accepted as indicative of a significant relationship between the amount of DPOAE loss and the measure in question. All of the above statistical measures and other computations were performed on a microcomputer (Apple, Macintosh PowerBook G4) using commercially available software (Microsoft Excel 2004 for the Macintosh).

III. RESULTS

A. Effects of noise exposure on DPOAEs and ABRs

Exposure to the 2-kHz OBN presented monaurally at 110 dB SPL for 2 h produced substantial reductions in DPOAE levels that were restricted to the exposed ear. The DPOAE losses largely reflected permanent cochlear damage as DP-grams obtained from 3 to 4 weeks postexposure showed little recovery. Figure 1(A) compares mean ABR threshold shifts (solid circles) to average DPOAE losses for average postexposure DP-grams (light lines) representing four primary-tone levels (see figure legend). Decreases in DPOAE levels at the $2f_1 - f_2$ were largely "bi-lobed" with an initial area of decrements evident between 2 and 6 kHz, and a second area of reduced emissions appearing in the high-frequency region between 12 and 20 kHz, with the greatest reductions occurring around 2.8 kHz, i.e., $\frac{1}{2}$-oct above the 2-kHz center frequency of the OBN (stippled bar).

It can be seen in Fig. 1(A) that noise exposure produced about a 20-dB threshold shift in the ABR at and above the exposure band that gradually sloped upward towards the "no change" dashed line. The ABR threshold shift was less complex than the DPOAE loss pattern, but, overall, similar patterns were apparent. In the plots of Figs. 1(B)–1(E), it is clear that the ABR threshold shifts correlated reasonably well with the DPOAE losses at all stimulation levels. This finding is consistent with the notion that DPOAE decrements reflect the "hearing loss" revealed by ABR threshold shifts. Overall, there was about a 0.4-dB change in DPOAE level for every dB of ABR threshold shift.

B. Suppression growth in normal ears

A primary goal of the present study was to examine DPOAE suppression over a broad frequency range typically covered by DP-grams so that various measures of suppression could be correlated with DPOAE frequency-loss patterns following noise exposure. In Figs. 2(A)–2(H), 3-dB contour plots of the amount of suppression for various ST levels either at $f_2 - 30$ Hz or $f_2 - 1$ oct at each f_2 frequency are illustrated for a normal rabbit ear. These plots visually depict the data used to calculate a number of pre- and postexposure suppression measures that are shown below in other figures. The plots were created with the ST at either $f_2 - 30$ Hz [Figs. 2(A)–2(D)] or $f_2 - 1$ oct [Figs. 2(E)–2(H)]. From inspection of these contour plots, it is obvious that STs produced increasingly more suppression as primary-tone pairs used to elicit the DPOAEs became less intense. In addition, it is clear that for the same primary-tone levels, STs near the f_2 site ($f_2 - 30$ Hz) were more effective in suppressing the DPOAE than STs at $f_2 - 1$ oct, which was considerably further away from the f_2 region.

Further, the amount of suppression for a given f_2 generally increased (darker bands) as the ST was raised in level with suppression beginning to occur when the ST was within approximately 10 dB of the level of f_2. In these plots, the spacing between the contour lines is indicative of the SG slope, with closely spaced lines being associated with steeper slopes. Some of the more notable findings that can be seen in these plots are the anomalies in suppression as a function of

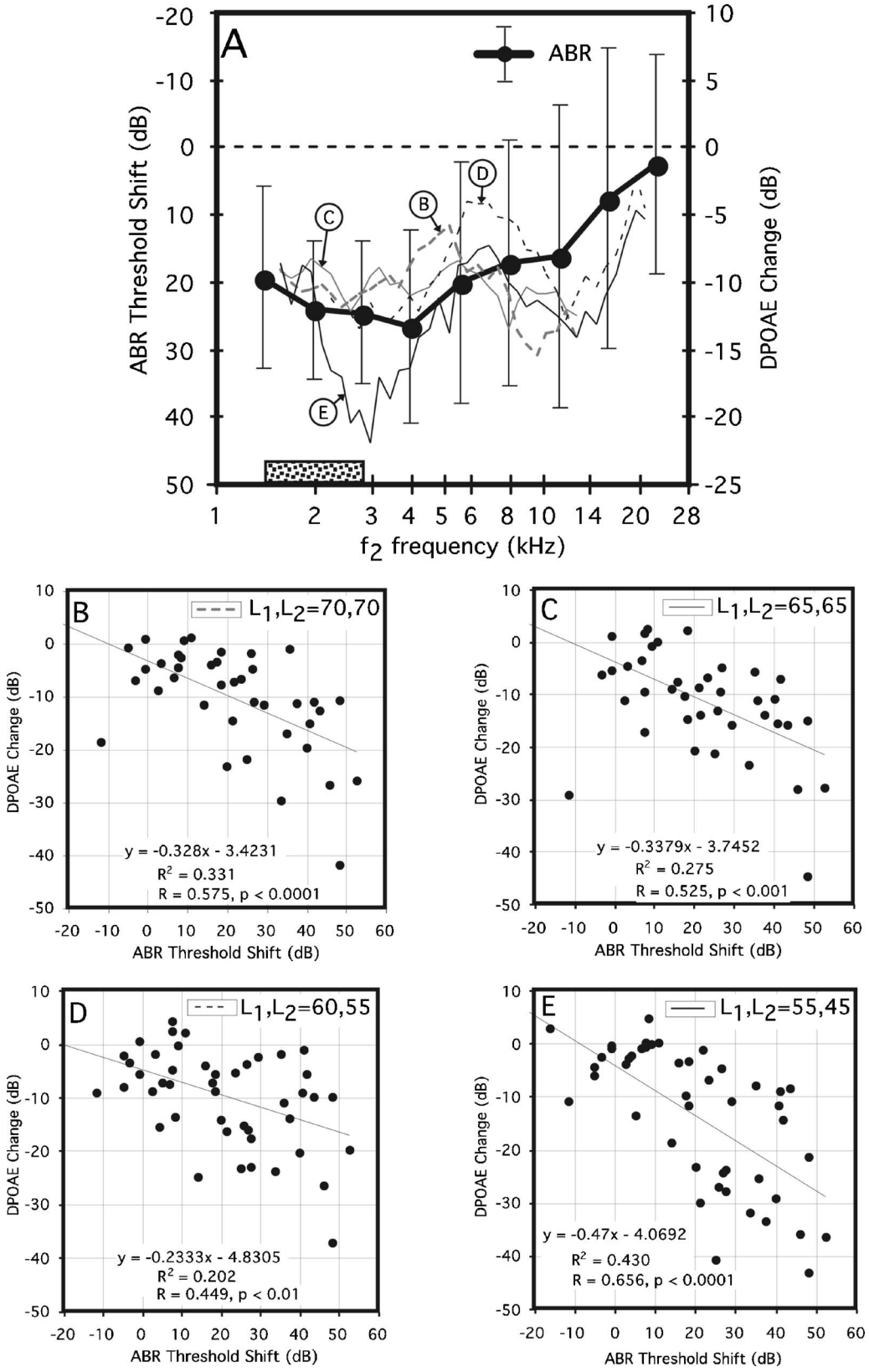

FIG. 1. Associations between permanent ABR threshold shifts and DPOAE losses following noise exposure. (A) Mean ABR threshold shifts compared to mean DP-gram alterations for four primary-tone levels (L_1,L_2=70,70;65,65;60,55;55,45 dB SPL) that are arranged in approximate ascending order, with the lowest level primary-tone combination being closest to the abscissa (thin solid line). Circled letters point to the average DP-gram associated with the corresponding correlation plots below. ABR threshold shifts were largest in the region of the exposure band and decreased toward the high frequencies. DPOAE changes tended to be bimodal with large losses from about 2–5 kHz and 8–15 kHz, with a less affected region between approximately 5 and 8 kHz. (B)–(E) correlations between ABR threshold shifts (abscissa) and DPOAE losses (ordinate) at corresponding f_2 frequencies for all noise-exposed ears (n =8) for the primary-tone levels indicated at top left of each plot. Significant correlations were obtained between ARB threshold shifts and DPOAE changes for all primary-tone levels, with the strongest correlation at the lowest primary-tone level (E). In this and subsequent figures, the stippled bar at the lower left indicates the frequency extent of the OBN exposure. Error bars= ±1 sd.

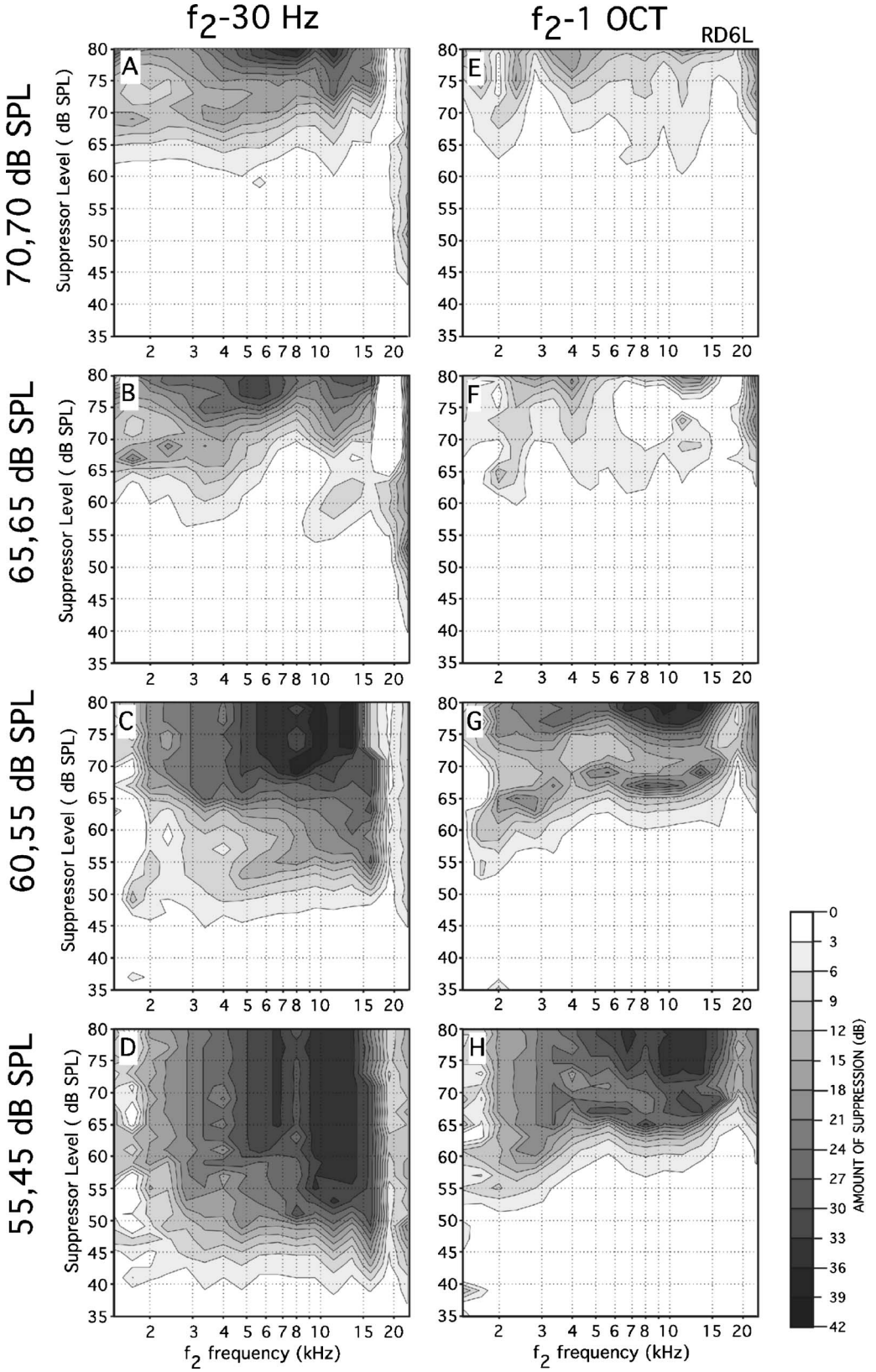

FIG. 2. Examples of 3-dB suppression-contour plots showing details of the amount of suppression in a normal rabbit ear [i.e., the left ear (L) of rabbit RD6] as a function of ST level and f_2 frequency for two the ST conditions and four primary-tone levels. (A)–(D) Results for an ST at f_2-30 Hz near the f_2 place. (E)–(H) results for an ST 1 octave (f_2-1 oct) below f_2. It can be seen that STs near f_2 (left column) were more effective suppressors with lower suppression thresholds (i.e., 3-dB contours) than STs near the "tail" of the STC (right column). These contour plots reveal many anomalies in the amount of suppression as a function of f_2 frequency and irregularities in the spacing of the contour lines across frequency indicative of great variability in SG slope.

f_2 frequency. For example, a large irregularity can be seen in the 60,55-dB SPL f_2-30 Hz contour plot [Fig. 2(C)] when STs were 50–65 dB SPL and f_2 was between 5 and 10 kHz. Other aberrations can be observed in most of the other plots.

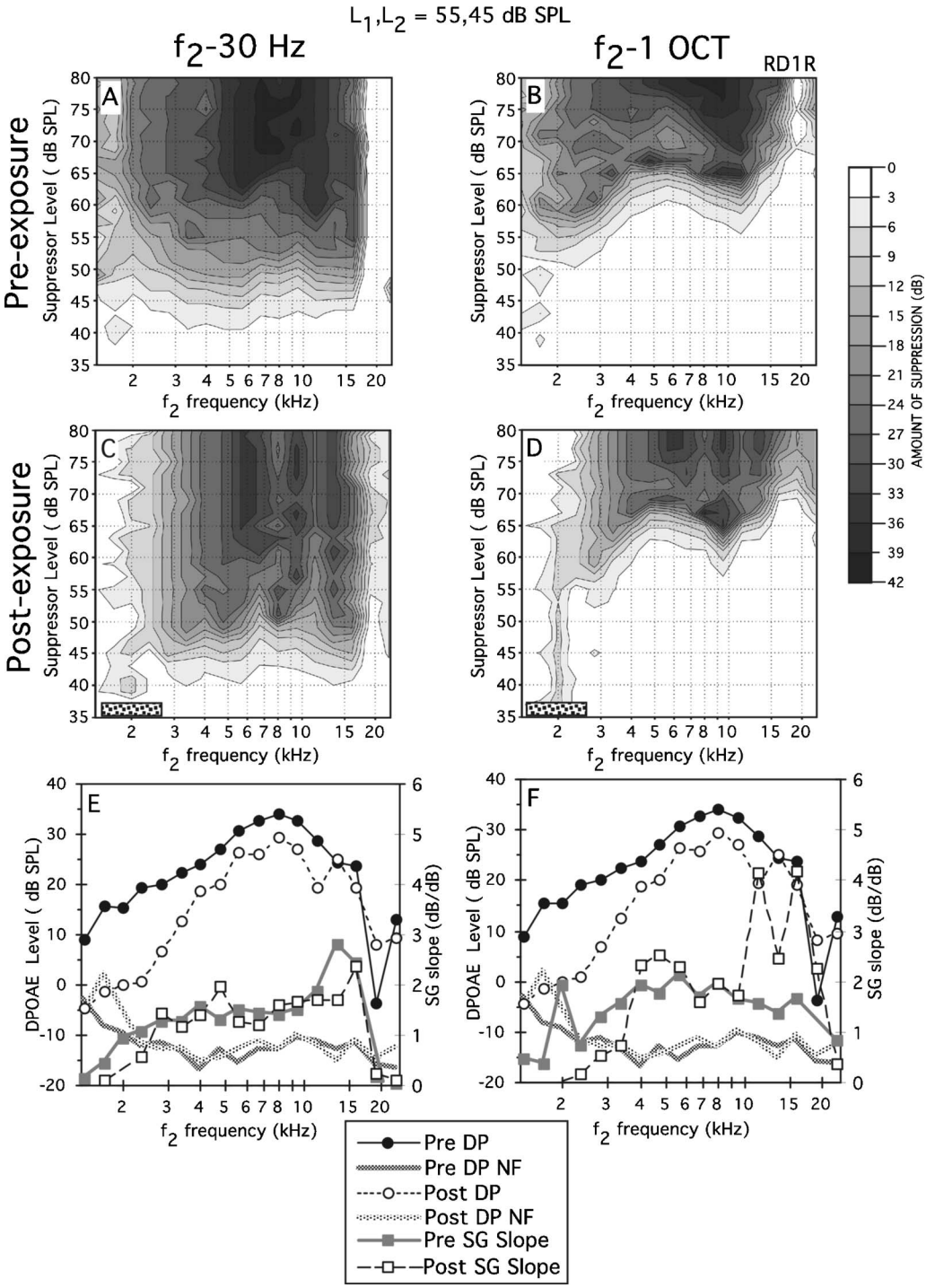

FIG. 3. Example from the right (R) ear of rabbit RD1 showing "moderate" noise damage. Upper panels show pre- (A, B) and postexposure (C, D) suppression contours corresponding to the DP-gram conditions described below. It is difficult to observe any systematic effects of noise on these plots as a function of f_2, except from about 1–2 kHz where the DPOAEs were reduced to NF levels. It can be seen for this rabbit that suppression thresholds represented by the 3-dB contours remained relatively unchanged across frequency for both conditions. Bottom plots (E, F) show DP-grams (repeated in both right and left columns) obtained before noise exposure (solid circles) and at 3 week postexposure (open circles). Preexposure SG slopes (solid squares) compared to their postexposure counterparts (open squares) are shown for f_2-30 Hz (E) and f_2-1 oct (F). In this rabbit SG slopes tended to be slightly shallower over the lower frequencies, where noise-induced DPOAE losses were greatest, than at the higher ones. However, it is clear that SG slope changes did not adequately follow the pattern of DPOAE losses as revealed in the related DP-grams.

For example, some of these presented as "holes" as can be seen in Fig. 2(B) over the 6- to 10-kHz region where suppression was absent for a range of ST levels. Contrary to what might be expected, the amount of suppression for a given ST level was not uniform across frequency in many instances.

C. Effects of noise on DPOAEs and SG slopes in individual ears

In Figs. 3 and 4 individual examples of the effects of noise exposure on both DPOAE 3-dB suppression-contour plots [(A)–(D)] and SG slopes [(E)–(F)] are presented. The

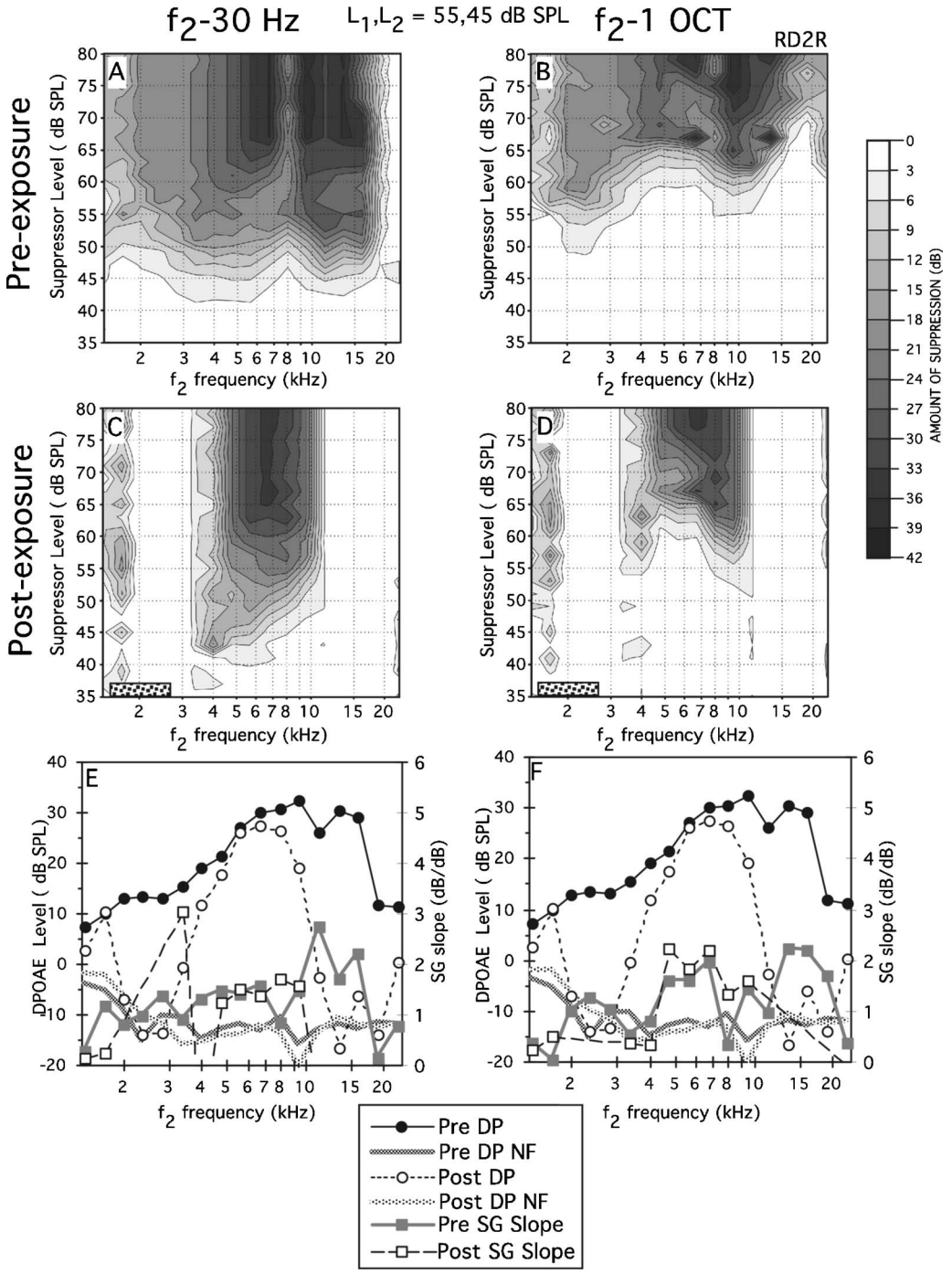

FIG. 4. Examples from the R ear of rabbit RD2 showing "severe" noise damage. In this rabbit DPOAEs were essentially reduced to the NF over the low- (1–3 kHz) and high-frequency (12–20 kHz) regions. Suppression contours [(A)–(D) show postexposure "gaps" (C, D) where DPOAEs approached the NF. In the region of measurable DPOAEs, there were no clear changes in SG, along with little change in suppression thresholds. Below, DP-grams (E, F) obtained before (solid circles) noise exposure are compared to their postexposure (open circles) counterparts. In this rabbit, although DPOAEs were reduced to the NF at low and high frequencies, there was a region of relatively normal DPOAEs centered at 6 kHz. Corresponding measure of SG slopes before (solid squares) and after (open squares) exposure are plotted for the two ST conditions (i.e., f_2-30 Hz, f_2-1 oct). Overall, there was no apparent tendency for SG slopes to track the DPOAE-loss pattern on either the ascending or descending side of the area of normal DPOAEs centered at 6 kHz.

latter values were calculated from the associated contour plots showing the amount of suppression as a function of f_2 frequency with the ST at either f_2-30 Hz (panel E) or f_2-1 oct (panel F). For the right ear (R) of rabbit RD1 shown in Fig. 3, the postexposure DPOAEs (open circles) show one variety of loss pattern in which DPOAEs at and within one octave above the 2-kHz exposure band were primarily affected with the highest frequencies appearing to be relatively unchanged [Figs. 3(E) and 3(F)] as compared to the preexposure DPOAEs (solid circles). More moderate versions of this DPOAE-loss pattern were also obtained in other rabbits (not shown), where essentially all the emissions for frequencies above 6 kHz returned to baseline levels.

It can be seen that the preexposure SG-slope values (gray squares) across f_2 frequency were rather variable for both f_2-30 Hz (E) and f_2-1 oct (F), which represents a

finding that might be expected given the above descriptions of the irregularities in the related contour plots. However, the region over which the SG slopes were calculated (i.e., 1–15 dB of suppression) was considerably more uniform (first five contours) than when the ST reached higher levels [e.g., Fig. 3(A)]. When the ST was at f_2-30 Hz (E) there was little difference in SG slopes before (gray squares) as compared to after noise exposure (open squares), except for the lowest frequencies, where slopes clearly decreased. However, there was little tendency for the SG slopes to "follow" the DPOAE-loss pattern in any systematic way. For the f_2-1 oct condition (F), similar findings were observed in that the SG slopes also tended to be lower in the 2- to 5-kHz range of f_2 frequencies following noise exposure. For this ST location, SG slope actually increased in the 10- to 20-kHz range following exposure to the OBN.

Figure 4 presents similar individual data for the R ear of rabbit RD2 that experienced considerably more severe noise damage than rabbit RD1 of Fig. 3. Specifically, as indicated in Figs. 4(E) and 4(F), DPOAEs were reduced to near-NF levels for most frequencies below 3 kHz and above approximately 12 kHz. This DPOAE-loss pattern is clearly revealed in the contour plots of Figs. 4(C) and 4(D), where suppression could not be measured because of the extremely low-level DPOAEs in both the low- and high-frequency regions. Examination of the SG slopes [Figs. 4(E) and 4(F)] where they were measurable revealed variable slope changes with some being shallower and others being steeper following noise exposure. Although this rabbit exhibited a distinct DPOAE-loss pattern with a region of nearly normal DPOAEs postexposure (~5–8 kHz), again, there was no clear tendency for the SG-slope changes to mirror the DPOAE damage pattern.

D. Average DPOAE suppression measures before and after noise exposure

To determine if there was an overall effect of noise exposure on suppression measures, averages for DPOAE levels, SG slopes, suppression thresholds, and tip-to-tail values were computed across ears before and after noise exposure. Mean pre- (solid circles) and postexposure (open squares) noise exposure DP-grams and SG slopes at f_2-30 Hz and f_2-1 oct as a function of f_2 frequency are plotted in the left, middle, and right columns, respectively, of Fig. 5 for the four primary-tone levels (rows). Inspection of the average DP-grams in Figs. 5(A)–5(D) reveals a clear effect of noise exposure at all primary-tone levels. Individual paired t tests revealed significant DPOAE losses at and above the exposure band (stippled bar) as well as at several of the highest frequencies tested. In contrast, mean SG slopes when the ST was at f_2-30 Hz [Figs. 5(E)–5(H)] showed only one significant difference near 20 kHz for the 65,65-dB SPL primary-tone condition [Fig. 5(F)]. Likewise, differences in the average f_2-1 oct slopes were significant only at approximately 3 kHz for the lowest primary-tone level of 55,45 dB SPL [Fig. 5(L)]. However, there was a tendency for the f_2-1 oct SG slopes to be shallower for the two lowest primary-tone levels [Figs. 5(K) and 5(L)] in the 2- to 4-kHz region where the aftereffects of the noise exposure were sizeable.

Figure 6 presents similar data for suppression thresholds at f_2-30 Hz and f_2-1 oct, along with tip-to-tail measures before (solid circles) and 3–4 weeks after (open squares) the OBN exposure. Here, it is clear that suppression thresholds at f_2-30 Hz [Figs. 6(A)–6(D)] remained unchanged across all f_2 frequencies tested. And, essentially similar results were obtained at f_2-1 oct [Figs. 6(E)–6(H)], except for two significant points in the damage region at primary-tone levels of 55,45 dB SPL [Fig. 6(H)]. For this particular level and f_2 range, there was a trend for suppression thresholds over the low-frequency region to be slightly lower after the exposure. The last column of plots in Figs. 6(I)–6(L) show average tip-to-tail measures before and after noise exposure. Only two significant points were obtained for this measure at the two highest primary-tone levels [Figs. 6(I) and 6(J)], and they seemed unrelated to the corresponding DPOAE-loss patterns, which were, on average, similar to those described above in Fig. 5.

E. Correlations between noise-induced changes in DPOAEs and suppression-based measures

Overall, average suppression measures compared before and after the OBN exposure that produced significant reductions in mean DPOAEs failed to reveal similar patterns of change for suppression-derived measures across f_2 frequencies. However, small and consistent changes in these suppression-based measures may have been obscured by the averaging process that minimizes individual differences in the DPOAE-loss patterns. To test this hypothesis, changes revealed by taking preexposure DPOAE levels from postexposure ones were correlated using linear regression with similar changes computed for the various suppression indices. With this procedure, it was possible to determine if larger noise-induced decrements in DPOAEs were associated with bigger effects on the various suppression measures. The results of this approach for SG slopes at f_2-30 Hz and f_2-1 oct are shown in Figs. 7(A)–7(H) for all four primary-tone level conditions. It can be seen that in six of the eight cases there were significant correlations between DPOAE-level reductions and changes in SG slopes. In all of these instances, SG slopes became shallower (decreased) as DPOAE losses increased. Although many of these correlations were significant, there was substantial scatter in the data and the variance (i.e., R^2) accounted for was relatively small ranging from approximately 6% to 22%.

Similar analyses for suppression thresholds at f_2-30 Hz and f_2-1 oct, along with tip-to-tail measures, are plotted in Fig. 8. Only one correlation for f_2-30 Hz thresholds [Figs. 8(A)–8(D)] was significant for 65,65-dB SPL primary-tone levels [Fig. 8(B)], in which larger DPOAE changes were associated with slight threshold elevations. At other primary-tone levels, this measure of suppression showed no association with the aftereffects of noise on DPOAEs. Threshold measures obtained at f_2-1 oct [Figs. 8(E)–8(H)] were equally unimpressive in that, again, a significant effect on suppression threshold was obtained, but, this time, only for the lowest primary-tone level at 55,45 dB

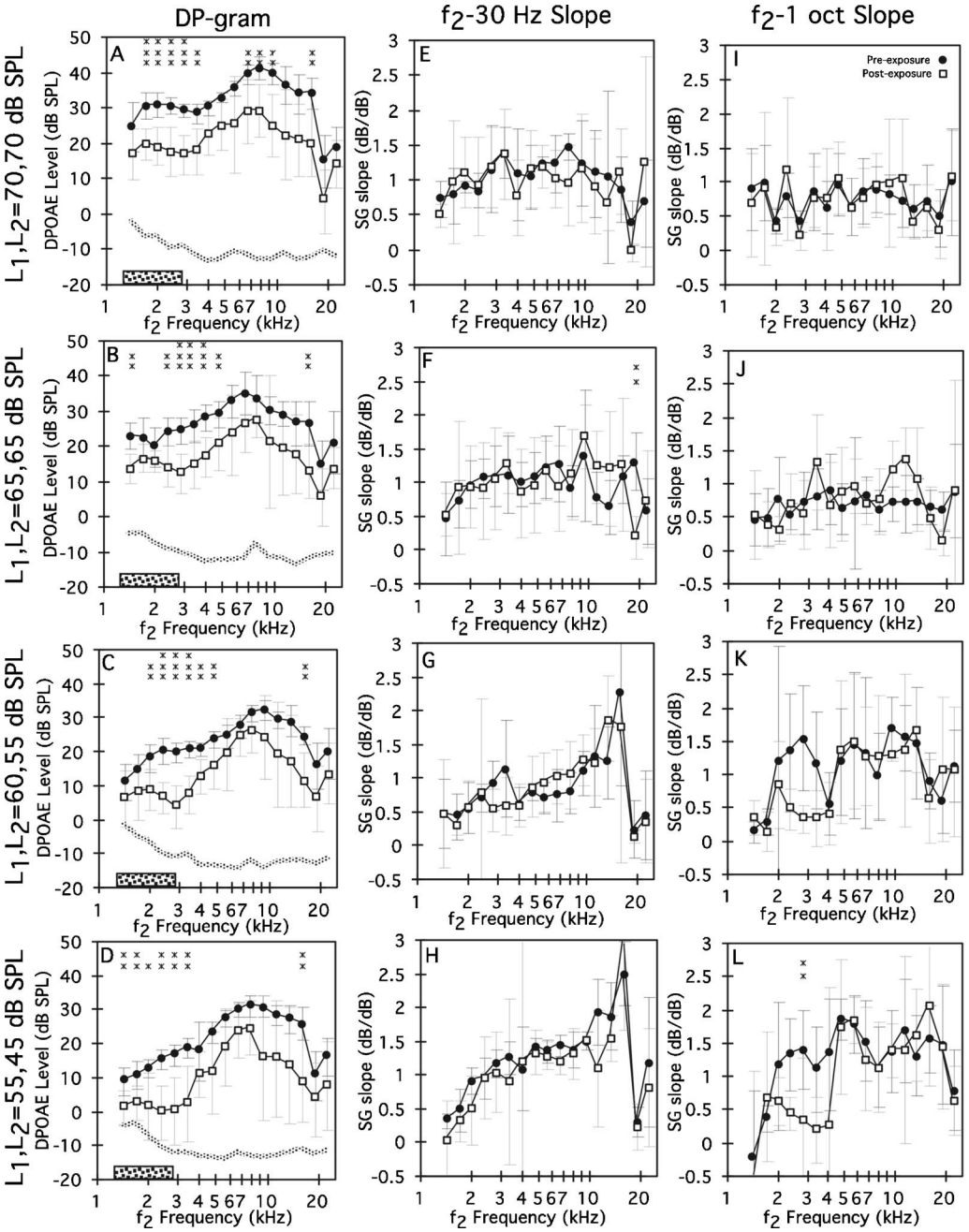

FIG. 5. Mean DP-grams and SG slopes computed before and after noise exposure for all four primary-tone levels. Average postexposure (open squares) DP-grams [(A)–(D)] clearly revealed consistent and significant losses as compared to preexposure levels (solid circles) regardless of primary-tone level. Similar comparisons for average SG slopes computed at f_2-30 Hz and f_2-1 oct demonstrated only two significant and seemingly spurious differences. However, at the two lowest primary-tone levels with STs at f_2-1 oct (K, L), SG slopes appeared to show a consistent trend towards reduced values in the 2–4-kHz region. The double and triple asterisks along the top of the plots indicate statistically significant differences at the $p<0.01$ and $p<0.001$ levels, respectively.

SPL [Fig. 8(H)]. In this instance, opposite results were apparent with thresholds decreasing with increased reductions in DPOAE levels. The last column of Fig. 8 shows similar plots for tip-to-tail differences. Here, it is clear that for the lowest test level [Fig. 8(L)], there was a significant tendency for tip-to-tail values to decrease in the presence of substantial decrements in DPOAE levels. Similar trends were observed for higher L_1, L_2 levels [Figs. 8(I) and 8(J)], but none of these were significant. Overall, for both suppression thresholds and tip-to-tail measures, the results of the regression analyses were not particularly convincing in that neither of these measures were very sensitive to noise-induced alterations to DPOAEs. However, for very low-level primaries, increasing cochlear dysfunction as indicated by greater changes in DPOAE levels was associated with both decreased suppression thresholds at f_2-1 oct and reduced tip-to-tail values.

IV. DISCUSSION

A number of previous studies have examined DPOAE STCs and other DPOAE-suppression parameters under sev-

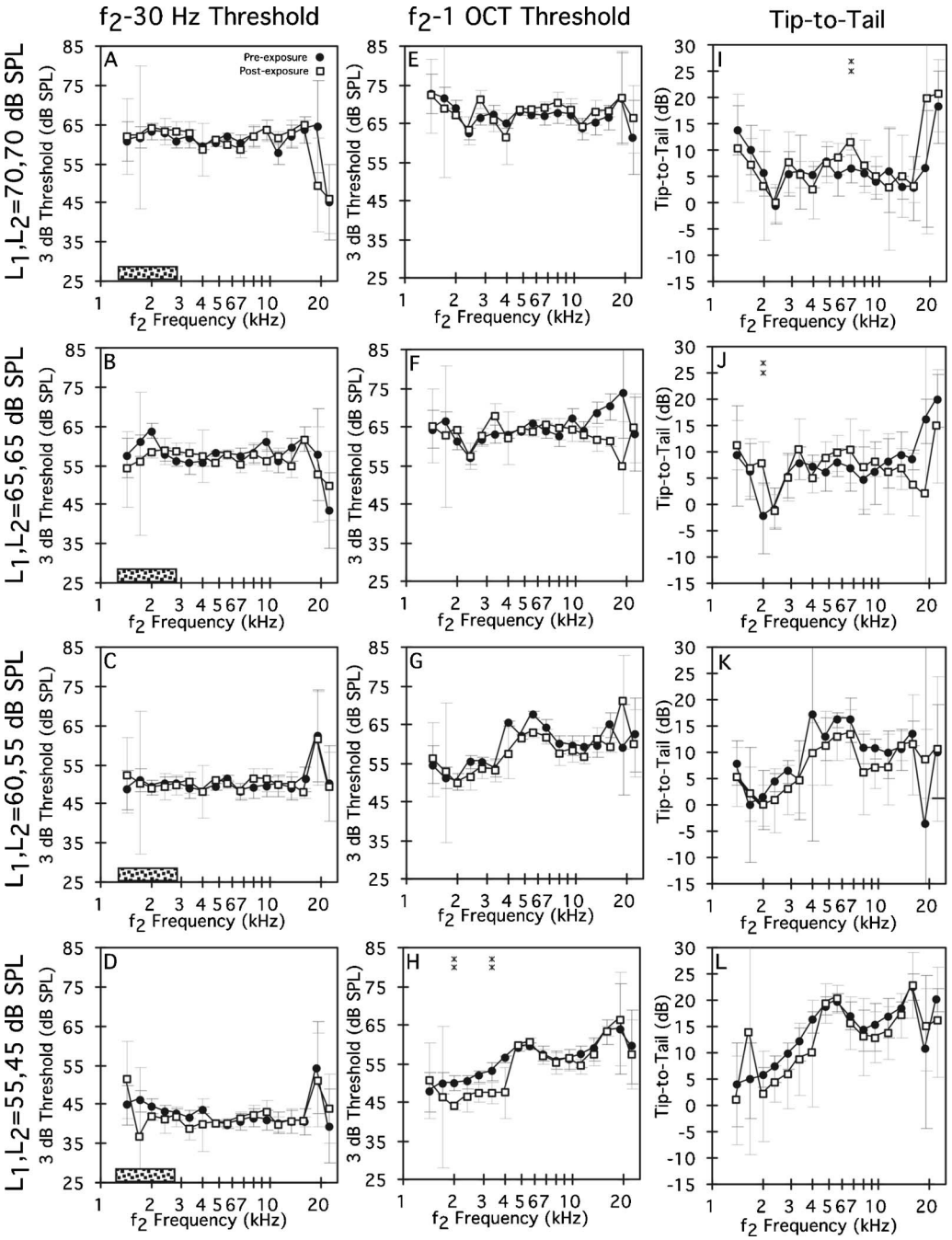

FIG. 6. Mean suppression thresholds and tip-to-tail measures computed before (solid circles) and after (open squares) noise exposure for four primary-tone levels. It can be seen that there were no systematic changes in these derived DPOAE-suppression measures across rabbits.

eral conditions including during normal development in human infants (e.g., Abdala, 1998, 2001b, 2004), in humans with SNHL (Abdala and Fitzgerald, 2003; Gorga *et al.*, 2003), and following deliberate cochlea insults in experimental preparations (Martin *et al.*, 1998a; Howard *et al.*, 2002, 2003). All these investigations typically based their findings on measures taken at only a few f_2 frequencies that evoked the $2f_1-f_2$ DPOAE. This approach may be adequate to describe DPOAE-suppression measures in normal ears, if it can be assumed that the underlying cochlear function is relatively invariant as a function of frequency. However, such an assumption may not be entirely defendable. For example, even during normal development, Abdala (1998) found little or no differences in suppression measures between premature neonates at 3000 Hz compared to adults, while the same measures collected at 1500 and 6000 Hz were different between the two subject populations. Consequently, even in "normal" ears the assumption of homogenous cochlear function across frequency needs to be viewed with caution. In ears with SNHL, cochlear function across frequency is by definition not uniform. Thus, suppression measures obtained at just a few f_2 frequencies may give false impressions regarding the overall sensitivity of these measures to cochlear insult.

In the present study, SG functions were obtained at two locations on the DPOAE STC, namely near the "tip," i.e.,

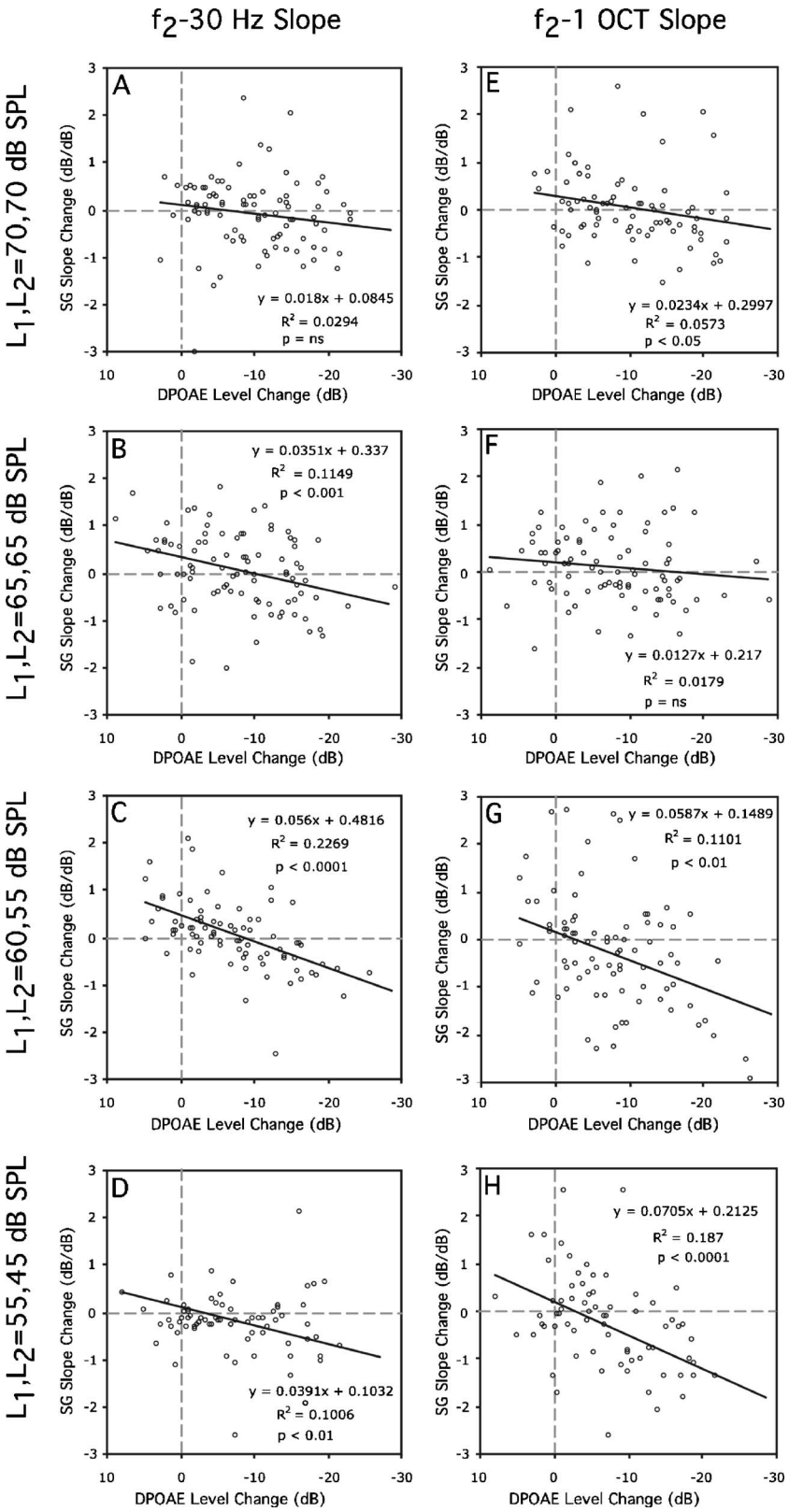

FIG. 7. Correlations computed between DPOAE losses and SG-slope changes at four primary-tone levels following noise exposure. SG slopes tended to decrease with increasing modifications in DPOAE levels in response to STs near f_2 [(A)–(D)] as well as for STs an octave below f_2 [(E)–(H)]. This relationship was significant in the majority of instances, thus establishing a tendency for SG slope to become shallower postexposure as DPOAEs decreased from their preexposure levels. In this and the subsequent figure, negative values on the abscissa represent instances when DPOAEs levels were enhanced following noise exposure.

near f_2 at f_2-30 Hz, and in the "tail' of the STC, i.e., at a distant site from f_2 at f_2-1 oct. From these measures, estimates of SG slopes, suppression thresholds, and STC tip-to-tail values were derived. It would be expected that sensitive measures of cochlear abnormality would be capable of "tracking" the functional damage pattern in, for example, ears with SNHL. To test this hypothesis, SG functions were obtained at the same f_2 frequencies used to collect DP-grams so that changes in these suppression parameters could be related in a straightforward manner to the pattern of cochlear dysfunction produced by deliberate noise exposure. It was anticipated that if the above-noted suppression measures were sensitive to cochlear malfunction, the pattern of DPOAE losses would be reflected by similar patterns of

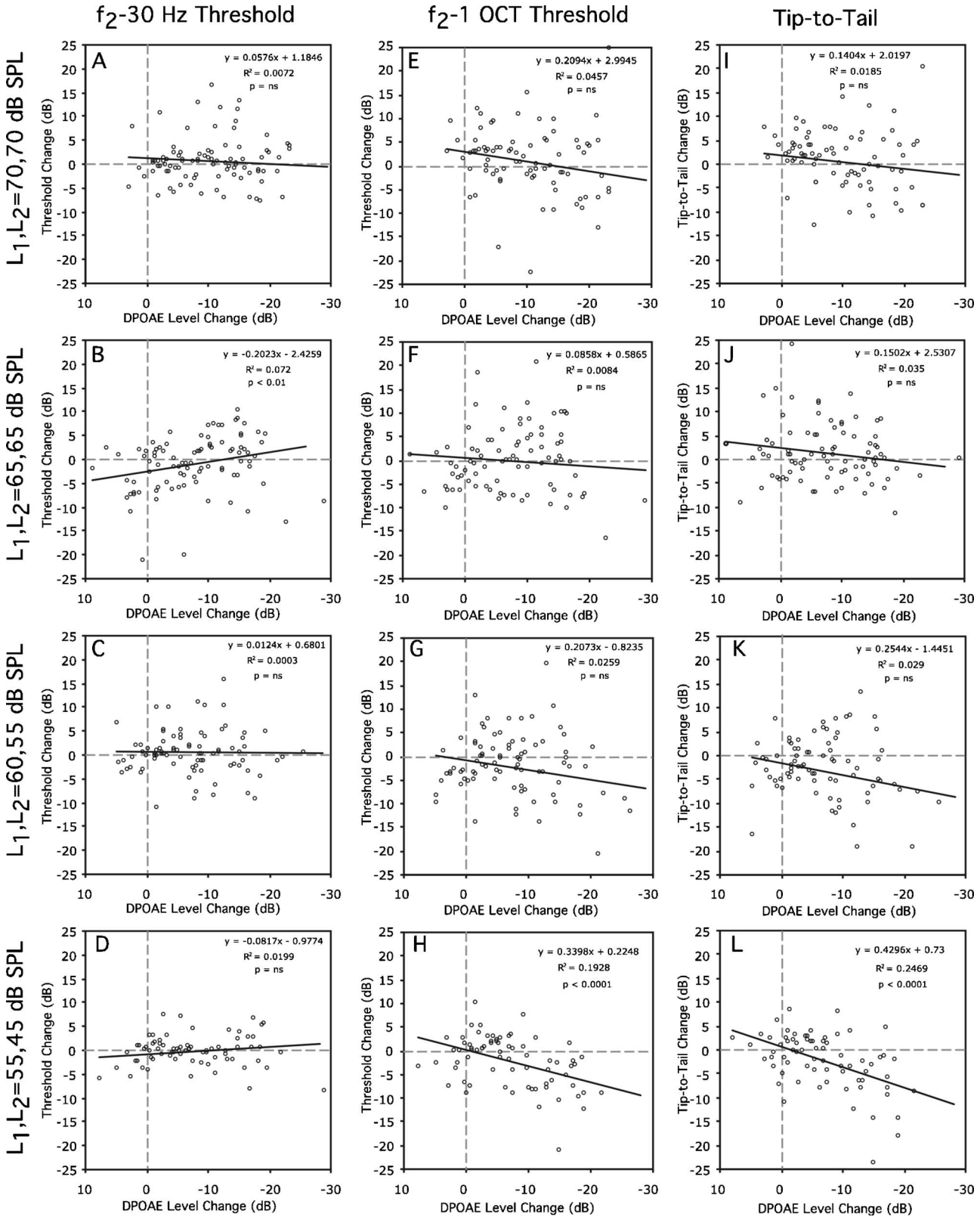

FIG. 8. Relation of suppression-threshold and tip-to-tail changes to reductions in DPOAE levels at four primary-tone levels. Suppression thresholds at $f_2 - 30$ Hz showed little evidence of a consistent correlation with changes in DPOAEs. However, both suppression thresholds at $f_2 - 1$ oct and tip-to-tail measures showed reliable decreases with noise-induced reductions in DPOAE levels.

change across frequency in SG slopes and in the various other suppression characteristics measured here. In general, this expectation was not confirmed by the results of the present investigation in that suppression measures averaged across subjects did not reflect the pattern of DPOAE loss as revealed by average DP-grams. However, when the amount of DPOAE loss was expressed as postexposure minus preexposure level differences, postexposure alterations were

weakly related to similarly calculated changes in SG slopes, suppression thresholds at f_2-1 oct, and tip-to-tail values in that significant correlations were obtained, depending upon primary-tone levels, for these specific suppression parameters.

A. Effects of noise exposure on DPOAEs and ABRs

The pattern of DPOAEs following noise exposure was in agreement with the results of previous studies in our laboratory and with the typical characteristics of noise-induced outer hair cell (OHC) damage in rabbits (Franklin *et al.*, 1991; Howard *et al.*, 2003). This DPOAE-loss pattern was generally confirmed in the present study by the pattern of noise-induced threshold shifts in ABRs. The finding of substantial correlations between ABRs and DPOAE measures was consistent with the notion that DPOAE losses as described by the DP-gram can reliably detect noise-induced injury to OHCs (e.g., Hamernik and Qiu, 2000; Davis *et al.*, 2004, 2005).

The most robust correlation between DPOAEs and ABRs was obtained for the lowest primary-tone level of $L_1, L_2 = 55, 45$ dB SPL, which is consistent with previous observations that lower primary-tone levels are more sensitive to cochlear dysfunction (e.g., Sutton *et al.*, 1994; Vazquez *et al.*, 2001). However, overall, highly significant correlations were obtained between ABR measures and DPOAE levels regardless of primary-tone level. These findings are consistent with recent investigations suggesting that DPOAEs are probably associated with the stereociliary transduction apparatus in that, at high levels of acoustic stimulation, DPOAEs are present even in mice lacking prestin, the molecular motor protein responsible for cochlear amplification (Liberman *et al.*, 2004). High-level DPOAEs can also map structurally intact OHCs in the absence of cochlear tuning (Carvalho *et al.*, 2004) and can, as well, assess the functional integrity of OHCs presumably at the level of their transduction channels (Avan *et al.*, 2003).

B. SG and SG slopes in normal and noise-damaged ears

One of the goals of this investigation was to characterize SG and SG slopes over a wide range of f_2 frequencies. One notable finding (see Fig. 2) was the variability in the contour plots of SG across frequency with respect to the amount of suppression that could be obtained for a given ST level. For example, sometimes "holes" were obtained in these plots where the ST was ineffective over a restricted but significant area of the plot. These findings suggest that previous results obtained at only a few frequencies may not be representative of a broader frequency span, especially in ears with SNHL. Such anomalies in the amount of suppression seemed to be "real" and not related to calibration artifacts in that they appeared in different places for different rabbits [e.g., compare the plots of Fig. 2(D) with those of Figs. 3(A) and 4(A)].

Other details previously described for SG can also be observed in the contour plots of Fig. 2. Thus, it can be seen that suppressors near f_2 (f_2-30 Hz) were more effective than suppressors more distant at f_2-1 oct. This difference is apparent in a variety of STC studies (e.g., Harris *et al.*, 1992; Brown and Kemp, 1984; Martin *et al.*, 1987, 1998b; Kummer *et al.*, 1995; Abdala *et al.*, 1996; Gorga *et al.*, 2002, 2003), and is more obvious at lower primary-tone levels. This finding is consistent with previous suggestions (Gorga *et al.*, 2002; Abdala and Chatterjee, 2003) that f_2 can be viewed as a probe and the ST as a masker.

In normal human ears SG slopes below f_2 have been reported by Abdala (1998) to be between 1 and 1.4 dB/dB. Kummer *et al.* (1995) noted slopes in the range of 1.5 and 2 dB/dB, and recently Gorga *et al.* (2002) uncovered similar slopes between 1.5 and 2.5 dB/dB, depending upon f_2 levels. In humans, SG slopes tend to be shallower for STs closer to f_2 (Kummer *et al.*, 1995; Gorga *et al.*, 2002), but this effect seems to be level- and frequency-dependent. In general, SG slopes in normal rabbits ranged from 0.5 to 1.5 dB/dB and tended to be somewhat shallower for STs at f_2-1 oct. Overall, SG slopes in rabbits also appeared to be a result of a complex interaction of ST frequency with respect to f_2 and the levels of the primary tones.

Although noise overexposure produced, on average, substantial decrements in DPOAEs (Fig. 5), there was little evidence overall for significant changes in SG slope, either near the tip of the STC (f_2-30 Hz) or in the STC tail region (f_2-1 oct). However, for f_2-1 oct at the two lowest primary-tone levels, there was a tendency for SG slopes to be shallower than for higher-level primaries. This tendency for low-frequency ST slopes to become shallower was also observed in humans with SNHL (Gorga *et al.*, 2003). In a small group of children with SNHL, Abdala and Fitzgerald (2003) described a contradictory trend for SG slopes in that they were abnormally steep. However, during development, neonates showed shallower SG for STs lower in frequency than f_2 (Abdala 2001a,b, 2004; Abdala and Chatterjee, 2003). Overall, though, in the noise-exposed rabbits of the present study, mean changes in SG slopes did not "track" average noise-induced alterations in DP-grams, thus suggesting that this measure was less sensitive to the aftereffects of overexposure, or that high variability in the data concealed the adverse effects of the OBN exposure on SG.

Regression analyses (e.g., Fig. 7) revealed a tendency for SG slopes both near f_2 and in the STC tail region to decrease (i.e., become shallower) as the reductions in DPOAE levels increased. Thus, the majority of the data collected here suggests that with sufficient noise damage, as indicated by reduced DPOAE magnitudes, SG slope trends were in the downward direction. In most cases, the scatter was appreciably large, thus suggesting that the variability in the SG-slope measures was a large contributor to the inability of this metric to track average changes in DPOAEs.

Shallower slopes presumably imply that the excitation pattern of the ST was more restricted or "focal" and that there was less upward spread of masking (Abdala and Fitzgerald, 2003) following noise exposure, because ST was less effective at the f_2 place. This explanation is not particularly compelling, because it would be expected that noise-induced damage would, if anything, decrease the sharpness of tuning and that this outcome would lead to broader excitation patterns. In the present study, the dysfunctional region

was not just restricted to the ST place, but often encompassed the f_2 place as well. This results in a very complicated situation that makes it difficult to predict the effects of noise overexposure on the slopes of SG. The overall result may depend upon the combined effects of damage to the active process affecting cochlear-amplifier gain and tuning at both the ST and f_2 sites.

C. Suppression thresholds in normal and noise damaged ears

The general phenomenon of "suppression threshold" is clearly evident in the SG contour plots of Fig. 2. Threshold in these plots represents the ST level required to produce the first 3-dB contour line. Thus, suppression thresholds with the ST at f_2-30 Hz were approximately 60 dB SPL for the $L_1=L_2=70,70$ dB SPL primary-tone condition and were considerably lower at 42 dB SPL for the $L_1,L_2=55,45$ dB SPL primary-tone combination. These results are consistent with STC tip thresholds in rabbits (Martin *et al.*, 1998a; Howard *et al.*, 2002, 2003) and similar relationships between primary-tone levels and suppression thresholds were also found for humans (e.g., Abdala *et al.*, 2001a,b; Gorga *et al.*, 2003; Martin *et al.*, 2003). Typically, suppression thresholds are within 10 dB of the level of the primary tones used to evoke the DPOAE, which is a general property of suppression in a nonlinear system such as the cochlea (Fahey *et al.*, 2000). This generalization also held true for suppression thresholds averaged across rabbits (see Fig. 6). As might be expected, thresholds were consistently higher for the f_2-1 oct condition in which the ST was more distant from the f_2 place.

Regardless of the ST condition (i.e., f_2-30 Hz or f_2-1 oct) there was no overall mean difference in suppression thresholds following noise exposure. A similar result was noted in a previous study (Howard *et al.*, 2003) for permanently noise-damaged rabbits where STC tip thresholds, on average, did not appear to be affected by noise exposure. Thus, in this and in a prior study, changes in suppression thresholds did not track the average pattern of DPOAE reduction produced by noise overexposure. Interestingly, in humans with SNHL, there also was little difference in suppression thresholds revealed by mean STCs (Gorga *et al.*, 2003).

Regression analyses revealed that suppression thresholds at f_2-30 Hz (i.e., equivalent to a STC tip threshold measure) across primary-tone levels [see Figs. 8(A)–8(D)] were not correlated with the extent of DPOAE decrements. However, during temporary noise insults in rabbits (Howard *et al.*, 2002), STC-tip thresholds tended to show very small, but significant, increases as DPOAE losses increased. In contrast, just the opposite effect was noted using loop diuretics to reversibly affect DPOAEs (Martin *et al.*, 1998a). For example, for a ST at f_2-1 oct, suppression thresholds consistently decreased as the reductions in DPOAE level increased. In terms of STCs, this infers that the tails of the STC were lowered with respect to the tips. During development, STC tip thresholds in adults were generally elevated relative to either term newborns or 3-month-old infants (Abdala, 2004). Like other suppression measures, it appears that depending upon the circumstances, alterations in cochlear function can have differing effects on STC tip thresholds.

D. Tip-to tail measures in normal and noise damaged ears

It has been suggested that tip-to-tail differences derived from STCs can provide estimates of cochlear-amplifier gain (e.g., Mills, 1998; Pienkowski and Kunov, 2001). In the present study, suppression thresholds at f_2-30 Hz and f_2-1 oct were used as representatives of STC tip and tail regions, respectively, to derive tip-to-tail difference measures of cochlear-amplifier gain. As primary-tone levels are increased it would be expected that the cochlear amplifier would be saturated and tip-to-tail differences or "gain" would decrease. This effect was observed in the present study [see Figs. 6(I)–6(L)] where tip-to-tail differences were about 5–7 dB at primary-tone levels of $L_1=L_2=70,70$ dB SPL, and increased to somewhere between 10 and 20 dB depending upon f_2 frequency at primary-tone levels of $L_1,L_2=55,45$ dB SPL. Similar results were obtained previously in rabbits over a wider range of primary-tone levels (Howard *et al.*, 2003). In humans, comparable effects of primary-tone level were observed for tip-to-tail differences from inspection of STCs obtained at different primary-tone levels (e.g., Gorga *et al.*, 2002, 2003; Martin *et al.*, 2003). In the present study, mean tip-to-tail measures [see Figs. 6(I) and 6(J)] were not changed following permanent noise-induced changes in DPOAE levels. These findings are in agreement with similar average data obtained in another group of rabbits with permanent noise-induced reductions in DPOAEs (Howard *et al.*, 2003). However, in the present study, regression analyses revealed that noise-induced decrements in DPOAEs were accompanied by decreases in tip-to-tail values. This outcome is consistent with the finding that f_2-1 oct suppression thresholds decreased, while suppression thresholds at f_2-30 Hz were unchanged. These results in rabbits are similar to those described by other investigators comparing tip-to-tail measures between hearing-impaired patients and normal-hearing human subjects (Gorga *et al.*, 2003).

V. CONCLUSIONS

DPOAEs showed good correlations with permanent noise-induced hearing loss as assessed by ABRs. Thus, DPOAEs decreased approximately 0.4 dB for every dB of ABR threshold shift. Moreover, all primary-tone levels were capable of detecting "hearing loss," but the $L_1=L_2=55,55$ dB SPL primary-tone combination produced the best correlation with ABR threshold shifts. The noise-exposure protocol produced permanent postexposure changes in DPOAEs that on average were significantly different from their corresponding preexposure values.

Contour plots of SG as a function of f_2 frequency revealed that growth of suppression was not uniform across frequency and that many anomalies were apparent in these plots. Overall, none of the suppression-based measures including SG slopes, suppression thresholds, or tip-to-tail mea-

sures were capable of "tracking" the pattern of noise-induced alterations to DPOAEs. This outcome suggests that the great variability apparent in the SG-contour plots from which these measures were extracted severely limited the ability of these measures to follow the DPOAE-loss pattern.

In contrast to the mean analyses, regression assessments relating the change in DPOAEs following noise exposure to the alterations in related measures of suppression revealed that for all three measures (SG slopes, suppression thresholds, and tip-to-tail measures) there were in some cases significant tendencies for these indices to change as the amount of DPOAE loss increased. In these instances, SG slopes tended to decrease or become shallower, and suppression thresholds at f_2-1 oct also decreased while those at f_2-30 Hz were unaffected, apparently accounting for the tendency for tip-to-tail measures to decrease with increasing reductions in DPOAE levels.

In summary, when obtained under controlled conditions, the present findings were consistent with previous findings in rabbits in that measures of suppression were relatively insensitive to substantial changes in DPOAE levels produced by various cochlear insults. Thus, measures of SG slope, suppression thresholds, and tip-to-tail values, even when collected across the same f_2 range and primary-tone levels, did not accurately mirror the related pattern of DPOAE loss. Although these measures were sometimes significantly correlated with the amount of DPOAE loss, in general, such metrics were characterized by great inconsistency. Such variability of these measures severely limited their usefulness for the detection of noise-induced cochlear dysfunction in rabbits, even under very controlled situations where a within-subjects postexposure minus preexposure experimental design was employed.

ACKNOWLEDGMENTS

This work was supported in part by the Public Health Service (NIDCD, DC000613, DC003114), the Research Fund of the Department of Otolaryngology, University of Colorado Health Sciences Center, Denver CO, and a grant to the University of Colorado School of Medicine (NIDDK: DK007496). The authors thank two anonymous reviewers for their many helpful comments and suggestions.

Abdala, C. (**1998**). "A developmental study of distortion product otoacoustic emission ($2f_1-f_2$) suppression in humans," Hear. Res. **121**, 125–138.

Abdala, C. (**2000**). "Distortion product otoacoustic emission ($2f_1-f_2$) amplitude growth in human adults and neonates," J. Acoust. Soc. Am. **107**, 446–456.

Abdala, C. (**2001a**). "Maturation of the human cochlear amplifier: distortion product otoacoustic emission suppression tuning curves recorded at low and high primary tone levels," J. Acoust. Soc. Am. **110**, 1465–1476.

Abdala, C. (**2001b**). "DPOAE suppression tuning: cochlear immaturity in premature neonates or auditory aging in normal-hearing adults?" J. Acoust. Soc. Am. **110**, 3155–3162.

Abdala, C. (**2004**). "Distortion product otoacoustic emission ($2f_1-f_2$) suppression in 3-month-old infants: Evidence for postnatal maturation of human cochlear function?" J. Acoust. Soc. Am. **116**, 3572–3580.

Abdala, C., and Chatterjee, M. (**2003**). "Maturation of cochlear nonlinearity as measured by distortion product otoacoustic emission suppression growth in humans," J. Acoust. Soc. Am. **114**, 932–943.

Abdala, C., and Fitzgerald, T. S. (**2003**). "Ipsilateral distortion product otoacoustic emission ($2f_1-f_2$) suppression in children with sensorineural hearing loss," J. Acoust. Soc. Am. **114**, 919–931.

Abdala, C., Sininger, Y. S., Ekelid, M., and Zeng, F. G. (**1996**). "Distortion product otoacoustic emission suppression tuning curves in human adults and neonates," Hear. Res. **98**, 38–53.

Avan, P., Bonfils, P., Gilain, L., and Mom, T. (**2003**). "Physiopathological significance of distortion-product otoacoustic emissions at $2f_1-f_2$ produced by high- versus low-level stimuli," J. Acoust. Soc. Am. **113**, 430–441.

Brown, A. M., and Kemp, D. T. (**1984**). "Suppressibility of the $2f_1-f_2$ stimulated acoustic emissions in gerbil and man," Hear. Res. **13**, 29–37.

Carvalho, S., Mom, T., Gilain, L., and Avan, P. (**2004**). "Frequency specificity of distortion-product otoacoustic emissions produced by high-level tones despite inefficient cochlear electromechanical feedback," J. Acoust. Soc. Am. **116**, 1639–1648.

Davis, B., Qiu, W., and Hamernik, R. P. (**2004**). "The use of distortion product otoacoustic emissions in the estimation of hearing and sensory cell loss in noise-damaged cochleas," Hear. Res. **187**, 12–24.

Davis, B., Qiu, W., and Hamernik, R. P. (**2005**). "Sensitivity of distortion product otoacoustic emissions in noise-exposed chinchillas," J. Am. Acad. Audiol., **16**, 69–78.

Fahey, P. F., Stagner, B. B., Lonsbury-Martin, B. L., and Martin, G. K. (**2000**). "Nonlinear interactions that could explain distortion product interference response areas," J. Acoust. Soc. Am. **108**, 1786–1802.

Franklin, D. J., Lonsbury-Martin, B. L., Stagner, B. B., and Martin, G. K. (**1991**). "Altered susceptibility of $2f_1-f_2$ acoustic-distortion products to the effects of repeated noise exposure in rabbits," Hear. Res. **53**, 185–208.

Gorga, M. P., Neely, S. T., Dorn, P. A., and Konrad-Martin, D. (**2002**). "The use of distortion product otoacoustic emission suppression as an estimate of response growth," J. Acoust. Soc. Am. **111**, 271–284.

Gorga, M. P., Neely, S. T., Dierking, D. M., Dorn, P. A., Hoover, B. M., and Fitzpatrick, D. F. (**2003**). "Distortion product otoacoustic emission suppression tuning curves in normal-hearing and hearing-impaired human ears," J. Acoust. Soc. Am. **114**, 263–278.

Hamernik, R. P., and Qiu, W. (**2000**). "Correlations among evoked potential thresholds, distortion product otoacoustic emissions and hair cell loss following various noise exposures in the chinchilla," Hear. Res. **150**, 245–257.

Harris, F. P., Probst, R., and Xu, L. (**1992**). "Suppression of the $2f_1-f_2$ otoacoustic emission in humans," Hear. Res. **64**, 133–141.

Howard, M. A., Stagner, B. B., Lonsbury-Martin, B. L., and Martin, G. K. (**2002**). "Effects of reversible noise exposure on the suppression tuning of rabbit distortion-product otoacoustic emissions," J. Acoust. Soc. Am. **111**, 285–296.

Howard, M. A., Stagner, B. B., Foster, P. K., Lonsbury-Martin, B. L., and Martin, G. K. (**2003**). "Suppression tuning in noise-exposed rabbits," J. Acoust. Soc. Am. **114**, 279–293.

Kemp, D. T. (**1979**). "Evidence of mechanical nonlinearity and frequency selective wave amplification in the cochlea," Arch. Oto-Rhino-Laryngol. **224**, 37–45.

Kummer, P., Janssen, T., and Arnold, W. (**1995**). "Suppression tuning characteristics of the $2f_1-f_2$ distortion-product otoacoustic emission in humans," J. Acoust. Soc. Am. **98**, 197–210.

Liberman, M. C., Zuo, J., and Guinan, J. J., Jr. (**2004**). "Otoacoustic emissions without somatic motility: can stereocilia mechanics drive the mammalian cochlea?" J. Acoust. Soc. Am. **116**, 1649–1655.

Martin, G. K., Jassir, D., Stagner, B. B., and Lonsbury-Martin, B. L. (**1998a**). "Effects of loop diuretics on the suppression tuning of distortion-product otoacoustic emissions in rabbits," J. Acoust. Soc. Am. **104**, 972–983.

Martin, G. K., Jassir, D., Stagner, B. B., Whitehead, M. L., and Lonsbury-Martin, B. L. (**1998b**). "Locus of generation for the $2f_1-f_2$ vs $2f_2-f_1$ distortion-product otoacoustic emissions in normal-hearing humans revealed by suppression tuning, onset latencies, and amplitude correlations," J. Acoust. Soc. Am. **103**, 1957–1971.

Martin, G. K., Lonsbury-Martin, B. L., Probst, R., Scheinin, S. A., and Coats, A. C. (**1987**). "Acoustic distortion products in rabbit ear canal. II. Sites of origin revealed by suppression contours and pure-tone exposures," Hear. Res. **28**, 191–208.

Martin, G. K., Stagner, B. B., Jassir, D., Telischi, F. F., and Lonsbury-Martin, B. L. (**1999**). "Suppression and enhancement of distortion-product otoacoustic emissions by interference tones above f_2. I. Basic findings in rabbits," Hear. Res. **136**, 105–123.

Martin, G. K., Villasuso, E. I., Stagner, B. B., and Lonsbury-Martin, B. L. (**2003**). "Suppression and enhancement of distortion-product otoacoustic emissions by interference tones above f_2. II. Findings in humans," Hear.

Res. **177**, 111–122.
Mills, D. M. (**1998**). "Interpretation of distortion product otoacoustic emission measurements. II. Estimating tuning characteristics using three stimulus tones," J. Acoust. Soc. Am. **103**, 507–523.
Pienkowski, M., and Kunov, H. (**2001**). "Suppression of distortion product otoacoustic emissions and hearing threshold," J. Acoust. Soc. Am. **109**, 1496–1502.
Sutton, L. A., Lonsbury-Martin, B. L., Martin, G. K., and Whitehead, M. L. (**1994**). "Sensitivity of distortion-product otoacoustic emissions in humans to tonal overexposure: time course of recovery and effects of lowering L_2," Hear. Res. **75**, 161–174.
Vazquez, A. E., Luebke, A. E., Martin, G. K., and Lonsbury-Martin, B. L. (**2001**). "Temporary and permanent noise-induced changes in distortion product otoacoustic emissions in CBA/CaJ mice," Hear. Res. **156**, 31–43.
Whitehead, M. L., McCoy, M. J., Lonsbury-Martin, B. L., and Martin, G. K. (**1995**). "Dependence of distortion-product otoacoustic emissions on primary levels in normal and impaired ears. I. Effects of decreasing L_2 below L_1," J. Acoust. Soc. Am. **97**, 2346–2358.

Use of stimulus-frequency otoacoustic emission latency and level to investigate cochlear mechanics in human ears[a)]

Kim S. Schairer,[b)] John C. Ellison, Denis Fitzpatrick, and Douglas H. Keefe
Center for Hearing Research, Boys Town National Research Hospital, 555 N. 30th Street, Omaha, Nebraska 68131

(Received 16 January 2006; revised 9 May 2006; accepted 21 May 2006)

Stimulus frequency otoacoustic emission (SFOAE) sound pressure level (SPL) and latency were measured at probe frequencies from 500 to 4000 Hz and probe levels from 40 to 70 dB SPL in 16 normal-hearing adult ears. The main goal was to use SFOAE latency estimates to better understand possible source mechanisms such as linear coherent reflection, nonlinear distortion, and reverse transmission via the cochlear fluid, and how those sources might change as a function of stimulus level. Another goal was to use SFOAE latencies to noninvasively estimate cochlear tuning. SFOAEs were dominated by the reflection source at low stimulus levels, consistent with previous research, but neither nonlinear distortion nor fluid compression become the dominant source even at the highest stimulus level. At each stimulus level, the SFOAE latency was an approximately constant number of periods from 1000 to 4000 Hz, consistent with cochlear scaling symmetry. SFOAE latency decreased with increasing stimulus level in an approximately frequency-independent manner. Tuning estimates were constant above 1000 Hz, consistent with simultaneous masking data, but in contrast to previous estimates from SFOAEs.
[DOI: 10.1121/1.2214147]

PACS number(s): 43.64.Jb, 43.64.Kc, 43.64.Ri [BLM] Pages: 901–914

I. INTRODUCTION

A. Sources of SFOAEs

Stimulus frequency otoacoustic emissions (SFOAE) are generated in the cochlea in response to sound. They can be generated by continuous tones, or primaries, of frequencies f_1 and f_2 presented at levels L_1 and L_2, respectively, and the SFOAE is recorded at either of the primary frequencies. Another way to specify the primaries is "probe" and "suppressor," meaning the SFOAE is recorded at the frequency of the probe that is presented in the presence of a suppressor. A review of the methods for extracting SFOAEs can be found in Schairer *et al.* (2003). The goals of this study are to measure SFOAE latency as a function of both stimulus frequency and level, to evaluate alternative source mechanisms of SFOAEs, and to use SFOAE latencies to indirectly estimate cochlear tuning using the SFOAE-source theory of linear coherent reflections.

Two theories based on forward and reverse transmission of mechanical energy along the basilar membrane (BM) have been proposed to account for the generation of SFOAEs. The first theory is linear coherent reflection (Shera and Guinan, Jr., 2003; Shera and Zweig, 1993; Zweig and Shera, 1995). This theory predicts that at low levels, SFOAEs are generated by coherent (i.e., phase-sensitive) reflections from a random distribution of impedance irregularities along the BM. Thus, the SFOAE measured at the probe frequency is dominated by energy reflected from impedance irregularities at the peak of the traveling wave near the tonotopic place of the probe frequency. The linear coherent reflection mechanism centers on the cochlear mechanics at the limit of low stimulus levels [below approximately 20 dB sound pressure level (SPL)] where the outer hair cell (OHC) functioning is linear (Zwicker, 1983; Zwicker and Schloth, 1984). However, it is important to note that the basic mechanism of linear coherent reflection is a linear scattering of the forward traveling wave along the BM due to a distribution of inhomogeneities in transmission characteristics. This basic "linear" mechanism is assumed present even at moderate and high stimulus levels in which the compressive nonlinearity of BM mechanics limits the growth of response near tonotopic place. The second theory posits that, in response to a sinusoidal excitation, a nonlinear distortion component is created on the BM, which thereby acts as a SFOAE source at the probe frequency (Brass and Kemp, 1993). Irrespective of the generator mechanism, a nonlinear SFOAE residual is measured using a "suppression paradigm," in which the presence of a second sinusoidal tone is assumed to suppress the traveling wave on the BM at the probe frequency, and this suppressed response is compared at the probe frequency with the response to the probe tone alone. The nonlinear SFOAE residual may be extracted even if the second tone does not fully suppress the probe tone, however, the maximum emission amplitude will not be produced (because suppression is incomplete), and other nonlinear effects may be produced. Both theories (linear coherent reflection and nonlinear distortion) require nor-

[a)]Portions of this work were presented in Schairer, K. S., Fitzpatrick, D., Goodman, S., Ellison, J. E., and Keefe, D. H. "Using level-dependent latencies to identify dominant SFOAE sources." Presented at the American Auditory Society 2004 Scientific and Technology Meeting Program, Scottsdale, AZ, March, 2004.

[b)]Electronic mail: kschairer@wisc.edu

mal, active function of the OHC, with its associated nonlinear response growth properties that influence the cochlear mechanics.

A third theory of SFOAE generation is based on forward transmission of mechanical energy along the BM to the tonotopic place, but reverse transmission of the SFOAE through cochlear fluid. Ren (2004) reported data that he interpreted as contradicting theories that stated that the return of energy forming a (DPOAE) is through backward, or reverse, traveling waves. Ren used scanning-laser interferometry to monitor BM vibrations at the f_1, f_2, and DPOAE frequencies $(2f_1-f_2)$ and concluded that only forward traveling waves were observed. Ren suggested that energy is returned to the base of the cochlea through a compression wave in the cochlear fluids, rather than through a reverse traveling wave on the BM, to generate emissions. Such a mechanism might also be present in SFOAE generation. This would contradict the nonlinear-distortion and coherent reflection theories, which are based on a reverse mechanical wave present on the BM. The current SFOAE data were collected with f_2/f_1 of 1.02–1.03, which is similar to the smallest f_2/f_1 ratio of 1.05 that Ren used.

The time it takes for the compression wave to travel from the tonotopic place to the stapes through the cochlear fluid is much shorter than the characteristic forward travel time for the mechanical traveling wave on the BM between stapes and tonotopic place, and is approximated as zero within the limits of our measurement precision. Thus, if SFOAE generation was dominated by this source, the latency of the resulting emission would be approximately equal to the forward travel time on the BM. A level-dependent transition between coherent-reflection emission and the compressional-wave mechanism would be associated with a reduction in SFOAE latency by a factor of approximately one-half.

Although it is generally accepted that SFOAEs are dominated by the linear coherent reflection source at low to moderate stimulus levels (40 dB SPL and slightly higher), it is less clear which source dominates SFOAE generation at higher stimulus levels. The next section describes how the SFOAE latency estimate τ, which is derived from the gradient of the SFOAE phase $\phi(f)$ by

$$\tau = -(1/2\pi)d\phi(f)/df, \tag{1}$$

can be used to separate the different sources. Latency estimates are used in the current experiment to characterize changes in dominant sources as a function of stimulus level.

B. Using SFOAE latency estimates to separate sources

In the current study, f_1 is the probe frequency at which the SFOAE is recorded, f_2 is the suppressor frequency, and $f_1<f_2$. The latency as a function of frequency has been used to separate the different mechanisms in DPOAE, which may be generated near the region of f_2 and a SFOAE in the region of $2f_1-f_2$. The DPOAE latency is defined by a relation analogous to Eq. (1), except that $\phi(f)$ is the phase at the DPOAE frequency as a function of the frequency that is swept. Procedures include sweeping f_2 with a fixed f_2/f_1, sweeping f_2 with a fixed f_1, or sweeping f_1 with a fixed f_2 (Kalluri and Shera, 2001; Knight and Kemp, 2000; Tubis *et al.*, 2000). The resulting DPOAE latency depends on the choice of the frequency sweep procedure. If f_2 is swept at fixed f_2/f_1, then the region of interaction, in relation to f_2 and f_1, will be constant, and the phase of the emission that arises from this region will be nearly constant as a function of f_2. This is reflected as zero group delay from the cochlea, but there may be delays associated with the middle ear and ear canal. Thus, nonlinear distortion sources at $2f_1-f_2$ are characterized by short, near-zero latencies that change gradually as a function of frequency. A similar method can be used to separate sources for SFOAEs, based on sweeping the probe tone at f_1 and using a suppressor tone f_2 such that f_2/f_1 is fixed.

The SFOAE phase is predicted to change rapidly as the probe frequency changes according to the linear coherent-reflection theory, because the energy is reflected from spatial irregularities at the peak of the traveling wave at the tonotopic place of the stimulus. Thus, linear coherent-reflection sources are characterized by steep phase gradients, and longer latencies that change as a function of frequency.

Multiple internal reflections also contribute to the SFOAE phase, and the individual internal reflections can be separated by time-domain analyses of SFOAE responses (Konrad-Martin and Keefe, 2005). In the bidirectional theory of SFOAE transmission, SFOAEs propagate in the reverse direction from the tonotopic region of the cochlea to the basal end of the cochlea, at which place the SFOAE is partially transmitted through the middle ear into the ear canal and partially reflected to form an internal reflection of the SFOAE. Such an internally reflected SFOAE is proportional to the basal reflectance at the oval window, and propagates in the forward direction to the tonotopic place where it may be rereflected in the reverse direction as an additional component of the SFOAE. This rereflected component is proportional to the apical reflectance. This process of reflections near the tonotopic place and the basal end of the cochlea produces a sequence of multiple internal reflections, such that the total SFOAE signal recorded in the ear canal is a sum of the SFOAE in the absence of such internal reflections and the partially transmitted SFOAE components associated with each internal reflection. If the magnitude of the product of the basal reflectance and apical reflectance is small compared to unity, then the effect of multiple internal reflections on the SFOAE phase can be modeled using a perturbative model. Such a model predicts a quasi-periodic fine structure, in which the phase is the sum of the SFOAE phase in the absence of internal reflections and an oscillatory term (Talmadge *et al.*, 1998; Zweig and Shera, 1995). The product of basal and apical reflectance magnitudes has been measured in a human ear as having an upper bound of 0.125 (Konrad-Martin and Keefe, 2003), which is sufficiently small to validate such a perturbative approach. The methodology described below for the current study smoothes the unwrapped SFOAE phase prior to calculating its phase gradient. This smoothing operation removes the fine structure associated with multiple internal reflections. Therefore, these multiple

internal reflections are unlikely to contaminate the SFOAE latency measurements reported herein. In addition, the effects on SFOAEs of multiple internal reflections diminish with increasing level, so that their impact on SFOAE latencies, even if present at low levels, would diminish at higher probe levels.

The original formulation of linear coherent-reflection theory, which was based on one-dimensional BM mechanics, proposed that SFOAE latency is determined by the BM latency (i.e., group delay) at the traveling wave peak (Zweig and Shera, 1995). This one-dimensional theory predicted that the forward and reverse BM travel times were equal. It follows that, except for any short latencies associated with ear-canal and middle-ear transmissions, the SFOAE delay is predicted to be approximately twice the travel time to the tonotopic place of the stimulus on the BM. Because the BM is tuned to higher frequencies toward the base and lower frequencies toward the apex, emissions that are dominated by coherent reflection are predicted to have latencies that decrease as frequency increases. These predictions are supported at low stimulus levels (and at least at higher frequencies) in measurements from cats, guinea pigs, and humans (Dreisbach *et al.*, 1998; Shera and Guinan, Jr., 2003). A more recent formulation of the linear coherent reflection theory based on a two-dimensional model of BM mechanics predicts that the SFOAE latency is somewhat less than twice the BM group delay (Shera *et al.*, 2005). Because of the lack of knowledge of BM group delay in human cochleae, the simpler prediction of the one-dimensional formulation of the linear coherent emission theory is mainly used in this report.

One current question is how SFOAE latency varies with stimulus levels, and because SFOAE latencies are expected to be related to BM latencies, it is relevant to consider published data on phase nonlinearity in BM mechanics. The amplitude of BM motion varies with stimulus level according to a compressive nonlinearity (Rhode, 1971). At low levels, the traveling wave peak for a sinusoidal stimulus is sharper than at higher levels, and occurs near the tonotopic or resonant place on the BM that corresponds to the frequency of the stimulus. As stimulus intensity increases, the peak broadens and shifts to a lower frequency. The nonlinearity in the magnitude of BM response to a pure tone is a compressive nonlinearity near the tonotopic place, and this nonlinearity in response magnitude is accompanied by a nonlinearity in the BM phase near the tonotopic place in the basal cochlear region of the squirrel monkey (Rhode and Robles, 1974), guinea pig (Nuttall and Dolan, 1993; Sellick *et al.*, 1982), cat (Cooper and Rhode, 1992), chinchilla (Ruggero *et al.*, 1997), and gerbil (Ren and Nuttall, 2001). Rhode and Cooper (1996) reported a qualitatively similar nonlinear BM phase response in the apical turn of the chinchilla cochlea. For measurements at the best-frequency (BF) place, the main pattern was that the phase at the BF typically varied little with the stimulus level, whereas the phase delay increased with increasing stimulus level at frequencies slightly below BF and decreased at frequencies above BF. This phase pattern is similar to neural patterns observed in single auditory nerve fibers (Anderson *et al.*, 1971), which suggests that BM nonlinearity is the source of this neural nonlinearity. Most of these studies of BM mechanics did not report the change in the slope of the BM phase with the stimulus level, which is needed to predict the latency to the BF place, but the results of all these studies are consistent with a decrease in the BM group delay at BF with an increasing stimulus level. An exception is that of Ruggero *et al.* (1997), who reported that the BM group delay in the tonotopic region of a 10 kHz tone in one cochlea decreased from 0.99 ms for 10-dB tones to 0.61 ms for 90-dB tones. The ratio of these group delays was approximately 0.6 between the highest and lowest stimulus levels.

If SFOAE latency is closely related to BM motion, as assessed through the group delay at the tonotopic place, then one would expect SFOAE latency to decrease as the stimulus level increases as long as SFOAEs are predominantly generated near the tonotopic place. However, there are complications with this comparison. First, BM measurements are taken at one point on the BM, whereas SFOAEs are recorded in the ear canal. Ear canal measurements of SFOAEs necessarily include reverse-propagation effects. Second, independent estimates of the group delay of the BM traveling wave are not available in human cochleae. These measurements cannot be done in humans, and hypotheses necessarily must rely on estimates from animal models (and possibly damaged cochleae), which may be functionally different than undamaged human cochleae. Thus, measurements of SFOAE latency in human ears provide noninvasive data on BM mechanics that are otherwise unavailable.

Goodman *et al.* (2003) used the SFOAE phase and time-domain analysis of data recorded in guinea pig ears to determine if variations in the SFOAE level as a function of frequency (i.e., microstructure) were due to variations in reflectance (e.g., impedance irregularities), and/or interference of two sources that varied in phase as a function of frequency (i.e., sources with different latencies). They concluded that SFOAE microstructure is due to a complex addition of two components, one with a slowly rotating phase (the nonlinear-distortion component) and one with a rapidly rotating phase (the linear coherent-reflection component). They stated that other sources were involved, such as variations in reflectance along BM and effects of multiple internal reflections. Linear reflection was described for one example as dominant at most levels, but the nonlinear-distortion component was dominant at a high level (86 dB pSPL).

In the current study, SFOAE latency was estimated at probe frequencies from 500 to 4000 Hz in 16 normal-hearing adult ears, and at probe levels of 40 to 70 dB SPL. Three possible outcomes of the experiment are described in the next section. Because independent estimates of BM travel time cannot be made, it is assumed that the latencies estimated in the lowest probe-level condition are estimates of the round-trip travel time, and that one half of those latencies represent forward travel time.

C. Possible outcomes

One possible outcome would be that SFOAE latency is independent of level. Latencies would decrease as frequency increases in accord with the linear coherent-reflection theory

at all probe levels. Latencies would be the same between the 40- and 70-dB SPL probe levels conditions and approximately equal to the round-trip travel time. This would suggest that SFOAEs are dominated by the linear coherent reflection source at higher levels, and that the BM travel time does not change as a function of level in normal human ears.

A second possible outcome would be that SFOAE latencies at high stimulus levels are short (near zero) and independent of frequency, as compared to long, and frequency dependent at lower levels. This would suggest that SFOAEs are dominated by nonlinear distortion at higher levels.

A third possible outcome would be that SFOAE latencies decrease with increasing stimulus level, but remain substantially larger than those expected if SFOAEs were dominated by nonlinear distortion at high levels. This decrease in latency might occur in two ways, one due to BM nonlinearity, and the other due to a level-dependent transition in the reverse BM signal between a mechanically generated transmission at lower stimulus levels and an acoustic compressional wave at higher stimulus levels.

With respect to BM nonlinearity, as reviewed above, the BM group delay decreases with increasing stimulus level. With the view that SFOAEs are generated within the region of the tonotopic place, it would be expected that SFOAE latencies would also decrease with increasing stimulus level. The extent of the change cannot be predicted. However, if SFOAEs are generated at higher stimulus levels by a combination of nonlinear distortion and coherent reflection, as in the theory of Talmadge *et al.* (2000), then SFOAE latency might decrease as probe levels increase, but to a lesser degree than if nonlinear distortion were the dominant source alone. Influences on OAEs due to nonlinearity associated with the stiffness of the OHC cilia have also been proposed (Liberman *et al.*, 2004).

With respect to the acoustic compressional wave mode, latency would be approximately one half of the latency predicted by the linear coherent-reflection theory. That is, latency would be equal to the time it takes for the traveling wave to peak at the tonotopic place (forward transmission time), because the reverse transmission would be through the fluid with negligible delay. However, the fact that BM nonlinearity also may reduce latency at high stimulus levels suggests that if both these mechanisms were present, the latency might be reduced by a factor even smaller than 0.5.

II. METHODS

A. Subjects

Sixteen adults (8 females, 8 males) ages 19 to 33 years (mean=23.75 years) participated as paid volunteers. The procedures were explained, and each subject signed a consent form before testing began. Subjects had air-conduction thresholds equal to or less than 15 dB (HL) at audiometric test frequencies of 250 to 8000 Hz in the test ear. Air-bone gaps were no greater than 10 dB, and tympanometry using a 226-Hz probe tone suggested normal middle-ear pressure and admittance (ranges: −50 to +35 daPa, 0.3 to 1.5 mL) in the test ear on the day of the test. Subjects were seated in a sound-attenuated booth during OAE testing, and were allowed to sleep or read quietly during data collection.

B. Stimuli and procedure

Stimuli were generated by an in-house software program, using a 24-bit Card Deluxe sound card (Digital Audio Labs) and transmitted to an Etymotic ER-10C low-noise probe microphone and receiver system that was modified to provide an extended 20-dB range of output. Stimuli were presented in a double-evoked procedure (Keefe, 1998) in a set of three intervals defined as follows. Stimulus f_1 was presented in interval one, f_2 in interval two, and both primaries were presented simultaneously in interval three. Responses were also acquired in each of the three intervals. SFOAEs were measured over the frequency range 500–4000 Hz, with separate recording sessions for each octave in the range. A real-time high-pass filter with cutoff frequency f_c was used to attenuate low-frequency noise below f_c, with f_c=250 Hz for measurements between 500 and 1000 Hz, f_c=500 Hz for measurements between 1000 and 2000 Hz, and f_c=650 Hz for measurements between 2000 and 4000 Hz.

The primary frequency ratio (suppressor to probe, or f_2 to f_1) was maintained in the range 1.02–1.03 at 65 frequency steps per octave, with variability in the frequency ratio arising from choosing each frequency from one of the center frequencies of the discrete Fourier transform response (DFT) bins. The sample rate was fixed at 32 000 Hz, but the number of samples differed across the three octaves in order to maintain the same number of frequency steps and similar frequency ratios across the three octaves. The response-buffer size, equal to the number of frequency bins of the DFT, was 4096 samples for SFOAEs from 500 to 1000 Hz, 2048 samples from 1000 to 2000 Hz, and 1024 samples from 2000 to 4000 Hz. The corresponding step size in frequency between adjacent SFOAEs was approximately 8 Hz from 500 to 1000 Hz, 16 Hz from 1000 to 2000 Hz, and 31 Hz from 2000 to 4000 Hz octave. Data were acquired at probe levels (L_1) of 40, 50, 60, 65, and 70 dB SPL, with a suppressor level (L_2) that was always 15 dB above L_1. A suppressor level of 15 dB was chosen because in preliminary studies, it was the best compromise between providing enough suppression to elicit a nonlinear residual across the range of desired L_1 conditions, and producing an adequate signal-to-noise ratio (SNR), which is reduced at higher stimulus levels due to level-dependent variability of the responses. Further, if the suppressor level was much more than 15 dB, it would have restricted the highest level of L_1 that could have been presented due to subject protection issues (i.e., limitation of exposure to loud stimuli) and the fact that probe distortion was observed at higher levels than those used in the experiments. An alternative method to achieve higher probe levels might be to use tone-burst stimuli.

Within each of the three stimulus/response intervals, the buffers just described were repeated six times, and the first two repetitions were discarded to remove stimulus artifact arising from buffer transitions. Between 500 and 1000 Hz, the entire buffer (i.e., set of three intervals) was repeated 16

times, for a total of 64 responses in the average SFOAE. Between 1000 and 4000 Hz, the entire buffer was repeated eight times, for a total of 32 responses in the average. More averaging was used in the lower octave to improve the signal-to-noise ratio (SNR). These procedures are similar in form, if not in exact numbers of repetitions, to procedures described more fully in Schairer *et al.* (2003).

Data were acquired in the left ear in eight subjects, and in the right ear in eight other subjects. Stimulus levels were varied (i.e., $L_1 = 40-70$ dB SPL) at each f_1 before moving to the next f_1. Data were collected over four to six sessions of 1 to 2.5 h each. The entire procedure was repeated in the right ear of subject PH02 and the left ear of subject PH12, with approximately two months between the first and second tests.

C. Analysis

In order to extract the nonlinear residual OAE (P_d) at the probe frequency of f_1, the sound pressure (P_1) was recorded in response to f_1 in interval one, P_2 in response to f_2 in interval two, and P_{12} in response to the combined presentation of the two stimuli in the third interval. The OAE pressure (P_d) was calculated as follows:

$$P_d = P_1 + P_2 - P_{12}. \quad (2)$$

The DFTs of the average pressure wave forms were calculated and evaluated at the probe frequency f_1. Note that although other OAEs are elicited (i.e., at distortion product frequencies), only the data from the frequency bin of the probe are presented. The distortion products and internal reflections may have an effect on the emission recorded at the probe frequency in the ear canal, but those effects were not specifically identified in this analysis. Also note that because the suppressor was always 15 dB above the probe level, full suppression may not have been obtained, particularly at low levels. The noise level (SPL) was calculated as the standard error of the responses across the repetitions of the entire buffer (Schairer *et al.*, 2003). System distortion was estimated by presenting the experimental conditions in a Bruel and Kjaer Ear simulator (coupler) Type 4157 (IEC 711 standard).

The SFOAE phase (at f_1) was calculated relative to the probe-stimulus phase as the phase of the SFOAE P_d (at f_1) minus the phase of the P_1 stimulus (at f_1). At each probe level, the resulting phase spectrum over frequency was unwrapped. A problem is that phase unwrapping is sensitive to the presence of noise, and any such errors in phase unwrapping introduce discontinuities in the phase gradient, and hence in SFOAE latency. To avoid this problem, Shera and Guinan (2003) included only SFOAE phase data at which the SNR $>$ 15 dB. Discontinuities in the phase gradients remained in the current data after imposing this SNR criterion. Shera and Guinan used a three-point interpolation to calculate a phase gradient, and hence a latency. To reduce noise, Shera and Guinan used a locally weighted scatter plot smoothed (loess) technique to calculate a latency estimate across subjects that varied smoothly with frequency. There is a tradeoff in requiring a higher SNR in order to have a smoother phase, and the fact that the range of SNR in SFOAE responses is limited. An alternative phase-smoothing technique was used in the current study to calculate SFOAE latencies, and is described after presenting the SFOAE phase results.

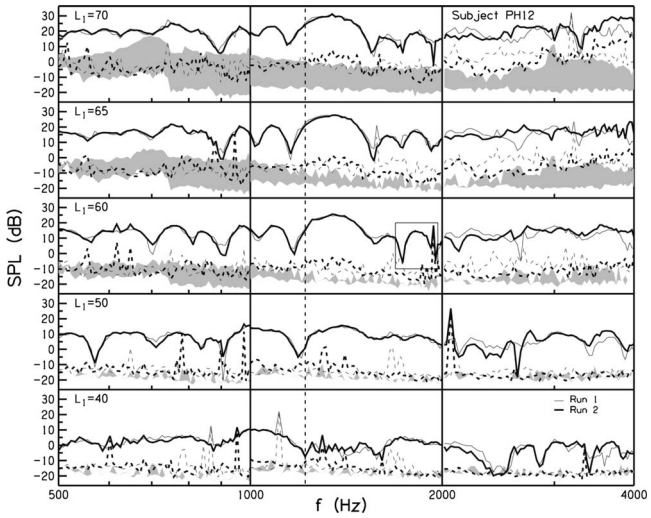

FIG. 1. Repeatability for SFOAE level in decibel SPL as a function of the probe frequency (f_1) in hertz for example subject PH12. The suppressor frequency (f_2), number of samples, and the number of stimulus repetitions were different across the three octaves, and were selected to maintain a f_2/f_1 ratio of 1.02–1.03 for 65 frequency steps per octave with a constant signal-to-noise ratio. Probe levels (L_1) of 70 to 40 dB SPL are shown in the different rows, top to bottom. Suppressor levels (L_2) were 15 dB above L_1. The thin lines represent run 1, and thick lines represent run 2, which was obtained about two months after the first run. The solid lines represent emission level, and the dashed lines represent the noise (or variability of the response). The shaded regions denote the area between the distortion and noise recorded in a coupler. The root-mean-square (rms) errors between emission levels from runs 1 and 2 were calculated across the three octaves in each condition, and they are shown in Table I. The vertical dashed line is centered on a minimum in the lowest L_1 condition, to help the reader see the shift in the minimum to lower frequencies as L_1 increases. The responses in the square in the $L_1 = 60$ condition are described in the text for a comparison to the phase plots in Fig. 3.

III. RESULTS

A. SFOAE level

The repeatability of individual-ear responses is first described. For subjects PH12 and PH02, Figs. 1 and 2 show the SFOAE level measured in two runs as a function of f_1 and as a function of L_1 from 70 to 40 dB SPL from the top to the bottom rows. The solid lines represent the emissions and the dashed lines represent the noise. The gray shading represents the region between the distortion and noise recorded in an IEC 711 standard coupler. Any emissions that fall into this region are questionable.

Noise level increased with increases in level for both subjects. This is consistent with previous studies that demonstrated stimulus level-dependent variability in input-output functions at probe frequencies of 1000, 2000, and 4000 Hz (Schairer *et al.*, 2003; Schairer and Keefe, 2005). This stimulus level-dependent increase in noise was not observed in the coupler. The shaded areas increased with increasing level because the distortion recorded in the coupler increased without a corresponding increase in noise level.

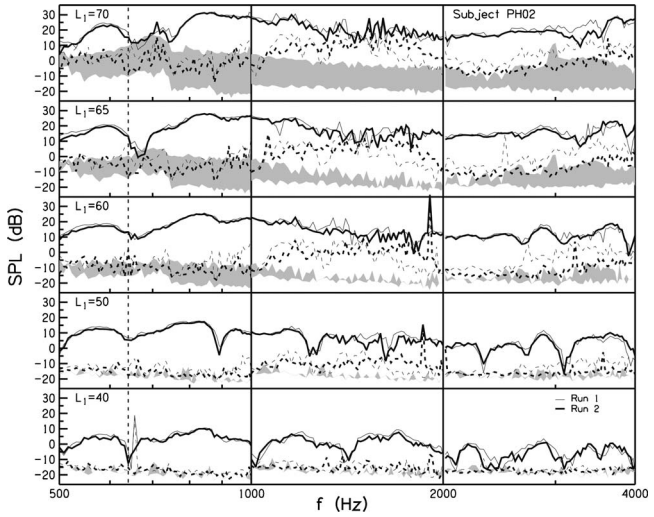

FIG. 2. Repeatability of SFOAE SPL for subject PH02 in the same format as for Fig. 1.

The fine structure, i.e., the pattern of maxima and minima in SFOAE level, in PH12's ear was repeatable in general in run 1 (thin line) and run 2 (thick line), although less repeatable between 2000 and 4000 Hz. The linear coherent-reflection theory predicts that minima in the SFOAE level occur because wavelets that are scattered from random spatial fluctuations, and that vary in phase, cancel each other to varying degrees at different frequencies (Zweig and Shera, 1995). Although DPOAE fine structure increases with decreasing stimulus level (He and Schmiedt, 1997; He and Schmiedt, 1993), such a trend in SFOAE fine structure was not clearly observed in the current study.

For subject PH12, the minima tended to move to lower frequencies as L_1 increased. The dashed vertical line is centered at a minimum in the $L_1=40$ condition as a guide to show how the minimum gradually shifted to lower frequencies with increases in L_1. The SNR was repeatable except for a few sharp maxima in the noise floor (perhaps when the subject moved), and the higher noise level in run 1 across the 2000–4000 Hz range. The presence of noise peaks, such as around 2000 Hz in the $L_1=50$ condition where SNR becomes 0, was associated with a discontinuity in SFOAE phase and hence latency.

The fine structure for PH02 was repeatable and did not decrease with decreasing stimulus level as much as for PH12. The minima in the fine structure also did not show the same trend toward lower frequencies with increasing level, as seen in PH12. Differences in noise in one octave relative to the others may have occurred because each octave was recorded in a separate session. However, the noise was larger in the 1000 to 2000 Hz range for both runs (relative to the flanking frequency ranges) in subject PH02. If the increased noise were due to changes in subject state or poor probe fit, it would not be expected to be repeatable. Because it was repeatable, it suggests that this ear may be more susceptible to level-dependent response variability in the 1000–2000 Hz range.

TABLE I.

Subject	L_1 condition	RMS error (in dB) of SNR run 1 vs run 2	RMS error (in cycles) of phase run 1 vs run 2
PH02	40	*4.46*	*1.32*
	50	6.55	1.01
	60	*8.55*	*0.10*
	65	8.28	0.71
	70	7.21	0.64
PH12	40	5.30	0.12
	50	5.83	1.06
	60	7.03	0.28
	65	7.05	0.88
	70	6.96	0.30

Repeatability was quantified by calculating the root-mean-square (rms) error of the SNR (in decibels) across the two runs summed over all frequencies in each L_1 condition. Table I shows the rms error in all conditions for both subjects (with minimum and maximum levels in bold italics). The errors in SNR ranged from 4.46 dB for subject PH02 in the $L_1=40$ condition to 8.55 dB for the same subject in the $L_1=60$ condition. An important contributor to this error was the presence of large noise spikes at a few frequencies. The noise spikes were most likely due to subject movements that momentarily increased the variability of the response. Once the variability increased, there were not enough stimulus presentations to average out the variability for that particular data point.

B. SFOAE phase

Figures 3 and 4 show repeated measurements of the unwrapped SFOAE phase spectra for subjects PH12 and PH02. Parameters are represented as in Figs. 1 and 2, except in Figs. 3 and 4, the dashed lines represent the phase estimated from the coupler measurements. As expected, there was no

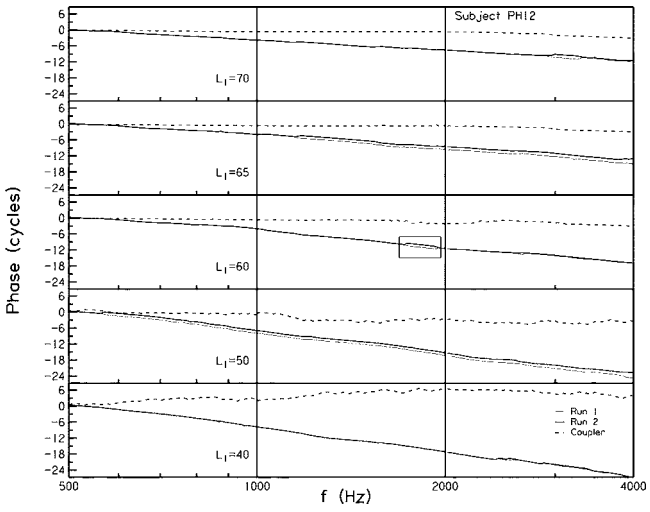

FIG. 3. Repeatability for SFOAE phase for subject PH12 as a function of f_1. Parameters are represented as in Fig. 2, except in this figure, the dashed lines represent the phase estimated from the coupler measurements. The rms errors between phase from runs 1 and 2 in each condition are shown in Table I. The phase measurements in the square in the $L_1=60$ condition are described in the text for comparison with the level measurements in Fig. 1.

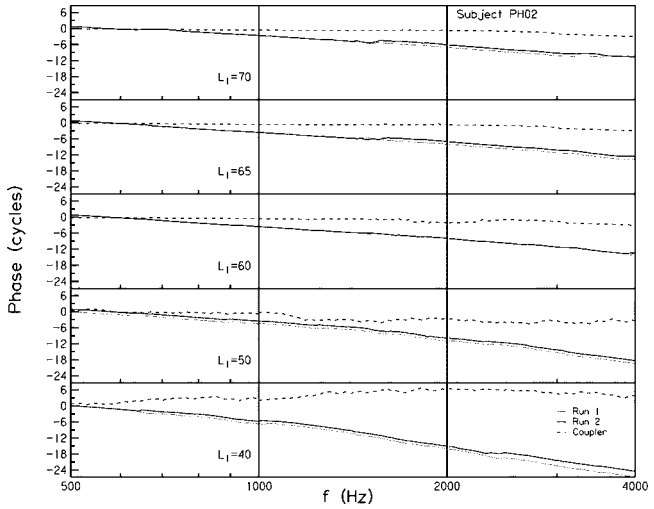

FIG. 4. Repeatability for SFOAE phase for subject PH02 in the same format as Fig. 3.

frequency or level dependence of phase in the coupler. In each subject's ear, the SFOAE phase decreased with increasing frequency, and its phase gradient became shallower as L_1 increased.

The SFOAE phase differed across the two runs at frequencies in which the SNR was reduced by noise spikes. However, the SFOAE phase difference between the two runs was sometimes small even at frequencies where the SNR was small. For subject PH12, in the $L_1=60$ condition over a range from 1000 to 2000 Hz, there was a sharp notch in emission level (see square in Fig. 1), but there was a difference in SNR across the two runs because the noise was larger in run 1. The corresponding SFOAE phases (see square in Fig. 3) deviated from each other. At a slightly higher frequency, there was a peak in the noise for run 2 and (coincidentally) a notch in emission level in run 1, and the SFOAE phases in overlapped again. This is similar to the steps in phase corresponding to minima in the amplitude microstructure observed in guinea pig (Goodman *et al.*, 2003).

The rms errors in SFOAE phase from runs 1 and 2 were calculated across the three octaves, and are shown in Table I. The rms errors ranged from 0.10 cycles in the $L_1=60$ condition for subject PH02 to 1.32 cycles in the $L_1=40$ condition for the same subject. A rms phase error of one or more cycles likely corresponds to an effect of noise in the phase-unwrapping operation.

It might be expected that the smallest SNR error would be associated with the smallest rather than the largest phase error. A comparison of the emission level (Fig. 2) and phase (Fig. 4) for this subject explains the trend. In the $L_1=40$ condition in Fig. 2, there was a sharp notch in emission level for both runs near 640 Hz, and a peak in the noise at a slightly higher frequency for run 1. Otherwise, the SNR was similar across the three octaves for both runs. In the phase plot for the corresponding condition in Fig. 4, there was a deviation in the phase near 640 Hz, which is likely associated with the noise spike in the SNR. Such a spike would produce an error in the phase unwrapping that might influence all higher frequencies, thus leading to a large rms phase error, as was observed. The effect of the noise spike at 640 Hz would produce only a localized spike in the SFOAE latency near 640 Hz.

C. Spline method to smooth SFOAE phase

SFOAE latency was calculated using two approaches in this study using different subject inclusion criteria. These approaches were to (1) unwrap phase, estimate the latency in each ear from phase gradients based on a three-point-finite-difference method, and smooth latency across frequency using a loess approach or (2) unwrap phase, smooth the phase across frequency for each ear using a smoothed cubic-spline interpolation, and then calculate latency as the derivative of the spline function. The first approach replicated the method of Shera and Guinan (2003). Because the calculation of the phase gradient is highly sensitive to noise, Shera and Guinan used an inclusion criterion that the SFOAE SNR exceed 15 dB. Our simulations for a tone in Gaussian noise showed that smaller SNR criteria than 15 dB were inadequate for extracting the signal phase gradient from noise at the frequency of the tone, and that even a 18 dB SNR criterion might be advisable. However, an inclusion criterion of 15 dB SNR may exclude many SFOAE responses, e.g., at frequencies where the noise is high, the stimulus level is low, or near a minimum in the fine structure of the SFOAE SPL.

In the second method, the SFOAE phase was fitted using a smoothed cubic-spline interpolation (based on the function CSAPS in the MATLAB SPLINE TOOLBOX) in which the phase data were weighted at each frequency by the measured SFOAE SNR. The benefit of this approach is that SNR criterion of 6 dB could be used. Thus, SFOAE responses with SNR between 6 and 15 dB that would have been excluded with the Shera and Guinan (2003) method were retained in the smoothed spline approach. Other inclusion criteria with larger SNR criteria than 6 dB were explored in analyses using the smoothed spline procedure, but the advantages of excluding individual noisy data were more than offset by the advantages of including more data at the lower and upper end of the frequency range and by the smoothing phase rather than the phase gradient. The SFOAE latency was calculated using Eq. (1) by differentiating the spline fitting function.

While a cubic spline function fits a smooth line through a given set of data, i.e., the unwrapped phase over a discrete set of frequencies, the resulting smooth line does not pass through each data point but it minimizes, instead, the roughness, or curvature, of the line. A smoothing parameter p is an input to the MATLAB command CSAPS, and is chosen in the range from 0 to 1, such that $p=0$ corresponds to a least-squares linear fit to the data, which is the maximal smoothing that can be applied, while $p=1$ corresponds to a cubic spline function with no smoothing, but which passes through each data point.

The effect of smoothing the unwrapped SFOAE phase response in subject PH02 is shown in Fig. 5, which plots results obtained at varying L_1 for an inclusion criterion that the SFOAE SNR exceeded 6 dB and using $p=0.1$. In this

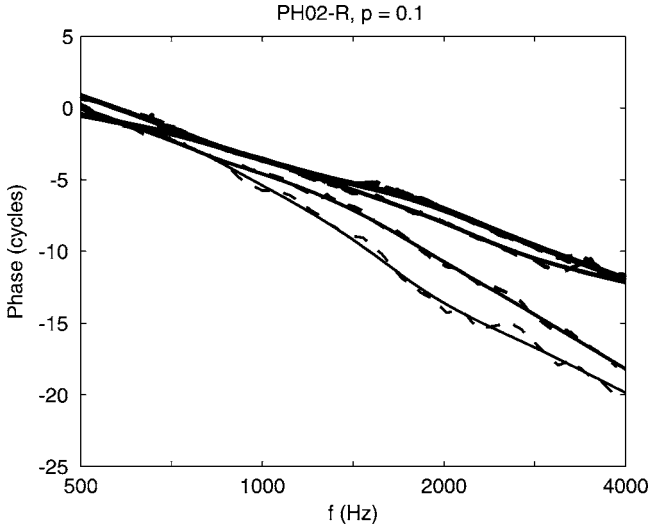

FIG. 5. The unwrapped SFOAE phase response for subject PH02 is shown for the raw data (dashed lines) and the smoothed spline fit to the data (solid lines) with $p=0.1$. Increasing line thickness represents SFOAE responses measured at increasing L_1 (40, 50, 60, 65, and 70 dB SPL). Raw data are plotted only for SNR > 15 dB SPL while the smoothed spline fit was calculated for data satisfying SNR > 6 dB.

and all subsequent spline fits, the spline was calculated on a logarithmic (i.e., octave) frequency axis, because all results were plotted on this axis, even though the latency is defined with respect to a derivative of the spline function fitting the phase $\phi(f)$ on the linear frequency axis [see Eq. (1)]. Note that in Fig. 5 (and in Fig. 6, which is derived from Fig. 5), the lines representing the two highest level conditions are difficult to differentiate because they overlap (i.e., the data for this subject were nearly identical in those conditions). Only the data points that satisfied the SNR criteria were included because it would have made the figure even more difficult to interpret if all data points were included. Refer to Fig. 7 to see another comparison of the two different SNR rules, and how they affected the estimated latencies.

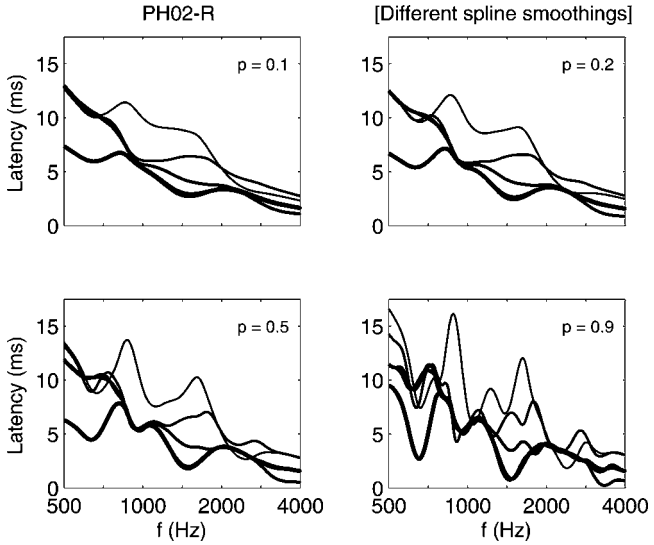

FIG. 6. Effect of smoothed spline fit parameter p on the resulting estimates of SFOAE latency in ms. Stimulus level is encoded by line thickness as in Fig. 5, and each panel represents a particular value of p ranging over 0.1, 0.2, 0.5, and 0.9.

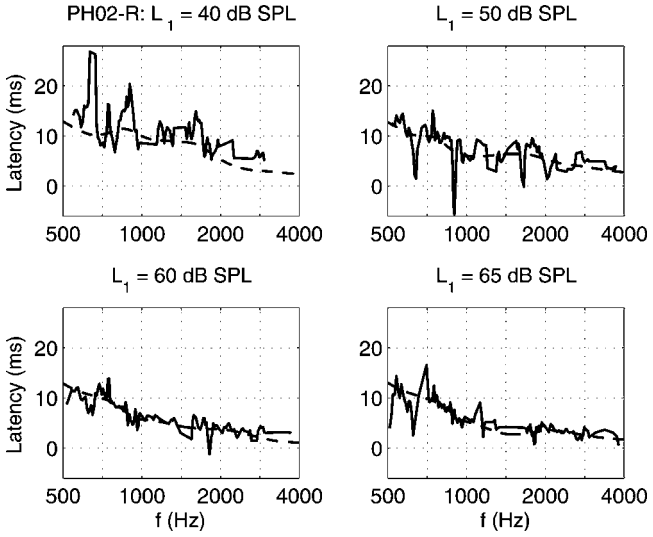

FIG. 7. Comparison for subject PH02 of the SFOAE latency in ms obtained using the smoothed-spline procedure (dashed line) versus that obtained using a three-point finite difference method (solid line). The inclusion criteria were 6 dB for the smoothed-spline method and 15 dB for the three-point finite difference method. Each panel shows SFOAE latency for fixed L_1 (40, 50, 60, and 65 dB SPL).

D. SFOAE latency

The influence of varying p on estimating the SFOAE latency is shown in Fig. 6 for the same subject PH02. With small amounts of smoothing ($p=0.9$), the SFOAE latency curve fluctuated with small values occurring in frequency ranges where the SNR was poor. With progressively smaller values of p at 0.5, 0.2, and 0.1, the estimated latency for the subject was much smoother. The smoothing achieved by using $p=0.1$ corresponds to the smoothed phase response in Fig. 5, and was used for all subsequent analyses.

SFOAE latency estimates are compared for the same subject PH02 in Fig. 7 at four L_1 levels (40, 50, 60, and 65 dB SPL) for estimates calculated using the smoothed spline fit to the phase versus those calculated using a method similar to that of Shera and Guinan (2003), i.e., data were included if the SNR > 15 dB, and a three-point-finite-difference approximation was used to calculate the latency. The single-subject latencies estimated using the smoothed spline fits were smoothed at all L_1 in this and other subjects. However, the latencies estimated using the finite-difference method applied to the unsmoothed phase were much noisier, particularly at low L_1 where the SNR was poorer, although always at least 15 dB. Nevertheless, the underlying mean trends of these latency estimates were similar.

Group results are next discussed. One of the 16 subjects had a low SFOAE SNR across much of the frequency range, and the resulting estimates of SFOAE latency were difficult to interpret. This subject was excluded from the group results, which were thus based on responses in 15 subjects, for which the mean and the standard error (SE) of the mean were calculated.

It is convenient to represent the SFOAE latency $\tau_{SF}(f,L_1)$ as a function of frequency and stimulus level in terms of a dimensionless SFOAE latency $N_{SF}(f,L_1)$ defined by

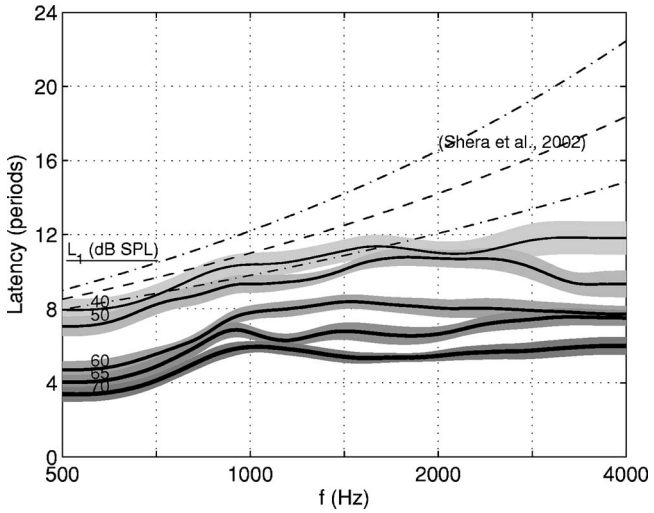

FIG. 8. The group means of SFOAE latency (solid lines) are plotted nondimensionally in units of the numbers of periods at the SFOAE frequency, with increasing line thickness representing increasing L_1 (40, 50, 60, 65, and 70 dB SPL). The gray fill pattern about each mean represents ±1 SE of the mean SFOAE latency. The three dashed lines show the mean and the 95% confidence interval of the SFOAE latencies reported by Shera *et al.* (2002) for a stimulus level of 40 dB SPL.

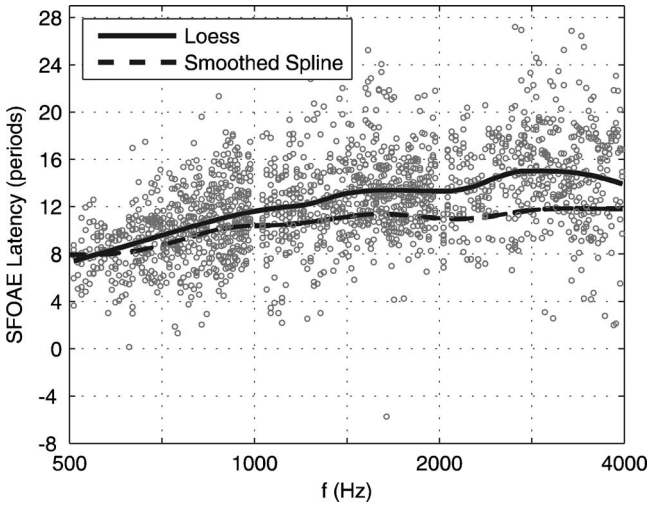

FIG. 9. Group measurements of SFOAE latency in periods measured with $L_1=40$ dB SPL are shown for latencies calculated using the smoothed spline fit of SFOAE phase and using a three-point finite difference method followed by a loess fit to the data. The raw three-point finite difference estimates of SFOAE latency are shown as circle symbols (1735 estimates), such that the phase data were only included if the SNR > 15 dB. The loess fit to these data is shown as the solid line. The smoothed spline fit to these data, based on an inclusion criterion that the SNR > 6 dB, is shown as the dashed line (see the same curve in Fig. 8 for $L_1=40$ dB SPL).

$$N_{SF}(f,L_1) = f \times \tau_{SF}(f,L_1), \tag{3}$$

in which $N_{SF}(f,L_1)$ is the SFOAE latency measured as the number of periods at the SFOAE frequency f (Shera and Guinan, Jr., 2003). This representation is useful in assessing the extent to which the cochlea satisfies a scaling symmetry. In a scaling-symmetric cochlea, $N_{SF}(f,L_1)$ is predicted to be independent of frequency (Zweig and Shera, 1995).

Figure 8 shows the group mean ± SE of the dimensionless SFOAE latencies $N_{SF}(f,L_1)$, which are plotted as black lines and gray fills, respectively, at each L_1, such that the mean $N_{SF}(f,L_1)$ at the lowest L_1 is the thinnest line in this and subsequent figures. At each L_1, $N_{SF}(f,L_1)$ was approximately constant from 1000 to 4000 Hz, and was shorter below 1000 Hz. The latency $N_{SF}(f,L_1)$ in the $L_1=40$ condition was approximately 11–12 periods. The latency $N_{SF}(f,L_1)$ decreased with increasing level in a systematic manner, although the SE of the latencies at L_1's of 40 and 50 dB SPL had substantial overlap from 500 to 3000 Hz. The corresponding power-law fits to $N_{SF}(f,L_1)$ reported by Shera *et al.* (2002) for a L_1 of 40 dB SPL are also plotted for the mean and 95% confidence interval about the mean of their subject group data. The latency results at 40 dB SPL are in agreement with current results at low frequencies. However, the mean latency reported by Shera *et al.* exceed the current results somewhere in the range above 1200–1800 Hz, depending on the choice of criterion, with the largest discrepancies observed at 4000 Hz (latency estimates of 18 periods versus 12 periods).

To better understand the possible reasons underlying this discrepancy above 1200–1800 Hz in the SFOAE latencies, the group SFOAE latencies in the current study were also calculated using the three-point finite difference method, in which a SNR inclusion criterion of 15 dB was used and the loess smoother was applied to the group results (Shera *et al.*, 2002; Shera and Guinan, Jr., 2003). It is sufficient to compare results at the particular L_1 of 40 dB SPL common to both studies. The results for the current dataset show that the loess procedure estimated a slightly higher SFOAE latency than did the smoothed spline procedure (see Fig. 9), but the loess fit remained lower at high frequencies than the power-law fit reported by Shera *et al.* (2002). For example, the loess fit at 4000 Hz in the current data was approximately 14–15 periods, which is less than the mean of 18 periods reported by Shera *et al.* and slightly below their 95% confidence interval (see Fig. 8). Both the smoothed-spline and loess fits to the SFOAE latency data show a substantially constant number of periods between 1000 and 4000 Hz. No SE was calculated in the loess procedure, but the scatter in the group data of Fig. 9, which is consistent with the scatter in the individual-ear data in Fig. 7, is considerably larger than the SE results found using the smoothed-spline fits (see Fig. 8). Thus, the loess procedure partially accounts for the discrepancy in the SFOAE latency results of Shera *et al.* compared to the current study using the smoothed spline procedure, but the choice of procedure does not account for the magnitude of the discrepancy at 4000 Hz.

The level dependence of SFOAE latency in the current group results was assessed by calculating the change in latency as a function of L_1 relative to the latency measured at the lowest level. Each ratio of the SFOAE latency at L_1's of 50, 60, 65, and 70 dB SPL to that at L_1 of 40 dB SPL is plotted in Fig. 10. Each ratio is the same, whether latencies are measured as $\tau_{SP}(f,L_1)$ (in ms) or as $N_{SF}(f,L_1)$ (in periods). At the largest L_1(70 dB SPL), the latency was reduced to approximately one half of its value at the lowest L_1, independent of frequency (to within the SEs of measurement).

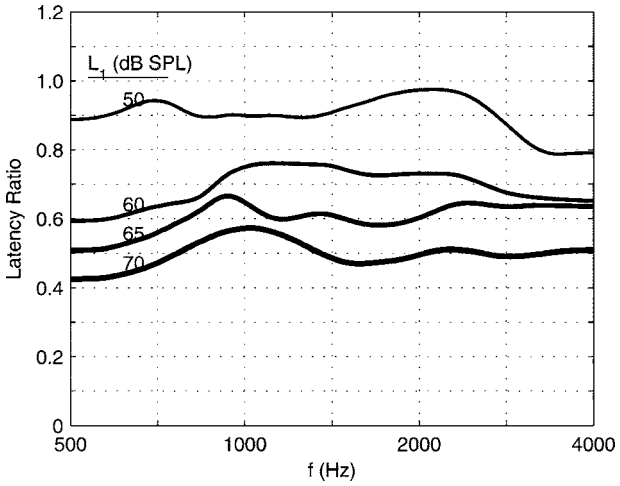

FIG. 10. The effect of L_1 on mean SFOAE latency is illustrated by plotting the ratio of the SFOAE latency in each L_1 condition relative to the latency in the L_1=40 dB SPL condition.

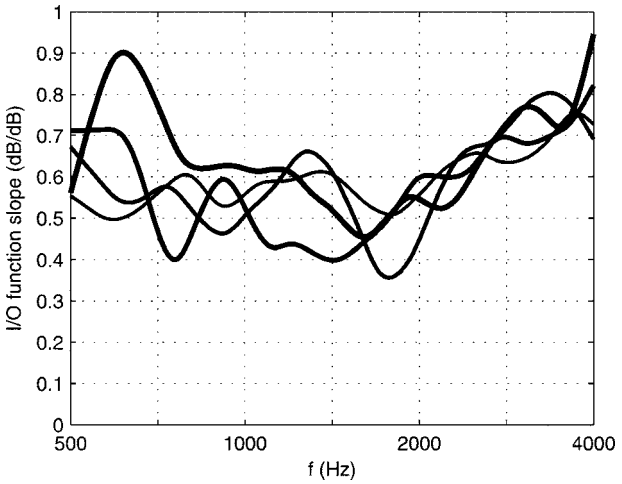

FIG. 12. The slope of the SFOAE input-output functions (in dB/dB) are plotted versus frequency. Thicker lines represent responses at increasing L_1 ranging from 50, 60, 65, and 70 dB SPL.

E. Group SFOAE SPL results

Although the primary emphasis of this study concerns SFOAE latency effects with level, the measurements also provided group results of how SFOAE SPL varied with L_1. The mean ±1 SE of the SFOAE SPL are plotted in Fig. 11 (gray lines and gray fills, respectively) as a function of L_1. A smoothed-spline approximation using a smoothing parameter p of 0.995 was applied to the mean data to produce a slowly varying estimate of mean SPL (black lines in Fig. 11). The main level effect is that the SFOAE SPL increased compressively with increasing L_1. The SFOAE SPL increased with frequency from 500 up to 1000 Hz, and then decreased with frequency up to 2000 Hz. The SFOAE SPL between 2000 and 4000 Hz was approximately constant for L_1 =40–50 dB SPL, and increased with increasing frequency for L_1=60–70 dB SPL.

The measurements of SFOAE SPL at each frequency at L_1 ranging from 40 to 70 dB SPL form a SFOAE input/output (I/O) function. The slope of this I/O function was calculated as the change in SFOAE SPL between each pair of adjacent L_1 levels (so that the slope has units of dB/dB), and is plotted versus frequency in Fig. 12. These slopes are parametrized by the higher of the pair of adjacent L_1 levels, namely, at 50, 60, 65, and 70 dB SPL, such that increasing line thickness represents increasing L_1. The four slope curves tend to overlay one another across frequency, except that the slope at the highest level is slightly larger between 600 and 800 Hz and around 4000 Hz. It follows that the slope of the SFOAE I/O function was approximately independent of L_1 up to 65 dB SPL. The SFOAE I/O function slope varied across frequency, with slopes in the range of 0.5–0.6 dB/dB for frequencies from 500 up to 2200 Hz, and larger slopes at higher frequencies reaching 0.75 dB/dB at 4000 Hz.

These values are similar to the estimates of compressive growth in Schairer *et al.* (2003), which ranged from 0.44 to 0.61 dB/dB for frequencies of 1000–4000 Hz. In the Schairer *et al.* study, a two-slope model of SFOAE I/O function was able to predict the compression and slope of SFOAEs elicited with equal-frequency primaries. This SFOAE model was similar to one used in fitting BM I/O functions (Yates *et al.*, 1990). The SFOAE compression range reported in Schairer *et al.* (2003) exceeded the slopes of BM I/O functions reported by Yates *et al.* (1990), and this is also true for the current data. However, it was suggested that some of the difference may be due to the fact that measurements of BM nonlinearity assess forward-transmission effects only, whereas measurements of SFOAE nonlinearity represent forward- and reverse-transmission effects.

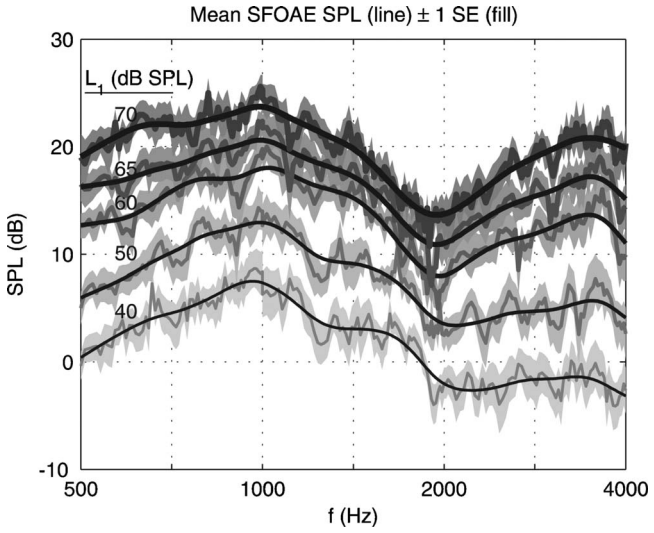

FIG. 11. The mean SFOAE SPL are plotted (gray lines) with ±1 SE (gray fills), with increasing line thickness and increasing fill darkness representing increasing L_1 (40, 50, 60, 65, and 70 dB SPL). The smoothed mean SFOAE SPL are plotted as black lines for each L_1, and agree with the unsmoothed SPL to within ±1 SE.

IV. DISCUSSION

The main goal of the current study was to examine how SFOAE latency changed as a function of level, and learn what it suggests about changes in dominant SFOAE sources as a function of level. The latency results are addressed in the

context of the possible outcomes described in the Introduction (Sec. I C.). Next, the SFOAE latency measurements are used to estimate cochlear tuning.

A. SFOAE sources as a function of stimulus level

The first possible outcome was that SFOAE latencies would be equal at all stimulus levels. However, we found that for any given probe frequency, the SFOAE latency decreased as probe level increased (Figs. 8 and 10). The second possible outcome was that SFOAE latencies in the highest probe-level condition would be near zero. If nonlinear distortion were the dominant source of SFOAEs at the highest probe level, then the latency would be short (near zero) and constant as a function of probe frequency. This was not the case. In the highest probe-level condition, the estimated SFOAE latency was significantly larger than 0 ms and was not constant as a function of frequency (see Figs. 7, 8, and 10).

The experimental results were in accord with the third possible outcome, namely, that SFOAE latencies decreased with increasing stimulus level but remained nonzero. One might expect ear-canal and middle-ear transmission to account for no more than 0.2 ms of round-trip travel time, but the minimum SFOAE latencies were approximately an order of magnitude larger than these travel times, which indicates that SFOAE latencies were dominated by cochlear transmission effects.

These results support the theory that the active process underlying the phase nonlinearity of BM mechanics is also responsible for the nonlinearity in SFOAE latency. SFOAE latencies decreased by approximately 0.5 from the highest stimulus level (70 dB SPL) relative to the lowest (40 dB SPL) (see Fig. 10). The BM group delays reported by Ruggero *et al.* (1997) decreased by approximately 0.6 from the highest stimulus level (90 dB SPL) relative to the lowest (10 dB SPL). One might expect in any case a greater range of nonlinearity in the non-invasive *in vivo* SFOAE measurements than in an invasive animal measurement, and there is the additional confounding factor of species differences. The underlying similarity in the level-dependent SFOAE latency results and the nonlinear BM phase measurements suggest that BM nonlinearity is responsible for the observed SFOAE latency effects. Combined measurements of SFOAEs and BM group delay at the tonotopic place in a mammalian cochlea would be useful in further investigating this relationship.

A nonlinear coherent-reflection or other nonlinear-distortion mechanism may also contribute to the response at high stimulus levels, but the results suggest that it is not the dominant source inasmuch as there was substantial latency at all stimulus levels (e.g., Fig. 5).

As described in the Introduction, another mode in which SFOAE latencies might decrease with stimulus level is if the reverse transmission of the SFOAE is via a slower mechanical transmission at low stimulus levels and via a faster acoustical compression-wave transmission at high stimulus levels. The SFOAE latency at low stimulus levels is consistent with the theory of linear coherent reflection (Shera and Guinan, Jr., 2003). Thus, if the compressional-wave mode is involved in SFOAE generation, it would likely be at higher stimulus levels, even though there is no nonlinear theory of SFOAE generation that predicts such a transition between modes of generation. If SFOAE generation is dominated by a compression-wave source, the latency should be approximately equal to the forward transmission time, because reverse transmission via an acoustic compression wave in the cochlear fluid would have a delay that is almost negligible compared to that of forward transmission. In the absence of other nonlinear effects, it follows that SFOAE latencies would be reduced by a factor of one half if an acoustic compressional mode was substituted for the mechanical-transmission mode. A reduction of latency by one half was observed at high levels in the results of Fig. 10. However, to the extent that the phase nonlinearity of BM mechanics would also reduce SFOAE latency at higher stimulus levels, a reduction by one half due to a dominance of the compression-wave mode would seem likely to reduce the latency by more than a factor of one half. Because such a reduction was not observed, there appears insufficient evidence in the current results to favor the compressional-wave hypothesis, although further research is warranted.

These results are consistent with a coherent-reflection model of SFOAE generation, in which the level-dependent changes in the BM transfer-function phase reduced the SFOAE latency at higher levels. This model of SFOAE generation is assumed in the next section, which uses the measurements of SFOAE latency across frequency and stimulus level to predict effects on cochlear tuning.

B. Using SFOAE latency to estimate Q_{ERB}

In the current data, the $N_{SF}(f,L_1)$ satisfied scaling symmetry above 1000 Hz, meaning that at a given stimulus level, the round-trip travel time was a constant number of periods regardless of frequency (above 1000 Hz). Because the assumption of scaling symmetry is met, it follows that SFOAE latency can be used to estimate mechanical resonance bandwidth in cochlear mechanics because bandwidth is related to the forward travel time from the ear canal to the peak place of excitation on the BM (Zweig, 1976; Zweig and Shera, 1995). This forward travel time is $N_{BM}(f,L_1)$ when measured in units of the number of periods of the stimulus tone. A prediction of the one-dimensional coherent-reflection theory, is that the round-trip SFOAE travel time is twice the forward travel time, so that $N_{SF}(f,L_1)=2\times N_{BM}(f,L_1)$. Cochlear tuning is quantified in terms of a quality factor Q_{ERB}, which is defined as the ratio of the stimulus frequency to the equivalent rectangular bandwidth (ERB) of the mechanical resonance on the BM. The roundtrip latency N_{SF} of SFOAEs elicited by a low-level sinusoid would thus be proportional to Q_{ERB}. Based on the additional assumption that the best auditory tuning measured behaviorally is constrained by the auditory tuning imposed by cochlear mechanics, the tuning and round-trip latency are related by

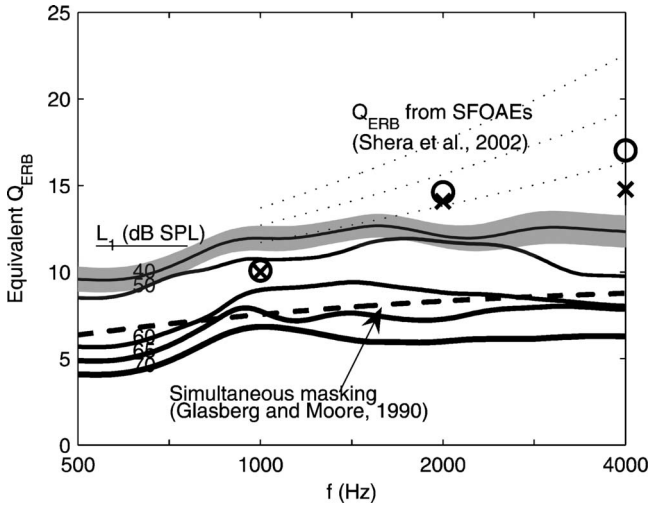

FIG. 13. The equivalent Q_{ERB} (solid lines) derived from the group mean of the SFOAE latencies are plotted with increasing line thickness representing increasing L_1 (40, 50, 60, 65, and 70 dB SPL). The gray fill pattern about the equivalent Q_{ERB} at L_1=40 dB SPL represents the effect of ±1 SE of the SFOAE latency mean on the estimate of equivalent Q_{ERB}. The three dashed thin lines show the mean and its 95% confidence interval of the equivalent Q_{ERB} (Shera *et al.*, 2002) based on SFOAE latencies measured at a stimulus level of 40 dB SPL (also plotted in Fig. 8). The plotting symbols (*x* and *o*) at 1000, 2000, and 4000 Hz are psychophysical measurements of Q_{ERB} based on a forward masking procedure using a pair of roex models (Oxenham and Shera, 2003). The dashed thick line plots the Q_{ERB} obtained from simultaneous masking measurements (Glasberg and Moore, 1990).

$$Q_{ERB} = kN_{BM} = kN_{SF}/2, \tag{4}$$

in which Q_{ERB} represents either the degree of tuning on the BM or the degree of psychophysical tuning, which can be measured behaviorally using a forward-masking paradigm (Shera *et al.*, 2002). The coefficient of proportionality k is assumed to vary more slowly with frequency than either Q_{ERB} or N_{SF}, is known to be similar in the cat and guinea pig, and is assumed to be correspondingly similar in humans.

Using the mean k reported by Shera *et al.* ($k=2.3f^{-0.07}$, where the unit of f is kilohertz), an equivalent $Q_{ERB}(f,L)$ was calculated as a function of frequency and stimulus level using the measured SFOAE latencies (the effects of the variability in estimating k is outside the scope of the present analyses). The results are shown in the solid-line curves of Fig. 13 in which each curve corresponds to a particular L_1. The SE of N_{SF} (see Fig. 8) was used to calculate an approximate SE for Q_{ERB} (at L_1=40 dB SPL), but no additional variability associated with the confidence interval of k was included. Also shown in Fig. 13 are the mean Q_{ERB} and its 95% confidence interval measured using SFOAE latency (dashed lines; Shera *et al.*, 2002), and the psychophysical values of Q_{ERB} measured using a forward-masking paradigm with a low-level probe signal in a notched-noise masker (Oxenham and Shera, 2003). These psychophysical data were measured at 1000, 2000, and 4000 Hz, and Q_{ERB} was calculated using a pair of roex models, shown as individual symbols in Fig. 13. Finally, an alternative set of psychophysical measurements of Q_{ERB} are shown for the case of simultaneous masking of a probe tone in a notched-noise masker (Glasberg and Moore, 1990). Simultaneous masking is thought to involve suppression and "line-busy" effects at the peripheral level that are not part of forward masking. The present interest is to compare the frequency dependence of these various estimates of auditory tuning, irrespective of the detailed mechanisms underlying each measure of behavioral tuning. Although data are available above 4000 Hz in previous data sets (Oxenham and Shera, 2003; Shera *et al.*, 2002), the data are truncated to the range for which estimates are available for comparison from the current data set.

The simultaneous-masking data support the view that auditory tuning is relatively constant across frequency ($Q_{ERB} \approx 12$), except that the slight reduction to $Q_{ERB}=10$ at 500 Hz suggests broader tuning at 500 Hz compared to higher frequencies. The emission-based measurement of Q_{ERB} by Shera *et al.* (2002) showed an increase in Q_{ERB} at higher frequencies, which suggests sharper tuning at 4000 Hz than at 2000 or 1000 Hz. This measurement is directly related to the increase in N_{SF} at higher frequencies reported by Shera *et al.* and plotted in Fig. 8. It is notable that the psychophysical measurements of Q_{ERB} via forward masking (Oxenham and Shera, 2003) are substantially below the confidence limits of their emission-based measurements of Q_{ERB} at 4000 Hz in Fig. 13; the deviation is in the direction toward the current emission-based estimates of Q_{ERB} at the L_1 of 40 dB SPL. It is difficult to judge from this plot whether the forward-masking estimates of Q_{ERB} increase with increasing frequency from 2000 to 4000 Hz, or whether they are independent of frequency. Forward-masking estimates at additional frequencies would be helpful between 1000 and 4000 Hz in understanding the relationship. It should be noted that data in the Oxenham and Shera paper included data points at 6000 and 8000 Hz (not shown), and taken together with the data points shown here, Q_{ERB} does appear to increase.

While forward-masking experiments at low probe levels show sharper tuning overall than do the simultaneous masking experiments, it is unclear whether their frequency dependence is the same or different. The emission-based estimates of Q_{ERB} in the current study are relatively constant across frequency from 1000 to 4000 Hz and suggest broader tuning from 500 to 1000 Hz, which is consistent with the simultaneous-masking estimates of Q_{ERB}. Emission-based estimates of Q_{ERB} have also been reported at 2700 and 4000 Hz over a similar range of stimulus levels using a pair of transient SFOAE measurement procedures (Konrad-Martin and Keefe, 2005). These results show the expected decrease in N_{SF} and Q_{ERB} with increasing stimulus level, but the Q_{ERB} estimated at the lowest stimulus levels (close to 40 dB SPL) are more similar to the results of Shera *et al.* (2002) than to the current results. The reasons for the differences between the Konrad-Martin and Keefe and the current results are unknown.

V. CONCLUSIONS

1. SFOAE latency was found to decrease with increasing stimulus level. The low-level measurements of SFOAE latency (at 40 dB SPL) are consistent with the linear co-

herent reflection theory of SFOAE generation and are inconsistent with the theories of SFOAE generation based on nonlinear distortion or fluid compression. This does not mean that nonlinear distortion and/or fluid compression does not occur at low levels, only that they are not the dominant source, or that their contribution is negligible as measured in the ear canal. The higher-level measurements of SFOAE latency (at 65–70 dB SPL) were approximately half the value of the latency at low levels. The reduction in SFOAE latencies is consistent with previous measurements of BM phase nonlinearity in mammalian cochleae.

2. The SFOAE latency at a given stimulus level is approximately equal to a constant number of stimulus periods between 1000 and 4000 Hz, which supports the prediction of cochlear scaling symmetry, and is slightly reduced between 500 and 1000 Hz. The SFOAE latencies at 40 dB SPL were slightly less between 2000 and 4000 Hz than latencies reported by Shera *et al.* (2002).
3. The prediction of Zweig and Shera (1995) that SFOAE latency predicts cochlear tuning with a coefficient of proportionality similar to that of other mammals (Shera *et al.*, 2002) was applied to the present data. The results show that cochlear tuning was approximately constant between 1000 and 4000 Hz and slightly broader between 500 and 1000 Hz.

ACKNOWLEDGMENTS

Work was supported by NIH R01 DC03784, R03 DC06342, P30 DC04662, and T32 DC00013. The authors thank two anonymous reviewers for helpful suggestions and comments in revising this manuscript.

Anderson, D. J., Rose, J. E., Hind, J. E., and Brugge, J. F. (**1971**). "Temporal position of discharges in single auditory nerve fibers within the cycle of a sine-wave stimulus: Frequency and intensity effects," J. Acoust. Soc. Am. **49**, 1131–1139.

Brass, D., and Kemp, D. T. (**1993**). "Suppression of stimulus frequency otoacoustic emissions," J. Acoust. Soc. Am. **93**, 920–939.

Cooper, N. P., and Rhode, W. S. (**1992**). "Basilar membrane mechanics in the hook region of cat and guinea-pig cochleae: Sharp tuning and nonlinearity in the absence of baseline position shifts," Hear. Res. **63**, 163–190.

Dreisbach, L. E., Siegel, J. H., and Chen, W. (**1998**). "Stimulus-frequency otoacoustic emissions measured at low- and high-frequencies in untrained human subjects," *Abstracts of the Twenty-First Annual Midwinter Research Meeting of the Association for Research in Otolaryngology*, Mt. Royal, NJ, pp. 349–349.

Glasberg, B. R., and Moore, B. C. (**1990**). "Derivation of auditory filter shapes from notched-noise data," Hear. Res. **47**, 103–138.

Goodman, S. S., Withnell, R. H., and Shera, C. A. (**2003**). "The origin of SFOAE microstructure in the guinea pig," Hear. Res. **183**, 7–17.

He, N., J., and Schmiedt, R. A. (**1993**). "Fine structure of the 2 f1-f2 acoustic distortion product: Changes with primary level," J. Acoust. Soc. Am. **94**, 2659–2669.

He, N., and Schmiedt, R. A. (**1997**). "Fine structure of the 2 f1-f2 acoustic distortion products: effects of primary level and frequency ratios," J. Acoust. Soc. Am. **101**, 3554–3565.

Kalluri, R., and Shera, C. A. (**2001**). "Distortion-product source unmixing: A test of the two-mechanism model for DPOAE generation," J. Acoust. Soc. Am. **109**, 622–637.

Keefe, D. H. (**1998**). "Double-evoked otoacoustic emissions. I. Measurement theory and nonlinear coherence," J. Acoust. Soc. Am. **103**, 3489–3498.

Knight, R. D., and Kemp, D. T. (**2000**). "Indications of different distortion product otoacoustic emission mechanisms from a detailed f1, f2 area study," J. Acoust. Soc. Am. **107**, 457–473.

Konrad-Martin, D., and Keefe, D. H. (**2005**). "Transient-evoked stimulus-frequency and distortion-product otoacoustic emissions in normal and impaired ears," J. Acoust. Soc. Am. **117**, 3799–3815.

Konrad-Martin, D., and Keefe, D. H. (**2003**). "Time-frequency analyses of transient-evoked stimulus-frequency and distortion-product otoacoustic emissions: testing cochlear model predictions," J. Acoust. Soc. Am. **114**, 2021–2043.

Liberman, M. C., Zuo, J., and Guinan, J. J., Jr. (**2004**). "Otoacoustic emissions without somatic motility: can stereocilia mechanics drive the mammalian cochlea?," J. Acoust. Soc. Am. **116**, 1649–1655.

Nuttall, A. L., and Dolan, D. F. (**1993**). "Two-tone suppression of inner hair cell and basilar membrane responses in the guinea pig," J. Acoust. Soc. Am. **93**, 390–400.

Oxenham, A. J., and Shera, C. A. (**2003**). "Estimates of human cochlear tuning at low levels using forward and simultaneous masking," J. Assoc. Res. Otolaryngol. **4**, 541–554.

Ren, T. (**2004**). "Reverse propagation of sound in the gerbil cochlea," Nat. Neurosci. **7**, 333–334.

Ren, T., and Nuttall, A. L. (**2001**). "Basilar membrane vibration in the basal turn of the sensitive gerbil cochlea," Hear. Res. **151**, 48–60.

Rhode, W. S. (**1971**). "Observations of the vibration of the basilar membrane in squirrel monkeys using the Mossbauer technique," J. Acoust. Soc. Am. **49**, 1218–1231.

Rhode, W. S., and Cooper, N. (**1996**). "Nonlinear mechanics in the apical turn of the chinchilla cochlea *in vivo*," Aud. Neurosci. **3**, 101–121.

Rhode, W. S., and Robles, L. (**1974**). "Evidence from Mossbauer experiments for nonlinear vibration in the cochlea," J. Acoust. Soc. Am. **55**, 588–596.

Ruggero, M. A., Rich, N. C., Recio, A., Narayan, S. S., and Robles, L. (**1997**). "Basilar-membrane responses to tones at the base of the chinchilla cochlea," J. Acoust. Soc. Am. **101**, 2151–2163.

Schairer, K. S., Fitzpatrick, D., and Keefe, D. H. (**2003**). "Input-output functions for stimulus-frequency otoacoustic emissions in normal-hearing adult ears," J. Acoust. Soc. Am. **114**, 944–966.

Schairer, K. S., and Keefe, D. H. (**2005**). "Simultaneous recording of stimulus-frequency and distortion-product otoacoustic emission input-output functions in human ears," J. Acoust. Soc. Am. **117**, 818–832.

Sellick, P. M., Patuzzi, R., and Johnstone, B. M. (**1982**). "Measurement of basilar membrane motion in the guinea pig using the Mossbauer technique," J. Acoust. Soc. Am. **72**, 131–141.

Shera, C. A., and Guinan, J. J., Jr. (**2003**). "Stimulus-frequency-emission group delay: A test of coherent reflection filtering and a window on cochlear tuning," J. Acoust. Soc. Am. **113**, 2762–2772.

Shera, C. A., Guinan, J. J., Jr., and Oxenham, A. J. (**2002**). "Revised estimates of human cochlear tuning from otoacoustic and behavioral measurements," Proc. Natl. Acad. Sci. U.S.A. U.S.A. **99**, 3318–3323.

Shera, C. A., Tubis, A., and Talmadge, C. L. (**2005**). "Coherent reflection in a two-dimensional cochlea: Short-wave versus long-wave scattering in the generation of reflection-source otoacoustic emissions," J. Acoust. Soc. Am. **118**, 287–313.

Shera, C. A., and Zweig, G. (**1993**). "Order from chaos: Resolving the paradox of periodicity in evoked otoacoustic emissions," in *Biophysics of Hair Cell Sensory Systems*, edited by H. Duifhuis, J. W. Horst, P. van Dijk, and S, M. van Netten (World Scientific, Singapore) pp. 54–63.

Talmadge, C. L., Tubis, A., Long, G. R., and Piskorski, P. (**1998**). "Modeling otoacoustic emission and hearing threshold fine structures," J. Acoust. Soc. Am. **104**, 1517–1543.

Talmadge, C. L., Tubis, A., Long, G. R., and Tong, C. (**2000**). "Modeling the combined effects of basilar membrane nonlinearity and roughness on stimulus frequency otoacoustic emission fine structure," J. Acoust. Soc. Am. **108**, 2911–2932.

Tubis, A., Talmadge, C. L., Tong, C., and Dhar, S. (**2000**). "On the relationships between the fixed-f1, fixed-f2, and fixed-ratio phase derivatives of the 2f1-f2 distortion product otoacoustic emission," J. Acoust. Soc. Am. **108**, 1772–1785.

Yates, G. K., Winter, I. M., and Robertson, D. (**1990**). "Basilar membrane nonlinearity determines auditory nerve rate-intensity functions and cochlear dynamic range," Hear. Res. **45**, 203–219.

Zweig, G. (**1976**). "Basilar membrane motion," Cold Spring Harb Symp. Quant Biol. **40**, 619–633.
Zweig, G., and Shera, C. A. (**1995**). "The origin of periodicity in the spectrum of evoked otoacoustic emissions," J. Acoust. Soc. Am. **98**, 2018–2047.
Zwicker, E. (**1983**). "Delayed evoked oto-acoustic emissions and their suppression by Gaussian-shaped pressure impulses," Hear. Res. **11**, 359–371.
Zwicker, E., and Schloth, E. (**1984**). "Interrelation of different oto-acoustic emissions," J. Acoust. Soc. Am. **75**, 1148–1154.

Effects of hearing loss and spectral shaping on identification and neural response patterns of stop-consonant stimuli

Ashley W. Harkrider,[a] Patrick N. Plyler, and Mark S. Hedrick
Department of Audiology and Speech Pathology, 457 South Stadium Hall, The University of Tennessee, Knoxville, Tennessee 37996

(Received 5 August 2005; revised 18 April 2006; accepted 21 April 2006)

In order to determine the effects of hearing loss and spectral shaping on a dynamic spectral speech cue, behavioral identification and neural response patterns of stop-consonant stimuli varying along the /b-d-g/ place-of-articulation continuum were measured from 11 young adults (mean age=27 years) and 10 older adults (mean age=55.2 years) with normal hearing, and compared to those from 10 older adults (mean age=61.3 years) with mild-to-moderate hearing impairment. Psychometric functions and N1-P2 cortical evoked responses were obtained using consonant-vowel (CV) stimuli with frequency-independent (unshaped) amplification as well as with frequency-dependent (shaped) amplification that enhanced *F*2 relative to the rest of the stimulus. Results indicated that behavioral identification and neural response patterns of stop-consonant CVs were affected primarily by aging and secondarily by age-related hearing loss. Further, enhancing the audibility of the *F*2 transition cue with spectrally shaped amplification partially reduced the effects of age-related hearing loss on categorization ability but not neural response patterns of stop-consonant CVs. These findings suggest that aging affects excitatory and inhibitory processes and may contribute to the perceptual differences of dynamic spectral cues seen in older versus young adults. Additionally, age and age-related hearing loss may have separate influences on neural function. [DOI: 10.1121/1.2204588]

PACS number(s): 43.64.Ri, 43.64.Qh, 43.64.Sj [WPS] Pages: 915–925

I. INTRODUCTION

Older adults with (Dorman *et al.*, 1985; Plyler and Hedrick, 2002) and without (Harkrider *et al.*, 2005) hearing loss have difficulty utilizing the *F*2 formant transition for the identification of stop consonants. Plyler and Hedrick (2002) reported that increasing the overall presentation level of stop-consonant stimuli does not improve identification and results in smaller shifts in phonetic boundaries in older listeners with impaired hearing versus young listeners with normal hearing. Moreover, reduced stop-consonant identification and reduced phonetic boundary shifts are not correlated with the hearing sensitivity of the older listeners with impaired hearing, suggesting that the contribution of age to performance should be explored.

Dorman *et al.* (1985) measured psychometric functions to stimuli along the /b-d-g/ continuum in young listeners with normal hearing, elderly listeners with normal hearing, and elderly listeners with hearing impairment. Results indicated that categorical boundaries of elderly listeners differed from those of young controls for all three phonemes. However, performance did not differ between elderly listeners with versus without normal hearing. This finding suggested that age, not hearing sensitivity, may contribute to altered phonetic categories based on dynamic spectral cues.

Harkrider *et al.* (2005) compared psychometric functions and N1-P2 cortical responses to stop-consonant stimuli along the /b-d-g/ continuum in young and older listeners with normal hearing. Consistent with the findings of Dorman *et al.* (1985), older listeners with normal hearing had different phonetic categories in response to *F*2 formant transitions varying along the place-of-articulation continuum versus young normal controls. Additionally, N1-P2 cortical responses to these time-varying spectral cues differed between young and older listeners with normal hearing. Thus, it appears that older listeners with normal hearing have disrupted encoding of the *F*2 formant transition; a conclusion also reached when investigating a temporal speech cue, voice onset time (Tremblay *et al.*, 2002, 2003).

Schneider *et al.* (1994) and Frisina and Frisina (1997) have hypothesized that this impaired temporal coding results from an age-related loss of neural synchrony. Neural synchrony of nerve fibers is enhanced with an increase in stimulus level (Martin, 1991) and neurons in relative refractory will fire only to subsequent higher-level stimulation (Koester, 1991). Thus, if an age-related loss of neural synchrony contributes to differences in categorical perception and neural response patterns between young and older listeners, increasing the amplitude of the speech cue should reduce these differences. In accord, Harkrider *et al.* (2005) obtained psychometric functions and cortical evoked responses using consonant-vowel (CV) stimuli along a /b-d-g/ continuum in young and older listeners with normal hearing. All stimuli were presented in an unshaped and in a spectrally shaped condition; controlling for overall presentation level. Results demonstrated that when the same stop-consonant stimuli are spectrally shaped to enhance the audibility of the *F*2 formant transition relative to the rest of the stimulus, older listeners have perceptual categories and N1-P2 auditory evoked potentials (AEPs) that are more similar to those of younger

[a]Electronic mail: aharkrid@utk.edu

listeners for some stimuli. Thus, neural deficits due to aging may only reduce the responsiveness of neurons. However, neural deficits associated with age-related hearing loss may reduce neural responsiveness and distort coding of auditory information. This would explain why older listeners with hearing impairment often do not demonstrate improvements in speech perception with amplification.

Providing flat amplification of the speech signal to listeners with sloping sensorineural hearing loss may significantly increase the audibility of the stop consonant; however, flat amplification would not enhance the audibility of the *F*2 formant transition relative to the rest of the stimulus. Furthermore, increasing the overall presentation level of the stimulus may increase susceptibility to the deleterious effects of the upward spread of masking, making accurate consonant identification more difficult. As was shown with older listeners with normal hearing (Harkrider *et al.*, 2005), providing spectrally shaped amplification to older hearing-impaired listeners to enhance gain in the mid-to-high-frequencies may significantly increase neural responsiveness to the *F*2 formant transition cue, thereby decreasing differences in behavioral and/or neurophysiological performance relative to young, normal controls. Alternatively, unlike the findings in older, normal-hearing listeners (Harkrider *et al.*, 2005), spectrally shaped amplification may not reduce differences in behavioral and/or neurophysiological performance of older hearing-impaired listeners relative to young normal controls. Differences in the effects of spectral shaping on perception and neural response patterns of dynamic spectral cues in older listeners with versus without hearing loss could shed light on the neural deficits contributing to altered perception of *F*2 formant transitions in listeners with hearing loss. If reduced neural responsiveness (decreased audibility) is the primary mediating factor, then spectral shaping to enhance the *F*2 formant transition should improve identification and normalize neural response patterns to the cue, like it did in the older normal-hearing subjects. If reduced responsiveness in combination with improper coding (distortion) by residual neurons is responsible, then spectral shaping to enhance the *F*2 formant transition should not improve identification or normalize neural response patterns to the cue.

In the current study, behavioral and N1-P2 neural responses to unshaped and spectrally shaped stop-consonant stimuli from older individuals with normal hearing, older individuals with hearing impairment, and young individuals with normal hearing were compared. The purposes of the study were to: (1) Examine differences in behavioral and neural response patterns of the *F*2 formant transition among the three groups of listeners and (2) determine if spectral shaping will decrease differences in behavioral identification and neural response patterns of the *F*2 formant transition in older listeners with hearing impairment relative to young, normal controls. Results may help to separate effects of aging from effects of age-related hearing loss on the perception of dynamic spectral information presented via frequency-dependent and frequency-independent amplification.

Based on previous findings in older individuals with hearing impairment (e.g., Dorman *et al.*, 1985; Plyler and Hedrick, 2000) and older individuals with normal hearing (Harkrider *et al.*, 2005), it was predicted that: (1) Behavioral and neural response patterns would differ among the three groups, (2) spectral shaping would reduce but not eliminate differences in categorization abilities and neural response patterns of stop-consonant stimuli between young, normal controls and older listeners with and without hearing impairment, and (3) the amount of influence of spectral shaping on behavioral and neural responses would differ for older listeners with versus without hearing loss.

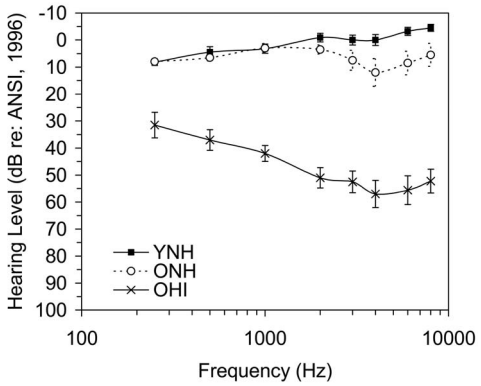

FIG. 1. Audiometric thresholds (means ± one standard error) for the test ear are shown for young (YNH, $n=11$) and older (ONH, $n=10$) listeners with normal hearing and older listeners with hearing impairment (OHI, $n=10$).

II. METHODS

A. Participants

Participants were 11 young normal-hearing adults (mean=27 years; range=22–34 years; 5 males), 10 older normal-hearing adults (mean=55.2 years; range=43–65 years; 5 males), and 10 older hearing-impaired adults (mean =61.3 years; range=49–73 years; 5 males). All participants passed an otoscopic examination and a tympanometric screen. Participants with normal hearing had pure-tone thresholds of 15 dB hearing level or better at frequencies 0.25, 0.5, 1, 2, 3, 4, 6, and 8 kHz in their test ear. Participants with hearing impairment had moderate high-frequency hearing losses. Mean audiometric thresholds for the test ear are shown, in Fig. 1. For experimental testing, stimuli were presented to the better ear of adults with normal hearing (6 right ears, 4 left ears), and to the ear that most closely matched the target range of high-frequency hearing loss for adults with hearing impairment (8 right ears, 2 left ears). Medical history, as reported by the subjects, indicated that all participants were right-handed and had no history of otologic or neurologic injury or disorder. Data from participants with normal-hearing collected under the same stimulus conditions as for the hearing-impaired for both unshaped and shaped stimuli are reported originally in Harkrider *et al.* (2005). Data from the young normal-hearing individuals to the unshaped stimuli are used as the "gold standard" for comparison to data from the older normal-hearing and hearing-impaired individuals to unshaped and shaped stimuli.

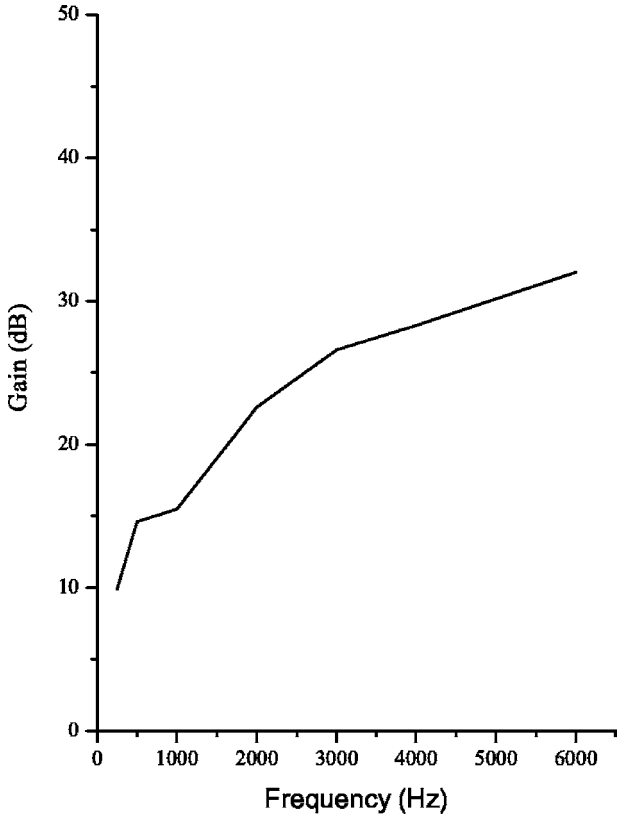

FIG. 2. Gain as a function of frequency applied to the shaped stimuli using DSL targets.

B. Stimuli

1. Unshaped stimuli

A 15-step /bɑ/-/dɑ/-/gɑ/ continuum was generated using the cascade configuration of Klatt's formant synthesizer (Klatt, 1980) at a sampling rate of 10 kHz. The total duration of each stimulus was 100 ms while the duration of the first and second formant transitions was 40 ms. The starting frequency of the first formant was 0.15 kHz, which increased until it reached steady state at 0.75 kHz. The onset frequency of the second formant varied from 0.9 to 2.3 kHz in 0.1 kHz steps in order to create the /bɑ/-/dɑ/-/gɑ/ perceptual continuum. The frequencies of the third and fourth formants were 2.4 and 3.3 kHz throughout the duration of the stimulus. The amplitude of the second formant was −3 dB relative to the first formant; the amplitude of the third formant was −6 dB relative to the first formant.

2. Spectrally shaped stimuli

Spectral shaping of the stop-consonant stimuli was performed using a commercially available signal processing software package (Cool Edit Pro, Adobe) to improve the audibility of the transition cue relative to the rest of the stimulus. Spectral shaping was applied to approximate the desired sensation level targets (DSL v4.1 software) for conversational speech, assuming linear amplification for a listener with a mild-to-moderate sensorineural hearing loss (Cornelisse *et al.*, 1995) (Fig. 2). In an attempt to minimize the upward spread of masking and enhance audibility of the *F*2 formant transition, spectral shaping was selected to minimize gain at the low frequencies and enhance gain in the mid-to-high frequencies, where *F*2 formant information is carried for /b-d-g/ phonemes. Shaping was verified by measuring one-third octave root-mean-square (rms) levels in a Zwislocki coupler using a sound level meter (slow averaging, C weighting).

3. Stimuli levels

The rms output level of the shaped stimuli was 82 dB sound pressure level (SPL) and was equal to the rms output level of the unshaped stimuli to control for overall presentation level. Thus, shaped stimuli were amplified more for the frequencies of the *F*2 formant transition relative to the rest of the stimulus (spectrally shaped amplification), while unshaped stimuli were amplified equally at all frequencies (spectrally unshaped amplification). Stimuli were presented at the same intensity level to all subjects (e.g., Tremblay *et al.*, 2003). Equal sensation levels across groups were not used to avoid differential effects of presentation level on stop consonant perception (Dorman and Dougherty, 1981; Plyler and Hedrick, 2002). Equal rms output levels ensured that any perceptual and/or electrophysiological differences in responses obtained by unshaped versus shaped stimuli can be attributed to shaping of the signal as opposed to overall level differences. Calibration of unshaped and shaped stimuli was performed using a sound level meter with slow averaging and C weighting.

C. Procedure

1. Behavioral apparatus

The stop-consonant stimuli were digitally controlled by a signal generation system (Tucker-Davis Technologies, System II) interfaced to a microcomputer. Digital signal generation and control of the research protocol was accomplished by interactive signal generation and control software (CSRE version 4.5). The digital stimuli were routed from the microcomputer to the digital-to-analog (D/A) converter (TDT-DD1). The output of the D/A converter was routed to a low-pass filter (TDT-PF1, 4.9 kHz low-pass), then to a programmable attenuator (TDT-PA4), and then to the headphone buffer (TDT-HB) before being delivered to an insert earphone (Etymotic, ER-3A) located in a sound-treated examination room (Industrial Acoustics Company).

2. Behavioral procedures

Participants were seated in the examination room and instructed to view a computer monitor through the examination room window. Following each stimulus presentation, participants indicated which stop consonant they perceived by selecting the appropriate symbol displayed on the monitor (B or D or G) via the computer mouse. Each subject participated in a criterion session prior to experimental testing. The criterion session involved identification of six exemplar stimuli one unshaped and one shaped for each of the three phonemes). Exemplar stimuli had *F*2 onset frequencies of 0.9 kHz, 1.6 kHz, and 2.3 kHz. These three stimuli were judged by two independent listeners to represent the best examples of /bɑ/, /dɑ/, and /gɑ/. During one criterion trial,

the 6 stimuli were presented 5 times for a total of 30 presentations. Experimental testing commenced when the participants achieved at least 50% correct within a trial. All participants achieved 50% correct after at least six trials.

In the experimental session, each of the 30 stimuli (shaped and unshaped) were randomly presented over 20 trials for a total of 600 responses. Generation of random stimulus orders and online data collection was performed for each group using a commercially available identification program (CSRE, version 4.5). Psychometric functions displaying the percentage identification as a function of onset frequency were generated for the shaped and unshaped conditions for each phoneme.

3. Electrophysiological apparatus

N1 and P2 cortical potentials were recorded using the stop-consonant stimuli that produced the greatest perceptual difference within the /b/ and /d/ and /g/ categories defined by greater than 50% identification following shaping for each listener. The stimuli were routed through a 16-bit D/A converter (Tucker-Davis Technologies, model ZDA1) using a 10 kHz sampling rate, low-pass filtered at 4.9 kHz, and delivered to the test ear via an electrically shielded insert earphone (Etymotic Research, model ER-3A). The level of the stimulus was equal to that used in the behavioral session and was delivered to the test ear at a rate of 1.1 s. Tucker-Davis Technologies SigGen and BioSig software was used for data acquisition. Electroencephalogram (EEG) activity was differentially amplified (gain: 1×10^5) (Tucker-Davis Technologies, model DB4) and filtered. The rejection rate of these filters was −6 dB/octave and the bandwidth was DC −40 Hz. The cortical potentials were digitized via a 16-bit analog-to-digital (A/D) converter (Tucker-Davis Technologies, model AD1) at a sampling rate of 10 kHz. The time window was −100–550 ms and one average waveform consisted of 250 sweeps. Each response was replicated.

4. Electrophysiological procedures

N1 and P2 cortical potentials were acquired with a four-channel electrode configuration, using gold-plated electrodes applied to the surface of the scalp. Prior to electrode placement, the skin was cleansed with a mild facial scrub and a conductive paste applied. Electrodes were held in place with medical tape. The electrode placements were designated according to the 10–20 international system (Jasper, 1958). The noninverting electrodes were placed on the vertex of the head (Cz), on the left side of the vertex (C5), and on the ipsilateral mastoid. The inverting electrode was placed on the nasion (Nz) and the ground electrode was placed on the forehead (Fpz). Electrode impedances were then measured at 30 Hz. An electrode was replaced if its measured impedance was >3 kΩ or not within 1 kΩ of the others. The electrooculogram (EOG), used to develop an eye-blink rejection rule for each subject, was recorded by electrodes placed on the right superior orbit and the right inferior orbit. Eye-blink rejection was set at a level equivalent to that of the smallest recorded EOG during a series of ten blinks performed just prior to data collection. Additionally, an EEG artifact rejection algorithm was applied to the on-line averaging waveform. If the peak voltage within a sample exceeded ±50 μV, that sample was excluded from the averaged waveform. Excluding sweeps within preset EOG and EEG artifact rejection limits, 250 sweeps were averaged per individual mean AEP waveform. Rejection rates averaged 11.4% and were never greater than 15% per run for any participant ensuring that the number of stimulus presentations was similar across subjects and stimulus conditions.

During the recording session, the participants were in a sound-treated booth, comfortably reclined in an armchair with their heads and necks well supported. Participants were instructed to sit quietly, watch a closed-captioned-movie of their choice, and not sleep. A total of 24 individual mean AEP waveforms [2 electrodes (Cz and C5) ×3 phonemes (/b/, /d/, /g/)×2 shaping conditions (unshaped and shaped) ×2 runs] per subject were acquired. The order of phoneme and shaping condition (shaped versus unshaped) was randomized across participants.

D. Data analysis

1. Behavioral data analysis

In order to best characterize perception of stop-consonant place of articulation using psychometric functions, two quantifiable procedures were used. First, phonetic boundary locations corresponding to 50% points were calculated in Hz from each listener's shaped and unshaped psychometric functions. To determine 50% points; percent unshaped /b/ scores were converted to z scores and a linear least-squares fit was used to obtain an estimate of the 50% point, which was the phonemic boundary for unshaped /b/. The same process was used to determine phonemic boundaries for shaped /b/, unshaped /d/, shaped /d/, unshaped /g/, and shaped /g/ stimuli. Because boundaries could not always be measured, an area under the curve (Hedrick *et al.*, 1995) also was computed for shaped and unshaped psychometric functions. The area under the curve was calculated by adding the number of percent /b/ (or /d/ or /g/) responses obtained across the continuum of $F2$ onset transitions. The sum was divided by the total number of transition steps for the continuum. The boundary and area under the curve measurements have been shown to yield similar results (Hedrick *et al.*, 1995).

2. Analysis of cortical evoked potentials

Individual mean waveforms and group grand-mean waveforms were analyzed as described below. For all waveforms, the 100 ms prestimulus period was used for baseline correction, allowing for reliable absolute peak amplitude measures. Each EEG waveform was analyzed separately by three research assistants using Tucker-Davis Technologies software (BioSig®). Slow cortical potential peaks were identified based on response windows in previously reported literature (e.g., Martin *et al.*, 1999; Hakrider and Hedrick, 2005; Harkrider *et al.*, 2005), as well as those obtained from the grand-mean waveforms. The response window for N1 was 80–200 ms, and the latency with the greatest positive amplitude following N1 was identified as P2. Absolute laten-

cies and peak amplitudes (referenced to the prestimulus baseline) were recorded. A polarity inversion of the response at the mastoid electrode was used, if necessary, to aid in the indentification of slow cortical potentials measured at Cz and C5 electrodes. A reliability check indicated that the three research assistants recorded the same latencies and amplitudes for all but nine evoked potential components and these discrepancies were very small. Thus, reliability was very good. Latency and amplitude measures were recorded from the Cz electrode site.

For the purpose of presentation and for comparison with the results of other studies, AEP response latencies were corrected for delays imposed during data acquisition. The length of the tubes for the insert earphone causes a 0.9 ms delay and the amplifier/filter combination causes a 2 ms group delay. Thus, 2.9 ms in addition to the time between sweep onset and stimulus onset was subtracted from the raw latency values.

III. RESULTS

A. Behavioral

Mean psychometric functions for each phoneme are presented in Fig. 3 for the older, listeners without and with hearing impairment to the unshaped and shaped stimuli. For comparison, psychometric functions for each phoneme also are presented for the young adults with normal hearing to the unshaped stimuli. Means and standard deviations for categorical boundaries and areas under the curve are presented for all groups in Tables I and II, respectively.

Two three-factor ANOVAS with repeated measures were conducted, one on categorical boundaries and one on the area under the curve measures. The factors were group (three levels, young normal hearing versus older normal hearing versus older hearing impaired), shaping (repeated measures on two levels, unshaped versus shaped) and phoneme (repeated measures on three levels, /b/ versus /d/ versus /g/). Because the within-subject factor, phoneme, had three levels, Mauchly's test of sphericity was conducted to determine if the homogeneity-of-variance-of-differences assumption was violated for the main effect of this factor or for its interaction with the other within-subject factor, shaping condition. The sphericity test indicated significant violations for the main effect of phoneme on the ANOVA on categorical boundary. Thus, the *p*-values associated with the Greenhouse-Geisser adjusted degrees of freedom were used for the averaged test of significance for phoneme on categorical boundary. Sphericity-assumed adjusted degrees of freedom were used for the averaged tests of significance in all other cases. Significance was revealed at p values <0.05. To test for significant main effects, posthoc pair-wise comparisons using the Tukey's least-significant difference (LSD) approach to control for Type I error with three groups were used (Green *et al.*, 2000; Day and Quinn, 1989). The sources of any significant interactions were identified with internal ANOVAs, graphs, and posthoc pair-wise comparisons using the Tukey's LSD approach.

It should be noted that not all subjects had categorical boundaries to all six stimuli using the criteria for calculating boundaries discussed previously. Thus, a small number of subjects ($n=11$) was used for statistical analyses on this measure. As expected, the ANOVA on categorical boundary revealed a significant main effect for phoneme ($F_{1,3,10,5}=259.5; p<0.001$), such that boundaries shifted to higher frequencies for /b/ to /d/ to /g/. Significant group by phoneme ($F_{2.6,10.5}=5.547; p=0.0.18$) and group by shaping condition ($F_{2,8}=4.444; p=0.048$) interactions were found. Posthoc tests indicated that younger listeners had smaller /d/ categories than older listeners with normal hearing ($p<0.05$) and with hearing loss ($p<0.05$). There were no differences in /d/ categories between older listeners without and with hearing impairment ($p>0.05$). Additionally, shaping decreased differences in categorization of stop-consonant CV stimuli in older versus younger listeners ($p<0.05$). Specifically, shaping the phonemes caused the categorical boundaries from older listeners to shift in frequency so that they more closely approximated the boundaries obtained from young, normal-hearing listeners to unshaped phonemes (the gold standard comparison). There were no differences in the effects of shaping on categorical boundaries between older listeners without and with hearing impairment ($p>0.05$).

The ANOVA on the area under the curve included data from all 31 listeners and revealed a main effect for shaping ($F_{1,28}=4.240; p=0.049$). The interactions between group and phoneme ($F_{4,56}=2.601; p=0.046$), phoneme by shaping condition ($F_{2,56}=7.209; p=0.002$), and group by phoneme by shaping condition ($F_{4,56}=2.684; p=0.041$) were also significant. Posthoc tests indicated that, as with categorical boundary, /d/ categories were larger in older versus younger listeners ($p<0.05$) but did not differ between the two groups of older listeners ($p>0.05$). Spectral shaping decreased differences in area under the curve between younger and older listeners, but the effect was dependent on the phoneme and group. Specifically, for older normal-hearing listeners, shaping made the area under-the-curve measures more similar to younger normal-hearing listeners for /d/ ($P<0.05$). For older hearing-impaired listeners, shaping made the area under-the-curve measures more similar to younger normal-hearing listeners for /d/ ($p<0.05$) and /g/ ($p<0.05$). Thus, for the area under the curve, there were differences in the effects of spectral shaping on older listeners with hearing loss versus older listeners without hearing loss.

B. Electrophysiological

Grand average waveforms for each phoneme are presented in Fig. 4 for older listeners with and without hearing impairment to the unshaped and shaped stimuli. For comparison, average waveforms from the young normal-hearing listeners to unshaped stimuli also are presented in Fig. 4. N1 and P2 latencies and peak amplitudes were recorded for each individual's average waveforms (Table III). Mauchly's test of sphericity indicated a significant violation for the main effect of phoneme in the ANOVA on N1 amplitude and P2 latency. A significant violation for the interaction of phoneme and shaping condition was found in the ANOVAs on N1 latency, P2 latency, and P2 amplitude. Thus, the p values associated with the Greenhouse-Geisser adjusted degrees of freedom were

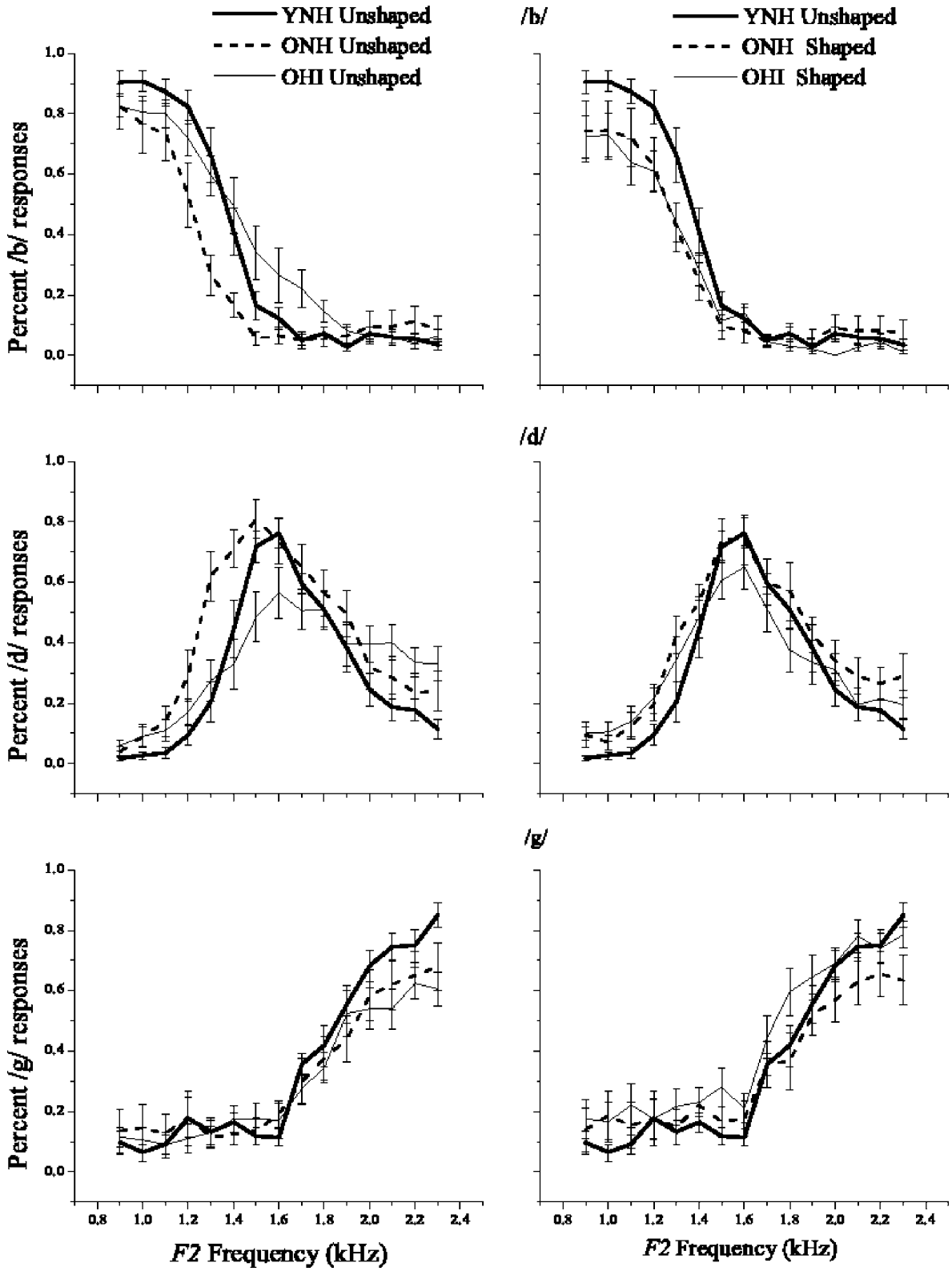

FIG. 3. Grand average psychometric functions for older normal-hearing (ONH=dash, $n=10$) and older hearing-impaired (OHI=light solid, $n=10$) listeners to /b/ (top), /d/ (middle), and /g/ (bottom) stop consonants in unshaped (left panels) and shaped (right panels) conditions. For comparison, grand average psychometric functions for young normal-hearing listeners (YNH=bold solid, $n=11$) to the unshaped stimulus conditions are displayed in both left and right panels. Error bars denote one standard error from the mean.

used for the averaged test of significance for those respective main effects or interactions. Sphericity-assumed adjusted degrees of freedom were used for the averaged tests of significance in all other cases. Significance was revealed at p values <0.05. To test for significant main effects, posthoc pairwise comparisons using the Tukey's LSD approach to control for Type I error with three groups were used (Green *et al.*, 2000; Day and Quinn, 1989). The sources of any sig-

TABLE I. Means and standard deviations (S.D.) for categorical boundaries (Hz) from young normal-hearing, older normal-hearing, and older hearing-impaired listeners for unshaped (US) and shaped (S) stop-consonant stimuli.

Stimuli	US/b/	S/b/	US/d_b/	S/d_b/	US/d_g/	S/d_g/	US/g/	S/g/
Young normal hearing (n=4)								
Mean	1363.3	1398.0	1388.8	1464.8	1729.8	1836.0	1754.0	1905.3
S.D.	*111.8*	*67.1*	*101.8*	*124.4*	*52.4*	*19.5*	*67.2*	*66.0*
Older normal hearing (n=4)								
Mean	1189.5	1267.0	1197.3	1291.5	1852.5	1836.3	1852.5	1863.3
S.D.	*81.0*	*76.3*	*72.8*	*82.6*	*151.3*	*140.4*	*151.3*	*140.4*
Older hearing impaired (n=3)								
Mean	1483.3	1269.3	1497.7	1321.0	1840.7	1793.3	1895.7	1802.3
S.D.	*104.1*	*140.3*	*90.7*	*161.3*	*42.1*	*143.5*	*100.3*	*134.2*

nificant interactions were identified with internal ANOVAs, graphs, and posthoc pair-wise comparisons using the Tukey's LSD approach.

The three-factor ANOVA on N1 latency revealed a main effect for phoneme ($F_{2,26}$=0.023; p=0.023). A significant interaction between phoneme and shaping condition was also found ($F_{1.6,41.3}$=4.064; p=0.033). Posthoc tests revealed that N1 latencies to /d/ versus /g/ differed significantly (mean difference =4.14 ms; $p<0.05$) while latencies to /b/ versus /d/ (mean difference =−3.14 ms; $p>0.05$) and /b/ versus /g/ (mean difference =0.99 ms; $p>0.05$) were not different. Additionally, with shaping, N1 latencies significantly increased for /b/ and /g/ and decreased for /d/ phonemes ($p<0.05$).

N1 amplitudes were much larger for the older group with hearing loss compared with the older normal-hearing group, with the young normal controls having the smallest amplitudes. A significant group by phoneme interaction ($F_{3.2,42.2}$=2.937; p=0.040) was found. According to posthoc tests, N1 amplitudes in young listeners were smaller than those in older listeners with normal hearing for /g/ ($p<0.05$). Additionally, N1 amplitudes in young listeners were smaller than those in older listeners with hearing impairment for /d/ ($p<0.05$) and /g/ ($p<0.01$) phonemes.

The ANOVA on P2 latency revealed a significant main effect for group ($F_{2,26}$=3.442; p=0.047). Subsequent testing showed that P2 latencies were significantly longer for older versus younger listeners with normal hearing ($p<0.05$). Although P2 latencies appeared prolonged for older listeners with hearing impairment versus young listeners with normal hearing, these differences approached but did not reach statistical significance ($p>0.05$). No statistical latency differences were found between the two groups of older listeners ($p>0.05$).

The ANOVA on P2 amplitude revealed a significant group by phoneme interaction ($F_{4,52}$=2.717; p=0.039). Posthoc testing demonstrated that versus younger listeners, older listeners without hearing loss had significantly larger P2 amplitudes for /b/ ($p<0.05$) and /d/ ($p<0.05$) but not /g/ phonemes ($p<0.05$). Similarly, versus young listeners, older listeners with hearing loss had significantly larger P2 amplitudes for /b/ ($p<0.05$) and /d/ ($p<0.05$), but not /g/ ($p<0.05$).

TABLE II. Means and standard deviation (S.D.) for areas under the curve (average % of a given phoneme) for young normal-hearing, older normal-hearing, and older hearing-impaired listeners for unshaped (US) and shaped (S) stop-consonant stimuli.

Stimuli	US/b/	S/b/	US/d/	S/d/	US/g/	S/g/
Young normal hearing						
Mean	1.256	1.185	1.164	1.129	1.262	1.360
S.D.	*0.169*	*0.166*	*0.148*	*0.134*	*0.121*	*0.205*
Older normal hearing						
Mean	1.074	1.108	1.395	1.321	1.196	1.239
S.D.	*0.129*	*0.153*	*0.199*	*0.244*	*0.208*	*0.189*
Older hearing impaired						
Mean	1.299	1.051	1.219	1.190	1.160	1.412
S.D.	*0.228*	*0.205*	*0.233*	*0.237*	*0.161*	*0.180*

IV. DISCUSSION

A. Group differences in identification and neural response patterns of stop-consonant CVs

Psychometric functions reveal that categorization of the *F*2 formant transition cue along the /b-d-g/ place-of-articulation continuum differs among the three groups such that /d/ categories are larger in older listeners without and with hearing loss versus, young normal controls. Notably, performance does not differ between the two groups of older listeners. Results are consistent with Dorman *et al.* (1985) in three similar groups of subjects. Moreover, older adults with or without normal hearing also have a harder time than younger adults perceiving temporal speech cues, such as voice onset time (e.g., Tremblay *et al.*, 2003). Because older adults with hearing loss perform similarly to older adults with normal hearing, categorization of stop-consonant CVs appears to be affected primarily by aging, not age-related hearing loss. This may explain why, within a group of hearing impaired individuals, listeners with better hearing sensitivity are as likely to have difficulty utilizing the *F*2 formant transition cue as are listeners with poorer hearing sensitivity, regardless of the presentation level of the stimulus (Plyler and Hedrick, 2002).

Additionally, in the current study, neural response patterns to the *F*2 formant transition cue differs among the three groups such that N1 and P2 amplitudes are smaller and P2 latencies are shorter to most stimulus conditions in younger versus older listeners, regardless of hearing status. Results

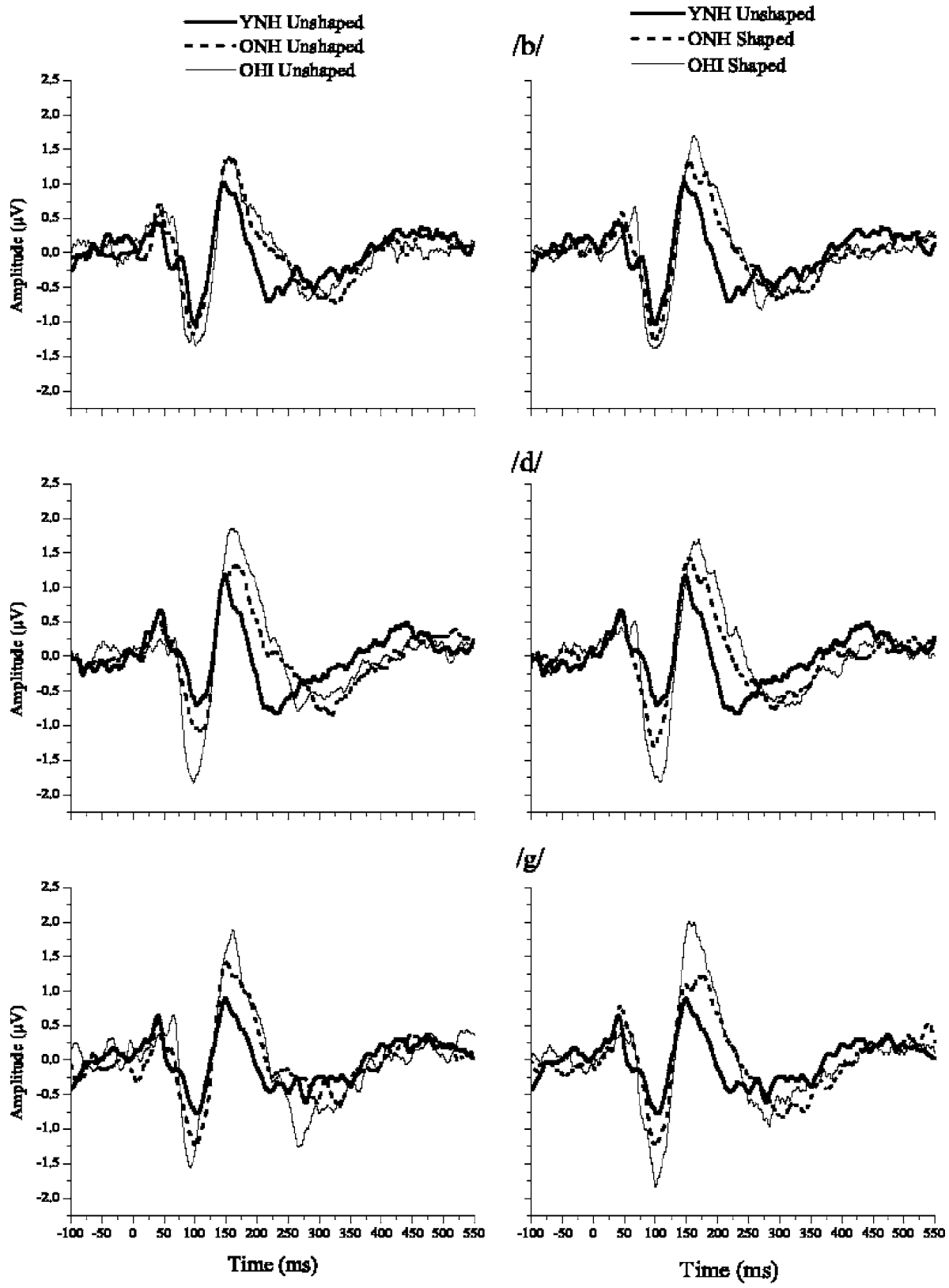

FIG. 4. Grand average waveforms for older normal-hearing (ONH=dash, $n=10$) and older hearing-impaired (OHI=light solid, $n=10$) listeners to /b/ (top), /d/ (middle), and /g/ (bottom) stop consonants in unshaped (left panels) and shaped (right panels) conditions. For comparison, grand average waveforms for young normal-hearing listeners (YNH=bold solid, $n=11$) to the unshaped stimulus conditions are displayed in both left and right panels.

are consistent with previous findings (Pfefferbaum *et al.*, 1979; Kelly-Ballweber and Dobie, 1984; Woods and Clayworth, 1986; Harkrider *et al.*, 2005) and suggest that, like categorization, neural response-patterns to various speech cues are affected primarily by aging. However, Tremblay *et al.* (2003) also reported larger N1 amplitudes in older adults with hearing loss versus older adults with normal hearing to voiceless stimuli, concluding that N1 amplitudes are influ-

TABLE III. Means and standard deviations (S.D.) for N1 latency (ms), N1 amplitude (nV), P2 latency (ms), and P2 amplitude (nV) for unshaped (US) and shaped (S) stop-consonant stimuli in young ($n=11$) and older listeners with normal hearing ($n=10$) and older listeners with hearing impairment ($n=10$).

Stimuli	US/b/	S/b/	US/d/	S/d/	US/g/	S/g/
Young normal hearing						
N1 Latency						
Mean	105.9	106.3	115.4	108.1	110.2	106.3
S.D.	*11.1*	*11.6*	*16.7*	*10.5*	*13.6*	*13.3*
N1 Amplitude						
Mean	−1201.8	−1149.5	−1074.6	−1283.1	−829.6	−976.1
S.D.	*635.5*	*552.4*	*446.2*	*484.6*	*709.4*	*544.2*
P2 Latency						
Mean	146.5	152.7	153.9	156.4	154.0	148.7
S.D.	*14.5*	*13.4*	*11.9*	*17.4*	*20.9*	*9.7*
P2 Amplitude						
Mean	1274.0	1181.9	1437.1	1200.3	1265.0	1498.3
S.D.	*856.5*	*728.8*	*775.8*	*805.1*	*833.3*	*908.2*
Old normal hearing						
N1 Latency						
Mean	107.4	114.5	115.8	113.7	108.1	112.1
S.D.	14.9	21.2	18.6	19.9	17.2	16.2
N1 Amplitude						
Mean	−1505.0	−1775.5	−1614.0	−1734.3	−1817.3	−1649.8
S.D.	*857.2*	*996.6*	*859.9*	*1255.3*	*920.2*	*1047.0*
P2 Latency						
Mean	185.9	165.9	164.3	160.3	158.1	161.0
S.D.	*94.5*	*22.0*	*18.5*	*13.0*	*13.7*	*22.6*
P2 Amplitude						
Mean	1733.5	1874.4	1827.1	1954.4	1750.5	1640.8
S.D.	*694.5*	*733.1*	*833.9*	*881.9*	*832.6*	*646.5*
Old hearing impaired						
N1 Latency						
Mean	104.6	107.0	110.2	104.1	99.7	106.1
S.D.	*11.9*	*11.4*	*14.8*	*7.9*	*14.4*	*9.5*
N1 Amplitude						
Mean	−2020.3	−1932.0	−2288.8	−2317.6	−2258.1	−2382.2
S.D.	*1418.3*	*1206.0*	*1729.9*	*1469.0*	*1336.5*	*1248.5*
P2 Latency						
Mean	160.7	167.7	162.4	165.0	157.9	160.1
S.D.	*15.9*	*15.1*	*15.6*	*11.3*	*8.6*	*10.9*
P2 Amplitude						
Mean	1772.3	2155.1	2128.4	2077.3	2167.9	2455.0
S.D.	*884.7*	*958.9*	*849.1*	*1063.9*	*1261.8*	*1290.2*

enced by age-related hearing loss. Similarly, present findings demonstrate that N1 amplitudes are larger for the older group with hearing loss compared with the older normal-hearing group ($p=0.06$), indicating that differences in N1 amplitudes to stop-consonant CVs may be due primarily to aging, but may also may be affected by age-related hearing loss.

Because overall presentation level was controlled across groups, sensation levels differed for normal-hearing versus hearing-impaired individuals. Large changes in amplitude and small changes in latency can be found when signals are presented at different sensation levels. However, evoked potential amplitudes typically decrease as sensation level decreases. In the present study, the results showed an increase in amplitude for the hearing-impaired listeners relative to the normal hearing listeners (consistent with Tremblay *et al.*, 2003). One would expect the opposite to occur (smaller amplitudes for hearing-impaired listeners) if the sensation level was influencing the amplitude findings.

B. Effects of spectral shaping on group differences in perception of stop-consonant CVs

Spectral shaping decreases differences in categorization of stop-consonant CVs in older versus young listeners. However, the effects of spectral shaping differ depending on the hearing status of the older listeners and on the phoneme being tested. Specifically, for older normal-hearing listeners with shaping, the /d/ category becomes more similar to the unshaped /d/ category of the young control group. For older listeners with hearing impairment, with shaping, the /d/ and /g/ categories are more similar to the unshaped /d/ and /g/ categories of the young control group. These results suggest that differences in categorization of $F2$ cues due to aging and age-related hearing loss are minimized with spectrally shaped stimuli.

Spectral shaping does not appear to alter neural response patterns of stop-consonant CVs in older listeners with hearing impairment. However, it does alter the neural response patterns of stop-consonant CVs in older adults with normal hearing. Specifically, as reported in Harkrider *et al.* (2005), with shaping, P2 latencies are more similar and N1 amplitudes are less similar to those measured from young adults with normal hearing to unshaped stimuli. The differential effects of spectral shaping on neural response patterns from the two groups of older listeners suggest that the effects of aging, but not age-related hearing loss, on neural responsiveness to stop-consonant CVs can be minimized with spectral shaping.

C. The aging brain, age-related hearing loss, and dynamic spectral cues

Because neural response patterns are different between younger and older listeners, it appears that aging affects excitatory and inhibitory processes and may contribute to the perceptual differences of dynamic spectral cues seen in older versus young adults. Specifically, P2 latencies were longer and N1 and P2 amplitudes were larger in older compared to younger listeners. Prolonged P2 latencies have been associated with age-induced deficits in processing of complex speech sounds (Tremblay *et al.*, 2003; Harkrider *et al.*, 2005). Large N1 and P2 amplitudes have been attributed to age-related deficits in central inhibition (e.g., Pfefferbaum *et al.*, 1979; Kelly-Ballweber and Dobie, 1984; Woods and Clayworth, 1986; Tremblay *et al.*, 2003; Harkrider *et al.*, 2005), perhaps compounded by age-related hearing loss (Tremblay *et al.*, 2003).

Additionally, in the current study, because spectral shaping has a differential effect on neural responses from older listeners with normal hearing compared to those with hearing loss, age and age-related hearing loss appear to have separate influences on neural function. Harkrider *et al.* (2005) showed that spectrally shaping the CV stimuli reduces some differences in neural response patterns and perceptual categorization between young normal listeners versus older listeners

with normal hearing. Specifically, shaping the CV stimuli resulted in reduced P2 latencies for older normal-hearing listeners so that they approximated those of younger listeners to unshaped stimuli. Moreover, with shaping, N1 and P2 amplitudes from older listeners with normal hearing became even more different relative to those from young controls to unshaped stimuli. These findings suggest that amplifying the *F*2 formant transition cue relative to the rest of the CV stimulus enhances neural synchrony, which may be reflected in shorter latency and larger amplitude AEPs. Thus, Harkrider *et al.* (2005) concluded that, in older listeners with normal hearing, difficulties with perception of spectral cues may be attributed to reduced neural synchrony of intact neurons simultaneous with weaker central inhibition. Further, enhancing the audibility of the *F*2 transition cue appeared to overcome, at least partially, the effects of aging on neural response patterns and categorization ability of stop-consonant CVs. The site of this asynchrony is unknown, it could be at the level of the auditory periphery (like auditory neuropathy/dys-synchrony) or it maybe higher in the system. However, in general, individuals, with peripheral auditory neuropathy/dys-synchrony do not benefit from standard amplification (Miyamoto *et al.*, 1999).

The present findings reveal that, unlike with older normal-hearing listeners, spectrally shaping the CV stimuli does not reduce differences in neural response patterns between older listeners with hearing impairment and young listeners with normal hearing. Yet, it does reduce differences in categorization ability between these two groups. Difficulties with perception of dynamic spectral cues in older listeners with hearing impairment may be due, in part, to a decrease in neural synchrony of intact neurons and weaker central inhibition relative to young controls. However, because spectral shaping does not alter AEPs in this group, there appears to be more to the explanation. It is possible that, in this group of older listeners with hearing loss, aging reduces neural responsiveness of intact neurons causing decreased audibility and potential central deficits due to auditory deprivation, while the hearing loss causes additional peripheral effects, such as distortion, due to cochlear damage and/or improper encoding by residual neurons. Although if this were the case, one might assume that no matter the presentation level of the speech stimuli, older listeners with hearing impairment would have more difficulty identifying and categorizing dynamic spectral cues than normal-hearing younger or older listeners. In fact, this was not so. Even though AEPs from the older hearing-impaired adults are unaltered by spectrally shaping the CVs, their categorization abilities are more like those of the young controls with shaping for /d/ and /g/ phonemes. Thus, explanations for the finding that shaping improves behavioral performance but does not alter neural response patterns of stop-consonant CVs are needed.

The higher variability in AEP measures from the older adults with hearing impairment versus the groups with normal hearing (Table III) may be responsible, in part, for the lack of statistically significant findings on the main effect of shaping on AEPs in this group. However, larger standard deviations from this group did not preclude achieving significance in other statistical comparisons. Another possibility is that, relative to older normal-hearing listeners, older hearing-impaired listeners have more room for improvement in the categorization of the /d/ and /g/ phonemes (left panels in Fig. 3). Thus, when audibility of the cue is enhanced for the individuals with hearing loss (right panels in Fig. 3), they demonstrate more benefit than older normal-hearing listeners. It is also possible that age differences between the two groups of older listeners may contribute to differential effects of shaping on AEP measures. Older normal-hearing listeners were slightly younger (mean=55.2 years) than older, hearing-impaired adults (mean=61.3 years) and, perhaps, the aging effects on their nervous systems were less dramatic and easier to overcome than those on the nervous systems of older listeners with hearing impairment. However, age-matching the participants across the two groups did not alter any statistical findings. Another possibility is that older listeners with hearing impairment learn to subtly adapt their perceptual categories in response to the altered neural response patterns. Reasons for the differences in the effects of spectrally shaped amplification on the AEPs from the two groups of older listeners are likely complex and will require further study.

In order to more clearly define the separate effects of age and age-related hearing loss on perception and neural response patterns of dynamic spectral cues, the next step may be to examine the same responses to the same stimuli in young hearing-impaired listeners. However, it may be difficult to directly compare data from young hearing-impaired listeners with older hearing-impaired listeners because the configuration, duration, and etiology of the hearing losses between the two groups are often different. Each of these factors has the potential to alter the central auditory nervous system in different ways and could confound any data comparisons between the two groups, making findings difficult to interpret.

V. CONCLUSIONS

1. Differences in behavioral identification and neural response patterns were found between young normal-hearing listeners and older listeners, regardless of hearing sensitivity. Thus, identification and neural response patterns of stop-consonant CVs appear to be affected primarily by aging, not age-related hearing loss.
2. Differences in behavioral identification of *F*2 formant transitions by both groups of older listeners relative to young controls are minimized with spectrally shaped stimuli. Therefore, enhancing the audibility of the *F*2 transition cue partially overcomes the effects of aging and age-related hearing loss on categorization ability.
3. Unlike with older normal-hearing listeners (Harkrider *et al.*, 2005), differences in neural response patterns to stop-consonant CVs from older hearing-impaired listeners are not minimized relative to normal controls when spectral shaping is applied to the stimuli. Therefore, enhancing the audibility of the *F*2 formant transition does not overcome the effects of age-related hearing loss on neural function.
4. The differential effect of shaping on neural response pat-

terns of older listeners with normal hearing compared to older listeners with hearing impairment suggests that age and age-related hearing loss have separate influences on neural function. Because spectral shaping to enhance the *F*2 formant transition normalizes neural response patterns to the cue in older normal-hearing individuals, the primary influence of aging may be a decrease in neural synchrony, leading to reduced audibility of the cue. Because spectral shaping to enhance the *F*2 formant transition does not normalize neural response patterns to the cue in older hearing-impaired listeners, age-related hearing loss appears to cause reduced neural synchrony in combination with improper coding by residual neurons, resulting in decreased audibility and distortion of the cue.

ACKNOWLEDGMENTS

This work was supported by a Professional Development Award from The University of Tennessee. The authors thank our reviewers for comments on earlier drafts of the manuscript. H. Hamby, K. Lowery, and J. Rigsby are also acknowledged for their assistance with data collection and analysis.

American National Standards Institute. (1996). "Specification for audiometers," ANSI S3.6-1996, New York.

Cornelisse, L., Seewald, R., and Jamieson, D. (**1995**). "The input/output formula: A theoretical approach to the fitting of personal amplification devices," J. Acoust. Soc. Am. **97**, 1854–1864.

Day, R. W., and Quinn, G. P. (**1989**). "Comparisons of treatments after an analysis of variance in ecology," Ecol. Monogr. **49**, 433–463.

Dorman, M. F., and Dougherty, K. (**1981**). "Shifts in phonetic identification with changes in signal presentation level," J. Acoust. Soc. Am. **69**, 1439–1440.

Dorman, M. F., Marton, K., and Hannley, M. T. (**1985**). "Phonetic identification by elderly normal and hearing-impaired listeners," J. Acoust. Soc. Am. **77**, 664–670.

Frisina, D., and Frisina, R. D. (**1997**). "Speech recognition in noise and presbycusis: relations to possible neural mechanisms," Hear. Res. **106**, 95–104.

Green, S. B., Salkind, N. J., and Akey, T. M. (**2000**). *Using SPSS for Windows. Analyzing and Understanding Data*, 2nd Ed. (Prentice–Hall, Upper Saddle River, N.J.), pp. 227–229.

Harkrider, A. W., and Hedrick, M. S. (**2005**). "Acute effects of nicotine on auditory gating," Hear. Res. **202**, 114–128.

Harkrider, A. W., Plyler, P. N., and Hedrick, M. S. (**2005**). "Effects of age and spectral shaping on perception and neural representation of stop consonant stimuli," Clin. Neurophysiol. **116**, 2153–2164.

Hedrick, M. S., Schulte, L., and Jesteadt, W. (**1995**). "Effect of relative and overall amplitude on perception of voiceless stop consonants by listeners with normal and impaired hearing," J. Acoust. Soc. Am. **98**, 1292–1303.

Jasper, H. H.. (**1958**). "Report of the committee on methods of clinical examination in electro-encephalography: The ten-twenty electrode system," Electroencephalogr. Clin. Neurophysiol. **10**, 371–375.

Kelly-Ballweber, D., and Dobie, R. A. (**1984**). "Binaural interaction measured behaviorally and electrophysiologically in young and old adults," Audiology **23**, 181–194.

Klatt, D. (**1980**). "Software for a cascade/parallel formant synthesizer," J. Acoust. Soc. Am. **67**, 971–995.

Koester, J. (**1991**). "Voltage-gated ion channels and the generation of the action potential," in *Principles of Neural Science*, 3rd Ed., edited by E. R. Kandel, J. H. Schwartz, and T. M. Jessell (Appleton and Lange, Connecticut).

Martin, J. H. (**1991**). "Coding and processing of sensory information," in *Principles of Neural Science*, 3rd Ed., edited by E. R. Kandel, J. H. Schwartz, and T. M. Jessell (Appleton and Lange, Connecticut).

Martin, B., Kurtzberg, D., and Stappells, D. (**1999**). "The effects of decreased audibility produced by high-pass noise masking on N1 and the mismatch negativity to speech sounds /bɑ/ and /dɑ/," J. Speech Lang. Hear. Res. **42**, 271–286.

Miyamoto, R. T., Kirk, K. I., Renshaw, J., and Hussain, D. (**1999**). "Cochlear implantation in auditory neuropathy," Laryngoscope **109**, 181–185.

Pfefferbaum, A., Ford, J. M., Roth, W. T., Hopkins, W. F., and Kopell, B. S. (**1979**). "Event related potential changes in healthy aged females," Electroencephalogr. Clin. Neurophysiol. **46**, 81–86.

Plyler, P. N., and Hedrick, M. S. (**2002**). "The effects of stimulus presentation level on stop consonant identification in normal and hearing-impaired listeners," J. Am. Acad. Audiol **13**, 154–l59.

Schneider, B. A., Pichora-Fuller, M. K., and Kowalchuk, D. (**1994**). "Gap detection and the precedence effect in young and old adults," J. Acoust. Soc. Am. **95**, 980–991.

Tremblay, K. M., Piskosz, M., and Souza, P. (**2002**). "Aging alters the neural representation of speech cues," NeuroReport **13**, 1865–1870.

Tremblay, K., Piskosz, M., and Souza, P. (**2003**). "Effects of age and age-related hearing loss on the neural representation of speech cues," Clin. Neurophysiol. **114**, 1332–1343.

Woods, D. L., and Clayworth, C. C. (**1986**). "Age related changes in human middle latency auditory evoked potentials," Electroencephalogr. Clin. Neurophysiol. **65**, 297–303.

Identification of syllables in noise: Electrophysiological and behavioral correlates

Ricky Kaplan-Neeman,[a] Liat Kishon-Rabin, Yael Henkin, and Chava Muchnik
Department of Communication Disorders, Sackler Faculty of Medicine, Tel-Aviv University, Israel

(Received 19 July 2005; revised 31 May 2006; accepted 2 June 2006)

This study was designed to characterize the effect of background noise on the identification of syllables using behavioral and electrophysiological measures. Twenty normal-hearing adults (18–30 years) performed an identification task in a two-alternative forced-choice paradigm. Stimuli consisted of naturally produced syllables /da/ and /ga/ embedded in white noise. The noise was initiated 1000 ms before the onset of the speech stimuli in order to separate the auditory event related potentials (AERP) response to noise onset from that to the speech. Syllables were presented in quiet and in five SNRs: +15, +3, 0, −3, and −6 dB. Results show that (1) performance accuracy, d', and reaction time were affected by the noise, more so for reaction time; (2) both N1 and P3 latency were prolonged as noise levels increased, more so for P3; (3) /ga/ was better identified than /da/, in all noise conditions; and (4) P3 latency was longer for /da/ than for /ga/ for SNR 0 through −6 dB, while N1 latency was longer for /ga/ than for /da/ in most listening conditions. In conclusion, the unique stimuli structure utilized in this study demonstrated the effects of noise on speech recognition at both the physical and the perceptual processing levels.
 [DOI: 10.1121/1.2217567]

PACS number(s): 43.64.Sj, 43.72.Dv, 43.71.Gv [ALF] Pages: 926–933

I. INTRODUCTION

Verbal communication most commonly takes place in background noise. This communication is known to be disrupted when the energy of the noise and that of the speech signal interact at the same frequency bands, resulting in reduced speech recognition (Rosen and Fourcin, 1986; Moore, 1997). The use of *auditory event related potentials (AERPs)* for studying manifestations of speech perception in noise allows for additional insight to this speech perception process (Whiting *et al.*, 1998; Martin *et al.*, 1997, 1999; Martin and Stapells, 2005). In general, AERP studies demonstrated that discriminating speech in noise resulted in slower and less efficient processing. Interestingly, this was evident also when speech recognition scores were high. (Whiting *et al.*, 1998; Martin *et al.*, 1997, 1999; Martin and Stapells, 2005). For example, the discrimination between /ba/ and /da/ in various background noises resulted in prolongation of AERP components as well as in reduced amplitudes. This effect was found more pronounced in AERPs that are believed to reflect the closure and completion of the speech perception process (i.e., P3) in attended and nonattended tasks (Kutas and Dale, 1997).

One major outcome common to these studies was the difficulty in obtaining AERP peaks at a SNR of zero and below despite high recognition scores (Martin *et al.*, 1997, 1999; Whiting *et al.*, 1998, Martin and Stapells, 2005). Examination of the methodology suggests that one possible reason for this difficulty may be related to the fact that both the speech signal and the noise were initiated at the same time. This in turn produced overlapping *onset responses* that did not allow separating the AERPs elicited by the noise from those elicited by the speech-plus-noise. Therefore, when exploring the neurophysiologic manifestations of speech perception in background noise, it is important to identify the optimal time period between the onsets (of the noise and the speech-plus-noise) that will elicit separate prominent and identifiable waveforms. Preliminary investigations conducted in our lab showed that when the noise was initiated 1 s before that of the speech signal a full separation of the waveforms was obtained. This is illustrated in Fig. 1. It can be seen that when noise was initiated 50 ms prior to the speech stimulus, the overlapping waveforms did not permit clear identification of all AERP components (especially N1 and P2) [Fig. 1(a)]. In contrast, when noise was initiated 1 s before that of the speech stimulus, clear identifiable AERPs were evident, separately for the noise and for the speech-plus-noise [Fig. 1(b)].

The main purpose of the present study was to investigate the process of speech recognition in difficult and easy noisy conditions, by normal-hearing adults, using electrophysiological measures while implementing stimuli structure that allows separating AERPs to the noise from those of the speech-plus-noise. Behavioral measures were obtained as well in order to supplement the electrophysiological data and provide a quantative measure for the "end-product" of the speech recognition process. In order to reduce the effect of linguistic information on the identification process, and thus limit the parameter under study to acoustic-phonetic, stimuli included /da/ and /ga/. These syllables differ by one significant phonetic feature, place of articulation, known to be susceptible to noise (Miller and Nicely, 1955; Boothroyd, 1984; Hornsby *et al.*, 2005).

[a]Address for correspondence: Department of Communication Disorders, Sheba Medical Center, Tel Hashomer, 52621 Israel. Electronic mail: rkneeman@012.net.il

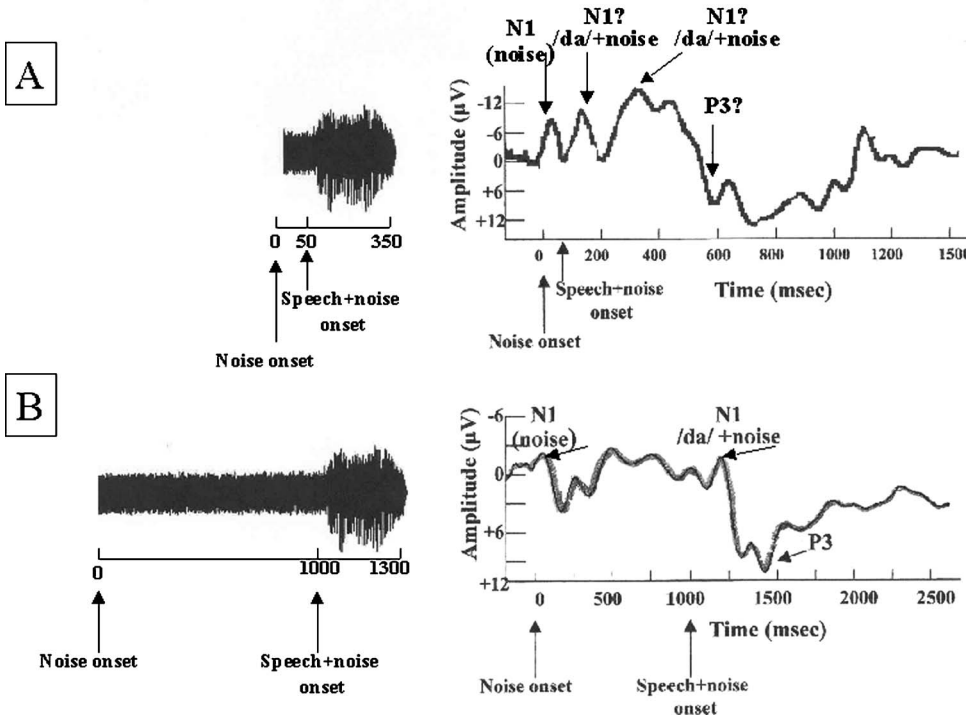

FIG. 1. AERPs of an individual subject elicited by the noise and by /da/ +noise in SNR of +15 dB at Cz (a) when noise initiated 50 ms prior to the syllable, and (b) when noise initiated 1000 ms prior to the syllable. Note the different time scale for (a) and (b) that stemmed from the different stimulus structure.

II. METHODS

A. Subjects

Twenty young adult females (mean age 21.5 years; range 18–30) were paid to participate in the study. All were right-handed, native Hebrew speakers, with normal hearing sensitivity (≤15 dBHL) within the frequency range of 250 to 8000 Hz (ANSI, 1996).

B. Stimuli

Stimuli consisted of naturally spoken consonants-vowel (CV) syllables, /da/ and /ga/. The two consonants /d,g/ were chosen since they differ by the phonetic feature place of articulation which is prone to be affected by noise (Miller and Nicely, 1955; Boothroyd, 1984; Hornsby *et al.*, 2005). Moreover, spectral differences between them are evident mainly in the steepness of the second and third formant transitions of the consonant burst to the steady state of the vowel, with the transition of /ga/ steeper than that of /da/ in Hebrew natural speech stimuli (Kishon-Rabin *et al.*, 2003). Thus, the distinction between the two phonemes in noise may be difficult, even for normal-hearing young adults.

Stimuli were digitally recorded by a female native Hebrew speaker in a soundproof room via a JVC MV40 microphone, using the Sound-Forge software (Version 4.5a), with a sampling rate of 22 050 Hz and 16 bits quantization level. The spectrographic and waveform displays of the stimuli are shown in Fig. 2. Based on preliminary testing, the two syllables were edited to create equal duration of voicing lead and equal duration of the steady-state portion of the vowel in order to minimize secondary acoustic cues for identification. Total duration of each syllable was 300 ms. Amplitude normalization was carried out in two stages: First, voicing lead and the remaining part of the syllable, i.e., burst, formant transitions, and vowel steady-state amplitudes, were normalized separately, according to the softest segment of the two syllables[1]. Second, the syllables were normalized as a whole. Careful attention was given to ensure that no transients were introduced, i.e., segments were removed only at zero crossing points, at the end or at the beginning of a cycle.

In order to demonstrate the detrimental effect of noise on both easy and difficult noise conditions, syllable identification was tested in quiet and at five signal-to-noise ratios (SNRs): +15, +3, 0, −3, and −6 dB, in a "sound-treated" room. As SNR of 0 dB was found to be a significant point in which AERP responses were difficult to obtain (Martin *et al.*, 1997,1999; Whiting *et al.*, 1998; Martin and Stapells, 2005), small steps of 3 dB around this point were selected, in addition to the favorable condition of +15 dB.

White noise was used as a masker because its flat spectrum across all frequencies will mask more efficiently the high frequencies that characterize the second formant transition of the two syllables. Because other noises, like speech-shaped or multi-talker babble, are known to be characterized by a flat spectrum below 0.8 KHz with an attenuation rate of 5–10 dB per octave above 0.8 Khz, the high-frequency acoustic cues used for the identification of place of articulation feature can be detected in these noises (Jiang *et al.*, 2006; Nittrouer *et al.*, 2003; Gordon-Salant, 1985).

The noise was generated by the Sound-Forge software, low passed at 5 KHz, gated with a 10-ms cosine-raised rise-fall time and a total duration of 1300 ms. In order to prevent the effect of frozen noise that might provide secondary cues for identification, four different segments of noise were mixed with each of the CV syllables. The CV syllables were mixed with the noise at different SNRs by varying the level of the masking noise and keeping the level of the speech stimuli constant. SNRs were computed using the root mean square (rms) function.

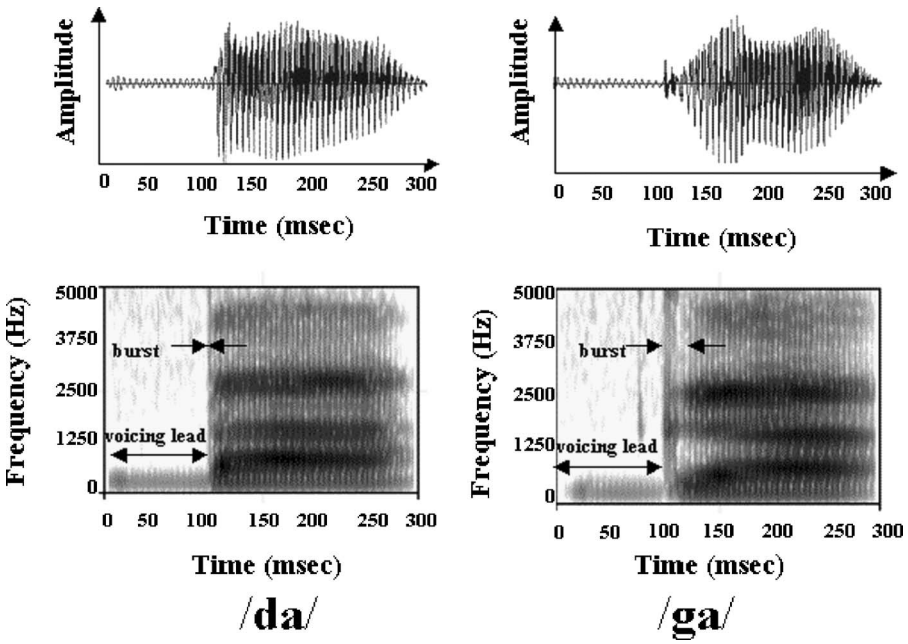

FIG. 2. Waveforms and spectrogram analysis for /da/ and /ga/. Note the voicing lead portion that includes minimal energy, and the different burst duration of each syllable.

C. AERP recording

Brain electrical activity was recorded from 11 sites on the scalp via electrocap tin electrodes referenced to the chin. Recording locations were standard international 10-20-system location: F3, Fz, F4, T3, C3, Cz, C4, T4, P3, Pz, P4. Electrodes impedances were kept under 5 kΩ. A ground electrode was placed on the left mastoid, and electrodes above and below the left eye monitored eye movements.

An Orgil™ Brain Performance Measurement (BPM) System sampled the brain electrical activity at 256 Hz. A/D resolution was 0.1 μV per bit, and the band pass was 0.1–100 Hz. Single-trial waveforms were saved for off-line eye-movement correction, base-line correction, averaging, and digital filtering.

D. Procedure

Subjects were seated in a comfortable armchair. After electrode application they were instructed to fixate their eyes on a colored spot on the wall in front of them and refrain from blinking during a recording block. The stimuli were presented using a Grason-Stadler GSI-16 audiometer via TDH-50 headphones at 65 dBHL in a semi-random order: the "quiet" (i.e., syllables without noise) condition was always the first to be presented and the succeeding SNR was chosen randomly. Note, however, that the SNR=−6 did not follow the quiet condition in order to allow some accommodation to the noise. Subjects performed a two-alternative forced-choice identification task, labeling the syllables either as /da/ or /ga/. They were instructed to press one of two buttons corresponding to the appropriate syllable, placing equal emphasis on speed and accuracy. Each block consisted of 300 single trials, 150 tokens of each syllable. The interstimulus interval between two consecutive stimuli from offset to onset was 2000 ms. Short breaks were provided between blocks, upon subjects' request. The AERP recording lasted approximately 2.5 h for each subject. Single-trial waveforms were saved for off-line analysis in the Orgil™ system computer, which also provided measures of behavioral reaction time and percent-correct identification.

The Institutional Review Board of the Tel-Aviv University approved experimentation. Participants signed an informed consent form for their participation in the study.

E. Data analysis

The latency and amplitude of the AERP components N1, P2, N2, and P3 were obtained from each subject in quiet and in the different SNRs. Peak latency was defined as the time from stimulus onset to the point of the most negative or positive peak in a preselected time window, based on grand-averaged waveforms across subjects. Thus, N1 was defined as the most negative peak in the 160–228-ms time window, P2 as the most positive peak in the 230–374-ms time window, N2 was the most negative peak in the 280–574-ms time window, and P3 was the most positive peak in the 380–843-ms time window. Amplitude was defined as the voltage difference between the peak and the average voltage over the 200-ms preceding stimulus onset.

Multivariate analysis of variance for repeated measures with two levels of task (/da/, /ga/) and six levels of condition (quiet, +15, +3, 0, −3, −6) was performed on the AERP components latency and amplitude as well as on the behavioral measures: accuracy (percent correct) and reaction time. The level of significance was set to $p<0.05$. Contrast analysis was employed when significant differences among tasks and conditions were found.

III. RESULTS

A. Behavioral measures

1. Accuracy

Word identification accuracy in the different listening conditions (quiet and the different SNRs) for the two syllables (/da/, /ga/) are presented in Fig. 3(a). A MANOVA test was conducted to separate the main effects of syllable, lis-

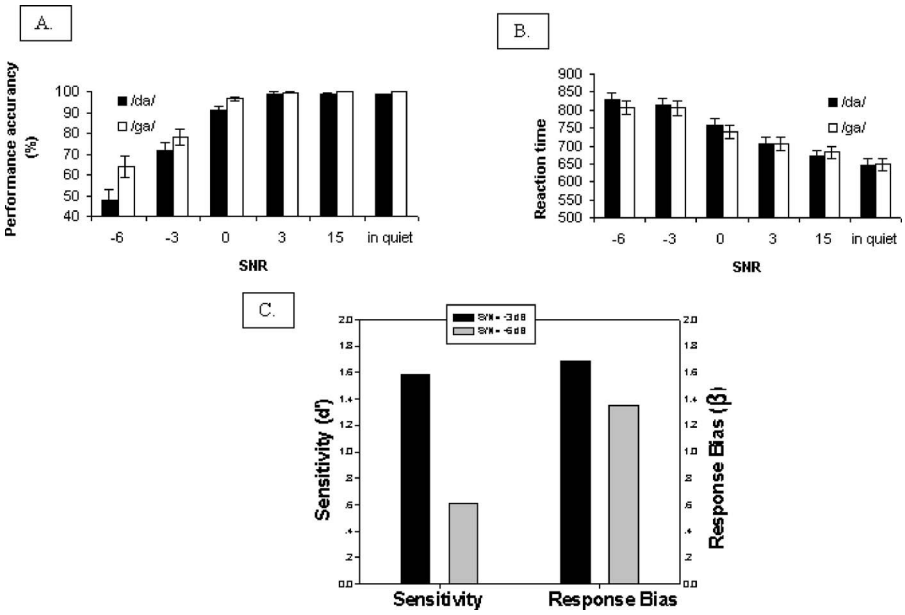

FIG. 3. Psychoacoustic data: (a) The mean (±1 SE) percentages of correct syllable identification; (b) reaction time (in ms) in the quiet condition and in the different SNRs for /da/ and /ga/, and (c) Sensitivity (d') and bias (β) in SNRs −3 and −6 dB.

tening condition, and their interaction: syllable × listening condition. The results revealed that both main effects and interaction were significant [$F(1,19)=10.42$, $p=0.004$; $F(5,15)=31.96$, $p<0.0001$; $F(5,15)=2.95$, $p=0.04$; for syllable, listening condition and syllable × listening condition, respectively]. Specifically, the average identification of the syllable /ga/ (90.87%) was better than /da/ (83.66%). A tendency of better identification of /ga/ was manifested in almost all SNRs. Contrast analysis of the listening condition revealed significant differences ($p \leqslant 0.02$) among each of the SNRs and the quiet condition (with the exception of SNR = +15 dB).

The decrease in performance with decreasing SNR was different for /da/ than for /ga/. This interaction is illustrated in Fig. 3(a). Contrast analysis revealed that for quiet and the more favorable listening conditions (SNR = +15, +3 dB), identification was similar for both syllables. At SNR of 0, however, it was more difficult to identify /da/ than /ga/, a difference of 5.66 percentage points [$F(1,19)=16.61$, $p<0.0006$]. This difference increased to 16.27 percentage points at SNR of −6 dB, but did not reach statistical significance.

Performance accuracy in a two-alternative-forced-choice task can be described by a hit and false-alarm rate, which in turn can be reduced to a single measure of sensitivity. The sensitivity measure, d', proposed by signal detection theory (Macmillan and Creelman, 2005), was calculated and showed decreased sensitivity to the recognition in noise as SNR decreased from −3 to −6 [1.58 and 0.61, respectively, $t(18)=5$, $p<0.001$], as can be seen in Fig. 3(c). Furthermore, a β calculation, a measure of bias, suggests relatively unchanged β with decrease of SNR from −3 to −6 [1.69 and 1.35, respectively, $t(18)=1.15$, $p<0.05$]. Thus, while sensitivity to performance decreased, no "bias,"[2] or favoritism towards one syllable was demonstrated and the better recognition of /ga/ was not due to listeners' preference of this syllable.

2. Reaction time

Figure 3(b) shows the means (±1 SE) of reaction times in the listening conditions: quiet and the different SNRs for each of the syllables. While the effect of listening condition was significant [$F(5,15)=44.19$, $p<0.0001$], the effects of syllable as well as the interaction syllable × listening condition were not found to be significant. Specifically, it was found that reaction time was the shortest in the quiet condition and was prolonged significantly between each successive condition ($p<0.01$) (RT = 676.2, 705.7, 749, 809, and 817.4 ms for SNR = +15, +3, 0, −3, and −6 dB, respectively).

B. Auditory event related potentials

For the purpose of this study the latencies and amplitudes of AERPs from the midline electrodes (Fz, Cz, Pz), which yielded the largest amplitudes, were analyzed. The paradigm used in the present study resulted in two distinguishable sets of AERP peaks: N1 and P2 elicited by the noise alone, with minor changes of latency and amplitude regardless of noise intensity, and N1, P2, N2 and P3 elicited by the syllables in noise that were prolonged in latency and decreased or increased in amplitude as noise level increased.

1. Latency

Individual subject's responses elicited to /ga/ in the quiet condition and at SNR = +15, 0, and −6 dB are displayed in Fig. 4. Responses are displayed for Cz, which yielded the largest amplitudes. The effect of noise in the different SNRs on *N1 latencies* is shown in Table I. A significant main effect of syllable on N1 latency [$F(1,19)=13.69$, $p=0.0015$] was found. Specifically, N1 latency for /ga/ was longer (221.3 ms), than for /da/ (205.6 ms) across SNRs. In addition, a main effect of listening condition was found [$F(5,15)=12.55$, $p<0.0001$] with a significant prolongation

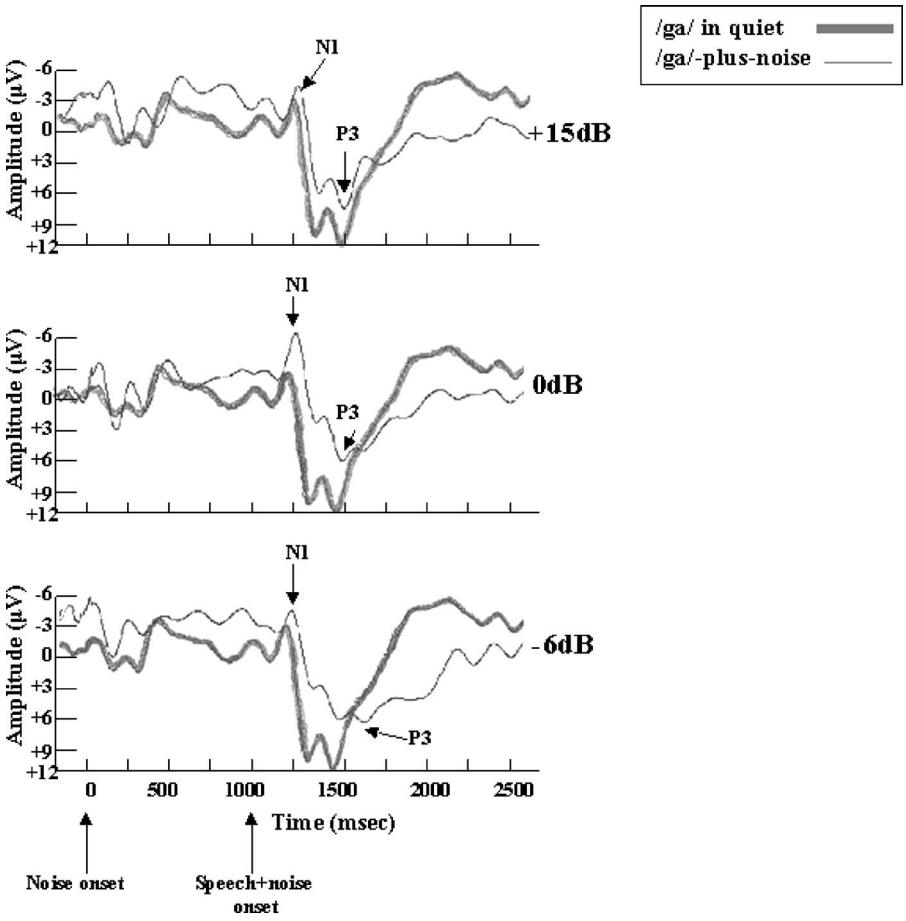

FIG. 4. Superimposition of individual subject's waveforms elicited by /ga/ in the quiet condition (thick line) and at SNR of +15, 0, and −6 dB (thin line) at Cz. The arrows indicate N1 and P3 at the different SNRs.

of N1 as SNR decreased from +15 to −6 dB ($p<0.05$). The interaction syllable × listening condition was not significant.

The effect of noise on P2 and N2 latencies across SNRs were inconsistent. In some subjects latencies of these components were prolonged in all noise conditions, however in other subjects prolongation occurred only at negative SNRs. As a result the main effects of syllable and listening condition on P2 and N2 latencies were not significant.

The effect of noise in the different SNRs on *P3 latencies* is shown in Table I. A significant main effect of syllable [$F(1,19)=11.6$, $p=0.01$] suggested that in general P3 latency was longer for /da/ (605.5 ms) than for /ga/ (554.2 ms). A significant main effect of listening condition on P3 was also found [$F(5,15)=19.45$, $p=0.01$]. Analyses of contrasts revealed that a significant prolongation of P3 latency occurred at SNR ≤ 0 compared to the quiet condition. The data in Table I suggest a tendency for the noise to have a greater effect on P3 for /da/ than for /ga/ as SNR decreases. This interaction, however, was not significant.

In order to evaluate the processing time that elapsed from the elicitation of N1 to that of P3, we subtracted N1 latencies from P3 latencies. The resulting N1−P3 measure for both syllables in the different listening conditions is shown in Table I. The data suggests significantly prolonged N1−P3 for /da/ compared to /ga/, especially at SNRs equal to or less than zero. Significant main effects of syllable [$F(1,19)=81.8$, $p<0.0001$], and listening condition [$F(5,15)=11.92$, $p<0.0001$], as well as a significant interaction syllable × listening condition [$F(5,15)=21.42$, $p<0.0001$] were found. Contrast analysis of listening condition revealed a significant difference between SNR of 0 and the quiet condition [$F(1,19)=24.34$, $p<0.0001$] The interaction syllable × listening condition revealed significant differences between /ga/ and /da/ only at SNR of 0 [$F(1,19)=19.29$, $p<0.0003$].

TABLE I. Mean (±SD) N1 and P3 latencies and brain processing time (BPT) (P3 latency minus N1 latency) in ms for both syllables. Peak latencies were measured where amplitudes were maximal (N1 at Cz and P3 at Pz).

SNR	/ga/N1	/da/N1	/ga/P3	/da/P3	/ga/ BPT	/da/ BPT
In quiet	188.8(25.5)	138.6(23.6)	482.7(63.5)	522.3(81.5)	293.9 (38)	383.7(52.5)
+15	200.8(26.5)	204.5(24.6)	512.9(72.8)	533.9(79.9)	312.1(46.3)	329.4(55.3)
+3	227.4(24.6)	210.3(33.7)	570.7(68.6)	505.9(132.28)	343.3 (44)	295.6(98.58)
0	230.3(16.4)	232.9 (42)	567.3(41.6)	672.8(112.6)	337(25.2)	439.9(70.6)
−3	234.1 (14)	216(15.9)	580.2(88.1)	671.8(85.3)	346.1(74.1)	455.8(69.41)
−6	246.2 (22)	231.4(14.6)	611.6(83.9)	727.6(76.4)	365.4(61.9)	496.2(61.8)

TABLE II. Mean (±SD) of N1 amplitudes (in μV) for both syllables measured at Cz.

SNR	/ga/	/da/
In quiet	11.53(2.34)	6.77(2.34)
+15	8.21(1.93)	5.96(2.11)
+3	8.55(1.35)	7.28(3.49)
0	7.55(2.02)	4.88(2.52)
−3	6.77(1.8)	7.74(2.83)
−6	7.35(3.6)	10.1(2.79)

2. Amplitude

A general decrease in /ga/ N1 amplitude from quiet to an SNR of −6 can be seen in Table II. For the N1 amplitude of /da/, however, the effect of noise was not monotonic: it decreased up to an SNR of 0, after which no clear tendency was evident. A significant main effect of listening condition was found [$F(5,15)=5.24$, $p<0.0001$]. Contrast analysis of listening condition revealed a significant decrease between each two consecutive SNRs ($p<0.05$). The main effect of syllable, as well as the interaction syllable × listening condition, were not significant. The effect of noise on the amplitudes of the other AERP components P2, N2, and P3 was not monotonic and did not reach significance.

IV. DISCUSSION

The present study was designed to evaluate the effect of background noise on the identification of naturally produced syllables using behavioral and electrophysiological measures. Our main findings can be summarized as follows: (1) both performance accuracy and reaction time were affected by the noise, more so for reaction time, which was prolonged even in the highest SNR (+15); (2) both N1 and P3 latencies were prolonged as noise levels increased, more so for P3; (3) /ga/ was better identified than /da/, in all noise conditions; and (4) P3 latency and N1−P3 brain processing time were longer for /da/ than for /ga/ for SNR 0 through −6 dB, while N1 latency was longer for /ga/ than for /da/ in most listening conditions.

A. Behavioral measures

The finding that sensitivity and recognition are reduced and reaction time is prolonged by the noise support recent speculations that these measures provide partially independent sources of information that possibly complement one another (Mackersie *et al.*, 1999; Oates *et al.*, 2002). While sensitivity as reflected by d' was affected only at zero or negative SNRs, reaction time measure was found to be more susceptible to the timing of the process, delayed already with the introduction of noise, thus manifesting difficulties that were not apparent otherwise. The results of the present study are in agreement with studies that investigated the effect of different factors related to speech perception on performance accuracy and reaction time [e.g., noise (Pratt, 1981), amplification via hearing aids (Gatehouse and Gordon, 1990), speech in noise (Whiting *et al.*, 1998), and phonetic versus semantic processing (Henkin *et al.*, 2002)].

One of the unexpected results of this study is that listeners showed greater sensitivity to /ga/ compared to /da/ with decreasing SNR, as revealed by both performance accuracy and unchanged ß values. It was hypothesized that because /ga/ has a steeper second formant transition it will be more susceptible to the effect of noise. Furthermore, specific efforts were made to select stimuli that are similar in the direction of the formant transition, thus minimizing the possibility of secondary acoustic cues influencing the identification in noise (see Sec. II). The unpredicted findings raised the possibility that greater sensitivity of the identification of /ga/ in noise may be related to other acoustic cues to the perception of place of articulation that were not considered previously. In a recent study investigating the identification functions of /ba, da, ga/ on a continuum of second formant transition, Hebrew speaking listeners were found not to rely entirely on second formant transitions for the identification of the back voiced plosive /ga/ (Kishon-Rabin *et al.*, 2003). Additional inquiries into the data showed that the *duration of the burst* of /ga/ was longer (20.54 ms) than that of /da/ (8.21 ms) and therefore may serve as an important acoustic cue for the identification of this phoneme. Similar findings were found in Dutch, where subjects relied on burst duration for identification of plosives (Ernestus and Mak, 2004). It is known that noise has a larger detrimental effect on spectral compared to temporal information (Miller and Nicely, 1955; Boothroyd, 1984), thus explaining the greater difficulties of identifying /da/ compared to /ga/ in noise. It should be noted that although the phonemes /da/ and /ga/ are both part of the phonemic inventory of the Hebrew and English languages and are similarly described by the same phonological system, it is possible that they are acoustically different because of differences in pronunciation as well as the influence of the following vowel (Kishon-Rabin *et al.*, 1999). In order to extend our findings to the voiced plosives in other languages, such as English, additional investigations specific to each language are required.

B. Auditory event related potentials

One of the major aims of this study was to investigate the identification process of syllables in noise using AERP indices in a stimuli structure that will not obscure the responses of the speech stimuli by the robust responses to the noise. After several pilot studies, it was found that inserting a 1000-ms noise segment prior to the onset of the syllable enabled us to record two distinct sets of AERPs, one to the noise and the other to the syllable in noise. As a result identifiable AERPs were documented at all noise conditions, including negative SNRs.

The main AERP finding of the present study suggests a differential effect of noise on N1 and P3 latency. N1 latency increased as SNR decreased from the favorable listening condition of SNR=+15 dB. In contrast, P3 latency was significantly prolonged only at SNRs equal to or less than 0 dB. A possible explanation for these findings relates to the perceptual processes that each of these components is believed to reflect. N1 is traditionally classified as an obligatory response, reflecting the initial stages of the auditory process-

ing, and is known to be affected by the physical characteristics of the stimuli (Naatanen and Picton, 1987; Martin *et al.*, 1997). Once noise is added to the stimuli, these characteristics change and in turn elicit responses showing reduced temporal precision. A similar effect was demonstrated by Oates *et al.*, (2002) investigating AERPs in sensory-neural hearing loss. These authors postulated that the prolonged N1 latencies were a consequence of the physiological changes that occur within the cortex when sensory-neural hearing impairments were present. It might be suggested, therefore, that the cortical activity of speech perception in noise is slowed down in a way that resembles a state of sensory-neural hearing loss.

The P3 component, on the other hand, is assumed to reflect higher-order cognitive operations, such as recognition and classification, thus representing the closure or completion of the speech perception process (Kutas and Dale, 1997; Salisbury *et al.*, 2002). It was reported to be affected by several factors such as the difficulty of linguistic processing (Henkin *et al.*, 2002) and the amount of information available to reach a conscious decision (Oates *et al.*, 2002; Salisbury *et al.*, 2002). In the present context, the increase of P3 latency in negative SNRs may be explained by the decrease in the information conveyed by the syllables due to masking and the increase in listeners' uncertainty regarding their identification. Under favorable noise conditions, however, noise did not degrade performance and no significant increase in P3 latency was evident.

The differential effect of background noise on N1 and P3 can also be explained by the auditory scene analysis theory (Bregman, 1990). N1 latency prolongation at all noise conditions could be considered an index of a stage determined by the incoming acoustic data, affected by the physical characteristics of the stimuli, namely the addition of noise: a bottom-up process. The P3 latency prolongation only at unfavorable noise conditions, on the other hand, might reflect the consequence of a more detailed analysis by controlled mechanisms of linguistic knowledge: a top-down process (Alain *et al.*, 2001).

In order to ensure that the prolongation of P3 latency is not secondary to the prolongation of the N1 component, the latencies of N1 were subtracted from those of P3 (N1−P3). A considerable prolongation of N1−P3 was evident, especially for /da/, as SNR decreased to less than zero. These results may be the manifestation of the difficulty that listeners encountered while identifying /da/ at negative SNR values. The finding that both N1 and P3 latencies were prolonged suggests that the presence of background noise has a significant impact on the initial stages of stimulus processing when the stimuli are first registered as well as on the later cognitive levels of speech processing when the decisions are made. Moreover, this impact (i.e., latency prolongation) appears to be enhanced at the later stages of processing, presumably reflecting the reduction of acoustic information due to the noise and difficulties in linguistic decision making.

One of the interesting findings of this study is the reverse pattern of N1 and P3 latency prolongation for syllables /da/ and /ga/, in quiet as well as in noise. While N1 latency for /ga/ was *longer* than for /da/, P3 latency was *longer* for /da/ than for /ga/. If we assume the traditional definition of N1 as an obligatory response to the acoustic stimulus, we would expect N1 latency to be equal for both syllables when masked at a given SNR (considering the syllables were matched in their physical dimensions). Alternatively, one would predict that, if at all, N1 latency may be longer for /da/ than for /ga/ because P3 latency was longer for /da/, implying difficulty in syllables identification process. The unexpected findings (as indicated above) might be explained by the longer burst duration (for /ga/), which elicited a longer N1 latency in all listening conditions. Thus, regardless of the physical circumstances (i.e., existence of background noise), the acoustic cue for identification was already processed at the N1 level, reflecting not only detection of the stimuli but also some kind of a preclassification process. This finding lends support to the assumption that N1 is a mixed component also signaling the arrival of potentially discriminable information to the auditory cortex (Martin and Boothroyd, 1999; Sharma and Dorman, 2000; Sinai and Pratt, 2003). For recognition, however, listeners were required to finalize the classification-categorization process of the stimuli, reflected by P3 latency.

Some evidence of the difficulties associated with the identification of the syllables in noise can be found in the AERP amplitude data. The N1 amplitude of /ga/ showed a gradual decrease as SNRs decreased from quiet to SNR =−6 dB. It is suggested that acoustic changes of the stimuli may have affected the synchronous firing of neural populations generating the N1 response, thus causing a reduction in N1 amplitude. The N1 amplitude for /da/, however, showed a different pattern and decreased only at SNRs greater than 0 dB. The same inconsistency across syllable type holds for P2, N2, and P3 amplitude. If variations in P3 amplitude are assumed to reflect the degree or quality with which the information is processed (Polich and Herbst, 2000), then the addition of the noise might have damaged the quality of the response to /da/, being more susceptible to noise, resulting in disorganized and desynchronized responses. The greater effort to identify /da/ might have caused the inconsistency in response characteristics. Only when acoustic conditions deteriorated, the trend of decreased amplitude was evident, as found in difficult task situations by other studies (Polich, 1987; Whiting *et al.*, 1998; Henkin *et al.*, 2002). Alternatively, as suggested by Tampas and Harkrider (2006), the inconsistency in response to /da/ might reflect underlying differences in cortical inhibition. Specifically, recent studies interpreted changes in AERP amplitudes as indication of increased brain excitability or a reduced inhibition capacity (Harkrider and Champlin, 2001; Harkrider and Hedrick, 2005). Thus, reduced amplitudes may reflect the suppression of brain electrical activity to the irrelevant stimulus (noise) whereas enhanced amplitudes may presumably reflect failure of cortical inhibitory mechanisms. Overall, it appears that the amplitude measure as found in the present study cannot serve as a consistent and reliable indicator of the effect of noise on CV syllables identification processes.

C. Conclusions

This study supports the following conclusions:

(1) The novel stimuli structure used here enabled the separation of AERP responses to the noise from those elicited when identifying speech-plus-noise.
(2) Reaction time measure was found to be more sensitive than performance accuracy to the introduction of background noise, demonstrating the slowing down of the identification process despite high recognition scores.
(3) Multiple temporal and spectral cues are probably involved in phoneme identification. Phonemes cued by temporal information, however, appear to be more resilient to noise than those cued spectrally. This finding may be language dependent and requires further investigation.
(4) AERPs delineated the effect of noise on the identification process from the initial stages of detection and preclassification (N1) to the completion of the stimuli evaluation process (P3).

ACKNOWLEDGMENTS

This research was partially supported by the Tel-Aviv University and the Yairi Fund. The authors also wish to thank Professor Hillel Pratt for his insightful comments, Esther Shabtay for the statistical analysis, and Dr. Shlomo Gilat for technical assistance.

[1]Syllables were normalized in two parts because the 100-ms voicing lead has very little energy, being practically unheard, as opposed to the second part of the syllable, composed of burst, transitions, and vowel, containing most of the syllable's energy. Because syllables were normalized according to the softest segment, it was necessary to separate the voicing lead part from the other part, otherwise the overall intensity would have been reduced markedly.

[2]Beta- the index that describes the location of a criterion that divides the decision axis between values that lead to "yes" and "no" responses (Macmillan and Creelman, 2005, p. 47).

Alain, C., Arnott, S. R., and Picton, T. W. (**2001**). "Bottom-up and top-down influence on Auditory Scene Analysis: Evidence from event-related brain potentials," J. Exp. Psychol. Hum. Percept. Perform. **27**, 1072–1089.

ANSI (**1996**). American National Standard Specification for Audiometers ANSI S3.6-1996 (American National Standards Institute, New York).

Boothroyd, A. (**1984**). "Auditory perception of speech contrasts by subjects with sensorineural hearing loss," J. Speech Hear. Res. **27**, 134–144.

Bregman, A. S. (**1990**). *Auditory Scene Analysis: The Perceptual Organization of Sound* (Bradford Books, MIT, Cambridge, Ma).

Ernestus, M. and Mak, W. M. (**2004**). "Distinctive phonological features differ in relevance for both spoken and written word recognition," Brain Lang **90**, 378–392.

Gatehouse, S. and Gordon, J. (**1990**). "Response times to speech stimuli as measures of benefit from amplification," Br. J. Audiol. **24**, 63–68.

Gordon-Salant, S. (**1985**). "Recognition of digitized CV syllables in multitalker babble," Audiology **24**, 241–253.

Harkrider, A. W. and Champlin, C. A. (**2001**). "Acute effect of nicotine on non-smokers: III. LLRs and EEGs," Hear. Res. **160**, 99–110.

Harkrider, A. W. and Hedrick, M. S. (**2005**). "Acute effect of nicotine on auditory gating in smokers and non-smokers," Hear. Res. **202**, 114–128.

Henkin, Y., Kishon-Rabin, L., Gadoth, N., and Pratt, H. (**2002**). "Auditory event-related potentials during phonetic and semantic processing in children," Audiol. Neuro-Otol. **7**, 228–239.

Hornsby, B. W. Y., Trine, T. D., and Ohde, R. N. (**2005**). "The effect of high presentation levels on consonants feature transmission," J. Acoust. Soc. Am. **118**, 1719–1729.

Jiang, J., Chen, M., and Alwan, A. (**2006**) "On the perception of voicing in syllable-initial plosives in noise," J. Acoust. Soc. Am. **119**, 1092–1105.

Kishon-Rabin, L., Dayan, M., and Michaeli, O. (**2003**). "Effect of second-formant transitions on the perception of Hebrew voiced stop consonants," J. Basic Clin. Physiol. Pharmacol. **14**, 151–164.

Kishon-Rabin, L., Taitelbaum, R., Tobin, Y., and Hildesheimer, M. (**1999**). "The effect of partially restored hearing on speech production of postlingually deafened adults with multi channel cochlear implants," J. Acoust. Soc. Am. **106**, 2843–2857.

Kutas, M. and Dale, A. (**1997**). "Electrical and magnetic readings of mental functions," in *Cognitive Neuroscience*, edited by M. D. Rugg (Psychology Press, UK) pp. 197–242.

Mackersie, C., Neuman, A. C., and Levitt, H. (**1999**). "Response time and word recognition using a modified-rhyme monitoring task: list equivalency and time-order effects," Ear Hear. **20**, 515–520.

Macmillan, N. A. and Creelman, C. D. (**2005**). *Detection Theory: A User's Guide* (Erlbaum, London), pp 3–47.

Martin, B. A. and Boothroyd, A. (**1999**). "Cortical, auditory, event-related potentials in response to periodic and aperiodic stimuli with the same spectral envelope," Ear Hear. **20**, 33–44.

Martin, B. A. and Stapells, D. R. (**2005**). "Effects of low-pass noise masking on auditory event-related potentials to speech," Ear Hear. **26**, 195–213.

Martin, B. A., Kurtzberg, D., and Stapells, D. R. (**1999**). "The effects of decreased audibility produced by high-pass noise masking on N1 and the mismatch negativity to speech sounds /ba/ and /da/," J. Speech Lang. Hear. Res. **42**, 271–286.

Martin, B. A., Sigal, A., Kurtzberg, D., and Stapells, D. R. (**1997**). "The effects of decreased audibility by high-pass noise masking on cortical event-related potentials to speech sounds /ba/ and /da/," J. Acoust. Soc. Am. **101**, 1585–1599.

Miller, G. A. and Nicely, P. E. (**1955**). "An analysis of perceptual confusions among some English consonants," J. Acoust. Soc. Am. **27**, 338–352.

Moore, B. C. J. (**1997**). *An Introduction to the Psychology of Hearing* (Academic, London), pp. 272–305.

Naatanen, R., and Picton, T. W. (**1987**). "The N1 wave of human electric and magnetic response to sound: A review and an analysis of the component structure," Psychophysiology **24**, 375–425.

Nittrouer, S., Wilhelmsen, M., Shapely, K., Bodily, K., and Creutz, T. (**2003**) "Two reasons not to bring your children to cocktail parties," J. Acoust. Soc. Am. **113**, 2254.

Oates, P. A., Kurtzberg, D., and Stapells, D. R. (**2002**). "Effects of sensorineural hearing loss on cortical event-related potential and behavioral measures of speech-sound processing," Ear Hear. **23**, 399–415.

Polich, J. (**1987**). "Task difficulty, probability, and inter-stimulus interval as determinants of P300 from auditory stimuli," Electromyogr. Clin. Neurophysiol. **68**, 311–320.

Polich, J., and Herbst, K. L. (**2000**). "P300 as a clinical assay: rationale, evaluation, and findings," Int. J. Psychophysiol **38**, 3–19.

Pratt, R. L. (**1981**). "On the use of reaction time as a measure of intelligibility," Br. J. Audiol. **15**, 253–255.

Rosen, S. and Fourcin, A. (**1986**). "Frequency selectivity and the perception of speech," in *Frequency Selectivity in Hearing*, edited by B. C. J. Moore (Academic, London).

Salisbury, D. F., Desantis, M. A., Shenton, M. E., and McCarley, R. W. (**2002**). "The effect of background noise on P300 to suprathreshold stimuli," Psychophysiology **39**, 111–115.

Sharma, A. and Dorman, M. F. (**2000**). "Neurophysiologic correlates of cross-language phonetic perception," J. Acoust. Soc. Am. **107**, 2697–2703.

Sinai, A. and Pratt, H. (**2003**). "Semantic processing of unattended words and pseudowords in first and second language: an ERP study," J. Basic Clin. Physiol. Pharmacol. **14**, 177–190.

Tampas, J. W. and Harkrider, A. W. (**2006**). "Auditory evoked potentials in females with high and low acceptance of background noise when listening to speech," J. Acoust. Soc. Am. **119**, 1548–1561.

Whiting, K. A., Martin, B. A., and Stapells, D. R. (**1998**). "The effects of broadband noise masking on cortical event-related potentials to speech sounds /ba/ and /da/," Ear Hear. **19**, 218–231.

Effects of level and frequency on the audibility of partials in inharmonic complex tones

Brian C. J. Moore,[a] Brian R. Glasberg, Kai En Low, Thomas Cope, and Wei Cope
Department of Experimental Psychology, University of Cambridge, Downing Street, Cambridge CB2 3EB, England

(Received 15 November 2005; revised 31 May 2006; accepted 31 May 2006)

The effect of level and frequency on the audibility of partials was measured for complex tones with partials uniformly spaced on an equivalent rectangular bandwidth (ERB_N) number scale. On each trial, subjects heard a sinusoidal "probe" followed by a complex tone. The probe was mistuned downwards or upwards (at random) by 4.5% from the frequency of one randomly selected partial in the complex. The subject indicated whether the probe was higher or lower in frequency than the nearest partial in the complex. The frequencies were roved from trial to trial, keeping frequency ratios fixed. In experiment 1, the level per partial, L, was 40 or 70 dB SPL and the mean frequency of the central partial, f_c, was 1201 Hz. Scores for the highest and lowest partials in the complexes were generally high for all spacings. Scores for the inner partials were close to chance at 0.75-ERB_N spacing, and improved as the spacing was increased up to 2 ERB_N. For intermediate spacings, performance was better for the lower level used. In experiment 2, L was 70 dB SPL and f_c was 3544 Hz. Performance worsened markedly for partial frequencies above 3544 Hz, consistent with a role of phase locking. [DOI: 10.1121/1.2216906]

PACS number(s): 43.66.Fe, 43.66.Hg, 43.66.Dc [AJO] Pages: 934–944

I. INTRODUCTION

People with normal hearing have the ability to "hear out" some of the individual partials in complex tones (Ohm, 1843; Helmholtz, 1863). This ability has been quantified in several studies using both harmonic tones (Plomp, 1964; Plomp and Mimpen, 1968; Gibson, 1970; Bernstein and Oxenham, 2003) and inharmonic tones (Plomp, 1964; Soderquist, 1970; Fine and Moore, 1993; Moore and Ohgushi, 1993). For harmonic complex tones with equal-amplitude harmonics, the results of most studies indicate that harmonics with numbers up to about 5 to 8 can be heard out, whereas higher harmonics are unresolved. When the harmonic of interest is pulsed on and off, above-chance performance is possible up to somewhat higher harmonic numbers (Gibson, 1970; Bernstein and Oxenham, 2003); however, it is not clear whether this method gives a valid measure of the ability to hear out partials (Moore *et al.*, 2006). Plomp (1964) and Plomp and Mimpen (1968) proposed that a partial can only be heard out from a complex tone when it is separated from neighboring partials by more than one critical bandwidth (Zwicker, 1961).

Moore and Ohgushi (1993) studied the audibility of partials in complex tones whose partials were uniformly spaced on an ERB_N-number scale, where ERB_N refers to the equivalent rectangular bandwidth of the auditory filter as determined for young, normally hearing listeners at moderate sound levels (Glasberg and Moore, 1990; Moore, 2003); it is conceptually similar to the critical bandwidth as described by Zwicker (1961), but different in numerical value, especially at low frequencies (Moore and Sek, 1995). Moore and Ohgushi (1993) suggested that, if the ability to hear out partials depends primarily on the extent to which the partials are resolved in the cochlea, then, for a given ERB_N spacing, the ability to hear out partials should be the same for all partials within the complex tone. Their results showed that the highest and lowest ("edge") partials in each complex tone were especially easily heard out, and the ability to hear out the edge partials remained above chance even when the partials were closely spaced (0.75-ERB_N spacing). In contrast, scores for the "inner" partials were close to chance when the spacing was 0.75 ERB_N and increased to become near perfect when the spacing was increased up to 2 ERB_N. For intermediate spacings, performance for the inner partials did not vary monotonically with the frequency of the partials. Discounting the nonmonotonicities, there was an overall trend for performance to worsen with increasing frequency of the inner partials. Moore and Ohgushi suggested that this might reflect a role of phase locking in the ability to hear out partials; phase locking becomes less precise for frequencies above about 1000 Hz (Anderson, 1973; Johnson, 1980; Palmer and Russell, 1986). Phase locking can also be used to explain why the edge partials are especially easy to hear out (Moore and Ohgushi, 1993; Moore, 2003).

In the present experiments, we used a method similar to that of Moore and Ohgushi (1993) to measure the ability to hear out partials in complex tones with partials uniformly spaced on an ERB_N-number scale. The present study extends previous studies in the following ways. First, we examined the effect of overall level. In previous studies only a single level has been used. It is known that the bandwidths of the auditory filters increase with increasing level, mainly because the filters get broader on their low-frequency sides (Weber, 1977; Moore and Glasberg, 1987; Glasberg and Moore, 1990; 2000; Baker *et al.*, 1998; Rosen *et al.*, 1998).

[a]Author to whom correspondence should be addressed. Electronic mail: bcjm@cam.ac.uk

If the ability to hear out partials depends on peripheral filtering, then that ability should be better at a low level than at a high level. Our first experiment tested this prediction.

The second new aspect is that we extended the frequency range covered by the partials, to include frequencies well above the highest frequency at which phase locking is thought to occur (at least in animals), namely 4–5 kHz (Anderson, 1973; Johnson, 1980; Palmer and Russell, 1986). This was done to provide a stronger test of the idea that the ability to hear out partials depends partly on phase locking, as suggested by Ohgushi (1978), Hartmann *et al.* (1990), Moore and Ohgushi (1993), Hartmann and Doty (1996), and de Cheveigné (1999). Plomp (1964) and Plomp and Mimpen (1968) measured the ability to hear out partials in harmonic complex tones with 12 harmonics, using fundamental frequencies up to 2000 Hz. The number of audible harmonics tended to decrease with increasing fundamental frequency, once the fundamental frequency was above 125 Hz. This meant that the frequency separation between adjacent harmonics required for a given harmonic to be heard out with 75% accuracy, expressed as a proportion of the frequency of the harmonic, increased with increasing frequency. The proportion was about 0.15 at 1000 Hz (corresponding to about 1.15 ERB_N) and 0.24 at 8000 Hz (corresponding to about 2.2 ERB_N). These results are consistent with the idea that phase locking has some influence on the ability to hear out partials in complex tones, but that it does not play an essential role.

One difficulty in interpreting the results of Plomp (1964) and Plomp and Mimpen (1968) is connected with the method used. Their subjects used a three-way switch to listen either to the complex tone, or to one of two sinusoids. One of the sinusoids had the same frequency as a partial in the complex tone, and the other had a frequency midway between that of the partial and the adjacent higher or lower one. The subject was allowed to switch freely between the three tones, and was required to decide which of the two sinusoids coincided in frequency with the partial in the complex tone. The score (varying between 50 and 100 percent) was used as an index of how well the partial could be heard out from the complex tone. The problem in interpreting the results arises from the fact that subjects were allowed to switch as many times as desired between the complex tone and the comparison sinusoids before making a decision. This makes it difficult to evaluate absolute levels of performance (for example to calculate values of the detectability index, d'), since effectively each trial was composed of an unknown number of subtrials. A second problem with this technique is that subjects may spend more time making their judgments in difficult conditions, which would affect the pattern of results across conditions. Like Moore and Ohgushi (1993), we used a task similar to that of Plomp (1964), but modified so as to be a true two-interval, two-alternative forced-choice task. On each trial, subjects had to indicate whether a sinusoidal "probe" was higher or lower in frequency than the nearest partial in the complex tone that was presented after the probe.

The third aspect of the present work is connected with a methodological problem that was present for most previous studies examining the ability to hear out partials in complex tones. The problem is that subjects may have learned the correct responses associated with specific probes using the feedback that was provided; they could then achieve above-chance performance even if the partial that was "probed" could not be heard out at all from the complex tone. To check whether this occurred, Soderquist (1970) ran some trials in which only the probe tones were presented, without the complex tone. Subjects were asked to indicate what the correct response would have been if the complex tone had been presented. Two out of the eight subjects scored above chance on this test ($p<0.04$), indicating that these two subjects had learned the correct answers associated with the frequencies of some of the probe tones. The other subjects did not score above chance. To prevent the use of such a strategy in the present experiments, we followed a procedure introduced by Bernstein and Oxenham (2003); the frequencies of all partials in a given complex tone were randomly varied (roved) from trial to trial.

The final new aspect of the present work is connected with the nonmonotonicities in the functions relating performance to the frequency of the partial found by Moore and Ohgushi (1993). They suggested two possible explanations for the nonmonotonicities. The first is that they might arise from irregularities in the transmission of the sound through the middle ear, which would result in some partials having a higher effective level than others. Moore and Ohgushi investigated the effect of increasing the level of a partial that was relatively poorly identified, and found that a 5-dB increase in level was sufficient to improve performance substantially. They concluded that only minor irregularities in middle-ear transmission, on the order of 5 dB, would be required to account for the nonmonotonicities in the data. Irregularities of this magnitude are apparent in middle-ear transfer functions obtained from human cadavers (Puria *et al.*, 1997; Aibara *et al.*, 2001). Equal-loudness contours (ELCs) for individual subjects are also consistent with the idea that there are irregularities in middle-ear transmission (Mauermann *et al.*, 2004). For levels close to absolute threshold, such ELCs show a distinct fine structure (rapid changes with frequency), which is thought to be influenced by the cochlear active mechanism (Mauermann *et al.*, 2004). Within a given individual, the pattern of this fine structure is reasonably consistent across levels at low levels, but for levels above 40 dB SPL the pattern is no longer related to that seen at levels close to absolute threshold. Nevertheless, irregularities of the order of 5 dB remain in the ELCs, and the level required for equal loudness can change by 5 dB when the frequency is changed by 2% or less. These remaining irregularities may reflect changes in middle-ear transmission with frequency.

If the nonmonotonicities in the data of Moore and Ohgushi (1993) did result from irregularities in middle-ear transmission, then one might expect the pattern of the results to vary across subjects. While there were some individual differences in the patterns across the four subjects used, three of the four subjects showed good performance for the partial centered at 1000 Hz, and less good performance for the partials adjacent to that.

A second explanation for the irregularities in the data is connected with the special status of the 1000-Hz partial. Moore and Ohgushi suggested that performance might have

been especially good for the 1000-Hz partial, as it was the only partial that was common to all of the complex tones used. As described earlier, subjects might have built up a memory for the pitch of the 1000-Hz partial over a series of trials, and have compared the pitch of the probe to this memory representation rather than to the pitch of the nearest partial in the complex tone. In the present experiments, the possibility of subjects building up a memory for the pitch of any of the partials was eliminated by the procedure of randomizing the frequencies of all partials from trial to trial. Also, we tested more subjects than Moore and Ohgushi (1993); if the nonmonotonicities arise from irregularities in middle-ear transmission, testing more subjects should improve the chances of finding individual differences in the pattern of nonmonotonicities. Our use of two levels also provided a test of the possible role of irregularities in middle-ear transmission. If such irregularities play an important role in determining the pattern of nonmonotonicities, then that pattern should be similar for the two levels used.

II. GENERAL METHOD

The method was similar to that used by Roberts and Bregman (1991) and by Moore and Ohgushi (1993). On each trial subjects were presented with a sinusoidal tone followed by a complex tone. The sinusoid will be referred to as the "probe." Subjects were told that the probe was close in frequency to one of the partials in the complex tone, but was actually slightly higher or lower in frequency than that partial. On half the trials, chosen at random, the probe was higher in frequency than the partial by 4.5%, and on the other half it was lower by 4.5%. Subjects were asked to indicate, by pressing the appropriate button on the response box, whether the probe was higher or lower in frequency than the "closest" partial in the complex. Correct-answer feedback was provided after each trial by lights on the response box. The partial that was "probed" was varied randomly from trial to trial. The frequencies of all partials in the complex tone were randomly varied (roved) from trial to trial by multiplying them by a factor randomly chosen within the range 0.9 to 1.1, while keeping the frequency ratios between partials fixed. The frequency of the probe was multiplied by the same factor.

It should be noted that Demany and Ramos (2005) found that when a probe tone was presented *after* an inharmonic complex tone, subjects could not reliably tell whether the probe was identical to one of the components in the complex or fell midway between two components. However, when the probe was separated from one of the components by a small amount in frequency (e.g., one semitone), subjects could tell whether the probe was higher or lower in frequency than that component. It is not known whether similar results would be obtained for a probe presented before the complex (as in our experiment), but in any case, the ±4.5% shift of the probe from the frequency of the component, as used here, was in the range where subjects can make the judgment reliably if the components in the complex are sufficiently widely spaced.

Before testing proper started, subjects were given training, starting with easy conditions and working towards more difficult conditions. Training started with a "complex" tone containing a single sinusoid with a nominal frequency of 1000 Hz. In this case, the task was a simple frequency discrimination task (but with roving, as described above). Then, the number of partials in the complex tone was increased to two, with widely separated frequencies. When subjects scored better than 90% with this complex, the number of partials was increased to three with widely spaced frequencies, and then to five. Some subjects who found the task to be easy skipped the training with intermediate numbers of components. Subjects were then given training runs with the complex tones to be used in the experiment proper, which contained between five and 11 partials. After this training, performance appeared to remain largely stable.

In the experiment proper, each partial in a complex was probed ten times in a given run, five times with the probe lower in frequency than the relevant partial in the complex, and five time with it higher. Five runs were obtained for each complex tone, giving a total of 50 judgments for each partial. In a few cases, when scores for the first few runs were close to 100% for all partials, testing stopped after fewer than five runs.

III. EXPERIMENT 1: EFFECTS OF LEVEL

In this experiment we examined the effects of level on the ability to hear out partials from complex tones whose partials all had frequencies within the range where phase locking is thought to occur (Anderson, 1973; Johnson, 1980; Palmer and Russell, 1986). The frequency of the highest partial used was 3158 Hz.

A. Stimuli

The partials in each complex tone were equally spaced on an ERB_N-number scale. The relationship between ERB_N-number, E, and frequency, f (Hz), was assumed to be as suggested by Glasberg and Moore (1990),

$$E = 21.4 \log_{10}(0.00437f + 1). \quad (1)$$

The spacings used were 0.75, 1.0, 1.5, and 2 E. The mean frequency of the central partial was always 1201 Hz, corresponding to $E=17$. The mean frequencies of all partials for each spacing used are given in Table I. The complex tone with 2-E spacing contained nine partials. All of the other complex tones contained 11 partials. Note that the smallest frequency spacing is greater than 9.5%, so a probe tone that is mistuned by 4.5% is always closer to the target partial than to any other (but only a little closer for the 0.75-E spacing).

The pure tone and the complex tone each had a steady-state duration of 800 ms, with 20-ms raised-cosine rise/fall ramps. This relatively long duration was chosen to reduce perceptual fusion of the partials produced by their synchronous gating (Moore *et al.* 1986). The interstimulus interval was 300 ms. The pure tones and each partial in the complex tones all had the same level, which was either 40 or 70 dB SPL. The 40-dB level was chosen to be as low as possible subject to the constraint that every partial was at least 20 dB above the absolute threshold for every subject. The 70-dB

TABLE I. Frequencies of the partials in the complex tones for each spacing used in experiment 1. The frequency of the middle partial is given in bold type.

Spacing	Frequency, Hz										
2.0 *E*		375	520	700	924	**1201**	1545	1972	2501	3158	
1.5 *E*	408	520	652	806	988	**1201**	1452	1747	2094	2501	2980
1.0 *E*	605	700	806	924	1055	**1201**	1364	1545	1747	1972	2222
0.75 *E*	726	806	893	988	1090	**1201**	1322	1452	1594	1747	1913

level was chosen to be the highest level found comfortable for all subjects; according to the loudness model described by Moore *et al.* (1997), the loudness of the monaurally presented complex tone with 1.5-*E* spacing was 22.2 sones, corresponding to a loudness level of 84.6 phons. The starting phases of the partials in each complex tone were chosen randomly for each trial.

Stimuli were generated digitally on-line using a Tucker-Davis Technologies (TDT) system II. The stimuli were played through a 16-bit digital-to-analog converter (TDT, DD1) at a 50-kHz sampling rate, low-pass filtered at 8 kHz (Kemo VBF8/04), attenuated (TDT, PA4), and presented via a headphone buffer (TDT, HB6), a manual attenuator (Hatfield 2125), and one earpiece of a Sennheiser HD580 headphone, which has a diffuse-field response. Levels specified are equivalent diffuse-field levels. Levels at the eardrum would have been higher for frequencies around 3000 Hz (Moore *et al.* 1998). Subjects were tested individually in a double-walled sound-attenuating chamber.

B. Subjects

Seven subjects (three male, four female) were used, all with no reported history of hearing disorders. Their absolute thresholds were better than 20 dB HL for audiometric frequencies from 250 to 8000 Hz (ISO 389-8, 2004). Their ages ranged from 21–26 years and all had some degree of musical training, including taking formal examinations in performance on the piano or the violin. One was a director of music for a Cambridge college. Musically trained subjects were chosen, since subjects without such training often have difficulty with this task (Fine and Moore, 1993). All subjects were paid for their participation. One subject (S6) was available only for a limited time, and she was not tested using the 0.75-ERB_N spacing. One subject (S2) was author KEL.

C. Results

Figure 1 gives an overview of the scores for the bottom partial (bottom panels), the inner partials in each complex (middle panels, scores averaged across all inner partials), and top partial (top panels). The scores are averaged across cases when the probe was lower in frequency than the closest partial and when it was higher in frequency; these scores were generally similar for the larger spacings of the partials, but were not always similar for the smaller spacings (0.75 and 1 *E*), as is described in more detail later in the paper. Left and right columns show results for levels per component of 40 and 70 dB SPL, respectively. Each symbol shows results for one subject. For the bottom partial, scores were close to 100% for all subjects for the 2-*E* spacing. With decreasing *E*, scores decreased only slightly for most subjects, but decreased markedly for one (S6) at the 70-dB level and for two (S6 and S7) at the 40-dB level. For the top partial, scores were above 90% for most subjects for the 2-*E* spacing. With decreasing spacing, scores decreased by amounts that varied across subjects, and one subject (S2) showed a distinct dip in performance for the 1.5-*E* spacing for the 70-dB level. For both the bottom and top partials, scores for most subjects remained above chance even for the smallest spacing used. Scores averaged across the inner partials were close to the chance level of 50% for the smallest spacing used, and increased with increasing spacing. For the 2-*E* spacing, all subjects except S6 achieved scores above 80% for the 40-

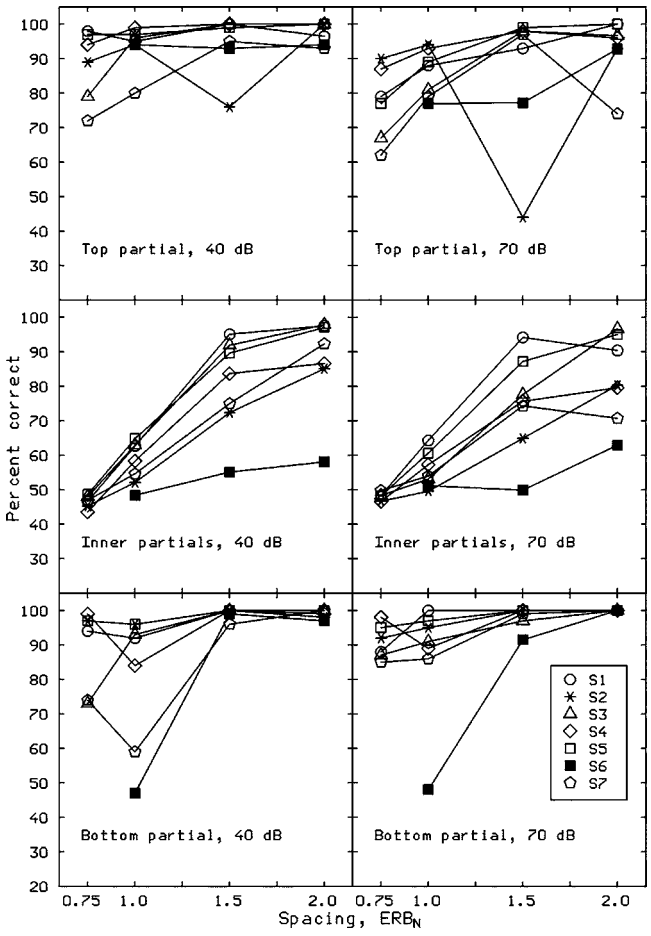

FIG. 1. Scores for the top partial in each complex (top panels), inner partials (middle panels, scores averaged across all inner partials), and the bottom partial in each complex (bottom panels), averaged across cases when the probe was lower in frequency than the closest partial and when it was higher in frequency and plotted as a function of spacing. Left and right columns show results for levels per component of 40 and 70 dB SPL, respectively. Results for each subject are identified by a different symbol.

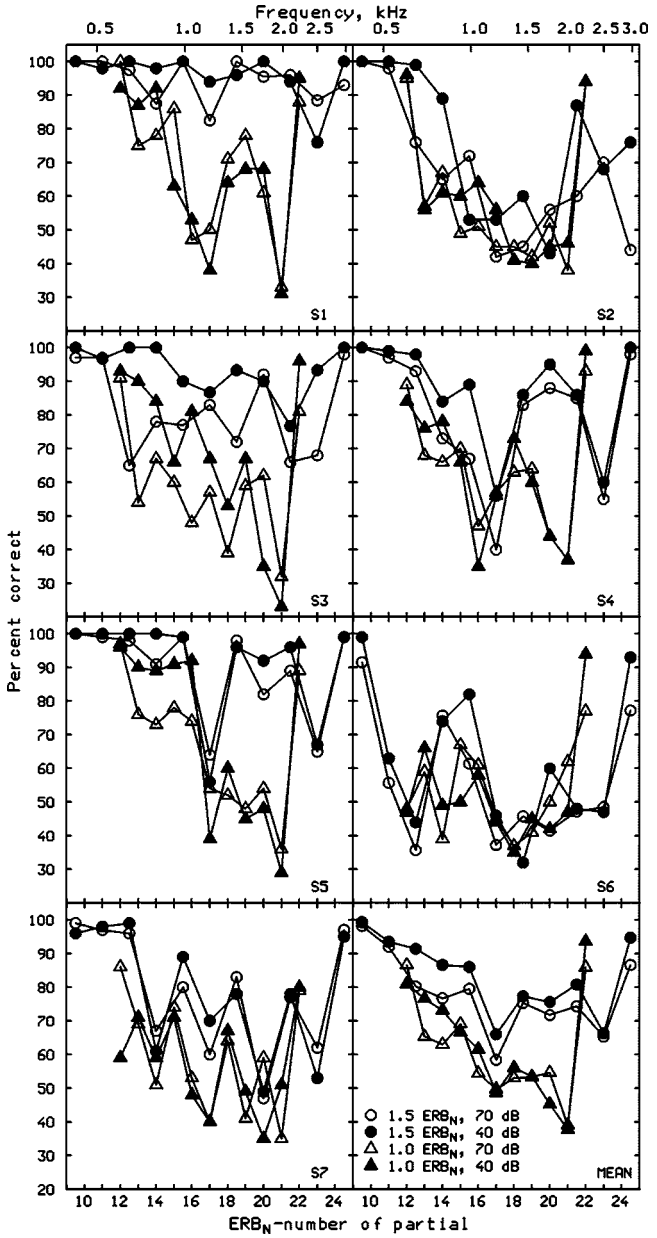

FIG. 2. Scores for each subject and averaged across subjects (bottom-right panel) for the complex tones with partials spaced by 1 *E* (triangles) and 1.5 *E* (circles), plotted as a function of the ERB_N-number (*E*) of the partial. Scores are averaged across cases when the probe was lower in frequency than the closest partial and when it was higher in frequency. Filled and open symbols show results for the levels of 40 and 70 dB SPL per component, respectively.

dB level and above 70% for the 70-dB level. The relatively high scores for the edge partials are consistent with the results of Moore and Ohgushi (1993) and with other research showing that edge partials are easier to hear out from complex tones than inner partials (Plomp, 1964; Moore, 1973b; Moore *et al.*, 1984).

Figure 2 shows the scores for individual subjects and averaged across subjects (bottom-right panel) for the complex tones with partials spaced by 1 *E* (triangles) and 1.5 *E* (circles). The scores are plotted as a function of *E* and are averaged across the cases when the probe was lower in frequency than the closest partial and when it was higher in frequency. Filled and open symbols show results for the levels of 40 and 70 dB SPL per component, respectively. The large differences in overall performance across subjects could reflect differences in frequency selectivity, but this seems unlikely to account for the whole effect, as differences in frequency selectivity across normally hearing subjects are relatively small (Moore, 1987; Wright, 1996). The individual differences in performance found here may be related to differences in musical experience and aptitude across subjects (Soderquist, 1970; Fine and Moore, 1993).

Scores for the lowest partials were high for all subjects except S7 for the 1-*E* spacing. Scores for the highest partials were high for all subjects except S2 for the 1.5-*E* spacing. Scores for the inner partials often varied nonmonotonically with *E*, as found by Moore and Ohgushi (1993). However, unlike what was found by Moore and Ohgushi, the pattern of the results varied markedly across subjects. As a result, the mean scores for the inner partials varied relatively smoothly with *E*, except for a slight dip in scores for the spacing of 1.5 *E* when *E* was 17. To confirm that there was no systematic relationship between the irregularities for different subjects, the scores for each spacing and each value of *E* were normalized by dividing the score for a given subject by the mean score across subjects, for the inner partials only. We then calculated, separately for each spacing and each level, the correlation between the scores of each subject (as a function of *E*) and the scores of every other subject. Since this gave a total of 156 possible correlations, the probability of obtaining a few large positive or negative correlations by chance is rather high. The correlations were approximately equally often positive and negative. The largest positive correlation was 0.97 and the largest negative correlation was −0.78; 85% of the correlations fell within the range −0.5 to +0.5. There were no pairs of subjects for whom scores were consistently correlated across spacings. This analysis confirms that the pattern of irregularities was not consistently related across subjects. The individual variability suggests that the irregularities result from factors intrinsic to each subject, rather than from some property of the stimuli.

Further insight into the cause of the nonmonotonicities can be gained by considering separately the scores when the probe was mistuned upwards from the corresponding partial in the complex and when it was mistuned downwards. The differences between the scores for these two cases were often rather large for the two smallest spacings. Figure 3 shows examples of the results for the complex tone with 0.75-*E* spacing and a level of 40 dB SPL per partial. Results for these four subjects were selected because they all showed distinct nonmonotonicities in the functions relating percent correct to *E*. As for the results shown in Fig. 2 for wider spacings, the pattern of results in Fig. 3 varies markedly across subjects, confirming that the nonmonotonicities result from factors intrinsic to each subject. For each subject, there were some partials for which scores were quite different when the probe was mistuned upwards by 4.5% (filled circles) and when it was mistuned downwards by 4.5% (open circles). For example, for the partial with $E=17$, the score for S7 was 84% for the former case, and 22% for the latter case. The low score when the partial was mistuned downwards suggests that the probe was judged relative to a lower partial

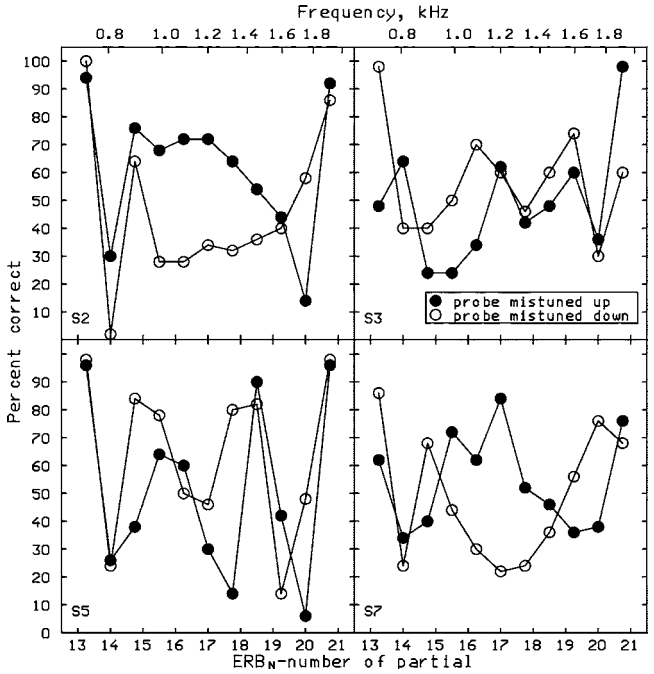

FIG. 3. Examples of individual results for the complex tone with 0.75-*E* spacing and a level of 40 dB SPL per partial. Results are shown separately for the case when the probe was lower in frequency than the closest partial and when it was higher in frequency.

in the complex, rather than to the "intended" partial (the one closest to the probe in frequency, which was higher in frequency than the probe). Errors produced by judging the pitch of the probe relative to the "wrong" partial in the complex would be expected to be greater for the smallest spacings. For example, for the 0.75-*E* spacing, when the probe was 4.5% lower in frequency than the 1201-Hz partial, it was only 5.2% higher in frequency than the 1090-Hz partial. Since 5.2% is only a little larger than 4.5%, the task would be very difficult, and any factor that led to a small increase in salience of the 1090-Hz partial relative to the 1201-Hz partial would be expected to lead to a high proportion of systematic errors. The results did indeed show a higher proportion of systematic errors for the smaller spacings than for the larger spacings.

S5 showed good performance for the eighth partial ($E = 18.5$) and poor performance for the seventh and ninth partials. This subject showed a similar but less marked pattern when the level per partial was 70 dB SPL. Since the frequencies of partials 8, 9, and 10 were separated by less than 10%, and the frequencies of all components were roved from trial to trial over the range 0.9 to 1.1 times the nominal values, this pattern of results suggests that good performance may be associated with the position of a partial within a sequence, independently of its absolute frequency. This is inconsistent with the idea that the nonmonotonicities in performance are caused solely by irregularities in the middle-ear transfer function. However, no other examples were found where performance was good for a given partial at both levels and poor for the partials spaced at ±0.75 *E* from that partial.

For some subjects, the scores for the second-highest partial in the complex tone with 1-*E* spacing (Fig. 2) were well below the chance level of 50%, indicating systematic errors. Indeed, the mean score for this partial was below chance (about 40%) for both levels. These particularly low scores can be partly explained in terms of the high salience of the pitch of the highest partial. It appears that, when the frequency of the probe was 4.5% above the frequency of the second-highest partial, the pitch of the probe was often judged relative to that of the highest partial rather than that of the closest partial. Hence, subjects consistently responded that the partial in the complex was higher in pitch than the probe, leading to scores that were close to zero in some cases (e.g., 2% at both levels for S6). When the probe was 4.5% lower in frequency than the second-highest partial, scores were usually somewhat above the chance level, but this was not always the case. For example, for the 1-*E* spacing, subject S3 scored 40% and 22% for the levels of 40 and 70 dB SPL, respectively. The low scores in these cases cannot be attributed to the high salience of the pitch of the highest partial; if S3 had compared the pitch of the probe to that of the highest partial, she would have achieved high scores. It appears that, for S3, and for some of the other subjects (S4 and S5 for the level of 40 dB SPL), the pitch salience of the second-highest partial was lower than that of both of the adjacent partials.

If the nonmonotonicities in the functions relating percent correct to *E* result partly from irregularities in middle-ear transmission, one would expect the pattern of nonmonotonicities to be similar for the two levels tested. To assess the extent to which this was true, we calculated the correlation between scores for the two levels, separately for each spacing and each subject. The calculation was based on scores for the inner partials only. The results are shown in Table II. The correlations are all positive, and in 19 cases out of 27 the correlation is significant at $p < 0.05$ (one-tailed test). This indicates that there is a reasonable degree of similarity in the pattern of results for the two levels, consistent with the idea that the nonmonotonicities arise partly from irregularities in middle-ear transmission.

In the mean results (bottom-right panel in Fig. 2), scores for the inner partials generally worsen with increasing *E*, especially for the 1-*E* spacing. A similar trend was found by Moore and Ohgushi (1993). The trend for worse performance at higher frequencies is consistent with the finding of Plomp (1964) and of Plomp and Mimpen (1968) that the frequency spacing necessary for a given partial to be heard out was greater than a critical band at high frequencies, but less than a critical band at low frequencies. This trend may indicate a role of phase locking in the ability to hear out partials.

Scores for the lower level (filled symbols) were often slightly better than scores for the higher level (open symbols), although this was not the case for all subjects or all values of *E*. In the mean data, the effect of level was greater for *E* in the range 12–14 than for higher values of *E*.

To assess the statistical significance of the effects described above, the data shown in Fig. 2 were subjected to a rationalized arcsine transform (Studebaker, 1985) and then to a within-subjects analysis of variance (ANOVA), with factors level (40 or 70 dB SPL), partial number (1 to 11), and spacing (1 or 1.5 *E*). The main effect of level was significant,

TABLE II. Correlation coefficients between scores for the two levels (40 and 70 dB SPL) for the inner partials, for each subject and each spacing of the partials. The number of samples (N) is given in each case. Significant correlations ($p<0.05$, one-tailed test) are indicated by *.

Subject	Spacing	Correlation	N
S1	0.75	0.44	9
S1	1.0	0.79*	9
S1	1.5	0.45	9
S1	2.0	0.87*	7
S2	0.75	0.92*	9
S2	1.0	0.59*	9
S2	1.5	0.66*	9
S2	2.0	0.41	7
S3	0.75	0.69*	9
S3	1.0	0.50	9
S3	1.5	0.14	9
S3	2.0	0.45	7
S4	0.75	0.67*	9
S4	1.0	0.90*	9
S4	1.5	0.93*	9
S4	2.0	0.95*	7
S5	0.75	0.87*	9
S5	1.0	0.96*	9
S5	1.5	0.94*	9
S5	2.0	0.56	7
S6	1.0	0.60*	9
S6	1.5	0.74*	9
S6	2.0	0.88*	7
S7	0.75	0.65*	9
S7	1.0	0.65*	9
S7	1.5	0.94*	9
S7	2.0	0.50	7

performance being better at the lower level; $F(1,6)=7.48$, $p=0.034$. The main effect of partial number was significant; $F(10,60)=22.27$, $p<0.001$. The main effect of spacing was significant, performance being better at the wider spacing; $F(1,6)=39.65$, $p<0.001$. The interaction of partial number and level was significant; $F(10,60)=4.28$, $p<0.001$. *Post hoc* tests, based on the least-significant differences test, indicated that the effect of level was significant ($p<0.05$) for partials with numbers 2, 3, 4, 5, and 11, but not for any other partials. Finally, the interaction of spacing and level was significant; $F(1,6)=19.42$, $p=0.005$. *Post hoc* tests indicated that the effect of level was significant for both spacings, but the effect was larger for the 1.5-E spacing than for the 1-E spacing.

To assess whether the effects of level were consistent with an excitation-pattern model, excitation patterns of the complex stimuli were calculated using the method described by Glasberg and Moore (1990), but with the diffuse-field outer-ear transfer function and middle-ear transfer function described by Moore *et al.* (1997). It was assumed that the audibility of a partial was related to the magnitude of the local peak produced by that partial in the excitation pattern. This was quantified as the mean difference in excitation level between the peak and the local minima on each side spaced at ±0.5 of the E spacing from the frequency at the peak; the resulting quantity will be called the peak-to-valley ratio (PVR). Consider as an example the results for the complex tone with components spaced by 1 E. When the level per component was 40 dB SPL, the PVR varied from 1.6 to 1.8 dB across partials (mean=1.66, SD=0.07). When the level per component was 70 dB SPL, the PVR varied from 0.85 to 1.05 dB (mean=0.98, SD=0.06). The effect of increasing level on the PVR was relatively constant across partials. Thus, consideration of the excitation pattern alone would lead to the prediction that the worsening of performance with increasing level would be roughly the same for all inner harmonics. Also, performance for the inner partials would be predicted to be roughly independent of the number of the partial. Clearly, these predictions are not consistent with the data, suggesting that factors other than the PVR affect the ability to hear out partials in complex tones.

In summary, the results show that performance was slightly worse at the higher level than at the lower level, as expected from the broadening of the auditory filter with increasing level. Performance for intermediate spacings and for inner partials tended to worsen with increasing frequency of the partials, suggesting a role of phase locking in the ability to hear out partials. Distinct nonmonotonicities in the functions relating percent correct to the frequency of the partial occurred in the results for individual subjects. The pattern of the nonmonotonicities varied across subjects, but was similar across the two levels for a given subject. These findings suggest that the monotonicities arise from some factor intrinsic to each subject.

IV. EXPERIMENT 2: THE AUDIBILITY OF PARTIALS AT HIGHER FREQUENCIES

This experiment was similar to experiment 1, except that the partials fell in a higher frequency range; this was done to provide a further assessment of the role of phase locking. The highest partials fell above 5000 Hz, which is roughly the highest frequency at which phase locking has been observed in mammals (Anderson, 1973; Johnson, 1980; Palmer and Russell, 1986). Only a single level was used for each subject.

A. Method

As before, the partials in each complex tone were equally spaced on an E scale. The spacings used were 1.0, 1.5, 2, 2.5, and 3 E. They were chosen to include larger spacings than used in experiment 1, since pilot experiments showed that scores were often well below 100% for a spacing of 2 E. The mean frequency of the central partial was always 3544 Hz, corresponding to $E=26$. The number of partials varied from 11 to five, depending on the spacing. The mean frequencies of all partials for each spacing used are given in Table III. Otherwise, the stimuli, method and training were the same as for experiment 1.

Six subjects (three male, three female) were used, all with no reported history of hearing disorders. Their absolute thresholds were better than 20 dB HL for audiometric frequencies from 250 to 8000 Hz (ANSI, 2004). Their ages ranged from 19–21 years and all had some degree of musical training, including taking formal examination in piano, violin, or singing. Four subjects were paid for their partici-

TABLE III. Frequencies of the partials in the complex tones for each spacing used in experiment 2. The frequency of the middle partial is given in bold type.

Spacing	Frequency, Hz										
3.0 *E*				1747	2501	**3544**	4984	6973			
2.5 *E*				1972	2653	**3544**	4710	6237			
2.0 *E*			1747	2222	2812	**3544**	4451	5577	6973		
1.5 *E*		1747	2094	2501	2980	**3544**	4205	4984	5898	6973	
1.0 *E*	1972	2222	2501	2812	3158	**3544**	3973	4451	4984	5577	6237

pation; the remaining two, S9 and S10, are authors WC and TC, respectively. One subject (S7) had taken part in experiment 1. A single level was used for each subject. This was 70 dB SPL per partial for all subjects except S9. She found that level to be uncomfortably loud, so she was tested using a level of 55 dB SPL per partial.

B. Results

Figure 4 shows scores for the bottom partial (bottom panel), the inner partials (middle panel, scores averaged across all inner partials), and the top partial (top panel). The scores are averaged across cases when the probe was lower in frequency than the closest partial and when it was higher in frequency. Each symbol shows results for one subject. For the bottom partial, which had a frequency of 1747 or 1972 Hz, scores for spacings of 1.5 *E* and above were mostly high (above 90%) except for S11 at all spacings and S7 for the spacing of 2.5 *E*. For the top partial, which had a frequency of 6237 or 6973 Hz, performance was generally poorer than for the bottom partial, and scores did not improve monotonically with increasing spacing. All subjects performed poorly for the spacing of 2.5 *E*. These results contrast with those obtained in experiment 1, where most subjects scored very well for the top partial for most spacings. For the inner partials, performance was close to the chance level of 50% for the spacing of 1 *E*, and generally improved with increasing spacing. Again, however, there was a "dip" in performance for some subjects for the 2.5-*E* spacing.

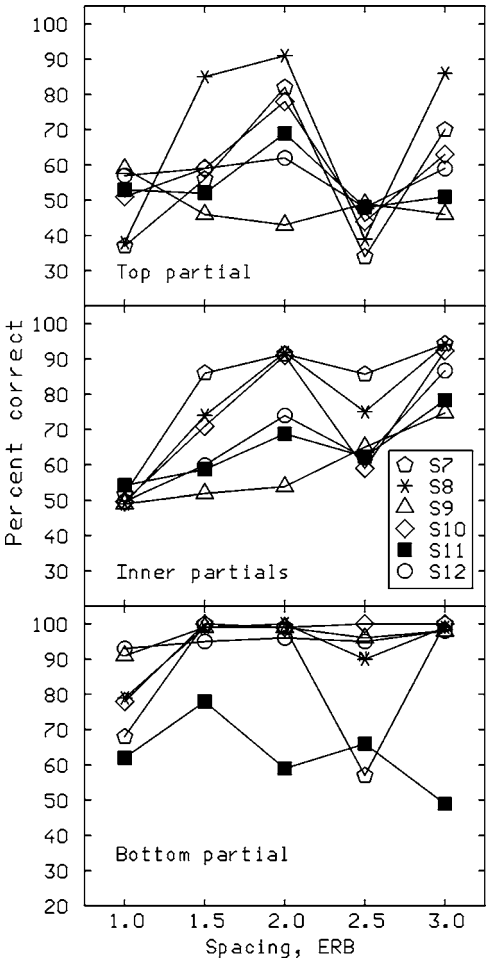

FIG. 4. As Fig. 1, but showing results of experiment 2 for the single level used with each subject.

Figure 5 shows the scores for each subject for each spacing. The scores are plotted as a function of *E* and are averaged across cases when the probe was lower in frequency than the closest partial and when it was higher in frequency. The pattern of the results varied markedly across subjects, especially for the smaller spacings, for which performance often varied nonmonotonically with frequency. For the spacing of 3 *E*, five of the six subjects achieved relatively high scores (>90%) for partials with frequencies up to 3544 Hz, but performance tended to fall off for the two highest partials, which had frequencies of 4984 and 6073 Hz. Only S8 achieved relatively high scores for all partials with the spacing of 3 *E*.

Figure 6 shows the scores averaged across subjects for each spacing, plotted as a function of *E*. Scores were averaged across the cases when the probe was lower in frequency than the closest partial and when it was higher in frequency. For the largest spacing, performance worsened monotonically with increasing frequency of the partial, once the frequency exceeded 2501 Hz. A within-subjects ANOVA of the data for the 3-*E* spacing showed a significant effect of the *E* value of the partial; $F(4,20)=4.14$, $p=0.013$. However, for the other spacings, performance was nonmonotonically related to the frequency of the partial and the pattern of the results was rather irregular.

As was found in experiment 1, the nonmonotonicities were often associated with systematic errors. This is illustrated in Fig. 7, which shows individual scores for the 2.5-*E* spacing, plotted separately for the case when the probe was mistuned upwards from the corresponding partial in the complex (filled squares) and the case when it was mistuned downwards (open squares). For all subjects except S10, there are some partials for which scores differ substantially for the

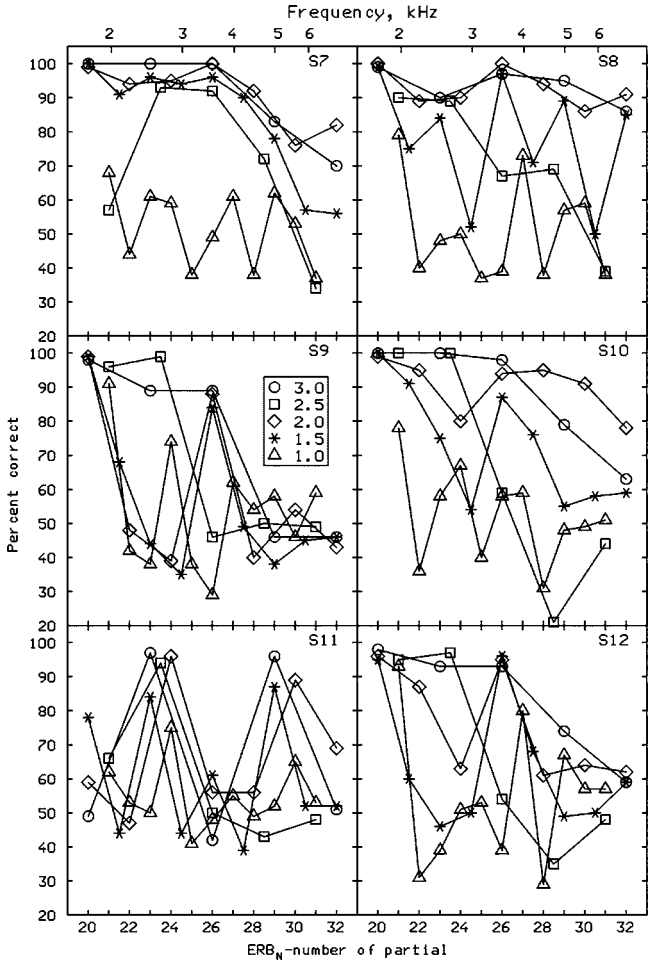

FIG. 5. As Fig. 2, but showing results of experiment 2 for all spacings for the single level used with each subject.

two cases. The patterns differ markedly across subjects. For example, for the lowest partial, S11 got a high score when the probe was mistuned downwards and a low score when it was mistuned upwards, while S7 showed the opposite pattern.

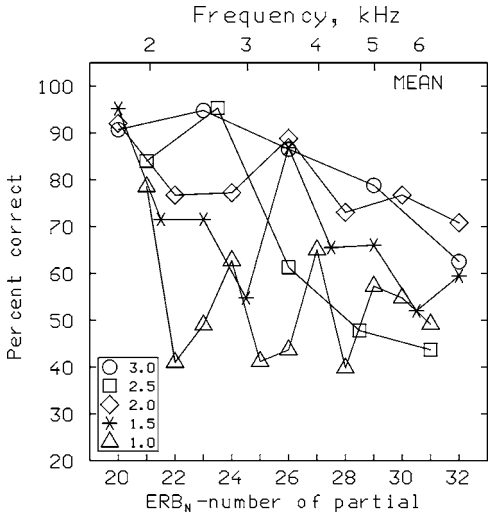

FIG. 6. Results of experiment 2, showing scores averaged across subjects for each spacing, plotted as a function of the ERB_N-number of the partial. Scores are averaged across the cases when the probe was lower in frequency than the closest partial and when it was higher in frequency.

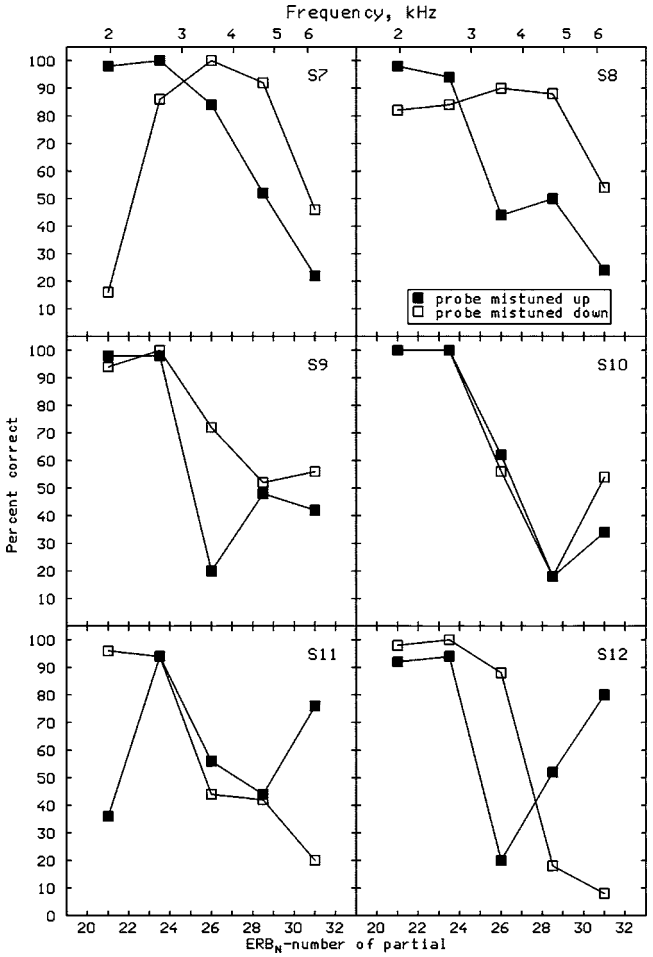

FIG. 7. Individual scores for the 2.5-*E* spacing, plotted separately for the case when the probe was mistuned upwards from the corresponding partial in the complex (filled squares) and the case when it was mistuned downwards (open squares).

We were concerned that some of the irregularities in the pattern of the results might have occurred because the frequency response of the headphone used (Sennheiser HD580) can show distinct peaks and dips at high frequencies, the pattern of which varies across listeners depending on the geometry of the ear canal (Moore *et al.*, 1998; Tan *et al.*, 2003). To check on this, four of the subjects, S8, S9, S10, and S12, were tested using an Etymõtic Research ER-2 insert earphone, which is designed to give a flat response at the eardrum for frequencies up to about 14 000 Hz. S8 was available only for a limited time, and was tested using spacings of 1.5, 2, and 2.5 *E* only. The other subjects were tested for all of the spacings used previously. For each subject, the pattern of results was similar to that obtained when the Sennheiser HD580 earphone was used, although the magnitudes of the peaks and dips in the functions relating performance to the ERB_N-number of the partial did vary somewhat across earphone type. It is also noteworthy that overall performance was similar for the two earphone types, suggesting that there was no long-term learning. To quantify the degree of similarity between results for the two earphones, we calculated, separately for each subject and each spacing, the correlation between the scores obtained with the HD580 earphone and with the ER2 earphone. The results are shown in Table IV.

TABLE IV. Correlation coefficients between scores obtained using Sennheiser HD580 and Etymõtic Research ER-2 earphones, for such subject and each spacing of the partials. The number of samples (N) is given in each case. Significant correlations ($p<0.05$, one-tailed test) are indicated by *.

Subject	Spacing	Correlation	*N*
S8	1.5	0.75*	9
S8	2.0	0.66	7
S8	2.5	0.89*	5
S9	1.0	0.91*	11
S9	1.5	0.94*	9
S9	2.0	0.97*	7
S9	2.5	0.95*	5
S9	3.0	0.96*	5
S10	1.0	0.93*	11
S10	1.5	0.98*	9
S10	2.0	0.70*	7
S10	2.5	0.98*	5
S10	3.0	0.79	5
S12	1.0	0.98*	11
S12	1.5	0.95*	9
S12	2.0	0.80*	7
S12	2.5	0.89*	5
S12	3.0	0.75	5

The correlations are all above 0.66 and many are above 0.9. All but three of the correlations are significant at $p<0.05$ (one-tailed). These correlations indicate a high degree of similarity between the results obtained using the two types of earphone. We conclude that the irregularities observed in the main part of experiment 2 were not the result of peaks and dips in the response of the earphone.

V. DISCUSSION

A notable difference between the results for experiments 1 and 2 is that in experiment 1 the top partial was heard out with higher accuracy than the adjacent inner partials, whereas in experiment 2 this was not the case. Even when the partials were separated by more than 2 *E*, performance for the top partial in experiment 2 was far from perfect. This difference in results for the two experiments is consistent with the idea that edge partials are more easily heard out than inner partials only for frequencies where phase locking is available. As discussed by Moore and Ohgushi (1993), neurons with characteristic frequencies (CFs) close to the frequency of a given partial will phase lock to that partial, provided the frequency separation of partials is sufficient, and provided the frequency of the partial is not too high. For an inner partial in a complex tone, the pattern of phase locking in neurons with CFs close to the frequency of the partial will be disturbed by the partials on either side, making it more difficult to extract the pitch of that partial, especially when the partials are closely spaced. In contrast, neurons tuned just below the lower edge frequency, or just above the higher edge frequency, will show a pattern of phase locking that is less disturbed by the other partials. When the top partial has a frequency above the range where phase locking occurs, as in our experiment 2, then there will be no special status for the top partial.

It is possible that part of the general trend for performance to worsen at high frequencies is related to the worsening of frequency discrimination at high frequencies. For the highest frequency used (6973 Hz), the frequency difference limen (FDL) for sinusoidal tones is typically about 1% (Moore, 1973a; Wier *et al.*, 1977; Sek and Moore, 1995), which is considerably less than the 4.5% frequency difference between the probe and the nearest partial used here. However, FDLs for components within complex tones are higher than for sinusoids presented in isolation (Moore *et al.*, 1984; Gockel *et al.*, 2006), so it is possible that part of the worsening in performance at high frequencies found here happened because subjects had difficulty hearing the difference in frequency between the probe and the target partial. In any case, the worsening in frequency discrimination at high frequencies has often been ascribed to loss of phase locking (Moore, 1973a; Goldstein and Srulovicz, 1977; Heinz *et al.*, 2001), so this explanation of the worsening in performance also depends ultimately on phase locking.

Frequency selectivity may play a role in allowing partials to be heard out primarily because partials have to be separated sufficiently by the auditory filters to give a relatively undisturbed temporal representation of their frequencies. For partials separated by less than 1 *E*, the temporal representation of individual inner partials may be so disturbed that pitches corresponding to the partials cannot be heard, even at low frequencies. As the spacing of partials is increased, the temporal representation will be progressively less disturbed by adjacent partials, and the partials will get easier to hear out. Resolution by the auditory filters does not seem to be sufficient to make partials easy to hear out. For the higher-frequency partials used in experiment 2, performance was often much less than perfect even when the partials were separated by 2 *E* or more. It appears that both resolution by the auditory filters and sufficiently precise phase locking are required for a partial to be heard out with high accuracy.

In both experiments, distinct nonmonotonicities were found in the functions relating percent correct to the ERB_N-number of the partial. Similar nonmonotonicities were found by Moore and Ohgushi (1993). However, they found a similar pattern across the four subjects used, whereas we found strong individual differences in the patterns. Further, the results of experiment 1 showed that the scores for a given spacing was often significantly correlated across the two levels used for a given subject, indicating that the pattern of the nonmonotonicities was reasonably consistent across the two levels. The results of experiment 2 showed that the nonmonotonicities were not related to the frequency response of the specific earphone used, since the pattern of results was similar for the Sennheiser HD580 earphone (which has a diffuse-field response) and the Etymõtic Research ER-2 earphone (which has a flat response at the eardrum), for each of the four subjects tested using both earphones. Overall, the results suggest that the nonmonotonicities are not determined by the stimuli themselves, as delivered to the eardrum. Rather, they result from factors intrinsic to each subject. We suggest that the nonmonotonicities might be related to irregularities (non smooth frequency responses) in the trans-

mission of sound through the middle ear, the pattern of which might vary from one person to another. However, further work is needed to assess the validity of this suggestion.

ACKNOWLEDGMENTS

This work was supported by the MRC (UK). Authors T. Cope and W. Cope were supported by studentships from the Grindley Fund. We thank Andrew Oxenham and two reviewers for helpful comments on earlier versions of this paper.

Aibara, R., Welsh, J. T., Puria, S., and Goode, R. L. (**2001**). "Human middle-ear sound transfer function and cochlear input impedance," Hear. Res. **152**, 100–109.

Anderson, D. J. (**1973**). "Quantitative model for the effects of stimulus frequency upon synchronization of auditory discharges," J. Acoust. Soc. Am. **54**, 361–364.

ANSI (2004). ANSI S3.6-2004 Specification for Audiometers (American National Standards Institute, New York).

Baker, R. J., Rosen, S., and Darling, A. M. (**1998**). "An efficient characterization of human auditory filtering across level and frequency that is also physiologically reasonable," in *Psychophysical and Physiological Advances in Hearing*, edited by A. R. Palmer, A. Rees, A. Q. Summerfield, and R. Meddis (Whurr, London).

Bernstein, J. G., and Oxenham, A. J. (**2003**). "Pitch discrimination of diotic and dichotic tone complexes: Harmonic resolvability or harmonic number?" J. Acoust. Soc. Am. **113**, 3323–3334.

de Cheveigné, A. (**1999**). "Pitch shifts of mistuned partials: A time-domain model," J. Acoust. Soc. Am. **106**, 887–897.

Demany, L., and Ramos, C. (**2005**). "On the binding of successive sounds: Perceiving shifts in nonperceived pitches," J. Acoust. Soc. Am. **117**, 833–841.

Fine, P. A., and Moore, B. C. J. (**1993**). "Frequency analysis and musical ability," Music Percept. **11**, 39–53.

Gibson, L. (**1970**). "The ear as an analyzer of musical tones," 80th Meeting of the Acoustical Society of America paper HH3, 63.

Glasberg, B. R., and Moore, B. C. J. (**1990**). "Derivation of auditory filter shapes from notched-noise data," Hear. Res. **47**, 103–138.

Glasberg, B. R., and Moore, B. C. J. (**2000**). "Frequency selectivity as a function of level and frequency measured with uniformly exciting notched noise," J. Acoust. Soc. Am. **108**, 2318–2328.

Gockel, H., Moore, B. C. J., Carlyon, R. P., and Plack, C. J. (2006). "Effect of duration on the frequency discrimination of individual partials in a complex tone and on the discrimination of fundamental frequency," J. Acoust. Soc. Am. (submitted).

Goldstein, J. L., and Srulovicz, P. (**1977**). "Auditory-nerve spike intervals as an adequate basis for aural frequency measurement," in *Psychophysics and Physiology of Hearing*, edited by E. F. Evans and J. P. Wilson (Academic, London).

Hartmann, W. M., and Doty, S. L. (**1996**). "On the pitches of the components of a complex tone," J. Acoust. Soc. Am. **99**, 567–578.

Hartmann, W. M., McAdams, S., and Smith, B. K. (**1990**). "Hearing a mistuned harmonic in an otherwise periodic complex tone," J. Acoust. Soc. Am. **88**, 1712–1724.

Heinz, M. G., Colburn, H. S., and Carney, L. H. (**2001**). "Evaluating auditory performance limits. I. One-parameter discrimination using a computational model for the auditory nerve," Neural Comput. **13**, 2273–2316.

Helmholtz, H. L. F. (**1863**). *Die Lehre von den Tonempfindungen als physiologische Grundlage für die Theorie der Musik* (Vieweg, Braunschweig).

ISO 389-8 (2004). "Acoustics—Reference zero for the calibration of audiometric equipment—Part 8: Reference equivalent threshold sound pressure levels for pure tones and circumaural earphones," (International Organization for Standardization, Geneva).

Johnson, D. H. (**1980**). "The relationship between spike rate and synchrony in responses of auditory-nerve fibers to single tones," J. Acoust. Soc. Am. **68**, 1115–1122.

Mauermann, M., Long, G. R., and Kollmeier, B. (**2004**). "Fine structure of hearing threshold and loudness perception," J. Acoust. Soc. Am. **116**, 1066–1080.

Moore, B. C. J. (**1973a**). "Frequency difference limens for short-duration tones," J. Acoust. Soc. Am. **54**, 610–619.

Moore, B. C. J. (**1973b**). "Some experiments relating to the perception of complex tones," Q. J. Exp. Psychol. **25**, 451–475.

Moore, B. C. J. (**1987**). "Distribution of auditory-filter bandwidths at 2 kHz in young normal listeners," J. Acoust. Soc. Am. **81**, 1633–1635.

Moore, B. C. J. (**2003**). *An Introduction to the Psychology of Hearing*, 5th ed. (Academic, San Diego).

Moore, B. C. J., and Glasberg, B. R. (**1987**). "Formulae describing frequency selectivity as a function of frequency and level and their use in calculating excitation patterns," Hear. Res. **28**, 209–225.

Moore, B. C. J., and Ohgushi, K. (**1993**). "Audibility of partials in inharmonic complex tones," J. Acoust. Soc. Am. **93**, 452–461.

Moore, B. C. J., and Sek, A. (**1995**). "Auditory filtering and the critical bandwidth at low frequencies," in *Advances in Hearing Research*, edited by G. A. Manley, G. M. Klump, C. Köppl, H. Fastl, and H. Oeckinghaus (World Scientific, Singapore).

Moore, B. C. J., Alcántara, J. I., and Dau, T. (**1998**). "Masking patterns for sinusoidal and narrowband noise maskers," J. Acoust. Soc. Am. **104**, 1023–1038.

Moore, B. C. J., Glasberg, B. R., and Baer, T. (**1997**). "A model for the prediction of thresholds, loudness and partial loudness," J. Audio Eng. Soc. **45**, 224–240.

Moore, B. C. J., Glasberg, B. R., and Peters, R. W. (**1986**). "Thresholds for hearing mistuned partials as separate tones in harmonic complexes," J. Acoust. Soc. Am. **80**, 479–483.

Moore, B. C. J., Glasberg, B. R., and Shailer, M. J. (**1984**). "Frequency and intensity difference limens for harmonics within complex tones," J. Acoust. Soc. Am. **75**, 550–561.

Moore, B. C. J., Glasberg, B. R., Flanagan, H. J., and Adams, J. (**2006**). "Frequency discrimination of complex tones; assessing the role of component resolvability and temporal fine structure," J. Acoust. Soc. Am. **119**, 480–490.

Ohgushi, K. (**1978**). "On the role of spatial and temporal cues in the perception of the pitch of complex tones," J. Acoust. Soc. Am. **64**, 764–771.

Ohm, G. S. (**1843**). "Über die Definition des Tones, nebst daran geknüpfter Theorie der Sirene und ähnlicher tonbildender Vorrichtungen (On the definition of a tone and related theory of a siren and similar tone-producing devices)," Ann. Phys. Chem. **59**, 513–565.

Palmer, A. R., and Russell, I. J. (**1986**). "Phase-locking in the cochlear nerve of the guinea-pig and its relation to the receptor potential of inner hair-cells," Hear. Res. **24**, 1–15.

Plomp, R. (**1964**). "The ear as a frequency analyzer," J. Acoust. Soc. Am. **36**, 1628–1636.

Plomp, R., and Mimpen, A. M. (**1968**). "The ear as a frequency analyzer. II," J. Acoust. Soc. Am. **43**, 764–767.

Puria, S., Rosowski, J. J., and Peake, W. T. (**1997**). "Sound-pressure measurements in the cochlear vestibule of human-cadaver ears," J. Acoust. Soc. Am. **101**, 2754–2770.

Roberts, B., and Bregman, A. S. (**1991**). "Effects of the pattern of spectral spacing on the perceptual fusion of harmonics," J. Acoust. Soc. Am. **90**, 3050–3060.

Rosen, S., Baker, R. J., and Darling, A. (**1998**). "Auditory filter nonlinearity at 2 kHz in normal-hearing listeners," J. Acoust. Soc. Am. **103**, 2539–2550.

Sek, A., and Moore, B. C. J. (**1995**). "Frequency discrimination as a function of frequency, measured in several ways," J. Acoust. Soc. Am. **97**, 2479–2486.

Soderquist, D. R. (**1970**). "Frequency analysis and the critical band," Psychonomic Sci. **21**, 117–119.

Studebaker, G. (**1985**). "A rationalized arcsine transform," J. Speech Hear. Res. **28**, 455–462.

Tan, C. T., Moore, B. C. J., and Zacharov, N. (**2003**). "The effect of nonlinear distortion on the perceived quality of music and speech signals," J. Audio Eng. Soc. **51**, 1012–1031.

Weber, D. L. (**1977**). "Growth of masking and the auditory filter," J. Acoust. Soc. Am. **62**, 424–429.

Wier, C. C., Jesteadt, W., and Green, D. M. (**1977**). "Frequency discrimination as a function of frequency and sensation level," J. Acoust. Soc. Am. **61**, 178–184.

Wright, B. A. (**1996**). "Auditory filter asymmetry at 2000 Hz in 80 normal-hearing ears," J. Acoust. Soc. Am. **100**, 1717–1721.

Zwicker, E. (**1961**). "Subdivision of the audible frequency range into critical bands (Frequenzgruppen)," J. Acoust. Soc. Am. **33**, 248.

Spectral-peak selection in spectral-shape discrimination by normal-hearing and hearing-impaired listeners

Jennifer J. Lentz[a)]
Department of Speech and Hearing Sciences, Indiana University, Bloomington, Indiana 47405

(Received 17 August 2005; revised 18 May 2006; accepted 30 May 2006)

Spectral-shape discrimination thresholds were measured in the presence and absence of noise to determine whether normal-hearing and hearing-impaired listeners rely primarily on spectral peaks in the excitation pattern when discriminating between stimuli with different spectral shapes. Standard stimuli were the sum of 2, 4, 6, 8, 10, 20, or 30 equal-amplitude tones with frequencies fixed between 200 and 4000 Hz. Signal stimuli were generated by increasing and decreasing the levels of every other standard component. The function relating the spectral-shape discrimination threshold to the number of components (N) showed an initial decrease in threshold with increasing N and then an increase in threshold when the number of components reached 10 and 6, for normal-hearing and hearing-impaired listeners, respectively. The presence of a 50-dB SPL/Hz noise led to a 1.7 dB increase in threshold for normal-hearing listeners and a 3.5 dB increase for hearing-impaired listeners. Multichannel modeling and the relatively small influence of noise suggest that both normal-hearing and hearing-impaired listeners rely on the peaks in the excitation pattern for spectral-shape discrimination. The greater influence of noise in the data from hearing-impaired listeners is attributed to a poorer representation of spectral peaks. [DOI: 10.1121/1.2216564]

PACS number(s): 43.66.Fe, 43.66.Sr, 43.66.Ba [JHG] Pages: 945–956

I. INTRODUCTION

Multichannel models of spectral-shape discrimination have been able to account for performance when stimuli are either spectrally sparse (i.e., stimulus components are separated by a frequency distance greater than the bandwidth of an auditory filter; Kidd *et al.*, 1991; Green, 1992; Lentz and Richards, 1997) or spectrally dense (Farrar *et al.*, 1987), but the application of multichannel models to jointly account for spectral-shape discrimination sensitivity of sparse and dense stimuli has had limited success (Versfeld, 1997; Lentz *et al.*, 1999). When modeling spectrally sparse stimuli, the number of "bands" (or the number of random variables that are used in the formation of a decision variable) is generally assumed to be the same as the number of stimulus components; those bands are also assumed to be independent (Berg and Green, 1990). When stimuli have greater numbers of components and are spectrally dense, this assumption no longer leads to accurate predictions of performance, and models that include imperfect frequency resolution become necessary (Bernstein and Green, 1987; Farrar *et al.*, 1987; Summers and Leek, 1994; Ellermeier, 1996).

Lentz *et al.* (1999) attempted to jointly model spectral-shape discrimination performance of sparse and dense stimuli using a bank of filters that represent the frequency analysis of the auditory system as a front end to a multichannel linear decision model (Durlach *et al.*, 1986). When all frequency channels were input to the decision model, Lentz *et al.* found that the model could only account for spectral-shape discrimination sensitivity of sparse and dense stimuli if the filters had bandwidths twice as narrow as measured using the notched-noise method. These very narrow filters effectively functioned as a peak-selection algorithm for their spectrally sparse stimuli. Because including a peak-selection algorithm into the Lentz *et al.* model has the potential to make the model more parsimonious with previous estimates of frequency selectivity, the following experiment tests whether spectral-shape discrimination is based on spectral peaks alone and expands the Lentz *et al.* model to include a peak-selection algorithm.

Controlled spectral-shape discrimination experiments illustrate that the auditory system is able to compare and contrast levels across frequency (Spiegel *et al.*, 1981; Green and Kidd, 1983; Green *et al.*, 1983; see also Green, 1988 for an overview). In these experiments, stimuli typically consist of the sum of tones, and listeners discriminate between a standard stimulus and a stimulus with a different spectral shape, or spectral profile. Sensitivity for detecting changes in spectral shape is dependent on the number of tones in the stimulus, the frequency spacing of the tones, and the type of spectral change. For tasks in which listeners detect a single increment added to a background of tones, spectral-shape discrimination sensitivity improves with the addition of tones when stimulus components are separated by frequency distances greater than the bandwidth of an auditory filter (i.e., for spectrally sparse stimuli; Green *et al.*, 1983; Green *et al.*, 1984; Bernstein and Green, 1987). As stimuli become spectrally dense, larger spectral prominences are needed for spectral-shape discrimination (Bernstein and Green, 1987).

Whether the auditory system uses spectral peaks or the entire stimulus in spectral-shape discrimination has important implications for the implementation of psychophysical

[a)]Address correspondence to Jennifer J. Lentz, Ph.D., Dept. of Speech and Hearing Sciences, 200 S. Jordan Ave., Bloomington, IN 47405. Phone: (812) 855-8945; fax: (812) 855-5531; electronic mail: jjlentz@indiana.edu

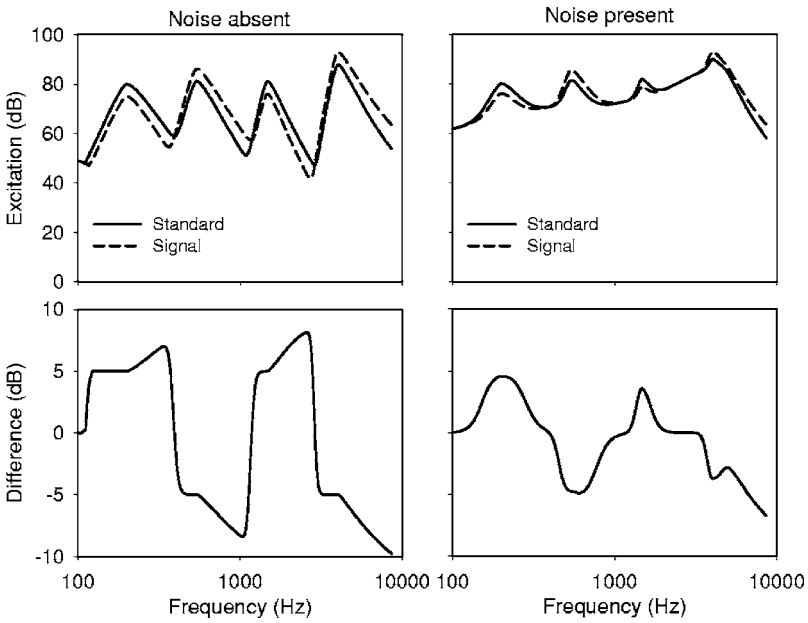

FIG. 1. The upper panels plot the excitation patterns of a standard stimulus made of four equal-amplitude components (solid line) and a signal stimulus created by decreasing and increasing the levels of every other stimulus component by 5 dB (dashed line). The left and right panels indicate the excitation patterns generated in the absence and in the presence of noise, respectively. The lower panels indicate the difference in excitation between the signal and the standard excitation patterns.

models, as selecting the appropriate channels has the potential to have a drastic effect on predicted performance. For example, broadband stimuli activate a wide frequency range of auditory channels, and each of those channels could carry information indicating that two stimuli have different spectral shapes. If the auditory system selectively uses channels that represent high intensities rather than a large spectral change between stimuli, then the actual performance might be poorer than predicted by a psychophysical model.

Figure 1 illustrates this logic by plotting excitation patterns for two stimuli in the upper left panel and the difference in the excitation patterns between those two stimuli in the lower left panel. The solid line in the upper left panel indicates a normal-hearing excitation pattern for a standard stimulus having four equal-amplitude components presented at a level of 80-dB SPL. The dashed line indicates the excitation pattern of a signal stimulus that was generated by decreasing components one and three by 5 dB and increasing components two and four by 5 dB. The difference excitation pattern in the lower left panel illustrates that the high-frequency edges of the excitation-pattern peaks have a change in excitation that exceeds 5 dB. In this way, a system that uses the entire excitation pattern would have more spectral-contrast information available than a system that selectively uses only the peaks (that have changes in excitation equaling about 5 dB) in the excitation pattern. However, peak selection would make spectral-shape discrimination relatively impervious to noise, as noise would mask the change in excitation at the high-frequency edges of the peaks.

The influence of noise on the excitation pattern is illustrated in the right panels of Fig. 1, which show excitation patterns generated when a 50 dB/Hz-broadband noise is added to the stimuli used in the left panels.[1] The upper right panels indicate standard+noise (solid line) and signal +noise (dashed line) excitation patterns. The difference in the noise-added excitation patterns (lower right panel) shows marked changes from the difference between noise-absent excitation patterns (lower left panel). Here, the noise reduces the spectral change in the frequency channels surrounding the excitation-pattern peaks.

The use of peaks in spectral-shape discrimination also has important implications for modeling and evaluating the effects of hearing loss. Hearing-impaired listeners who have poorer-than-normal frequency selectivity have a poorer representation of spectral peaks. Using stimuli with very dense spectra, Summers and Leek (1994) and Leek and Summers (1996) showed that the great difficulty experienced by listeners with hearing loss on spectral-shape discrimination tasks is primarily due to their reduced frequency selectivity. For spectrally sparse stimuli, Lentz and Leek (2003) showed that listeners with hearing loss have similar abilities to normal-hearing listeners in discriminating changes in spectral shape. However, differences in the decision weights of normal-hearing and hearing-impaired listeners when comparing levels across frequency (Doherty and Lutfi, 1996, 1999; Lentz and Leek, 2003) indicate some effect of hearing impairment, even when the stimuli are spectrally sparse. If reduced frequency selectivity changes the shape and the size of the spectral peaks, then the observed differences in decision weights might be a result of impaired peripheral processing.

The following experiment tests the hypothesis that the normal and impaired auditory systems use only the peaks in the excitation pattern for spectral shape discrimination. Spectral shape discrimination ability is measured in the presence and in the absence of a noise stimulus. The noise stimulus effectively blocks the change in excitation that is present on the edges of the peaks of the excitation pattern between signal and standard stimuli, leaving only the peaks available to cue excitation changes. If thresholds are little influenced by the presence of noise, then it will be concluded that the auditory system relies greatly on spectral peaks for spectral shape discrimination.

TABLE I. Audiometric thresholds of test ear for normal-hearing and hearing-impaired listeners (dB HL *re*: ANSI, 1996).

			Frequency (Hz)						
Observer	Age	Test ear	250	500	1000	2000	3000	4000	8000
NH1	43	R	10	5	10	10	10	10	20
NH2	40	R	10	10	10	0	0	0	10
NH3	40	R	5	0	0	0	0	0	5
NH4	48	R	10	5	5	10	10	10	5
NH5	57	L	0	5	5	0	0	0	10
HI1	78	L	10	20	35	50	45	50	65
HI2	38	R	20	20	35	35	50	50	60
HI3	64	L	10	10	25	45	50	55	60
HI4	58	L	10	15	25	35	60	65	65
HI5	19	R	30	35	60	65	35	45	45

II. METHODS

A. Observer characteristics

Five normal-hearing listeners and five hearing-impaired listeners participated in the experiment. The ages of the normal-hearing listeners ranged between 40 and 57 years, with a mean of 45.6 years, whereas ages of the hearing-impaired listeners ranged between 19 and 78 years, averaging 51.4 years. All normal-hearing listeners had pure tone audiometric thresholds of 10-dB HL or better between 250 and 4000 Hz and 20-dB HL or better at 8000 Hz. For normal-hearing listeners, the right ear was tested unless the right ear did not meet the criterion for normal hearing. Hearing-impaired listeners were selected so that the mean pure tone average threshold at 1000, 2000, and 4000 Hz was greater than 35-dB HL in their better ear (the test ear). Hearing losses were moderate and bilateral; the site of lesion was presumed to have a cochlear origin based on air and bone-conduction thresholds and normal immittance audiometry. The audiometric configurations for all test ears and the participants' ages are reported in Table I.

A sixth normal-hearing listener was excluded from the study due to an inability to achieve spectral-shape discrimination thresholds below −8.3 dB for *at least one* of the stimulus conditions. This criterion was set based on a roving-level distribution that was employed to reduce the use of overall level cues (described in the stimuli). Thresholds above this criterion level might be due to a contribution of single-channel intensity-based cues, and only thresholds below this criterion can be assured to reflect across-frequency processing.

B. Stimuli

The standard stimuli were the sum of 2, 4, 6, 10, 20, or 30 equal-amplitude sinusoids ranging from 200–4000 Hz, spaced equidistantly on a logarithmic scale, and rounded to the nearest 4 Hz. On each stimulus presentation, the starting phases of the component tones were selected randomly and independently from a uniform distribution ranging from 0 to 2π rad. The signal stimulus was generated by decreasing and increasing the levels of every other component. The up components were increased by the same decibel amount as the down components were decreased ($\Delta L_{up} = \Delta L_{down}$). Signal strength is described as the change in amplitude of the up components relative to the mean amplitude of the standard components [i.e., $20\log(\Delta A/A)$; sig re stan, in dB]. Each spectral component in the standard was presented at a mean level of 80-dB SPL. Stimuli were 250 ms in duration, with 30 ms cosine-squared rise/fall times.

When present, a 50-dB SPL/Hz noise stimulus was generated by summing tones up to 5000 Hz with amplitudes drawn from a Rayleigh distribution and phases randomly drawn from a uniform distribution that ranged from 0 to 2π rad. The noise components were separated by 1 Hz, yielding 1 s of independent noise. A 250-ms sample was randomly selected from the 1-s noise sample, and a new 1-s sample was generated for each noise stimulus presented. Noise stimuli had 30-ms cosine-squared rise/fall times. When present, the noise was added to the standard and signal stimuli such that onsets and offsets were shared.

Signal, standard, and noise stimuli were generated and summed digitally, and then played through one channel of a 24-bit digital-to-analog converter (DAC; TDT System III RP2.1) at a sampling rate of 4096×10^{-5} s (about 24414 Hz).[2] The output of the DAC was fed into a programmable attenuator that was adjusted to appropriately calibrate the stimuli. The output was fed into the right headphone of a Sennheiser HD 250 II Linear headset.

To reduce the impact of local intensity cues, measurements were obtained with across-interval level randomization in which the overall levels of the stimuli were varied on every presentation. The stimulus levels were randomly altered via the external attenuator based on draws from a uniform distribution with a mean of 0 dB, an 8 dB range, and a 0.1 dB gradation. The overall level across stimulus component number and roving levels ranged from a minimum of 79-dB SPL to a maximum of 98.8-dB SPL.

C. Procedure

Spectral-shape discrimination thresholds in the presence and in the absence of noise were estimated using a modified two-alternative forced-choice task, with trial-by-trial signal strengths chosen according to a three-down, one-up adaptive tracking procedure estimating the 79% correct point on the psychometric function ($d' = 1.14$; Levitt, 1971). Observers were seated in a sound-attenuating room and heard three sounds separated by 450 ms. The first interval contained a standard stimulus, and the second and third intervals contained signal or standard stimuli, the order of which was selected randomly with equal likelihood. Listeners indicated which interval contained the signal stimulus by responding using a button box. Correct-answer feedback was provided to the listener following each trial.

At the beginning of every track, the signal strength was set to 10 or 15 dB above an estimate of the listener's final threshold. The initial step size of the tracking procedure was 4 dB, and after three reversals the step size was reduced to 2 dB. The track continued until a total of nine reversals of

the direction of the track were obtained. The mean of the signal strengths at the last six reversal points was taken as threshold.

To control for the learning effects that are often present in spectral-shape discrimination experiments, a randomized block design was used to collect 12 threshold estimates per stimulus. The experimental design included six different numbers of components, and two noise conditions (noise present and noise absent) for a possible 12 experimental combinations. For each observer a number of components (N) and whether noise was present or absent was chosen at random. Three threshold estimates were obtained for the condition selected, and then three estimates were obtained for the remaining noise condition. Once six threshold estimates were obtained for a given N (three noise present, and three noise absent), a new N was selected randomly and the process repeated. After three thresholds were obtained for all stimulus types, three new thresholds were estimated with the stimulus types run in reverse order. Two additional sets of three threshold estimates were run with the stimulus types in their original and reverse order. Thresholds reported here represent the average of the last nine threshold estimates.

D. Modeling

An excitation-pattern model based on psychophysical estimates of frequency selectivity was used as a front-end to a linear multichannel decision model developed by Durlach *et al.* (1986; see Lentz *et al.*, 1999) according to the following procedures. Standard stimuli were generated at levels corresponding to levels ranging between 76- and 84-dB SPL per component in 1-dB steps. To shorten processing time, noise stimuli were simulated by summing equal-amplitude components at a frequency spacing of 10 Hz (i.e., the Rayleigh-distributed amplitudes were not included). The levels of frequency components were corrected such that the noise stimulus had the same overall level as that used in the psychophysical experiment, and due to the summation used in the excitation-pattern model, this noise yielded identical results to a noise made from components spaced by 1 Hz (also verified through spot checks). The elimination of the amplitude variance on the noise only has a small influence on the magnitude of an "encoding" noise source used in the decision model. For each N, signal stimuli were generated at 5 different signal strengths, which were selected to yield predicted d' values spanning between about 0.9 and 1.4.

In the peripheral auditory simulations, all stimuli were passed through 201 Roex filters, as described by the Glasberg and Moore (1990) filter bank, with center frequencies ranging between 89 and 8562 Hz. Filter center frequencies were spaced by 0.154 ERB, where ERB is defined as the Equivalent Rectangular Bandwidth of the filter. The power at the output of each filter was computed to generate the excitation patterns. The impaired auditory peripheral simulation included modifications to the Glasberg and Moore (1990) filter bank to accommodate reduced frequency selectivity. When the average hearing level at any filter center frequency exceeded 40-dB SPL, scaling of the auditory filter bandwidths was accomplished in the following way. First, the average hearing levels of the clinical audiograms were linearly interpolated so that a hearing level corresponding to each auditory filter center frequency was derived. Hearing levels corresponding to frequencies below 250 Hz were set to equal the hearing level at 250 Hz. Second, the bandwidth of each auditory filter is scaled by ERB_{HL}/ERB_{NH}, where ERB_{HL} is given by Glasberg and Moore (1986) as $ERB_{HL} = -0.135 + 0.0097HL_{SPL}$, with ERB_{HL} defined in kHz and HL_{SPL} defined as absolute threshold in dB SPL. ERB_{NH} is the approximate ERB at 1 kHz of a normal-hearing listener (0.133 kHz) because the previous equation was derived by Glasberg and Moore (1986) for an auditory filter centered at 1 kHz. In this way, the bandwidth of each auditory filter was broadened by an amount relative to the hearing level at that auditory filter's center frequency. The filter tail parameter was set to equal −25.2 dB. Note that this yields impaired filters having the same symmetry as the normal filters. For both healthy and impaired excitation pattern simulations, when the level at a filter's output was below the threshold of audibility for a filter's center frequency, the output level was set to be equal to the threshold of audibility (using the average audiograms).

Two types of models were evaluated: (1) the whole-spectrum model, in which the entire excitation pattern was the input to the channel model; and (2) the peaks-only model, in which the peaks in the excitation pattern were preserved and input to the channel model. The peaks-only excitation pattern was generated by first determining the maximum excitation of each peak in the standard excitation pattern. When the power at the output of a single auditory filter is P_c dB below the excitation of the nearest peak (a peak defined as excitation that exceeds excitation in adjacent frequency regions), the output of that filter is set to the corresponding threshold of audibility.

Figure 2 illustrates excitation patterns for four-component standard stimuli in the presence and in the absence of noise. For the whole-spectrum excitation patterns (top panels), the spectral representation is similar for normal-hearing and hearing-impaired listeners in the low frequencies, but the reduced frequency selectivity of the impaired auditory system degrades the spectral contrast in the high frequencies. The added noise stimulus broadens the spectral peaks and decreases the depth of the valleys in both the normal-hearing and hearing-impaired simulations. Also, the noise stimulus leads to a visible degradation of the high-frequency spectral peaks in the hearing-impaired model. For the peaks-only excitation patterns ($P_c = 5$ dB; bottom panels), spectral peaks are present for all frequency components, but broader peaks are associated with hearing impairment and the presence of noise.

The Durlach *et al.* (1986) channel model was implemented by using the formula described by van Trees (1968) as $(d')^2 = [\Delta_1, \ldots, \Delta_M] G [\Delta_1, \ldots, \Delta_M]^T$, where $[\Delta_1, \ldots, \Delta_M]$ indicates the mean change in level between signal and standard excitation patterns for channels 1 to M, G is the inverse of the covariance matrix, and T denotes the matrix transpose. Recall that the signal stimuli were generated using five signal strengths chosen to yield predicted d' values spanning between about 0.9 and 1.4. The Δ vector and

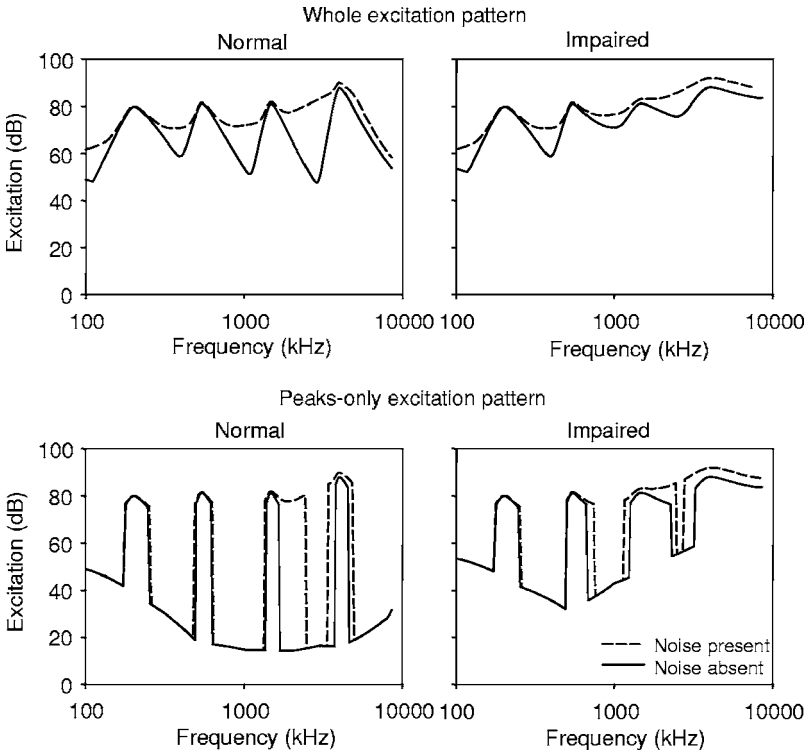

FIG. 2. Normal-hearing and hearing-impaired excitation patterns for a four-component stimulus are plotted in the left and right panels, respectively. Noise-present excitation patterns are plotted as the dashed lines, and noise-absent excitation patterns are plotted as the solid lines. The whole-spectrum model is illustrated in the upper panels, and the peak-selection model in which filters having output levels 5 dB below the nearest peak in excitation are set to the threshold of audibility is indicated in the lower panels.

the covariance matrix were estimated by corrupting the excitation patterns generated for each stimulus in the following way: Independently drawn deviates from a Normal distribution having a mean of 0 and a standard deviation of σ were added to the output of the each of the 201 frequency channels to generate 1000 randomly perturbed standard and 1000 randomly perturbed signal stimuli for each N and each signal strength. Here, σ is the standard deviation of "internal" or "encoding" noise needed to approximate imperfect auditory sensitivity. Random draws were taken from the group of excitation patterns generated at the nine different overall levels to simulate roving levels (i.e., 76–84-dB SPL per component in 1 dB steps). The correlated noise source generated by the rove is reflected in the covariance matrix, which was estimated by averaging the signal and standard covariance matrices. Psychometric functions at each of the five signal strengths were constructed. A linear least-squares fit to the psychometric function was used to determine a final estimate of threshold corresponding to $d' = 1.14$.

The two models were implemented by means of a partial grid search, using the single parameter, σ, for the whole-spectrum model and the two parameters, σ and P_c, for the peaks-only model. Note that the whole-spectrum model is the same as the peaks-only model with a P_c that is greater than the maximum excitation present in the excitation pattern. Hearing-impaired data were modeled separately from normal-hearing data. The proportion of variance accounted for in the average data (thresholds versus the number of stimulus components) was maximized in the noise-absent conditions by varying the value of σ or σ and P_c, depending on the model being fitted. Note that average data were used because, as will be illustrated in the results section, variability in the pattern of thresholds related to N is present across observers. The parameters σ and P_c were fixed, and then noise-present data were predicted using the simulated noise stimuli added to the multi-component stimuli.

The σ and P_c parameters differentially influence the pattern of the function relating predicted threshold to number of stimulus components. The parameter σ (the standard deviation of an encoding noise distribution) has the influence of either raising or lowering the entire function. Figure 3 illustrates that an increase in σ is associated with an upward shift in the function relating threshold to N (poorer sensitivity), whereas a decrease in σ is associated with a downward shift in the predicted threshold (better sensitivity). Changes to the number of channels also influence predicted sensitivity (Lentz *et al.*, 1999); an increase in the number of channels

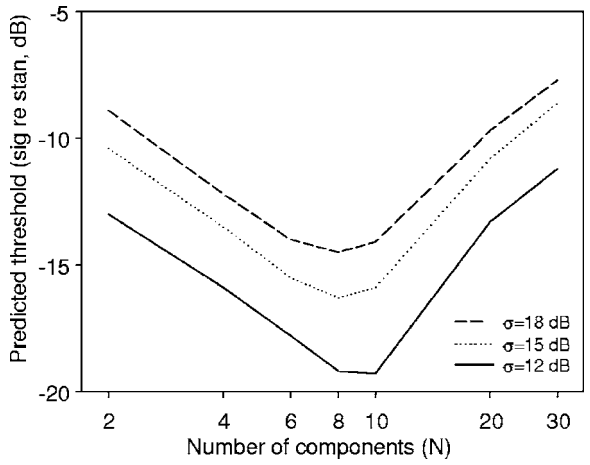

FIG. 3. The influence on model predictions for a change in the standard deviation of the "encoding" noise, σ, is illustrated. Predicted thresholds are plotted as a function of the number of stimulus components. Model predictions are based on noise-absent stimuli, normal-hearing auditory filter bandwidths, and $P_c = 7$ dB.

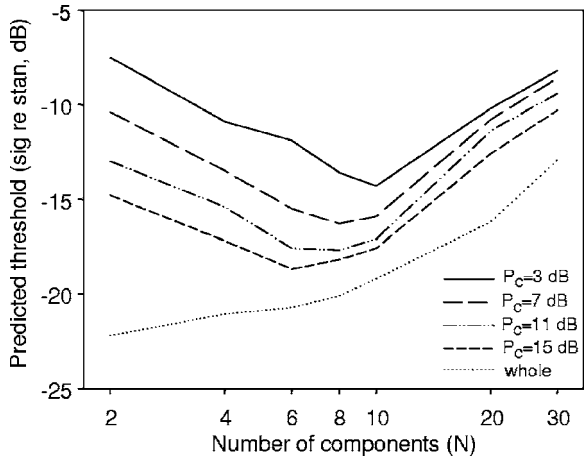

FIG. 4. The influence on model predictions for a change in the P_c parameter is illustrated. Predicted thresholds are plotted as a function of the number of stimulus components. Model predictions are based on noise-absent stimuli, normal-hearing auditory filter bandwidths, and $\sigma=15$ dB.

(leading to better sensitivity) would necessitate an increase in σ (leading to poorer sensitivity) to yield the same predictions. Thus, the magnitude of σ has little absolute meaning, as it must be interpreted in the context of the number of channels.

In contrast to the encoding noise parameter, the peak-selection parameter, P_c, influences the shape of the function relating threshold to N. The influence of the P_c parameter on the shape of the function is illustrated in Fig. 4. Changes in the P_c parameter are associated with changes in overall sensitivity, in that larger values of P_c (broader spectral peaks) lead to a greater number of channels cueing the spectral-shape change and subsequently lower thresholds (better sensitivity). Larger P_c values also lead to a smaller N at which thresholds begin to rise, but the P_c parameter has little effect on the slope of the function relating threshold to N at small N. Note that in this implementation of the model P_c is not allowed to be 0, as this would obliterate all spectral information.

III. RESULTS

A. Experimental data

Figure 5 plots thresholds obtained from the individual listeners (upper five panels) and the thresholds averaged across listeners (bottom panels) as a function of the number of stimulus components. A repeated-measures ANOVA treating group membership as a between-subjects variable and number of components and whether noise was present or absent as within-subjects variables reveals significant main effects and two-way interactions in the data. Thresholds are dependent on the number of components $[N;F(6,48)=12.4;p<0.001]$, and, across most listeners, there is a general pattern of an initial decrease in threshold followed by a subsequent increase in threshold as N increases. Only NH2 in the noise-present condition and HI1 in the noise-absent condition do not show this pattern in their data.

The average data from normal-hearing listeners (bottom left panel) also indicate that the function relating threshold to N has a "W" shape. While there are some individual differences in the shape of the function relating threshold to N across observers, three of the five normal-hearing listeners show this W shape in their noise-absent data (NH1, NH3, and NH5; also reported by Lentz *et al.*, 1999), and four of the listeners show the W shape in the noise-present data, though individual observers show this W shape to different degrees. For example, the noise-present data of NH1 have a very pronounced W, with thresholds at $N=8$ being 10 dB higher than thresholds at $N=4$ or $N=10$. In contrast, the noise-present data obtained from NH3 indicate a less-pronounced W shape, as thresholds at $N=8$ are only 1.2 dB higher than thresholds at $N=6$. In general, data obtained from hearing-impaired listeners (right panel) do not have the W shape in either condition: the W shape is evident only for HI5 when noise is absent and HI2 when noise is present.

The fact that thresholds vary nonmonotonically with increasing N suggests that listeners are comparing levels across frequency and not relying on single-channel intensity cues for discrimination. In addition, all average thresholds in the noise-absent conditions, except those obtained from the hearing-impaired listeners at $N=20$ and $N=30$, are below the -8.3 dB level-detection limit. Thus, on average, the noise-absent data do not reflect judgments based on overall intensity changes.

The general shape of the functions relating threshold to N is different for normal-hearing and hearing-impaired listeners, as revealed by a significant interaction between group membership and the number of components $[F(6,48)=2.9;p<0.015]$. For normal-hearing listeners, thresholds begin to consistently rise with increasing N when the stimulus contains more than 10 components. In contrast, thresholds obtained from the hearing-impaired listeners begin to rise at the smaller N of 6 or 8. For the larger N's, hearing-impaired listeners show poorer spectral-shape discrimination sensitivity than normal-hearing listeners. These two results (the smaller N at which thresholds begin to rise and the poorer the spectral-shape discrimination sensitivity at large N for hearing-impaired listeners) likely reflect the poorer frequency selectivity in the impaired auditory system [see also Summers and Leek (1994) and Leek and Summers (1996)].

On average, it appears that spectral-shape discrimination is poorer for hearing-impaired than for normal-hearing listeners, but this finding is not statistically significant $[F(1,8)=3.6;\ p=0.09]$, perhaps due to the small group size and large variability in performance across listeners. It is evident from the individual data (also reflected in the large error bars on the average data) plotted in Fig. 5 that overall spectral-shape discrimination sensitivity varies across listeners, regardless of whether they have hearing loss or not. For example, NH2 has very poor spectral-shape discrimination sensitivity compared to the other normal-hearing listeners and some of the hearing-impaired listeners.

The repeated-measures ANOVA also reveals a significant main effect of whether noise was present or absent $[F(1,8)=92.5;p<0.001]$ and a significant interaction between group membership and whether noise was present or absent $[F(1,8)=11.6;p<0.01]$. On average, the presence of noise leads to an increase in spectral-shape discrimination threshold by 2.6 dB. However, the spectral-shape discrimina-

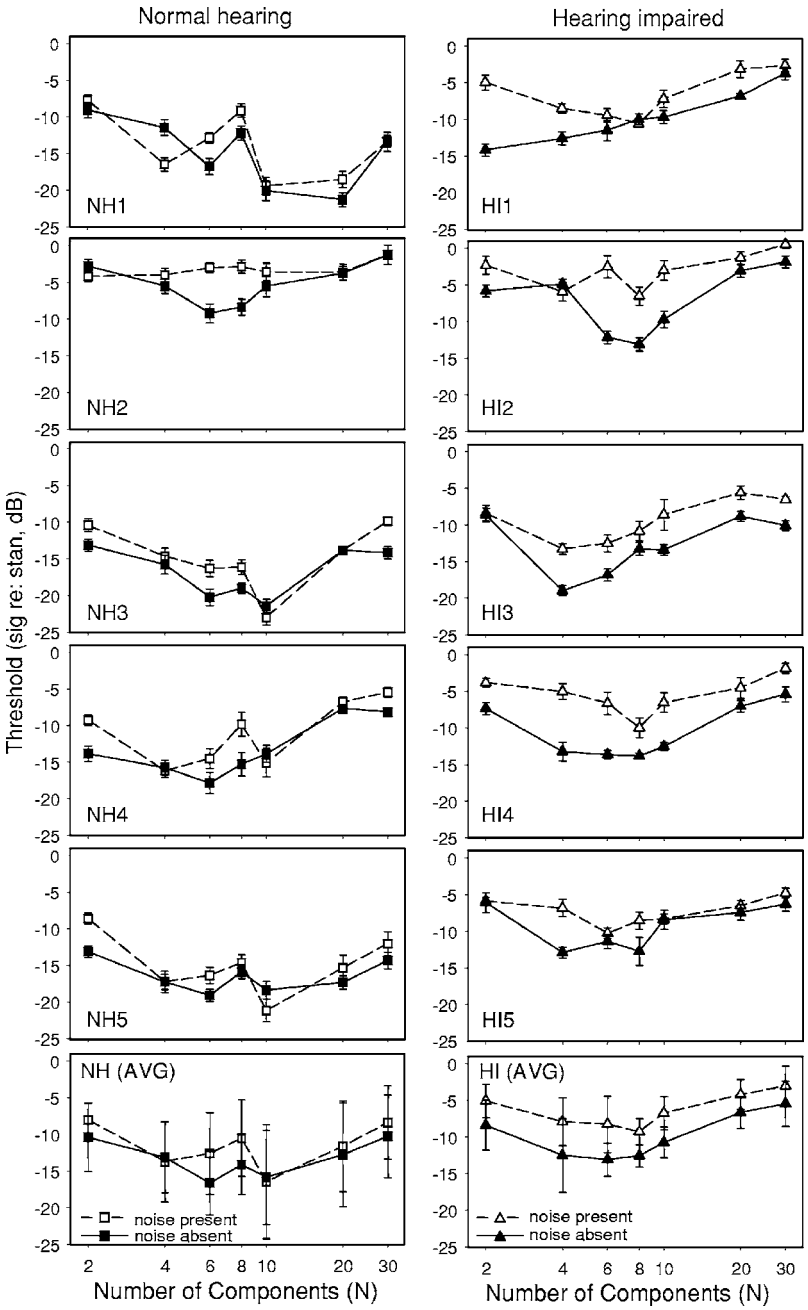

FIG. 5. Spectral-shape discrimination thresholds are plotted for five normal-hearing listeners (left panels) and five hearing-impaired listeners (right panels) as a function of the number of stimulus components. Averaged data are plotted in the bottom panels for each group. Filled and unfilled symbols denote noise-absent and noise-present conditions, respectively. For the individual data, error bars indicate standard errors of the mean across nine threshold replicates, whereas, for the averaged data, error bars indicate standard deviations across five listeners.

tion sensitivity of the hearing-impaired listeners is influenced by the noise to a greater extent than for the normal-hearing listeners (1.7 dB for normal-hearing listeners and 3.5 dB for hearing-impaired listeners). For the normal-hearing listeners, thresholds at $N=6$ and $N=8$ are more greatly influenced by the presence of the noise stimulus—these two thresholds alone are 3.8 dB higher than the corresponding noise-absent thresholds. However, the general pattern is a small effect of noise. Using slightly different stimuli, Green and Forrest (1986) also found that spectral-shape discrimination thresholds of normal-hearing listeners were not influenced by a noise stimulus having a spectrum level 30 dB below the level per component. In contrast, thresholds obtained from hearing-impaired listeners for all numbers of components are influenced by the presence of noise.

The relatively small effect of the noise on spectral-shape discrimination thresholds of normal-hearing listeners is consistent with the hypothesis that the auditory system uses only the peaks in the excitation pattern when discriminating between sounds with different spectral shapes. The small effect of noise on the spectral-shape discrimination threshold indicates that masking the information-bearing edges of peaks in the excitation pattern does not greatly degrade performance and suggests that only the peaks are used for spectral-shape discrimination. Hearing-impaired listeners, however, were influenced by the presence of noise to a greater extent than normal-hearing listeners. This result might imply that the impaired auditory system does not rely on the spectral peaks to the same extent as the normal-hearing listeners because reduced frequency selectivity broadens the peaks and makes them less pronounced. An alternative explanation is that the

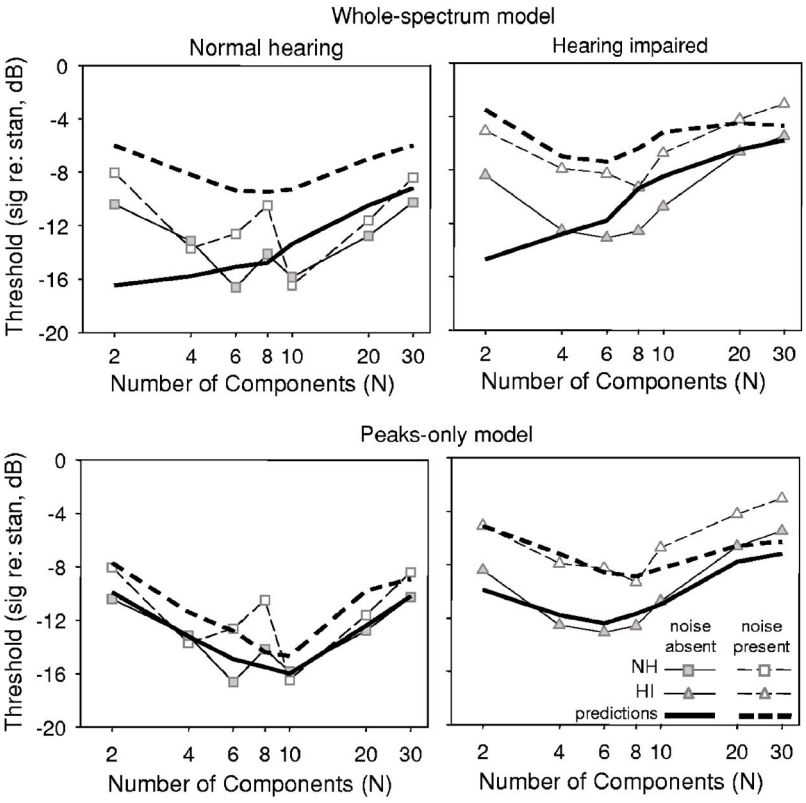

FIG. 6. Model predictions for the whole-spectrum and peaks-only models are plotted in the upper and lower panels, respectively. Normal-hearing data and predictions are indicated in left panels, whereas hearing-impaired data and predictions are indicated in the right panels. Noise-absent predictions are shown by the bold, solid lines, and noise-present predictions are shown with the bold, dashed lines. Averaged data from Fig. 5 are replotted with the noise-absent data as filled symbols and the noise-present data as the unfilled symbols.

impaired auditory system does rely on the spectral peaks, but the broader spectral peaks are more susceptible to noise. These two alternatives will be explored further in the modeling.

B. Modeling results

Model predictions are plotted along with the average normal-hearing and hearing-impaired data in Fig. 6. Whole-spectrum model predictions are plotted in the upper panels, whereas peaks-only predictions are plotted in the lower panels. Normal-hearing and hearing-impaired data and predictions are shown in the left and right panels, respectively.

The upper left panel illustrates that normal-hearing data are poorly predicted by the whole-spectrum model. The best-fitting whole-spectrum model predictions of the noise-absent data (bold, solid line; $\sigma=27$ dB) do not well capture the trends present in the data. The model predicts that thresholds increase with increasing N for all N and predicts better-than-measured thresholds at small N. The model fits to the noise-absent data more closely captures the initial decrease in threshold with increasing N and the subsequent increase in threshold with increasing N, but the whole-spectrum model predicts that noise-present thresholds (bold, dashed line) should be much higher than noise-absent thresholds. The elevated noise-present thresholds are not observed in the data, as thresholds are only 1.7 dB higher when noise is present over when noise is absent. Thresholds for small N are predicted to be about 10 dB higher in the noise-present conditions than in the noise-absent conditions, and the effect of noise is predicted to decrease with increasing N, to a value of 3.2 dB at $N=30$. The whole-spectrum model accounts for less than 45% of the variance in the data, and it is clear that it fails considerably to predict trends present in the normal-hearing data.

The whole-spectrum model shows a similar failure to predict the hearing-impaired data in the noise-absent conditions. As with the predictions of the normal-hearing data, predicted thresholds in the noise-absent condition (bold, solid lines; obtained using $\sigma=28$ dB) consistently increase with increasing N. However, model predictions of the noise-present conditions (dashed, solid lines) show an improvement in the goodness-of-fit, with a major improvement in capturing the initial decrease in threshold with increasing N. The general shape of the function relating the predicted threshold to N is also similar to the shape of the measured data. The whole-spectrum model, however, does not predict the consistent influence of noise on the threshold for all N.

Because the whole-spectrum model fails to capture the decrease in threshold with increasing N for small N, and the effect of noise is not appropriately predicted for normal-hearing and hearing-impaired listeners, a second model was used in which the whole-spectrum model was modified to include a peak-selection algorithm (see Fig. 6, bottom panel). Normal-hearing noise-absent data were best fit using the peak-selection model with $\sigma=13$ dB and $P_c=4$ dB, accounting for 85% of the variance in the data. Model predictions (bold, solid lines) accurately predict the pattern of thresholds observed in the dataset. The main deficiency is that the W shape is not captured by the model. However, peak-selection model fits are superior to the model fits obtained from the whole-spectrum model.

When the noise-present data are predicted using the same parameters as the noise-absent conditions, the model

has more difficulty predicting the data, accounting for only 49% of the variance. In general, the model predicts that noise would lead to an average 1.8 dB increase in the spectral-shape discrimination threshold, an increase that is very similar to the average 1.7 dB effect of noise in the normal-hearing data. The shape of the predicted function is similar to the shape of the data. However, the pronounced W shape in the noise-present dataset again is not captured by the model, and no change to the model parameters can predict the W shape (see Figs. 3 and 4). The cause of the W shape in the data is unknown, but perhaps it is related to a shift from a peak-selection process used at small N (i.e., when a stimulus leads to a highly peaked excitation pattern) to a different decision process for stimuli having less peaked excitation patterns.

Noise-absent data from hearing-impaired listeners are best fit using the peak-selection model with $\sigma=19$ dB and $P_c=3$ dB, accounting for 85% of the variance in the data. The general shape of the function is very similar to that observed in the data, but the change in the predicted threshold with increasing N at large N is somewhat shallower than measured. Part of the failure in the model to capture the subtle trends present for large N might be that the auditory filter bandwidths used in the model were estimated rather than measured. To test whether changes in auditory filter bandwidth might lead to better predictions to the data collected from hearing-impaired listeners, the peaks-only model was run using scaled auditory filter bandwidths. Even better fits (over 92% of the variance accounted for) could be obtained using narrower auditory filter bandwidths. However, even with this modification, the rise in threshold with increasing N at large N is somewhat underpredicted. Clearly, the fits to the hearing-impaired data are robust, with the peaks-only model being a much better predictor of performance than the whole-spectrum model. Despite using optimal processing and generalization of frequency selectivity, the model fits do quite well in predicting the trends present in the hearing-impaired data.

The best-fitting parameters differ from those estimated from the normal-hearing data, with σ being larger to fit the hearing-impaired data (19 and 13 dB for the hearing-impaired and normal-hearing listeners, respectively), and P_c being only 1 dB different from the P_c that best-fit the normal-hearing data (3 and 4 dB for the hearing-impaired and normal-hearing data, respectively). The higher value of σ for hearing-impaired listeners might be consistent with the idea that hearing impairment can be modeled as a "second noise" (e.g., Humes *et al.*, 1988). The similarity of P_c values between the two groups suggests that processing of stimuli with different spectral shapes is very similar for normal-hearing and hearing-impaired listeners and indicates that the impaired auditory system still accomplishes some form of peak selection. The peaks-only model also predicts the data obtained from hearing-impaired listeners much better than the whole-spectrum model.

As in the predictions of the normal-hearing data, the peaks-only model does not predict the noise-present data as well as the noise-absent data, accounting for only 61% of the variance in the noise-present data. The general pattern of predicted thresholds versus N is similar to the observed pattern in the data. Unlike the normal-hearing data, the hearing-impaired data tended not to show the W shape in the function relating threshold to N. The main failure of the model to capture the trends in the hearing-impaired data is at large N where predicted thresholds are *better* than measured. Increasing the value of σ would improve the goodness-of-fit, but then the better predictions of thresholds at large N would come at the expense of more poorly predicted thresholds at small N. Changing the peak-selection parameter (P_c) does not improve the goodness of fit.

The major failure of the whole-spectrum model is to capture the decrease in threshold with increasing N when N is small for both groups of listeners. Including a peak-selection algorithm into the model successfully depicts this initial decrease in threshold. The peaks-only model captures some of the increase in threshold in the presence of noise, but generally the peaks-only model does not predict the noise-present data as well as the noise-absent data. However, the relative success of the peaks-only model in predicting both normal-hearing and hearing-impaired data compared to the whole-spectrum model suggests that listeners in both groups use the peaks in spectral-shape discrimination. The higher relative thresholds for the hearing-impaired listeners in the presence of the noise, then, could be due to differences in frequency selectivity between the two groups, rather than differences in the listeners' decision processes when discriminating between sounds with different spectral shapes.

IV. DISCUSSION

A. Peak selection in spectral-shape discrimination

Support for the conclusion that spectral-shape discrimination of sounds with a peaked excitation pattern is accomplished by selecting the peaks can be found in both the experimental data and the modeling predictions. First, the experimental data from normal-hearing listeners indicate that the presence of a noise stimulus has only a modest influence on the spectral-shape discrimination threshold. If the entire excitation pattern were used for the decision, it would be anticipated that the presence of noise would lead to a large increase in threshold. This prediction is supported by the very large influence of noise on the spectral-shape discrimination threshold predicted by the whole-spectrum model. Second, the peaks-only model is able to capture the trends apparent in the noise-absent data, though the model fits are not as robust as observed for the noise-present conditions. The peaks-only model captures trends in the normal-hearing and hearing-impaired data equally well, supporting the conclusion that the impaired auditory system also relies on spectral peaks for discriminating between sounds with different spectral shapes. Taken together, the experimental data and the multichannel modeling suggest that the healthy and the impaired auditory systems rely on spectral peaks in the stimulus for spectral-shape discrimination when the stimulus has pronounced spectral peaks.

Previous spectral-shape discrimination data are consistent with the hypothesis that the auditory system relies mostly on the spectral peaks to discriminate between sounds

with different spectral shapes when those stimuli lead to peaked excitation patterns. These experiments indicate that the central auditory system may not greatly rely on the edges of the excitation pattern peaks. For example, Green *et al.* (1984) had listeners detect a single tone added in phase to the 1000-Hz central component of a three-component background and varied the spacing of the frequency components. The sensitivity for detecting a single tone added to a three-component background improved by only 4 dB when stimulus components were separated by a frequency ratio of 1.38 versus a frequency ratio of 5 (see also Green *et al.*, 1983). If the auditory system used the edges of the peaks in the excitation pattern, it might be expected that a larger improvement in threshold would have been measured.

Other evidence of using the spectral peaks for spectral-shape discrimination is that spectral-shape discrimination data do not show evidence of the near-miss to Weber's law (Mason *et al.*, 1984; Green and Mason, 1985; Versfeld and Houtsma, 1995; Lentz, 2005). The near-miss to Weber's law reflects a decrease in the ratio relating the intensity discrimination difference limen of a single tone to the intensity of that tone ($\Delta I/I$) with increasing intensity (Riesz, 1928; Viemeister, 1972; Moore and Raab, 1974). For intensity discrimination of tones, the change in excitation at the high-frequency edge of the peak in the excitation pattern provides a useful cue to the auditory system that one tone is more intense than another. Because spectral-shape discrimination experiments show no evidence for the near-miss to Weber's law (even in the absence of overall level randomization), the edges of the excitation pattern peaks might not be important for spectral-shape discrimination. These results suggest that using only the spectral peaks might be an inherent property of auditory processing for broadband listening.

These arguments regarding peak selection for spectral-shape discrimination have support in the vowel-perception literature, where it has been suggested that the frequencies of the spectral peaks (i.e., formants) provide more important cues to vowel identity than the overall shape of the spectrum (Assmann and Summerfield, 1989). Assmann and Summerfield (1989) measured single- and double-vowel identification for synthetic vowels and "vowels" with only six harmonics. The six-harmonic "vowels" contained equal-amplitude harmonic pairs, with each pair corresponding to one of the first three formant frequencies. Overall levels of performance did not differ significantly between the two vowel types, despite the richer spectrum of the synthesized vowels, indicating that the low-level valleys did not provide informative cues to the identities of the vowels.

Spectral enhancement mediated by suppression in the auditory nerve (Houtgast, 1972; Sidwell and Summerfield, 1985), might provide a mechanism for selecting the spectral peaks in a complex stimulus. Physiologic studies have also shown that the temporal responses of auditory nerve fibers are dominated by the spectral peaks in a vowel-like stimulus (e.g., Young and Sachs, 1979; Delgutte and Kiang, 1984). Enhancement of the spectral peaks in a stimulus also occurs in the impaired auditory system, although the enhancement is not as pronounced as for normal-hearing listeners (Sidwell and Summerfield, 1985; Thibodeau, 1991).

Because the results of the current experiment suggest that the edges of the peaks in the excitation pattern do not contribute greatly to spectral-shape discrimination, the selection of spectral peaks might be described as a process leading to a loss of information, indicating that two stimuli have different spectral shapes. However, as has been shown here, the presence of a low-level noise does not greatly alter sensitivity to changes in spectral shape. In contrast, the whole-spectrum model predicts a large decrease in spectral-shape discrimination sensitivity. Selecting for the spectral peaks would provide a mechanism allowing the ear to function similarly under noisy and quiet conditions.

Thresholds obtained from hearing-impaired listeners were elevated by noise by a greater amount than those obtained from normal-hearing listeners. However, the small influence of noise (3.5 dB) and the success of the peaks-only model lead to the conclusion that hearing-impaired listeners also rely on the spectral peaks to discriminate between sounds with different spectral shapes. Because hearing-impaired listeners have poorer frequency selectivity than normal-hearing listeners, the spectral peaks in a stimulus are more easily masked by the presence of noise. Thus, a major limitation experienced by the hearing-impaired listeners in spectral-shape discrimination might be reduced frequency selectivity, which impacts the perception of both spectrally sparse and spectrally dense stimuli, especially in the presence of a background noise.

B. Modeling implications

A modification of the whole-spectrum multichannel model by including a peak-selection algorithm leads to an improvement of model fits, but the peaks-only model does not capture all trends in the data. Including a peaks-only excitation pattern has the effect of accurately predicting the initial decrease in threshold with increasing numbers of components that has been commonly reported in spectral-shape discrimination data (see Bernstein and Green, 1987; Green, 1992). This modified version of the model, while very successful at predicting the general trends of spectral-shape discrimination for normal-hearing and hearing-impaired listeners, has two notable discrepancies between the predictions and the data. One discrepancy is that the model could not capture distinct W shape present in the data of the majority of the normal-hearing listeners. The inability of the model to capture this shape suggests a difference in the auditory processes responsible for coding spectral shape for stimuli with different spectral characteristics. The model also fails to predict the increase in threshold with increasing N ($N>8$) observed for hearing-impaired listeners. Consideration of each of these discrepancies might lead to insight regarding the processes that code spectral shape in the normal and impaired auditory systems.

The inability of the peaks-only model to capture the W shape in the data from normal-hearing listeners suggests that there could be differences in the underlying processes for stimuli with peaked excitation patterns, stimuli with excitation patterns intermediate to peaked and flat, and stimuli with flat excitation patterns. Spectral-shape discrimination of

sparse stimuli has been modeled fairly extensively in the past, and for the most part, multichannel models have been highly successful at predicting performance (see Berg and Green, 1990; Green, 1992; Lentz and Richards, 1997). However, despite the widespread support for an optimal combination of channel outputs, listeners do not always optimally combine information across frequency when the stimuli are spectrally sparse (Lentz and Leek, 2003). Stimulus characteristics and task demands could play a large role in the decision rules adopted by normal-hearing and hearing-impaired listeners.

Spectrally dense stimuli might also be subject to shifts in decision rules, depending on whether stimuli are spectrally flat or spectrally peaked, but there are few quantitative evaluations of a multichannel model to spectrally dense stimuli. Farrar *et al.* (1987) successfully applied a multichannel model to the discrimination of noise bursts modeled after English consonants. Other applications of excitation patterns to the spectral-shape discrimination of spectrally dense stimuli have used a modified version of the multichannel model. Summers and Leek (1994) successfully modeled spectral-shape discrimination of stimuli having a sinusoidally rippled spectral envelope using a simple "two-channel" algorithm in which a minimum excitation level was subtracted from a maximum excitation level. Versfeld (1997) also argued that a modification of the multichannel model in which only a limited number of channels are combined would lead to better predictions of spectral-shape discrimination of narrow bands of noise. Applied to the current model, using a subset of channels will only improve predictions if a different number of channels is used for spectrally sparse stimuli than for spectrally dense stimuli.

The presence of the W shape in the normal-hearing data could arise from differences in the decision processes adopted by listeners across stimuli with different spectral densities (or different spectral shapes, such as peaked or flat), but another possible explanation of the W shape is that temporal cues could play a role in the presence of the W shape. As the spectral density of the stimuli used in this experiment increases, the temporal interactions between adjacent components would also increase, leading to a second cue present in the current experiment. Support for the idea that temporal cues might be at play here is found in an auxiliary experiment by Lentz *et al.* (1999). They showed that temporal cues could have a modest influence on spectral-shape discrimination sensitivity. However, none of the subjects who participated in the auxiliary experiment had data that reflected the W shape (in conditions both with and without reliable temporal cues). These subjects ($N=3$) received a large amount of practice on the spectral-shape discrimination tasks (about 18 h). Another explanation is that the W shape might reflect different decision strategies across spectral densities with the spectral-shape change being more difficult to learn for certain types of stimuli. Why this might differ for normal-hearing and hearing-impaired listeners is unclear.

As mentioned previously, the peaks-only model does not successfully capture the increase in threshold for spectrally dense stimuli, especially for the hearing-impaired listeners. Perhaps the decision strategies adopted by listeners with hearing loss are different from those adopted by listeners with normal hearing for both spectrally sparse and spectrally dense stimuli. Using spectrally sparse stimuli, Doherty and Lutfi (1996) and Lentz and Leek (2003) showed that listeners with hearing loss adopt decision strategies that are different to the strategies adopted by listeners with normal hearing. Whether these results on spectrally sparse stimuli are due to peripheral or central differences in auditory processing remains unknown, but if spectral shape processing does differ for spectrally sparse (or spectrally peaked) and spectrally dense (or spectrally flat) sounds, there could also be differences in the decision strategies adopted by normal-hearing and hearing-impaired listeners for spectrally dense sounds. Differences in decision strategies could lead to differences in the success of the model at predicting thresholds for large N. Better fits of the model might also be expected if actual auditory filter bandwidth estimates were used.

V. SUMMARY AND CONCLUSIONS

The current experiment shows that the presence of noise has little effect on spectral-shape discrimination ability for normal-hearing listeners and leads to a moderate increase in threshold for hearing-impaired listeners. An excitation pattern model based on psychophysical estimates of frequency selectivity and a peak-selection algorithm coupled with a linear multichannel decision model is able to account for more than 85% of the variance in the data for normal-hearing and hearing-impaired groups in conditions when noise is absent. The relatively small influence of noise on spectral-shape discrimination sensitivity and the success of a multichannel model that included a peak-selection algorithm suggest that the normal and impaired auditory systems selectively use peaks in the excitation pattern. It is therefore concluded that the somewhat larger influence of noise on spectral-shape discrimination sensitivity for hearing-impaired listeners is due to a broadening of peaks in the excitation pattern rather than an inability to use those peaks.

ACKNOWLEDGMENTS

This work was supported by Grant DC 005825 from the National Institute on Deafness and Communication Disorders. The author thanks Melissa Ferrello and Melissa Woods for assistance during data collection and Larry Humes for helpful comments on this manuscript.

[1]The noise used for the excitation patterns contain equal-amplitude components.

[2]The TDT RP2.1 does not generate aliased stimuli below the sampling rate, eliminating the need for an antialiasing filter.

ANSI (1996) S3.6-1996. "Specification for audiometers," American National Standards Institute, New York.

Assmann, P. F., and Summerfield, Q. (**1989**). "Modeling the perception of concurrent vowels: vowels with the same fundamental frequency," J. Acoust. Soc. Am. **85**, 327–338.

Berg, B. G., and Green, D. M. (**1990**). "Spectral weights in profile listening," J. Acoust. Soc. Am. **88**, 758–766.

Bernstein, L. R., and Green, D. M. (**1987**). "The profile-analysis bandwidth," J. Acoust. Soc. Am. **81**, 1888–1895.

Delgutte, B., and Kiang, N. Y. (**1984**). "Speech coding in the auditory nerve: I. Vowel-like sounds," J. Acoust. Soc. Am. **75**, 866–878.

Doherty, K. A., and Lutfi, R. A. (**1996**). "Spectral weights for overall level discrimination in listeners with sensorineural hearing loss," J. Acoust. Soc. Am. **99**, 1053–1058.
Doherty, K. A., and Lutfi, R. A. (**1999**). "Level discrimination of single tones in a multitone complex by normal-hearing and hearing-impaired listeners," J. Acoust. Soc. Am. **105**, 1831–1840.
Durlach, N. I., Braida, L. D., and Ito, Y. (**1986**). "Towards a model for discrimination of broadband signals," J. Acoust. Soc. Am. **80**, 63–72.
Ellermeier, W. (**1996**). "Detectability of increments and decrements in spectral profiles," J. Acoust. Soc. Am. **99**, 3119–3125.
Farrar, C. L., Reed, C. M., Ito, Y., Durlach, N. I., Delhorne, L. A., Zurek, P. M., and Braida, L. D. (**1987**). "Spectral-shape discrimination. I. Results from normal-hearing listeners for stationary broadband noises," J. Acoust. Soc. Am. **81**, 1085–1092.
Glasberg, B. R., and Moore, B. C. (**1986**). "Auditory filter shapes in subjects with unilateral and bilateral cochlear impairments," J. Acoust. Soc. Am. **79**, 1020–1033.
Glasberg, B. R., and Moore, B. C. (**1990**). "Derivation of auditory filter shapes from notched-noise data," Hear. Res. **47**, 103–138.
Green, D. M. (**1988**). *Profile Analysis: Auditory Intensity Discrimination* (Oxford University Press, New York).
Green, D. M. (**1992**). "The number of components in profile analysis tasks," J. Acoust. Soc. Am. **91**, 1616–1623.
Green, D. M., and Forrest, T. G. (**1986**). "Profile analysis and background noise," J. Acoust. Soc. Am. **80**, 416–421.
Green, D. M., and Kidd, G. (**1983**). "Futher studies of auditory profile analysis," J. Acoust. Soc. Am. **73**, 1260–1265.
Green, D. M., and Mason, C. R. (**1985**). "Auditory profile analysis: Frequency, phase, and Weber's Law," J. Acoust. Soc. Am. **77**, 1155–1161.
Green, D. M., Kidd, G., Jr., and Picardi, M. C. (**1983**). "Successive versus simultaneous comparison in auditory intensity discrimination," J. Acoust. Soc. Am. **73**, 639–643.
Green, D. M., Mason, C. R., and Kidd, G., Jr (**1984**). "Profile analysis: Critical bands and duration," J. Acoust. Soc. Am. **75**, 1163–1167.
Houtgast, T. (**1972**). "Psychophysical evidence for lateral inhibition in hearing," J. Acoust. Soc. Am. **51**, 1885–1894.
Humes, L. E., Espinoza-Varas, B., and Watson, C. S. (**1988**). "Modeling sensorineural hearing loss. I. Model and retrospective evaluation," J. Acoust. Soc. Am. **83**, 188–202.
Kidd, G., Mason, C. R., Uchanski, R. M., Brantley, M. A., and Shah, P. (**1991**). "Evaluation of simple models of auditory profile analysis using random reference spectra," J. Acoust. Soc. Am. **90**, 1340–1354.
Leek, M. R., and Summers, V. (**1996**). "Reduced frequency selectivity and the preservation of spectral contrast in noise," J. Acoust. Soc. Am. **100**, 1796–1806.
Lentz, J. J. (**2005**). "Profile analysis: the effects of rove on sparse spectra," J. Acoust. Soc. Am. **118**, 2794–2797.
Lentz, J. J., and Leek, M. R. (**2003**). "Spectral shape discrimination by hearing-impaired and normal-hearing listeners," J. Acoust. Soc. Am. **113**, 1604–1616.
Lentz, J. J., and Richards, V. M. (**1997**). "Sensitivity to changes in overall level and spectral shape: an evaluation of a channel model," J. Acoust. Soc. Am. **101**, 3625–3635.
Lentz, J. J., Richards, V. M., and Matiasek, M. R. (**1999**). "Different auditory filter bandwidth estimates based on profile analysis, notched noise, and hybrid tasks," J. Acoust. Soc. Am. **106**, 2779–2792.
Levitt, H. (**1971**). "Transformed up-down methods in psychoacoustics," J. Acoust. Soc. Am. **49**, 467–477.
Mason, C. R., Kidd, G., Jr., Hanna, T. E., and Green, D. M. (**1984**). "Profile analysis and level variation," Hear. Res. **13**, 269–275.
Moore, B. C., and Raab, D. H. (**1974**). "Pure-tone intensity discrimination: some experiments relating to the near-miss to Weber's law," J. Acoust. Soc. Am. **55**, 1049–1054.
Riesz, R. R. (**1928**). "Differential intensity sensitivity of the ear for pure tones," Phys. Rev. **31**, 867–875.
Sidwell, A., and Summerfield, Q. (**1985**). "The effect of enhanced spectral contrast on the internal representation of vowel-shaped noise," J. Acoust. Soc. Am. **78**, 495–506.
Spiegel, M. F., Picardi, M. C., and Green, D. M. (**1981**). "Signal and masker uncertainty in intensity discrimination," J. Acoust. Soc. Am. **70**, 1015–1019.
Summers, V., and Leek, M. R. (**1994**). "The internal representation of spectral contrast in hearing-impaired listeners," J. Acoust. Soc. Am. **95**, 3518–3529.
Thibodeau, L. M. (**1991**). "Performance of hearing-impaired persons on auditory enhancement tasks," J. Acoust. Soc. Am. **89**, 2843–2850.
van Trees, H. L. (**1968**). *Detection, Estimation, and Modulation Theory* (Wiley, New York).
Versfeld, N. J. (**1997**). "Discrimination of changes in the spectral shape of noise bands," J. Acoust. Soc. Am. **102**, 2264–2275.
Versfeld, N. J., and Houtsma, A. J. M. (**1995**). "Discrimination of changes in the spectral shape of two-tone complexes," J. Acoust. Soc. Am. **98**, 807–816.
Viemeister, N. F. (**1972**). "Intensity discrimination of pulsed sinusoids: the effects of filtered noise," J. Acoust. Soc. Am. **51**, 1265–1269.
Young, E. D., and Sachs, M. B. (**1979**). "Representation of steady-state vowels in the temporal aspects of the discharge patterns of populations of auditory-nerve fibers," J. Acoust. Soc. Am. **66**, 1381–1403.

Effect of noise on the detectability and fundamental frequency discrimination of complex tones

Hedwig Gockel[a)]
MRC Cognition and Brain Sciences Unit, 15 Chaucer Road, Cambridge CB2 2EF, United Kingdom

Brian C. J. Moore
Department of Experimental Psychology, University of Cambridge, Downing Street, Cambridge CB2 3EB, United Kingdom

Christopher J. Plack
Department of Psychology, Lancaster University, Lancaster LA1 4YF, United Kingdom

Robert P. Carlyon
MRC Cognition and Brain Sciences Unit, 15 Chaucer Road, Cambridge CB2 2EF, United Kingdom

(Received 5 July 2005; revised 2 May 2006; accepted 9 May 2006)

Percent correct performance for discrimination of the fundamental frequency (F0) of a complex tone was measured as a function of the level of a background pink noise (using fixed values of the difference in F0, ΔF0) and compared with percent correct performance for detection of the complex tone in noise, again as a function of noise level. The tone included some low, resolvable components, but not the fundamental component. The results were used to test the hypothesis that the worsening in F0 discrimination with increasing noise level was caused by the reduced detectability of the tone rather than by reduced precision of the internal representation of F0. For small values of ΔF0, the hypothesis was rejected because measured performance fell below that predicted by the hypothesis. However, this was true only for high noise levels, within 2–4.5 dB of the level required for masked threshold. The results indicate that the mechanism for extracting the F0 of a complex tone with resolved harmonics is remarkably robust. They also indicate that adding a background noise to a complex tone containing resolved harmonics is not a good means for equating its pitch salience with that of a complex tone containing only unresolved harmonics. [DOI: 10.1121/1.2211408]

PACS number(s): 43.66.Hg, 43.66.Fe, 43.66.Dc [JHG] Pages: 957–965

I. INTRODUCTION

The perception of the pitch of complex tones plays an important role in melody recognition, extraction of speech intonation, and the segregation of competing sounds. There have been many experimental studies and computational models aimed at elucidating both the underlying mechanisms of pitch perception and the limits of fundamental frequency (F0) discrimination. With some exceptions (Bilsen, 1973; Hoekstra, 1979; Horst *et al.*, 1984; Scheffers, 1984; Moore and Glasberg, 1991), the majority of those studies have focused on the perception of complex tones presented in quiet. The present study addresses instead the limitations on F0 discrimination imposed by the presence of competing noise and focuses on two issues. The first involves a direct comparison between percent correct performance for the detection of a complex tone and the discrimination of its F0, both as a function of background noise level. By measuring performance on both tasks in the same listeners, and by developing a simple quantitative model of the relationship between the two, we determine the extent to which discrimination performance is limited by detectability. The second issue concerns the question of whether it is possible to equate the salience of the pitches of two tones by adding noise to the one that is initially more salient.

Several researchers have addressed the effect of noise on frequency discrimination for pure tones (Harris, 1966; Henning, 1967; Cardozo, 1974; Hoekstra, 1979; Dye and Hafter, 1980; Sinnott and Brown, 1993; Scheffers, 1984). In most of these studies, thresholds for frequency discrimination, FDLs, have been measured over a range of signal-to-noise ratios, and sometimes, but not always, the masked threshold of the tone in noise has also been measured. The study of Cardozo (1974) is of particular interest, since he measured percent correct performance for both detection and frequency discrimination of a 1000-Hz tone in noise, as a function of the signal-to-noise ratio. A four-alternative forced-choice task was used in both tasks. The detection task was somewhat unusual in that the subject had to indicate in which of the four intervals the tone was *not* present. In the frequency-discrimination task, the subject had to indicate in which of the four intervals the tone was higher in frequency (above 1000 Hz by an amount Δf). Cardozo defined the detection "threshold" as the signal level required for 62.5% correct (corresponding to a detectability index, $d' = 1.19$). In the frequency-discrimination task, about 50% correct was achieved for $\Delta f = 16$ Hz when the tone was *at* the detection

a)Electronic mail: hedwig.gockel@mrc-cbu.cam.ac.uk

threshold. Frequency discrimination for that value of Δf improved rapidly with increasing signal level, up to about 83% correct when the signal was 3 dB above the detection threshold. Performance was poorer for smaller values of Δf and also increased less rapidly with increasing signal level. Remarkably, for relatively large values of Δf (above about 50 Hz), the signal level required for 62.5% correct in the frequency discrimination task was almost the same as the level required for 62.5% correct in the detection task. Also, for large values of Δf, the psychometric function for detection of the tone had the same slope as the functions for discrimination of the frequency of the tone. In other words, subjects could discriminate the difference in frequency as well as they could detect the tone.

Although there are some data on the F0 discrimination of complex tones in noise (Bilsen, 1973; Hoekstra, 1979; Horst *et al.*, 1984; Scheffers, 1984; Moore and Glasberg, 1991), we know of no experiment analogous to Cardozo's (1974), in which discrimination performance has been directly compared with detection performance for complex tones. Moore and Glasberg (1991) measured thresholds for detecting a change in F0 of complex tones containing low (resolvable) harmonics, as a function of the level of a pink noise background. They found that the resulting F0DLs were almost unaffected by the background noise except when the noise level was so high that the tones were "barely audible." However, the noise level was changed in rather large steps (4 dB) and detection thresholds for the tones in the noise were not measured.

Hoekstra (1979) measured thresholds (75% correct in a two-alternative forced-choice, 2AFC, task) for discrimination of the F0 of a pulse train that was passed through a $\frac{1}{3}$-oct filter centered at 2000 Hz. A background noise was passed through the same filter, and F0DLs were measured as a function of the level of the tone relative to its masked threshold in the noise; the masked threshold (75% correct in a 2AFC task) was determined separately for each F0 used, and the value of F0 varied from 200 to 20 Hz. When F0 was 100 Hz or less, so that the tone contained only rather high harmonics, it was not possible to measure F0DLs when the tone was less than about 8–10 dB above masked threshold. For the F0 of 200 Hz, F0DLs could be measured for levels at, or only slightly above, the masked threshold. For this F0, F0DLs decreased progressively with increasing signal level until the tone was 15 to 20 dB above masked threshold. For a given level relative to masked threshold, the F0DLs for the filtered pulse trains were always higher than the FDL for a pure tone centered at 2000 Hz, although the difference was small for the pulse train with F0=200 Hz. For most of Hoekstra's tones, the harmonics would have been too high to be resolved in the auditory system. It is generally assumed that only harmonics up to the fifth to eighth are resolvable (Plomp, 1964; Plomp and Mimpen, 1968; Moore and Ohgushi, 1993; Moore *et al.*, 2006). Bernstein and Oxenham (2003) suggested a somewhat higher limit, based on an experiment where the "target" harmonic was pulsed on and off, but the validity of their procedure has been questioned (Moore *et al.*, 2006). Even for the highest F0 used by Hoekstra, the lowest audible harmonic would have been the ninth, which would have been marginally, if at all, resolvable.

Scheffers (1984) measured the ratio of signal to pink noise level at which changes in F0 of fixed magnitude, ΔF0, could be detected with 75% accuracy in a 2AFC task (defined as threshold), for values of ΔF0 from 0.5% to 10%. The stimuli were vowel sounds, pulse trains (low-pass filtered at 4 kHz), and pure tones. Masked thresholds of the sounds in the pink noise were also measured; again, threshold was defined as the level corresponding to 75% correct in a 2AFC task. Changes of 5% or more in F0 could be detected with 75% accuracy for signal levels close to masked threshold, for all three types of stimuli. Again, the results suggest that, when the change in F0 is reasonably large, the F0 of the tones can be discriminated as well as the tones are detected. For smaller changes in F0, for example 1%, the signal level had to be 5–10 dB above masked threshold to allow 75% correct performance.

In summary, a few studies have assessed F0 discrimination in noise for various levels relative to the masked threshold and have demonstrated remarkably good F0 discrimination for tones containing resolved harmonics, even when the tones were at levels close to the masked threshold. However, we are not aware of any studies in which both signal detectability and F0 discrimination were measured as a function of signal-to-noise ratio.

In the present experiments, percent correct performance for detecting a complex tone in noise was measured as a function of noise level (with the signal level fixed) and compared with percent correct performance for the discrimination of the F0 of the same complex tone, again as a function of noise level. The tone included some low, resolvable components, but not the fundamental component. The results were used to test the hypothesis that the worsening in F0 discrimination with increasing noise level was caused by the reduced probability of the tone being detected rather than by reduced precision of the internal representation of F0 on trials where both tones in a 2AFC trial were detected. F0 discrimination for the complex tone in noise was also compared with that for a complex tone with unresolved harmonics presented in a low level of noise (designed only to mask combination tones, but not to interfere with discrimination or detection).

II. STIMULI AND GENERAL PROCEDURE

Stimuli were complex tones with a nominal F0 of 88 or 250 Hz. All tones were bandpass filtered between 1375 and 1875 Hz (3-dB down points, slopes of 48 dB/oct). For complex tones with equal-amplitude harmonics, harmonics with numbers up to about five to eight are resolved by the auditory system (Plomp, 1964; Plomp and Mimpen, 1968; Moore and Ohgushi, 1993; Bernstein and Oxenham, 2003; Moore *et al.*, 2006). Therefore, within the passband, the tones with the 88-Hz F0 contained only unresolved components (numbers 16–21), while the tones with the 250-Hz F0 contained mainly resolved components (numbers 6 and 7). All components were added in sine phase (starting phase of 0°) and had a level of 45 dB SPL. This low level was chosen to ensure

that possible distortion products would be at a low level. A continuous pink noise was presented. This either had a spectrum level of 15 dB (*re* 20 μPa) at 1 kHz (referred to as the baseline level) or a higher level. The background noise was low-pass filtered with a nominal cutoff frequency of 3900 Hz (slope 96 dB/oct). For the tones with a nominal F0 of 88 Hz, the noise was at the baseline level and was intended to mask possible distortion products, particularly combination tones occurring at F0 and low harmonics of F0 (Buunen *et al.*, 1974; Pressnitzer and Patterson, 2001). For the tones with a nominal F0 of 250 Hz, the level of the noise was increased by various amounts above baseline level, so as to manipulate the signal-to-noise ratio. Pink noise was used rather than white noise because the masking produced by pink noise varies less with frequency than for a white noise.

The complex tones were generated and bandpass filtered digitally. They were played out using a 16-bit digital-to-analog converter (CED 1401 plus), with a sampling rate that was varied between trials over the range 40 kHz±10%. This had the effect of randomly varying the F0 over the range ±10% (also producing a variation of ±10% in the duration and in the filter cutoff frequencies). This F0 randomization discouraged subjects from basing their decision on a long-term memory representation of the sound. The randomization was used in both experiments. In what follows, the random variation between trials is not explicitly discussed, and we describe only the nominal F0. The nominal stimulus duration was 400 ms, including 5-ms raised-cosine onset and offset ramps.

Stimuli were passed through an anti-aliasing filter (Kemo 21C30) with a cutoff frequency of 17.2 kHz (slope of 96 dB/oct) and presented monaurally, using Sennheiser HD250 headphones. Subjects were seated individually in an IAC double-walled sound-attenuating booth.

A two-interval two-alternative forced choice (2I-2AFC) task was used. The interval between the two stimuli within a trial was fixed at 500 ms. Each interval was marked by a light and visual feedback was provided following each response. The total duration of a single session was about 2 h, including rest times.

III. EXPERIMENT 1: EFFECT OF NOISE ON F0 DISCRIMINATION

A. Stimuli and procedure

Listeners had to discriminate between the F0s of two sequentially presented complex tones, which had a nominal F0 of either 88 or 250 Hz. For the tones with a nominal F0 of 250 Hz, the level of the noise was increased by various amounts above the baseline level (8, 10, 12, 14, and 16 dB). The value of ΔF0 was fixed at various amounts, chosen individually for each subject. They were selected on the basis of pilot runs, so that performance for F0 discrimination of the complex with a nominal F0 of 88 Hz (which, for noise levels at baseline, led to poorer performance than for the complex with a nominal F0 of 250 Hz) fulfilled the following criteria: (1) for the largest ΔF0, performance was relatively high but not perfect, and (2) for the smallest ΔF0, performance was relatively low but above chance level. Two subjects, who were available for a longer time, were tested using more than two ΔF0 values. The following values of ΔF0 were used: 2% and 4% for subject 1; 1%, 2%, and 3% for subject 2; 2% and 6% for subject 3; 2% and 5% for subject 4; 1% and 4% for subject 5; and 1%, 2%, 4%, and 6% for subject 6. Five blocks of 105 trials were run for each condition and subject. The first five trials in each block were considered as practice and results from these were discarded. Within a block of 105 trials, the condition (determined by the values of F0, ΔF0, and the noise level) was kept constant. The order of the conditions was counterbalanced within and across subjects. One block was run for each condition in turn, before additional blocks were run. The results reported are the mean of 500 trials for each condition and subject.

B. Subjects

Six subjects participated; all had some musical experience. All had taken part in previous experiments involving discrimination of the F0 of complex tones, so they were highly practiced. They ranged in age from 22 to 34 years. Their quiet thresholds at octave frequencies between 250 and 8000 Hz were below 15 dB HL (ANSI, 2004). Stimuli were presented to the left ear for four subjects and to the right ear for the other two.

C. Results and discussion

Figure 1 shows the results. Performance for the tones containing only unresolved components (solid symbols) lies between 60% and 93%. As expected, for the tone with resolved harmonics (open symbols connected by solid lines) performance declined with increasing noise level. However, for a given noise level, increases in ΔF0 did not always lead to improved performance. This was especially apparent for subject 6 (panel f), who was tested for more values of ΔF0 than the other subjects; for her, performance improved when ΔF0 was increased from 1% to 2%, but did not improve with further increases in ΔF0. One interpretation of this result is that, once the value of ΔF0 was sufficiently large, performance depended mainly on whether the tone was audible on both halves of each trial; if the tone was heard in both intervals, then the difference in F0 could be heard. The very poor F0 discrimination for the highest noise levels tested may reflect the fact that the tones were close to their masked threshold at this noise level. This interpretation was tested in experiment 2.

Table I shows the increase in noise level needed for each subject to achieve equal performance for F0 discrimination of complex tones with resolved and unresolved harmonics, for each ΔF0 used; this was estimated by interpolation. For all subjects, the increase in noise level needed to achieve equal performance decreases with increasing ΔF0. Thus, there is no *single* increment in noise level for each subject that leads to equal F0 discrimination of complexes with resolved harmonics (with increased noise) and complexes with unresolved harmonics (with baseline noise). Typically, the noise level required to equate discrimination performance across the two types of complex was 2–3 dB higher when ΔF0 was small (1% or 2%) than when it was larger (3%–

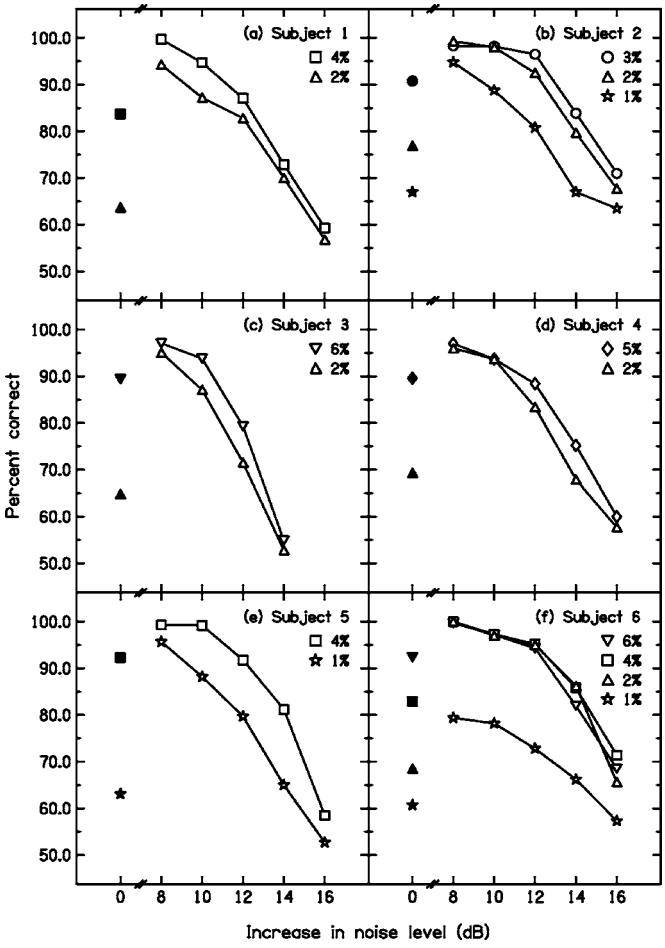

FIG. 1. Performance for F0 discrimination of complex tones filtered between 1375 and 1875 Hz (experiment 1). The parameter is the difference in F0 between the two halves of a trial, ΔF0. The solid symbols at the left-hand side of each panel show performance when the nominal F0 was 88 Hz (unresolved harmonics only). These tones were presented in the presence of a continuous pink background noise with a spectrum level of 15 dB at 1 kHz (the baseline level) that was low-pass filtered at 3900 Hz. The open symbols connected by solid lines show performance when the nominal F0 was 250 Hz (resolved components); performance is plotted as a function of the level of the background noise relative to the baseline level. Each panel gives results for one subject.

6%). A paired-samples t test, based on the noise level required to equate F0 discrimination for the largest and smallest values of ΔF0 used for each subject, showed that the difference was highly significant $[t(5)=11.3, p<0.001]$.

One might expect to be able to gradually reduce the pitch salience of a tone with resolved harmonics by adding increasing amounts of noise, so that this salience would eventually drop to that of a tone with unresolved harmonics. If F0 discrimination provides a direct measure of pitch salience, as is often assumed, then one might expect it to be possible to equate F0 discrimination for complex tones with resolved and unresolved harmonics by adding noise to the former, regardless of the value of ΔF0 used. In fact, it was not possible to choose a noise level which equated performance for resolved and unresolved harmonics for all ΔF0s. This could indicate that F0 discrimination does not provide a direct measure of pitch salience. However, it may also be the case that some other factor is involved.

One possible "other factor" is that F0 discrimination of the tone with resolved harmonics was determined not only by the salience of its pitch but also by its detectability. If the tone was not detected in one or both intervals of a given trial, then this would clearly lead to poorer performance. When ΔF0 was relatively large, the percentage correct F0 discrimination of the tone with resolved harmonics at low noise levels was typically 10%–15% better than for the tone with unresolved harmonics (and the same ΔF0 value). Hence, as the noise level was increased, only a small decrease in detectability would be required to lead to F0 discrimination the same as for the tone with unresolved harmonics. In contrast, when ΔF0 was relatively small (1% or 2%), the percentage correct F0 discrimination of the tone with resolved harmonics at low noise levels was typically 20%–30% better than for the tone with unresolved harmonics. In this case a larger decrease in detectability (corresponding to a higher noise level) would be required to equate F0 discrimination for the tones with resolved and unresolved harmonics. This could account for why the noise level required to equate performance for the tones with resolved and unresolved harmonics was higher for the smaller values of ΔF0. The effect of the noise on detectability of the tone with resolved harmonics was assessed in experiment 2.

TABLE I. Increase in noise level needed for each subject in order to produce F0 discrimination performance for the complex tone with resolved harmonics, RES, equal to that for the complex tone with unresolved harmonics, UNRES (with the baseline noise level), for various ΔF0's.

Subject	ΔF0 (%)	$P(c)$ UNRES (%)	Increase in noise level for RES (dB)
1	4	83.7	12.5
	2	63.7	15
2	3	90.8	13
	2	76.9	14.5
	1	67.0	14.5
3	3	89.4	10.6
	1	65.8	12.7
4	5	89.6	11.5
	2	69.3	13.7
5	2	92.3	11.9
	0.5	63.1	14.3
6	6	92.4	12.5
	4	84.2	14.5
	2	68.5	15.5
	1	60.7	15.5

IV. EXPERIMENT 2: EFFECT OF NOISE LEVEL ON DETECTION OF THE TONE

A. Stimuli, procedure, and subjects

The signal to be detected was the same tone with resolved harmonics as used in experiment 1. The nominal F0 was 250 Hz. Subjects had to indicate which of the two intervals in the 2-AFC task contained the tone. Detection performance was measured as a function of the level of the noise background. The noise used was the same as in experiment 1. Seven different noise levels (increased above baseline level by 8 to 20 dB, in steps of 2 dB) were tested.

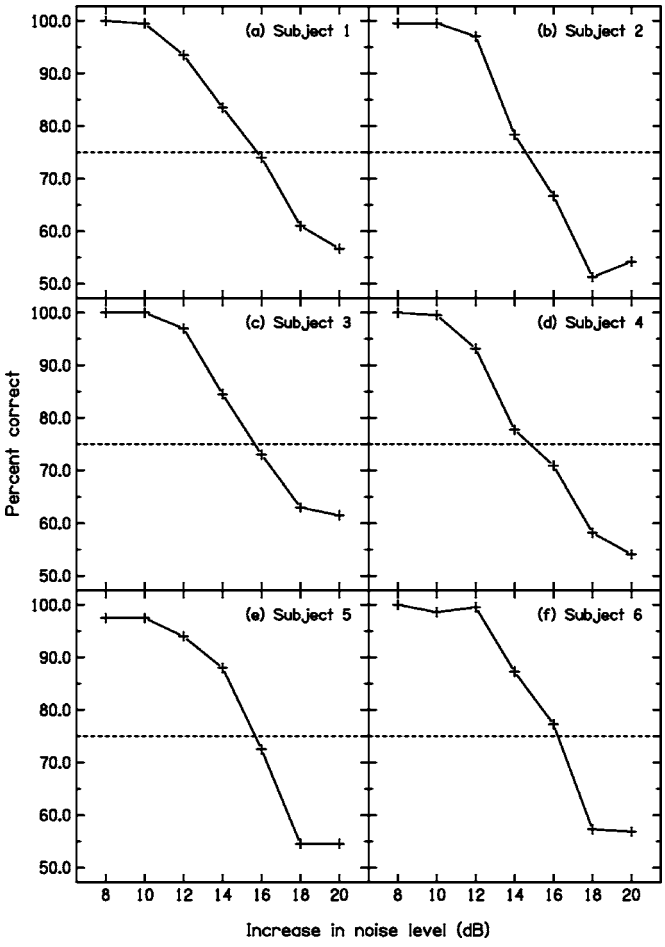

FIG. 2. Performance in a 2AFC task for detection of a complex tone with a nominal F0 of 250 Hz filtered between 1375 and 1875 Hz (experiment 2). Performance is plotted as a function of the level of the background noise relative to the baseline level.

Within a block of 140 trials, the order of the conditions was always from easy (lowest noise level) to hard (highest noise level). There were 20 repetitions of this cycle within a block. Between trials, the noise level was changed from its old to the desired value by changing the setting of the programmable attenuator in steps of 0.1 dB. This resulted in a smooth rather than sudden transition. The noise background was presented for 1 s at the new level before the next trial started. Ten blocks of 140 trials were run for each subject. The results shown are the mean of the 200 trials per condition. The six subjects were the same as for experiment 1.

B. Results and discussion

Each panel in Fig. 2 shows the results for one subject. The percent correct detection is at or close to 100% for the lower noise levels and decreases progressively with increasing noise level, as expected. Performance is generally just above the chance level of 50% for the highest noise level used. It is clear that, over the upper part of the range of noise levels used in experiment 1, one or both of the tones in a forced-choice trial would not have been detected on some trials.

We consider next the hypothesis that, in experiment 1, the decrease in F0 discrimination performance with increasing level was caused solely by the reduced probability that the tone would be detected, rather than by reduced precision in the internal estimate of F0. According to this hypothesis, when both tones in a trial were detected, discrimination of F0 was unaffected by the noise level and was as good as for the lowest noise level used.

To calculate the level of performance predicted on the basis of this hypothesis we assume first that, if the subject detects the tone in both intervals, the probability of discriminating F0 correctly corresponds to that observed in the 2AFC F0-discrimination task for a relative noise level of 8 dB (the lowest level used) for the ΔF0 under consideration. It is necessary also to make an assumption about what happens on trials for which one or both of the tones are not detected. One possibility is that subjects simply guess, in which case the probability of a correct response is 0.5. This represents a lower limit to the performance that can be expected based on the above hypothesis. Another possibility is that, on trials where the tone is detected in only one interval, subjects adopt the optimal strategy of labeling that interval as the one containing the higher F0 whenever the F0 is above 250 Hz and of labeling the interval as the one containing the lower F0 whenever the F0 is below 250 Hz. This optimal strategy assumes that subjects develop a long-term memory representation of the pitch corresponding to the mean of the range of stimuli presented, i.e., the range of F0s presented. This represents an upper limit to the performance that can be expected based on the above hypothesis. We focus here on derivation of the lower limit, since if the measured F0 discrimination performance falls below this lower limit, this would contradict the hypothesis. The use of the "optimal" strategy would lead to only a small improvement in predicted performance, and then mainly for the larger ΔF0 values at high noise levels, due to the randomization of F0 between trials.

As a first stage in the derivation, we converted the percent correct values for the detection data, obtained in the 2AFC task, to values of the detectability index, d' (Macmillan and Creelman, 1991). To reduce the effect of errors of measurement associated with individual data points, for each subject the data relating d' to the signal-to-noise ratio, R (expressed in linear power units), were fitted with a function of the form:

$$d' = kR, \tag{1}$$

where k is a fitting constant (Green and Swets, 1974). The function was fitted to the data for relative noise levels from 12 to 20 dB; the data for the two lowest noise levels were excluded, as d' is difficult to estimate accurately when performance is perfect, or nearly so. The root mean square (rms) difference between the measured d' values and the fitted values ranged from 0.083 to 0.405 across subjects, with a mean of 0.228, indicating that the fits were generally good. The fitted function was used to derive values of d' for each noise level used and these were converted to the probability of detecting the complex tone in a *one-interval task* (Macmillan and Creelman, 1991). We denote this probability, for a background noise level x dB above baseline, as $q(x)$.

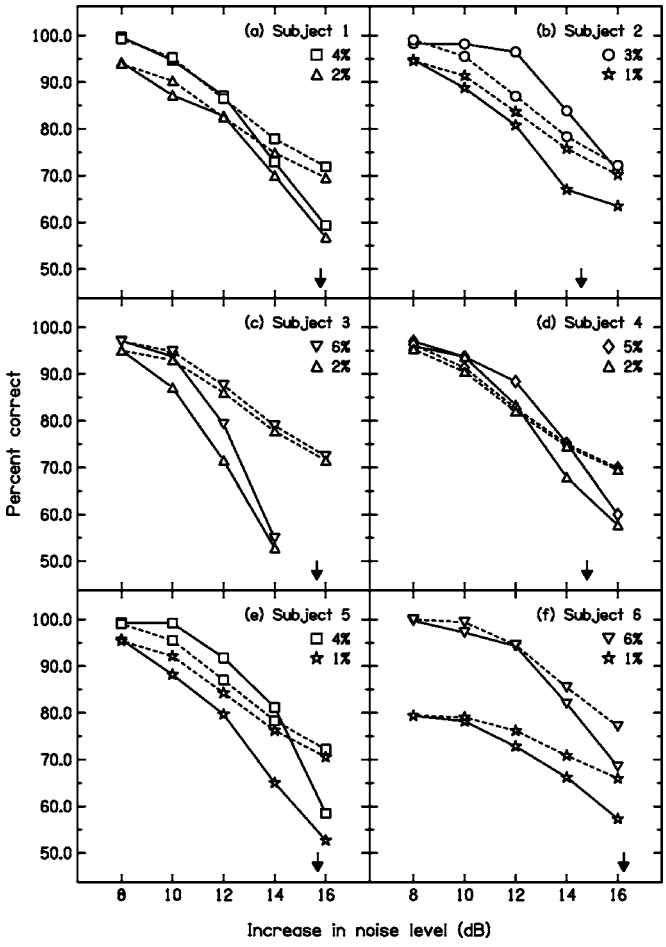

FIG. 3. Predictions of lower limit of performance for F0 discrimination of complex tones filtered between 1375 and 1875 Hz. The solid lines replot performance observed in experiment 1 for a nominal F0 of 250 Hz for the largest and smallest values of ΔF0 used for each subject. The dashed lines show the predicted lower limit of performance based on the assumption that F0 discrimination was limited by the detectability of the tones (see text for details). The down-pointing arrows indicate the noise level leading to 75% correct detection in a 2AFC task, as measured in experiment 2. Performance is plotted as a function of the level of the background noise relative to the baseline level.

In the F0-discrimination task, the probability of detecting both tones in a trial is $q^2(x)$. For trials where this occurs, the probability of correct F0 discrimination is assumed to be equal to that measured for a background noise that is 8 dB above the baseline level, $p(8)$. For trials where one or both tones are not detected, the probability of correct F0 discrimination is assumed to be 0.5. Therefore, the lower limit of proportion correct in the 2AFC F0-discrimination task for a background noise level x dB above the baseline level, $p(x)$, is given by the following expression:

$$p(x) = q^2(x) \cdot p(8) + 0.5[1 - q^2(x)]. \quad (2)$$

The dashed lines in Fig. 3 show the performance in the 2AFC F0-discrimination task predicted from Eq. (2); to avoid clutter, in cases where subjects were tested using more than two values of ΔF0, predictions are shown only for the smallest and largest values used. Recall that Eq. (2) gives the predicted lower limit to performance based on the above hypothesis. If actual performance falls below predicted performance, this implies that the above hypothesis is false, i.e., that the noise has an effect on F0 discrimination over and above its effect on the detection of the tone.

For the largest value of ΔF0 tested, measured performance fell close to or slightly above predicted performance for relative noise levels up to 12–14 dB, for all subjects except subject 3. For subject 3, measured performance matched predicted performance only for relative noise levels up to 10 dB. For all subjects except subject 2, measured performance for the largest value of ΔF0 fell below predicted performance for the relative noise level of 16 dB, indicating a deleterious effect of the noise on F0 discrimination *per se*. For the smallest value of ΔF0, measured performance fell below predicted performance for relative noise levels of 14 dB or higher for all subjects. For some subjects (3, 5, and 6) this first happened for relative noise levels of 10 or 12 dB. Overall, the results suggest that the noise had a deleterious effect on F0 discrimination *per se*, but only for relatively high noise levels, i.e., the hypothesis is rejected.

The finding of measured performance slightly better than predicted for some noise levels and values of ΔF0 may be accounted for by subjects making use of information from F0-discrimination trials in which only one of the two tones was detected. As noted earlier, on such trials the optimal strategy would be to label the interval in which the tone was detected as the one containing the higher F0 whenever the F0 was above 250 Hz, and to label that interval as the one containing the lower F0 whenever the F0 was below 250 Hz. Calculations of predicted performance based on the optimal strategy indicate that this would lead to only a small improvement in performance, as could be anticipated from the randomization of the mean F0 across trials. The improvement occurs mainly for relatively large values of ΔF0 and for high noise levels. The results of these calculations do not change our basic conclusion that the discrimination of F0 *per se* can be affected by the presence of noise, but only for noise levels within 2–4.5 dB of the level required to reach masked threshold (see below).

V. GENERAL DISCUSSION

The detection "threshold" can be defined as the noise level at which performance reached 75% (illustrated by the dashed horizontal lines in Fig. 2). This level was between 14.6 and 16.2 dB above the baseline level for all subjects. The threshold levels for individual subjects are shown by the down-pointing arrows at the bottom of each panel in Fig. 3. The noise level at which F0 discrimination performance fell below that predicted by Eq. (2) varied somewhat across subjects and across ΔF0 values, from about 10 dB (subject 3, ΔF0=2%) to 16 dB (subject 6, ΔF0=6%). For the larger ΔF0 values used, for three out of the six subjects (subjects 2, 4, and 5) F0 discrimination performance fell below that predicted only when the relative noise level was so high that detection performance was at or below threshold. For subject 2 with ΔF0=3%, measured performance did not fall clearly below predicted performance for any noise level. For those subjects and for large ΔF0s, discrimination performance was equal for a tone containing resolved harmonics and a tone

containing only unresolved components when the increase in noise level reduced the detectability of the former but presumably did not reduce the precision of the internal representation of its F0. Typically, for the smaller ΔF0 values used, measured performance first fell below predicted performance for relative noise levels of 12 to 14 dB. The noise only appeared to impair the precision of the internal representation of F0 when the noise level was within 2–4.5 dB of the level required to reach masked threshold. This indicates a remarkable degree of robustness in the mechanism for extracting the F0.

It is instructive to consider whether the results are consistent with models of frequency discrimination based on changes in the excitation pattern (Zwicker, 1956; Moore and Sek, 1994). According to Zwicker's model (Zwicker, 1956, 1970; Zwicker and Fastl, 1999) a change in frequency can just be detected if the excitation level at any point on the pattern changes by 1 dB. Moore and Sek (1994) proposed a model for the detection of frequency and/or amplitude modulation in which information could be combined from different points on the excitation pattern (see also Florentine and Buus, 1981); in this model the change in excitation level required for "threshold" ($d'=1$) is typically about 2–3 dB when the change is restricted to a small region of the excitation pattern (similar values were suggested by Buus and Florentine, 1995); somewhat smaller changes can be detected when the changes occur over a large region. To assess whether such models could account for our data, we calculated excitation patterns following the procedure described by Glasberg and Moore (1990), but using the transfer functions for the outer and middle ear described by Moore *et al.* (1997). The conditions of listening were specified as "diffuse field," as the Sennheiser headphones used here have a diffuse field response.

We started by calculating excitation patterns for two complex tones in noise with a difference in F0 of 4%; the two F0s were 245 and 255 Hz. The spectra of the tones specified as input to the excitation-pattern program took into account the effect of the bandpass filter used in the experiment. The excitation patterns obtained for a relative noise level of 8 dB (the lowest level used) are shown in Fig. 4. The patterns are shown only for center frequencies where the pattern is not dominated by the background pink noise. The largest difference in excitation level between the two patterns was 1.3 dB. This occurred over a very restricted range of center frequencies around 1416 Hz. The difference of 1.3 dB is only slightly larger than the criterion of 1 dB proposed by Zwicker and is markedly smaller than the criterion change required in the model of Moore and Sek (1994) for changes in excitation level in a restricted frequency region. However, performance was close to perfect for this value of ΔF0 and noise level. For the same ΔF0, but with a relative noise level of 14 dB, the maximum difference in excitation level between the two excitation patterns was only 0.5 dB; again this occurred over a restricted part of the pattern around 1416 Hz. Yet, several subjects (subjects 1, 2, 5, and 6) achieved scores over 70% for this value of ΔF0 or a smaller value. It seems implausible that such high scores could be achieved on the basis of such a small difference in the excitation pattern.

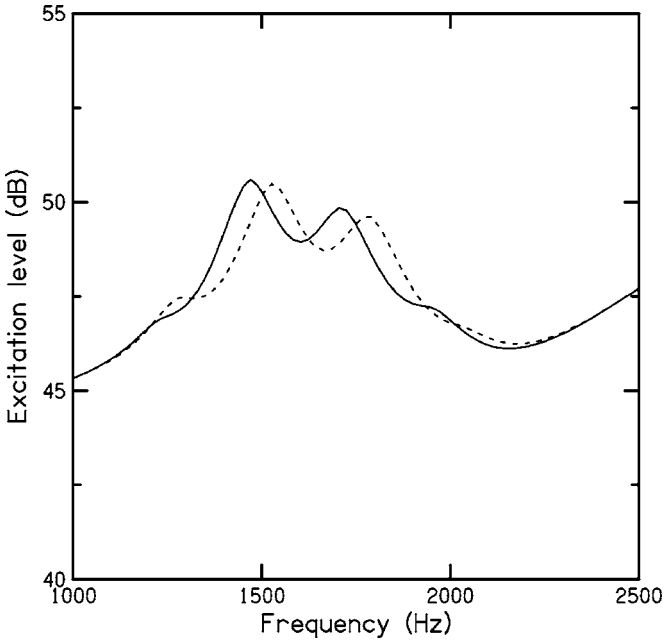

FIG. 4. Excitation patterns for two complex tones with F0=245 Hz (solid line) and 255 Hz (dashed line). The tones were presented in a background of pink noise with a level of 8 dB relative to the baseline level. The patterns are plotted only over the frequency range where they were not dominated by the noise.

Next, excitation patterns were calculated with ΔF0 =2%; the two F0s were 247.5 and 252.5 Hz. For a relative noise level of 8 dB, the largest difference in excitation level between the two was only 0.4 dB. This occurred over a restricted range of center frequencies around 1416 Hz. Yet, all subjects achieved scores over 90% for this value of ΔF0 and noise level. For a relative noise level of 14 dB, the largest difference decreased to only 0.25 dB. Yet, some subjects (subjects 1, 2, 4, and 6) achieved scores in the range 67%–86% under these conditions. Again, it seems implausible that such high scores could be achieved on the basis of such a small difference in the excitation pattern.

Note that the model does not even correctly predict the patterns of performance across conditions. For example, the excitation-level difference for ΔF0=4% and a relative noise level of 14 dB was slightly larger than the difference for ΔF0=2% and a relative noise level of 8 dB, yet performance was markedly worse for the former condition than for the latter.

We conclude that it is unlikely that F0 discrimination performance at the higher noise levels was based on changes in excitation level. It seems more likely that temporal information derived from phase locking was used. A similar conclusion was reached by Moore *et al.* (1984) on the basis of data on the frequency discrimination of individual components within complex tones. In principle, temporal information, if efficiently used, can provide much more precise information about the frequencies of individual components than place information (Siebert, 1970; Heinz *et al.*, 2001a). This applies also to conditions where background noise is present (Heinz *et al.*, 2001a, b).

We described earlier the idea that it might be possible to manipulate the pitch salience of a complex tone with resolved harmonics by varying the level of a background noise. The results presented here indicate that the addition of noise is not a good way to manipulate pitch salience, since the noise level required to reduce the precision of the internal representation of F0 is sufficiently high to markedly reduce the detectability of the tone. The observed effects of noise on F0 discrimination reflect the reduced detectability of the tone as much as, if not more than, the reduced pitch salience of the tone.

VI. SUMMARY AND CONCLUSIONS

Percent correct performance for detecting a complex tone in noise was measured as a function of noise level and compared with percent correct performance for discrimination of the F0 of the same complex tone, again as a function of noise level. The tone included some low, resolvable components, but not the fundamental component. The results were used to test the hypothesis that the worsening in F0 discrimination with increasing noise level was caused by the reduced detectability of the tone rather than by reduced precision of the internal representation of F0. For small values of ΔF0, it was shown that performance fell below that predicted by the hypothesis, but only for high noise levels, within 2–4.5 dB of the level required for masked threshold; at lower levels, the results were consistent with noise reducing performance by virtue of the reduced detectability of the tone. For large values of ΔF0, for some subjects, performance fell below that predicted only when the noise level was so high that it was at or above the level required for masked threshold. For one subject (for a large value of ΔF0) performance never fell below that predicted. The results indicate that the mechanism for extracting the F0 of a complex tone with resolved harmonics is remarkably robust, and operates with high precision even for noise levels sufficient to reduce detectability considerably. The results also indicate that the addition of noise is not a good way to manipulate the pitch salience of a tone with resolved components, since the noise level required to reduce the precision of the internal representation of F0 is sufficiently high to markedly reduce the detectability of the tone. In fact, the results indicate that, at high to medium levels of performance, addition of noise to a tone with resolved components can equate F0 discrimination of that tone to that for a complex tone with unresolved components purely by reducing the detectability of the former.

ACKNOWLEDGMENTS

This work was supported by EPSRC Grant No. EP/D501571/1. We thank Associate Editor John Grose and two anonymous reviewers for helpful comments on an earlier version of this paper.

ANSI (**2004**). *ANSI S3.6-2004 Specification for audiometers* (American National Standards Institute, New York).

Bernstein, J. G., and Oxenham, A. J. (**2003**). "Pitch discrimination of diotic and dichotic tone complexes: harmonic resolvability or harmonic number?" J. Acoust. Soc. Am. **113**, 3323–3334.

Bilsen, F. A. (**1973**). "On the influence of the number and phase of harmonics on the perceptibility of the pitch of complex signals,"Acustica **28**, 60–65.

Buunen, T. J. F., Festen, J. M., Bilsen, F. A., and van den Brink, G. (**1974**). "Phase effects in a three-component signal," J. Acoust. Soc. Am. **55**, 297–303.

Buus, S., and Florentine, M. (**1995**). "Sensitivity to excitation-level differences within a fixed number of channels as a function of level and frequency," in *Advances in Hearing Research*, edited by G. A. Manley, G. M. Klump, C. Köppl, H. Fastl, and H. Oekinghaus (World Scientific, Singapore).

Cardozo, B. L. (**1974**). "Some notes on frequency discrimination and masking," Acustica **31**, 330–336.

Dye, R. H., and Hafter, E. R. (**1980**). "Just-noticeable differences of frequency for masked tones," J. Acoust. Soc. Am. **67**, 1746–1753.

Florentine, M., and Buus, S. (**1981**). "An excitation-pattern model for intensity discrimination," J. Acoust. Soc. Am. **70**, 1646–1654.

Glasberg, B. R., and Moore, B. C. J. (**1990**). "Derivation of auditory filter shapes from notched-noise data," Hear. Res. **47**, 103–138.

Green, D. M., and Swets, J. A. (**1974**).*Signal Detection Theory and Psychophysics* (Krieger, New York).

Harris, J. D. (**1966**). "Masked DL for pitch memory," J. Acoust. Soc. Am. **40**, 43–46.

Heinz, M. G.,Colburn, H. S., and Carney, L. H. (**2001a**). "Evaluating auditory performance limits: I. One-parameter discrimination using a computational model for the auditory nerve," Neural Comput. **13**, 2273–2316.

Heinz, M. G., Colburn, H. S., and Carney, L. H. (**2001b**). "Evaluating auditory performance limits:II. One-parameter discrimination with random level variation," Neural Comput. **13**, 2317–2339.

Henning, G. B. (**1967**). "Frequency discrimination in noise," J. Acoust. Soc. Am. **41**, 774–777.

Hoekstra, A. (**1979**). "Frequency discrimination and frequency analysis in hearing," Ph.D. thesis, Institute of Audiology, University Hospital, Groningen, Netherlands.

Horst, J. W., Ritsma, R. J., and Wit, H. P. (**1984**). "Frequency discrimination in quiet and in noise for signals with triangular spectral envelopes," J. Acoust. Soc. Am. **76**, 1067–1075.

Macmillan, N. A., and Creelman, C. D. (**1991**). *Detection Theory: A User's Guide* (Cambridge U.P., Cambridge, England).

Moore, B. C. J., and Glasberg, B. R. (**1991**). "Effects of signal-to-noise ratio on the frequency discrimination of complex tones with overlapping or nonoverlapping harmonics," J. Acoust. Soc. Am. **89**, 2858–2865.

Moore, B. C. J., and Ohgushi, K. (**1993**). "Audibility of partials in inharmonic complex tones," J. Acoust. Soc. Am. **93**, 452–461.

Moore, B. C. J., and Sek, A. (**1994**). "Effects of carrier frequency and background noise on the detection of mixed modulation," J. Acoust. Soc. Am. **96**,741–751.

Moore, B. C. J., Glasberg, B. R., and Baer, T. (**1997**). "A model for the prediction of thresholds, loudness and partial loudness," J. Audio Eng. Soc. **45**, 224–240.

Moore, B. C. J.,Glasberg, B. R., and Shailer, M. J. (**1984**). "Frequency and intensity difference limens for harmonics within complex tones," J. Acoust. Soc. Am. **75**, 550–561.

Moore, B. C. J., Glasberg, B. R., Flanagan, H. J., and Adams, J. (**2006**). "Frequency discrimination of complex tones; assessing the role of component resolvability and temporal fine structure," J. Acoust. Soc. Am. **119**, 480–490.

Plomp, R. (**1964**). "The ear as a frequency analyzer," J. Acoust. Soc. Am. **36**, 1628–1636.

Plomp, R., and Mimpen, A. M. (**1968**). "The ear as a frequency analyzer II," J. Acoust. Soc. Am. **43**, 764–767.

Pressnitzer, D., and Patterson, R. D. (**2001**). "Distortion products and the pitch of harmonic complex tones," in *Physiological and Psychophysical Bases of Auditory Function*, edited by D. J. Breebaart, A. J. M. Houtsma, A. Kohlrausch, V. F. Prijs, and R. Schoonhoven (Shaker, Maastricht).

Scheffers, M. T. (**1984**). "Discrimination of fundamental frequency of synthesized vowel sounds in a noise background," J. Acoust. Soc. Am. **76**, 428–434.

Siebert, W. M. (**1970**). "Frequency discrimination in the auditory system: place or periodicity mechanisms," Proc. IEEE **58**, 723–730.

Sinnott, J. M., and Brown, C. H. (**1993**). "Effects of varying signal and noise levels on pure-tone frequency discrimination in humans and monkeys," J. Acoust. Soc. Am. **93**, 1535–1540.

Zwicker, E. (**1956**). "Die elementaren Grundlagen zur Bestimmung der In-

formationskapazität des Gehörs (The foundations for determining the information capacity of the auditory system)," Acustica **6**, 356–381.
Zwicker, E. (**1970**). "Masking and psychological excitation as consequences of the ear's frequency analysis," in *Frequency Analysis and Periodicity Detection in Hearing*, edited by R. Plomp and G. F. Smoorenburg (Sijthoff, Leiden).
Zwicker, E., and Fastl, H. (**1999**). *Psychoacoustics—Facts and Models, Second Edition* (Springer-Verlag, Berlin).

Adaptive control of vowel formant frequency: Evidence from real-time formant manipulation

David W. Purcell[a)]
Department of Psychology, Queen's University, Kingston, Ontario K7L 3N6, Canada

Kevin G. Munhall
Department of Psychology and Department of Otolaryngology, Queen's University, Kingston, Ontario K7L 3N6, Canada

(Received 10 February 2006; revised 26 May 2006; accepted 31 May 2006)

Auditory feedback during speech production is known to play a role in speech sound acquisition and is also important for the maintenance of accurate articulation. In two studies the first formant (F1) of monosyllabic consonant-vowel-consonant words (CVCs) was shifted electronically and fed back to the participant very quickly so that participants perceived the modified speech as their own productions. When feedback was shifted up (experiment 1 and 2) or down (experiment 1) participants compensated by producing F1 in the opposite frequency direction from baseline. The threshold size of manipulation that initiated a compensation in F1 was usually greater than 60 Hz. When normal feedback was returned, F1 did not return immediately to baseline but showed an exponential deadaptation pattern. Experiment 1 showed that this effect was not influenced by the direction of the F1 shift, with both raising and lowering of F1 exhibiting the same effects. Experiment 2 showed that manipulating the number of trials that F1 was held at the maximum shift in frequency (0, 15, 45 trials) did not influence the recovery from adaptation. There was a correlation between the lag-one autocorrelation of trial-to-trial changes in F1 in the baseline recordings and the magnitude of compensation. Some participants therefore appeared to more actively stabilize their productions from trial-to-trial. The results provide insight into the perceptual control of speech and the representations that govern sensorimotor coordination. [DOI: 10.1121/1.2217714]

PACS number(s): 43.66.Jh, 43.70.Aj [AL] Pages: 966–977

I. INTRODUCTION

Human movement shows a striking adaptability to a variety of conditions. We walk on surfaces that vary in regularity, traction, and compliance. We can control our arms and hands under a variety of lighting conditions and loads. We can speak at different rates and volumes, and even with pens clasped between our teeth. This adaptability could not exist without accurate perception of the movement environment, but it has long been known that strictly sensory-controlled movement could not account for coordination in rapid skills such as speech (e.g., Lashley, 1951). Closed-loop control schemes are too slow and lack stability. In recent years, motor research has focused on the role of "internal models" in accounting for such skilled movement. Internal models are neural representations of the kinematics, dynamics, and sensory consequences of movement that are thought to play a role in motor planning and control (Tin and Poon, 2005). According to this view, sophisticated internal models are learned through practice and are used to facilitate motor control when sensory feedback is insufficient. These representations permit the motor system to predict some of the internal and external conditions that could contribute to variability, and plan accordingly. The adaptability of motor skill over time is attributed to the plasticity of these internal models and their role in sensorimotor learning. In this paper we address how an internal representation of speech acoustics adapts when acoustic feedback is modified during speech production.

The first proposal for an internal model of this kind for speech production was made by Kawato (1989), though similar ideas of a motor program, or motor image or schema, have long histories in speech research. In the years since Kawato's paper, the concept of an internal model has been drawn on numerous times (Guenther, 1995; Perkell *et al.*, 1997; Munhall *et al.*, 2000; Jones and Munhall, 2000; Tremblay *et al.*, 2003). In spite of this popular support for the role of internal models in speech, there are few confirmed specifics about how these hypothetical mechanisms might work (cf. Guenther, 2003).

One of the primary candidates for an internal model in speech is an auditory representation. Auditory feedback is too slow to be used in moment-to-moment control, but hearing your own speech is an essential part of talking. The evidence that hearing has a strong impact on speech motor control comes from both clinical and laboratory studies. Babbling (Oller and Eilers, 1988) and learning to talk (Smith, 1975) are impaired in individuals with congenital hearing impairments. Postlingually deafened adults also show changes in many aspects of their speech (e.g., Wald-

[a)]Author to whom correspondence should be addressed. Currently affiliated with the National Centre for Audiology at the University of Western Ontario. Electronic-mail: purcelld@nca.uwo.ca

stein, 1990; Lane and Webster, 1991; Leder and Spitzer, 1993; Schenk *et al.*, 2003). Laboratory-induced manipulations to the loudness (Lane and Tranel, 1971), timing (Smith and Smith, 1962), fundamental frequency (Kawahara, 1995; Burnett *et al.*, 1998), or formant frequencies (Houde and Jordan, 1998, 2002) of auditory speech feedback all produce rapid changes in speech production.

In this paper we extend Houde and Jordan's (2002) approach by examining how individuals respond to manipulations of the first formant frequency of the vowels in monosyllables. Houde and Jordan's work was carried out with whispered speech, but the studies here and elsewhere (Purcell and Munhall, 2006; Villacorta *et al.*, 2004, 2005) have demonstrated the viability of manipulating voiced stimuli successfully. The present studies are modeled after sensorimotor manipulation studies outside of the speech literature, such as the use of prisms to displace the visual field and interfere with the visuomotor control of reaching (e.g., Stratten, 1896; Held, 1965), or the use of novel force fields to study the dynamics of motor control (Shadmehr, 2004). In the presence of a perceptual manipulation in these studies, the motor system compensates to achieve a goal. This compensation, of course, could occur if the movement was only guided in real time by sensory information. However, when the perceptual manipulation is removed an aftereffect or adaptation to the perceptual manipulation is observed. This persistence or learning in the motor system does not disappear immediately, indicating that a representation is involved in the control scheme.

Houde's approach, and the one we follow here, involves producing small incremental shifts in the frequency of the formants of vowels that participants hear themselves producing. Over successive trials the frequency of the produced and heard speech become farther and farther apart. Both compensation and adaptation have been demonstrated for formants (Houde and Jordan, 1998, 2002) and fundamental frequency (Jones and Munhall, 2000, 2002, 2005) with this paradigm. In the two experiments presented in this paper, we test fundamental aspects of the auditory-motor system: the sensitivity of the system to manipulations in different directions in the vowel space (experiment 1), the threshold for response to auditory manipulation (experiments 1 and 2), and the persistence of short-term alterations in the auditory-motor mapping (experiment 2).

II. EXPERIMENT 1

When an individual produces a series of the same vowel, the formant frequencies vary from trial to trial, but cluster around an average frequency, or possible vowel target, for that talker. Evidence shows that auditory feedback influences each of these vowel targets in the talker's vowel space. For example, individuals with cochlear implants may experience expanded vowel spaces following activation of their implants (e.g., Svirsky and Tobey, 1991; Perkell *et al.*, 1992; Economou *et al.*, 1992; Svirsky *et al.*, 1992), and talkers who discriminate auditory vowel contrasts more accurately also produce vowels with less variability in the formant frequencies (Perkell *et al.*, 2004). Thus, some type of auditory-motor mapping must be at play during vowel production.

In this paper we address two aspects of this mapping. First, we tested the threshold formant frequency at which participants began to compensate for a discrepancy between produced and heard vowel feedback. When feedback for F0 is shifted by very small amounts, there is at first no obvious response by the speech production system (Jones and Munhall, 2000). In this pitch-shift experiment, the acoustic feedback was systematically shifted in frequency from the spoken acoustics in small steps across utterances. Initially, participants did not change their production even though there was a widening frequency gap between uttered and heard speech. At some point the discrepancy between spoken acoustics and the feedback appears to cross some threshold and there is evidence of compensation in the participant's speech. We will call this point the **compensation threshold** and it presumably reflects a tolerance bound for sensorimotor control. While a great deal is known about psychoacoustic thresholds for formant frequencies (Kewley-Port and Watson, 1994; Kewley-Port *et al.*, 1996; Kewley-Port and Zheng, 1999; Kewley-Port, 2001; Liu and Kewley-Port, 2004), little is known about compensation thresholds, which must reflect a characteristic of the internal model for the auditory-motor control of speech.

The second goal of this study was to test whether the sensitivity to feedback manipulation is symmetrical around the talker's central formant tendency. Vowel spaces are not homogeneous in the distribution of vowel spacing (Lindblom, 1986; Maddieson, 1984), and factors such as proximity of adjacent vowels many influence the tolerance or compensation thresholds for individual vowels. In addition, the spatial variance of tongue movements during vowel production differs for vowel qualities and differs along the length of the tongue, presumably due to the properties of the tongue and its motor control (Perkell, 1996). All of these factors combined may introduce nonlinearities in the auditory feedback system.

A. Participants

Ten female participants varying in age from 18 to 24 years were tested in a single session. For each ear, hearing thresholds were measured at octave frequencies from 500 to 4000 Hz. All individuals had normal thresholds ($\leqslant$20 dB HL). No participants had known language or speech impairments, and all had learned English as their first language.

B. Equipment

Equipment was similar to that previously reported in Purcell and Munhall (2006). Participants' speech was transduced into an electrical signal with a type WH20 Shure headset microphone. A Tucker-Davis Technologies MA3 microphone amplifier with the +20-dB gain switch active was used to amplify the microphone signal. This signal was low-pass filtered with an analogue Frequency Devices type 901 filter using a cutoff frequency of 4500 Hz and gain of 0 dB. The filtered signal was digitized at 10 kHz with 16-bit precision

using a National Instruments PXI-6052E input/output board mounted in a PXI-1002 chassis. Real-time analysis and filtering of the voice was achieved using a National Instruments PXI-8176 embedded controller, and the altered voice was converted back to analogue by the 6052E at 10 kHz with 16-bit precision. A second Frequency Devices unit was employed to low-pass filter the altered feedback voice as above. A Madsen Midimate 622 audiometer added speech noise and amplified the signal for bilateral presentation of the same stimulus through Sennheiser "HD 265 linear" headphones. During practice trials, the microphone MA3 amplifier was adjusted between 30 and 50 dB for each individual so that vocalizations caused the Madsen input VU meter to read approximately 0 dB. Audiometer output gain was set so the headphone voice signal at each ear was approximately 80 dBA sound pressure level (SPL) with background speech shaped noise of approximately 50 dBA SPL. Calibration was performed using a Brüel &Kjær sound level meter and artificial ear Type 4153.

C. Experimental conditions

When normal feedback was not provided, the first formant (F1) of the vowel /ɛ/ was altered. Participants produced this vowel at normal speed in the CVC context of the word "head," and F1 was altered for the entire vowel (and incidentally the vocalic portion of the consonant "d"). Utterances were collected in sets of trials that will be referred to as blocks. Prior to any alteration of auditory feedback, baseline or "start" trials were collected with normal feedback at the beginning of each experimental block. These were followed by "ramp" trials where the magnitude of the shift was slowly increased in 4-Hz steps over 50 utterances. Shift magnitude was constant throughout each trial and was changed while the subject paused between utterances. Thus the manipulation of F1 was gradually changed from 0 Hz to a maximum of either ±200 Hz over the course of the 50 ramp trials. A positive shift was towards the vowel /æ/, and a negative shift was towards /ɪ/. The ramp trials were followed by "hold" trials where the maximum feedback change of ±200 Hz was employed. Auditory feedback was returned to normal with a step change following the hold trials. These last trials collected in each block with normal feedback were referred to as "end" trials. Both experiments employed naive subjects, and in an exit interview about 40% of participants were aware of some kind of change in the auditory feedback over the course of the experiment. The step change between the maximum formant shift and normal feedback (between the hold and end trials) was the point in the experiment where the manipulation would have been most apparent. Only 8% of individuals correctly identified that their vowels had been changed in the auditory feedback. Noticing the presence of feedback changes was not related to the pattern of compensatory behavior.

D. Experimental protocol

Experiments were performed in an Industrial Acoustics Company (IAC) sound-insulated room with participants seated in a comfortable chair. Individuals were asked to produce the words prompted on a video display using their normal speaking rate and level (vowels were not extended). Speaking level was monitored on the audiometer VU meter and was generally consistent over the course of an experiment. Each prompt lasted 1.5 s, and the interprompt interval was approximately 2.5 s.

At the start of each experiment, an automated screening program was used to prompt the participant to speak five extended tokens of seven English vowels spanning the vowel space (Ladefoged, 1982) in a CVC context (all /hVd/). The screening protocol was used to establish the best parameters for tracking the formants of each participant. The stability of the F1 estimate for the vowel /ɛ/ was evaluated, and the best linear predictive coding (LPC) model order in the range 8 through 12 (inclusive) was determined (Vallabha and Tuller, 2002). The best model order was selected as the order that produced F1 estimates with the smallest standard deviation (SD). This model order was then used for the rest of the experiment.

E. Online formant shifting and detection of voicing

Detection of voicing and formant shifting were performed as previously described in Purcell and Munhall (2006). Briefly, the manipulation of auditory feedback was achieved by filtering the voice in real-time. A simple statistical amplitude threshold technique was used to detect the onset of voicing in each trial. The first step in manipulating auditory feedback was to determine formants in the speech using an iterative Burg algorithm for estimating spectral parameters (Orfandidis, 1988). The sliding analysis window used in this procedure weighted older samples with an exponential decay chosen such that 50% of the area under the weighting curve applied to samples less than 8.6 ms old. The National Instruments system was capable of performing a new formant estimate every nine speech samples. This estimate of F1 was used to calculate filter coefficients such that a pair of spectral zeros deemphasized the existing formant, and a pair of spectral poles emphasized existing energy in the voice in the frequency region of the new desired formant. These filter coefficients were updated with each new formant estimate about every 900 μs.

F. Offline formant analysis

Prior to estimating formants offline, the record of each utterance was trimmed both before and after the vowel using a supervised semi-automated process. Rare vowels that were shorter than the mean duration minus two SDs were removed from further analysis, as were any trials where the participant clearly stumbled or failed to utter the correct word. The final preprocessing step was to trim all vowels to the duration of the shortest vowel in the set by truncating the tail. Vowel formants were calculated offline by sliding the analysis window ten speech samples (1 ms) per estimate, and used the same algorithm as the on-line experiment. Using the best model order for F1 of /ɛ/ helped reduce gross errors in tracking, however for some participants F2 was occasionally misinterpreted as F1. These bad estimates were removed using a histogram method where bins were declared unusable if they

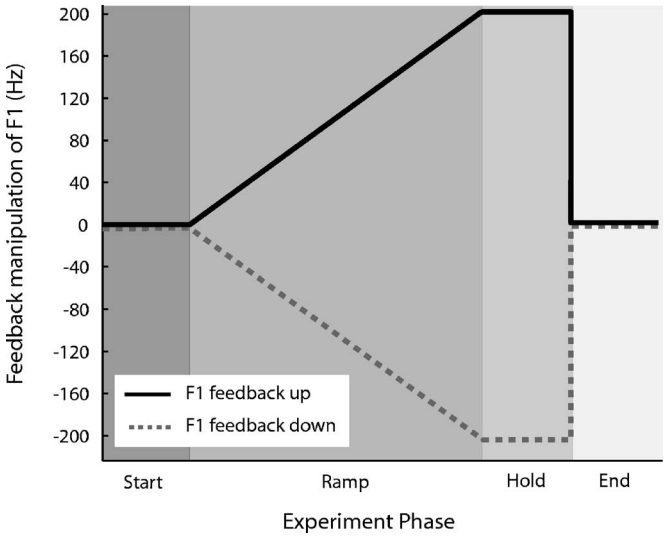

FIG. 1. Diagram of the time course of the manipulations made to the feedback of formant F1 from utterance to utterance. The four phases of the experiment (start, ramp, hold, and end) are indicated with shading of increasing lightness. The solid line is for the experimental condition where F1 of the test vowel /ɛ/ was pushed upwards towards the vowel /æ/, and the dash line indicates where F1 was shifted downwards towards /ɪ/.

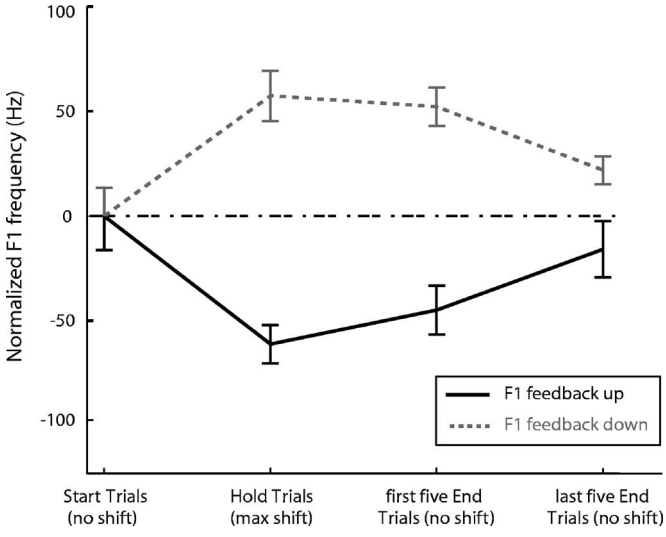

FIG. 2. Average changes in production measured with the microphone in response to the feedback manipulations in Fig. 1. The response is normalized to the average baseline F1 measurement in the start phase of the experiment. Average values are reported for the start, hold, and end phases of the experiment. The end phase has been subdivided into the means of the first and last five trials of that phase. Error bars are ±1 standard error. Note that the change in F1 production was in the opposite direction of the feedback manipulation in Fig. 1.

had counts of less than 5% of the average mode and were at least 150 Hz distant from the average mode. A single "steady-state" F1 value was determined for each trial by averaging F1 estimates in a 20-ms window (i.e., 20 estimates) beginning 50% of the way through the vowel. Mean values reported in the tables and figures were calculated by averaging these steady-state values across the relevant trials and participants.

G. Response evaluation

Changes in the production of F1 were evaluated against the average of the start trials that had normal auditory feedback. Compensation was calculated as the change in the production of F1 between the hold trials with the maximum feedback shift, and the start trials. Adaptation was calculated as the difference between the end trials with normal feedback, and the start trials. In both experiments, the onset of a response was estimated using the change point test (Donath *et al.*, 2002; Siegel and Castellan, 1988) applied to the steady-state F1 estimates.

H. Procedure

The ten participants were prompted to say the word "head" a total of 95 times for each of two shift directions. Half of the participants served first in a condition in which auditory feedback was shifted upward and then they experienced the same design with auditory feedback shifted downward. The order of shift direction was counterbalanced across participants. For each shift direction, auditory feedback was normal for 15 start trials. This was followed by 50 ramp trials where feedback was shifted to a maximum of either ±200 Hz. A further 15 hold trials were collected at the maximum shift, followed by 15 end trials with normal feedback. This is shown schematically in Fig. 1. After a short break, each participant then repeated the experiment, but with the manipulation in the opposite direction.

I. Results and discussion

On average, production of F1 changed in a direction opposite to the manipulation, as though the vocal control system were attempting to compensate for the manipulation. For both directions of F1 frequency manipulation the largest compensation occurred during the hold trials while altered feedback was at its maximum. However, even during the hold trials only partial compensation was observed. When feedback was returned to normal, F1 production did not immediately return to start values. In response to the auditory feedback manipulations in Fig. 1 (the stimulus), the mean F1 compensation and adaptation values are shown in Fig. 2 and Table I.

Repeated measures analysis of variance (ANOVA) using Greenhouse-Geisser corrections with factors of manipulation direction (up or down) and experiment phase (start, hold, and first or last five end trials) showed that there was a significant effect of direction $[F(1,7)=57.2, p<0.001]$ and a significant interaction between direction and experiment phase $[F(1.6,10.9)=14.5, p<0.001]$. There was no main effect of experiment phase because the responses were in opposite directions depending on whether feedback was altered up or down. Scheffé's method was used to detect significant differences between experiment phases for each manipulation direction. Hold trials were significantly different from start trials for both shift directions [up $F(3,27)=9.7$, $p<0.001$; down $F(3,21)=7.0, p<0.01$]. There was also a significant difference between the start and the first five end trials [up $F(3,27)=5.2$, $p<0.01$; down $F(3,21)=5.8$, $p<0.01$], but not the last five. Using a separate variance t test, there was also no significant difference between start trials for the two

TABLE I. Average data from experiment 1. There are ten individuals in the mean for the +200-Hz condition. The formant tracker was unstable for two participants when F1 was pushed −200 Hz, and this average therefore includes data from only eight individuals. The mean change points used one fewer participant in each condition because one person in each had an irrational change point (before the manipulation). All values are in Hz with between-subject standard error in parentheses. Compensation is the difference between mean F1 of the start and hold trials times the sign of the manipulation. Adaptation is the difference between the mean F1 of the start and end trials times the sign of the manipulation.

Condition	F1+200 Hz	F1−200 Hz
Measurement		
Start F1	775 (16.3)	769 (13.6)
F1 change point	64 (12.1)	89 (10.3)
Hold F1	713 (9.2)	827 (12.0)
First five end F1	730 (11.7)	822 (9.2)
Last five end F1	759 (13.5)	791 (6.7)
Compensation	61 (15.4)	58 (16.7)
Adaptation first five end	45 (15.0)	52 (16.6)
Adaptation last five end	16 (14.6)	22 (14.2)

manipulation directions. Although there was no statistical difference between the start trials for the two measurement directions, and no difference between the start trials and the last five end trials for a given direction, the means of the last five end trials in Fig. 2 suggest that production had not yet returned to baseline values. The order in which the manipulation direction was applied might therefore have had a subtle effect on an individual's production in the second part of the test. That is, the baseline F1 in the start trials of the second measurement block may have been slightly shifted in the direction of that block's manipulation as a remnant of the first measurement. This recovery from adaptation or deadaptation is explored in more detail in experiment 2.

The change point, or point during the ramp trials that production first changed significantly from the baseline value of the start trials, was identified using the change point test with the start and ramp trials. The mean of the individual participant change points is given for each manipulation direction in Table I. This measure will be considered a compensation threshold. There was no statistical difference between the mean change points for the different shift directions, as evaluated with a separate variance t test ($p < 0.14$). This compensation threshold (mean of both directions was 76 Hz) is above psychoacoustic formant thresholds observed for untrained individuals with background noise (Kewley-Port and Zheng, 1999; Kewley-Port, 2001) (recall noise level here was 50 dBA). However, this difference should be viewed as preliminary. A within-subject design, in which participants perform both tasks, is required because the responses to altered feedback and psychoacoustic thresholds vary markedly between participants. In the present data, compensation to the 200-Hz manipulation of F1 ranged from 9 to 126 Hz. That is to say, whereas one individual modified their F1 production by 9 Hz in response to this manipulation (essentially no significant change in production given the trial to trial variability), another modified theirs 14 times more. A large range of response magnitude is consistent with that observed in pitch-shift studies (e.g., Burnett *et al.*, 1998; Liu and Kewley-Port, 2004; Sivasankar *et al.*, 2005), but the reasons for such between-participant differences in susceptibility to altered feedback cannot be accounted for at present. In Kewley-Port and Watson's (1994) psychoacoustic difference thresholds for well-trained individuals, there were some large individual differences in performance for F2, but the range in F1 was generally smaller.

For both the size of the compensation and the compensation threshold, there were no statistically significant differences in the response for raising or lowering the frequency of F1 feedback. As shown in Table I, the compensation and adaptation values were similar (in Hz) for both directions. The directional sensitivity of the speech motor system therefore appears to be similar for F1 of the vowel /ɛ/. However, whether this symmetry generalizes to other vowels is unknown. Point vowels such as /æ/ that have no competing vowels in one F1 frequency direction may behave differently. The issue of the size of the "effective" stimulus also must be considered.

Among the front vowels, the difference in F1 between /ɪ/ and /ɛ/ is not the same as it is from /ɛ/ to /æ/. The values reported by Baken and Orlikoff (2002, Table 7-1, p. 260) between /ɛ/ and /ɪ/ for men and women are 140 and 180 Hz, respectively. The F1 differences between /ɛ/ and /æ/ for men and women are −130 and −250 Hz. If the vowel formant space is defined functionally by vowel categories, then linear manipulations like the ±200 Hz used here may not be treated uniformly by the auditory-vocal feedback system. Given the unsymmetrical F1 positioning of /ɪ/ and /æ/ in the vowel space with respect to /ɛ/ for women, it might be expected that the functional size of the manipulation employed here was larger for the shift from /ɛ/ towards /ɪ/. In the start trials, the measured average F1 difference between /ɛ/ and /ɪ/ was 174 Hz. Between /ɛ/ and /æ/ the mean difference was −217 Hz. Therefore on average, the manipulation may have been slightly functionally larger, with respect to this group's vowel categories, for the downward shift of F1 towards /ɪ/. Of course individual F1 spacing of the front vowels varies, so the relative functional manipulation size would change with the speaker. This issue is reminiscent of discussions of the metric for expressing the perceptual distance between vowels (e.g., Lindblom, 1986).

III. EXPERIMENT 2

Experiment 1 showed symmetrical compensation thresholds for raising and lowering of the first formant, and also demonstrated adaptations in both frequency directions that did not immediately return to the baseline level. In this experiment, we explored the dynamics of the deadaptation phase by recording a longer "end" phase in the experiment. The 15 trials recorded in experiment 1 were not enough to track the recovery from manipulation. Here, we also manipulated the length of the hold phase to begin to explore what conditions are influencing the adaptation persistence.

The effects of sensorimotor adaptation can persist for hours, days, and even longer in some cases, depending on the length of exposure to the manipulated sensory conditions, type of transformation, and activity following return to nor-

mal sensory conditions (Darainy *et al.*, 2006; Shadmehr and Brashers-Krug, 1997; Caithness *et al.*, 2004). For example, the vestibular-motor system of astronauts adapts during space flight and does not fully return to normal for more than a day after the return to earth's gravitational field (Paloski *et al.*, 2004). On the other hand, under some conditions the recovery from adaptation in saccadic eye movements that have been adapted using a target-jump paradigm can be quite rapid (Gaveau *et al.*, 2005).

There is little evidence from speech adaptation studies on the persistence of the effects. Jones and Munhall (2005) showed that the effect of adapted fundamental frequency during the production of Mandarin tones did not disappear in a short block of trials following return to normal feedback. Houde and Jordan (2002) report the puzzling observation that participants who had participated in an adaptation experiment showed baseline shifts in the direction of adaptation when they returned to the laboratory for recordings one month later. The baselines of the second phase of experiment 1 showed the same trend. This is not evident in the baseline start trials of Fig. 2 due to normalization, but it can be seen that the mean of the last five end trials plotted in Fig. 2 did not quite reattain the baseline, despite normal auditory feedback. In both Houde and Jordan's study and experiment 1, the gap between testing was filled with uncontrolled, natural speaking. Experiment 2 examined deadaptation under controlled conditions in which the number and content of participant productions were part of the design.

A. Participants

Forty-one participants varied in age from 18 to 23 year (nine females and five males in each of the hold 0 and hold 45 conditions, eight females and five males in the hold 15 condition). For each ear, hearing thresholds were measured at octave frequencies from 500 to 4000 Hz. Most individuals had normal thresholds ($\leqslant$20 dB HL), however there were two participants (one male and one female from the hold 45 condition) who had thresholds of 25 dB HL in one ear at one frequency. These individuals had typical responses and normal thresholds otherwise and were therefore included in the analysis. No participants had known language or speech impairments, and all had learned English as their first language.

B. Procedure

In this experiment F1 was shifted only in the upward direction to a maximum of +200 Hz (towards the vowel /æ/), and there were 20 start, 50 ramp, and 115 end trials. The first five start trials were not included in averages so that 15 trials were used as in experiment 1. Three different hold conditions were employed in a between-participants design with 0, 15, or 45 hold trials at the maximum feedback shift (the three conditions employed 14, 13, and 14 individuals, respectively). In the case of the hold 0 condition, the last five ramp trials were used to estimate compensation. All other features of the experiment were the same as in experiment 1.

TABLE II. Average data from experiment 2. There are 14 individuals in the means for the hold 0 and hold 45 conditions, and 13 for the hold 15 condition. The mean change point for each hold condition was the average of one fewer participant because either an individual did not have a statistically significant change point, or the change point was irrational (before the manipulation). All values are in Hz with between-subject standard error in parentheses. Compensation is the difference between the mean F1 of the start and hold trials. Residual adaptation is the difference between the mean F1 of the start trials and the last half of the end trials.

Condition	Hold 0	Hold 15	Hold 45
Measurement			
Start F1	670 (25.6)	693 (29.0)	692 (30.6)
F1 change point	73.5 (8.2)	79.0 (6.9)	93.5 (11.0)
Hold F1	616 (24.9)	624 (27.4)	645 (26.1)
Last half of end trials F1	647 (28.3)	681 (30.7)	672 (27.4)
Compensation	54 (9.5)	69 (8.1)	47 (11.0)
Adaptation last half of end trials	23 (10.2)	12 (7.9)	20 (10.5)

C. Results and discussion

Mean responses for the three different hold conditions are given in Table II. As in experiment 1, the average F1 production changed in the opposite direction of the manipulation of F1 in the auditory feedback. In experiment 2, F1 was raised in frequency (+200 Hz), so production of F1 in the hold trials tended to be lower than in the start trials. This effect extended well into the end trials that had normal feedback. The average response across participants for every trial is plotted in Fig. 3 for the hold 45 condition. Data for the hold 0 and 15 conditions were similar, but necessarily had fewer hold trials with the maximum feedback shift.

In the end trials shown in Fig. 3, F1 returns towards its original value in the start trials but does not reach the baseline level. The distribution of end trials for each of the three hold conditions is plotted in Fig. 4. Data from the different

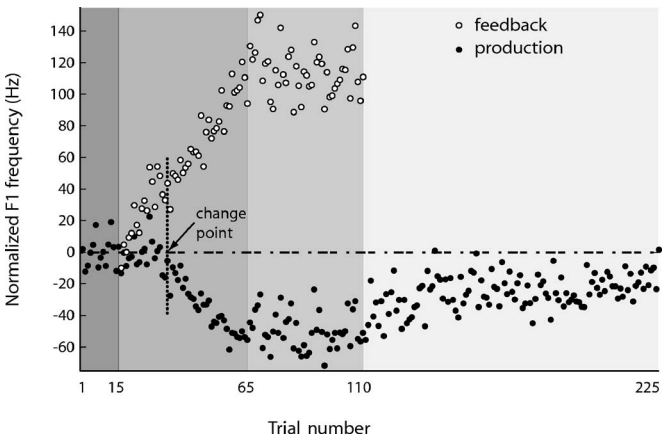

FIG. 3. Average F1 values across participants for each trial from the hold 45 condition of Experiment 2. Different phases of the experiment are again indicated with shading of increasing lightness as in Fig. 1 (from left to right these are start, ramp, hold, and end phases). Formant values are normalized with respect to the average baseline F1 in the start phase. Filled circles indicate production values of F1, whereas the open circles demarcate feedback F1 in the headphones (only shown where feedback differed from production). An arrow indicates the change point where production changed significantly from the baseline value in the start phase. This occurred when the feedback was altered 76 Hz on the 9th trial of the ramp phase.

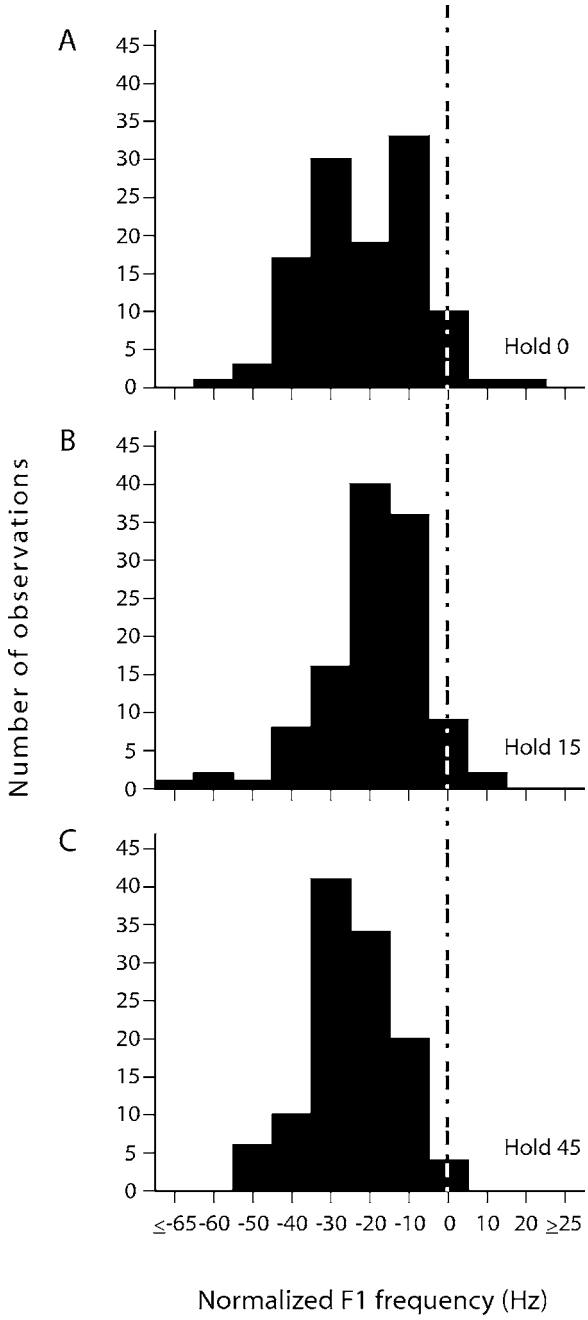

FIG. 4. Histograms of produced F1 in the end trials of all three hold conditions [panels (a), (b), and (c) are for hold conditions 0, 15, and 45, respectively]. Each bin was 10 Hz wide, and bin centers are labeled. Formant values are normalized with respect to the average baseline F1 in the start phase. The distributions of end trials overlap substantially across hold conditions, and all are shifted left (negative, or in the direction of compensation) relative to the average baseline F1 in the start phase.

hold conditions overlap substantially and did not differ in mean value ($p>0.80$, Scheffé's method applied to within-subject means). In order to analyze the dynamics of recovery from adaptation, the end trials from the three hold conditions were averaged. As can be seen in Fig. 5, adaptation decayed relatively quickly from its maximum over the first 15 end trials with normal feedback. Subsequently, the production of F1 appeared to asymptote at about −20 Hz relative to F1 in the start trials. In this experiment, it was not possible to separate the effects of time and utterance number on the

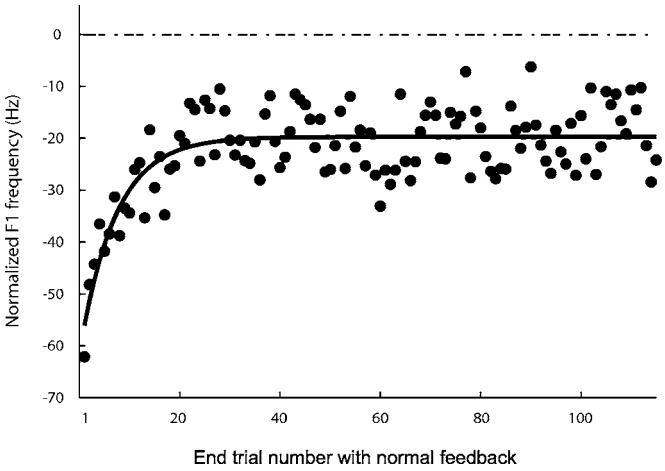

FIG. 5. Average F1 values across participants and hold conditions for each trial from the end phase of experiment 2. Each dot therefore represents mean data from 41 individuals for that trial. End phase trial numbers have been reindexed from 1 to 115 in this figure, but these correspond with trials 111 to 225 shown in Fig. 3. Formant F1 values are normalized with respect to the average baseline F1 in the start phase. An exponential has been fit to the values from each trial using a least squares cost function and is shown with a solid line (asymptote −19.8 Hz, intercept −61.7 Hz, and tau 0.141).

shape of the decay function because timing was rigidly paced. The average end trials were well modeled by a decaying exponential curve fit using a least squares cost function. Deadaptation in other sensorimotor systems shows similar exponential patterns (Davidson and Wolpert, 2004; Hopp and Fuchs, 2004).

An ANOVA with between-participant factor of hold condition (0, 15, and 45 hold trials), and within-participant factor of experiment phase (start, hold, and last half of end trials) was calculated. The mean of the last half of the end trials was chosen as an adaptation metric to avoid the rapid decay of adaptation during the first 15 end trials as shown in Fig. 5. There was a significant effect of experiment phase [$F(2,76)=55.5, p<0.001$], but not of hold condition. *Posthoc* comparisons using Scheffé's method showed that the hold trials had significantly lower F1 values than the start trials, for all three hold conditions [hold 0, $F(2,26)=14.8$, $p<0.001$; hold 15, $F(2,24)=33.9$, $p<0.001$; hold 45, $F(2,26)=11.2$, $p<0.001$]. Combining the three hold conditions, the last half of the end trials were significantly different from the start trials [$F(2,80)=5.6, p<0.01$]. In summary, the number of hold trials had no apparent effect on the compensation achieved, or the decay of adaptation with normal feedback.

During the ramp trials F1 did not change from baseline as soon as the feedback shift began (e.g., Fig. 3). Rather, the onset of compensation (change point) was delayed until a large enough discrepancy between produced and heard speech occurred. The change point shown in Fig. 3, calculated with the grand average data for this condition, was at a feedback manipulation of 76 Hz (in Table II, the arithmetic average of individual change points is 93.5 Hz for this hold condition). An ANOVA with the factor of hold condition (0, 15, and 45 hold trials) showed no difference in change points

TABLE III. Within-participant F1 production variability estimated as the standard deviation (SD) from token to token in the present analysis and those previously reported. Only select front vowels are given; data for other vowels may be available in the studies listed. Where different age groups were available, those closest in age to the young adults of the present study were chosen.

Study	Vowels	Speakers	Repetitions	SD (Hz)
Present	/ɛ/	41	15	29
Peterson and Barney (1952)	Entire vowel space	61	2	23
Kent (1973)	/ɪ/,/æ/	4	10	On order of 45
Kent and Forner (1979)	/ɪ/,/æ/	5	5	<60
Repp and Williams (1987)	/ɪ/,/æ/	2	4	20-30
Vallabha and Tuller (2004)	Entire vowel space	3	10	27
Pisoni (1980)	/ɪ/,/ɪ/,/ɛ/,/æ/	2	10	17, 23, 24, 38
Perkell and Nelson (1985)	/æ/	1	24	31
Beckman *et al.* (1995)	/ɪ/,/æ/	1	Not explicitly given	21, 45
Hawkins and Midgley (2005)	/ɪ/,/ɛ/,/æ/	5	4	22, 47, 56
Waldstein (1990)	/ɪ/,/ɪ/,/ɛ/,/æ/	7	8	22, 28, 46, 50

between the three hold conditions. This was expected since the experiment was identical until the hold trials themselves were reached.

One obvious feature of the data reported here is the variability in the talkers' formant values. Within-participant trial-to-trial variability in F1 was estimated by calculating SD in the start phase. Across participants the average SD was 29 Hz. In the literature, between-participant variability is generally what is reported, but within-participant values are available and are presented in Table III. Peterson and Barney (1952) recorded two tokens per speaker, and while this is a small set, their raw F1 data from across the English vowel space can be used to underestimate within-participant SD values. Select vowels are also available from the literature on the imitation of speech (e.g., Kent, 1973; Kent and Forner, 1979; Repp and Williams, 1987; Vallabha and Tuller, 2004). Interestingly, Pisoni (1980) found that mean F1 values were correlated between sessions, whereas F1 SD was not. Variability is also available from x-ray microbeam studies with single speakers (e.g., Perkell and Nelson, 1985; Beckman *et al.*, 1995). Individual token data in the appendix of Hawkins and Midgley (2005) can also be used to estimate variability in young male speakers. Additionally, Waldstein (1990) reports SD values for seven normal-hearing controls. The variability observed in the present study was quite similar to these previously reported values, as evident in Table III.

One important aspect of this variability is its sequential dependence. Due to delays in processing auditory feedback, the influence of one trial's perceived formant frequency should not be seen until the next trial. To evaluate this process an autocorrelation analysis was carried out across a range of lags for the start phase of the experiment (the nonstationary frequency changes in the other phases make this analysis complex for any other part of the data). The change in F1 between trials i and $i+1$ was calculated for every consecutive pair of start trials (using all 20 trials; there were 27 participants not missing any start trials included in this autocorrelation analysis), and the mean F1 value was subtracted from these difference scores before the normalized autocorrelation function was calculated at 11 lags, including a lag of zero. The autocorrelation values were then arithmetically averaged across individuals and are shown in Fig. 6(a). The negative lag-one correlation approached significance ($r=-0.37$, $p=0.10$), whereas greater lags had correlations closer to zero. This trend is reminiscent of the finding in learning force fields in which error on a given trial was predicted by the previous trial's error (Thoroughman and Shadmehr, 2000). The strength of this relationship was not uniform across participants with the range of lag-one correlations being from 0.04 to −0.73. The variability can be used to predict the size of F1 compensation during the hold phase of the experimental manipulation [Fig. 6(b)]. Participants who had strongly negative lag-one correlations during the start trials were more likely to produce large compensations during the hold trials, when feedback was maximally changed ($r=-0.44$, $p=0.02$).

IV. GENERAL DISCUSSION

Both studies demonstrated compensation and adaptation to modifications of acoustic feedback of the first formant frequency. When the frequency of F1 was shifted down (experiment 1) or up (experiments 1 and 2), participants compensated by varying F1 in the opposite frequency direction. In all conditions the average compensations were incomplete and only accounted for a portion of the frequency manipulation. Across all conditions in both experiments, the mean compensation was about 29% of the applied absolute formant manipulation of 200 Hz. The size of the compensation did not differ as a function of direction of shift, nor did the threshold for compensation. Adaptation of F1 frequency was observed in both experiments, and the pattern of adaptation was independent of direction of frequency manipulation. Finally, deadaptation showed an exponential pattern that was not influenced by amount of exposure to altered feedback. Within the limited range of conditions tested (0 to 45 hold trials), no differences were observed in F1 during the end trials following return to normal auditory feedback.

The observed compensation and adaptation are consistent with the findings of Houde and Jordan (Houde and Jordan, 1998, 2002) for whispered speech. Both Houde and Jordan and the present studies found similar ranges of

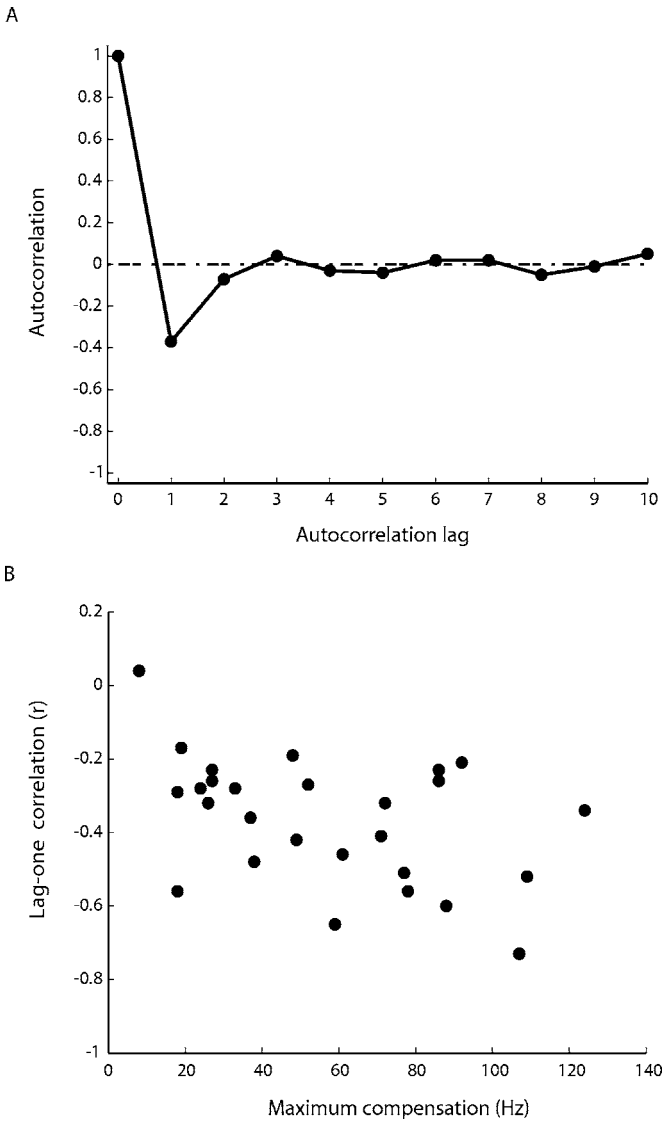

FIG. 6. Panel (a) shows the average autocorrelation of the normalized F1 difference between consecutive trials in the start phase, across subjects and at various lags. The average negative lag-one correlation was $r=-0.37$, whereas higher lags were close to zero. Panel (b) plots the lag-one autocorrelation values against compensation in the hold phase of the experiment (where maximum compensation was observed) for each individual. The cross correlation between these parameters was $r=-0.44$ and was statistically significant.

compensatory behavior and enduring aftereffects. In particular, Houde and Jordan and the studies reported here all show incomplete compensation in response to the formant manipulation. The relatively weak compensation (29%) could be due to a number of factors including nonlinear regions of the feedback response system, the single formant perturbations used in the studies reported here, and the possibility that the importance of auditory feedback may be modulated over time (see Purcell and Munhall, 2006).

Compensation and adaptation have also been demonstrated with manipulations of fundamental frequency feedback (Jones and Munhall, 2000, 2002, 2005), but F0 shows intriguing differences from the formant adaptations shown here and by Houde and Jordan. The F0 studies show negative aftereffects not observed with formants manipulations. For example, when feedback is raised in pitch, participants compensate by lowering their vocal pitch. When normal feedback is returned, the participants overshoot the baseline frequency and produce a higher pitch than baseline. Negative aftereffects such as this are the most common form of adaptation found in perception (e.g., Goldstein, 2006). This is also the form of aftereffect found in other sensorimotor adaptations such as prism adaptation (Held, 1965), and force field adaptations in arm (Lackner and DiZio, 2005) and speech (Tremblay *et al.*, 2003) movement. While the F1 compensation behavior is similar to that seen for F0, the behavior of F1 adaptation is quite different. Formant adaptation is positive, meaning that the produced formant frequencies simply remain near their compensation values. In this sense the phenomena is more like a recalibration of the F1 target or like Helson's (1951, 1964) idea of a change in adaptation level.

Adaptation-level theory as originally proposed (Helson, 1951, 1964) aimed to account for the maintenance of a functional neutral point in perception through computation of a weighted mean of perceived stimuli. While the idea of a shift in the average is consistent with the present data, the statistical pooling of stimulus values to determine this shift is at odds with the findings here and elsewhere. Experiment 2 revealed no relationship between the length of the hold phase and the rate of recovery. Other studies also show results that can not obviously be accounted for by a running average. Houde and Jordan's study involved a substantially more extended manipulation phase (over 2000 trials in the hold condition), but showed similar patterns of data to the present study. At the other extreme, Donath *et al.* (2002) found that production changes were evident in a subsequent utterance about 6 s after manipulation of feedback F0 in a single trial. Finally, Houde and Jordan raise the very surprising possibility that the adaptation persisted for a very long time. They reported that participants showed vestiges of their feedback manipulation when they returned to the laboratory a month following the study. The month of normal talking would surely have washed out any perturbation if a simple running average were at work.

Although it is unclear how long the adaptation lasts, there is consistent evidence about the shape of the recovery function. Both experiments show evidence for an initial period of rapid change. In a more detailed study of end trials, experiment 2 showed an exponential deadaptation towards baseline with an initial fast recovery and a mean F1 that was still below the baseline frequency even 115 trials following the end of the manipulation. This exponential function is consistent with studies of deadaptation following learning to move the arm in novel force fields (Davidson and Wolpert, 2004), and studies of recovery from adaptation of saccadic amplitude (Hopp and Fuchs, 2004). Retention curves in memory research of a very similar shape have been reported for more than 100 years, raising the possibility that the phenomenon being studied here is functionally a memory phenomenon. Rubin and Wenzel (1996), in a meta-analysis of 210 studies of retention curves in memory studies, showed

that the loss of information from memory could be fit very well by a range of different kinds of curve-fitting functions similar to the exponential.

The exponential in our analysis was chosen for convenience and was not derived for any theoretical reason. As Rubin and Wenzel (1996) found, it is difficult to distinguish subtly different mathematical functions in data that contain moderate variance. A more promising approach is to constrain the choice of curve-fitting procedures to those that have more appropriate theoretical underpinnings. For example, Wickelgren (1972) proposed an exponential power function for memory decay in which decay was proportional to the similarity of the stimuli being studied. Recent work by Jones and Munhall (2005) suggests that the decay of adaptation for F0 is related to similarity between the adaptation stimuli and the stimuli spoken after the return to normal feedback. When one Mandarin tone was adapted, the fundamental frequency of that tone remained altered longer than a tone that had not been adapted during the manipulation phase. The conditions that influence the decay of adaptation is a promising area for further studies.

Two kinds of variance are present in the current studies. Formant values varied between talkers and also within talkers' data. Second, compensation/adaptation varied significantly between individuals. Part of the variance in formant values can be attributed to formant estimation errors (Vallabha and Tuller, 2002), but it is apparent that there is real variability from token to token of a vowel as it is uttered by an individual. It has been pointed out previously (e.g., Broad, 1976; Kent and Forner, 1979) that this variability is similar to the difference limens found by Flanagan (1955). As mentioned above, more recently Kewley-Port and Watson (1994) have shown that well-trained individuals performing under ideal listening conditions can achieve better performance. However, more ordinary listening conditions, lack of training, and noise can raise thresholds above the estimates of SD reviewed in Table III (Kewley-Port and Zheng, 1999; Kewley-Port, 2001; Liu and Kewley-Port, 2004). Using the change point data here, it is interesting that the response began when manipulations were larger than two SDs beyond the baseline average value of F1. This suggests that some production variability is expected and tolerated by the feedback controller, but when production strays too far (near three SDs) a corrective mechanism is invoked. The fact that compensation was not reliably observed in the present study until the F1 manipulation was >60 Hz is congruent with the idea of managing a speech production system whose output is quite variable. There may be stability costs if a feedback system were to micro-manage off-target productions with deviations smaller than those reasonably expected from that production system (about ± 60 Hz). As noted above, the compensation threshold is higher than the best psychoacoustic performance for detecting changes in F1 (Kewley-Port and Watson, 1994), but under normal listening conditions a somewhat higher threshold may be expected. There may of course also be differences in psychoacoustic and feedback control system thresholds, and between pure listening and listening while speaking.

Why some participants do not compensate for the manipulations is unknown. However, the correlation between the lag-one autocorrelation and the magnitude of compensation observed in experiment 2 suggests that some participants are more actively stabilizing their productions from trial-to-trial even under normal feedback conditions. One possibility is that talkers weight the different types of feedback differently (e.g., Borden, 1979; Perkell, 1980). Some may rely more on kinesthetic feedback and thus are not influenced as much by acoustic feedback. The individual differences in response to manipulations such as delayed auditory feedback are consistent with this possibility (Howell and Archer, 1984). A second possibility is that talkers differ in what the control parameter for the vowel is. In carrying out this work, we have made a number of implicit assumptions about the representation of vowels and their perception: that formants are being tracked by talkers, that the acoustic space is a linear frequency space, and that a static formant estimate is sufficient for characterizing dynamic vowels in natural utterances. Strong arguments have been made against each of these assumptions (e.g., Lindblom, 1986; Strange, 1989), and it may be that our experimental approach does not capture perceptually pertinent patterns for some participants.

In closing, the present experiments have demonstrated that formant production is sensitive to auditory feedback and that some form of representation mediates vowel production. The studies have provided preliminary evidence about the sensitivity of the feedback system and its time constants. However, we still know little about this phonetic representation system, the conditions under which learning and adaptation occur, and its role in the broad context of communication (Pardo and Remez, 2006). Although it has been recognized for a long time that auditory feedback drives learning in speech production, progress in understanding this perception/production relationship has been slow. The approach taken here permits us to address this interaction directly. Beyond the theoretical importance of this work, there are a range of applied problems in which auditory-motor learning is primary. Second-language learning, articulation training of individuals with hearing impairments and cochlear implants, and many types of speech therapy involve perceptual learning and imitation. Thus, progress in this laboratory-based adaptation phenomenon has the potential for significant contributions to enduring problems in rehabilitation science.

ACKNOWLEDGMENTS

The authors would like to thank Reiner Wilhelms-Tricarico and Richard McGowan for their assistance in the development of the formant tracking and filtering algorithms. The authors would also like to thank Bryan Burt for his assistance in data collection, and Courtney Belfour and Sheena Kirkland for their work segmenting vowels from the recorded tokens. Research supported by the National Institute on Deafness and Other Communication Disorders, and the (Canadian) Natural Sciences and Engineering Research Council.

Baken, R. J. and Orlikoff, R. F. (**2000**). *Clinical Measurement of Speech and Voice* (Singular, San Diego).
Beckman, M. E., Jung, T. P., Lee, S. H., Dejong, K., Krishnamurthy, A. K., Ahalt, S. C., Cohen, K. B., and Collins, M. J. (**1995**). "Variability in the production of quantal vowels revisited," J. Acoust. Soc. Am. **97**, 471–490.
Borden, G. J. (**1979**). "An interpretation of research of feedback interruption in speech," Brain Lang **7**, 307–319.
Broad, D. J. (**1976**). "Toward defining acoustic phonetic equivalence for vowels," Phonetica **33**, 401–424.
Burnett, T. A., Freedland, M. B., Larson, C. R., and Hain, T. C. (**1998**). "Voice F0 responses to manipulations in pitch feedback," J. Acoust. Soc. Am. **103**, 3153–3161.
Caithness, G., Osu, R., Bays, P., Chase, H., Klassen, J., Kawato, M., Wolpert, D. M., and Flanagan, J. R. (**2004**). "Failure to consolidate the consolidation theory of learning for sensorimotor adaptation tasks," J. Neurosci. **24**, 8662–8671.
Darainy, M., Malfait, N., Towhidkhah, F., and Ostry, D. J. (**2006**). "Transfer and durability of acquired patterns of human arm stiffness," Exp. Brain Res. **170**, 227–237.
Davidson, P. R. and Wolpert, D. M. (**2004**). "Scaling down motor memories: de-adaptation after motor learning," Neurosci. Lett. **370**, 102–107.
Donath, T. M., Natke, U., and Kalveram, K. T. (**2002**). "Effects of frequency-shifted auditory feedback on voice F0 contours in syllables," J. Acoust. Soc. Am. **111**, 357–366.
Economou, A., Tartter, V. C., Chute, P. M., and Hellman, S. A. (**1992**). "Speech changes following reimplantation from a single-channel to a multichannel cochlear implant," J. Acoust. Soc. Am. **92**, 1310–1323.
Flanagan, J. L. (**1955**). "A difference limen for vowel formant frequency," J. Acoust. Soc. Am. **27**, 613–617.
Gaveau, V., Alayane, N., Salemme, R., and Desmurget, M. (**2005**). "Self-generated saccades do not modify the gain of adapted reactive saccades," Exp. Brain Res. **162**, 526–531.
Goldstein, E. B. (**2006**). *Sensation and Perception* (Wadsworth, Belmont, CA).
Guenther, F. H. (**1995**). "Speech sound acquisition, coarticulation, and rate effects in a neural network model of speech production," Psychol. Rev. **102**, 594–621.
Guenther, F. H. (**2003**). "Neural control of speech movements," in *Phonetics and Phonology in Language Comprehension and Production: Differences and Similarities*, edited by A. Meyer and N. Schiller (Mouton de Gruyter, Berlin), pp. 209–239.
Hawkins, S. and Midgley, J. (**2005**). "Formant frequencies of RP monophthongs in four age groups of speakers," J. Int. Phonetic Assoc. **35**, 183–199.
Held, R. (**1965**). "Plasticity in sensory-motor systems," Sci. Am. **213**, 84–94.
Helson, H. (**1951**). "Perception," in *Theoretical Foundations of Psychology*, edited by H. Helson (Van Nostrand, Toronto), pp. 348–389.
Helson, H. (**1964**). *Adaptation-Level Theory: An Experimental and Systematic Approach to Behavior* (Harper & Row, New York).
Hopp, J. J. and Fuchs, A. F. (**2004**). "The characteristics and neuronal substrate of saccadic eye movement plasticity," Prog. Neurobiol. **72**, 27–53.
Houde, J. F. and Jordan, M. I. (**1998**). "Sensorimotor adaptation in speech production," Science **279**, 1213–1216.
Houde, J. F. and Jordan, M. I. (**2002**). "Sensorimotor adaptation of speech I: Compensation and adaptation," J. Speech Lang. Hear. Res. **45**, 295–310.
Howell, P. and Archer, A. (**1984**). "Susceptibility to the effects of delayed auditory feedback," Percept. Psychophys. **36**, 296–302.
Jones, J. A. and Munhall, K. G. (**2000**). "Perceptual calibration of F0 production: evidence from feedback perturbation," J. Acoust. Soc. Am. **108**, 1246–1251.
Jones, J. A. and Munhall, K. G. (**2002**). "The role of auditory feedback during phonation: Studies of Mandarin tone production," J. Phonetics **30**, 303–320.
Jones, J. A. and Munhall, K. G. (**2005**). "Remapping auditory-motor representations in voice production," Curr. Biol. **15**, 1768–1772.
Kawahara, H. (**1995**). "Transformed auditory feedback: The collection of Data from 1993.1 to 1994.12 by a new set of analysis procedures," TR-H-120 (ATR Human Information Processing Research Laboratories, Kyoto), pp. 1–52.
Kawato, M. (**1989**). "Motor theory of speech perception revisted from the minimum torque-change neural network model," in *8th Symposium on Future Electron Devices*, Tokyo, Japan, pp. 141–150.
Kent, R. D. (**1973**). "The imitation of synthetic vowels and some implications for speech memory," Phonetica **28**, 1–25.
Kent, R. D. and Forner, L. L. (**1979**). "Developmental study of vowel formant frequencies in an imitation task," J. Acoust. Soc. Am. **65**, 208–217.
Kewley-Port, D. (**2001**). "Vowel formant discrimination II: Effects of stimulus uncertainty, consonantal context, and training," J. Acoust. Soc. Am. **110**, 2141–2155.
Kewley-Port, D. and Watson, C. S. (**1994**). "Formant-frequency discrimination for isolated English vowels," J. Acoust. Soc. Am. **95**, 485–496.
Kewley-Port, D. and Zheng, Y. (**1999**). "Vowel formant discrimination: Towards more ordinary listening conditions," J. Acoust. Soc. Am. **106**, 2945–2958.
Kewley-Port, D., Li, X., Zheng, Y., and Neel, A. T. (**1996**). "Fundamental frequency effects on thresholds for vowel formant discrimination," J. Acoust. Soc. Am. **100**, 2462–2470.
Lackner, J. R. and DiZio, P. (**2005**). "Motor control and learning in altered dynamic environments," Curr. Opin. Neurobiol. **15**, 653–659.
Ladefoged, P. (**1982**). *A Course in Phonetics* (Harcourt Brace Jovanovich, New York).
Lane, H. and Tranel, B. (**1971**). "Lombard Sign and Role of Hearing in Speech," J. Speech Hear. Res. **14**, 677–709.
Lane, H. and Webster, J. W. (**1991**). "Speech deterioration in postlingually deafened adults," J. Acoust. Soc. Am. **89**, 859–866.
Lashley, K. S. (**1951**). "The problem of serial order in behavior," in *Cerebral Mechanisms in Behavior*, edited by L. A. Jeffress (Wiley, New York).
Leder, S. B. and Spitzer, J. B. (**1993**). "Speaking fundamental frequency, intensity, and rate of adventitiously profoundly hearing-impaired adult women," J. Acoust. Soc. Am. **93**, 2146–2151.
Lindblom, B. (**1986**). "Phonetic universals in vowel systems," in *Experimental Phonology*, edited by J. J. Ohala and J. J. Jaeger (Academic P, Toronto), pp. 13–44.
Liu, C. and Kewley-Port, D. (**2004**). "Formant discrimination in noise for isolated vowels," J. Acoust. Soc. Am. **116**, 3119–3129.
Maddieson, I. (**1984**). *Patterns of Sounds* (Cambridge U.P., Cambridge).
Munhall, K. G., Kawato, M., and Vatikiotis-Bateson, E. (**2000**). "Coarticulation and physical models of speech production," in *Papers in Laboratory Phonology V: Acquisition and the Lexicon*, edited by M. Broe and J. Pierrehumbert (Cambridge U.P., Cambridge), pp. 9–28.
Oller, D. K. and Eilers, R. E. (**1988**). "The role of audition in infant babbling," Child Dev. **59**, 441–449.
Orfandidis, S. J. (**1988**). *Optimum Signal Processing, An introduction* (MacMillan, New York).
Paloski, W. H., Black, F. O., and Metter, E. J. (**2004**). "Postflight balance control recovery in an elderly astronaut: a case report," Otol. Neurotol. **25**, 53–56.
Pardo, J. S. and Remez, R. E. (**2006**). "The perception of speech," in *The Handbook of Psycholinguistics*, edited by M. Traxler and M. A. Gernsbacher (Elsevier, New York), to be published.
Perkell, J. (**1980**). "Phonetic features and the physiology of speech production," in *Language Production*, edited by B. Butterworth (Academic, London), pp. 337–372.
Perkell, J. (**1996**). "Properties of the tongue help to define vowel categories: Hypotheses based on physiologically-oriented modeling," J. Phonetics **24**, 3–22.
Perkell, J., Lane, H., Svirsky, M., and Webster, J. (**1992**). "Speech of cochlear implant patients: a longitudinal study of vowel production," J. Acoust. Soc. Am. **91**, 2961–2978.
Perkell, J. S. and Nelson, W. L. (**1985**). "Variability in production of the vowels /ɪ/ and /a/," J. Acoust. Soc. Am. **77**, 1889–1895.
Perkell, J. S., Guenther, F. H., Lane, H., Matthies, M. L., Stockmann, E., Tiede, M., and Zandipour, M. (**2004**). "The distinctness of speakers' productions of vowel contrasts is related to their discrimination of the contrasts," J. Acoust. Soc. Am. **116**, 2338–2344.
Perkell, J. S., Matthies, M. L., Lane, H., Guenther, F. H., Wilhelms-Tricarico, R., Wozniak, J., and Guiod, P. (**1997**). "Speech motor control: acoustic goals, saturation effects, auditory feedback and internal models," Speech Commun. **22**, 227–250.
Peterson, G. E. and Barney, H. L. (**1952**). "Control methods used in a study of the vowels," J. Acoust. Soc. Am. **24**, 175–184.
Pisoni, D. B. (**1980**). "Variability of vowel formant frequencies and the quantal theory of speech: a first report," Phonetica **37**, 285–305.
Purcell, D. W. and Munhall, K. (**2006**). "Compensation following real-time manipulation of formants in isolated vowels," J. Acoust. Soc. Am. **119**, 2288–2297.
Repp, B. H. and Williams, D. R. (**1987**). "Categorical Tendencies in Imitat-

ing Self-Produced Isolated Vowels," Speech Commun. **6**, 1–14.
Rubin, D. C. and Wenzel, A. E. (**1996**). "One hundred years of forgetting: A quantitative description of retention," Psychol. Rev. **103**, 734–760.
Schenk, B. S., Baumgartner, W. D., and Hamzavi, J. S. (**2003**). "Effect of the loss of auditory feedback on segmental parameters of vowels of postlingually deafened speakers," Auris Nasus Larynx **30**, 333–339.
Shadmehr, R. (**2004**). "Generalization as a behavioral window to the neural mechanisms of learning internal models," Hum. Mov. Sci. **23**, 543–568.
Shadmehr, R. and Brashers-Krug, T. (**1997**). "Functional stages in the formation of human long-term motor memory," J. Neurosci. **17**, 409–419.
Siegel, S. and Castellan, N. J. (**1988**). *Nonparametric Statistics for the Behavioral Sciences* (McGraw-Hill, Boston).
Sivasankar, M., Bauer, J. J., Babu, T., and Larson, C. R. (**2005**). "Voice responses to changes in pitch of voice or tone auditory feedback," J. Acoust. Soc. Am. **117**, 850–857.
Smith, C. R. (**1975**). "Residual hearing and speech production in deaf children," J. Speech Hear. Res. **18**, 795–811.
Smith, K. U. and Smith, W. M. (**1962**). *Delayed Sensory Feedback and Behavior* (Saunders, Philadelphia).
Strange, W. (**1989**). "Evolving theories of vowel perception," J. Acoust. Soc. Am. **85**, 2081–2087.
Stratten, G. (**1896**). "Some preliminary experiments on vision without inversion of the retinal image," Psychol. Rev. **3**, 611–617.
Svirsky, M. A. and Tobey, E. A. (**1991**). "Effect of different types of auditory stimulation on vowel formant frequencies in multichannel cochlear implant users," J. Acoust. Soc. Am. **89**, 2895–2904.
Svirsky, M. A., Lane, H., Perkell, J. S., and Wozniak, J. (**1992**). "Effects of short-term auditory deprivation on speech production in adult cochlear implant users," J. Acoust. Soc. Am. **92**, 1284–1300.
Thoroughman, K. A. and Shadmehr, R. (**2000**). "Learning of action through adaptive combination of motor primitives," Nature (London) **407**, 742–747.
Tin, C. and Poon, C. S. (**2005**). "Internal models in sensorimotor integration: Perspectives from adaptive control theory," J. Neural Eng. **2**, S147–S163.
Tremblay, S., Shiller, D. M., and Ostry, D. J. (**2003**). "Somatosensory basis of speech production," Nature (London) **423**, 866–869.
Vallabha, G. K. and Tuller, B. (**2002**). "Systematic errors in the formant analysis of steady-state vowels," Speech Commun. **38**, 141–160.
Vallabha, G. K. and Tuller, B. (**2004**). "Perceptuomotor bias in the imitation of steady-state vowels," J. Acoust. Soc. Am. **116**, 1184–1197.
Villacorta, V., Perkell, J. S., and Guenther, F. H. (**2004**). "Sensorimotor adaptation to acoustic perturbations in vowel formants," J. Acoust. Soc. Am. **115**, 2430.
Villacorta, V., Perkell, J. S., and Guenther, F. H. (**2005**). "Relations between speech sensorimotor adaptation and perceptual acuity," J. Acoust. Soc. Am. **117**, 2618.
Waldstein, R. S. (**1990**). "Effects of postlingual deafness on speech production: implications for the role of auditory feedback," J. Acoust. Soc. Am. **88**, 2099–2114.
Wickelgren, W. (**1972**). "Trace Resistance and Decay of Long-Term Memory," J. Math. Psychol. **9**, 418–455.

Cues for masked amplitude-modulation detection

Paul C. Nelson
Department of Biomedical and Chemical Engineering and Institute for Sensory Research, Syracuse University, Syracuse, New York 13244

Laurel H. Carney[a)]
Department of Biomedical and Chemical Engineering and Institute for Sensory Research and Department of Electrical Engineering and Computer Science, Syracuse University, Syracuse, New York 13244

(Received 4 October 2005; revised 17 May 2006; accepted 19 May 2006)

The ability of psychoacoustic models to predict listeners' performance depends on two key stages: preprocessing and the generation of a decision variable. The goal of the current study was to determine the perceptually relevant decision variables in masked amplitude-modulation detection tasks in which the modulation depth of the masker was systematically varied. Potential cues were made unreliable by roving the overall modulation depth from trial to trial or were reduced in salience by equalizing the envelope energy of the standard and target after the signal was added. Listeners' performance was significantly degraded in both paradigms compared to the baseline (fixed-level modulation masker) condition, which was similar to those used in previous studies of masking in the envelope-frequency domain. Although this observation was broadly consistent with a simple long-term envelope power-spectrum model, there were several aspects of the data that were not. For example, the steep rate of change in threshold with masker depth and the fact that an optimal amount of envelope noise could enhance performance were not predicted by decision variables calculated directly from the stimulus envelope. A physiologically based processing model suggested a realistic nonlinear mechanism that could give rise to these second-order features of the data. © *2006 Acoustical Society of America.* [DOI: 10.1121/1.2213573]

PACS number(s): 43.66.Mk, 43.66.Dc [JHG] Pages: 978–990

I. INTRODUCTION

Behaviorally relevant acoustic stimuli such as speech cannot be defined solely by their long-term audio-frequency composition. Temporal variations in a signal's spectrum and interactions between individual spectral components result in amplitude-modulated (AM) sounds. Viemeister (1979) used concepts from linear systems analysis as a framework to determine the effective temporal modulation transfer function (MTF) of the auditory system by measuring the just-noticeable modulation depth of a sinusoidally amplitude-modulated (SAM) noise for a range of modulation frequencies (f_m). Viemeister's approach has proven highly valuable as a first-order approximation of the system's (low-pass) properties and as a starting point for many other studies. For example, the modulation filter-bank model structure (e.g., Dau *et al.*, 1997a), which assumes that the envelope of the output of each audio-frequency channel passes through a bank of bandpass filters (broadly) tuned to f_m, is able to account for several perceptual findings that a low-pass preprocessor cannot explain (i.e., Dau *et al.*, 1997a, b, 1999; Ewert and Dau, 2000).

To predict psychophysical thresholds, the output of any model must be concisely quantified with some decision variable (DV). And while the preprocessing model structures are fundamentally different for the two models mentioned earlier, both the Viemeister (1979) model and the most recent implementations of the Dau model [the envelope power-spectrum model, Ewert and Dau, 2000; Ewert *et al.*, 2002; Ewert and Dau, 2004] assume an average rms DV at the output of their envelope-filtering process. This assumption has been shown to be reasonable for many types of AM-detection tasks, but it is not clear whether decision statistics that rely on local temporal envelope features (instead of average or long-term features) would be equally successful as quantifications of the model outputs.

The broad goal of the current set of experiments was to further elucidate which features of AM stimuli are perceptually salient and used by listeners in modulation detection tasks. To accomplish this, empirical data are presented that provide critical tests for various DVs. Paradigms from the audio-frequency tone-in-noise (TIN) detection literature that highlight shortcomings of long-term decision statistics in the spectral-frequency domain (roving-level and energy-equalized TIN detection) were translated into the modulation-frequency domain. Because the stimuli had envelope-frequency bandwidths smaller than the presumed modulation filter widths, the internal representation of the stimulus envelope was similar for the low-pass (Viemeister) model and the bandpass (Dau) model. An alternative model, developed to predict responses of inferior colliculus (IC) neurons to AM signals (Nelson and Carney, 2004), was tested alongside the previously proposed psychophysical (signal-processing) models. The working hypothesis was that a physiologically motivated model structure would shape the

[a)]Electronic mail: lacarney@syr.edu

 0001-4966/2006/120(2)/978/13/$22.50

internal representation of the stimulus more like the real system than "effective" signal-processing models.

There are two reasons to consider a *masked* AM-detection task (instead of pure, or unmasked, AM detection) to test our hypotheses. First, several reasonable techniques can be used to adjust a given model's unmasked detection abilities, which makes it difficult to dismiss one competing decision statistic over another. A more interesting reason is that real-world sounds have complex modulation spectra, so it is useful to consider envelope detection abilities and limitations for stimuli other than pure sinusoidal AM. Previous studies of masked-AM detection have focused on the effects of varying the frequencies of the signal and/or masker modulation (Houtgast, 1989; Bacon and Grantham, 1989; Strickland and Viemeister, 1996; Dau *et al.*, 1997a; Ewert and Dau, 2000; Ewert *et al.*, 2002). Here, masker level (or masker modulation depth) was the only systematically manipulated stimulus dimension. Predicted signal-detection thresholds based on a battery of potentially relevant DVs were compared to the masked thresholds measured psychophysically. Because several decision devices predicted statistically similar thresholds, a more detailed analysis of the relationships between DVs and listener responses on a trial-by-trial basis was also carried out.

A subset of the potential perceptually relevant decision devices investigated in the present study can be introduced in the context of previous work. Perhaps the most influential and straightforward DV assumed in previous AM-coding work is the long-term rms energy measured at the output of some envelope-filtering process. Such a statistic can explain the shape of the temporal modulation transfer function (with low-pass preprocessing: Viemeister, 1979; Strickland and Viemeister, 1996) and the envelope-frequency selectivity observed in experiments measuring sinusoidal AM-detection thresholds in the presence of a narrowband-noise masker modulation applied to the same carrier (with bandpass preprocessing: Ewert and Dau, 2000; Ewert *et al.*, 2002). Moore and Sek (2000) measured detection thresholds for stimuli with three AM-frequency components for three different phase configurations, and found no dependence of thresholds on the components' relative phases. This finding is also consistent with predictions of an average (rms) envelope statistic. Note that any local temporal structure present in the stimulus (or its internal representation) is discarded with an average (rms) metric.

Strickland and Viemeister (1996) concluded that the ratio of the maximum value to the minimum value of the envelope (max/min) was the best predictor of listeners' thresholds in a tone-on-tone modulation masking experiment. In contrast to the rms statistic, which averages over the entire temporal waveform, max/min makes decisions based on only two points in the envelope representation. Crest factor (ratio of maximum envelope value to the envelope rms) represents a compromise in some sense: a single value of the waveform is normalized by an averaged value. Lorenzi *et al.* (1999) accounted for performance in a (supra-threshold) modulation component phase discrimination task by basing decisions on the crest factor of a low-pass filtered version of the envelope of their stimuli. DVs based on the higher-order moments of envelope amplitude distributions have also been tested in various envelope-processing tasks (i.e., skewness: Lorenzi *et al.*, 1999; kurtosis: Strickland and Viemeister, 1996).

Another aspect of a signal with a complex modulation spectrum is its venelope, or second-order envelope (Shofner *et al.*, 1996; Ewert *et al.*, 2002; Lorenzi *et al.*, 2001a, b). Venelope cues could potentially be used in modulation masking experiments, especially in conditions with tonal maskers and noise signals (Ewert *et al.*, 2002). This line of reasoning parallels results from audio-frequency tone and noise masking experiments in which envelope cues have been shown to have various effects on detection performance, depending on the masker-signal configuration (i.e., the asymmetry of masking; see Derleth and Dau, 2000). It is reasonable to hypothesize that venelope fluctuations may also provide a detection cue for conditions with sinusoidal signals and random maskers (as measured in the present study), especially when first-order envelope cues are made unreliable or completely removed.

As an alternative to signal-processing-based DVs, threshold predictions were also made based on a physiologically motivated model for neural responses to AM tones (Nelson and Carney, 2004). The average firing rate of model inferior colliculus cells was tested as a physiologically realistic DV, alongside several of the signal statistics described earlier. In the model cells, firing rate increases monotonically with signal modulation depth. Interactions between strong inhibitory and weaker excitatory inputs result in a "hard" threshold modulation depth that limits the model's detection performance even in the absence of internal or external (stimulus-induced) noise sources. Model-cell rate MTFs are bandpass, with Q values (measured at the half-maximal-rate points) of approximately 1. This broad tuning is realized in the physiological model by assuming different time courses in the effective low-pass filtering properties of inhibition and excitation. The Q values are consistent with the signal-processing modulation filters derived recently by Dau and co-workers to predict several aspects of psychophysical envelope coding (Dau *et al.*, 1997a; Ewert and Dau, 2000; Ewert *et al.*, 2002). For the band-limited stimuli used in the present study, the filtering properties of the IC model cells have little effect on shaping the internal representation of the envelope. Again, the focus is on understanding the perceptually salient quantifications of the internally represented envelope (as opposed to testing the validity of a bandpass modulation filter versus a "smoothing" or low-pass modulation filter).

Independent of the chosen DV, simulations of psychophysical experiments must include some mechanism to limit model performance in the detection and discrimination of deterministic stimuli (without external noise). The most common way to do this is to add some amount of internal noise, either to the internal representation, or to the final value of the decision statistic in each interval. Ewert and Dau (2004) have provided some insight into the appropriate statistical description of the internal noise relevant to envelope-processing tasks. They measured AM depth-discrimination thresholds for a wide range of standard depths, and found the Weber fraction for sinusoidal carriers to be independent of

standard depth, as long as the standard was well above threshold. This can be accounted for in a model by assuming a constant *ratio* between the DVs in the target and standard interval at threshold, or by including an internal noise whose variance is proportional to the value of the assumed decision statistic. For low standard depths (i.e., −28 and −23 dB in $20 \log m$, where m is linear modulation depth), the situation was different. In this range, a constant increase in modulation depth was required to reach discrimination threshold (independent of the standard depth). This can be thought of as arising from a second type of internal noise process—one with a *fixed variance*, which dominates threshold measurements at low modulation depths. We will address Ewert and Dau's (2004) findings, but we will also consider model predictions with a fixed-variance noise only, as a "best-case scenario" for the various decision statistics (i.e., if a decision statistic predicts higher thresholds than the listeners' performance with the fixed-variance noise alone, it would certainly not be able to account for thresholds if the constant-ratio noise, or Weber-fraction noise, were also included).

Two specific paradigms that have been used in the audio-frequency domain to test the power spectrum model of masking were translated into the envelope-frequency domain in the current study: roving-level and equal-energy TIN detection. A within-trial rove in overall energy renders long-term rms cues unreliable, and models based on energy cues predict higher thresholds in a roving-level situation. The absolute amount of increase over fixed-level conditions depends on the rove range (Green, 1983). Kidd *et al.* (1989) found that roving the overall level by 32 dB in an audio-frequency TIN detection task did *not* have a significant effect on thresholds (for noise bandwidths greater than one-third of the psychophysically measured auditory-filter bandwidth). In another paradigm that challenges energy-based audio-frequency models of masking, Richards and Nekrich (1993) measured the detectability of tones in narrow bands of masking noise after the energy in the two observation intervals was equalized. Pure long-term energy models predict that such a task would be impossible (for subcritical bandwidths), but listeners performed the task reliably. Richards and Nekrich (1993) attributed their results to differences in the envelopes of the noise-alone and tone-plus-noise stimuli.

With this body of previous work in mind, we present here psychophysical masked-AM detection data and predicted thresholds based on a diverse set of decision statistics. Measured and simulated thresholds in roving-level and equal-energy conditions are compared to those from a baseline fixed-level masker condition, over a wide range of masker modulation depths.

II. PSYCHOPHYSICAL EXPERIMENT

A. Methods

1. Subjects and procedure

Four listeners with normal hearing participated in the experiment. Pure-tone thresholds for all of the subjects were less than 15 dB HL at octave frequencies between 500 Hz and 8 kHz. The authors served as two of the subjects (S2 and S3) and had experience in psychoacoustic measurements. The remaining two listeners had no previous experience. A training period, typically lasting three or more 1.5-h sessions, was provided in which masked and absolute modulation thresholds were estimated using procedures similar to those described in the following. Further training was provided for the roving-level and equal-envelope-energy (EEE) conditions (see the following). Data collection began when thresholds for a subject stabilized; there were typically no learning effects observed after four to five tracks on a given condition. The listeners became familiar with the different stimulus conditions, and were aware of the particular condition prior to the start of a track.

Masked SAM detection thresholds were obtained using an adaptive two-interval, two-alternative forced-choice (2I, 2AFC) procedure with a two-down, one-up stepping rule that estimated the modulation depth necessary for 70.7% correct detection (Levitt, 1971). This combination of parameters resulted in a threshold estimate that corresponded to a d' of about 0.8. In the randomly chosen target interval, the signal modulation was imposed along with a masker modulation on the tone carrier. The standard interval contained only the masker modulation. The signal modulation depth m at the beginning of a track was set well above threshold, and was varied initially by 3-dB steps (in $20 \log m$), and in steps of 1.5 dB after the first two reversals. The tracking procedure was run until 16 reversals were obtained; threshold for a given track was taken as the mean modulation depth of the last ten reversals. For each stimulus condition, thresholds presented here are the mean of four such estimates. Only tracks in which the standard deviation of the last ten reversals was less than 3 dB were included in further analysis. Across-subject average data are presented as the mean and standard deviation of the 16 threshold estimates (4 listeners $\times 4$ tracks per condition).

2. Apparatus and stimuli

Subjects listened diotically through calibrated Sennheiser HD 580 headphones while seated in a sound-treated booth. Stimuli were digitally generated at a sampling rate of 48.828 kHz and converted to analog signals via the TDT System III two-channel real-time processor (RP2.1) digital-to-analog converter and the TDT System III headphone buffer (HB7), with its gain set to −27 dB (to eliminate background noise). Signals were generated and presented with visual feedback using MATLAB. Noise waveforms were saved for both intervals on every trial (by recording random-number-generator seeds) so that the exact stimuli could be reconstructed for *post hoc* analysis (see Sec. III A 3).

The two intervals were each 600 ms in duration including 50-ms $\cos^2$ ramps, and were presented with a 500-ms interstimulus interval. Both the sinusoidal signal (always in sine phase) and the narrow-band Gaussian-noise masker modulation were applied to the envelope of a 2800-Hz tone carrier for the entire duration of the stimulus. The signal frequency was 64 Hz; the masker was centered on the signal frequency and had a bandwidth of 32 Hz. These parameters were chosen to satisfy several specific constraints. First, the modulation frequencies were low enough to avoid the introduction of audio-frequency spectral resolution cues that arise

when the sidebands generated by modulation are remote from the carrier frequency component. In addition, the bandwidth of the masker was wide enough to allow for the slower second-order (venelope) fluctuations to fall within a range that could potentially be detected in a 600-ms duration signal (the venelope energy was concentrated around 10 Hz). The AM signal and masker parameters were also influenced by modeling considerations, as described below.

Two statistically independent realizations of the masker were generated for the standard and target intervals. An additive approach, as opposed to the multiplicative one used in several related studies (Ewert and Dau, 2000; Ewert *et al.*, 2002; Houtgast, 1989), was used to combine the signal and masker. This allowed for more careful control of the envelope-frequency domain magnitude spectrum (i.e., addition of time-domain waveforms results in the addition of their frequency-domain spectra, whereas multiplication of time waveforms is equivalent to a convolution of their frequency spectra). The equation for the stimuli in both intervals is

$$s(t) = c\{\sin(2\pi f_c t)[1 + m\sin(2\pi f_m t) + M(t)]\},$$

where f_c is the carrier frequency, m is the stimulus modulation depth (zero in the standard interval), f_m is the signal modulation frequency, and $M(t)$ is the masker waveform (zero when measuring absolute thresholds). Masker level was defined in terms of the rms of $M(t)$. The compensation factor c was included so the overall power in both intervals was equivalent to that of a 65-dB SPL pure tone. Every stimulus was checked for over modulation caused by the stochastic nature of the narrow-band maskers; no envelope with a modulation index greater than one was presented to the listeners.

3. Conditions

The acoustic stimuli used in this experiment were similar to those described in Ewert *et al.* (2002). Different parameter variations, as well as minor procedural modifications, distinguish the two studies. Ewert *et al.* (2002) focused on frequency effects (of both signal and masker). Here, we explicitly considered the effect of masker level (i.e., the masker rms modulation depth) and the consequences of systematically controlling the availability of envelope-detection cues. Thresholds for three conditions were measured: (1) SAM detection with a fixed-level modulation masker, (2) SAM detection with a random 10-dB within-trial rove in masker level, and (3) SAM detection with EEE in the standard and target intervals (after the signal was added). The roving-level condition effectively made envelope energy an unreliable cue; the EEE condition strongly attenuated first-order envelope energy differences as a cue for detection. Thresholds from the fixed-level condition provided a baseline for evaluating the consequences of these two manipulations. Note that the fixed-level condition was comparable to those of previous studies (i.e., Ewert *et al.*, 2002).

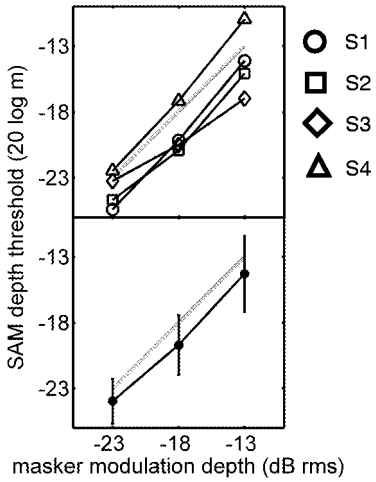

FIG. 1. Individual (top panel) and mean (bottom panel) masked-SAM detection sensitivity. Thresholds at these supra-threshold masker depths increased at a rate of about 1 dB ($20\log m$) per 1 dB (masker rms); the dashed lines in the two panels serve as a reference with a 1 dB/dB slope. Signal f_m=64 Hz; masker bandwidth=32 Hz, centered on signal frequency; SPL =65 dB; carrier f_c=2800 Hz; duration=600 ms. Standard deviations of individual listener threshold estimates were between 2 and 4 dB (error bars omitted for clarity).

B. Results and discussion

1. Fixed-level modulation masker

General trends in the results were similar across the four listeners, but individual sensitivity varied considerably in the masked-AM detection task. Both individual (upper panel) and mean thresholds (lower panel) are shown in Fig. 1 for the detection of a 64-Hz sinusoidal modulation in the presence of an additional masker modulation. The masker had a bandwidth of 32 Hz, and was always centered on the signal frequency. Signal thresholds are shown for a 10-dB range of masker modulation depths.

Thresholds increased monotonically as the masker level increased over this range of masker depths. Listener S4 was less sensitive than the other three subjects, while the thresholds of Subject S3 increased at a rate less than 1 dB/dB. Mean thresholds were 1–2 dB ($20\log m$) lower than the masker modulation depth (dB rms), and increased with a slope of 1 dB/dB. These results are consistent with those of Houtgast (1989), who measured detection thresholds for an 8-Hz sinusoidal signal modulation in the presence of a 2.8 -Hz bandwidth masker modulation. In contrast with the present study, Houtgast (1989) combined the signal and masker multiplicatively and imposed them on a noise carrier.

Somewhat less intuitive are the patterns of thresholds measured for lower-level maskers. In efforts to map out the entire range of masker modulation depths that produced masking while still avoiding overmodulation, for the purpose of the roving-level experiment (to follow), it became clear that some of the listeners' masked thresholds were *lower* than their pure AM-detection thresholds. This "facilitation" is illustrated in Fig. 2 in the form of nonmonotonic threshold versus masker level functions for two of the four listeners (S2 and S3). The thresholds for the three right-most points in each function are replotted from Fig. 1. Unmasked detection thresholds ranged from −25 to −30 dB (masker level=

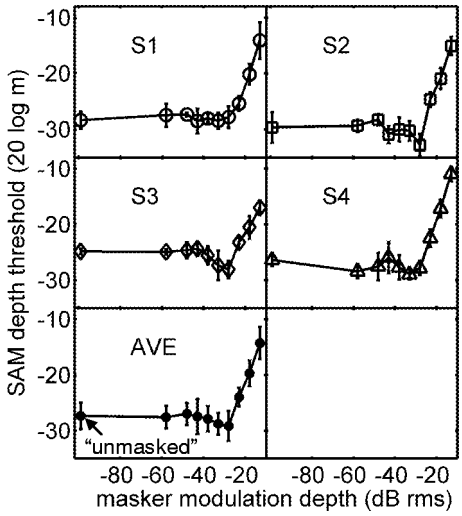

FIG. 2. Masked-detection thresholds for a wide range of masker modulation depths. Two of the listeners (S2 and S3) exhibited a nonmonotonic dependence of sensitivity on masker level; their thresholds were lower for a masker level of −28 dB than in the unmasked condition. The three right-most points in each panel are replotted from Fig. 1; these masker levels consistently caused "positive" masking without causing overmodulation.

−99 dB rms; left-most point on each plot), and were consistent with previously reported pure-tone SAM detection thresholds for comparable f_c, f_m, and SPL (i.e., Kohlrausch *et al.*, 2000). The external variability of the noise maskers began to influence thresholds between −40 and −30 dB rms. The presence of the region of facilitation was not related to absolute sensitivity to AM; the two subjects that exhibited the clearest facilitation had the lowest (S2) and highest (S3) thresholds in unmasked AM detection. In addition, the masker level that resulted in the most facilitation was the same for both listeners (−28 dB rms).

Strickland and Viemeister (1996) and Bacon and Grantham (1989) reported facilitation in some of their tone-on-tone modulation masking conditions, when the frequency of the masker was well below that of the signal. They accounted for this type of negative masking by assuming that their listeners were able to attend to the valleys of the masker when its fluctuations were slow enough, resulting in a temporally localized larger effective modulation depth. The facilitation illustrated in Fig. 2 is fundamentally different: the masker and signal occupy the same frequency region, and inherent fluctuations in the narrow-band masker made the timing of its valleys unpredictable to our listeners. Also, the negative masking effects in previous studies increased as the masker modulation depth increased; the effect observed in the current study is only measurable at very low masker depths (near or even below detection thresholds). Potential mechanisms underlying on-frequency, low-level noise-masker facilitation will be evaluated in Sec. III.

2. Roving-level modulation masker

The effect of introducing a random 10-dB within-trial rove in masker level on listeners' thresholds is shown in Fig. 3. Because the masker modulation depth was different in every interval, it was necessary to track on the level of the signal with respect to the level of the noise (i.e., the difference between the two in dB). Detection thresholds are plotted for a fixed-level (−18 dB rms) noise masker (filled bars) and for the roving level (uniformly distributed from −23 to −13 dB rms) noise masker (open bars). Individual and across-subject average thresholds are included in the figure.

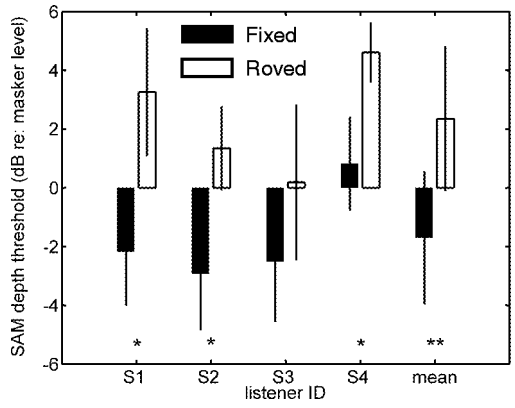

FIG. 3. Comparison of fixed-level thresholds at a masker depth of −18 dB (closed bars) and roving-level thresholds, where the masker depth was randomly chosen from a uniformly distributed 10-dB range centered on −18 dB (open bars). Asterisks indicate cases where the difference between the fixed- and roving-level thresholds was significant ($^{*}p<0.02$; $^{**}p<0.0001$).

In general, thresholds in the roving-level condition were 3–5 dB higher than those in the fixed-level case. The effect was significant (t-test, $p<0.02$) for three of the four individual listeners, and highly significant ($p<0.0001$) when the across-subject mean and variance was considered. The 10 -dB rove in masker level increased the mean thresholds by 4 dB. Unfortunately, the small dynamic range of AM maskers precluded the use of larger rove ranges in the present study (i.e., the masker must be intense enough to cause masking, but not so strong as to result in overmodulation, especially in the signal interval). Despite the limitations, the significant effect of this relatively small rove range contrasts with results from audio-frequency TIN detection experiments, where even a 32-dB rove in masker level did not significantly affect listeners' thresholds (except at the narrowest bandwidth tested, Kidd *et al.*, 1989). The convincing results of Kidd *et al.* (1989) provide a critical test that challenges the power spectrum model of masking in the audio-frequency domain. Qualitatively, models which assume the long-term energy of the (ac-coupled) envelope as the perceptually relevant quantity (e.g., Viemeister, 1979; Ewert and Dau, 2002) are not seriously challenged by the current results obtained with the roving-level modulation masker. A more careful analysis of this general statement is provided in Sec. III.

3. Equalized-envelope-energy modulation masker

As an alternative approach to test energy-based models, (long-term) first-order envelope cues were *removed* by forcing the rms modulation depth of the standard and target intervals to be the same, regardless of the level of the signal (in $20 \log m$). The task was the same as in the fixed-level and roving-level condition: listeners chose the interval containing the sinusoidal signal modulation. Pure long-term energy de-

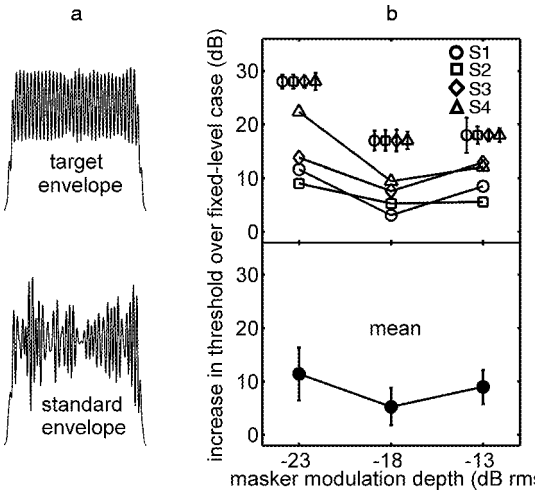

FIG. 4. Effect of equalizing the overall modulation depth in the two observation intervals after the signal was added. (a) Example wave forms: masker depth=−13 dB rms; signal added to target interval masker at a +20 dB SNR. (b) Increases in thresholds over comparable fixed-level conditions (absolute thresholds are shown along with model predictions in Fig. 7). Individual listener standard deviations are shown above the corresponding means [(b), top panel].

cision statistics did not provide any cues for detection in this paradigm (as long as the masker bandwidth was within the passband of the envelope-filtering process). Overmodulation was not an issue in the EEE condition: the average depth in both standard and target intervals was determined by the depth of the masker-alone modulation. Qualitatively, the signal-interval envelope fluctuations became more sinusoidal as m increased (but the overall rms modulation depth was the same in both the standard and target envelopes).

Example waveforms for a −13-dB rms standard depth are illustrated in Fig. 4(a) along with individual listener and mean thresholds for a 10-dB range of masker-alone modulation depths [Fig. 4(b)]. Note that absolute thresholds are not plotted in Fig. 4; instead, increases in threshold over the corresponding fixed-level masker condition are shown. The key result illustrated in Fig. 4 is that the listeners were able to perform the task, although measured thresholds were about 10 dB worse on average than in the fixed-level condition (in which the overall rms modulation depth was allowed to naturally vary across intervals). Perhaps the most striking aspect of the individual thresholds is the high variability both within and across listeners (note the expanded scale of the y axis). Anecdotally, the task became considerably more difficult in the EEE condition, and listeners reported the use of a very different strategy compared to that employed in the fixed-level case. The following sections quantitatively explore potential cues that could explain thresholds in all three masker configurations (fixed-level, roving-level, and EEE).

III. MODELING

A. Methods

1. Simulating threshold runs

Masked-detection thresholds were determined for each assumed DV using the same procedure, stimuli, and conditions as described in the psychophysical methods. The mean and standard deviation of 16 estimates were obtained (for comparison to the 4 subjects × 4 repetitions measured psychophysically). Only the steady-state portion of the envelope (the central 500 ms) was used to compute decision statistics.

Several DVs were calculated from the Hilbert envelopes of the stimuli and used in simulated tracking procedures: (1) rms ac-coupled envelope energy, (2) average local modulation depth, (3) average rate of model IC cell, (4) crest factor, (5) maximum local modulation depth, and (6) max/min ratio. The first three DVs can be considered "long-term," as they are based on an integrated representation of the entire steady-state envelope. The remaining three statistics assume that short-term fluctuations are salient perceptual cues in the masked modulation-detection task.

DVs based on local modulation depths [(2) and (5) in the list above] were calculated from a running ratio of the ac to dc envelope energy in each cycle of the signal modulation. More specifically, the max/min ratio was computed for every cycle of the steady-state envelope, and divided by the mean value of the envelope for that same time period. From the resulting 32 points (500 ms of a 64-Hz signal), an average value was computed (in the case of the average local depth DV), or the maximum value was extracted (for the maximum local depth DV).

Because the envelope-frequency spectra of the stimuli were always within the passband of a 64-Hz modulation bandpass filter and a modulation low-pass filter with a cutoff frequency of 150 Hz, there was no filtering applied to the Hilbert envelopes before determining the signal-based decision statistics. In this respect, predictions based on the model IC cell average rate are different from the others: rate MTFs of simulated IC neurons are bandpass. Again, this difference has very limited consequence for the stimuli presented in this study (but see EEE predictions). Only the cell tuned to the signal frequency (64 Hz) was considered. Implementation details for the physiological model were the same as in Nelson and Carney (2004), except the convolution of alpha functions and instantaneous rate functions was carried out in the frequency domain for computational reasons (see website for code: web.syr.edu/~lacarney). Model parameters were matched to those describing the cell in Figs. 8(c), 9–11 in Nelson and Carney (2004), except the auditory-nerve (AN) characteristic frequency (CF) was set to the stimulus carrier frequency (f_c=2800 Hz), and the strength of inhibition (re: excitation) at the level of the IC model cells ($S_{\mathrm{IC,INH}}$) was set to 1.1. Also, the stimulus presentation level was set to 24 dB SPL for simulations with the model IC cells. This SPL resulted in near-maximal synchrony at the level of model AN fibers (compared to responses at other SPLs), which translates into higher rates in model IC cell responses. Similar responses would be expected from off-CF AN fibers for stimuli presented at higher SPLs [e.g., Joris and Yin (1992), their Fig. 8(c)]. The decision to use low-SPL stimuli as inputs to the physiological model carries with it an assumption that the central nervous system is able to weight responses from peripheral channels that are least affected by saturation and/or compression. Such assumptions are at least indirectly supported by psychophysical work that shows improvements in modulation detection performance as the overall SPL is

increased (i.e., Kohlrausch *et al.*, 2000) despite the fact that saturation and compression are likely to be affecting near-CF responses.

Since the stimuli were deterministic, it was necessary to limit model performance in conditions without a masker (pure AM detection, or a masker level of −99 dB) by adding a Gaussian random variable to the final values of the decision statistics in each interval. The variance of this noise was adjusted to yield pure SAM detection thresholds of about −27 dB, and was held constant for all of the experimental conditions once it was determined.

2. Ruling out some potential cues

Several DVs were unable to predict trends or absolute thresholds comparable to those of the listeners in any of the masked-AM detection conditions (except at the lowest masker depths, where the task is essentially pure AM detection). Because of their poor performance in general, simulations based on skewness (the third central moment of the envelope amplitude distribution), kurtosis (the fourth moment), and venelope fluctuations are not included in the figures presented here. Predicted thresholds based on these three DVs were too high, often immeasurable, and also highly variable across the 16 estimates. The skewness of the point-by-point envelope distribution did not reliably change when the sinusoidal signal was added for any of the noise levels in this task. Values of venelope standard deviation and kurtosis consistently decreased when the tone was added, but only at modulation depths much higher than the listeners' thresholds.

Another decision statistic that was unable to predict performance in the current set of experiments was one based on a quantification of the instantaneous frequency (IF) of the envelope time waveform. A noise-alone modulated carrier would be expected to have higher variability in its envelope IF than that of a tone-plus-noise-modulated carrier. The bandwidth of the modulation maskers (32 Hz), along with external stimulus variability and the use of relatively low modulation depths, made envelope IF an unreliable cue for SAM detection in the present study. Tracking simulations based on a target-interval drop in envelope IF variance resulted in predicted thresholds that were highly variable across tracks and higher than the listeners' thresholds.

Several recent studies have used a cross-correlation calculation between a template response derived at some suprathreshold signal level and the "current" stimulus representation as a method to quantify model responses and predict psychophysical thresholds (i.e., Dau *et al.*, 1997a, b; Ewert and Dau, 2004). This technique is optimal in the sense that the signal is assumed to be known exactly, both in terms of its magnitude and phase, and has been shown to reasonably predict performance in a wide variety of psychoacoustical experiments, including modulation detection and modulation masking (Dau *et al.*, 1997a, b; 1999). Accounting for performance with such an optimal strategy comes at the expense of being able to identify the specific perceptually relevant features of the stimulus or response. As such, a correlation-based DV is fundamentally different from the other DVs considered in this study. It is interesting to point out that a template-based approach predicts no effect of masker-depth-roving or energy-equalization (simulations not shown). Furthermore, the templates for all three masker conditions (averaged over many noise tokens) are essentially identical: the sinusoidal signal is the only portion of the stimulus that remains after averaging many repetitions of the signal-plus-noise waveform. This aspect of the cross-correlation model contrasts with the tracking simulations and qualitative listener comments that all point to the use of a different cue in the EEE conditions as compared to the fixed-level and roving-level masker conditions.

3. Trial-by-trial response analysis: Decision-variable-reconstructed psychometric functions

The ability of a given decision statistic to track on realistic detection thresholds is necessary but not sufficient as a requirement for concluding that listeners are using the cue on a trial-by-trial basis. To further test each potential cue, several key conditions were analyzed by comparing the values of different DVs that were derived from the exact stimuli presented to the listeners during the tracking procedure. The first step in this analysis (which required no additional time of the listeners) was to save the standard and target interval waveforms as the listeners performed the 2I,2AFC task (in practice, only the MATLAB random number generator seeds were saved). To recreate the stimuli presented during the track, the only other variables needed were the modulation depths of the signal and masker in both intervals, and the masker-level configuration (i.e., fixed, roved, or equal-energy).

The logic behind the decision-variable-reconstructed psychometric (DVRP) functions was as follows: if listeners were using the assumed DV as a primary cue, then their performance should have systematically depended on the magnitude of the difference between the DVs calculated from the two intervals. If there was no difference, performance should have been at chance; for big differences, performance should have been near 100% correct. When percent correct was plotted as a function of the difference in DVs (target interval DV–standard interval DV), two shapes of the DVRP function were possible if the DV was salient and being consistently used by the listeners: monotonically increasing with high values of percent correct at large positive differences, and monotonically decreasing with the best performance when the difference between the target and standard DV was negative (i.e., the presence of the tone modulation was consistently signaled by a *lower* value of the DV). In general, the sign of the slope of the function indicated whether the signal interval corresponded to the higher or lower value of the DV.

Three representative masker conditions were analyzed with DVRP functions: (1) fixed-level masker (−18 dB rms), (2) roving-level masker (chosen from a uniform distribution from −23 to −13 dB rms, and (3) EEE masker (masker-alone depth of −18 dB rms). To generate each function, responses were combined across the four listeners and four tracks per condition. This resulted in approximately 80 observations per point in each function [16 tracks × ~50 trials per track/10 points (bins) per function]. The spacing of con-

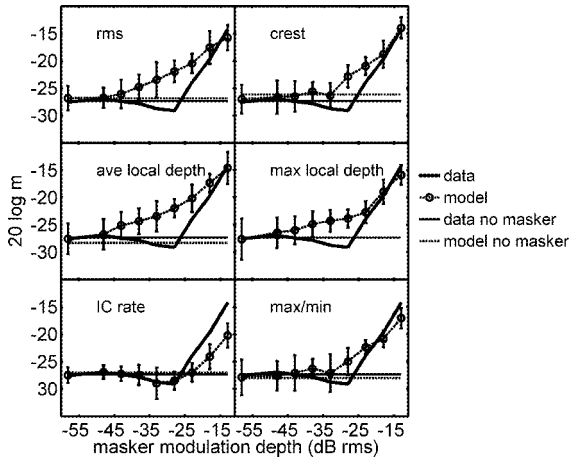

FIG. 5. Model thresholds from simulated tracks based on six DVs (o), along with the listeners' fixed-level data from Fig. 2 (solid lines, no symbols). Unmasked (pure) SAM detection thresholds are shown with the solid horizontal lines. Unmasked model thresholds (thick dashed lines) were set by adding a fixed-variance internal noise to the DV in each interval. Predictions based on long-term DVs are shown in the left column; local temporal features were included in the simulations summarized in the right column.

secutive points was not fixed; instead, a fixed number of responses were placed into unevenly spaced bins. There was no internal noise introduced to construct the DVRP functions; external stimulus variability was the only random factor included.

B. Results and discussion

1. Fixed-level modulation masker

Predictions for each of the decision statistics along with the average listener thresholds for the fixed-level masker condition are shown in Fig. 5. The solid horizontal line in each panel indicates the listeners' mean threshold with no masker. Dashed lines without symbols in Fig. 5 show corresponding unmasked detection performance for each tested cue, which was determined in the simulations by a fixed-variance noise added to the DVs.

First, consider the simulated thresholds in the left column of Fig. 5. These DVs (envelope rms, average local modulation depth, and IC cell average rate) make up the subset of the "long-term" statistics that predict performance broadly consistent with that of the listeners. However, each of them has shortcomings, even in this straightforward fixed-masker-level task (in which no detection cues have been manipulated). Average local depth and rms thresholds were almost identical (this is also true for the roving-level and equal-energy conditions), and suffered the same inconsistencies with the data. Specifically, the external variability of the stimulus caused increases in threshold at masker depths considerably lower than in the data. As a result, predicted thresholds based on envelope rms and average local depth were higher than the listeners' thresholds in the observed "dip" around −30 dB rms. Because the slope of the function was lower in the rms and average depth predictions than it was in the data, the curves reconverged at the highest masker levels tested.

Thresholds based on the average firing rate of a model IC cell are shown in the bottom row of the left column in Fig. 5. This threshold-masker level function distinguishes itself from any of the signal-based DV predictions in two important respects. First, the IC model correctly predicted a nonmonotonic dependence of signal sensitivity on masker modulation depth. Second, simulated thresholds were *lower* than the data at masker depths above −23 dB. The nonmonotonic shape was a direct result of the "hard" modulation-depth threshold that arises from the strong inhibitory inputs present in the model cell. In the absence of any internal noise or external signal variability, the model IC cell did not respond until the signal modulation depth was above ~−32 dB. This value was set by the strength of inhibition relative to the excitation: stronger inhibition results in higher thresholds. When an appropriate amount of noise was added to the sinusoidal signal (i.e., at a masker modulation depth of −28 dB rms), the instantaneous modulation depth rose above this hard threshold more often than it did with an equal-amplitude signal in "quiet," resulting in lower detection thresholds and a pronounced dip in the threshold-masker level function. At higher masker modulation depths (>−23 dB rms), the external variability of the masker swamped out this subtle effect. The fact that the absolute values of thresholds at these higher masker levels were lower in the simulations than in the data does not represent a fatal flaw. In fact, the inclusion of a Weber-fraction-type noise (i.e., one that is proportional to the stimulus or its response, see Ewert and Dau, 2004) would improve the match between model and data at these masker depths. The fit between other DVs and the data would not be improved by including this multiplicative type of internal noise because they predicted thresholds higher than the data, even with "fixed-variance" internal noise alone.

Local temporal features were incorporated in the simulated thresholds shown in the right column of Fig. 5. In general, the fit to the data was slightly better for these DVs than the other signal-based statistics: the overestimation of thresholds in the data's shallow notch was less severe, especially for the crest factor and max/min DVs. In a sense, it was surprising that predictions based on only two points of the modulating waveform (i.e., the max/min statistic) were more consistent with the listeners' performance than traditional long-term (rms) measures. Ewert and Dau (2002) showed that a pure long-term cue could account for several trends in the frequency effects of modulation masking, using a masker modulation depth of −10 dB rms. Interestingly, at comparable masker levels in the present study, long-term and local feature cues were all reasonable predictors of modulation detection thresholds (i.e., model thresholds were either similar to or lower than the data). From the thresholds measured here across the range of low masker depths, it seems fair to conclude that predicted performance based on DVs that incorporated temporally local features were as consistent with the listeners' performance as rms (time-averaged) cues. Implementation of the physiological model suggested a mechanism (namely, a modulation-depth threshold nonlinearity) that could be incorporated into models for envelope

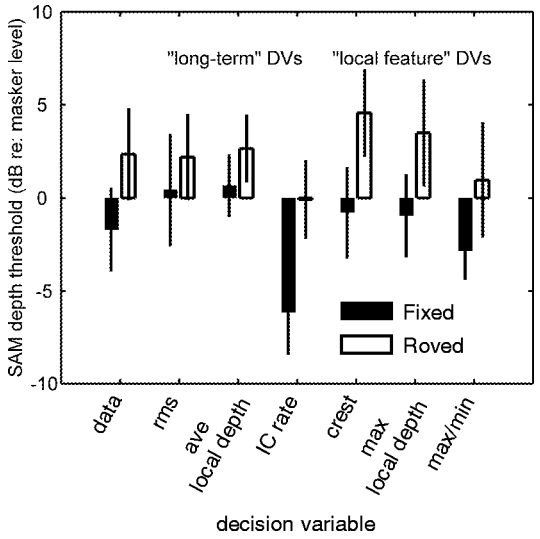

FIG. 6. Roving-level masker simulations and comparison with listeners' mean data. The format is the same as Fig. 3, but the thresholds of different DVs are shown instead of the performance of different listeners.

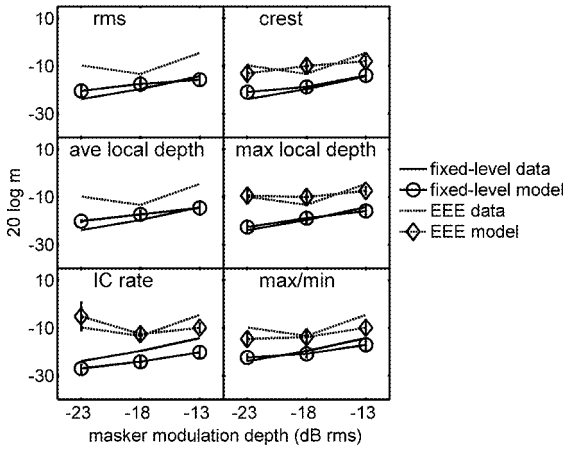

FIG. 7. Comparison of measured thresholds (lines with no symbols) and predicted thresholds (connected symbols with error bars) for EEE (dashed lines) and fixed-level conditions (solid lines). DVs are arranged as in Fig. 5. If a given combination of DV and masker condition resulted in overmodulation or tracks that did not converge, simulated thresholds were not plotted (this occurred with the rms and average local depth DVs in EEE conditions).

processing to account for the nonmonotonicity observed in the listeners' threshold-masker level functions.

2. Roving-level modulation masker

When the masker modulation depth was randomly chosen from a 10-dB uniformly distributed range of values centered at −18 dB rms on a trial-by-trial basis, mean psychophysical thresholds increased by about 4 dB over the −18 -dB fixed-level condition (Fig. 3). We can ask the simple question: how much are thresholds based on these different DVs affected by the same manipulation? Figure 6 answers this question by comparing the fixed-level and roving-level thresholds for each DV (the listeners' mean data are replotted from Fig. 3 at the far left). The simulated thresholds for fixed-level conditions in Fig. 6 are identical to those illustrated in Fig. 5 at a masker modulation depth of −18 dB rms, but replotted as a signal-to-noise ratio (SNR) for direct comparison to the roving-level condition, where the SNR was the tracking variable. Simulations using long-term DVs are represented in the first three columns to the right of the mean data. Thresholds with various combinations of local features included are shown in the last three pairs of bars.

Two aspects of the simulations are worth noting. First, all six of the tested DVs were affected by an amount that was consistent with the effect seen in the data: thresholds were increased by 2–6 dB when the masker level was roved. Also, thresholds based on the model IC cell's average firing rate were lower than those obtained with the signal-based statistics. Again, this is not a serious failure of the physiological model. The inclusion of a second noise source, proportional to the magnitude of the stimulus or response fluctuations, would increase thresholds at these (relatively high) masker modulation depths, while maintaining the difference between the fixed-level and roving-level conditions. The other DVs would not benefit from such a modification (with the possible exception of the max/min statistic), as their predicted thresholds were at or above the actual data with a fixed-variance noise source alone.

Despite the subtle differences between the effects predicted by the different DVs, the variability of the threshold estimates with respect to the small observed threshold elevation does not allow for strong conclusions supporting or disputing the validity of a specific DV in the roving-level task. The use of a larger rove range would have potentially produced more pronounced effects that could have critically tested the different DVs; unfortunately, the limited dynamic range that was available in the amplitude-modulation domain for this manipulation did not allow for definitive answers to these questions. In our paradigm, only masker modulation depths that clearly caused masking while also avoiding overmodulation were used.

3. Equalized-envelope-energy modulation masker

Predictions based on each of the tested DVs for the EEE conditions are compared to listeners' thresholds in Fig. 7 (dashed lines). The fixed-level thresholds are also replotted (solid lines) to provide a baseline for comparison to the EEE thresholds. Actual data are shown in each panel without symbols or error bars; DV predictions are shown with symbols and error bars (◇=EEE; ○=fixed-level). By definition, rms and average-local-depth metrics were unable to track on thresholds in the EEE conditions (the signal-plus-noise modulation depth was adjusted to have the same long-term rms depth as the corresponding noise-alone interval).

The only long-term DV that was able to consistently track on a reasonable signal level at threshold was the firing rate of a model IC cell. The predictions of the physiological IC model were comparable to the listeners' thresholds at masker depths of −18 and −13 dB rms. However, the IC model predicted that the difference between fixed-level and EEE thresholds should decrease with masker depth. This was not observed in the data. The fact that the IC rate DV could predict EEE thresholds at all was a result of the effective bandpass envelope filtering that preceded the decision device. Although the bandwidth of the stimuli was within the passband of the filter (the half-rate Q value is about 1, cor-

responding to a 64-Hz passband for the cell tuned to the signal modulation frequency), the resulting output spectra were nevertheless shaped by the cell's modulation-tuning properties. There was less attenuation of the energy concentrated near the peak of the modulation filter, so target-interval stimuli in the EEE conditions could elicit a larger response (higher firing rate) than the standard-interval stimuli. A similar effect would be expected for a rms DV following any realistic envelope bandpass filtering process. Still, such a cue did not predict the appropriate variation in EEE thresholds with masker depth, and the absolute difference between fixed-level and EEE thresholds was higher than observed in the data. The use of an invariant cue across all conditions was also not consistent with listeners' anecdotal reports suggesting that their strategy was very different between the fixed-level and equal-energy conditions.

The DVs that were the best predictors of the listeners' EEE data were those based on local temporal envelope features (Fig. 7, right column). Max/min, crest factor, and max local depth all accounted reasonably well for the difference in performance between the fixed-level and EEE thresholds as well as the absolute values of the thresholds and the higher variability associated with the EEE data. Importantly, the decision rule had to be switched for these three statistics: simulations selected the interval with the larger value of the DV in fixed-level conditions and the interval with the smaller value in EEE conditions as the target interval. This sign-flipping was qualitatively consistent with subjective accounts from the listeners that they had developed a different strategy (based on feedback) in the EEE paradigm: often the "smoother" or "more regular" envelope was reportedly chosen as the signal interval. Given this, the success of the local feature statistics in predicting the data was somewhat surprising, since the calculations were all heavily weighted by a small temporal portion of the envelope waveform. Nevertheless, the match to the data was quite good, and it was clear that the most straightforward way to account for the listeners' performance in the EEE conditions was to incorporate information about local fluctuations into the decision device. The finding that local temporal features were crucial for explaining the EEE data was different than the conclusions drawn from analogous audio-frequency energy-equalized TIN detection tasks (i.e., Richards and Nekrich, 1993), in which the overall flattening of the (long-term) envelope when a tone was added could explain performance consistent with that of the listeners. The corollary cue in the current experiment would be a drop in the (long-term) venelope energy, which we determined to be incapable of predicting performance consistent with the listeners.

4. Decision-variable-reconstructed psychometric functions

As an alternative method to compare and contrast different DVs (beyond predicting thresholds), we analyzed trial-by-trial decisions made by the listeners and considered how those choices correlated with the magnitude and direction of variation in each DV between the two stimuli presented to the listener. Figure 8 shows DVRP functions for three masker conditions and six DVs. The masker modulation

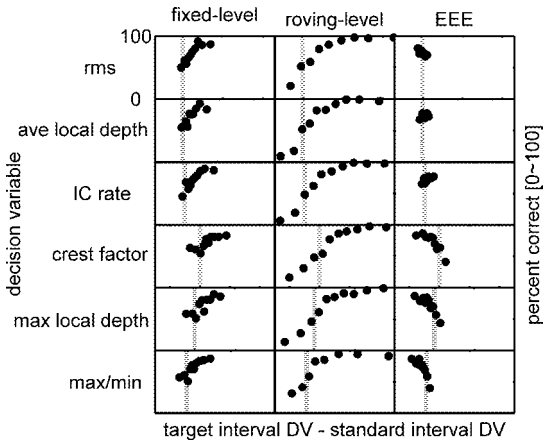

FIG. 8. Decision-variable-reconstructed psychometric functions for six DVs and three key masker configurations: fixed-level (−18-dB masker depth; left column), roving-level (masker depths randomly chosen from a 10-dB range centered at −18 dB; middle column), and equal-envelope-energy (−18-dB standard-interval masker depth). The range of differences plotted for each DV was determined by the range covered in the roving-level conditions. The ranges were: envelope rms: [−0.07 0.23]; average local depth: [−0.004 0.013]; model IC cell rate: [−6 18]; crest factor: [−0.3 0.5]; maximum local depth: [−0.01 0.02]; max/min ratio: [−1.46 4.00]. Vertical dashed lines indicate the zero-difference point on the x axis.

depth for all of the conditions shown was nominally −18 dB rms (note that this value was randomly chosen from a 10 -dB range in the roving-level conditions, and was effectively attenuated in the target interval for the EEE conditions). Fixed-level results are contained in the first column; roving-level and EEE analyses are shown in the second and third columns, respectively. The vertical dashed line in each panel indicates the point where the target and standard DVs were the same (i.e., their difference was zero). The ordinate limits are set at 0 and 100% correct in each panel. The x axes are fixed for each DV; they were determined by the largest range of variation observed across the three conditions (usually the roving-level case; see the figure caption for exact values).

DVRP functions for the fixed-level condition (left column) can be placed in one of two categories. The first three DVs (ac-coupled envelope rms, average local depth, and IC rate) all showed a consistent increase in percent correct as the target interval DV became larger than the DV measured in the corresponding standard interval. Also, these three cues were typically not "confused" by the task: the vast majority of the trials resulted in a positive difference between target and standard DV.

The second group of statistics is made up of DVs based on local temporal features (crest factor, max local depth, and max/min ratio). Listeners' percent correct increased for positive differences (target DV > standard DV) as they did for the long-term statistics in the top three rows, but a higher proportion of trials resulted in standard-interval DVs that were larger than the target-interval DVs (>20%; represented by points to the left of the vertical dashed line). This confusion suggested that long-term DVs may have been more reliable cues in the fixed-level masker conditions, because they were less susceptible to changes in local features caused entirely by the stochastic nature of the maskers.

Roving-level masker DVRP functions (Fig. 8, middle

column) spanned a wider range of DV differences than fixed-level or EEE-masker conditions, as expected. Because the roving-level DVRP functions were qualitatively similar, none of the six DVs (Fig. 8, middle column) can be considered more or less consistent than any of the others in this paradigm. In about one-quarter of the trials, percent correct dropped below chance (50%) when the cue in the standard interval was bigger than that in the target interval for all six of the tested DVs. It would be possible for the functions to be symmetric about zero if the listeners recognized conditions where the level-roving caused such a reversal in cue direction. This was not seen in any of the DVRP functions; the listeners tended to choose the interval with the larger DV value, regardless of the particular random combination of standard and target masker level. The similarity of the DVRP functions for the roving-level results makes it difficult to point out one DV as being more consistent with the data. Similar conclusions were made with the roving-level threshold-tracking simulations (Fig. 6).

The target-interval rms modulation depth was normalized to match that of the standard interval in the EEE conditions. DVRP functions for a −18-dB EEE masker are shown in the right column of Fig. 8. Compared to the fixed- and roving-level cases, the spread of DV differences is highly compressed for rms, average local depth, and IC rate decision statistics (Fig. 8, top three panels, right column). This reflects the stimulus manipulation; the fact that there was any spread in the rms DVRP was because only the steady-state portion (the central 500 ms) of the stimulus was used to compute the DVs, while the entire duration of modulation was equalized in the stimuli presented to the listeners (including the onset and offset ramps). Still, there were no strong trends in the upper three EEE DVRP functions of Fig. 8: percent correct was nearly independent of the DV difference, which was always close to zero. The situation was different for the local-feature-based DVs (bottom-right three panels in Fig. 8). High signal modulation depths resulted in low values of crest factor, max local depth, and max/min ratio. The tracking simulations (Fig. 7) and DVRP functions suggested that listeners were using a drop in the value of a DV that incorporated some local feature; max/min ratio predicted absolute thresholds that were slightly closer to the listeners' thresholds than crest factor or max local depth.

Analysis of DVRP functions provided a different angle on the same question that was addressed with the tracking simulations; the consistency between the two approaches is reassuring. The technique is promising for pulling apart decision statistics in other psychophysical tasks that include external stimulus variability, especially those with competing DVs that are weakly correlated with one another. The procedure requires no assumptions to be made about internal noise, and no additional time from the listeners. Analysis of adaptive tracking procedure responses has previously been validated as an efficient and accurate way to extract psychometric functions (Dai, 1995); the current implementation simply considered statistics based on the actual stimuli presented, instead of the signal level, or modulation depth, presented in each trial. In the context of the current simulations, two specific and important pieces of information are reinforced with the DVRP functions. First, they reiterate the notion that the sign or direction of the cue flips in EEE conditions for the local-feature DVs with respect to the direction of the cue in fixed- and roving-level masker conditions. Second, the proportion of DV calculations that elicit a larger value in the standard interval in the fixed-level conditions is higher for the short-term DVs than for the long-term DVs.

IV. GENERAL DISCUSSION

The remainder of this article is divided into three parts. In the first section, potential mechanisms underlying specific features of the fixed-level results are further discussed. Directions for future work are then detailed. Finally, the key psychophysical and modeling results are summarized.

A. Negative masking

The nonmonotonic relationship between sensitivity and noise level apparent in two of the four listeners in the fixed-level masker condition (Fig. 2) can be interpreted as stochastic resonance (for a recent review, see Wiesenfeld and Jaramillo, 1998). There are (at least) two straightforward mechanisms that could underlie such an effect. One possible explanation is that the listeners used a nonoptimal criterion that remained constant across noise level [see Tougaard (2000) for an analysis of such an assumption]. This interpretation is less than satisfying for several reasons. First, the presence of the nonmonotonicity is not related to the listeners' pure AM-detection thresholds (with no masker). If the effect was simply an epiphenomenon of poor criterion placement, the two listeners whose data suggest stochastic resonance should have been less sensitive than the other listeners at low masker depths. Another problem with the poor-criterion explanation is related to the types of mistakes that such a mechanism would predict. In low-masker-level conditions, the fixed DV criterion is never reached, and as a result, the signal is never "perceived" as being present. The opposite is true for the high masker levels, where even the noise-alone DV distribution lies above the fixed criterion: the above explanation suggests that the signal should sound as though it is present on every trial. These bias-related observations are also inconsistent with subjective impressions given by the listeners, and they suggest that some other mechanism may underlie the stochastic resonance effects.

Another mechanism that can explain the nonmonotonicity in our data is based on a combination of weak signals and a threshold nonlinearity (i.e., Ward *et al.* 2002). If a system does not respond to a subthreshold periodic stimulus, the addition of noise may push the input amplitude above threshold at a mean frequency related to the periodicity of the weak signal. An example of such a system with an envelope (modulation-depth) threshold is the physiological model tested here (Nelson and Carney, 2004). The ability of such a simple model to account for the effect highlights the potential advantages of using physiologically motivated model front-ends when predicting psychophysics to gain insight into underlying mechanisms. In addition to modeling work, there is also direct physiological evidence suggesting that central auditory neurons respond in a way consistent with a

modulation-depth threshold device. Adding a low-level noise modulation to a sinusoidal AM can both enhance neural synchronization to the tone and increase average firing rate over responses to the SAM tone alone in the frog auditory midbrain (Bibikov, 2002). The negative masking effects observed in the current study are also likely related to similar psychophysical measures in cochlear implant listeners of masked (electrically stimulated) modulation detection thresholds (e.g., Chatterjee and Robert, 2001).

B. Future directions

A main focus of future work will be to quantitatively relate actual (as opposed to modeled) midbrain physiological responses to psychophysical performance in AM detection tasks. To date, the relative roles of timing (i.e., synchronization to the envelope) and average rate information as neural substrates for AM perception at low modulation depths (near behavioral thresholds) remain unclear. The rate versus timing debate can be thought of as a discussion of underlying neural DVs, similar to the classifications of signal-based DVs as long-term or local-feature-containing. It is typically assumed that information about AM is largely transformed into an average-rate-based scheme by the level of the IC (which is one reason we only considered the rate responses of our model IC cell here), but the majority of the data supporting that view comes from stimuli with high modulation depths (for a review, see Joris *et al.*, 2004). The fact that our listeners could perform the EEE task suggests that the local temporal structure of AM stimuli is available as a cue under certain conditions. To reconcile these inconsistencies, we are currently recording responses in the awake rabbit IC to both pure SAM and noise-masked SAM across a wide range of modulation depths (from −35 to 0 dB in 20 log m).

Another issue that deserves further study is the effect of including a "Weber-fraction noise," along with the fixed-variance internal noise that was used here to limit performance with deterministic stimuli. Existing data suggest that tone-carrier AM-depth discrimination sensitivities may be determined by a fixed-variance noise at low modulation depths and a noise that is proportional to the elicited response at high modulation depths (i.e., Ewert and Dau, 2004). Assuming that the listeners were using an overall depth-related cue, then the fixed-level masker SAM detection paradigm can be thought of as depth discrimination task, with both external and internal noise processes playing a role. At the highest masker depths tested (−13 dB rms), most of the DV-derived thresholds are at or below the listeners' data (Fig. 5), suggesting the need for an additional source of noise at high modulation depths. This is consistent with the findings from the AM-depth discrimination literature. To better account for all of the data presented here, it seems necessary to implement a model with a modulation depth threshold, along with some form of local feature detection and two types of internal noise (fixed-variance and Weber-fraction).

C. Summary

(i) SAM depth thresholds in an on-frequency masked AM-detection task were influenced by external stimulus variability at very low masker modulation depths (i.e., −40 to −30 dB rms). Negative masking, or stochastic resonance, was observed in two of the four listeners at masker levels around −30 dB rms (Fig. 2).

(ii) Roving the overall modulation depth (Fig. 3) or equalizing the long-term envelope energies (Fig. 4) from trial to trial both resulted in significant increases in threshold. These findings contrast with observations in comparable TIN detection tasks in the audio-frequency domain.

(iii) Tracking simulations showed that several competing DVs were able to qualitatively account for performance for the fixed-level (baseline) and roving-level masker conditions (Fig. 5).

(iv) Reconstruction of psychometric functions based on a variety of DVs revealed that long-term statistics (averaged across the entire stimulus duration) may have been more robust cues in the fixed-level condition than statistics based on local temporal features. This was inferred because of the larger proportion of trials that resulted in the standard interval DV being larger than the corresponding target interval DV when local features were assumed to be the primary detection cues (Fig. 8).

(v) Thresholds in the EEE conditions could only be accounted for with a "local feature" DV, as long-term cues were minimized by equalizing the overall energy of the standard and target envelopes, after the sinusoidal signal was added. Listeners apparently chose the interval with a lower max/min ratio, crest factor, maximum local depth, or some other local feature cue in these conditions (Fig. 7).

(vi) Implementing a physiologically motivated model structure and comparing predictions based on its rate responses to the fixed-level data showed that a hard modulation-depth threshold mechanism can predict negative masking at low masker depths. This suggests that such a nonlinearity could be included (along with an internal noise source) to limit performance in the absence of external variability in a more complete model of envelope processing (Fig. 5).

ACKNOWLEDGMENTS

This research was supported by NIH-NIDCD F31-7268 (P.C.N.) and NIH-NIDCD R01-01641 (L.H.C., P.C.N.). We thank Magdalena Wojtczak, Karen Doherty, Yan Gai, and the reviewers for helpful comments on earlier versions of the manuscript.

Bacon, S. P., and Grantham, D. W. (**1989**). "Modulation masking: Effects of modulation frequency, depth, and phase," J. Acoust. Soc. Am. **85**, 2575–2580.

Bibikov, N. G. (**2002**). "Addition of noise enhances neural synchrony to amplitude-modulated sounds in the frog's midbrain," Hear. Res. **173**, 21–38.

Chatterjee, M., and Robert, M. E. (**2001**). "Noise enhances modulation sensitivity in cochlear implant listeners: stochastic resonance in a prosthetic sensory system?," J. Assoc. Res. Otolaryngol. **2**, 159–171.

Dai, H. (**1995**). "On measuring psychometric functions: A comparison of the constant-stimulus and adaptive up-down methods," J. Acoust. Soc. Am. **98**, 3135–3139.

Dau, T., Kollmeier, B., and Kohlrausch, A. (**1997a**). "Modeling auditory processing of amplitude modulation. I. Detection and masking with narrow-band carriers," J. Acoust. Soc. Am. **102**, 2892–2905.

Dau, T., Kollmeier, B., and Kohlrausch, A. (**1997b**). "Modeling auditory

processing of amplitude modulation. II. Spectral and temporal integration," J. Acoust. Soc. Am. **102**, 2906–2619.
Dau, T., Verhey, J., and Kohlrausch, A. (**1999**). "Intrinsic envelope fluctuations and modulation-detection thresholds for narrow-band noise carriers," J. Acoust. Soc. Am. **106**, 2752–2760.
Derleth, R. P., and Dau, T. (**2000**). "On the role of envelope fluctuation processing in spectral masking," J. Acoust. Soc. Am. **108**, 285–296.
Ewert, S. D., and Dau, T. (**2000**). "Characterizing frequency selectivity for envelope fluctuations," J. Acoust. Soc. Am. **108**, 1181–1196.
Ewert, S. D., and Dau, T. (**2004**). "External and internal limitations in amplitude-modulation processing," J. Acoust. Soc. Am. **116**, 478–490.
Ewert, S. D., Verhey, J. L., and Dau, T. (**2002**). "Spectro-temporal processing in the envelope-frequency domain," J. Acoust. Soc. Am. **112**, 2921–2931.
Green, D. M. (**1983**). "Profile analysis. A different view of auditory intensity discrimination," Am. Psychol. **38**, 133–142.
Houtgast, T. (**1989**). "Frequency selectivity in amplitude-modulation detection," J. Acoust. Soc. Am. **85**, 1676–1680.
Joris, P. X., Schreiner, C. E., and Rees, A. (**2004**). "Neural processing of amplitude-modulated sounds," Physiol. Rev. **84**, 541–577.
Joris, P. X., and Yin, T. C. T. (**1992**). "Responses to amplitude-modulated tones in the auditory nerve of the cat," J. Acoust. Soc. Am. **91**, 215–232.
Kidd, G., Jr., Mason, C. R., Brantley, M. A., and Owen, G. A. (**1989**). "Roving-level tone-in-noise detection," J. Acoust. Soc. Am. **86**, 1340–1354.
Kohlrausch, A., Fassel, R., and Dau, T. (**2000**). "The influence of carrier level and frequency on modulation and beat-detection thresholds for sinusoidal carriers," J. Acoust. Soc. Am. **108**, 723–734.
Levitt, H. (**1971**). "Transformed up-down methods in psychoacoustics," J. Acoust. Soc. Am. **49**, 467–477.
Lorenzi, C., Berthommier, F., and Demany, L. (**1999**). "Discrimination of amplitude-modulation phase spectrum," J. Acoust. Soc. Am. **105**, 2987–2990.
Lorenzi, C., Simpson, M. I. G., Millman, R. E., Griffiths, T. D., Woods, W. P., Rees, A., and Green, G. G. (**2001b**). "Second-order modulation detection thresholds for pure-tone and narrow-band noise carriers," J. Acoust. Soc. Am. **110**, 2470–2478.
Lorenzi, C., Soares, C., and Vonner, T. (**2001a**). "Second-order temporal modulation transfer functions," J. Acoust. Soc. Am. **110**, 1030–1038.
Moore, B. C. J., and Sek, A. (**2000**). "Effects of relative phase and frequency spacing on the detection of three-component amplitude modulation," J. Acoust. Soc. Am. **108**, 2337–2344.
Nelson, P. C., and Carney, L. H. (**2004**). "A phenomenological model of peripheral and central neural responses to amplitude-modulated tones," J. Acoust. Soc. Am. **116**, 2173–2186.
Richards, V. M., and Nekrich, R. D. (**1993**). "The incorporation of level and level-invariant cues for the detection of a tone added to noise," J. Acoust. Soc. Am. **94**, 2560–2574.
Shofner, W. P., Sheft, S., and Guzman, S. J. (**1996**). "Responses of ventral cochlear nucleus units in the chinchilla to amplitude modulation by low-frequency, two-tone complexes," J. Acoust. Soc. Am. **99**, 3592–3605.
Strickland, E. A., and Viemeister, N. F. (**1996**). "Cues for discrimination of envelopes," J. Acoust. Soc. Am. **99**, 3638–3646.
Tougaard, J. (**2000**). "Stochastic resonance and signal detection in an energy detector—Implications for biological receptor systems," Biol. Cybern. **83**, 471–480.
Viemeister, N. F. (**1979**). "Temporal modulation transfer functions based upon modulation thresholds," J. Acoust. Soc. Am. **66**, 1364–1380.
Ward, L. M., Neiman, A., and Moss, F. (**2002**). "Stochastic resonance in psychophysics and animal behavior," Biol. Cybern. **87**, 91–101.
Wiesenfeld, K., and Jaramillo, F. (**1998**). "Minireview of stochastic resonance," Chaos **8**, 539–548.

Effects of age and sequence presentation rate on temporal order recognition

Peter J. Fitzgibbons
Department of Hearing, Speech, and Language Sciences, Gallaudet University, Washington, DC

Sandra Gordon-Salant and Sarah A. Friedman
Department of Hearing and Speech Sciences, University of Maryland, College Park, Maryland

(Received 30 August 2005; revised 18 April 2006; accepted 25 May 2006)

The experiments examined the ability of younger and older listeners to identify the temporal order of sounds presented in tonal sequences. The stimuli were three-tone sequences that spanned two-octave frequency range, and listeners identified random permutations of tone order using labels of relative pitch. Some of the sequences featured uniform timing characteristics, and the sequence duty cycle was varied across conditions to examine the relative influence of tonal durations and intertone interval on recognition performance across a range of sequence presentation rates. Other stimulus sequences featured nonuniform timing with unequal tone durations and intertone intervals. The listeners were groups of younger and older persons with or without hearing loss. Results indicated that temporal order recognition was influenced primarily by sequence presentation rate, independent of tonal duration, tonal interval spacing, or sequence timing characteristics. The performance of older listeners was poorer than younger listeners, but the age-related recognition differences were independent of sequence presentation rate. There were no consistent effects of hearing loss on temporal ordering performance. © *2006 Acoustical Society of America.*
[DOI: 10.1121/1.2214463]

PACS number(s): 43.66.Mk, 43.66.Sr [JHG] Pages: 991–999

I. INTRODUCTION

This paper describes the results of an investigation that examined the abilities of younger and older listeners to correctly identify the presentation order of sound in simple stimulus sequences. The specific experiments are part of an ongoing project designed to explore the hypothesis that aging is accompanied by a gradual decline in auditory temporal processing that can influence listeners' perception of both speech and non-speech sequential sounds. Studies of speech recognition have consistently found that many elderly listeners have difficulty accurately perceiving sounds sequences that have been temporally modified in some manner. This is particularly evident for speech sequences delivered at rapid presentation rates, as might result from either fast talking or time compression techniques applied to speech wave forms (Wingfield *et al.*, 1985; Gordon-Salant and Fitzgibbons, 1993; Vaughan and Letowski, 1997; Tun, 1998). For rapid speech, the observed age-related decline in recognition performance is frequently offered as supporting evidence for a class of cognitive theories which postulate that aging is accompanied by a generalized slowing of information processing within the nervous system (Salthouse, 1996).

While the above studies report age-related difficulties in understanding rapid speech, the underlying sources of the problem are not easily identified. Study of the problem is complicated in part by the inherent spectral and temporal complexity of speech sounds, especially the speech sequences that characterize sentence-length stimuli. Additionally, factors related to the semantic and syntactic structure of speech sequences, and age-related changes in hearing sensitivity, can each exert a significant influence on the accuracy of speech processing among elderly listeners. However, in terms of acoustic modifications, one general characteristic of rapid speech is the shortened durations of some or all of the component phoneme segments and pause intervals, along with corresponding suprasegmental changes in overall sequence tempo and rhythm. Thus, any age-related reductions in sensitivity to either the segmental duration changes or the sequential timing characteristics could contribute to the diminished ability of older listeners to process rapid speech. Consideration of this possibility prompted us to examine age-related changes in temporal sensitivity using a combination of simple and complex nonspeech stimulus patterns that mimic some aspects of sentence-length speech sequences.

Currently, psychophysical measurements collected with relatively simple stimuli indicate that aging can be an important factor contributing to diminished temporal sensitivity. Some of the evidence refers to threshold measurements for the detection of brief temporal gaps inserted between successive acoustic markers, either pairs of non-speech or speech sounds. Generally, the gap thresholds measured for older listeners are found to be larger than those of younger listeners, with the age-related threshold differences being larger when measured with acoustic markers that feature spectral disparities (Schneider *et al.*, 1994, 1998; Snell, 1997; Lister *et al.*, 2002; Pichora-Fuller *et al.*, 2006). In other temporal sensitivity tasks, older listeners are observed to exhibit a reduced ability to discriminate changes in the duration of simple sounds, or silent intervals inserted between pairs of simple speech or nonspeech sounds (Abel *et al.*, 1990; Fitzgibbons and Gordon-Salant, 1995; Lister *et al.*, 2002; Grose *et al.*, 2001; Lister and Tarver, 2004). Also, the age-related difficul-

ties observed for duration discrimination with simple stimuli appear to become more pronounced for tasks that utilize complex stimulus sequences. For example, in one such task, we presented sentence-length tone sequences and measured listeners' ability to discriminate changes in the duration of a single target sequence component, either a tone or an embedded silent interval (Fitzgibbons and Gordon-Salant, 1995). Younger listeners performed this task with relatively little difficulty, but older listeners exhibited discrimination performance that was substantially poorer than that measured previously for the same target component presented in isolation. In a related experiment with tone sequences (Fitzgibbons and Gordon-Salant, 2004), it was observed that older listeners exhibited a reduced ability to discriminate changes in the overall timing, or tempo, within multitone sequences. The diminished temporal sensitivity of older listeners with these stimulus patterns was most evident at faster sequence presentation rates, and for sequences that featured irregular timing characteristics.

These results of the different discrimination tasks with simple and complex stimulus patterns indicate that some aspects of auditory temporal processing may undergo changes with aging. However, results collected in temporal discrimination tasks may not be predictive of those observed in more difficult tasks, such as sequence recognition. For example, even with nonspeech stimuli the temporal thresholds associated with discrimination tasks and recognition tasks can be substantially different, as we observed in an earlier investigation of temporal order processing (Fitzgibbons and Gordon-Salant, 1998). This previous study used stimulus sequences consisting of three tonal components of equal duration presented contiguously, with sequence rate altered by covariation of the component durations. Different task conditions required listeners to discriminate random changes of tone order, and also to identify the random orders using labels of relative tone pitch (e.g., high, medium, low). Results for younger listeners in the study confirmed that the tone durations required for order discrimination were substantially shorter than those required for order identification. Presumably, the longer stimulus durations required for the order identification task reflect the added processing demands associated with the requirement to label each tonal component. Relative to the younger listeners, the older listeners in the study required much longer tonal durations to perform the order discrimination task. However, for order identification, the age-related performance differences were restricted primarily to sequence conditions with relatively rapid presentation rates, where the tone durations approached values required by the older listeners for order discrimination. Other investigations of sequential processing also report findings indicating that tasks involving temporal order judgments can be quite difficult for many elderly listeners (Trainor and Trehub, 1989; Humes and Christopherson, 1991).

It is noteworthy that the elderly listeners in our earlier study exhibited difficulty for temporal order recognition with faster sequence presentation rates, but not with slower sequence rates. This outcome suggests the existence of an age-related limitation in processing speed, rather than a general difficulty among elderly listeners in performing the task demands associated with component labeling, storing, and recalling of order information. However, other results reported by Trainor and Trehub (1989) point to a different conclusion. Their sequential ordering task required younger and older listeners to distinguish between two alternatives of a four-tone sequence that differed only by the temporal ordering of two tonal components. Older listeners in this study also exhibited impaired sequencing abilities, but the magnitude of the observed age effects appeared to be independent of stimulus presentation rate, or specific factors related to processing speed. Thus, the influence of sequence rate and the nature of the processing difficulty exhibited by elderly listeners on temporal ordering tasks remain unclear. The present investigation is undertaken to examine these issues by investigating the specific sequence factors that influence temporal order processing in younger and older listeners. Additional motivation for this investigation comes from the collective findings of earlier temporal order recognition studies, as reviewed in various reports (e.g., Divenyi and Hirsh, 1974; Pinheiro and Musiek, 1985; Trainor and Trehub, 1989). The earlier studies, conducted primarily with young listeners, indicate that temporal order recognition can be difficult, particularly for tasks that require the labeling of individual sequence items comprised of less familiar nonspeech sounds. However, one common finding from these studies was the observation indicating that the introduction of silent intervals between successive items in sequential stimulus patterns acted to enhance temporal order recognition (e.g., Aaronson *et al.*, 1971; Peters and Wood, 1973; Warren, 1974). The improved recognition performance associated with the presence of interitem silent intervals was generally attributed to the increased availability of processing time that listeners used to encode individual sequence items for later recall. Similar observations were made more recently by Wingfield *et al.* (1999), who reported that the insertion of interitem pause intervals within rapid speech sequences effectively enhanced recognition performance, particularly for older listeners.

Thus, it appears that stimulus manipulations which increase available processing time may be beneficial for listeners participating in sequence recognition tasks. Unfortunately, the concept of processing time is not well defined, and in terms of stimulus parameters, it could be associated with item durations, interitem temporal spacing, overall sequence presentation rate, or some combination of these factors. However, if slowed processing is associated with aging, then order recognition among elderly listeners should be affected by variations in sequence timing, or item durations, particularly under the time constraints associated with faster sequence presentation rates. The present experiments are designed to examine these potential stimulus effects on sequential processing by measuring order recognition in younger and older listeners using uniformly timed tonal sequences in which tone durations and intertone intervals are systematically varied across a range of sequence presentation rates. Other measurements are collected to determine if the effects of sequence presentation rate on temporal order recognition for uniformly timed tone sequences pertain as well to stimulus sequences with nonuniform tone intervals. These com-

parisons are of interest in part because some of our earlier observations (Fitzgibbons and Gordon-Salant, 2004) indicated larger age-related differences in discrimination performance for stimulus sequences with non-uniform timing characteristics compared to those with uniform timing. Additionally, the timing characteristics associated with many meaningful sound sequences, such as rapid speech, are inherently nonuniform. Last, for all testing, we investigated the possible interactive effects of listener age and sensorineural hearing loss on temporal order recognition performance. Toward this end, performance was compared across four groups of listeners, who were matched according to age and degree of hearing loss.

II. METHOD

A. Subjects

Listeners in the main experiments with uniform stimulus sequences included 46 subjects assigned to four groups according to age and hearing status. Six of these listeners (one to two per listener group) were unavailable for subsequent testing with the nonuniform stimulus sequences, leaving a total of 40 listeners participating in these conditions. For the main experiments, one group of listeners included younger normal-hearing subjects (Yng Norm, $n=13$) ages 19–40 ($M=24.2$ years) with mean pure-tone thresholds $\leq$20 dB HL (re: ANSI, 2004) from 250 to 4000 Hz. Another group included younger listeners with hearing loss (Yng Hrg Loss, $n=9$) ages 19–42 ($M=28.2$ years) with mild-to-moderate sloping high frequency sensorineural hearing losses of hereditary or unknown etiologies. A third group of listeners included normal-hearing elderly listeners (Eld Norm, $n=9$) of 65–76 years ($M=71.8$ years) with mean pure-tone thresholds $\leq$20 dB HL from 250 to 4000 Hz. Last, an elderly group of listeners with hearing loss (Eld Hrg Loss, $n=15$) age 65–79 ($M=73.1$ years) also had mild-to-moderate sloping high-frequency hearing losses. The young and elderly listeners with hearing loss exhibited bilateral impairment of equivalent degree and configuration across the range of audiometric test frequencies. These subjects had a negative history of otologic disease, noise exposure, and family history of hearing loss. The probable etiology of hearing loss in the older listeners was presbycusis. Table I presents the mean subject data, showing ages, group sizes, and audiograms for the test ears of the four listener groups. The table also shows entries for listener group sizes (in parentheses) associated with the test conditions using the non-uniform stimulus sequences.

Additional criteria for subject selection included monosyllabic word recognition scores exceeding 80%, normal middle ear function as assessed by tympanometry, and acoustic reflex thresholds that were within the 90th percentile for a given pure tone threshold (Gelfand *et al.*, 1990). All listeners were in general good health, with no history of stroke or neurological impairment and possessed sufficient motor skills to provide responses using a computer keyboard. Additionally, all listeners passed a screening test for general cognitive awareness (Pfeiffer, 1975). Most of the listeners reported some degree of childhood exposure to musical instruments, but none received formal musical training as adults, or currently practiced as musicians. The listeners had not participated previously as subjects in listening experiments and were paid for their services in the study.

TABLE I. Average pure tone air conduction thresholds and standard deviations (in decibels HL, re: ANSI, 2004) across frequency, average listener age, and number of subjects for the four groups. Values in parentheses reflect group sizes for conditions with nonuniform stimulus sequences.

	Pure tone frequency					Age	N
	250	500	1000	2000	4000		
Yng Norm							
mean	7.3	5.0	4.6	6.2	1.5	24.2	13(11)
s.d.	3.2	6.2	5.0	5.3	7.4		
Eld Norm							
mean	10.0	7.2	8.9	10.0	14.1	71.8	9(8)
s.d.	5.3	5.9	3.9	5.3	5.2		
Yng Hrg Loss							
mean	23.3	22.2	27.2	43.9	45.0	28.2	9(7)
s.d.	14.1	17.2	14.7	6.6	16.2		
Eld Hrg Loss							
Mean	16.3	19.0	26.3	38.7	54.3	73.07	15(14)
s.d.	6.8	7.6	11.0	7.2	7.7		

B. Stimuli

All stimuli for the experiments were sequences of three pure tones generated using inverse fast Fourier transform (FFT) procedures with a digital signal processing board (Tucker-Davis Technologies AP2) and a 16-bit digital-to-analog (D/A) converter (Tucker-Davis Technologies DD1, 20 kHz sampling rate) that was followed by low-pass filtering (Frequency Devices 901F; 6000 kHz cutoff, 90 dB/oct). The tone frequencies for all sequences spanned a two octave range for ease of labeling, and were arbitrarily designated as low (L), 500 Hz; medium (M) 1000 Hz; and high (H) 2000 Hz.

For the uniform sequences, the tones within each sequence were equal in duration with each component having a 1 ms cosine-squared rise/fall envelope. Within each sequence, the onset-to-onset intervals between successive tones (the interonset interval, or IOI) were also equal, but were set to different fixed values across four conditions of sequence presentation rate; the IOI values were 500, 350, 250, or 150 ms, respectively, for each of the four sequence rate conditions. For each sequence rate condition, the tonal IOI included a combination of tone segment and silent interval, with the percentage of IOI filled by tone (the duty cycle) having a fixed value of 25, 50, 75, or 100 % in four separate test conditions conducted for each of the four sequence IOI values.

The nonuniform stimulus sequences were designed to examine the same four sequence rate conditions tested with the uniform sequences. Within the nonuniform sequences, each tonal IOI was different, with two of the values set to be 40% larger than, and 40% smaller than, a third mean IOI value that was fixed at 500, 350, 250, or 150 ms, respectively, in each of four sequence rate conditions. Thus, for the

nonuniform tone sequences, the mean IOI values were the same as those in the uniform sequences, for corresponding rate conditions. Additionally, within the nonuniform stimulus sequences, each tonal IOI was created to have a 50% duty cycle.

In total, there were 16 conditions with the uniform stimulus sequences, defined by the combination of four duty cycles tested at each of four sequence rates. There were four conditions with the nonuniform sequences, each associated with a different sequence rate but the same sequence duty cycle.

C. Procedures

The listening trials for the temporal order recognition task were single interval in which one stimulus sequence was presented with a tone order that was selected randomly from six possible permutations of the three tone frequencies. Using procedures of the earlier study (Fitzgibbons and Gordon-Salant, 1998) that were adapted from Divenyi and Hirsh (1974), listeners used labels of relative pitch to identify each sequence tone; that is, high (H), medium (M), and low (L), respectively, for the three tone frequencies of 2000, 1000, and 500 Hz. Listeners identified the stimulus sequence order for each recognition trial by keyboard response, selecting one of six keys (each labeled with a different sequence tone order: HML, HLM, MHL, MLH, LMH, LHM); a simple line drawing above each response key was also provided as a visual aid to depict the pitch-shift directions associated with each sequence ordering. The identification trials were listener paced, with a 3 s intertrial interval following each listener response; the stimulus presentation interval was also marked by a visual display on a computer monitor facing the listener. Percent-correct feedback was provided to listeners following each block of identification trials, but not for individual trials.

The 16 conditions with uniform sequences, comprising combinations of the four sequence duty cycles and four fixed IOI values, were tested in a different randomly determined order for each listener. Similarly, subsequent measurements collected for the four rate conditions with the nonuniform sequences were conducted using a different random order of the rate conditions for each listener. All testing was conducted using 50-trial blocks with duty cycle and sequence rate fixed within each block of listening trials. Prior to data collection, each listener was familiarized with the task and trained with the order identification task. Listeners practiced for 4–6 h in 2 h sessions that included 10–12 blocks of listening trials per session. The practice sessions included blocks of listening trials using relatively slow presentation rates with sequences featuring 1 s tonal durations. Listeners were required to demonstrate order recognition of at least 75% correct on three consecutive trial blocks with the practice sequences in order to participate in the experiments. The number of trial blocks required to achieve the performance criterion varied across individual listeners, but there was no systematic difference in the number of practice blocks required by younger and older listeners. Three listeners with normal hearing (two young, one elderly) could not perform the ordering task at criterion levels, and were excluded from further testing. For these listeners, the problem appeared to be related to difficulties in labeling tonal components according to relative pitch; similar problems were observed for a subset of listeners in our previous experiments (Fitzgibbons and Gordon-Salant, 1998). Listeners selected for the experiments were tested individually in a sound-attenuating booth, with all testing conducted monaurally via an insert earphone (Etymotic ER-3A) calibrated in a 2 cm^3 coupler (B&K DB0138). All stimuli were presented at 85 dB SPL, which corresponded to at least 30 dB sensation levels for the listeners with hearing loss. Testing was conducted in the better ear for listeners with hearing loss, and in the preferred ear for listeners with normal hearing. Excluding practice sessions, total time for data collection was about 12 h, scheduled in 2 h sessions over the course of 3–4 weeks.

III. RESULTS

A. Uniform sequences

The temporal order recognition performance of the listeners in the 16 conditions conducted with the uniformly timed stimulus sequences was initially analyzed to examine the specific effects of sequence duty cycle for each of the sequence IOI values. The individual percent-correct recognition scores for the blocks of listening trials in each condition were arcsine transformed and subjected to an analysis of variance (ANOVA) using a repeated measures design for the two within-subjects factors of duty cycle and IOI, and the between subject factors, age and hearing status. This initial analysis revealed a significant effect of sequence IOI $[F(3,126)=42.69, p<0.01]$, but the effect of sequence duty cycle was not significant $[F(3,126)=0.33, p>0.05]$, nor were any of the interaction effects involving duty cycle. Results that are representative of this outcome are displayed in the panels of Fig. 1, which show the mean percent correct scores for each group of listeners as a function of sequence IOI, with the parameter in the figure reflecting the sequence duty cycle. Each panel of the figure reveals that recognition performance improved progressively across increasing values of IOI, but results for each of the four duty cycles, ranging in value from 25 to 100 %, were virtually the same at each value of IOI for each of the listener groups.

Following evidence of negligible duty-cycle effects in the data, we collapsed the individual data across the four duty-cycle conditions for each of the IOI values for each group of listeners. These results are displayed in Fig. 2, which show the mean recognition performance of each listener group for each of the four sequence IOI values; error bars in the figure represent standard errors of the mean for each listener group. A repeated-measures ANOVA on the data of Fig. 2 was conducted using one within-subjects variable, IOI, and two between-subjects variables, age and hearing status. This analysis revealed significant main effects of sequence IOI $[F(3,540)=73.2, p<0.01]$ and age $[F(1,180)=8.57, p<0.01]$ with no other significant interactions involving IOI. There was no significant effect of hearing status $[F(1,180)=0.054, p>0.05]$ or interaction between age and hearing status $[F(1,180)=3.21, p>0.05]$ among the listener

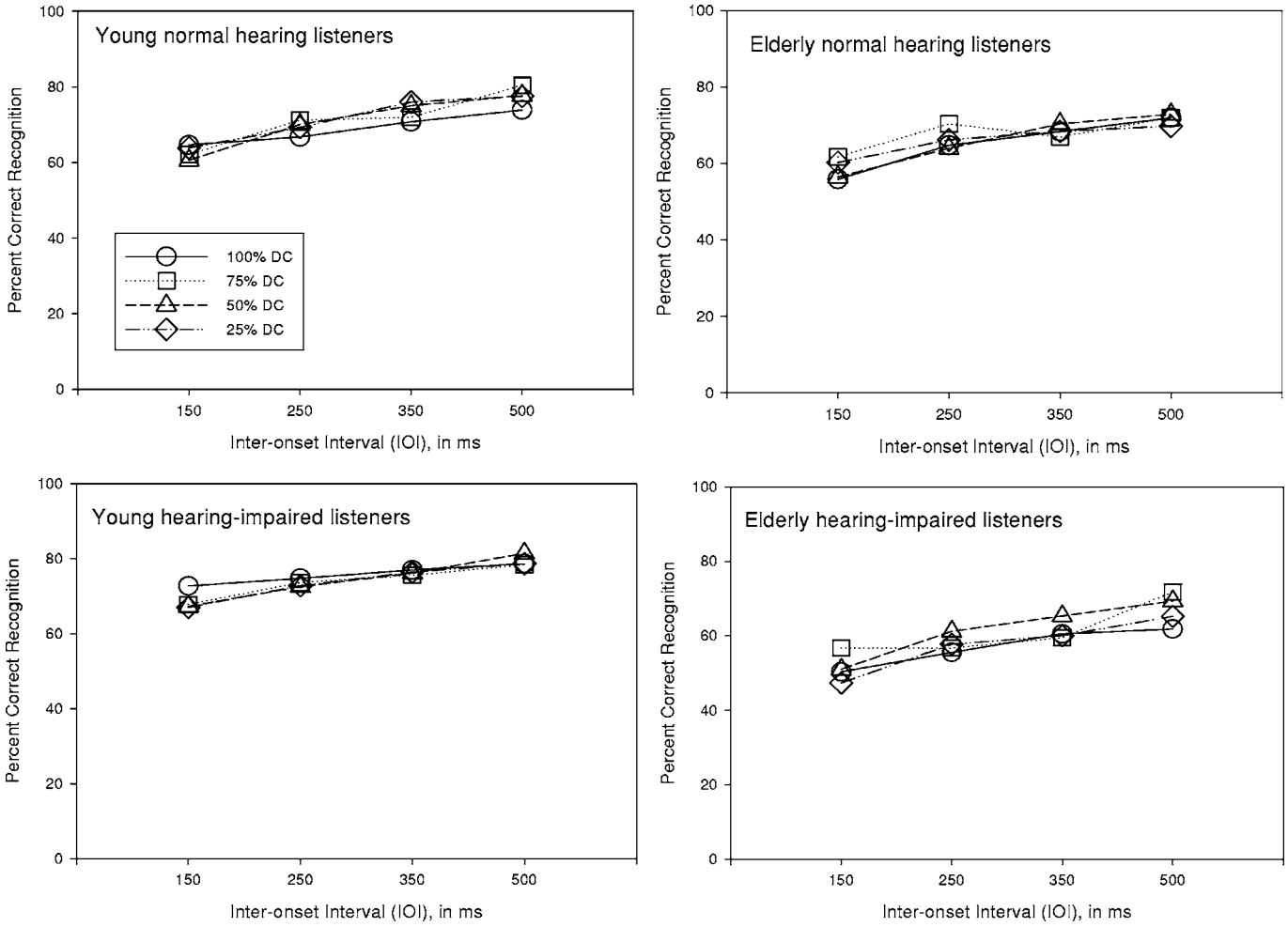

FIG. 1. Mean percent correct temporal order recognition scores for each group of listeners as a function of sequence interonset interval (IOI ms) for the uniform tone sequences. The parameter in the figure panels is the sequence duty cycle in percent.

groups. The main effect of IOI is reflected by the progressive improvement in recognition performance for each listener group with increasing values of sequence IOI. The main effect of age reflects the poorer performance of the older listeners relative to the young listeners. Each of these main effects is displayed more clearly in Fig. 3. This figure shows the mean recognition scores of the older and younger listeners, collapsed across hearing status, for each of the IOI con-

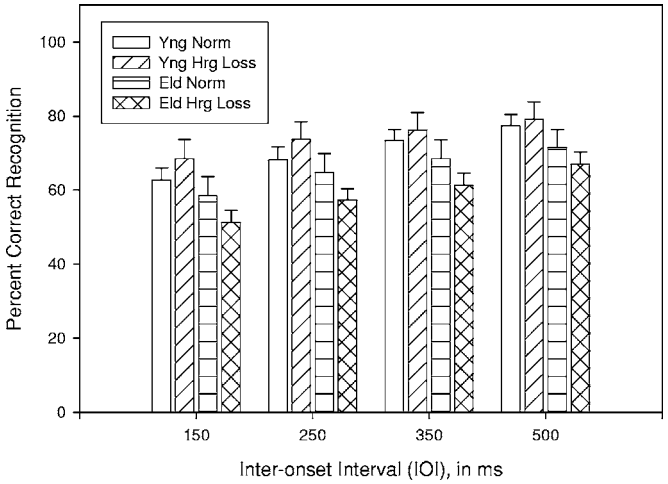

FIG. 2. Mean percent correct temporal order recognition scores for each listener group collapsed across duty cycle for each sequence IOI (ms) condition with the uniform tone sequences. Error bars show one standard error of the mean.

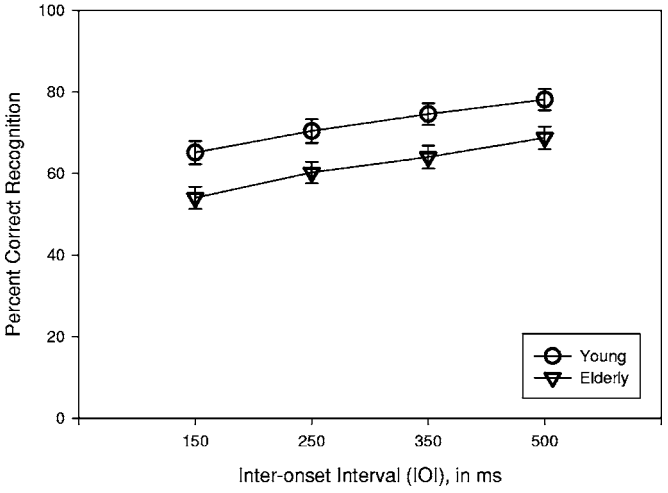

FIG. 3. Mean percent correct temporal order recognition scores for the younger and older listeners for each sequence IOI value (ms) with the uniform tone sequences. Error bars show one standard error of the mean.

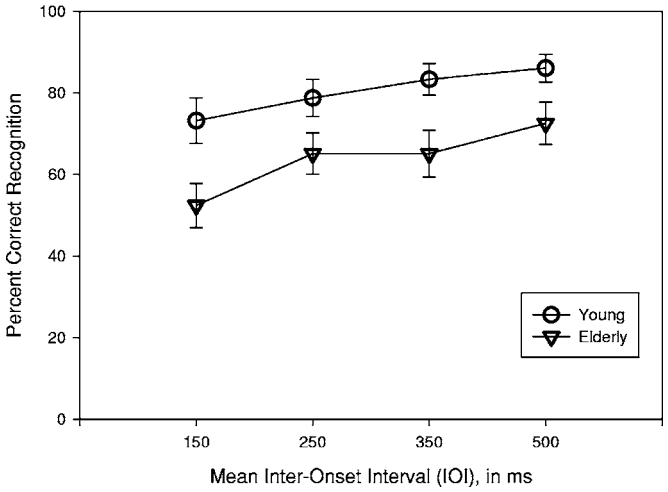

FIG. 4. Mean percent correct temporal order recognition scores for the younger and older listeners as a function of mean sequence IOI value (ms) for the nonuniform tone sequences. Error bars show one standard error of the mean.

ditions; vertical bars in the figure represent standard errors of the means. For each sequence IOI condition, the order recognition performance of the older listeners was poorer than that of the younger listeners.

B. Nonuniform sequences

The nonuniform stimulus sequences were used to examine the same four sequence rate conditions as measured with the uniform sequences. Individual IOIs within the nonuniform sequences differed, but the mean IOI values were the same as those of the uniform sequences for corresponding sequence rates. The percent-correct recognition data collected with these nonuniform sequences were also arcsine transformed and subjected to an ANOVA using a repeated-measures design with one within-subjects variable, mean IOI, and two between-subject variables, age and hearing status. Results of the analysis revealed significant main effects of IOI condition $[F(3,108)=24.3, p<0.01]$ and age $[F(1,36)=5.7, p<0.05]$, with no other significant interactions involving either of these two variables. Additionally, the effect of hearing status was not significant $[F(1,36)=0.025, p>0.05]$, nor was the interaction between age and hearing status $[F(1,36)=2.74, p>0.05]$ in these performance data. The significant effects from this analysis are displayed in Fig. 4, which shows the mean recognition performance, collapsed across hearing loss, as a function of average sequence IOI ms, for the groups of older and younger listeners; vertical bars in the figure represent standard errors of the means. The data for both groups of listeners reveal a progressive increase in recognition performance for increasing value of mean IOI. The mean performance of the older listeners was poorer than that of the younger listeners at each IOI value.

IV. DISCUSSION

A. Uniform sequences

The temporal ordering task with the three-tone sequences appeared to be difficult for many of the listeners, and none of the participants achieved perfect recognition performance for all of the sequence rates tested. For the uniform sequences, where IOI values are simply the reciprocal of sequence rate, the mean accuracy of order recognition for the younger listeners decreased progressively from about 78 to 66 % across sequence conditions of decreasing IOI values from 500 to 150 ms. This range of performance is substantially greater than chance level (16.7% correct for this six-choice task), indicating that, despite the perceived difficulty of labeling individual sequence tones, the listeners were capable of performing the ordering task. These results for the younger listeners were improved somewhat relative to those reported for younger listeners in our earlier temporal ordering study that used uniform contiguous three-tone sequences (Fitzgibbons and Gordon-Salant, 1998). Some degree of performance difference between the two studies was anticipated, because sequence tone frequencies in the previous investigation spanned a relatively narrow 1/3-octave range, whereas sequences in the present experiment featured a larger two-octave frequency range that was intended to facilitate the task of labeling individual tones according to relative pitch. Additional comparisons of the present results to those reported in other temporal ordering studies is hampered by the fact that performance measures in such tasks appear to depend on a large number of factors, including the number and type of components in sequences, and the response mode utilized in the order tasks. However, for ordering tasks like the present one, where listeners are required to name or attach labels to individual sequence items, component durations of 150–500 ms are frequently reported to be necessary for moderately trained listeners to achieve accurate ordering performance (Pinheiro and Musiek, 1985). Results collected from the younger listeners in the present study are consistent with this range of previous estimates.

The recognition performance of the older listeners with the uniform stimulus sequences shifted across changes of IOI value in a manner similar to that observed for the younger listeners. For these older listeners, mean performance levels decreased progressively from about 69 to 55 % across the range of decreasing IOI values from 500 to 150 ms. These performance levels were poorer than those of the younger listeners, but the magnitude of age-related deficit was fairly stable across the range of IOI values tested; that is, mean recognition performance of older listeners was about 10% poorer than that of younger listeners in each of the four sequence IOI conditions. The hearing status of listeners in the experiment did not prove to have a systematic influence on order recognition performance, and no significant interaction effects involving hearing loss and listener age emerged in the data analysis. However, there were performance trends in the individual group results that did appear to be related to hearing status. For example, inspection of Fig. 2 shows that among the younger listeners, the group with hearing loss performed somewhat better than those with normal hearing,

while the opposite was true for the older listeners; that is, the group with normal hearing performed better than the group with hearing loss. These group differences related to hearing loss were relatively small, and most likely reflected individual differences in the ordering abilities of the subjects sampled for each listener group. Several of the listeners within the younger group of subjects with hearing loss were observed to be among the better performers in the ordering tasks. The absence of systematic effects of hearing loss in the data was not surprising given the relatively high stimulus presentation levels, in conjunction with the mild degrees of listener hearing loss in the two-octave frequency range of the tonal sequence components.

The age-related performance differences seen in the present data differ from those observed in our earlier experiments with uniform contiguous tone sequences. The earlier results revealed no significant age-related performance differences on order identification across a range of longer sequence IOI values exceeding 250 ms, but did show a significant age-related decline in performance for a faster sequence rate featuring an IOI value of 100 ms. The earlier results also showed a relatively high degree of performance variability within listener groups, a situation that hampered analysis of age effects for several of the sequence rate conditions. By comparison, performance variability within subject groups of the present study was smaller and relatively uniform, an outcome that can probably be attributed to the use of more frequency-disparate tone sequences that were easier for listeners to label. The earlier study also examined listeners with hearing loss using high-frequency tone sequences narrowly spaced about 4 kHz, a spectral region associated with the greatest degree of sensitivity loss in the subjects with hearing impairment. The earlier results, like those of the present study, showed no significant influence of hearing loss on the temporal order recognition task.

A primary purpose of the present study was to investigate the relative importance of tonal duration, intertone interval, and sequence rate on temporal order recognition. This goal was motivated, in part, to help clarify interpretation of earlier results collected with contiguous tone sequences, for which changes in tonal durations are accompanied by changes of sequence presentation rate. Additionally, it is of general theoretical interest to identify the stimulus parameters most closely associated with the processing time required by listeners to perform a temporal ordering task. As mentioned previously, various earlier investigations with temporal sequencing tasks reported that the insertion of silent intervals between successive items in a stimulus sequence could facilitate listeners' recall of temporal order. The facilitating effects of interitem silent intervals were presumed to reflect the increased availability of processing time that listeners used to encode and store item order information for later recall (Aaronson 1971; Warren, 1974; Pinheiro and Musiek, 1985). Of course, this reasoning also requires that component durations are sufficient for listeners to process enough sensory information to distinguish the individual sequence items. In the present experiments, we examined these effects of component duration and interitem silent intervals within the tone sequences by systematically manipulating the tonal duty cycle from 25 to 100 %, while holding sequence presentation rate constant. Contrary to expectations, the sequence duty cycle had no significant influence on listeners' temporal order recognition, for any of the sequence rates examined. It was anticipated that older listeners, in particular, might benefit the most from duty cycles that afforded relatively larger intertone intervals, especially for the faster sequence rates in which processing time is limited. At the fastest sequence rate tested, with tonal IOI of 150 ms, intertone silent intervals took on values ranging from 0 to 112.5 ms as the duty cycle changed from 100 to 25 % across conditions. Similarly, for this same IOI condition, tone durations decreased from 150 to 37.5 ms through the range of decreasing duty cycle values. Despite these changes in parameter values, the order recognition performance of the older listeners remained stable. For all test conditions with the uniform stimulus sequences, the results from each group of listeners indicated that sequence IOI is the only stimulus factor that influenced temporal order recognition. Recognition performance improved progressively as the tonal IOI increased, an outcome that was independent of tone duration, or intertone interval, within the range of values examined. Thus, for these sequences, the introduction of intertone silent intervals would benefit order recognition only if the silent intervals acted to increase the tonal IOI, and thus slow sequence presentation rate.

B. Nonuniform sequences

The results collected from the subset of listeners in conditions with the nonuniform stimulus sequences allow additional examination of the stimulus factors that influence temporal order recognition. Recall that the nonuniform sequences had different IOI values, but the same sequence presentation rates that characterized the uniform sequences. The mean order recognition measurements of the younger listeners with the nonuniform sequences showed systematic effects of mean IOI, with performance accuracy shifting progressively from about 87 to 74 % across decreasing values of mean IOI from 500 to 150 ms. These mean performance levels are somewhat better than those cited above for the younger listeners with the uniform sequences. However, much of the improvement in mean performance of the younger listeners can be attributed largely to the sample of participants within younger groups tested with the nonuniform sequences. That is, inspection of individual results indicated that the individual subjects who were unavailable for testing with the nonuniform conditions were among the poorer performers in the previous conditions with uniform sequences. This was particularly the case for the group of younger listeners with hearing loss, which showed the largest improvement in mean performance with the nonuniform sequences.

Results collected from the older listeners with the nonuniform sequences exhibited similar effects of sequence IOI as seen in results obtained from the younger listeners. For the older listeners, accuracy in recognition performance shifted from about 74 to 54 % across the range of decreasing mean IOI value for the nonuniform sequences. The older listener

groups (each missing a single subject) produced equivalent mean recognition performance across the uniform and nonuniform sequences, for corresponding IOI conditions. Also, performance of these older listeners was consistently poorer than that of the younger listeners at each sequence IOI condition. The magnitude of the age-related performance difference was fairly stable across IOI conditions, with an average performance difference of 16.5%. The largest age-related performance difference occurred for the nonuniform sequence with the 150 ms mean IOI, but the magnitude of this difference was not sufficient to produce a significant interaction effect between listener age and mean IOI value in the data analysis.

The collective findings from measurements obtained with both the uniform and nonuniform stimulus sequences provide some additional insight about the role of stimulus and processing factors that influence temporal order recognition. If the stimulus sequence consists of equally timed events, as with the uniform tone sequences, then the time between successive component onsets appears to be the relevant processing interval for order recognition. We found no evidence to support the argument that component duration, or intercomponent silence, has an independent influence on tone order processing. Of course, it is possible that factors such as interitem spacing might have greater influence on the processing of longer stimulus sequences that contain a larger number of components than was evident for our three-tone stimulus patterns. Additionally, it is reasonable to assume that component durations need to be sufficient for item identification, with specific values perhaps depending on the complexity and number of the sequence items. For example, with speech sequences, changes in some segment durations (e.g., consonant sounds) are reported to impact recognition performance more than adjustments of other segment durations (e.g., vowel sounds) (Pickett, 1999). Also, accurate temporal order recognition of speech sequences comprised of vowel segments can be accomplished with shorter component durations than is required for sequences of unrelated nonspeech sounds (Pinheiro and Musiek, 1985).

The effects of tonal IOI seen in the performance measures collected with uniformly timed sequences tend to obscure possible independent effects of sequence presentation rate. However, measurements collected with the nonuniform sequences indicate that sequence rate, rather than tonal IOI, has the more important influence on temporal order recognition. On the basis of earlier discrimination data, we had anticipated that the mixing of tonal IOI values within a given sequence might be disruptive to the processing of temporal order. However, the recognition performance of most of the listeners was similar with the uniform and nonuniform sequences, if the presentation rate of the stimulus patterns was preserved. This equivalency in performance between the sequences with differing timing characteristics may be suggestive of the listening strategy employed by subjects in performing the temporal ordering task. For example, with uniformly timed sequences, the importance of tonal IOI implies that listeners may have attempted to identify and encode order information in a real-time serial manner during the course of sequence presentation. This strategy is based upon the assumption that component IOI is the relevant processing interval in sequential ordering tasks. However, this same listening strategy should produce different performance results if the tonal IOIs differ substantially within a sequence, as was the case for the nonuniform stimuli. This performance deficit with the nonuniform patterns did not occur, indicating that listeners may have extracted, or reconstructed, tone order information subsequent to sequence presentation. This processing strategy seems plausible, particularly for the relatively simple three-tone stimulus patterns used in this study.

The recognition performance of the older listeners in this study was poorer than that observed for the younger listeners, for both the uniform and nonuniform stimulus sequences. However, the source of the age-related performance differences is not evident. Unlike our previous findings with the contiguous sequences, the present results did not reveal an interaction between listener age and sequence presentation rate. Instead, the age-related performance differences were approximately equivalent across the range of sequence rate conditions tested. Of course, the fastest rate tested here (about 6.7 tone/s for 150 ms IOI) was slower than the fastest rate tested in our earlier study (10 tone/s), a rate difference that could explain some of the age-related performance differences between the studies. However, the observed stability of age effects across rate conditions may indicate a more general difficulty among older listeners with sequential pattern recognition, one that is not specifically related to sequence rate or diminished processing speed, at least at the sensory/perceptual level. Similar conclusions were reached by Trainor and Trehub (1989) from their temporal ordering experiments, as described previously. Recall that Trainor and Trehub also observed impaired temporal ordering abilities among older listeners, but the age-related difficulties were not specifically related to sequence presentation rates. However, these earlier experiments also featured a high degree of stimulus uncertainty, wherein stimulus presentation rates were randomly varied within a block of listening trials. The extent to which these procedural factors impacted the ordering performance of the older listeners is unknown.

As stated above, the present results did not reveal a specific interaction between sequence presentation rate and the magnitude of the age-related ordering differences. However, the observation of such an interaction may not be the only indicator of slowed processing among the elderly listeners. For example, inspection of the mean performance of the younger and older listeners (e.g., Figs. 3 and 4) shows that the older listeners required sequence IOI values of 350–500 ms to achieve the same performance levels demonstrated by the younger listeners for an IOI of 150 ms. These comparisons indicate that longer processing times were required by the older listeners to achieve the performance equivalence to the younger subjects. However, these comparisons do not indicate the source of slowed processing in the older listeners. Evidence exists for age-related differences in encoding of temporal information at various sites within the auditory pathway (e.g., Schneider and Pichora-Fuller, 2000; Simon *et al.*, 2004). Additionally, temporal order recognition involves a number of cognitive tasks, includ-

ing those specific to sound component labeling, short-term memory, and the storing and retrieval of order information. Any of these processes could undergo changes with aging to affect slowed processing, whether the stimuli are tone sequences like those used here, or any of the time-altered speech sequences used in some of the earlier speech recognition experiments. Greater study of these potential cognitive influences on the auditory processing of elderly listeners is warranted. Added support for this argument was offered recently by Humes (2005), who demonstrated via statistical regression analysis that many measures of auditory processing among elderly listeners are partially related to individual differences in cognitive function.

In summary, the present experiments used relatively simple stimulus sequences consisting of three tones of differing frequency. Listeners were required to identify different random orders of the tones by using labels of relative pitch to identify individual tonal components. Tones within the stimulus sequences were either equal in their durations with uniform timing, or unequal in duration with nonuniform timing. For both types of sequences, the temporal order recognition performance of listeners was influenced primarily by sequence presentation rate, showing progressively better recognition as the rate slowed. Factors related to tone duration, or intertone interval, had no systematic influence on recognition performance. The older listeners generally exhibited poorer recognition performance than younger listeners for each sequence rate condition tested. Temporal ordering tasks that require the naming of components in a sequence are difficult for many listeners, and are likely to involve several perceptual and cognitive processing factors. Investigation of these factors needs to be incorporated into subsequent studies of aging and auditory processing, particularly for complex sequential sounds.

ACKNOWLEDGMENT

This research was supported by an individual research grant (R37AG09191) from the National Institute on Aging.

Aaronson, D., Markowitz, N., and Shapiro, H. (**1971**). "Perception and immediate recall of normal and compressed auditory sequences," Percept. Psychophys. **9**, 339–344.

Abel, S., Krever, E., and Alberti, P. W. (**1990**). "Auditory detection, discrimination, and speech processing in ageing, noise-sensitive and hearing-impaired listeners," Scand. Audiol. **19**, 43–54.

ANSI (**2004**). ANSI S3.6-2004, "American National Standard Specification Tor Audiometers" (American National Standards Institute, New York).

Divenyi, P., and Hirsh, I. (**1974**). "Identification of temporal order in three-tone sequences," J. Acoust. Soc. Am. **56**, 144–151.

Fitzgibbons, P. J., and Gordon-Salant, S. (**1995**). "Age effects on duration discrimination with simple and complex stimuli," J. Acoust. Soc. Am. **98**, 3140–3145.

Fitzgibbons, P. J., and Gordon-Salant, S. (**1998**). "Auditory temporal order perception in younger and older adults," J. Speech Lang. Hear. Res. **41**, 1052–1060.

Fitzgibbons, P. J., and Gordon-Salant, S. (**2004**). "Age effects on discrimination of timing in auditory sequences," J. Acoust. Soc. Am. **116**, 1126–1134.

Gelfand, S., Schwander, T., and Silman, S. (**1990**). "Acoustic reflex thresholds in normal and cochlear-impaired ears: Effects of no-response rates on 90th percentiles in a large sample," J. Speech Hear Disord. **55**, 198–205.

Gordon-Salant, S., and Fitzgibbons, P. J. (**1993**). "Temporal factors and speech recognition performance in young and elderly listeners," J. Speech Hear. Res. **36**, 1276—1285.

Grose, J. H., Hall, J. W., III., and Buss, E. (**2001**). "Gap duration discrimination in listeners with cochlear hearing loss: effects of gap and marker duration, frequency separation, and mode of presentation," J. Assoc. Res. Otolaryngol. **2**, 388–398.

Humes, L. (**2005**). "Do 'auditory processing' tests measure auditory processing in the elderly?" Ear Hear. **26**, 109–119.

Humes, L., and Christopherson, L. (**1991**). "Speech identification difficulties of hearing-impaired elderly persons: The contribution of auditory processing deficits," J. Speech Hear. Res. **34**, 686–693.

Lister, J., Besing, J., and Koehnke, J. (**2002**). "Effects of age and frequency disparity on gap discrimination," J. Acoust. Soc. Am. **111**, 2793–2800.

Lister, J., and Tarver, K. (**2004**). "Effect of age on silent gap discrimination in synthetic speech stimuli," J. Speech Lang. Hear. Res. **47**, 257–268.

Peters, R. W., and Wood, T. J. (**1973**). "Perceived order of tone pulses." J. Acoust. Soc. Am. **54**, 315.

Pfeiffer, E. (**1975**). "A short portable mental status questionnaire for the assessment of organic brain deficit in elderly patients," J. Am. Geriatr. Soc. **23**, 433–441.

Pichora-Fuller, M. D., Schneider, B. A., Benson, N. J., Hamstra, S. J., and Storzer, E. (**2006**). "Effect of age on detection of gaps in speech and nonspeech markers varying in duration and spectral symmetry," J. Acoust. Soc. Am. **119**, 1143–1155.

Pickett, J. M. (**1999**). *The Acoustics of Speech Communication* (Allyn & Bacon, Needham Heights, MA).

Pinheiro, M. L., and Musiek, F. E. (**1985**). "Sequencing and temporal ordering in the auditory system," in *Assessment of Central Auditory Dysfunction*, edited by M. L. Pinheiro and G. L. Musiek, Williams & Wilkins, Baltimore.

Salthouse, T. A. (**1996**). "The processing speed theory of adult age differences in cognition," Psychol. Rev. **103**, 403–428.

Schneider, B. A., and Pichora-Fuller, M. K. (**2000**). "Implications of perceptual deterioration for cognitive aging research," in *The Handbook of Aging and Cognition*, 2nd ed. edited by F. I. M. Craik and T. A. Salthouse (Lawrence Erlbaum Assoc, Mahwah, NJ), Chap. 3, pp. 155–219.

Schneider, B. A., Pichora-Fuller, M. K., Kowalchuk, D., and Lamb, M. (**1994**). "Gap detection and the precedence effect in young and old adults," J. Acoust. Soc. Am. **95**, 980–991.

Schneider, B. A., Speranza, F., and Pichora-Fuller, M. K. (**1998**). "Age-related changes in temporal resolution: Envelope and intensity effects," Can. J. Exp. Psychol. **52**, 184–191.

Simon, H., Frisina, R. D., and Walton, J. P. (**2004**). "Age reduces response latency of mouse inferior colliculus neurons to AM sounds," J. Acoust. Soc. Am. **116**, 469–477.

Snell, K. B. (**1997**). "Age-related changes in temporal gap detection," J. Acoust. Soc. Am. **101**, 2214–2220.

Trainor, L. J., and Trehub, S. E. (**1989**). "Aging and auditory temporal sequencing: Ordering the elements of repeating tone patterns," Percept. Psychophys. **45**, 417–426.

Tun, P. A. (**1998**). "Fast, noisy speech: Age differences in processing rapid speech with background noise," Psychol. Aging **13**, 424–434.

Vaughan, N., and Letowski, T. (**1997**). "Effects of age, speech rate, and type of test on temporal auditory processing," J. Speech Lang. Hear. Res. **40**, 1192–1200.

Warren, R. M. (**1974**). "Auditory temporal discrimination by trained listeners," Cogn. Psychol. **6**, 237–256.

Wingfield, A., Poon, L. W., Lombardi, L., and Lowe, D. (**1985**). "Speech of processing in normal aging: Effects of speech rate, linguistic structure, and processing time," J. Gerontol. **40**, 579–585.

Wingfield, A., Tun, P. A., Koh, C. K., and Rosen, J. J. (**1999**). "Regaining lost time: Adult aging and the effect of time restoration on recall of time-compressed speech," Psychol. Aging **14**, 380–389.

The occurrence of the Coanda effect in pulsatile flow through static models of the human vocal folds

Byron D. Erath and Michael W. Plesniak[a)]
School of Mechanical Engineering, Purdue University, West Lafayette, Indiana 47907

(Received 3 August 2005; revised 12 May 2006; accepted 12 May 2006)

Pulsatile flow through a one-sided diffuser and static divergent vocal-fold models is investigated to ascertain the relevance of viscous-driven flow asymmetries in the larynx. The models were 7.5 times real size, and the flow was scaled to match Reynolds and Strouhal numbers, as well as the translaryngeal pressure drop. The Reynolds number varied from 0–2000, for flow oscillation frequencies corresponding to 100 and 150 Hz life-size. Of particular interest was the development of glottal flow skewing by attachment to the bounding walls, or Coanda effect, in a pulsatile flow field, and its impact on speech. The vocal folds form a divergent passage during phases of the phonation cycle when viscous effects such as flow separation are important. It was found that for divergence angles of less than 20 degrees, the attachment of the flow to the vocal-fold walls occurred when the acceleration of the forcing function was zero, and the flow had reached maximum velocity. For a divergence angle of 40 degrees, the fully separated central jet never attached to the vocal-fold walls. Inferences are made regarding the impact of the Coanda effect on the sound source contribution in speech. © *2006 Acoustical Society of America.* [DOI: 10.1121/1.2213522]

PACS number(s): 43.70.Aj [BHS] Pages: 1000–1011

I. INTRODUCTION

This paper addresses the development of the Coanda effect and its potential influence in phonation. Henri Coanda, a Romanian engineer, is credited with discovering that fluid issuing forth from a slot has a tendency to adhere to a surface placed adjacent, and at some acute angle, to the slot. He attributed this phenomenon to an imbalanced suctioning force caused by entrainment of the ambient fluid between the jet and the adjacent surface (Coanda, 1936). This phenomenon is commonly referred to as the Coanda effect, and is evident in many common engineering applications involving fluid mechanics.

The relevance of the Coanda effect in the production of speech sounds is at present unclear, but several investigators have suggested it plays an important role. McGowan (1988) and Z. Zhang, *et al.* (2002) have shown that there are two aeroacoustic source mechanisms in addition to the volume source due to time-varying glottal volume flow. The first of these is a dipole source due to pressure forces on the vocal-tract wall, related to fluctuations in the glottal jet. These fluctuations can arise from movement of the separation point, or from global changes in jet geometry, such as a switch from a symmetrical to an asymmetrical configuration due to the Coanda effect.

The effects of moving separation points on sound production are of particular interest in unvoiced speech, such as fricatives, where the monopole sound source is zero, and the dipole source becomes the dominant contributor. Initially proposed by Stevens (1971), the theory that the principal sound source of a turbulent jet arises from its interaction with its surrounding rather than from within the turbulent jet itself was substantiated by Shadle (1985). Using a simplified driven model of the vocal tract, Barney *et al.* (1999) concluded that acoustic sources may arise from nonacoustic flow-field interactions with flow boundaries, and may be geometry dependent. Using a formulation of Howe (1975), Krane (2005) showed that the dipole strength may be expressed in terms of the jet vorticity and the shape of the vocal tract. In addition to sound production arising from the interaction of the jet with solid surfaces, this derivation explicitly showed that the dipole mechanism is active where the flow has separated.

The Coanda effect has been shown to exhibit many of these qualities that are expected to contribute to the production of sound in voiced and unvoiced speech. Investigating a two-dimensional turbulent jet exhausted over an inclined adjacent flat plate, Borque and Newman (1960) observed a separation of the flow at the lip, followed by a reattachment point downstream. Newman (1961) later provided a comprehensive theoretical and experimental investigation of the Coanda effect, using an inclined adjacent flat plate for flow at moderately high Reynolds number. Basing his theory on conservation of momentum and undeflected jets, he determined that flow separation and reattachment lengths were a function of the angle of the plate to the flow axis. Furthermore, they showed that an imbalance in entrainment between the two sides of the jet results in the jet asymmetry that characterizes the Coanda effect.

Unfortunately, this previous work is limited to flows which are steady and are characterized by Reynolds numbers higher than those exhibited in speech. Both of these factors affect the entrainment rate of the jet, and hence, the occurrence of the Coanda effect. Turbulent shear layers have increased entrainment (Hussain, 1986) i.e., quicker formation of the Coanda effect, but shorter attachment lengths. Furthermore, in a study of fully pulsed axisymmetric jets with a

[a)]Author to whom correspondence should be addressed. Electronic mail: plesniak@ecn.purdue.edu

no-flow period, Bremhorst and Hollis (1990) found the entrainment rate to be nearly double that for steady jets. These findings suggest that there are many variables that may contribute to, or inhibit, the formation of asymmetric flows in the dynamic environment of speech.

The possibility of asymmetric flow configurations in speech has been proposed in the past. Initially suggested by Teager (1980), Teager and Teager (1981, 1983), and Kaiser (1983), their work was largely disregarded due to a lack of theoretical underpinning relating their observations to sound production. Furthermore, their inability to conclusively address issues of repeatability and reproducibility of their measurements, as well as the inherently invasive nature of the hot-wire measurements on which their findings were based, limited the acceptance of their work. Despite this controversy, inspection of their data and others is highly suggestive that glottal jet flows are often asymmetrical. It is widely accepted that the Coanda effect will form in steady vocal-tract flow investigations, as mentioned by Hirschberg (1992) and Krane (2005). Furthermore, experiments in dog larynges (Alipour and Scherer, 1995; Alipour *et al.* 1995a, 1995b) showed lateral spatial variations in the maximum glottal jet velocity. Although not explicitly investigating glottal flow asymmetries, Alipour and Scherer (1995) and Alipour *et al.* (1995a, 1995b) spatially reconstructed the nature of the flow from point-wise, temporal, hot-wire measurements. While spatial variations in the mean velocity field were evident, the inability to capture an instantaneous full-field realization prevented definitive characterization of the flow behavior. Furthermore, the spatial variability of the flow may have been influenced by interference of the relatively large-sized probe with the flow, when placed close to the excised larynges.

Due to the impetus of Teager and Teager (1983) and Kaiser (1983), considerable efforts have been directed to resolve the question of whether or not the Coanda effect will occur in the dynamic, high-frequency oscillations of phonation. Early work was performed by Pelorson *et al.* (1994, 1995) and Hirschberg *et al.* (1996) in impulsively started flows in three times life-size static vocal-fold models of varying geometric configurations. Unsteady flow was generated by abruptly opening a pressurized reservoir placed upstream of the models. A picture of the glottal flow dynamics was constructed by acquiring velocity measurements at the minimal constriction of the vocal-fold models, as well as measuring the static pressure time history on the facing vocal-fold models at the same location. Flow visualization was also employed to observe the spatial development of the glottal jet. By measuring the time necessary for the Coanda effect to fully establish in their models, they concluded that there was insufficient formation time available during the high-frequency oscillations inherent in phonation. Their conclusions were based on the assumption that the development of the Coanda effect takes a finite period of time to develop, and that this formation interval is proportional to the fundamental frequency. These results have been confirmed, recently, by Hofmans *et al.* (2003).

Using the same experimental setup of impulsively started flow through divergent glottal models, pressure measurements were obtained on both vocal-fold walls at the minimum constriction. The development of the Coanda effect was identified by a marked divergence in the pressure magnitude between the opposing walls. Again, the same necessary time scaling for the development of the Coanda effect was reported. These studies concluded that the Coanda formation time was longer than that afforded by the high-frequency oscillations of voicing. However, the results of Mongeau *et al.* (1997) suggest the importance of flow acceleration within the glottis when investigating the flow-field behavior. While they did not obtain spatial flow-field measurements, time-resolved hot-wire velocity measurements of flow through a modulated life-size rubber model of the vocal folds revealed that the flow largely behaved in a quasisteady manner, except during the opening one-fifth of the duty cycle when the flow was accelerating. While the experiments of Pelorson *et al.* (1994, 1995), Hirschberg *et al.* (1996), and Hofmans *et al.* (2003) have provided significant contributions to flow development and behavior within the glottis, they are all limited by their inability to accurately represent the flow dynamics (i.e., truly pulsatile flow) that occurs in voiced speech, as well as the inability to obtain the velocity time history in a nonintrusive manner. In particular, the duration of the flow acceleration resulting from the impulsively started flow is a significant fraction of a typical period of a glottal cycle. Consequently, there remains an unresolved issue regarding the development of the Coanda effect in phonation under pulsatile flow conditions.

An obvious advancement of previously performed work (as suggested by Pelorson *et al.*, 1995) is to investigate glottal flow behavior in the more physiologically applicable situation of a truly pulsatile flow field. The purpose of this study was to investigate the development of the Coanda effect in static models of the human glottis, subject to pulsatile flow, with a waveform comparable to physiological phonation conditions, and to determine which parameters govern its formation. Particle image velocimetry (PIV) was used to investigate flow through the glottal airspace. This noninvasive technique provides full-field, planar mean velocity statistics with high spatial resolution, an advancement over techniques previously employed in laryngeal flow investigations.

The choice of pulsatile flow through static vocal-fold models (rather than dynamic models) allows a focus on how time variations in glottal flow affect the occurrence of the Coanda effect, using a flow field that evolves in a dynamically similar manner to physiological flows. In this manner, the present study builds upon the previous work of Pelorson *et al.* (1994, 1995), Hirschberg *et al.* (1996), and Hofmans *et al.* (2003), adding only a single additional degree of complexity. The results reported herein provide insight into what factors are important in the development of the Coanda effect during phonation. Not only is the *in vitro* model used more physiologically accurate than those in previous similar studies, but the experimental technique provides accurate spatial distributions of the velocity field, obtained in a noninvasive manner. From these measurements, the time required for the formation of the Coanda effect, relative to a physiologically relevant pulsatile flow period, can be determined.

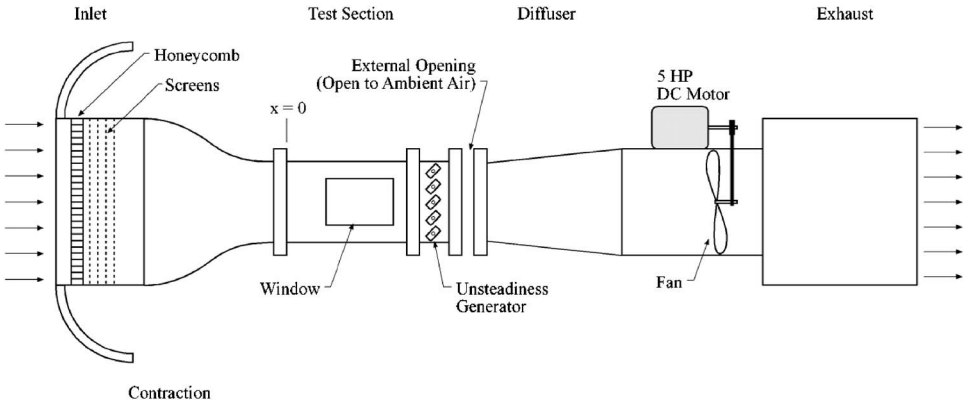

FIG. 1. Schematic of the wind tunnel.

II. METHODS

A. Experimental apparatus

All experiments were performed in a low-speed, open-circuit suction wind tunnel, as shown schematically in Fig. 1. The optically clear polycarbonate test section measured 30.5 cm (12.0 in.) by 30.5 cm (12.0 in.) in the spanwise directions (out of the page) and 122 cm (48.0 in.) in the streamwise direction (left-to-right).

An unsteadiness generator, consisting of five equally spaced rotating shutters placed downstream of the test section, was used to provide the periodic free-stream velocity fluctuations in the test section to replicate the unsteady physiological flow parameters. Matching the physiological flow required that an ellipsoidal cross-sectional geometry be used for each shutter so that the total area obstruction of the shutters varied in the streamwise direction throughout one rotation, producing a pulsatile flow with a zero mean flow component for part of the cycle. The shutter frequency, f_s, adjustable from 0–5 Hz, was controlled by a variable speed motor (Oriental Motors, 60 W, model US560-501W), with a 7.5:1 gear box (model 5GU7.5KA).

An optical encoder (US Digital, model E5s-360) with 0.5° resolution quadrature output was placed on the shutter shaft, and the quadrature output was sent to a digital frequency counter (Data Precision, model 5740) which recorded the shutter frequency with a resolution of ±0.001 Hz. The TTL output wave of the optical encoder also served as a variable external trigger based upon shutter phase, which was used for reference in the phase-averaged data acquisition. Shutter position, or phase ϕ, was defined as zero when the shutters were oriented such that the major diameter was vertical, and the shutters were fully closed. One flow pulse is produced by the shutters rotating 180°, from fully closed to open and then fully closed again.

Two devices were constructed to investigate the Coanda effect. The first was a one-sided diffuser, schematically shown in Fig. 2. The diffuser apparatus created a modified test section by dividing the existing wind tunnel test section into a top and bottom plane spanning the width of the original test section. The top half measured 16.23 cm (6.39 in.) high, while the bottom half measured 13.77 cm (5.41 in.) high. As flow passed through the top half of the modified test section it was accelerated through a fifth-order polynomial inlet contraction, with a contraction ratio of 22:1. The exit of the contraction formed the slot width of interest, and measured 7.5 mm (0.30 in.) in height. Extending from the lower edge of the slot was an adjacent plate which was angled at 20° away from the streamwise direction. The plate had a length-to-diameter ratio of 18.5. The total length of the apparatus was 42.0 cm (16.5 in.). The bottom half of the modified test section served as the bypass. Four stretched wire mesh screens were placed across the bottom section, mimicking the dynamic pressure drop across the *modified* test section. The screens were equally spaced 2.54 cm (1.00 in.) apart. All four screens had a porosity of 59%, and mesh size of 42, where mesh size is defined as the number of openings per linear inch.

The second apparatus, the glottal flow test section, was physiologically representative of the glottal airspace, based on dimensions reported by Scherer *et al.* (2001). A schematic showing its positioning in the wind tunnel is shown in Fig. 3. This apparatus, constructed of 1.27-cm (0.500 in.)-thick clear acrylic sheet, divided the original wind tunnel test sec-

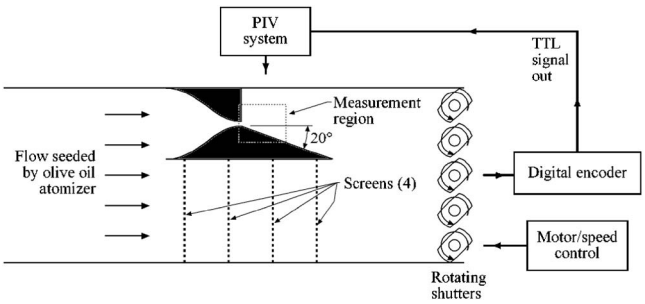

FIG. 2. One-sided diffuser test section.

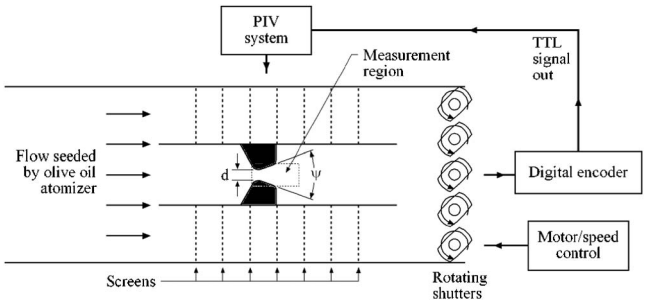

FIG. 3. Glottal flow test section.

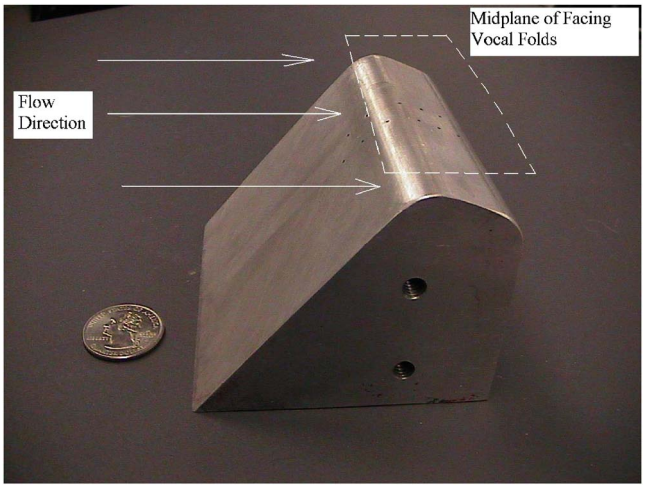

FIG. 4. Vocal-fold model, 7.5× scale $\Psi=40°$.

tion into three separate horizontal channels. The total length was 61.0 cm (24.0 in.). The top and bottom channels both measured 28.0 cm (11.0 in.) wide by 7.52 cm (2.96 in.) high, and served as bypasses to allow sufficient air flow to the fan. The middle channel acted as the vocal-tract test section. The opening was 30.5 cm (12 in.) wide by 12.9 cm (5.08 in.) high. A two-dimensional contraction, with a contraction ratio of 3.4:1, in the spanwise direction narrowed the middle channel to a constant width of 9.00 cm (3.54 in.). Three 7.5× scaled static vocal-fold model pairs with divergence angles of 10, 20, and 40° were machined according to the specifications of Scherer *et al.* (2001). Figure 4 shows (one-half of) one of the vocal-fold models with a divergence angle of 40°. Data were acquired with models positioned in the vocal-tract channel such that the exit plane of the models was located 33.0 cm (13.0 in.) downstream of the vocal-tract inlet, and 28.0 cm (11.0 in.) upstream of the exit. The height of the vocal-tract channel dictated that the glottal gap between the two models, d, was fixed at 0.30 cm (0.118 in.) (See Fig. 3). Wire mesh screens were used along the top and bottom bypasses to increase flow resistance so that the pressure drops were identical to the pressure drop across the center channel containing the vocal-fold models, thereby eliminating any undesirable pressure gradients when the flow exits the vocal-tract model. Seven screens were placed normal to the streamwise direction along the top and bottom bypasses, spanning the whole width and height. The mesh size of the screens was 80 (openings per linear inch), porosity was 19.4%, and wire diameter was 0.018 cm (0.0070 in.). They were spaced 5.08 cm (2.00 in.) apart, centered about the middle of the channels.

B. Data acquisition

The spatial flow field through the one-sided diffuser, and vocal-fold models, was measured using Particle image velocimetry (PIV). PIV is a noninvasive technique that provides detailed, spatially resolved flow fields. A particle-laden flow is illuminated with a thin laser sheet, formed by a pulsed Nd:YAG laser. The light scattered by the particles is captured by a charge-coupled device (CCD) camera creating an image of the particle cloud. With the time between each laser pulse, Δt (and therefore each image) precisely controlled, successive images are then cross correlated using a fast Fourier transform (FFT) algorithm to find the displacement, Δx, of the particles. Velocity vectors can then be determined according to $U=\Delta x/\Delta t$. Ensemble averages allow detailed statistics of the flow to be computed. See Grant (1997) and Raffel *et al.* (1998) for more details concerning the PIV technique.

TABLE I. Life-size and model parameters.

Apparatus Flow conditions	Physiological flow Pulsatile	One-sided diffuser Pulsatile	Glottal-flow Pulsatile
d (mm)	~0–1	7.5	3.0
U (m/s)	~0–30	4.0	7.40
f_s (Hz)	~100–250	1.78, 2.67	1.78
ν (Ns/m^2)	1.51×10^{-5}	1.51×10^{-5}	1.51×10^{-5}
ΔP_{trans} (cmH_2O)	~0–20	N.A.	0–0.267
Re	~0–5000	0–1987	0–1470
St	$\sim10^{-3}$	3.3×10^{-3}, 5.0×10^{-3}	7.22×10^{-4}
Ψ (Divergence angle, deg)	~40 to −40	40	10, 20, 40

Dynamic similarity between the measured model flow and glottal flow was established by matching the Reynolds number (Re), Strouhal number (St), and pressure distribution (C_p) to the physiological values inherent in phonation, where

$$\text{Re}=\frac{Ud}{\nu}, \tag{1}$$

$$\text{St}=\frac{fd}{U}, \tag{2}$$

$$C_p=\frac{\Delta P_{\text{trans}}}{1/2\rho U^2}. \tag{3}$$

In the above equations, U is the fluid velocity, d is the characteristic length scale, ν is the kinematic viscosity of the fluid, f is the frequency of the flow pulsations, ΔP_{trans} is the transglottal pressure drop, and ρ is the fluid density. The length scale, d, was chosen to be the height of the minimal constriction in the apparatus of interest, as shown in Fig. 3. Solving for U, f, and ΔP_{trans} results in U scaling as 1 over the model size, while f and ΔP_{trans} both scale as 1 over the model size squared. The life-size and scaled values for both apparatus can be found in Table I. The larger model size (7.5× life-size) was chosen to allow easier optical access, and better spatial resolution of the flow.

PIV data were taken in the anterior-posterior midplanes (Y-Z plane in experimental setup of Figs. 2 and 3). The flow was seeded using an olive oil atomizer (TSI, model #2) which incorporates six Laskin nozzles, and emits nearly monodisperse seed particles with diameters on the order of 1 μm. The seeding particles were inserted into the upstream

section of the wind tunnel via a flow loop which ran from the atomizer through a plenum chamber, before being drawn into the wind tunnel, 2.0 m (6.6 ft.) upstream of the test section, via two 2.54-cm (1.00 in.)-diameter perforated pipes placed along both side walls of the wind tunnel.

The area of interest was illuminated using a 500-mJ/pulse laser (New Wave, Nd: YAG) with a 532-nm wavelength and pulse duration of 5 ns. Images were captured by a digital camera (TSI PowerView 4MP, model 630051) with a 2000×2000 pixel CCD array. The image plane varied in size from ~30 mm square to ~60 mm square depending on the area of interest. The images were processed using an FFT correlator on a Nyquist grid, with 32^2 or 64^2 pixels, and 50% overlap. With peak-finding accuracy of ~0.1 pixels (Peterson, 2001) and subregion shifting of 8 to 16 pixels, the uncertainty in the mean velocity measurements was ~6%. The spatial resolution ranged from $\sim\pm0.24$ to 0.48 mm. The phase-averaged unsteady flow measurements were externally triggered from the optical encoder on the unsteadiness generators and thereby depended on the shutter frequency. The repeatability of the optical encoder was ±1/30th of a degree, which for a shutter frequency of 1.78 Hz results in a variation of ±0.104 ms. The number of image pairs (realizations) acquired for each data set varied between 100 and 1000. The number of realizations was chosen to ensure convergence of the ensemble mean, which was determined by comparing the average of N realizations to the average of $N+1$ realizations. The mean was considered converged when increasing N by 1 resulted in a minimal change in the average value. The number of realizations to be acquired at subsequent shutter positions was then chosen such that the average representation of the flow converged within 3% of the mean stationary value, thereby minimizing the amount of data that needed to be acquired, while still maintaining a sufficient level of accuracy. Vector validation was achieved by applying maximum, minimum, mean, median, and standard deviation statistics. Care was taken to not employ any interpolation, or "filling" processes that would alter the data sets.

The time history of velocity through the one-sided diffuser in pulsatile flow was measured using hot-wire anemometry (TSI, model IFA-300). The probe (TSI, model 1201-20) measured 0.20 cm (0.09 in.) wide, with a film diameter of 50.8 μm (2.0 μin.). The velocity was acquired at the throat by inserting the hot-wire wand from above, normal to the flow, such that the probe was flush against the upper diffuser wall, with the tip extending halfway across the diffuser throat, oriented so that the cross wire was normal to the flow direction. The maximum measured frequency response of the hot wire was ~100 kHz. The data samples were acquired at a rate of 600 Hz.

The unsteady time history of the flow velocity through the vocal-fold models was measured by laser Doppler velocimetry (LDV) (Dantec Dynamics Flowlite 1D). LDV has the added benefit over hot-wire anemometry of being a noninvasive technique which allows point-wise temporal resolution of the flow field. The interrogation volume was formed by two 1.38-mm-diameter beams produced by a helium-neon laser ($\lambda=632.8$ nm), with a frequency shift of 40 MHz. At the exit pupil of the focal lens the beam spacing was 38 mm with a divergence angle of 13.54°. The focal length of the beams was 160 mm, and the beam diameter at the focal length was ~0.1 mm, which corresponds to an ellipsoidal measurement volume of $\sim4.5\times10^{-3}$ mm^3. The measurement volume was positioned in the minimal glottal airspace between the two vocal-fold models, allowing capture of the streamwise velocity component. Signal processing was performed by flow-processing software (Dantec Dynamics BSA). Flow seeding specifications were the same as those used for the PIV measurements. The resulting acquired sample rate was on the order of 1 kHz for all of the measurements.

III. RESULTS

A. One-sided diffuser

Due to its simplicity, a one-sided diffuser design was chosen as a first approach to investigate the development of the unsteady Coanda effect. The simplified configuration allowed a broad investigation of the unsteady Coanda effect, while having the added benefit that the flow always attaches to one side, thereby simplifying spatial averaging of the mean velocity field. It also allows the flow conditions to be benchmarked with previous experiments performed on the Coanda effect (Borque and Newman, 1960; Newman, 1961). The results of this initial study were used to guide the approach taken in the subsequent investigation of the Coanda effect through more physiologically representative vocal-fold models. The frequency dependence of the Coanda effect was investigated by measuring the velocity field of pulsatile flow in the one-sided diffuser using phase-averaged PIV at two shutter frequencies (f_s); 1.81 and 2.67 Hz (102 and 150 Hz life-size). Figures 5(a) and 6(a), respectively, are temporal velocity traces at the slot (diffuser throat), plotted versus shutter phase, ϕ, in degrees, for the two aforementioned frequencies of interest. The location of the shutter positions, indicated as shutter phase ϕ, at which the PIV data were acquired is indicated on each plot by vertical lines, and is labeled as: (A) 20°; (B) 40°; (C) 60°; (D) 80°; (E) 95°; (F) 105°; (G) 115°; (H) 130°; (I) 145°; (J) 160°; and (K) 180°. Regions of acceleration ($\phi=40-105°$), maximum velocity ($\phi=105-115°$), and deceleration ($\phi=115-160°$) are indicated on each figure.

The temporal flow behavior is best explained by examining the time derivative of the velocity traces, or accelerations, plotted in Figs. 5(b) and 6(b) ($f_s=1.81$ and 2.67 Hz, respectively). As shown in Figs. 5(a) and 5(b), for a shutter frequency of 1.81 Hz the flow velocity begins accelerating shortly before point B, when the shutter phase is ~35°. Maximum acceleration of the flow occurs for a shutter phase of ~52°, after which the flow acceleration slowly diminishes, until the point of maximum velocity, and zero acceleration, is reached at point F. The flow then immediately decelerates, reaching maximum deceleration at a shutter phase of ~137°, before finally coming to rest at point J, $\phi=160°$. Figure 6(b) shows the time derivative of the velocity trace for a shutter frequency of 2.67 Hz. In comparison to Fig. 5(b), there is a slight lag between the two shutter positions arising from a small misalignment in the initial trigger

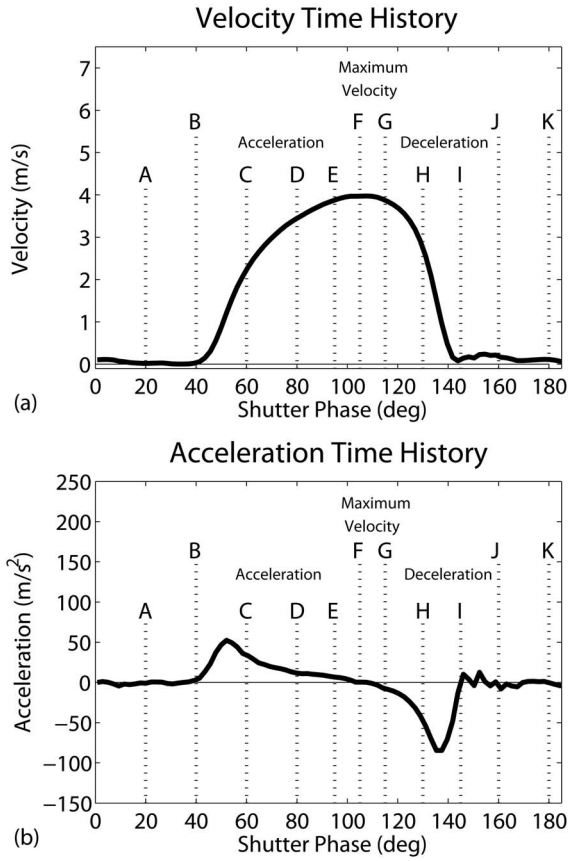

FIG. 5. (a) Velocity trace at the slot for a one-sided diffuser, with locations of phase-averaged data acquisition overlaid as vertical lines; f_s=1.81 Hz; (A) 20°; (B) 40°; (C) 60°; (D) 80°; (E) 95°; (F) 105°; (G) 115°; (H) 130°; (I) 145°; (J) 160°. (b) Acceleration of the velocity waveform at the slot for a one-sided diffuser, with locations of phase-averaged data acquisition overlaid as vertical lines; f_s=1.81 Hz; (A) 20°; (B) 40°; (C) 60°; (D) 80°; (E) 95°; (F) 105°; (G) 115°; (H) 130°; (I) 145°; (J) 160°.

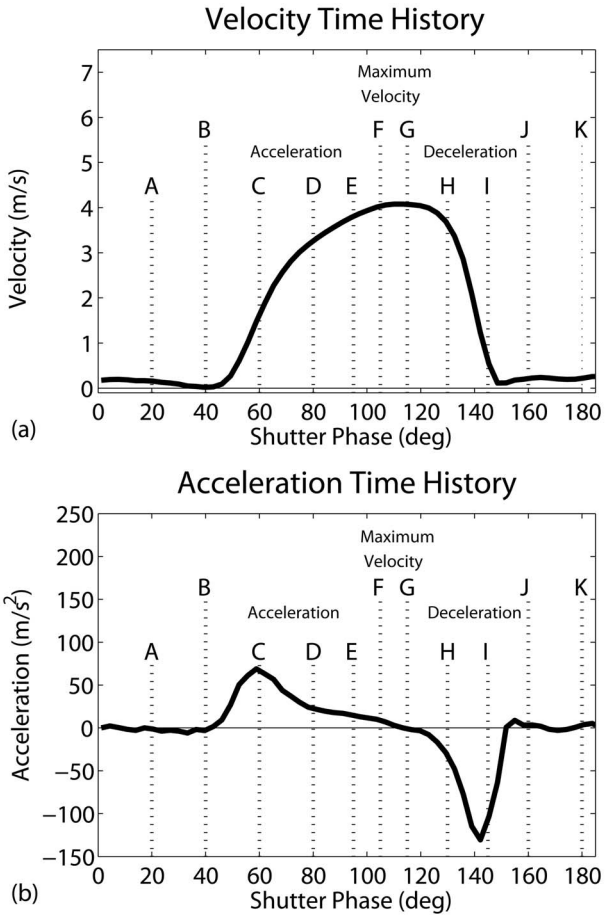

FIG. 6. (a) Velocity trace at the slot for a one-sided diffuser, with locations of phase-averaged data acquisition overlaid as vertical lines; f_s=2.67 Hz; (A) 20°; (B) 40°; (C) 60°; (D) 80°; (E) 95°; (F) 105°; (G) 115°; (H) 130°; (I) 145°; (J) 160°. (b) Acceleration of the velocity waveform at the slot for a one-sided diffuser, with locations of phase-averaged data acquisition overlaid as vertical lines; f_s=2.67 Hz; (A) 20°; (B) 40°; (C) 60°; (D) 80°; (E) 95°; (F) 105°; (G) 115°; (H) 130°; (I) 145°; (J) 160°.

position, although this difference does not affect the waveform characteristics. The flow initially accelerates slightly after point B, $\phi \sim 45°$. It follows the same pattern as described previously, with the maximum acceleration occurring for a shutter phase of ~57°, followed by a decline in the acceleration to the maximum velocity, and zero acceleration, at point G, where ϕ=115°. Deceleration reaches a maximum at a shutter phase of ~142°, before the flow is brought to rest at a shutter phase of 155°. The magnitude of the maximum acceleration and deceleration is about 25% greater for the 2.67-Hz case [Fig. 6(b)] than the 1.81-Hz case [Fig. 6(a)] due to the shorter opening and closing times inherent in the higher shutter frequency.

Phase-averaged PIV images were acquired at the previously specified shutter positions for a shutter frequency of 1.81 Hz (102 Hz life-size). The images are shown in Figs. 7(a)–7(c), representing a progression of the spatial flow field in time. The temporal location of the velocity field is referenced to the shutter positions, specified as points A through J in the velocity and acceleration waveform plots [see Figs. 5(a) and 5(b)], and is also represented as a vertical line, superimposed on the waveform plot, in the lower left corner of each image. Velocity magnitude is plotted, normalized by the maximum velocity (U_{max}=4.10 m/s) throughout the cycle. The contour plots range in color from blue to red, which corresponds to a normalized velocity of 0.0 to 1.0, respectively. White streamlines are superimposed on the plots. The spatial coordinates have been normalized by the maximum glottal gap (d=7.5 mm).

In Figs. 7(a)–7(c), f_s=1.81 Hz (102 Hz life-size), a leading vortex is observed for ϕ=65°. As it is convected downstream, the jet skews down toward the adjacent plate, and attachment occurs at a shutter phase of ϕ=105°, point F on the velocity and acceleration waveform graphs. Complete flow attachment was defined to be when the reattachment lengths of the pulsatile flow were equal to the reattachment lengths of the steady-flow measurements. The steady-flow measurements are not presented here, but can be found in Erath (2005). This point in time corresponds to the flow reaching maximum velocity, and the acceleration being zero [see Figs. 5(a) and 5(b)]. The streamwise reattachment length is approximately 5 diameters downstream of the slot. The jet remains attached to the surface throughout the remainder of the flow cycle, even after the maximum deceleration in the flow at $\phi \sim 145°$. The observation that the flow first attaches to the plate at the point of zero acceleration in this case as

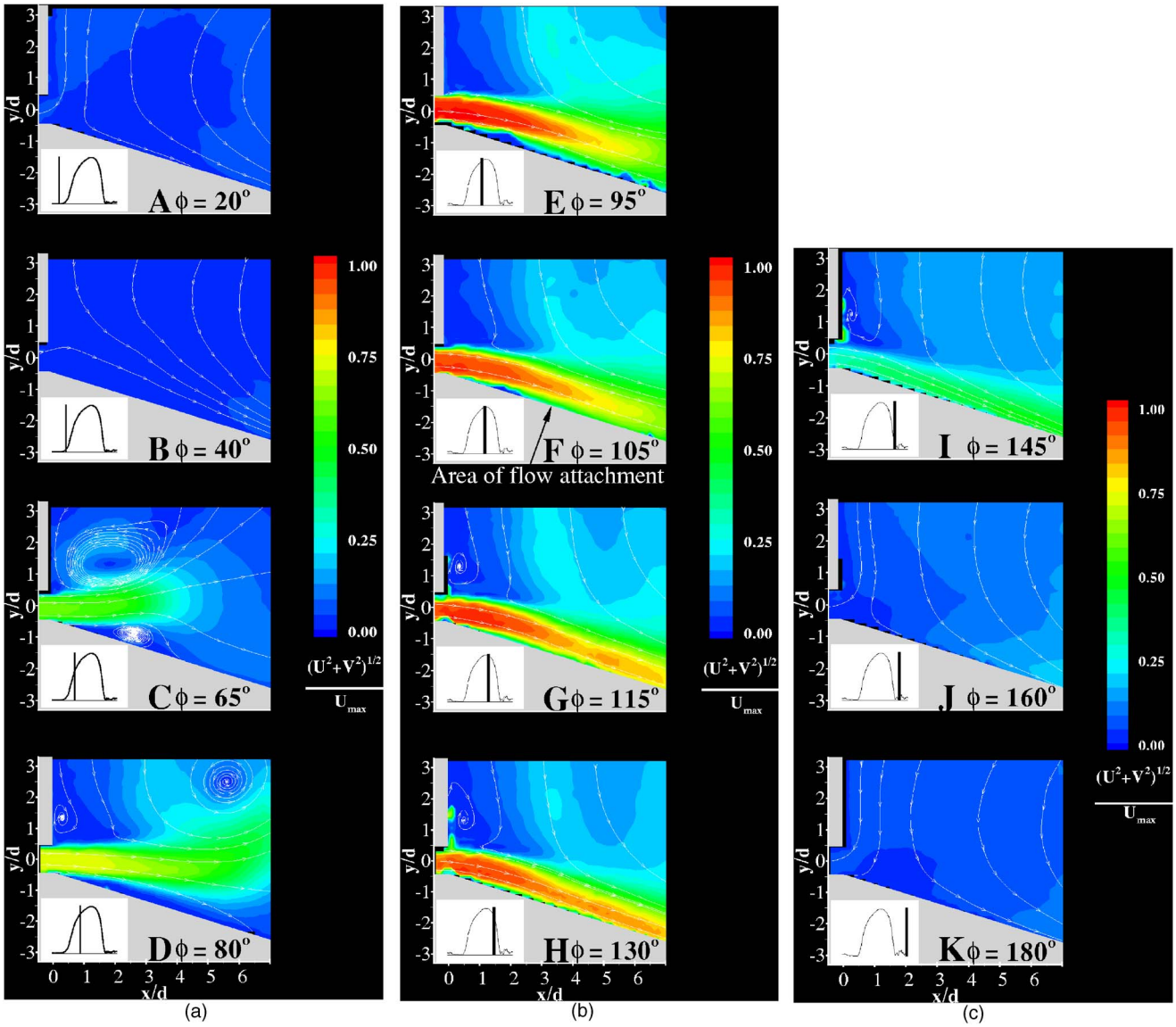

FIG. 7. (Color online) (a) Phase-averaged velocity field through a one-sided diffuser, f_s=1.81 Hz; ϕ=20° to 80°. (b) Phase-averaged velocity field through a one-sided diffuser, f_s=1.81 Hz; ϕ=95° to 130°. (c) Phase-averaged velocity field through a one-sided diffuser, f_s=1.81 Hz; ϕ=145° to 180°.

well as others to be presented suggests that the occurrence of the Coanda effect may be a function of the temporal velocity derivative, i.e., the flow acceleration.

Next, the development of the Coanda effect was investigated for a shutter frequency of 2.67 Hz (150 Hz life-size). If the time required for the development of the Coanda effect, as proposed by Pelorson *et al.* (1994), Hirschberg *et al.* (1996), and Hofmans *et al.* (2003), is constant (i.e., independent of pulsation frequency), then the phase at which the flow attaches will depend upon the pulse period. For example, when the flow is driven at 2.67 Hz, the phase at which it attaches would be 50% later in the pulse period, than for the case of 1.81 Hz. However, as shown in Fig. 8, the spatial and temporal behavior of the Coanda effect at the higher frequency (2.67 Hz) was identical to the flow field presented at the shutter frequency of 1.81 Hz. For brevity, only the velocity fields at the shutter phases of greatest interest (ϕ=65, 115, and 145°) are plotted for this frequency. For a complete account of the velocity fields at the higher frequency shutter phases, see Erath (2005). As in the lower frequency case, the initial leading vortex is observed at point C, where ϕ=65°. The jet is then skewed toward the plate in the subsequent images, before initially attaching to the surface at point G, a shutter phase of 115°. Referring back to the plots of the velocity and acceleration waveform [see Figs. 6(a) and 6(b)], this point again corresponds to the location of the flow where the velocity is a maximum, and the acceleration is zero. These results further confirm that the attachment of the Coanda effect is dependent upon the time derivative of the velocity waveform rather than an absolute time scale based on frequency.

B. Vocal-fold models

The velocity-dependent deflection of the Coanda jet was examined in the more physiologically relevant case of unsteady flow through the static vocal-fold models, at a shutter frequency of 1.81 Hz (100 Hz life-size). The model vocal-

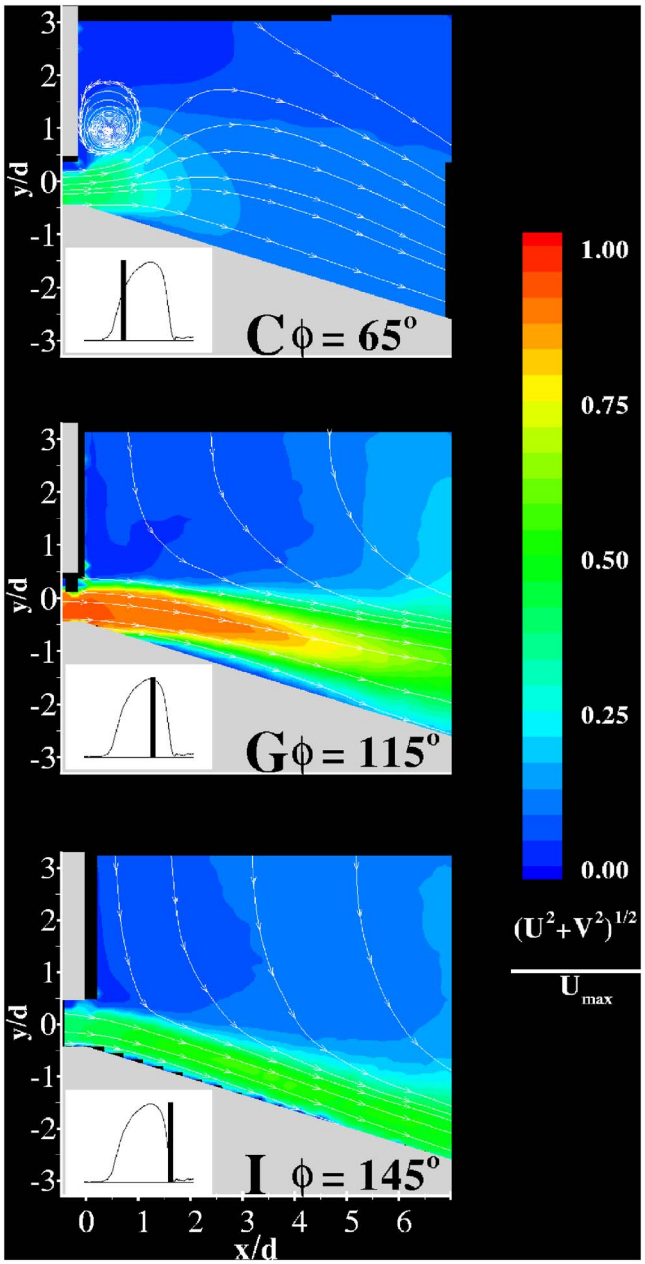

FIG. 8. (Color online) Phase-averaged velocity field through a one-sided diffuser, f_s=2.67 Hz; ϕ=65°, 115°, and 145°.

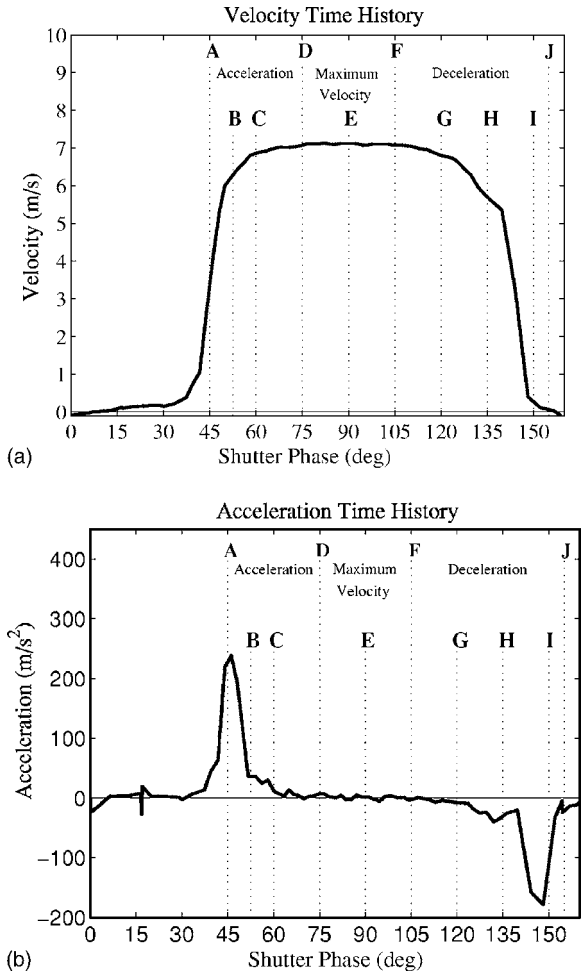

FIG. 9. (a) Velocity trace at the minimal glottal diameter, with locations of phase-averaged data acquisition represented by vertical lines: (A) 45°; (B) 52.5°; (C) 60°; (D) 75°; (E) 90°; (F) 105°; (G) 120°; (H) 135°; (I) 150°; (J) 155°, f_s=1.78 Hz (100 Hz life-size). (b) Time derivative of the velocity trace at the minimal glottal diameter, with locations of phase-averaged data acquisition represented by vertical lines: (A) 45°; (B) 52.5°; (C) 60°; (D) 75°; (E) 90°; (F) 105°; (G) 120°; (H) 135°; (I) 150°; (J) 155°, f_s=1.78 Hz (100 Hz life-size).

tract apparatus was placed in the wind tunnel, and the velocity waveform was acquired from LDV measurements for the pulsating flow conditions. The LDV measurements allowed noninvasive temporal resolution of the velocity. The waveform is shown in Fig. 9(a), with the corresponding plot of the acceleration shown in Fig. 9(b).

The location of the phase-averaged PIV data acquisition points is labeled on the plots as: (A) 45°; (B) 52.5°; (C) 60°; (D) 75°; (E) 90°; (F) 105°; (G) 120°; (H) 135°; (I) 150°; and (J) 155°. Areas of acceleration, maximum velocity, and deceleration are labeled on both graphs. The flow accelerates quickly, reaching a maximum at point A, before decelerating to zero at point D, where the maximum velocity occurs. The flow remains steady until point F, where it begins to decelerate, eventually reaching a maximum deceleration at a shutter phase of ~145°, before the velocity is brought to rest at point J.

Phase-averaged PIV measurements of pulsatile flow through the 7.5× scaled static vocal-fold models with divergence angles of 10, 20, and 40° were acquired, with 1000 velocity field realizations captured at each shutter phase. It was observed that, for each shutter phase, the jet deflection angle, i.e., the angle that the glottal jet deflected from the streamwise direction, varied significantly for the 1000 realizations. In some realizations the jet was deflected toward the lower wall, whereas in others it was skewed toward the upper wall. Typical phase-averaged analysis entails averaging all of the realizations for a given phase angle to achieve statistical convergence of the average flow representation. This method was inappropriate because the random behavior (flip flopping) of the jet deflection angle for a given phase, ϕ, would smear out any asymmetries or unsteadiness in the flow. To alleviate this concern, the inclusion of a particular vector field in the phase average was determined based on a

calculation of the jet deflection angle for that image pair. After calculating the jet deflection angle for each image pair (at constant shutter phase), a histogram of the distribution was plotted for each data acquisition set, and each vocal-fold model, with a resolution of $\pm 0.0625\Psi$, where Ψ is the total glottal divergence angle. The glottal jet trajectory at each shutter phase, represented by a histogram plot of the jet deflection angle for each data acquisition set, was observed to have a Gaussian-type distribution centered about the peak location (see Erath, 2005; Erath and Plesniak, 2006). The most prevalent jet deflection angle histogram bin contained ~75% of the total realizations at each shutter phase. The PIV velocity fields are presented as the average of the realizations corresponding to the dominant location of the glottal jet at each divergence angle and shutter phase. This method minimized the smearing of flow features due to over averaging, while allowing statistical convergence of the velocity field to be achieved. The result is a detailed representation of the velocity field for the "most probable" location of the glottal jet at any given shutter phase for each divergence angle. While the complete sequence of velocity fields for each shutter phase is presented for a divergence angle of 10°, only the critical shutter phases are plotted for divergence angles of 20 and 40°. The complete sequence of velocity fields at all of the shutter phases for these two divergence angles can be found in Erath (2005).

1. Ten-degree divergence

The phase-averaged PIV images are shown in Figs. 10(a)–10(c) for a vocal-fold divergence angle of $\Psi = 10°$. In these figures, the spatial coordinates have been normalized by the minimal glottal diameter, $d = 0.30$ cm (0.40 mm life-size), and the velocity magnitude has been nondimensionalized by the maximum fluid velocity ($U_{max} = 7.40$ m/s), for the complete cycle. The results are plotted as contours of normalized velocity magnitude from 0.0 to 1.0, ranging in color from blue to red, respectively. White streamlines are overlaid to highlight the flow patterns.

An initial leading vortex is evident during the acceleration of the flow. As the flow reaches its maximum velocity at point D, $\phi = 75°$, the Coanda effect is manifested as the jet deflects towards and attaches to the vocal-fold wall [see Fig. 10(b)]. This shutter phase corresponds to the instant when the velocity waveform reaches its maximum value, and the acceleration is zero [see Figs. 9(a) and 9(b)]. This again confirms that the formation of the Coanda effect is dependent upon the acceleration of the flow to maximum velocity. Once attached to the vocal-fold wall the flow remained attached throughout the remainder of the cycle, as in the case of the one-sided diffuser.

2. Twenty-degree divergence

The relevant flow-field behavior can be represented by the critical points of the flow, points B, D, and I, in the forcing waveform. These locations correspond to the initial acceleration of the flow, the point of maximum velocity, and deceleration of the flow preceding complete stoppage. For brevity, the velocity fields through the 20° divergent vocal-fold models are plotted at these critical shutter phases in Fig. 11. At point B ($\phi = 52.5°$) the flow accelerates through the slot, and a large leading vortex is formed. The velocity reaches a maximum and the acceleration of the flow goes to zero at point D ($\phi = 75°$). As with the smaller divergence angle, the flow attaches to the vocal-fold wall at this phase. It remains attached to the wall through the closing phases of the shutter as the flow decelerates (point I). Note that for a divergence angle (Ψ) of 20° the attachment length of the flow along the vocal-fold models is greater for point I than for point D (see Fig. 11), showing a propensity for the point of flow separation to move downstream throughout the cycle. Consequently, the jet also deflects further from the streamwise direction. For $\Psi = 10°$ the separation point of the flow from the vocal-fold model remained relatively steady throughout the cycle once the flow initially attached, separating at the onset of the exit radius.

3. Forty-degree divergence

The flow behavior is significantly different for a vocal-fold divergence angle of 40° (Fig. 12). Again, the velocity fields are only shown at the critical points (B, D, and I). While the flow initially behaves similarly to the previous cases, with a leading vortex, the flow remains unattached throughout the entire flow cycle, never skewing far enough towards a wall for the jet to completely attach. This can be seen at point D, where the velocity has reached a maximum, yet the flow remains symmetric about the midline. A slight deflection in the jet deflection angle is observed at point I; however, it is believed that this small skewing is a result of very slight geometrical asymmetries in the 40° divergent models. It was found that minimal variations of ~25 μm (0.001 in.) in the surface finish, as well as geometric variations between the two facing vocal-fold models of ~100 μm (0.004 in.), resulted in the flow preferentially skewing towards a particular wall. If not for slight imperfections in the 40° divergent model, the flow would be expected to remain symmetric throughout the complete cycle. A more in-depth discussion of the flow stability resulting from geometric variations can be found in Erath and Plesniak (2006).

IV. DISCUSSION

The investigation of pulsatile flow through a one-sided diffuser and static vocal-fold models has resulted in the identification of important flow structures that are expected to influence sound production in the vocal tract. Most notable is the flow asymmetry that arises due to the formation of the Coanda effect at divergence angles of 10 and 20°. The occurrence of the Coanda effect was shown to depend on the local unsteady acceleration rather than the cycle frequency, thereby emphasizing its importance in voiced as well as unvoiced speech. While these results seem to contradict the findings of Pelorson *et al.* (1994, 1995), Hirschberg *et al.* (1996), and Hofmans *et al.* (2003), they are actually consistent. As previously mentioned, a major shortcoming of their work was that the flow acceleration, generated by the impulsively opened valve, comprised a large portion

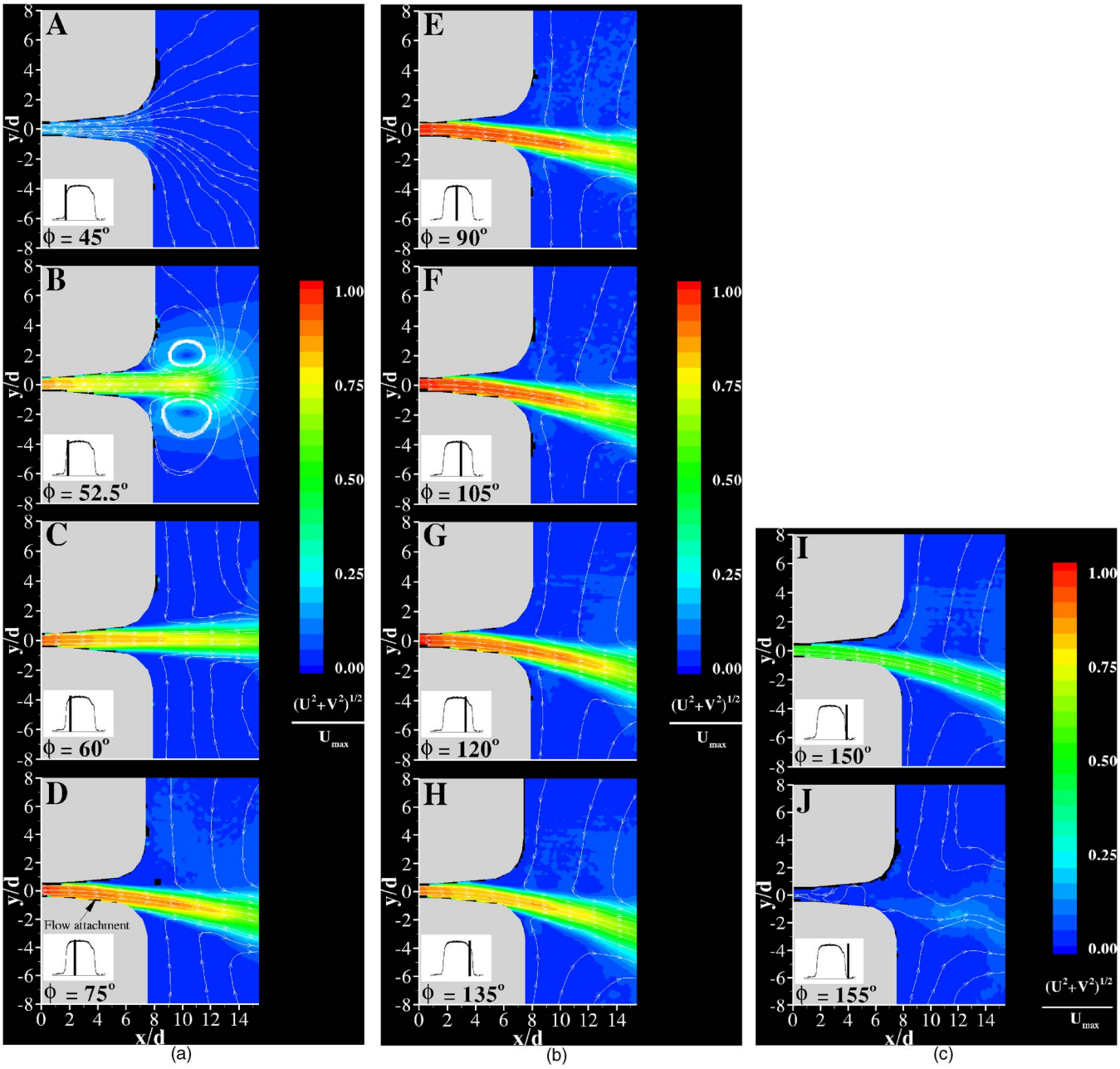

FIG. 10. (Color online) (a) Phase-averaged velocity field through a static vocal-fold model, $\Psi=10°$, $f_s=1.78$ Hz (100 Hz life-size); $\phi=45°$ to 75°. (b) Phase-averaged velocity field through a static vocal-fold model, $\Psi=10°$, $f_s=1.78$ Hz (100 Hz life-size); $\phi=90°$ to 135°. (c) Phase-averaged velocity field through a static vocal-fold model, $\Psi=10°$, $f_s=1.78$ Hz (100 Hz life-size); $\phi=150°$ to 155°.

(about one-fourth) of the total scaled glottal cycle. An inspection of their work reveals that the point at which the Coanda effect develops corresponds to the flow reaching maximum velocity and zero acceleration. In other words, had the impulsively started flow accelerated to maximum velocity quicker, as expected in the physiological case where the flow is pulsatile, the Coanda formation times would have been shorter also, and on the order of those reported in this work.

While no quantitative data have been presented regarding contribution of the Coanda effect to vocal-tract sound, the interaction of the jet with the vocal-fold walls is expected to contribute to the dipole sound source resulting from the unsteady force exerted on the fluid by the walls (see Z. Zhang, 2002). It also follows that the observed downstream deflection of the glottal jet towards the larynx walls may cause an interaction with the false vocal folds, as reported by Shadle (1985), C. Zhang *et al.* (2002), Krane (2005), and Howe and McGowan (2005). The moving separation point is expected to be of greatest consequence since flow separation is responsible for the varying flow resistance through the glottis, and ultimately, the production of voice (Titze, 1988; Hirschberg, 1992; McGowan, 1993). Furthermore, the presence of the Coanda effect would give rise to pressure differences between the two walls of the vocal folds, thereby directly affecting the forcing functions that drive the motion of the vocal folds (Scherer *et al.*, 2001).

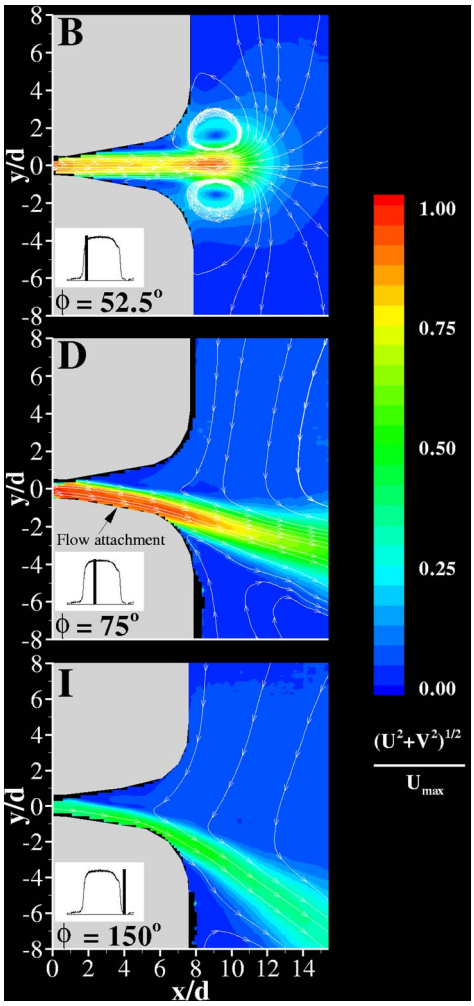

FIG. 11. (Color online) Phase-averaged velocity field through a static vocal-fold model, $\Psi=20°$, $f_s=1.78$ Hz (100 Hz life-size); $\phi=52.5°$, 75°, and 150°.

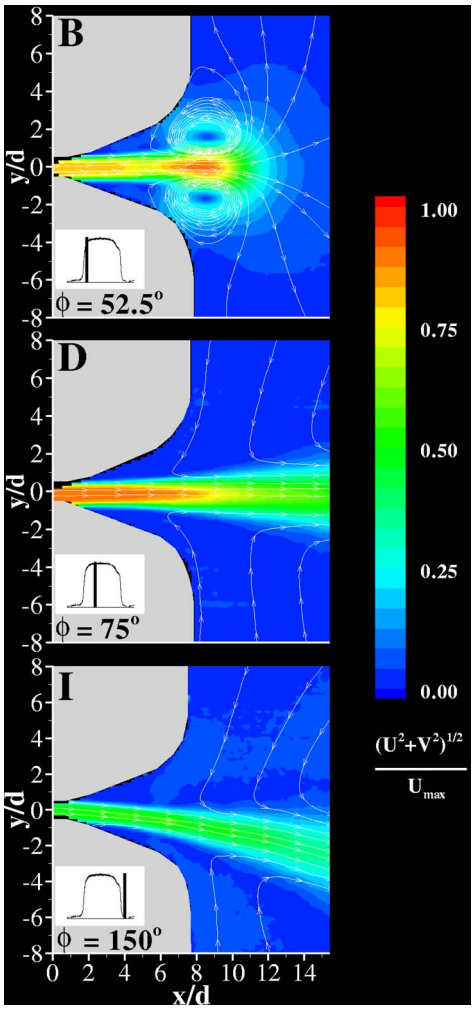

FIG. 12. (Color online) Phase-averaged velocity field through a static vocal-fold model, $\Psi=40°$, $f_s=1.78$ Hz (100 Hz life-size); $\phi=52.5°$, 75°, and 150°.

There are several shortcomings of the present simplified model with respect to the complex process of phonation. In particular, the dynamic motion of the vocal folds contributes to the flow velocity in the glottal airspace. Berke *et al.* (1989) observed that the velocity time history in excised canine larynges exhibited a small acceleration when the vocal folds began to close, a phenomenon which was attributed to flow displacement arising from the vocal folds' interaction with the fluid as they began to close. Furthermore, in the moments immediately following and preceding glottal opening and closure (when the glottal airspace is small) the dominant mechanism driving the fluid velocity is the motion of the vocal fold walls (Deverge *et al.*, 2003).

V. CONCLUSIONS

The development of the Coanda effect in pulsatile flow was investigated in an idealized one-sided diffuser, and in the more physiologically representative case of flow through static models of the vocal folds. The scaling of the Reynolds and Strouhal number and the pressure coefficient to physiological values lends confidence that these results are reasonable representations of *in vivo* laryngeal flows.

It was observed that the establishment of the Coanda effect in pulsatile flow depends more strongly on the local unsteady acceleration than on the pulsation frequency, as has been previously reported by Pelorson *et al.* (1994, 1995), Hirschberg *et al.* (1996), and Hofmans *et al.* (2003). These findings result from a more physiologically relevant scenario of a fully pulsatile flow field, and they are not contradictory to previous results (Pelorson *et al.*, 1995; Hofmans *et al.*, 2003) if those results are interpreted by using the findings presented here. The attachment of the Coanda jet to the adjacent wall consistently occurred when the forcing velocity waveform reached its maximum value, and the acceleration was zero, for glottal divergence angles $\leqslant 20°$. For a postcritical divergence angle of 40°, the flow never attached to a wall.

The separation point of the flow from the vocal-fold models also varied as a function of divergence angle, consistent with the findings of Newman (1961). For $\Psi=10°$, the flow detached from the vocal-fold models at the onset of the exit radius. Increasing Ψ to 20° resulted in the flow staying attached halfway around the exit radius. The presence of the Coanda effect in phonation is expected to influence sound production due to the drastic change in the separation point

of the flow, as well as the interaction of the skewed jet with the ventricular folds. The pressure distribution on each vocal fold arising from an asymmetric separated flow will also result in a difference in the aerodynamic forces acting on the two folds.

ACKNOWLEDGMENTS

This research was funded by the National Institutes of Health Grant RO1 DC03577. The authors would like to acknowledge Alison Templin for her assistance in data acquisition on the project.

Alipour, F., and Scherer, R. C. (**1995**). "Pulsatile airflow during phonaton: An excised larynx model," J. Acoust. Soc. Am. **97**, 1241–1248.

Alipour, F., Patel, V. C., and Scherer, R. C. (**1995a**). "Measurement of pulsatile flow in excised larynges with hot-wire anemometry," ASME FED-Vol 202 Indl. Papers in Fluids Eng. 1–5.

Alipour, F., Patel, V. C., and Scherer, R. C. (**1995b**). "An experimental study of pulsatile flow in canine larynges," J. Fluids Eng. **117**, 577–581.

Barney, A., Shadle, C. H., and Davies, P. O. A. L. (**1999**). "Fluid flow in a dynamic mechanical model of the vocal folds and tract. I. Measurements and theory," J. Acoust. Soc. Am. **105**, 444–455.

Berke, G. S., Moore, M. D., Monkewitz, P. A., Hanson, D. G., and Gerratt, B. R. (**1989**). "A preliminary study of particle velocity during phonation in an *in vivo* canine model," J. Voice **3**, 306–313.

Borque, C., and Newman, B. G. (**1960**). "Reattachment of a two-dimensional incompressible jet to an adjacent flat plate," The Aeronautical Quarterly Review, V.XI.

Bremhorst, K., and Hollis, P. G. (**1990**). "Velocity field of an axisymmetric pulsed, subsonic air jet," AIAA J. **28**, 2043–2049.

Coanda, H. (**1936**). "Device for deflecting a stream of elastic fluid projected into an elastic fluid," U.S. Patent No. 2,052,869, Sept. 1, 1936.

Deverge, M., Pelorson, X., Vilain, C., Lagree, P.-Y., Chentouf, F., Willems, J., and Hirschberg, A. (**2003**). "Influence of collision on the flow through *in vitro* rigid models of the vocal folds," J. Acoust. Soc. Am. **114**, 3354–3362.

Erath, B. D. (**2005**). "An experimental investigation of velocity fields in divergent glottal models of the human vocal tract," M.S. thesis, Purdue University.

Erath, B. D., and Plesniak, M. W. (**2006**). "An investigation of bimodal jet trajectory in flow through scaled models of the human vocal tract," Exp. Fluids (in press).

Grant, I. (**1997**). "Particle image velocimetry: A review," Proc. Inst. Mech. Eng., Part C: J. Mech. Eng. Sci. **211**, 55–76.

Hirschberg, A. (**1992**). "Some fluid dynamic aspects of speech," Bull. Commun. Parlee **2**, 7–30.

Hirschberg, A., Pelorson, X., Hofmans, G. C. J., van Hassel, R. R., and Wijnands, A. P. J. (**1996**). "Starting transient of the flow through an *in-vitro* model of the vocal folds," in *Vocal Fold Physiology: Controlling Complexity and Chaos*, edited by P. J. Davis and N. H. Fletcher (Singular, San Diego, CA), pp. 31–46.

Hofmans, G. C. J., Groot, G., Ranucci, M., Graziani, G., and Hirschberg, A. (**2003**). "Unsteady flow through *in-vitro* models of the glottis," J. Acoust. Soc. Am. **113**, 1658–1675.

Howe, M. S. (**1975**). "Contributions to the theory of aerodynamic sound, with application to excess jet noise and the theory of the flute," J. Fluid Mech. **71**(4), 625–673.

Howe, M. S., and McGowan, R. S. (**2005**). "Aeroacoustics of [s]," Proc. R. Soc. London, Ser. A **461**, 1005–1028.

Hussain, A. K. M. F. (**1986**). "Coherent structures and turbulence," J. Fluid Mech. **173**, 303–356.

Kaiser, J. F. (**1983**). "Some observations on vocal tract operation from a fluid flow point of view," in *Vocal Fold Physiology: Biomechanics, Acoustics, and Phonatory Control*, edited by I. R. Titze and R. C. Scherer (Denver Center for the Performing Arts, Denver, CO), pp. 358–386.

Krane, M. H. (**2005**). "Aeroacoustic production of low-frequency unvoiced speech sounds," J. Acoust. Soc. Am. **118**, 410–427.

McGowan, R. S. (**1988**). "An aeroacoustic approach to phonation," J. Acoust. Soc. Am. **83**, 696–704.

McGowan, R. S. (**1993**). "The quasisteady approximation in speech production," J. Acoust. Soc. Am. **94**, 3011–3013.

Mongeau, L., Franchek, N., Cooker, C. H., and Kubil, R. A. (**1997**). "Characteristics of a pulsating jet through a small modulated orifice, with application to voice production," J. Acoust. Soc. Am. **102**, 1121–1133.

Newman, B. G. (**1961**). "The deflexion of plane jets by adjacent boundaries—Coanda effect," in *Boundary Layer and Flow Control*, edited by G. V. Lachmann (Pergamon, New York), pp. 232–264.

Pelorson, X., Hirschberg, A., van Hassel, R. R., and Wijnands, A. P. J. (**1994**). "Theoretical and experimental study of quasisteady-flow separation within the glottis during phonation. Application to a modified two-mass model," J. Acoust. Soc. Am. **96**, 3416–3431.

Pelorson, X., Hirschberg, A., Wijnands, A. P. J., and Bailliet, H. M. A. (**1995**). "Description of the flow through *in-vitro* models of the glottis during phonation," Acta Acust. (Beijing) **3**, 191–202.

Peterson, S. D. (**2001**). "Experimental Investigations of Multiple Jets-In-Crossflow," Masters thesis, Purdue University.

Raffel, M., Willert, C., and Kompenhans, J. (**1998**). *Particle Image Velocimetry, A Practical Guide* (Springer, Berlin).

Scherer, R. C., Shinwari, D., DeWitt, K. J., Zhang, C., Kucinschi, B. R., and Afjeh, A. A. (**2001**). "Intraglottal pressure profiles for a symmetric and oblique glottis with a divergence angle of 10 degrees," J. Acoust. Soc. Am. **109**, 1616–1630.

Shadle, C. H. (**1985**). "The Acoustics of Fricative Consonants," Ph.D. thesis, Massachusetts Institute of Technology.

Stevens, K. N. (**1971**). "Airflow and turbulence noise for fricative and stop consonants: Static considerations," J. Acoust. Soc. Am. **50**, 1180–1192.

Teager, H. M. (**1980**). "Some observations on oral air flow during phonation," IEEE Trans. Acoust., Speech, Signal Process. **ASSP-28**(5), 599–601.

Teager, H. M., and Teager, S. M. (**1981**). "The effects of separated air flow on vocalization," in *Vocal Fold Physiology: Contemporary Research and Clinical Issues*, edited by D. M. Bless and J. H. Abbs (College-Hill, San Diego, CA), pp. 124–143.

Teager, H. M., and Teager, S. M. (**1983**). "Active fluid dynamic voice production models, or there is a unicorn in the garden," in *Vocal Fold Physiology: Biomechanics, Acoustics, and Phonatory Control*, edited by I. R. Titze and R. C. Scherer (Denver Center for the Performing Arts, Denver, CO), pp. 387–401.

Titze, I. R. (**1988**). "The physics of small-amplitude oscillation of the vocal folds," J. Acoust. Soc. Am. **83**, 1536–1552.

Zhang, C., Zhao, W., Frankel, S. H., and Mongeau, L. (**2002**). "Computational aeroacoustics of phonation. II. Effects of flow parameters and ventricular folds," J. Acoust. Soc. Am. **112**, 2147–2154.

Zhang, Z., Mongeau, L., and Frankel, S. H. (**2002**). "Experimental verification of the quasisteady approximation for aerodynamic sound generation by pulsating jets in tubes," J. Acoust. Soc. Am. **112**, 1652–1663.

Model-based classification of nonstationary vocal fold vibrations

Tobias Wurzbacher, Raphael Schwarz, and Michael Döllinger
Department of Phoniatrics and Pediatric Audiology, University Hospital Erlangen, Medical School, Erlangen, Germany

Ulrich Hoppe
Department of Audiology, University Hospital Erlangen, Medical School, Erlangen, Germany

Ulrich Eysholdt and Jörg Lohscheller
Department of Phoniatrics and Pediatric Audiology, University Hospital Erlangen, Medical School, Erlangen, Germany

(Received 19 October 2005; revised 11 May 2006; accepted 12 May 2006)

Classification of vocal fold vibrations is an essential task of the objective assessment of voice disorders. For historical reasons, the conventional clinical examination of vocal fold vibrations is done during stationary, sustained phonation. However, the conclusions drawn from a stationary phonation are restricted to the observed steady-state vocal fold vibrations and cannot be generalized to voice mechanisms during running speech. This study addresses the approach of classifying real-time recordings of vocal fold oscillations during a nonstationary phonation paradigm in the form of a pitch raise. The classification is based on asymmetry measures derived from a time-dependent biomechanical two-mass model of the vocal folds which is adapted to observed vocal fold motion curves with an optimization procedure. After verification of the algorithm performance the method was applied to clinical problems. Recordings of ten subjects with normal voice and ten dysphonic subjects have been evaluated during stationary as well as nonstationary phonation. In the case of nonstationary phonation the model-based classification into "normal" and "dysphonic" succeeds in all cases, while it fails in the case of sustained phonation. The nonstationary vocal fold vibrations contain additional information about vocal fold irregularities, which are needed for an objective interpretation and classification of voice disorders. © *2006 Acoustical Society of America.* [DOI: 10.1121/1.2211550]

PACS number(s): 43.70.Aj, 43.70.Bk, 43.70.Dn, 43.72.Ar [BHS] Pages: 1012–1027

I. INTRODUCTION

The visual examination of vocal fold oscillations in clinical routine is based on laryngeal endoscopic techniques. Endoscopic real-time recording systems, based on digital high-speed (HS) cameras, allow for observation and interpretation of aperiodic, irregular, and nonstationary vocal fold vibrations.[1–3] HS systems have successfully been used to reveal the nature of vocal fold oscillations in the case of normal voices and in different kinds of dysphonia.[4–9]

Commonly, vocal fold vibrations are assessed during a stationary vocalization, for example the phonation of a sustained vowel at a constant pitch and intensity level. This phonation paradigm originates historically from the stroboscopic examination situation,[10,11] since stroboscopy is technically confined to the steady state. The sustained phonation paradigm has also been used for HS examinations, although the HS technique is not restricted to a stationary vocalization process. However, sustaining a vowel excludes the investigation of dynamic phonation transitions comprised in the everyday use of speech, resulting in an incomplete characterization of phonation. As an example, short segments for two stationary phonations at different pitches of HS recorded vocal fold vibrations are given in Fig. 1. The female subject, age 55 years, has a right-sided unilateral recurrent laryngeal nerve paralysis. In each graph the upper and lower curves represent the deflections from the glottal midline of the left and right vocal fold. Within the two recordings the effect of the paralysis on the vocal fold vibrations is quite different. At the fundamental frequency $f_0=235$ Hz, the stability of the oscillation amplitude of both vocal folds is disturbed. The mean amplitude ratio between the right and left vocal fold is 4/3. In contrast, at the pitch $f_0=395$ Hz the oscillation amplitudes of both curves are stable, while the mean amplitude ratio turned to 2/3. As a result the acoustic voice signal of the low-pitched phonation sounds much hoarser than the high-pitched phonation. The example demonstrates the principal disadvantage of a stationary phonation paradigm, which focuses just on the investigation of vocal fold vibrations at one pitch: the voice disorder of the investigated subject emerges quite differently at different pitch frequencies. The effects of a voice disorder on vocal fold vibrations depend on the fundamental frequency. During the medical examination with a stationary phonation it may happen that the patient phonates at a pitch, where only minor vocal fold asymmetries appear and thus the extent of the voice disorder is not detected. Therefore, a stationary phonation condition may underdiagnose a voice disorder. To overcome this drawback, nonstationary phonation paradigms can be applied for

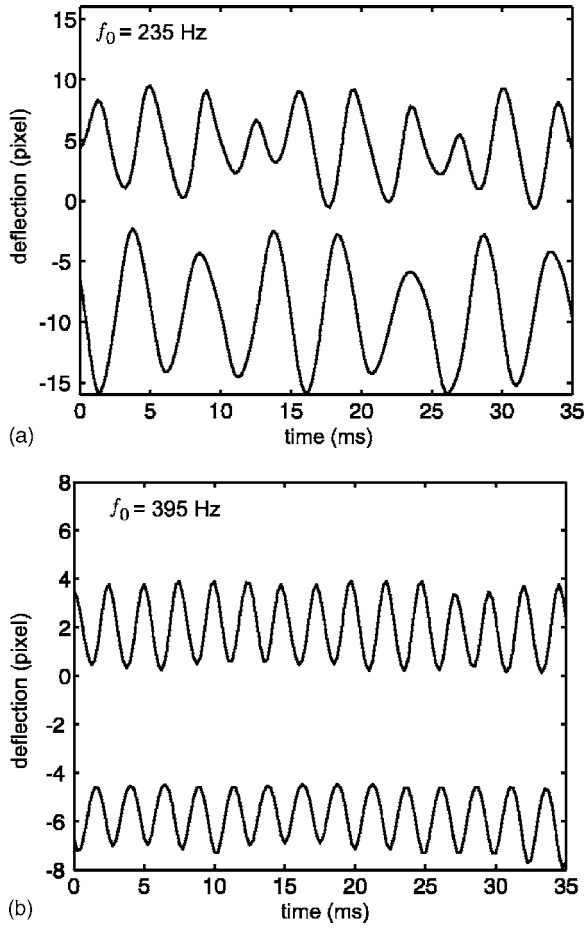

FIG. 1. Two segments of SSP vocal fold oscillations at the medial position of the vocal folds at different pitches for a female subject suffering from right-sided unilateral recurrent laryngeal nerve paralysis. In graph (a) at pitch f_0=235 Hz and in graph (b) at pitch f_0=395 Hz. In each graph the upper (lower) curve represents the oscillations of the left (right) vocal fold. The glottal midline is located at deflection 0. The paralyzed side oscillates farther away from the midline than the healthy side.

the voice diagnosis, which incorporate dynamical transitions scanning a broader phonation regime and preserving the practicability for endoscopic examination.

Currently, alternative nonstationary phonation paradigms for endoscopic HS recordings are under investigation. Some studies have focused on the nonstationary vocal fold onset to detect and classify dynamical vocal fold abnormalities.[12,13] Recent work has also investigated a pitch raise paradigm for normal voices to gain more insight in nonstationary laryngeal mechanisms.[14,15] Glottal and articulatory parameters changed significantly during the pitch raise: vocal fold length increased, the amplitude of the vocal fold oscillation as well as the glottal area decreased, and the sound pressure level changed.

In this work the potential of a monotonous pitch raise (MPR) paradigm for endoscopic HS examinations is opposed to the conventionally sustained stationary phonation (SSP) condition. Ten healthy subjects and ten subjects diagnosed with different kinds of voice disorders were examined using both conventional SSP and the proposed nonstationary MPR phonation paradigm. The study investigates whether the MPR is more suitable for detecting a voice pathology than the SSP paradigm. For this purpose the observed vocal fold vibrations are classified into a normal and a pathological group.

From a clinical point of view, an efficient method to classify vocal fold vibrations is of particular interest. The basic idea behind the classification is a quantitative analysis of left to right asymmetries and irregularities of the vocal fold vibrations. The vocal folds of normal voices vibrate more symmetrical and regular than pathological ones.[7,16] The aim is to derive quantitative parameters that describe the degree of symmetry and stability of vocal fold vibrations. In a preliminary investigation, a simple curve analysis of the HS observed vocal fold vibrations with respect to side differences in envelope and frequency failed to separate the examined subjects into a normal and a pathological group. The absence of important vocal fold vibration characteristics, such as oscillation shape and collision information, may arise as a possible explanation.

In former studies the quantitative analysis of stationary sustained vibrations was successfully performed by adapting the dynamics of a biomechanical two-mass model (2MM) to the observed vibrations.[7,8,17] As shown, the 2MM vibration characteristics can simulate a wide variety of normal and pathological vocal fold vibrations.[7,8,18–24] Therefore, the 2MM offers a comprehensive curve analysis of vocal fold vibrations. However, the work of Döllinger *et al.*[7] was not focused on the clinical application but rather on the methodology to obtain parameter values by global optimization in case of a stationary phonation.

In this paper a 2MM-based approach for the analysis and the quantitative interpretation of nonstationary vocal fold vibrations is presented. In order to simulate nonstationary vibrations, the original constant 2MM parameters are modified to be time dependent. An optimization procedure is developed that adapts the time-dependent 2MM dynamics to nonstationary vocal fold vibrations. The performance of the optimization procedure is verified with synthetically generated vocal fold vibrations and the optimization procedure is applied to real clinical problems. The parameters of the 2MM have no direct assignment to anatomical vocal fold structures[25] and thus are not interpreted in a physiological way. However, the optimized model parameters capture time-dependent characteristics of vocal fold vibrations and are used for categorization purpose. The further clinical treatment and the therapy outcome can be assessed with the optimized parameters. Within this study it is shown that these parameters enable a separation of normal and pathological voices in the case of a nonstationary pitch raise phonation.

II. METHODS

A. Data acquisition

Vocal fold vibrations were recorded in real-time with a HS camera system during phonation. A rigid endoscope (90° optic, 9-mm diameter) coupled to a HS camera (256 $\times$256 pixel spatial and 4000-Hz temporal resolution, Wolf

TABLE I. Itemization of subjects for the endoscopical HS recordings with normal and pathological voice.

Subject ID	Disease
1–10	normal voice
11–14	functional dysphonia
15	functional dysphonia+nodules
16	Reinke's edema; postsurgery
17	vocal fold polyp
18,19	unilateral recurrent laryngeal nerve paralysis
20	unilateral recurrent laryngeal nerve paralysis; postsurgery

Corp. Knittlingen, Germany) was placed into the oropharynx. Details on the general recording situation can be found in the literature.[2,7]

HS recordings of two different phonation paradigms are explored:

(1) SSP—sustained stationary phonation: An endoscopic HS image series was recorded during sustained phonation of the vowel /a/ at a comfortable, constant pitch and intensity. It is the conventional examination paradigm in clinical endoscopy.
(2) MPR—monotonous pitch raise: An endoscopic HS image series was recorded during a monotonic increase of the pitch frequency during the phonation of the vowel /a/. The subjects were instructed to phonate from a low pitch up to an arbitrary higher one.

Within the study HS recordings of each examination paradigm were performed from two different groups as listed in Table I:

(1) Normal voice group: The first group consisted of ten subjects (ten female, 20.4±3.8 years) with a normal voice, which exhibited neither history nor clinical signs of a voice disorder.
(2) Pathological voice group: The second group included subjects diagnosed with different kinds of voice disorders (nine female, one male; 39.2±11.2 years). The group is subdivided in functional (ID 11–15) and organic (ID 16–20) voice disorders. Each pathology has an influence on the vibration characteristic and destabilizes the symmetry of vocal fold oscillations.

Potential effects on the vocal fold vibration characteristic due to different ages in both subject groups are neglected, since permanent hormonal vocal changes do not occur until the menopause.[26] In the average both subject groups are younger.

In all 40 HS recordings were performed. The digital image data, delivered by the CCD sensor, are permanently stored and permit the application of image processing algorithms.[12,27] The aim of the image analysis is to extract the vibrating vocal fold edges within the HS recordings. This is achieved by segmenting the time-varying opening of the glottis. Figure 2 shows a segmented image of the endoscopic HS series. The segmented contours of the vocal fold edges and the glottal axis are depicted as white lines. The glottal

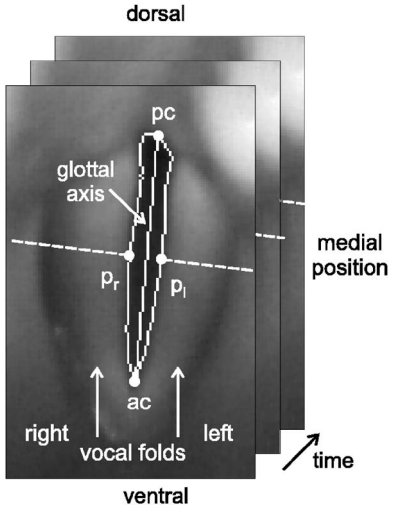

FIG. 2. A segmented HS image. The vocal fold edges and the glottal axis are marked as white lines. Four specific points are indicated as white filled circles: ac—anterior commissure, pc—posterior commissure, p_l and p_r—vocal fold edge points at medial position for the left and right sides. The moving points p_l and p_r are tracked over time. Their distances to the glottal axis form the experimental trajectories $d_\alpha^{\mathrm{HS}}(t)$.

axis is defined as linear regression of the glottal area and connects the posterior (pc) and anterior (ac) commissure. The glottal length $l^{\mathrm{HS}}(t)$ is defined as the distance between the two commissures and is calculated for each cycle at the maximum open condition of the glottis.

Of particular interest is to describe the movements of the vocal folds as a function of time at one specific position. Commonly, the medial position of the vocal folds is used, since this typically corresponds to the point of maximum oscillation amplitude.[17] Within Fig. 2, the vocal fold edge points at the medial position are marked by the points p_l and p_r. The time-varying deflections of these opposing vocal fold edge points from the glottal axis are regarded as experimental trajectories $d_\alpha^{\mathrm{HS}}(t)$ for the left ($\alpha=l$) and right ($\alpha=r$) side. This functional description can be directly derived from the segmented images.

Errors of the image processing arise in the case of reduced endoscopic image quality. In the process glottal segmentation, a threshold level was used to determine whether a particular pixel of the image belongs to the glottis or marks a vocal fold edge. If the transition from the glottis to the vocal folds is blurred within the image, an uncertainty of the segmentation of the pixel arises. The uncertainty influences the deflection of the extracted experimental trajectories $d_\alpha^{\mathrm{HS}}(t)$. Typical deflections are about ten pixels for low-pitched voices and about five pixels for high-pitched voices. The accuracy of the segmented deflections is in the order of one pixel. A difference of one pixel in deflection results in relative image processing errors of about $\varepsilon_{\mathrm{img}}=10\%$ for large deflections at low pitches and $\varepsilon_{\mathrm{img}}=20\%$ for small deflections at high pitches. The high relative error $\varepsilon_{\mathrm{img}}$ results from the limited spatial resolution of the CCD chip of the HS camera rather than from an imprecise segmentation of the glottis.

Since there is no metric information within the endoscopic image data, the glottal length $l^{\mathrm{HS}}(t)$ and the trajecto-

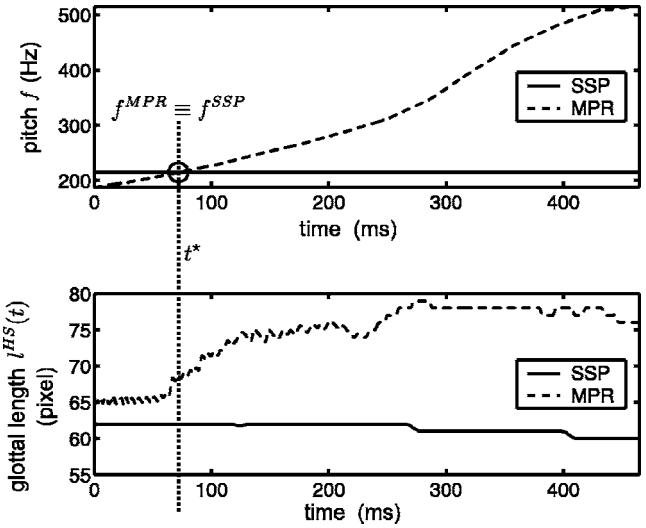

FIG. 3. Steps in the estimation of a conversion factor for the experimental trajectories $d_\alpha^{\mathrm{HS}}(t)$ from pixel to metrical units. The upper graph illustrates the pitches for the two phonation paradigms SSP and MPR of the female subject ID 1. At the time instant $t=t^\star$ the pitches between both paradigms are equal and marked with a circle. At the intersection point the physical glottal lengths l^{SSP} and $l^{\mathrm{MPR}}(t^\star)$ are approximately equal and are related to the extracted glottal length $l^{\mathrm{HS}}(t)$, which are shown on the lower graph, of the image processed HS sequence.

ries $d_\alpha^{\mathrm{HS}}(t)$ are just given in pixel units. For the model-driven classification it is necessary to convert the trajectories into metric units. In accordance to literature, a conversion factor γ^{SSP} for the SSP condition can be estimated:[7,8]

The conversion factor γ^{SSP} is estimated by relating the physical glottal length $l^{\mathrm{SSP}}(t)$ to the extracted glottal length $l^{\mathrm{HS}}(t)$. Both lengths, l^{SSP} and l^{HS}, are constant in the SSP condition:

$$\gamma^{\mathrm{SSP}} = \frac{l^{\mathrm{SSP}}}{l^{\mathrm{HS}}}. \tag{1}$$

However, the value of l^{SSP} given in literature[28–31] has a wide spread for males and females. Within this work the glottal length l^{SSP} is assumed to be 0.7 cm for females and 1.4 cm for males, which lies within the range of literature values and is identical to the lengths chosen in former works.[7,8]

In contrast to the constant glottal length during SSP, the glottal length increases during MPR.[14] The estimation of a conversion factor γ^{MPR} for the MPR trajectories is illustrated in Fig. 3. At the time instant $t=t^*$, where the pitches between SSP and MPR paradigm are equivalent $f^{\mathrm{MPR}} \equiv f^{\mathrm{SSP}}$, the physical glottal length $l^{\mathrm{MPR}}(t)$ of the pitch raise is approximated by the glottal length l^{SSP} of the stationary phonation:

$$l^{\mathrm{MPR}}(t^*) \approx l^{\mathrm{SSP}}. \tag{2}$$

From Eq. (2), which relates the dimensions of MPR to SSP recordings, the MPR conversion factor is derived as

$$\gamma^{\mathrm{MPR}} = \gamma^{\mathrm{SSP}} \frac{l^{\mathrm{HS}}}{l^{\mathrm{HS}}(t^*)}. \tag{3}$$

For all 20 subjects the intersection points of the pitches between SSP and MPR are determined and a conversion factor γ^{MPR} is estimated for the nonstationary MPR trajectories.

B. Model-based classification

The classification of the observed trajectories $d_\alpha^{\mathrm{HS}}(t)$ is based on the analysis and quantification of left to right oscillation asymmetries. For this purpose a model-based approach is proposed. For the quantitative analysis of $d_\alpha^{\mathrm{HS}}(t)$ the model has to reproduce the form and the time course of the observed trajectories. The 2MM, originally introduced for sound synthesis, is a low-dimensional model that is able to reproduce various kinds of vocal fold vibrations, such as normal, chaotic, and pathological vibration behaviors.[7,18–24] Other, more complex biomechanical models, which aim at a more physiologically realistic representation, like multi-mass[32–34] or finite element[35,36] models with numerous parameters, or the additional coupling of a vocal tract to the model,[18,37] simulate also vocal fold vibrations. However, the low-dimensional 2MM reproduces the oscillations of two opposing vocal fold edge points with the optimization of only a few parameters. Within the study the optimized parameters serve to quantify the kind of oscillation and are not interpreted in a physiological way. Therefore, the lower number of parameters in the 2MM is advantageously compared to the large number of parameters in more complex vocal fold models, since more parameters mean more computational costs. Additionally, a large number of optimization parameters leads to ambiguities in the sense that different optimized parameter sets result in the same model dynamics. Hence, a unique assignment between vocal fold oscillations and the optimized model parameters, which are needed for the classification, is refused. In the case of the proposed model-based classification, the ability of the 2MM to reproduce different types of vocal fold vibrations serves to quantify left to right asymmetries of $d_\alpha^{\mathrm{HS}}(t)$ rather than a physiological modeling with a realistic extraction of laryngeal tensions.

1. Time-varying 2MM for nonstationary vocal fold vibrations

The original form of the biomechanical 2MM enables the modeling of stationary vocal fold vibrations. However, the adaptation of the 2MM to MPR trajectories requires a model that is capable of simulating nonstationary vocal fold oscillations. Therefore, a time-dependent 2MM(t) with time-varying model parameters is derived from the 2MM setup of Steinecke *et al.*[23] A more detailed description of the stationary 2MM and the definition of the model parameters can be found in the literature.[7,18,23] In the following, a brief summary of the 2MM(t) is depicted with special attention to the time-dependent extensions (Fig. 4). Within the 2MM(t) one vocal fold is represented by two coupled oscillators, which are set into vibration by a subglottal air pressure $P_s(t)$. A change in $P_s(t)$ mainly affects the amplitude of the model's oscillation and, to some minor extent, the oscillation frequency.[14,38,39] The subglottal pressure $P_s(t)$ can be seen as a measure for the energy flowing into the system.[7] The coupling between the lower and upper masses is represented by spring constants $k_{c\alpha}(t)$. The rest positions of the masses are denoted as $x_{0,i\alpha}(t)$ and the glottal length of the model is $l(t)$. Incorporated nonlinearities are the driving Bernoulli force

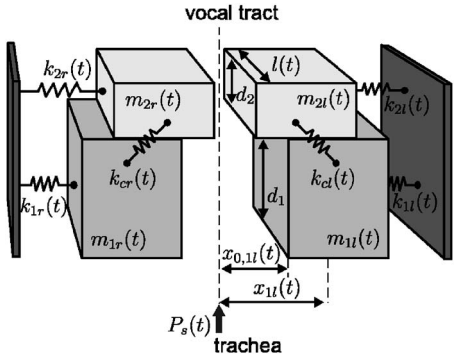

FIG. 4. Schematic representation of the 2MM(t) with time-varying parameters. The 2MM(t) emulates vocal fold vibrations and serves to quantify left to right asymmetries rather than a physiological modeling. Each vocal fold is represented by two coupled $k_{c\alpha}(t)$ masses $m_{i\alpha}(t)$ of thickness d_i with length $l(t)$. Each mass is coupled to a rigid wall by a spring $k_{i\alpha}(t)$ and a damping $r_{i\alpha}(t)$ element (damping elements not shown to keep clarity of the drawing). From the rest positions $x_{0,i\alpha}(t)$ only a lateral displacement $x_{i\alpha}(t)$ is allowed for the masses, which are set to vibrations by the subglottal air pressure $P_s(t)$.

$F_B(t)$, which acts only on the lower masses in the quasilaminar flow approach, and the impact forces $I_{i\alpha}(t)$. Indices used for the parameters denote the lower $(i=1)$ and upper $(i=2)$ plane of the model. The impact forces $I_{i\alpha}(t)$, which are represented by spring constants $c_{i\alpha}(t)$, act as additional restoring forces when the model's masses get into contact. The vibrating masses of thickness d_i and spring tensions of the model are denoted by the parameters $m_{i\alpha}(t)$ and $k_{i\alpha}(t)$, which predominantly influence the frequency as well as the amplitude of the oscillation.[40,41] Due to the time dependency of the masses $m_{i\alpha}(t)$, the more general form of Newton's second law

$$F_{i\alpha}(t) = m_{i\alpha}(t) \cdot \dot{v}_{i\alpha}(t) + v_{i\alpha}(t) \cdot \dot{m}_{i\alpha}(t), \tag{4}$$

is used, where the time derivatives $\dot{m}_{i\alpha}(t)$ of masses are accounted for in the equations of motion.[20,42,43] Damping coefficients $r_{i\alpha}(t)$ are chosen according to Ishizaka *et al.*,[18]

$$r_{i\alpha} = 0.16\sqrt{(m_{1\alpha}(t) + m_{2\alpha}(t)) \cdot (k_{1\alpha}(t) + k_{2\alpha}(t))}. \tag{5}$$

The model is described by a system of four coupled differential equations

$$\begin{aligned} m_{1\alpha}(t)\ddot{x}_{1\alpha}(t) &= b_{0,1\alpha}(t)x_{1\alpha}(t) + b_{1,1\alpha}(t)\dot{x}_{1\alpha}(t) \\ &\quad + b_{2,1\alpha}(t)x_{2\alpha}(t) + I_{1\alpha}(t) + F_B(t), \\ m_{2\alpha}(t)\ddot{x}_{2\alpha}(t) &= b_{2,2\alpha}(t)x_{1\alpha}(t) + b_{0,2\alpha}(t)x_{2\alpha}(t) \\ &\quad + b_{2,1\alpha}(t)\dot{x}_{2\alpha}(t) + I_{2\alpha}(t), \end{aligned} \tag{6}$$

where $x_{i\alpha}(t)$ are the lateral displacements of the masses $m_{i\alpha}(t)$.[23,44] The time-dependent coefficients are formed by the model parameters as

$$b_{0,i\alpha}(t) = -k_{i\alpha}(t) - k_{c\alpha}(t) - \dot{m}_{i\alpha}(t),$$

$$b_{1,i\alpha}(t) = -r_{i\alpha}(t) - \dot{m}_{i\alpha}(t),$$

$$b_{2,i\alpha}(t) = k_{c\alpha}(t) - \dot{m}_{i\alpha}(t).$$

The impact forces are defined as

$$I_{i\alpha}(t) = -\Theta(-a_i(t))\frac{c_{i\alpha}(t)a_i(t)}{2l(t)}, \tag{7}$$

where $\Theta(x)=1$ for $x>0$ and $\Theta(x)=0$ for $x\leqslant 0$ and $a_i(t) = a_{il}(t)+a_{ir}(t) = l(t)(x_{0,il}(t)+x_{0,ir}(t)) + l(t)(x_{il}(t)+x_{ir}(t))$ is the instantaneous glottal area, composed of the rest positions $x_{0,i\alpha}(t)$ and the displacements $x_{i\alpha}(t)$ of the masses. The driving force reads

$$F_B(t) = l(t)d_1P_1(t), \tag{8}$$

where

$$P_1(t) = P_s(t)\left(1 - \Theta(a_{\min}(t))\left(\frac{a_{\min}(t)}{a_1(t)}\right)^2\right)\Theta(a_1(t)) \tag{9}$$

is the pressure acting on the lower masses $m_{1\alpha}(t)$. The area $a_{\min}(t) = \min(a_{1l}(t), a_{2l}(t)) + \min(a_{1r}(t), a_{2r}(t))$ represents the minimal area between the left and right masses of the 2MM(t).

An analytical solution of Eq. (6) is not known.[45] The four second-order differential equations in (6) are rewritten to eight coupled first-order differential equations and then they are numerically solved by a fourth-order Runge-Kutta method with a step size h fixed to the frame rate of the HS recordings $h=1/(4000\ \text{Hz})$. Thus, each time sample of the HS observed vocal fold displacements can directly be compared with the resultant displacements $x_{i\alpha}(t)$ of the numerical solution. Theoretical trajectories $d_\alpha(t)$ are computed from the calculated displacements $x_{i\alpha}(t)$ as

$$d_\alpha(t) = \min(x_{1\alpha}(t), x_{2\alpha}(t)). \tag{10}$$

This is analogous to $d_\alpha^{\text{HS}}(t)$ measured from the endoscopic view of the vocal folds.

2. Scaling and optimization parameters

In the model the time-variant parameters $k_{i\alpha}(t)$, $m_{i\alpha}(t),\ldots$ are expressed in terms of Ishizaka's *et al.*[18] standard parameters $k_{0,i\alpha}, m_{0,i\alpha},\ldots$ by introducing factors $Q_\alpha(t)$, $R_\alpha(t)$, and $U(t)$:

$$\begin{aligned} &k_{i\alpha}(t) = k_{0,i\alpha} \cdot Q_\alpha(t), \quad k_{c\alpha}(t) = k_{0,c\alpha} \cdot Q_\alpha(t), \\ &m_{i\alpha}(t) = m_{0,i\alpha}/Q_\alpha(t), \quad c_{i\alpha}(t) = c_{0,i\alpha} \cdot Q_\alpha(t), \\ &x_{0,i\alpha}(t) = x_{0,i\alpha} \cdot R_\alpha(t), \quad P_s(t) = P_{s0} \cdot U(t). \end{aligned} \tag{11}$$

The factors $Q_\alpha(t)$ primarily influence the fundamental frequency of the oscillations. The scaling of the springs and masses with $Q_\alpha(t)$ couples four model parameters of one side into one single optimization factor. The reciprocal coupling of tensions and masses was proposed and justified in earlier works.[7,44] This coupling reduces the number of free parameters and assures a unique association between the scaling factors $Q_\alpha(t)$ and the model trajectories $d_\alpha(t)$ generated with $Q_\alpha(t)$.[46] In case of an independent optimization of spring tensions and model masses, the generated theoretical trajectories cannot be assigned to a unique data set. Hence, the results of an independent optimization of tension and masses would not be meaningful. Through the reciprocal coupling of spring tensions $k_{i\alpha}(t)$ and model masses $m_{i\alpha}(t)$ by the scaling factors $Q_\alpha(t)$, the damping coefficients $r_{i\alpha}(t)$ after Eq. (5)

become time invariant. With the factors $R_\alpha(t)$ it is possible to adjust the rest positions of the model masses and to control the average distance of the vocal folds to the glottal axis during the oscillation. The factor $U(t)$ changes the standard subglottal pressure $P_{s_0}=8$ cm H_2O and contributes to adjust the amplitudes of the theoretical trajectories $d_\alpha(t)$.

The five scaling factors compose a set

$$S(t) := [Q_l(t), Q_r(t), R_l(t), R_r(t), U(t)] \tag{12}$$

that is used to influence the vibration characteristic $d_\alpha(t)$ of the model. The independent scaling of the left and right model sides with $Q_\alpha(t)$ and $R_\alpha(t)$ allows for left and right asymmetries in the model. Depending on $S(t)$, both symmetrical and asymmetrical vocal fold vibrations can be simulated.

The model parameters are scaled with the proposed set $S(t)$ for the normal and the pathological voice diseases given in Table I. Modifications of the scaling mechanism depending on the type of the disease could improve the model-based classification. For example, it would be more reasonable for the pathological subject ID 17, with a vocal fold polyp, to scale just the model masses $m_{i\alpha}(t)$ instead of the coupled scaling of the masses and tensions with $Q_\alpha(t)$ as in Eq. (11). However, a disease-dependent scaling implies that the patient is already diagnosed by a medical doctor. In the case of an application as a screening method, which decides if a patient has irregular vocal fold vibrations, no detailed assumptions on the model scaling $S(t)$ can be made. It is important that the scaling $S(t)$ enables us to simulate a wide variety of vocal fold vibrations and that the calculated solution is unique within the optimization space. The proposed set $S(t)$ of scaling parameters, defined in Eq. (11), fulfills these requirements.

3. Classification criteria

The model-based classification of vibration patterns makes use of the left to right oscillation asymmetries represented by the factors $Q_\alpha(t)$ and $R_\alpha(t)$ of the model parameter set $S(t)$. As a measure of asymmetry between the oscillations of the left and right side of the model, the ratios

$$Q(t) = \frac{Q_l(t)}{Q_r(t)} \quad \text{and} \quad R(t) = \frac{R_l(t)}{R_r(t)} \tag{13}$$

are introduced. Perfect oscillation symmetry is obtained for $Q(t)=1$ and $R(t)=1$. If the left and right side scaling factors differ from each other, the ratios are no longer equal to one and indicate asymmetries in vocal fold vibrations. The subglottal pressure factor $U(t)$ captures no left to right asymmetries and is thus not used as a classification criterion.

Time-varying asymmetries within nonstationary vocal fold vibrations are mapped to time variations of the two symmetry factors $Q(t)$ and $R(t)$. The asymmetries are described and visualized by a two-dimensional curve

$$C(t) := C(Q(t), R(t)) \tag{14}$$

in the $Q(t)$-$R(t)$ plane. An example is given in Fig. 5(a). A curve $C(t)$ that represents symmetric and regular vibrations is closed to the point of perfect symmetry $P_{\text{sym}} := (1,1)$ in the $Q(t)$-$R(t)$ plane. Asymmetric and irregular oscillations are indicated by a scattered curve with a wide spread in the $Q(t)$-$R(t)$ plane. Three characteristics are derived from the curve $C(t)$ that describe the degree of asymmetry in vocal fold vibrations. Figures 5(a) and 5(b) help to clarify these definitions. Figure 5(b) shows a magnified part of Fig. 5(a).

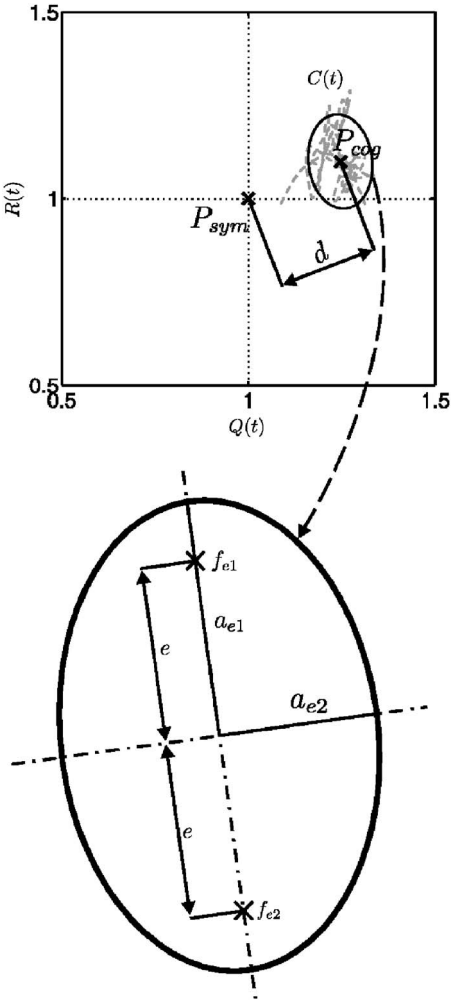

FIG. 5. Definition of measurements used for classification. (a) $Q(t)-R(t)$ plane with the curve $C(t)$ and the fitted ellipse. The distance d between the point of perfect symmetry $P_{\text{sym}}=(1,1)$ and the center of gravity P_{cog} of the curve $C(t)$ is also shown. (b) Enlarged ellipse with the semi-major and semi-minor axes a_{e1} and a_{e2}. The two focal points are denoted as f_{e1}, f_{e2} and the linear eccentricity as e.

(i) Distance $d=\|P_{\text{sym}}-P_{\text{cog}}\|_2$. The variable d is the distance from the center of gravity P_{cog} of the curve $C(t)$ to the symmetry point P_{sym} in the $Q(t)$-$R(t)$ plane [Fig. 5(a)]. It indicates the mean degree of left to right oscillation asymmetry over time. Small values represent small asymmetries.

(ii) Ellipse area $a=a_{e1}a_{e2}\pi$. An ellipse with the semi-major and semi-minor axes a_{e1}, a_{e2} is fitted to the curve $C(t)$ [Figs. 5(a) and 5(b)]. The length of each axis is chosen to include 95% sampling points of $C(t)$ along the axis.[47] The area a is a measure for the oscillation stability over time: the larger a, the larger the instability of oscillation.

(iii) Ellipse linear eccentricity $e=\sqrt{a_{e1}^2-a_{e2}^2}$. The linear eccentricity e equals the distance from the center to one of the focal points f_{e1}, f_{e2} of the ellipse [Figs. 5(a) and 5(b)]. The linear eccentricity e of the ellipse is used to characterize the kind of oscillation asymmetry over time. Large values of e indicate that one asymmetry type, either $Q(t)$ or $R(t)$, outweighs the other. Small values of e indicate a balance of the two asymmetry factors.

The three asymmetry characteristics are combined to a single measure Ψ that summarizes the asymmetry and instability of vocal fold vibrations. The combination of the criteria is a scalar rating value defined as

$$\Psi := e \cdot d + a. \tag{15}$$

The rating Ψ consists of the ellipse area a added to the product of linear eccentricity e and distance d. The rating emphasizes the time-variant asymmetries of the curve $C(t)$ by the incorporated two ellipse measures that characterize the time-variant deviations of $C(t)$ in the $Q(t)$-$R(t)$ plane. Small rating values of Ψ represent symmetrical and stable vocal fold oscillations. Asymmetric or instable vocal fold oscillations are represented by large values of Ψ. Classification of vocal fold vibrations is based on the derived rating value Ψ.

C. Parameter optimization of the time-varying two-mass model

In order to derive the curve $C(t)$ and the rating value Ψ a parameter set $S(t)$ of the 2MM(t) has to be determined by an optimization procedure. Optimization means finding proper values of the parameter set $S(t)$ that adapts the model dynamics $d_\alpha(t)$ to experimental trajectories $d_\alpha^{\mathrm{HS}}(t)$. For each numerical calculated time step of $d_\alpha(t)$, one time sample of the parameter set $S(t)$ is necessary. Optimization of the five-element set $S(t)$ for each time step of an entire experimental trajectory of about 1 s (number of samples $N=4000$) would be computationally expensive. However, the complexity can be reduced because laryngeal muscle contractions and associated movements of laryngeal structures are continuous functions and are slow relative to the numerical integration scheme used for the vocal fold model. Hence, a slow continuous parameter variation takes place. Rather, a slow continuous parameter variation takes place: the sampling period (0.25 ms) of the numerical Runge-Kutta calculation scheme is less than typical time constants for muscle contraction ($\sim$30 ms) and mechanical delays ($\sim$20 ms).[48–50] Thus, it is unnecessary to optimize every time step of $S(t)$.

In the following an optimization procedure is introduced that takes advantage of the continuous parameter variations. A flow chart of the algorithm is depicted in Fig. 6. For the adaptation of the 2MM(t) dynamics $d_\alpha(t)$, the algorithm divides the experimental trajectories $d_\alpha^{\mathrm{HS}}(t)$ into B blocks. Successive blocks overlap by one sample. This ensures the continuity of the parameters during optimization. Each block b represents one period of oscillation, from oscillation maximum to maximum, with N_b samples. For typical pitch frequencies ranging from 100 to 500 Hz, the duration time of

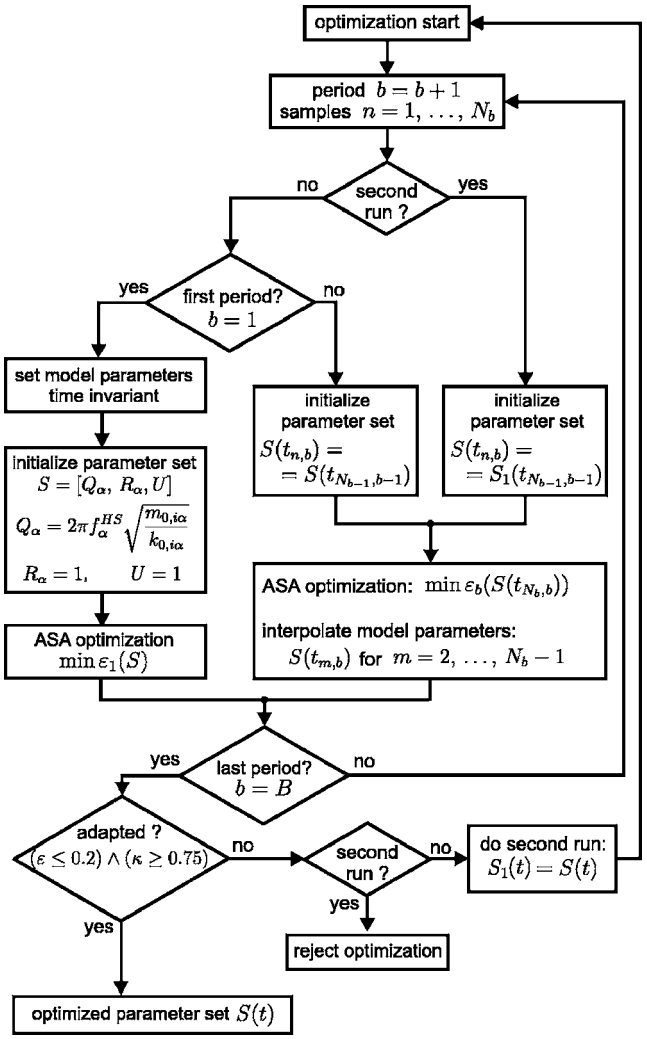

FIG. 6. Flow chart of the adaptation of the 2MM(t) dynamics to HS observed nonstationary vocal fold vibrations $d_\alpha^{\mathrm{HS}}(t)$. From $d_\alpha^{\mathrm{HS}}(t)$ successive periods are extracted and are reproduced by the model. The model parameters are optimized with a global optimization algorithm called "Adaptive Simulated Annealing."[51]

one period is 2–10 ms. Therefore, the number of samples is $N_b=8,\ldots,40$ for the given sampling rate of 4000 Hz. The time samples of the parameters $S(t)$ and trajectories are indexed as $t_{n,b}$, where b represents the actual period and n is the time sample within the period b.

For the optimization, the error

$$\varepsilon_b=\frac{1}{N_b}\sum_{n=1}^{N_b}(d_\alpha(t_{n,b})-d_\alpha^{\mathrm{HS}}(t_{n,b}))^2 \tag{16}$$

between experimental and theoretical trajectories is minimized for each period $b=1,\ldots,B$. The error ε_b is also called objective function. Since the behavior of the 2MM(t) is nonlinear and the objective function ε_b has a nonconvex structure with multiple local minima, a global optimization method is used for minimization: a stochastic optimization procedure, "Adaptive Simulated Annealing" (ASA), is applied to the problem.[51,52]

The optimization of the parameter set $S(t)$ starts at period $b=1$ of the experimental trajectories $d_\alpha^{\mathrm{HS}}(t_{n_0,0})$ with $n_0=0,\ldots,N_0$. For the first oscillation period a constant param-

eter set $S=S(t_{n_0,0})$ is assumed. Hence, the parameter samples are constant $S=S(t_{n_0,0})$ over the first period. Initial values for these parameters are derived by using a simple mass-spring oscillator equation[7]

$$Q_\alpha(t_{n_0,1}) = 2\pi f_\alpha^{\mathrm{HS}} \sqrt{\frac{m_{0,i\alpha}}{k_{0,i\alpha}}}, \tag{17}$$

where f_α^{HS} is the fundamental frequency of period $b=1$. The other factors of the parameter set $S=S(t_{n_0,1})$, $R=R_\alpha(t_{n_0,1})$, and $U=U(t_{n_0,1})$, are set to one. Following the initialization the ASA optimization of the first period is performed. The five elements of the constant parameter set S are optimized until the objective function ε_1 gets a minimal value.

After the optimization of the first period all the consecutive periods $b=2,\ldots,B$ are processed. The values of $S(t_{n,b})$ are initialized with the last values of the optimization outcome of the previous block $S(t_{N_{b-1},b-1})$. Since two successive periods overlap by one sample, the end state $S(t_{N_{b-1}},b-1)$ of period $b-1$ is identical to the start state $S(t_{1,b})$ of period b. Hence, the first sample values $S(t_{1,b})$ of the actual period b are fixed. Only the last values of the parameter set $S(t_{N_b,b})$ are optimized. The parameter values between the fixed start values $S(t_{1,b})$ and the last time samples $S(t_{N_b,b})$ are obtained by linear interpolation.

For each period the optimization procedure results in adapted but not in identical trajectories. Therefore, a slight oscillation forms around the true values of the parameter set $S(t)$. After executing the optimization procedure for all B blocks, a low-pass filter is applied to the elements of $S(t)$ to remove these artifacts caused by the period by period processing. Such artifacts are zigzag variations of the parameters between succeeding periods.

The similarity between the experimental trajectories $d_\alpha^{\mathrm{HS}}(t)$ and the adapted theoretical trajectories $d_\alpha(t)$ and the adapted theoretical trajectories $d_\alpha(t)$ is measured with two criteria:

(i) Normalized error ε—serves to quantify the match between the entire adapted and observed trajectories. The mean of the objective function values ε_b of Eq. (16) is normalized to the mean signal energy

$$E_s := 1/N \cdot \sum_{n=1}^{N} d_l^{\mathrm{HS}}(t_n)^2 + d_r^{\mathrm{HS}}(t_n)^2 \tag{18}$$

over all N time steps of the left and right trajectories $d_\alpha^{\mathrm{HS}}(t)$:

$$\varepsilon = \frac{\sum_{b=1}^{B} \varepsilon_b}{B \cdot E_s}. \tag{19}$$

Especially deflection differences between the trajectories are captured with the normalized error ε. A value of $\varepsilon=0.2$ is still acceptable, since the ε measure can be compared to the image processing error $\varepsilon_{\mathrm{img}}$ (Sec. II A), which lies in the same order of magnitude for small vocal fold deflections at high pitches.

(ii) Correlation coefficient κ—measures how close the shape of the adapted trajectories $d_\alpha(t)$ met the experimental curves $d_\alpha^{\mathrm{HS}}(t)$. Between $d_\alpha(t)$ and $d_\alpha^{\mathrm{HS}}(t)$ the standard correlation coefficient κ_α (also known as Pearson's correlation) is calculated for each side $\alpha=l,r$ of the trajectories. The average yields $\kappa := (\kappa_l+\kappa_r)/2$. It is used as another independent measure for similarity between the experimental and theoretical trajectories.

A similarity of

$$(\varepsilon \leqslant 0.2) \wedge (\kappa \geqslant 0.75) \tag{20}$$

between $d_\alpha^{\mathrm{HS}}(t)$ and $d_\alpha(t)$ serves as the criterion that the adaptation succeeded and the optimization is accepted. If the values exceed the given bounds, then the optimization algorithm is started again. At the second run, the algorithm starts each block optimization with the optimized parameters of the first optimization run as initial parameters. If the values ε and κ still exceed the bounds after the second run, then the adaptation failed and the calculated symmetry quotients $Q(t)$ and $R(t)$ are rejected.

With the proposed optimization the 2MM(t) can be adapted to nonstationary vocal fold vibrations. Furthermore, it can also be applied to SSP trajectories, since SSP trajectories are a special case of nonstationary trajectories. In contrast to the SSP adaptation results of former works,[7] which suffered from the inability to model interperiod fluctuations, the period by period optimization is capable of modeling such vibration characteristics. Thus, the developed model-based optimization scheme can also be applied to classify stationary vocal fold vibrations.

D. Verification and application to synthetic data

The correct localization of the global minimum of the objective function ε_b in Eq. (16) cannot be guaranteed in principle, since it is a nonconvex function with many local minima. The minima in the chosen objective function ε_b result from different model vibration characteristics $d_\alpha(t)$, induced by different parameter sets $S(t)$, which fit more or less the observed experimental trajectories $d_\alpha^{\mathrm{HS}}(t)$. In order to estimate the performance and the probability of how often the proposed optimization algorithm delivers acceptable results, tests with 500 synthetically trajectories with the 2MM(t) were produced. The 500 simulated trajectories are subdivided in 250 stationary and 250 nonstationary trajectories. The synthetic trajectories are generated with predefined stationary and nonstationary parameter sets $S^*(t)$ with different tensions, subglottal pressure levels, and rest positions. For the nonstationary case the time course of the parameters had varying slopes with linear and exponential increases. In order to simulate a wide variety of symmetrical and asymmetrical vocal fold vibrations (pitch frequencies from 100 up to 500 Hz, amplitudes from 0.3 to 1.3 mm,[31] with and without glottal closure), the factors of the predefined parameter are set in the following range: $Q_\alpha^* \in \{0.8,\ldots,4\}$, $R_\alpha^* \in \{0.5,\ldots,2\}$, and $U^* \in \{0.8,\ldots,5\}$.

The predefined parameter sets $S^*(t)$ were compared to the outcome of the ASA optimization $S(t)$. Since the classification based on the calculated symmetry quotients $Q(t)$ and $R(t)$, the classification is not affected by errors of the optimization factor $U(t)$. Thus, $U(t)$ is not incorporated in the

evaluation of the algorithm's performance. The measure of how reliable the predefined symmetry quotients are calculated with the period by period optimization is defined as the relative error at one time point t_n averaged over all N time steps:

$$\varepsilon_{\mathrm{rel}} = \frac{1}{N} \cdot \sum_{n=1}^{N} \frac{|S^*(t_n) - S(t_n)|}{S^*(t_n)}. \tag{21}$$

The predefined data sets are calculated more precisely, if the relative error $\varepsilon_{\mathrm{rel}}$ is small. An acceptable relative error is $\varepsilon_{\mathrm{rel}}=0.1$, since a change of 10% in the symmetry quotients $Q(t)$ and $R(t)$ corresponds to deflection differences between the trajectories of about 5%. This is less than the errors $\varepsilon_{\mathrm{img}}$ (Sec. II A) induced by the image processing and thus acceptable.

It has to be guaranteed that a good match between $d_\alpha^{\mathrm{HS}}(t)$ and $d_\alpha(t)$, which is measured with the values ε and κ, also yields in a low relative error $\varepsilon_{\mathrm{rel}}$. Otherwise, the calculated symmetry quotients would not be interpretable, due to ambiguities that arise if two different optimization sets $S(t)$ would generate the same trajectories $d_\alpha(t)$. For the estimation of the relation between the relative error of symmetry quotients and the matching of trajectories only those data sets are evaluated that lie inside the boundaries given in Eq. (20). Data sets with values outside the boundaries are discarded, since in such cases the global optimization delivers nonacceptable results.

III. RESULTS

The applicability of the model-based parameter extraction is presented for the classification of HS recorded vocal fold vibrations. First, the accuracy of the proposed optimization is demonstrated with 500 predefined data sets. Second, the model adaptation is applied to 40 HS recordings of 20 subjects for classification. Finally, the corresponding rating values are presented, which are used for classifying normal and pathological vocal fold oscillations.

A. Synthetic data sets

The predefined synthetic data and the calculated trajectories serve to verify the proposed optimization scheme. The evaluation with the synthetic data sets clarify how accurate the predefined symmetry quotients are calculated, how reliable the optimization adapts the model dynamics to the predefined oscillation pattern, and how often the parameter optimization fails.

Figure 7 displays the relation between the correlation coefficient κ and the normalized error ε of Eq. (19). Both values measure the accuracy of the match between the adapted trajectories $d_\alpha(t)$ and the predefined synthetic trajectories. The closer the data points are to the lower left corner of Fig. 7, the better the match between the trajectories. A trust-region, which is defined by the bounds $(\varepsilon \leqslant 0.2) \wedge (\kappa \geqslant 0.75)$, is delimited by dashed lines within Fig. 7. The values of the optimization run inside the region are accepted. The close match inside the region is indicated by the mean values $\varepsilon=4.3\pm3.7\%$ and $\kappa=0.95\pm0.05$ for the stationary case and $\varepsilon=4.2\pm2.8\%$ and $\kappa=0.95\pm0.05$ for the nonstationary case. The values outside the region denote less accurate matching between the trajectories. Those optimization runs and the calculated symmetry measures $Q(t)$ and $R(t)$ are discarded. This is the case in 3.4% out of all the synthetic data sets.

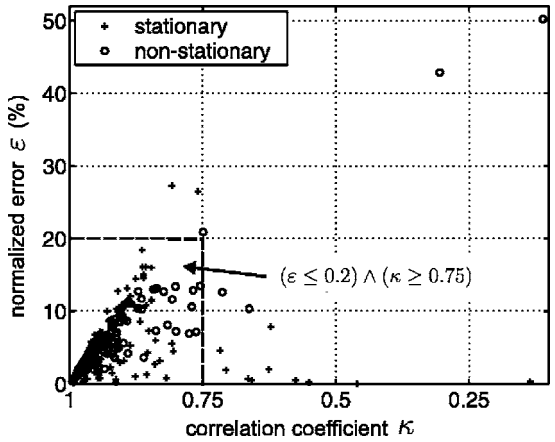

FIG. 7. The two values κ and ε, which measure the similarity between a given and the adapted trajectories, are plotted against each other. The + marks and the ○ marks denote the evaluation results for the predefined synthetic stationary and nonstationary data sets $S^*(t)$. If both similarity measures lie within the given bounds $(\varepsilon \leqslant 0.2) \wedge (\kappa \geqslant 0.75)$, then the optimization results are accepted. Otherwise the results are rejected.

In Fig. 8 the probability $\Pr(\varepsilon_{\mathrm{rel}} \leqslant \xi)$ that the relative error $\varepsilon_{\mathrm{rel}}$ of the symmetry quotients $Q(t)$ and $R(t)$ is lower than or equal to a boundary ξ is illustrated for the stationary and nonstationary synthetic data sets. The graphs show the probability in calculating the correct predefined symmetry quotients $Q(t)$ and $R(t)$ dependent on a given relative error level $\varepsilon_{\mathrm{rel}}$. The probability increases with an increase of the accepted relative error. For a boundary of $\varepsilon_{\mathrm{rel}}=10\%$ the symmetry quotients are calculated with a probability of 95% and 99% for the stationary and nonstationary case.

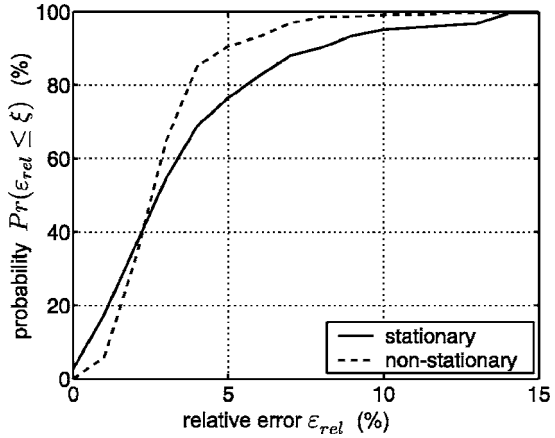

FIG. 8. Result of the evaluation with predefined stationary and nonstationary data sets $S^*(t)$. The graph displays the probability of getting the symmetry quotients $Q(t)$ and $R(t)$ for a given relative error $\varepsilon_{\mathrm{rel}}$ acceptance level. For a relative error of $\varepsilon_{\mathrm{rel}}=10\%$ the symmetry quotients $Q(t)$ and $R(t)$ are obtained to 95% for the stationary and to 99% for the nonstationary case with the proposed period by period optimization method.

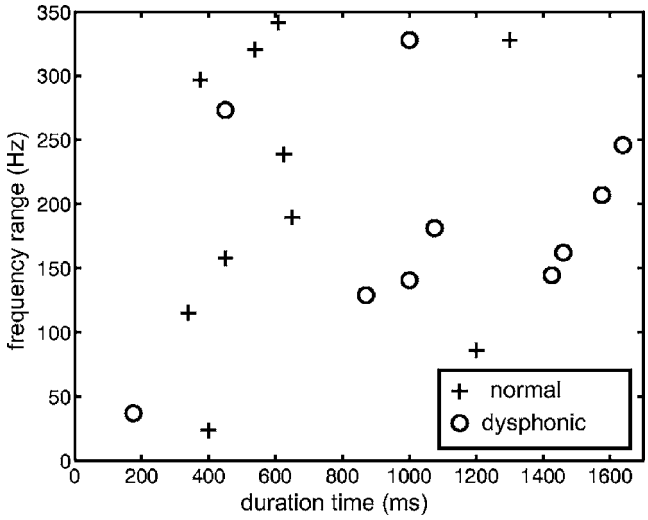

FIG. 9. Plot of the MPR duration time and the covered MPR frequency range (highest-lowest frequency) of the investigated normal (plus +) and pathological voice (circles ○) subjects. The values scatter for both groups: the normal as well as the pathologic voices can cover a wide frequency range up to 350 Hz. The pathological subjects spend more time for the MPR frequency shift.

B. Model dynamics adapted to HS recordings

During the endoscopic HS examination each individual subject interpreted and executed the MPR paradigm in a slightly different way. They performed the pitch raise in a frequency range and duration time that was comfortable for them. In Fig. 9 the covered frequency range (highest-lowest frequency) is plotted versus the duration time of the pitch raise. The group of the pathological voice subjects covers a wide mean frequency range 185±83 Hz, just as well the subject group with normal voices 210±113 Hz. However, the pathological subjects spend more time for the MPR frequency shift on average (1067±482 ms vs 649±336 ms).

The adapted theoretical trajectories $d_\alpha(t)$ match the experimental $d_\alpha^{\mathrm{HS}}(t)$ curves of the normal voices. An overview of the similarity between both trajectories is given in Table II. The normalized error ε of the adaptation for the normal voice subjects ranges from 2.6% up to 8.2% with a median of 5.7% for the SSP phonation. The correlation coefficients κ between the experimental $d_\alpha^{\mathrm{HS}}(t)$ and the adapted theoretical trajectories $d_\alpha(t)$ ranges from 89.3% up to 97.1%. The median correlation coefficient κ amounts 94.6%. For the MPR paradigm in Table II, the extremal values for the normalized error ε and the correlation coefficient κ are 3.5% to 18.5% and 85.8% to 96.7%. The corresponding medians are 5.5% and 94.0%, respectively.

Detailed values for the adaptation quality of theoretical $d_\alpha(t)$ to experimental trajectories $d_\alpha^{\mathrm{HS}}(t)$ of the pathological voices can be found in Table III. For the SSP phonation the normalized error ε ranges from 3.9% to 14.7% with a median of 6.9%. The correlation coefficient κ has a median of 94.6% and spreads from 75.9% to 95.9%. In the case of the MPR paradigm the values of the normalized error ε and the correlation coefficient κ cover a range from 4.8% to 18.0% and 82.2% to 95.5%. Their respective medians are 6.8% and 92.5%.

TABLE II. Values of the optimization for SSP and MPR phonation for the normal voices. Normalized error ε and correlation coefficients κ in percent between experimental $d_\alpha^{\mathrm{HS}}(t)$ and adapted theoretical $d_\alpha(t)$ trajectories.

Subject ID normal	Normalized error ε (%)		Correlation κ (%)	
	SSP	MPR	SSP	MPR
1	2.6	10.5	97.1	90.8
2	5.2	4.4	89.3	95.2
3	3.1	3.5	96.5	96.7
4	2.8	5.9	96.3	93.7
5	6.8	6.7	95.0	93.1
6	6.1	4.9	94.2	94.2
7	7.3	18.5	90.9	85.8
8	8.2	5.0	92.8	95.4
9	7.2	15.4	90.8	80.9
10	2.8	3.8	96.6	94.6
First quartile	2.8	4.4	90.9	90.8
Median	5.7	5.5	94.6	94.0
Third quartile	7.2	10.5	96.5	95.2

As an exemplarily adaptation result, short sections of nonstationary MPR trajectories $d_\alpha^{\mathrm{HS}}(t)$ and the corresponding adapted theoretical curves $d_\alpha(t)$ for a normal (ID 1) and a pathological subject (ID 18) are shown in Figs. 10(a) and 10(b). In both cases, the adapted trajectories (black dashed lines) match the experimental trajectories (gray solid lines) in frequency, amplitude, and phase. The displacement of the trajectories decreases within the depicted signal sections, as a result of the nonstationary MPR phonation. The normalized error ε and the correlation coefficient κ are read out of Tables II and III: 10.5% and 90.8% for the normal voice subject; 7.3% and 92.6% for the pathological voice subject. The normal voice in Fig. 10(a) is characterized by symmetrical oscillations of the left and right side: frequency and displacement of the masses from glottal midline are equal for both sides. There is no phase shift between the left and right

TABLE III. Values of the optimization for SSP and MPR phonation for the pathological voices. Normalized error ε and correlation coefficients κ in percent between experimental $d_\alpha^{\mathrm{HS}}(t)$ and adapted theoretical $d_\alpha(t)$ trajectories.

Subject ID pathologic	Normalized error ε (%)		Correlation κ (%)	
	SSP	MPR	SSP	MPR
11	4.5	5.0	90.7	95.5
12	7.2	11.6	87.8	89.2
13	6.5	10.3	93.2	87.8
14	5.0	4.8	95.9	93.3
15	8.5	5.6	86.9	93.5
16	3.9	10.0	94.7	88.2
17	6.0	5.8	92.5	94.0
18	9.7	7.3	82.4	92.6
19	8.8	6.2	75.9	92.4
20	14.7	18.0	86.2	82.2
First quartile	5.0	5.6	90.9	88.2
Median	6.9	6.8	94.6	92.5
Third quartile	8.8	10.3	96.5	93.5

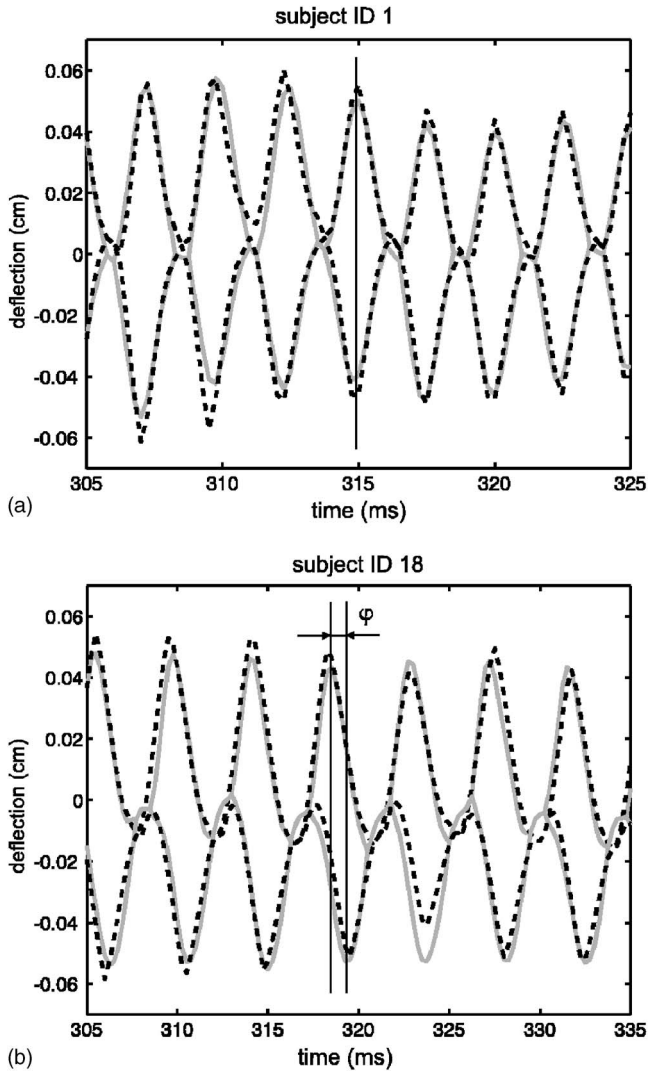

FIG. 10. Sections of nonstationary (MPR) experimental $d_\alpha^{\mathrm{HS}}(t)$ (solid, gray) and adapted theoretical $d_\alpha(t)$ (dashed, black) trajectories. The vertical lines mark the maximum displacements of the left and right vocal fold side of one oscillation cycle. (a) There is no phase shift for the normal voice subject (ID 1, female) between the left and right side vocal fold vibration. (b) There is a phase shift of $\varphi=1$ rad for the pathological voice subject (ID 18, female) between the left and right side vocal fold vibration.

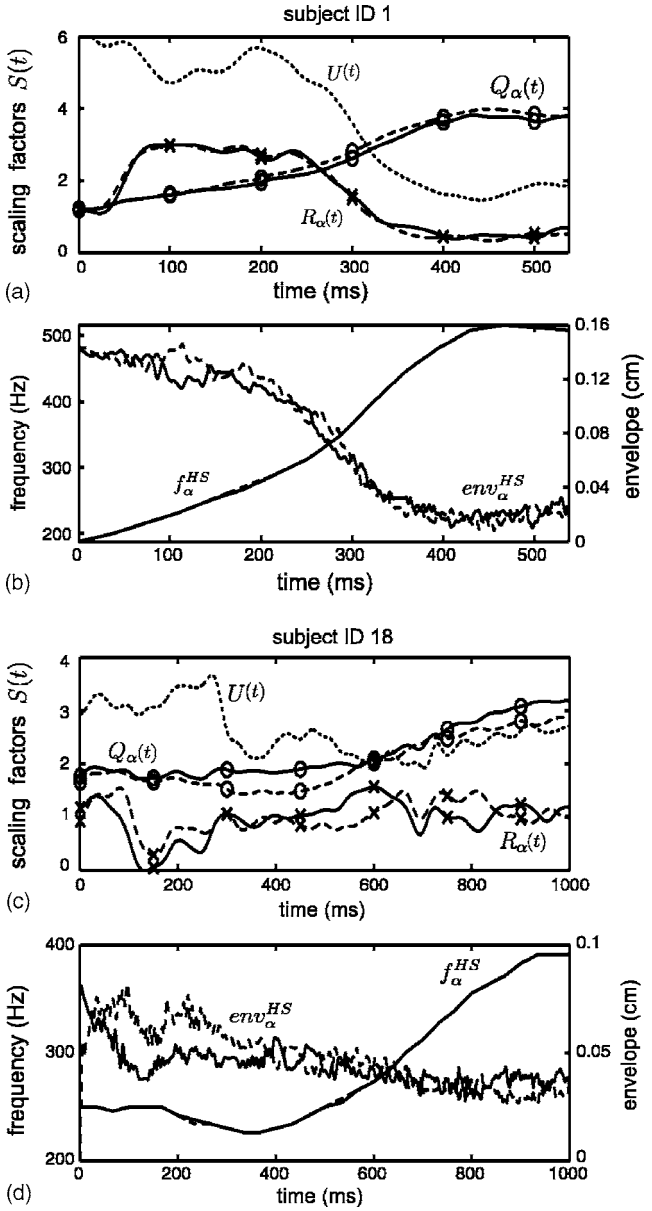

FIG. 11. The set $S(t)$ of the five optimization factors of the 2MM(t), which led to the adapted theoretical trajectories in Fig. 10. In graphs (a) and (c) the optimized parameter set for a normal voice subject (ID 1, female) and a pathological voice subject (ID 18, female) are depicted. The individual factors are marked as $Q_l(t)$: solid lines with ○ marks; $Q_r(t)$: dashed lines with ○ marks; $R_l(t)$: solid lines with × marks; $R_r(t)$: dashed lines with × marks; $U(t)$: dotted lines. Graphs (b) and (d) illustrate the corresponding frequency f_α^{HS} and envelope $\mathrm{env}_\alpha^{\mathrm{HS}}$ profiles. Left sides ($\alpha=l$) are identified as solid, the right sides ($\alpha=r$) as dashed lines.

side. In contrast, the oscillations of the pathological subject exhibit a phase shift $\varphi=1$ rad [Fig. 10(b)]. The right side trajectory (lower curve) lags behind the left side trajectory (upper curve). The left and right side trajectories are not symmetrical. However, the occurrence of a phase shift φ alone is not sufficient to decide if vocal fold vibrations belong to a hoarse speaker. Trajectories of hoarse voices were observed that did not have a phase shift as well as trajectories of normal voices that exhibited a phase shift. For instance, the normal voice subject ID 10 has a phase shift of $\varphi=1.2$ rad.

C. Optimized parameters and classification

The adaptation of the 2MM(t) dynamics $d_\alpha(t)$ to the experimental trajectories $d_\alpha^{\mathrm{HS}}(t)$ leads to a set of optimized model parameters $S(t)$. For an example, the adapted trajectories $d_\alpha(t)$ in Fig. 10 are generated with the corresponding optimized model parameters depicted in Fig. 11(a). The time variations of the left and right optimization factors $Q_l(t)$, $Q_r(t)$ and $R_l(t)$, $R_r(t)$ and the subglottal pressure factor $U(t)$ are plotted. For the normal voice (subject ID 1) the curves of the optimized factors are smooth. The curve progression between the left and the right side factors look alike and indicates symmetrical oscillations. The corresponding frequency f_α^{HS} and envelope $\mathrm{env}_\alpha^{\mathrm{HS}}$ profiles of the MPR recording are given in Fig. 11(b). During the MPR the frequencies f_α^{HS} of the left ($\alpha=l$) and right ($\alpha=r$) side rise symmetrically from 200 to 500 Hz, while the envelopes $\mathrm{env}_\alpha^{\mathrm{HS}}$ decrease from 0.14 to 0.03 cm. In contrast to this normal voice, the param-

eters of the pathological voice (subject ID 18) fluctuate during the MPR time in Fig. 11(c). Differences between the left and the right side factors $Q_l(t)$ and $Q_r(t)$ emerge at the time instance around 400 ms and at the last 200 ms of the MPR duration time. Both factors $Q_\alpha(t)$ increase from 1.7 to about 3 in the same time period. The factors $R_l(t)$ and $R_r(t)$ differ from each other and vary around one. The differences in the left to right factors imply asymmetric oscillations. The described left to right asymmetries are quantitatively expressed in the dimensionless quotients $Q(t)$ and $R(t)$ of Eq. (13). In Fig. 11(d) the frequency f_α^{HS} and the envelope $\mathrm{env}_\alpha^{\mathrm{HS}}$ profiles are depicted for the recorded MPR sequence of subject ID 18. During the first 180 ms of the MPR the left and right side frequency f_α^{HS} is about 250 Hz; in the next 200 ms f_α^{HS} decreases to 230 Hz. In the following 500 ms a linear increase of f_α^{HS} up to 390 Hz takes place. The frequency f_α^{HS} keeps constant for the remaining 100 ms of the recording. The envelope $\mathrm{env}_\alpha^{\mathrm{HS}}$ profile decreases from 0.06 to 0.04 cm. Larger differences between the left and right side envelope occur during the first 400 ms of the recording.

The asymmetries captured with the factors $Q(t)$ and $R(t)$ are visualized by the two-dimensional parameter curve $C(t)$ in the $Q(t)$-$R(t)$ plane. Within this plane symmetry is located in the point $P_{\mathrm{sym}}=(1,1)$, while asymmetries are deviations from P_{sym}. Figure 12 illustrates the curve $C(t)$ for the MPR phonation of the ten normal voice subjects for the MPR phonation. The mean distance d of the curve's center of gravity is 0.13 ± 0.07. Around the center of gravity the ellipse is plotted, which serves as decision criterion for the time-variant asymmetries of the curve $C(t)$ in the $Q(t)$-$R(t)$ plane. The ellipses cover different amounts of sections in the $Q(t)$-$R(t)$ plane: the mean ellipse area is 0.04 ± 0.02. The form of the ellipses ranges from circlelike (ID 7 or ID 10) to elongated (ID 1 or ID 3, for example). The mean ellipse linear eccentricity e is 0.21 ± 0.1.

Figure 13 depicts the curves $C(t)$ and the corresponding ellipses in the $Q(t)$-$R(t)$ plane for the MPR phonation of the pathologic voice subjects. Compared to the values of the normal voices, the three characteristics d, a, and e are increased: they amount 0.17 ± 0.1, 0.18 ± 0.1, and 0.48 ± 0.17. Enlarged oscillation asymmetries are indicated by these three increased values. The curve's center of gravity is farther away from the symmetry point $P_{\mathrm{sym}}=(1,1)$, the ellipse spans a larger area a in the $Q(t)$-$R(t)$ plane, and the higher linear eccentricity e results in more squished ellipse forms as for the averaged normal voice subjects.

The rating value Ψ describes the degree of left to right asymmetries for the adapted SSP and MPR oscillations. The rating Ψ combines the three criteria d, a, and e. The two summands of the rating Ψ are coded in light $(d\cdot e)$ and dark gray (a). Small rating values stand for small left to right asymmetries. Figure 14(a) shows the rating Ψ for the normal and pathological voice subjects for the stationary SSP paradigm. The rating Ψ is in the same order of magnitude for both subject groups, except for the pathologic subjects ID 19 and ID 20. For these two subjects Ψ has increased values of 0.85 and 1.9. The median rating value Ψ for the normal voices is 0.025 and 0.065 for the pathological voices. The ranges of the rating values between the normal and pathological voice group overlap. A Wilcoxon rank sum test confirms the hypothesis at a significant level of 0.05 that the

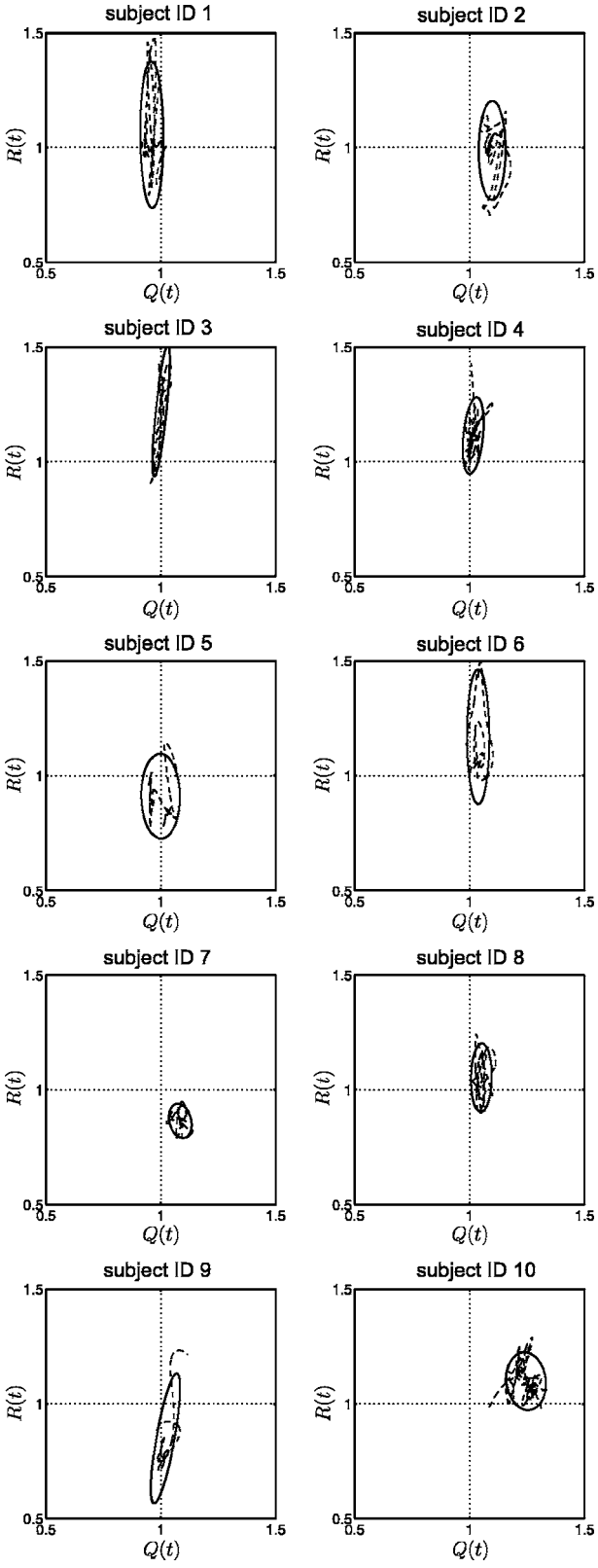

FIG. 12. Plots of the curve $C(t)$ for the normal voice subjects in the $Q(t)-R(t)$ plane for MPR phonation. Perfect symmetry is located at the point $P_{\mathrm{sym}}=(1,1)$. Deviations from P_{sym} indicate left to right asymmetries. An ellipse is drawn around the center of gravity for each curve. The axes lengths of the ellipses are determined to include 95% of samples along each axes.

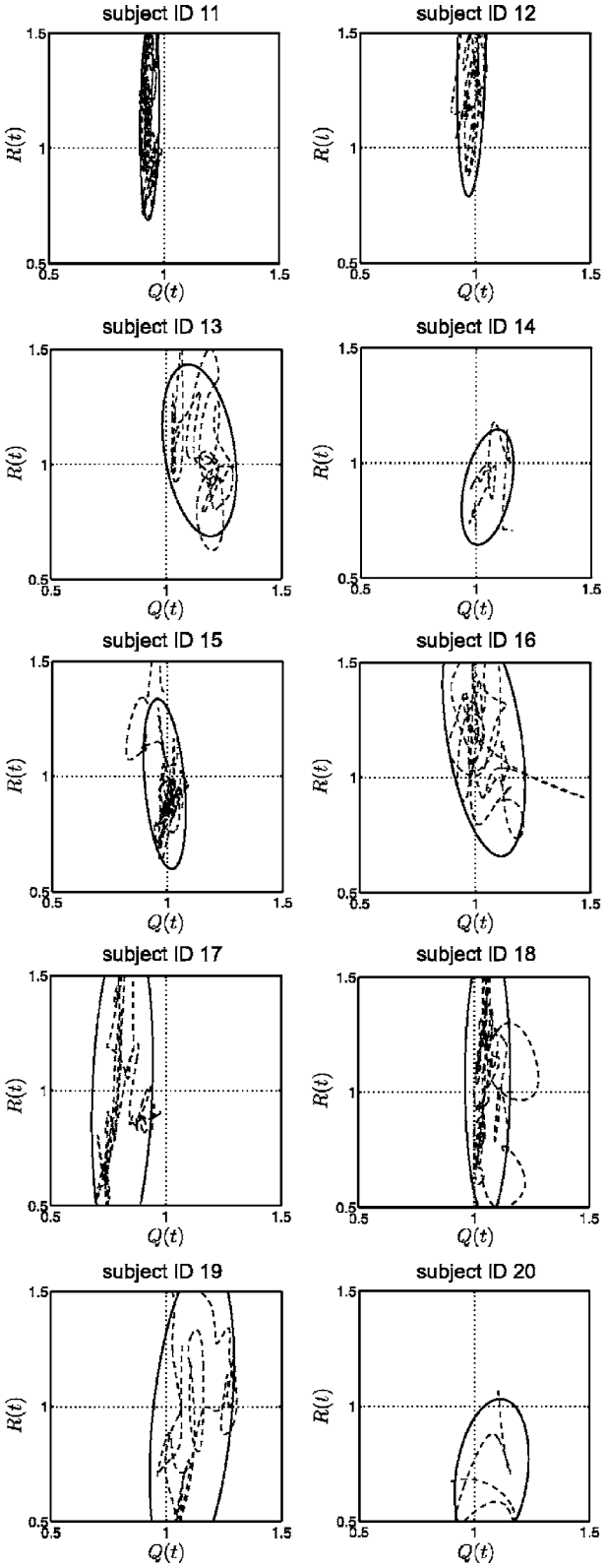

FIG. 13. Plots of the curve $C(t)$ for the pathological voice subjects in the $Q(t)-R(t)$ plane for MPR phonation. Explanations are given in the caption of Fig. 12.

rating values Ψ of both groups are not significantly different. A separation in normal and pathological voices fails with the rating value Ψ for the investigated subjects in the SSP paradigm.

In contrast to the rating Ψ in the case of the SSP paradigm, Fig. 14(b) illustrates the rating Ψ for the individual subjects in the case of the nonstationary MPR paradigm. For each normal voice subject the rating value Ψ is less than 0.1, whereas Ψ is greater than 0.1 for all of the pathological voice subjects. Three pathological voice subjects (ID 11, 14, and 15) have a relatively low rating Ψ about 0.11, due to smaller asymmetries in the adapted symmetry factors. The other ratings Ψ of the pathological voices range from 0.23 to 0.47. The corresponding medians of the rating values are 0.06 for the normal group and 0.25 for the pathological voice group. The hypothesis that the rating values Ψ of both groups are descended from an identical population is rejected at a significance level of 0.05 with a Wilcoxon rank sum test. Thus, a separation between the normal and pathological voice groups is possible. A classification between the two voice groups is reached with the rating value Ψ in the nonstationary MPR condition.

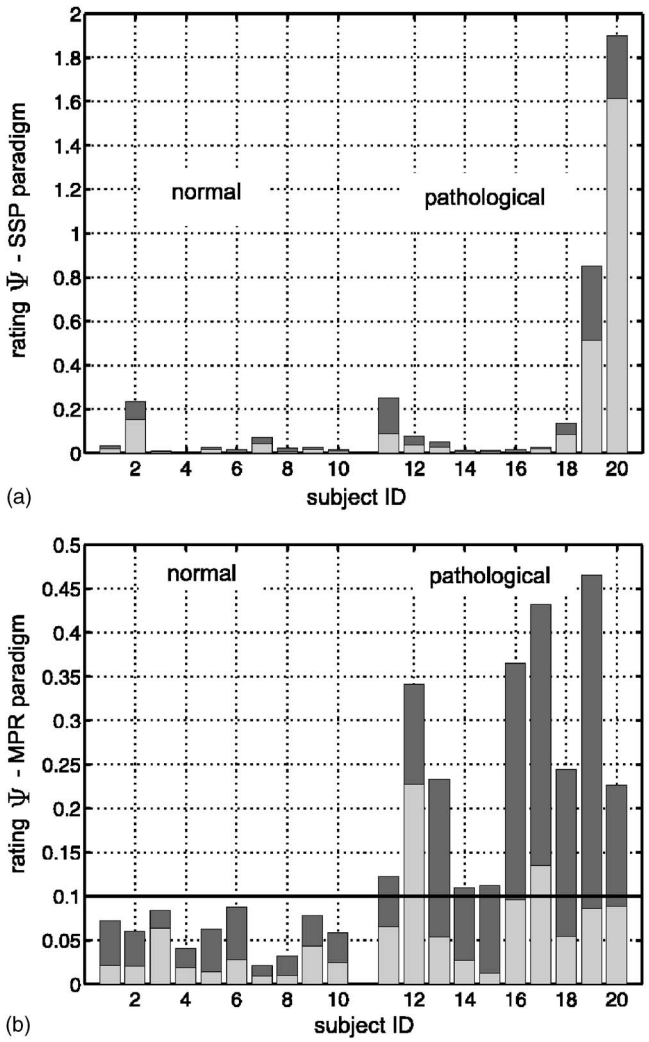

FIG. 14. Comparison of rating values Ψ for the SSP and MPR phonation. The two summands that contribute to Ψ are coded in light ($e \cdot d$) and dark (a) gray. (a) Rating values Ψ for the individual subjects for the SSP. A separation into groups of normal and pathological voices fails. (b) Rating values Ψ for the individual subjects for the MPR phonation. A separation between both groups is possible with a boundary of $\Psi = 0.1$ (black horizontal line).

IV. DISCUSSION

Endoscopic HS recordings of the larynx are useful for the visualization of irregular, transient, and nonstationary vocal fold vibrations.[9,44] Typically, a sustained stationary phonation paradigm SSP, which is used for stroboscopic techniques, is also applied for the HS examination of normal and pathological vocal fold vibrations.[6–8,53] Conclusions on vocal fold vibration behavior are only possible for the observed static laryngeal configuration, which is characterized by constant muscle tensions, constant subglottal pressure levels, and constant positions of the cartilaginous framework of the larynx. An alternative phonation paradigm, a monotonous pitch raise MPR, is investigated for the endoscopic HS recordings. The MPR is one representative of nonstationary phonation paradigms and requires continuous adjustments of laryngeal muscles.[14,15] Therefore, dynamical transitions influence the vocal fold vibrations. Compared to a stationary phonation, the dynamical transitions of the MPR examination are closer to the running speech in everyday life, which is characterized by transient and nonstationary processes. Hence, the MPR paradigm allows a more comprehensive description of the laryngeal motorics.

Both the normal and the dysphonic voice group are able to perform the nonstationary MPR phonation during the endoscopy. The voice disorder of the investigated dysphonic subjects does not influence the frequency range negatively. On average, they cover a frequency range comparable to the normal voice subjects (Fig. 9). Thus, even for dysphonic subjects, the MPR phonation paradigm can be applied in the clinical HS examination of the larynx.

The extraction of the experimental trajectories $d_\alpha^{\mathrm{HS}}(t)$ from the recorded HS sequences by image processing performs well for the MPR paradigm. Compared to SSP, where typically short time segments (50–250 ms) are sufficient to characterize the vocal fold oscillation pattern,[7,8,44] the phonation time of MPR is longer. In the average of the examined normal and pathological voices, the MPR duration time takes 858 ± 458 ms. The image processing is capable to detect and track the oscillations of vocal fold edges during this time period, even in cases with varying and inhomogeneous illumination situations of the larynx. In the SSP and MPR recordings the image processing has a typical uncertainty of one pixel, which has an influence on the extracted deflections from the glottal axis of the vocal fold vibrations. The resulting error depends on the camera resolution and the deflection of the vibrations and is in a range of 10% with respect to the oscillation amplitude (Sec. II A).

The objective of the study is to extract quantitative parameters from the experimental stationary and nonstationary trajectories $d_\alpha^{\mathrm{HS}}(t)$ that can be used for classification purposes. The calculation of quantitative parameters is based on a parameter optimization of a biomechanical vocal fold model, the 2MM. Nonstationary vocal fold oscillations, as resulting from the phonation of a MPR, require the proposed time-dependent parameters of the 2MM(t).[44] The introduced time-varying model parameters, as springs, masses, rest positions of the masses, and the subglottal pressure, enable us to simulate nonstationary MPR vocal fold vibrations. These time-variant model parameters affect the oscillation dynamics as frequency, amplitude and waveform of the theoretical trajectories $d_\alpha(t)$ over time. The presented 2MM(t) can emulate symmetric vocal fold vibrations of the left and right side as well as asymmetrical vibrations. The different vibration characteristics are obtained by adjusting the introduced scaling factors, which are pooled in the parameter set $S(t)$.

The adaptation of the 2MM(t) dynamics to nonstationary vocal fold vibrations is enabled by the optimization scheme. The verification of the optimization scheme with 500 synthetic data sets reveals that the method is applicable to adapt the model dynamics to the predefined curves as well as to approximate the symmetry quotients $Q(t)$ and $R(t)$ of the predefined data sets (Figs. 7 and 8). The symmetry quotients $Q(t)$ and $R(t)$ are calculated with a probability greater than 95% with the proposed optimization, at an accuracy of $\varepsilon_{\mathrm{rel}} = 10\%$. An error level of $\varepsilon_{\mathrm{rel}} = 10\%$ corresponds to deflection differences between the trajectories of about 5%, which is less than the errors induced by the quantization errors during image segmentation (Sec. II A).

The symmetry factors $Q(t)$ and $R(t)$ and the scaling factor $U(t)$ are calculated with different accuracies. The error for $Q(t)$ is smaller than for $R(t)$ and $U(t)$. The factors $Q_\alpha(t)$ scale four model parameters (three different spring tensions $k_{0,i\alpha}$, $k_{0,c\alpha}$, and $c_{0,i\alpha}$ as well as the masses $m_{0,i\alpha}$), whereas $R_\alpha(t)$ and $U(t)$ scale just one model parameter. As a result, variations of $R_\alpha(t)$ and $U(t)$ induce smaller changes in the model dynamics than variations in $Q_\alpha(t)$. Therefore, the factors $Q_\alpha(t)$ dominate the model dynamics and influence the objective function ε_b, Eq. (16), of the optimization at most. The symmetry factor $Q(t)$ is calculated with the highest accuracy by the optimization. The optimization factor $U(t)$ is calculated with the lowest accuracy. Since $U(t)$ captures no left to right asymmetries, it is not included in the classification criterion. Hence, it cannot negatively affect the classification. The results of the verification with the synthetic data sets demonstrate that the proposed optimization algorithm is able to adapt the time-dependent 2MM(t) dynamics and to calculate the predefined symmetry quotients with a high accuracy in the average.

The adaptation of the theoretical trajectories $d_\alpha(t)$ to the 40 experimental trajectories $d_\alpha^{\mathrm{HS}}(t)$ succeeded, as indicated by the values in Tables II and III. The optimization does not only adapt the 2MM(t) dynamics to nonstationary vocal fold vibrations, but also enables us to simulate and adapt interperiod fluctuations that perturb stationary vocal fold vibrations. Interperiod fluctuations superimpose slight frequency and intensity variations on the stationary trajectories. This appears especially for dysphonic patients who are often not able to sustain a vowel at a constant pitch and loudness. Previous development of adapting a non-time-dependent 2MM to stationary vocal fold vibrations suffered from the inability to simulate the aforementioned interperiod fluctuations.[7] With the proposed time-dependent approach errors due to interperiod fluctuations are systematically eliminated.

The quantitative and objective assessment of vocal fold oscillation asymmetries bases on the quotients $Q(t)$ and $R(t)$ of the optimized model scaling factors $Q_\alpha(t)$ and $R_\alpha(t)$. Left to right vocal fold vibration asymmetries are mapped to a

two-dimensional parameter curve $C(t)$ defined through both symmetry factors $Q(t)$ and $R(t)$. A visual interpretation of the asymmetries is possible in the $Q(t)$-$R(t)$ plane. The time-dependent asymmetries of $Q(t)$ and $R(t)$ are captured in the variations of the curve $C(t)$ and are characterized by the surrounding ellipse. The curve $C(t)$ reflects the asymmetries of the optimized model parameters and therefore the asymmetries in the adapted vocal fold oscillations. In contrast to the stationary phonation, where the curve $C(t)$ qualifies only time-dependent asymmetries, i.e., interperiod fluctuations, $C(t)$ provides additional pitch-dependent information in the nonstationary MPR phonation.

From the curve $C(t)$ a rating value Ψ is calculated that quantifies different degrees of vocal fold asymmetries. One part of the rating Ψ is the distance d from the center of gravity P_{cog} of the curve $C(t)$ to the symmetry point $P_{\mathrm{sym}} = (1,1)$. The distance d describes the mean degree of asymmetry and can be regarded as a counterpart of the asymmetries that are observable in stationary adaptation approaches. In addition, the two ellipse measures, linear eccentricity e and ellipse area a, contribute to the rating $\Psi = e \cdot d + a$. They describe time-dependent asymmetries and cannot be revealed in case of a non-time-dependent approach.

The rating values Ψ for the SSP condition of the normal and pathological voices are depicted in Fig. 14(a). In the case of a SSP paradigm only the portions of a voice disorder that become manifest at the specific pitch and intensity are quantified. The pathological subjects ID 11 to 18 phonated in a pitch and intensity region where their voice disorder did not appear. The calculated left to right asymmetries Ψ of vocal fold vibrations are in the same range (from 0.1 to 0.5) as for the normal voice subjects. Therefore, the normal and pathological voices cannot be separated from each other.

In the case of the MPR paradigm, which scans a broader phonation regime than SSP, the rating Ψ exploits the pitch-dependent variations of the curve $C(t)$. The combined evaluation of time-invariant (d), time-variant (a and e), and pitch-dependent (d, a, and e) criteria enables a quantitative separation and thus a classification of vocal fold oscillations. A distinction between the subjects of the normal and the pathological voice group is possible with the rating value Ψ in the nonstationary pitch raise condition. Not only are the organic voice disorders (subjects ID 16–20) correctly assigned, but also the functional voice disorders (subjects ID 11–15) are distinguishable from the normal voice subjects.

The automatic optimization procedure enables the quantification of vocal fold vibrations, which is essential for the objective diagnosis of voice disorders. The rating value Ψ displays the degree of time-varying vocal fold asymmetries and thus a high-grade dysphony correlates to high rating values. In a further study the investigations will focus on the potential of the proposed approach to quantify the outcome of voice therapy. Additionally, it will be investigated if even different kinds of dysphonia can be separated from each other.

V. CONCLUSION

In contrast to the stationary phonation, the vocal fold vibrations of a pitch raise contain active changes of the vocal fold vibration state. Hence, additional information of vocal fold movements is available. The pitch-dependent evolution of left to right oscillation asymmetries and the stability of vocal fold vibrations can be extracted from the high-speed recordings. In a time-dependent biomechanical model approach, the model dynamics are adapted to the observed vocal fold vibrations. The optimized model parameters enable us to visualize and to quantify left to right vocal fold asymmetries within a two-dimensional parameter curve. From this curve a rating value is derived that assesses the degree of asymmetry. Based on this rating value it is shown that just in the case of the nonstationary phonation paradigm a classification into a group of normal and dysphonic voice subjects succeeds. The combination of a nonstationary examination procedure and a quantitative model-based analysis is sensitive for the detection of pitch- and time-dependent vocal fold irregularities and enables a classification of vocal fold vibrations.

ACKNOWLEDGMENTS

This work was supported by grant from the Deutsche Forschungsgemeinschaft (DFG) Project No. DFG HO 2177/2. Parts of this work used a software developed by Lester Ingber and other contributors.

[1] H. Hirose, "High-speed digital imaging of vocal fold vibration," Acta Oto-Laryngol. **458**, 151–153 (1988).
[2] T. Wittenberg, M. Moser, M. Tigges, and U. Eysholdt, "Recording, processing and analysis of digital highspeed sequences in glottography," Mach. Vision Appl. **8**, 399–404 (1995).
[3] H. K. Schutte, J. G. Svec, and F. Sram, "First results of clinical application of videokymography," Laryngoscope **108**, 1206–1210 (1998).
[4] D. Maurer, M. Hess, and M. Gross, "High-speed imaging of vocal fold vibrations and larynx movements within vocalizations of different vowels," Ann. Otol. Rhinol. Laryngol. **105**, 975–981 (1996).
[5] S. Niimi and M. Miyaji, "Vocal fold vibration and voice quality," Folia Phoniatr Logop **52**, 32–38 (2000).
[6] J. Neubauer, P. Mergell, U. Eysholdt, and H. Herzel, "Spatio-temporal analysis of irregular vocal fold oscillations: biphonation due to desynchronization of spatial modes," J. Acoust. Soc. Am. **110**, 3179–3192 (2001).
[7] M. Döllinger, U. Hoppe, F. Hettlich, J. Lohscheller, S. Schuberth, and U. Eysholdt, "Vibration parameter extraction from endoscopic image series of the vocal folds," IEEE Trans. Biomed. Eng. **49**, 773–781 (2002).
[8] R. Schwarz, U. Hoppe, M. Schuster, T. Wurzbacher, U. Eysholdt, and J. Lohscheller, "Classification of unilateral vocal fold paralysis by endoscopic digital high-speed recordings and inversion of a biomechanical model," IEEE Trans. Biomed. Eng. **53**, 1099–1108 (2006).
[9] U. Eysholdt, F. Rosanowski, and U. Hoppe, "Irregular vocal fold vibrations caused by different types of laryngeal asymmetry," Eur. Arch. Otorhinolaryngol. **260**, 412–417 (2003).
[10] J. Wendler, "Stroboscopy," J. Voice **6**, 49–54 (1992).
[11] B. Schneider, J. Wendler, and W. Seidner, "The relevance of stroboscopy in functional dysphonias," Folia Phoniatr Logop **54**, 44–54 (2002).
[12] U. Eysholdt, M. Tigges, T. Wittenberg, and U. Pröschel, "Direct evaluation of high-speed recordings of vocal fold vibrations," Folia Phoniatr Logop **48**, 163–170 (1996).
[13] Patrick Mergell, H. Herzel, T. Wittenberg, M. Tigges, and U. Eysholdt, "Phonation onset: vocal fold modeling and high-speed glottography," J. Acoust. Soc. Am. **104**, 464–470 (1998).
[14] U. Hoppe, F. Rosanowski, M. Döllinger, J. Lohscheller, and U. Eysholdt, "Visualization of the laryngeal motorics during a glissando," J. Voice **17**, 370–376 (2003).
[15] O. Rasp, J. Lohscheller, M. Döllinger, U. Eysholdt, and U. Hoppe, "The pitch raise paradigm: a new task for real-time endoscopy of non-stationary phonation," Folia Phoniatr Logop **58**, 175–185 (2006).
[16] I. Tokuda and H. Herzel, "Detecting synchronization in an asymmetric vocal fold model from time series data," Chaos **15**, 013702 (2005).

[17]M. Döllinger, T. Braunschweig, J. Lohscheller, U. Eysholdt, and U. Hoppe, "Normal voice production: computation of driving parameters from endoscopic digital high speed images," Methods Inf. Med. **42**, 271–276 (2003).
[18]K. Ishizaka and J. L. Flanagan, "Synthesis of voiced sounds from a two-mass model of the vocal cords," Bell Syst. Tech. J. **51**, 1233–1268 (1972).
[19]K. Ishizaka and N. Isshiki, "Computer simulation of pathological vocal-cord vibration," J. Acoust. Soc. Am. **60**, 1193–1198 (1976).
[20]T. Koizumi, S. Taniguchi, and S. Hiromitsu, "Two-mass models of the vocal cords for natural sounding voice synthesis," J. Acoust. Soc. Am. **82**, 1179–1192 (1987).
[21]J. C. Lucero, "Dynamics of the two-mass model of the vocal folds: Equilibria, bifurcations, and oscillation region," J. Acoust. Soc. Am. **96**, 3104–3111 (1993).
[22]D. A. Berry, H. Herzel, I. R. Titze, and K. Krischer, "Interpretation of biomechanical simulations of normal and chaotic vocal fold vibrations with empirical eigenfunctions," J. Acoust. Soc. Am. **95**, 3595–3604 (1994).
[23]I. Steinecke and H. Herzel, "Bifurcations in an asymmetric vocal fold model," J. Acoust. Soc. Am. **97**, 1571–1578 (1995).
[24]J. J. Jiang, Y. Zhang, and J. Stern, "Modeling of chaotic vibrations in symmetric vocal folds," J. Acoust. Soc. Am. **110**, 2120–2128 (2001).
[25]B. H. Story and I. R. Titze, "Voice simulation with a body-cover model of the vocal folds," J. Acoust. Soc. Am. **97**, 1249–1260 (1994).
[26]J. Wendler, W. Seidner, G. Kittel, and U. Eysholdt, *Lehrbuch der Phoniatrie und Pädaudiologie* (Thieme, Stuttgart, 1996).
[27]J. Lohscheller, M. Döllinger, M. Schuster, R. Schwarz, U. Eysholdt, and U. Hoppe, "Quantitative investigation of the vibration pattern of the substitute voice generator," IEEE Trans. Biomed. Eng. **51**, 1394–1400 (2004).
[28]S. Schuberth, U. Hoppe, M. Döllinger, J. Lohscheller, and U. Eysholdt, "High-precision measurement of the vocal fold length and vibratory amplitude," Laryngoscope **112**, 1043–1049 (2002).
[29]M. C. Su, T. H. Yeh, C. T. Tan, C. D. Lin, O. C. Linne, and S. Y. Lee, "Measurement of adult vocal fold length," J. Laryngol. Otol. **116**, 447–449 (2002).
[30]T.-Y. Hsiao, C.-L. Wang, C.-N. Chen, F.-J. Hsieh, and Y.-W. Shau, "Elasticity of human vocal folds measured in vivo using color doppler imaging," Ultrasound Med. Biol. **28**, 1145–1152 (2002).
[31]M. Schuster, J. Lohscheller, P. Kummer, U. Eysholdt, and U. Hoppe, "Laser projection in high-speed glottography for high-precision measurements of laryngeal dimensions and dynamics," Eur. Arch. Otorhinolaryngol. **262**, 477–481 (2005).
[32]I. R. Titze, "The human vocal cords: A mathematical model, part I," Phonetica **28**, 129–170 (1973).
[33]I. R. Titze, "The human vocal cords: A mathematical model, part II," Phonetica **29**, 1–21 (1974).
[34]D. Wong, M. Ito, N. B. Cox, and I. R. Titze, "Observation of perturbations in a lumped-element model of the vocal folds with application to some pathological cases," J. Acoust. Soc. Am. **89**, 383–394 (1991).
[35]J. J. Jiang, C. E. Diaz, and D. G. Hanson, "Finite element modeling of vocal fold vibration in normal phonation and hyperfunctional dysphonia: implications for the pathogenesis of vocal fold nodules," Ann. Otol. Rhinol. Laryngol. **107**, 603–609 (1998).
[36]F. Alipour, D. A. Berry, and I. R. Titze, "A finite element model of vocal fold vibration," J. Acoust. Soc. Am. **108**, 3003–3012 (2000).
[37]P. Mergell and H. Herzel, "Modelling biphonation—the role of the vocal tract," Speech Commun. **22**, 141–154 (1997).
[38]I. R. Titze, "On the mechanics of vocal-fold vibration," J. Acoust. Soc. Am. **60**, 1366–1380 (1976).
[39]I. R. Titze and J. Sundberg, "Vocal intensity in speakers and singers," J. Acoust. Soc. Am. **91**, 2936–2946 (1992).
[40]I. R. Titze, "On the relation between subglottal pressure and fundamental frequency in phonation," J. Acoust. Soc. Am. **85**, 901–906 (1989).
[41]I. R. Titze, E. S. Luschei, and M. Hirano, "Role of the thyroarytenoid muscle in regulation of fundamental frequency," J. Voice **3**, 213–224 (1989).
[42]H. B. Nudelman and B. D. Hoyt, "Comments on Two-mass models of the vocal cords for natural sounding voice synthesis," J. Acoust. Soc. Am. **85**, 2220–2221 (1989).
[43]T. Koizumi, S. Taniguchi, and S. Hiromitsu, "Reply to 'Comments on "Two-mass models of the vocal cords for natural sounding voice synthesis,"'" J. Acoust. Soc. Am. **85**, 2221–2223 (1989).
[44]P. Mergell, I. R. Titze, and H. Herzel, "Irregular vocal-fold vibration—High-speed observation and modeling," J. Acoust. Soc. Am. **108**, 2996–3002 (2000).
[45]U. Hoppe, "Mechanisms of Hoarseness—Visualization and Interpretation by Means of Nonlinear Dynamics," in *Kommunikationsstörungen, Berichte aus Phoniatrie und Pädaudiologie, Band 7*, edited by U. Eysholdt (Shaker, Aachen, 2001).
[46]M. Döllinger, "Parameter Estimation of Vocal Fold Dynamics by Inversion of a Biomechanical Model," in *Kommunikationsstörungen, Berichte aus Phoniatrie und Pädaudiologie, Band 10*, edited by U. Eysholdt (Shaker, Aachen, 2002).
[47]L. F. Oliveira, D. M. Simpson, and J. Nadal, "Calculation of area of stabilometric signals using principal component analysis," Physiol. Meas **17**, 305–312 (1996).
[48]A. B. Pealman and F. Alipour, "Comparative study of the physiological properties of the vocalis and cricothyroid muscles," Acta Oto-Laryngol. **105**, 372–378 (1988).
[49]I. R. Titze, B. Story, M. Smith, and R. Long, "A reflex resonance model of vocal vibrato," J. Acoust. Soc. Am. **111**, 2272–2282 (2002).
[50]D. L. Morgan and U. Proske, "Vertebrate slow muscle: its structure, pattern of innervation and mechanical properties," Physiol. Rev. **64**, 103–168 (1984).
[51]L. Ingber, "Lester Ingber's Archive: Adaptive Simulated Annealing," http://www.ingber.com/, (2005).
[52]L. Ingber, "Very fast simulated re-annealing," Math. Comput. Modell. **12** (8), 967–973 (1989).
[53]L. Li, P. N. Galatsanos, and D. Bless, "Eigenfolds: A new Approach for Analysis of Vibrating Vocal Folds," IEEE International Symposium on Biomedical Imaging, Washington, DC (2002).

Interarticulator cohesion within coronal consonant production[a)]

Christine Mooshammer[b)]
Institut für Phonetik und digitale Sprachverarbeitung, Christian-Albrechts Universität, Kiel, 24098 Germany

Philip Hoole
Institut für Phonetik und sprachliche Kommunikation, Ludwig-Maximilians-Universität, Munich, Germany

Anja Geumann
School of Computer Science and Informatics, UCD, Dublin, Ireland

(Received 3 May 2005; revised 29 March 2006; accepted 5 May 2006)

If more than one articulator is involved in the execution of a phonetic task, then the individual articulators have to be temporally coordinated with each other in a lawful manner. The present study aims at analyzing tongue-jaw cohesion in the temporal domain for the German coronal consonants /s, ʃ, t, d, n, l/, i.e., consonants produced with the same set of articulators—the tongue blade and the jaw—but differing in manner of articulation. The stability of obtained interaction patterns is evaluated by varying the degree of vocal effort: comfortable and loud. Tongue and jaw movements of five speakers of German were recorded by means of electromagnetic midsagittal articulography (EMMA) during /aCa/ sequences. The results indicate that (1) tongue-jaw coordination varies with manner of articulation, i.e., a later onset and offset of the jaw target for the stops compared to the fricatives, the nasal and the lateral; (2) the obtained patterns are stable across vocal effort conditions; (3) the sibilants are produced with smaller standard deviations for latencies and target positions; and (4) adjustments to the lower jaw positions during the surrounding vowels in loud speech occur during the closing and opening movement intervals and not the consonantal target phases. [DOI: 10.1121/1.2208430]

PACS number(s): 43.70.Bk, 43.70.Aj [AL] Pages: 1028–1039

I. INTRODUCTION

In the execution of a speech task, e.g., complete occlusion of the vocal tract with the lips, the articulators involved constitute a system with multiple degrees of freedom. Therefore, it is generally acknowledged that multiarticulatory tasks are not accomplished by individual control of each composite articulator. Instead, hierarchically ordered coordinative structures are assumed to orchestrate spatially and temporally the individual movements, thereby simplifying the control of multiple muscle activities (see, e.g., Fowler *et al.*, 1980).

Coordinative structures as organizational units have been included in speech production models with radically different assumptions concerning the nature of the motor plan. Thus, for example the task dynamic model (Saltzman and Munhall, 1989) is based around the concept of key vocal-tract constrictions, while the DIVA model (Guenther *et al.*, 1998, 1999) assumes that the goals of speech movements are defined in an auditory or perceptual space. As a further key issue the temporal aspect of speech motor control has been given much attention in recent years because it was found that the contributing articulators do not all start moving at the same time but with a certain order and timed with respect to specific articulatory events of each other (see, e.g., Gracco and Abbs, 1986). The focus of most studies was on the strength of the functional linkage between varying component articulators such as lip-jaw vs tongue tip-jaw in Hertrich and Ackermann (2000) or lip-jaw vs velum-jaw in Kollia *et al.* (1995) and across varying suprasegmental conditions (stress and speech tempo in Kelso *et al.*, 1986; speech tempo in DeNil and Abbs, 1991; Nittrouer *et al.*, 1988; Nittrouer, 1991; and Shaiman *et al.*, 1995). Up to now, no articulatory timing data have been available for varying manners of articulation within a single set of component articulators. The general aim of the current study is to investigate the timing of the tongue tip and jaw for the coronal consonants /s, ʃ, t, d, n, l/, i.e., for consonants produced with the same set of articulators but different constriction degrees and additional features such as voicing or velar opening.

A fixed succession of articulatory events for achieving a phonetic goal has been interpreted as strong interarticulator cohesion and evidence for coordinative structures (see Fowler *et al.*, 1980; Saltzman and Munhall, 1989). For example, for the bilabial closure a very consistent advancement of the upper lip velocity peak for the closing movement relative to the lower lip and jaw velocity peaks has been found (see, e.g., Gracco and Abbs, 1986; Gracco, 1988; van Lieshout, 1995; Kollia *et al.*, 1995). The stability of such relatively time-locked interarticulator cohesion has been experimentally tested by varying external parameters such as speech rate and stress placement. The assumption is that the task-specific organizationally invariant timing of composite articulators is achieved by a motor program which function-

[a)]Portions of this work were presented at the 15th International Congress of Phonetic Sciences, Barcelona, Spain, August 2003.

[b)]Author to whom correspondence should be addressed. Electronic mail: timo@ipds.uni-kiel.de

ally organizes multiarticulate speech movements for a phonetic gesture, while local parameters of the pattern, such as speech tempo, are left to vary freely and are considered parameters of the program (see Shaiman *et al.*, 1995).

The timing between the executing organs is assumed to be almost invariant and stronger for gestures within a phoneme than between phonemes (see Saltzman *et al.*, 1998). The evidence for different degrees of cohesion, termed "glue" by Saltzman *et al.* (2000), was found by perturbation experiments: the relative timing was shifted to a lesser degree when the perturbation occurred within an actively controlled gesture rather than at the borders.

In former studies the strength of cohesion has been found to vary with several aspects, e.g., closing movements are more tightly coupled than opening movements (e.g., Gracco, 1988; Hertrich and Ackermann, 2000). Furthermore, articulators controlled by different tract variables such as the vocal folds and velum exhibit a smaller degree of interarticulator cohesion with the jaw than articulators controlled by a single tract variable such as upper lip and jaw (see, e.g., Gracco and Löfqvist, 1994; Kollia *et al.*, 1995) as measured by a greater variability in timing parameters. This tendency implies that interarticulator cohesion is stronger than intergestural cohesion. Finally, consistent timing relationships between articulators are more often found for the peak velocity as compared to on- and offsets of movements (Gracco, 1988; van Lieshout 1995).

Evidence for a fixed timing relationship between the upper lip and the jaw across suprasegmental manipulations was found by, e.g., Kelso *et al.* (1986) using a phase plane plot, which shows the velocity of the jaw during a VCV sequence on one axis and its position on the other. The timing relationship to the upper lip was then expressed as an angle in this plane. This phase angle varies with phonetic identity but not with speech rate and stress according to Kelso *et al.* (1986). However, later studies yielded contradictory results: the phase angle was found to decrease if the jaw cycle duration decreased, e.g., at fast speech rate or for unstressed syllables more of the cycle was occupied by the upper lip lowering for bilabial consonants (see Nittrouer *et al.*, 1988; Shaiman *et al.*, 1995) or the tongue tip closing and closure for apical consonants (Nittrouer, 1991). These latter results indicate that rate and stress manipulations do also affect the spatiotemporal relationships among articulators.

Most studies focused on bilabial consonants and the spatiotemporal coordination between the lips and the jaw. Up to now, the *timing* between the involved articulators for different manners of articulation has not been studied. However, a number of studies have examined the *spatial* contribution of the jaw to the production of vowels and consonants with varying manners and places of articulation. Since in the present study articulatory properties of the coronal consonants will be investigated, only earlier results on /s, ʃ, t, d, n, l/ will be reviewed here. Based on jaw positions, previous studies found that the jaw's contribution varies for these consonants, e.g., a closed and very precisely controlled jaw position is essential for the sibilants /s/ and /ʃ/ in order to provide a second noise source by a small distance between the upper and lower teeth (Geumann *et al.*, 1999; see also, e.g., Shadle, 1990; Lee *et al.*, 1994; Howe and McGowan, 2005). For /l/ a low jaw position is advantageous in order to provide space for the more apical articulation—as opposed to a flat and laminal articulation—and to avoid lateral contact between the tongue sides and the posterior parts of the alveolar ridge (see, e.g., Lindblad and Lundqvist, 1999 and Geumann, 2001a). Geumann (2001a) suggested that apicality also seems to play a role for the voiced stop /d/ which is then produced with a lower jaw position than /t/, but as Dart (1991) and Geumann (2001a) pointed out, the choice between an apical or laminal articulation in languages such as French, English, and German depends on the speaker. Highly consistent results have been found for the jaw positions during /t/, which were only slightly lower than the sibilants' and almost as invariant (see, e.g., Kühnert *et al.*, 1991; Keating *et al.*, 1994; Lee *et al.*, 1994; Geumann *et al.*, 1999).

The present study aims at investigating the temporal coordination between the tongue tip and the jaw for the coronal consonants /s, ʃ, t, d, n, l/ in German. As was found for spatial parameters, the jaw does not contribute uniformly to the production of the consonants under consideration. In the first part of the Results section, jaw and tongue tip positions will be analyzed for the coronal consonants. Whether the differential role of the jaw also has consequences for the timing between the jaw and the tongue tip will be assessed in the second part by analyzing the intervals between specific articulatory events of the tongue tip and the jaw in VCV sequences, such as the closing movement offset and opening movement onset. In addition to these latencies, the latencies of the peak velocities are taken into account because it was found that the peak muscle activation correlates quite well with peak velocities (see Gracco, 1988). One specific hypothesis concerning the timing is that, if the task of the jaw is simply to lift the tongue tip up towards the alveolars, the tongue tip and the jaw should move in relative synchrony, with any time lag attributable to differences in kinematic properties of the articulators involved such as generally slower jaw movements as compared to tongue tip movements (see Tasko and Westbury, 2002). A third aim of this study is to investigate the strength of temporal cohesion for varying manners of articulation. Therefore, the variability of positions and latencies was compared for the six coronal consonants.

In order to check whether the observed differences between manners of articulation are stable across different conditions, the data were recorded at two vocal effort levels: normal and speaking up without shouting. As was found, e.g., by Schulman (1989) and Geumann (2001a), the excursion of the jaw movement towards the vowel is larger in loud speech, whereas the consonants were less affected. Therefore, speaking up can be interpreted as an up scaling for the vowel-directed movement but not the consonant related, and the closing gesture will be mainly affected because of lower jaw positions during the vowel. If tight cohesion obtains, then the temporal and spatial tongue-jaw coordination during the consonants should not be affected by the lower jaw positions of the surrounding vowels. Furthermore, Dromey and Ramig (1998) showed that token-to-token variability of articulatory measures decreased for higher levels of vocal ef-

fort. More subtle differences in timing between manners of articulation are therefore expected to be found more easily in loud speech.

II. METHOD

A. Speakers

Five native speakers of German, one female (AW) and four male (KH, RS, SR, UR), were recorded by means of electromagnetic midsagittal articulography. The age of the speakers ranged from 23 to 31 and none of the speakers had a known history of speech or hearing problems. The speakers were students or faculty staff of the Institute of Phonetics and Speech Communication at the University of Munich. They were not familiar with the aims of this study.

B. Speech material

This study is based on the same set of data as reported in Geumann *et al.* (1999); Geumann (2001a, b). The six coronal consonants /s, ʃ, t, d, n, l/ were recorded in symmetrical VCV sequences. The vowel context consisted of /i/, /e/, and /a/. Only items with surrounding low vowels /a/ will be considered here because jaw movements for high vowels were too small and noisy for analysis of movement kinematics. The first vowel was always stressed and long and the second one unstressed but unreduced. All VCV sequences were embedded in the carrier phrase "*Hab das Verb____ mit dem Verb____ verwechselt*" (I mixed up the verb____ with the verb)____ and occurred equally often in the first and in the second positions. Therefore, both target sequences received contrastive sentence accent. The sentences were repeated six times in randomized order, which gives 12 repetitions per item and vocal effort condition. Stimuli were presented on a computer screen.

The increase in vocal effort was elicited by instructing the subjects to speak as loud as possible without shouting. They were told to imagine that, with the microphone turned off, they had to be heard in the control room adjacent to the recording room. In the normal condition, the speakers were instructed to speak at a comfortable vocal effort level. Since both conditions were randomly varied, the loud condition was additionally marked on the prompt screen below the test sequence.

By measuring the rms amplitude during the vowels, we assessed whether all speakers increased the intensity significantly (for details see Geumann, 2001a). Speakers varied in the amount of vocal effort increase. Speaker UR almost shouted; he generally spoke with the highest intensity for loud speech and largest difference between the two vocal effort levels (mean sentence intensity for UR for the normal condition was 61 dB and for the loud condition 72 dB). The smallest changes were observed for speakers AW and KH, with a change from normal to loud vocal effort level of about 5 dB.

C. Procedure

Articulatory data were collected by using the electromagnetic midsagittal articulograph AG100 manufactured by Carstens Medizinelektronik (for details on the measurement principle see Hoole and Nguyen, 1999). Four sensors were glued on the tongue surface by using dental cement (Ketac). For the current study only the tongue tip sensor, placed approximately 1 cm behind behind the apex, was analyzed. For monitoring jaw movements three sensors were placed on the outer and inner surface of the lower gums and the angle of the chin. Two sensors on the bridge of the nose and the upper incisors were recorded for the correction of head movements.

After the recording session, data were rotated to the occlusal plane and the origin of the new coordinate system was located at the lower edge of the upper incisors. The procedure to orient the data with the horizontal axis parallel to the occlusal plane was as follows: The investigator made a trace of the subject's hard palate during the experiment using a spare sensor. Then, this trace was aligned with a hard-palate trace taken from a dental impression placed in the EMMA apparatus. A plastic t-bar bearing two sensors was placed on the dental impression (resting on the upper incisors at the front and the second molars at the back) to provide a definition of occlusal plane orientation.

The articulatory data were sampled at a frequency of 500 Hz. For further processing all signals were downsampled to 250 Hz and low-pass filtered with a finite impulse response (FIR) filter (Kaiser window design, −6 dB at 50 Hz). Horizontal, vertical, and tangential velocities were calculated and smoothed with a further Kaiser window filter (−6 dB at 20 Hz).

The measured tongue tip signal is composed of the active tongue tip and the jaw. Thus, the tongue tip signal has to be decomposed into the active tongue tip movement and the passive consequence of the jaw movements (for an extensive overview see Westbury *et al.*, 2002), which is complicated by the fact that the measured jaw movement consists of a rotational and a translational component. From MRI data (for details of data acquisition see Hoole *et al.*, 2000) for each speaker the exact position of the mandibular condyle was obtained and mapped onto the EMMA coordinates. Distances between condyle and outer jaw and condyle and tongue sensors on the midsagittal plane were calculated at the temporal midpoint of consonant production for each speaker. The tongue-to-condyle distance in percent of the outer-jaw-to-condyle distance was taken as a weighting factor for the jaw. This procedure, which follows that of Edwards (1985), was applied because simple subtraction neglects the fact that jaw rotation affects the tongue tip to a greater degree than the tongue back. The resulting signals are termed intrinsic tongue tip for the remainder of this article.

D. Analysis

Figure 1 shows the labeling criteria. In the upper part the speech signal, the vertical jaw movement, and the derived tangential velocity of the utterance [ˈa:sa] are presented. The last two panels show the vertical intrinsic tongue tip movement and again the derived tangential velocity signal. Movement cycles of the intrinsic tongue tip[1] and jaw were segmented into closing and opening intervals by using a 20% threshold criterion of the peak tangential velocity as shown

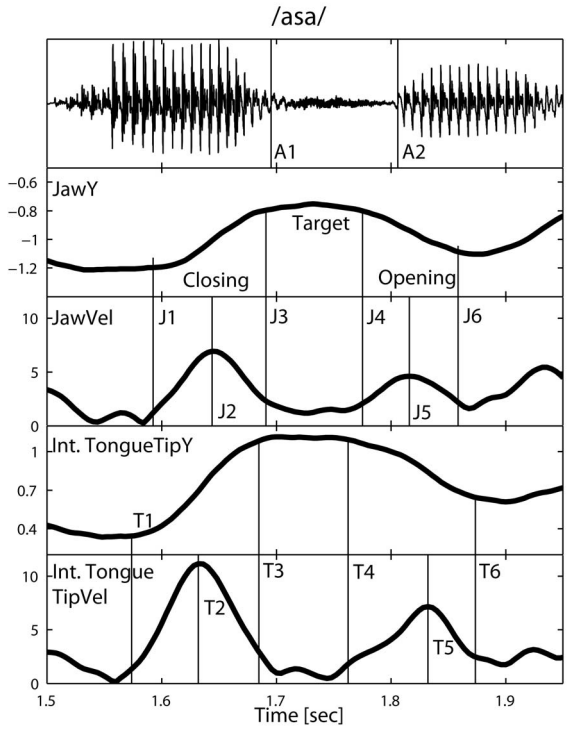

FIG. 1. Labeling criteria: Upper to lower panel: audio signal of [ˈa:sa] by speaker RS, vertical jaw movement in cm, tangential velocity signal of jaw in cm/s, vertical intrinsic tongue tip signal in cm, tangential velocity signal of intrinsic tongue tip in cm/s. Vertical lines: acoustical on- and offset of the consonant (A1 and A2), for the intrinsic tongue tip and the jaw, respectively, onset of closing movements (T1 and J1), peak velocity of the closing movement (T2 and J2), offset of the closing movement (T3 and J3), onset of the opening movement (T4 and J4), peak velocity of the opening movement (T5 and J5), and the offset of the opening movement (T6 and J6).

in this figure. The threshold criterion was applied because the onset of an opening or closing movement cannot be consistently labeled by simply using a zero crossing (or minimum when analyzing the tangential velocity) of the velocity signal, since usually multiple zero crossings occur during and after the target phase. As was shown by Kroos *et al.* (1997), a 20% threshold of the tangential velocity yields the most stable results as assessed by comparing the variability of data for selected absolute and relative threshold values. The hold duration for the consonant was defined operationally as the interval between the offset of the closing movement and the onset of the opening movement (see in Fig. 1 time points T4-T3 for the intrinsic tongue tip hold phase and J4-J3 for the jaw hold phase). Even though we are aware of the fact that this interval, in which relatively little movement occurs, is not the same as the intended target of an abstract gesture, this phase will be termed *target* of the intrinsic tongue tip or jaw for reasons of simplicity.

From these landmarks latencies were computed by subtracting the corresponding time points of the tongue tip from the jaw, with the number landmarks shown in Fig. 1. The following tongue-jaw latencies were calculated: the velocity peaks of the closing movement ($\mathrm{Lat}V_{\mathrm{cl}}$=J2-T2), the target achievement ($\mathrm{Lat}_{\mathrm{on}}$=J3-T3), the end of the target ($\mathrm{Lat}_{\mathrm{off}}$=J4-T4), and the velocity peaks of the opening movement ($\mathrm{Lat}V_{\mathrm{op}}$=J5-T5) (the abbreviations given in brackets are used for the tables below).

Latencies were also calculated in relation to the acoustic onset and offset of the consonants. The former was set at the end of high energy in *F*2 for the obstruents or a general energy drop for the nasal or the lateral. The offset was specified at the burst for /t, d/, the beginning of regular voicing for the sibilants, and a rise in energy for the nasal and the lateral. Because the intrinsic tongue tip hold phase onset and offset was well aligned with the acoustically defined events, only the jaw closing movement offset relative to the acoustically defined consonant onset ($\mathrm{AcJaw}_{\mathrm{on}}$=J3-A1) and the jaw opening movement onset relative to the acoustically defined consonant offset ($\mathrm{AcJaw}_{\mathrm{off}}$=J4-A2) are discussed in this study. For all latencies negative values indicate a jaw advancement and positive values a tongue tip advancement.

The latencies for consonantal target onsets and offsets were highly correlated with the acoustic duration of the consonants, which varied between the mean values of 130 ms for /s/ and 40 ms for /d/. Therefore, the latencies $\mathrm{Lat}_{\mathrm{on}}$, $\mathrm{Lat}_{\mathrm{off}}$, $\mathrm{AcJaw}_{\mathrm{on}}$, and $\mathrm{AcJaw}_{\mathrm{off}}$ were normalized individually to the acoustic consonant durations, i.e., the latencies were divided by the corresponding acoustic duration (A2-A1). Because no reasonable reference duration could be used for the latencies of the velocity peaks, no normalization was applied to $\mathrm{Lat}V_{\mathrm{cl}}$ and $\mathrm{Lat}V_{\mathrm{op}}$.

Intrinsic tongue tip and jaw positions were extracted at the 20% threshold of the closing movement onset during the initial vowel (time points T1 and J1), the target onset and offset (T3, T4, J3, J4), and the opening movement offset during the final vowel (T6 and J6) as shown in Fig. 1. In order to abstract from individual vocal-tract size differences *z* scores were calculated for all positional data. For computing the *z* scores, speaker-specific means and standard deviations of the jaw and the intrinsic tongue tip movement signals were calculated for the stretches when the subjects actually spoke. The means pooled for all trials were subtracted from measurement points and then divided by the standard deviation.

Cohesion strength was assessed by calculating statistics for the variability of temporal and spatial parameters. As measure for the variability simple standard deviations were used instead of the coefficients of variation; this is independent of the magnitude of the mean and might therefore be more appropriate. However, since *z* scores and latencies varied around zero, coefficients of variation could not be calculated.

E. Data exclusion

For the computation of latencies some data had to be excluded because, for the opening gesture towards the second /a/, no jaw downward movement could be detected and/or because the highest jaw position was sometimes not achieved during the consonant but during the following unstressed vowel. At normal vocal effort level exclusion was necessary for 19% of all /d/, 12% of the /n/ realizations, and 27% of the /l/ (11, 7, and 16 items, respectively). The only sound for which some items had to be excluded at loud speech was the voiced stop; the four instances were all produced by speaker SR.

TABLE I. Manner (MN) and vocal effort (VE) effects on the jaw (left) and intrinsic tongue tip (right) positions during the first vowel (V1), the consonant (C) and the second vowel (V2) and on the closing and opening displacements. Statistics are based on repeated measures ANOVAs with Greenhouse-Geisser ε corrected degrees of freedom in brackets. Results of pairwise *t*-tests with Bonferroni adjustments are also given with < indicating lower positions or smaller displacements.

			Jaw			Intrinsic tongue tip		
			MN	VE	MN:VE	MN	VE	MN:VE
Pos.	V1	*F*(df)	1.75 (2.1, 8.6)	13.05 (1, 4)* N>L	3.61 (2.9, 11.5)*	0.22 (1.6, 6.4)	3.6 (1, 4)	0.78 (2.3, 9.4)
	C	*F*(df)	26.9 (1.8, 7.2)*** s∫>dnl, t>nl	7.74 (1, 4)*	3.63 (1.3, 5.2)	16.96 (2.1, 8.4)** s<∫tdnl, t∫>1	77.7 (1, 4)***	3.2 (2.5, 9.9)
	V2	*F*(df)	7.19 (2.8, 11.4)**	12.41 (1, 4)* N>L	0.87 (1.6, 6.4)	1.66 (1.9, 7.5)	1.0 (1, 4)	1.59 (2.5, 9.8)
Disp.	Clos	*F*(df)	23.7 (2.4, 9.6)*** s∫>nl, td>1	14.4 (1, 4)* N<L	4.95 (1.5, 5.9)	13.5 (1.9, 7.7)*** s<∫tdn<1, ∫<dn	0.74 (1, 4)	0.74 (1.5, 6.0)
	Op	*F*(df)	32.6 (1.6, 6.4)*** ∫std>1, s∫>n	15.1 (1, 4)*	4.0 (1.8, 7.4)	25.4 (2.1, 8.4) s<∫tdn<1, ∫<dn	6.89 (1, 4)	3.39 (1.7, 6.7)

$^{*}p<0.05$.
$^{**}p<0.01$.
$^{***}p<0.001$.

These numbers of exclusion and their specific distribution, i.e., only voiced consonants, can be interpreted in terms of an obligatory closed-jaw position for the voiceless obstruents on the one hand and either a transitory lower jaw target (no turning point) or no obligatory jaw target at all for the voiced coronals on the other hand. The latter assumption does not seem to hold if the data for loud vocal effort are taken into account for which exclusion was restricted to four voiced stops, all produced by one speaker. Since the timing for the closing movement might already be affected if no consonant-related jaw target is reached, these items were excluded for all latencies. For the latencies of the peak velocities items were excluded when double-velocity peaks of equal height occurred in either the jaw or the intrinsic tongue tip tangential velocity signal. For the closing gesture a double-velocity peak occurred for 14 cases (1.9%) and for the opening gesture for 26 cases (3.6%).

F. Statistics

Analyses of variance were calculated for individual speakers and pooled over all speakers using the script language R (R Development Core Team, 2005). For the individual speakers all valid data were included. Main effects and interactions were computed. Independent variables were manner of articulation (MN) and vocal effort level (VE).

In order to evaluate speaker-independent strategies, additionally ANOVAs pooled over all speakers were calculated based on the data averaged over up to 12 repetitions so that each speaker contributed only one experimental score per condition (see, e.g., Max and Onghena, 1999). This data reduction is necessary in order to avoid artificially inflating the error terms and degrees of freedom. Whether manner of articulation and vocal effort affected positional and temporal data was evaluated by calculating repeated-measures ANOVAs with the within-subject factors MN and VE. Degrees of freedom were corrected by calculating the Greenhouse-Geisser epsilon in order to avoid violation of the sphericity assumption. Therefore, fractional degrees of freedom are often given in the tables. Pairwise *t*-tests with Bonferroni adjustments for multiple comparisons were carried out for individual statistics and for the repeated-measure ANOVAs in order to assess significant differences between the six-level-factor MN.

III. RESULTS

A. Positions and movement amplitudes

First, systematic effects of manner of articulation and vocal effort on spatial parameters were evaluated by calculating repeated-measures ANOVAS with manner and vocal effort as repeated factors. Subject means of jaw and intrinsic tongue tip positions during the first vowel, the consonant, and the second vowel and of the closing and opening amplitudes served as dependent variables (see Table I). Figure 2 shows the displacements of the jaw (left) and the intrinsic tongue tip (right) during the closing (upper panels) and the opening movements (lower panels). All data are *z*-transformed, i.e., scaled in standard deviations. The height of the white bars indicates the magnitude of the movement amplitudes for the normal condition and gray bars for the loud condition. The zero line for the bars in the upper figures specifies the articulator position in the normal effort condition during the initial /a/ for the closing movement (see T1 and J1 in Fig. 1) and the final /a/ for the opening movements in the lower figures (see also T6 and J6 in Fig. 1). The tops of the bars correspond to the maximal excursions of the articulators during the consonant.

Jaw positions during the consonant were significantly affected by manner but only slightly by vocal effort (see the tops of the bars in panels on the left side). For the jaw positions during the vowels, depicted as the lower edges of the bars, the opposite was the case: for the vowels the jaw position was significantly lower for loud speech but manner of articulation affected the jaw position only slightly, reaching significance only for the second vowel. Therefore, jaw dis-

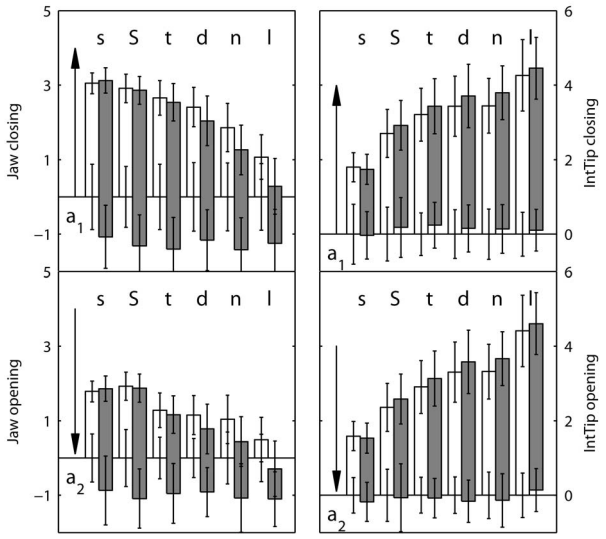

FIG. 2. Positions and displacements of the jaw (left) and the intrinsic tongue tip (right) during the closing (upper panels) and the opening movements (lower panels). All data are *z*-transformed, i.e., scaled in standard deviations. The height of the white bars indicates the magnitude of the amplitudes for the normal condition and gray bars for the loud condition. The zero line in the upper panels corresponds to the articulator position in the normal effort condition during the initial /a/ for the closing movement and the final /a/ for the opening movements in the lower figures. The tops of the bars indicate the position of the articulators during the consonantal target phase.

placements, shown in Fig. 2 as the height of the bars, increased significantly for loud speech mainly because of the lower jaw positions during the vowels.

Manner effects on jaw positions during the consonant were tested by pairwise *t*-tests using the Bonferroni adjustments for multiple comparisons; this yielded significantly higher jaw positions for the sibilants as compared to /d, l, n/. The voiceless stop /t/ was produced with a jaw position between the sibilants (no significant difference) and the voiced stop /d/. The lateral was realized with the greatest jaw opening. The effect of vocal effort increased with decreasing consonant-specific position, i.e., more extensive jaw lowering in loud speech was found for consonants with an already open jaw position. However, even in the case of the lateral the *t*-test did not indicate a significant vocal effort effect. Looking at individuals, four of the speakers had a significantly lower jaw position in the loud condition during the nasal and two speakers during the lateral. Only one speaker produced /t/ and /d/ with a significantly lower position, and no speaker varied the jaw position during the sibilants over the two vocal effort conditions.

As can also be seen in Fig. 2, jaw opening movements towards the second vowel were smaller than the closing movements. This can be attributed to the fact the initial vowel received the main stress and second vowel was unstressed but unreduced, i.e., not a schwa vowel.

The intrinsic tongue tip position during the consonant varied with manner of articulation, with significantly lowest position and smallest amplitudes for the sibilant /s/. /ʃ/ was produced with a significantly higher tongue tip position, which can be attributed to its more retracted place of articulation as compared to /s/. For the production of the lateral the tongue tip had to move more than for the other consonants (not significant for /l/ vs /d, n/). Thus, the pattern of movement amplitudes for manner of articulation is inversely related for the jaw and the intrinsic tongue tip: the more the jaw moves the smaller is the intrinsic tongue tip movement (see the sibilant /s/) and vice versa for the lateral. Intrinsic tongue tip positions during vowels were affected neither by vocal effort nor by manner of articulation. However, repeated-measures ANOVAs revealed a significant main effect of vocal effort on the intrinsic tongue tip position during the consonant. Since the *t*-tests pooled for all consonants and split by consonant did not reach significance, and the difference between normal and loud speech was very small (loud speech: mean 1.68, s.d 1.04; normal speech: mean 1.5, s.d 0.97) this result will be neglected.

To summarize the results in the spatial domain, manner of articulation affected both the tongue tip and the jaw positions during the consonant, whereas for the vowels only the jaw positions for the final unstressed vowels showed some significant effects for manner variations. Generally, the results from the literature are confirmed: the sibilants and the voiceless stop are produced with a closer jaw position compared to the remaining consonants under consideration here. Vocal effort increase was accompanied by a significantly more open jaw position during the vowels, while for the consonants effects were smaller and less consistent (significant only for the nasal (four speakers) and the lateral (two speakers)). The intrinsic tongue tip positions during the vowels and consonants remained unaffected by vocal effort changes.

B. Temporal coordination

Temporal interarticulator coordination between the tongue tip and the jaw was assessed by analyzing the latencies between the two articulators as well as between the jaw and the acoustically defined landmarks. In the first part, manner and effort effects on the latencies during the consonant target phase are discussed and then in the second part the latencies of the closing and opening velocity peaks. The aim of this section is to determine whether differences in the spatial extent of jaw involvement are accompanied by differences in the temporal coordination close to the constriction phase of the consonants.

As was pointed out in Sec. II D the significantly longer acoustic durations of the fricatives influence the latencies. Therefore, target on- and offsets were normalized to the acoustic consonant durations individually. Results are shown in Fig. 3 with 0 and 1 denoting the acoustically defined begin and end of the consonant respectively (see A1 and A2 in Fig. 1). Unfilled bars show the target duration and relative timing of the intrinsic tongue tip target achievement and release (T3 and T4 in Fig. 1), gray bars the relative hold durations of the jaw (J3 and J4 in Fig. 1). If the lower border of the white bar is close to zero, then the acoustic onset of this consonant (A1) is at the same time as the onset of the intrinsic tongue tip target phase (T3). The height of the lower white bar shows the normalized latency of the target onset (Lat_{on}), i.e., how much later the jaw achieves the target as compared to the tongue tip. For example, the lower white bar for /t/ of

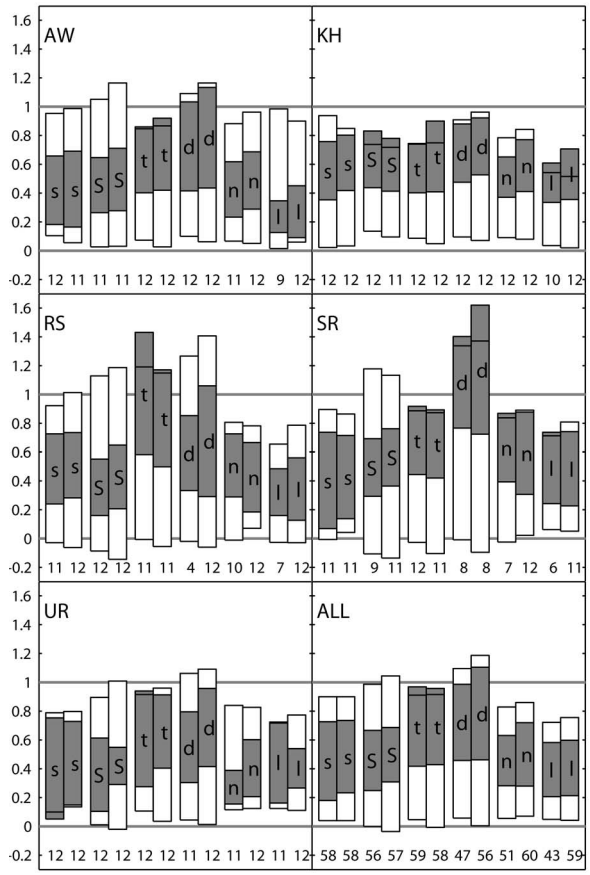

FIG. 3. Normalized durations of intrinsic tongue tip (unfilled boxes) and jaw target (gray boxes) on- and offsets for normal (left) and loud speech (right). Zero denotes the acoustically defined onset of the consonant and 1 the offset with number of measured items.

speaker AW is longer than for /l/, which corresponds to a longer positive onset latency for /t/ than for /l/ and therefore to a later jaw target achievement for /t/ than for /l/. In contrast, in only one case, /s/ of speaker UR, no lower white bar but a gray bar is shown, which indicates a negative onset latency and that the jaw achieves its target earlier than the tongue tip. Accordingly, the height of the upper white bar gives the normalized latency of the onset of the opening movement (Lat_{off}), i.e., the interval during which the jaw has already started the opening movement and the tongue tip still maintains the target position, indicating a negative offset latency (see, e.g., /s/ for all speakers). If no upper white bar is shown and the gray bar is overlapping the upper edge of the white bar, as, e.g., for /t/ of speaker RS, then the tongue tip starts the opening movement before the jaw, corresponding to a positive offset latency.

The results of ANOVAS for individual speakers are given in Table II, with manner and VE (vocal effort) as independent variables and the normalized latency between tongue tip and jaw movement at the target onset (Lat_{on}) and at the target offset (Lat_{off}) as dependent variables. Positive values indicate that the jaw moves later and negative values that it moves earlier than the intrinsic tongue tip. Furthermore, the differences between the acoustic onset and offset of the consonants and the jaw target onset and offset ($AcJaw_{on}$ and $AcJaw_{off}$) were also analyzed in order to check whether the specified events of jaw movements are coordinated with acoustically defined landmarks such as the on-and offset of nasality or the burst noise.

Generally, on- and offsets of the intrinsic tongue tip tend to vary with the acoustically defined on-and offsets, shown in Fig. 3 as the close proximity of the upper and lower edges of the white bars with the horizontal line at 0 indicating the acoustical onset and the line at 1 indicating the acoustical offset, respectively. There are also some less well-aligned examples: For the postalveolar sibilant the intrinsic tongue tip hold interval was longer than the acoustically defined consonant (shown by the longer white bars overlapping over the two long horizontal lines at 0 and 1 in Fig. 3, especially clear for speakers RS and SR), which can be attributed to the fact that the tongue tip sensor is probably placed in front of the relevant articulator for the postalveolar and therefore does not capture all parts of the relevant movement for the constriction. Only speaker KH, whose articulation of /ʃ/ was much more fronted, had a shorter plateau for the postalveolar fricative compared to the acoustic duration. The intrinsic tongue tip plateau also frequently exceeded the acoustically defined consonant offset for the voiced stop (see especially speakers RS and SR). This can be attributed to the difficulties in labeling the end of the plateau, since during /d/ most speakers showed a high amount of lingual forward and downward movement, probably due to its more apical articulation as reported in the Introduction.

The consonantal target was generally reached first with the tongue tip and then with the jaw, indicated by the lower white boxes in Fig. 3. This short time lag might be attributable to specific kinematic properties of the involved articulators, such as generally slower jaw movements as mentioned above in the Introduction. Only for the alveolar fricative of speaker UR did the jaw reach the target before the tongue tip.

Manner of articulation had significant effects on the timing between the tongue tip and the jaw for several articulatory events. For the stops the onset latency (Lat_{on}) was longer as compared to the other consonants, which implies a longer jaw delay as shown by the longer lower white bars in Fig. 3. This was significant for four speakers and for the tests pooled over all speakers. Furthermore, the onset of the jaw opening movement was consistently somewhat later than or happened at the same time as the onset of the tongue tip opening movement (no upper white bars) for the voiceless stop, whereas the jaw started its opening movement only rarely before the tongue tip for the other consonants (upper white bars). Relative to the acoustic onset of the consonant the jaw reached its target latest for both stops, as shown for the variable $AcJaw_{on}$ (only /d/ for speaker KH) and started its opening movement latest ($AcJaw_{off}$). Therefore, the gray boxes in Fig. 3 are shifted towards the upper end of the white boxes for the stops. For the other consonants the jaw target interval tends to be centered in the middle of the tongue tip target interval with positive onset latencies, i.e., the jaw reaches its maximum later than tongue tip, and negative offset latencies, i.e., the jaw starts its downward movement before the tongue tip.

Comparing the two sibilants /s/ and /ʃ/, the jaw target

TABLE II. Manner (MN) and vocal effort (VE) effects on onset and offset latencies between the tongue tip and the jaw (Lat_{on} and Lat_{off}) as well as between the acoustically defined onset and the jaw target achievement ($AcJaw_{on}$) and the acoustically defined offset and the jaw target offset ($AcJaw_{off}$). Statistics are based on two-way ANOVAs for individual speakers. Results of pairwise *t*-tests with Bonferroni adjustments are also given with > indicating a later jaw timing.

Speaker	Effect	Df	Lat_{on}	Lat_{off}	$AcJaw_{on}$	$AcJaw_{off}$
AW	MN	5	32.41***	31.38***	44.48***	54.29***
	VE	1	2.50	0.90	0.41	7.85**
	MN:VE	5	1.61	1.05	0.68	0.17
		125	td > ʃn > sl	td > ns ʃl	td > ʃn > sl	d > t > s ʃ n > l
KH	MN	5	2.27	7.56***	4.33**	10.71***
	VE	1	4.26*	5.55*	1.82	11.10**
	MN:VE	5	0.14	1.07	0.43	2.07
		129	L > N	t ʃ l > snd L > N	d > snl	d > snl, t > l L > N
RS	MN	5	17.83***	22.61***	24.05***	44.19***
	VE	1	0.15	1.73	1.17	0.03
	MN:VE	5	2.39*	0.91	1.24	2.98*
		114	N: t > ns ʃ l L: t > nl, d > n	t > nlts > ʃ	t > dsn ʃ l, d > l	N: t > dsn ʃ l, d > l L: td > sn ʃ l
SR	MN	5	27.00***	27.54***	29.08***	50.43***
	VE	1	0.20	0.65	0.01	1.15
	MN:VE	5	0.69	1.62	0.66	1.20
		105	d > t ʃ > sln	td > s, tdnls > ʃ	d > tn ʃ ls, t > ls	d > tnl ʃ s, t > ʃ s
UR	MN	5	21.94***	16.08***	14.30***	21.15***
	VE	1	32.20***	0.87	27.88***	0.16
	MN:VE	5	1.59	5.69***	0.70	3.94**
		129	td > nls, ʃ > ns L > N	N: tsl > n, tl > ʃ L: ts > ʃ nl, d > ʃ	dt > l ʃ ns L > N	N: t > l ʃ n, ds > n L: dt > sn ʃ l, s > ʃ l

*$p < 0.05$.
**$p < 0.01$.
***$p < 0.001$.

achievement was significantly earlier for /s/ than for /ʃ/ for three speakers. The jaw also tended to start the opening movement earlier for /ʃ/ but this was significant only for two speakers.

Vocal effort affected the tongue-tip jaw coordination only inconsistently. As can be seen in Table II, only for speakers KH and UR did vocal effort increase have a significant main effect with a later jaw target achievement for both speakers and a later jaw target offset for speaker UR (see lower with boxes in Fig. 3). Latencies pooled over all speakers (Table III), however, did not show significantly different means for vocal effort increase. Interactions between the two factors manner and vocal effort were significant in some cases, e.g., for speaker RS the jaw started its downward movement early for /t/ and later for /ʃ/ when spoken loudly. However, no consistent pattern of vocal effort effects on the timing parameters during the consonant could be found.

Time points further away from the consonant target phases were also affected by manner and vocal effort variations as shown in Table IV. The velocity peak latency of the closing gesture ($LatV_{cl}$) indicated no significant manner-dependent variation when all speakers were pooled. For individual speakers the timing of the closing velocity peaks did vary with manner of articulation, but no consistent pattern could be found. Most consonants were produced with a slight jaw advancement, apart from speakers KH and UR for /l/ and speaker RS for /ʃ/, who showed a later closing velocity peak for the jaw. Vocal effort affected $LatV_{cl}$ of /s/ for

TABLE III. Manner (MN) and vocal effort (VE) effect on onset (left) and offset (right) latencies between the tongue tip and the jaw (Lat) and acoustically defined landmarks and the jaw (AcJaw). Statistics are based on repeated measures ANOVAs with Greenhouse-Geisser ε corrected degrees of freedom in brackets. Results of pairwise *t*-tests with Bonferroni adjustments are also given > indicating later jaw events.

		Onset			Offset		
		MN	VE	MN:VE	MN	VE	MN:VE
Lat	*F*(df)	6.65 (1.7, 6.9)* df > ls, d > n	2.74 (1, 4)	2.46 (1.8, 7.1)	3.90 (3.3, 13.0)* t > ʃ	0.27 (1, 4)	0.6 (2.3, 9.3)
AcJaw	*F*(df)	7.21 (1.9, 7.7)* d > n ʃ ls, t > ls	0.9 (1, 4)	1.66 (1.8, 7.2)	7.83 (2.3, 9.1)** td > sn ʃ l	10.01 (1, 4)*	1.54 (2.0, 8.1)

*$p < 0.05$.
**$p < 0.01$.
***$p < 0.001$.

TABLE IV. Manner (MN) and vocal effort (VE) effects on latencies of the closing (left: LatV_{cl}) and opening (right: LatV_{op}) velocity peaks. Statistics for individual speakers are based on two-way ANOVAS and the statistics pooled overall speakers are based on repeated measures ANOVAs with Greenhouse-Geisser ε corrected degrees of freedom in brackets. Results of pairwise *t*-tests with Bonferroni adjustments are also given with > indicating later jaw events.

		LatV_{cl}			LatV_{op}		
		MN	VE	MN:VE	MN	VE	MN:VE
AW	*F*(df)	2.24(5, 123)	0.07 (1, 123)	1.78 (5, 123)	44.3 (5, 121)*** d > tnl > s∫	4.56 (1, 121)*	1.62 (5, 121) t: N < L
KH	*F*(df)	10.6 (5, 127)*** ls > ∫, *l* > ndt	2.72 (1, 127)	2.74 (5, 127)* s: N > L	11.6 (5, 121)*** *l* > td, ln > ∫s	3.33 (1, 121)	1.19 (5, 121)
RS	*F*(df)	4.97 (5, 106)*** ∫ > sld	6.44 (1, 106)* N > L	1.83 (5, 106) s: N > L	47.0 (5, 112)*** tndls > ∫, dnt > s	5.56 (1,112)* N > L	5.82 (5, 112)*** t,d: N < L
SR	*F*(df)	46.42 (5, 105)*** ∫tndl > s, ∫ > *l*	6.60 (1, 105)*	0.63 (5, 105) n: N > L	29.7 (5, 102)*** lnd > st > ∫	0.87 (1, 102)	2.38 (5, 102)*
UR	*F*(df)	7.34 (5, 127)*** tsd∫n > *l*	1.42 (1, 127)	1.09 (5, 127) s:N > L	14.7 (5, 120)*** sldnt > ∫	8.71 (1, 120)** N > L	1.89 (5, 120) t: N < L
All	*F*(df)	0.85 (1.5, 5.8)	10.12 (1, 4)*	0.85 (2.2, 8.6)	8.2 (2.6, 10.4)** nldst > ∫	19.51 (1, 4)*	2.2 (1.6, 6.3) t: N < L

$^{*}p < 0.05$.
$^{**}p < 0.01$.
$^{***}p < 0.001$.

three speakers with an earlier jaw velocity peak in loud speech. The latency of the opening velocity peaks was negative and longer for /∫/ (for speakers AW and KH also for /s/) than for the other consonants, i.e., the jaw velocity peak occurred earlier than the intrinsic tongue tip velocity peak for the sibilants. Another tendency was that in loud speech the jaw velocity peak occurred later after the voiceless stop, which was significant for three speakers and when pooled over all speakers.

Summarizing the results for manner effects, it was found that two differential patterns emerge for the six analyzed coronal consonants: The first pattern looks more symmetrical, with a jaw target achievement occurring shortly after the tongue tip target achievement and the jaw target offset before the offset of the tongue tip. Therefore, the jaw hold interval is always shorter than the tongue interval and lies approximately in the middle of the tongue tip target interval. As can be seen in Fig. 3, for most speakers the sibilants and the sonorants are produced with this timing pattern. The second pattern is asymmetrical in the sense that the jaw target is achieved in the second half of the tongue tip target phase and the jaw also starts its opening movement later than the tongue tip. This pattern emerges for the two stops (see also Fig. 3).

For vocal effort, due to a high amount of speaker-dependent variability, only some tendencies could be observed: The consonants with the least spatial variability as well as the highest jaw position, i.e., /s, ∫, t/, showed very inconsistent differences in the onset and offset of the jaw target. Significant timing differences, reported in Table IV, were always in the direction to accommodate both requirements: a lower jaw for loudly produced vowels and a high jaw target for segmental needs. For example, for the alveolar fricative /s/ the latency of the velocity peaks of the closing movement slightly decreased (as shown in Table IV, column MN:VE for LatV_{cl} significant for speakers KH, RS, and UR), i.e., the jaw reached its peak velocity somewhat earlier than the tongue tip in normal condition (mean=−10 ms) and with a more pronounced advancement in loud speech (mean=−18 ms). This seems to be a possible strategy in order to anticipate an early onset of the jaw target, whereas for /∫/ and /t/ the jaw target onset did not matter as much. For the voiceless stop a high jaw position has to be maintained until the burst. Because of the required lower jaw position for the following vowel in loud speech the necessary jaw displacement increases, which in the case of /t/ also leads to a later jaw opening velocity peak (mean for all speakers for the normal condition: −9 ms vs loud: 6 ms). As shown in Table IV, this is significant for speakers AW, RS, and UR as well as the pooled speakers.

C. Spatial and temporal variability

In order to assess the interarticulator cohesion, the standard deviations of temporal parameters were compared for the analyzed consonants assuming that temporally more precisely articulated consonants exhibit a stronger interarticulator cohesion. Standard deviations of intrinsic tongue tip and jaw positions during the consonant were also analyzed in order to compare the relevance of the two articulators for the coronal consonants. Results of repeated-measures ANOVAs and pairwise *t*-tests are given in Table V. Concerning the spatial variability, the jaw positions clearly varied less during the voiceless obstruents /s, ∫, t/. A generally higher variability for loud speech was observed for the jaw positions, which is contrary to the results of Dromey and Ramig (1998). The accuracy of intrinsic tongue tip position during the consonant varied neither with manner of articulation nor with vocal effort.

For the offset latencies Lat_{off} and $AcJAw_{off}$, significantly smaller variances were obtained for the sibilants as compared to the lateral and the voiced stop. The velocity peak latency of the closing movement was significantly more variable for /∫/ as compared to the other consonants.

TABLE V. Manner (MN) and vocal effort (VE) effects on standard deviations of positions (upper part) and onset offset latencies between the tongue tip and the jaw (Lat), the acoustically defined landmarks and the jaw (AcJaw) and the peak velocities (Lat*V*). Statistics are based on reported measure ANOVAs with Greenhouse-Geisser ε corrected degrees of freedom in brackets. Results of pairwise *t*-tests with Bonferroni adjustments are also given with > indicating more variability.

		Jaw			Intrinsic-tongue-tip		
		MN	VE	MN:VE	MN	VE	MN:VE
Pos	F (df)	7.16 (2.2, 8.9)* ln > tsʃ	8.93 (1, 4)* L > N	2.59 (2.1, 8.3)	1.11 (2.4, 9.5)	1.1 (1, 4)	0.88 (1.8, 7.2)
		Onset			Offset		
		MN	VE	MN:VE	MN	VE	MN:VE
Lat	F (df)	1.42 (1.5, 6.1)	0.01 (1, 4)	0.96 (1.9, 7.7)	4.8 (2.1, 8.5)* ld > ʃs	0.05 (1, 4)	0.37 (1.8, 7.4)
AcJaw	F (df)	1.56 (1.6, 6.2)	0.44 (1, 4)	1.26 (2.0, 8.1)	12.0 (2.4, 9.6)** dlt > sʃ, n > ʃ	0.18 (1, 4)	0.23 (1.6, 6.6)
LatV	F (df)	10.3 (1.6, 6.5)* ʃ > sntd	1.61 (1, 4)	1.04 (1.9, 7.5)	1.0 (2.9, 11.5)	1.29 (1, 4)	1.03 (2.2, 8.8)

*$p < 0.05$.
**$p < 0.01$.
***$p < 0.001$.

In conclusion, during the consonants significantly less spatial and temporal variability was found for the sibilants, whereas for the voiceless stop only the spatial jaw positioning was more precise than for /n, l/ but not the timing.

IV. SUMMARY AND DISCUSSION

This study investigated the timing between the tongue tip and the jaw of the German coronal consonants /s, ʃ, t, d, n, l/ in a low vowel context. We hypothesized that the contribution of the jaw differs for various manners of articulation, and that this is reflected in the strength of cohesion between the tongue tip and the jaw. The strength of the cohesion was investigated by analyzing the variability of temporal and spatial parameters. Vocal effort changes were introduced as a control condition. The assumption was that consonants with a tight temporal and spatial coupling between the tongue tip and the jaw should not change due to vocal effort variation. We obtained the following results:

(1) With respect to tongue-jaw coordination, two different patterns emerged: a symmetrical one with later jaw target onsets and earlier offsets within the tongue target phase, and an asymmetrical pattern with a late jaw target onset and an offset which occurs approximately simultaneously with the tongue tip target offset. The sibilants /s, ʃ/ were produced predominantly with a symmetrical pattern and the voiceless plosive with an asymmetrical one. For the remaining coronal consonants /d, l, n/ a preference for a symmetrical pattern could be observed but with a high amount of speaker-dependent variability.
(2) Increasing vocal effort had very little consistent effects on the analyzed timing parameters during the consonants. However, the timing of velocity peaks was affected for two consonants: the jaw-closing velocity peak was advanced for /s/ in loud speech and the jaw-opening velocity peak was delayed for /t/ in loud speech.
(3) Sibilants were produced with the least amount of spatial and temporal variability. The voiceless stop showed reduced variability only in the spatial domain. The remaining consonants /d, n, l/ were generally more available and the sonorants also more frequently affected by the vocal effort condition.

These results will be discussed in terms of lingual-mandibular coordination for producing different manners of articulation, and implications for speech motor control.

A. The role of the coordination between the tongue tip and the jaw

The most striking result of this study is the very consistent difference in lingual-mandibular timing between the voiceless stop on the one hand and the sibilants on the other hand. For the remaining consonants, which were also produced with a lower and more variable jaw position, speakers varied in their preferred timing pattern. This confirms the results from previous studies that the jaw does not contribute uniformly to the achievement of consonantal coronal constrictions. In this section various explanations for the emergence of these two timing patterns will be discussed.

As was suggested in the Introduction, a late jaw target for the voiceless stop is produced in order to achieve a salient burst. In Mooshammer *et al.* (2003) we argued that the explosion noise might be enhanced by an obstacle noise source, namely the lower teeth. Among stops it is only the alveolar in which the lower teeth are immediately downstream of the place of articulation, and indeed current evidence suggests that bilabial or velar stops are generally produced with lower and more variable jaw positions (see, e.g., Lee, 1996; Hoole and Kühnert, 1996). This assumption is

supported by the high and almost invariant jaw position which was found in most studies for /t/. Furthermore, a late jaw target, starting the opening movement somewhat later than the tongue tip, was not obligatory for the voiced stops, which were fully voiced for all speakers in the current study. As can be seen in Fig. 3, only speaker SR exhibits an asymmetrical timing pattern with a late jaw target in this case. Finally, in Geumann (2001a) it was found that for three speakers the jaw was significantly lower during the voiced stop compared to the voiceless, which can be attributed to an accommodation to the jaw targets of the neighboring vowels (see also the higher contextual variability for /d/ as found in Geumann, 2001a). This option does not exist for the voiceless stop since a prominent burst is required. It is an interesting hypothesis that the well-known fact that the voiced stop is produced with a weaker and less audible burst (Ladefoged and Maddieson, 1996) might be partly attributable to the lower jaw position and the earlier jaw opening movement onset.

An alternative or additional factor might be that the asymmetrical pattern of the tongue-jaw coordination is a consequence of the target planning: Fuchs *et al.* (2001, in press) and Löfqvist and Gracco (2002) hypothesized that for stops the articulator aims at reaching a target planned above the constriction location (palate or upper lip) for ensuring a rapid pressure buildup. Furthermore, a target above the palate also has the advantage that no precise positioning of the tongue or lower lip is required for the stop as opposed to fricatives, for example. Hence, when the tongue tip crashes into the palate before reaching its target, the jaw might still continue to move upwards to achieve its planned goal. Evidence for these considerations can be found by the late jaw target achievement compared to the fricatives and the sonorants, but palate impact alone cannot explain why the jaw opening movement is timed with the burst and why a high and less variable jaw position seems to be an obligatory characteristic of the voiceless alveolar stop.

B. Implications for speech motor control

Generally, our results confirm that coordinative structures orchestrate individual articulators in a task-specific and flexible manner in order to reduce the degrees of freedom. On the one hand the same executing organs, tongue tip and jaw, can act together and—by combining a variety of spatial and temporal patterns—create distinctive sounds. The tongue tip and jaw are temporally highly fine-tuned but not necessarily moving in synchrony, as was shown here for the voiceless stop. Therefore, the analyzed articulators can move quite independently of each other and recombine in a flexible manner. On the other hand the temporal patterns during the consonantal target regions were quite stable across two vocal effort conditions, which speaks for a high degree of cohesion for producing coronal consonants.

It was proposed by Gracco (1988) and Hertrich and Ackermann (2000) that opening movements are produced with a lesser degree of cohesion than closing movements (see the Introduction). In contrast, we found that the onset of the opening movement and the relative timing of the contributing articulators at this time point might even be crucial for distinguishing different sounds. Even though the analyzed consonants are not solely distinguished on the basis of the two observed movement patterns, symmetrical and asymmetrical, the latter pattern seems to aim at the production of a prominent burst and therefore provides important cues for the contrast between the voiced and the voiceless stops (by additionally raising the jaw less for the former) and the contrast between different places of articulation. Besides implications for the kind of control underlying the observed kinematics, this result also supports the assumption that intergestural cohesion is stronger within segments than in between (see, e.g., Saltzman *et al.*, 1998), and that—as suggested by the perturbation experiment of Gomi *et al.* (2002)—the cohesion is stronger during the achievement of the goal than further away. In the current study consistent temporal adjustments due to changes in the condition, namely vocal effort, were mainly found at the peak velocities, i.e., during the transition between successive targets (see also delayed jaw peak velocity after /t/ in loud speech). The timing of the consonantal target onsets and offsets, however, was not consistently affected by vocal effort changes.

As was already discussed, the jaw's task varies significantly for the analyzed consonants. Even though many studies emphasize that the jaw is more sluggish due its heaviness than other articulators, the speaker seems nevertheless capable of controlling jaw positions and its movement course in a very exact way. As was found by Lindblom and Lubker (1985), subjects can judge the amount of jaw movement more accurately than their tongue movements. The authors argue that—besides the perceptual distinctiveness—the higher awareness of the speaker for jaw positioning might play an important role for the tendency to favor contrasts along the dimension of opening for the composition of vowel systems. Our study suggests that the speaker's higher awareness of jaw positions is probably exploited for the distinction of consonants to a greater degree than assumed in earlier studies.

ACKNOWLEDGMENTS

This work was partially supported by the German Research Council (DFG) Ti69/31 and GWZ 4/8-1, P.1. We also thank Jonathan Harrington, Barbara Kühnert, Christian Geng, and Susanne Fuchs for very valuable comments on earlier drafts of this paper. Peter Dalgaard and Ernst Dombrowski gave invaluable advice regarding statistics and solutions in R. Furthermore, this work was inspired and initiated by very fruitful discussions of the first author with Peter Alfonso and Pascal van Lieshout during her postdoc term in Knoxville, 2001, supported by a DAAD grant. We also want to express our gratitude to the two anonymous reviewers and the editor, Anders Löfqvist, for their insightful comments and suggestions.

[1]For reasons of consistency the intrinsic tongue tip signal was used for labeling for all consonants, even though there is some variation in place of articulation: the sibilant /ʃ/ is usually more retracted than the alveolar consonants.

Dart, S. (1991). "Articulatory and acoustic properties of apical and laminal articulations," UCLA Working Papers in Phonetics **79**, 1–155.
De Nil, L., and Abbs, J. (**1991**). "Influence of speaking rate on the upper lip, lower lip, and jaw peak velocity sequencing during bilabial closing movements," J. Acoust. Soc. Am. **89**, 845–849.
Dromey, C., and Ramig, L. O. (**1998**). "Intentional changes in sound pressure level and rate: Their impact on measures of respiration, phonation, and articulation," J. Speech Lang. Hear. Res. **41**, 1003–1018.
Edwards, J. (**1985**). "Contextual effects on lingual-mandibular coordination," J. Acoust. Soc. Am. **78**, 944–948.
Fowler, C., Rubin, P., Remez, R., and Turvey, M. T. (**1980**). "Implications for speech production of a general theory of action," in *Language Production, Volume 1: Speech and Talk*, edited by B. Butterworth (Academic, London), pp. 373–420.
Fuchs, S., Perrier, P., and Mooshammer, C. (**2001**). "The role of the palate in tongue kinematics: An experimental assessment in VC sequences from EPG and EMMA data," Proceedings Eurospeech, Aalborg, Denmark **3**, pp. 1487–1490.
Fuchs, S., Perrier, P., Geng, C., and Mooshammer, C. (**2006**). "What role does the palate play in speech motor control? Insights from tongue kinematics for German alveolar obstruents," in *Towards a Better Understanding of Speech Production Processes*, edited by J. Harrington and M. Tabain (Psychology Press, New York), pp. 149–164
Geumann, A. (**2001a**). "Invariance and variability in articulation and acoustics of natural perturbed speech," *Forschungsberichte des Instituts für Phonetik und Sprachliche Kommunikation der Universität München*, **38**, pp. 265–393.
Geumann, A. (**2001b**). "Vocal intensity: Acoustic and articulatory correlates," in *Proceedings of the 4th International Speech Motor Conference*, edited by B. Maassen, W. Hulstijn, R. Kent, H. Peters, and P. van Lieshout (Uitgeverij Vantilt, Nijmegen), pp. 70–73.
Geumann, A., Kroos, C., and Tillmann, H. G. (**1999**). "Are there compensatory effects in natural speech?" Proceedings of the 14th International Congress Phonetic Sciences, San Francisco, **1**, pp. 399–402.
Gomi, H., Honda, M., Ito, T., and Murano, E. (**2002**). "Compensatory articulation during bilabial fricative production by regulating muscle stiffness," J. Phonetics **30**, 261–279.
Gracco, V. (**1988**). "Timing factors in the coordination of speech movements," J. Neurosci. **8**, 4628–4639.
Gracco, V., and Abbs, J. (**1986**). "Variant and invariant characteristics of speech movements," Exp. Brain Res. **65**, 156–166.
Gracco, V., and Löfqvist, A. (**1994**). "Speech motor coordination and control: Evidence from lip, jaw, and laryngeal movements," J. Neurosci. **14**, 6585–6587.
Guenther, F., Hampson, M., and Johnson, D. (**1998**). "A theoretical investigation of reference frames for the planning of speech movements," Psychol. Rev. **105**, 611–633.
Guenther, F. H., Espy-Wilson, C. Y., Boyce, S. E., Matthies, M. L., Zandipour, M., and Perkell, J. S. (**1999**). "Articulatory tradeoffs reduce acoustic variability during American English /r/ production," J. Acoust. Soc. Am. **107**, 2854–2865.
Hertrich, I., and Ackermann, H. (**2000**). "Lip-jaw and tongue-jaw coordination during rate-controlled syllable repetitions," J. Acoust. Soc. Am. **107**, 2236–2247.
Hoole, P., and Kühnert, B. (**1996**). "Tongue-jaw coordination in German vowel production," in Proceedings of the 4th Speech Production Seminar, Autrans, France, pp. 97–100.
Hoole, P., and Nguyen, N. (**1999**). "Electromagnetic articulography in coarticulation research," in *Coarticulation: Theory, Data and Techniques*, edited by W. H. Hardcastle and N. Hewlett (University Press, Cambridge), pp. 260–269.
Hoole, P., Wismüller, A., Leinsinger, G., Kroos, C., Geumann, A., and Inoue, M. (**2000**). "Analysis of tongue configuration in multi-speaker, multivolume MRI data," in *Proceedings of the 5th Seminar on Speech Production: Models and Data*, Seeon, Germany, pp. 157–160.
Howe, M., and McGowan, R. (**2005**). "Aeroacoustics of [s]," Proc. R. Soc. London, Ser. A **461**, 1005–1028.
Keating, P., Lindblom, B., Lubker, J., and Kreiman, J. (**1994**). "Variability in jaw height for segments in English and Swedish VCVs," J. Phonetics **22**, 407–422.
Kelso, J., Saltzman, E., and Tuller, B. (**1986**). "The dynamical perspective on speech production: Data and theory," J. Phonetics **14**, 29–59.
Kollia, B., Gracco, V., and Harris, K. (**1995**). "Articulatory organization of mandibular, labial, and velar movements during speech," J. Acoust. Soc. Am. **98**, 1313–1324.
Kroos, C., Hoole, P., Kühnert, B., and Tillmann, H. (**1997**). "Phonetic evidence for the phonological status of the tense-lax distinction in German," *Forschungsberichte des Instituts für Phonetik und Sprachliche Kommunikation der Universität München* **35**, 17–25.
Kühnert, B., Ledl, C., Hoole, P., and Tillmann, H. (1991). "Tongue-jaw interactions in lingual consonants," PERILUS **14**, 21–25.
Ladefoged, P., and Maddieson, I. (**1996**).*The Sounds of the World's Languages* (Blackwell, Oxford).
Lee, S. (**1996**). "Orals, gutturals, and the jaw," in *Phonology and Phonetic Evidence: Papers in Laboratory Phonology IV*, edited by B. Cornell and A. Arvaniti (Cambridge University Press, Cambridge), pp. 235–241.
Lee, S., Beckman, M., and Jackson, M. (**1994**). "Jaw targets for strident fricatives," in *Proceedings of the International Conference on Spoken Language Processing*, Yokohama, pp. 37–40.
Lindblad, P., and Lundqvist, S. (**1999**). "How and why do the tongue gestures of [t], [d], [l], [n], [s], and [r] differ?," *Proceedings of the 14th International Congress of Phonetic Sciences*, pp. 417–420.
Lindblom, B., and Lubker, J. (**1985**). "The speech Humunculus and a problem of phonetic linguistics," in *Phonetic Linguistics, Essays in Honor of Peter Ladefoged*, edited by V. Fromkin (Academic, Orlando), pp. 169–192.
Löfqvist, A., and Gracco, V. (**2002**). "Control of oral closure in lingual stop consonant production," J. Acoust. Soc. Am. **111**, 2811–2827.
Max, L., and Onghena, P. (**1999**). "Some issues in the statistical analysis of completely randomized and repeated measures designs for speech language and hearing research," J. Speech Lang. Hear. Res. **42**, 261–270.
Mooshammer, C., Geumann, A., Hoole, P., Alfonso, P., van Lieshout, P., and Fuchs, S. (**2003**). "Coordination of lingual and mandibular gestures for different manners of articulation," in *Proceedings of the 15th International Congress Phonetic Sciences*, pp. 81–84.
Nittrouer, S. (**1991**). "Phase relations of jaw and tongue tip movements in the production of VCV utterances," J. Acoust. Soc. Am. **90**, 1806–1815.
Nittrouer, S., Munhall, K., Kelso, J., and Tuller, B. (**1988**). "Patterns of interarticulator phasing and their relation to linguistic structure," J. Acoust. Soc. Am. **84**, 1653–1661.
R Development Core Team (2005). "R: A language and environment for statistical computing. R Foundation for Statistical Computing," Vienna, Austria; URL: ⟨http://www.R-project.org.⟩
Saltzman, E., and Munhall, K. (**1989**). "A dynamical approach to gestural patterning in speech production," Ecological Psychol. 1, 333–382.
Saltzman, E., Löfqvist, A., and Mitra, S. (**2000**). "'Glue' and 'clocks:' Intergestural cohesion and global timing," in *Papers in Laboratory Phonology V: Acquisition and the Lexicon*, edited by M. B. Broe and J. B. Pierrehumbert (Cambridge University Press, Cambridge), pp. 88–101.
Saltzman, E., Löfqvist, A., Kay, B., Kinsella-Shaw, J., and Rubin, P. (**1998**). "Dynamics of intergestural timing: A perturbation study of lip-larynx coordination," Exp. Brain Res. **123**, 412–424.
Schulman, R. (**1989**). "Articulatory dynamics of loud and normal speech," J. Acoust. Soc. Am. **85**, 295–312.
Shadle, C. (**1990**). "Articulatory-acoustic relationships in fricative consonants," in *Speech Production and Speech Modelling*, edited by W. Hardcastle and A. Marchal (Kluwer, Dordrecht), pp. 187–209.
Shaiman, S., Adams, S., and Kimelman, M. (**1995**). "Timing relationships of the upper lip and jaw across changes in speaking rate," J. Phonetics **23**, 119–128.
Tasko, S., and Westbury, J. (**2002**). "Defining and measuring speech movement events," J. Speech Lang. Hear. Res. **45**, 127–142.
van Lieshout, P. (**1995**). *Motor Planning and Articulation in Fluent Speech of Stutterers and Nonstutterers* (NICI, Nijmegen).
Westbury, J., Lindstrom, M., and McClean, M. (**2002**). "Tongue and lips without jaws: A comparison of methods for decoupling speech movements," J. Speech Lang. Hear. Res. **45**, 651–662.

Lexical frequency and voice assimilation

Mirjam Ernestus,[a] Mybeth Lahey, and Femke Verhees
Max Planck Institute for Psycholinguistics & Radboud University Nijmegen, Wundtlaan 1, 6525 XD Nijmegen, The Netherlands

R. Harald Baayen
Radboud University Nijmegen & Max Planck Institute for Psycholinguistics, Wundtlaan 1, 6525 XD Nijmegen, The Netherlands

(Received 14 July 2005; revised 11 February 2006; accepted 12 May 2006)

Acoustic duration and degree of vowel reduction are known to correlate with a word's frequency of occurrence. The present study broadens the research on the role of frequency in speech production to voice assimilation. The test case was regressive voice assimilation in Dutch. Clusters from a corpus of read speech were more often perceived as unassimilated in lower-frequency words and as either completely voiced (regressive assimilation) or, unexpectedly, as completely voiceless (progressive assimilation) in higher-frequency words. Frequency did not predict the voice classifications over and above important acoustic cues to voicing, suggesting that the frequency effects on the classifications were carried exclusively by the acoustic signal. The duration of the cluster and the period of glottal vibration during the cluster decreased while the duration of the release noises increased with frequency. This indicates that speakers reduce articulatory effort for higher-frequency words, with some acoustic cues signaling more voicing and others less voicing. A higher frequency leads not only to acoustic reduction but also to more assimilation. © *2006 Acoustical Society of America.* [DOI: 10.1121/1.2211548]

PACS number(s): 43.70.Fq, 43.70.Bk, 43.71.An [AL] Pages: 1040–1051

I. INTRODUCTION

In everyday speech, words are often acoustically reduced compared to their citation form. In a study of conversational American English, Johnson (2004) found that at least one segment was missing in 25% of the words, while a complete syllable was absent in no less than 6% of the words. Similarly, Ernestus (2000) showed that words and fixed expressions may loose all their unstressed syllables in conversational Dutch. Thus, *eigenlijk* [ˈɛixələk] "actually" may be realized as [ˈɛik] and *in ieder geval* [ɪn ˈidər xəˈvɑl] "in any case" as [ˈivɑl].

Several studies have shown that segments are more likely to be shorter or absent in words with a high frequency of occurrence (see, e.g., Zipf, 1935; Fidelholz, 1975; Bybee, 2001). Thus, Jurafsky *et al.* (2001), studying a large corpus of English telephone conversations, reported that word final /t/s and /d/s tend to be shorter and have a greater probability to be completely absent in words of a higher frequency of occurrence. On the basis of the same corpus, Bell *et al.* (2003) showed that a higher frequency of occurrence also correlates with shorter acoustic durations for function words. Similar results have been obtained for spontaneous Dutch: Pluymaekers, Ernestus, and Baayen (2005) found that Dutch affixes tend to be shorter and their segments to be more often absent in words of a higher frequency.

The present study broadens the scope of quantitative research on the role of lexical frequency in speech production by investigating the correlation between frequency and degree of assimilation. The test case is regressive voice assimilation (RVA) in Dutch affecting obstruent clusters spanning morpheme boundaries.

In Dutch, all syllable-final obstruents are voiceless (final devoicing). Before the voiced plosives /b/ and /d/, however, they may be realized as voiced, a phenomenon referred to as regressive voice assimilation (e.g., Booij, 1995; Wetzels and Mascaró, 2001). Thus, the compound *wetboek* "law book," consisting of the parts *wet* [ʋɛt] "law" and *boek* [buk] "book," is generally pronounced as [ʋɛdbuk], and *twaalfduizend* "twelve thousand," consisting of *twaalf* [tʋɑlf] "twelve" and *duizend* [duyzənt] "thousand," as [tʋɑlvduyzənt]. RVA is described in the literature as obligatory within derived words and more frequent in compounds than across words (Loots, 1983; Booij, 1995). Furthermore, RVA is less frequent in obstruent clusters preceded by another voiceless obstruent (Demeulemeester, 1962), in women's speech (Kaiser, 1958; Slis, 1982, 1986), and at lower speech rates (Kaiser, 1958; Slis, 1982; Menert, 1994).

The voicing of obstruents in clusters as perceived by the listener is cued by several characteristics of the acoustic signal. Van den Berg (1986) showed that the most important cue for Dutch clusters is the presence of glottal vibration. The first obstruent of a cluster is perceived as voiced if glottal vibration is present during its final part, or during the initial part of the second obstruent. This second obstruent is perceived as voiced if glottal vibration is present during its final part. Other cues to the perception of voicing are the duration of the obstruents and the duration of the preceding vowel (van den Berg, 1987). Longer cluster-final obstruents tend to be perceived as voiceless. Longer preceding vowels favor the perception of the initial obstruents as voiced. The voicing of

[a]Electronic mail: mirjam.ernestus@mpi.nl

 0001-4966/2006/120(2)/1040/12/$22.50

single obstruents is cued by additional characteristics of the acoustic signal (for an overview, see van Alphen and Smits, 2004), including the duration of the plosive's release noise (the burst and the following period of aspiration), which tends to be shorter for voiced than for voiceless plosives (e.g., Slis and Cohen, 1969). The relevance of most of these additional subtle cues has not been investigated for obstruents in clusters.

Several competing hypotheses may be formulated concerning the correlation between frequency and degree of RVA. Two hypotheses depart from the idea that highly frequent morphologically complex words which are losing their internal morphological structure become more similar to monomorphemic words (cf. Ernestus, 2000: 34; see also Booij, 1995). This change might affect RVA in two ways. First, since RVA is more frequent across weaker (prosodic) boundaries (Booij, 1995), it might also be more frequent and stronger in high-frequency complex words in which boundaries are weakened. This would lead to higher percentages of completely voiced obstruent clusters and to more voiced clusters. Second, since completely voiceless clusters are typical for Dutch monomorphemic words (Zonneveld, 1983), one might also predict that RVA should occur less often or be weaker in high frequency complex words: A cluster with only one voiced obstruent would be closer to the ideal for monomorphemic words than a completely voiced cluster. The assumption underlying both lines of reasoning is that frequency of occurrence affects all acoustic cues for voicing in such a way that they all signal more voicing (first hypothesis) or less voicing (second hypothesis) in high frequency words. We will therefore refer to these hypotheses as Phonemic hypotheses.

Alternatively, we can formulate a hypothesis, which we will call the Subphonemic hypothesis, based on the observation that speakers tend to realize words of a higher frequency with less articulatory effort. Reduction in articulatory effort may affect a wide range of acoustic characteristics signaling voicing. Some of these characteristics may signal more voicing and others less voicing in words realized with less articulatory effort. For the listener, the net result of a higher frequency therefore will depend on the precise details of how articulatory reduction affects the different acoustic characteristics of the signal and on the extent to which these characteristics cue perceived voicing.

We pitted these hypotheses against each other by means of the subcorpus Library for the blind, part of the recently developed Spoken Dutch Corpus (Oostdijk, 2000; Oostdijk *et al.*, 2002). This subcorpus consists of parts of stories read aloud for the blind. It contains over 900 000 words, recorded with hardly any background noise, and it is therefore ideal for acoustic measurements. There are both male and female speakers, of very different ages (born between 1917 and 1974), and originating from all parts of the Netherlands. All recordings are transcribed orthographically.

We first classified obstruents in clusters from this subcorpus as voiced, voiceless, or absent. We investigated the predictive value of lexical frequency for these classifications (Sec. II). Whereas the Phonemic hypotheses predict a correlation between the classifications and frequency, this correlation is not compelling for the Subphonemic hypothesis as the effects of frequency on the different characteristics of the acoustic signal may cancel each other out for perceived voicing. We then proceeded with detailed analyses of four important cues to voicing (Sec. III). In contrast to the Subphonemic hypothesis, the Phonemic hypotheses predict that these cues all signal either more voicing or less voicing at higher frequencies. Finally, by combining the voice classifications from Sec. II and the acoustic measurements from Sec. III, we tested whether frequency has a predictive role for the classifications in addition to the acoustic measurements (Sec. IV).

II. PHONETIC TRANSCRIPTIONS

A. Method

We studied obstruent clusters resulting from the concatenation of morphemes (e.g., the compound *voetbal* "football" resulting from the concatenation of *voet* and *bal*). The first obstruent in these clusters is realized as voiceless in word final position. We restricted ourselves to bilabial (/p/), labiodental (/f/), and alveolar (/s/, /t/) obstruents as cluster-initial obstruents. The second obstruent in the cluster was either /b/ or /d/, which may induce RVA of the preceding obstruent. We excluded clusters of only alveolar or only bilabial plosives, since they tend to be realized as single plosives (e.g., Booij, 1995). Furthermore, we only studied obstruent clusters preceded by a sonorant (consonant or vowel), as especially these clusters show RVA (Demeulemeester, 1962). The speakers were educated in the Western and Southern parts of the Netherlands, but we also considered a small number of speakers born in the Western or Southern parts of the Netherlands but educated in other regions.

The resulting data set contained 908 word tokens, realized by 84 men and 79 women. The majority (107) of speakers were educated in the West, and a minority in the South (29) or in other regions (27). We decided not to include the speakers' regional background in the analyses, a decision that hardly affected the results of the statistical analyses reported in this paper, as was shown by explorative analyses. The data set contained 321 compound tokens, 138 prefixed word tokens, and 449 suffixed word tokens. Of the suffixed word tokens, 14 are prosodic compounds according to the phonological literature (e.g., Booij, 1995), as they end in suffixes with full vowels.

Three phoneticians, native speakers of Dutch, classified the obstruents in the clusters as voiced, voiceless, or absent. One phonetician came from the center of the Western part, henceforth the West, another from the West of the Southern part, henceforth the South-West, and the third phonetician came from the very South of the Southern part, henceforth the South, of the Netherlands.

Transcribers tend to base their classifications not only on the acoustic signal but also on their expectations (e.g., Vieregge, 1987). We attempted to minimize the role of the phoneticians' expectations based on their knowledge of words (and word frequencies) by presenting them only with a small part of each word, the part consisting of the obstruent cluster, the preceding vowel, and the following vowel. Some obstruent clusters were separated from their surrounding vow-

TABLE I. Absolute and relative numbers of obstruent clusters unanimously classified as completely voiced (+voice +voice), unassimilated (−voice +voice), completely voiceless (−voice −voice), as containing just the second obstruent (absent present), or other.

Categorization	Assimilation	*N*	Percentage
+voice +voice	Regressive	261	42.9%
−voice +voice	None	121	19.9%
−voice −voice	Progressive	151	24.8%
Absent present		57	9.4%
Other		19	3.1%

els by intervening sonorant consonants, and these consonants were then also included in the stretches of speech presented to the phoneticians. Thus, the phoneticians listened to *oetba* from *voetbal* "football" and to *endbla* from *ochtendblad* "morning paper."

B. Results

Table I shows the classifications of the 609 obstruent clusters on which the three phoneticians were in full agreement (67.1% of the classified clusters). In this table, the clusters are classified as completely voiced, as unassimilated (i.e., the initial obstruent as voiceless and the final obstruent as voiced), as completely voiceless, as realized without the initial obstruent, or as other (the final obstruent is absent or the initial obstruent is voiced while the final obstruent is voiceless).

As expected, the majority (43%) of clusters were classified as completely voiced, reflecting RVA. Unexpected is the high percentage (25%) of completely voiceless clusters, reflecting progressive voice assimilation. This type of assimilation was at least as frequent as no assimilation (20%).

The frequency measure that we considered for predicting the realization of the obstruent clusters is the frequency with which the two morphemes forming the obstruent cluster co-occur in derived words and compounds. Thus, the frequency for the realization of the *tb* cluster in the prefixed word *ont+bijt* "breakfast" was the frequency of *ontbijt* itself plus the frequency of *ontbijtje* "small breakfast," *ontbijten* "to have breakfast," *ontbijtservies* "breakfast set," etc. We determined these cumulative frequencies on the basis of the CELEX lexical database (Baayen, Piepenbrock, and Gulikers, 1995). The distribution of these frequencies was heavily skewed, and we therefore applied a logarithmic transformation (with base *e*). Henceforth, we will refer to these transformed cumulative frequencies simply as frequency. Furthermore, we will refer with Word to that part of the word token under consideration that consists of the two morphemes contributing to the obstruent cluster and on which the frequency count is based (e.g., *ontbijt* both for *ontbijt* itself and for *ontbijtservies*).

We analyzed all classifications contributed by each of the three phoneticians, irrespective of whether the phoneticians were in full agreement. We first investigated whether frequency predicts assimilation by comparing clusters realized without assimilation with completely voiced clusters on the one hand and with completely voiceless clusters on the other hand. In a next step, we studied the role of frequency in whether an assimilated cluster is completely voiced versus voiceless. Finally, we investigated whether frequency is a predictor for the absence of the initial obstruent.

The boxplots in Fig. 1 show the frequency distributions for these four types of classifications. The boxes show the interquartile ranges, the dots in the boxes denote the medians, and the "whiskers" extend to the observations within 1.5 times the interquartile range. Outliers beyond this range are represented by individual circles.

All statistical analyses in this study made use of stepwise multilevel models of covariance with speaker and Word as crossed grouping factors (Pinheiro and Bates, 2000; Baayen, Tweedie, and Schreuder, 2002; Baayen, 2004; Quené and van der Bergh, 2004; Bates and Sarkar, 2005). Such models obviate the necessity of separate Fl and F2 analyses. Note that the by-item covariate frequency is confounded with the random effect of Word. Hence, our multilevel models are conservative with respect to the contribution of this covariate.

For the analyses of the phonetic classifications, we used generalized linear mixed models with a binomial link function, using penalized quasilikelihood (e.g., Venables and Ripley, 2002). Such models predict the probability of a (binary) classification. We entered as predictors the speakers' Gender and Year of birth (minus 1900), the Type of the first obstruent in the cluster (fricative versus plosive), the Second obstruent (/b/ versus /d/), the Morphological class of the word (prefixed, suffixed, or compound), and Phonetician (three levels). We entered Frequency as the last predictor, again keeping the models as conservative as possible with respect to this covariate.

We first investigated the probability that a cluster was perceived as completely voiced versus unassimilated. A higher frequency increased the probability that the cluster was perceived as completely voiced ($\hat{\beta}=0.14$, with $\hat{\beta}$ denoting the estimated (unstandardized) regression coefficient, following the notation of, e.g., Chatterjee, Hadi, and Price, 2000, $F(1,1664)=4.23, p<0.05$), though the effect was small (see Fig. 1). Furthermore, men's clusters were more often classified as completely voiced (68.9% completely voiced classifications and 31.1% unassimilated classifications) than women's clusters [56.2% completely voiced classifications and 43.8% unassimilated classifications, $F(1,1664)=10.43$, $p=0.001$], and the phonetician from the West classified fewer clusters (57.9%) as completely voiced than the phoneticians from the South-West (68.2%) and the South (63.3%, $F(2,1664)=17.81$, $p<0.0001$), who did not differ from each other in their classifications ($p>0.05$).

In the second analysis, we investigated the likelihood that a cluster was realized as completely voiceless versus unassimilated. A higher frequency increased the probability that the cluster was perceived as completely voiceless [$\hat{\beta}=0.19$, $F(1,1252)=4.38$, $p<0.05$]. In addition, the phonetician from the West classified clusters as completely voiceless (50.0% completely voiceless classifications and 50% unassimilated classifications) more often than the phonetician from the South (48.8% completely voiceless classifications)

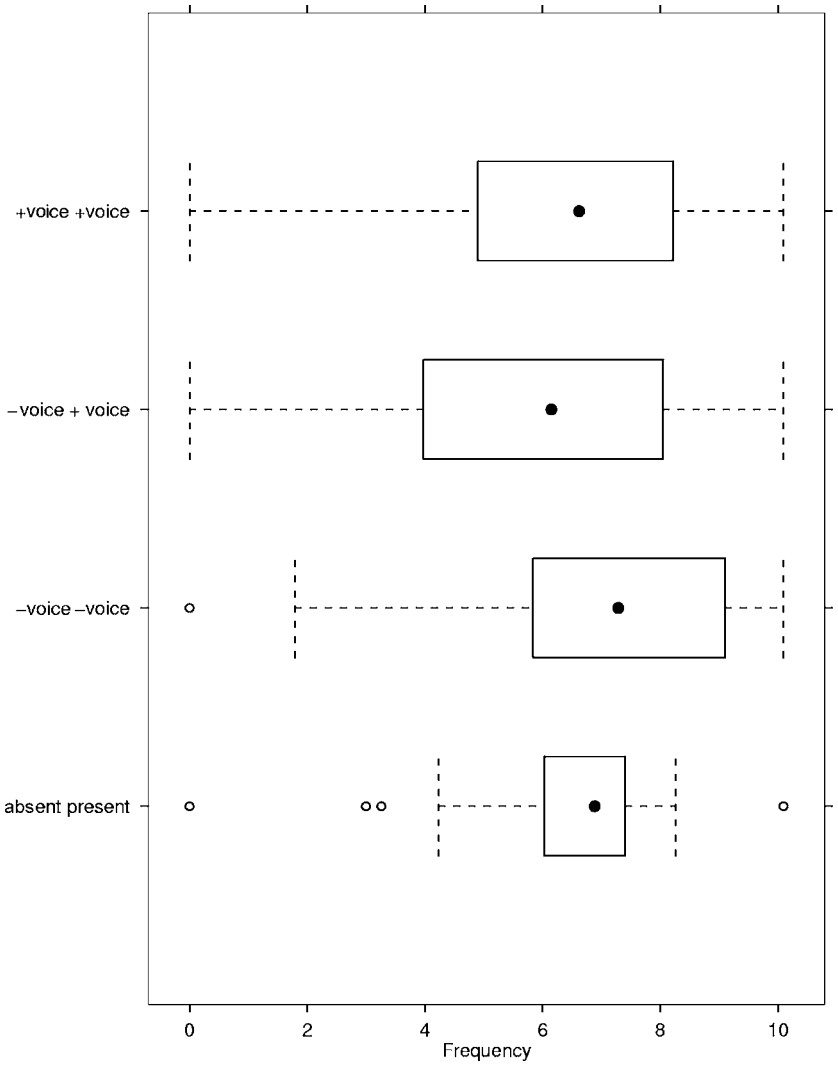

FIG. 1. Boxplot for the frequency distributions of the clusters that were classified as completely voiced (+voice +voice), unassimilated (–voice +voice), completely voiceless (–voice –voice), or as containing just the second obstruent (absent present).

but less often than the phonetician from the South-West [54.7%, $F(2,1252)=3.39$, $p<0.05$]. These two phoneticians from the South also differed significantly from each other in their classifications [$F(1,1117)=4.50$. $p<0.05$].

Third, we compared the completely voiced and the completely voiceless classifications. Plosive-initial clusters were more often classified as completely voiced (78.5% completely voiced classifications and 21.5% completely voiceless clusters) than fricative-initial clusters [58.4% completely voiced clusters, $F(1,1691)=5.02$, $p<0.05$] and the phoneticians from the South (64.4%) and South-West (64.0%) classified more clusters as completely voiced than the phonetician from the West [57.9%, $F(2,1691)=5.03$, $p<0.01$]. Frequency was not predictive.

Finally, we modeled the presence versus absence of the initial obstruent. The model did not converge when Word was included as a random effect. Hence, we report the model with only speaker as random effect. The initial obstruent was more likely to be absent in higher-frequency words [$\hat{\beta}=0.0002$, $F(1,2630)=111.64$, $p<0.0001$]. Furthermore, especially plosives were often absent [in 30.8% of cases, versus fricatives in 2.5% of cases, $F(1,2630)=115.57$, $p<0.0001$] and obstruents were more often classified as absent before /b/ (19.3% of the obstruents before /b/) than before /d/ [4.8%, $F(1,2630)=19.72$, $p<0.0001$]. These observations point to the generalization that especially alveolar plosives preceding /b/ are frequently absent.

C. Discussion

Our data document a correlation between a word's frequency of occurrence and voice assimilation. We observed that clusters are more often perceived as completely voiced or completely voiceless in higher-frequency words. Especially the words with completely voiceless clusters and those with unassimilated clusters differed significantly with respect to their average frequency.

The high percentage of clusters perceived as completely voiceless is unexpected given the literature on Dutch phonology. The received wisdom is that in Dutch progressive voice assimilation is restricted to clusters ending in fricatives or in the initial plosives of function words (e.g., Demeulemeester, 1962; Zonneveld, 1983; Booij, 1995; Rietveld and van Heuven, 2001; but see Slis, 1986). Such clusters were not included in our data set, and, hence, our data show that this generalization is incorrect. Progressive voice assimilation also affects clusters ending in plosives that do not belong to function words, but to stems, to suffixes, or to content words

in compounds (cf. Slis, 1986). This falsifies phonological theories in which the initial plosives of function words receive special status because they would be the only plosives showing progressive voice assimilation (e.g., Zonneveld, 1983).

The phonetician from the South classified obstruents as voiced more often than the phonetician from the West, while the phonetician from the South-West patterned in general with the phonetician from the South. Since obstruent devoicing is more common in the West than in the South of the Netherlands (e.g., Collins and Mees, 1981: 159; Gussenhoven and Bremmer, 1983: 57), this suggests that the phoneticians' classifications reflected the likelihoods of voiced and voiceless obstruents in their own regiolects. This would be in line with the study by Coussé *et al.* (2004), who showed that trained phoneticians classify Dutch vowels as short or long in accordance with their own regional variety of Dutch.

Especially alveolar plosives before /b/ were classified as absent (cf. Mitterer and Ernestus, 2006). In languages related to Dutch, such as English (Marslen-Wilson, Nix, and Gaskell, 1995) and German (Wiese, 1996), alveolar plosives have been claimed to assimilate to the place of articulation of the following obstruent. Hence, a /tb/ cluster may be realized as a /pb/ or /bb/ cluster, which is difficult to distinguish from a single /b/. Also the high deletion rate in Dutch /tb/ clusters might be argued to be due to place assimilation. If so, alveolar plosives should be frequently absent also before velar plosives: A /tk/ cluster would be realized as a /kk/ cluster, and hence it should be difficult to distinguish from a single /k/. In order to test this prediction, the three phoneticians transcribed all 163 /tk/ clusters from the subcorpus Library for the blind consisting of an alveolar plosive and a velar plosive, in the context of surrounding sonorants and realized by speakers educated in the Western or Southern parts of the Netherlands. The /t/ was classified as absent in only one cluster. We conclude that the perceived high deletion rate of /t/ in /tb/-clusters is unlikely to result from place assimilation.

The explanation offered by Browman and Goldstein (1990: 360) for the absence of /t/ before /b/ in English appears to be more promising for our Dutch data. Browman and Goldstein argue that the absence of alveolar plosives before bilabial plosives may be the consequence of coarticulation. Bilabial plosives are realized with a constriction at the lips, and they thus can mask all sounds that are simultaneously realized within the vocal tract. If they are realized simultaneously with an alveolar plosive, they can mask at least the release of this alveolar plosive, which is the most important cue to its recognition. In such cases, the alveolar plosive is acoustically absent, although its articulatory gestures are present. Alveolar plosives cannot be masked by velar plosives, as velar plosives are realized with a constriction in the back of the mouth. The account by Browman and Goldstein thus not only explains the high deletion rate of /t/ before /b/, but also the low deletion rate of /t/ before /k/.

We now turn to detailed analyses of the acoustic characteristics of the speech signal that cue perceived voicing. We investigated whether frequency correlates with the duration of several components of the cluster and with the duration of the preceding vowel. Recall that according to the Phonemic hypotheses, these durations should all signal either more or less voicing at higher frequencies. The Subphonemic hypothesis predicts that in higher-frequency words the acoustic characteristics are realized with less articulatory effort.

III. ACOUSTIC MEASUREMENTS

A. Method

Our data set contained 732 obstruent clusters, of which 711 had also been investigated in the classification study above. The obstruents in the additional 21 clusters could not be reliably classified as voiced, voiceless, or absent, due to background noise, whereas they could be measured accurately. Conversely, the data set lacked the 197 clusters incorporated in the classification data set that could not be reliably measured because of background noise or that were classified as containing only one obstruent.

Recall that voiced obstruents typically follow longer vowels than voiceless obstruents, that they are typically shorter than voiceless obstruents, and also contain shorter release noises. In addition, voiced obstruents in clusters tend to be produced with glottal vibration during their final parts (see Sec. I). Since clusters typically contain at best one interruption in glottal vibration, which starts during the first obstruent, the duration of glottal vibration provides information on its temporal location (i.e., the longer the period, the greater the chance that the final parts of both obstruents are realized with glottal vibration). We decided to measure the duration of the vowel preceding the obstruent cluster, the duration of the obstruent cluster itself, the period of glottal vibration during the cluster, and the duration of the release noise in the cluster.

In case the preceding vowel was separated from the obstruent cluster by a sonorant consonant (as in *ochtendblad* "morning paper" in which the cluster /tb/ is preceded by /n/), we included the duration of this sonorant in our measurement of the vowel, since it is in general impossible to determine exactly where the vowel ends in the acoustic signal and where the following sonorant consonant starts. We defined the beginning of the vowel as the beginning of the regular wave form with the characteristics of the vowel, and the end of the vowel (plus sonorant consonant) as the (sudden) end of this regular wave form. The end of the obstruent cluster was defined as the beginning of the regular wave form with the characteristics of the following sonorant. We assumed glottal vibration to be present in that part of the obstruent cluster where the wave form was periodic, the spectrogram contained a voice bar, and where we could hear the vocal fold vibration. Finally, we defined release noise to start at the sudden increase in amplitude after a closure and to end where the acoustic signal was regular or flat again. All measurements were in seconds. Figure 2 shows the segmentation for a token of the Word *afbeeld* "depict" containing the cluster /fb/.

The two phoneticians from the South and South-West of the Netherlands who previously had classified the clusters, made the acoustic measurements. Each phonetician mea-

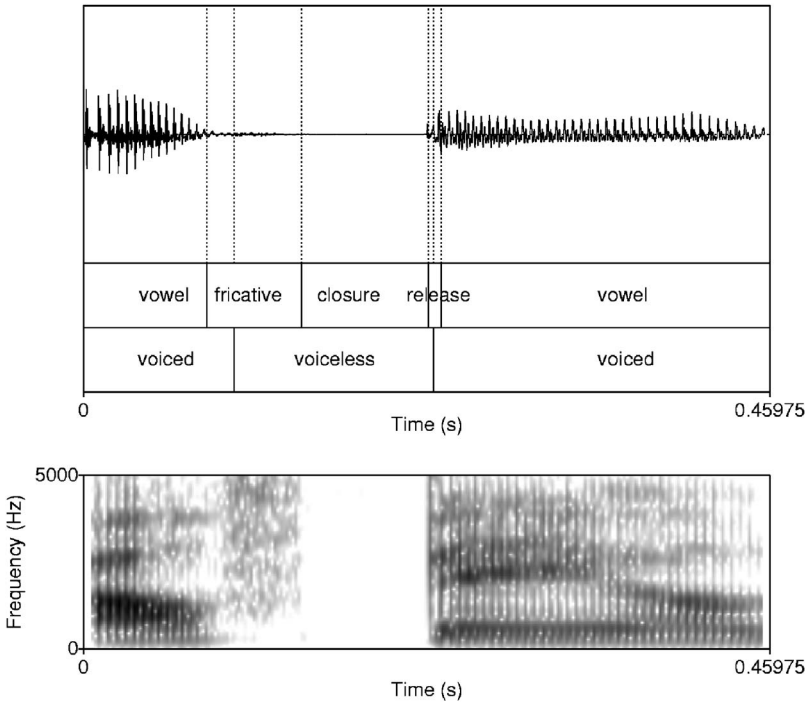

FIG. 2. Segmentation of [ɑfbe] from *afbeeld* "depict."

sured half of the clusters. One year later, each phonetician measured the durations for 100 tokens a second time. The first and second measurements differed on average 5 ms, with a standard deviation (after removal of one outlier) ranging from 4 ms (for cluster and burst duration) to 8 ms (for the period of glottal vibration).

B. Results

We considered as predictors for the acoustic measurements the speakers' Gender and Year of birth (minus 1900), the Type of the first obstruent in the cluster (fricative versus plosive), the Second obstruent (/b/ versus /d/), and the Morphological class of the word (prefixed, suffixed, or compound). Since listeners interpret segment durations relative to the durations of surrounding segments (Miller, 1981), we entered as predictor for the duration of the preceding vowel also the duration of the cluster. For the other durations, we entered the acoustic duration of the preceding vowel, its phonological length (long versus short, see, e.g., Booij, 1995), and whether this vowel was stressed. Together, these additional predictors reflect speech rate. Finally, we entered Frequency as predictor.

1. Cluster duration

We first studied the duration of the obstruent cluster. Frequency correlated negatively with cluster duration [$\hat{\beta}=-0.002$, $F(1,729)=18.63$, $p<0.0001$]. In addition, clusters ending in /b/ (mean: 0.136 s) were on average 16 ms longer than those ending in /d/ [mean: 0.120 s, $F(1,729)=10.78$, $p=0.001$].

Cluster duration itself may be predictive for the other acoustic durations signaling voicing. For instance, it is an obvious predictor for the duration of the period of glottal vibration during the cluster, since, by definition, this period cannot be longer than the cluster itself. We therefore included cluster duration as a covariate in the statistical models for the durations of the period of glottal vibration, the release noise, and the preceding vowel. Since cluster duration correlates with Frequency, we decided not to include raw cluster duration. In order to avoid collinearity between our predictors (cluster duration and Frequency), we first fitted cluster duration against Frequency and entered the resulting residuals as covariates in the models. These residuals (henceforth Cluster residuals) show a correlation of $r=0.79$ ($p<0.0001$) with the cluster durations. In other words, greater cluster residuals imply longer clusters.

2. Period of glottal vibration

Of the 732 clusters, 253 were realized without any glottal vibration. We analyzed the complete absence versus presence of at least some glottal vibration by means of a generalized linear mixed model with a binomial link function. Women realized obstruent clusters more often without glottal vibration (in 43.8% of cases) than men [24.6%, $F(1,727)=9.08$, $p<0.01$]. Obstruent clusters ending in /d/ were more often realized without glottal vibration (in 47.2% of cases) than obstruent clusters ending in /b/ [6.6%, $F(1,727)=180.29$, $p<0.0001$]. Furthermore, we found that for clusters preceded by vowels longer than 120 ms, a longer vowel implied a higher probability of complete absence of glottal vibration [linear effect of vowel duration: $\hat{\beta}=-3.84$, $F(1,727)=646$, $p=0.01$; quadratic effect: $\hat{\beta}=15.34$, $F(1,727)=10.87$, $p=0.001$].

The attested effects of gender and the Second obstruent are as expected. The larynx of men and women differ in their properties (e.g., shape, size, mass, stiffness) such that the oscillation conditions of the vocal folds are more restricted for women than for men (Lucero and Koenig, 2005). Furthermore, the oral volume can be expanded to a greater extent, both passively and actively, during the production of a

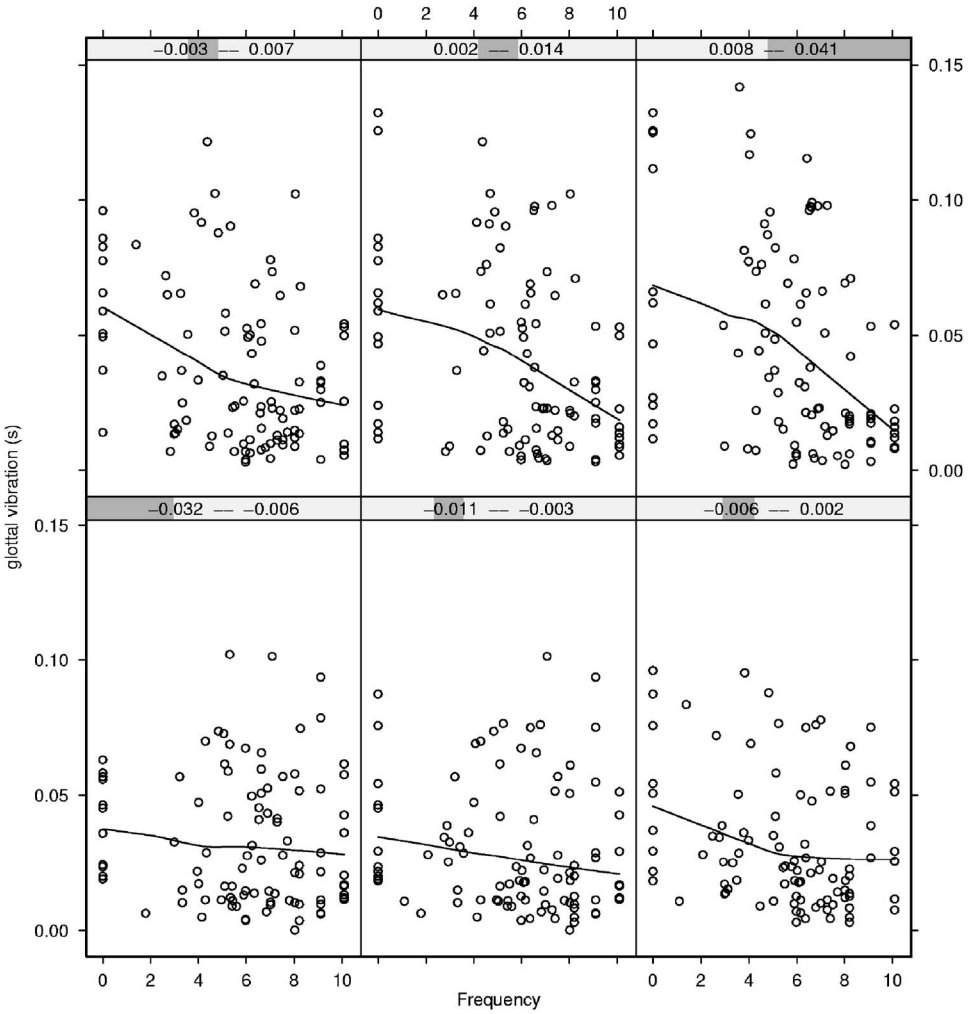

FIG. 3. The interaction of frequency and Cluster residuals on the duration of the period of glottal vibration. Every panel represents 97 clusters ordered by Cluster residuals: The bottom left panel represents the 97 clusters with the smallest Cluster residuals and the top right panel the 97 clusters with the greatest Cluster residuals (see the bar at the top of each panel). The solid line in each panel represents a nonparametric scatterplot smoother.

bilabial than an alveolar plosive (Ohala, 1983). As a consequence, the difference between the sub- and supraglottal air pressure, which is necessary for glottal vibration, is more easily maintained during [b] than [d].

In 137 out of the 479 clusters realized with glottal vibration, the vocal folds vibrated continuously from beginning to end. Men realized clusters with continuous glottal vibration more often (in 36.0% of cases) than women [in 19.2% of cases, $F(1,729)=12.55$, $p<0.001$]. Furthermore, clusters ending in /b/ were more often (in 33.3% of cases) produced with continuous glottal vibration than those ending in /d/ [24.8%, $F(1,729)=17.80$, $p<0.0001$]. These patterns are in line with those observed for the complete absence versus presence of some glottal vibration.

Finally, we modeled the length of the period of glottal vibration by means of linear regression analysis. Our data set only included the 342 clusters that were partly produced with glottal vibration. We did not include the clusters that were realized completely with or without glottal vibration since this would have led to an extreme bimodal distribution of the dependent variable, with a first peak at 0 s and a second peak at approximately 0.12 s, the average duration of the clusters.

We found a main effect of Frequency [$F(1,337)=6.25, p<0.05$] and of cluster residuals [$\hat{\beta}=0.85, F(1,337)=4.11, p<0.05$], in addition to an interaction of Frequency with Cluster residuals [$F(1,337)=12.08, p<0.001$]. Figure 3 illustrates the effect of Frequency and its interaction with Cluster residuals. Each panel in this trellis graph shows the correlation between Frequency (X axis) and the duration of the period of glottal vibration (Y axis) for clusters with the cluster residuals specified at the top of the panel. Cluster residuals increase from the bottom left panel to the bottom right panel and then from the top left panel to the top right panel. In general, frequency correlates negatively with the period of glottal vibration, but this effect is attenuated for clusters with smaller Cluster residuals.

In addition, the period of glottal vibration was, unsurprisingly, longer in clusters with greater Cluster residuals [$\hat{\beta}=0.85, F(1,337)=4.11, p<0.05$] and in clusters ending in /b/ [mean duration in clusters ending in /b/ was 0.051 s. and in clusters ending in /d/ 0.029 s, $F(1,337)=31.40, p<0.0001$]. The effects of these two variables varied with speaker (all $p<0.001$).

3. Duration of the release noise

We investigated the total duration of the release noise(s) in the cluster. In fricative-initial clusters, only the final plosive is realized with a release noise, while in plosive-initial clusters, both the initial and the final plosive may be realized with release noises.

Frequency was a significant nonlinear predictor in the

model [linear: $\hat{\beta}=-0.00045$, $F(1,725)=0.67, p>0.1$, quadratic: $\hat{\beta}=0.00013, F(1,725)=11.04, p<0.001$]. From a log frequency of 4 onwards, the total duration of the release noises increased approximately linearly with increasing frequency. From 0 to 4, the duration increased only slightly with frequency. Furthermore, the total duration of the release noises was greater in clusters with greater cluster residuals [$\hat{\beta}=0.071, F(1,725)=11.23, p<0.001$]. It was also greater if the initial obstruent was a plosive [mean duration of 0.033 s for plosive-initial clusters versus 0.021 s for fricative-initial clusters: $F(1,725)=72.36, p<0.0001$], and if the final plosive was /d/ [mean duration for /d/-final clusters: 0.0232 s; for /b/-final clusters: 0.0230 s, $F(1,726)=29.06, p<0.0001$]. The effect of the Type of the first obstruent varied with both speaker and Word while the effect of the Second obstruent varied with speaker (all $p<0.001$). Finally, the total duration of the release noises increased with longer durations of the preceding vowel [$\hat{\beta}=0.019, F(1,725)=4.87, p<0.05$].

4. Duration of the preceding vowel

Finally, we studied the duration of the vowel preceding the obstruent cluster, which is also a cue to perceived voicing in Dutch, though less strong than in English (Slis and Cohen, 1969). As expected, phonologically long vowels were on average longer (mean: 0.150 s) than phonologically short vowels [mean: 0.101 s, $F(1,728)=210.13, p<0.0001$] and stressed vowels were on average longer (mean: 0.120 s) than unstressed vowels [mean: 0.077 s, $F(1,728)=47.53, p<0.0001$]. Furthermore, vowels preceding fricative-initial clusters were longer (mean: 0.119 s) than those preceding plosive-initial clusters [mean: 0.099 s, $F(1,728)=7.69, p<0.01$]. Frequency, however, was not predictive for the duration of the preceding vowel.

C. Discussion

Summing up, as frequency increases, both the cluster and the period of glottal vibration become shorter, while the total release noise becomes longer. We now consider what these results imply with respect to the relation between frequency and articulatory effort.

Shorter periods of glottal vibration, as observed in words of higher frequencies, imply less articulatory effort. One necessary condition for the realization of glottal vibration is that the supraglottal air pressure is lower than the subglottal pressure. During the realization of fricatives, the air pressure above the glottis also has to be higher than the pressure beyond the constriction. These two requirements can be met simultaneously with undue effort only for a short time. In order to reduce articulatory effort, speakers may relax the adduction of the glottis, terminating glottal vibration but facilitating the realization of frication. During the realization of plosives, the air passing the vocal folds cannot escape from the vocal tract, and pressure builds up above the glottis. As a consequence, glottal vibration may simply stop in long plosives or in clusters of plosives, on average after 65 ms (Ohala, 1983). Since only little articulatory effort is necessary for glottal vibration in short clusters, reduction in articulatory effort hardly affects these clusters. This explains the observed interaction between Cluster residuals and Frequency for the period of glottal vibration (Fig. 3).

Reduction in articulatory effort is also achieved by reduction in the magnitudes of the constricting and release gestures, necessary for the production of the cluster, and by temporal overlap of these articulatory gestures. This results in shorter obstruent clusters. Moreover, it may result in longer release noises: If a plosive is realized with reduced constricting gestures, overlapping with the release gestures, its constriction is (partly) taken over by the release noise, which is consequently lengthened. As a consequence, the plosive may even sound as a fricative (cf. Ernestus, 2000: 203).

In conclusion, the attested correlations between the acoustic durations and frequency reflect reduction in articulatory effort. Our data are thus in line with the Subphonemic hypothesis, which states that a higher lexical frequency results in reduction of articulatory effort affecting a wide range of characteristics of the acoustic signal.

Shorter periods of glottal vibration and longer release noises result in less perceived voicing, whereas shorter obstruent clusters result in more perceived voicing (e.g., Slis and Cohen, 1969; van den Berg, 1986, 1987). Thus, in words of higher frequency, some cues signal more while others signal less perceived voicing. This finding is also in line with the Subphonemic hypothesis, while falsifying the two Phonemic hypotheses.

In Sec. II, we observed that frequency correlates with the phonetic classification of clusters as completely voiced, unassimilated, or completely voiceless. The three phoneticians listened only to the obstruent clusters and the surrounding vowels (plus intervening sonorant consonants, if present). In the majority of cases, they thus could not recognize the words, and their classifications could not be affected by their knowledge of the words, including the words' frequencies. This leads to the prediction that frequency is not a predictor for the phoneticians' classifications over and above the acoustic durations measured in Sec. III. We tested this prediction in Sec. IV.

IV. NATURE OF THE FREQUENCY EFFECTS IN THE CLASSIFICATIONS

A. Method

We combined our acoustic measurements with the voice classifications obtained in Sec. II. The resulting data set contained 711 clusters. Since every cluster was classified by three phoneticians, it consisted of in all 2133 classifications. We investigated whether frequency is a predictor for the phoneticians' judgments over and above the acoustic measurements, by means of stepwise generalized linear multilevel models with a binomial link function.

B. Results

Figure 4 shows the distributions of the durations of the complete cluster, of the period of glottal vibration during the cluster, of the release noise(s), and of the preceding vowel,

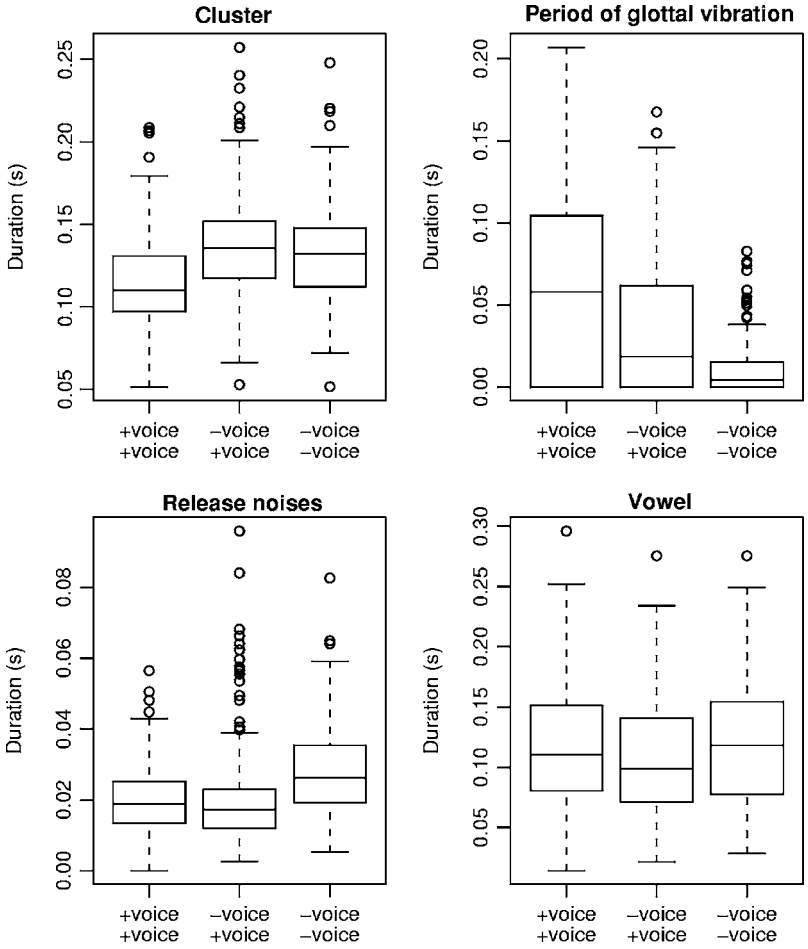

FIG. 4. Distribution of the durations of the obstruent cluster, of the period of glottal vibration, of the total release noise(s), and of the preceding vowel for completely voiced (+voice +voice), unassimilated (–voice +voice), and completely voiceless (–voice –voice) clusters.

for obstruent clusters classified as completely voiced, as unassimilated (–voice +voice), and as completely voiceless.

We investigated the relevance of Frequency, by contrasting unassimilated clusters first with completely voiced and then with completely voiceless clusters. Our independent variables were Frequency, entered as the first predictor, the durations of the preceding vowel, of the period of glottal vibration, of the release noise, and of the cluster. In addition, we included (interactions with) the speakers' Gender and Year of birth (minus 1900), the Type of the first obstruent in the cluster (fricative, plosive), the Second obstruent (/b/, /d/), the Morphological class of the word (prefixed, suffixed, compound), and Phonetician.

The probability ($\hat{\beta}$'s for log-odds) that a cluster was classified as completely voiced versus unassimilated decreased with increasing cluster duration [$\hat{\beta}=-68.68, F(1,1431)=153.27, p<0.0001$], increased nonlinearly with the period of glottal vibration [linear: $\hat{\beta}=-13.38, F(1,1431)<1, p>0.1$; quadratic: $\hat{\beta}=421.62, F(1,1431)=88.71, p<0.0001$], and also increased with the duration of the preceding vowel [$\hat{\beta}=11.52, F(1,1431)=10.21, p<0.01$]. Furthermore, the phoneticians tended to classify plosive-initial clusters as completely voiced more often (69.84%) than fricative-initial clusters [57.9%, $F(1,1431)=16.40, p<0.0001$]. Finally, Phonetician emerged as significant [$F(1,1431)=27.03, p<0.0001$]. Frequency was not predictive.

The probability that a cluster was classified as completely voiceless versus unassimilated increased with longer release noises [$\hat{\beta}=133.38, F(1,1157)=86.47, p<0.0001$] while it decreased with longer periods of glottal vibration [$\hat{\beta}=-40.50, F(1,1157)=42.99, p<0.0001$], and with the duration of the preceding vowel [$\hat{\beta}=-12.56, F(1,1157)=12.28, p<0.0005$; note that the sign of the coefficient of this partial effect is negative even though Fig. 4 suggests that it should be positive. This difference in sign is due to by-Word differences that are taken into account in the multilevel analysis but that are ignored in the overall means depicted in Fig. 4]. In addition, the phoneticians tended to classify more fricative-initial clusters (51.7%) than plosive-initial clusters (42.3%) as completely voiceless [$F(1,1157)=8.62, p<0.005$]. Again, Frequency was no longer predictive.

Finally, the probability that a cluster was classified as completely voiceless versus completely voiced decreased with longer periods of glottal vibration [$\hat{\beta}=-114.02, F(1,1448)=100.31, p<0.0001$] and with longer preceding vowels [$\hat{\beta}=-32.49, F(1,1448)=39.49, p<0.01$], but increased with longer release noises [$\hat{\beta}=176.04, F(1,1448)=229.12, p<0.0001$] and longer obstruent clusters [$\hat{\beta}=71.54, F(1,1448)=39.49, p<0.0001$]. These results are as expected given the literature on acoustic cues for the perceptual voicing of single obstruents and obstruent clusters (e.g., Slis, 1982; van den Berg 1986, 1987).

C. Discussion

The durations of the complete cluster, of the period of vocal fold vibration, of the release noises, and of the preceding vowel cued perceived voicing, which is consistent with the observations in the literature (e.g., Slis and Cohen, 1969; van den Berg, 1986, 1987). The distinction between completely voiced and unassimilated clusters was mainly cued by the period of vocal fold vibration, followed by the duration of the complete cluster, as can be seen in Fig. 4. The duration of the release noises was not predictive, probably because plosive-initial clusters tend to be realized without their initial plosives in connected speech. The perceived voicing of the final obstruent was signaled mainly by the period of glottal vibration and by the duration of the release noise(s) (see Fig. 4).

Frequency only has a predictive value for the unassimilated versus completely voiced and completely voiceless classifications if the acoustic characteristics of the speech signal are left out of consideration (compare the models developed in this section with those in Sec. II). This suggests that the correlations between the classifications and frequency observed in Sec. II were carried exclusively by the acoustic cues to voicing. Frequency affected the classifications only indirectly through the acoustic cues, which we predicted given that the phoneticians did not listen to complete words, but to fragments just containing the clusters with the surrounding vowels.

Our finding that frequency is not predictive for the voice classifications over and above the studied acoustic characteristics is also supported by the combination of the models developed in the different sections of this paper. The models showing frequency effects on the acoustic characteristics discussed in Sec. III combined with the acoustic models for perceived voicing (this section) show exactly the same correlations between frequency and the phoneticians' classifications as revealed in Sec. II.

First, we discuss the probability of a completely voiceless cluster versus an unassimilated cluster. This probability is especially high for plosive-initial clusters. It increases with the duration of the release noise(s) and decreases with the period of glottal vibration and with the duration of the preceding vowel. For higher-frequency words, the duration of the release noise(s) is longer and the period of glottal vibration is shorter. The frequency effects on these two cues thus work in the same direction and lead to increased probabilities for completely voiceless clusters in higher-frequency words. Hence, the combined acoustic models lead to exactly the same conclusion as the direct analysis of the role of frequency in the classifications.

Second, we consider the probability of a completely voiced cluster versus an unassimilated cluster. This probability is especially high for fricative-initial clusters. It decreases with cluster duration while it increases with the period of glottal vibration and with vowel duration. As frequency increases, both the cluster and the period of glottal vibration become shorter. The frequency effects on the two cues to voicing therefore work in opposite directions. Hence, the net effect of frequency on the classifications depends on the strength of the frequency effects on the durations of the cluster and the period of glottal vibration as well as on the contributions of these two durations to perceived voicing.

$$\mathrm{lo} = -68.682 * \mathrm{cd} - 13.383 * \mathrm{gv} + 421.626 * \mathrm{gv}^2 \quad (1)$$

$$\mathrm{cd} = 0.15 - 0.002 * \mathrm{Freq} \quad (2)$$

$$\mathrm{gv} = -0.018 + 0.541 * \mathrm{cd} + 0.007 * \mathrm{Freq} - 0.064 * \mathrm{Freq} * \mathrm{cd} \quad (3)$$

Equation (1) shows part of the model developed above for the log odds (lo) of a completely voiced versus an unassimilated cluster. It shows the coefficients for the durations of the cluster (cd) and the period of glottal vibration (gv), ignoring the variables that are insensitive to Frequency. Equation (2) is the acoustic model for the duration of /b/-final clusters (Clusters ending in /d/ are predicted to be 4 ms shorter), with Freq standing for frequency. The model for the period of glottal vibration built in Sec. III contained cluster residuals as predictor. Equation (3) shows the model with raw cluster duration instead of Cluster residual as predictor, for /b/-initial words (in /d/-initial words the period of glottal vibration is predicted to be 7 ms shorter). Combining the three equations and varying Frequency from 0 to 10 reveals an almost linear positive correlation between Frequency and the log-odds: The higher the frequency, the higher the probability of a completely voiced cluster, also exactly as concluded in Sec. II.

V. GENERAL DISCUSSION

Several studies have documented that segments tend to be shorter in higher-frequency words (e.g., Jurafsky *et al.*, 2001; Bell *et al.*, 2003; Pluymaekers *et al.*, 2005). The present study is the first to report a correlation between lexical frequency and voice assimilation. It is based on a Dutch corpus of read speech. Three phoneticians classified obstruents as voiced, voiceless, or absent in clusters consisting of a morpheme-final obstruent and the voiced initial plosive of the following morpheme. Completely voiced clusters (RVA) as well as completely voiceless clusters (progressive assimilation) occurred more often in higher-frequency words. Unassimilated clusters typically occurred in words of a lower frequency.

The high percentage of words with completely voiceless clusters (25%) shows that progressive voice assimilation also occurs in Dutch word-internal clusters ending in plosives. This is in contrast with the received wisdom according to which progressive voice assimilation in Dutch would be restricted to fricative-final clusters and to clusters ending in the initial voiced plosives of function words (e.g., Demeulemeester, 1962; Zonneveld, 1983; Booij, 1995; Rietveld and van Heuven, 2001; but see Slis, 1986). Thanks to larger corpora, we now have the means to go beyond introspection and laboratory speech, and discover the, sometimes, surprising characteristics of connected speech.

Acoustic analyses showed that as frequency increased, clusters tended to be shorter, to be realized with shorter periods of glottal vibration, and to have longer release noises.

This indicates that speakers tend to realize higher-frequency words with reduced articulatory effort. The probability of a completely voiceless versus unassimilated cluster is correlated with the durations of the period of glottal vibration and the release noises, which both signal less voicing at higher frequencies. The probability of a completely voiced versus unassimilated cluster, in contrast, is co-determined by the period of glottal vibration, which signals less voicing at higher frequencies, and by cluster duration, which signals more voicing in higher-frequency words. The opposite effects of frequency on these acoustic cues may explain why the effect of frequency on the perception of clusters as completely voiced versus unassimilated is small.

The frequency that we studied for each cluster was the sum of the frequencies of all words containing the morphemes that form the cluster. Thus, the frequency studied for the *tb* cluster in *ontbijt* "breakfast" was based on the frequencies of, among others, *ontbijt* itself, *ontbijtje*, and *ontbijtbord*. It might be argued that another frequency measure is in fact more important, namely, the frequencies of the morphemes in the complex words. If these frequencies are low, one might expect less assimilation due to a greater likelihood of compositional production (see also Bien, Levelt, and Baayen, 2005; Hay and Baayen, 2005). We therefore added the frequencies of the individual morphemes (e.g., *ont* and *bijt*), cumulated over all words in which they occur in the CELEX morphological parsings, as predictors to our models for the acoustic measurements. These morpheme frequencies turned out never to be predictive.

The present findings challenge full decomposition models of speech production. In the model by Levelt, Roelofs, and Meyer (1999) for instance, the production of a morphologically complex word such as /vutbɑl/ "football", implies the activation of the word's lemma ("football"), followed by the activation of its morphological constituents (the lexemes /vut/ and /bɑl/). In turn, lexemes activate their associated phonemes and syllables. Since the model locates frequency effects at the level of the lexeme, it cannot straightforwardly explain a frequency effect of the lemma on clusters consisting of the last phoneme of the first lexeme and the first phoneme of the second lexeme.

The present frequency effects also have implications for our understanding of speech comprehension. Previous research has documented that phoneme transitions that are infrequent within morphemes may be more frequent at morpheme boundaries, and that listeners use low-probability junctural transitions as cues for detecting morphological structure (e.g, Seidenberg, 1987; Hay, 2003). The predictivity of lexical frequency for subtle acoustic details of obstruent clusters documented in the present study shows that subphonemic cues may also contribute to the identification of morphological structure. Morphologically complex words produced with little assimilation at the subphonemic level, that is, with well-articulated obstruent clusters, tend to be less frequent and therefore are more easily recognized via their parts. In contrast, words showing more assimilation between their parts, that is, with hypo-articulated clusters, tend to be of a higher-frequency and are more likely to be accessed on the basis of their full forms (e.g., Hay and Baayen, 2005).

Finally, the frequency effects documented in this study are completely unexpected given phonological theory, in which assimilation is described in terms of a phoneme sharing its phonological feature with a neighboring phoneme (e.g., Booij, 1995). Our findings show that voice assimilation is graded. Moreover, the different cues to voicing may be affected independently from each other. The literature on acoustic cues to voicing (e.g., Slis and Cohen, 1969; van den Berg, 1986, 1987) in combination with the literature on the relation between lexical frequency and articulatory effort (e.g., Jurafsky *et al.*, 2001; Bell *et al.*, 2003; Pluymaekers *et al.*, 2005) allows us to understand the observed independent and partly opposite effects of frequency on the fine-grained acoustic cues to voicing and their consequences for the perception of voicing in obstruent clusters.

Baayen, R. H. (**2004**). "Statistics in psycholinguistics: A critique of some current gold standards," Mental Lexicon Working Papers, pp. 1–45.

Baayen, R. H., Piepenbrock, R., and Gulikers, L. (**1995**). *The CELEX Lexical Database (CD-ROM)* (Linguistic Data Consortium, University of Pennsylvania, Philadelphia, PA).

Baayen, R. H., Tweedie, F. J., and Schreuder, R. (**2002**). "The subjects as a simple random effect fallacy: Subject variability and morphological family effects in the mental lexicon," Brain Lang **81**, 55–65.

Bates, D. M., and Sarkar, D. (**2005**). *The lme4 library*, on-line available: http://lib.stat.cmu.edu/R/CRAN/.

Bell, A., Jurafsky, D., Fosler-Lussier, E., Girand, C., Gregory, M., and Gildea, D. (**2003**). "Effects of disfluencies, predictability, and utterance position on word form variation in English conversation," J. Acoust. Soc. Am. **113**, 1001–1024.

Bien, H., Levelt, W. M. J., and Baayen, R. H. (**2005**). "Frequency effects in compound production," PNAS **102**, 17876–17881.

Booij, G. E. (**1995**). *The Phonology of Dutch* (Clarendon, Oxford).

Browman, C. P., and Goldstein, L. (**1990**). "Tiers in articulatory phonology, with some implications for casual speech," in *Between the Grammar and Physics of Speech*, Papers in Laboratory Phonology Vol. 1, edited by J. Kingston and M. E. Beckman (Cambridge University Press, Cambridge), pp. 341–376.

Bybee, J. L. (**2001**). *Phonology and Language Use* (Cambridge University Press, Cambridge).

Chatterjee, S., Hadi, A., and Price, B. (**2000**). *Regression Analysis by Example* (Wiley, New York).

Collins, B., and Mees, I. (**1981**). *The Sounds of English and Dutch* (Leiden University Press, Leiden).

Coussé, E., Gillis, S., Kloots, H, and Swerts, M. (**2004**). "The influence of the labeller's regional background on phonetic transcriptions: Implications for the evaluation of spoken language resources," in *Proceedings of the Fourth International Conference on Language Resources and Evaluations*, edited by M. T. Lino, M. F. Xavier, F. Fereirra, R. Costa, and R. Silva, pp. 1447–1450.

Demeulemeester, F. (**1962**). "Assimilatie van stemloze explosieven en fricatieven voor b en d" ("Assimilation of voiceless plosives and fricatives before b and d"), Taal en Tongval **14**, 20–36.

Ernestus, M. (**2000**). *Voice Assimilation and Segment Reduction in Casual Dutch: A Corpus-Based Study of the Phonology-Phonetics Interface* (LOT, Utrecht).

Fidelholz, J. (**1975**). "Word frequency and vowel reduction in English," in *Papers from the 11th Regional Meeting of the Chicago Linguistic Society*, edited by R. E. Grossman, L. J. San, and T. J. Vance, Vol. **11**, pp. 200–213.

Gussenhoven, C., and Bremmer, R. H. J. (**1983**). "Voiced fricatives in Dutch: Sources and present-day usage," North-Western Europ. Lang. Evol. **2**, 55–71.

Hay, J. (**2003**). *Causes and Consequences of Word Structure* (Routledge, New York).

Hay, J. B., and Baayen, R. H. (**2005**). "Shifting paradigms: Gradient structure in morphology," Trends in Cognitive Science **9**, 342–348.

Johnson, K. (**2004**). "Massive reduction in conversational American English" in *Spontaneous Speech: Data and Analysis, Proceedings of the First Session of the Tenth International Symposium* (The National International Institute for Japanese Language, Tokyo, Japan), pp. 29–54.

Jurafsky, D., Bell, A., Gregory, M., and Raymond, W. D. (**2001**). "Probabilistic relations between words: Evidence from reduction in lexical production," in *Frequency and the Emergence of Linguistic Structure*, edited by J. L. Bybee and P. Hopper (Benjamins, Amsterdam), pp. 229–254.

Kaiser, L. (**1958**). "Onderzoek naar assimilatieverschijnselen" ("Research in assimilation phenomena"), in *Album Edgard Blancquaert: De Gehuldigde Aangeboden ter Gelegenheid Van Zijn Emeritaat Door Kollega's Vakgenoten en Oud-Leerlingen* (George Michels, Tongeren), pp. 31–41.

Levelt, W. J. M., Roelofs, A., and Meyer, A. S. (**1999**). "A theory of lexical access in speech production," Behav. Brain Sci. **22**, 1–38.

Loots, W. (**1983**). "Syntax and assimilation of voice in Dutch," in *Sound Structures: Studies for Antonie Cohen*, edited by M. van den Broecke, V. van Heuven, and W. Zonneveld (Foris, Dordrecht), pp. 173–180.

Lucero, J. C., and Koenig, L. L. (**2005**). "Phonation thresholds as a function of laryngeal size in a two-mass model of the vocal folds (L)," J. Acoust. Soc. Am. **118**, 2798–2801.

Marslen-Wilson, W., Nix, A., and Gaskell, G. (**1995**). "Phonological variation in lexical access: Abstractness, inference and English place assimilation," Lang. Cognit. Processes **10**, 285–308.

Menert, L. (**1994**). "Experiments on voice assimilation in Dutch: Prosodic structures and tempo," Ph.D. dissertation, University of Utrecht, Utrecht.

Miller, J. L. (**1981**). "Some effects of speaking rate on phonetic perception," Phonetica **38**, 159–180.

Mitterer, H., and Ernestus, M. (**2006**). "Listeners recover /t/s that speakers reduce: Evidence from /t/-lenition in Dutch," J. Phonetics, **34**, 73–103.

Ohala, J. J. (**1983**). "The origin of sound patterns in vocal tract constraints," in *The Production of Speech*, edited by P. F. MacNeilage (Springer, Berlin), pp. 189–216.

Oostdijk, N. (**2000**). "The Spoken Dutch Corpus Project," The ELRA Newsletter **5**, 4–8.

Oostdijk, N., Goedertier, W., Eynde, F. van, Boves, L., Martens, J., Moortgat, M., and Baayen, R. H. (**2002**). "Experiences from the Spoken Dutch Corpus Project," in *Proceedings of the Third International Conference on Language Resources and Evaluation*, edited by M. González Rodríguez and C. Paz Suarez Araujo, pp. 340–347.

Pinheiro, J. C., and Bates, D. M. (**2000**). *Mixed-effects Models in S and S-PLUS* (Statistics and Computing, Springer, New York).

Pluymaekers, M., Ernestus, M., and Baayen, R. H. (**2005**). "Lexical frequency and acoustic reduction in spoken Dutch," J. Acoust. Soc. Am. **118**, 2561–2569.

Quené, H., and van der Bergh, H. (**2004**). "On multi-level modeling of data from repeated measures designs: A tutorial," Speech Commun. **43** 103–121.

Rietveld, A., and van Heuven, V. (**2001**). *Algemene Fonetiek (General Phonetics)* (Coutinho, Bussum).

Seidenberg, M. (**1987**). "Sublexical structures in visual word recognition: Access units or orthographic redundancy," in *Attention and Performance XII*, edited by M. Coltheart (Erlbaurn, Hove), pp. 245–264.

Slis, I. H. (**1982**). "Assimilatie van stem in het Nederlands" ("Assimilation of voice in Dutch"), Glot **5**, 235–261.

Slis, I. H. (**1986**). "Assimilation of voice in Dutch as a function of stress, word boundaries, and sex of speaker and listener," J. Phonetics **14**, 311–326.

Slis, I. H., and Cohen, A. (**1969**). "On the complex regulating the voiced-voiceless distinction, II," Lang Speech **12**, 80–102; (**1969**) **12**, 137–155.

van Alphen, P. M., and Smits, R. (**2004**). "Acoustical and perceptual analysis of the voicing distinction in Dutch initial plosives: The role of prevoicing," J. Phonetics **32**, 455–491.

van den Berg, R. (**1986**). "The effect of varying voice and noise parameters on the perception of voicing in Dutch two-obstruent sequences," Speech Commun. **5**, 355–367.

van den Berg, R. (**1987**). "Effects of durational factors on the perception of voicing in Dutch two-obstruent sequences," J. Phonetics **15**, 259–271.

Venables, W. N., and Ripley, B. D. (**2002**). *Modern Applied Statistics with S-Plus* (Springer, New York).

Vieregge, W. H. (**1987**). "Basic aspects of phonetic segmental transcription," in *Probleme der Phonetischen Transkription (Problems with Phonetic Transcriptions)*, edited by A. Almeida and A. Braun (Franz Steiner Verslag Wiesbaden GMBH, Stuttgart), pp. 5–55.

Wetzels, W., and Mascaró, J. (2001). "The typology of voicing and devoicing," Lang. **77**, 207–244.

Wiese, R. (**1996**). *The Phonology of German* (Clarendon, Oxford).

Zipf, G. K. (**1935**). *The Psycho-Biology of Language* (Houghton Mifflin, Boston).

Zonneveld, W. (**1983**). "Lexical and phonological properties of Dutch devoicing assimilation," in *Sound structures: Studies for Antonie Cohen*, edited by M. van den Broecke, V. van Heuven, and W. Zonneveld (Foris, Dordrecht), pp. 297–312.

An amplitude quotient based method to analyze changes in the shape of the glottal pulse in the regulation of vocal intensity

Paavo Alku[a] and Matti Airas
Laboratory of Acoustics and Audio Signal Processing, Helsinki University of Technology, P.O. Box 3000, Fin-02015 TKK, Finland

Eva Björkner and Johan Sundberg
Department of Speech, Music and Hearing, Royal Institute of Technology, Lindstedtsvägen 24, SE-10044, Stockholm, Sweden

(Received 16 February 2006; revised 10 May 2006; accepted 17 May 2006)

This study presents an approach to visualizing intensity regulation in speech. The method expresses a voice sample in a two-dimensional space using amplitude-domain values extracted from the glottal flow estimated by inverse filtering. The two-dimensional presentation is obtained by expressing a time-domain measure of the glottal pulse, the amplitude quotient (AQ), as a function of the negative peak amplitude of the flow derivative (d_{peak}). The regulation of vocal intensity was analyzed with the proposed method from voices varying from extremely soft to very loud with a SPL range of approximately 55 dB. When vocal intensity was increased, the speech samples first showed a rapidly decreasing trend as expressed on the proposed AQ-d_{peak} graph. When intensity was further raised, the location of the samples converged toward a horizontal line, the asymptote of a hypothetical hyperbola. This behavior of the AQ-d_{peak} graph indicates that the intensity regulation strategy changes from laryngeal to respiratory mechanisms and the method chosen makes it possible to quantify how control mechanisms underlying the regulation of vocal intensity change gradually between the two means. The proposed presentation constitutes an easy-to-implement method to visualize the function of voice production in intensity regulation because the only information needed is the glottal flow wave form estimated by inverse filtering the acoustic speech pressure signal. © *2006 Acoustical Society of America.* [DOI: 10.1121/1.2211589]

PACS number(s): 43.70.Jt, 43.70.Gr [BHS] Pages: 1052–1062

I. INTRODUCTION

The regulation of vocal intensity is an inherent feature in speech communication. Our everyday life is full of events in which we want to vary the volume of speech: in order to emphasize something, in order to be heard over a longer distance, in noisy environments, or, for example, in order to convey emotional content (such as anger) in the speech message. Intensity of sound is defined in physics as a measure of power per unit of area (e.g., Young and Freedman, 1996). In speech science, the term *vocal intensity* is commonly used to refer to the acoustic energy of speech, and it is typically quantified by using the sound pressure level (SPL) (Titze, 1994). Healthy speakers are able to produce voiced sounds over a wide range of intensity levels. In a study by Coleman *et al.* (1977), for example, voices of female and male subjects were analyzed by having each subject produce the maximum and minimum SPL of which he or she was capable. The values obtained, measured at a distance of 6 in. from the speaker, showed that the speech samples produced in soft and (very) loud phonation varied between 48 and 126 dB.

Changing sound intensity in audio equipment corresponds simply to amplitude scaling, i.e., multiplication with a constant that is either larger than unity (amplification) or smaller than unity (attenuation). In contrast to this, intensity regulation of natural speech uses various mechanisms realized by the human voice production apparatus. Consequently, varying speech intensity is reflected in changes of many acoustical features of the speech wave form, such as the fundamental frequency ($F0$), formant values, and the spectral tilt of the produced speech sound, rather than in pure amplification/attenuation of the signal wave form alone. According to Titze (1994), there are three basically distinct mechanisms to control the intensity of the human voice. They correspond to adjustments of the vocal apparatus below the larynx, within the larynx, and above the larynx. Below the larynx, intensity can be regulated by controlling the aerodynamic output of the lungs to the vocal system. The key variable in this process is subglottal pressure[1] (Ladefoged and McKinney, 1963; Bouhuys *et al.*, 1968). Within the larynx, there are methods to regulate intensity by modifying the vibration of the vocal folds and hence changing the amount of aerodynamic power converted into acoustic power. These methods correspond, for example, to an increase in the flow amplitude or to a decrease in the length of the glottal closing phase and they are typically reflected by a changed value of subglottal pressure. Above the larynx, vocal intensity can be modified by adjusting the resonances of the vocal cavity, especially the first formant, to coincide with the harmonics

[a]Electronic mail: paavo.alku@tkk.fi

of the glottal source. This method to control vocal intensity is called formant tuning, but it is not typically used in intensity regulation of conversational speech (Titze, 1994).

In the late 1950s and early 1960s, a number of investigations were carried out on the intensity regulation of speech (Van den Berg, 1956; Ladefoged and McKinney, 1963; Isshiki, 1964, 1965). These studies addressed mainly the impacts of subglottal pressure and air flow rate on vocal intensity. The key role of the subglottal pressure on vocal intensity was demonstrated, for example, in a study by Ladefoged and McKinney (1963), who reported that the peak sound pressure level (in dB) rose linearly as a function of subglottal pressure (presented on the logarithmic scale) for the middle part of the subglottal pressure range. On the other hand, Isshiki (1964, 1965) studied intensity regulation as controlled by two factors, the contraction of the laryngeal adductor muscles and the expiratory force. He reported that in low frequency phonation the flow rate remained almost unchanged, or even slightly decreased, with the increase in voice intensity reflecting the use of laryngeal control. In contrast to this phenomenon, the flow rate of high frequency phonation showed a large increase when voice intensity was raised indicating the use of expiratory muscle control. These results were supported in a laryngeal electromyography study by Hirano *et al.* (1970). Subsequently, Isshiki's approach to the study of vocal intensity based on respiratory and laryngeal phenomena has been used in various investigations. Stathopoulos and Sapienza (1993a, 1993b) for example, compared respiratory and laryngeal function in intensity variation between males and females and between adults and children. In addition, the two factors suggested by Isshiki have been used in studies comparing intensity regulation of normal and disordered voices (e.g., Makiyama *et al.*, 2005) as well as in studies addressing sustained and transient increases of intensity (Finnegan *et al.*, 2000). Even though the roles of the laryngeal adductor muscles and the expiratory force have been studied widely since they were originally proposed by Isshiki, it is worth noting that there is still a lack of understanding on how these two major factors interact when vocal intensity is regulated.

The early studies on intensity regulation of speech did not, however, address the relationship between the excitation of (voiced) speech created by the vibrating vocal folds, the glottal volume velocity wave form, and vocal intensity. Later, when the use of inverse filtering became widely used, numerous experiments were conducted to study the behavior of the glottal volume velocity wave form in intensity regulation of speech. These studies show, in terms of the amplitude-based parameters of the glottal flow (Fig. 1), that raising the vocal intensity is accomplished typically by an increase of the ac flow and also (but perhaps not so clearly) by a decrease of the minimum flow (Holmberg *et al.*, 1988; Hertegård and Gauffin, 1991; Titze, 1992b; Sulter and Wit, 1996). Furthermore, increasing vocal intensity corresponds to changing the shape of the glottal pulse so that the length of the open phase decreases (Dromey *et al.*, 1992; Sapienza *et al.*, 1998; Hodge *et al.*, 2001) and, in particular, the length of the glottal closing phase decreases (Holmberg *et al.*, 1988; Sulter and Wit, 1996). The increase of the ac flow and the decrease of the duration of the glottal closing phase both amplify the negative peak amplitude of the flow derivative (Sundberg *et al.*, 1993). This parameter, depicted by d_{peak} in Fig. 1, is also called the maximum flow declination rate (Holmberg *et al.*, 1988; Stathopoulos and Sapienza, 1993a, 1993b). It has been shown in various studies (e.g., Holmberg *et al.*, 1988; Gauffin and Sundberg, 1989; Fant, 1993; Stathopoulos and Sapienza, 1993b; Sapienza and Stathopoulos, 1994; Sulter and Wit, 1996; Alku *et al.*, 1999) that d_{peak} is closely related to vocal intensity. The important role of d_{peak} characterizing the behavior of the voice source in intensity regulation is demonstrated by the fact that the mapping between SPL (in dB) and d_{peak} (on the logarithmic scale) can be approximated very closely with an increasing linear function (Gauffin and Sundberg, 1989; Alku *et al.*, 1999).

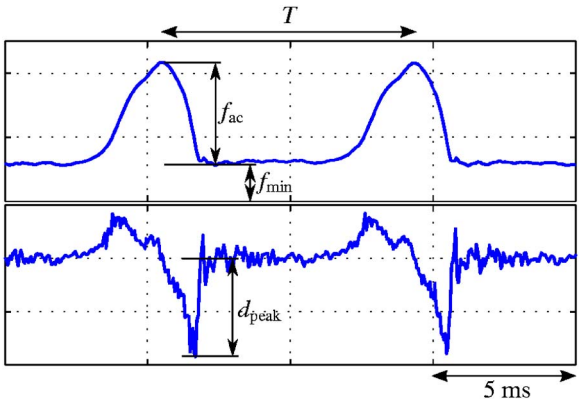

FIG. 1. (Color online) Glottal flow pulse (upper graph) and its first derivative (lower graph) computed from natural speech using inverse filtering. The amplitude-domain quantities shown as: f_{ac}=peak-to-peak flow (also called the ac flow), f_{min}=minimum of the flow (also called the dc offset), d_{peak}=negative peak amplitude of the flow derivative (also called the maximum airflow declination rate). Length of the fundamental period is denoted by T.

Titze and Sundberg studied the regulation of vocal intensity in speakers and singers by presenting analytic and empirical models to predict sound pressure levels from glottal wave form parameters (Titze, 1992a; Titze and Sundberg, 1992). In their studies, the role of minimum lung pressure to initiate phonation, the phonation threshold pressure, was essential. The authors addressed, among other things, the question of how subglottal pressure affects the vocal intensity. It was shown that the doubling of excess pressure over the threshold caused an 8–9 dB increase in SPL. The first 6 dB of this increase was explained by an increase in the glottal flow amplitude, whereas the remaining 2–3 dB came from changing the shape of the flow pulse to a less symmetric form. Similar results were also reported by Fant (1982), whose theoretical calculations yielded the SPL increase of 9.5 dB as a result of doubling subglottal pressure. According to Fant, 2 dB of this rise in vocal intensity is caused by changes in the glottal flow pulse form during the closing phase.

The relationship between vocal intensity and $F0$, or its perceptual counterpart, loudness, has also been studied widely (e.g., Gramming *et al.* 1988; Strik and Boves, 1992; Titze and Sundberg, 1992; Alku *et al.*, 2002). Attention has been focused especially on the voice range profile (VRP),

also called the phonetogram, which is a display of vocal intensity range versus $F0$ (Damste, 1970; Gramming and Sundberg, 1988; Åkerlund *et al.*, 1992; Titze, 1992b; Coleman, 1993). In one of their VRP studies, Gramming *et al.* (1988) reported that the mean pitch increased by about a half-semitone when intensity was increased by one decibel. According to their findings, the increased value of $F0$ can be expected as a passive result of raising the subglottal pressure in order to produce louder sounds.

The present study addresses the question of how speakers change the characteristics of the glottal pulse when vocal intensity is increased. Given the essential role of intensity regulation in voice communication, this issue is undoubtedly of great importance in speech science. Previous studies, however, have paid little attention to methodologies to visualize how the glottal pulse characteristics change when intensity is regulated. Therefore, a new method is presented which makes it possible to analyze how a rise in vocal intensity is contributed to by the following two glottal source related mechanisms both of which raise the negative peak amplitude of the flow derivative: (a) changing of the glottal pulse to a more asymmetric form versus (b) increasing of the glottal flow amplitude. Rather than using the ordinary approach (e.g., Holmberg *et al.*, 1988; Stathopoulos and Sapienza, 1993a, 1993b; Södersten *et al.*, 1995; Sulter and Wit, 1996), in which speech samples are divided into few intensity categories (typically three: soft, normal, loud), this study analyzes voices, the intensity of which rose from low to high in small steps of approximately 5 dB. This approach, previously used also by Sundberg *et al.* (2005), was chosen because it allows a more detailed insight into the intensity regulation mechanisms in speech. Furthermore, many of the previous studies on intensity regulation of speech have used a rather narrow SPL range between soft and loud phonations. For example, the difference between loud and soft male voices was, on average, 11 dB in the study by Holmberg *et al.* (1988), 15 dB in the study by Sapienza *et al.* (1998), and 18 dB in the study by Hodge *et al.* (2001). In contrast to these studies, the present survey aimed to gather information on vocal intensity regulation mechanisms by using phonations that had SPL dynamics much closer to the extreme limits achievable by normal speakers.

II. MATERIAL AND METHODS

A. Speech material

Speech data were-collected from ten adult Finnish speakers (five females and five males) with no history of speech, voice, or hearing disorders. The ages of the female speakers varied between 42 and 54 and those of the males between 33 and 45 years. The acoustic speech pressure wave form was recorded using a condenser microphone (Brüel&Kjaer 4176) placed at a distance of 40 cm from the lips of the speaker. The distance was carefully controlled before each phonation, an important precaution in order to be able to compare the amplitude features of the estimated glottal flows between different phonations.(see Sec. II D). Intraoral pressure was simultaneously recorded using a pressure transducer (Frøkjær-Jensen Electronics, Manophone, MF710) connected to the subject's mouth with a plastic catheter. For the computation of SPL values, we also recorded a calibration signal generated by a Brüel&Kjaer 4231 calibrator. During the recording, the subject phonated with the catheter placed between the lips in the corner of the mouth. The recordings were made in an anechoic chamber and all of the subjects sat while producing the sounds.

The speaking task was to produce a series of the word /pa:p:a/ with increasing vocal intensity. First, each subject was asked to repeat the production of the word /pa:p:a/ several times as softly as possible without whispering. The output level of the speech signal was measured by means of a sound level meter (Brüel&Kjaer 2225), whose LED display was visible to both the subject and the experimenter. When the subject had learned to repeat the production of the test word as softly as possible with a consistent SPL value, the recording of the first sample was conducted. The subject was then asked to produce the word /pa:p:a/ by increasing the sound pressure level by 5 dB. In order to do this, the subject again watched the LED display of the sound level meter and gave multiple productions until the desired SPL increase from the preceding representation was achieved. When the desired SPL value was reached, five repetitions of the /pa:p:a/ word were recorded. The same procedure was then repeated several times with the subject increasing the value of SPL by 5 dB until she or he reached the loudest sample required with a SPL value of 105 dB. (Some subjects also voluntarily produced an even louder sound with an SPL value of 110 dB.) All the subjects found this procedure straightforward and they achieved the desired SPL value after a few productions of the word /pa:p:a/. Importantly, the subjects were given no other restrictions regarding their voice production, permitting the speakers to choose pitch and phonation type freely during the recording.

Both the acoustic speech pressure wave form and the intraoral pressure signal were directly transmitted to a computer via an audio card (Turtle Beach Tahiti, Turtle Beach Systems) with a frequency response from dc up to 20 kHz. Each recorded speech sample comprised five productions of the /pa:p:a/ repetitions, from which the middle one was always selected and stored for further analyses. The wave forms were digitized using a sampling frequency of 22.050 kHz and a resolution of 16 bits. The bandwidth of the signals was 11 kHz. In the computer, the acoustic speech signals were first high-pass filtered with a linear phase FIR filter, with a cut-off frequency of 60 Hz, in order to remove any possible low-frequency air pressure variations picked up during the recordings.

B. Inverse filtering

In order to estimate the glottal volume velocity wave forms, we used an inverse filtering technique, which estimates the glottal excitation directly from the acoustic speech pressure wave form as recorded in a free field, i.e., no flow mask was used. The method used was a slightly modified version of the technique described by Alku (1992). The modification concerned the modeling of the vocal tract transfer function, which was based on an all-pole modeling tech-

nique, called Discrete All-Pole Modeling (DAP) (El-Jaroudi and Makhoul, 1991), instead of the conventional Linear Predictive Coding (LPC) used by Alku (1992). The difference between DAP and LPC is that the former is based on the Itakura-Saito distortion criterion in determining an optimal all-pole filter, whereas the latter uses the least squares error criterion. Consequently, the formants of the vocal tract, particularly for high-pitched voices can be more accurately estimated by DAP than by LPC (El-Jaroudi and Makhoul, 1991). An accurate modeling of the vocal tract transfer function is crucial from the point of view of glottal inverse filtering. As reported by Alku and Vilkman (1994), the application of DAP instead of LPC in modeling the vocal tract transfer function decreases the amount of formant ripple in the estimated glottal flows.

The inverse filtering method used in the present study estimates the vocal tract transfer function applying the above-mentioned DAP technique by first canceling the average effect of the glottal source from the speech spectrum using low-order all-pole filtering. In order to be able to compare the different phonations in terms of the value of d_{peak}, a normalization method described in detail in Alku *et al.* (1998) was used. In this method, the dc gain of the vocal tract model used in inverse filtering is adjusted to unity. This makes possible an analysis of the amplitude features of the glottal flow on an amplitude scale, which is arbitrary (i.e., it does not yield the absolute flow values), but remains the same for all the voices analyzed. The length of the analysis window was 50 ms. For some of the low-pitched male voices, the length of the time window was increased to 70 ms in order to cover at least four glottal cycles. In order to estimate the glottal flow over sustained phonation, the analysis window of inverse filtering was set at the middle of the long vowel in the/pa:p:a/word.

C. Computation of sound pressure level and subglottal pressure

The SPL values were determined on the dB scale using the energy computation[2] and the SPL value of the calibration tone (94 dB) as follows:

$$L_p = 94\ \text{dB} + 10 \log_{10} \frac{E_s}{E_c}, \tag{1}$$

where L_p is speech *SPL*, E_s is the energy of the speech signal, and E_c is the energy of the equally long calibration signal. It is worth noting that Eq. (1) here yields the SPL value of a speech signal with linear weighting at a distance of 40 cm from the speaker's lips. In order to be able to compare the results of inverse filtering to SPL values, the analysis window of the SPL computation was adjusted to start from the same position as in inverse filtering. However, the window length in SPL computation was longer (100 ms) than that of inverse filtering.

Estimates of subglottal pressure (P_s) were computed from the oral-pressure measurements, a practice widely used in voice production studies. In this approach, the subglottal pressure of a vowel is estimated from the oral-pressure measurements during the stop consonants surrounding the vowel.

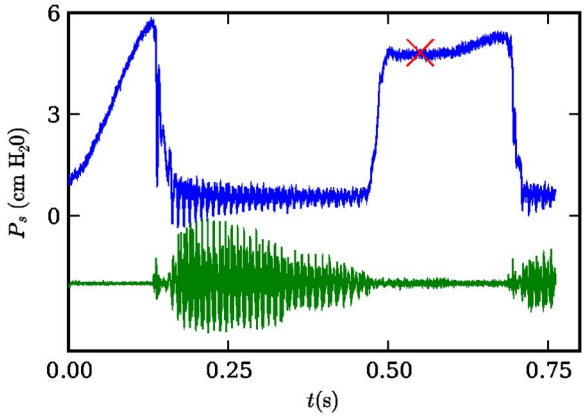

FIG. 2. (Color online) Example of the oral-pressure (upper graph) and the speech pressure wave form (lower graph) phonated by a male subject. Two magnified sections of the oral-pressure signal correspond to the /p/-occlusions of the /pa:p:a/ word. The second of these, at the instant indicated by a cross, was used for the computation of the subglottal pressure value.

If several steady-state pressure values are available, it is possible to use interpolation of consecutive oral-pressure values (e.g., Löfqvist *et al.*, 1982; Holmberg *et al.*, 1988; Hertegård *et al.*, 1995). In the present study, however, there were only two /p/-occlusions, the prevocalic and postvocalic /p/-occlusion of the /pa:p:a/ word, available in the digital signals stored in the computer. From these two measurements, the subglottal pressure was estimated by taking into account only the postvocalic /p/-occlusion because it was found to be more stable. The value of P_s was estimated by searching for the "knee" of the oral-pressure wave form during the postvocalic /p/-occlusion (see Fig. 2). The "knee" was determined subjectively by the experimenter by searching for the point in the rising phase of the oral-pressure signal at which the signal reached a plateau level (a similar procedure has been used, for example, in Hertegård *et al.*, 1995).

D. Amplitude quotient as a function of the negative peak amplitude of the glottal flow derivative

In the quantification of the time-based features of the glottal flow it has become accepted that these are computed by measuring the *time intervals* between certain events such as glottal opening and closure as well as the instant of the maximal flow (Holmberg *et al.*, 1988; Cummings and Clements, 1995; Sulter and Wit, 1996; Vilkman *et al.*, 1997). However, it is also possible to measure time-domain features of the glottal closing phase using the *amplitude-domain* values extracted from the glottal flow and its first derivative. This is based on the voice source parametrization schemes developed both independently and in parallel by Fant and his co-authors (Fant and Lin, 1988; Fant *et al.*, 1994; Fant 1995, 1997) and Alku and Vilkman (Alku and Vilkman, 1996a, 1996b; Alku *et al.*, 2002). In these studies, the application of the ratio between the peak-to-peak amplitude of the glottal flow and the negative peak amplitude of the flow derivative was analyzed in the parametrization of the glottal source. This ratio was shown by Fant and his coauthors to yield "a measure of effective decay time of the glottal flow pulse" and it was initially used as a method to reduce the number of

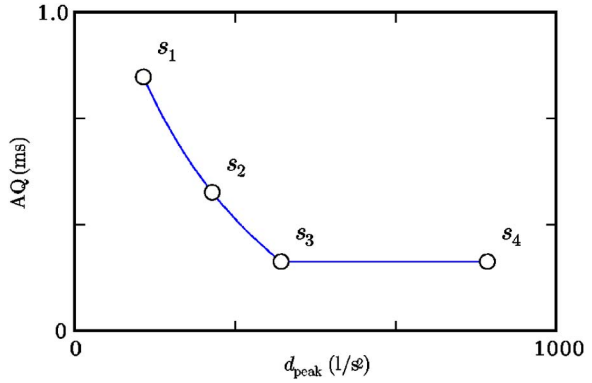

FIG. 3. (Color online) Illusory behavior of amplitude quotient (AQ) as a function of the negative peak amplitude of the flow derivative (d_{peak}); both quantities are expressed on linear scales using arbitrary values on the ordinate and abscissa. Four speech samples (s_1,s_2,s_3,s_4) were created by increasing vocal intensity. Increasing intensity from s_1 to s_3 was carried out by shortening the length of the glottal closing phase, which implies that the value of AQ decreases when d_{peak} is raised. Increasing intensity from s_3 to s_4, however, was achieved by a multiplication of the ac flow of the glottal pulse, which implies that the value of AQ remains constant when d_{peak} is raised.

the LF parameters in modeling the glottal source (Fant *et al.*, 1994; Fant 1995, 1997). The ratio between the two amplitude domain quantities is named the amplitude quotient (AQ) and its normalized version (with respect to the length of the fundamental period) is called the normalized amplitude quotient (NAQ) (Alku *et al.*, 2002). Using the notations given in Fig. 1, the definition of AQ is as follows:[3]

$$\mathrm{AQ} = \frac{f_{\mathrm{ac}}}{d_{\mathrm{peak}}}. \tag{2}$$

It has been shown that AQ has the following two important features (Alku *et al.*, 2002; Bäckström *et al.*, 2002; Gobl and NiChasaide, 2003). First, AQ is a time-domain quantity that correlates closely with the length of the glottal closing phase, but is always smaller than the true closing phase (except for the nonrealistic triangular-shaped flow, for which AQ becomes equal to the length of the closing phase). Second, computation of AQ is straightforward because it does not involve the extraction of the time instant of glottal closure. Hence, the quantification of the time-based features of the glottal closing phase with AQ (or with NAQ) is more robust against distortion such as the formant ripple present in glottal flows estimated by inverse filtering.

In our previous Studies, AQ (and NAQ) has been used in the quantification of the glottal flow when, for example, the phonation type is changed (Alku and Vilkman, 1996a, b) or as a measure of perceived phonatory pressedness in singing (Sundberg *et al.*, 2004; Björkner *et al.*, in press). Instead of treating AQ as such, the present study introduces a new application for AQ especially well suited for the analysis of intensity regulation. This new means of exploiting AQ is based on a two-dimensional presentation shown in a schematic form in Fig. 3, where AQ (y axis, linear scale) is plotted against d_{peak} (x axis, also on a linear scale). This straightforward presentation will demonstrate how changing d_{peak} which takes place in intensity regulation, will affect AQ in different ranges of d_{peak}.

Let us assume that when an illusory speaker repeats a vowel sound several times, gradually increasing the vocal intensity after each phonation, the corresponding values of d_{peak} and AQ of each speech sample will result as depicted in the two-dimension presentation, shown in Fig. 3. Keeping in mind that SPL has a strong positive correlation with d_{peak} (Gauffin and Sundberg, 1989), it is obvious that the first speech sample, depicted by s_1 in Fig. 3, with the lowest vocal intensity has a small value of d_{peak}. Moreover, it is likely (e.g., Holmberg *et al.*, 1988) that the speaker has used a rounded glottal pulse with gradual opening and closing in the production of this speech sample and, consequently, the length of the glottal closing phase is extended. Given the strong correlation between the length of the glottal closing phase and AQ (Alku *et al.*, 2002), this also implies that the first speech sample has a large value of AQ. The location of the next speech sample, with slightly larger vocal intensity (depicted by s_2 in Fig. 3), is characterized by a larger value of d_{peak} and a smaller value AQ, provided that the intensity increase was achieved by a reduction of the length of the glottal closing phase. Consequently, in this simplified schematic presentation, one would expect that the speech samples of increasing vocal intensity will follow a decreasing function as shown in Fig. 3. According to the definition of AQ [Eq. (2)] the prerequisite for this decrease demands that the increase of d_{peak} [denominator in Eq. (2)] be larger than the increase of f_{ac} [nominator in Eq. (2)]. More specifically, if we also assume that the increase of intensity is achieved by keeping the ac flow constant and by enlarging d_{peak} merely by affecting the shape of the glottal closing phase, the decreasing function between s_1 and s_2 in Fig. 3 will be a hyperbola. [This can be easily seen in Eq. (2), which shows that AQ becomes proportional to $1/d_{peak}$ when f_{ac} is a constant.] Let us continue the simplified example by assuming that after the production of the next sample, depicted by s_3 in Fig. 3, the speaker abruptly changes the intensity regulation strategy so that the length of the glottal closing phase is no longer shortened, but the vocal intensity is still to be raised. In other words, the illusory speaker starts to produce louder speech sounds by amplifying only the amplitude of the flow pulse. Since a (pure) multiplication of a signal with a constant corresponds to multiplying the derivative of the signal with the same constant, it is clear, according to Eq. (2) that the value of AQ will not be affected in this case. In Fig. 3, this implies that the new speech sample, depicted by s_4, has a larger value of d_{peak} than the previous sample, but (exactly) the same value of AQ. In other words, the function between AQ and d_{peak} changes from a hyperbola into a horizontal line between s_3 and s_4.

Even though the above-noted example is illusory, it can be used to analyze the intensity regulation of natural speech. In particular, when speech samples of gradually increasing intensity are expressed in the AQ-d_{peak} presentation, with this scheme it is possible to demonstrate how a speaker's means of increasing his or her vocal intensity changes from affecting the shape of the glottal closing phase to the strategy based on amplifying the flow signal magnitude but keeping the pulse shape more or less constant. In the next section,

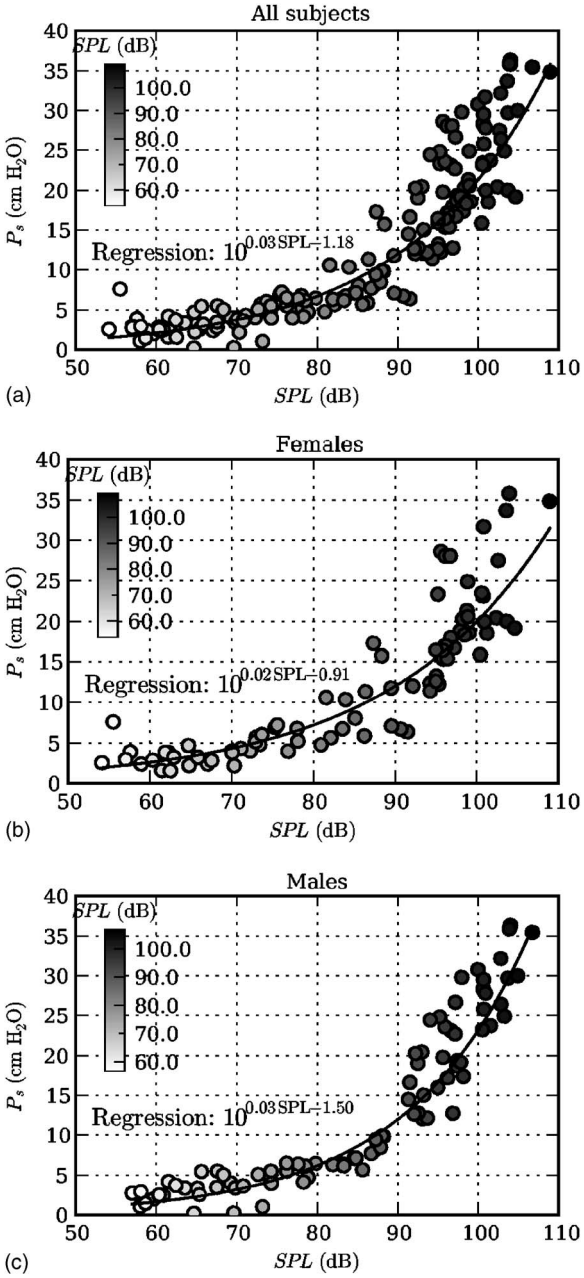

FIG. 4. Subglottal pressure (P_s) as a function of sound pressure level (SPL). Each circle denotes a speech sample whose SPL value is also expressed on a grey scale. Optimal exponential function, fitted by the regression analysis to the data, is shown as a continuous curve. (a) All speakers (n=10), (b) female speakers (n=5), (c) male speakers (n=5).

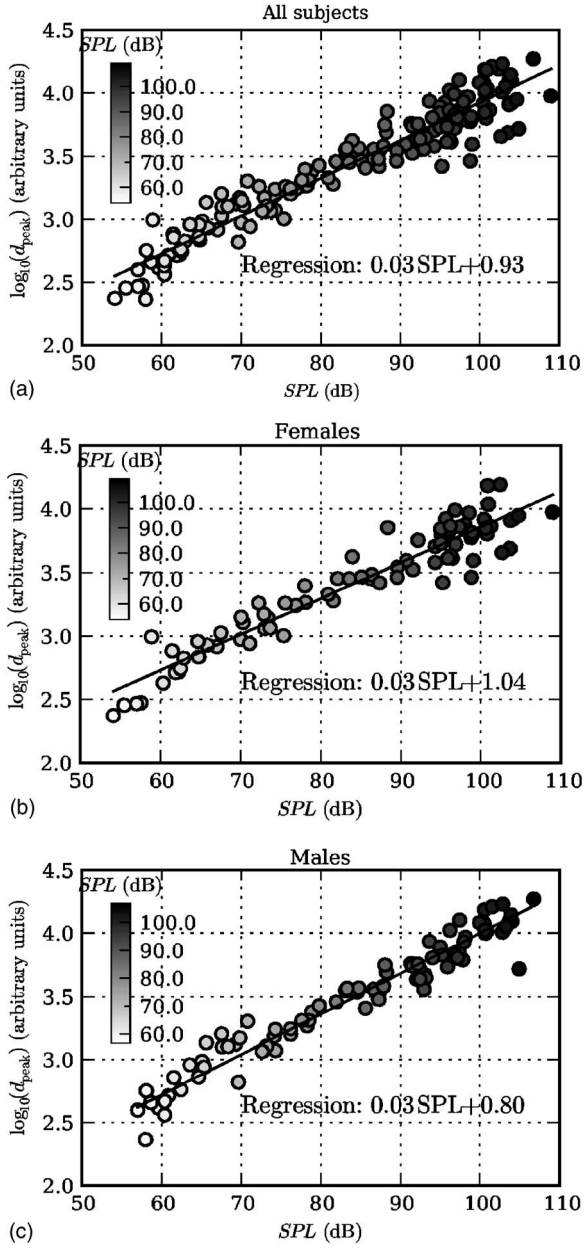

FIG. 5. Negative peak amplitude of the glottal flow derivative (d_{peak}) as a function of SPL. Each circle denotes a speech sample whose SPL value is also expressed on a grey scale. Optimal linear function, fitted by the regression analysis to the data, is shown as a continuous line. (a) All speakers (n=10), (b) female speakers (n=5), (c) male speakers (n=5).

this approach will be used together with other sources of information (subglottal pressure and SPL) extracted from natural speech samples.

III. RESULTS

Since the speaking task in the present study was to create voices of increasing intensity, the data obtained are presented in this section by expressing every sample with a grey scale denoting the SPL value of the sound (see grey scale bar in Figs. 4–6). The data are depicted separately for female and male speakers but also by combining the two genders sexes. The presentation of the results comprises four stages, corresponding to Figs. 4–7, respectively. The reasons for this kind presentation are as follows. First, since subglottal pressure is known to be one of the key parameters underlying intensity regulation (Stevens, 1977), it is reasonable to present the behavior of P_s as a function of SPL which was the parameter that the subjects controlled in the recordings. The data obtained in these analyses are shown in Fig. 4. Second, the negative peak amplitude of the flow derivative is expressed (on a logarithmic scale) as a function of SPL (Fig. 5) in order to demonstrate how the well-known, strong correlation of d_{peak} and SPL (Gauffin and Sundberg, 1989) was reflected in the speech samples of the present study characterized by substantial dynamics in sound pressure level values. Third, the data are presented by using the proposed

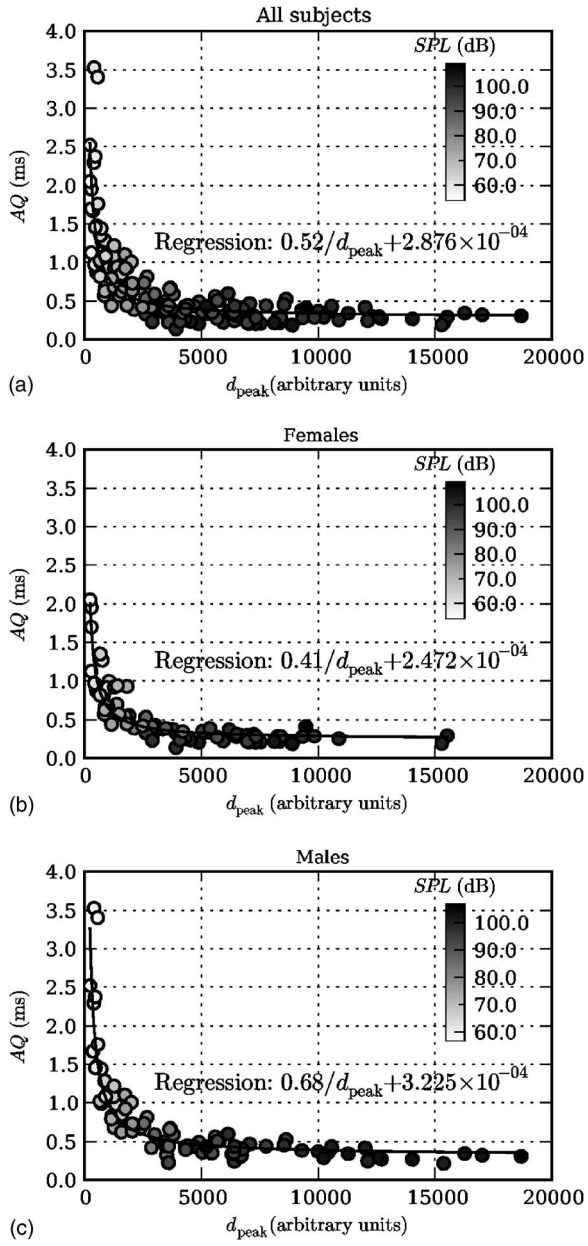

FIG. 6. AQ as a function of the negative peak amplitude of the glottal flow derivative (d_{peak}). AQ is a measure for the glottal closing phase length and it is defined according to Eq. (2) from two amplitude-domain quantities, the peak-to-peak flow, and the negative peak amplitude of the glottal flow derivative. Each circle denotes a speech sample whose SPL value is also expressed on a grey scale. Optimal hyperbolic function, fitted by the regression analysis to the data, is shown as a continuous curve. (a) All speakers (n=10), (b) female speakers (n=5), (c) male speakers (n=5).

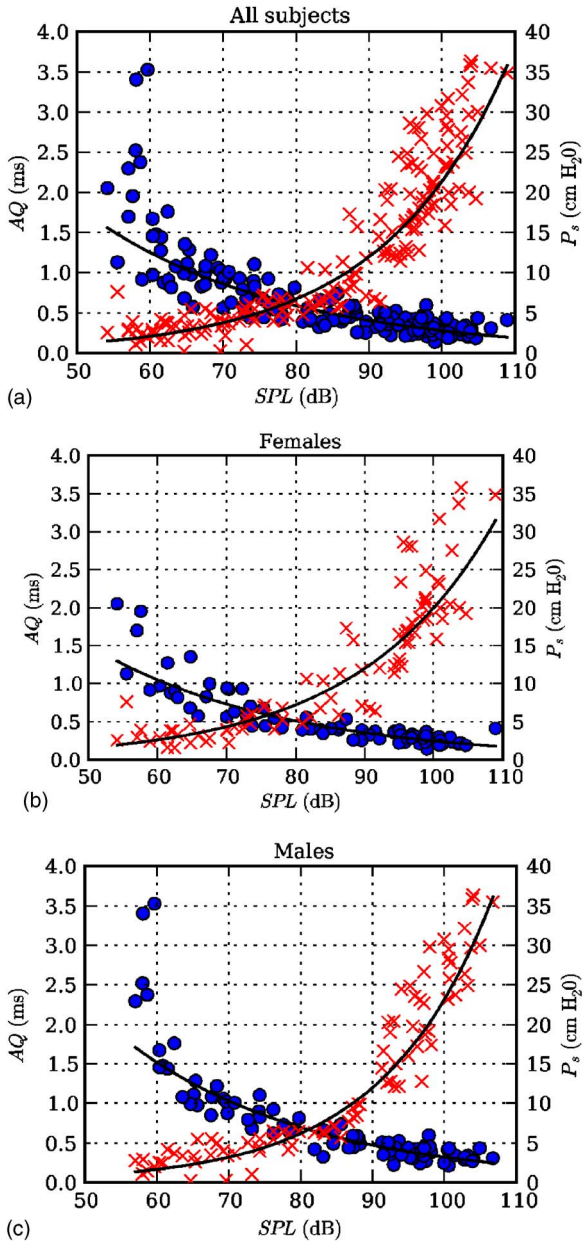

FIG. 7. (Color online) AQ (circles) and subglottal pressure (P_s, crosses) as a function of SPL. Optimal exponential functions, fitted by the regression analysis to AQ and P_s values, are shown by descending and ascending curves, respectively. (a) All speakers (n=10), (b) female speakers (n=5), (c) male speakers (n=5).

AQ-d_{peak} relationship in Fig. 6. Finally, Fig. 7 shows a combinatory expression of both AQ and P_s as a function of SPL in order to demonstrate how these two distinct features underlying intensity regulation behaved as a function of SPL.

The range of SPL values produced by males[4] (57–111 dB) was almost the same as that of females (54–109 dB). As expected, based on previous studies (e.g., Van den Berg, 1956; Ladefoged and McKinney, 1963), subglottal pressure increased when SPL was raised. The lowest pressure values measured equaled 1.6 cm H_2O and 1.1 cm H_2O for male and female subjects, respectively. The largest P_s values of males and females equaled 35.8 cm H_2O and 36.3 cm H_2O, respectively. It is worth noting that the range of P_s values measured in the present study is considerably larger than in many previous studies, in which glottal flow characteristics underlying intensity regulation have been analyzed. The range of P_s was 3.3–15.4 cm H_2O for males and 3.2–13.1 cm H_2O for females in the study by Holmberg *et al.* (1988). In the study by Södersten *et al.* (1995), in which only female voices were analyzed, the range of P_s was 3.2–20.4 cm H_2O.

When the subglottal pressure is plotted against the sound pressure level the data points appear to follow an exponentially rising curve. Figure 4 shows the data scatterplot together with an exponential function that was optimally fit to the data by using regression analysis. In the log-transformed

domain, into which the regression line was fitted, the correlation coefficient of SPL and log-transformed P_s was 0.893 (for all subjects), indicating a very large correlation between the subglottal pressure and the sound pressure level.

The strong correlation of SPL and the negative peak of the glottal flow derivative, as demonstrated previously in several studies (e.g., Gauffin and Sundberg, 1989), is supported by the current results as shown by the plot of log-transformed d_{peak} versus SPL depicted in Fig. 5. The correlation of SPL, and log-transformed d_{peak} is also high with a correlation coefficient value of 0.959 for all subjects. The close correlation of d_{peak} and SPL is further emphasized in Fig. 6, which shows the AQ parameter values as a function of d_{peak}: the distribution of the data point value in the grey scale closely follows that of the SPL scale.

Figure 6 illustrates the speech samples using the proposed AQ-d_{peak} graph. The data depicted in Fig. 6 follow the schematic trends discussed, using the hypothetical speaker, in Sec. II D: the value of AQ was largest for the voices of low SPL, but it started to decrease rapidly when the vocal intensity was increased (i.e., when d_{peak} rose). This decline of AQ, however, soon began to approach a saturation point after which there was only a minor change in the parameter value even though d_{peak} rose considerably. This behavior is illustrated in Fig. 6 by the regression curve fit to the data. The constant in the regression formula indicates that while SPL (and therefore, also the value of d_{peak}) was increased, the average value of AQ asymptotically approached 0.2877 ± 0.05290 ms. This value may be considered the average lower limit of AQ in intensity regulation. Furthermore, the curve indicates that at low SPL values, vocal intensity was dominantly controlled by AQ variation.

The different control strategies of vocal intensity for the voices of low and high SPL are further illustrated in Fig. 7, in which both the AQ and P_s values are shown in the same plot. In general, the value of AQ decreased when vocal intensity increased. This behavior is feasible because of two results already shown in previous studies: First, there is a strong correlation between AQ and the length of the glottal closing phase (Alku *et al.*, 2002) and, second, there are many studies in which the shortening of the glottal closing phase coinciding with the raising of the intensity has been reported (e.g., Holmberg *et al.*, 1988). Correspondingly, above approximately 85 dB, P_s changed much more rapidly than AQ, suggesting that in that region the SPL changes were mainly caused by changes in the subglottal pressure. In the intermediate zone, 70–85 dB, both AQ and P_s affected the SPL equally.

The gender sex differences of the above-mentioned curves were also assessed. By plotting subglottal pressures against SPL values for females and males [Figs. 4(b) and 4(c), respectively], the statistical significance of the regression line differences was examined by comparing full and reduced ANCOVA models. The comparison indicated that while there were no significant gender sex differences in the intercept term, the slope did differ significantly ($p=0.0013$). Thus, it is suggested that the subglottal pressure rises more rapidly as a function of SPL for males than for females. When $\log(d_{peak})$ is plotted against SPL, as shown in Figs. 5(b) and 5(c) for females and males, respectively, the analysis of ANCOVA models indicates that there was a statistically significant difference in the intercept term ($p < 2 \cdot 10^{-16}$), indicating that at a given SPL value, female voices exhibited larger d_{peak} values than males. Even the regression slopes differed significantly ($p=0.0048$), although this effect was not as strong as the intercept. When AQ is plotted against the d_{peak} values [Figs. 6(b) and 6(c) for females and males, respectively], the regression coefficients indicate that the level of the horizontal asymptote of the hyperbola was higher for males, and that the scaling factor of the hyperbola was higher for males than for females as well. The scaling factor value differences are also clearly visible in Figs. 7(b) and 7(c), which show AQ and P_s plotted against the SPL values. In the lower SPL range, AQ values declined more rapidly for males than for females. The significance of the gender sex differences in the hyperbolas was examined by calculating the difference between male data points and the female regression curve, and then by fitting another hyperbola to the acquired cross-residue. The results indicated that there were significant differences both in the k coefficient ($p < 2 \cdot 10^{-16}$) and in the level of the horizontal asymptote c ($p < 2 \cdot 10^{-16}$).

IV. DISCUSSION

Since the publication of the classic studies by Isshiki (Isshiki, 1964, 1965), there have been various investigations on respiratory and laryngeal mechanisms underlying regulation of vocal intensity. Respiratory mechanisms can be examined by either directly measuring the respiratory system or by analyzing respiratory activity using subglottal pressure (Stathopoulos and Sapienza, 1993a). Laryngeal means to control vocal intensity have been typically performed by using an inverse filtering approach in which the estimated glottal flow is quantified in terms of its amplitude-domain features, time-domain features, or both (e.g., Holmberg *et al.*, 1988). Both the respiratory and laryngeal mechanisms have been studied, based mostly on speaking tasks where intensity is varied across a few categories, typically three, namely soft, normal, and loud phonation.

This study proposed a new approach for the analysis of intensity regulation in which a time-domain measure of the glottal flow, the amplitude quotient, is presented as a function of the negative peak amplitude of the flow derivative. The resulting two-dimensional graph, the AQ-d_{peak} presentation, was used in the analysis of the glottal function of voices that varied from extremely soft to very loud. In addition to the proposed AQ-d_{peak} presentation, two conventional measurements, the subglottal pressure and the sound pressure level, were used. The extensive dynamics in both of these measurements, approximately 35 cm H_2O for P_s and 55 dB for SPL, indicate that the speakers took advantage of different mechanisms of intensity regulation when performing the speaking task requested. It is of special interest to note that for the softest voice samples, that is, on the lower SPL range between approximately 55 and 70 dB, the increase of subglottal pressure was very modest even though the SPL values changed by almost 15 dB. This indicates that there must

have been other means to vary the vocal intensity. However, for loud speech samples, that is, on the higher SPL range between approximately 95 and 110 dB, P_s rose very rapidly together with the SPL increase, suggesting that for these voice samples, raising the subglottal pressure may become the dominant way to increase the vocal intensity.

In the production of real speech, gradually increasing in intensity, it is unnatural to change abruptly from laryngeal means to respiratory mechanisms. Instead, speakers will most likely start regulating intensity of soft samples mostly by taking advantage of laryngeal means which then will be gradually accompanied by respiratory mechanisms when louder samples are to be produced. In the production of the loudest samples, the regulation is mostly dominated by the respiratory mechanisms. In the present study, this phenomenon was described by the AQ-d_{peak} graph as the convergence of the speech samples of increasing intensity toward an asymptote. This asymptote, available with the help of the proposed presentation, implies that there is a (theoretical) maximum limit of pressedness in intensity regulation. Hence, the presentation of speech samples of different intensity levels on the AQ-d_{peak} graph makes it possible to quantify how control mechanisms underlying regulation of vocal intensity change gradually from laryngeal to respiratory means.

In the study by Holmberg *et al.* (1988), the glottal function was addressed in three intensity categories (soft, normal, and loud) by using a wide range of parameters. The speech data of their study consisted of a short /pæ/ syllable produced in a string of five repetitions. The authors speculated that syllable productions in soft, normal, and loud categories might reflect the use of three different "vocal modes" and therefore they might represent intensity regulation conditions that are not compatible with those used in the production of sustained vowels. The authors of the present study agree with this speculation but, based on the results obtained in this research, we argue that the phonations in distinct "vocal modes" could be explained rather by the use of few intensity categories than by the use of syllable productions. Hence, if intensity regulation is studied over several phonations of gradually increasing SPL values, which was the case in the present study in which every subject produced on average 17 voice samples of different SPL values, it is unlikely that speakers can adapt a special "vocal mode" in each production. Therefore, speech samples analyzed in the present investigation might better reflect a continuous changing of the vocal function from the low intensity voice production to the generation of high intensity speech.

Previous studies on vocal intensity regulation have shown that, as a general trend, the length of the glottal closing phase becomes shorter when intensity rises (e.g., Holmberg *et al.*, 1988). This overall behavior was also corroborated by the present study as indicated by Fig. 7, which shows that the AQ values decrease as a function of SPL. Gender sex differences, however, appeared in the changing AQ when intensity was raised. The present study indicated that the horizontal asymptote level of the AQ-d_{peak} graph was significantly higher for males. In addition, the steepness of the graph was also significantly sharper for males as compared to females. Both of these two observations reflect the physical differences in the vocal fold length between genders sex, which results, in general, in a longer closing phase duration, that is, a larger AQ value, in male glottal pulses than in females. The more abrupt steepness AQ-d_{peak} graphs for males also implies that the male voice production mechanism is able to generate glottal flow pulses in low intensity phonation that have a long closing phase, that is, a large value of AQ, and a small value of d_{peak}. Vocal intensity increase for this kind of glottal pulses can be effectively controlled by laryngeal means resulting in a great decrease in the glottal closing phase. Consequently, the AQ-d_{peak} graph will show a steep decrease in particular for male voices at the lowest SPL range.

Comparing gender sex differences found in the present study to those reported in previous ones is somewhat problematic because of the following issues. First, the present study applied a speaking task in which the intensity was increased gradually by 5 dB steps whereas the majority of the previous investigations have applied speaking tasks comprising only few discrete loudness categories. Second, the extensive dynamic range in the SPL values of the present study implies that the change from low-intensity voice productions to high-intensity phonations might have been accomplished by the use of vocal strategies which are different from those used in studies involving considerably smaller SPL dynamics. Third, and most important, most of the previous studies have used glottal source parametrization methods based on normalized time-based values, such as the closing quotient (ClQ), that is, the ratio between the glottal closing phase duration and the length of the fundamental period (e.g., Holmberg *et al.*, 1988; Sulter and Wit, 1996). The present investigation, however, used the AQ measurement, which quantifies the glottal closing phase in absolute time units. It is, therefore, difficult to gauge how much changes in the glottal closing phase characteristics reported in previous investigations are due to changes in the glottal closing phase length, that is, the numerator of ClQ, and how much they reflect the change of the fundamental period, that is, the denominator of ClQ.

Despite these differences, explaining how the gender sex differences demonstrated by the AQ-d_{peak} of the present study are related to the previous ClQ-based investigations on vocal intensity is feasible. In the study by Holmberg *et al.* (1988), it was found that male voices showed a significantly smaller ClQ value in normal and loud phonation than females. However, there was no significant male-female difference in ClQ for soft voices. We may speculate that these results reported by the above-mentioned study on ClQ are actually in line with the results of the present study even though the relationship between the two is perhaps not the most obvious one. It is, for example, possible that in producing soft voices both the female and male speakers in that study might have used the same "vocal mode" resulting in glottal pulses that are of similar shapes, but of different time-lengths, for the two genders sexes. [A stylized illustration is provided in Fig. 10, p. 519, in Holmberg *et al.* (1988)]. Parametrization of this kind of glottal pulse will in fact result in small ClQ differences between males and females, as reported in Holmberg *et al.* (1988), but, importantly, in larger

AQ values in male voices than in female speech as, indeed, was indicated by the AQ-d_{peak} graphs of low-intensity voices in the present study. Moreover, it can be argued that the speakers in the study by Holmberg *et al.* (1988) most likely used means other than respiratory ones when changing vocal intensity from soft to normal speech, because if this intensity change was based solely on the respiratory mechanism, the same "vocal mode" would have been used by both males and females in normal loudness as well. Consequently, one would not have expected to find a gender sex difference in ClQ in normal loudness either. However, the existence of the gender sex difference in normal and loud phonations in the study by Holmberg *et al.* (1988) indicates that the intensity increase from soft voices was accomplished by means other than respiratory; that is, most likely by changes in the time-based characteristics of the glottal closing phase. In the present study, this indicates the occurrence of voice samples on a steep decreasing portion of the AQ-d_{peak} graphs when intensity is increased at the lowest part of the SPL range. Finally, a possible explanation why ClQ values of males in the study by Holmberg *et al.* (1988) were *smaller* than those of females in normal and loud speech while the horizontal level of the AQ-d_{peak} graphs of males in the present study were *larger* than that of females is the difference in the normalization of the time-based parameters involved. In other words, it is possible that if intensity increase in female and male voices is accomplished by the reduction of both the glottal closing phase and the fundamental period, but if the latter happens more rapidly for males, a smaller ClQ value is to be expected for them, as reported in Holmberg *et al.* (1988). However, since the absolute length of the closing phase is still typically larger in male speech, it is understandable why the proposed AQ-d_{peak} graph showed a higher horizontal asymptote level for males than for females.

V. CONCLUSIONS

Regulation of vocal intensity was analyzed by means of a new method, the AQ-d_{peak} graph, from voices whose SPL varied from extremely low to very high. When vocal intensity was increased, the speech samples first showed a rapidly decreasing trend when expressed on the proposed AQ-d_{peak} graph. The hypothetical correspondence of this behavior is a hyperbola, indicating that the speakers have mainly manipulated the length of the glottal closing phase in the regulation of vocal intensity. When intensity was further raised, the location of the speech samples on the AQ-d_{peak} converged toward a horizontal line, the asymptote of the hyperbola. This indicates that the decrease of AQ starts to diminish even though d_{peak} continues to rise which, in turn, implies that the speakers have started to increase their vocal intensity by amplifying the ac flow of the glottal pulse.

When interpreted according to Isshiki (1964, 1965), the behavior of the AQ-d_{peak} graph, as summarized earlier, implies that the intensity regulation strategy changes from laryngeal means, represented by the rapidly decreasing part of the hyperbola, to respiratory mechanisms, represented by the horizontal asymptote. The behavior of the AQ-d_{peak} graph in the speech samples of the current study was in line with results reported in several other investigations on intensity regulation in showing that increasing vocal intensity corresponds typically to the decreasing of the glottal closing phase, reflected in the current study by AQ, and to the increasing of the negative peak amplitude of the glottal flow derivative. In contrast to many previous studies, however, the current research proposes a new means to visualize the function of voice production, which might be of use in investigating intensity regulation of speech and could supplement existing voice production analysis tools such as the phonetogram. The proposed presentation is easy to implement because the only information needed is the glottal flow wave form estimated by inverse-filtering the acoustic speech pressure signal.

ACKNOWLEDGMENTS

This work was supported by the Academy of Finland (Project No. 200859), by the European Community's Human Potential Programme under Contract No. HPRN-CT-2002-00276 [HOARSE-network], and by the KAUTE foundation.

[1]Instead of using the term "subglottal pressure" Titze frequently uses the term "lung pressure" to refer to the mean subglottal pressure as estimated during oral occlusion (Fant, 1997).

[2]The energy of a digital signal is computed as the (infinite) sum of squares of the signal samples (Oppenheim and Schafer, 1975).

[3]It should be noticed in Eq. (2) that the domain of AQ is time, because this quotient is defined as a ratio between a flow value and a value of the *time derivative* of the flow. If inverse filtering is based on digital signal processing, which is typical in voice source analysis today, the values of f_{ac} and d_{peak} usually extracted from discrete-time wave forms that are expressed using integer numbers as the time variable. In this case, AQ in Eq. (2) needs to be divided by the sampling frequency in order to express the parameter value in seconds.

[4]Measurement of subglottal pressure failed for some of the high SPL speech samples produced by male subjects due to clipping of the intraoral pressure waveforms in the analog-to-digital conversion. Therefore, these phonations could not be included in those analyses in which subglottal pressure values are required, but they were used in all other analyses.

Åkerlund, L., Gramming, P., and Sundberg, J. (**1992**). "Phonetogram and averages of sound pressure levels and fundamental frequencies of speech: Comparison between female singers and nonsingers," J. Voice **6**, 55–63.

Alku, P. (**1992**). "Glottal wave analysis with Pitch Synchronous Iterative Adaptive Inverse Filtering," Speech Commun. **11**, 109–118.

Alku, P., Bäckström, T., and Vilkman, E. (**2002**). "Normalized amplitude quotient for parameterization of the glottal flow," J. Acoust. Soc. Am. **112**, 701–710.

Alku, P., and Vilkman, E. (**1994**). "Estimation of the glottal pulseform based on discrete all-pole modeling," in Proceedings of the International Conference on Spoken Language Processing, Yokohama, Japan, pp. 1619–1622.

Alku, P., and Vilkman, E. (**1996a**). "A comparison of glottal voice source quantification parameters in breathy, normal, and pressed phonation of female and male speakers," Folia Phoniatr Logop **48**, 240–254.

Alku, P., and Vilkman, E. (**1996b**). "Amplitude domain quotient for characterization of the glottal volume velocity waveform estimated by inverse filtering," Speech Commun. **18**, 131–138.

Alku, P., Vilkman, E., and Laukkanen, A.-M. (**1998**). "Estimation of amplitude features of the glottal flow by inverse filtering speech pressure signals," Speech Commun. **24**, 123–132.

Alku, P., Vintturi, J., and Vilkman, E. (**1999**). "On the linearity of the relationship between the sound pressure level and the negative peak amplitude of the differentiated glottal flow in vowel production," Speech Commun. **28**, 269–281.

Alku, P., Vintturi, J., and Vilkman, E. (**2002**). "Measuring the effect of fundamental frequency raising as a strategy for increasing vocal intensity in soft, normal and loud phonation," Speech Commun. **38**, 321–334.

Björkner, E., Sundberg, J., and Alku, P. (in press). "Subglottal pressure and normalized amplitude quotient variation in classically trained baritone singers," Logoped. Phoniatr. Vocol.
Bouhuys, A., Mead, J., Proctor, D., and Stevens, K. (**1968**). "Pressure-flow events during singing," Ann. N.Y. Acad. Sci. **155**, 165–176.
Bäckström, T., Alku, P., and Vilkman, E. (**2002**). "Time-domain parameterization of the closing phase of glottal airflow waveform from voices over a large intensity range," IEEE Trans. Speech Audio Process. **10**, 186–192.
Coleman, R. F. (**1993**). "Sources of variation in phonetograms," J. Voice **7**, 1–14.
Coleman, R. F., Mabis, J. H., and Hinson, J. K. (**1977**). "Fundamental frequency-sound pressure level profiles of adult male and female voices," J. Speech Hear. Res. **20**, 197–204.
Cummings, K. E., and Clements, M. A. (**1995**). "Analysis of the glottal excitation of emotionally styled and stressed speech," J. Acoust. Soc. Am. **98**, 88–98.
Damste, H. (**1970**). "The phonetogram," Pract. Otorhinolaryngol. (Basel) **32**, 185–187.
Dromey, C., Stathopoulos, E., and Sapienza, C. (**1992**). "Glottal airflow and electroglottographic measures of vocal function at multiple intensities," J. Voice **6**, 44–54.
El-Jaroudi, A., and Makhoul, J. (**1991**). "Discrete all-pole modeling," IEEE Trans. Acoust., Speech, Signal Process. **39**, 411–423.
Fant, G. (1982). "Preliminaries to analysis of the human voice source," STL-QPSR 4, Dept. of Speech Communication and Music Acoustics, Royal Institute of Technology, Stockholm, pp. 1–27.
Fant, G. (**1993**). "Some problems in voice source analysis," Speech Commun. **13**, 7–22.
Fant, G. (1995). "The LF-model revisited. Transformations and frequency domain analysis," STL-QPSR 2-3, Dept. of Speech Communication and Music Acoustics, Royal Institute of Technology, Stockholm, pp. 119–156.
Fant, G. (**1997**). "The voice source in connected speech," Speech Commun. **22**, 125–139.
Fant, G., Kruckenberg, A., Liljencrants, J., and Båvegård, M. (1994). "Voice source parameters in continuous speech. Transformation of LF-parameters," in Proceedings of the International Conference on Spoken Language Processing, Yokohama, Japan, pp. 1451–1454.
Fant, G., and Lin, Q. (1988). "Frequency domain interpretation and derivation of glottal flow parameters," STL-QPSR 2-3, Dept. of Speech Communication and Music Acoustics, Royal Institute of Technology, Stockholm, pp. 1–21.
Finnegan, E., Luschei, E., and Hoffman, H. (**2000**). "Modulations in respiratory and laryngeal activity associated with changes in vocal intensity during speech," J. Speech Lang. Hear. Res. **43**, 934–950.
Gauffin, J., and Sundberg, J. (**1989**). "Spectral correlates of glottal voice source waveform characteristics," J. Speech Hear. Res. **32**, 556–565.
Gobl, C., and Ni Chasaide, A. (**2003**). "Amplitude-based voice source parameters for measuring voice quality," in Proceedings of the ISCA Workshop on Voice Quality: Functions, Analysis and Synthesis, Geneva, Switzerland, pp. 151–156.
Gramming, P., and Sundberg, J. (**1988**). "Spectrum factors relevant to phonetogram measurement," J. Acoust. Soc. Am. **83**, 2352–2360.
Gramming, P., Sundberg, J., Ternström, S., Leanderson, R., and Perkins, W. (**1988**). "Relationship between changes in voice pitch and loudness," J. Voice **2**, 118–126.
Hertegård, S., and Gauffin, J. (**1991**). "Insufficient vocal fold closure as studied by inverse filtering," in *Vocal Fold Physiology: Acoustics, Perceptual and Physiological Aspects of Voice Mechanisms*, edited by J. Gauffin and B. Hammarberg (Singular, San Diego), pp. 243–250.
Hertegård, S., Gauffin, J., and Lindestad, P-Å. (**1995**). "A comparison of subglottal and intraoral pressure measurements during phonation," J. Voice **9**, 149–155.
Hirano, M., Vennard, W., and Ohala, J. (**1970**). "Regulation of register, pitch and intensity of voice," Folia Phoniatr (Basel) **22**, 1–20.
Hodge, S., Colton, R., and Kelley, R. (**2001**). "Vocal intensity characteristics in normal and elderly speakers," J. Voice **7**, 503–511.
Holmberg, E., Hillman, R., and Perkell, J. (**1988**). "Glottal airflow and transglottal air pressure measurements for male and female speakers in soft, normal, and loud voice," J. Acoust. Soc. Am. **84**, 511–529.
Isshiki, N. (**1964**). "Regulatory mechanism of voice intensity variation," J. Speech Hear. Res. **7**, 17–29.
Isshiki, N. (**1965**). "Vocal intensity and air flow rate," Folia Phoniatr (Basel) **17**, 92–104.
Ladefoged, P., and McKinney, N. P. (**1963**). "Loudness, sound pressure, and subglottal pressure in speech," J. Acoust. Soc. Am. **35**, 454–460.
Löfqvist, A., Carlborg, B., and Kitzing, P. (**1982**). "Initial validation of an indirect measure of subglottal pressure during vowels," J. Acoust. Soc. Am. **72**, 633–635.
Makiyama, K., Yoshihashi, H., Mogitate, M., and Kida, A. (**2005**). "The role of adjustment of expiratory effort in the control of vocal intensity: Clinical assessment of phonatory function," Otolaryngol.-Head Neck Surg. **132**, 641–646.
Oppenheim, A., and Schafer, R. (**1975**). *Digital Signal Processing* (Prentice Hall, Englewood Cliffs, NJ).
Sapienza, C., and Stathopoulos, E. (**1994**). "Comparison of maximum flow declination rate: Children versus adults," J. Voice **8**, 240–247.
Sapienza, C., Stathopoulos, E., and Dromey, C. (**1998**). "Approximations of open quotient and speed quotient from glottal airflow and EGG waveforms: Effects of measurement criteria and sound pressure level," J. Voice **12**, 31–43.
Stathopoulos, E., and Sapienza, C. (**1993a**). "Respiratory and laryngeal function of women and men during vocal intensity variation," J. Speech Hear. Res. **36**, 64–75.
Stathopoulos, E., and Sapienza, C. (**1993b**). "Respiratory and laryngeal measures of children during vocal intensity variation," J. Acoust. Soc. Am. **94**, 2531–2543.
Stevens, K. N. (**1977**). "Physics of laryngeal behavior and larynx models," Phonetica **34**, 264–279.
Strik, H., and Boves, L. (**1992**). "Control of fundamental frequency, intensity and voice quality in speech," J. Phonetics **20**, 15–25.
Sulter, A., and Wit, H. (**1996**). "Glottal volume velocity waveform characteristics in subjects with and without vocal training, related to gender, sound intensity, fundamental frequency, and age," J. Acoust. Soc. Am. **100**, 3360–3373.
Sundberg, J., Fahlstedt, E., and Morell, A. (**2005**). "Effects on the glottal voice source of vocal loudness variation in untrained female and male voices," J. Acoust. Soc. Am. **117**, 879–885.
Sundberg, J., Thalen, M., Alku, P., and Vilkman, E. (**2004**). "Measuring perceived phonatory pressedness in singing from flow glottograms," J. Voice **18**, 56–62.
Sundberg, J., Titze, I., and Scherer, R. (**1993**). "Phonatory control in male singing: A study of the effects of subglottal pressure, fundamental frequency, and mode of phonation on the voice source," J. Voice **7**, 15–29.
Södersten, M., Hertegård, S., and Hammarberg, B. (**1995**). "Glottal closure, transglottal airflow, and voice quality in healthy middle-aged women," J. Voice **9**, 182–197.
Titze, I. (**1992a**). "Phonation threshold pressure: A missing link in glottal aerodynamics," J. Acoust. Soc. Am. **91**, 2926–2935.
Titze, I. (**1992b**). "Acoustic interpretation of the voice range profile (Phonetogram)," J. Speech Hear. Res. **35**, 21–43.
Titze, I. (**1994**). *Principles of Voice Production* (Prentice-Hall, Englewood Cliffs, NJ).
Titze, I., and Sundberg, J. (**1992**). "Vocal intensity in speakers and singers," J. Acoust. Soc. Am. **91**, 2936–2946.
Van den Berg, J. W. (**1956**). "Direct and indirect determination of the mean subglottic pressure," Folia Phoniatr. **8**, 1–24.
Vilkman, E., Lauri, E-R., Alku, P., Sala, E., and Sihvo, M. (**1997**). "Loading-changes in time-based parameters of glottal flow waveforms in different ergonomic conditions," Folia Phoniatr. **49**, 247–263.
Young, H. D., and Freedman, R. A. (**1996**). *University Physics* (Addison-Wesley, Reading, MA), p. 612.

Effects of language experience and stimulus complexity on the categorical perception of pitch direction

Yisheng Xu, Jackson T. Gandour,[a] and Alexander L. Francis
Department of Speech, Language, & Hearing Sciences, Purdue University, West Lafayette, Indiana 47907-2038

(Received 16 December 2005; revised 18 May 2006; accepted 19 May 2006)

Whether or not categorical perception results from the operation of a special, language-specific, speech mode remains controversial. In this cross-language (Mandarin Chinese, English) study of the categorical nature of tone perception, we compared native Mandarin and English speakers' perception of a physical continuum of fundamental frequency contours ranging from a level to rising tone in both Mandarin speech and a homologous (nonspeech) harmonic tone. This design permits us to evaluate the effect of language experience by comparing Chinese and English groups; to determine whether categorical perception is speech-specific or domain-general by comparing speech to nonspeech stimuli for both groups; and to examine whether categorical perception involves a separate categorical process, distinct from regions of sensory discontinuity, by comparing speech to nonspeech stimuli for English listeners. Results show evidence of strong categorical perception of speech stimuli for Chinese but not English listeners. Categorical perception of nonspeech stimuli was comparable to that for speech stimuli for Chinese but weaker for English listeners, and perception of nonspeech stimuli was more categorical for English listeners than was perception of speech stimuli. These findings lead us to adopt a memory-based, multistore model of perception in which categorization is domain-general but influenced by long-term categorical representations.
 [DOI: 10.1121/1.2213572]

PACS number(s): 43.71.−k, 43.71.An, 43.71.Hw [KEG] Pages: 1063–1074

I. INTRODUCTION

Categorical perception (CP) has been one of the most extensively studied phenomena in speech perception for nearly 50 years because it is believed to reflect some fundamental aspects of the processing of speech sounds (see Harnad, 1987, for an overview). Up to the present, the bulk of CP research has been directed to segmental features of speech, i.e., consonants and vowels. Though not without controversy, the consensus opinion has been that consonant features are perceived in a mostly categorical fashion whereas vowel features are not (e.g., Liberman *et al.*, 1957; Fry *et al.*, 1962). Recently there has been increasing interest in suprasegmental features of speech (e.g., pitch: Francis *et al.*, 2003; Hallé *et al.*, 2004). In this regard, *tone languages* are especially advantageous because contrasts in pitch height and/or direction are exploited to minimally distinguish lexical items (Gandour, 1978). Mandarin Chinese, for example, has four lexical tones: e.g., ma^1 "mother," ma^2 "hemp," ma^3 "horse," ma^4 "scold". These four tones can be described phonetically as high level, high rising, falling rising, and high falling, respectively (Howie, 1976).

Earlier research on the categorical nature of tone perception reveals the importance of pitch movement (level versus contour) and the influence of language experience (tonal versus nontonal). With respect to pitch movement, a continuum ranging from one (or more) level tone to another is not perceived categorically (Thai—Abramson, 1979; Cantonese—Francis *et al.*, 2003), whereas a continuum ranging from a high level tone to a high rising contour tone is perceived categorically (Mandarin—Wang, 1976; Cantonese—Francis *et al.*, 2003). Using a stimulus continuum ranging from a Mandarin Tone 2 (high rising) to a Tone 1 (high level), cross-language comparisons show that native speakers perceive this tonal contrast in a categorical manner but that speakers of a nontone language (English) do not (Wang, 1976). In a more recent cross-language CP study of lexical tones (Taiwan Mandarin—Hallé *et al.*, 2004), it is argued that there is a gradient in the degree of CP—as measured by the slope of identification curve, the peakedness of identification response time, and the peakedness of discrimination performance—that varies depending on a listener's degree of familiarity with lexical tones. Using three tonal continua (1 versus 2; 2 versus 4; 3 versus 4), their results show that Taiwanese listeners' perception of tones shows a higher degree of CP ("quasicategorical") than that of listeners of a nontone language (French). Despite their lack of familiarity with lexical tones, French listeners are still able to make their identification and discrimination judgments on the basis of psychophysical factors alone. Their theoretical explanation is based on a cross-linguistic model of speech perception, PAM, perceptual assimilation model (Best *et al.*, 2001). According to this account, lexical tones in Taiwanese are not necessarily difficult for French speakers to perceive, but they are perceived in a noncategorical manner because they are *not assimilable* to any phonemic unit of French, and thus do not invoke phonetic perception processes specific to French. This model essentially stems from a view that CP relies on a speech mode of perception based on native phoneme categories (Liberman *et al.*, 1967; Studdert-Kennedy *et al.*, 1970).

[a]Electronic mail: gandour@purdue.edu

Whether CP is restricted to a special speech mode is still a matter of controversy. Earlier data showed that CP occurs in synthetic speech stimuli but not in their spectrally rotated nonspeech correlates (Liberman *et al.*, 1961). Subsequently, CP has been reported for nonspeech continua as well. For example, CP has been observed using a noise-lead time continuum that contrasts the onset of a noise relative to a buzz (Miller *et al.*, 1976) and a tone onset time continuum that contrasts the relative onset time of two component tones (Pisoni, 1977). These findings demonstrate that it is the temporal order of two acoustic events which underlies the CP phenomenon rather than a mechanism unique to speech (e.g., voice onset time). By varying the amplitude rise time of simple sawtooth stimuli, CP has also been demonstrated with a pluck-bow continuum simulating the sounds of music instruments (Cutting and Rosner, 1974; Cutting, 1982). More recently, Mirman *et al.* (2004) compared the degree of CP between a nonspeech continuum employing a rapid-changing cue (amplitude rise time of noise) and another nonspeech continuum employing a steady-state cue (spectral notch center frequency of noise). They concluded that CP is more dependent on rapid-changing than steady-state acoustic cues, which correlates with differences in the degree of CP between stop consonants and static vowels. Another line of evidence supporting a domain-general view comes from the observations of CP in nonhuman animals (e.g., chinchilla: Kuhl and Miller, 1975; monkey: Kuhl and Padden, 1983) when they are presented with speech continua employing temporal-order or rapid-changing cues. Based on these findings, some researchers believe that CP may result from natural sensory discontinuities (Pastore *et al.*, 1977; Kuhl, 1981; Stevens, 1981). According to this hypothesis, the phoneme boundaries in speech simply occur at regions of heightened natural auditory sensitivities.

None of the major explanations of CP appears to be completely adequate on its own (Rosen and Howell, 1987). Some of these shortcomings may be attributed to issues of experimental design. In the extant literature, for example, CP studies have compared native to non-native language listeners and speech to nonspeech stimuli, but as far as we know, no previous study has attempted to incorporate both factors into a single experimental design. We argue that it is important to look at these two intersecting factors of the phenomenon concurrently in order to achieve a better understanding of CP. In this cross-language (Chinese, English) study of the categorical nature of tone perception in Mandarin Chinese, we include both variables: language group (native versus nonnative) and stimulus type (speech versus nonspeech). For the two language groups, one is comprised of native speakers of Mandarin, the other of native speakers of English who are unfamiliar with Mandarin or any other tone language. For the two stimulus types, we employ a physical continuum ranging from a high rising to high level tone in Mandarin in comparison to homologous harmonic tones. In an effort to equalize the stimuli between speech and nonspeech, we opted to use linear instead of curvilinear contours. Linear ramps commonly occur in nonspeech contexts but represent at best a crude approximation of natural speech tonal contours, and therefore are less likely to give any perceptual advantage to the native listeners. This experimental design permits us to evaluate the effect of language experience by comparing Chinese and English groups; to determine whether CP is speech-specific or domain-general by comparing speech to nonspeech stimuli for both Chinese and English listeners; and to examine whether CP involves a separate categorical process, over and above regions of sensory discontinuity, by comparing speech to nonspeech stimuli for English listeners. In so doing, we are led to develop a multistore model of CP. By adapting earlier multistore information processing models (e.g., Atkinson and Shiffrin, 1968; Cowan, 1988) as well as previous memory-based interpretations of CP (e.g., Pisoni, 1975; Macmillan, 1987), this new model enables us to provide a unified account of the CP phenomenon.

II. METHOD

A. Subjects

Thirty native speakers of Mandarin Chinese (13 males; 17 females) and thirty native speakers of American English (15 males; 15 females) participated in this experiment. The two groups were similar in age (Mean±s.d.: Chinese =27.5±2.9; English=23.2±4.3) and years of formal education (Mean±s.d.: Chinese=18.7±2.8; English=15.9±3.3). All participants exhibited normal hearing sensitivity (pure-tone air conduction thresholds of 20 dB HL or better in both ears at frequencies of 0.5, 1, 2, and 4 kHz). All Chinese listeners were from mainland China, and none had received any formal instruction in English until after the age of 11. No English listener had any previous exposure to Chinese or for that matter any other tone language. None of the participants, Chinese or English, had more than five years of formal musical training, and none had any recent musical training (within the past five years). All participants were paid for their participation. They gave informed consent in compliance with a protocol approved by the Institutional Review Board of Purdue University.

B. Stimuli

Two sets of stimuli were constructed for this experiment: speech (S) and nonspeech (NS) (Fig. 1). The speech stimuli were derived from the Mandarin syllable [i] with a high level tone (Tone 1: yi^1, "clothing") that was produced by a male native speaker. The nonspeech stimuli were harmonic tones that exhibited the same pitch, amplitude, and duration parameters as the speech stimuli. The speech and nonspeech stimuli differed from one another only in spectral components. Each set consisted of seven stimuli derived from the same pitch continuum ranging in equal steps from a *level* to a *rising* linear ramp.

The fundamental frequency (F_0) contours of the pitch continuum were modeled by seven linear functions:

$$f_i(t) = (f_2 - f_{1,i})t/d + f_{1,i}, \quad i = 1,2,\ldots,7. \tag{1}$$

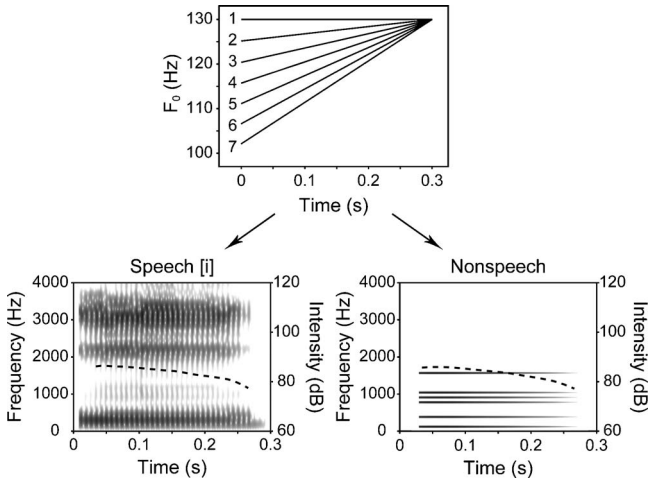

FIG. 1. Synthetic speech (Mandarin [i] syllables) and nonspeech (harmonic tones) stimuli based on the same F_0 continuum (top panel). The bottom-left panel shows a broadband spectrogram of the Step 1 speech stimulus. The bottom-right panel shows a narrowband spectrogram of its nonspeech homologue. Their intensity envelopes (dashed lines) are closely matched.

The constant d was the duration of the stimuli (0.3 s). The offset frequency (f_2) was fixed at 130 Hz. Onset frequencies ($f_{1,i}$) were separated on a psychoacoustic scale by an equal step size of 0.1200 ERB (equivalent rectangular bandwidth) (Table I). The conversions from frequency (f) in Hz to ERB-rate (E) in ERB and vice versa were based on Eq. (2) (Greenwood, 1961):

$$E = 16.7 \log_{10}(f/165.4 + 1),$$
$$f = 165.4(10^{E/16.7} - 1). \tag{2}$$

Using PRAAT software (Boersma and Weenink, 2003), speech stimuli were resynthesized from the Tone 1 natural speech template. Its duration was first scaled to 0.3 s. The F_0 contour of this speech template was then replaced with Eq. (1) by applying PSOLA (pitch-synchronous overlap and add) resynthesis (Valbret *et al.*, 1992). The two ends of the continuum, Step 1 and Step 7, were judged qualitatively to be good exemplars of Mandarin Tones 1 (yi^1, "clothing") and 2 (yi^2, "aunt"), respectively, by three Chinese listeners who did not participate in the experiment.

Nonspeech stimuli were composed of six equal-amplitude harmonics (1, 3, 6, 7, 8, 12) of the F_0 (cf. Francis and Ciocca, 2003). Harmonics 2, 4, 5, 9, 10, and 11 were omitted to increase perceptual dissimilarity with the speech stimuli. These harmonic tones were first created with:

TABLE I. Frequency (f) in Hz and ERB-rate (E) in ERB of the F_0 onset in each stimulus.

Step	f (Hz)	E (ERB)	Step size (Hz)	Step size (ERB)
1	130.00	4.2063	4.85	0.1200
2	125.15	4.0863	4.77	0.1200
3	120.38	3.9663	4.69	0.1200
4	115.70	3.8463	4.61	0.1200
5	111.08	3.7263	4.54	0.1200
6	106.55	3.6063	4.46	0.1200
7	102.08	3.4863		

$$y(t) = \frac{1}{6}\sum_{i=1}^{6} \sin 2\pi h_i[(f_2 - f_1)t/2d + f_1]t,$$
$$h_i = 1,3,6,7,8,12. \tag{3}$$

The resulting wave forms were then multiplied by the amplitude envelope of the speech template sample by sample, and peak normalized to the same intensity level.

For the practice tasks, speech and nonspeech stimuli were similarly constructed using a seven-step pitch continuum ranging from level to rising F_0 contours. However, the practice stimuli differed from the experimental stimuli in terms of both F_0 and spectral properties. F_0 offset frequency was set one octave higher (at 260 Hz) than that of the experimental stimuli. Despite the octave shift, psychophysical step size was maintained (0.1200 ERB) in order to preserve perceptual equivalence of pitch movement (Hermes and van Gestel, 1991). The practice speech stimuli were resynthesized from a Mandarin /a/ syllable produced with a high level tone by a female native speaker. The practice nonspeech stimuli were composed of six harmonics, but most were different (1, 3, 4, 5, 9, 11) from those used in the experimental stimuli.

C. Procedures

Chinese (C) and English (E) listeners were assigned to one of four subgroups according to stimulus set (speech, S; nonspeech, NS). There were 15 participants per subgroup: CS=Chinese group, speech condition; ES=English group, speech condition; CNS=Chinese group, nonspeech condition; ENS=English group, nonspeech condition. Each participant was asked to perform identification and discrimination tasks in either the speech or nonspeech condition. The two tasks were presented in random order across participants.

1. Identification task

In the identification task, participants listened to stimuli from the speech/nonspeech continuum presented in isolation. They were instructed to press the left mouse button upon hearing a "level" pitch, or the right mouse button upon hearing a "rising" pitch. There were 20 occurrences of each of the seven stimuli (140 trials) presented in random order. The rate of presentation was self-paced. Once a response was collected, the next stimulus was presented automatically following a 1-s pause.

2. Discrimination task

In the discrimination task, stimuli were presented in pairs with a 500-ms interstimulus interval (ISI). This ISI duration was selected to maximize differences in the performance of between- versus within-category discrimination (Pisoni, 1973). A total of 170 pairs were presented in random order. Of these pairs, 100 consisted of two different stimuli separated by two steps on the speech/nonspeech continuum (*different* pairs), in either forward (1-3, 2-4, 3-5, 4-6, 5-7) or reverse order (3-1, 4-2, 5-3, 6-4, 7-5). There were 10 occurrences of each of the ten 2-step pairs. The remaining 70 pairs

contained one of the seven stimuli on the speech/nonspeech continuum paired with itself (*same* pairs). There were ten occurrences per stimulus pair. After hearing each pair, participants were instructed to judge whether the two stimuli were the same or different, and to respond by pressing a mouse button (left="same," right="different"). The rate of presentation was self-paced as in the identification task.

All the stimuli were presented binaurally at ~72 dB SPL through a pair of Sony MDR-7506 headphones. Stimulus presentation and response collection were implemented using E-PRIME software (Schneider *et al.*, 2002).

3. Practice tasks and subject prescreening

Prior to each of the two experimental tasks, participants were asked to perform a similar identification or discrimination task using a different set of speech/nonspeech stimuli. These two practice tasks were designed primarily to familiarize them with task requirements in order to stabilize their performance in the actual experiment. Another objective was to minimize differences in task difficulty between language groups that might be attributed to the non-native (English) listeners' unfamiliarity with Chinese sounds. Finally, they allowed us to identify individuals who were unable to reach our threshold criterion for task performance.

After the practice identification task, separate binomial tests were performed on each participant's percentage of "level" responses to Step 1 and the percentage of "rising" responses to Step 7. After the practice discrimination task, a binomial test was performed on the percentage of correct "same" and "different" discriminations. A significance threshold of $p<0.05$ (significantly above chance) was used to determine whether the subject could proceed to the experimental tasks. Only 3 out of 63 participants, one Chinese and two English, failed to pass the prescreening threshold, and thus were excluded from the experiment.

D. Data analysis

To investigate the effects of language experience (native or non-native) and domain specificity (speech or nonspeech) on identification and discrimination performance, we obtained individual measures for each subject based on three essential characteristics of CP: sharp category boundary, corresponding discrimination peak, and prediction of discrimination from identification (Treisman *et al.*, 1995).

1. Identification function and categorical boundary

Based on the binomial distribution of the identification scores and the sigmoid shape of the response function, a logistic regression [generalized linear model, see Eq. (4)] between the *identification score* (P_I) and a repeated measures predictor, *step number* (x), was adopted to obtain the mean identification function for each subgroup:

$$\log_e\left(\frac{P_I}{1-P_I}\right)=b_0+b_1x. \tag{4}$$

Note that x can be treated as a continuous variable proportional to the ERB-rate scale although we only sampled at discrete steps on the continua. Since the identification functions for "level" and "rising" responses are symmetrical, only the latter was analyzed. The GEE (Generalized Estimating Equations) (Liang and Zeger, 1996) estimated regression coefficient b_1 was used to evaluate the slope of the fitted logistic curve (Kutner *et al.*, 2005, p. 567), which is an indication of the *sharpness* of the categorical boundary. The effects of language group (GROUP=C,E) and stimulus set (STIM=S,NS) on b_1 were estimated by their interactions with step number x in the generalized linear model using GROUP, STIM, and x as predictors. We derived the mean position of the categorical boundary in each subgroup from the value of step number (x_{cb}) corresponding to the 50% identification score,

$$\begin{aligned} &b_0+b_1x_{cb}=\log_e\left(\frac{0.5}{1-0.5}\right)=0 \\ &\Rightarrow x_{cb}=-\frac{b_0}{b_1}. \end{aligned} \tag{5}$$

Similarly, x_{cb} for each subject was derived from individual logistic response functions, and then analyzed by a two-way ANOVA for GROUP and STIM effects. Other dependent measures described in the following sections—P_{bc}, P_{wc}, P_{pk}, z, D—were analyzed by similar ANOVA models.

2. Obtained discrimination scores and related measures

In order to compute the obtained discrimination score (P), we divided the 170 discrimination trials into five 2-step comparison units. Each unit was comprised of all the trials in four types of pairwise comparisons (AB, BA, AA, and BB) for stimuli A and B separated by two steps. There were 40 trials in each unit. Adjacent comparison units contained overlapping AA or BB trials (e.g., the ten 3-3 pairs were included in both 1-3 and 3-5 units). P for each comparison unit was defined by

$$P=P(''S''|S)\cdot P(S)+P(''D''|D)\cdot P(D). \tag{6}$$

The percentages of "same" ("S") and "different" ("D") responses of all the same (S) and different (D) trials (i.e., the correct responses) in each comparison unit were represented by two conditional probabilities, $P(\text{"}S\text{"}|S)$ and $P(\text{"}D\text{"}|D)$, respectively. $P(S)$ and $P(D)$ were the probabilities of S (AA or BB) and D (AB or BA) trials in each unit, which were both equal to 0.5 in this experiment.

The obtained discrimination data for each subject were then examined by three different measures: *between-category* discrimination sensitivity (P_{bc}), measured from the comparison unit corresponding to the categorical boundary (x_{cb}) determined from the subgroup identification functions (for all subjects in this experiment, $P_{bc}=P_{35}$); *within-category* discrimination sensitivity (P_{wc}), which was the average of the two comparison units (P_{13} and P_{57}) at the ends of the continuum (cf. Pisoni, 1973); and *peakedness* of the discrimination function (P_{pk}), estimated by the difference between P_{bc} and P_{wc}.

3. Prediction of discrimination from identification

The predicted discrimination score P^* was computed using Eq. (7) (Pollack and Pisoni, 1971),

$$P^* = [1 + (P_A - P_B)^2]/2, \quad (7)$$

where the identification scores (as one of the two categories, uniformly either "level" or "rising") of the two stimuli A and B in a comparison unit. This equation was drawn from an extreme assumption that same-different discrimination is solely determined by the identification of the two stimuli as the same or different categories [covert identification; the original model was discussed in Liberman *et al.* (1957)].

The predictability of discrimination from identification was examined on two aspects in terms of the degree of CP (Liberman *et al.*, 1957). First, the correlation between the predicted and obtained discrimination scores, i.e., the similarity in the shape of the two discrimination curves, especially the position of the discrimination peaks, was measured by Fisher's z-transformed correlation coefficient (z) to obtain normally distributed data for ANOVA. Second, the distance between the two discrimination curves was measured by the mean difference ($P - P^*$) between the obtained and predicted discrimination scores. The underestimation of discrimination from identification is presumably due to the involvement of continuous perception in the discrimination task (Macmillan, 1987).

III. RESULTS

A. Logistic identification functions

The estimated regression coefficients for the mean logistic response functions of the four subgroups (CS, CNS, ES, ENS) are presented in Table II. These parameters were used to plot the identification functions in Fig. 2.

B. Sharpness of the category boundary

In the generalized linear model for logistic regression, a significant two-way interaction ($Z=3.45$; $p=0.0006$) was observed between GROUP and step number x, indicating that Chinese listeners showed sharper category boundaries (larger b_1; see Table II) than English for both speech and nonspeech stimuli. This difference can also be visualized from the logistic response functions in Fig. 2. The STIM $\times$ x interaction and GROUP $\times$ STIM $\times$ x interaction were not significant.

C. Position of the category boundary

The position of the category boundary (x_{cb}) computed from subgroup and individual logistic regressions is presented in Table II. A two-way ANOVA on individual x_{cb} yielded only a significant STIM main effect [$F(1,56)=4.72$; $p=0.0341$]. For both language groups (Chinese, English), although the mean category boundaries for both speech and nonspeech were approximately centered at the middle of the continua ($x_{cb} \approx 4$), the boundary of the speech continuum was slightly shifted toward the "rising" end ($\approx$0.34 step; Fig. 2) as compared to the nonspeech continuum.

TABLE II. GEE estimates of regression coefficients (b_0, b_1) and the derived categorical boundary (x_{cb}) for each subgroup (C=Chinese, E=English; S=speech; NS=nonspeech).

Subgroup	b_0	b_1	$x_{cb}=-b_0/b_1$
CS	−10.3094	2.4266	4.2485
CNS	−8.1686	2.0855	3.9169
ES	−4.4333	1.0611	4.1780
ENS	−5.0307	1.3146	3.8268

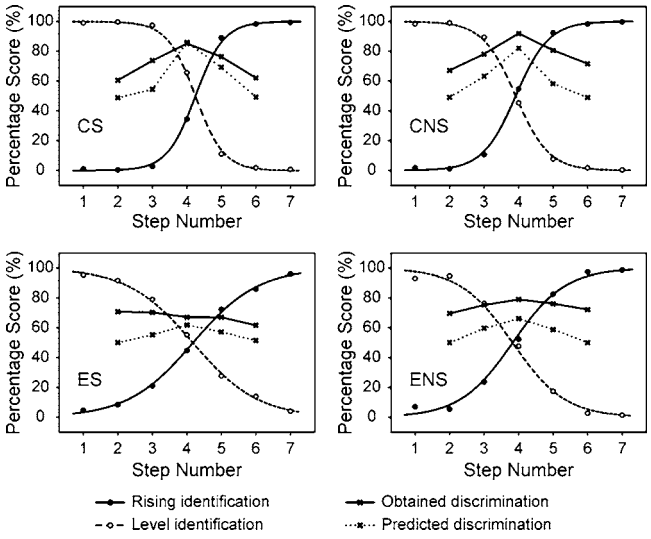

FIG. 2. Logistic identification functions ("level" and "rising") and two-step discrimination curves ("obtained" from the discrimination scores and "predicted" from the identification scores) for each subgroup (C=Chinese; E=English; S=speech; NS=nonspeech). The "level" logistic response functions (dashed lines) were plotted by reflecting the "rising" logistic response functions (solid lines) across the 50% horizontal line ($P_{level}=1-P_{rising}$).

D. Between-category discrimination

A two-way ANOVA revealed significant GROUP [$F(1,56)=69.44$; $p<0.0001$] and STIM [$F(1,56)=23.89$; $p<0.0001$] main effects on between-category discrimination sensitivity (P_{bc}) [Fig. 3(a)]. The GROUP $\times$ STIM interaction effect was not significant, indicating that Chinese listeners showed better between-category discrimination sensitivity than English in both speech (mean: CS=86.5%; ES=68.5%) and nonspeech (CNS=92.2%; ENS=80.3%) stimulus sets. For both language groups, nonspeech stimuli yielded better between-category discrimination sensitivity than speech.

E. Within-category discrimination

A two-way ANOVA showed significant GROUP [$F(1,56)=4.75$; $p=0.0335$] and STIM [$F(1,56)=11.09$; $p=0.0015$] main effects on within-category discrimination sensitivity (P_{wc}) [Fig. 3(b)]. The GROUP $\times$ STIM interaction effect was not significant, indicating that English listeners showed better within-category discrimination sensitivity than Chinese in both speech (mean: CS=62.7%; ES=67.6%) and nonspeech (CNS=69.6%; ENS=72.3%) stimulus sets. For both language groups, nonspeech stimuli yielded better within-category discrimination sensitivity than speech.

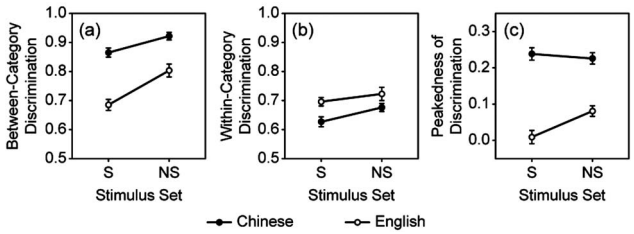

FIG. 3. Discrimination score in percentage correct: (a) between-category; (b) within-category; (c) peakedness of discrimination. (S=speech; NS=nonspeech.)

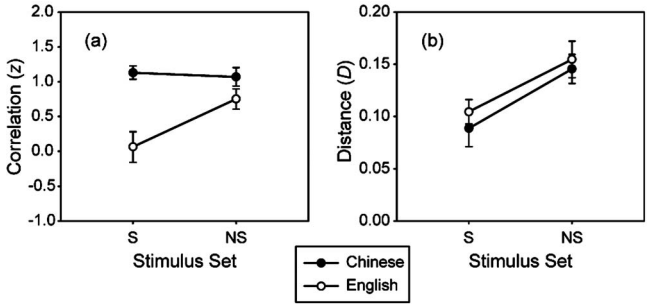

FIG. 4. The relationship between predicted and obtained discrimination curves: (a) Fisher's z-transformed correlation; (b) mean distance. (S=speech; NS=nonspeech.)

F. Peakedness of discrimination

A two-way ANOVA on peakedness of discrimination (P_{pk}) showed a significant GROUP×STIM interaction [$F(1,56)=6.61$; $p=0.0128$; Fig. 3(c)]. Tukey adjusted multiple comparisons indicated that Chinese listeners obtained a higher discrimination peak than English for both speech and nonspeech stimuli ($p_{adjusted}<0.0001$). In addition, English listeners achieved a higher discrimination peak in response to nonspeech than speech stimuli ($p_{adjusted}=0.0157$). Student t-tests for P_{pk} in each of the four subgroups showed that only the mean P_{pk} of the ES subgroup was not significantly greater than zero ($p=0.5777$). A significant discrimination peak was observed in all of the other three subgroups (CS, CNS, ENS; for mean $P_{pk}>0$, $p<0.0001$).

G. Correlation between predicted and obtained discrimination

A two-way ANOVA on the z-transformed correlation between the predicted and obtained discrimination scores revealed a significant GROUP×STIM interaction [$F(1,56)=5.85$; $p=0.0188$; Fig. 4(a)]. Tukey adjusted multiple comparisons indicated that English listeners, when performing the speech discrimination task (ES subgroup), showed significantly lower correlation than the other three subgroups (ES<CS, $p_{adjusted}<0.0001$; ES<CNS, $p_{adjusted}=0.0001$; ES<ENS, $p_{adjusted}=0.0136$). This result is consistent with the shapes of subgroup discrimination curves shown in Fig. 2.

H. Underestimation of discrimination by identification

A two-way ANOVA showed only a significant effect of STIM [$F(1,56)=12.13$; $p=0.0010$] on the mean distance between the obtained and predicted discrimination functions [Fig. 4(b)]. For both language groups, underestimation of discrimination by identification was greater in nonspeech than in speech stimuli.

IV. DISCUSSION

A. Categorical perception of tone

Identification and discrimination tasks reveal classical patterns of CP in Chinese listeners for both speech (CS) and nonspeech (CNS) stimuli varying along a linear F_0 continuum from level to rising. The results for the speech stimuli (CS) are comparable to those for stop consonants (Liberman *et al.*, 1957, 1961) in terms of defined characteristics of CP: a sharp category boundary, a corresponding discrimination peak, and predictability of discrimination from identification. The exhibition of CP for pitch direction is dependent on a listener's experience with a tone language (CS) as shown by the lack of similar CP effects in nontone language listeners (ES). For Chinese listeners, some aspects of CP—sharp identification boundary and discrimination peak—extend to homologous nonspeech stimuli. (CNS). Regardless of language group, discrimination scores in the nonspeech tasks (CNS, ENS) are better overall than those in the speech tasks (CS, ES). This may be related to differences in the complexity between the two sets of stimuli. (See Sec. IV C.)

One explanation for CP claims that it arises from variations in natural auditory sensitivity along some acoustic continuum without any reference to speech-specific mechanisms (Pastore *et al.*, 1977; Stevens, 1981). Interestingly, both speech and nonspeech stimuli in this study yield identification boundaries near the middle of the F_0 continuum regardless of language experience. This finding is inconsistent with a previous claim of separate linguistic and psychophysical boundaries on a synthetic speech continuum varying in pitch direction from level to rising (Wang, 1976). Wang reported two separate boundaries in a comparison between Chinese ($n=2$; linguistic) and English ($n=2$; psychophysical) listeners. The current study, on the other hand, employs two continua, speech and nonspeech, in addition to a much larger sample size ($n=15$) per language group. We argue that the nonspeech continuum is a *sine qua non* for making a direct comparison of the relationship between the two boundary types. Prima facie, this overlap in identification boundaries, irrespective of stimulus type or language group, may be construed to support natural auditory sensitivities as the driving force behind CP. By this account, the presence of a psychophysical boundary due to the heterogeneity of natural auditory sensitivities along the continuum predicts that the identification boundary and discrimination peak would co-occur in the same location for both speech and nonspeech stimuli. The fact that no discrimination peak is observed at the identification boundary in the speech task for the English group (ES) runs counter to the auditory-explanation. We further propose that the relatively small discrimination peak that is observed in response to the nonspeech stimuli for the English group (ENS) is likely due to memory rather than auditory mechanisms. (See Sec. IV B.)

In multidimensional scaling of listeners' perception of

linear F_0 ramps (level, falling, rising), cross-language comparisons show that the relative importance of the pitch height and direction dimensions varies depending on a listeners' familiarity with specific types of pitch patterns that occur in the tone space of their native language (Gandour and Harshman, 1978; Gandour, 1983). Pitch height distinguishes tones, either static or dynamic, that differ according to average F_0, while direction of change distinguishes primarily rising from nonrising tones. The perceptual salience of the direction dimension is greater for native speakers of tone languages, including Mandarin Chinese, than for speakers of nontone languages (English), while English listeners give greater weight to the height dimension than do tone language speakers. Such cross-language differences in perceptual weighting suggest that linguistic experience directs attention to linguistically relevant properties of the auditory signal. In this experiment, the fact that Chinese listeners show as much CP for nonspeech sounds as for speech sounds, whereas English listeners do not, suggests that Chinese listeners' CP for nonspeech sounds does not result simply from the presence of an innate region of heightened sensitivity. Otherwise English listeners would be expected to show the same CP effects in the ENS condition as the Chinese listeners did in the CNS condition. We therefore conclude that Chinese listeners' nonspeech performance must derive at least in part from their experience with listening to Chinese pitch patterns. These data lead us to infer that Chinese listeners' native language experience has changed the way they process pitch patterns regardless of the stimulus context in which these patterns are embedded. Although the basis for cross-language differences in CP may emerge from linguistic experience, the effects of such experience is not specific to speech perception (contra Studdert-Kennedy *et al.*, 1970). More generally, we predict CP effects whenever listeners are asked to judge auditory features that are similar to linguistically relevant speech parameters in their native language no matter whether they are presented in the context of natural speech or not.

B. Memory mechanisms of categorical perception

Instead of attributing CP effects to natural auditory sensitivities or speech-specific processes, we explain the data from this experiment by memory mechanisms involved in the CP tasks and their interactions with different levels of stimulus complexity between speech and nonspeech.

1. The dual-process model

The interpretation of CP by the contribution of distinct memory codes was first proposed by Fujisaki and Kawashima (1969, 1970, 1971), often referred to as the dual-process model (Macmillan, 1987, p. 55), and extensively discussed by Pisoni and colleagues in a series of experiments on phoneme discrimination (Pisoni, 1973; Pisoni and Lazarus, 1974; Pisoni, 1975). In this model, short-term memory (STM) recruited in CP tasks is divided into a continuous auditory short-term store and a categorical phonetic short-term store (Pisoni, 1975, pp. 8–9). The auditory memory code is subject to rapid decay and is dominant in within-category discrimination. The phonetic memory code is more stable due to "contact" with representations residing in long-term memory, and is dominant in between-category discrimination. Overall discrimination sensitivity is determined by the sum of these two types of memory available in the decision-making stage after decay. Both auditory and phonetic modes-coexist during the discrimination task but subjects operate exclusively in phonetic mode during the identification task. The dual-process model can successfully account for the underestimation of discrimination by identification observed in applications of the classical Haskins model (Liberman *et al.*, 1957), including the present experiment. Pisoni (1973) also employed the model to interpret differences in the degree of CP between consonants and vowels (Fry *et al.*, 1962; Stevens *et al.*, 1969), arguing that auditory STM appears to make a greater contribution to the discrimination of vowels as compared to stop consonants.

The dual-process model can account for our finding that Chinese listeners showed a sharper identification boundary and higher discrimination peak than English listeners. These language-dependent effects presumably indicate the role of phonetic memory in the CP tasks. However, because this model claims that CP effects emerge from a speech-specific phonetic mode, it cannot explain the robust categorical effects for nonspeech discrimination in the Chinese listeners (CNS) or the quasicategorical effects in the English listeners (ENS), as well as those well-documented observations of CP for certain nonspeech continua (Cutting and Rosner, 1974; Miller *et al.*, 1976; Pisoni, 1977; Mirman *et al.*, 2004). Moreover, although a dual-process model can account for the observed increase of between-category discrimination by the existence of phonetic memory, it cannot account for the observed decrease of within-category discrimination in Chinese listeners as compared to English. According to the dual-process model, both Chinese and English listeners would be expected to show similar within-category discrimination unless we admit a culture-bound difference in auditory sensitivity (Tanner and Rivette, 1964; Stagray and Downs, 1993; for contra evidence, see Burns and Sampat, 1980).

2. Signal-detection models

Another approach to CP utilizing memory mechanisms was based on Durlach and Braida's (1969) quantitative model for intensity perception. This approach employs a continuous theory of perception, i.e., signal detection theory (SDT: Green and Swets, 1966; Macmillan and Creelman, 1991). Again, two modes of memory operation are assumed: a *trace* mode and a *context-coding* mode. In the trace mode, the sensory memory trace of a previously heard stimulus is maintained for comparison with the sensation of a following stimulus; the trace is subject to temporal decay and interference, called trace variance. In the context-coding mode, the sensation of each stimulus is compared to a general stimulus context; the variance of this mode increases with the width of the context (i.e., overall stimulus range). The total variance is the sum of the two sources of memory variances plus the basic sensory variance, which is presumed to be constant. These two memory operations reflect domain-general processes that exist in both speech and nonspeech perception. Applying this model to CP explains the discrepancy between

fixed/roving discrimination and identification sensitivity as a function of differential contributions of trace and context-coding modes (Macmillan *et al.*, 1977; Macmillan, 1987). The vowel-consonant difference in CP can also be explained by the differential amount of context-coding variance (Ades, 1977; Macmillan *et al.*, 1988). The notion of context-coding now allows us to examine CP not only on the basis of stimulus sensitivity, but also in terms of task context (Macmillan *et al.*, 1977; Gerrits and Schouten, 2004).

A major limitation of SDT models is that they do not distinguish between short-term and long-term components in the context-coding mode, as pointed out by Macmillan *et al.* (1988, p. 1277). According to Durlach and Braida's (1969, p. 374) original definition, context may be derived either from the stimuli presented in the actual experiment (experimental context) or from a much larger set of stimuli from earlier experience (permanent context). Unfortunately, only factors related to the experimental context were considered in these models (Durlach and Braida, 1969; Braida *et al.*, 1984), thus making it impossible to measure any experience-dependent effects on CP. In the present experiment, this distinction is crucial. Cross-language differences in the sharpness of the identification boundary and discrimination peak can only be explained in terms of differences in the two groups' long-term experience with their respective native languages, and *not* in terms of differences in experimental context (which was identical for Chinese and English listeners). The current formulation of SDT models, however, does not incorporate a formal distinction between the effects of experimental and permanent context. Such models are therefore unable to give a full account of our data.

A more recent SDT model (van Hessen and Schouten, 1992) has incorporated a *labeling* process. The total variance consists of sensory variance and three sources of memory variance: trace, context-coding (temporary context), and labeling (permanent context). In this model, however, the categorical nature of the labeling process is not clearly distinguished from continuous sensory encoding. Moreover, CP reflects access to *permanent* phoneme labels only. The quasicategorical effects observed in our experiment are left unexplained in the case of nonspeech discrimination for English listeners (ENS) since they do not have access to permanent phoneme labels for such pitch stimuli.

3. A multistore model of CP

In our view, both dual-process and SDT models recognize CP as a complex phenomenon that emerges from at least two memory processes. Yet neither of these two models recognizes *categorization* as a process inherent to perception.

The SDT models attempted to explain CP by adapting a theory for continuous sensory processes (Macmillan *et al.*, 1977; Macmillan, 1987). We argue that the internal responses generated by the categorization process obey the rule of *discrete* probability distributions, fundamentally different from the sensory-level continuous Gaussian distributions assumed by SDT. In the case of binary internal responses, the probability for each response as a function of the stimulus value can be modeled by sigmoidal functions [e.g., a logistic function; see Eq. (4) and related commentary in Sec. II]. This discrete distribution generates a local maximum of perceptual sensitivity at the category boundary [cf. Eq. (7)]. Its mechanism represents essentially the same labeling process as described in the Haskins model. The dual-process model incorporated the categorization process as a separate memory mechanism parallel to sensory processing. But this process was treated as a special mode for speech perception only, whereas we claim that it is independent of domain or modality. This argument is supported not only by CP of melodic music intervals (Burns and Ward, 1978) and color hues (Bornstein, 1987), but also by observations from visual and auditory processing in other species (Herrnstein and Loveland, 1964; Kuhl and Miller, 1975; Freedman *et al.*, 2001; Ohl *et al.*, 2001). In addition, although categorization is often observed to be related to long-term memory representations, it can nevertheless operate automatically on certain novel stimulus features, resulting in temporary representations stored in short-term categorical memory. (See Sec. IV B 4.)

This short-term categorical store is to be distinguished from (continuous) sensory memory. A model that contains only sensory memory would fail to predict the differential experimental outcomes between speech (ES) and nonspeech (ENS) stimuli for the English listeners. In the former case, we observe no CP effects; in the latter, we observe a quasi-categorical effect. Thus, separate memory processes must be recruited for encoding continuous and categorical information. Furthermore, this short-term categorical store is to be distinguished from categorical representations stored in long-term memory. A model that contains only a long-term categorical store cannot account for the quasicategorical effect of ENS since English listeners have no previous exposure to Mandarin tones. More important, our proposed short-term categorical memory differs from the traditional view of this store that serves only as an intermediate buffer between sensory and long-term memory (Atkinson and Shiffrin, 1968). We claim that it can operate in parallel with fine-grain sensory memory and produce a CP effect independent of long-term memory. To account for our data, we introduce a new multistore model including sensory, short-term, and long-term memory components (Fig. 5).

a. Sensory memory. Two separate sensory stores have been proposed for auditory memory (Cowan, 1984, 1987). According to Cowan (1984), the *sensory memory trace* is derived from unanalyzed raw sensory data with possible temporal integration. Its lifetime has been estimated to be about 300 ms (i.e, cannot last beyond the duration of one trial in delayed discrimination tasks with parameters that are comparable to those used in this experiment). The *analyzed sensory memory* contains fine-grain analyzed sensory codes including steady-state (e.g., pitch height), time-varying (e.g., pitch slope), and event-timing (e.g., onset time or duration) information. Its lifetime is on the order of seconds. This relatively longer sensory store is necessarily required for the context-coding in the Durlach-Braida model (1969).

b. Short-term categorical memory. As hypothesized, this memory store captures only those critical features of the stimuli that are used for perceptual categorization. The strategy of such a separate memory process is to improve computational efficiency and to reduce working memory load by omitting most of the irrelevant details in sensory inputs. The likelihood that categorical encoding runs parallel to fine-

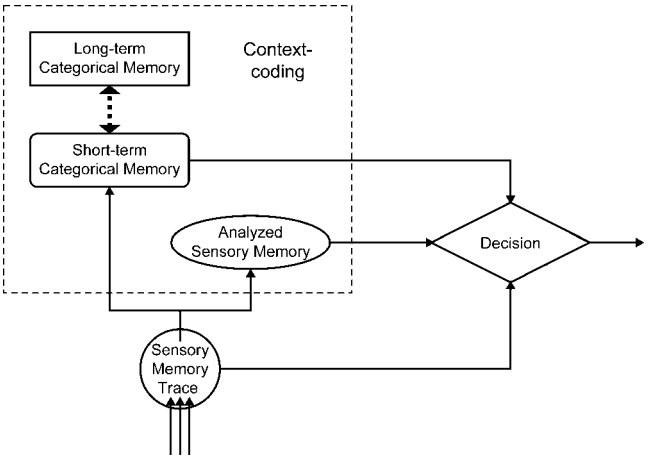

FIG. 5. A multistore model of CP. It includes four memory stores: *sensory memory trace, analyzed sensory memory, short-term categorical memory, and long-term categorical memory*. Information is encoded in a hierarchical order but short-term categorical memory and analyzed sensory memory can be processed in parallel. All the sensory and short-term categorical components are subject to memory decay. The available memory traces after decay are input for *decision-making*. If long-term categorical memory is also available, it will interact with short-term categorical memory via both top-down and bottom-up mechanisms. All the memory components with relatively longer lifetime are involved in context-coding.

grain sensory encoding is supported by duplex perception for certain speech or music stimuli (Liberman *et al.*, 1981; Pastore *et al.*, 1983). In the present experiment, we argue that this memory component is responsible for the quasicategorical effect observed in the English listeners' response to the nonspeech stimuli (ENS). Beyond our data, it also provides an explanation for other CP phenomena generated by nonspeech stimuli (Cutting and Rosner, 1974; Miller *et al.*, 1976; Pisoni, 1977). (See Sec. IV B 4)

c. Long-term categorical memory. Short-term categorical representations can be permanently preserved in long-term memory as a result of perceptual learning. These long-term categorical representations may serve as *templates* to be activated later by *bottom-up matching* of similar features. They also provide *top-down expectations* in the encoding of short-term categorical memory that allow listeners to better direct selective attention to a critical stimulus feature or dimension (Grossberg, 1980, 1999; Francis and Nusbaum, 2002). Moreover, this conversion from temporary to permanent representations increases the automation of categorical processing which, in turn, leads to a reduction of working memory load and an enhancement of categorization accuracy (Shiffrin and Schneider, 1977; Johnson and Ralston, 1994). In this experiment, we argue that this memory component is responsible for the stronger CP effects observed in Chinese listeners in both speech (CS) and nonspeech (CNS) conditions as compared to English listeners.

d. Memory variance and decision-making. Similar to the "resistance network" proposed by SDT models (van Hessen and Schouten, 1992), we hypothesize that the relative dominance of each memory resource for the input of decision-making (Fig. 5) is determined by the variance of that memory component. Memory variances may come from encoding, decay, or limited memory capacity. Since this experiment is not aimed at studying the effects of interstimulus interval (measure of *decay*) or number of categories (measure of *capacity*), our discussion is limited to the *encoding* variance related to stimulus complexity. (See Sec. IV C.)

e. Context-coding. Our model also extends the concept of context-coding (Fig. 5) that originated in the Durlach-Braida model (1969). In a CP task, subjects not only process sensory and categorical information of the target stimuli, but also integrate residual information from previous stimuli. Thus, context-coding may be involved with those memory components that span multiple stimuli and trials, i.e., analyzed sensory memory and short- and long-term categorical memory (Fig. 5). For example, in analyzed sensory memory, sensitivity decreases as a function of the width of the stimulus continuum in roving discrimination (Berliner and Durlach, 1973). In categorical memory, various factors (e.g., speaker normalization effects) may influence the location of category boundaries on a physical stimulus continuum (for a review, see Repp and Liberman, 1987). In addition, if both sensory and categorical memory resources are available in a roving discrimination task, the discrimination peak can be sharpened by the experimental context (see Sec. IV B 4 c).

4. Applications of the multistore model

Whereas this model does provide a full account of our CP data on tonal perception, it more importantly yields fresh perspectives on long-standing issues of controversy related to CP.

a. Nonspeech CP. By our model, we interpret varying degrees of CP that have been observed in some nonspeech continua, but not in others, to be attributable to stimulus-dependent categorization mechanisms based on *intrinsic* and *extrinsic* references. Both mechanisms may operate in the short-term categorical memory. An intrinsic reference is defined by the comparison of two acoustic levels changing across time (e.g., direction of pitch movement or formant transition) or the temporal order of two events inside a stimulus (e.g., temporal order of acoustic cues for voicing relative to the release of stop consonants). Categorization of intrinsic features is less demanding on working memory because computation can be carried out within each stimulus as in judgments of pitch direction herein. Most of the nonspeech continua exhibiting a CP effect have been based on acoustic features with intrinsic references (Cutting and Rosner, 1974; Miller *et al.*, 1976; Pisoni, 1977). In contrast, steady-state features such as the formant contrast of static vowels or the pitch contrast of level tones lack intrinsic references. Categorical encoding of these acoustic features is dependent on extrinsic references that are based on either a normalized acoustic level derived from other stimuli in the context or the best matched exemplar in memory. In either case, working memory load may be increased by computations required to integrate across a sequence of stimuli or to evaluate the fitness among multiple exemplars. This explains why steady-sate nonspeech continua were not categorically perceived if presented in isolation (Mirman *et al.*, 2004).

b. Degree of CP. We argue that the distinction between intrinsic and extrinsic references also determines the degrees of CP for speech continua. Macmillan *et al.* (1988), for example, found that the context variance of vowels (extrinsic reference) is up to three times larger than that for consonants (intrinsic reference). Similarly, it also explains the greater degree of CP in judgments of pitch direction (intrinsic) of linear ramps in this experiment (cf. contour tones: Wang, 1976; Francis *et al.*, 2003; Hallé *et al.*, 2004) relative to judgments of pitch height (extrinsic) of level tones (Abramson, 1979; Francis *et al.*, 2003). In agreement with the CP

data, it has also been shown that contour tones are less context-dependent than level tones (Fox and Qi, 1990; Francis *et al.*, 2003; Wong and Diehl, 2003).

c. Acquired similarity versus acquired distinctiveness. A peak in roving discrimination can emerge from simultaneously available sensory and categorical information depending on the task context (Macmillan, 1987; Kewley-Port *et al.*, 1988). If within-category trials are presented in a fixed discrimination task, a categorical distinction is not available because the stimuli always belong to the same category. In this fixed task context, discrimination relies only on sensory information. However, if such trials are presented in a roving discrimination task, they are also affected by the categorical distinction of between-category trials. If both types of information draw subjects' attention, conflicting sensory ("different") and categorical ("same") labels may be generated for two different stimuli within the same category. This conflicting information may result in less accurate within-category discrimination. In this sense, a discrimination peak is sharpened by the interdependency between the two types of trials in a roving task context. Thus, in our roving discrimination task, cross-language differences reveal that *both* an enhancement of between-category *and* a reduction of within-category discrimination contribute to the peakedness of discrimination. Such an explanation based on task context may help to resolve the persistent controversy about whether CP stems from "acquired similarity" (Kuhl, 1991) or "acquired distinctiveness" (Liberman *et al.*, 1961). Iverson and Kuhl (2000) have investigated this question by directly comparing roving and fixed discrimination tasks, and conclude that these two aspects of CP derive from independent mechanisms. However, their results are also consistent with the model proposed herein. The ratios between roving and fixed discrimination sensitivities across a vowel continuum with 60-mel formant frequency intervals indicate that within-category discrimination is significantly lower in the roving discrimination task (roving/fixed ≈ 0.6) but between-category discrimination is very close between the two tasks (roving/fixed ≈ 0.9). This result follows directly from our account that invokes a unified mechanism to explain these two aspects of CP.

C. Effects of stimulus complexity

The speech stimuli exhibit a greater complexity than the nonspeech stimuli according to at least three operational criteria. First, the existence of high-order unresolved harmonics in the speech stimuli reduces the ratio of spectral energy distribution in low-order resolved harmonics. Given the equivalent overall spectral energy between speech and nonspeech, it yields a lower pitch salience for the speech stimuli because resolved harmonics contribute more to pitch perception than do unresolved harmonics (Stagray *et al.*, 1992; Shackleton and Carlyon, 1994). Second, pitch judgments of the voice fundamental frequency (F_0) in the speech stimuli may be influenced by a pitch percept ("sibilant pitch") evoked by spectral energy allocation, which is determined by F_2 and higher formants (Traunmüller, 1987). Third, the fact that a *vowel* is perceived in the speech stimuli may interfere with pitch judgments due to a perceptual integration between segmental and suprasegmental dimensions (Carrell *et al.*, 1981; Repp and Lin, 1990).

Stimulus complexity affects the encoding variance of the memory components differentially in our multistore model. The short-term (sensory and categorical) memory components involve real-time encoding processes, and thus are subject to this type of encoding variance. With respect to sensory memory, encoding variance caused by stimulus complexity decreases overall pitch sensitivity, affecting both within- and between-category discrimination. This effect is demonstrated by lower discrimination scores and a smaller distance between obtained and predicted discrimination curves when comparing speech to nonspeech across the two language groups. With respect to short-term categorical memory, increased stimulus complexity makes it more difficult to extract categorical features and to form robust memory representations. It selectively affects between-category discrimination resulting in a reduced peakedness of discrimination. The absence of a significant peak for English listeners in the speech discrimination task (ES) may indicate that their discrimination judgments are based exclusively on continuous sensory encoding.

In contrast, the activation of permanent categorical representations does not involve any real-time encoding since they are stored *a priori* in long-term memory. Thus, this long-term component involved in CP tasks is less affected by stimulus complexity, especially when it operates dominantly in a top-down manner (Grossberg, 1999). In the current experiment, we observe that adult native Chinese listeners easily recognize pitch patterns associated with Mandarin tonal categories irrespective of stimulus set. This finding is presumably due to overlearned pitch representations that result from long-term exposure to their native language. It is therefore not surprising that we observe no effect on the peakedness of discrimination between speech and nonspeech stimuli for the Chinese listeners.

If an increase in stimulus complexity reduces the overall pitch sensitivity, we can also explain why the location of the identification boundary differs as a function of the stimulus continuum for both language groups. Although the physical step size of the speech continuum is equal to that of the nonspeech continuum, the perceptual step size of the speech continuum must be smaller due to this lowered sensitivity. We further assume that the mean decision-making criterion is constant for both stimulus sets in the identification task. Because the level end of the continuum is represented by a flat contour, there is no F_0 movement during the course of its trajectory. This stimulus is therefore likely to serve as an anchor point. As a consequence, subjects need more steps to make a "rising" response in the speech stimuli as compared to nonspeech, which results in a small boundary shift toward the rising end of the speech continuum.

D. Neurophysiological evidence for multistore memory processing

The putative memory components in our model appear to be consistent with recent findings from the brain imaging literature. A magnetoencephalography (MEG) study (Lu *et al.*, 1992) shows that the physiological lifetime of auditory sensory memory is significantly longer for auditory association cortex than for primary auditory cortex. This evidence

provides an anatomical basis for the distinction between *analyzed sensory memory* and the *sensory memory trace* proposed in our model. In another MEG experiment Luo *et al.* (2005) compared categorical versus simple auditory discrimination. They demonstrated that alpha-band activities are enhanced in auditory areas for nonspeech stimuli, and in frontal areas for both speech and nonspeech stimuli. Moreover, the alpha-band brain activity in auditory areas was stronger when directly comparing the categorical discrimination of newly learned nonspeech categories to long-term speech categories. These findings not only suggest a distinction between categorical and continuous auditory processing, but also point to different neural networks for the activation of *short-term* and *long-term categorical memory*.

V. CONCLUSION

A multistore model consisting of *unanalyzed* and *analyzed sensory memory, short-term* and *long-term categorical memory*, and parallel processing of sensory and categorical information offers a unified account of CP that explains not only the data herein but also a wide range of disparate data from the extant literature. Short-term categorical memory is hypothesized to be domain-general, inherent to the perceptual system, and separate from continuous sensory processes. Differential effects of stimulus complexity on these memory stores further support their distinctive contributions in CP tasks. Although this model is at an early stage of development, it offers promise of illuminating some of the topics of controversy surrounding CP over the past half-century.

ACKNOWLEDGMENTS

Research supported in part from the National Institutes of Health and the Purdue Research Foundation (J.G.). This article is based on part of a doctoral dissertation completed by Y.X. at Purdue University in December 2005.

Abramson, A. S. (**1979**). "The noncategorical perception of tone categories in Thai," in *Frontiers of Speech Communication Research*, edited by B. Lindblom and S. Öhman (Academic, London), pp. 127–134.

Ades, A. E. (**1977**). "Theoretical notes. Vowels, consonants, speech, and nonspeech," Psychol. Rev. **84**, 524–530.

Atkinson, R. C., and Shiffrin, R. M. (**1968**). "Human memory: A proposed system and its control processes," in *The Psychology of Learning and Motivation: Advances in Research and Theory*, edited by K. W. Spence and J. T. Spence (Academic, New York), pp. 89–195.

Berliner, J. E., and Durlach, N. I. (**1973**). "Intensity perception. IV. Resolution in roving-level discrimination," J. Acoust. Soc. Am. **53**, 1270–1287.

Best, C. T., McRoberts, G. W., and Goodell, E. (**2001**). "Discrimination of non-native consonant contrasts varying in perceptual assimilation to the listener's native phonological system," J. Acoust. Soc. Am. **109**, 775–794.

Boersma, P., and Weenink, D. (**2003**). "PRAAT: Doing phonetics by computer," (Version 4.1.12) [Computer program]. Retrieved May 8, 2003, from http://www.praat.org/.

Bornstein, M. H. (**1987**). "Perceptual categories in vision and audition," in *Categorical Perception: The Groundwork of Congnition*, edited by S. R. Harnad (Cambridge University Press, New York), pp. 287–300.

Braida, L. D., Lim, J. S., Berliner, J. E., Durlach, N. I., Rabinowitz, W. M., and Purks, S. R. (**1984**). "Intensity perception. XIII. Perceptual anchor model of context-coding," J. Acoust. Soc. Am. **76**, 722–731.

Burns, E. M., and Sampat, K. S. (**1980**). "A note on possible culture-bound effects in frequency discrimination," J. Acoust. Soc. Am. **68**, 1886–1888.

Burns, E. M., and Ward, W. D. (**1978**). "Categorical perception—phenomenon or epiphenomenon: Evidence from experiments in the perception of melodic musical intervals," J. Acoust. Soc. Am. **63**, 456–468.

Carrell, T. D., Smith, L. B., and Pisoni, D. B. (**1981**). "Some perceptual dependencies in speeded classification of vowel color and pitch," Percept. Psychophys. **29**, 1–10.

Cowan, N. (**1984**). "On short and long auditory stores," Psychol. Bull. **96**, 341–370.

Cowan, N. (**1987**). "Auditory sensory storage in relation to the growth of sensation and acoustic information extraction," J. Exp. Psychol. Hum. Percept. Perform. **13**, 204–215.

Cowan, N. (**1988**). "Evolving conceptions of memory storage, selective attention, and their mutual constraints within the human information-processing system," Psychol. Bull. **104**, 163–191.

Cutting, J. E. (**1982**). "Plucks and bows are categorically perceived, sometimes," Percept. Psychophys. **31**, 462–476.

Cutting, J. E., and Rosner, B. S. (**1974**). "Categories and boundaries in speech and music," Percept. Psychophys. **16**, 564–570.

Durlach, N. I., and Braida, L. D. (**1969**). "Intensity perception. I. Preliminary theory of intensity resolution," J. Acoust. Soc. Am. **46**, 372–383.

Fox, R., and Qi, Y. Y. (**1990**). "Context effects in the perception of lexical tone," J. Chin. Linguist. **18**, 261–283.

Francis, A. L., and Ciocca, V. (**2003**). "Stimulus presentation order and the perception of lexical tones in Cantonese," J. Acoust. Soc. Am. **114**, 1611–1621.

Francis, A. L., Ciocca, V., and Ng, B. K. (**2003**). "On the (non)categorical perception of lexical tones," Percept. Psychophys. **65**, 1029–1044.

Francis, A. L., and Nusbaum, H. C. (**2002**). "Selective attention and the acquisition of new phonetic categories," J. Exp. Psychol. Hum. Percept. Perform. **28**, 349–366.

Freedman, D. J., Riesenhuber, M., Poggio, T., and Miller, E. K. (**2001**). "Categorical representation of visual stimuli in the primate prefrontal cortex," Science **291**, 312–316.

Fry, D. B., Abramson, A. S., Eimas, P. D., and Liberman, A. M. (**1962**). "The identification and discrimination of synthetic vowels," Lang Speech **5**, 171–189.

Fujisaki, H., and Kawashima, T. (**1969**). "On the models and mechanisms of speech perception," Annual Report of the Engineering Research Institute, Faculty of Engineering, University of Tokyo, Vol. **28**, pp. 67–73.

Fujisaki, H., and Kawashima, T. (**1970**). "Some experiments on speech perception and a model for the perceptual mechanism," Annual Report of the Engineering Research Institute, Faculty of Engineering, University of Tokyo, Vol. **29**, pp. 207–214.

Fujisaki, H., and Kawashima, T. (**1971**). "A model of the mechanisms for speech perception-quantitative analysis of categorical effects in discrimination," Annual Report of the Engineering Research Institute, Faculty of Engineering, University of Tokyo, Vol. **30**, pp. 59–68.

Gandour, J. (**1978**). "The Perception of Tone," in *Tone: A linguistic survey*, edited by V. Fromkin (Academic, New York), pp. 41–76.

Gandour, J. (**1983**). "Tone perception in Far Eastern languages," J. Phonetics **11**, 149–175.

Gandour, J., and Harshman, R. A. (**1978**). "Crosslanguage differences in tone perception: A multidimensional scaling investigation," Lang Speech **21**, 1–33.

Gerrits, E., and Schouten, M. E. (**2004**). "Categorical perception depends on the discrimination task," Percept. Psychophys. **66**, 363–376.

Green, D. M., and Swets, J. A. (**1966**). *Signal Detection Theory and Psychophysics* (Wiley, New York).

Greenwood, D. D. (**1961**). "Critical bandwidth and the frequency coordinates of the basilar membrane," J. Acoust. Soc. Am. **33**, 1344–1356.

Grossberg, S. (**1980**). "How does a brain build a cognitive code?," Psychol. Rev. **87**, 1–51.

Grossberg, S. (**1999**). "The link between brain learning, attention, and consciousness," Conscious Cogn **8**, 1–44.

Hallé, P. A., Chang, Y.-C., and Best, C. T. (**2004**). "Identification and discrimination of Mandarin Chinese tones by Mandarin Chinese vs. French listeners," J. Phonetics **32**, 291–453.

Harnad, S. R. (ed). (**1987**). *Categorical Perception: The Groundwork of Cognition* (Cambridge University Press, New York).

Hermes, D. J., and van Gestel, J. C. (**1991**). "The frequency scale of speech intonation," J. Acoust. Soc. Am. **90**, 97–102.

Herrnstein, R. J., and Loveland, D. H. (**1964**). "Complex visual concept in the pigeon," Science **146**, 549–551.

Howie, J. (**1976**). *Acoustical Studies of Mandarin Vowels and Tones* (Cambridge University Press, Cambridge).

Iverson, P., and Kuhl, P. K. (**2000**). "Perceptual magnet and phoneme boundary effects in speech perception: Do they arise from a common

mechanism?," Percept. Psychophys. **62**, 874–886.
Johnson, K., and Ralston, J. V. (**1994**). "Automaticity in speech perception: Some speech/nonspeech comparisons," Phonetica **51**, 195–209.
Kewley-Port, D., Watson, C. S., and Foyle, D. C. (**1988**). "Auditory temporal acuity in relation to category boundaries; Speech and nonspeech stimuli," J. Acoust. Soc. Am. **83**, 1133–1145.
Kuhl, P. K. (**1981**). "Discrimination of speech by nonhuman animals: Basic auditory sensitivities conducive to the perception of speech-sound categories," J. Acoust. Soc. Am. **70**, 340–349.
Kuhl, P. K. (**1991**). "Human adults and human infants show a 'perceptual magnet effect' for the prototypes of speech categories, monkeys do not," Percept. Psychophys. **50**, 93–107.
Kuhl, P. K., and Miller, J. D. (**1975**). "Speech perception by the chinchilla: Voiced-voiceless distinction in alveolar plosive consonants," Science **190**, 69–72.
Kuhl, P. K., and Padden, D. M. (**1983**). "Enhanced discriminability at the phonetic boundaries for the place feature in macaques," J. Acoust. Soc. Am. **73**, 1003–1010.
Kutner, M. H., Nachtsheim, C. J., Neter, J., and Li, W. (**2005**). *Applied Linear Statistical Models* (McGraw-Hill Irwin, Boston).
Liang, K. Y., and Zeger, S. L. (**1996**). "Longitudinal data analysis using general linear models," Biometrika **73**, 13–22.
Liberman, A. M., Cooper, F. S., Shankweiler, D. P., and Studdert-Kennedy, M. (**1967**). "Perception of the speech code," Psychol. Rev. **74**, 431–461.
Liberman, A. M., Harris, K. S., Hoffman, H. S., and Griffith, B. C. (**1957**). "The discrimination of speech sounds within and across phonemic boundaries," J. Exp. Psychol. **54**, 358–368.
Liberman, A. M., Harris, K. S., Kinney, J. A., and Lane, H. (**1961**). "The discrimination of relative onset-time of the components of certain speech and non-speech patterns," J. Exp. Psychol. **61**, 379–388.
Liberman, A. M., Isenberg, D., and Rakerd, B. (**1981**). "Duplex perception of cues for stop consonants: Evidence for a phonetic mode," Percept. Psychophys. **30**, 133–143.
Lu, Z. L., Williamson, S. J., and Kaufman, L. (**1992**). "Human auditory primary and association cortex have differing lifetimes for activation traces," Brain Res. **572**, 236–241.
Luo, H., Husain, F. T., Horwitz, B., and Poeppel, D. (**2005**). "Discrimination and categorization of speech and non-speech sounds in an MEG delayed-match-to-sample study," Neuroimage **28**, 59–71.
Macmillan, N. A. (**1987**). "Beyond the categorical/continuous distinction: A psychophysical approach to processing modes," in *Categorical Perception: The Groundwork of Cognition*, edited by S. R. Harnad (Cambridge University Press, New York), pp. 53–85.
Macmillan, N. A., and Creelman, C. D. (**1991**). *Detection Theory: A User's Guide* (Cambridge University Press, Cambridge, UK).
Macmillan, N. A., Goldberg, R. F., and Braida, L. D. (**1988**). "Resolution for speech sounds: Basic sensitivity and context memory on vowel and consonant continua," J. Acoust. Soc. Am. **84**, 1262–1280.
Macmillan, N. A., Kaplan, H. L., and Creelman, C. D. (**1977**). "The psychophysics of categorical perception," Psychol. Rev. **84**, 452–471.
Miller, J. D., Wier, C. C., Pastore, R. E., Kelly, W. J., and Dooling, R. J. (**1976**). "Discrimination and labeling of noise-buzz sequences with varying noise-lead times: An example of categorical perception," J. Acoust. Soc. Am. **60**, 410–417.
Mirman, D., Holt, L. L., and McClelland, J. L. (**2004**). "Categorization and discrimination of nonspeech sounds: Differences between steady-state and rapidly-changing acoustic cues," J. Acoust. Soc. Am. **116**, 1198–1207.
Ohl, F. W., Scheich, H., and Freeman, W. J. (**2001**). "Change in pattern of ongoing cortical activity with auditory category learning," Nature (London) **412**, 733–736.
Pastore, R. E., Ahroon, W. A., Baffuto, K. J., Friedman, C., Puleo, J. S., and Fink, E. A. (**1977**). "Common-factor model of categorical perception," J. Exp. Psychol. Hum. Percept. Perform. **3**, 686–696.
Pastore, R. E., Schmuckler, M. A., Rosenblum, L., and Szczesiul, R. (**1983**). "Duplex perception with musical stimuli," Percept. Psychophys. **33**, 469–474.
Pisoni, D. B. (**1973**). "Auditory and phonetic memory codes in the discrimination of consonants and vowels," Percept. Psychophys. **13**, 253–260.
Pisoni, D. B. (**1975**). "Auditory short-term memory and vowel perception," Mem. Cognit. **3**, 7–18.
Pisoni, D. B. (**1977**). "Identification and discrimination of the relative onset time of two component tones: Implications for voicing perception in stops," J. Acoust. Soc. Am. **61**, 1352–1361.
Pisoni, D. B., and Lazarus, J. H. (**1974**). "Categorical and noncategorical modes of speech perception along the voicing continuum," J. Acoust. Soc. Am. **55**, 328–333.
Pollack, I., and Pisoni, D. B. (**1971**). "On the comparison between identification and discrimination tests in speech perception," Psychonomic Sci. **24**, 299–300.
Repp, B. H., and Liberman, A. M. (**1987**). "Phonetic category boundaries are flexible," in *Categorical Perception: The Groundwork of Cognition*, edited by S. R. Harnad (Cambridge University Press, New York), pp. 89–112.
Repp, B. H., and Lin, H. B. (**1990**). "Integration of segmental and tonal information in speech perception: A cross-linguistic study," J. Phonetics **18**, 481–495.
Rosen, S., and Howell, P. (**1987**). "Auditory, articulatory and learning explanations of categorical perception in speech," in *Categorical Perception: The Groundwork of Cognition*, edited by S. R. Harnad (Cambridge University Press, New York), pp. 113–160.
Schneider, W., Eschman, A., and Zuccolotto, A. (**2002**). *E-Prime Reference Guide* (Psychology Software Tools Inc., Pittsburgh).
Shackleton, T. M., and Carlyon, R. P. (**1994**). "The role of resolved and unresolved harmonics in pitch perception and frequency modulation discrimination," J. Acoust. Soc. Am. **95**, 3529–3540.
Shiffrin, R. M., and Schneider, W. (**1977**). "Controlled and automatic human information processing. II. Perceptual learning, automatic attending, and a general theory," Psychol. Rev. **84**, 127–190.
Stagray, J. R., and Downs, D. (**1993**). "Differential sensitivity for frequency among speakers of a tone and a nontone language," J. Chin. Linguist. **21**, 144–162.
Stagray, J. R., Downs, D., and Sommers, R. K. (**1992**). "Contributions of the fundamental, resolved harmonics, and unresolved harmonics in tone-phoneme identification," J. Speech Hear. Res. **35**, 1406–1409.
Stevens, K. N. (**1981**). "Constraints imposed by the auditory system on the properties used to classify speech sounds," in *The Cognitive Representation of Speech*, edited by T. F. Myers, J. Laver, and J. Anderson (North-Holland, Amsterdam).
Stevens, K. N., Liberman, A. M., Studdert-Kennedy, M., and Ohman, S. E., (**1969**). "Crosslanguage study of vowel perception," Lang Speech **12**, 1–23.
Studdert-Kennedy, M., Liberman, A. M., Harris, K. S., and Cooper, F. S. (**1970**). "Theoretical notes. Motor theory of speech perception: A reply to Lane's critical review," Psychol. Rev. **77**, 234–249.
Tanner, W. P. Jr., and Rivette, G. L. (**1964**). "Experimental study of "tone deafness"," J. Acoust. Soc. Am. **36**, 1465–1467.
Traunmüller, H. (**1987**). "Some aspects of the sound of speech sounds," in *The Psychophysics of Speech Perception*, edited by M. E. Schouten (Martinus Nijhoff, Dordrecht), pp. 293–305.
Treisman, M., Faulkner, A., Naish, P. L., and Rosner, B. S. (**1995**). "Voice-onset time and tone-onset time: The role of criterion-setting mechanisms in categorical perception," Q. J. Exp. Psychol. A **48**, 334–366.
Valbret, H., Moulines, E., and Tubach, J. P. (**1992**). "Voice transformation using PSOLA," Speech Commun. **11**, 513–546.
van Hessen, A. J., and Schouten, M. E. (**1992**). "Modeling phoneme perception. II. A model of stop consonant discrimination," J. Acoust. Soc. Am. **92**, 1856–1868.
Wang, W. S.-Y. (**1976**). "Language change," Ann. N.Y. Acad. Sci. **208**, 61–72.
Wong, P. C., and Diehl, R. L. (**2003**). "Perceptual normalization for inter- and intratalker variation in Cantonese level tones," J. Speech Lang. Hear. Res. **46**, 413–421.

Neural correlates of intelligibility in speech investigated with noise vocoded speech—A positron emission tomography study

Sophie K. Scott[a)]
Department of Psychology and Department of Phonetics and Linguistics, University College London, Gower Street, London WC1E 6BT, United Kingdom

Stuart Rosen and Harriet Lang
Department of Phonetics and Linguistics, University College London, Gower Street, London WC1E 6BT, United Kingdom

Richard J. S. Wise
MRC CSC, Hammersmith Hospital, Ducane Road, London W12 0NN, United Kingdom

(Received 13 August 2003; accepted 25 April 2006)

Functional imaging studies of speech perception in the human brain have identified a key role for auditory association areas in the temporal lobes (bilateral superior temporal gyri and sulci) in the perceptual processing of the speech signal. This is extended to suggest some functional specialization within this bilateral system, with a particular role for the left anterior superior temporal sulcus (STS) in processing intelligible speech. In the current study, noise-vocoded speech was used to vary the intelligibility of speech parametrically. This replicated the finding of a selective response to intelligibility in speech in the left anterior superior temporal sulcus, in contrast to the posterior superior temporal sulcus, which showed a response profile insensitive to the degree of intelligibility. These results are related to theories of functional organization in the human auditory system, which have indicated that there are separate processing streams, with different functional roles, running anterior and posterior to primary auditory cortex. Specifically, it is suggested that an anterior stream processing intelligibility can be distinguished from a posterior stream associated with transient representations, important in spoken repetition and working memory. © *2006 Acoustical Society of America.* [DOI: 10.1121/1.2216725]

PACS number(s): 43.71.Rt, 43.64.Sj [PFA] Pages: 1075–1083

I. INTRODUCTION

The use of functional neuroimaging techniques that allow relatively precise anatomical localization [positron emission tomography (PET) and functional magnetic resonance imaging (fMRI)] has developed our understanding of the cortical basis of human speech perception, and the relationship with the functional neuroanatomy of audition. Work on the anatomy of the auditory cortex of the nonhuman primate (mostly in the rhesus macaque) has shown both parallel and serial (hierarchical) anatomical connections and neural processing in core, belt, and parabelt auditory regions (Rauschecker, 1998; Kaas and Hackett, 1999). This has been usefully applied to the findings from studies that have shown a similar architecture for sound processing in the human brain [e.g., Talavage *et al.*, 2000, Hall *et al.*, 2002; see Scott and Johnsrude (2003) for a review]. Importantly, these functional-anatomical studies have highlighted the rostral-caudal organization of the primate auditory cortex. In particular, the response to conspecific vocalizations more strongly activates temporal lobe regions lateral and anterior to the primary auditory cortex (Rauschecker, 1998). By contrast, Tian and colleagues demonstrated neurons posterior to primary auditory cortex that responded to the spatial localization of a vocalization but were largely insensitive to specific calls. These results, along with others, have led to the hypothesis that there are at least two "streams" of auditory processing: one directed anteriorly to identify the sound and another directed posteriorly that represents the spatial localization of the sound. Although this framework is not universally accepted (e.g., Middlebrooks, 2002), this functional-anatomical interpretation gains support from detailed anatomical connectivity studies in the macaque. These have shown segregation of superior temporal-prefrontal projections for anterior and posterior white matter tracts, which could form the basis for separate streams of auditory processing (Romanski *et al.*, 1999).

In the current study, we aimed to elaborate the roles of the rostral and caudal auditory cortex in speech processing in the human primate. Functional imaging studies of speech perception have shown extensive involvement of bilateral superior temporal lobe regions, including the primary auditory cortex (PAC), and over the lateral superior temporal gyrus (STG), a region corresponding to the parabelt cortex in nonhuman primates (Binder *et al.*, 2000). Activation typically extends down to the superior temporal sulcus (STS).

[a)]Address for correspondence: Institute of Cognitive Neuroscience, University College London, 17 Queen Square, London WC1N 3AR, UK. Electronic mail: sophie.scott@ucl.ac.uk

However, the neural activation measured in these studies (as indexed by regional cerebral blood flow) is always determined relative to a baseline condition, and the precise pattern of activation seen depends on the baseline condition selected. The selection of the baseline condition(s) can influence the degree to which the neural response to speech is left lateralized. Speech relative to silence (Wise *et al.*, 1991, 1999) typically shows a response in the bilateral primary auditory cortex, as there is no control for general auditory stimulation. Studies that employ an auditory baseline condition, which attempts to control for some of the acoustic structure in the speech signal, have found that speech-specific responses are seen bilaterally along much of the length of the lateral STG and STS. This has been shown for human vocalizations contrasted with signal-correlated noise (Mummery *et al.*, 1999) and its variants (Belin *et al.*, 2000), where the amplitude envelope variation (but not the spectral detail) of the speech signal is matched in the baseline stimuli.

This apparent bilateral representation of speech has led to the claim that the processing of speech is mediated bilaterally, and that a left hemisphere specialization for language occurs later in the neurolinguistic system (Hickok and Poeppel, 2000). However, symmetry of activation in the left and right dorsolateral temporal lobes need not imply that both cerebral hemispheres are performing identical computations on the input. A recent study of phonological structure indicated a role for the left lateral STG in the processing of phonological structure in speech (Jacquemot *et al.*, 2003) and a paper from our group indicated that neural responses as a function of intelligibility in speech (both normal and noise-vocoded) are also lateralized to the left temporal lobe (Scott *et al.*, 2000).

Scott *et al.* (2000) contrasted two forms of intelligible speech (normal and six-channel noise-vocoded) (Shannon *et al.*, 1995) against spectrally rotated equivalents (Blesser, 1972), in an attempt to use a baseline condition that more adequately controlled for the acoustic structure in speech. Spectral rotation preserves the overall pattern of spectro-temporal variation in speech (i.e., formants are clearly visible) as well as the original pitch contours of the speech, but the inversion in the spectral domain renders the speech unintelligible. Scott *et al.* (2000) demonstrated a left lateralized stream of speech processing, running lateral and anterior to the PAC, in which the processing of speech, noise vocoded speech, and rotated speech was observed in the bilateral STG and posterior STS and the processing of intelligible speech alone was seen more rostrally, in the anterior left STS. In contrast, responses in the right anterior STG/STS were greater to both speech-based stimuli (normal and rotated speech) than the two noise excited conditions, suggesting a preferential processing in right STG/STS for stimuli with dynamic, melodic pitch variation. This interpretation is supported by studies of the neural processing of pitch variation (Zatorre and Belin, 2001) and musical patterns (Patterson *et al.*, 2002), both of which have demonstrated a predominantly right lateralized response to pitch variation. The responses of the left and right anterior STG/STS can thus be distinguished. In addition, these anterior responses were compatible with hypotheses, based on nonhuman primate research, that there is an anterior "what" stream of auditory processing (Rauschecker, 1998). The left lateralized, anterior response to intelligible speech has been replicated and extended using fMRI (Narain *et al.*, 2003; Specht and Ruel, 2003) and has also been demonstrated in primate neural responses to conspecific vocalizations. (Poremba *et al.*, 2004)

In contrast to this emphasis on anterior temporal lobe regions, many (but not all) clinical studies on speech perception, based on lesion-deficit analyses in aphasic patients, emphasize the left *posterior* STS as a region that maps sound on to meaning. In our previous PET study (Scott *et al.*, 2000) this region did not show a speech-specific response, as it had the same stimulus response profile as the lateral STG, responding to speech, noise vocoded speech and rotated speech irrespective of intelligibility. We have suggested (Scott *et al.*, 2000; Wise *et al.*, 2001) that the posterior STS is involved in the short-term representation of sound input that might be mapped onto the production of words, rather than an acoustic-phonetic mapping onto lexical structures. Consistent with this potential distinction between anterior and posterior STS functions, small lesions of the left posterior STS result in conduction aphasia, where patients can understand spoken language, but cannot repeat words (Anderson *et al.*, 1999; Quigg and Fountain, 1999). These findings suggest that it might be possible to identify different response profiles to acoustic stimuli between the lateral STG and posterior STS, which was not possible in our previous study (Scott *et al.*, 2000), as both regions were equally activated by speech, noise vocoded speech, and rotated speech.

The current study was a replication and elaboration of our previous study. A parametric design was used, rather than the paired contrasts used previously. In parametric designs, a stimulus property is varied along a dimension in a number of steps, and regional cerebral blood flow (rCBF) changes that vary linearly with this variable are identified using a covariate analysis. This increases the sensitivity of the design, relative to functional imaging studies that rely on subtraction techniques. The number of channels in noise-vocoded speech (Shannon *et al.*, 1995) was varied from 1 to 16, to give a dimension of intelligibility and permit a correlational analysis of the rCBF changes that covary with this manipulation. Spectral rotation was again used as a control for complexity, since increasing the number of channels in noise-vocoded speech necessarily increases the spectro-temporal detail. In addition, to compare responses in the anterior and posterior STG and STS, a contrast of conditions in which some (if not all) of the lexical items were intelligible, against those where little if any of the stimuli can be understood was planned, to test the hypothesis that the posterior STS might show sensitivity to any potentially relevant spectro-temporal detail in the signal, rather than to overall degree of intelligibility.

Positron emission tomography (PET) was used to index neural activity. A disadvantage of PET is that the total number of scans performed is limited by the dose of radioactivity administered, which means that single-subject analyses are not normally possible and that grouped data are typically presented. PET has, however, several advantages for such investigations. It is relatively quiet (relative to the high levels of acoustic noise generated in fMRI). Most critically, the

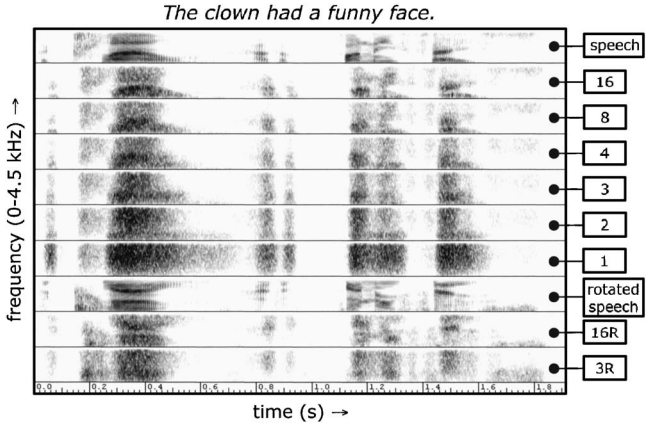

FIG. 1. Spectrograms of the stimuli used and of the original speech and rotated speech stimuli.

signal recorded in PET is equipotent across the cortex and subcortical regions, in contrast with fMRI, where the echo planar imaging (EPI) sequence normally used to measure the blood oxygen level dependent (BOLD) response is subject to signal loss due to artefact and geometric distortion (Devlin *et al.*, 2000). This effect is most dramatic in the anterior temporal lobes, regions which are of critical importance in speech perception (Scott *et al.*, 2000). Finally, the rCBF values which are measured to index neural activity are linear with respect to activity, unlike the BOLD response typically measured in fMRI (Dhankhar *et al.*, 1997).

II. METHOD

A. Stimuli

Speech was noise vocoded to l, 2, 3, 4, 8, and 16 channels, over the frequency range 70 Hz to 4 kHz using essentially the technique described by Shannon *et al.* (1995). The input waveform was passed through a bank of 1, 2, 4, 8, or 16 analysis filters (each a sixth-order Butterworth IIR, with three orders per upper and lower side) with frequency responses that crossed 3 dB down from the pass-band peak. Envelope detection occurred at the output of each analysis filter by full-wave rectification and second-order Butterworth low-pass filtering at 20 Hz. These envelopes were then multiplied by a white noise, and each filtered by a sixth-order Butterworth IIR output filter identical to the analysis filter. The rms level from each output filter was then set to be equal to the rms level of the original analysis outputs, before being summed together. Cross-over frequencies for both the analysis and output filters were calculated using an equation (and its inverse) relating position on the basilar membrane to its best frequency (Greenwood, 1990).

Spectrograms of the stimuli are shown in Fig. 1.

The control for complexity was noise-vocoded spectrally rotated speech. The original (low-pass filtered) speech was spectrally rotated around 2 kHz (Blesser, 1972), filtered so as to have the same long-term average spectrum as ordinary speech, then noise vocoded with 3 and 16 channels. These two conditions provide a control for neural activity that has an increase in spectro-temporal complexity without an increase in intelligibility. The stimuli were the BKB (Foster *et al.*, 1993) and IHR (MacLeod and Summerfield, 1987) sentences, spoken by an adult British English speaking male. These are short concrete sentences with three or four key words.

B. Participants

There were seven right-handed participants (six men and one woman), all with normal hearing. The average age was 38 (range 30–62). All the participants were able to understand the noise-vocoded speech after pretraining and in later testing (see Sec. IV). All gave written informed consent, which was approved by the Research Ethics Committee of Imperial College School of Medicine/Hammersmith, Queen Charlotte's & Chelsea & Acton Hospitals. Permission to administer radioisotopes was given by the Department of Health (UK).

Participants were pretrained on five channel noise-vocoded speech (NVC speech), by presenting them with a sentence and asking them to repeat back what they heard (these sentences were not included in the later scanning and intelligibility testing). If participants were incorrect, then they were given feedback and played the stimulus again until all sentences could be repeated correctly on the first presentation. This took fewer than 20 sentences for each participant. A different number of channels was used for pretraining to ensure that all the noise-vocoding conditions during scanning were novel (i.e., that no one condition was more familiar than the others), while also providing training that fell within the mid range of the overall number of channels presented.

C. PET scanning

PET scanning was performed with a Siemens HR++ (966) PET scanner operated in high-sensitivity 3D mode. Sixteen scans were performed on each subject, using the oxygen-15-labeled water bolus technique. All subjects were scanned while lying supine in a darkened room with their eyes closed. There were two scans for each stimulus condition, 1-, 2-, 3-, 4-, 8-, and 16-channel noise-vocoded speech and 3- and 16-channel rotated noise-vocoded speech. Stimulus presentation was for 1 min, throughout which the sentences were played continuously. The stimulus conditions were presented in a random order. The loudness was set at a comfortable level, determined for each subject, and this level was kept constant over the scanning sessions. The sentence presentations began 15 s before the scanning commenced, and each sentence presented was novel (i.e., there were no repeats). The subjects were instructed to listen passively "for meaning" in the scanning sessions. Passive listening reduces the likelihood that the observed activations are due to task-specific controlled processing, which would be involved if the subjects were required to make explicit responses or try and remember the sentences they heard (Scott and Wise, 2003). Thus, this study focused on the implicit, automatic mechanisms of speech perception. After the completion of scanning, each subject was tested on each condition, using a measure of the number of key words repeated correctly (16 sentences were presented per condition, scored as number

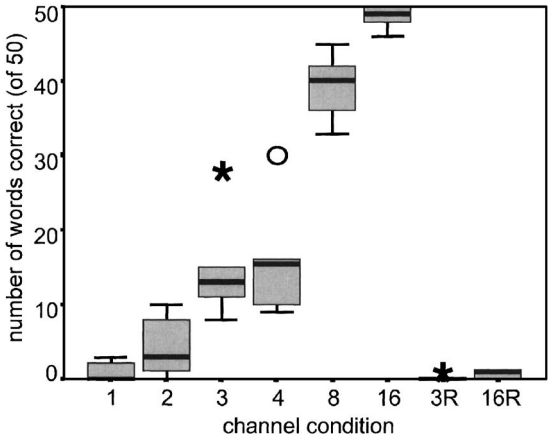

FIG. 2. Boxplots of the performance obtained for six of the seven subjects after PET scanning (one not being available for testing). The box indicates the interquartile range of values obtained, with the median indicated by the solid horizontal line. The range of measurements is shown by the whiskers except for points more than 1.5 (indicated by "o") or 3 box lengths ("*") from the upper or lower edge of the box. Scores are the number of key words reported correctly in a set of 16 sentences.

correct out of 50 key words). The sentences used were different for each testing condition and different from those used in training.

III. ANALYSIS

The images were analyzed using statistical parametric mapping (SPM99b, Wellcome Department of Cognitive Neurology, http://www.fil.ion.ucl.ac.uk/spm). All scans from each subject were realigned to eliminate head movements between scans and normalized into a standard stereotactic space. Images were then smoothed using an isotropic 10-mm, full width half-maximum, Gaussian kernel, to allow for variation in gyral anatomy and to improve the signal-to-noise ratio. Specific effects were investigated, voxel-by-voxel, using appropriate contrasts to create statistical parametric maps of the t statistic, which were subsequently transformed into Z scores. The analysis included a blocked analysis of covariance (AnCova) with global counts as a covariate to remove the effect of global changes in perfusion across scans. The threshold for significance was set at $P<0.05$, corrected for analyses across the whole volume of the brain ($P<0.000\,001$, uncorrected; Z score >4.7) [further details of this analysis technique are given in Scott *et al.* (2004)].

The main statistical analysis of the rCBF data aimed to identify the rCBF changes that correlate with the number of channels in NVC, but not with the rotated NVC stimuli. Intelligibility is most simply related to the logarithm of the number of channels (Faulkner *et al.*, 2001). The use of the logarithmic transform was supported by a logistic regression on the data presented in Fig. 2. With a single continuous predictor variable, using the logarithm of the number of channels led to a much better fit than the use of the number of channels directly. Therefore, we modeled for rCBF changes that correlate positively with the log number of channels and masked inclusively for regions where the two rotated conditions (16R and 3R) were significantly less responsive than their unrotated equivalents $[(3+16)>(3R+16R)]$. The use of inclusive masking was an attempt to identify voxels that are both more activated by unrotated NVC speech than by rotated speech, and which also show a sensitivity to the log number of channels in the noise vocoded speech. This contrast does not, however, explicitly exclude voxels in which there is a difference between the rotated conditions, i.e., the possibility remains that the analysis does not rule out voxels driven solely by acoustic complexity. A parallel analysis was therefore used in which the voxels that increased with the log number of channels were identified, but an exclusive mask was used to remove voxels which were sensitive to the differences between the 1, 3R, and 16R stimuli $[16R>3R>1]$, i.e., which were driven by increases in acoustic complexity. This analysis was thus a second attempt to identify voxels which correlate with the number of channels, but which are not solely responding to acoustic properties of the stimuli. The SPM package does not allow the simultaneous application of multiple masking conditions, so these two analyses were performed separately. The results of these parallel analyses are shown in Table I.

To test the hypothesis that the posterior STS might be responding to the conditions where there was the potential for intelligible speech, regardless of the actual degree of intelligibility, a contrast was planned comparing all the conditions where there was some intelligibility (3, 4, 8, and 16 channels) over those where there was little or none (1, 2, 3R, and 16R). Exclusive masking was used to exclude neural responses which were significantly activated overall by increasing numbers of channels. This subtraction contrast was designed therefore to reveal responses which are sensitive to a degree of spectro-temporal structure, sufficient for some speech perception, but not sensitive to specific increases in the number of channels.

IV. RESULTS

The behavioral data are shown in Fig. 2. This clearly demonstrates a relationship between the number of channels and the intelligibility of the speech, consistent with previous studies (Shannon *et al.*, 1995). Likewise, the intelligibility of the rotated sequences was negligible, as in previous studies (Scott *et al.*, 2000; Narain *et al.*, 2003).

Figures 3 and 4 and Table I show the neural correlates of increasing numbers of channels of NVC speech in the input, controlling for overall spectro-temporal complexity (by inclusive masking for $[(3+16)>(3R+16R)]$). RCBF increases can be seen in both temporal lobes, over the lateral STG, running lateral and anterior to the primary auditory cortex (PAC). In the left temporal lobe, however, the response to intelligibility passes rostrally down the temporal lobe, extending as far as the temporal pole. There was a peak in the left lateral superior temporal gyrus (STG), the left STS, and the left anterolateral temporal pole. The peak in the right temporal lobe was in the antero-lateral STG. The plots for the rCBF changes for each peak are shown in Figs. 4(a)–4(d). There is some sensitivity to acoustic complexity in the left lateral STG/STS peaks [Fig. 4(b) and 4(c)]: the response to 16R is greater than that to 3R, but the response to

TABLE I. Peaks of activations two contrast. Contrast 1: Activity correlated with the log channel number and for which there was greater activation for the unrotated stimuli than the rotated stimuli. Contrast 2: Activity correlated with the log channel number and for which there is no increase in activation for the increasing numbers of channels for the rotated speech conditions.

Contrast 1: peaks increasing with log number of channels, masking inclusively for regions where $(3+16)>(3R+16R)$		MMN coordinates		
Region	Z score	x	y	z
Right antero-lateral STG	5.96	64	−4	−2
Left lateral STG	4.52	−64	−28	8
Left anterior STS	5.6	−62	−10	0
Left temporal pole	4.73	−48	16	−16
Contrast 2: peaks increasing with log number of channels, masking exclusively for regions where $(16R>3R>1)$		**MMN coordinates**		
Region	Z score	x	y	z
Right lateral STG	5.36	64	−6	−4
Leftanterior STG/STS	5.01	−64	−8	4
Left temporal pole	4.73	−48	16	−16

the unrotated stimuli is greater still (indeed, no contrast in this study identified peak responses where the response to the unrotated stimuli was the same or smaller than to the rotated stimuli). When exclusive masking for acoustic structure (16R>3R>1) is used with the intelligibility contrast, the more posterior STG peak is not seen, confirming that it is sensitive to acoustic structure (Table I). The left temporal pole response shows no difference between 3R and 16R, suggesting insensitivity to acoustic complexity [Fig. 4(d)]. The left anterior STS peak shows a "midway" response: the pattern of activation follows the behavioral relationship between the number of channels and intelligibility, and the peak is not excluded by the 16R>3R>1 mask for acoustic sensitivity. This peak does, however, show some acoustic sensitivity to the difference between the 16R and 3R conditions [Fig. 4(c)].

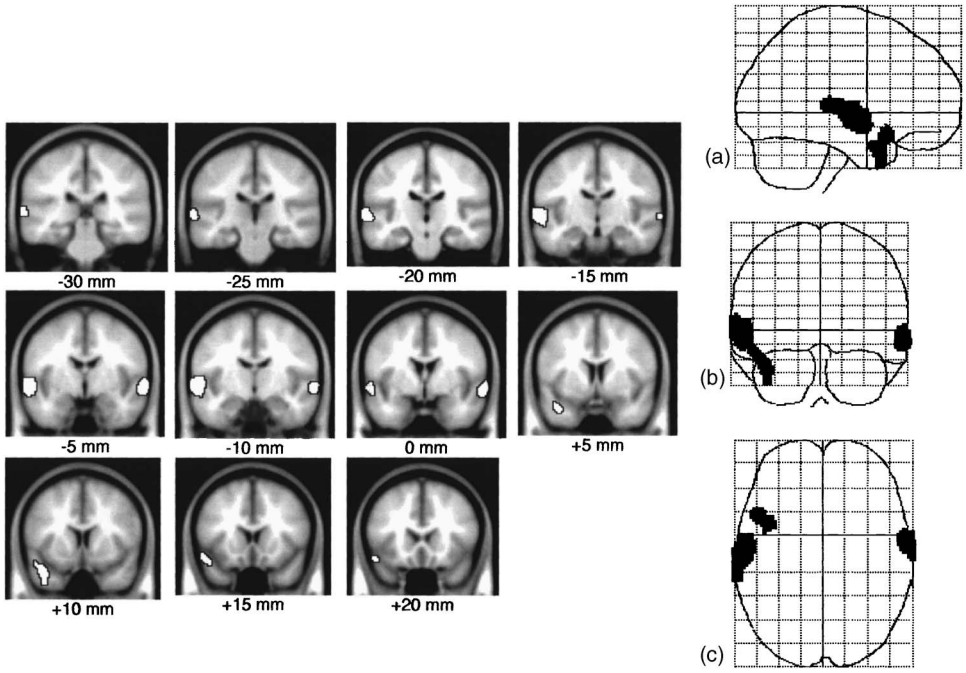

FIG. 3. Regions where activity increased with the number of channels (expressed logarithmically), masked inclusively for regions in which the unrotated stimuli were significantly higher than their rotated equivalents (voxel-level significance $P<0.0001$, unconnected for whole brain analysis). In the panels on the left, the activation is superimposed on coronal slices of an average T1 weighted MRI image (the Montreal Neurological Institute template, used in SPM99). The panel on the top left shows the most posterior activation, and the subsequent panels show the activation at slices, 0.5 cm apart, moving in an anterior direction. These panels show the activation running along the left STS, extending into STG in a posterior direction and into the medial and ventral temporal lobe in the anterior direction. The numbers below each panel refer to the distance along the y plane of MNI coordinates. The panels also show right STS activation in the slices between −15 and 0 mm. The panels on the right show the same activation, this time projected onto a "glass brain;" this lacks anatomical detail but shows all the activations on the same figure. Panel (a) shows a sagittal view, with the brain viewed from the side; panel (b) shows a coronal view, with the brain viewed from the back, and panel (c) shows an axial view, with the brain viewed from above.

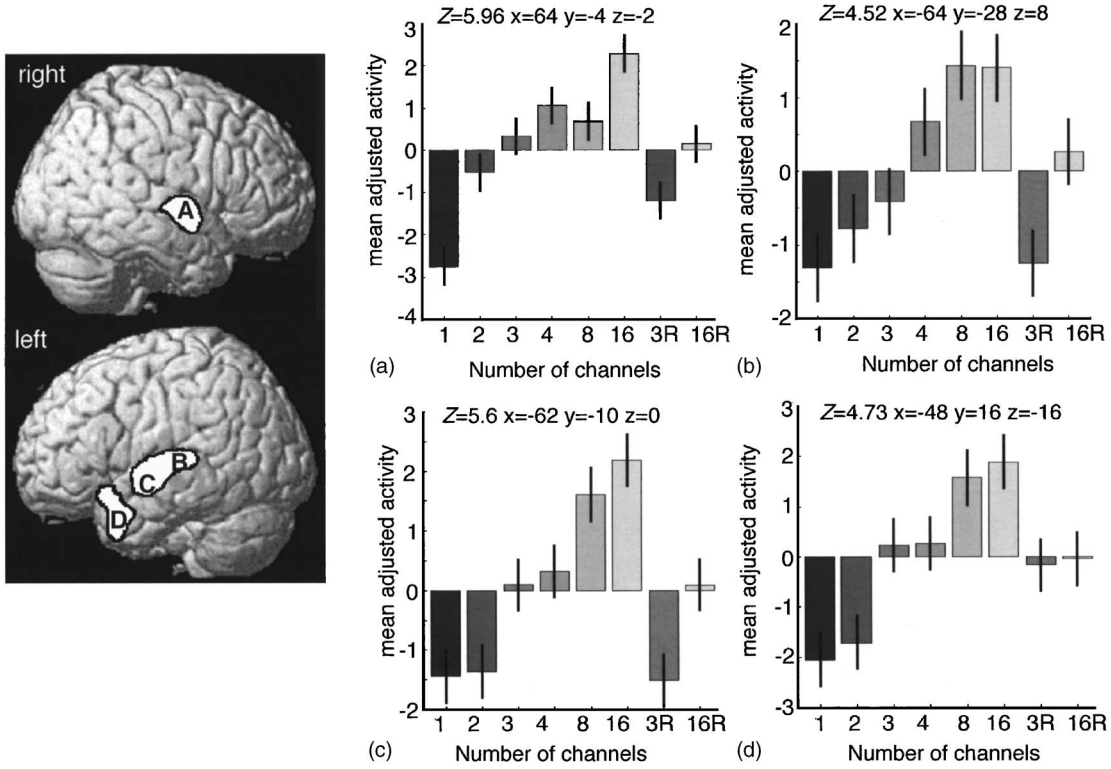

FIG. 4. Regions where activity increased with the number of channels (expressed logarithmically), masked inclusively for regions in which the unrotated stimuli were significantly higher than their rotated equivalents (voxel-level significance $P<0.0001$, uncorrected for whole brain analysis). The activations are rendered on the right and left hemispheres. The plots (a)–(d) show the rCBF variations with condition for each of the peaks: (a) shows the peak in the right STG, and (b)–(d) show the three peaks in the left temporal lobe.

The peak in the right STG is principally driven by differences between the single channel condition and the higher channel conditions, i.e., by some degree of spectral structure and variation [Fig. 4(a)]. There is also an elevated response to the 16-channel condition. If the contrast is repeated, with an exclusive mask for regions showing some sensitivity to spectral structure (i.e., [(2, 3, 4, 8, 16, 3R, and 16R) $>$ 1]), then the right STG activation is not seen. In contrast, the peaks in the left temporal lobe, which vary with the number of channels in a more linear fashion (though not with the rotated conditions), remain unchanged by this mask.

The planned contrast of conditions with sufficient spectro-temporal structure for some comprehension (3, 4, 8, and 16) over unintelligible conditions (1, 2, 3R, and 16R), with exclusive masking for regions that respond to increasing number of channels, shows a purely left lateralized response (Fig. 5). The activation runs posterior and lateral to the PAC, into the posterior STS. There are peaks at $x=-60$,

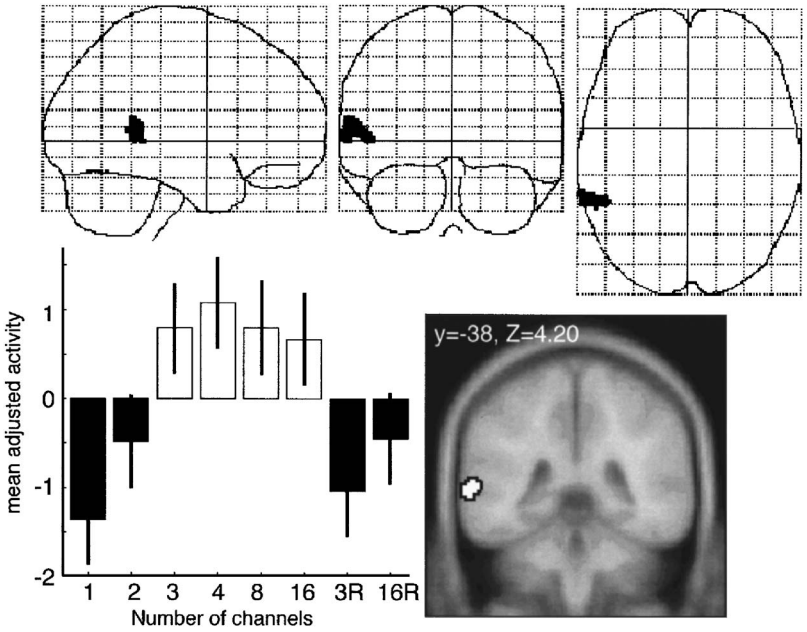

FIG. 5. Regions where the activation was increased for the conditions 3, 4, 8, and l6 over the conditions 1, 2, 3R, and 16R, masked exclusively for regions which increased logarithmically with the increasing number of channels. This shows a region in the left posterior STS, shown on a glass brain projection in the upper panels, and on a coronal slice from an average MRI template. The plot shows the rCBF profile of the peak closest to the posterior STS peak in Scott *et al.* (2000) which was located at −.64, −.38, 0.

$y=-44$, $z=10$ ($Z=4.33$) and $x=-64$, $y=-38$, $z=2$ ($Z=4.20$), and the plot for the latter is shown in Fig. 5. These peaks reflect activations which are not solely driven by increasing numbers of channels.

V. DISCUSSION

This study has thus presented strong evidence that, as in our previous study, intelligible speech is (predominantly) processed in the left anterior temporal lobe, and that there is a rostrally directed stream of processing of the speech signal. Importantly, there is a sensitivity to increases in the number of channels that are associated with intelligibility in regions lateral to PAC, in very similar regions to those which respond to amplitude modulations (contrasted with unmodulated noise) in fMRI studies (Giraud *et al.*, 2000; Hart *et al.*, 2003). Hart and colleagues specifically identified regions in the lateral STG, adjacent to the PAC, that respond selectively to amplitude modulations in the speech AM range. This lateral STG region shows sensitivity to phonological structure in speech (Jacquemot *et al.*, 2003), and in the current study the response profile indicates some specialization for speech specific information, although it is also sensitive to aspects of acoustic structure. This suggests that the neural regions involved in processing amplitude modulation are also important initial stages in the processing of the speech signal. Descriptively, there is also the appearance of hierarchical processing of the signal (Scott and Johnsrude, 2003): the most posterior peak in the left STG shows a linear relationship between the number of channels from 1 to 8 (but not to the rotated stimuli), whereas the more anterior peaks (STS, temporal pole) have profiles more similar to the intelligibility data, where 1 and 2 channels, and 3 and 4 channels activate this area to a similar degree.

This study also revealed a response to intelligible speech in the right lateral STG, not seen in our previous study. This may be a consequence of the use of a more sensitive parametric design. There are three other potential factors which may affect this result. There is an enhanced response in the right lateral STG to all the NVC conditions relative to the single channel condition—that is, there is increased activation for each condition with some spectral structure, relative to the one channel condition. This suggests that the right STG is sensitive to changes in spectral structure, or perhaps to the pitch sensation consequent upon this. There is also an enhanced response in the right lateral STG to the 16-channel condition. Since the intelligible speech with 16 channels sounds recognizably like the original speaker [and informal listening suggests those up to 8 do not (Warren *et al.*, under review)], right temporal lobe mechanisms involved in speaker recognition might be activated along with increased intelligibility (Van Lancker *et al.*, 1989). It is also possible that, since the increased number of channels leads to a stronger sense of pitch (Xu *et al.*, 2002), the activation may reflect processing of the variation in pitch (due to the original speech intonation), which is known to lead to greater right STG/STS involvement (Patterson *et al.*, 2002). An effect of pitch variation should be attenuated by use of rotated stimuli as a baseline, since these preserve dynamic pitch variation. However the rotated stimuli do evoke a weaker pitch sensation than the unrotated stimuli. Further studies will allow us to clarify the reasons for this finding.

The use of a parametric design allows us to draw a distinction within the left temporal lobe between the lateral STG and the posterior STS. In our previous study (Scott *et al.*, 2000), these both responded to speech, rotated speech, and NVC speech equally. Lateral STG, like the anterior temporal lobe, shows a sensitivity to the number of channels in the NVC speech and a reduced sensitivity to the rotated stimuli, consistent with these regions forming an auditory "what" pathway [Figs. 4(b) and 4(c)] (Rauschecker, 1998; Scott *et al.*, 2000; Scott and Johnsrude, 2003). The posterior STS, however, is activated equally by the 3-, 4-, 8-, and 16-channel NVC speech conditions, despite considerable intelligibility differences across these conditions.

The left posterior STS therefore does not appear to be part of the same functional system as the antero-laterally directed pattern of hierarchical acoustic processing (Scott and Johnsrude, 2003; Wise *et al.*, 2001). Unlike the anterior STG, the posterior STS does not receive direct monosynaptic input from primary auditory areas, being at least two synapses away (Galuske *et al.*, 1999). Left posterior STS has been identified as having an important role in the rehearsal or production of spoken repetition (e.g., Wise *et al.*, 2001), and in the representation of sequences in auditory short-term memory rehearsal (Buchsbaum *et al.*, 2001). The posterior STS is activated by some acoustic stimuli (Mummery *et al.*, 1999; Hall *et al.*, 2002; Giraud and Price, 2001) and is associated with plasticity in the recovery of speech perception after aphasic stroke (Leff *et al.*, 2002). We have speculated previously that the posterior STS will show sensitivity to stimulus properties in *potentially* pronounceable sequences (Scott *et al.*, 2000), where the stimuli with some potential were speech, NVC speech, and rotated speech. Rotated speech is not necessarily pronounceable *per se*, but it preserves the temporal structure of the speech and thus the overall suprasegmental structure of the speech, and can indeed be understood after lengthy training (Blesser, 1972). The left posterior STS may therefore be responding to the saliency of this speechlike signal rather than to its overall intelligibility. The current study supports this position: the peak in the posterior STS is revealed by contrasting the four conditions in which there were *some* intelligible items with those in which there were none. The peak does not, however, show sensitivity to the number of channels and consequent variation in intelligibility. Thus the posterior STS shows a sensitivity to aspects of the acoustic structure of the sound sequences and the potential for meaningful structure to emerge from this. Such a response would be predicted by models which represent the acoustic structure of incoming sequences in some form of "buffer," for example the syllable processing model of Hartley and Houghton (1996). In this model, based on the errors made in word and nonword repetition tasks, the incoming speech signal is represented in a manner consistent with the underlying phonological structure of that language at the syllable (i.e., suprasegmental) level, with an emphasis on the sonority profile and the onset/rhyme distinction. If the posterior STS does play an important part in the processing

of such structure, then it would not be expected to simply detect intelligibility *per se*, but more structural, surapsegmental sequential elements that relate the incoming sound to how it might be spoken, and which are preserved in NVC speech with only a few channels.

Speech perception can also lead to activation in more posterior STS/inferior parietal cortex. We have recently replicated the original Scott *et al.* (2000) study with fMRI (Narain *et al.*, 2003) and found, in addition to a left anterior STS response, intelligibility-related activation which lies at the junction of the STS and in the left inferior parietal lobe, posterior ($y=-.64$) to the caudal STS activation described in this paper ($y=-44,-.38$) and that in our earlier PET study ($y=-.38$) (Scott *et al.*, 2000). The role of this more elusive posterior activation, and its relation to semantic processing, will be elaborated in further studies.

A recent fMRI study (Davis and Johnsrude, 2003) also used varying numbers of channels in NVC speech resulting in low, medium, and high intelligibility. In their study three different manipulations of intelligibility were constructed: NVC speech of 4, 8, and 15 channels, varying the signal-to-noise ratio of speech in noise and interrupting sentences with random sections of signal correlated noise (Schroeder, 1969). In addition to extensive pilot testing, performance during scanning was measured on line by using an explicit intelligibility judgment (not subsequently used for analysis). The contrast of increasing intelligibility (from the pilot testing) revealed a distributed system running anterior and posterior to PAC, into the ventral temporal lobes and prefrontal cortex. Evidence was found for a distinction between form-dependent processes (those that showed a response dependent on a particular manipulation condition) and form-independent processing (responses which were intelligibility specific but not sensitive to the type of stimulus manipulation). The design, however, included no formal control for the acoustic structure of the stimuli, which varied greatly both across manipulations and with intelligibility. Thus this study was not able to distinguish different patterns of activation within the hierarchical pattern of responses seen. For example, some regions in bilateral STG were reported to show a mixture of form-dependent and -independent responses: a control for acoustic aspects of the stimuli would have enabled these responses to be more clearly described. Without this, the "form-independent" regions are only independent of the form variations included in the study itself. This design also assumes that there are no important differences between the neural resources recruited by the three types of speech manipulation. There is some evidence that this assumption may be incorrect. We have previously demonstrated that the perception of speech in noise (energetic masking) is associated with activity in the prefrontal and parietal cortex, and that SNR level-independent responses are seen in the left ventral prefrontal and supplementary motor regions (Scott *et al.*, 2004). These regions are not activated by the manipulation of channel number in the current study, suggesting that there is not a complete overlap of the neural regions associated with these two manipulations of intelligibility. Furthermore, as discussed in the Introduction, the BOLD response typically measured in fMRI is associated with severe signal loss and distortion in the anterior temporal lobes. The most anterior peak reported for the intelligibility contrast in Davis and Johnsrude's study had a y coordinate of -34, and the most anterior peak associated with intelligibility in the current study is $+16$. This 5-cm difference may well be the result of signal loss in these more anterior regions arising from the use of fMRI.

Our current study of noise vocoded speech differs in several ways. Our use of a passive paradigm ensures that the activations seen will be associated with auditory processing of the input, rather than with explicit decision-making aspects of the task. It would be interesting to determine the extent to which the prefrontal activations seen in the Davis and Johnsrude (2003) paper would remain if a passive task were used. Our use of a wider range of channels also enables us to delineate brain regions which respond to increases across a wider range of NVC speech conditions, with special reference to the lower number of channel conditions, where intelligibility varies greatly. The smallest number of channels used by Davis and Johnsrude (2003) was four. From Fig. 2, and the plots in Fig. 4, we can identify both behavioral and neural responses that are sensitive to variation in the numbers of channels from one to four. Our use of two rotated NVC speech conditions enables us to explicitly distinguish between neural responses to auditory structural complexity changes and those which are associated with intelligibility. The use of PET enables us to identify peaks of activity that lie in very anterior temporal lobe regions (Table I, Figs. 3 and 4).

These factors explain why we are able to identify neural responses, associated specifically with intelligibility, in anterior temporal lobe regions not reported by Davis and Johnsrude (2003). Our design also permits the delineation of a difference between anterior and posterior auditory association cortical responses, consistent with the differing functions ascribed to these (Scott and Johnsrude, 2003; Wise *et al.*, 2001). This is also a consequence of the use of a passive design: if the posterior STS is important in transient representations of auditory inputs, then its role might be expected to change in an explicit, decision making task, as outlined by Buchsbaum and colleagues.

Thus we have argued for a distributed neural system involved in the processing of intelligible speech, which divides into two broad streams of processing: an anterior lateral stream associated with the acoustic-phonetic, semantic, and syntactic information which contributes to meaning in the speech signal (but not to all acoustic structure) and a posterior STS region sensitive to any potentially relevant structure in the incoming signal, regardless of the specific degree of acoustic detail. This is broadly within the parameters of the known neuroanatomy of the primate auditory cortex. Of course both anterior and posterior routes converge in prefrontal and premotor cortical regions (reviewed in Scott and Johnsrude, 2003) to form an interacting network.

ACKNOWLEDGMENTS

SKS and RJSW are both supported by grants from the Wellcome Trust. Many thanks to Sam Eaton-Rosen for help in creating Fig. 1.

Anderson, J. M., Gilmore, R., Roper, S., Crosson, B., Bauer, R. M., Nadeau, S., Beversdorf, D. Q., Cibula, J., Rogish, M. III, Kortencamp, S., Hughes, J. D., Gonzalez Rothi, L. J., and Heilman, K. M. (**1999**). "Conduction aphasia and the arcuate fasciculus: a reexamination of the Wernicke-Geschwind model," Brain Lang **70**, 1–12.

Belin, P., Zatorre, R. J., Lafaille, P., Ahad, P. and Pike, B. (**2000**). "Voice-selective areas in human auditory cortex," Nature (London) **403**, 309–312.

Binder, J. R., Frost, J. A., Hammeke, T. A., Bellgowan, P. S., Springer, J. A., Kaufman, J. N., and Possing, E. T. (**2000**). "Human temporal lobe activation by speech and nonspeech sounds," Cereb. Cortex **10**, 512–528.

Blesser, B. (**1972**). "Speech perception under conditions of spectral transformation: I. Phonetic characteristics," J. Speech Hear. Res. **15**, 5–41.

Buchsbaum, B. R., Hickok, G., and Humphries, C. (**2001**). "Role of left posterior superior temporal gyrus in phonological processing for speech perception and production," Cogn. Sci. **25**, 663–678.

Davis, M. H., and Johnsrude, I. S. (**2003**). "Hierarchical processing in spoken language comprehension," J. Neurosci. **23**, 3423–3431.

Devlin, J. T., Russell, R. P., Davis, M. H., Price, C. J., Wilson, J., Moss, H. E., Matthews, P. M., and Tyler, L. K. (**2000**). "Susceptibility-induced loss of signal: comparing PET and fMRI on a semantic task," Neuroimage **65**, 589–600.

Dhankhar, A., Wexler, B. E., Fulbright, R. K., Halwes, T., Blamire, A. M., and Shulman, R. G. (**1997**). "Functional magnetic resonance imaging assessment of the human brain auditory cortex response to increasing word presentation rates," J. Neurophysiol. **77**, 476–483.

Faulkner, A., Rosen, S., and Wilkinson, L. (**2001**). "Effects of the number of channels and speech-to-noise ratio rate of connected discourse tracking through a simulated cochlear implant speech processor," Ear Hear. **22**, 431–438.

Foster, J. R., Summerfield, A. Q., Marshall, D. H., Palmer, L., Ball, V., and Rosen, S. (**1993**). "Lip-Reading the BKB sentence lists - corrections for list and practice effects," Br. J. Audiol. **27**, 233–246.

Galuske, R. A. W., Schuhmann, A., Schlote, W., Bratzke, H., and Singer, W. (**1999**). "Interareal connections in the human auditory cortex," Neuroimage **9**, S994.

Giraud, A. L., and Price, C. J. (**2001**). "The constraints functional imaging places on classical models of auditory word processing," J. Cogn Neurosci. **13**, 754–765.

Giraud, A. L., Lorenzi, C., Ashburner, J., Wable, J., Johnsrude, I., Frackowiak, R., and Kleinschmidt, A. (**2000**). "Representation of the temporal envelope of sounds in the human brain," J. Neurophysiol. **84**, 1588–1598.

Greenwood, D. D. (**1990**). "A cochlear frequency-position function for several species—29 years later," J. Acoust. Soc. Am. **87**, 2592–2605.

Hall, D. A., Johnsrude, I. S., Haggard, M. P., Palmer, A. R., Akeroyd, M. A., and Summerfield, A. Q. (**2002**). "Spectral and temporal processing in human auditory cortex," Cereb. Cortex **12**, 140–149.

Hart, H. C., Palmer, A. R., and Hall, D. A. (**2003**). "Amplitude and frequency-modulated stimuli activate common regions of human auditory cortex," Cereb. Cortex **13**, 773–781.

Hartley, T., and Houghton, G. (**1996**). "A linguistically constrained model of short-term memory for nonwords," J. Mem. Lang. **35**, 1–31.

Hickok, G., and Poeppel, D. (**2000**). "Towards a functional neuroanatomy of speech perception," Trends in Cognitive Science **4**, 131–138.

Jacquemot, C., Pallier, C., LeBihan, D., Dehaene, S., and Dupoux, E. (**2003**). "Phonological grammar shapes the auditory cortex: a functional magnetic resonance imaging study," J. Neurosci. **23**, 9541–9546.

Kaas, J. H., and Hackett, T. A. (**1999**). "'What' and 'where' processing in auditory cortex," Nat. Neurosci. **12**, 1045–1047.

Leff, A., Crinion, J., Scott, S., Turkheimer, F., Howard, D., and Wise, R. (**2002**). "A physiological change in the homotopic cortex following left posterior temporal lobe infarction," Ann. Neurol. **51**, 553–558.

MacLeod, A., and Summerfield, Q. (**1987**). "Quantifying the contribution of vision to speech perception in noise," Br. J. Audiol. **21**, 131–141.

Middlebrooks, J. C. (**2002**). "Auditory space processing: here, there or everywhere?" Nat. Neurosci. **5**, 824–826.

Mummery, C. J., Ashburner, J., Scott, S. K., and Wise, R. J. S. (**1999**). "Functional neuroimaging of speech perception in six normal and two aphasic subjects," J. Acoust. Soc. Am. **106**, 449–457.

Narain, C., Scott, S. K., Wise, R. J. S., Rosen, S., Leff, A., Iversen, S. D., and Matthews, P. M. (**2003**). "Defining a left-lateralised response specific to intelligible speech using fMRI," Cereb. Cortex **13**, 1362–1368.

Patterson, R. D., Uppenkamp, S., Johnsrude, I. S., and Griffiths, T. D. (**2002**). "The processing of temporal pitch and melody information in auditory cortex," Neuron **36**, 767–776.

Poremba, A., Malloy, M., Saunders, R. C., Carson, R. E., Herscovitch, P., and Mishkin, M. (**2004**). "Species-specific calls evoke asymmetric activity in the monkey's temporal poles," Nature (London) **427**, 448–451.

Quigg, M., and Fountain, N. B. (**1999**). "Conduction aphasia elicited by stimulation of the left posterior superior temporal gyrus," J. Neurol., Neurosurg. Psychiatry **66**, 393–396.

Rauschecker, J. P. (**1998**). "Cortical processing of complex sounds," Curr. Opin. Neurobiol. **8**, 516–521.

Romanski, L. M., Tian, B., Fritz, J., Mishkin, M., Goldman-Rakic, P. S., and Rauschecker, J. P. (**1999**). "Dual streams of auditory afferents target multiple domains in the primate prefrontal cortex," Nat. Neurosci. **2**, 1131–1136.

Schroeder, M. R. (**1969**). "Reference signal for signal quality studies," J. Acoust. Soc. Am. **44**, 1735–1736.

Scott, S. K., and Johnsrude, I. S. (**2003**). "The neuroanatomical and functional organization of speech perception," Trends Neurosci. **26**, 100–107.

Scott, S. K., and Wise, R. J. S. (**2003**). "Functional imaging and language: A critical guide to methodology and analysis," Speech Commun. **41**, 7–21.

Scott, S. K., Blank, S. C., Rosen, S., and Wise, R. J. S. (**2000**). "Identification of a pathway for intelligible speech in the left temporal lobe," Brain **123**, 2400–2406.

Scott, S. K., Rosen, S., Wickham, L., and Wise, R. J. S. (**2004**). "A positron emission tomography study of the neural basis of informational and energetic masking effects in speech perception," J. Acoust. Soc. Am. **114**, 813–821.

Shannon, R. V., Zeng, F. G., Kamath, V., Wygonski, J., and Ekelid, M. (**1995**). "Speech recognition with primarily temporal cues," Science **270**, 303–304.

Specht, K., and Reul, J. (**2003**). "Functional segregation of the temporal lobes into highly differentiated subsystems for auditory perception: an auditory rapid event-related fMRI-task," Neuroimage **20**, 1944–1954.

Talavage, T. M., Ledden, P. J., Benson, R. R., Rosen, B. R., and Melcher, J. R. (**2000**). "Frequency-dependent responses exhibited by multiple regions in human auditory cortex," Hear. Res. **150**, 225–244.

Tian, B., Reser, D., Durham, A., Kustov, A., and Rauschecker, J. P. (**2001**). "Functional specialization in rhesus monkey auditory cortex," Science **292**, 290–293.

Van Lancker, D. R., Kreiman, J., and Cummings, J. (**1989**). "Voice perception deficits: neuroanatomical correlates of phonagnosia," J. Clin. Exp. Neuropsychol **11**, 665–674.

Warren, J. D., Scott, S. K., Price, C. J., and Griffiths, T. D. (under review). "Distinct human brain mechanisms for the separation and analysis of voices," Neuroimage.

Wise, R., Chollet, F., Hadar, U., Friston, K., Hoffner, E., and Frackowiak, R. (**1991**). "Distribution of cortical neural networks involved in word comprehension and word retrieval," Brain **114**, 1803–1817.

Wise, R. J., Scott, S. K., Blank, S. C., Mummery, C. J., Murphy, K., and Warburton, E. A. (**2001**). "Separate neural subsystems within 'Wernicke's area'," Brain **124**, 83–95.

Wise, R. J. S., Greene, J., Buchel, C., and Scott, S. K. (**1999**). "Brain regions involved in articulation," Lancet **353**, 1057–1061.

Xu, L., Tsai, Y., and Pfingst, B. E. (**2002**). "Features of stimulation affecting tonal-speech perception: implications for cochlear prostheses," J. Acoust. Soc. Am. **112**, 247–258.

Zatorre, R. J., and Belin, P. (**2001**). "Spectral and temporal processing in human auditory cortex," Cereb. Cortex **11**, 946–953.

Radiation forces exerted on arbitrarily located sphere by acoustic tweezer

Jungwoo Lee and K. Kirk Shung
Department of Biomedical Engineering, University of Southern California, Los Angeles, California 90089

(Received 25 July 2005; revised 30 May 2006; accepted 31 May 2006)

In a previous paper acoustic radiation force on a lipid sphere in a 100-MHz focused Gaussian field was calculated to demonstrate the acoustic tweezer effect near the focus. The theoretical formulation was based on the situation where the sphere is centered along the beam axis. Given intensity distribution independent of the x axis, it was then approximated by a cylindrical model for the sake of simplicity. Only the axial forces were considered because no lateral forces exist due to an object's symmetry. However, it was difficult to employ the same technique to the more general case when it is off the beam axis. To overcome the limitation, in this paper the previous model is modified to compute two additional lateral forces by carrying out the projection over arbitrary incident planes to restrict the integration limits. For different sizes of the sphere, the magnitudes of the net forces in three orthogonal directions are computed. The results show that the acoustic tweezer can be realized more easily in the lateral directions than in the axial directions. Differing from the axisymmetric case, the spheres of small sizes tend to be more strongly attracted than the larger ones in the lateral directions. © *2006 Acoustical Society of America.* [DOI: 10.1121/1.2216899]

PACS number(s): 43.80.Gx, 43.80.Jz [CCC] Pages: 1084–1094

I. INTRODUCTION

The precise dynamic control of small particles as diverse as atoms, living cells, or organelles has been a challenging issue in physical and biological sciences. Over the past decades the use of an optical tweezer[1–3] has brought forth revolutionary achievements in guiding and trapping minuscule particles. The development of this unique means was made possible by the radiation force arising from the momentum of optical energy. Recently, this technique has been extensively applied to many biological applications such as the measurement of the forces involved in motor molecules and the mechanical properties of white blood cells. However, there are several drawbacks concerning the use of laser. First, it is hard to observe the phenomenon in light opaque media. Second, due to its shallow depth of penetration, this technique may be difficult to apply to regions deeper into the medium. Third, the high intensities of laser itself may inflict severe damage to living tissues. These problems may be partially alleviated, if not completely, by using acoustic energy where the particles might be driven by the acoustic radiation force.[4–6]

In a previous paper,[7] the feasibility of the acoustic tweezer effect or trapping by a single ultrasonic beam was theoretically demonstrated in ray acoustics regime where a particle size much larger than an ultrasonic wavelength is considered. Only the axial radiation force on a lipid particle placed on the beam axis was calculated in a Gaussian-distributed ultrasound beam generated by a 100-MHz transducer with an F number of 1. It was shown that a steep intensity variation is the most critical factor to create the acoustic counterpart similar to an optical tweezer. Since the particle size of interest is in the range of tens of nanometers to tens of micrometers, the use of high-frequency ultrasound is essential. Another requirement for the acoustic tweezer was that the acoustic impedance of a particle has to be slightly smaller than that of a surrounding medium. Although optical tweezers also have a similar restriction, i.e., the refractive index of a particle must be larger than that of a surrounding medium, this has not prevented them from finding many useful applications. Hence, this limitation should not pose a problem in applying an acoustic tweezer to other types of particles. One solution would be to replace the surrounding medium by a fluid whose acoustic impedance is slightly higher than the particle's.

To simply verify the existence of an acoustic tweezer, in the previous paper[7] all the calculations were done for the axisymmetric case where the radiation force has only an axial component along the beam propagation. In the off-axis situation individual rays impinging on an object produce asymmetric radiation forces about the beam axis. This results in significant forces in lateral directions perpendicular to the axial ones. Therefore, the calculation procedure should account for not only the axial radiation forces but also the lateral ones. Due to the geometrical complexity the formulation becomes much more complicated. In the next two sections, we will take into consideration the radiation forces when a particle is centered on the YZ plane and subsequently extend those formulations to an arbitrarily located sphere. The simulation data and further analysis will be presented in Secs. IV and V. Finally, concluding remarks will be given in Sec. VI.

Throughout the paper, all the results and the derivations are based on the ray acoustics approach, and other effects such as acoustic streaming and thermodynamics are ignored for the sake of simplicity.

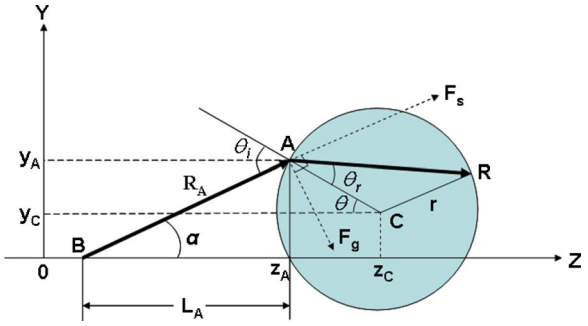

FIG. 1. (Color online) 2D schematic diagram of the sphere centered at an arbitrary location C. It is hit by an incident ray at the point A and the ray is equivalently considered to come from the point B due to the beam convergence. The scattering force F_s is applied in the direction of the incident ray, while the gradient force F_g is in the direction of the intensity gradient or perpendicular to F_s. R_A and r are the length of $\overline{AB}$ and the radius of the sphere; θ_i and θ_r are the incident and the refracted angles; θ is the angle between $\overline{CA}$ and the line $y=y_c$; α is the angle between $\overline{AB}$ and the z axis.

II. RADIATION FORCES ON SPHERE CENTERED ON *YZ* PLANE: 2D MODEL

In this section we will derive the mathematical expressions to calculate the radiation force when a sphere is located at an arbitrary position (y_c, z_c) as shown in Fig. 1. As an incident beam propagates from the left to the right, it exerts a force on a sphere consisting of two components, the scattering and the gradient forces. As defined both in ray acoustics and in geometrical optics, the former originated from reflection is proportional to the beam intensity and points at the incident direction, whereas the latter arising from refraction is proportional to the gradient of intensity and points at the direction of the intensity gradient.[3,7] The two components are perpendicular to each other and produce the radiation forces not only in the axial direction but also in the lateral direction.[2,8] In order to compute the asymmetric force created by an individual ray, both the axial and the lateral forces caused by the scattering and the gradient forces have to be added up at the same time. Therefore, the net force $d\vec{F}$ by an individual ray can be expressed as

$$d\vec{F} = d\vec{F}_s + d\vec{F}_g, \tag{1}$$

where $d\vec{F}_s$ and $d\vec{F}_g$ represent the scattering and the gradient forces, respectively. Each of them can also be given by

$$d\vec{F}_s = \frac{IdS\cos\theta_i}{c_w}\vec{s}, \tag{2}$$

$$d\vec{F}_g = \frac{IdS\cos\theta_i}{c_w}\vec{g}, \tag{3}$$

$$dS = r^2\sin\theta d\theta, \tag{4}$$

where $\vec{s}$ and $\vec{g}$ are the unit vectors in the directions of the scattering and the gradient forces; I and c_w are the acoustic intensity and the speed of sound in water, respectively; θ_i and r are the incident angle and the radius of the sphere; θ is the angle that a line $\overline{CA}$ makes with respect to the z axis as shown in Fig. 1. The symbol dS given by $r^2\sin\theta d\theta$ indicates the differential area over which an incident ray hits on a particle. The scattering and the gradient forces have different forms due to their directions. Decomposed in the y and z directions, they are denoted as

$$d\vec{F}_s = \frac{IdS\cos\theta_i}{c_w}\vec{s} = \frac{IdS\cos\theta_i}{c_w}(\vec{s_z} + \vec{s_y}) = (dF_{sz}, dF_{sy}), \tag{5}$$

$$d\vec{F}_g = \frac{IdS\cos\theta_i}{c_w}\vec{g} = \frac{IdS\cos\theta_i}{c_w}(\vec{g_z} + \vec{g_y}) = (dF_{gz}, dF_{gy}), \tag{6}$$

where the subscript sz, for example, indicates the z component of the scattering force. However, internal scatterings inside the sphere were not considered in the above equations. If including an infinite number of internal reflections in the formulation, we must insert additional terms into Eqs. (5) and (6) to account for them, which are given by

$$Q_s = 1 + R\cos 2\theta_i - \sum_{n=0}^{\infty} T^2R^n\cos\{2\theta_i - 2\theta_r + n(\pi - 2\theta_r)\}$$
$$= 1 + R\cos 2\theta_i - \frac{T^2[\cos(2\theta_i - 2\theta_r) + R\cos 2\theta_i]}{1 + R^2 + 2R\cos 2\theta_r}, \tag{7}$$

$$Q_g = -R\sin 2\theta_i + \sum_{n=0}^{\infty} T^2R^n\sin\{2\theta_i - 2\theta_r + n(\pi - 2\theta_r)\}$$
$$= -R\sin 2\theta_i + \frac{T^2[\sin(2\theta_i - 2\theta_r) + R\sin 2\theta_i]}{1 + R^2 + 2R\cos 2\theta_r}, \tag{8}$$

$$R = \left|\frac{Z_2/\cos\theta_r - Z_1/\cos\theta_i}{Z_2/\cos\theta_r + Z_1/\cos\theta_i}\right|^2, \tag{9}$$

$$T = 1 - R, \tag{10}$$

where θ_i and θ_r are the incident and refracted angles; Z_1 and Z_2 are the acoustic impedances in the surrounding medium and the particle; R and T are Fresnel reflection and transmission coefficients.[9] Q_s and Q_g define the fractions of the peak force transferred to the sphere by an incident ray in the directions of the propagation and the intensity gradient, respectively. Substituting Eqs. (7)–(10) into Eqs. (5) and (6), we obtain

$$d\vec{F}_s = Q_s\frac{IdS\cos\theta_i}{c_w}\vec{s}$$
$$= Q_s\frac{IdS\cos\theta_i}{c_w}(s_z, s_y) = (dF_{sz}, dF_{sy}), \tag{11}$$

$$d\vec{F}_g = Q_g\frac{IdS\cos\theta_i}{c_w}\vec{g}$$
$$= Q_g\frac{IdS\cos\theta_i}{c_w}(g_z, g_y) = (dF_{gz}, dF_{gy}). \tag{12}$$

To obtain the equations for the unit vectors, we need to describe the position vectors representing points A, B, and C in terms of the parameters specified in Fig. 1. They are

$$\vec{OA} = (z_C - r\cos\theta, y_C + r\sin\theta), \tag{13}$$

$$\vec{OB} = (z_C - r\cos\theta - L_A, 0), \tag{14}$$

$$\vec{OC} = (z_C, y_C), \tag{15}$$

where z_c and y_c are the coordinates of the center of the sphere. The point B is the center of curvature of the phase front on the beam axis for the consideration of divergence of the beam. It is an equivalent source point for an incident ray hitting point A. Hence, $\vec{s}$ and $\vec{g}$ can be expressed by

$$\vec{s} = \frac{\vec{BA}}{|\vec{BA}|} = \frac{\vec{OA} - \vec{OB}}{R_A} = \left(\frac{L_A}{R_A}, \frac{y_C + r\sin\theta}{R_A}\right), \tag{16}$$

$$\vec{g} = \left(\frac{y_C + r\sin\theta}{R_A}, -\frac{L_A}{R_A}\right), \tag{17}$$

$$R_A = z_A + \frac{\pi^2\lambda^2}{z_A}, \tag{18}$$

$$L_A = \pm\sqrt{R_A^2 - (y_C + r\sin\theta)^2}, \tag{19}$$

where R_A is the radius of the curvature of the incident ray and L_A is the horizontal distance between the points A and B; z_A is the z coordinate of the point A; λ is the ultrasonic wavelength. Note that L_A has the same sign as z_A's. The unit vector $\vec{g}$ can be easily calculated by employing the fact that it is orthogonal to $\vec{s}$ and is directed towards the beam axis.

After combining Eqs. (4) and (16)–(19) with Eqs. (1), (11), and (12), we can derive the equations of the net radiation forces in the y and z directions over a differential area by an incident ray, which are defined by

$$dF_z = dF_{sz} + dF_{gz} = \frac{r^2 I d\theta \sin\theta\cos\theta_i}{c_w R_A}\{Q_s L_A + Q_g(y_C + r\sin\theta)\}, \tag{20}$$

$$dF_y = dF_{sy} + dF_{gy} = \frac{r^2 I d\theta \sin\theta\cos\theta_i}{c_w R_A}\{Q_s(y_C + r\sin\theta) - Q_g L_A\}. \tag{21}$$

As integrating dF_z and dF_y over θ, they lead to

$$F_z = \int_{\theta_{\min}}^{\theta_{\max}} \frac{r^2 I \sin\theta\cos\theta_i}{c_w R_A}\{Q_s L_A + Q_g(y_C + r\sin\theta)\}d\theta, \tag{22}$$

$$F_y = \int_{\theta_{\min}}^{\theta_{\max}} \frac{r^2 I \sin\theta\cos\theta_i}{c_w R_A}\{Q_s(y_C + r\sin\theta) - Q_g L_A\}d\theta. \tag{23}$$

Given the acoustic intensity I, therefore, Eqs. (22) and (23) represent the net radiation forces in the y and z directions generated by incident rays. Suppose that the intensity I is given as

$$I = \frac{4P}{\pi w(z)^2}\exp\left[\frac{-2y^2}{w(z)^2}\right], \tag{24}$$

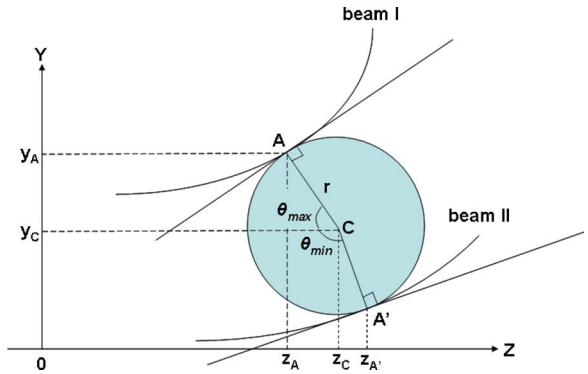

FIG. 2. (Color online) 2D determination of $\theta_{\min}$ and $\theta_{\max}$ used by Eq. (32). Two tangential beams I and II contact the sphere at the points A and A'. Extended spots at the focal point are introduced for each of them. Both $\theta_{\min}$ and $\theta_{\max}$ represent the angles made with the line $y=y_c$ by $\overline{CA'}$ and $\overline{CA}$, respectively.

$$w(z) = w_0\sqrt{1 + \left(\frac{\lambda z}{\pi w_0^2}\right)^2}, \tag{25}$$

where $w(z)$ and w_0 determine the beamwidths at z and at the focal point; P is the incident acoustic power emitted by a source. Finally, the net forces in both directions are given by

$$F_z = \frac{2P}{\pi c_w}\int_{\theta_{\min}}^{\theta_{\max}}\left\{\frac{r}{w(z)}\right\}^2\exp\left[\frac{-2y^2}{w(z)^2}\right]\frac{\cos\theta_i}{R_A}\{Q_s L_A + Q_g(y_C + r\sin\theta)\}\sin\theta d\theta, \tag{26}$$

$$F_y = \frac{2P}{\pi c_w}\int_{\theta_{\min}}^{\theta_{\max}}\left\{\frac{r}{w(z)}\right\}^2\exp\left[\frac{-2y^2}{w(z)^2}\right]\frac{\cos\theta_i}{R_A}\{Q_s(y_C + r\sin\theta) - Q_g L_A\}\sin\theta d\theta. \tag{27}$$

Note that the magnitude of each of the forces is reduced by a factor of 2. The reason is that the integration is carried out from $\theta_{\min}$ to $\theta_{\max}$ rather than 0 to $\theta_{\max}$. In this case, unlike the previous work where a sphere was symmetrically positioned about the beam axis, the upper and the lower limits of θ have different values because of its asymmetry and need to be determined separately.

The method to specify the integration range in Eqs. (26) and (27) is to find the extreme angles at which incident rays tangentially strike a sphere. Figure 2 shows the configuration for calculating them. At points A and A' both the incident beam and the sphere share the same tangent line simultaneously. To approximate the beam tangent to the sphere, we need to modify Eq. (25) to Eq. (27) and introduce an extended spot size to closely consider the beam profile,[10]

$$w(z) = y = mw_0\sqrt{1 + \left(\frac{\lambda z}{\pi w_0^2}\right)^2}, \tag{28}$$

where m is a positive real number. From Eq. (28), the tangent line can be expressed as

$$y = \left(\frac{m\lambda z_A}{\pi w_0 y_A}\right)(z - z_A) + y_A = M(z - z_A) + y_A, \tag{29}$$

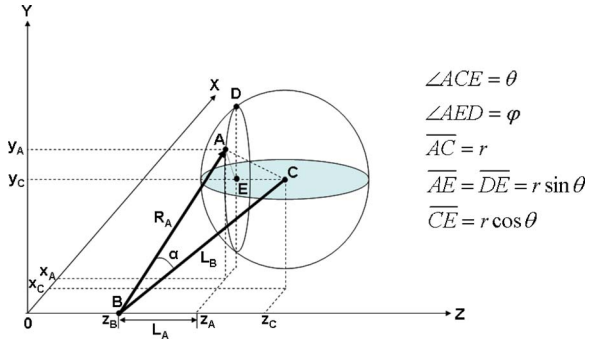

FIG. 3. (Color online) 3D geometry of the sphere centered at an arbitrary location C. The incident beam from the source point B arrives at the point A. The plane AED is perpendicular to the plane $y=y_c$; θ and φ are the elevational and the azimuthal angles according to our convention; α is the angle between $\overline{AB}$ and $\overline{BC}$; L_A and L_B are the lengths of z_A-z_B and $\overline{BC}$; R_A and r are the length of $\overline{AB}$ and the radius of the sphere.

$$m = \frac{y}{w_0\sqrt{1+\left(\frac{\lambda z}{\pi w_0^2}\right)^2}}. \tag{30}$$

For the incident ray to tangentially contact the sphere, the distance between the center of the sphere and the point A must be equal to the radius of the sphere, that is

$$\frac{|M(z_C - z_A) - (y_C - y_A)|}{\sqrt{M^2+1}} = r. \tag{31}$$

Two solutions may exist on the sphere to satisfy Eq. (31). Each of the two is originated either from the upper or the lower half of the sphere. Once they are numerically found, it is straightforward to calculate $\theta_{\min}$ and $\theta_{\max}$ by

$$\theta_{\min} \text{ or } \theta_{\max} = \arctan\left(\frac{y_C - y_A}{z_C - z_A}\right). \tag{32}$$

According to Eqs. (26), (27), and (32), we can obtain the analytical expressions for the net radiation forces. In the next section, we will extend the above formulations to the force on an arbitrarily located sphere.

III. RADIATION FORCE ON ARBITRARILY CENTERED SPHERE: 3D MODEL

Consider a sphere of the radius r centered at an arbitrary point $C(x_c, y_c, z_c)$ in Fig. 3. In the spherical coordinate the x components of the unit vectors in the scattering and the gradient directions must be added to the previous formulations. Thus, Eqs. (5) and (6) should be changed to

$$\begin{aligned} d\vec{F}_s &= Q_s\frac{IdS\cos\theta_i}{c_w}\vec{s} = Q_s\frac{IdS\cos\theta_i}{c_w}(s_x, s_y, s_z) \\ &= (dF_{sx}, dF_{sy}, dF_{sz}), \end{aligned} \tag{33}$$

$$\begin{aligned} d\vec{F}_g &= Q_g\frac{IdS\cos\theta_i}{c_w}\vec{g} = Q_g\frac{IdS\cos\theta_i}{c_w}(g_x, g_y, g_z) \\ &= (dF_{gx}, dF_{gy}, dF_{gz}), \end{aligned} \tag{34}$$

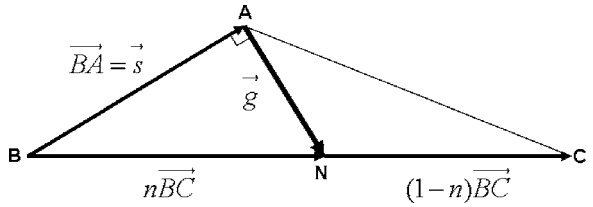

FIG. 4. Scattering and gradient vectors on the incident plane ABC in Fig. 3. They are denoted as $\vec{BA}$ and $\vec{AN}$. They are calculated by their orthogonality to each other. Here, n is a positive real number.

$$dS = r^2\sin\theta d\theta d\varphi, \tag{35}$$

where the differential area dS must consider the additional angular parameter φ in the spherical coordinate system. Assume that the Gaussian intensity distribution is given by

$$I = \frac{P}{\pi w(z)^2}\exp\left[\frac{-2(x^2+y^2)}{w(z)^2}\right]. \tag{36}$$

Note that the other parameters mentioned in this section are the same as the ones in previous section. The unit vectors $\vec{s}$ and $\vec{g}$ in Eqs. (33) and (34), however, need to be modified in terms of the parameters illustrated in Fig. 3. The unit vector of the scattering component $\vec{s}$ can be expressed by

$$\begin{aligned} \vec{s} &= \frac{\vec{BA}}{|\vec{BA}|} \\ &= \frac{\vec{OA} - \vec{OB}}{R_A} \\ &= \left(\frac{x_C - r\sin\theta\sin\varphi}{R_A}, \frac{y_C + r\sin\theta\cos\varphi}{R_A}, \frac{L_A}{R_A}\right) \\ &= \left(\frac{x_A}{R_A}, \frac{y_A}{R_A}, \frac{L_A}{R_A}\right). \end{aligned} \tag{37}$$

Meanwhile, since it is more involved to find the unit vector of the gradient component $\vec{g}$ than $\vec{s}$, Fig. 4 gives another view of the incident plane ABC. Using the fact that $\vec{g}$ is perpendicular to $\vec{s}$, we can deduce

$$\vec{BA}\cdot(\vec{BA} - n\vec{BC}) = 0, \tag{38}$$

and

$$\begin{aligned} n &= \frac{|\vec{BA}|^2}{\vec{BA}\cdot\vec{BC}} \\ &= \frac{R_A^2}{x_A x_C + y_A y_C + L_A(L_A + r\cos\theta)} \\ &= \frac{R_A}{L_B\cos\alpha}. \end{aligned} \tag{39}$$

From Eq. (39), $\vec{g}$ can be defined as

$$\vec{g} = \frac{\vec{AN}}{|\vec{AN}|} = \frac{n\vec{BC} - \vec{BA}}{|n\vec{BC} - \vec{BA}|}, \tag{40}$$

and the denominator can be written as

$$n\vec{BC} - \vec{BA} = [x_A - nx_C, y_A - ny_C, L_A - n(L_A + r\cos\theta)]. \tag{41}$$

Its magnitude is calculated from

$$\begin{aligned} |n\vec{BC} - \vec{BA}| &= \sqrt{(x_A - nx_C)^2 + (y_A - ny_C)^2 + (L_A - n(L_A + r\cos\theta))^2} \\ &= \sqrt{(x_A^2 + y_A^2 + L_A^2) + n^2(x_C^2 + y_C^2 + (L_A + r\cos\theta)^2) - 2n(x_A x_C + y_A y_C + L_A(L_A + r\cos\theta))}. \end{aligned} \tag{42}$$

From Fig. 4,

$$x_A^2 + y_A^2 + L_A^2 = R_A^2, \tag{43}$$

$$x_C^2 + y_C^2 + (L_A + r\cos\theta)^2 = L_B^2, \tag{44}$$

and from Eq. (39),

$$x_A x_C + y_A y_C + L_A(L_A + r\cos\theta) = \frac{R_A^2}{n}. \tag{45}$$

Substituting Eqs. (39) and (43)–(45) into Eq. (42), Eq. (42) can be rewritten as

$$\begin{aligned} |n\vec{BC} - \vec{BA}| &= \sqrt{R_A^2 + \left(\frac{R_A}{L_B\cos\alpha}\right)^2 \times L_B^2 - 2n \times \frac{R_A^2}{n}} \\ &= R_A\sqrt{\frac{1}{\cos^2\alpha} - 1} \\ &= R_A\tan\alpha. \end{aligned} \tag{46}$$

As combining Eqs. (39)–(41) with (46), we can yield the unit vector $\vec{g}$ as

$$\begin{aligned} \vec{g} &= \frac{n\vec{BC} - \vec{BA}}{|n\vec{BC} - \vec{BA}|} \\ &= \frac{1}{R_A\tan\alpha} \times \left(x_A - \frac{R_A}{L_B\cos\alpha}x_C, y_A \right. \\ &\quad \left. - \frac{R_A}{L_B\cos\alpha}y_C, L_A - \frac{R_A}{L_B\cos\alpha}(L_A + r\cos\theta)\right), \end{aligned} \tag{47}$$

where α is determined by

$$\alpha = \arccos\left(\frac{R_A^2 + L_B^2 - r^2}{2R_A L_B}\right). \tag{48}$$

Therefore, the net radiation forces over the differential area dS in three orthogonal directions by an incident ray can be calculated by

$$\begin{aligned} dF_x &= dF_{sx} + dF_{gx} \\ &= \frac{P}{\pi c_w}\left(\frac{r}{w(z)}\right)^2 \exp\left[\frac{-2(x^2+y^2)}{w(z)^2}\right]\frac{\cos\theta_i}{R_A} \\ &\quad \times\left\{\left(Q_s + \frac{Q_g}{\tan\alpha}\right)x_A - \frac{R_A Q_g}{L_B\sin\alpha}x_C\right\}\sin\theta d\theta d\varphi, \end{aligned} \tag{49}$$

$$\begin{aligned} dF_y &= dF_{sy} + dF_{gy} \\ &= \frac{P}{\pi c_w}\left(\frac{r}{w(z)}\right)^2 \exp\left[\frac{-2(x^2+y^2)}{w(z)^2}\right]\frac{\cos\theta_i}{R_A} \\ &\quad \times\left\{\left(Q_s + \frac{Q_g}{\tan\alpha}\right)y_A - \frac{R_A Q_g}{L_B\sin\alpha}y_C\right\}\sin\theta d\theta d\varphi, \end{aligned} \tag{50}$$

$$\begin{aligned} dF_z &= dF_{sz} + dF_{gz} \\ &= \frac{P}{\pi c_w}\left(\frac{r}{w(z)}\right)^2 \exp\left[\frac{-2(x^2+y^2)}{w(z)^2}\right]\frac{\cos\theta_i}{R_A} \\ &\quad \times\left\{\left(Q_s + \frac{Q_g}{\tan\alpha} - \frac{R_A Q_g}{L_B\sin\alpha}\right)L_A - \frac{rR_A Q_g\cos\theta}{L_B\sin\alpha}\right\} \\ &\quad \times\sin\theta d\theta d\varphi. \end{aligned} \tag{51}$$

As far as the angles θ and φ are concerned, we need to specify their integration intervals to calculate the forces generated by incident beams. For the azimuthal angle φ, its range is simply between 0 and 2π, while the limits $\theta_{\min}$ and $\theta_{\max}$ should be carefully computed for the elevational angle θ in Fig. 5(a). Note that all the incident beams are assumed to come from points on the beam axis and thus have circular symmetry around the z axis. We can then consider this problem in the same way as in the cylindrical model. The only difference is that the y coordinate of the center of the sphere should be changed from y_c to $\sqrt{x_c^2+y_c^2}$ in Fig. 5(b). $\sqrt{x_c^2+y_c^2}$ is the projected length of y_c over the plane containing the points C, P and the origin at the same time. Due to the circular symmetry of the incident beam, thus, the method used to find the limits $\theta_{\min}$ and $\theta_{\max}$ in previous section can be applied to this case as well. In other words, we can still use Eqs. (28)–(32) to figure out those limits by using $\sqrt{x_c^2+y_c^2}$

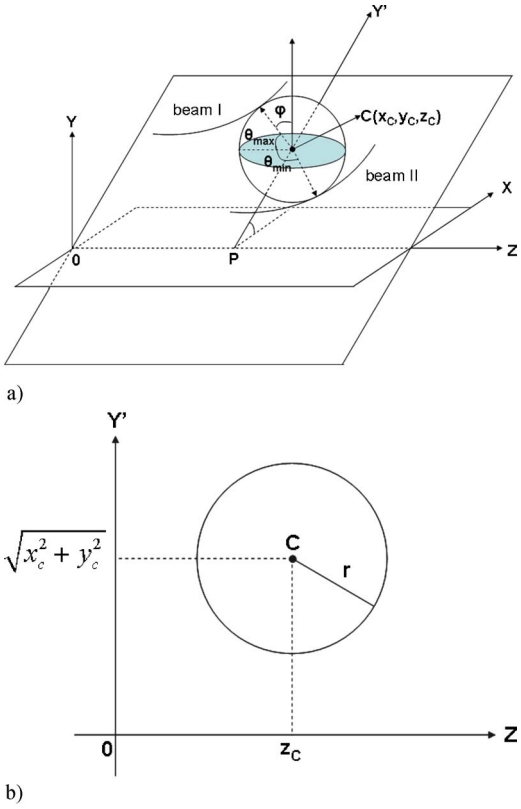

FIG. 5. (Color online) $\theta_{\min}$ and $\theta_{\max}$ in the spherical coordinate system. (a) 3D configuration of the sphere (b) Projection of the sphere onto the $Y'Z$ plane. The 2D approach to find them is also used but modified to fit the 3D case where φ are between $-\pi/2$ and $3\pi/2$. By projecting the sphere onto the $Y'Z$ plane and applying the 2D method to the case, the integration ranges in terms of θ are obtained. In the 3D case, the value of $\sqrt{x_c^2+y_c^2}$ is needed rather than y_c in the 2D model.

instead of y_c. Once $\theta_{\min}$ and $\theta_{\max}$ are found, Eqs. (49)–(51) are integrated in terms of θ and φ. The resultant radiation forces can be represented by

$$F_x = \frac{P}{\pi c_w}\int_0^{2\pi}\int_{\theta_{\min}}^{\theta_{\max}}\left(\frac{r}{w(z)}\right)^2 \exp\left[\frac{-2(x^2+y^2)}{w(z)^2}\right] \times\cos\theta_i\left\{\left(Q_s+\frac{Q_g}{\tan\alpha}\right)x_A-\frac{R_A Q_g}{L_B\sin\alpha}x_C\right\}\sin\theta d\theta d\varphi, \tag{52}$$

$$F_y = \frac{P}{\pi c_w}\int_0^{2\pi}\int_{\theta_{\min}}^{\theta_{\max}}\left(\frac{r}{w(z)}\right)^2 \exp\left[\frac{-2(x^2+y^2)}{w(z)^2}\right] \times\cos\theta_i\left\{\left(Q_s+\frac{Q_g}{\tan\alpha}\right)y_A-\frac{R_A Q_g}{L_B\sin\alpha}y_C\right\}\sin\theta d\theta d\varphi, \tag{53}$$

$$F_z = \frac{P}{\pi c_w}\int_0^{2\pi}\int_{\theta_{\min}}^{\theta_{\max}}\left(\frac{r}{w(z)}\right)^2 \exp\left[\frac{-2(x^2+y^2)}{w(z)^2}\right] \times\frac{\cos\theta_i}{R_A}\left\{\left(Q_s+\frac{Q_g}{\tan\alpha}-\frac{R_A Q_g}{L_B\sin\alpha}\right)L_A -\frac{rR_A Q_g\cos\theta}{L_B\sin\alpha}\right\}\sin\theta d\theta d\varphi. \tag{54}$$

TABLE I. Simulation parameters.

Center frequency	100 MHz
Wavelength (λ)	15 μm
Lateral beam width	15 μm
Aperture size	3 mm
Focal length	3 mm
F-number	1
Input acoustic power	1 mW
Peak incident intensity	141 W/cm^2
Peak incident pressure	1.5 MPa
Acoustic impedance of water	1.5 MRayls
Acoustic impedance of fat	1.4 MRayls
Speed of sound in water	1500 m/s
Speed of sound in fat	1450 m/s
Density of water	1000 kg/m^3
Density of fat	950 kg/m^3
Diameter of fat	120 μm(8λ) to 210 μm(14λ) in increment of 30 μm(2λ)

So far we have derived the analytical expressions for the net radiation forces in the spherical coordinates. The numerical results concerning the radiation forces obtained via Eqs. (52)–(54) will be presented in next section.

IV. RESULTS

Lateral and axial radiation forces are calculated based on the equations derived in Sec. III. For the simulation a lipid or fat sphere is chosen as a target whose characteristics meet the criteria stated previously[7] and insure a minimal reflection. A 100-MHz focused Gaussian transducer with F number of 1 interrogates the sphere and its circular aperture size is 3 mm. The simulation parameters such as beam characteristics and material constants are summarized in Table I. Figure 6 depicts the flow chart for the calculation procedure. Through a number of trials, the number of incident rays N to allow the numerical convergence was chosen as 10^4. This means that the portion of the sphere exposed to the incident beams is discretized into the same number of differential areas. Figure 7(a), for instance, illustrates the acoustic intensity distribu-

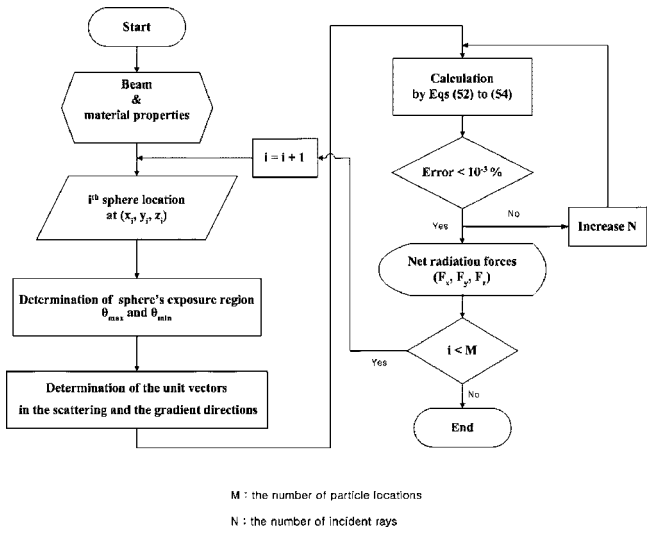

FIG. 6. Simulation algorithm for the 3D asymmetric radiation force. For the numerical convergence, M and N are set to be 200 and 10^4, respectively.

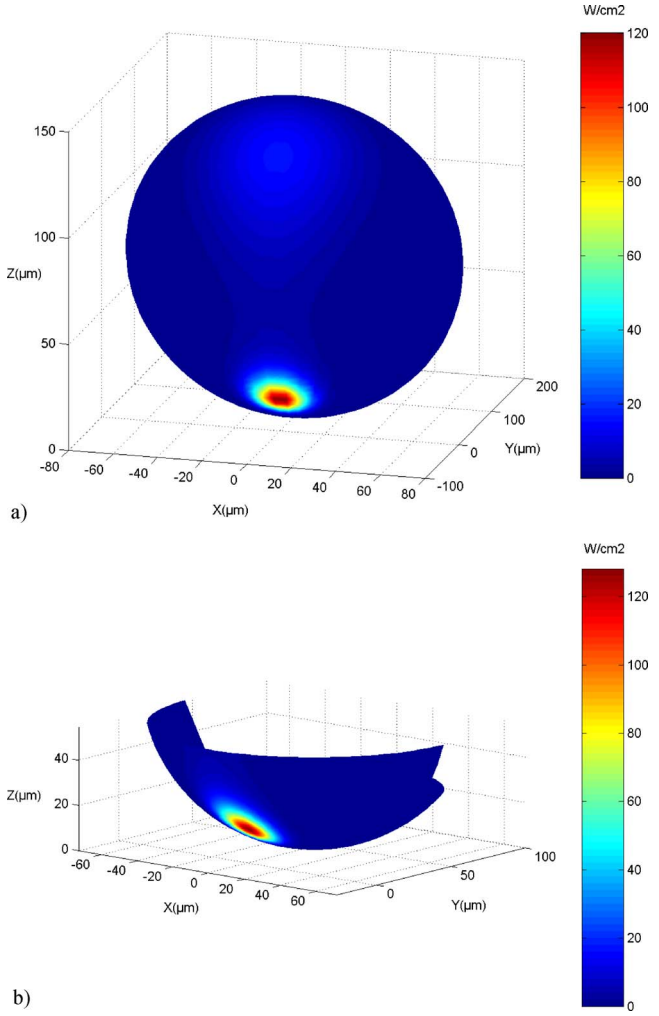

FIG. 7. (Color online) Intensity distribution either (a) over the entire sphere or (b) over the limited area specified by $\theta_{\min}$ and $\theta_{\max}$. Here, a 100-MHz Gaussian beamwidth at the focal point is one wavelength λ, 15 μm, and its peak intensity is 141 W/cm^2. The sphere is centered at a point $(0,3\lambda,5\lambda)$.

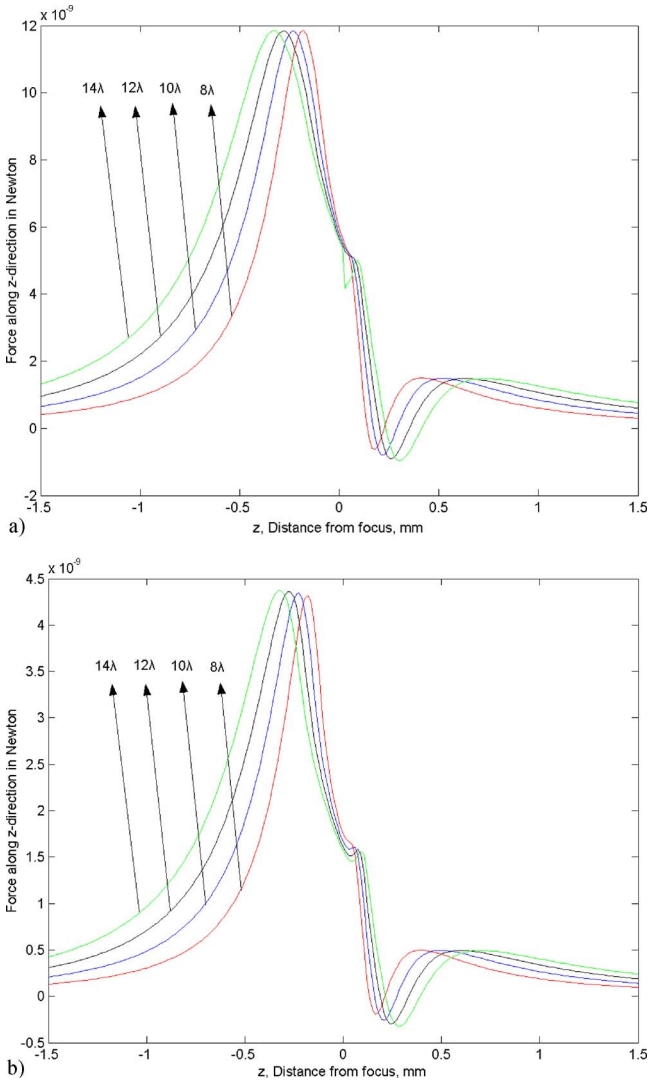

FIG. 8. (Color online) Magnitude plot of axial radiation force either (a) by the 3D model or (b) by the 2D one. For four different sizes of the sphere, the magnitudes of the forces are displayed as its location varies from −1.5 to 1.5 mm in the z direction. The peak intensity and the beamwidth at the focus remains unchanged as in Fig. 7.

tion over the sphere centered at a point (0, 3λ, 5λ). At the same position, the exposure region represented by pairs of (θ,φ) can be determined and displayed as shown in Fig. 7(b). When combined with the unit vectors $\vec{s}$ and $\vec{g}$ computed by Eqs. (37) and (47), the net radiation forces in the spherical coordinates can finally be calculated according to Eqs. (52)–(54). In Fig. 8, the net forces on the beam axis for the 2D and 3D cases are compared as a function of the sphere's location from −100λ to 100λ on the beam in order to contrast the difference. The size of the sphere is varied from 8λ to 14λ. It can be readily seen that the magnitude of the forces in the 3D case is increased relative to the 2D model. This is because the part of the sphere off the axis also contributes to the net forces. It is quite interesting to see that the observations obtained for the 2D case are still valid in the 3D model. Further discussion will follow in the subsequent section. Figure 9 shows the net forces in the x, y, and z directions when the sphere is centered at (λ,λ) on the XY plane. Its location varies along the z direction. In contrast to the results in Fig. 8, the net forces in the x and y directions are no longer negligible due to the asymmetry of the incident beams over the sphere. Thus, all three components of the forces become considerable, whereas only its z component is so in the presence of the axial symmetry. Figure 10 is illustrated for the reader to appreciate how each force component varies as the sphere moves farther away from the focal point. Note that the sphere is centered at $(5\lambda,5\lambda)$ on the XY plane.

V. DISCUSSION

In the calculation of the net radiation force in a 3D model, two crucial elements must be carefully considered. One is the direction of the scattering and the gradient forces and the other is the angular ranges to account for the portion of the sphere on which the radiation forces are exerted.

First, it is straightforward to find the direction of the scattering force $\vec{s}$ since it is the direction of the incident beam. The method to determine the direction of the gradient force $\vec{g}$ on the other hand is more complicated and employs the fact that the two vectors are perpendicular to each other. The convention chosen here for $\vec{g}$ is such that the gradient

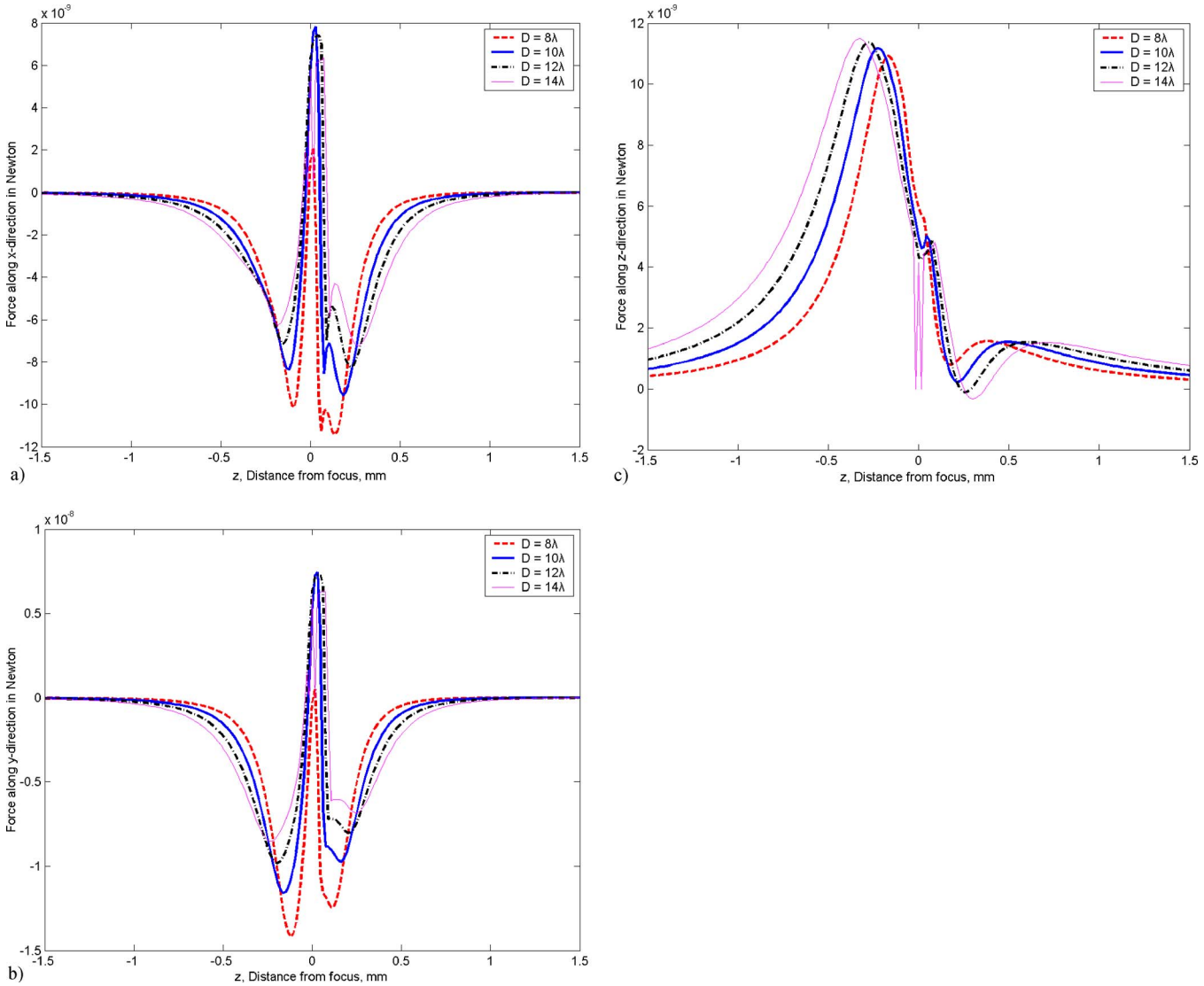

FIG. 9. (Color online) Plots of asymmetric radiation forces (a) x component; (b) y component; (c) z component. The sphere keeps centered at a point (λ,λ) on the XY plane as its location varies from -1.5 to 1.5 mm in the z direction. The parameter values in Table I are used to obtain the plots. The net forces were calculated by increasing the sphere's size from 8λ to 14λ.

force is always acting towards the beam axis. That is why Eq. (8) has an opposite sign compared to Ashkin's.[2] The gradient force plays a more important role in the realization of an acoustic tweezer than does the scattering force. The intensity gradient may create an attractive force on the sphere, whereas the scattering force tries to push it away from the beam source under any circumstances. Note that a negative force on the sphere implies an attractive movement towards the beam source according to our convention.

Second, not only the unit vectors but also the angular ranges are important. They depend on the position of the sphere as the beam convergence is considered. In particular, the elevational angle θ is more significant than the azimuthal angle φ. In this paper, the former is determined by the radius of the curvature of the incident rays, which differs from a previous approach.[11] In other words, the conventional method regards θ simply as varied from 0 to $\pi/2$ and approximates the case where the beam uniformly illuminates the sphere. But, this is not true for the tightly focused beam and we needed to consider both $\theta_{\min}$ and $\theta_{\max}$ at the same time. Therefore, we first derived Eqs. (28)–(32) for the 2D case and later applied them to the 3D model. It was possible due to the circular symmetry of the beam about the beam axis.

Figure 7(b) indicates the part of the sphere illuminated by the incident beams where the peak intensity over the sphere was calculated to be 141 $\mathrm{W/cm^2}$. We needed to integrate Eqs. (52)–(54) only over that limited region instead of the whole spherical surface as shown in Fig. 7(a). To validate the current theory, it can be easily seen that the 3D model is reduced to the 2D case when φ set to be 0.

In Fig. 8(a), the net radiation forces for the different sizes of the sphere were plotted along the beam axis. For comparison, the results from the 2D model were also displayed in Fig. 8(b). Note that the geometry of the sphere has axial symmetry about the beam axis and thus only the net force in the z direction is meaningful here. It is not surprising to discover the close similarity between them, since the elevational range θ remains fixed no matter what the azimuthal

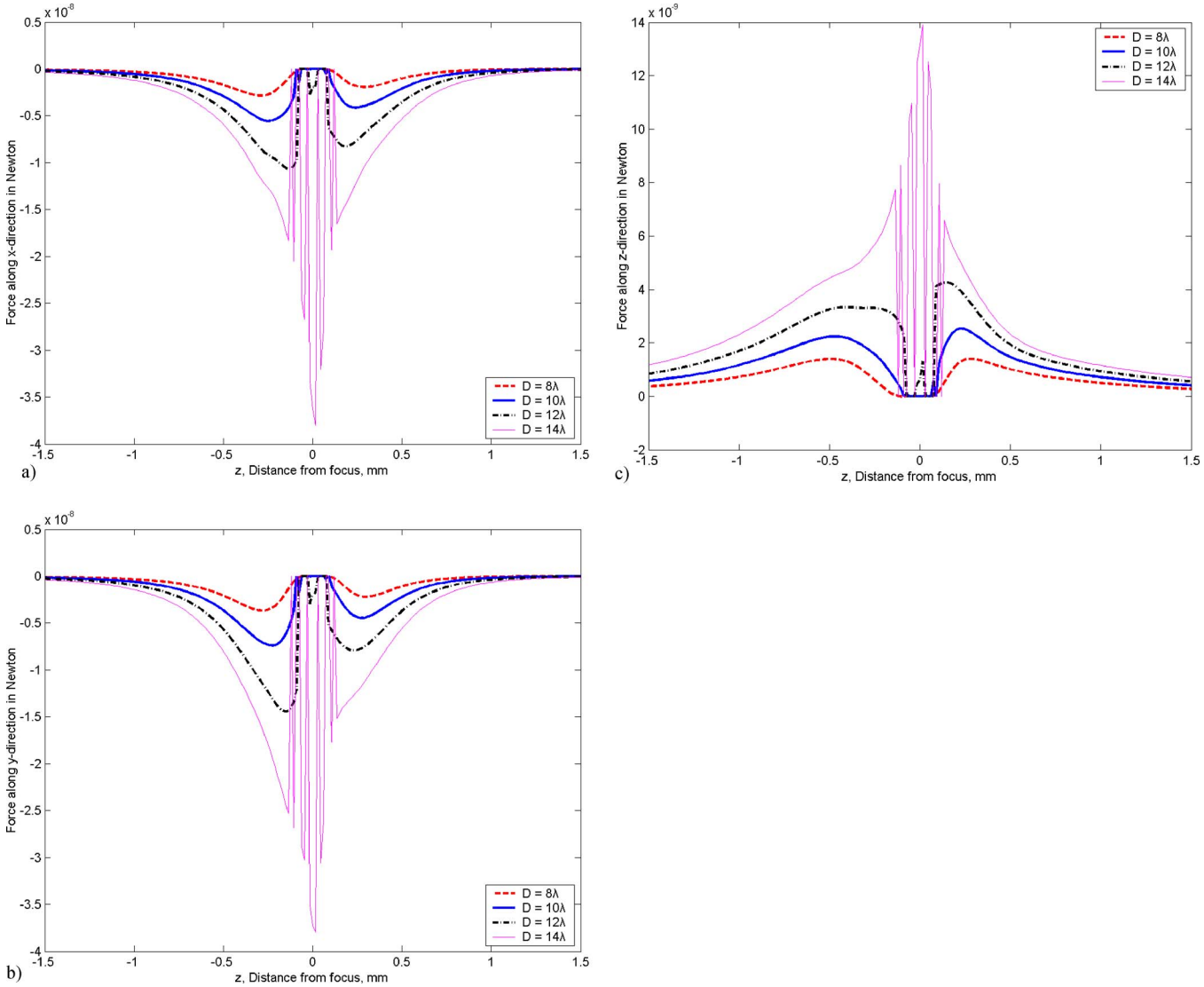

FIG. 10. (Color online) Plots of asymmetric radiation forces (a) x component; (b) y component; (c) z component. The sphere keeps centered at a point $(5\lambda, 5\lambda)$ on the XY plane as its location varies from -1.5 to 1.5 mm in the z direction. Given the parameters in Table I, the net forces were calculated by increasing the sphere's size from 8λ to 14λ. As compared with Fig. 9, the larger sphere creates the stronger force for the most part. In particular, the tweezer effect can always be seen in the x and y directions, not in the z direction, wherever the sphere is.

angle φ is. Only the magnitude of those forces increases because of the extra terms from the sphere off its axis. Table II summarizes the numerical data including the maximum trapping force, its axial position, and the tweezer range where negative forces are generated. Typically, the tweezer or trapping range does not change as much as the maximum trapping force. It is also interesting to see that the maximum trapping forces for the 3D case are nearly three times as large as those for the 2D model. The maximum trapping point in the spherical model is shifted farther away from the beam source than in the 2D case. For the sphere of 210 μm, for example, the maximal trapping point was at $z=300$ μm, while it was at $z=285$ μm in the 2D case. Hence, within the trapping range, the sphere can be more strongly trapped than

TABLE II. Summarized data by simulation where the beam width is $\lambda=15$ μm and the acoustic impedance of the sphere is 1.4 MRayls.

	Max. trapping force (10^{-10} N)		Max. trapping point (μm)		Tweezer range (μm)	
Diameter (μm)	2D	3D	2D	3D	2D	3D
120	−2.0	−6.2	165	180	133–212	141–226
150	−2.6	−7.9	210	225	160–273	172–289
180	−3.0	−9.0	240	255	188–333	203–352
210	−3.2	−9.6	285	300	216–391	235–413

expected in our previous work. The above results suggest the significance of including the third dimension into the theoretical formulation.

Let us assume that the sphere is centered at (λ,λ) on the XY plane and its location changes in parallel with the z axis. Figure 9 shows the results of the asymmetric forces in the x, y, and z directions. As shown in the figure, each of three components of the forces has almost the same order of magnitude. Figures 9(a) and 9(b) reveal several intriguing observations. First, the smaller sphere is more likely to generate the stronger attractive or negative force around the focal point, which is opposite to our previous findings. Second, there are two tweezer ranges, before and beyond the focus, rather than just one. The z components of the forces, however, in Fig. 9(c) demonstrate a similar pattern to the one observed in Fig. 8(a) except that they rapidly fluctuate around the focus for the sphere size $D=14\lambda$. A possible explanation for the fluctuation is that a larger sphere experiences more abrupt changes in the intensity gradient over its surface than a smaller one. Similarly, the tweezer behavior in the z direction vanishes for $D=14\lambda$.

Consider a sphere that is centered at $(5\lambda,5\lambda)$ on the XY plane, even farther off the beam axis. As its location varies along the z axis, the net forces in three directions were calculated and plotted in Fig. 10. Differing from Fig. 9, the results in the x and y directions indicate that the tweezer effect is realized more extensively and the larger sphere gives rise to the stronger attractive force. As compared with Figs. 9(a) and 9(b), Figs. 10(a) and 10(b) show that the sphere can be trapped more strongly even when it is placed in the region of a lower intensity. This also means that the gradient force tends to be more dominant as the sphere moves farther away from the beam axis. Even though the strength of the force decreases towards the low-intensity area, it can still be seen that the gradient force prevails over the scattering force in these two directions. Note that this finding applies only to the x and y components of the net force. From Figs. 9 and 10, it was found that the acoustic tweezer in the x and y directions can always be realized.

It has been suggested by Wu that acoustic streaming may cause acoustic trapping to become unstable because a force due to streaming will be exerted on the particle.[12] Work by Nyborg indicates that the streaming velocity depends on the sound attenuation stemming from the gradient of radiation pressure.[13] Nowicki computed axial streaming velocities for a "weakly" focused Gaussian beam, which means a focal length much greater than the transducer's aperture size, and showed that the measurement of streaming velocities was in good agreement with the theoretical values with both 3.5- and 32-MHz focused ultrasound beams.[14]

Although the approach used by Nowicki applies only to weakly focused beam as opposed to acoustic trapping where a tightly focused beam is required, it is still worthwhile to make a rough estimation as to the possible magnitude of the force that may be caused by acoustic streaming from their formulation. To evaluate the effect of streaming on an acoustic tweezer, expressions derived by Nowicki were used to calculate axial streaming velocities at 100 MHz; and the results are illustrated in Figs. 11–13 with the same set of conditions as we did for the radiation force calculation. The drag force F_d due to streaming can be calculated by[15]

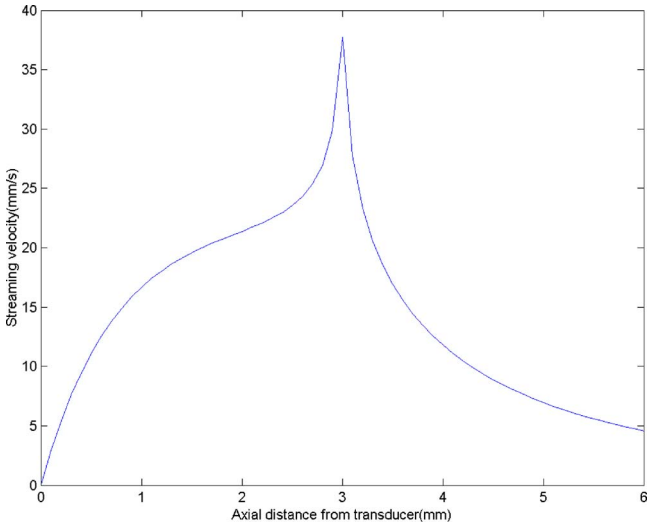

FIG. 11. (Color online) Axial streaming velocity by a 100-MHz transducer of $F\#=1$. Focal length=3 mm, transducer aperture=3 mm.

$$F_d = 3\pi\mu v_s w, \tag{55}$$

where v_s is the streaming velocity and w is the beamwidth; μ is the dynamic viscosity of medium. The streaming velocity is found to be about 20 mm/s in the trapping region and results in a drag force of 2.8 nN. It exceeds the negative radiation force of 1 nN. For the trapping range and radiation force, refer to Table II. Therefore, the streaming undermines the tweezer effect and makes it unstable. For a more strongly focused beam such as $F\#=0.5$, however, the streaming velocities shown in Fig. 12 yield a drag force estimated to be 2–3 nN. For comparison, the axial radiation force is illustrated in Fig. 13. With $F\#=0.5$, the negative radiation force is approximately 7.5 nN, which is much greater than the drag force caused by streaming.

It is important to note that the discussion given above may be a moot point because the analysis is for an ultrasonic

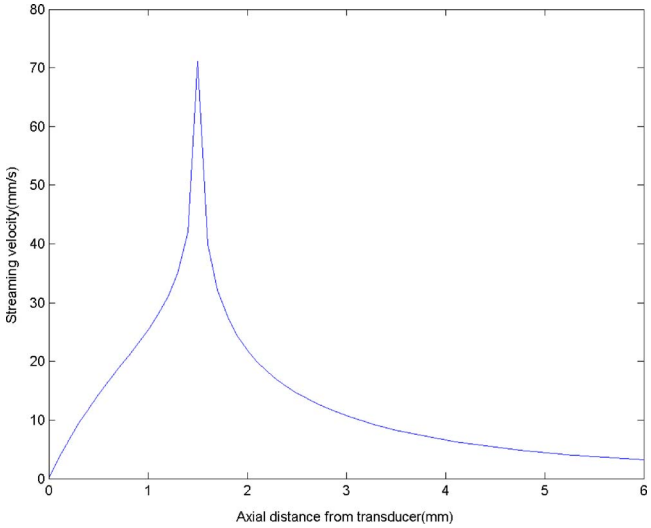

FIG. 12. (Color online) Axial streaming velocity by a 100-MHz transducer of $F\#=0.5$. Focal length=1.5 mm, transducer aperture=3 mm.

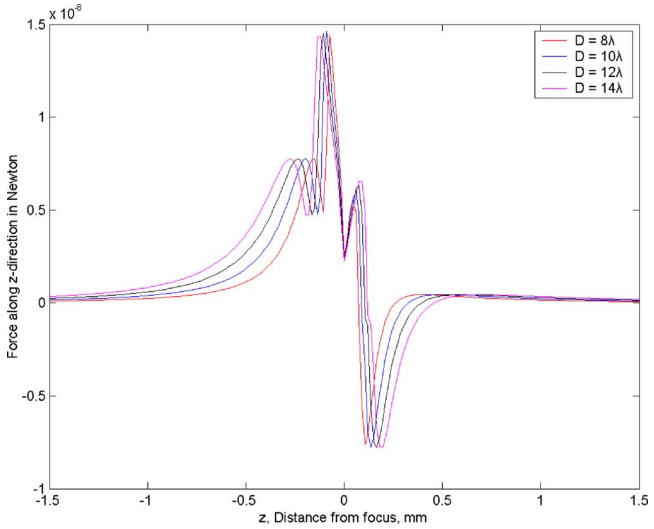

FIG. 13. (Color online) Axial radiation forces for $F\#=0.5$.

beam propagating in a homogeneous fluid. When a sphere much larger than the beam diameter is placed in the path of a highly focused ultrasound beam, the effect of streaming may be so small that it is not as significant as what the previous analysis may indicate. Since the prerequisite for acoustic trapping to occur is a highly focused beam with a sharp intensity distribution and a width smaller than the sphere diameter, in such an arrangement the lateral beam intensity surrounding the sphere exerting a force on the fluid would be much smaller than the beam intensity on the sphere. This would render the previous analysis meaningless.

VI. CONCLUSION

In the paper we have derived analytical expressions for the net radiation forces in the 3D spherical coordinate system and used them to calculate the force based on the ray acoustics. In this analysis, a 100-MHz focused ultrasound beam with a Gaussian profile is assumed for trapping a lipid sphere of varying size. Due to the geometry in the spherical model, the calculation of these forces was more complicated than in the 2D case. The results show that, unlike the axisymmetric situation, not only the scattering force but also the gradient force may make considerable contribution to the asymmetric radiation force. The results also showed that the tweezer can be realized more readily in the lateral directions than in the axial directions, and its strength depends on the position of a target. Moreover, it was observed that in the lateral directions small spheres are more likely to be attracted than large ones at the vicinity of the focal point.

ACKNOWLEDGMENT

This work has been supported by NIH Grant No. P41-EB2182.

[1]A. Ashkin, J. M. Dziedzic, J. E. Bjorkholm, and S. Chu, "Observation of a single-beam gradient force optical trap for dielectric particles," Opt. Lett. **11**(5), 288–290 (1986).
[2]A. Ashkin, "Forces of a single beam gradient laser trap on a dielectric sphere in the ray optics regime," Biophys. J. **61**, 569–582 (1992).
[3]A. Ashkin, "Optical trapping and manipulation of neutral particles using lasers," Proc. Natl. Acad. Sci. U.S.A. **94**, 4853–4860 (1997).
[4]L. V. King, "On the acoustic radiation pressure on spheres," Proc. R. Soc. London, Ser. A **147**, 212–240 (1934).
[5]W. L. Nyborg, "Radiation pressure on a small rigid sphere," J. Acoust. Soc. Am. **42**, 947–952 (1967).
[6]T. Hasegawa and K. Yosioka, "Acoustic radiation force on fused silica spheres and intensity determination," J. Acoust. Soc. Am. **58**, 581–585 (1975).
[7]J. W. Lee, K. L. Ha, and K. K. Shung, "A theoretical study of the feasibility of acoustical tweezers: Ray acoustics approach," J. Acoust. Soc. Am. **117**(5), 3273–3280 (2005).
[8]E. Sidick, S. D. Collins, and A. Knoesen, "Trapping forces in a multiple-beam fiber-optic trap," Appl. Opt. **36**, 6423–6433 (1997).
[9]L. E. Kinsler, A. R. Frey, A. B. Coppens, and J. V. Sanders, *Fundamentals of Acoustics*, 4th ed. (Wiley, New York, 2000).
[10]S. Nemoto and H. Togo, "Axial force acting on a dielectric sphere in a focused laser beam," Appl. Opt. **37**, 6386–6394 (1998).
[11]T. Schut, G. Hesselink, B. Grooth, and J. Greve, "Experimental and theoretical investigations on the validity of the geometrical optics model for calculating the stability of optical traps," Cytometry **12**, 479–485 (1991).
[12]J. Wu, "Acoustical tweezers," J. Acoust. Soc. Am. **89**(5), 2140–2143 (1991).
[13]W. L. Nyborg, "Acoustic streaming," in *Physical Acoustics IIB* (Academic, New York, 1965), pp. 265–331.
[14]A. Nowicki, "Acoustic streaming: Comparison of low amplitude linear model with streaming velocities measured by 32 MHz Doppler," Ultrasound Med. Biol. **23**(5), 783–791 (1997).
[15]R. L. Mott, *Applied Fluid Mechanics*, 6th ed. (Prentice Hall, Englewood Cliffs, NJ, 2005).

Classification of communication signals of the little brown bat

Karla V. Melendez
Neuroscience Program, University of Illinois Urbana-Champaign, Urbana, Illinois 61801

Douglas L. Jones
Department of Electrical and Computer Engineering, University of Illinois Urbana-Champaign, Urbana, Illinois 61801

Albert S. Feng
Department of Molecular and Integrative Physiology and Neuroscience Program, University of Illinois Urbana-Champaign, Urbana, Illinois 61801

(Received 22 February 2006; revised 8 May 2006; accepted 12 May 2006)

Little brown bats, *Myotis lucifugus*, are known for their ability to echolocate and utilize their echolocation system to navigate, and locate and identify prey. Their echolocation signals have been characterized in detail but their communication signals are less well understood despite their widespread use during social interactions. The goal of this study was to develop an automatic classification algorithm for characterizing the communication signals of little brown bats. Sound recordings were made overnight on five individual male bats (housed separately from a large group of captive bats) for 7 nights, using a bat detector and a digital recorder. The spectral and temporal characteristics of recorded sounds were first analyzed and classified by visual observation of a call's temporal pattern and spectral composition. Sounds were later classified using an automatic classification scheme based on multivariate statistical parameters in MATLAB. Human- and machine-based analysis revealed five discrete classes of bat's communication signals: downward frequency-modulated calls, steep frequency-modulated calls, constant frequency calls, broadband noise bursts, and broadband click trains. © *2006 Acoustical Society of America.*
[DOI: 10.1121/1.2211488]

PACS number(s): 43.80.Ka [JAS] Pages: 1095–1102

I. INTRODUCTION

Echolocating bats are highly vocal animals and rely on a sonar system to locate, identify, and track moving prey, avoid obstacles, and orient in 3D space (Grinnell, 1995; Neuweiler 2000; Schuller and Moss, 2004). They possess an exquisite auditory system which analyzes the spectral and temporal characteristics of their sonar signals to reveal detailed information about their surroundings. During echolocation, they emit either a constant frequency (CF), or a frequency-modulated (FM), or a CF-FM combination signal (Fenton, 1984). Much research has focused on understanding their echolocation signals, which are known to vary both intra- and interspecifically (Griffin *et al.*, 1960; Masters *et al.*, 1995; Parsons and Jones, 2000). Much less is known about their communication calls in spite of these animals' extensive and complex social interactions (Kanwal *et al.*, 1994; Behr and von Helversen, 2004).

The communication calls of several species of echolocating bats have been characterized; vocal signals have been shown to convey information for courtship and mating (Barclay *et al.*, 1979; Thomas *et al.*, 1979), maternal reunion with offspring (Balcombe, 1990; Matsumura, 1979, 1981), avoiding predators, and defending or advertising feeding areas (Fenton, 1985; Wilkinson and Bohman, 1998). These studies show that communication calls may consist of several variations of CF and FM signals, such as a descending, rippled FM, or a long, quasi-CF (Kanwal *et al.*, 1994; Ohlemiller *et al.*, 1996; Kanwal *et al.*, 2004; Ma *et al.*, 2006). Most of the earlier studies relied on visual inspection of the call's spectrograms. Only more recently have rigorous statistical analyses been applied to characterize communication calls of a few bat species, as performed in songbirds (Mallett and Pepperberg, 2002), primates (Fisher and Hammerschmidt, 2002), cetaceans (Ford, 1989; Boisseau, 2005), and the bat's echolocation signals (Obrist, 1995; Burnett and Masters, 1999; Parsons and Jones, 2000; Kanwal *et al.*, 2001). In particular, the communication calls of the mustached bats *Pternotus parnellii parnellii* (Kanwal *et al.*, 1994), the lesser spear-nosed bat *Phyllostomus discolor* (Esser and Schubert, 1998), the greater spear-nosed bat *Phyllostomus hastatus* (Boughman and Schubert, 1998), and the greater horseshoe bat *Rhinolophus ferrumequinum* (Ma *et al.*, 2006) have now been parsed out using discriminant function analysis (DFA), principal components analysis (PCA), and spectrographic analysis.

In the little brown bat, *Myotis lucifugus*, analysis of their communication calls is limited to visual inspection of their call spectrograms (Fenton, 1976; Barclay *et al.*, 1979). These studies identified a variety of calls that included broadband and FM call signals, as summarized in Table I (Barclay *et al.*, 1979). Visual inspection is generally qualitative, difficult to conduct on large datasets, and thus subject to the interpretation of the investigators. In this study, we developed an automatic classification scheme for classifying the little brown bat's communication calls statistically. Classification and regression tree analysis (CART) and PCA were used to confirm the accuracy of the automatic classification algorithm. This

TABLE I. Summary of calls from *Myotis lucifugus* obtained through visual inspection of spectrograms. Values are means ± standard deviation (Barclay *et al.* 1979).

Class	*n*	Duration (ms)	Max freq(kHz)	Min freq(kHz)
Squeak	73	28.7±28.3	29.8±10.7	20.9±5.4
Discontinuous double-note	116	30.2±7.3	67.7±10.5	34.1±5.5
Continuous double-note	14	28.9±7.5	65.4±14.3	35.0±6.0
Copulation call	38	61.3±14.8	11.4±2.6	9.5±2.2
Isolation call	283	21.0±8.8	38.6±17.2	22.2±5.1
Sine wave	9	242.8±50.5	51.6±5.7	30.3±3.6
Long squeak-straight FM	37	42.7±14.9	58.6±6.2	33.3±6.0
Long squeak-curved FM	13	89.0±24.0	57.7±10.4	33.9±8.2
Short squawk	50	62.6±61.8		
Long squawk	153	591±238		
Long squawk (buzz)	48	1040±251		
Audible buzz	216	2±1		

automatic classification scheme allows standardized analyses of large sound file datasets and identification of the most robust spectrographic features whose parameters can be adjusted to classify bat's communication signals.

II. METHODS

Adult male little brown bats, *Myotis lucifugus*, were collected from Starved Rock State Park in Utica, IL and kept in a flight cage ($1.9 \times 0.9 \times 0.9$ m), in an environmental room maintained at 27 °C and 60% relative humidity. Food (meal worms) and water were changed daily and made available *ad lib*.

A. Recordings of calls

Recordings were conducted between November 2004 and April 2005, after at least 1 month of captivity during which bats became accustomed to the new environment and diet. For recordings, a bat was housed in a recording cage placed 2.5 m in front of a bat detector with a frequency range of 10–120 kHz (D240X; Pettersson Elektronik AB, Uppsala, Sweden; Jones *et al.*, 2003; Ibanez *et al.*, 2001) linked to a Nagra ARES-BB digital recorder. The recording cage had a size of $30.5 \times 25.4 \times 20.3$ cm, which was confined to the maximal sound reception cone of the ultrasonic microphone of the bat detector. Calls from each bat were recorded overnight for 7 consecutive nights. Anechoic foam (7.62 cm thick) was placed behind the cage to eliminate echoes (Fig. 1). Additionally, calls from the entire group in the flight cage were recorded over a 7-night period to observe any novel call types that might emerge specifically in group settings.

B. Analysis of calls

1. Call features

Once recorded, calls were analyzed on a personal computer using BATSOUND PRO computer software (Peterrsson Elektronik AB) and later with MATLAB (Parsons and Jones, 2000; Jones *et al.*, 2003). We studied 15 spectrographic features as potential aids in classification: maximum frequency, maximum time, minimum frequency, minimum time, center frequency, center time, duration, kurtosis (freq), kurtosis (time), skew (freq), skew (time), spread (freq), spread (time), standard deviation (freq), and standard deviation (time). Features were chosen based on visual analysis of calls and/or usage in previous bat sound classification studies (Barclay *et al.*, 1979; Kanwal *et al.*, 1994).

Maximum frequency and time were defined as that corresponding to the 97th percentile of the signal's summed total magnitude. Minimum frequency and time were defined as that of the third percentile of the signal's summed total magnitude. Center frequency and time corresponded to the center of mass. To account for the variability within calls in this study, kurtosis, skew, spread, and standard deviation were chosen to describe both the frequency and time distributions of each call type. Kurtosis described the degree of peakedness of call's distribution. Skew described the degree of asymmetry of the call's distribution {[signal length * center – (signal length/2) −1]/(signal length/2)}. Spread delin-

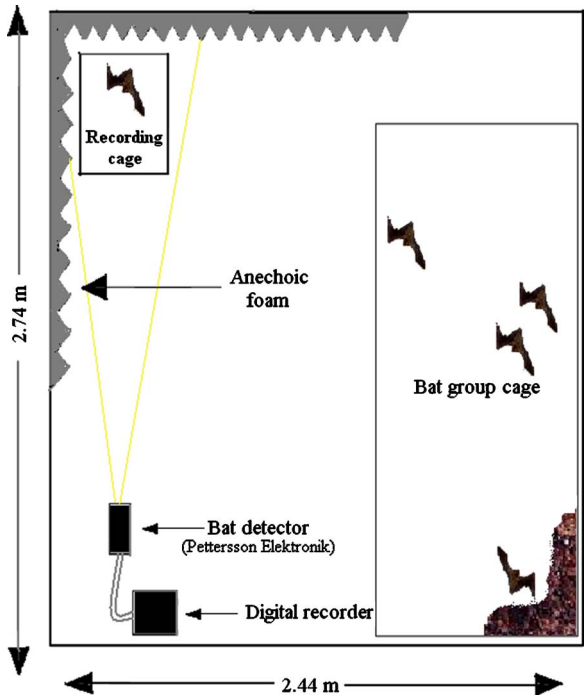

FIG. 1. Experimental setup for sound recordings from individual bats.

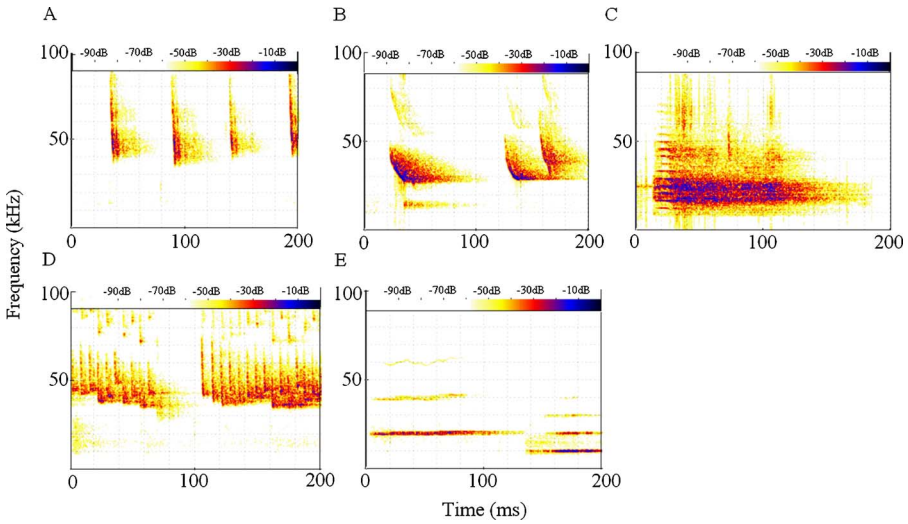

FIG. 2. Spectrograms of call types (FFT size 1024, Hamming window). (a) Steep frequency modulated; (b) downward frequency modulated; (c) broadband noise burst; (d) broadband click train; (e) constant frequency.

eated the range of a particular call [(max −min)/signal length]. Standard deviation showed the square root of the call's variance (Kenney and Keeping, 1962). Next, files were subjected to four types of analysis: manual classification, automatic classification, classification and regression tree analysis (CART), and principal components analysis (PCA).

2. Manual classification algorithm

First, a subset of call spectrograms (approximately 25%) was manually inspected and classified into five categories based on the call's spectrographic contours (Fig. 2) and Kanwal *et al.*'s (1994) classification scheme: steep FM (StFM), downward FM (DFM), broadband noise burst (BNB), broadband clicks train (BCT), and constant frequency (CF). Next, each manually classified call was plotted on a 3D graph (Fig. 3) whose axes consisted of different combinations of call features. Upper and lower boundaries were recorded for features that showed tight clustering of a particular call. For example, Fig. 3 shows that the boundaries of skew (time) for StFMs are −0.3 and −0.45. Different combinations of features were plotted until each call type could be distinguished by unique feature boundaries (Table II).

3. Automatic classification

Second, all calls were classified automatically using the features and feature boundaries derived from the manual classification algorithm. Calls that were clipped were eliminated from the automatic classification. Features that did not provide unique information about a particular class, and thus not included in Table II, were removed from the automatic classification algorithm.

4. Classification and regression tree analysis (CART)

CART analysis (Brieman *et al.*, 1984) was used to verify the best features and boundaries chosen from 3D graph analysis. CART is a type of decision tree analysis which splits all of the dependent variables (call classes) using the optimal predictor variables (call features). The CART algorithm determines thresholds for the predictor variables, and

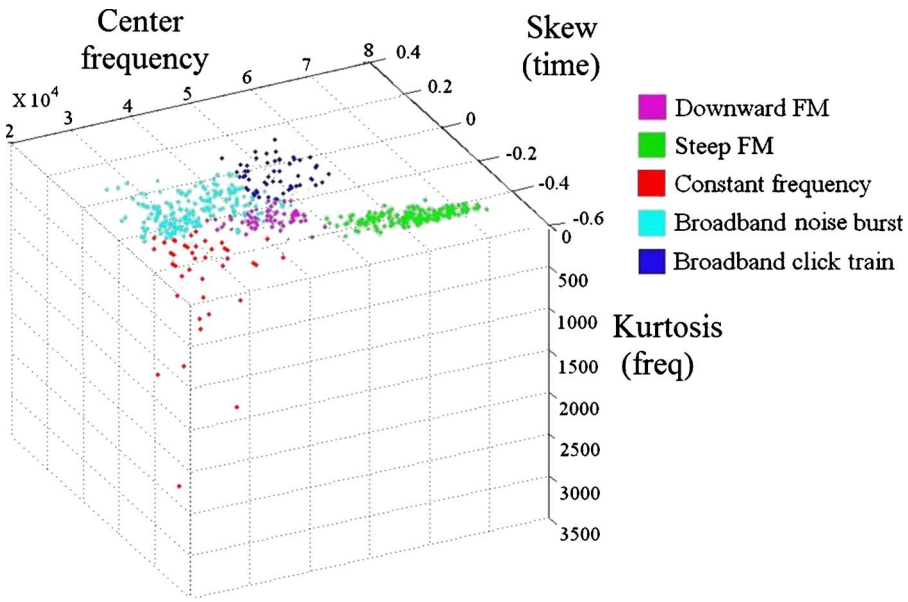

FIG. 3. Example of 3D plot used to determine the best feature set and feature boundaries for automatic classification. Features and feature boundaries that displayed clustering of individual classes were used in the automatic classification algorithm.

TABLE II. Manual classification parameters. A subset of call spectrograms (approximately 25%) was manually inspected and classified into five categories based on the call's spectrographic contours. Next, each classified call was plotted on a 3D graph (Fig. 3) whose axes consisted of different combinations of call features. Lower and upper boundaries were recorded for features that showed tight clustering of a particular call.

Class	Feature	Lower boundary	Upper boundary
Steep frequency modulated	Center frequency	50 kHz	75 kHz
	Kurtosis (freq)	N/A	100
	Skew (time)	−0.45	−0.3
Downward frequency modulated	Center frequency	35 kHz	50 kHz
	Kurtosis (freq)	N/A	100
	Skew (time)	−0.4	−0.15
	Duration	N/A	60 ms
Broadband click train	Center frequency	45 kHz	60 kHz
	Kurtosis (freq)	N/A	100
	Skew (time)	−0.15	0.15
Broadband noise burst	Kurtosis (freq)	N/A	250
	Skew (time)	−0.2	0.1
	Std (time)	N/A	0.03
Constant frequency	Center frequency	30 kHz	45 kHz
	Kurtosis (freq)	250	N/A
	Skew (time)	−0.3	−0.1

the branches are based on whether or not the values for the dependent variable are greater or less than these thresholds. The splitting continues until it reaches a leaf which corresponds to a labeled predictor variable. In this case, the *parent node* is the call feature which best splits the call classes into two groups. *Child nodes* continue to split the remaining call classes using the remaining robust call features until the CART algorithm terminates. The terminal nodes are typically mutually exclusive subgroups of the calls (Davuluri *et al.*, 2000; Bevilacqua *et al.*, 2003; Lemon *et al.*, 2003).

In this study, all 15 features were originally included in the CART analysis. The CART algorithm decided which of the 15 features provided unique information about a particular call type and then discarded the unused features in the final tree. Since this procedure is very similar to the manual classification algorithm in approach, CART results and manual classification results were compared, and *K*-fold cross validation was used to test the CART algorithm. In *k*-fold cross-validation ($k=10$), the data were divided into ten subsets of approximately equal size. The tree was trained ten times, each time leaving out one of the subsets from training, and using only the omitted subset to compute the accuracy of CART (Brieman *et al.*, 1984; Witten and Frank, 2005).

TABLE III. Percentage of calls. Totals were derived using the automatic classification algorithm. Calls that were clipped were removed from the dataset.

Class	Number of calls	Percentage
Broadband noise burst	2451	62.45%
Steep FM	655	16.69%
Downward FM	448	11.41%
Broadband click train	216	5.50%
Constant frequency	155	3.95%
Total	**3925**	**100.0%**

5. Principal components analysis (PCA)

Once the CART accuracy was computed, a custom-designed MATLAB program performed PCA to verify the number of features retained. PCA generates a set of uncorrelated variables (i.e., principal components) by computing linear combinations of the original variables (features). The first principal component is the linear combination of features that explains the most variance in the data. The last principal component is the remaining combination of features that explains the least variance in the data. Therefore, PCA allows one to verify if combinations of each of the features retained account for all of the variance (Wold *et al.*, 1987). Accuracy as a function of the number of principal components was also computed using CART and tenfold cross validation by first projecting the original feature vectors onto the principal components vectors (i.e., calculating their inner product).

III. RESULTS

A total of 3925 calls was recorded from five male bats (Table III). The group recordings were included in the total number of calls because they did not display any further variation.

A. Description of calls

Five features were derived from the manual classification scheme and included in the automatic classification

TABLE IV. Summary of calls from male *Myotis lucifugus* using the features and feature boundaries from the automatic classification algorithm. Values are means ± standard deviation.

Class	Center freq (kHz)	Duration (ms)	Kurtosis (freq)	Skew (time)	Std deviation (time)
Steep FM	60.0	39.10	34.81	−0.38	0.23
	±0.24	±1.20	±0.98	$\pm 1.6\times10^{-3}$	$\pm 7.2\times10^{-4}$
Downward FM	42.6	43.59	49.67	−0.27	0.24
	±0.19	±0.46	±1.01	$\pm 2.7\times10^{-3}$	$\pm 9.4\times10^{-4}$
Broadband noise burst	33.2	160.10	72.95	−0.11	0.26
	±0.14	±2.68	±0.83	$\pm 1.3\times10^{-3}$	$\pm 4.2\times10^{-4}$
Broadband click train	49.7	118.91	40.91	−0.06	0.26
	±0.26	±7.93	±1.82	$\pm 4.2\times10^{-3}$	$\pm 2.2\times10^{-3}$
Constant frequency	36.1	64.61	472.8	−0.20	0.24
	±0.30	±2.50	±34.75	$\pm 4.6\times10^{-3}$	$\pm 1.4\times10^{-3}$

TABLE V. Accuracy of automatic classification. A subset of manually classified calls was classified using the automatic classification algorithm and results were later compared to CART and PCA.

Class	Automatic/Manual classification (# of calls)	Percent accurate
Steep FM	162/168	96.43
Downward FM	53/68	77.94
Broadband click train	97/114	85.09
Broadband noise burst	345/403	85.61
Constant frequency	33/38	86.84
Total	**690/791**	**87.23**

scheme: center frequency, duration, kurtosis (frequency), skew (time), and standard deviation (time). Means and standard deviations of calls were calculated for the five features (Table IV). Center frequencies of each class were in the ultrasonic range (33.2–60.0 kHz); however, their lowest frequencies were sometimes in the human audible range (Fig. 2). Total durations for communication calls were between 40–120 ms, much longer than the 1–10-ms range for the species' echolocation calls (Fenton, 1984).

The following are the mean values for call features (Table IV). Two types of FM signals were found. Steep FM (StFM) signals had a center frequency of ~60 kHz and duration of ~40 ms. Downward FM (DFM) signals had a center frequency of 43 kHz and duration of 44 ms. Two types of broadband signals were found. The broadband noise bursts (BNB) were the most common (Table III) with a center frequency of 33 kHz and a duration of 160 ms. BNBs are often associated with *Myotis lucifugus* agonistic calls and are similar to the *squawks* and *buzzes* found in Barclay *et al.* (1979) study. The broadband click trains (BCT) were a series of clicks with a center frequency of 50 kHz. The duration of the trains was ~119 ms long. Finally, constant frequency (CF) signals were found with a center frequency of ~36 kHz and duration of ~65 ms.

B. Automatic classification accuracy

A subset of approximately 800 manually classified calls was used to determine the accuracy of the automatic classification scheme (Table V). First, the calls were divided into different classes using visual observation. Then, each class was processed using the automatic classification scheme. The automatic classification scheme had approximately 87% accuracy overall. The confusion matrix (Table VI) displays the number and call class of inaccurately classified calls.

TABLE VI. Confusion matrix. The call classes that were misclassified are shown.

Class	Steep FM	Downward FM	Broadband click train	Broadband noise burst	Constant frequency
Steep FM	162	1	2	3	0
Downward FM	1	53	4	10	0
Broadband click train	0	7	97	10	0
Broadband noise burst	3	14	29	345	12
Constant frequency	0	1	0	4	33

C. CART and PCA

The CART algorithm, as implemented in MATLAB, was used to confirm the accuracy of best features and boundaries included in the automatic classification algorithm. The features and feature boundaries chosen by CART were slightly different from those chosen in manual classification (Fig. 4), including minimum frequency, center frequency, center time, kurtosis (frequency), kurtosis (time), skew (time), spread (frequency), and maximum time in its feature set. Using tenfold cross validation, CART results showed an average accuracy of 89.71% (±3.37). Figure 5 shows CART analysis using the five features derived from manual classification alone [i.e., center frequency, duration, kurtosis (frequency), skew (time), and standard deviation (time)]. An average accuracy of 86.57% (±3.23) was calculated using tenfold cross validation.

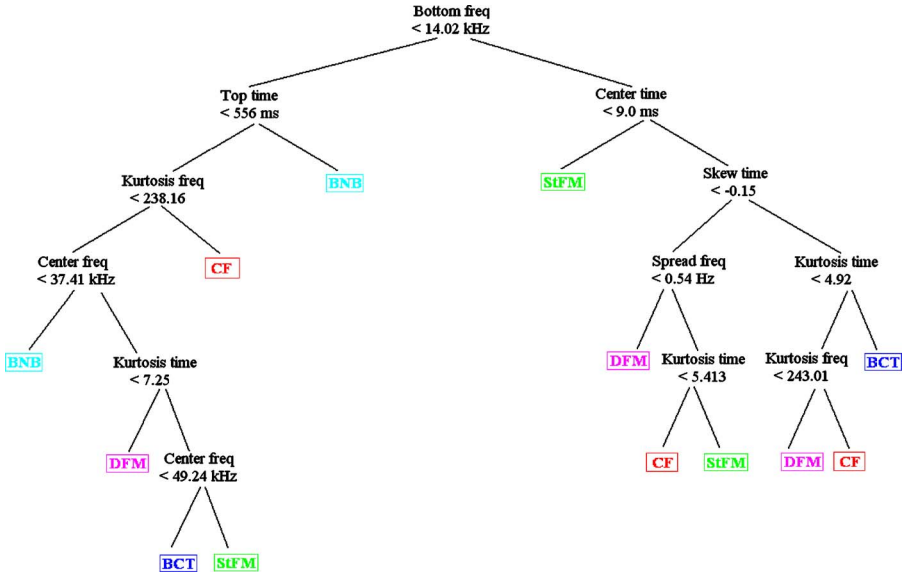

FIG. 4. Pruned tree generated by CART using all 15 features.

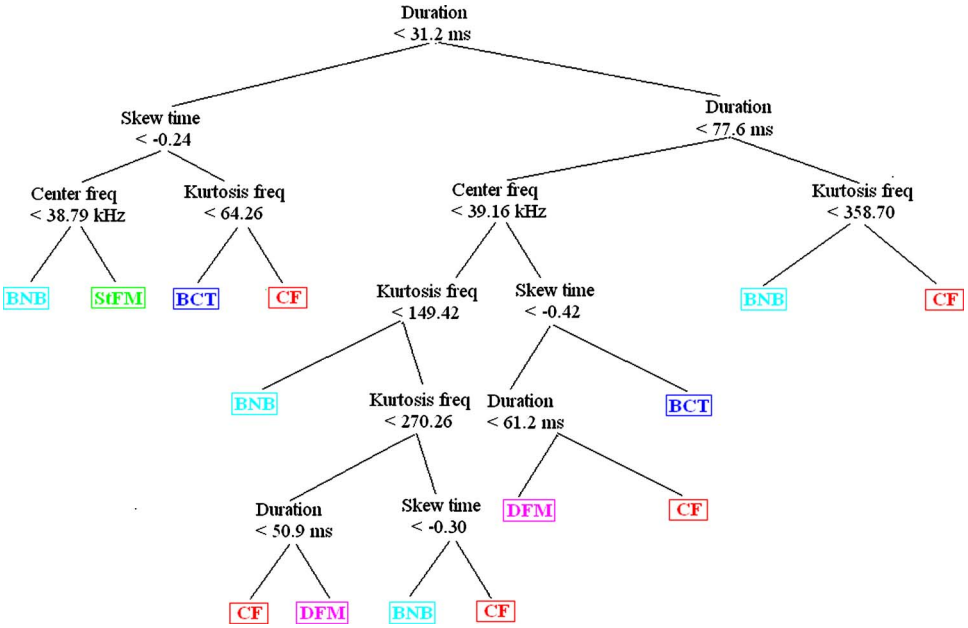

FIG. 5. Pruned tree generated by CART using the five features derived from manual classification.

PCA was then used to analyze the amount of variance explained by all 15 features (Fig. 6). PCA showed that six linear combinations (i.e., principal components) of all 15 features were most useful in explaining the data. The original feature vectors were then projected (inner product) onto the principal components vectors, and accuracy as a function of the number of principal components was assessed using CART and tenfold cross validation (Fig. 7). Accuracy remained above approximately 80% using six or more principal components.

IV. DISCUSSION

The communication repertoire of *Myotis lucifugus* was previously studied by Fenton and colleagues in the late 1970's. Since then, much progress has been made in sound classification technology. For example, programs such as MATLAB and WEKA (Witten and Frank, 2005) can be used to automatically classify large datasets in little time. Automatic classification parameters can also be easily manipulated to classify other calls in the species' repertoire by adding new features and feature boundaries when needed (e.g., interpulse interval duration or repetition rate). Such programs reduce subjectivity and therefore allow replicable results across researchers. In addition to newer technology, there is also a new understanding of the importance of studying bat communication calls. Several studies (Fenton, 1985; Kanwal *et al.*, 1994; Wilkinson and Bohman, 1998) show that bat communication calls are more spectrographically complex than echolocation calls, and thus may require more complex auditory processing. Although this study was limited to only male *Myotis lucifugus* due to permit restrictions, it nonetheless reveals the diversity of the species' communication calls.

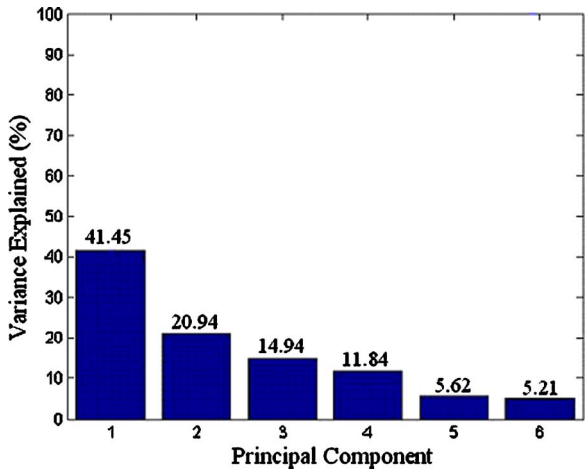

FIG. 6. Principal components analysis of all 15 features, showing the amount of variance in the data that is explained by each principal component.

Five primary communication call types were found: downward FM, steep FM, broadband noise burst, broadband click train, and constant frequency. As shown in Table VI, there was some overlap in the classification of call types because different calls may share similar acoustic features. For example, the DFM calls were sometimes misclassified as BNBs. This is understandable since DFM calls do have components similar to BNBs (e.g., broad bandwidth) (Fig. 2). The machine is therefore unable to "ignore" features which may not aid in defining its overall shape in a small number of cases. Two other class variations were also identified, upward FM (UFM) and brief broadband noise burst (bBNB). However, UFM and bBNB signals occurred infrequently and were thus removed from the dataset. The UFM signals were similar to the copulation calls found by Barclay *et al.* (1979), and would presumably occur more frequently in the presence of females. The bBNB signals were similar to the audible buzzes included in Barclay *et al.*'s (1979) study. Many other calls recorded by Barclay *et al.* are also expected to occur only in the presence of females, such as in mother-young interactions or during pair bonding. For example, the *double-note* and *isolation calls* (Table I) were recorded within a nursery colony, as juveniles sought communication with their mothers. *Copulation* calls were emitted by males during copulation or attempted copulation (Barclay *et al.*, 1979).

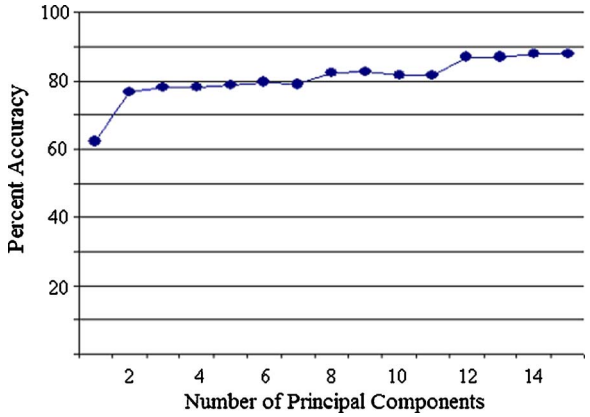

FIG. 7. Accuracy as a function of the number of principal components computed using CART and tenfold cross validation.

In terms of classification schemes, CART is robust and functions by continually splitting large groups into two subgroups based on features until the terminal groups are mutually exclusive. In this study, CART started with the entire bat call repertoire and all 15 features, then split it into individual classes, which served as the terminal groups. CART performed as well as full PCA (accuracy ~89% for both), suggesting that eight features used by CART (Fig. 4) were completely sufficient for classification. When five features were used in manual classification (Table II), there was approximately 87% accuracy, suggesting that five features can classify nearly all of the data. When only these five features were included in CART analysis, the accuracy was nearly identical (~87%). The five features had a higher accuracy than PCA with five (Fig. 7), suggesting that this specific set of features captures essentially all of the information useful for classification.

As is the case in most animal communication studies, the main goal is to determine the behavioral relevance of different call types. Follow-up studies will be conducted to determine the behavior that is associated with each class identified in this study.

ACKNOWLEDGMENTS

This research was supported by NIDCD Grant R01-DC-04998 to Albert S. Feng. We thank Andreas F. Ehmann from the UIUC Electrical Engineering Dept. for a wealth of technical support, particularly for his intellectual contributions to algorithm design and CART and PCA analysis. We thank Bryce Paschold for his help in data collection. We thank the Illinois Department of Natural Resources for permitting collection of bats. We also thank the UIUC Department of Animal Resources and Xinming Wang for assistance in care and collection of the bats.

Balcombe, J. P. (**1990**). "Vocal recognition of pups by mother Mexican free-tailed bats, *Tadarida brasiliensis mexicana*," Anim. Behav. **39**, 960–966.

Barclay, R. M. R., Fenton, M. B., and Thomas, D. W. (**1979**). "Social behavior of the little brown bat, *Myotis lucifugus*," Behav. Ecol. Sociobiol. **6**, 137–146.

Behr, O., and von Helversen, O. (**2004**). "Bat serenades—complex courtship songs of the sac-winged bat (*Saccopteryx bilineata*)," Behav. Ecol. Sociobiol. **56**, 106–115.

Bevilacqua, M., Braglia, M., and Montanari, R. (**2003**). "The classification and regression tree approach to pump failure rate analysis," Reliab. Eng. Syst. Saf. **79**, 59–67.

Boisseau, O. (**2005**). "Quantifying the acoustic repertoire of a population: The vocalizations of free-ranging bottlenose dolphins in Fiordland, New Zealand," J. Acoust. Soc. Am. **117**, 2318–2329.

Boughman, J. W., and Wilkinson, G. S. (**1998**). "Greater spear-nosed bats discriminate group mates by vocalizations," Anim. Behav. **55**, 1717–1732.

Brieman, I., Friedman, J., Olshen, R., and Stone, C. J. (**1984**). *Classification and Regression Trees* (Wadsworth, Belmont, CA).

Burnett, S. C., and Masters, W. M. (**1999**). "The use of neural networks to classify echolocation calls of bats," J. Acoust. Soc. Am. **106**, 2189.

Davuluri, R. V., Suzuki, Y., Sugano, S., and Zhang, M. Q. (**2000**). "CART classification of human 5' UTR sequences," Genome Res. **10**, 1807–1816.

Esser, K. H., and Schubert, J. (**1998**). "Vocal dialects in the lesser spear-nosed bat *Phyllostomus Discolor*," Naturwiss. **85**, 347–349.

Fenton, M. B. (**1976**). "Variation in the social calls of little brown bat (*Myotis lucifugus*)," Can. J. Zool. **55**, 1151–1157.

Fenton, M. B. (**1984**). "Echolocation: implications for ecology and evolution of bats," Q. Rev. Biol. **59**, 33–53.

Fenton, M. B. (**1985**). *Communication in the Chiroptera* (Indiana University Press, Bloomington).

Fisher, J., and Hammerschmidt, K. (**2002**). "An overview of the Barbary macaque, *Macaca sylvanus*, vocal repertoire," Folia Primatol. **73**, 32–45.

Ford, J. K. B. (**1989**). "Acoustic behaviour of resident killer whales (*Orcinus orca*) off Vancouver Island, British Columbia," Can. J. Zool. **67**, 727–745.

Griffin, D. R., Webster, F. A., and Michael, C. R. (**1960**). "The echolocation of flying insects by bats," Anim. Behav. **8**, 141–154.

Grinnell, A. D. (**1995**). "Hearing in bats: An overview," in *Hearing by Bats*, edited by A. N. Popper and R. R. Fay (Springer, New York), pp. 1–36.

Ibanez, C., Juste, J., Garcia-Mudarra, J. L., and Agirre-Mendi, P. T. (**2001**). "Bat predation on nocturnally migrating birds," Proc. Natl. Acad. Sci. U.S.A. **98**, 9700–9702.

Jones, G. Webb, P. I., Sedgeley, J. A., and O'Donnell, C. F. (**2003**). "Mysterious *Mystacina*: how the New Zealand short-tailed bat (*Mystacina tuberculata*) locates insect prey," J. Exp. Biol., **206**, 4209–4216.

Kanwal, J. S., Peng, J. P., and Esser, K. H. (**2004**). "Auditory communication and echolocation in the mustached bat: computing for dual functions within single neurons," in *Echolocation in Bats and Dolphins 29*, edited by J. A. Thomas, C. F. Moss, and M. Vater (The University of Chicago Press, Chicago) pp. 201–208.

Kanwal, J. S., Matsumura, S., Ohlemiller, K., and Suga, N. (**1994**). "Analysis of acoustic elements and syntax in communication sounds emitted by mustached bats," J. Acoust. Soc. Am. **96**, 1229–1254.

Kazial, K. A., Burnett, S. C., and Masters, W. M. (**2001**). "Individual and group variation in echolocation calls of big brown bats, *Eptesicus fuscus* (Chiroptera: Vespertilionidae)," J. Mammal. **82**, 339–351.

Kenney, J. F., and Keeping, E. S. (**1962**). *Mathematics of Statistics*, Pt. 1, 3rd ed. (Van Nostrand, Princeton, NJ).

Lemon, S. C., Roy, J., Clark, M. A., Friedmann, P. D., and Rakowski, W. (**2003**). "Classification and regression tree analysis in public health: Methodological review and comparison with logistic regression," Ann. Behav. Med. **26**, 172–181.

Ma, J., Kohta, K., Zhang, S., and Metzner, W. (**2006**). "Vocal communication in adult greater horseshoe bats, *Rhinolophus ferrumequinum*," J. Comp. Physiol., A **18**, 1–16.

Mallett, J., and Pepperberg, I. (**2002**). "Identifying bird species from bird song using frequency component analysis," J. Acoust. Soc. Am. **111**, 2391.

Masters, W. M., Raver, K. A. S., and Kazial, K. A. (**1995**). "Sonar signals of big brown bats, *Eptesicus fuscus*, contain information about individual identity, age and family affiliation," Anim. Behav. **50**, 1243–1260.

Matsumura, S. (**1979**). "Mother-infant communication in a horseshoe bat (*Rhinolophus ferrumequinum nippon*): development of vocalizations," J. Mammal. **60**, 76–84.

Matsumura, S. (**1981**). "Mother-infant communication in a horseshoe bat (*Rhinolophus ferrumequinum nippon*): Vocalization in three-week old infants," J. Mammal. **62**, 20–28.

Neuweiler, G. (**2000**). *The Biology of Bats* (Oxford University Press, Oxford).

Obrist, M. K. (**1995**). "Flexible bat echolocation—the influence of individual, habitat and conspecifics on sonar signal design," Behav. Ecol. Sociobiol. **36**, 207–219.

Ohlemiller, K. K., Kanwal, J. S., and Suga, N. (**1996**). "Facilitative responses to species-specific calls in cortical FM-FM neurons of the mustached bat," NeuroReport **7**, 1749–1755.
Parsons, S., and Jones, G. (**2000**). "Acoustic identification of twelve species of echolocating bat by discriminant function analysis and artificial neural networks," J. Exp. Biol. **203**, 2641–2656.
Schuller, G., and Moss, C. F. (**2004**). "Vocal control and acoustically guided behavior in bats," in *Echolocation in Bats and Dolphins* edited by J. A. Thomas, C. F. Moss, and M. Vater (The University of Chicago Press, Chicago), pp. 3–16.
Thomas, D. W., Fenton, M. B., and Barclay, R. M. R. (**1979**). "Social behaviour of the little brown bat, Myotis lucifugus. I. Mating behaviour," Behav. Ecol. Sociobiol. **6**, 129–136.
Wilkinson, G. S., and Boughman, J. W. (**1998**). "Social calls coordinate foraging in greater spear-nosed bats," Anim. Behav. **55**, 337–350.
Witten, I. H., and Frank, E. (**2005**). *Data Mining: Practical Machine Learning Tools and Techniques*, 2nd ed. (Morgan Kaufmann, San Francisco).
Wold, S., Esbensen, K., and Geladi, P. (**1987**). "Principal components analysis," Chemom. Intell. Lab. Syst. **2**, 37–52.

Acoustic properties of humpback whale songs

Whitlow W. L. Au[a)]
Marine Mammal Research Program, Hawaii Institute of Marine Biology, University of Hawaii, P.O. Box 1106, Kailua, Hawaii 96734

Adam A. Pack
The Dolphin Institute, 420 Ward Avenue, Suite 212, Honolulu, Hawaii 96814

Marc O. Lammers
Marine Mammal Research Program, Hawaii Institute of Marine Biology, University of Hawaii, P.O. Box 1106, Kailua, Hawaii 96734

Louis M. Herman
The Dolphin Institute, 420 Ward Avenue, Suite 212, Honolulu, Hawaii 96814

Mark H. Deakos
The Hawaii Association for Marine Education and Research, Inc., PMB #175, 5095 Napilihau Street 109B, Lahaina, Hawaii 96761

Kim Andrews
Marine Mammal Research Program, Hawaii Institute of Marine Biology, University of Hawaii, P.O. Box 1106, Kailua, Hawaii 96734

(Received 6 January 2006; revised 17 April 2006; accepted 12 May 2006)

A vertical array of five hydrophones was used to measure the acoustic field in the vertical plane of singing humpback whales. Once a singer was located, two swimmers with snorkel gear were deployed to determine the orientation of the whale and position the boat so that the array could be deployed in front of the whale at a minimum standoff distance of at least 10 m. The spacing of the hydrophones was 7 m with the deepest hydrophone deployed at a depth of 35 m. An eight-channel TASCAM recorder with a bandwidth of 24 kHz was used to record the hydrophone signals. The location (distance and depth) of the singer was determined by computing the time of arrival differences between the hydrophone signals. The maximum source level varied between individual units in a song, with values between 151 and 173 dB *re* 1 μPa. One of the purposes of this study was to estimate potential sound exposure of nearby conspecifics. The acoustic field determined by considering the relative intensity of higher frequency harmonics in the signals indicated that the sounds are projected in the horizontal direction despite the singer being canted head downward anywhere from about 25° to 90°. High-frequency harmonics extended beyond 24 kHz, suggesting that humpback whales may have an upper frequency limit of hearing as high as 24 kHz. © *2006 Acoustical Society of America.* [DOI: 10.1121/1.2211547]

PACS number(s): 43.80.Ka, 43.80.Lb [JAS] Pages: 1103–1110

I. INTRODUCTION

There is a growing concern on the effects of anthropogenic sounds on marine mammals, especially on mysticetes or baleen whales (NRC, 2003). As noise in the oceans continues to increase (Richardson *et al.*, 1995) there is a need to have appropriate regulations limiting the production of man-made sounds. However, one of the major problems in establishing standards and enacting regulations and guidelines is our poor understanding of the hearing sensitivity and frequency range of hearing of baleen whales. Our knowledge of the hearing capabilities of baleen whales is extremely limited and, without having any audiograms, we cannot estimate the sound pressure levels at various frequencies at which a whale may be affected behaviorally or when it will incur temporary and even permanent hearing threshold shifts. However, we can gain insight as to the amount of acoustic energy baleen whales, such as humpback whales, typically tolerate by knowing the source levels of their song emissions. This notion was expressed in the National Research Council's report on Ocean Noise and Marine Mammals (NRC, 2003), which stated that it is first critical to obtain information on what vocalizations are produced during normal conspecific interactions that might reveal information about the susceptibility of marine mammals to sounds of human origin. Humpback whales on their low-latitude wintering grounds produce so-called "social sounds" (Pack *et al.*, 2005; Silber, 1986) as well as a complex and structured series of vocalizations termed "song" (Payne *et al.*, 1983; Payne and McVay, 1971; Winn and Winn, 1978). While social sounds appear to be produced by females as well as males (Pack *et al.*, 2005), songs are produced exclusively by male humpbacks (Darling

[a)]Author to whom correspondence should be addressed. Electronic mail: wau@hawaii.edu

and Berube, 2001; Glockner, 1983). Although singers typically are lone males, singing sometimes occurs in the presence of other whales. For example, a male humpback will occasionally sing while escorting a female with her calf (Baker and Herman, 1984; Darling and Berube, 2001; Frankel *et al.*, 1995; Herman and Tavolga, 1980). Typically, the "singing escort" is within 100 m and approaches within one to two whale lengths of the mothercalf pair. Also, Darling and Berube (2001) documented 14 cases in which a male humpback whale approached close to a singer. Thus, by obtaining good source level measurements, we can also estimate the maximum amount of acoustic energy singing humpback whales expose to conspecifics.

The list of studies involving humpback whale songs is long and extends from 1970 (Winn *et al.*, 1970; Payne and McVay 1971) to the present time (Mercado *et al.*, 2005). Helweg *et al.* (1992) have written an excellent review on the current understanding of humpback whale songs. The various aspects of humpback whale songs that have been studied include geographic and seasonal variations in songs (Au *et al.*, 2000; Helweg *et al.*, 1998; Cerchio *et al.*, 2001), evolution of song structure throughout the year and between years (Guinee *et al.*, 1983; Payne *et al.*, 1983), size of singers (Spitz *et al.*, 2002), and the behavioral and spatial pattern of singers (Frankel *et al.*, 1995; Tyack, 1981), to name a few.

In all these studies the source levels produced by singing humpback whales have been almost entirely ignored. Frankel (1994) estimated the source level of singing humpback whales to be about 140 to 170 dB *re* 1 μPa with data collected from an array of hydrophones where most of the whales were 2 to 8 km away. The propagation losses were estimated using a simple cylindrical spreading model which is always subject to uncertainty when dealing with shallow coastal waters of varying depth. Furthermore, no consideration was given to the difference in source levels for different units.

The source levels of nonsong emissions of humpback whales in southeast Alaska, a summer feeding ground, have previously been measured by Thompson *et al.* (1986). Levenson (1972) has also reported on nonsong emissions of humpback whales. Thompson *et al.* (1986) measured grunts, moans, pulse trains, and other externally produced water interactive sounds such as slaps. Maximum source levels were 162–171 dB for low-frequency pulse trains from a visible feeding whale, 179–181 dB for blowhole shrieks, and 181–185 dB for trumpet like horn blasts. The values provided by Thompson *et al.* (1986) were considerably higher than those reported by Levenson (1972), who found a range of 144–175 dB *re* 1 μPa at 1 m for 64 *song* components from humpback whales in the Atlantic. However, the source levels of sounds produced by singing and nonsinging whales can be considerably different because of differences in the characteristics of nonsong and song emissions.

The Hawaiian Islands is the principal area of congregation for wintering North Pacific humpback whales (Calambokidis *et al.*, 2001). Humpback whales migrate to Hawaii from Southwest Alaska each winter to mate and give birth, though neither event has ever directly been observed. Most singing by humpbacks takes place on the winter grounds, although singing also occurs, but not as widespread, during the northbound migration (Norris *et al.*, 1999) and in the summer feeding grounds (Clark and Clapham, 2004).

In this study, the acoustic characteristics of singing humpback whales were measured with a vertical line array of five hydrophones deployed in close proximity to the whales. From these measurements, the distance of a whale from the array could be accurately estimated and the source level determined. Other features of the sound emissions such as the extent of the high-frequency harmonics and the directionality of the high-frequency components of the sounds were also investigated.

II. METHODS

Recordings of humpback whales (*Megaptera novaeangliae*) were made in the waters of the Auau channel between the islands of Maui, Lanai, Kahoolawe, and Molokai from 22–25 February 2002. The waters of this region contain one of the densest concentrations of humpback whales in the Hawaiian Island chain during the winter and spring months (Herman and Tavolga, 1980; Mobley *et al.*, 1999). Singers were located using a hand-held two-element horizontal hydrophone array termed "Aquahead" (Pack *et al.*, 2003). Singing humpback whales often suspend themselves in the water column with the longitudinal axis of their body between 0° and 75° from the vertical. Eventually they rise to the surface to expel spent gases and to recharge their respiratory system with fresh air before submerging again to take up a singing posture. When a singer was spotted surfacing to recycle its air supply and then resubmerging again, two swimmers with snorkeling gear entered the water. One swimmer was equipped with a digital video camera in an underwater housing, and also a hand-held 200–400-kHz range finder to determine the body length of the whale as it surfaced using underwater videogrammetry (Spitz *et al.*, 2000). The other swimmer swam to the location at the surface above the whale and indicated the heading of the whale. The whale was usually at a depth of about 15 to 25 m. The boat was then driven in front of the submerged whale, the engine was turned off, and a vertical array of five hydrophones was deployed (Fig. 1) while a swimmer oriented the boat by tugging on the bow line. Both the whale and the boat would drift over a period of minutes.

The hydrophones were spaced 7 m apart with the shallowest hydrophone submerged to a depth of 7 m. The whale's song was recorded on an eight-channel Teac TASCAM (Model DA-78HR) for as long as the whale remained in the vicinity of the boat. The sampling rate of the TASCAM was set at 48 kHz. The hydrophones were constructed of lead zirconate titanate (PZT) piezoelectric ceramic tubes having an o.d. of 1.3 cm, a wall thickness of 1.1 mm, and a length of 1.3 cm. The inner diameter of the tube was filled with corprene (a cork-neoprene material) and the element was encapsulated in degassed epoxy. The sensor was attached to an amplifier-line driver having a gain of 30 dB. The hydrophones were calibrated in a test tank and had similar responses and a sensitivity of approximately -175 ± 3 dB *re* 1 v/μPa between 100 Hz and 15 kHz. The

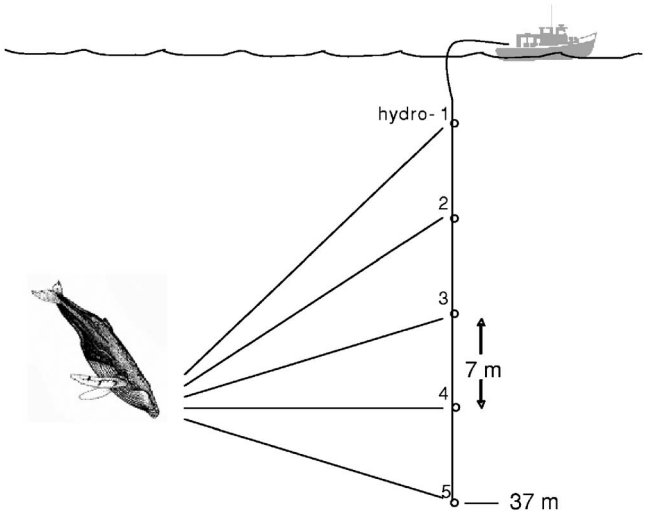

FIG. 1. Experimental geometry showing a singing humpback whale and the vertical array of hydrophones.

program Cool-Edit Pro was used to digitally transfer the multi-channel recordings from the TASCAM to a PC via a Mixtreme PCI card. Cool-Edit Pro controlled the Mixtreme card that performed as the interface to transfer the data.

To determine the source level of the singing whale, an accurate distance between the whale and the array was needed. By using the signals from three of the hydrophones the whale could be localized in depth and distance from the array. The localization of any sound source using the signals received by a line array can be achieved by determining the time of arrival differences between the center hydrophone and the other two hydrophones. The specific equations relating the time of arrival differences to the location of the source are given in the appendix of Lammers and Au (2003). The differences in the time of arrival of the signal at the three hydrophones are determined by calculating the cross-correlation integral for the signals measured by any two of the hydrophones. The time difference occurs at the time corresponding to the peak in the cross-correlation integral.

There are several ways to describe the acoustic source level of a singing humpback. The source level can be described in terms of the peak-to-peak, the root mean square (rms), and the energy flux density of the acoustic pressure. The rms source level can be expressed as

$$\mathrm{SL_{rms}} = 20 \log \sqrt{\frac{1}{T}\int_0^T p^2(t)dt} + 20 \log R$$
$$= \mathrm{SE} - 10 \log T, \quad (1)$$

where SE is the source energy flux density, T is the duration of the signal, $p(t)$ is the acoustic pressure waveform, and R is the range of the source from the measuring hydrophone. The source level will be presented in terms of the peak-to-peak, the rms, and the energy flux density of the acoustic pressure. The duration of the signal will be determined by calculating the energy flux density [the integral in Eq. (1)], choosing the time at which the energy is between 1% and 99% of the maximum energy.

III. RESULTS

The vertical hydrophone array was deployed in the near vicinity of nine singing humpback whales. The duration of each recording varied from 1 to 17 min depending on how long the whale remained in the vicinity of the boat. For the shortest recording, the whale moved out of the vicinity of the boat only a minute after the array was deployed. Four themes were aurally classified from the songs recorded for the nine whales, although this process can be very subjective and other researchers may actually identify different numbers of themes.

Payne *et al.* (1983) defined a humpback whale song unit as "the shortest sounds in the song which seem continuous to the human ear." We aurally classified nine distinct units and confirmed our judgment by examination of the spectrograms of the songs. An example of the waveform and spectrogram of each of the nine units is shown in Fig. 2 and the aural description of the units is listed in Table I. The descriptions were agreed upon by two listeners discussing their subjective sense of the best description.

The spectrograms can be separated into two groups, those units that have some tonal quality and higher frequency harmonics (units C, E, E_2, and H) and those that are relatively broadband with rumble, grunts, or gurglelike qualities

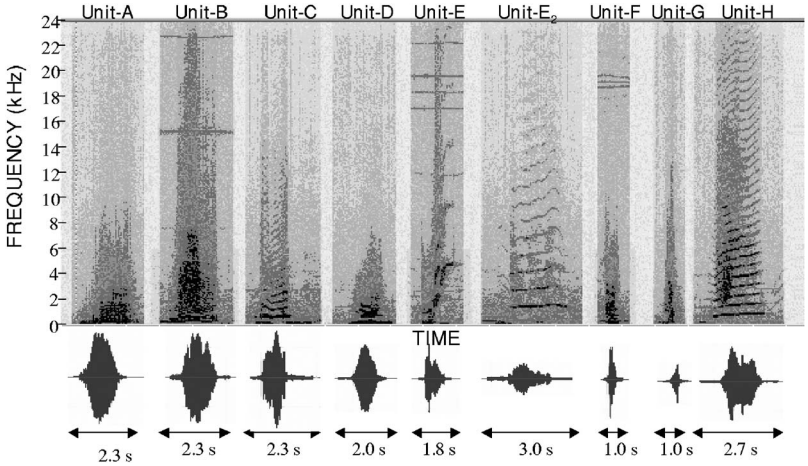

FIG. 2. Spectrogram and waveform representation of the nine units contained in the humpback whale songs during the winter season in Hawaiian waters in 2002. The units were from the recordings of several whales and were chosen because they showed the characteristics of the unit most clearly.

TABLE I. Aural description of the nine units for the humpback whale songs during the 2002 wintering season in Hawaii.

Unit	Description
A	vibrating upsweep
B	double upsweep
C	frequency sweeping cry
D	flat tonal groan
E	low gulp jumping to very sharp upsweep
E_2	high-frequency tonal wail
F	short low-frequency downsweep
G	short low-frequency upsweep
H	mid-frequency tonal wail

and with weak harmonics (units A, B, D, F, and G). The units with some tonal elements and high-frequency harmonics were described as cries or wails. Four distinct themes were found for the nine whales that we recorded. The sequence of units producing each theme is listed in Table II.

We found that certain units resulted in relatively unambiguous peaks in the cross-correlation function whereas others did not. Unit A was one of the better units to use, however, only three whales had this unit for a sufficient length of time to provide a good track. The tracks of three humpback whales given in terms of the horizontal distance from the boat and the depth of the whales are shown in Fig. 3. Once the whales sounded and moved into their singing position in the water column, they seemed to be relatively stationary whereas the boat housing the array was free to drift with the engine turned off. However, the three tracks show that the depth of the whale varied from about 15 m for whale E4 to slightly over 10 m for whales I2 and L2.

The peak-to-peak and rms source levels and the source energy flux density for the three whales tracked in Fig. 3 are shown in Table III for the nine units. Several results are noteworthy. The relationship between the rms source level and the peak-to-peak source level is slightly different for the different units. SL_{pp} was between 17 and 20 dB greater than SL_{rms}, and variation is probably due to difference in the shape of waveform shown in Fig. 3. If we consider the difference between SL_{pp} and SL_{rms} across the 778 units for the results on Table III, the following relationship is obtained,

TABLE II. The general sequence of units producing the four themes observed in the recordings of nine singers. There is considerable variability in a theme associated with the number of or sequence of the units. The units in parentheses are those that are repeated seemingly randomly from one to seven times, depending on the specific whale.

Theme	Units
1	B C (B-C) D D A
2	D A D E F D (E-F-D) E A
3	A F F F A F F E F D (E-F-D) E2 E
	A F F F A F F F F E E E [without (E-F-D)]
4	G G G G H

The specific number of F units can vary between 2 and 7, and E units between 1 and 3.
Sometimes the H unit is not emitted.

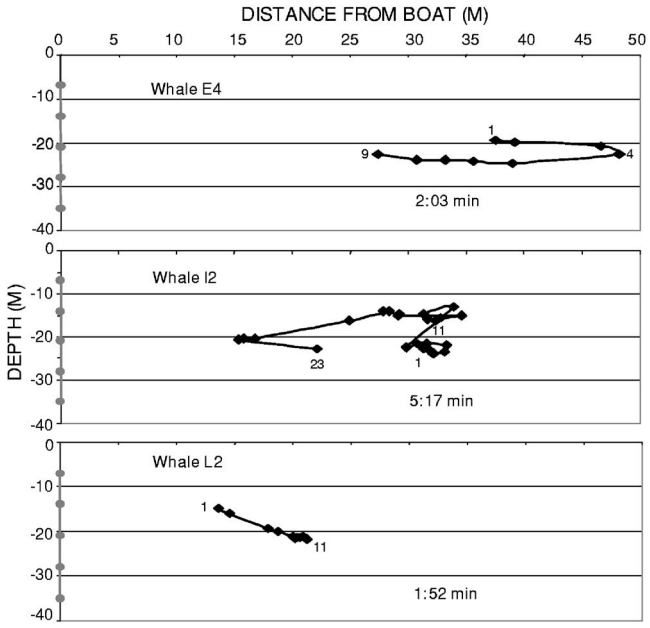

FIG. 3. Tracks of three singing humpback whales from the boat carrying the vertical line array. The numbers next to the points are the order of the localization with 1 being the first localization. The time shown on each plot is the total amount of time the whale was localized. The circles on the left vertical axis represent the hydrophones in the line array.

$$SL_{rms} = SL_{pp} - 17.1 \pm 2.7 \text{ dB}, \quad (2)$$

where 2.7 is the standard deviation. For a continuous sine wave signal, the difference between the peak-to-peak and the rms values is 9 dB. The 17.1 dB difference for the humpback whale originates from the pulse nature of the units and the slow rise and fall times of the waveforms.

The highest average rms source level recorded was 169 dB for whale E4 producing units A and D, and for whale I2 producing unit B. Unfortunately, units B and C were not recorded for whale E4. The lowest average rms source level was 149 dB for whale I2 producing unit G and whale L2 producing unit F, representing a unit-related 20-dB range in the average source levels. Unit H produced by whale I2 was not considered since only a single H unit was attributed to whale I2. The source level for unit E_2 was also among the lowest levels for all three whales.

The numerical values of SL_{rms} and SE are very similar, keeping in mind that the units of measurements are different. The duration of the units typically varied between 0.4 and 1.4 s except for units E_2 and H, of which we had very few samples. From Eq. (1), the difference in the value of SL_{rms} and SE is in the 10 log T term. With durations close to unity, the log term is negligible. For a duration of 0.4 s, the 10 log term is only 4 dB.

The variation in the mean and standard deviation of SL_{rms} for the nine units of the three tracked whales are shown in Fig. 4. An analysis of variance test was applied to the units produced by the three whales to test if the source levels were significantly different. If they were significantly different, the Tukey HSD *posthoc* test was applied to determine which pairs were significantly different at $p < 0.05$. If only two whales were involved, as in units B and C, a two-tailed t test was applied to determine if the levels were sig-

TABLE III. Results of source level estimation for the three whales whose tracks are shown in Fig. 3. The unit for SL_{pp} and SL_{rms} is dB *re* 1 μPa and the unit for SE is dB *re* 1 μPa^2 s.

Unit	SL_{pp} (dB)	SL_{rms} (dB)	SE (dB)	T (s)	N
		Whale E4			
A	184±4	169±3	169±4	0.9±0.2	19
B					
C					
D	184±4	169±3	169±4	0.9±0.2	19
E	178±2	162±2	160±2	0.7±0.1	17
E_2	172±2	153±3	156±2	2.3±0.9	9
F	173±3	156±3	152±3	0.4±0.2	64
G	181±3	162±4	158±3	0.5±0.3	27
H	179±1	162±0	162±1	1.0±0.2	2
		Whale I2			
A	182±2	165±3	165±2	1.1±0.6	26
B	184±1	169±2	169±1	1.1±0.1	15
C	180±5	162±8	163±7	1.3±0.5	12
D	176±4	161±5	159±4	0.6±0.2	73
E	179±3	163±3	160±3	0.6±0.3	50
E_2	171±6	151±7	155±5	2.9±2.1	9
F	171±6	154±7	151±6	0.5±0.2	39
G	170±3	149±2	147±2	0.8±0.6	16
H	165	144	152	5.7	1
		Whale L2			
A	181±3	164±2	165±3	1.4±0.6	42
B	181±3	164±2	165±2	1.2±0.4	23
C	183±2	167±3	166±2	0.9±0.2	21
D	173±6	160±4	157±5	0.6±0.2	56
E	177±4	160±4	158±4	0.6±0.2	52
E_2	172±4	153±5	157±3	3.3±2.0	26
F	167±3	149±4	148±4	0.8±0.3	143
G	177±3	157±3	155±2	0.6±0.2	18
H	169±7	153±10	156±8	1.8±0.0	2

nificantly different at $p<0.05$. Whale E4 produced louder sounds than the other two whales for units A and G. For the other units, the level of whale E4 was not significantly different from either whale I2 or L2. Whale L2 had the lowest source level when producing units B, D, E, and F. However, for units C and G, whale L2 sounds were louder than those of whale I2. Unit H was hardly recorded for the three whales, occurring twice for whale E4 and L2 and once for whale I2.

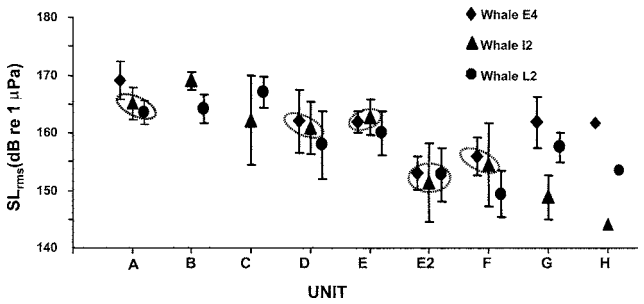

FIG. 4. The mean and standard deviation of the rms source level of the different units for the three whales tracked in Fig. 3. The means that are enclosed within a dashed oval are not significantly different. All other units are significantly different at $p<0.05$.

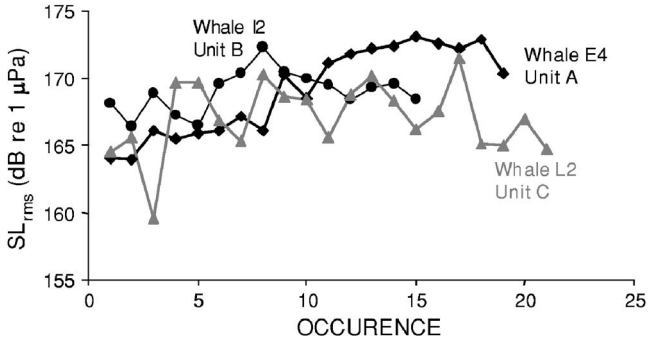

FIG. 5. The rms source level for the unit having the highest intensity for each of the three whales tracked in Fig. 3.

The rms source levels for the most intense unit emitted by the three whales are shown in Fig. 5. Unit A had the highest average source level for whale E4 with a maximum of 173 dB. The source level remained above 170 dB on nine occasions during the period the whale was tracked. Unit B was the most intense unit emitted by whale I2, reaching a level of 172 dB. Six emissions of unit B sounds were equal to or above 170 dB source level. Unit C was the most intense unit emitted by whale L2, with the highest level being 172 dB. However, only 4 of the 27 units were above 170 dB. Although the average source level of unit A emitted by whale E4 was the same as unit B emitted by whale I2, Fig. 5 clearly show that whale E4 emitted higher level signals than whale I2 but had a greater range between the lowest and highest levels which brought down its average source level for unit A.

There were three units (E, E_2, and H) that had very-high-frequency harmonics that extended beyond 24 kHz, which was the upper limit of the TASCAM recorder. The spectrogram and frequency spectrum of unit H sounds produced by three different whales are shown in Fig. 6. These spectrograms show the highest harmonic levels ever reported. The frequency spectra plots alongside the spectrograms indicate that the higher frequency harmonics do not drop off very rapidly. The frequency spectra were computed in Matlab using a 1024-point fast Fourier transform algorithm and a rectangular window. At a frequency of 10 kHz, the amplitude of the spectra is about −20 dB below peak amplitude for whales E4 and F4 and about −22 dB for whale L2. At a frequency of 22 kHz, the amplitude of the spectra is between −38 and −42 dB below the peak amplitude. Although unit H was recorded only 11 times total from nine whales, representing the least recorded unit, it was selected to be reported in Fig. 5 because of its unusually high-frequency harmonic structure.

The source levels measured by four of the five hydrophones in the array for unit H sounds from whale E4 and a unit E_2 sound from whale L2 are shown in Fig. 7. During the field measurements, one hydrophone in the array consistently malfunctioned, which limited the angular resolution of our measurements. Units H and E_2 were specifically chosen because both units were rich in high-frequency harmonics so that the sound field at the fundamental and harmonic frequencies could be easily determined. The closed circles for the fundamental frequency are the estimated source level

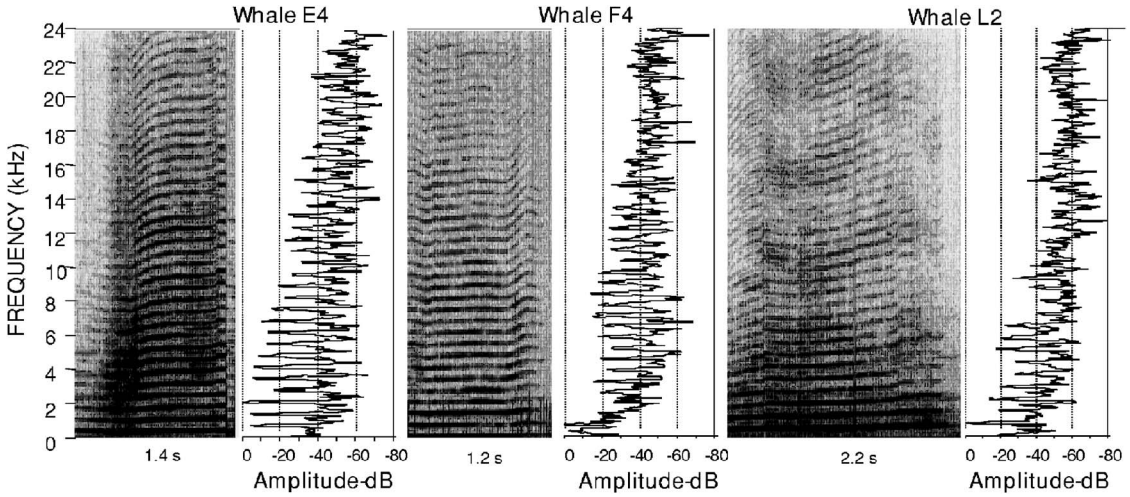

FIG. 6. Spectrogram showing the frequency versus time variation of unit H sounds and corresponding frequency spectra plotting relative amplitude as a function of frequency. The plots depict the high-frequency nature of unit H sounds showing harmonics extending beyond 24 kHz for three different whales.

from each of the four working hydrophones. Specific points were not shown for the higher harmonics to keep the plots relatively simple and uncluttered. The line connecting the points for the fundamental frequency consist of a third-order polynomial fitted to the four source levels.

The polar plots suggest that a beam has started to form in the vertical plane at the fundamental frequency of 750 Hz for whale E4. The same is true for whale L2 having a fundamental frequency of 1406 Hz. As the frequency increases the beam becomes narrower, however, there is an anomaly between the fifth and seventh harmonic for whale E4, where the beam of the seventh harmonic is slightly larger than for the fifth harmonic. The reason for this anomaly is not known, but may be related to the orientation of the whale. The angle of the whale to the vertical was not ascertained and the array was initially positioned directly in front of the whale; however, the whale could easily pivot about its longitudinal axis to modify the geometry between the array and the whale.

IV. DISCUSSION AND CONCLUSIONS

The use of a vertical line array has been instrumental in determining some of the basic acoustic properties of singing humpback whales. Although humpback whale songs have been recorded and studied for over three decades, only rough estimates of source level have been reported. The results of

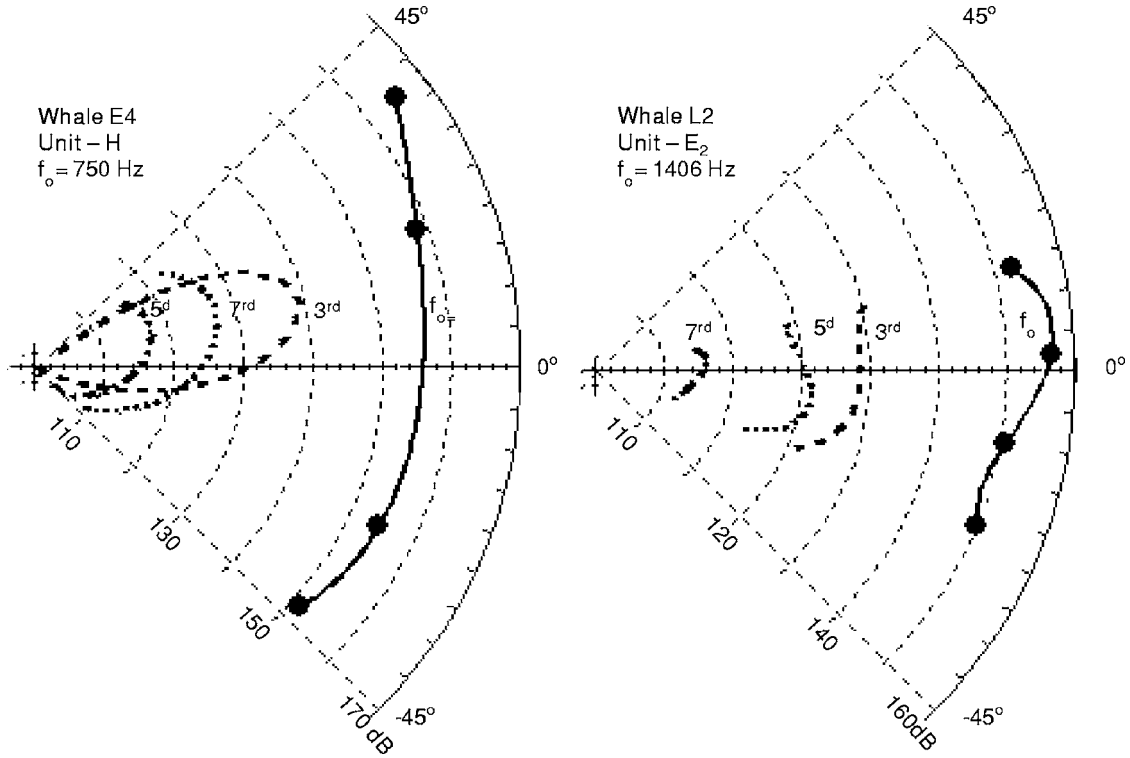

FIG. 7. Polar plot of the rms source level for whale E4 projecting a unit H sound and for whale L2 projecting a unit E_2 sound.

this study indicate that the source level for the different units are not the same but can vary as much as 20 dB between the least intense and the most intense units. The higher level units were the longer broadband units with durations of about 2 s that are described as rumbles, grunts, or gurgles, whereas the lower level units were units with some tonal quality or short broadband sounds such as units F and G. In an anthropomorphic sense, we can usually shout much louder than we can sing. It seems that the same tendency may be true for humpback whales.

The level of anthropogenic sounds that baleen whales should be exposed to is a topic under much discussion (NRC, 2003). The source level results can be used to estimate the level of sounds that other whales are exposed to when in the vicinity of a singer. Singing escorts have been estimated to be as close as two whale lengths away (about 28 m) from a cow-calf pair and other males have been observed to swim within approximately two whale lengths of a singer (Darling and Berube, 2001). If we assume a whale length as approximately 12–14 m, then sounds from a singer would be only about 28 dB lower at the location of the conspecific so that the conspecific would be exposed to sounds with average value of approximately 141 dB for the duration of the song. However, if the higher levels of unit A signals emitted by whale E4 are considered, then a conspecific may be exposed to sounds having a rms level of 147 dB. This also assumes that the singing whale will not lower the level of its output in the near presence of other whales.

The maximum source level of 173 dB measured in this study for whale E4 is slightly lower than the maximum of 175 dB for a moan and much lower than the 190 dB for a grunt measured by Thompson *et al.* (1986) of humpback whales vocalizing on the Alaskan summer feeding grounds. However, this is not unreasonable because a humpback whale will often sing continuously for many minutes whereas the nonsong sounds measured by Thompson *et al.* (1986) were probably not produced regularly over a long period of time. Therefore, the amount of acoustic energy emitted by a singing humpback whale during a dive that may last up to tens of minutes may indeed be greater than the amount of acoustic energy emitted by the nonsinging whales in their feeding grounds. Unfortunately, Thompson *et al.* (1986) did not provide any clues as to the temporal properties of the sounds they measured.

A simpler method of measuring the source level of singing humpback whales is to adapt the videogrammetry technique of Spitz *et al.* (2000) but include a recording system in an underwater housing that the swimmer would also carry. In this technique the distance to the whale is obtained with the use of a high-frequency (200–400 kHz) hand-held acoustic depth sounder (Spitz *et al.* 2002). A benefit to this technique is that the size of the singer can be estimated and the relationship between size and source levels can be established.

There are very little data available that could provide any indication of the upper frequency limit of hearing in baleen whales. A knowledge of the high-frequency harmonics in a signal may provide clues to the upper frequency of hearing in an organism. If the popular notion that animals generally hear the totality of the sounds they produce is applied in this study, then we could conclude that humpback whales probably hear to frequencies beyond 24 kHz. The harmonic structure shown in Fig. 6 is very prominent and certainly suggests that the high-frequency harmonics extend beyond 24 kHz. Although at that frequency, the level of the signal is reduced by 40 to 50 dB from its maximum value; the large dynamic range of the mammalian ear should be able to accommodate this range of acoustic intensity (Yost, 1994). There are several reasons why such high-frequency harmonics have not been previously reported. The most prevalent reason is that cassette tape recorders have been typically used in the past and these recorders have limited bandwidth. However, in the present age, there are many different types of portable digital recorders commercially available and these generally have analog bandwidths up to about 24 kHz or higher.

Initially, it was surprising to see the beginning of directivity in the sound field at the fundamental frequency of units H and E_2. However, a fundamental frequency of 750 Hz for unit H is associated with a wavelength close to 2 m. The average length of a male humpback whale is approximately 12–14 m (Winn and Reichley, 1985) so that considering the ratio of the linear measurement of the head close to the blowhole from photographs, one can estimate a diameter of roughly 1.5–1.7 m. Here we are assuming that the sound source is in the vicinity of the blowhole (Aroyan *et al.* 2000). Therefore, for the head diameter to wavelength ratio, we have $d/\lambda \sim 0.75-0.85$. For unit E_2 and whale L2, the wavelength corresponding to the fundamental frequency of 1406 Hz is close to 1 m so that $d/\lambda \sim 1.5-1.7$. A linear circular transducer will exhibit a directional characteristic when d/λ is close to unity (Urick, 1983). The fundamental frequencies of other units such as units A and B are relatively low at about 210 Hz. For these units $d/\lambda \sim 0.21-0.24$ so that the sound has no directivity at the fundamental frequency.

Singing humpback whales often suspend themselves with the longitudinal axis of their bodies between 0° and 75° from the vertical. The direction of the higher frequency harmonics suggests that the beam of the sound is directed slightly above the horizon. This implies that the sound generator is directing sounds at a steep angle above the animals' head. For low-frequency fundamentals of 200–400 Hz, the beam will be nearly omni-directional so that the orientation of the whales with respect to the vertical is not relevant. However, for the high-frequency harmonics, the orientation of the whale will affect how these harmonics propagate in the horizontal distance. Unfortunately, the precise position of the whales with respect to the vertical was not measured so the angle above the head of the whales cannot be accurately estimated. Humpback whales may be unique in the directions at which sounds are emitted from the head. It seems that most mammals emit sound in the forward direction with respect to their head.

There has been very little work done on understanding the acoustics of humpback whale sounds. In this project, we have only touched the surface of this intriguing subject. However, more needs to be done in order to gain a deeper

appreciation of the physics and physiology of sound production in not only humpback whales but in baleen whales in general.

ACKNOWLEDGMENTS

This work was sponsored in part by the Office of Protective Resources of the National Marine Fishery Service in Silver Springs, MD, Dr. Roger Gentry, program officer, and the Office of Naval Research, Dr. Robert Gisiner, program officer. Jake and Fiona Eberts and the Arthur M. Blank foundation also provided financial support. We thank Dr. Patrick Miller of the Gatty Marine Laboratory, University of St Andrews, who provided considerable guidance in selecting the TASCAM and the technique to extract the digital data directly from the tape into a PC. The Dolphin Institute and its members provided support for field activities. Our thanks to Elia Herman, Siri Hakala, Kira Goetschius, and Dan Gubitz for their assistance in the field and to Michiel Schotten, Wu-Jung Lee, and Alison Stimpert for assistance in the final analysis of the data. All observations and recordings of humpback whales were carried out under NOAA Federal Permit No. 707-1531-02 and State Permit SH2002-01, L. M. Herman and A. A. Pack, Principal Investigators. This is HIMB contribution 1229.

Aroyan, J. L., McDonald, M. A., Webb, S. C., Hildebrand, J. A., Clark, D., Laitman, J. T., and Reidenberg, J. S. (**2000**). "Acoustic model of sound production and progagation," in *Hearing in Whales and Dolphins*, edited by W. W. L. Au, A. N. Popper, and R. R. Fay(Springer-Verlag, New York), pp. 409–417.

Au, W. W. L., Mobley, J., Burgess, W. C., Lammers, M. O., and Nachtigall, P. E. (**2000**). "Seasonal and diurnal trends of chorusing humpback whales wintering in waters off western Maui," Marine Mammal Sci. **16**, 530–544.

Baker, C. S., and Herman, L. M. (**1984**). "Aggressive behavior between humpback whales (*Megaptera novaeanglaie*) wintering in Hawaiian waters," Can. J. Zool. **62**, 1922–1937.

Calambokidis, J., Steiger, G. H., Straley, J. M., Herman, L. M., Cerchio, S., Salden, D. R., Urban, R. J., Jacobsen, J. K., von Ziegesar, O., Balcomb, K. C., Gabriele, C. M., Dahlheim, M. E., Uchida, S., Ellis, G., Miyamura, Y., De Guevara, P. P., Yamaguchi, M., Sato, F., Mizroch, S. A., Schlender, L., Rasmussen, K., Barlow, J., and Quinn II, T. J. (**2001**). "Movements and population structure of humpback whales in the North Pacific," Marine Mammal Sci. **17**, 769–794.

Cerchio, S., Jacobsen, J. K., and Norris, T. F. (**2001**). "Temporal and geographical variation in songs of humpback whales, Megaptera novaeangliae: synchronous change in Hawaiian and Mexican breeding assemblages," Anim. Behav. **62**, 313–329.

Clark, C. W., and Clapham, P. J. (**2004**). "Acoustic monitoring on a humpback whale (*Megaptera novaenagliae*) feeding ground shows continual singing into late spring," Proc. R. Soc. London, Ser. B **271**, 1051–1057.

Darling, J. D., and Berube, M. (**2001**). "Interactions of singing humpback whales with other males," Marine Mammal Sci. **17**, 570–584.

Frankel, A. S. (**1994**). "Acoustic and visual tracking reveals distribution, song variability and social roles of humpback whales in Hawaiian waters," unpublished Ph.D. dissertation, University of Hawaii, Honolulu.

Frankel, A. S., Clark, C. W., Herman, L. M., and Gabriele, C. M. (**1995**). "Spatial distribution, habitat utilization, and social interactions of humpback whales, Megaptera novaeangliae, off Hawai'i, determined using acoustic and visual techniques," Can. J. Zool. **73**, 1134–1146.

Glockner, D. A. (**1983**). "Determining the sex of humpback whales (*Megaptera novaeangliae*) in their natural environment," in *Communication and Behavior of Whales*, edited by R. Payne (Westview, Boulder, CO).

Guinee, L. N., Chiu, K., and Dorsey, E. M. (**1983**). "Changes over time in the song of known individual whales," in *Communication and Behavior of Whale*, edited by R. Payne (Westview, Boulder, CO).

Helweg, D. A., Frankel, A.S., Mobley, J., and Herman, L. M. (**1992**). "Humpback whale song: Our current understanding," in *Marine Mammal Sensory Systems*, edited by J. A. Thomas, R. A. Kastelein, and A. S. Supin (Plenum, New York), pp. 459–483.

Helweg, D. A., Cato, D. H., Jenkins, P.F., Garrigue, C., and McCauley, R. D. (**1998**). "Geographic variation in South Pacific humpback whale songs," Behav. Ecol. **135**, 1–27.

Herman, L. M., and Tavolga, W. N. (**1980**).*The Communication Systems of Cetaceans* (Wiley Interscience, New York).

Lammers, M. O., and Au, W. W. L. (**2003**). "Directionality in the whistles of Hawaiian spinner dolphin (*Stenella longirostris*): A signal feature to cue direction of movement?," Marine Mammal Sci. **19**, 249–264.

Levenson, C. (**1972**). "Characteristics of sounds produced by humpback whales (*Megaptera novaeangliae*)," U.S. Naval Oceanographic Office Tech. Note No. 7700-6-72, St. Louis, MO.

Mercado, E. I., Herman, L. M., and Pack, A. A. (**2005**). "Song copying by humpback whales: Themes and variations," Anim. Cognition **8**, 93–102.

Mobley, J. R. J., Bauer, G. B., and Herman, L. M. (**1999**). "Changes over a ten-year interval in the distribution and relative abundance of humpback whales (*Megaptera novaeangliae*) wintering in Hawaiian waters," Aquat. Mamm. **25**, 63–72.

Norris, T. F., McDonald, M., and Barlow, J. (**1999**). "Acoustic detections of singing humpback whales (*Megaptera novaeangliae*) in the eastern North Pacific during their northbound migration," J. Acoust. Soc. Am. **106**, 506–514.

NRC (National Research Council (**2003**). *Ocean Noise and Marine Mammals* (National Academy, Washington, DC).

Pack, A. A., Au, W. W. L., Lammers, M. O., Herman, L., and Deakos, M., (**2003**). "Determining the Acoustic Field and Transmission Characteristics for Singing Humpback Whales on the Hawaiian Winter Grounds," paper presented at the 15th Biennial Conference on the Biology of Marine Mammals, Greensboro, NC, 14–19 December.

Pack, A. A., Herman, L. M., Deakos, M. H., Hakala, S., Craig, A. S., Olson, J. R., Spitz, S. S., Herman, E., Goetschius, K., and Lammers, M. O. (**2005**). "First report of sounds recorded from individual humpback whale calves on the Hawaiian wintering grounds," paper presented at the 16th Biennial Conf. Biology of Mar. Mammals, San Diego, CA.

Payne, K., Tyack, P., and Payne, R. (**1983**). "Progressive changes in the songs of humpback whales (*Megaptera novaeangliae*): a detailed analysis of two seasons in Hawaii," in *Communication and Behavior of Whales*, edited by R. Payne (Westview, Boulder CO), pp. 9–57.

Payne, R. S., and McVay, S. (**1971**). "Songs of humpback whales," Science **173**, 585–597.

Richardson, W. J., Greene, Jr., C.R., Malme, C. I., and Thomson, D. H. (**1995**). *Marine Mammals and Noise* (Academic, San Diego).

Silber, G. (**1986**). "The relationship of social vocalizations to surface behavior and aggression in the Hawaiian humpback whale (*Megaptera novaeangliae*)," Can. J. Zool. **72**, 805–811.

Spitz, S. S., Herman, L. M., and Pack, A. A. (**2000**). "Measuring size of humpack whales (*Megaptera novaeangliae*) by underwater videogrammetry," Marine Mammal Sci. **16**, 664–676.

Spitz, S. S., Herman, L. M., Pack, A. A., and Deakos, M. H. (**2002**). "The relation of body size of male humpback whales to their social roles on the Hawaiian winter grounds," Can. J. Zool. **80**, 1938–1947.

Thompson, P. O., Cummings, W. C., and Ha, S. J. (**1986**). "Sounds, source levels, and associated behavior of humpback whales, Southeast Alaska," J. Acoust. Soc. Am. **80**, 735–740.

Tyack, P. L. (**1981**). "Interactions between singing Hawaiian humpback whales and conspecifics nearby," Behav. Ecol. Sociobiol. **8**, 105–116.

Urick, R. J. (**1983**). *Principles of Underwater Sound* (McGraw Hill, New York).

Winn, H. E., and Reichley, N. E. (**1985**). "Humpback Whale *Megaptera novaeangliae* (Borowski, 1781)," in *Handbook of Marine Mammals: The Sirenians and Baleen Whales* edited by S. H. Ridgway and R. Harrison (Academic, San Diego), Vol. **3**, pp. 241–273.

Winn, H. E., and Winn, L. K. (**1978**). "The song of the humback whale (*Megaptera novaeangliae*) in the West Indies," Mar. Biol. (Berlin) **47**, 97–114.

Winn, H. E., Perkins, P. J., and Poulter, T. (**1970**). "Sounds of the humpback whale," paper presented at the 7th Annual Conf Biological Sonar, Stanford Research Institute, Menlo Park, CA.

Yost, W. A. (**1994**).*Fundamentals of Hearing*(Academic, San Diego).

Artificial neural network discrimination of black-capped chickadee (*Poecile atricapillus*) call notes

Carly M. Nickerson, Laurie L. Bloomfield, and Michael R. W. Dawson
Department of Psychology, University of Alberta, Edmonton, Alberta, T6G 2P9, Canada

Christopher B. Sturdy
Department of Psychology, Centre for Neuroscience, University of Alberta, Edmonton, Alberta, T6G 2P9, Canada

(Received 9 March 2006; revised 11 April 2006; accepted 12 May 2006)

Artificial neural networks were trained to discriminate between two different notes from the "chick-a-dee" call of the black-capped chickadee (*Poecile atricapillus*). An individual note was represented as a vector of nine summary features taken from note spectrograms. A network was trained to respond to exemplar notes of one type (e.g., A notes) and to fail to respond to exemplar notes of another type (e.g., B notes). After this training, the network was presented novel notes of the two different types, as well as notes of the same two types that had been shifted upwards or downwards in frequency. The strength of the response of the network to each novel and shifted note was recorded. When network responses were plotted as a function of the degree of frequency shift, the results were very similar to those observed in birds that were trained in an analogous task [Charrier *et al.*, J. Comp. Psychol. **119**(4), 371–380 (2005)]. The implications of these results to simulating behavioral studies of animal communication are discussed.
 [DOI: 10.1121/1.2211509]

PACS number(s): 43.80Ka., 43.80.Lb, 43.80.Jz [JAS] Pages: 1111–1117

I. INTRODUCTION

An artificial neural network (ANN) is a computer program that can learn to accomplish tasks such as pattern recognition (Pao, 1989). It is a simulation of neuron-like processors that accept incoming signals from one or more other processors, convert these signals into a level of internal activity, and finally convert this activity into an output signal. Signals are sent through weighted, modifiable connections that are analogous to synapses. A brief tutorial on ANNs is provided by Dawson *et al.* (2006). For a more extensive introduction to such networks, a number of sources are available (Bachetl and Abrahamsen, 1991; Caudill and Butler, 1992; Dawson, 2004; Gluck and Myers, 2001; Quinlan, 1991; Ripley, 1996).

ANNs are increasingly popular statistical tools in the study of animal vocalization and communication. For example, they have been used to classify bat species on the basis of echolocation calls (Parson and Jones, 2000), to categorize different calls produced by false killer whales (Murray *et al.*, 1998), to identify dolphin echolocation clicks (Houser *et al.*, 1999), to recognize stress calls of domestic pigs (Schon *et al.*, 2001), to distinguish particular female sea lions on the basis of their mother-pup contact calls (Campbell *et al.*, 2002), to assign a variety of Manitoban songbirds to their species on the basis of recorded songs (MaIlraith and Card, 1997), and to classify the component notes of the "chick-a-dee" call of the black-capped chickadee (Dawson *et al.*, 2006).

In addition to their statistical use, ANNs can also serve as models of animal behavior. In particular, ANNs provide interesting accounts of classical conditioning and discrimination learning (Dawson and Spetch, 2005; Delamater *et al.*, 1999; Gluck and Myers, 2001; Pearce, 1987). In such simulations, a single output unit of a network represents an animal's response. The unit is trained to turn on when the unconditioned stimulus (US) is presented, and to turn off when the US is absent. A set of input units is used to represent the present or absence of a particular conditioned stimulus (CS). For example, consider a simple network with two input units that are used to represent the presence of conditioned stimuli A and B (e.g., Dawson and Spetch, 2005). To simulate a positive patterning paradigm, this network would be trained to turn on when both input units were activated to represent a compound stimulus (i.e., AB+), and to turn off when only one input unit was activated to represent that only one of the stimulus components was present (i.e., A−, B−).

The purpose of this paper is to examine the ability of such a network to deal with what would appear to be a more complicated discrimination learning task from the animal communication literature (Charrier *et al.*, 2005). In the simulations below, rather than representing individual CSs (local representation), each input unit represents the value of a stimulus feature. An individual stimulus is defined by the entire vector of input unit values (distributed representation). The network is trained to respond to some feature vectors, and to not respond to others. There are two questions addressed in the simulations below. First, can a simple network perform discrimination learning when it is defined in this distributed fashion? Second, if such discrimination learning is possible, how well does the behavior of the networks resemble the choice behavior of animals trained to perform an analogous task?

A. Chickadee discriminations of notes and frequency-shifted notes

The chick-a-dee call of the black-capped chickadee (*Poecile atricapillus*) contains four note types (A, B, C, and D) produced in a fixed order (A→B→C→D), but note types can be repeated or omitted to produce chickadee calls with seemingly infinite combinations of notes (e.g., ACCCCD, ABDDD). Many researchers are interested in the composition of this call, as it more closely resembles human language syntax than any other animal system (Haliman and Ficken, 1986). As a result, numerous studies have explored the regularities, and the information contained, in chickadee call syntax (Baker *et al.*, 1987; Charrier and Sturdy, 2005; Clucas *et al.*, 2004; Ficken *et al.*, 1994; Freeberg and Lucas, 2002; Haliman *et al.*, 1985).

However, in addition to the study of the syntax of the chickadee call, an analysis of its constituent notes is also important. This is because the individual notes in a call can themselves communicate crucial information, such as the individual identity and gender of the caller (Charrier *et al.*, 2004). Playback studies have shown that chickadees can discriminate the calls of their own flock from those of foreign flocks (Nowicki, 1983), a function that is apparently mediated by D notes (Mammen and Nowicki, 1981). C notes may indicate the location or availability of food sources (Freeberg and Lucas, 2002). Individual A, B, C, and D notes can be used to distinguish black-capped chickadees from another species, the mountain chickadee *P. gambeli* (Dawson *et al.*, 2006).

Discrimination learning provides one paradigm for studying the ability of chickadees to process component notes of the chickadee call. For example, Charrier *et al.* (2005) first trained black-capped chickadees to discriminate two individual note types (e.g., A and B) by responding after hearing one (by visiting a feeder) and by withholding a response after hearing the other (by refraining from visiting a feeder). Then, they studied the responses of the birds to modified notes in a second phase. Birds were presented notes that had been frequency shifted up or down by between 0.5 and 2.5 standard deviations, in 0.5-SD steps. The responses of the birds to these shifted notes (i.e., whether or not the birds flew to a feeder) were used as an index of how the birds classified the transformed stimuli. Charrier *et al.* found, for example, that shifting the frequency of A notes down resulted in them being classified as being "B-like," while shifting the frequency of B notes upwards produced behavior that indicated that they were classified as being "A-like."

The purpose of the present study is to explore the ability of simple ANNs to simulate the experiment conducted by Charrier *et al.* (2005). In a training phase, ANNs learned to discriminate between two different types of notes from the chickadee call. In different conditions, this discrimination learning used the same pairings as those studied by Charrier *et al.* (i.e., A+B−, A−B+, B+C−, and B−C+). In a generalization phase, the ANNs were presented novel notes from the call, as well as notes whose frequency had been shifted up or down. Of interest was whether the networks could learn to discriminate between different note types, and whether the responses of the networks to the novel and shifted notes would simulate the behavioral data collected previously by Charrier *et al.*

II. MATERIALS AND METHODS

A. Training stimuli

Sixty notes that were originally used by Charrier *et al.* (2005) were used to create training set to teach ANNs to discriminate between different note types (A, B, and C). Twenty notes each of A, B, and C-note types were randomly selected from black-capped chickadee calls obtained from Colorado, USA and Ontario, Canada. Equal representations of both sources were used and all notes were of high quality. The notes were bandpassed filtered (1–10 kHz) to remove background noise and call-note amplitude was equalized using SIGNAL v 4.0 (Beeman, 2002; Engineering Design, CA). Only non-D notes were utilized, as D notes cannot be quantified on the same features as the A, B, and C notes; more specifically, D notes are acoustically dissimilar from non-D notes and are rarely confused with adjacent notes. For example, D notes are longer duration and consist of a harmonic series (Charrier *et al.*, 2004).

For each note, nine acoustic features were measured using a standard methodology (Nowicki and Nelson, 1990) that was also employed by Charrier *et al.* (2004) and Dawson *et al.* (2006). These features consisted of SF (start frequency), EF (end frequency), PF (peak frequency), AD (ascending duration), DD (descending duration), TD (total duration), FM_{asc} (slope of the ascending frequency modulation), FM_{desc} (slope of the descending frequency modulation), and F_{max} (highest amplitude frequency).

The frequency measurements (SF, EF, PF) were obtained in a digital spectrogram (window size 1024 points, frequency precision=43 Hz) using a cutoff amplitude of −35 dB relative to peak amplitude in the note. Maximum frequency (F_{max}) was measured in a power spectrum using a window size of 4096 points (frequency precision=11 Hz). We measured the main (highest amplitude) harmonic of A and B notes, and the fundamental harmonic of C notes. The duration measurements (AD, DD, TD) were quantified in a digital spectrogram (window size 256 points, temporal precision=5.8 ms). FM_{asc}, slope of ascending frequency (Hz/ms), and FM_{desc}, slope of descending frequency (Hz/ms), were calculated using the following formulas: (PF−SF)/(AD) and (EF−PF)/(DD), respectively. Therefore, nine summary features formed a vector that was used to describe each note, and was used as a stimulus for the ANN to discriminate.

Prior to being presented to the network, each of the nine features for the training set was converted into a z score. Dawson *et al.* (2006) had done this to reduce the range of the input features (which can cause problems when networks are trained) while maintaining the essential characteristics of the raw data.

B. Probe and shifted stimuli

A set of 330 test stimuli was also created to examine the responses of ANNs to notes to which they had not been

TABLE I. Examples of feature vectors used to represent notes as inputs to the networks. The examples below are based on one A note (0 SD shift), and are produced by shifting the frequency values of this note upwards or downwards. All feature values have been converted into z scores as described in the text.

	Input unit encoding of note features								
Frequency shift in SD	SF	PF	EF	AD	DD	TD	FM_{asc}	FM_{desc}	F_{max}
−2.5	0.38	−1.04	0.59	−1.43	1.40	−0.92	−0.47	2.01	−0.94
−2.0	0.64	−0.53	1.17	−1.43	1.40	−0.92	−0.47	2.01	−0.42
−1.5	0.89	−0.01	1.75	−1.43	1.40	−0.92	−0.47	2.01	0.10
−1.0	1.15	0.50	2.32	−1.43	1.40	−0.92	−0.47	2.01	0.62
−0.5	1.40	1.02	2.90	−1.43	1.40	−0.92	−0.47	2.01	1.13
0	1.65	1.53	3.48	−1.43	1.40	−0.92	−0.47	2.01	1.65
0.5	1.91	2.04	4.06	−1.43	1.40	−0.92	−0.47	2.01	2.17
1.0	2.16	2.54	4.63	−1.43	1.40	−0.92	−0.47	2.01	2.69
1.5	2.42	3.07	5.21	−1.43	1.40	−0.92	−0.47	2.01	3.20
2.0	2.67	3.58	5.79	−1.43	1.40	−0.92	−0.47	2.01	3.72
2.5	2.92	4.10	6.36	−1.43	1.40	−0.92	−0.47	2.01	4.24

exposed to during training. Thirty of these were probe notes (10 A, 10 B, 10 C) used by Charrier *et al.* (2005) which were standard notes that were randomly sampled according to the same procedures that were described for the training stimuli. These 30 probe notes were then linearly shifted upwards or downwards in frequency to create the remaining 300 test stimuli, using the same shifts as those studied by Charrier *et al.*

Shifted notes were created by raising or lowering each probe note's frequency while maintaining natural amplitude and temporal structure. In essence, the entire spectrogram was shifted in frequency, and then the frequency features used to represent the spectrogram were recomputed. The only features that were changed by this procedure were SF, PF, EF, and F_{max}. These features were manipulated by either adding or subtracting those values used by Charrier *et al.* (2005) from the SF, PF, EF, and F_{max} values within each vector for each note (see Table I for examples of positive and negative frequency-shifted vectors). Charrier *et al.* (2005) shifted each probe note up or down by the following standard deviations of frequency: ±0.5, ±1.0, ±1.5, ±2.0, ±2.5 SD. Each of the 30 test notes in the current study was treated in exactly the same fashion, creating 10 new shifted notes for each, and ultimately producing 330 stimuli (10 standard and 100 shifted A, B, and C notes, respectively; see Table I for an example from one note). The SDs used to shift the three different note types were 800 Hz for A notes, 500 Hz for B notes, and 150 Hz for C notes (Charrier *et al.*, 2004, 2005). The nine-feature vectors used to represent each test stimulus were also converted to z scores, using the means and standard deviations of the training stimuli.

C. Network architecture

The networks trained in this study were integration devices (Dawson, 2004). An integration device is a perceptron (Rosenblatt, 1962) that uses the sigmoid-shaped logistic equation as an activation function in its output unit. Each network had one output unit, used to represent the strength of its response to a presented stimulus. Each network also had nine input units, each of which represented the value of a summary feature when a stimulus note was presented to the network.

D. Discrimination learning

To conduct discrimination learning with a network, 40 patterns (i.e., the vectors representing 40 different notes) were selected from the 60 training stimuli that were described earlier. Twenty patterns were all notes of one type (A, B, or C), and the remaining patterns were all notes of another type. The network was trained to respond to every instance of one note type, and not to respond to every instance of the other. Following Charrier *et al.* (2005), four different combinations of note type/response type pairings were used: A+B−, A−B+, B+C−, and B−C+.

Prior to training an individual network, all of its connection weights were set to random values selected from the range between −0.1 and 0.1. The biases of the output units (i.e., the "thresholds" of the logistic activation functions) were initialized to 0. Because a network began with small, random connection weights, 20 different networks were trained in independent simulations. Each network was viewed as a "subject" in an experiment, with the results of the experiment being averaged over each subject.

The networks were trained with a gradient descent version of the delta rule (Dawson, 2004, 2005). This rule modifies network weights in a fashion that is identical to how the output unit weights in a more complex multilayer network (i.e., a network that has a layer of processors between input and output units) are trained by the generalized delta rule (Rumelhart *et al.*, 1986). Such a learning rule presents a stimulus, measures the error in the network's response to the stimulus, and then uses this error to modify the connection weights in the network. These modifications are such that the next time the pattern is presented to the network, its response error will be smaller. During a training sweep, each pattern is presented once, and connection weights are modified after each presentation. The order in which patterns are presented

is randomized every sweep. A dependent measure of interest is the number of sweeps of training required for a network to converge to a solution.

The networks were trained with the ROSENBLATT program (Dawson, 2005) that is available free of charge from ⟨http://www.bcp.psych.ualberta.ca/%7emike/Software/Rosenblatt/index.html⟩. The learning rate for the simulations was 0.5, with zero momentum. Training ends once the network generates a "hit" to every pattern. A hit occurs when the network produces a response of 0.9 or more to every pattern to which it is supposed to respond, or when it produces a response of 0.1 or less to every pattern to which it is not supposed to respond.

E. Testing responses to probe notes and shifted notes

After a network was trained according to the procedure described above, it was presented 20 probe notes and 200 shifted notes that had not been used during discrimination learning. As in the Charrier *et al.* (2005) study, the probe notes and the shifted notes were of the same two types as those presented during discrimination learning. For instance, in the A+B− condition, a network would be presented the 10 probe A notes, the 10 probe B notes, the 100 shifted A notes (i.e., each probe note shifted up or down by the amount previously described), and the 100 shifted B notes. The dependent measure for this phase of the study was the strength of a network's response to each of these 220 new stimuli.

III. RESULTS

A. Discrimination learning

The first question of interest was whether simple ANNs could learn this discrimination task when a distributed code was used to represent stimulus notes. The results indicated that this was not a problem for this architecture, because every network in every condition converged to a solution. The average number of sweeps required for this was 639.1 for the ten networks in the A−B+ condition, 638.9 for the A+B− condition, 259.4 for the B−C+ condition, and 259.3 for the B+C− condition. There were no significant differences in speed of learning between the networks in the two AB conditions, or between the networks in the two BC conditions. When all of the AB condition networks and all of the BC condition networks were treated as being in the same learning condition, it was found that the speed of convergence for the BC networks was significantly faster than that of the AB networks ($t=259.308$, $df=18$, $p<0.0001$).

B. Responses to shifted notes

The second question of interest was how the trained networks would respond to the novel notes (probe notes and shifted notes). In particular, to what extent would network responses to these notes simulate the responses of birds?

Figure 1 presents a plot of the average network responses to novel A notes and B notes after both the A−B+ and the A+B− discrimination learning. Qualitatively, these results are very similar to the bird responses that were reported by Charrier *et al.* (2005). Consider the A notes in the A−B+ condition. When they are shifted up in frequency, there is little change in response: the networks continue not to respond to these notes. However, when the notes are shifted down in frequency, these notes become more "B-like," because the networks begin to generate weaker responses to them. Now consider the B notes in the same condition. When they are shifted up, these notes become more "A-like," because the networks reduce their response to them. When they are shifted down, the networks actually increase their response, indicating that the notes seem more "B-like". A similar account can be made for the other two lines in the graph (from the A+B− condition), which are essentially mirror images of the two lines that have just been discussed.

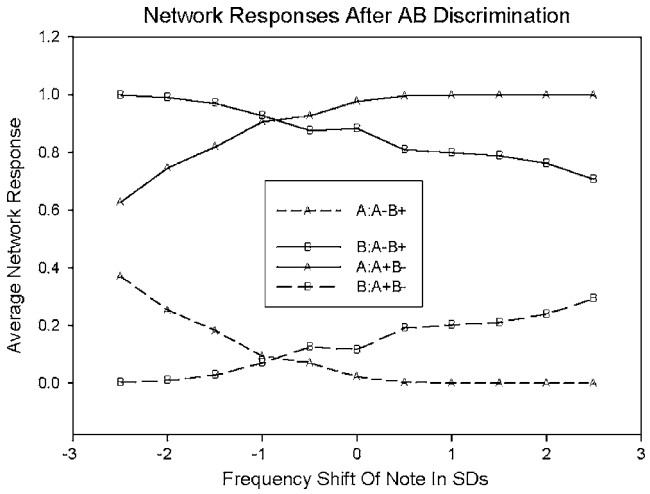

FIG. 1. Average response of networks to shifted notes after AB discrimination learning. The symbol (A, B) indicates the type of note presented to the network. Solid lines represent results from trials in which the network was trained to respond to a note, while dashed lines represent results from trials in which the network was trained to not respond to a note.

Figure 2 presents a plot of the average network re-

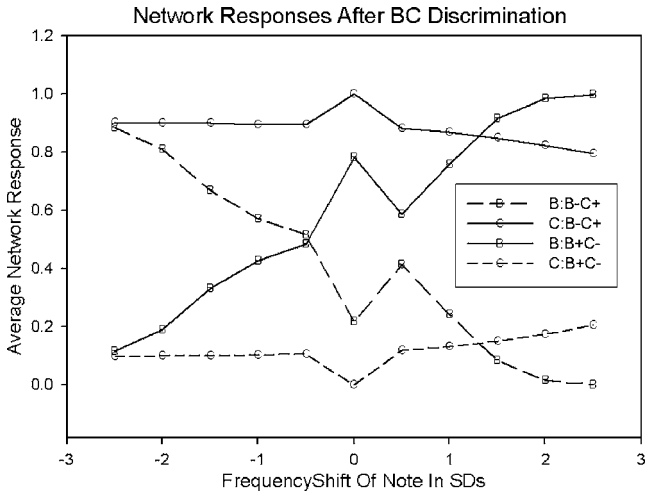

FIG. 2. Average response of networks to shifted notes after BC discrimination learning. The symbol (B, C) indicates the type of note presented to the network. Solid lines represent results from trials in which the network was trained to respond to a note, while dashed lines represent results from trials in which the network was trained not to respond to a note.

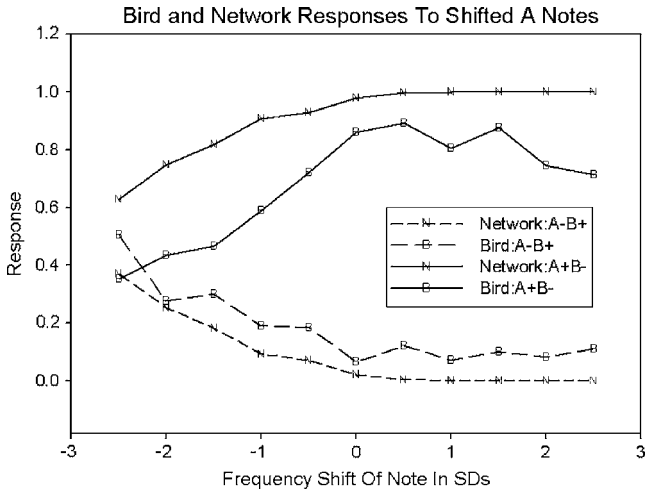

FIG. 3. Comparison of average response of black-capped chickadees and ANN to shifted A notes after AB discrimination learning. The symbol (B, N) indicates whether the function is produced by a bird (B) or an ANN (N). Solid lines represent results from A+B− trials, while dashed lines represent results from A−B+ trials.

sponses to novel B notes and C notes after both the B−C+ and the B+C− discrimination learning. Again, these results are very similar to the bird responses that were reported by Charrier *et al.* (2005). Consider the B notes in the B−C+ condition. When these notes are shifted up in frequency, there is a decrease in network response. However, when the notes are shifted down in frequency, these notes become more "C-like," because the networks begin to generate stronger responses to them. Now consider the C notes in the same condition. Regardless of whether they were shifted up or down, there was little effect of the shift on network response. This is consistent with the result of Charrier *et al.*, who found no significant effect of frequency shift on bird responses to C notes. Again, a similar account can be made for the other two lines in the graph (from the B+C− condition), which are essentially mirror images of the two lines that have just been discussed (Fig. 3).

To provide an additional quantitative assessment of the relationship between the network and animal responses, correlations were computed between the data used to plot the eight different lines in Figs. 1 and 2, and the analogous data used by Charrier *et al.* (2005) to plot average chickadee responses to shifted notes in their Figs. 4 and 5. Each of these correlations is based upon 11 pairs of responses, and is presented in Table II. As can be seen from this table, for all eight graphs there was a substantially high positive correlation, indicating that the network responses were excellent simulations of the bird responses. The overall correlation between the two datasets (i.e., between all 88 data pairs taken as a group) was 0.69.

IV. DISCUSSION

To summarize, a number of simple ANNs were trained to discriminate between two different component notes from the chick-a-dee call of the black-capped chickadee. After this training was accomplished, the network was presented novel notes that had been shifted in frequency. When the responses of networks to shifted notes was compared to the responses of birds trained in an analogous task, a high degree of correspondence was observed.

Previous research has shown that the nine summary features used to represent stimuli in the current study can be used to classify important aspects of the chick-a-dee call. For example, Dawson *et al.* (2006) demonstrated that component notes of this call (i.e., A, B, and C notes) could be classified to a high degree of accuracy on the basis of these features. This was true for both ANNs and linear discriminant analysis. Similarly, (Dawson *et al.*, 2006) represented A, B, C, and D notes with these summary features. They found that linear discriminant analysis could use these features, for any of the four note types, to discriminate black-capped chickadees from mountain chickadees.

While this previous research has indicated that the summary features used in the current study are extremely useful with respect to the statistical analysis of these notes, it says little about whether the birds themselves might be sensitive to similar features when processing the different notes in the chick-a-dee call. The simulation results in the current paper are one step towards modeling how the birds themselves might process and respond to the component notes.

The goal of simulation research is to develop models that are strongly equivalent to the agents or the phenomena that are being modeled (Pylyshyn, 1984). A strongly equivalent model of how chickadees discriminate component notes would generate the same performance as the birds, and would do so by exploiting the same procedures, mechanisms, and representations. A fundamental issue in validating simulations is collecting evidence to support the claim that they are strongly equivalent. This is particularly problematic when a researcher does not have direct access to the entity being simulated (e.g., the internal processes used by chickadees to identify notes). What kind of evidence is available to simulation researchers?

TABLE II. Correlations between bird responses and network responses to shifted notes for the eight different lines plotted in Figs. 1 and 2 in the current paper, and in Figs. 4 and 5 from Charrier *et al.* (2005).

Relations between responses to shifted A and B notes after AB discrimination learning			Relations between responses to shifted B and C notes after BC discrimination learning		
	A−B+ Condition	A+B− Condition		B−C+ Condition	B+C− Condition
A	0.97	0.92	**B**	0.86	0.66
B	0.83	0.79	**C**	0.85	0.75

Pylyshyn (1984) has suggested that one type of information that can be used to evaluate a simulation is error evidence: when the simulation makes mistakes, are these mistakes similar to those generated by the modeled subjects? The current results provide error evidence that can be used to evaluate the ANNs. When both the ANNs in the current study, and the birds in the Charrier *et al.* (2005) study, were presented the shifted notes, these were novel and deviant stimuli. The extent to which the responses (e.g., misclassifications) of the birds correspond to the responses of the ANNs is the extent to which error evidence supports these networks as models of the bird behavior. The high degree of correspondence that was observed between the two types of data (Table II) indicates that these ANNs are excellent models of chickadee discriminations between note types.

What, then, do these networks say about this discrimination learning task? First, they indicate that a linear combination of the nine summary features that were taken from the spectrograms provides sufficient information to accomplish this task. Second, the likelihood of responding to a note can be modeled as a nonlinear function of these combined features (e.g., the sigmoid activation function). Third, higher-order featural combinations (of the sort that would be provided by the hidden units in a multilayer network) are not required to accomplish this task.

This last point is relevant to a more general implication of the current simulation results. One important issue in the discrimination learning literature concerns how animals process information contained in compound stimuli. One approach to this issue is elemental (Rescorla, 1973, 1988, 2003; Rescorla and Wagner, 1972; Wagner, 2003). According to this approach, animals independently process the elemental components that define a compound stimulus. A second approach to this issue is configural (Pearce, 1987, 1994, 1997, 2002; Pearce and Bouton, 2001; Wasserman and Miller, 1997). According to this approach, compound stimuli are processed holistically: while a compound stimulus is related to its components, there is additional information that is represented that reflects the notion that a compound stimulus is not merely the sum of each element.

The elemental and configural approaches have strong implications for representing stimuli to be presented to ANNs. A typical elemental representation would have a single input unit representing the presence or absence of the elements of a compound stimulus, and no other input units (e.g., Pearce, 1997, p. 131). For example, a simple network would use two units that could represent the presence of stimulus elements A and B. The presence of the compound stimulus AB would be indicated by turning both of these units on as an elemental representation. In contrast, a typical configural representation includes additional units that are turned on only when a compound stimulus is presented (e.g., Pearce, 1997, p. 132). For example, three units would be required to represent compound stimulus AB: one for element A, another for element B, and a third to represent unique configural properties (AB). This third element is only activated when all of the stimulus compounds are presented. More complex configural representations—in particular, those that can be changed via learning—are represented in the hidden units of multilayer networks (Delamater *et al.*, 1999).

The current simulations provide a stimulus representation that does not fit neatly into any of the categories described above. The reason for this is that the networks use a representation that appears to be elemental from the description in the preceding paragraph. However, the stimuli that are presented to the network are feature configurations. Indeed, Dawson *et al.* (2006) found that all of the presented features were necessary for classifying chickadee call notes. The fact that the current networks were able to learn to discriminate note types on the basis of vectors of stimulus features suggests that configural learning may not necessarily require the presence of units that explicitly represent configurations of elements. Further studies of this sort of representation are required to explore the implications of networks like ours to the elemental/configural debate.

ACKNOWLEDGMENTS

This research was supported by an NSERC Discovery Grant, an Alberta Ingenuity New Faculty Grant, a Canada Foundation for Innovation (CFI) New Opportunities Grant as well as start-up and CFI partner funding from the University of Alberta to C.B.S. and NSERC and SSHRC research grants to M.R.W.D. L.L.B. was supported by an NSERC PGS-B and an Alberta Ingenuity Studentship. This research was approved by the University of Alberta Biological Sciences Animal Care Committee (Protocol No. 351201, originally approved on 14 November 2001) and the University of Calgary Life and Environmental Sciences Animal Care Committee (Protocol No. BI2001-028 originally approved on 29 November 2001). Birds were captured under an Environment Canada, Canadian Wildlife Service Scientific permit (Permit No. WSA-1-02, originally approved on 25 January 2002) and Alberta Fish and Wildlife Research permits (Nos. 4619 GP, 4621 GP, and 8734 GP) and collection licenses (Nos. 088 CN, 089 CN, and 147 CN) that were originally approved on 21 December 2001. Correspondence can be addressed to C.B.S.

Baker, M. C., Bjerke, T. K., Lampe, H. U., and Espmark, Y. O. (**1987**). "Sexual-response of female yellowhammers to differences in regional song dialects and repertoire sizes," Anim. Behav. **35**, 395–401.

Bechtel, W., and Abrahamsen, A. (**1991**). *Connectionism And The Mind* (Basil Blackwell, Cambridge, MA).

Beeman, Kim. (2002). SIGNAL 4.0 Reference Guide (Engineering Design, Berkeley, CA).

Campbell, G. S., Gisiner, R. C., Helweg, D. A., and Milette, L. L. (**2002**). "Acoustic identification of female Steller sea lions (*Eumetopias jubatus*)," J. Acoust. Soc. Am. **111**(6), 2920–2928.

Caudill, M., and Butler, B. (**1992**). *Understanding Neural Networks* (MIT Press, Cambridge, MA), Vol. **1**.

Charrier, I., and Sturdy, C. B. (**2005**). "Call-based species recognition in black-capped chickadees," Behav. Processes **70**(3), 271–281.

Charrier, I., Bloomfield, L. L., and Sturdy, C. B. (**2004**). "Note types and coding in Parid vocalizations. I. The chick-a-dee call of the black-capped chickadee (*Poecile atricapilla*)," Can. J. Zool. **82**, 769–779.

Charrier, I., Lee, T. T. Y., Bloomfield, L. L., and Sturdy, C. B. (**2005**). "Acoustic mechanisms of note-type perception in black-capped chickadee (*Poecile atricapillus*) calls," J. Comp. Psychol. **119**(4), 371–380.

Clucas, B. A., Freeberg, T. M., and Lucas, J. R. (**2004**). "Chick-a-dee call syntax, social context, and season affect vocal responses of Carolina

chickadees (*Poecile carolinensis*)," Behav. Ecol. Sociobiol. **57**(2), 187–196.
Dawson, M. R. W. (**2004**). *Minds And Machines: Connectionism And Psychological Modeling* (Blackwell, Malden, MA).
Dawson, M. R. W. (**2005**). *Connectionism: A Hands-on Approach*, 1st ed. (Blackwell Pub, Malden, MA).
Dawson, M. R. W., and Spetch, M. L. (2005). "Traditional perceptrons do not generate the overexpectation effect," Neur. Info. Proc. – Letters and Reviews **7**(1), 11–17.
Dawson, M. R. W., Charrier, I., and Sturdy, C. B. (**2006**). "Using an artificial neural network to classify black-capped chickadee (*Poecile atricapillus*) call note types," J. Acoust. Soc. Am. **199**(5), 3161–3172.
Dawson, M. R. W., Bloomfield, L. L., Charrier, I., and Sturdy, C. B. (**2006**). "Using non-D notes of the 'chick-a-dee' call to discriminate the black-capped chickadee (*Poecile atricapillus*) from the mountain chickadee (*Poecile gambeli*)," J. Comp. Psychol. **120**(2), 147–153.
Delamater, A. R., Sosa, W., and Katz, M. (**1999**). "Elemental and configural processes in patterning discrimination learning," Q. J. Exp. Psychol. B **52B**, 97–124.
Ficken, M. S., Hailman, E. D., and Hailman, J. P. (**1994**). "The chick-a-dee call system of the Mexican chickadee," Condor **96**(1), 70–82.
Freeberg, T. M., and Lucas, J. R. (**2002**). "Receivers respond differently to chick-a-dee calls varying in note composition in Carolina chickadees, *Poecile carolinensis*," Anim. Behav. **63**, 837–845.
Gluck, M. A., and Myers, C. (**2001**). *Gateway to Memory: An Introduction to Neural Network Modeling of the Hippocampus and Learning* (MIT Press, Cambridge, MA).
Hailman, J. P., and Ficken, M. S. (**1986**). "Combinatorial animal communication with computable syntax—chick-a-dee calling qualifies as language by structural linguistics," Anim. Behav. **34**, 1899–1901.
Hailman, J. P., Ficken, M. S., and Ficken, R. W. (1985). "The chick-a-dee calls of *Parus atricapillus*—a recombinant system of animal communication compared with written English," Semiotica **56**(3–4), 191–224.
Houser, D. S., Helweg, D. A., and Moore, P. W. (**1999**). "Classification of dolphin echolocation clicks by energy and frequency distributions," J. Acoust. Soc. Am. **106**(3), 1579–1585.
Mammen, D. L., and Nowicki, S. (**1981**). "Individual differences and within flock convergence in chickadee calls," Behav. Ecol. Sociobiol. **9**(3), 179–186.
McIlraith, A. L., and Card, H. C. (**1997**). "Birdsong recognition using backpropagation and multivariate statistics," IEEE Trans. Signal Process. **45**(11), 2740–2748.
Murray, S. O., Mercado, E., and Roitblat, H. L. (**1998**). "The neural network classification of false killer whale (*Pseudorca crassidens*) vocalizations," J. Acoust. Soc. Am. **104**(6), 3626–3633.
Nowicki, S. (**1983**). "Flock specific recognition of chickadee calls," Behav. Ecol. Sociobiol. **12**(4), 317–320.
Nowicki, S., and Nelson, D. A. (**1990**). "Defining natural categories in acoustic signals: Comparison of 3 methods applied to chick-a-dee call notes," Ethnology **86**(2), 89–101.
Pao, Y.-H. (**1989**). *Adaptive Pattern Recognition And Neural Networks* (Addison-Wesley, Reading, MA).
Parson, S., and Jones, G. (**2000**). "Acoustic identification of twelve species of echolocating bat by discriminant function analysis and artificial neural networks," J. Exp. Biol. **203**, 2641–2656.
Pearce, J. M. (**1987**). "A model for stimulus generalization in Pavlovian conditioning," Psychol. Rev. **94**(1), 61–73.
Pearce, J. M. (**1994**). "Similarity and discrimination: A selective review and a connectionist model," Psychol. Rev. **101**, 587–607.
Pearce, J. M. (**1997**). *Animal Learning And Cognition: An Introduction* (Psychology Press, East Sussex).
Pearce, J. M. (**2002**). "Evaluation and development of a connectionist theory of configural learning," Anim. Learn Behav. **30**(2), 73–95.
Pearce, J. M., and Bouton, M. E. (**2001**). "Theories of associative learning in animals," Annu. Rev. Psychol. **52**, 111–139.
Pylyshyn, Z. W. (**1984**). *Computation And Cognition* (MIT Press, Cambridge, MA).
Quinlan, P. (**1991**). *Connectionism And Psychology* (University of Chicago Press, Chicago, IL).
Rescorla, R. A. (**1973**). "Evidence for the unique stimulus account of configural conditioning," J. Comp. Physiol. Psychol. **85**, 331–338.
Rescorla, R. A. (**1988**). "Pavlovian conditioning: Its not what you think it is," Am. J. Psychol. **43**(3), 151–160.
Rescorla, R. A. (**2003**). "Contemporary study of Pavlovian conditioning," Span. J. Psychol. **6**, 185–195.
Rescorla, R. A., and Wagner, A. R. (**1972**). "A theory of Pavlovian conditioning: Variations in the effectiveness of reinforcement and nonreinforcement," *Classical Conditioning II: Current Research And Theory*, edited by A. H. Black and W. F. Prokasy (Appleton-Century-Crofts, New York), pp. 64–99.
Ripley, B. D. (**1996**). *Pattern Recognition And Neural Networks* (Cambridge University Press, Cambridge, U.K.).
Rosenblatt, F. (**1962**). *Principles Of Neurodynamics* (Spartan, Washington).
Rumelhart, D. E., Hinton, G. E., and Williams, R. J. (**1986**). "Learning representations by back-propagating errors," Nature (London) **323**, 533–536.
Schon, P. C., Puppe, B., and Manteuffel, G. (**2001**). "Linear prediction coding analysis and self-organizing feature map as tools to classify stress calls of domestic pigs (*Sus scrofa*)," J. Acoust. Soc. Am. **110**(3), 1425–1431.
Wagner, A. R. (**2003**). "Context-sensitive elemental theory," Q. J. Exp. Psychol. B **56**(1), 7–29.
Wasserman, E. A., and Miller, R. R. (**1997**). "What's elementary about associative learning?," Annu. Rev. Psychol. **48**, 573–607.

Testing the odontocete acoustic prey debilitation hypothesis: No stunning results

Kelly J. Benoit-Bird
College of Oceanic and Atmospheric Sciences, Oregon State University, 104 COAS Administration Building, Corvallis, Oregon 97331, and
Hawaii Institute of Marine Biology, University of Hawaii, PO Box 1106, Kailua, Hawaii 96734

Whitlow W. L. Au
Hawaii Institute of Marine Biology, University of Hawaii, P.O. Box 1106, Kailua, Hawaii 96734

Ronald Kastelein
SEAMARCO, Julianalaan 46, 3843 CC Harderwijk, The Netherlands

(Received 19 January 2006; revised 9 May 2006; accepted 12 May 2006)

The hypothesis that sounds produced by odontocetes can debilitate fish was examined. The effects of simulated odontocete pulsed signals on three species of fish commonly preyed on by odontocetes were examined, exposing three individuals of each species as well as groups of four fish to a high-frequency click of a bottlenose dolphin [peak frequency (PF) 120 kHz, 213-dB peak-to-peak exposure level (EL)], a midfrequency click modeled after a killer whale's signal (PF 55 kHz, 208-dB EL), and a low-frequency click (PF 18 kHz, 193-dB EL). Fish were held in a 50-cm diameter net enclosure immediately in front of a transducer where their swimming behavior, orientation, and balance were observed with two video cameras. Clicks were presented at constant rates and in graded sweeps simulating a foraging dolphin's "terminal buzz." No measurable change in behavior was observed in any of the fish for any signal type or pulse modulation rate, despite the fact that clicks were at or near the maximum source levels recorded for odontocetes. Based on the results, the hypothesis that acoustic signals of odontocetes alone can disorient or "stun" prey cannot be supported. [DOI: 10.1121/1.2211508]

PACS number(s): 43.80.Ka, 43.80.Nd [JAS] Pages: 1118–1123

I. INTRODUCTION

The idea that odontocete cetaceans can use sound to debilitate their prey was first proposed by Bel'kovich and Yablokov (1963) and later reviewed by Norris and Mohl (1983). Odontocetes, or toothed whales, a group of approximately 70 species in six families, are predators that feed on a range of prey including cephalopods, crustaceans, fish, birds, and other marine mammals. As a group, they rely on sound for orientation, navigation, communication, and predator and prey detection (Reynolds and Rommel, 1999). It has been proposed that loud, impulsive sounds made by cetaceans in the vicinity of prey can stun, disorient, and debilitate their prey, rather than just being used to find prey.

Support for the prey-stunning hypothesis includes observations of dolphins in laboratory and field settings. Data that sperm whales have intact squid lacking any bite marks in their stomachs led Norris and Mohl (1983) to suggest that the squid, rapid swimmers that are highly maneuverable, must be immobilized by the whale before consumption. A number of observations (summarized in Marten *et al.*, 2001; summarized in Norris and Mohl, 1983) that fish appeared lethargic and fish schools were depolarized by feeding dolphins in both captive and wild circumstances have been considered consistent with prey stunning by dolphins, though the mechanism has not been tested.

Evidence to support the prey-stunning hypothesis also comes from results that show acoustic signals can indeed cause a loss of buoyancy control, abdominal hemorrhage, and even death in fish. Explosives including TNT and dynamite with exposure levels between 229 and 234 dB and black powder with an exposure level between 234 and 244 dB have been shown to cause debilitation (Hubbs and Rechnitzer, 1952). Spark discharges with exposure levels between 230 and 242 dB can cause similar effects on fish (Zageski, 1987), though negative results have been reported for some cephalopods (Mackay and Pegg, 1988). An airgun exposing fish to an average of 216 dB peak-to-peak has been shown to cause death and debilitation in fish after multiple exposures over several hours (Marten *et al.*, 2001). Acoustic stunning of some fish has also been shown from high-amplitude pure tones (Hastings, 1995). Most of the acoustic signals that have experimentally shown to cause prey debilitation have rapid rise times (several tens of microseconds or less) and high pressures (>210 dB peak-to-peak), as do dolphin clicks. However, most of the received threshold levels shown to cause responses to these sounds are 10 to 25 dB above the maximum intensity recorded for dolphin clicks (Au, 1993). In other words, they contain about 300 times more energy than a single echolocation click. Only repeated exposure to the airgun every 15 s for 4 h caused debilitation at received sound levels reported for dolphin sounds.

Perhaps the most interesting evidence towards potential prey stunning by odontocetes comes from a very different animal taxa. Snapping shrimp produce broadband, impulsive sounds that reach source levels of 220 dB peak-to-peak

 0001-4966/2006/120(2)/1118/6/$22.50

(Schmitz *et al.*, 2000). Snapping shrimp have been shown to stun their prey using a single snap (Herberholz and Schmitz, 1999). Although it is not known if the mechanism for stunning by snapping shrimp is the sound itself or the mechanical stress caused by the cavitating bubble or the jet of water, these are some of the first data to suggest that a biologically created sound, rather than anthropogenic sounds, could cause debilitating effects on prey and serve a predatory function.

While the hypothesis that odontocete signals can directly cause debilitation in their prey has not been directly tested, the hypothesis has been attractive to both scientists and the popular media. In the last decade, Norris and Mohl's 1983 synthesis of the hypothesis has been cited 35 times. Some of these papers invoke acoustic prey stunning as a mechanism to explain their results despite the lack of direct support for the mechanism. Media coverage of papers that have discussed the prey-stunning hypothesis (Cranford, 1999; Marten *et al.*, 2001) has included dramatic headlines such as "Killer clicks" (New Scientist, 31 January 2001) and "Porpoise stun gun" (Science Frontiers No. 29: Sep–Oct 1993). The Santa Cruz County Sentinel (26 April 1998) summarized one study saying, "mysterious monsters are killing fish with murderous death beams." The general acceptance of the hypothesis by both professional and lay people led us to attempt a direct test of the hypothesis that odontocete acoustic signals can debilitate or disorient prey.

II. METHODS

A. Study area

The experiment was conducted in an outdoor tank at the field station of the Netherlands National Institute for Coastal and Marine Management (RIKZ) at Jacobahaven, Zeeland, The Netherlands in a freestanding rectangular tank 7.0 m long and 4.0 m wide with a water depth of 2.0 m. The tank rested on a 3-cm-thick layer of hard-pressed Styrofoam to reduce contact noise from the environment and was covered by a canopy to improve the clarity of video recordings. The water in the tank was pumped directly from the nearby Oosterschelde (a lagoon of the North Sea). The salinity was 30%–33%, the *p*H 7.9–8.1, nitrogen concentration <5 mg/l, and nitrate concentration <0.1 mg/l. The water was circulated via a sand, UV light, and carbon filter. To make the environment inside the tank as quiet as possible, the filter unit had a low-noise "whisper" pump. To reduce contact noise entering the pool, the pump and filter unit were also placed on hard-pressed rubber. Water parameters (temperature, salinity, oxygen, and nitrate) were measured daily and remained well within the boundaries suitable for normal activity of the fish.

B. Subjects

We tested the effects of simulated odontocete clicks on three species of fish: Atlantic herring (*Clupea harengus*), sea bass (*Dicentrarchus labrax*), and Atlantic cod (*Gadus morhua*). The Animal Welfare Commission of the Netherlands government stipulated that the fish used must feed readily in captivity, so they had to come from aquaria, though all were originally wild-caught. Sea bass and cod were fed to satiation each day after the sessions on a diet of raw fish. Herring were similarly fed a diet of Trouvit pellets size no. 00 (Nutreco Aquaculture). Fish were returned to the aquaria following the experiment to comply with animal care regulations.

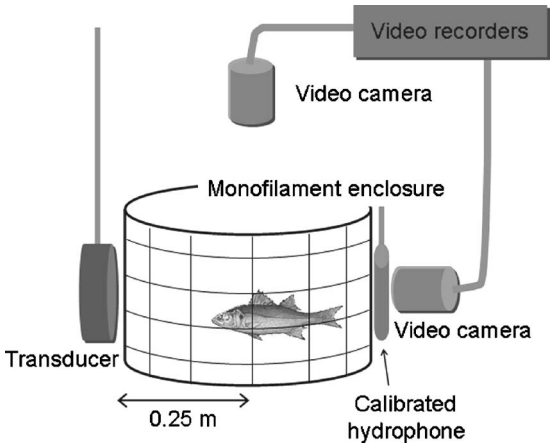

FIG. 1. Experimental setup. The fish is enclosed in monofilament enclosure next to an acoustic transducer. While in the cage, the subjects were videotaped from above and from the side.

Fish species were chosen to represent a variety of swimbladder types because of the hypothesis that the mechanism of fish debilitation is the interaction of the acoustic signal with air-filled cavities in the fish. The herring species has a modified form of the primitive swimbladder as a physostome, with air bladder extensions to the lateral line and labyrinth (Blaxter *et al.*, 1979; 1981). Species in this family have been shown to be especially sensitive to sound including high frequencies (Mann *et al.*, 1997) and the Pacific herring (*Clupea pallassi*) and American shad (*Alosa sapidissima*) have even been shown to respond to echolocation signals (Mann *et al.*, 1998; Wilson and Dill, 2002). We hypothesized that the herring was the most likely candidate for stunning because of these anatomical adaptations. Sea bass is a euphysoclistous fish; they are physostomous as juveniles but physoclistous as adults (Chatain, 1986). Cod have the most derived swimbladder form, a completely closed physoclist bladder. The swimbladder has also been shown to play a role in the hearing abilities of cod (Sand and Enger, 1973). If debilitation occurred, the variety of swimbladder types used could help elucidate the mechanism of acoustic interaction with the fish.

C. Experimental setup

For testing, fish were placed inside a 0.5-m-diameter, 0.3-m-high cylindrical monofilament enclosure supported by a plastic ring on the top and bottom (Fig. 1). This allowed the fish to swim freely while keeping the subjects positioned in front of the transducer producing the stimulus. The enclosure was suspended 1 m below the water's surface with the acoustic transducer placed immediately adjacent to the enclosure, making the subject fish, on average, 0.25 m away from the source of the stimuli. Two underwater video cameras were focused on the net enclosure, one looking directly down on the enclosure from above, and one looking from the side, directly across from the transducer. These cameras al-

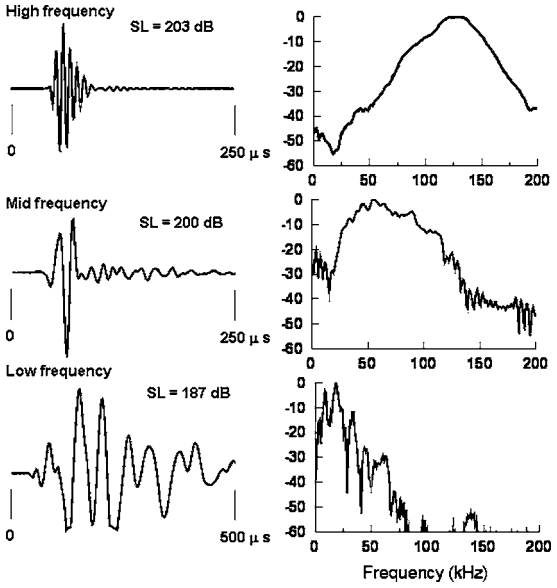

FIG. 2. Acoustic stimuli used in the experiment were three synthetic odontocete echolocation signals recorded using the calibration hydrophone. The waveforms (time-amplitude plots) of each signal are shown on the left, and the spectra (frequency-amplitude) plots on the right.

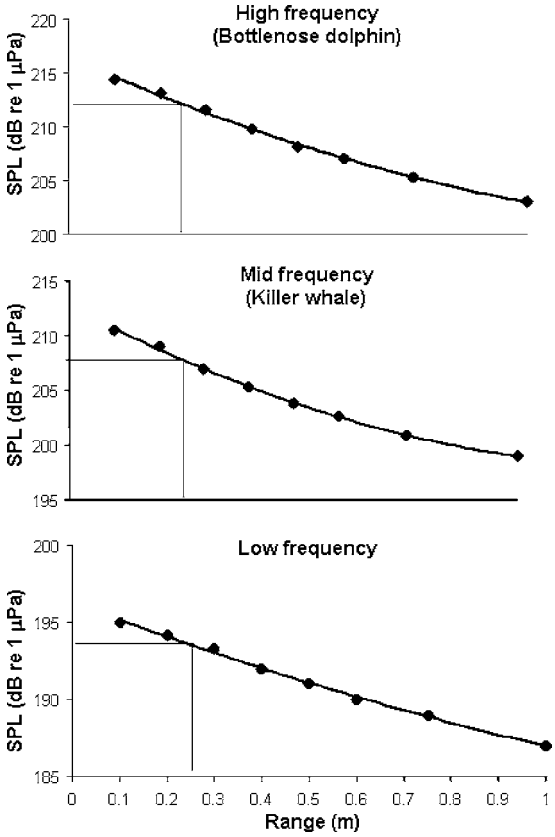

FIG. 3. The measured sound-pressure level of each of the three signals as a function of range from the source transducer. The levels the fish were exposed to at the center of the cage, indicated by the paired lines, were calculated based on these curves.

lowed us to observe the behavior of the fish without causing disturbance, and permitted us to make sure the fish was centered in front of the acoustic transducer when the stimulus was presented. The size of the enclosure was a compromise between allowing fish movement and controlling exposure level. Previous studies of stunning have observed loss of buoyancy control and changes in small-scale swimming behavior which this size enclosure should not limit.

Individual fish or fish in groups of four were placed inside the enclosure and allowed to acclimate to their new conditions for at least 30 min. The behavior of the fish was recorded using the two video cameras for 5 min prior to the presentation of the acoustic stimuli and 5 min postexposure for comparison. The hypothesis was that fish would be dramatically affected by the presentation of clicks so we looked for changes in activity level that would indicate avoidance or loss of swimming ability as well as changes in tilt or roll angle of greater than 30 deg, indicating loss of buoyancy control. We also looked for fish survival for 1 week following the experiments as an indication of long-term internal damage. We were prepared to immediately euthanize any fish that appeared to be in extreme distress immediately following acoustic exposure.

D. Stimuli

A variety of odontocete species have been hypothesized to debilitate their prey with echolocation clicks, so we simulated clicks of three different species in our experiment. The clicks as recorded by a calibration hydrophone are shown in Fig. 2. Clicks were produced using a function generator computer plug-in board with a sampling rate of 1 MHz. We measured the source level and the exposure level of each signal using a calibrated B&K 8103 hydrophone placed at a variety of ranges from the transmit transducer; the results are shown in Fig. 3. The first signal we tested, a bottlenose dolphin (*Tursiops truncatus*) click, had a peak frequency of 120 kHz and a source level of 203 dB *re*: 1 μPa peak-to-peak, exposing fish in the middle of the cage to levels of 213 dB *re*: 1 μPa peak-to-peak. This signal was produced using a custom-built planar transducer consisting of a 1–3 composite piezoelectric element of 6.4 cm diameter. This transducer has a 12.5-deg beamwidth in the far field, and though its beamwidth in the near field is unknown, subject fish were often directly in front of the transducer during the experiment, exposing them to the highest possible sound levels. The second signal, a killer whale (*Orcinus orca*) click (Au *et al.*, 2004), had a peak frequency of 55 kHz and had a source level of 200 dB *re*: 1 μPa peak-to-peak, exposing the fish to a level of 208 dB *re*: 1 μPa peak-to-peak. The final, low-frequency click had a peak frequency of 18 kHz and a source level of 187 dB *re*: 1 μPa peak-to-peak, exposing the fish to 193 dB *re*: 1 μPa peak-to-peak (Fig. 3). Both of these lower-frequency signals were produced using a custom-built transducer consisting of three piezoelectric ceramic spheres having diameters of 5.0, 3.8, and 1.3 cm and stacked in a column. Each sphere has a different resonance frequency and the three were driven in parallel so that the transducer has a low directivity index. The frequency range, duration, amplitude, and energy flux density of each of the three simulated clicks were comparable to the clicks produced by a range of odontocete species, providing comparable acoustic exposure to natural clicks, and thus should affect the subjects in the same way as natural clicks.

Clicks were presented to three individual sea bass and three individual cod as well as groups of four individuals of each species in two ways. The first was at static, regular pulse rates of 100, 200, 300, 400, 500, 600, and 700 clicks/second for exposure times ranging from a minimum of 7 s up to 1 min. This type of click presentation is most similar to regular echolocation by odontocetes at close ranges (less than 0.4 m, Evans and Powell, 1967). We also presented clicks in modulated pulse "sweeps." Clicks repetition rate increased from 100 to 700 clicks/s over either 1.1, 2.2, or 3.2 s. This click pattern is similar to the "terminal buzz" produced by echolocating animals as they make the final approach to a target (Au, 1993). We presented this signal type to three individuals cod and three individual herring as well as to a group of four cod and a group of four herring.

E. Behavioral parameters

To observe effects on buoyancy control, the video data were used to determine the tilt and roll angle of each fish in both individual and group tests every minute for the 15 min pre- and postsound exposure. To determine if fish avoided the sound's source, the percent of time each fish spent in each quadrant of the cage was recorded for the pre- and postexposure observation periods. To measure fish movement, the number of times each fish crossed between the quadrants of the cage was compared from pre- and postexposure periods.

F. Statistics

Tilt and roll angle of each fish in both individual and group tests every minute for the 15-min pre- and postsound exposure was compared using a repeated-measures analysis of variance (ANOVA). A series of paired *t*-tests was used to compare the pre- and postexposure quadrant residence time for each fish to determine if fish avoided the transducer. To measure fish movement, the number of times each fish crossed between the quadrants of the cage was compared from pre- and post-exposure periods using a paired *t*-test.

III. RESULTS

No clear changes in behavior were observed during the relatively short ensonification period. To observe effects on buoyancy control, the video data were used to determine the tilt and roll angle of each fish in both individual and group tests every minute for the 15-min pre- and postsound exposure (Fig. 4). A repeated-measures ANOVA revealed no significant differences between pre- and postexposure angles and showed no interaction of this with signal type, the number of fish in the cage, or species (Tables I and II, $p > 0.05$).

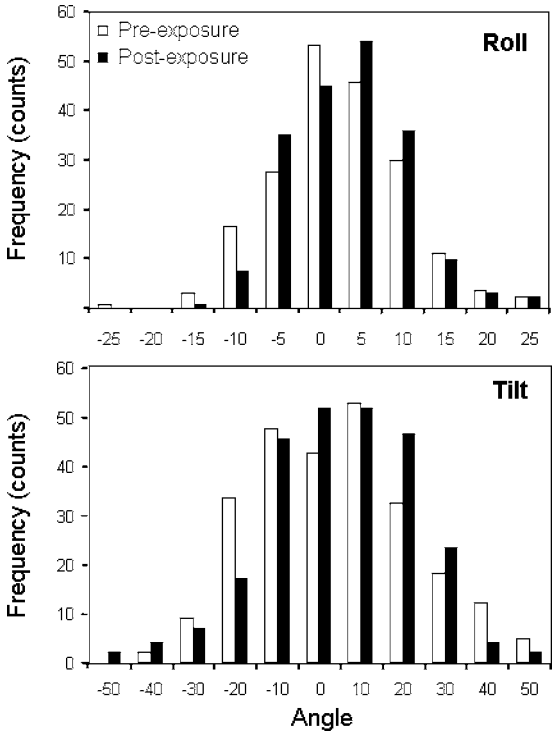

FIG. 4. The distribution of fish roll (top) and tilt (bottom) angles before and after exposure to the acoustic stimulus. An angle of zero represents a vertical orientation. There were no significant differences between pre- and postexposure periods and no significant effects of species, number of animals in the cage, or signal type, so all stimuli and fish species results are pooled in this graph.

To determine if fish avoided the sound's source, the percent of time each fish spent in each quadrant of the cage was recorded for the pre- and postexposure observation periods. A series of paired *t*-tests was used to compare the pre- and postexposure quadrant residence time for each fish (Table III). No significant differences were observed in any of the four quadrants ($p > 0.05$). This suggests that there was no avoidance of the sound's source.

To measure fish movement, the number of times each fish crossed between the quadrants of the cage was compared from pre- and postexposure periods using a paired *t*-test. No

TABLE I. Repeated-measures ANOVA for fish roll angle pre- and postexposure to acoustic stimuli.

Source	SS	*df*	MS	*F*	*p*
Pre vs post	31.61	1	31.61	0.55	0.46
*Signal	1095.51	18	60.86	1.06	0.40
*Group size	57.13	1	57.13	0.99	0.32
*Species	30.19	2	15.09	0.26	0.77
*Signal *Group size	886.39	13	68.18	1.19	0.29
*Signal *Species	1676.07	36	46.56	0.81	0.77
*Group size *Species	1.10	1	1.10	0.02	0.89
*Signal *Group size *Species	635.66	12	52.97	0.92	0.53
Error (pre vs post)	9664.05	168	57.52		

TABLE II. Repeated-measures ANOVA for fish tilt angle pre- and postexposure to acoustic stimuli.

Source	SS	*df*	MS	*F*	*p*
Pre vs post	196.23	1	196.23	0.60	0.44
*Signal	5893.71	18	327.43	1.00	0.46
*Group size	213.63	1	213.63	0.65	0.42
*Species	1085.74	2	542.87	1.66	0.19
*Signal *Group size	5231.02	13	402.39	1.23	0.26
*Signal *Species	10284.76	36	285.69	0.87	0.68
*Group size *Species	183.00	1	183.00	0.56	0.46
*Signal *Group size *Species	5910.46	12	492.54	1.51	0.13
Error (pre vs post)	54943.68	168	327.05		

significant difference was observed (mean difference $=0.0044\pm0.0016$ 95% CI, $t=0.62$, df$=170$, $p=0.43$).

We did not have any mortality or even slight abnormal behavior of our subjects, indicating no severe internal injuries from the testing.

IV. DISCUSSION

We did not observe any measurable changes in the behavior of any of the species of fish in any of the conditions we tested either during or following exposure to odontocete clicks. There were no noticeable changes in swimming activity, no apparent loss of buoyancy control that would be indicated by tilting or rolling of the fish, and no movement away from the transducer. In order for prey stunning by regular or terminal buzz clicks to be a viable mechanism for fish capture by odontocetes, the fish would need to be dramatically and noticeably affected by the acoustic signals, which was not apparent in our results. In addition, we did not have any mortality of the tested fish, which might indicate internal damage from the acoustic signals.

We tested a large number of variables including the frequency of the signal, pulse rate, and pulse sweeping. Our choice of the three signal types was to ensure that a wide frequency range was covered in the event that stunning might have a frequency dependency. These signals also covered the full range of frequencies employed by odontocetes from the relatively low frequency in the range used by the sperm whale to the high-frequency bottlenose dolphin. Fish in our experiment were subjected to very high levels of sounds for exposure times that are long relative to odontocete acoustic behavior during foraging.

Norris and Mohl (1983) proposed that the final click sweep, or terminal buzz, was the most likely signal to induce fish stunning. These non-"usual" clicks have very short interclick intervals (Madsen *et al.*, 2005; 2002) with between 50 and 200 clicks per second. The clicks in this terminal phase as the odontocete closes in on the prey are typically lower in amplitude than "regular" echolocation clicks, by about 15 dB. Our terminal buzz signals reached 700 pulses per second for 7 s to 1 min, with a maximum amplitude of 213 dB *re*: 1 μPa. We can describe a pulsed odontocete signal, $p(t)$, using the normalized waveform method of Au (1993) as

$$p(t) = \frac{A_{pp}}{2} s_N(t), \tag{1}$$

where A_{pp} is the peak-to-peak amplitude in μPa and s_N is the normalized waveform. The energy flux density of a single click will be

$$e = \frac{A_{pp}^2}{4\rho c}\int_0^T s_N(t)^2 dt = \frac{A_{pp}^2}{4} u \,.\, \frac{1}{\rho c}, \tag{2}$$

where u=the integral of the square of the normalized waveform and T is the duration of the waveform. The total energy flux density for N clicks will be simply

$$e_T = N\frac{A_{pp}^2}{4} u \,.\, \frac{1}{\rho c}. \tag{3}$$

In the extreme experimental condition of 700 clicks per second for 7 s to 1 min time period, we exposed fish subjects to over 8 to 70 [from Eq. (3)] times more acoustic energy than would an odontocete emitting terminal buzz signals with a peak-to-peak SPL of 213 dB (4.5×10^{10} μPa) at a rate of 200 clicks per second for 3 s (Madsen *et al.*, 2005). Even if we assume an odontocete emitting terminal buzz signals at twice the amplitude (9×10^{10} μPa) at the same repetition rate and duration, our extreme case would represent 2 to 17

TABLE III. Paired sample *t*-tests comparing pre- and postexposure time spent in each quadrant of the cage by each fish. All species were pooled in this analysis.

		95% Confidence interval of the difference				
Quadrant	Mean paired differences	Lower	Upper	*t*	*df*	*p*
A	−0.0034	−0.0118	0.0050	−0.80	170	0.43
B	−0.0060	−0.0127	0.0007	−1.78	170	0.08
C	0.0007	−0.0073	0.0087	0.17	170	0.86
D	0.0087	−0.0049	0.0223	1.27	170	0.21

times more acoustic energy. In most of our experimental conditions, the fish subjects were exposed to more acoustic energy than would be expected for animals in the wild based on the observations of wild odontocete foraging.

We tested these signals on multiple individuals of different sizes representing three species commonly consumed by odontocetes. These fish were selected based on their potential as prey species, their swimbladder morphology, and their availability in captivity. It has been proposed that acoustic signals can interact with the air-filled swimbladder to result in stunning. We chose a physoclistous, euphysoclistous, and physostomous fish species to be able to test for this effect, though no differences in response were exposed. We also tested any group effects by exposing groups of four individuals of a single species together. We did not observe any changes in coordination or coherence of individual fish within the groups.

If stunning does occur in the wild, its induction may require a stress other than or in addition to the acoustic signal. Perhaps additional sensory cues are required. For example, perhaps the fish are stressed or stunned by seeing a large predator or by the pressure wave created by the dolphins as they approach their prey. Another possible explanation is that the odontocete acoustic behavior that induces stunning is different than has been described by previous studies. For example, the "bang" sound reported by (Marten *et al.*, 2001). These relatively long, high-amplitude sounds were recorded in the wild and in the laboratory. However, their source, the phonation system or a body movement like a tail slap, is not known. Despite the use of signals near the maximum source levels recorded for odontocete clicks, we could not induce stunning or even disorientation in the fish tested. Our results do not support the hypothesis that odontocetes use their clicks alone to induce stunning in prey.

ACKNOWLEDGMENTS

We thank Sander van de Huel for assistance conducting the experiments. Jan van der Veen, Sea aquarium "het Arsenaal," The Netherlands, lent us most of the study animals, and Gerard Visser, Michaël Laterveer, and Peter van Putten (all of the Oceanium Department of Blijdorp Zoo), provided the herring and transported them to the study site. Gijs Rutjes (Coppens International) provided some of the sea bass. We thank Mardi Hastings for valuable discussions about this work and Brigitte Kastelein and the volunteers of SEAMARCO for logistical support. The facilities of the research station were made available thanks to Dick Vethaak (RIKZ), Roeland Allewijn (RIKZ), and Wanda Zevenboom (North Sea Directorate). This work was supported by the U.S. Office of Naval Research and the Netherlands Ministry for Agriculture, Nature, and Food Quality (DKW-program 418: North Sea and Coast. This project complied to the Dutch standards for animal experiments (Chris Pool, head of the Committee for Animal Experiments of RIKZ) and was conducted under University of Hawaii Animal Care Protocol 04-019. This is HIMB contribution 1234.

Au, W. W. L. (**1993**). *The Sonar of Dolphins* (Springer, New York).

Au, W. W. L., Ford, J. K. B., Horne, J. K., and Newman Allman, K. A. (**2004**). "Echolocation signals of free-ranging killer whales (*Orcinus orca*) and modeling of foraging for chinook salmon (*Oncorhynchus tshawytscha*)," J. Acoust. Soc. Am. **115**, 901–909.

Bel'kovich, V. M., and Yablokov, A. V. (1963). "Marine animals share experience with designers," Nauka Zhizn' **30**, 61–64.

Blaxter, J. H. S., Denton, E. J., and Gray, J. A. B. (**1979**). "The herring swimbladder as a gas reservoir for the acoustico-lateralis system," J. Mar. Biol. Assoc. U.K. **59**, 1–10.

Blaxter, J. H. S., Denton, E. J., and Gray, J. A. B. (**1981**). "The auditory bullae-swimbladder system in late stage herring larvae," J. Mar. Biol. Assoc. U.K. **61**, 315–326.

Chatain, B. (**1986**). "The swim bladder in *Dicentrarchus labrax and Sparus auratus*. 1. Morphological aspects of development," Aquaculture **53**, 303–311.

Cranford, T. (**1999**). "The sperm whale's nose: Sexual selection on a grand scale?" Marine Mammal Sci. **15**, 1133–1157.

Evans, W. W., and Powell, B. A. (**1967**). "Discrimination of different metallic plates by an echolocating delphinid," *in Animal Sonar Systems: Biology and Bionics*, edited by R. J. Busnel (Laboratoire de Physiologie Acoustique, Jouy-en-Josas, France), pp. 363–382.

Hastings, M. C. (**1995**). "Acoustic stunning of marine animals," J. Acoust. Soc. Am. **98**, 2940–2941.

Herberholz, J., and Schmitz, B. (**1999**). "Flow visualisation and high speed video analysis of water jets in the snapping shrimp (*Alpheus heterochaelis*)," J. Comp. Physiol., A **185**, 41–49.

Hubbs, C. L., and Rechnitzer, H. B. (**1952**). "Report on experiments designed to determine effects of underwater explosions on fish life," California Fish and Game Bulletin **38**, 333–366.

Mackay, R. S., and Pegg, J. (**1988**). "Debilitation of prey by intense sounds," Marine Mammal Sci. **4**, 356–359.

Madsen, P. T., Wahlberg, M., and Mohl, B. (**2002**). "Male sperm whale (*Physeter macrocephalus*) acoustics in a high-latitude habitat: Implications for echolocation and communication," Behav. Ecol. Sociobiol. **53**, 31–41.

Madsen, P. T., Johnson, M. P., Aguilar de Soto, N., Zimmer, W. M. X., and Tyack, P. L. (**2005**). "Biosonar performance of foraging beaked whales (*Mesoplodon densirostris*)," J. Exp. Biol. **208**, 181–194.

Mann, D. A., Hastings, M. C., and Popper, A. N. (**1998**). "Detection of ultrasonic tones and simulated dolphin echolocation clicks by a teleost fish, the American shad (*Alosa sapidissima*)," J. Acoust. Soc. Am. **104**, 562–568.

Mann, D. A., Lu, Z., and Popper, A. N. (**1997**). "A clupeid fish can detect ultrasound," Nature (London) **389**, 341.

Marten, K., Herzing, D. L., Poole, M., and Allman, K. N. (**2001**). "The acoustic predation hypothesis: Linking underwater observations and recording during odontocete predation and observing the effects of loud impulsive sounds on fish," Aquat. Mamm. **27**, 56–66.

Norris, K. S., and Mohl, B. (**1983**). "Can odontocetes debilitate prey with sound?" Am. Nat. **122**, 85–104.

Reynolds, J. E. III, and Rommel, S. A. (**1999**). *Biology of Marine Mammals* (Smithsonian Institution Press, Washington).

Sand, O., and Enger, P. S. (**1973**). Evidence for an auditory function of the swimbladder in the cod," J. Exp. Biol. **59**, 405–414.

Schmitz, B., Versluis, M., von der Heydt, A., and Lose, D. (**2000**). "A unique way of sound production in the snapping shrimp (*Alpheus heterochaelis*)," J. Acoust. Soc. Am. **108**, 2542.

Wilson, B., and Dill, L. M. (**2002**). "Pacific herring respond to simulated odontocete echolocation sounds," Can. J. Fish. Aquat. Sci. **59**, 542–553.

Zageski, M. (**1987**). "Some observations on the prey stunning hypothesis," Marine Mammal Sci. **3**, 275–279.